

**FIRE SUPPRESSION
SYSTEM PERFORMANCE
OF
ALTERNATIVE AGENTS
IN AIRCRAFT ENGINE
AND
DRY BAY
LABORATORY
SIMULATIONS**

SP 890: Vol. I

RICHARD G. GANN, EDITOR

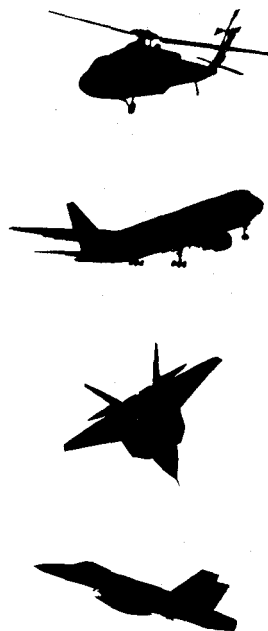
NIST

Certain commercial products are identified in this report in order to specify adequately the equipment used. Such identification does not imply recommendation by the National Institute of Standards and Technology, nor does it imply that this equipment is the best available for the purpose.

**Building and Fire Research Laboratory
National Institute of Standards
and Technology
Gaithersburg, MD 20899**

**U.S. Department of Commerce
Ronald H. Brown, Secretary
Technology Administration
Mary L. Good,
Under Secretary for Technology**

**National Institute of Standards
and Technology
Arati Prabhakar, Director**



November 1995

National Institute of Standards
and Technology

Special Publication 890, Vol. I

Natl. Inst. Stand. Technol.

Spec. Publ. 890, Vol. I

781 pages (Nov. 1995)

CODEN: NSPUE2

U.S. Government Printing Office
Washington: 1995

For sale by the Superintendent
of Documents

U.S. Government Printing Office
Washington, DC 20402

EXECUTIVE SUMMARY

Richard G. Gann
Building and Fire Research Laboratory

Halon 1301 (CF_3Br), one of the chemicals identified as detrimental to stratospheric ozone, had become the choice for suppressing in-flight fires in nearly all types of aircraft. Production of new halon 1301 was stopped on January 1, 1994, and efforts are underway to identify near-term replacements for critical applications, focussing on available or currently emerging chemicals and technologies. In particular, the three military services and the Federal Aviation Administration (FAA) have pooled resources to provide solutions for two applications: engine nacelles and dry (avionics) bays, while realizing that there are other aircraft areas also in need of protection. This project was managed at Wright Patterson Air Force Base (WPAFB), with oversight provided by a Technology Transition Team of the four sponsors.

The first major objective of the program was to identify the optimal available alternative fluid(s) for use in suppressing fires in aircraft engine nacelles and dry (avionics) bays. In October, 1993, based on extensive laboratory research and real-scale testing at WPAFB, the sponsors decided on a reduced list of candidates for each application; for engine nacelles: C_2HF_5 (HFC-125), C_3HF_7 (HFC-227ea), and CF_3I ; for dry bays: C_2HF_5 , C_3F_8 (FC-218), and CF_3I . Much of the laboratory-scale research leading to that decision has been described in NIST Special Publication 861, *Evaluation of Alternative In-Flight Fire Suppressants for Full-Scale Testing in Simulated Aircraft Engine Nacelles and Dry Bays*. That report documents the comprehensive experimental program to screen the performance of possible suppressant chemicals as a means to identify the best candidates for subsequent full-scale aircraft fire extinguishment evaluation at Wright Laboratory, and addresses the compatibility of these agents with flight systems, people, and the environment. In particular, apparatus and measurement methods suited to aircraft applications are carefully described, and extensive performance data are provided and analyzed. The reader is referred to that report as a prerequisite and companion to the current document.

The subsequent research described in this report falls into two broad categories:

Part 1: Knowledge to help differentiate among chemicals, leading to selection of the optimal currently available option(s) for in-flight fire suppression

Fire Suppression Efficiency. Most of the laboratory-scale information was reported in SP 861. In new studies in a deflagration/detonation tube, simulating fire suppression in a dry bay, FC-218 provided the best overall performance; HFC-125 was comparable under many conditions. CF_3I had the greatest positive impact at low addition levels, but showed non-monotonic behavior of flame speed and shock pressure at higher levels. In fire suppression efficiency measurements in a turbulent spray burner simulating engine nacelle fires, CF_3I was found to be more efficient than either HFC-125 or HFC-227ea. However, at an elevated temperature of 150 °C, the three chemicals performed equally on a mass basis.

Stability During Storage. There should be no problems with designing long-term storage capability for any of the four agents. The agents were tested for chemical stability in the presence of likely storage materials for over a year under typical in-use pressures and temperatures. The stability of HFC-125, HFC-227ea, and FC-218 was excellent. Samples of CF_3I were observed to be stable at 23 °C; however, during exposure at 100 °C and especially at 150 °C, small amounts of CO_2 and an unknown chemical appeared whose concentration increased with exposure time. Each of the four chemicals is compatible with a choice of materials for the storage containers: gasket materials, lubricants, and metals. Each agent caused only minor swelling in at least three of the elastomers and at most moderate swelling in the greases. The long-term deformation of the seven elastomers showed that at least two elastomers are compatible with each of the agents. The long-term stability of the seven elastomers, evaluated using compression set measurements, showed that at least two elastomers were not subject to excessive permanent deformation in each of the four agents. Long-term immersion of coupons of container metals at storage temperatures and pressure in each of the four candidate agents or halon 1301 produced little mass change or visual corrosion, although CF_3I showed some small interaction with three of the metals at high temperature. Slow strain rate tests of the metals in four of the agents at 20 °C and 150 °C and 5.86 MPa showed no difference from metal samples immersed in inert argon. CF_3I was not compatible with a titanium alloy at elevated temperature.

Safety Following Discharge. Predictions of the production of HF during fire suppression indicate that fires in dry bays are suppressed sufficiently quickly that only small amounts will be formed. For engine nacelle fires, the model developed here predicts that HFC-227ea, HFC-125 and FC-218 would produce similar amounts, while the more efficient CF_3I would produce far less. Exposure to surfaces heated by the fire would produce more HF from CF_3I than from an equal amount of the other three chemicals. Samples of aircraft materials that might be located near or downstream of an engine nacelle fire were immersed in 1 % or 10 % aqueous HF and then stored at 100 % relative humidity for 30 days at 22 °C. No significant degradation was seen. While accidentally-discharged CF_3I will decompose under both normal outdoor and indoor lighting, laboratory measurements and dispersion modeling show that the concentrations of potentially toxic photolysis products (HF, COF_2) are not likely to be sufficient to hinder prompt escape.

Discharge Performance. All four of the chemicals can be expected to discharge and disperse well from their storage and distribution systems at temperatures near 20 °C. At the lower temperatures experienced during high altitude flight or cold weather operation, CF_3I and HFC-227ea, with their higher boiling points, would not disperse as well as the other two chemicals.

Optimal Currently Available Option. Based on the results available in October, 1994, we recommended the selection of HFC-125 as the optimal candidate for Phase III examination for both engine nacelle and dry bay fire suppression. FC-218 possesses an extremely long environmental lifetime. While CF_3I was the most efficient suppressant, being virtually a drop-in replacement for halon 1301 in some tests, it had three drawbacks: its inhalation toxicity in cardiac sensitization testing, inconclusive stability and materials compatibility data, and a relatively high boiling point. HFC-227ea has a similar boiling point, and thus would also perform less well at low temperatures. The knowledge that has accrued in the final year of the project has not changed our perspective on this recommendation. During the fall 1994 meetings of the Technology Transition Team, these data and the results of an extensive and carefully constructed series of real-scale live-fire tests at Wright Patterson Air Force Base led the Team to recommend HFC-125 as the candidate for Phase III evaluation for both applications.

Part 2: Knowledge to assist in the development of engineering design criteria and suppressant system certification

Agent Discharge Behavior. The rate at which a suppressant will emerge from its storage container depends on the thermodynamic properties of the stored fluid and any pressurizing gas as well as the initial conditions in the container. Effective design of the suppression hardware requires quantitative performance measures for these chemicals. The NIST computer code PROFISSY accurately calculates binary vapor-liquid equilibria within the storage bottle, data needed by storage system designers. Laboratory data show that the nitrogen dissolved in the stored liquid agent significantly affects the agent discharge whether in a direct release system for dry bays or a piping system for engine nacelles. A NIST-developed storage bottle discharge model, which incorporates nitrogen degassing, generally predicts agent discharge times to within a factor of two, but occasionally a factor of four. The only required inputs for the model are the initial conditions in the vessel. For plumbed engine nacelle systems, a new, validated model can be used to facilitate calculations of transient, two-phase pipe flow. We have developed a flow chart to organize the use of these tools into a coherent process for optimal design of a new discharge system.

Engine Nacelle Fire Suppression Guidance. The selection of the mass of agent to be stored on an aircraft should be based on the amount needed to quench the worst realistic fire. For engine nacelles with ribs and other obstructions, this is a baffle-stabilized pool fire. Heating the air stream and, to a lesser extent, increasing the pressure, increases the mass of agent needed for flame extinction, while the fuel flow had no significant effect. A step-by-step procedure has been developed that gives guidance in determining fire suppressant concentrations and discharge times for flame extinguishment. It shows the relative importance of agent injection duration, air flow and velocity, agent/air mixing mode, and fire scenario. A reasonable target concentration for an agent in the fire zone is that needed to quench the most flammable fuel/air mixture, both ensuring flame suppression and preventing re-ignition during the period of injection.

Real-Time Concentration Measurement. Determination of the dispersion of the suppressant following discharge requires measurements of its concentration that are well-resolved in both time and space. We examined two instruments (based on thermal conductivity and infrared absorption) in order to assess their ability to perform *in situ* measurements with the ~1 ms time resolution needed for dry bay applications. Neither performed well. Both were improved extensively and showed potential. However, both need further work to be useful in practical systems. A review of the sensing literature shows a number of alternative approaches, but none that could be accurately adapted to this application without a significant development and testing effort. The most promising are time-resolved mass spectrometry and mid- and near-infrared absorption combined with fiber optics to provide easy access and the needed spatial resolution.

Certification Guidance. HFC-125 closely replicates the physical and dispersion properties of halon 1301. Thus it is an excellent simulant for hardware development and can be used to certify those engine nacelle fire suppression systems that still rely on halon 1301. The mixing time for agent entrainment behind an obstacle is different under non-fire conditions than for fire conditions. A method for using the non-fire data to approximate the fire suppression concentration has been developed.

Interaction with Metal Fires. In laboratory experiments, none of the four alternative chemicals nor halon 1301 showed exacerbation of burning of magnesium or titanium rods. It is not explicitly known

why the flare-ups observed during the introduction of halon 1301 to real metal fires were not observed here. However, it may be useful to know that in the circumstances replicated in the laboratory tests, the alternative agents did not worsen the combustion relative to that with halon 1301 present.

TABLE OF CONTENTS

Page

Executive Summary

<i>R.G. Gann</i>	iii
------------------------	-----

PART 1

1. Introduction <i>R.G. Gann</i>	1
2. Suppression of High Speed Flames and Quasi-detonations <i>G.W. Gmurczyk, W.L. Grosshandler</i>	9
3. Photodegradation of CF_3I <i>M.R. Nyden</i>	77
4. Effect of Suppressants on Metal Fires <i>T.J. Ohlemiller, J.R. Shields</i>	97
5. Compatibility with Metals <i>M.R. Stoudt, J.L. Fink, J.F. Dante, R.E. Ricker</i>	121
6. Interactions of Agents with Elastomers <i>G.B. McKenna, F. Horkay, P.H. Verdier, W.K. Waldron, Jr.</i>	201
7. Agent Stability Under Storage <i>R.H. Harris</i>	249

PART 2

8. Optimization of System Discharge <i>J.C. Yang, T.G. Cleary, I. Vázquez, C.I. Boyer, M.D. King, B.D. Breuel, C.A. Womeldorf, W.L. Grosshandler, M.L. Huber, L. Weber, G. Gmurczyk</i>	407
--	-----

(continued in Volume II)

1. INTRODUCTION

Richard G. Gann
Building and Fire Research Laboratory

Contents

Page

1. INTRODUCTION	1
1.1 Background	2
1.1.1 Stratospheric Ozone Depletion	2
1.1.2 Aircraft Fire Suppression	2
1.1.3 Prior Work	3
1.2 Objectives and Task Summary	3
1.3 Acknowledgments	4
1.4 References	5

1.1 Background

1.1.1 Stratospheric Ozone Depletion. In a remarkably short period of time, the world has identified, responded to, and ameliorated a new threat to the global climate (WMO, 1995). Following a mechanism first proposed by Rowland and Molina in 1974, chemically stable chlorine-, bromine-, and iodine-containing molecules rise to the stratosphere and are quantitatively photodissociated by ultraviolet radiation. The halogen atoms then catalytically convert ozone (O_3) molecules, whose chemistry shields the earth's surface from excess ultraviolet radiation, into oxygen (O_2) molecules, which have no such filtration effect. The evidence supporting this hypothesis soon became substantial, and the international political community produced a landmark agreement in 1987, the *Montreal Protocol on Substances That Deplete the Ozone Layer*. Subsequent international amendments to this and, domestically, the U.S. Clean Air Act of 1990 have led to restrictions on both production and use of identified ozone-depleting substances (ODSs).

Halon 1301 (CF_3Br) is one of the detrimental compounds identified in this process. It is used principally as a fire suppressant, and had become the choice for many applications where effective, efficient, and clean fire control is needed. Ideally, a typical year's production of halon 1301 would be loaded into fire suppression systems, where it would reside for many years until called upon to quench the infrequent fire. In practice, most of the chemical was released sooner, in training exercises, during system testing, from discharge of the suppression system when no fire was present, or from negligent handling. In the evolving regulatory process, future uses of halon 1301 were restricted, and its production was stopped on January 1, 1994 with limited allowances made for certain developing countries.

Many of the systems being protected by halon 1301 are essential to military readiness; and in 1991, the Deputy Director, Defense Research and Engineering in the Department of Defense initiated an urgent research program to identify near-term alternatives for weapons systems use, mostly by September 1996. This research focusses on commercially available or currently emerging chemicals and technologies.

1.1.2 Aircraft Fire Suppression. One of the most important uses of halon 1301 is the suppression of in-flight fires in nearly all types of aircraft. The three military services and the Federal Aviation Administration (FAA) have pooled resources to provide solutions for a number of problems as the aviation community reduces and eventually eliminates its reliance on halon 1301. The research and engineering projects have been carried out at laboratories of the Army, Navy, Air Force and FAA, and at the National Institute of Standards and Technology (NIST). The research program focussed on two applications: engine nacelles and dry (avionics) bays, while realizing that there are other aircraft areas also in need of protection.

The requirements for engine nacelle fire protection in commercial and military aircraft are similar. The interior of the nacelle is nominally tubular in shape, often with ribs and multiple other obstructions. Two types of fires are possible: spray fires, such as from a ruptured fuel line or hydraulic fluid line, and pool fires, resulting from either liquid settling on the bottom surface of the nacelle. Either fire type can be stabilized behind an obstruction, posing an additional difficulty for the fire suppressant. Currently, halon 1301 is stored in cylinders at pressures of ca. 2 MPa - 4 MPa. When a thermal sensor detects an abnormal, overheated condition, the flight of the airplane is leveled and the appropriate halon 1301 bottle is discharged. The part gas, part liquid agent flows through up to several meters of tubing to the engine nacelle. Once released, it rapidly fills the nacelle volume. The certification process requires that enough agent be available to maintain a minimum concentration (ca. 6 % by volume) throughout the nacelle for a minimum time interval (0.5 s) to ensure that the fire will

be extinguished and not re-ignite. Many systems have a duplicate bottle to be used as a back-up should the first shot be unsuccessful.

The dry bay fire is specific to military aircraft. These bays are cluttered compartments, typically 0.2 m^3 - 3 m^3 in volume, located along the wings and fuselage. An incident incendiary shell could penetrate both the bay wall and that of an adjacent fuel storage volume, leading to a deflagration and loss of the aircraft. Such fires must be quenched automatically within a few tens of milliseconds.

1.1.3 Prior Work. The first major objective of the four-agency program was to identify the optimal available alternative fluid(s) for use in suppressing fires in aircraft engine nacelles and dry (avionics) bays. This project was managed at Wright Patterson Air Force Base, with oversight provided by a Technology Transition Team of the four sponsors. In October, 1993, based on extensive laboratory research and real-scale testing at Wright-Patterson Air Force Base, the sponsors decided on a reduced list of candidates for each application:

Engine Nacelle	Dry Bay
C_2HF_5 (HFC-125, pentafluoroethane)	C_2HF_5 (HFC-125, pentafluoroethane)
C_3HF_7 (HFC-227ea, 1,1,1,2,3,3,3-heptafluoropropane)	C_3F_8 (FC-218, octafluoropropane)
CF_3I (trifluoroiodomethane)	CF_3I (trifluoroiodomethane)

Much of the laboratory-scale research leading to that decision was performed at NIST and has been described in *Evaluation of Alternative In-Flight Fire Suppressants for Full-Scale Testing in Simulated Aircraft Engine Nacelles and Dry Bays* (Grosshandler *et al.*, 1994). That report documents the comprehensive experimental program to screen the performance of possible suppressant chemicals as a means to identify the best candidates for subsequent full-scale aircraft fire extinguishment evaluation at Wright Laboratory, and addresses the compatibility of these agents with flight systems, people, and the environment. In particular, apparatus and measurement methods suited to aircraft applications are carefully described, and extensive performance data are provided and analyzed. The reader is referred to that report as a prerequisite and companion to the current document.

1.2 Objectives and Task Summary

The research described in this report has multiple origins, but falls into two broad categories:

Part 1: Knowledge to help differentiate among chemicals, leading to selection of the optimal currently available option(s) for in-flight fire suppression. These projects are described in Part 1. Section 2 of Part 1 (which follows this introduction) provides further data and explanation of previously identified phenomena regarding potential suppression of dry bay fires. Section 3 addresses the potential for degradation of photosensitive CF_3I following an accidental discharge. Research on the effectiveness of halon 1301 alternatives on metal fires is discussed in Section 4. Sections 5 and 6 continue to longer exposure times (from Grosshandler *et al.*, 1994) the measurements and analysis of the compatibility of the candidate agents with metals and organic materials that might be used in storage vessels. Section 7 similarly extends the prior study of the stability of the agents themselves during long-term storage.

Part 2: Knowledge to assist in the development of engineering design criteria and suppressant system certification. Section 8 develops understanding of and equations for calculating the dispersion of the agent from the storage bottle and subsequent plumbing. Section 9 provides guidance on the agent concentration requirements for flame suppression in engine nacelles. Section 10 develops a predictive capability for the formation of toxic and corrosive hydrogen fluoride (HF) during fire suppression. Section 11 reviews approaches to making the high-speed, real-time measurements of suppressant concentration needed both for research and certification, and describes our research on two of the approaches. Section 12 documents our search for and identification of a surrogate chemical for certification testing of aircraft fire suppression systems in which halon 1301 is still used.

Section 13 provides a summary of the results and puts them in the context of the fire suppression problems under consideration.

1.3 Acknowledgments

The work described in Sections 2 and 5-11 were co-sponsored by four agencies of the U.S. Government:

Wright Laboratory
Flight Dynamics Directorate
Vehicle Subsystems Division
Survivability Enhancement Branch
Mr. Michael Bennett
Lt. Gretchen Brockfeld
Lt. Gregg Caggianelli

Army Aviation and Troop Command
Mr. Michael Clauson

Naval Air Systems Command
Subsystems Branch
Fuel and Fluid Power Systems Section
Mr. James Homan

Department of Transportation
Federal Aviation Administration
Technical Center
Ms. Louise Speitel

The work in Sections 4 and 12 were sponsored by the Naval Air Systems Command, under the active guidance of Mr. David Thurston and Mr. William Leach, respectively. The work in Section 3 was performed under NIST internal funding.

The overall Program Manager was Mr. Michael Bennett of the Wright Laboratory. His energy and engineering perception were essential to the successful completion of the research reported here. Lt. Gregg Caggianelli and Lt. Brett Poole provided expert assistance in carrying out the full-scale instrumentation tests reported in Section 11.

Numerous staff from industrial firms provided advice, materials, and their time. They are credited in the individual sections.

Finally, full credit is due to Ms. Paula Garrett for her extensive efforts in bringing this manuscript to reality.

1.4 References

Grosshandler, W.L., Gann, R.G., and Pitts, W.M., Eds., *Evaluation of Alternative In-Flight Fire Suppressants for Full-Scale Testing in Simulated Aircraft Engine Nacelles and Dry Bays*, Special Publication 861, National Institute of Standards and Technology, Gaithersburg, MD, 1994.

Molina, M.J. and Rowland, F.S., "Stratospheric Sink for Chlorofluoromethanes: Chlorine Atom-Catalyzed Destruction of Ozone," *Nature* 249, 810 (1974).

Executive Summary, Scientific Assessment of Ozone Depletion: 1994, World Meteorological Organization, Geneva, 1995.

PART 1

AGENT SELECTION PROCESS

2. SUPPRESSION OF HIGH SPEED FLAMES AND QUASI-DETONATIONS

Grzegorz W. Gmurczyk
Science Applications International Corporation
and
William L. Grosshandler
Building and Fire Research Laboratory

Contents

Page

2. SUPPRESSION OF HIGH SPEED FLAMES AND QUASI-DETONATIONS	9
2.1 Background	10
2.2 Technical Approach and Task Summary	11
2.3 Experimental Set-up	12
2.3.1 Design	12
2.3.2 Operation	16
2.4 Experimental Results	16
2.4.1 Conditions	16
2.4.2 Measurement Signals	20
2.4.3 Combustion Characteristics	20
2.4.3.1 Ethene/Air Mixtures	23
2.4.3.2 Propane/Air Mixtures	26
2.4.4 Suppression Characteristics	26
2.4.4.1 C ₂ HF ₅ Performance	32
2.4.4.2 C ₃ F ₈ Performance	43
2.4.4.3 CF ₃ I Performance	52
2.4.4.4 Relative Performance of C ₂ HF ₅ , C ₃ F ₈ , and CF ₃ I	61
2.4.5 Uncertainty Analysis	61
2.5 Summary of Results	66
2.6 Conclusions	73
2.7 Acknowledgments	74
2.8 References	74

2.1 Background

A dry bay is a normally confined space adjacent to a fuel tank in which a combustible mixture and an ignition source could co-exist following penetration by an anti-aircraft projectile. They vary considerably in volume, typically being in the range of 0.2 to 3.0 m³. They are located in the wings and fuselage, and their shape is most often irregular. Aspect ratios up to 10:1 are not uncommon. The bays may or may not be ventilated, and are usually cluttered with electronic, hydraulic and mechanical components. Compared to the events leading to engine nacelle fire suppression, the required timing is two orders-of-magnitude faster for dry bay protection.

The previous study using a deflagration/detonation tube (Grosshandler *et al.*, 1994) was concerned with establishing a comprehensive experimental program to screen the performance of over a dozen agents. The experiments were designed to cover the range of conditions that might occur in a dry bay. Although actual measurements of fuel concentrations in a dry bay during live-fire testing have never been made, one could envision a worst-case situation in which the fuel is vaporized and partially premixed with the air just prior to ignition, producing a rapidly moving turbulent flame. If the suppressing agent were not well mixed and the dry bay geometry were conducive, the turbulent flame could accelerate, generating a shock wave ahead of it and transitioning to a detonation before encountering the agent. Ethene was chosen as the fuel in the previous study because it was known to detonate easier than many other hydrocarbons. This provided the most severe test for all the agents under conditions that were not duplicated in any of the other bench-scale studies.

Three chemicals were selected by the Technology Transition Team to be included in the complete full-scale experimental matrix conducted at Wright Patterson AFB (Carbaugh, 1993): HFC-125, FC-218 and CF₃I. Measurements in the previous detonation/deflagration tube study revealed a volume factor (VF) for FC-218 that was lower than the VF for HFC-125. More significant was the high over-pressure experienced for HFC-125 mass fractions below 25 %. With the deflagration/detonation tube operating with a lean ethene/air mixture, 21 % HFC-125 in the test section produced a quasi-detonation with a pressure ratio of 37:1, double the pressure build-up when no agent was present. The FC-218 behaved quite differently, and effectively reduced the pressure ratio at concentrations near 21 %. These results favored the selection of FC-218 over HFC-125 for dry bay protection.

Few flame suppression experiments had been conducted with CF₃I that were applicable to dry bays. The previous detonation/deflagration tube results indicated an unusual behavior that could also be observed with CF₃Br, but to a lesser extent. Both chemicals were equally effective in low concentrations at reducing the pressure build-up. At mass fractions greater than about 10 % the chemistry is altered and the pressures began to rise. Increasing the CF₃Br concentration benefitted suppression at mass fractions greater than 20 %, and total suppression of the flame occurred above 30 %. Pressure ratios in the CF₃I tests continued to rise up to a mass fraction of 30 %, reaching a pressure greater than the uninhibited mixture. That is, adding 30 % CF₃I to a lean ethene/air flame exacerbated the situation. It took a mass fraction of almost 45 % to completely suppress the pressure build-up.

The maximum pressure ratios observed in full-scale live-fire testing of uninhibited propane air mixtures are less than 7:1, and photographic evidence from full-scale dry bay testing suggests that turbulent flame speeds are below 300 m/s (Bennett, 1993). The previous experiments created uninhibited pressure ratios up to 25:1 and quasi-detonation velocities over 1100 m/s. By changing the fuel from ethene to propane, and by adjusting the geometry of the detonation/deflagration tube, the pressure ratio and velocity of the combustion wave can be reduced, allowing determination of whether or not a dangerous over-pressure arises during suppression under conditions that represent more likely threat scenarios.

The specific objectives of the current research project are the following:

- a. To determine the effectiveness of HFC-125, relative to FC-218, in suppressing high speed turbulent propane/air flames using the detonation/deflagration tube apparatus.
- b. To determine the conditions in the detonation/deflagration tube (equivalence ratio, tube geometry) which lead to excessive pressure build-up during suppression by HFC-125 of propane/air mixtures initially at room temperature and pressure.
- c. To determine the effectiveness of CF_3I , relative to FC-218, in suppressing high speed turbulent propane/air flames using the detonation/deflagration tube apparatus.
- d. To recommend a ranking of the three agents for full-scale dry bay applications based upon the current and previous suppression experiments.

2.2 Technical Approach and Task Summary

The detonation/deflagration tube is a unique apparatus for evaluating a fire suppressant in a highly dynamic situation. A shock wave precedes the flame, with obstructions in the flow, if any, promoting intense mixing of the fresh reactants with the combustion products and causing the pressure waves to interact with the mixing region. Given enough distance, the initially subsonic flame (deflagration) can accelerate dramatically, reaching the supersonic regime (detonation), and increasing the temperature of the reaction zone behind the shock as well as further adding to the heat release rate. Depending upon the geometric details, the wave can approach its theoretical Chapman-Jouguet velocity and accompanying high pressure ratio. Even a slight variation in composition of the reactants near the limit of detonation can cause a dramatic change in the wave velocity and cause destructive pressures to be attained.

Extensive literature exists describing the kinetics and dynamics of flame/shock wave systems formed within classical detonation tubes (e.g., Lefebvre *et al.*, 1992; Nettleton, 1987; Lee, 1984; Baker *et al.*, 1983; Westbrook, 1982). Chapman and Wheeler (1926) were the first to note that a methane/air flame could be accelerated to a terminal velocity in a shorter distance within a circular tube by placing obstacles into the flow. Lee *et al.* (1984) built on this observation to study quasi-detonations in hydrogen/air and hydrocarbon/air mixtures.

A quasi-detonation propagates more slowly than a true detonation due to pressure losses in the flow, but its structure is more complex than a true detonation, and the mechanism of its propagation is not fully understood. Although obstructed flow is more difficult to analyze than the flow in a smooth-walled tube, the complex obstructed arrangement has been investigated here because it more closely simulates a potentially damaging condition in the dry bay. The present construction of the detonation/deflagration tube facility is designed to compare both obstructed and unobstructed flow conditions.

Because the fire extinguishant is unlikely to be released prior to the establishment of a turbulent flame, the traditional experiment in which the flame inhibitor is premixed with the fuel and air prior to ignition does not replicate the chemistry critical to the actual situation. The NIST facility has been designed to provide a quiescent air/fuel/agent environment into which an uninhibited, fully turbulent flame propagates. The desire to rapidly suppress a flame and the associated pressure build up in such a situation is the primary objective behind this study. An ideal agent would quench the exothermic chemistry at low concentrations and prevent the further build-up of pressure waves; however, the

incident mechanical shock can only be reduced through viscous damping, and remains even when the chemistry has been satisfactorily interrupted. Shock/flame wave velocity and pressure ratio were the two dependent parameters that were measured as a means to characterize the extent of flame suppression. The velocity was determined by the time it took for the pressure wave to travel the distance between two pressure transducers. The pressure ratio was evaluated from the average amplitude of the first pressure pulse recorded by each transducer, normalized by the initial pressure.

A number of specific tasks were performed using the detonation/deflagration tube apparatus. First, experiments were conducted to determine the range of Mach numbers and pressure ratios obtainable in the tube using propane rather than ethene. The objective of this task was to produce in a predictable manner high speed turbulent flames (with Mach numbers between 1 and 2 and pressure ratios between 3 and 10) by manipulating the initial conditions in the tube. The variables at our disposal were the propane/air ratio, the fuel partial pressure, and the length of the tube and internal spiral. The conditions which led to repeatable subsonic flames were noted. Next, the pressure ratios and Mach numbers were measured in lean, stoichiometric and rich propane/air mixtures over a range of HFC-125, FC-218 and CF_3I mass fractions in the test section of the tube. The initial conditions were chosen to produce uninhibited Mach numbers below 2.0 and pressure ratios smaller than 10.

2.3 Experimental Set-up

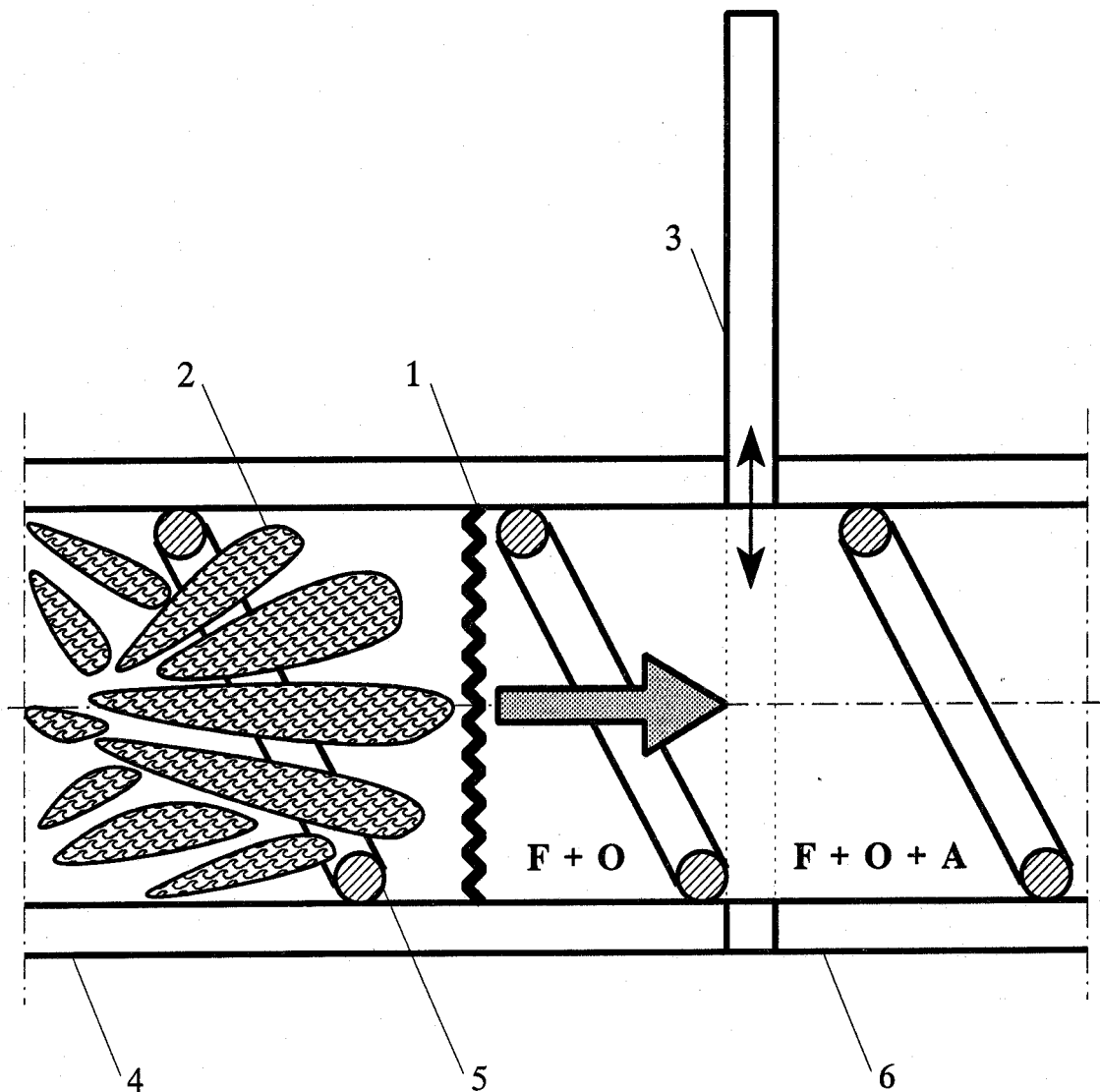
2.3.1 Design. The two-sectional detonation/deflagration tube was designed (Gmurczyk *et al.*, 1993, 1994) to examine the performance of the alternative agents in a highly dynamic situation, in which the pressure effects on the chemistry are thought to be important. Using the detonation/deflagration tube, the effectiveness of a fire fighting agent in suppressing a high speed, premixed flame or quasi-detonation can be rated by the extent to which it decelerates the propagating flame and simultaneously attenuates the hazardous shock which is always ahead of the flame.

A primary feature of the set-up is that the conditions of the ignition event do not affect the suppression process itself. Also, because an agent of interest is premixed with the fuel and air in a section of the tube separated from the ignition event, the influence of entrainment of the agent into the flame is minimized. The tube is closed to allow the increase in pressure to interact with the combustion chemistry.

The heart of the facility is shown schematically in Figure 1. The left hand side of the picture shows a fragment of the driver section (flame/shock generation region) of the tube separated by a partition from the test section (flame/shock suppression/attenuation region) of the tube on the right hand side of the picture. The flame/shock system propagating within a combustible mixture is fully established before entering the region occupied by a suppressant premixed with the same combustible mixture.

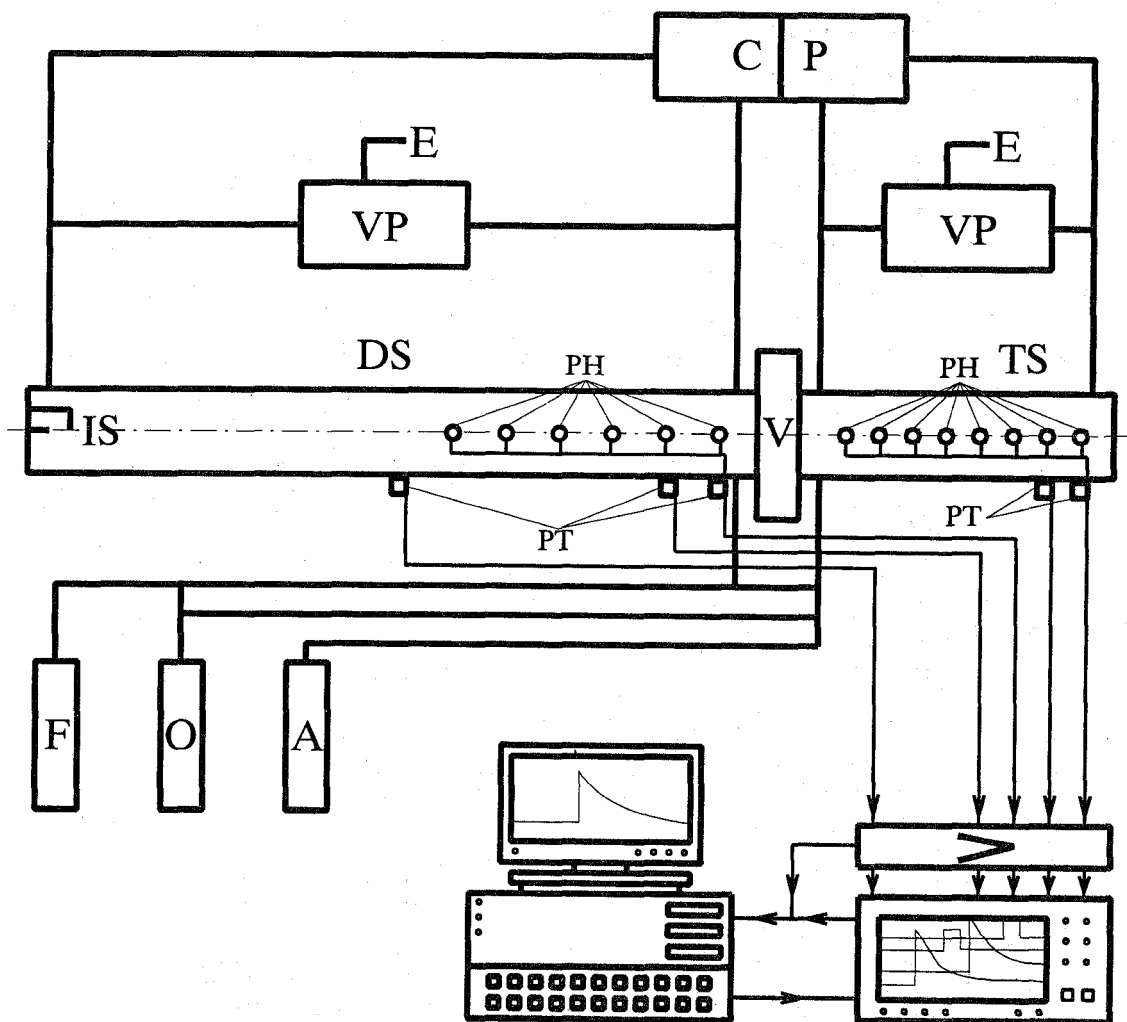
The driver section is 5 m long (see Figure 2) and is equipped at the closed end with a spark plug. This section is filled with the combustible mixture of ethene or propane and air of various compositions. The gas handling system (see Figure 3) consists of a vacuum pumping network; pressurized gas cylinders for the fuel, oxidizer and agent; and a dual circulating pump (Metal Bellows MB 602 XP).¹

¹ Certain trade names and company products are mentioned in the text or identified in an illustration in order to specify adequately the experimental procedure and equipment used. In no case does such identification imply recommendation or endorsement by the National Institute of Standards and Technology, nor does it imply that the products are necessarily the best available for the purpose.



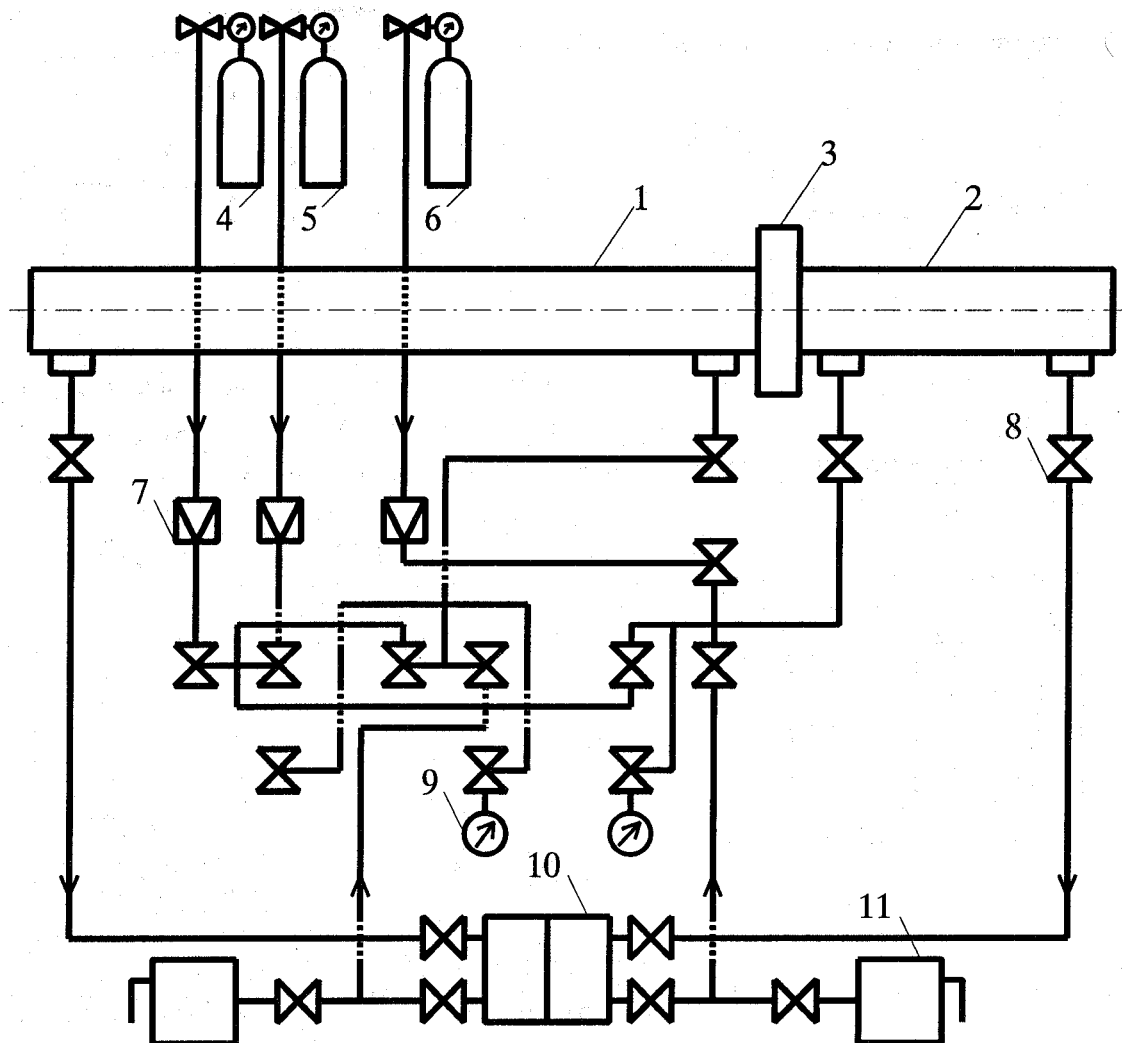
1 - SHOCK WAVE, 2 - TURBULENT FLAME, 3 - GATE VALVE,
4 - DRIVER SECTION, 5 - SPIRAL INSERT, 6 - TEST SECTION,
F - FUEL, O - OXIDIZER, A - AGENT

Figure 1. Schematic of the combustion/suppression process in the detonation/deflagration tube.



DS - DRIVER SECTION, TS - TEST SECTION, V - GATE VALVE,
 IS - IGNITION SYSTEM, CP - CIRCULATION PUMP,
 VP - VACUUM PUMP, E - EXHAUST, F - FUEL, O - OXIDIZER,
 A - AGENT, PH - FAST PHOTODIODE, PT - PIEZOELECTRIC
 PRESSURE TRANSDUCER, > - BLOCK OF AMPLIFIERS

Figure 2. Schematic of the detonation/deflagration tube facility designed and installed at NIST.



1 - DRIVER SECTION, 2 - TEST SECTION, 3 - GATE VALVE,
 4 - FUEL, 5 - OXIDIZER, 6 - AGENT, 7 - METERING VALVE,
 8 - ON-OFF VALVE, 9 - STATIC PRESSURE TRANSDUCER,
 10 - DUAL CIRCULATION PUMP, 11 - VACUUM PUMP

Figure 3. Schematic of the detonation/deflagration tube gas handling system.

The ignition energy is delivered in a micro-explosion of a tin droplet short-circuiting the tips of nichrome electrodes connected to an 80 V power supply. Spiral-shaped obstructions made of 6.4 mm stainless steel rods with a pitch equal to the inner diameter of the tube are inserted into the tube, to produce an area blockage ratio of 44 %, close to the value which is known to promote a high-speed or quasi-detonation regime of combustion.

The second section of the detonation/deflagration tube contained the gaseous agent along with the same fuel/air mixture used in the driver section. The diameter is the same and its length is either 2.5 m or 5.0 m. The flame and shock signals serving to determine velocities and pressures were taken 2.2 m downstream behind the gate valve when the 2.5 m long test section of the tube was installed. The 5 m test section was used without the spiral insert. The additional length was used to eliminate the reflected shock wave that sometimes interfered with a slower moving primary reaction front. The flame signals serving to determine velocities in the long tube were taken close to the entrance region of the test section, 0.3 m downstream behind the gate valve, to better ascertain the immediate impact of the inhibitors on the flame dynamics; the shock signals were measured 2.2 m into the test section, which is the same location used for the short tube.

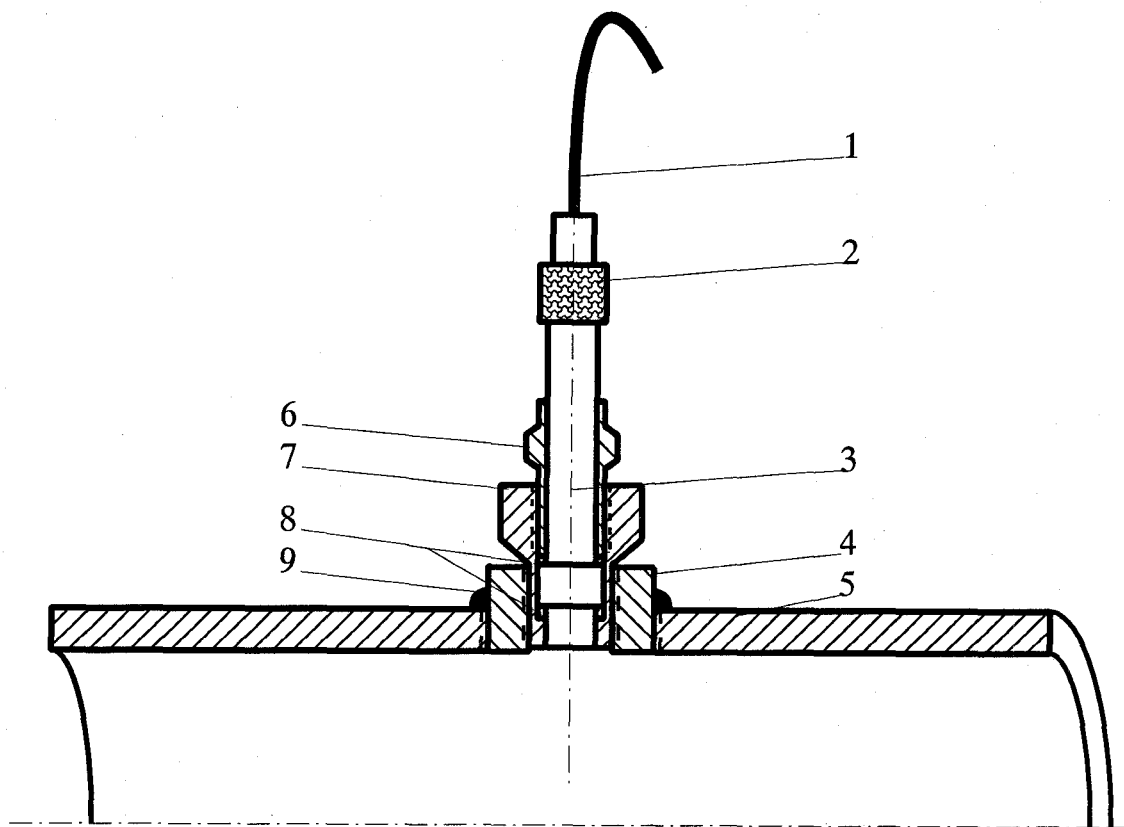
The driver and test sections are separated from each other by a 50 mm inner diameter, stainless steel, gate valve (MDC model GV-2000M-SP), which remains closed until just before ignition. Kistler model 603B1 dynamic piezoelectric pressure transducers (with dual mode charge amplifiers model 5010A10) and Siemens model BPX 65 silicon planar PIN high speed photodiodes are located along the test section to monitor the strength and speed of the combustion wave. Refer to Figures 4, 5, and 6. Their output was recorded either with a 50 MHz IBM Personal Computer with 32 bit EISA data acquisition board or with a fast, multi-channel, digital storage oscilloscope (Le Croy model 9314 M). In the latter case the data were also stored in the computer, since full communication was possible.

2.3.2 Operation. The whole system is evacuated to 10^{-1} Pa before filling the two sections separately with the desired mixtures, which are attained through the method of static partial pressures measured with Omega PX811 high accuracy absolute pressure gauges. The fuel/air ratio and total pressures are held constant across the gate valve. After filling, the gases are homogenized independently using a double, spark-free circulating pump, recirculating the entire tube volume a total of 20 times. The mixtures are then left for five minutes to become quiescent. About 10 s prior to ignition, the gate valve is opened manually. After ignition, the flame propagates into the driver section and accelerates quickly due to the intense turbulence created by the interactions of the flow with the obstacles. This generates a shock wave ahead of the flame. After passing through the open gate valve the flame/shock system encounters the same combustible mixture and a certain amount of agent in the test section. Depending on the concentration of the agent, the flame may be extinguished (or enhanced) and the pressure wave may be attenuated (or amplified).

2.4 Experimental Results

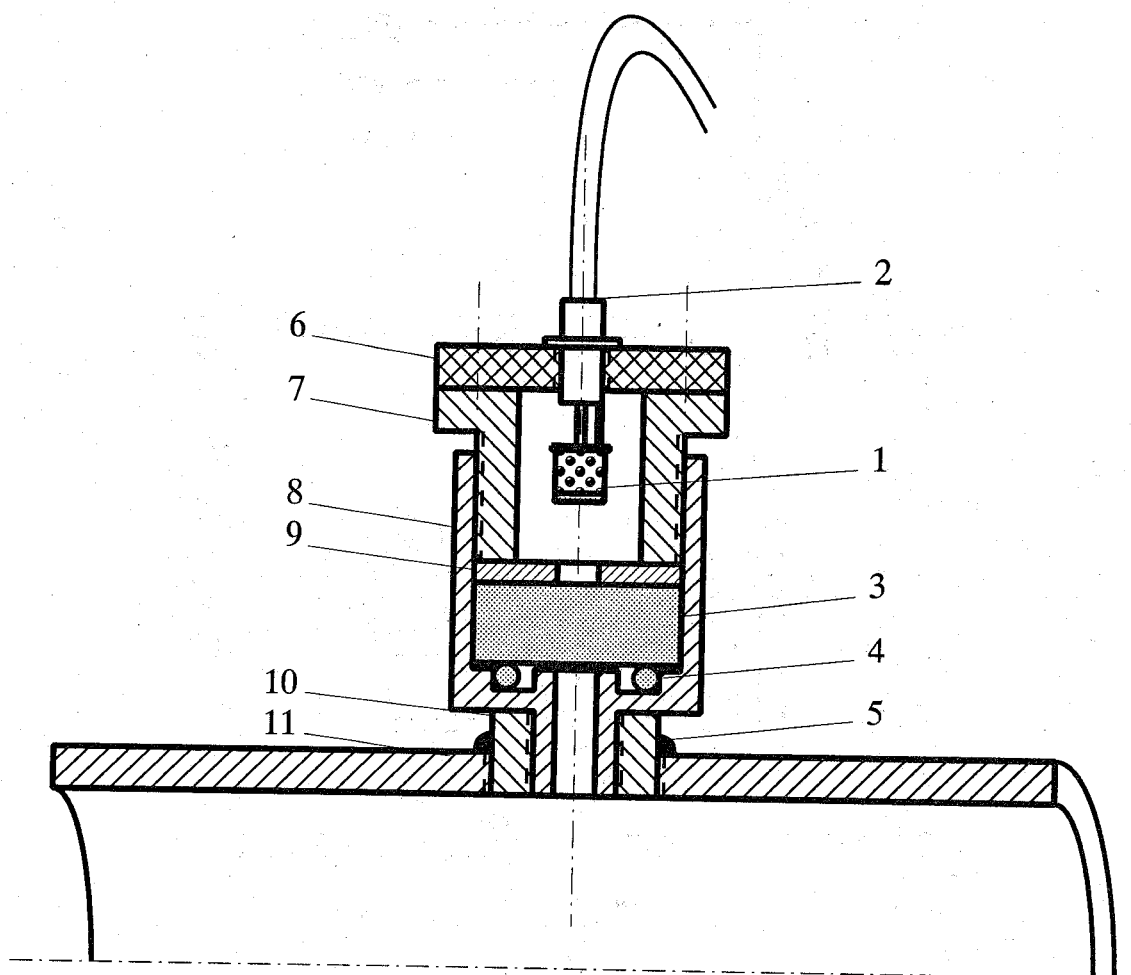
2.4.1 Conditions. The following independent parameters were changed during the course of the experiments:

- type of suppressant (C_2HF_5 , C_3F_8 , and CF_3I);
- concentration of suppressant;



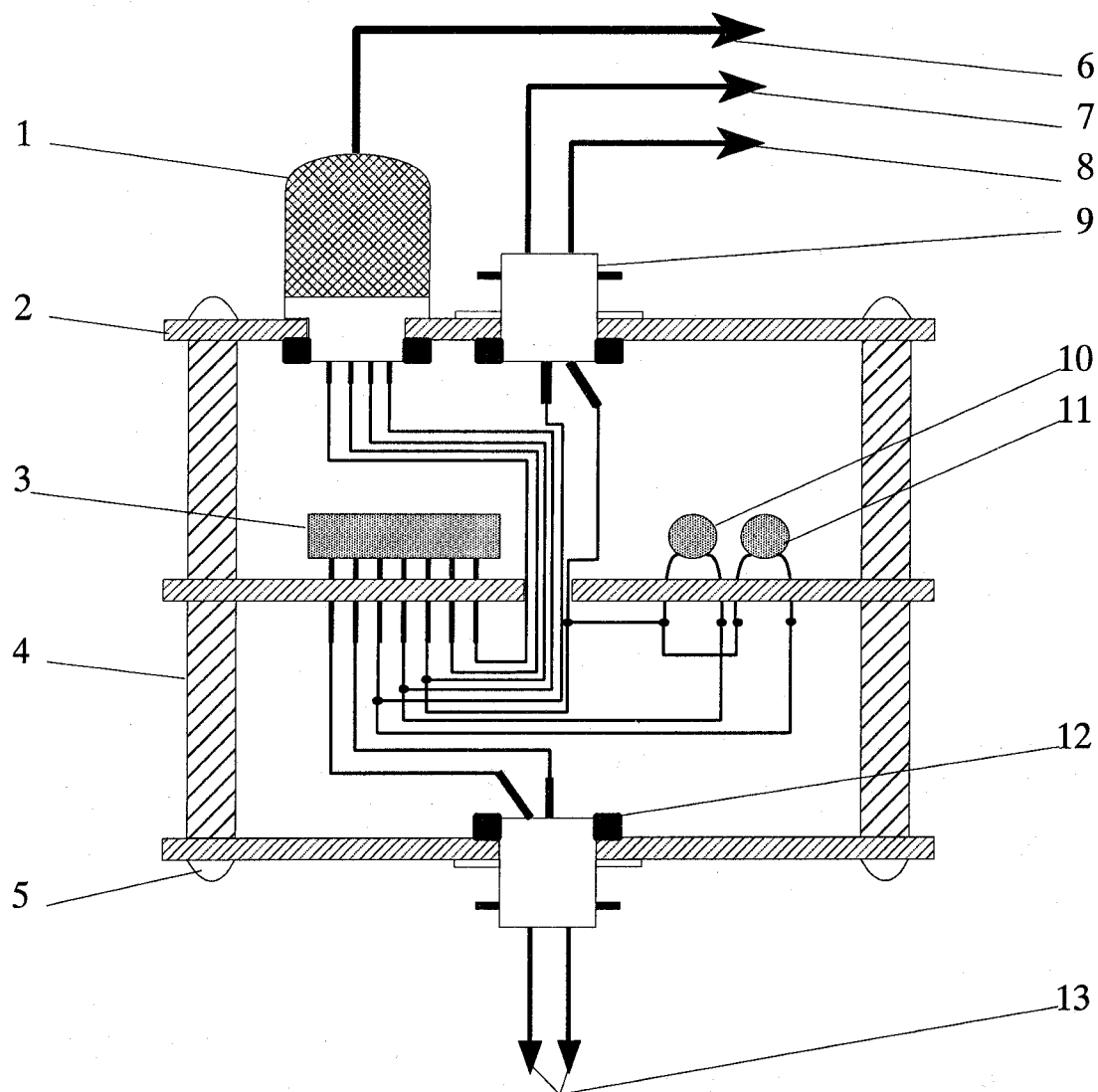
1 - LOW-NOISE CABLE, 2 - CABLE CONNECTOR, 3 - PIEZO-ELECTRIC PRESSURE TRANSDUCER, 4 - STUB, 5 - TUBE, 6 - RETAINING NUT, 7 - HOLDER, 8 - SEALS, 9 - SEAL WELD

Figure 4. Schematic of the piezoelectric dynamic pressure transducer mounting.



1 - PHOTODIODE, 2 - BNC CABLE, 3 - QUARTZ WINDOW,
4 - "O" RING, 5 - SEAL WELD, 6 - COVER, 7 - BUSH, 8 - CASE
9 - WASHER, 10 - STUB, 11 - TUBE

Figure 5. Schematic of the fast photodiode mounting.



1 - DIN CONNECTOR, 2 - CIRCUIT BOARD, 3 - OPERATIONAL AMPLIFIER, 4 - STANDOFF, 5 - SCREW, 6 - TO POWER SUPPLY, 7 - SIGNAL OUTPUT, 8 - GROUND, 9 - BNC CONNECTOR, 10, 11 - CAPACITORS, 12 - NUT, 13 - TO PHOTODIODE

Figure 6. Schematic of the fast photodiode amplifier.

- type of fuel (ethene or propane);
- equivalence ratio of the combustible mixture (lean, stoichiometric, rich)
- geometry of the tube (2.5 m or 5 m long test section, with or without spiral).

The initial temperature of the mixtures was ambient ($22\text{ }^{\circ}\text{C} \pm 3\text{ }^{\circ}\text{C}$) and the initial pressure was $100 \pm 0.6\text{ kPa}$. The oxidizer used in all experiments was breathing grade air. Ethene and propane (CP grade 99.5 % volume purity) were chosen as the fuels; ethene because it is known that detonations can be obtained in a tube of this geometry simply by varying the stoichiometry, and propane because it more closely resembles a jet fuel and can reproduce turbulent flames with pressure ratios under 10:1 and wave speeds down to sonic conditions. The extinguishing compounds were used as supplied by the manufacturers.

The partial pressure measurements were affected by the uncertainty of the static pressure transducer ($\pm 0.3\text{ kPa}$ maximum uncertainty after combining non-linearity, hysteresis, repeatability, and temperature effects), the uncertainty of the digital display device ($\pm 0.015\text{ kPa}$), the uncertainty associated with the purity of the gases ($\pm 0.5\text{ %}$ of partial pressure reading), and the uncertainty associated with possible gas losses in the circulation pump (up to 0.3 % of the partial pressure reading, in the worst case). Assuming that the errors were directly additive, the partial pressure for any component in the mixture was uncertain to less than 0.32 kPa plus 0.3 % of the reading.

2.4.2 Measurement Signals. Figure 7 shows representative signals coming from two fast photodiodes which indicate the presence of radiation (peak response at 850 nm) associated with the reaction front traveling in the tube. Figure 8 displays signals from two piezoelectric pressure transducers which represent a pressure jump associated with the shock wave ahead of the primary reaction zone. The time difference between the occurrence of the signals allows one to determine flame and shock velocities. The amplitude of the pressure signals permits determination of the pressure ratio of the shock.

The uncertainty of the determination of the shock wave amplitude was affected by the combined uncertainty of the dynamic pressure transducer ($\pm 1\text{ %}$ of the reading), the combined uncertainty of the transducer amplifiers ($\pm 0.5\text{ %}$ of the reading), the combined uncertainty of the digital data acquisition system ($\pm 0.5\text{ %}$), and the combined uncertainty of the digital readout device ($\pm 0.2\text{ %}$). Assuming additivity of errors, the resultant accuracy of determining the shock wave amplitude is $\pm 2.2\text{ %}$. The uncertainty of the determination of the shock time differences was affected by the same elements, as well as the transducer rise time ($< 2\text{ }\mu\text{s}$). The shock speed can thereby be estimated to be uncertain to less than $\pm 4.4\text{ %}$ of the reported reading (accounting for the differential nature of this measurement). The uncertainty of the determination of the flame travel time was affected primarily by the rise time of the photodiode, which is 30 ns . The combined uncertainty of the magnitude of the photodiode signal is estimated to be $\pm 2\text{ %}$ of the range.

2.4.3 Combustion Characteristics. The combustion generated in the driver section creates a shock wave followed by a chemically reacting region. The dependent parameters that were used to characterize the combustion within the test section of the tube are the pressure rise across the shock, the speed of the shock, and the speed of the chemically reacting radiation front. A secondary reaction was sometimes observed following the reflection of the incident shock wave from the end wall. The incident (or forward-travelling) shock wave speed and pressure ratio were determined from the

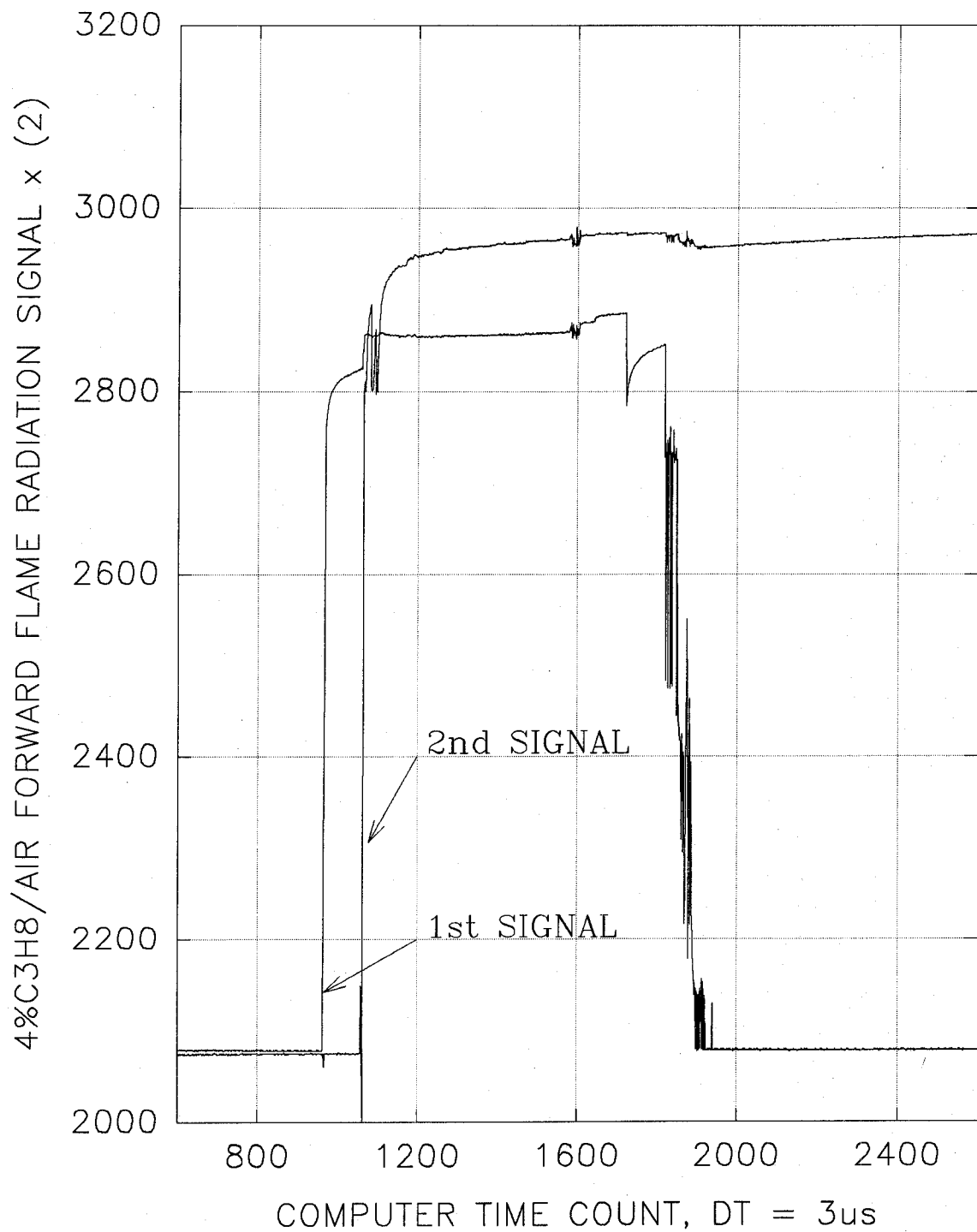


Figure 7. Typical measurement signals representing flame radiation detected by the photodiodes.

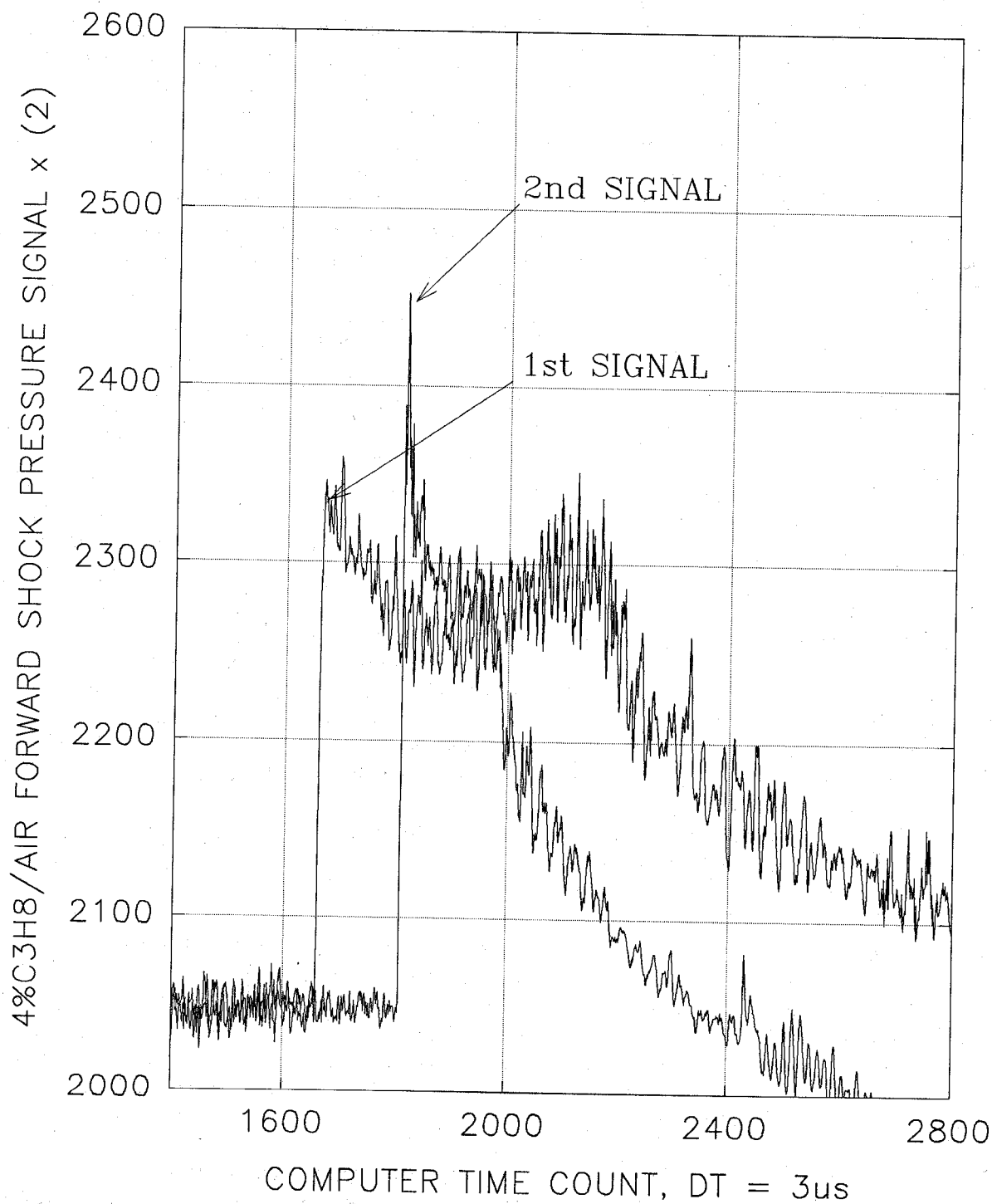


Figure 8. Typical measurement signals representing shock pressure detected by the dynamic pressure transducers.

piezoelectric transducer signals, and the time between activation of the photodiodes was used to calculate the forward-travelling radiation (or flame) front.

The repeatability of the measurements was affected by the following factors: preparation of the mixtures; circulation/homogenization of the mixtures; opening of the gate valve; the ignition parameters; formation/propagation of the flame/shock; vibrations of the spiral insert; and ambient temperature changes (ambient air pressure and humidity changes did not affect the results as air was supplied from a gas cylinder). Because each of these factors has an indeterminate randomness associated with it, a single test condition was repeated eleven times to quantify the precision of the experiment: a lean mixture of propane and air, with no suppressant, and the 10 m long tube with no spiral in the test section. More than twenty replicates would have been required to produce a meaningful standard deviation as specified by Taylor and Kuyatt (1994); thus, in the present study the maximum, rather than standard, deviation is used to indicate the precision of the inferred results. The mean of the eleven tests and maximum absolute deviations are as follows: flame speed, $334 \text{ m/s} \pm 38 \text{ m/s}$; shock speed, $681 \text{ m/s} \pm 25 \text{ m/s}$; and shock pressure ratio, 8.16 ± 0.38 .

2.4.3.1 Ethene/Air Mixtures. Figure 9 shows the dependence of the forward shock wave velocity versus equivalence ratio of the ethene/air mixture for the cases with and without the spiral insert in the 2.5 m test section. The equivalence ratio was changed to cover the full range of various combustion/flammability modes detectable by the installed apparatus. The shock wave generated by an accelerating flame is detectable for equivalence ratios between 0.5 and 2.12 for the two geometric configurations. The maximum shock velocity of nearly 2000 m/s was recorded for a rich mixture with the spiral absent. Except for the extreme lean and rich cases, with shock velocities less than 500 m/s, the flame was intimate with the shock.

Figure 10 displays the respective forward shock pressure ratios in the ethene/air mixture versus equivalence ratio for the two geometric configurations. Interestingly, the maximum pressure ratio of 35 was recorded for the situation with the spiral, which indicates clearly that transverse shock reflections from the wall play an important role in the whole process. However, in general, the shape of the pressure ratio curves corresponds well with the shape of the velocity curves.

There are four modes of combustion observed in the detonation/deflagration facility:

- a. Low-speed deflagration: generates a weak pressure wave in which the flame front is uncoupled. A typical pressure wave velocity is 400 m/s and pressure ratio is 1.5 for the two geometric configurations.
- b. High-speed deflagration: generates a strong pressure wave that is coupled with the flame front, the velocity of the flame is the same as the velocity of the pressure wave, and the shock-flame distance is on the order of centimeters. A typical velocity is 800 m/s and pressure ratio is 16 for the lean mixtures, and 1400 m/s and 20 for the rich mixtures, respectively, when the spiral insert is in the tube. When the spiral is not present in the tube the respective parameters are as follows: 700 m/s and 7 for the lean mixtures, and 600 m/s and 3 for the rich mixtures.
- c. Quasi-detonation: associated with the occurrence of high velocities and pressure ratios. The flame front is coupled with the pressure wave, the velocity of the flame is the same as the velocity of the pressure wave, and the shock-flame distance is on the order of millimeters. Typical velocities are 1200 m/s to 1500 m/s and pressure ratios are 20 to 35 over broad lean and rich ranges for the situation with the spiral insert in place. When the spiral is not present the transition from the high-speed deflagration mode to a detonation is gradual. The velocities

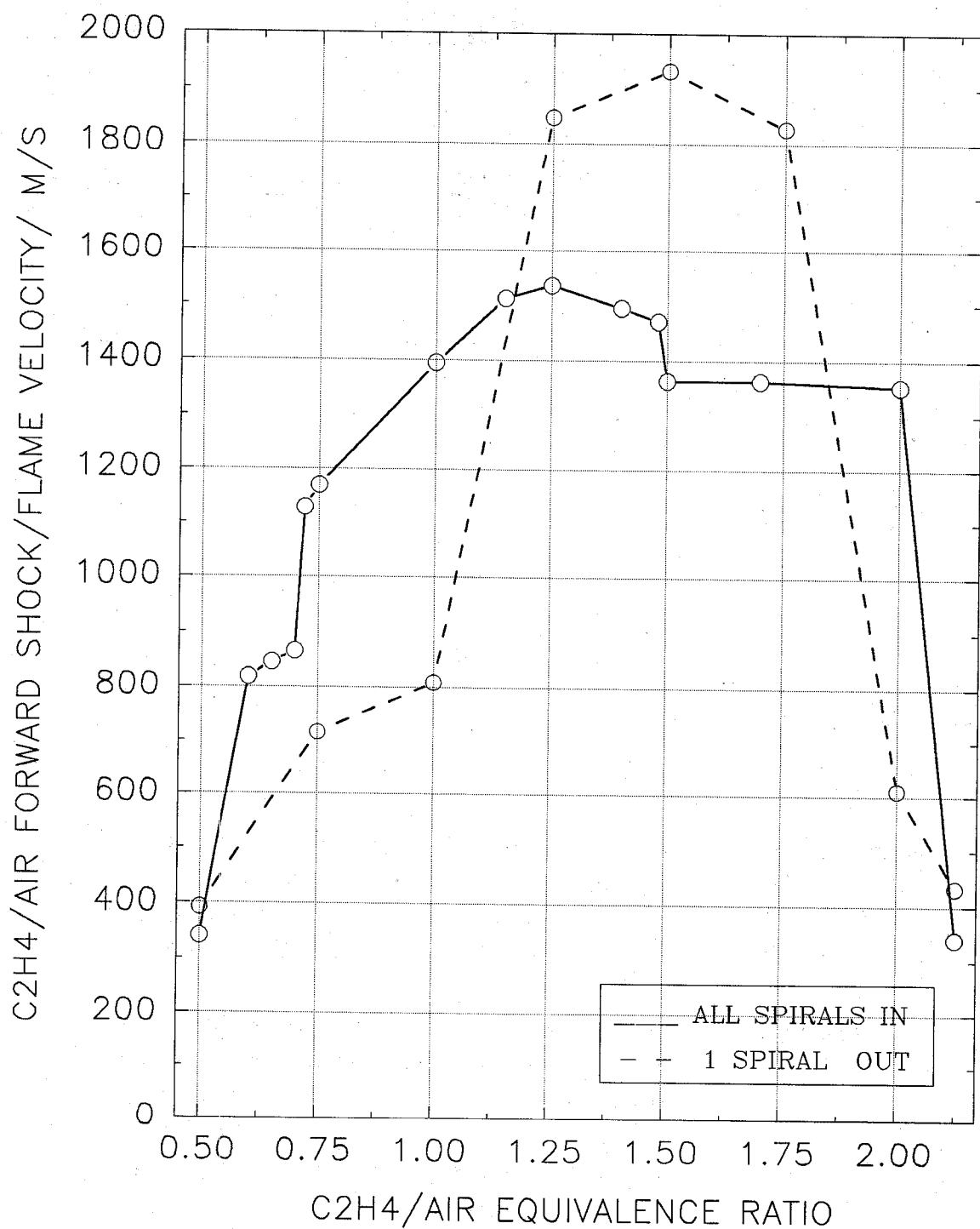


Figure 9. Combustion modes in the ethene/air mixtures - shock/flame velocities (2.5 m test section).

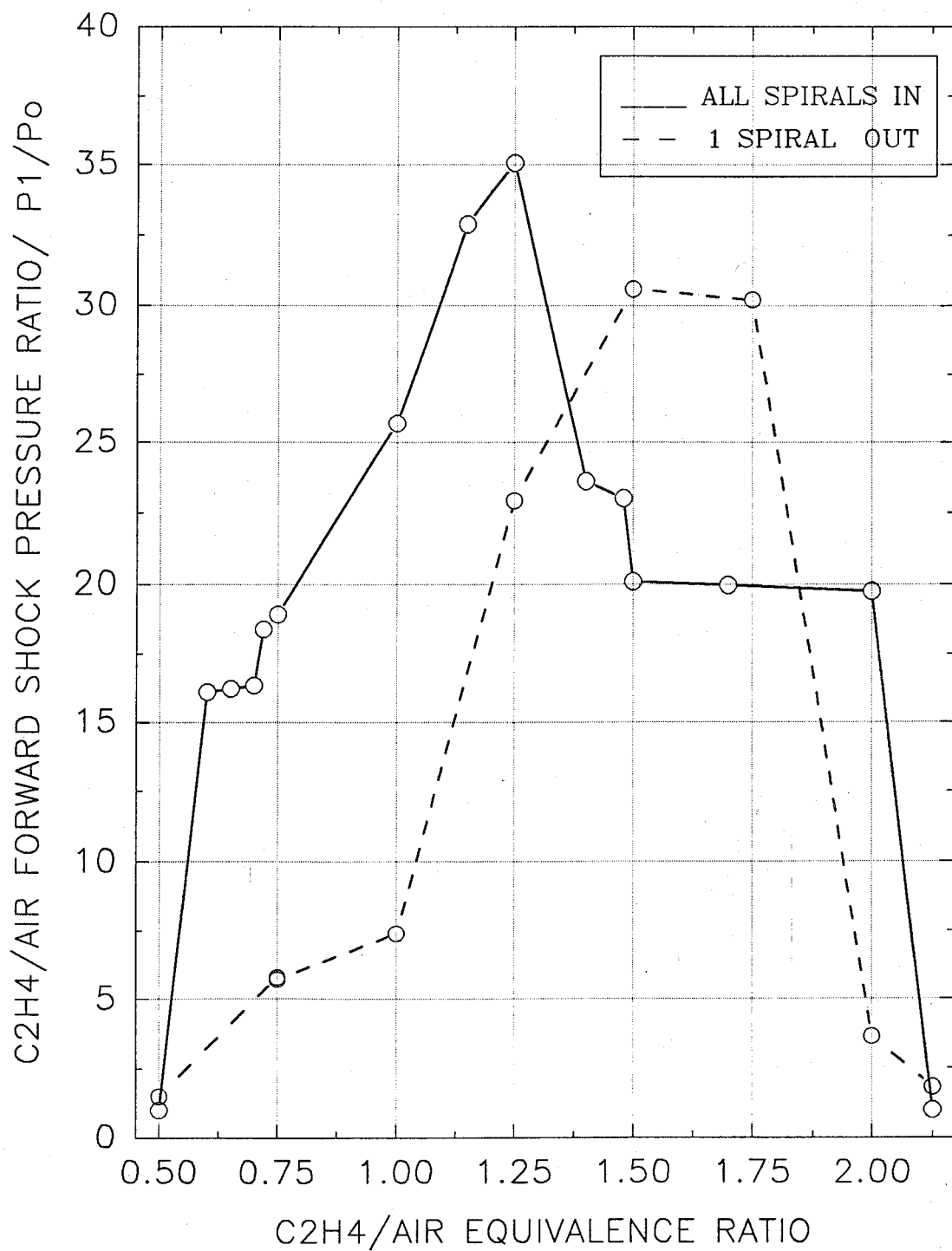


Figure 10. Combustion modes in the ethene/air mixtures - shock pressure ratios (2.5 m test section).

and pressure ratios are significantly lower. This mode occurs on the rich side of the ethene/air mixture.

- d. Chapman-Jouguet detonation: occurs only in the rich ethene/air mixture without the spiral insert. The flame front is coupled with the pressure wave, the velocity of the flame is the same as the velocity of the pressure wave, and the shock-flame distance is undetectable. A typical velocity is 1900 m/s and pressure ratio is 30. The velocity corresponds to the theoretical equilibrium thermodynamic estimates; however, the pressure ratios are 1/3 higher, which may indicate the occurrence of an over-driven detonation mode.

2.4.3.2 Propane/Air Mixtures. Uninhibited propane/air mixtures were evaluated in the 2.5 m test section as well, with and without the spiral insert in the test section. Figure 11 shows the dependence of the forward shock wave velocity on equivalence ratio. The shock wave generated by the accelerating flame was detectable for equivalence ratios between 0.65 and 1.45, both with the spiral present and absent. The maximum shock velocity of about 1300 m/s was recorded for the stoichiometric case with the spiral in place, much less than was found in the ethene/air mixture. The flame velocity was the same as the shock velocity for wave speeds above 800 m/s. This means that the propane generated reaction front can be more easily decoupled from the shock wave than in the ethene/air mixture. Figure 12 displays the respective forward shock pressure ratios in the propane/air mixture versus equivalence ratio. Here the maximum pressure ratio of 27 corresponds to the maximum velocity for the situation with the spiral. In general, the shape of the pressure ratio curves corresponds closely to the shape of the velocity curves.

Three of the four combustion modes observed with the ethene/air experiments were identified when propane was the fuel: low-speed deflagration, high-speed deflagration, and quasi-detonation. The Chapman-Jouguet condition was not observed, and when the spiral was not present in the test section, the quasi-detonation regime of combustion disappeared. There are other differences between the two fuels, as well. The combustion modes at higher velocities overlap totally in the ethene/air mixture for the cases with and without the spiral, while the propane/air mixture is characterized by a clear separation between the combustion modes for the two arrangements. Also, the regime of equivalence ratios for which combustion is detectable in the tube is much broader for the ethene/air mixture. Furthermore, the detonation process is unable to develop in the propane/air mixture when the spiral insert is missing from the tube. However, it is noteworthy that for the first time a quasi-detonation in a propane/air mixture has been recorded in the presence of the spiral obstacle. This finding extends the results of Lee (1984) and Peraldi *et al.* (1986).

2.4.4 Suppression Characteristics. The performance of the three extinguishing compounds (C_2HF_5 , C_3F_8 , and CF_3I) are analyzed by comparing the velocity and pressure ratio suppression characteristics in the lean, stoichiometric, and rich ethene/air and propane/air mixtures, with and without the presence of obstacles in the test section. (Note: the spiral inserts are always present in the driver section.) Pure nitrogen was placed in the test section as a benchmark to compare its performance to the above alternatives. The fully nitrogen-suppressed pressure ratios, shock speeds and combustion wave speeds are compared to the totally uninhibited fuel/air mixtures in Table 1.

In the ethene/air mixtures, as one might expect, the flame velocity is zero when the test section is filled with N_2 , but only under lean and stoichiometric conditions. In the rich mixture the velocity is slightly higher than zero. This means that the residual flame from the driver section of the tube enters the suppression section, since the flame velocity was measured just behind the gate valve separating the two sections of the tube. The respective forward shock velocities decrease because of

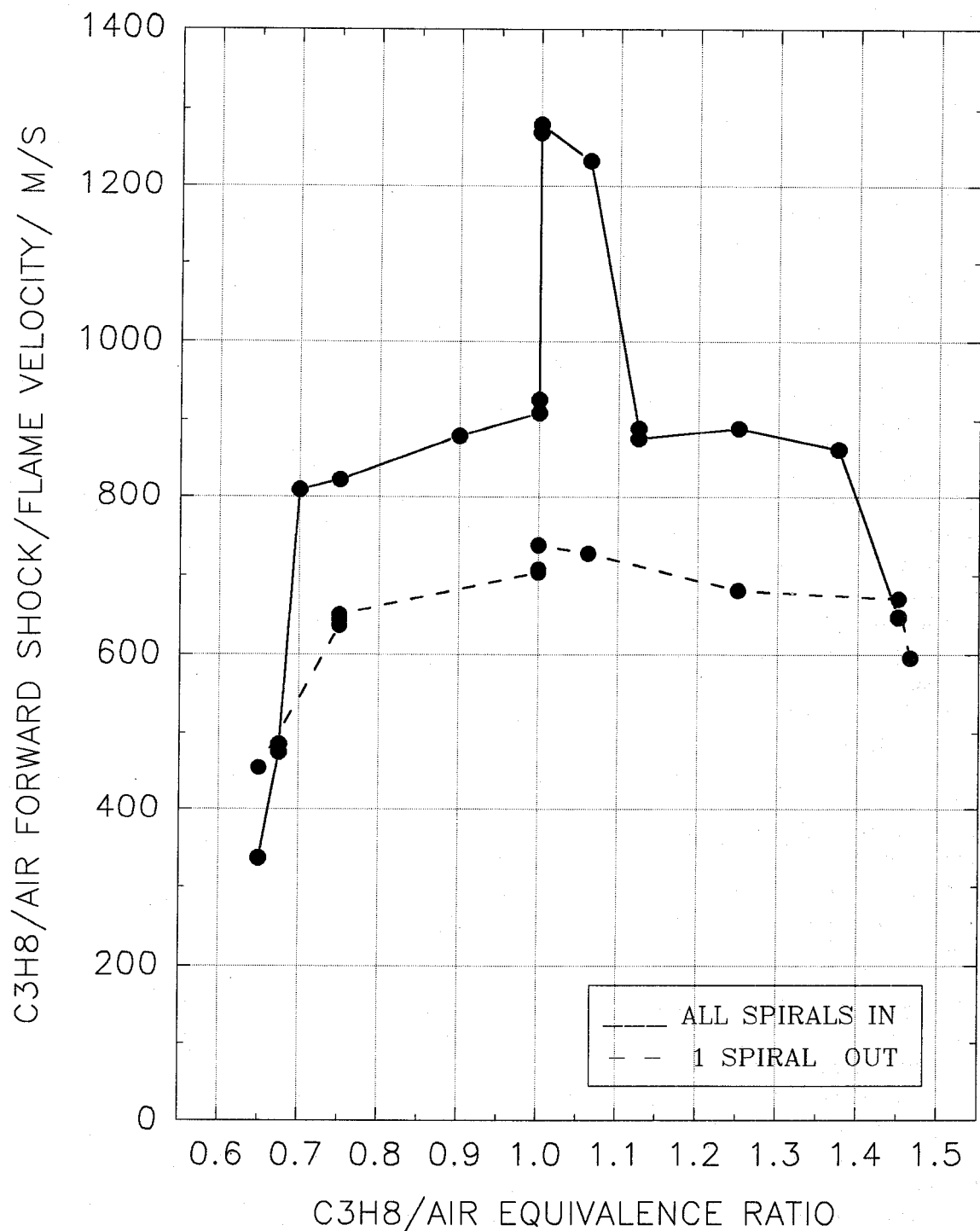


Figure 11. Combustion modes in the propane/air mixtures - shock/flame velocities (2.5 m test section).

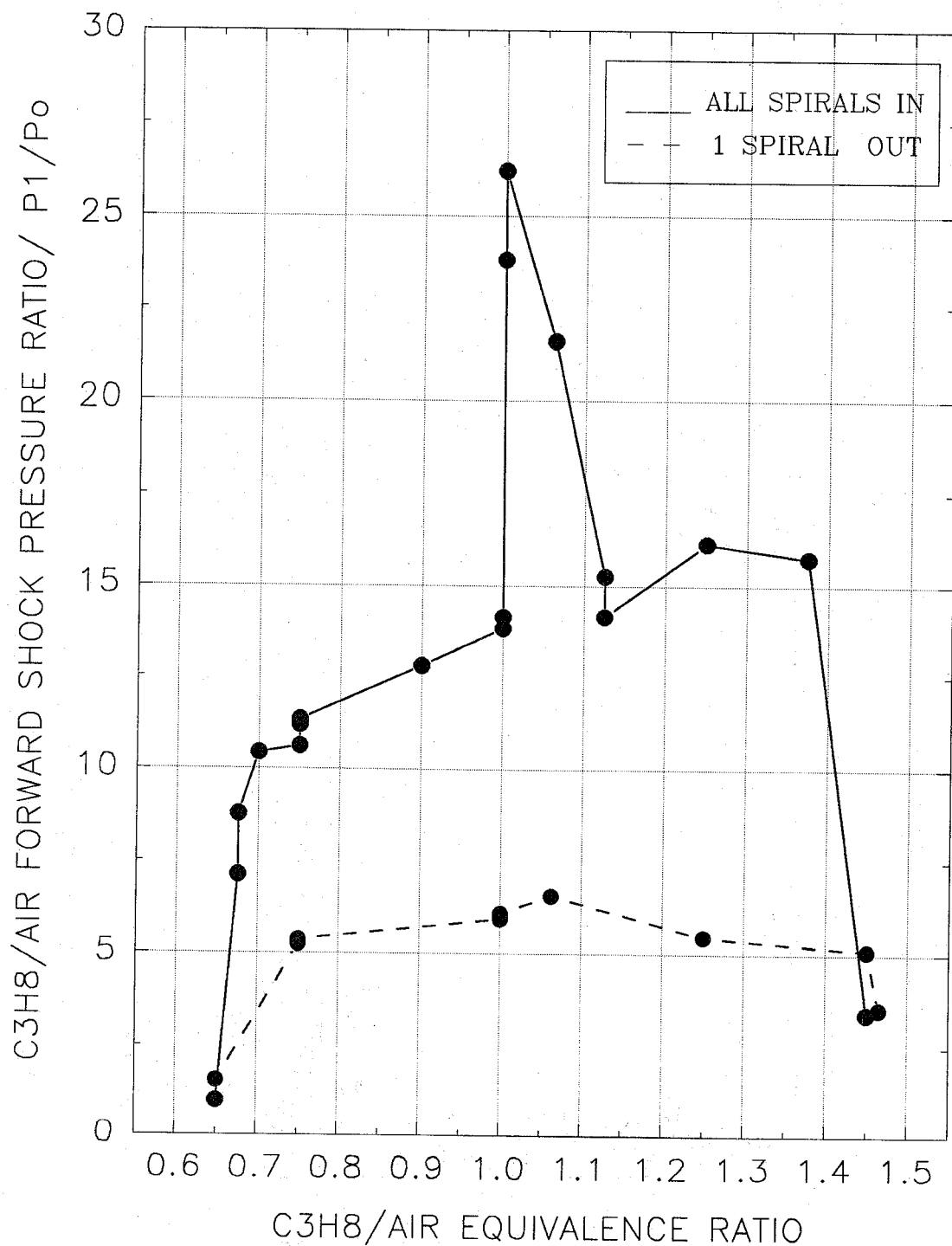


Figure 12. Combustion modes in the propane/air mixtures - shock pressure ratios (2.5 m test section).

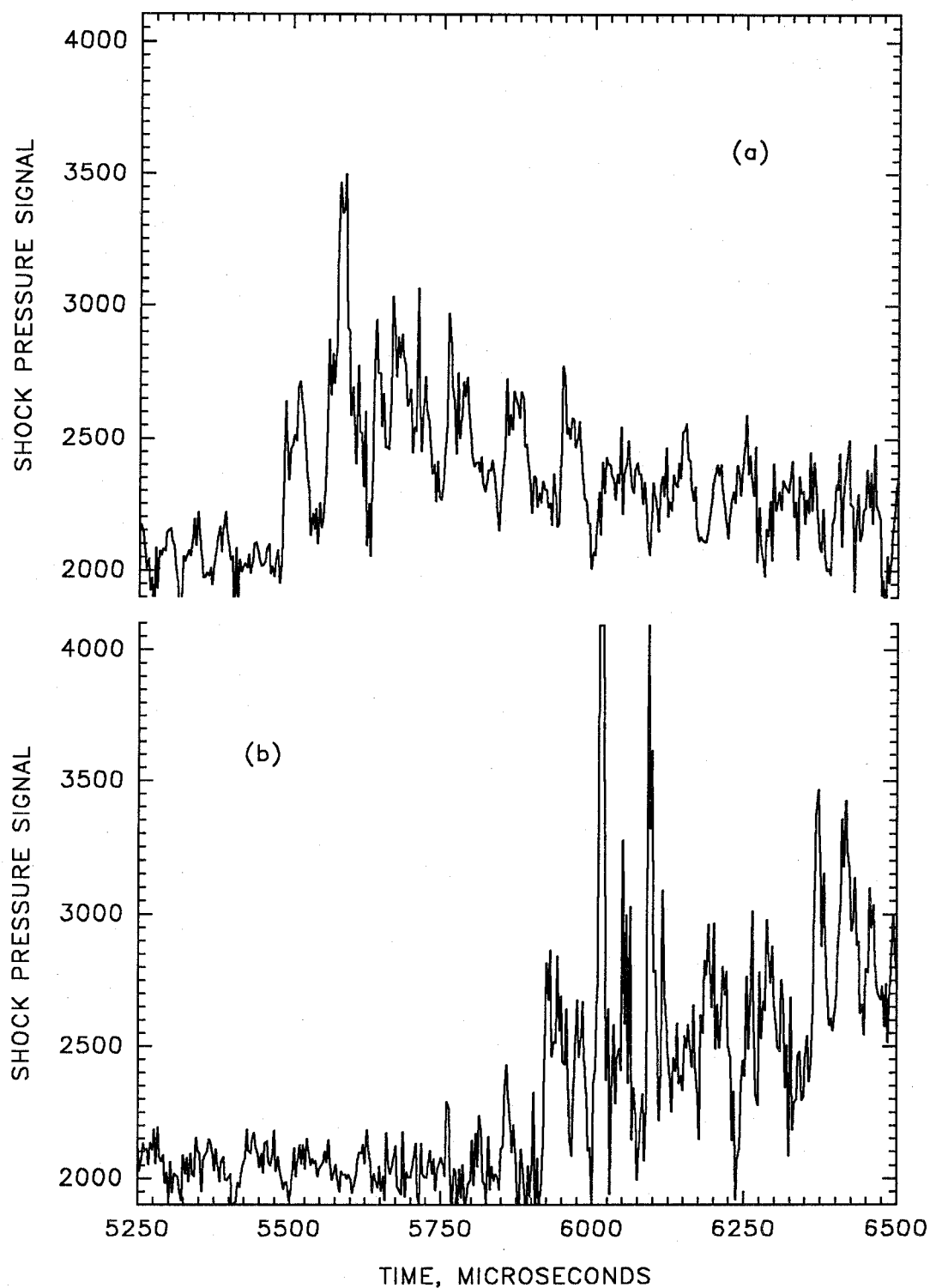


Figure 13. Pressure traces taken in CF_3I -inhibited C_3H_8 /air mixture (a) 2.04 m into test section, and (b) 2.37 m into test section.

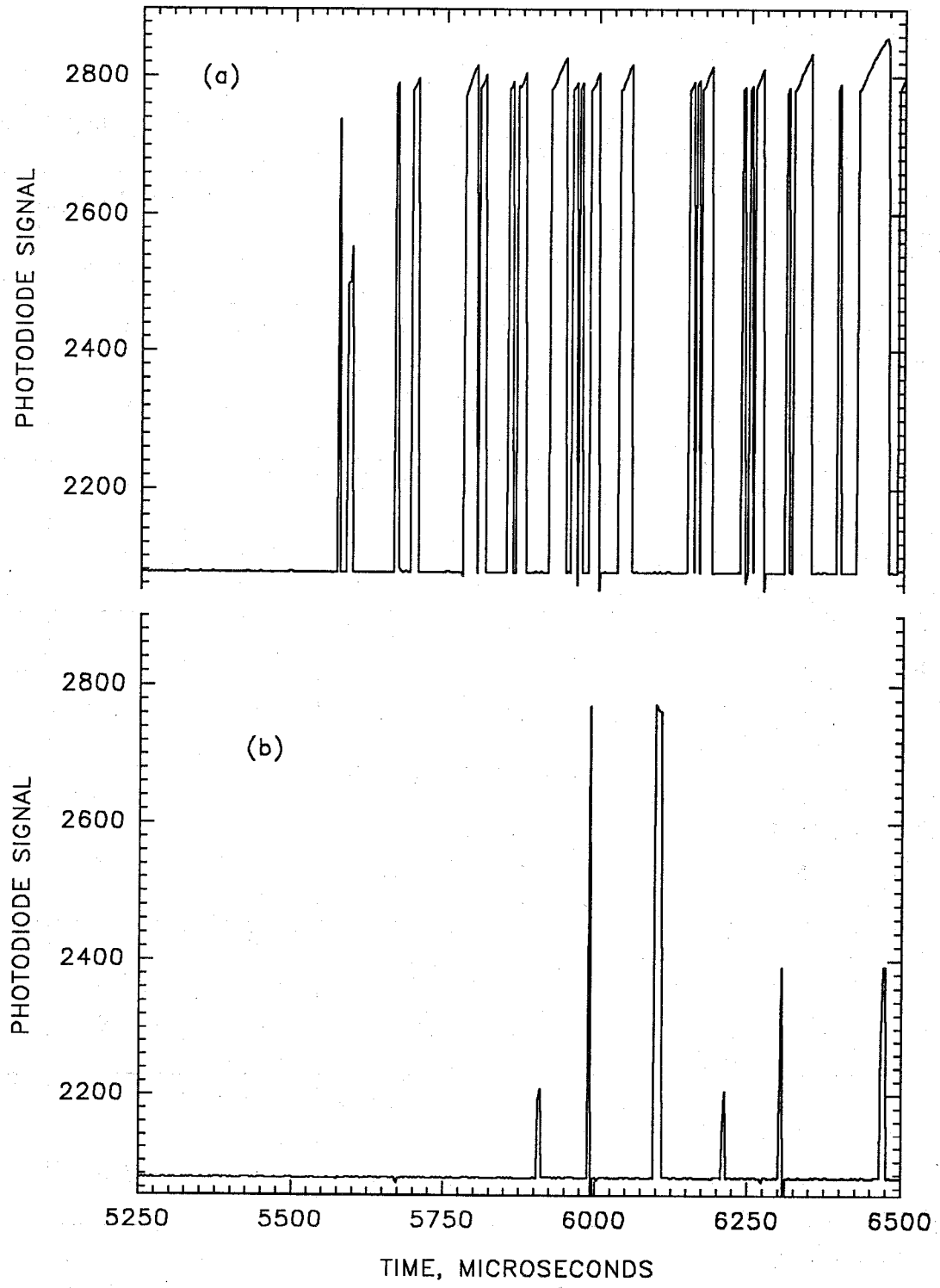


Figure 14. Photodiode signals from CF_3I -inhibited $\text{C}_3\text{H}_8/\text{air}$ mixture, taken (a) 2.04 m into test section, and (b) 2.37 m into test section.

Table 1. Pressure ratios, shock speeds and combustion wave speeds comparing fully suppressed (100% N₂) to totally unsuppressed (0% N₂) test conditions

Fuel Mixture	Test Section	0% Nitrogen			100% Nitrogen		
		P ₁ /P ₀	V _{shock} (m/s)	V _{comb} (m/s)	P ₁ /P ₀	V _{shock} (m/s)	V _{comb} (m/s)
C ₂ H ₄ , Φ=0.75	2.5 m (spiral)	18	1170	1170	2.5	440	0
	5.0 m (no spiral)	6.2	710	600	4.1	600	0
C ₂ H ₄ , Φ=1.00	2.5 m (spiral)	26	1400	1400	3.5	450	0
	5.0 m (no spiral)	6.5	720	720	4.7	660	0
C ₂ H ₄ , Φ=1.25	2.5 m (spiral)	35	1530	1530	*	*	*
	5.0 m (no spiral)	11	940	930	5.0	730	20
C ₃ H ₈ , Φ=0.86	2.5 m (spiral)	11	815	815	*	*	*
	5.0 m (no spiral)	8.1	690	330	4.5	575	103
C ₃ H ₈ , Φ=1.00	2.5 m (spiral)	13.5	900	900	*	*	*
	5.0 m (no spiral)	8.8	695	620	4.7	619	105
C ₃ H ₈ , Φ=1.25	2.5 m (spiral)	16	890	890	*	*	*
	5.0 m (no spiral)	8.3	690	510	4.5	586	45

* no data available

the disappearance of the energy supplied by exothermic chemical reactions, and the forward shock pressure ratios drop most significantly when the spiral is present.

In the propane/air mixtures, in every case the flame velocity is higher than zero, which means that 100 % nitrogen cannot fully extinguish the flame in the propane/air mixtures within a short distance. When compared to the flame propagating in the ethene/air mixtures, the initial velocity in nitrogen is lower but it is more stable on contact with an inert environment. The respective forward shock velocities in the propane/air mixtures are approximately proportional to the initial shock velocities established in the driver section of the tube. The respective forward shock pressure ratios at the three equivalence ratios correspond well to the relative behavior of the shock velocities.

The interaction of the combustion wave with the inhibited fuel/air mixture is a dynamic process which does not reach a steady state within the test section. Figure 13 shows two pressure traces taken 0.33 m apart in a CF_3I inhibited propane/air mixture. The photodiode measurements taken at the same two locations are shown in Figure 14. The initial and peak pressures can be seen to increase with the distance that the wave travels, indicating that the CF_3I is promoting the development of the shock wave. The flame radiation, on the other hand, diminishes as the combustion wave travels from the 2.04 m to 2.37 m position. The on-off behavior of the photodiodes also suggests that the combustion zone is thick and highly nonuniform in intensity.

The suppression data presented in this section have been measured at two different locations, depending upon the configuration. The pressure transducers and photodiodes were mounted 2.04 m and 2.37 m beyond the gate valve in the 2.5 m test section (with the spiral); in the 5.0 m test section (without spiral) the photodiodes were moved to locations 0.21 m and 0.38 m after the gate valve, while the pressure transducers remained at the 2.04 m and 2.37 m locations.

2.4.4.1 C_2HF_5 Performance. The primary motivation for conducting more research in the detonation/deflagration tube is shown in Figure 15. The data for the lean C_2H_4 /air mixture in the 2.5 m test section containing the spiral insert was collected in the earlier NIST study (Grosshandler *et al.*, 1994). The shock pressure ratio reaches a maximum of 37:1 for a 6 % mixture of C_2HF_5 . This is more than double the pressure increase had no suppressant been added, clearly an untenable situation were it to occur in a dry bay.

The tube geometry and fuel were altered to reduce the severity of the initial conditions to determine the impact on the combustion dynamics. The data points indicated by triangles in Figure 15 were taken with no spiral insert in the 5.0 m long test section. The initial shock pressure ratio is reduced by a factor of 3, and remains below 9:1 out to a partial pressure fraction of 10 %. The sensitivity of the $\text{C}_2\text{HF}_5/\text{C}_2\text{H}_4$ /air mixture to small perturbations in the detonation/deflagration tube became apparent when the 6 % experiment was repeated and resulted in a detonation. Except for that one case, removing the spiral greatly reduced the severity of the combustion wave.

Removing the spiral has a similar effect on the shock/combustion wave speed, plotted in Figure 16. The combustion process is completely extinguished when the C_2HF_5 partial pressure reaches 10 %, as compared to about 15 % when the spiral is present in the test section.

Ethene is known to be highly reactive (which is one reason it was selected for the previous study), but it is less representative of a vaporized jet fuel than propane. The original experiments were repeated with C_3H_8 instead of C_2H_4 , and these are also plotted (filled circles) in Figures 15 and 16. The C_3H_8 mixture produces significantly lower pressure ratios, never exceeding 15:1 when the spiral is present. The initial shock/combustion wave speed is cut in half by the change in fuel, and the flame radiation is fully extinguished at partial pressure fractions about 4 % lower.

The equivalence ratio of the C_2H_4 /air mixture was varied from lean to rich in the obstructed tube. The pressure increase across the shock wave is plotted in Figure 17 as a function of the partial pressure fraction of C_2HF_5 added to the test section. When the equivalence ratio is increased to $\Phi=1.0$

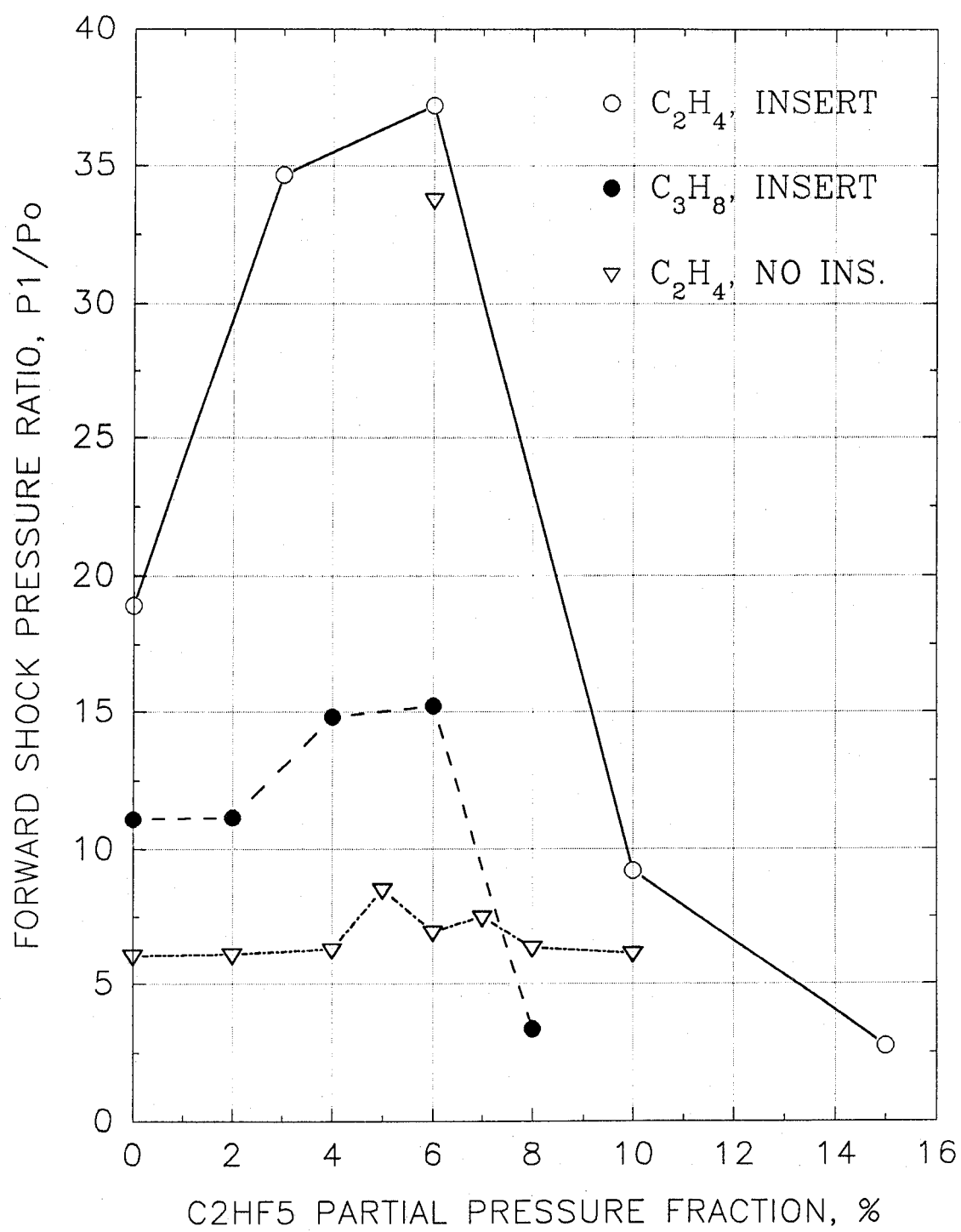


Figure 15. Shock pressure ratio in lean, C_2HF_5 -inhibited hydrocarbon/air mixtures, showing impact of spiral insert and fuel-type on suppression process.

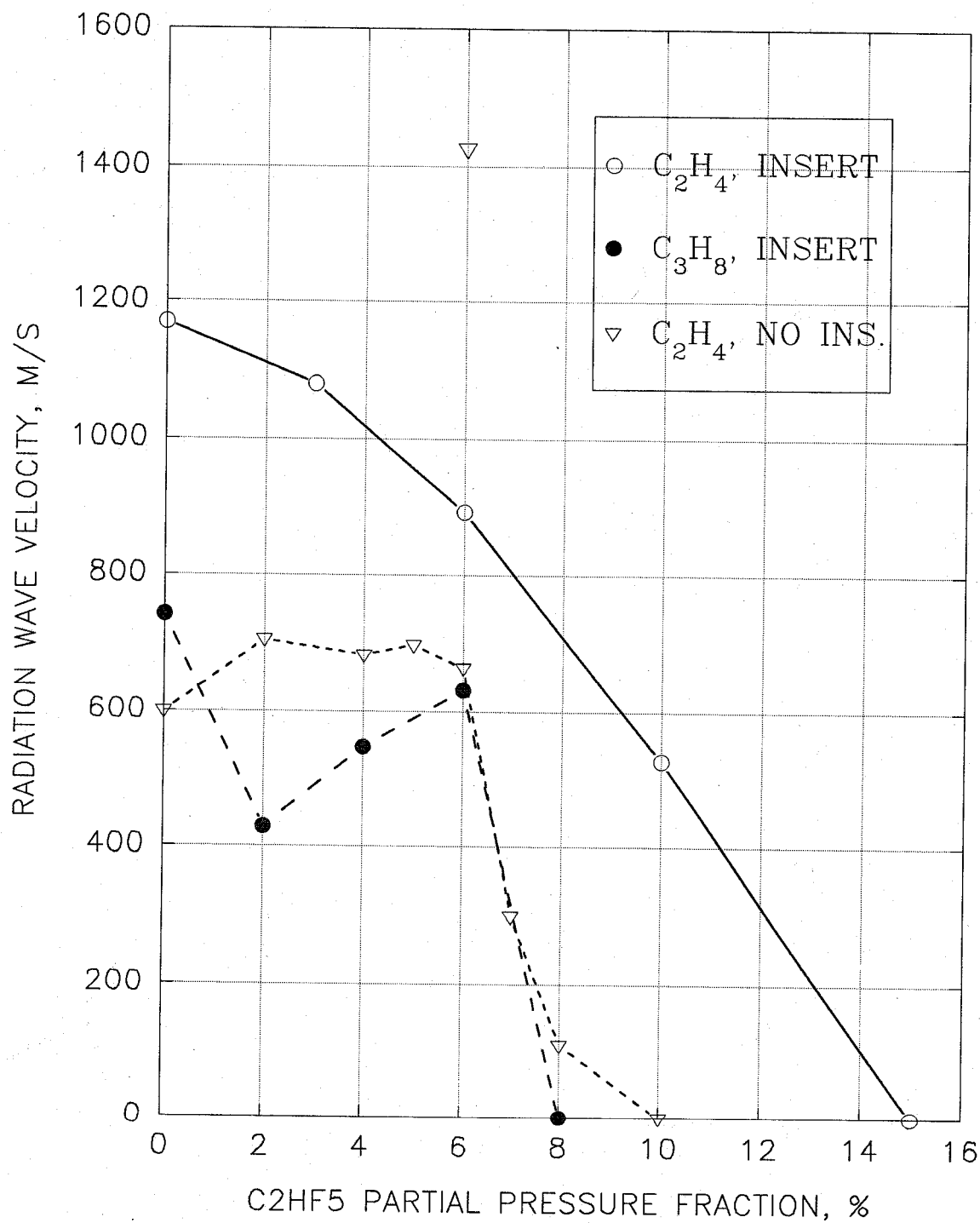


Figure 16. Shock/combustion wave speed in lean, C₂HF₅-inhibited hydrocarbon/air mixtures showing the impact of spiral insert and fuel-type on suppression behavior.

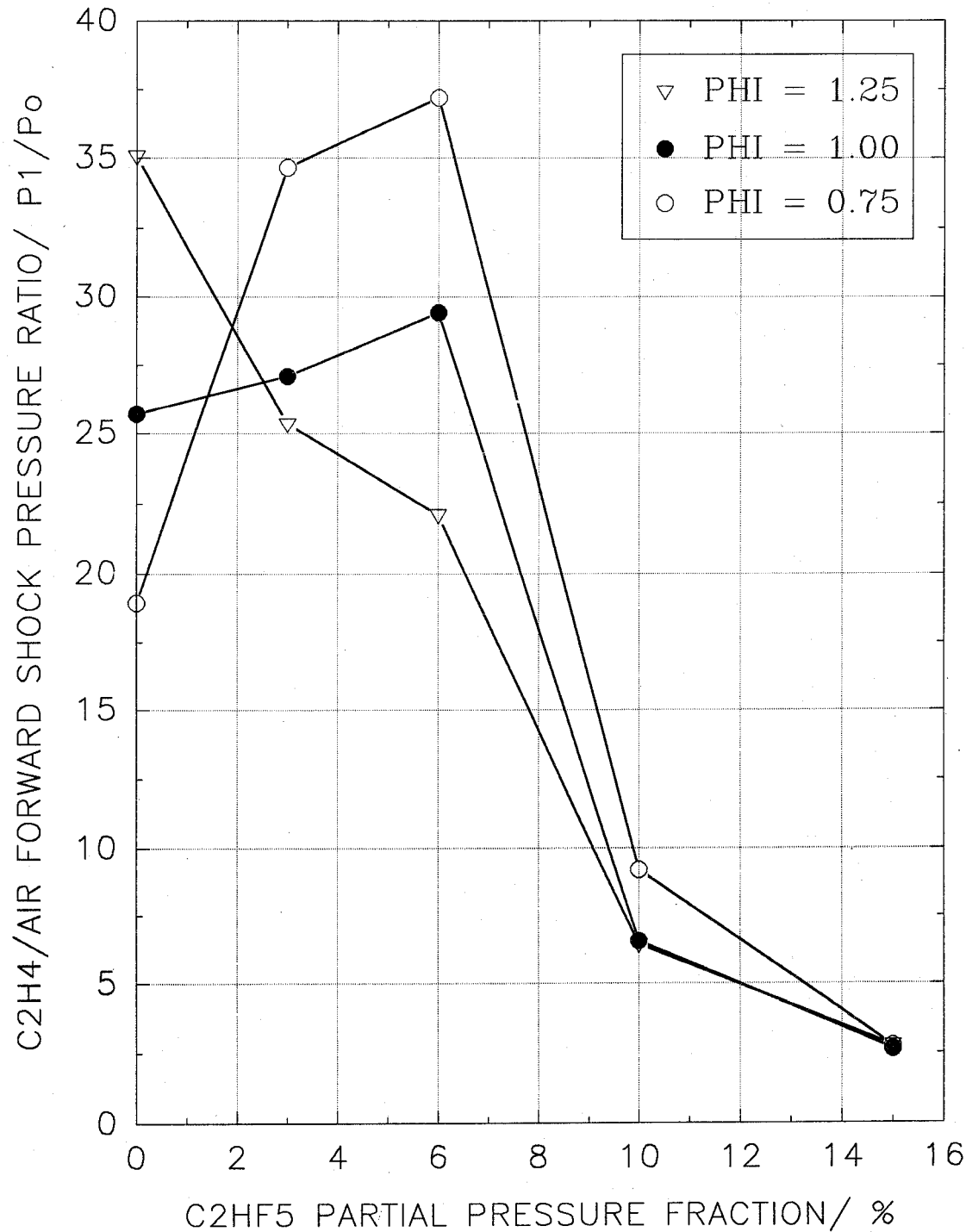


Figure 17. Shock pressure ratios in C_2HF_5 /ethene/air mixtures (2.5 m, with spiral).

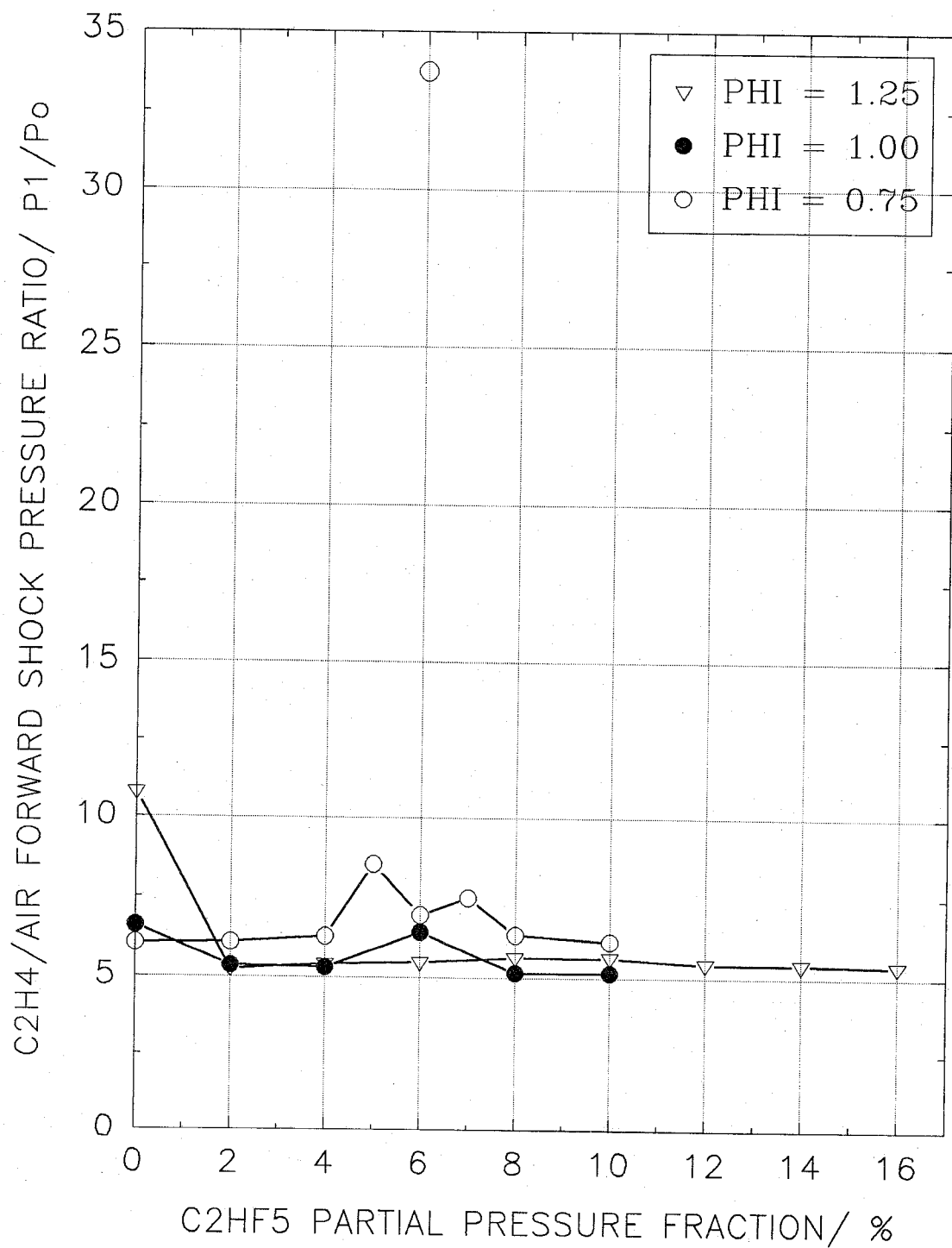


Figure 18. Shock pressure ratios in C_2HF_5 /ethene/air mixtures (5.0 m, no spiral).

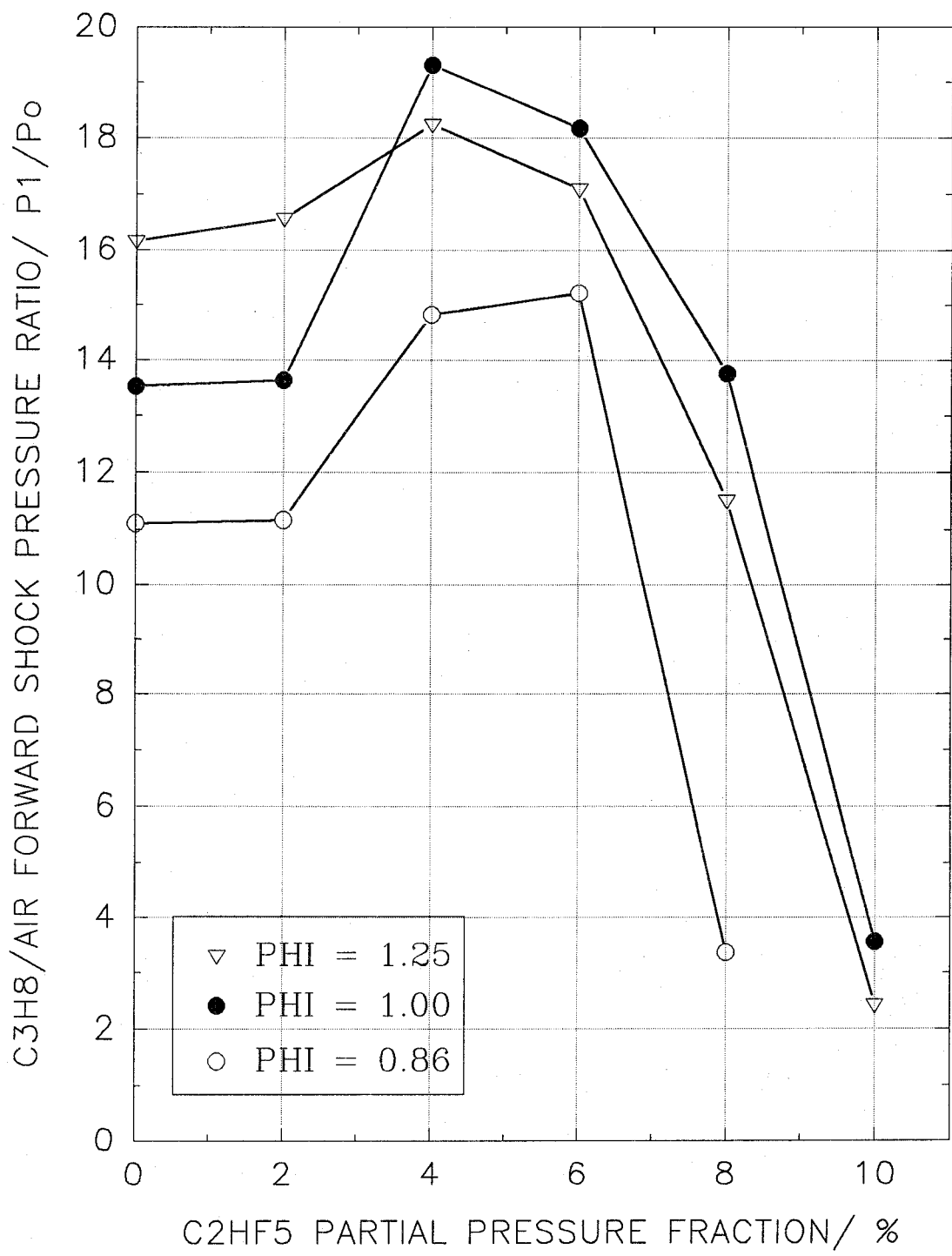


Figure 19. Shock pressure ratios in C_2HF_5 /ethene/air mixtures (2.5 m, spiral).

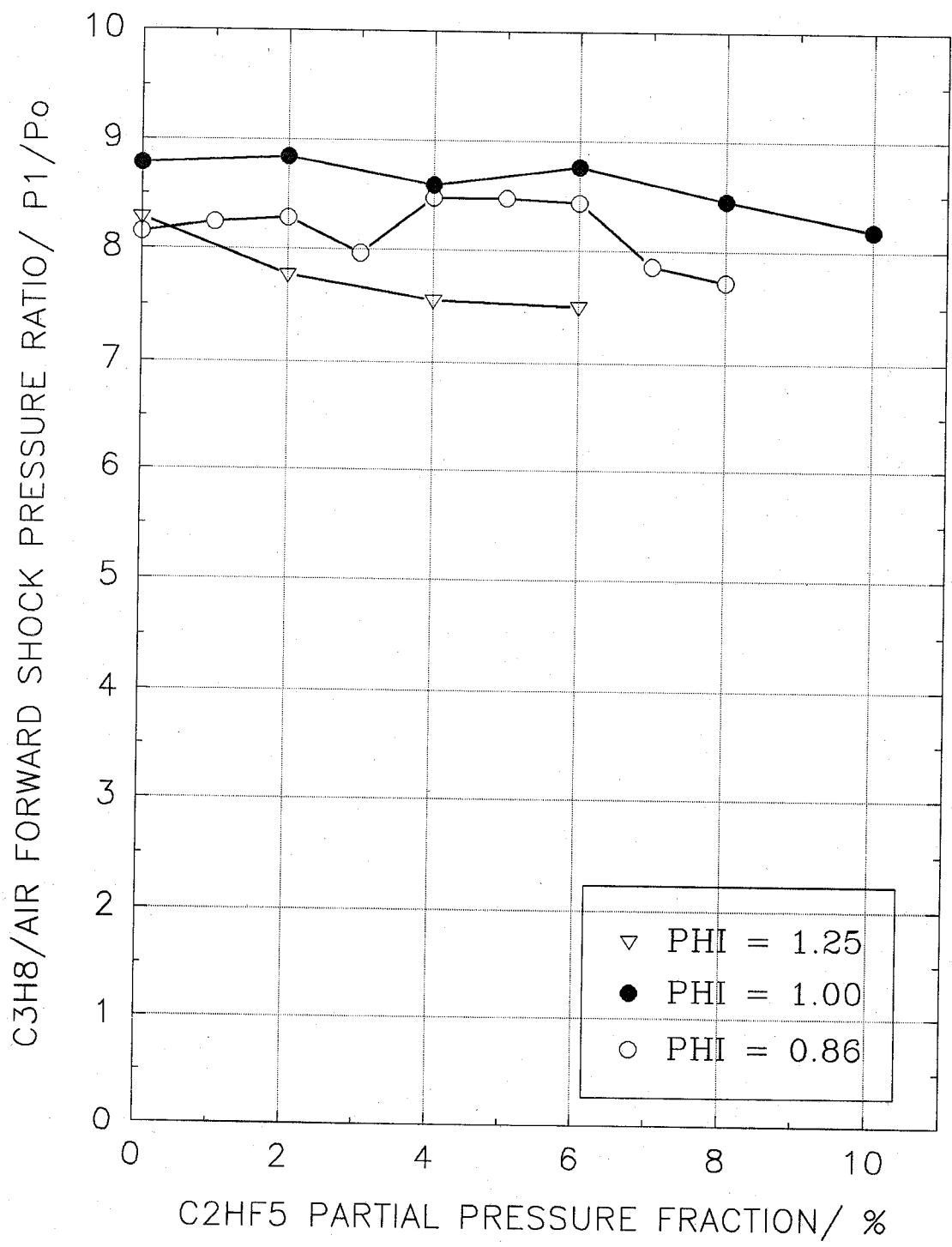


Figure 20. Shock pressure ratios in C_2HF_5 /propane/air mixtures (5 m, no spiral).

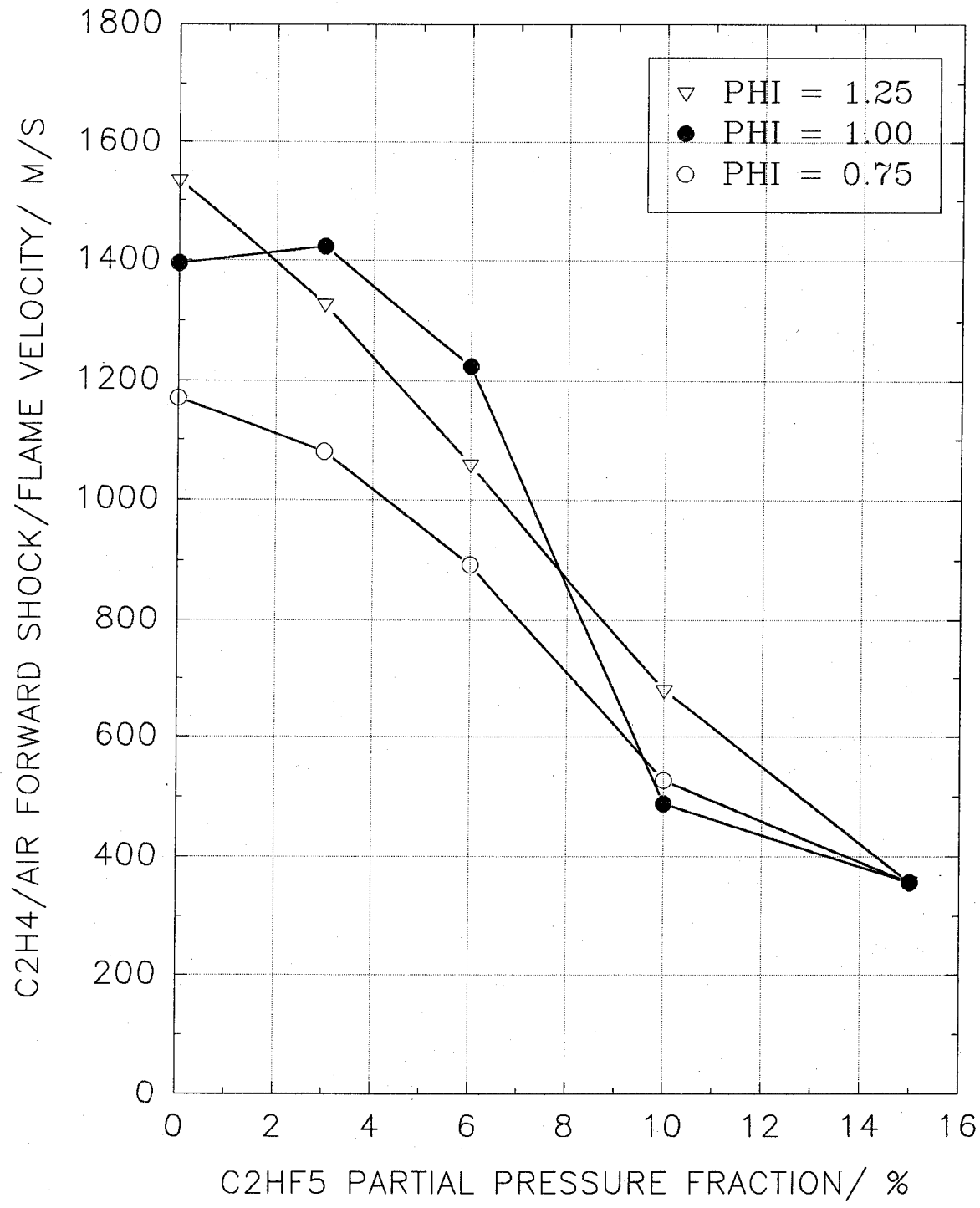


Figure 21. Shock/combustion wave speed in C₂HF₅/C₂H₄/air mixtures (2.5 m, spiral).

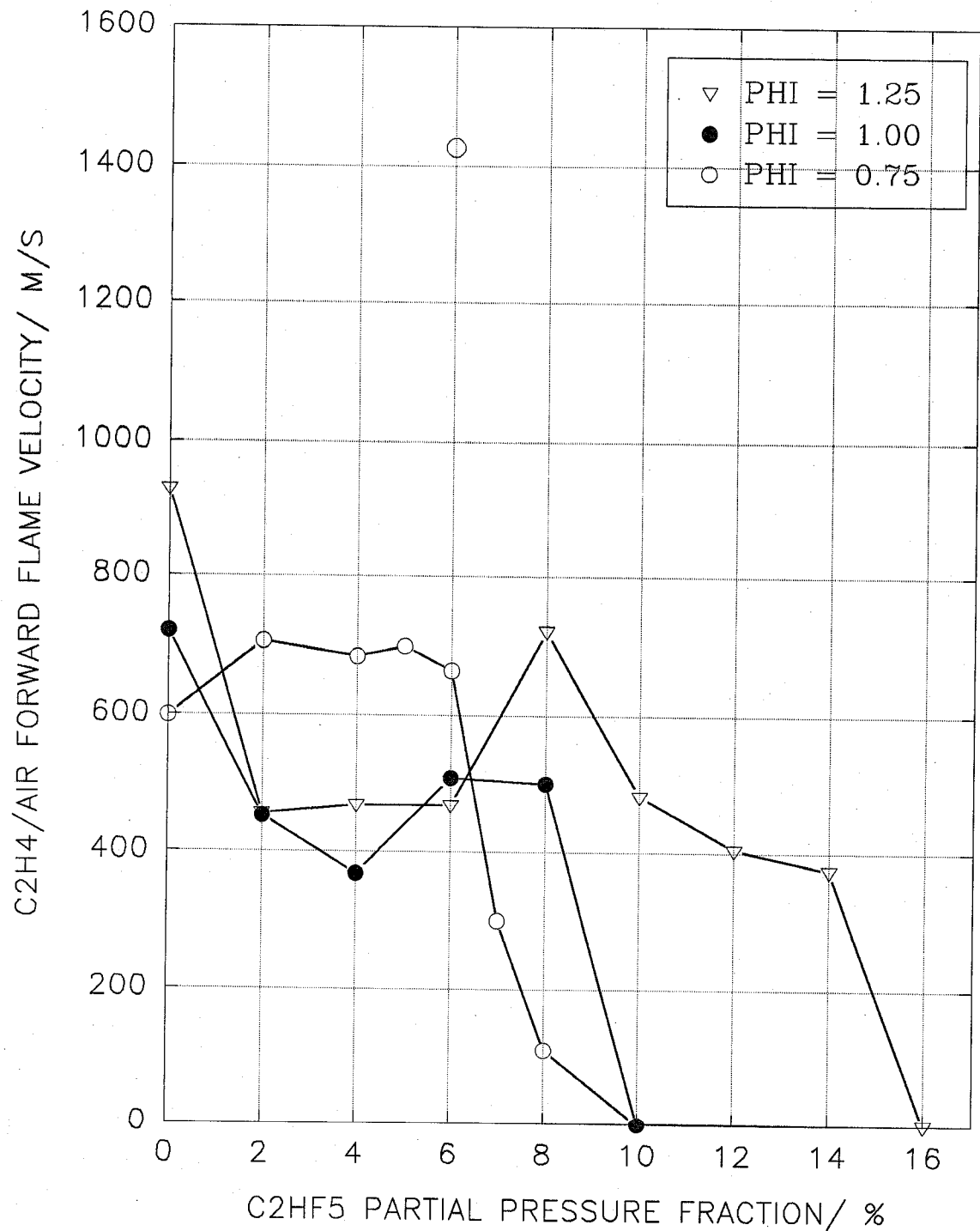


Figure 22. Combustion wave speed in C₂HF₅/C₂H₄/air mixtures (5 m, no spiral).

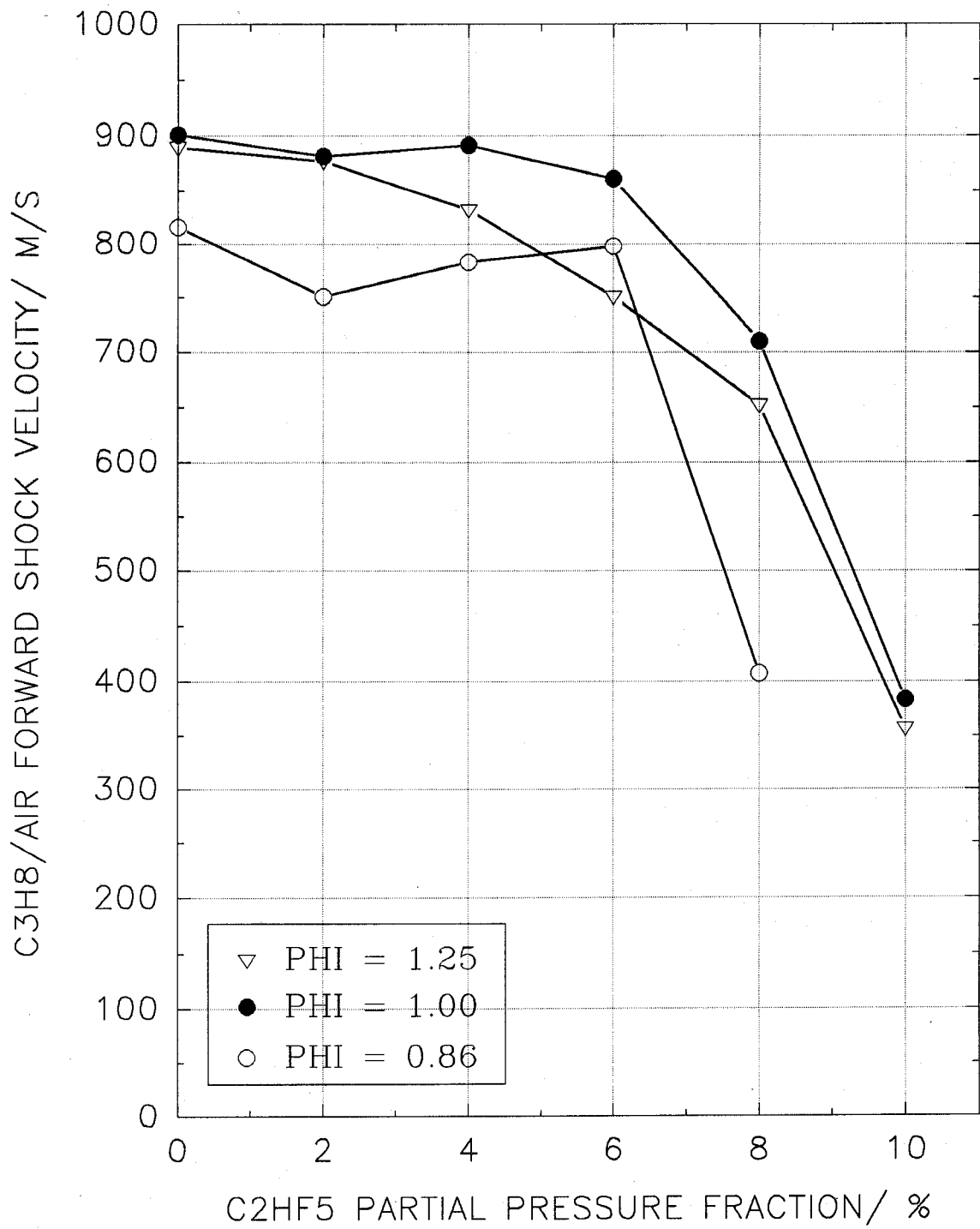


Figure 23. Shock/combustion wave speed in C_2HF_5/C_3H_8 /air mixtures (2.5 m, spiral).

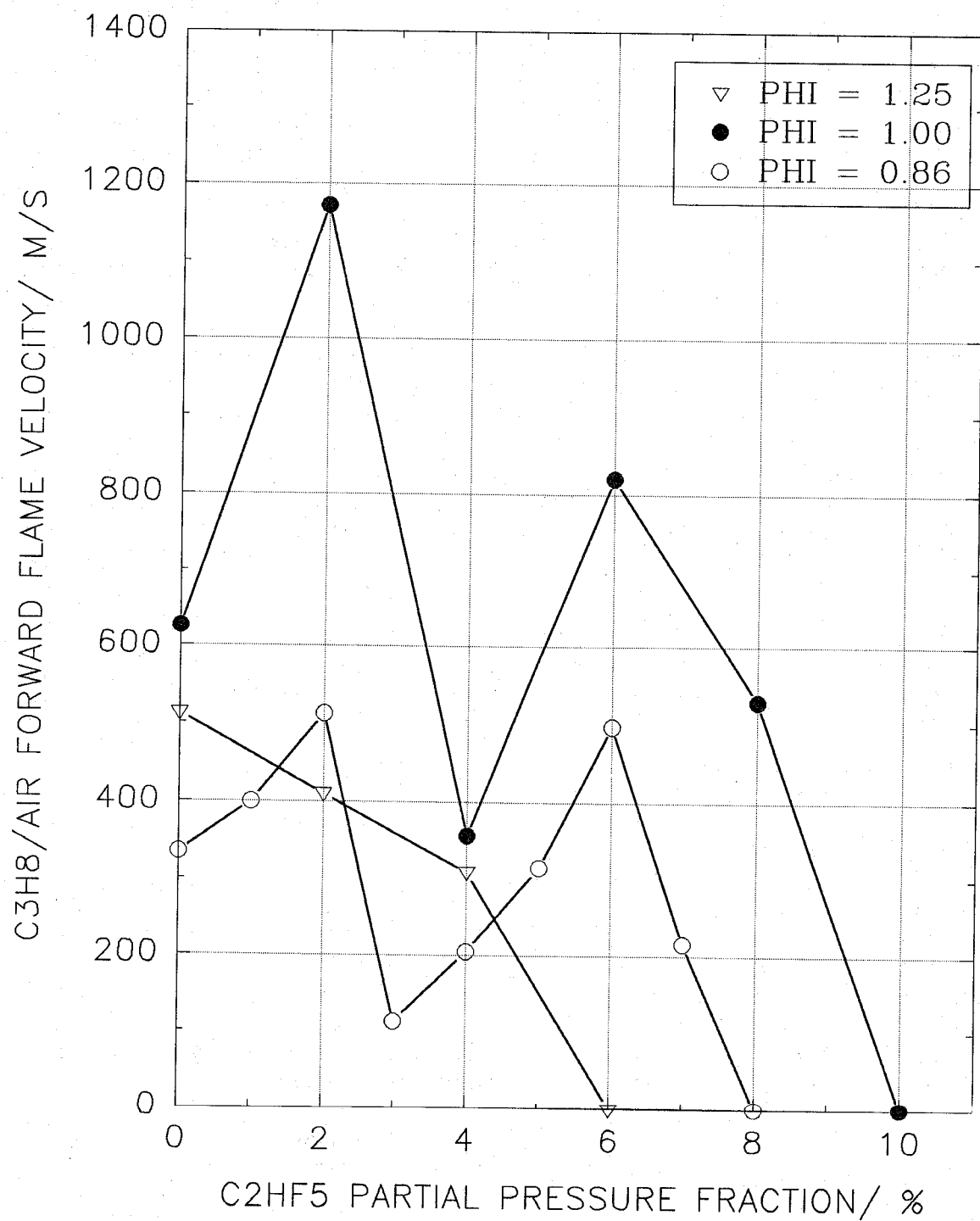


Figure 24. Combustion wave speed in C_2HF_5/C_3H_8 /air mixtures (5 m, no spiral).

and $\Phi=1.25$, the pressure rise in the uninhibited (partial pressure fraction = 0) test section increases substantially. However, the suppressant does not significantly worsen the situation for the stoichiometric mixture, and it is much more effective for the rich condition.

When the shorter, obstructed test section is replaced with the 5.0 m long unobstructed test section, the strength of the shock wave is decreased by a factor of about 3, as can be seen in Figure 18. For the rich and stoichiometric mixtures, adding as little as 2 % C_2HF_5 reduces the severity of the pressure build up. Additional agent has little impact on the pressure ratio. The behavior of the agent under lean conditions is less deleterious in the test section without the spiral in place. However, a small enhancement in pressure can be seen at a partial pressure fraction of 5 %. A single test at 6 % exhibited extreme pressures, although that data point could not be repeated.

Replacing ethene with propane cuts in half the pressures generated by the shock passing through the 2.5 m test section with the spiral insert. Figure 19 is a plot of P_1/P_0 as a function of the amount of HFC-125 added and the fuel/air equivalence ratio. The stoichiometric condition is the most dangerous with propane (compare to Figure 17), but for all equivalence ratios, the propane shock wave is easier to attenuate than the ethene-generated shock. In the long test section without the spiral insert, neither stoichiometry nor the amount of C_2HF_5 have much effect on the shock pressure ratio (see Figure 20).

The ethene/air mixture produces a quasi-detonation when the spiral is present in the 2.5 m test section. Thus, the shock and combustion wave travel together at the same speed. Figure 19 shows the wave speeds measured for this geometry as a function of stoichiometry and the amount of HFC-125 in the test section. Notice that the wave speed for the lean mixture decreases about monotonically with C_2HF_5 partial pressure, which is in contrast to the more complex behavior exhibited by the pressure ratio shown in Figure 17. When there is no spiral insert in the test section, the flame becomes decoupled from the shock. The flame velocities for different C_2HF_5/C_2H_4 /air mixtures are plotted in Figure 22. The flame speed is much slower than the shock speed and goes to zero when the HFC-125 reaches a partial pressure fraction of 10 % for $\Phi = 0.75$ and 1.0. A 16 % partial pressure fraction is required when the fuel/air ratio is rich. The outlying point for the lean mixture with 6 % agent has the correspondingly high pressure ratio shown in Figure 18. The rather chaotic looking behavior in Figure 22 can be partially attributed to the location of the photodiodes (0.3 m beyond the gate valve), where the gradient in agent concentration is high and the wake created by the gate valve may be influencing the flow field.

The shock and combustion wave travel together when propane is the fuel and the spiral insert is in the 2.5 m test section. The behavior of the wave speed (see Figure 23) is qualitatively similar to the ethene system, although the maximum speeds are lower and the amount of C_2HF_5 required to quench the combustion (*i.e.*, speed < 400 m/s) is a couple of percent lower with propane. Figure 24 shows the combustion wave speed without a spiral insert. The stoichiometric mixture produces the fastest flame, and is quenched when the C_2HF_5 partial pressure fraction is 10 %. Comparing this plot to Figure 22, it is interesting to note that the rich propane flame can be fully suppressed at a concentration less than half the value required to suppress rich ethene combustion.

2.4.4.2 C_3F_8 Performance. The perfluoropropane (FC-218) does not produce the high overpressures found when C_2HF_5 is added to the lean ethene mixture in the presence of the spiral insert. Figure 25 shows the shock pressure ratio measured in the obstructed configuration with the C_3F_8/C_2H_4 /air mixture. There is a slight enhancement when the partial pressure fraction is 2 %, but otherwise the drop-off in P_1/P_0 with agent concentration is well-behaved. The lean mixture is the easiest and the rich mixture the most difficult to suppress with C_3F_8 , which is opposite to the results observed when C_2HF_5 was the agent.

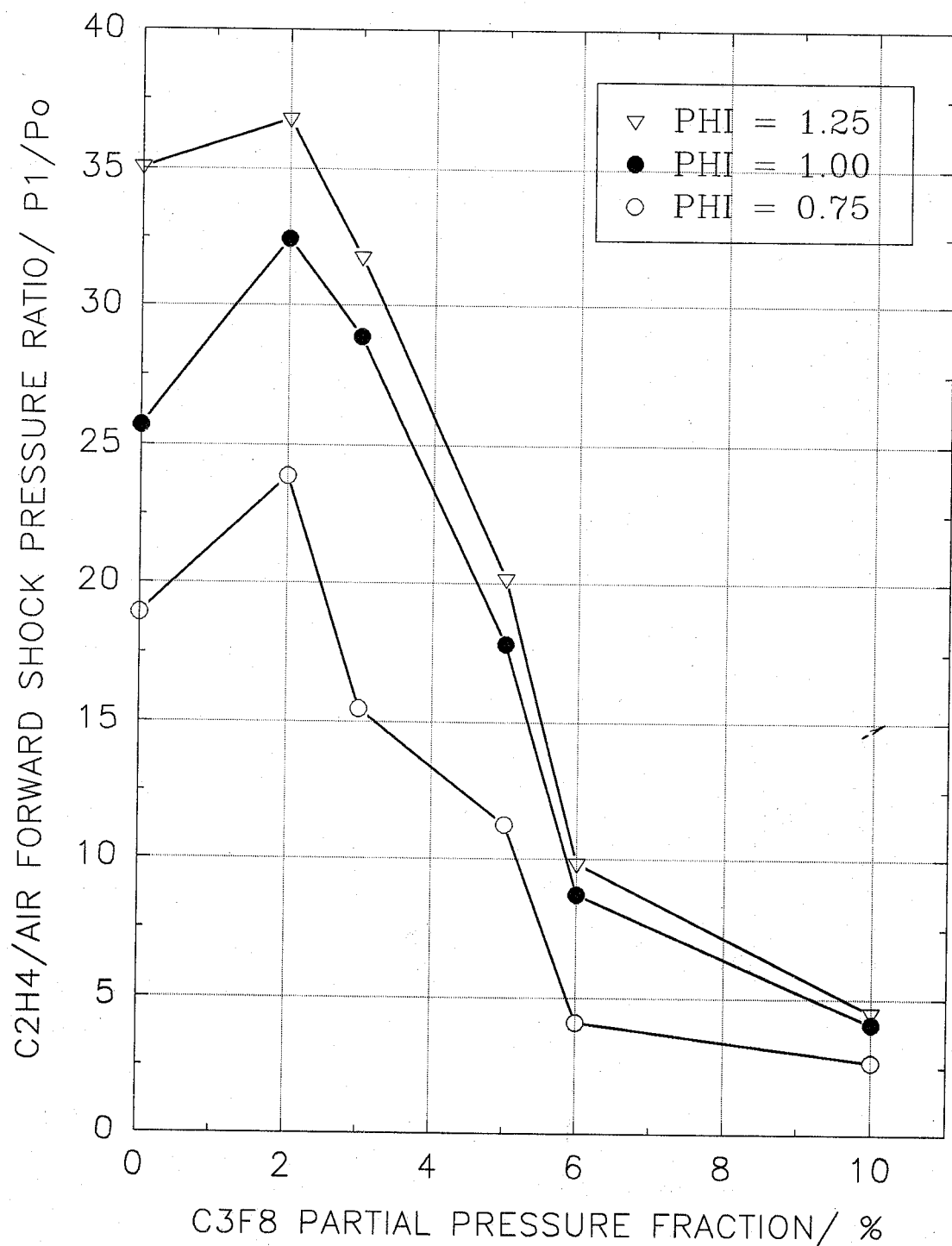


Figure 25. Shock pressure ratio in C₃F₈/C₂H₄/air mixtures (2.5 m, no spiral).

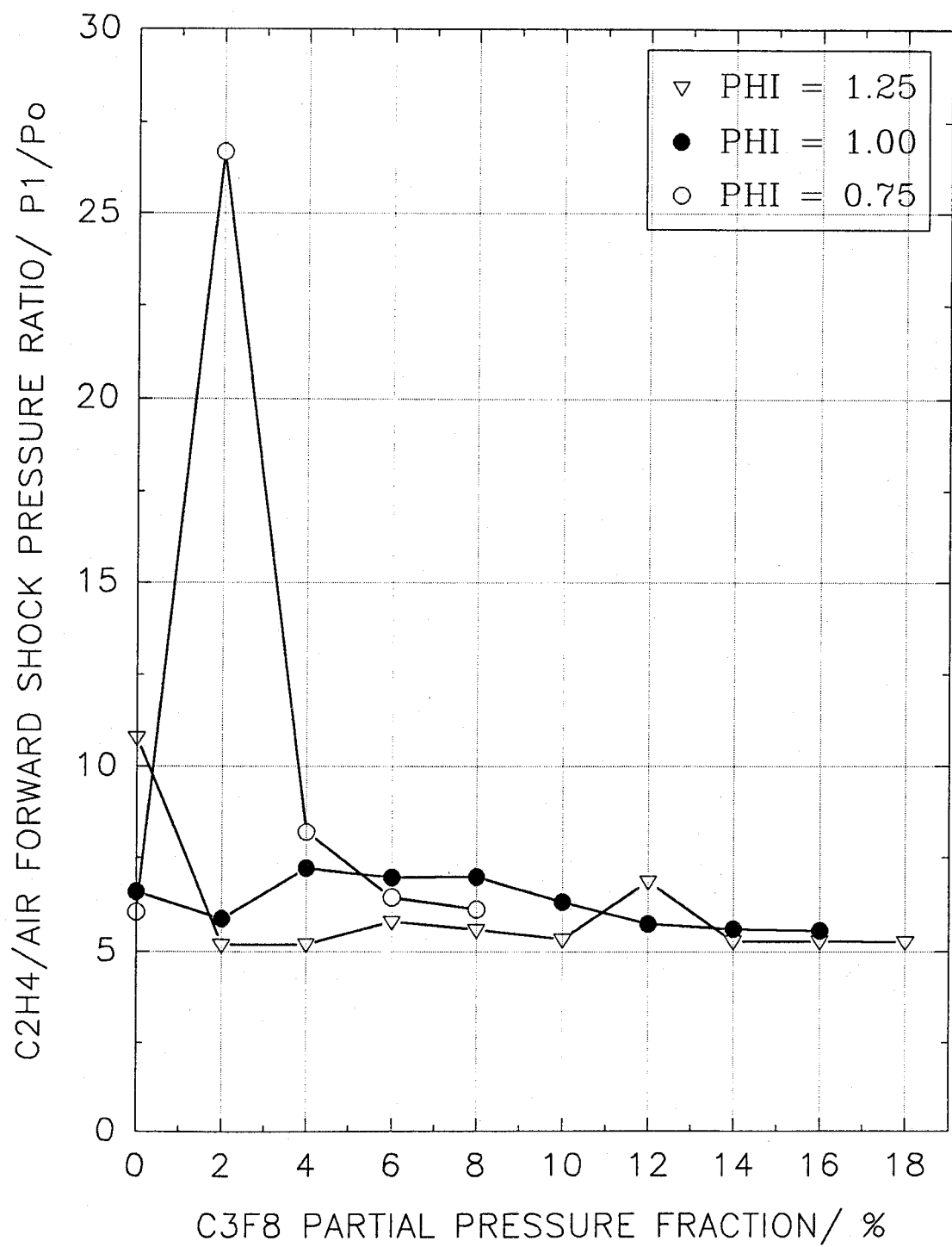


Figure 26. Shock pressure ratio in C_3F_8/C_2H_4 /air mixtures (5 m, no spiral).

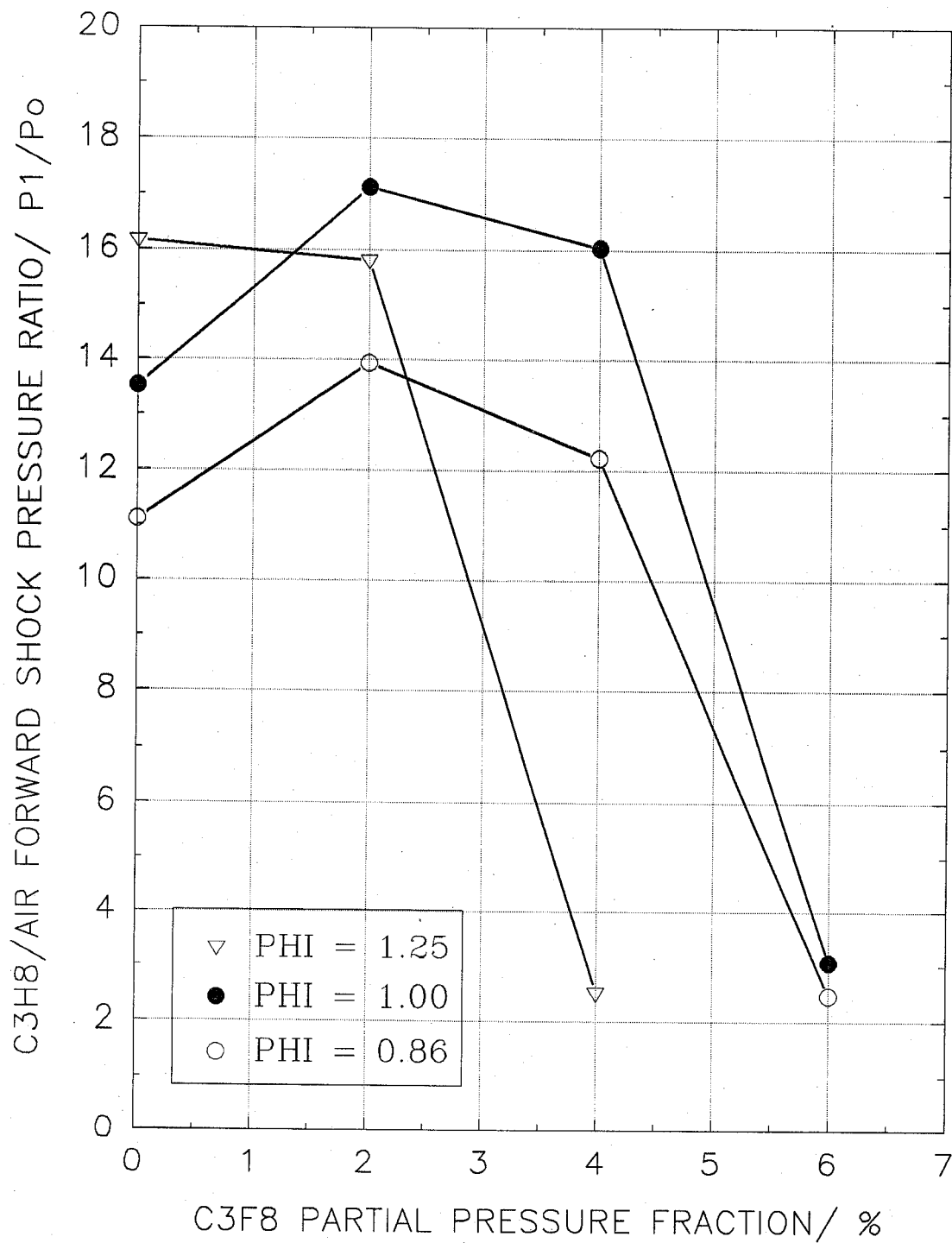


Figure 27. Shock pressure ratio in C_3F_8/C_3H_8 /air mixtures (2.5 m, spiral).

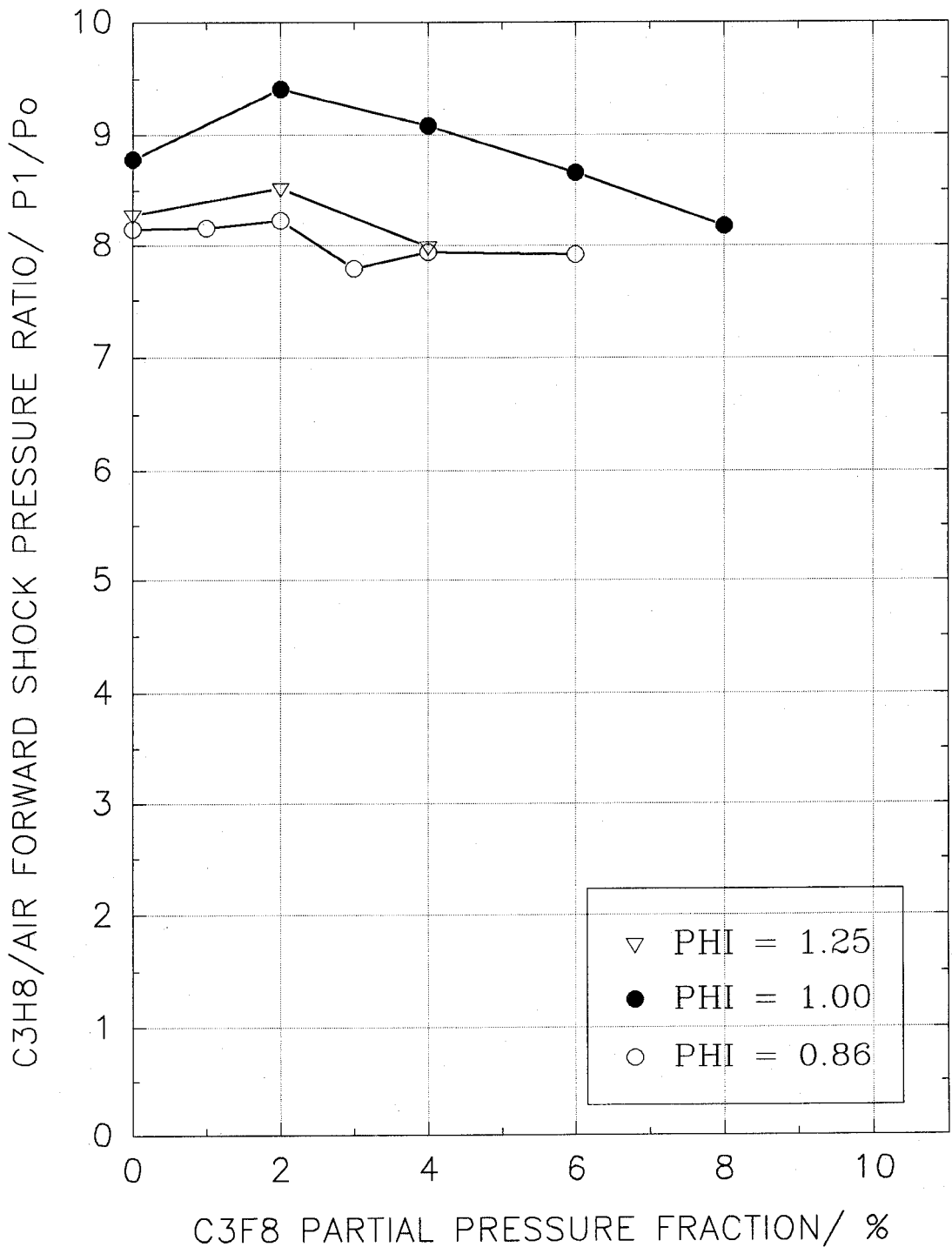


Figure 28. Shock pressure ratio in C_3F_8/C_3H_8 /air mixtures (5 m, no spiral).

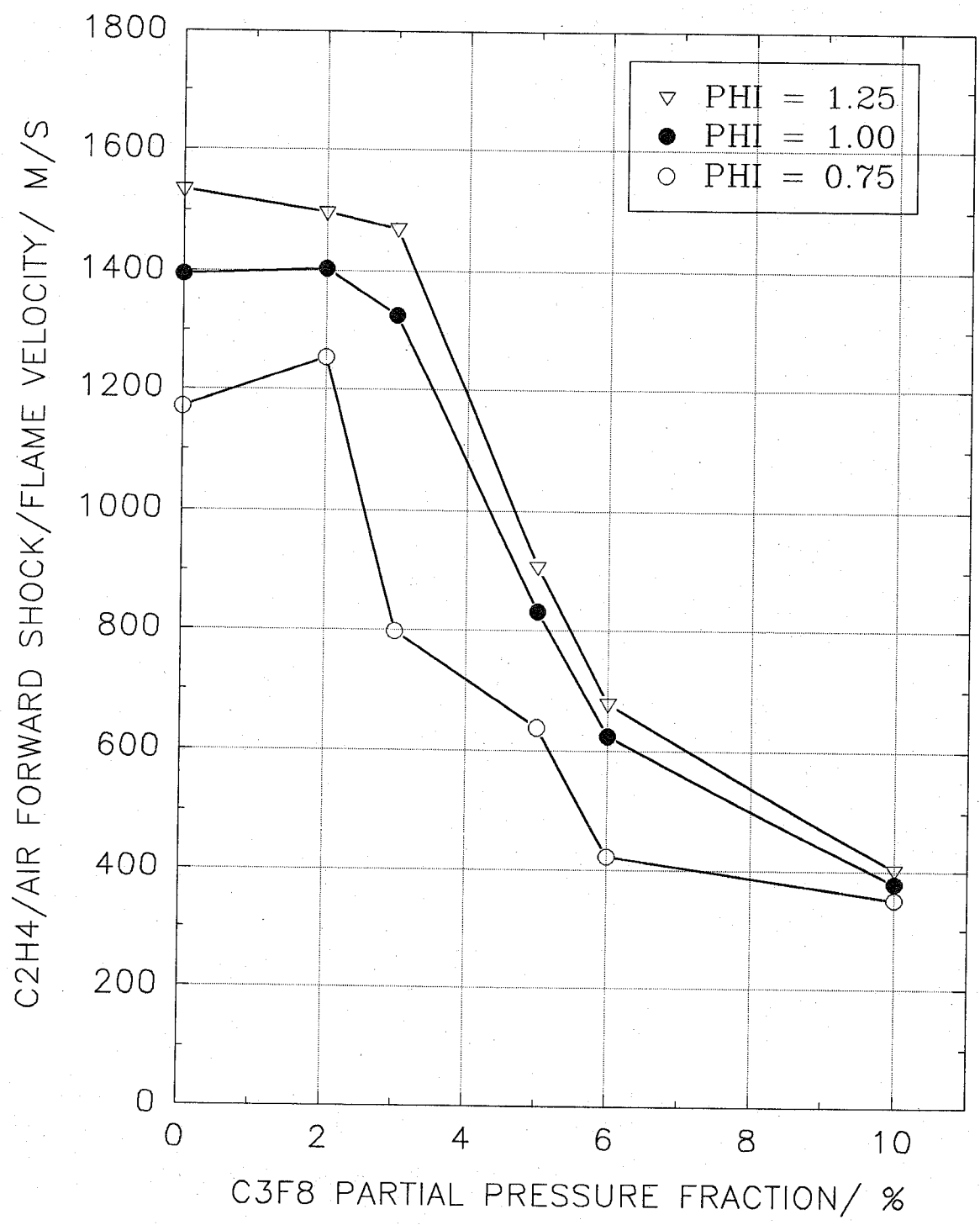


Figure 29. Shock/combustion wave speed in C₃F₈/C₂H₄/air mixtures (2.5 m, spiral).

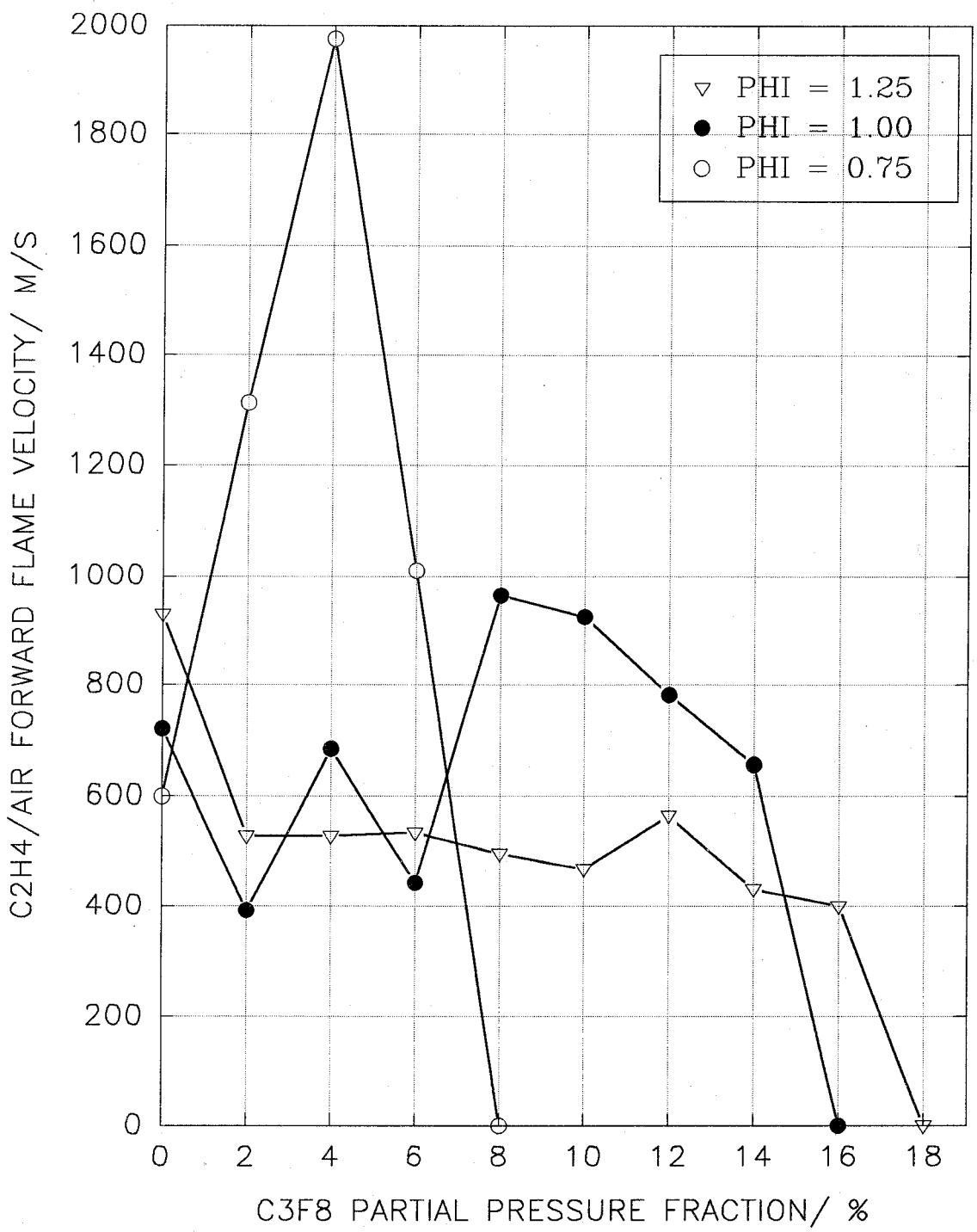


Figure 30. Combustion wave speed in C₃F₈/C₂H₄/air mixtures (5 m, no spiral).

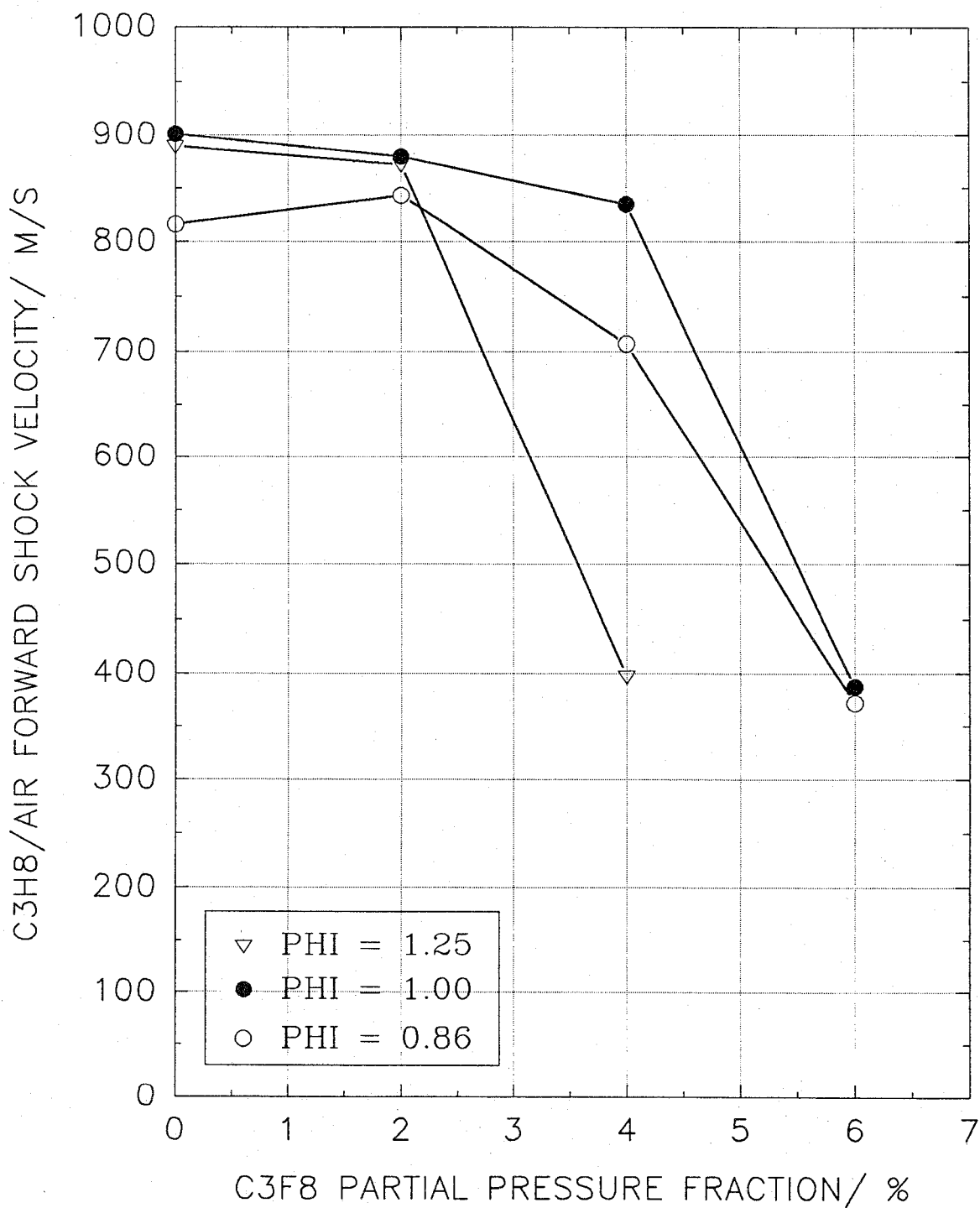


Figure 31. Shock/combustion wave speed in C_3F_8/C_3H_8 /air mixtures (2.5 m, spiral).

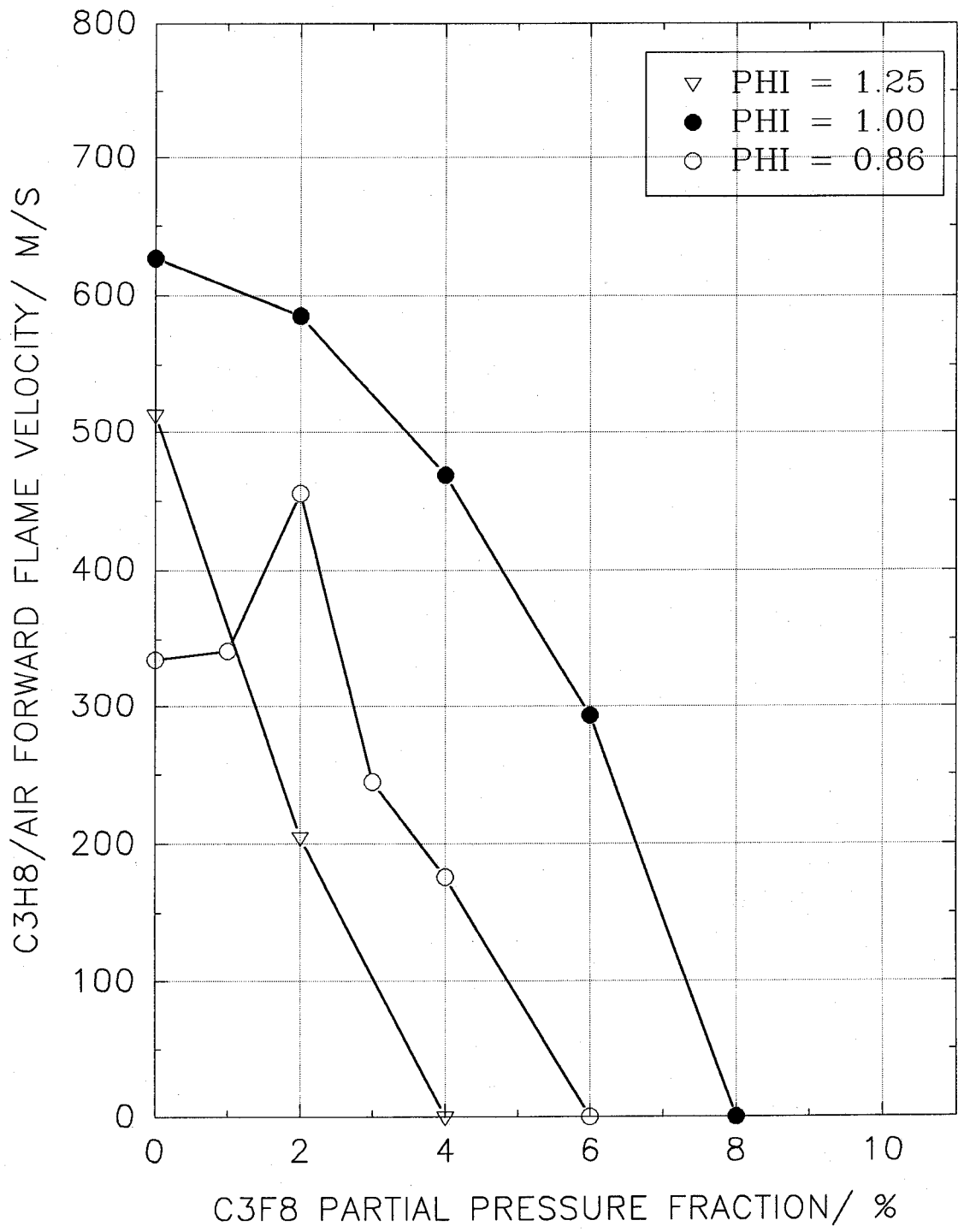


Figure 32. Combustion wave speed in C₃F₈/C₃H₈/air mixtures (5 m, no spiral).

By removing the spiral, the pressure rise across the shock is greatly reduced, and the suppression behavior of C_3F_8 is very similar to C_2HF_5 , as can be seen by comparing Figure 26 to Figure 18. The pressure spike in the lean mixture containing C_3F_8 cannot be easily explained, but may have something to do with the sensitivity of the ethene/air reaction to small perturbations. Note that a spike is also present in Figure 18, but that is hypothesized to be related to the hydrogen in the HFC-125 and its impact on the chain branching reactions.

The FC-218 does a much better job than HFC-125 in reducing the pressure buildup in the obstructed propane/air experiments. Figure 27 shows that a 4 % partial pressure fraction of C_3F_8 attenuates the shock wave traveling through the rich mixture as effectively as 2.5 times as much C_2HF_5 . Suppression of the lean propane mixture requires 6 % C_3F_8 , compared to 8 % C_2HF_5 . Figure 28 compares the shock pressure ratios for the lean, stoichiometric and rich propane/air mixtures in the 5 m long test section without the spiral insert. The FC-218 has little impact on the strength of the shock wave under these conditions. The same statement applies to HFC-125 (see Figure 20).

The combined shock and combustion wave speeds are plotted in Figure 29 for the C_3F_8 -suppressed C_2H_4 /air mixture in the obstructed 2.5 m long test section. The speed decreases with the addition of FC-218 more quickly, dropping below 400 m/s at a partial pressure fraction of 10 % (compared to 15 % when HFC-125 is the agent). Removing the insert results in the combustion wave speeds shown in Figure 30. The very high speed for the lean mixture with 4 % C_3F_8 corresponds to a Chapman-Jouguet detonation, a result that is difficult to have predicted, especially since full suppression is attained when only 8 % C_3F_8 is added to the mixture. The rich flame travels more slowly at low agent concentrations, but is not fully extinguished until the partial pressure fraction is 18 %. The speed of the propane combustion waves are plotted in Figures 31 and 32, with and without the spiral insert, respectively. The FC-218 out-performs the HFC-125 under both arrangements (compare to Figures 23 and 24). Under the worst conditions, only 8 % C_3F_8 is necessary to annihilate the propane flame.

2.4.4.3 CF_3I Performance. The suppression behavior of CF_3I is more complicated than either C_2HF_5 or C_3F_8 . This complexity is demonstrated in Figure 33, which shows that small concentrations of CF_3I dramatically reduce the shock pressure ratio generated in the obstructed 2.5 m long test section filled with C_2H_4 /air mixtures. However, the pressures rise as the agent partial pressure fraction is increased to 6 %, equalling or exceeding the totally uninhibited values. For the most reactive mixture ($\Phi = 1.25$), it takes over 13 % CF_3I to reduce the pressure ratio to below 5.1, as compared to about 12 % for C_2HF_5 and less than 10 % for C_3F_8 . The unpredictable behavior extends to the test configuration with no spiral insert (see Figure 34). In these tests, it is the richest condition that is the best behaved. For an equivalence ratio of 0.75, the pressure increases to a factor greater than 36:1 when the partial pressure fraction of CF_3I is 4 %. This peak shifts to 8 % when the C_2H_4 /air mixture is stoichiometric. Similar peaks were observed when HFC-125 and FC-218 were used (compare to Figures 18 and 26), but only for $\Phi = 0.75$. The precision of the CF_3I suppression measurements were checked by repeating four times the 8 % CF_3I in stoichiometric ethene/air mixture. The maximum absolute deviations of flame and shock velocities and pressure ratio were 157 m/s, 15 m/s and 0.97 respectively. This level of precision provides confidence that the trends observed in all the experimental sequences are real and meaningful.

The shock pressure ratio generated in obstructed lean, stoichiometric and rich CF_3I/C_3H_8 /air mixtures is shown in Figure 35. The behavior is similar to that observed with C_2H_4 , except that the stoichiometric mixture requires much more agent to get under control. With the spiral removed (Figure 36), the pressure ratio drops down more quickly when propane is the fuel, but the stoichiometric condition persists.

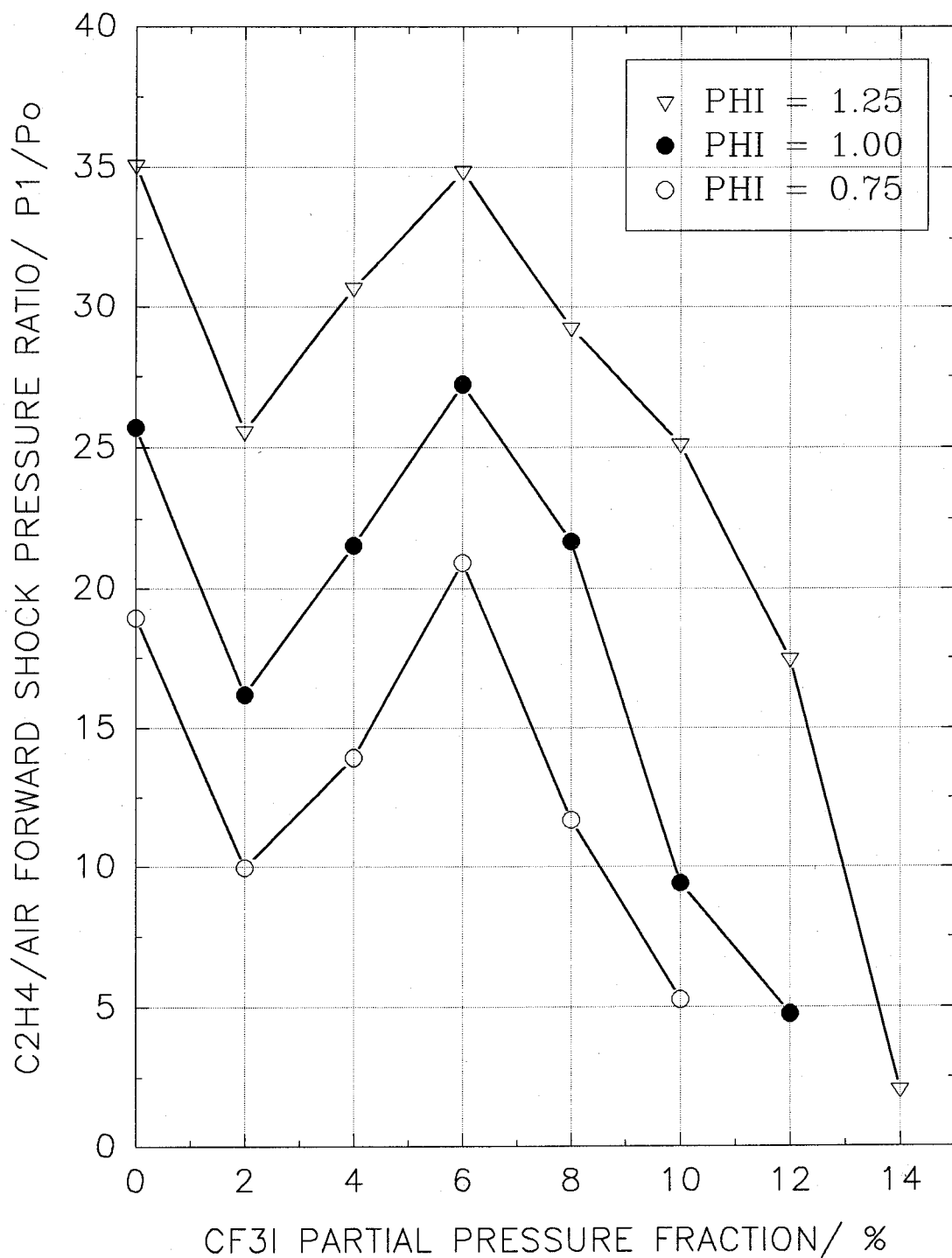


Figure 33. Shock pressure ratio in CF_3I/C_2H_4 /air mixtures (2.5 m, no spiral).

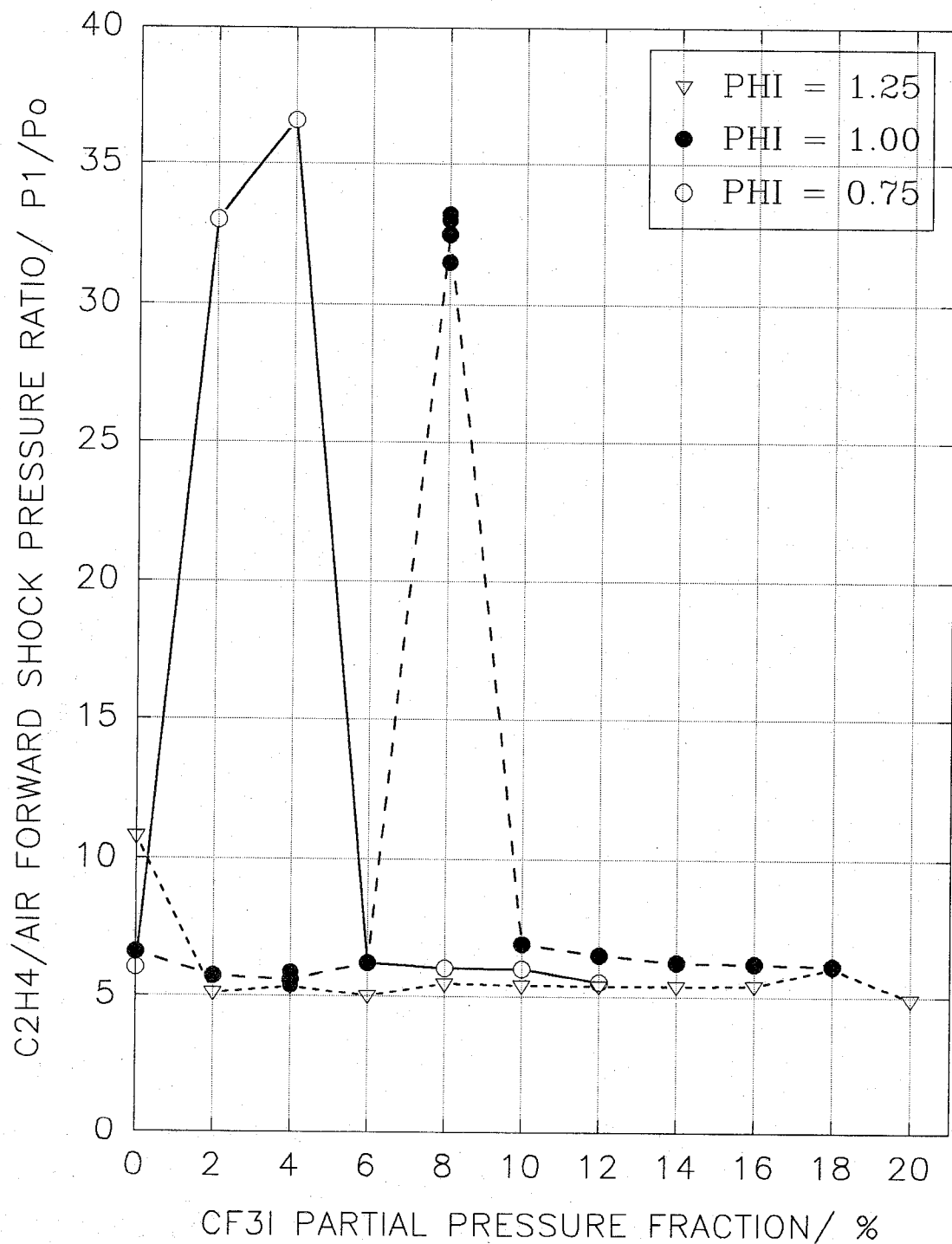


Figure 34. Shock pressure ratio in CF_3I/C_2H_4 /air mixtures (5 m, no spiral).

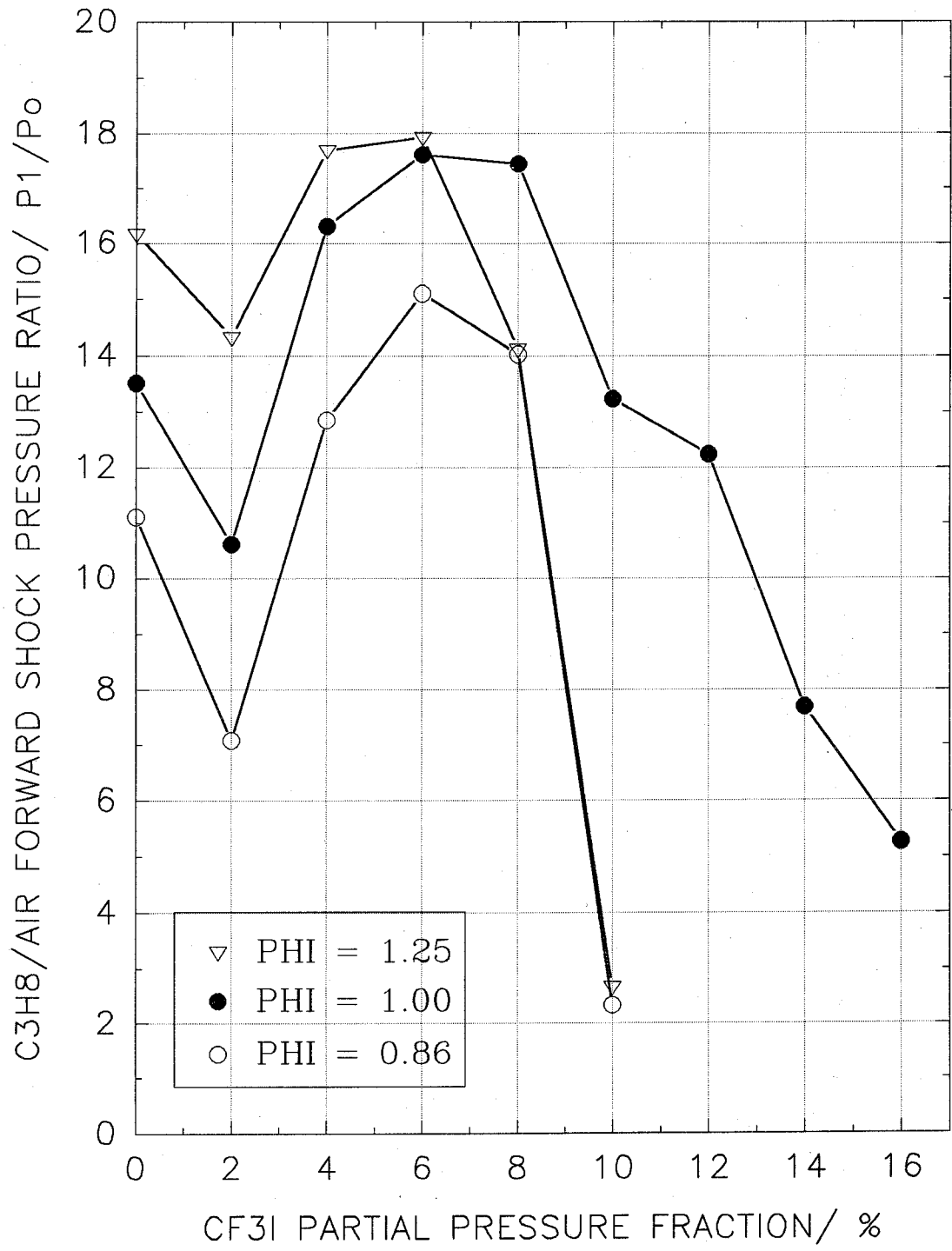


Figure 35. Shock pressure ratio in $\text{CF}_3\text{I}/\text{C}_3\text{H}_8/\text{air}$ mixtures (2.5 m, spiral).

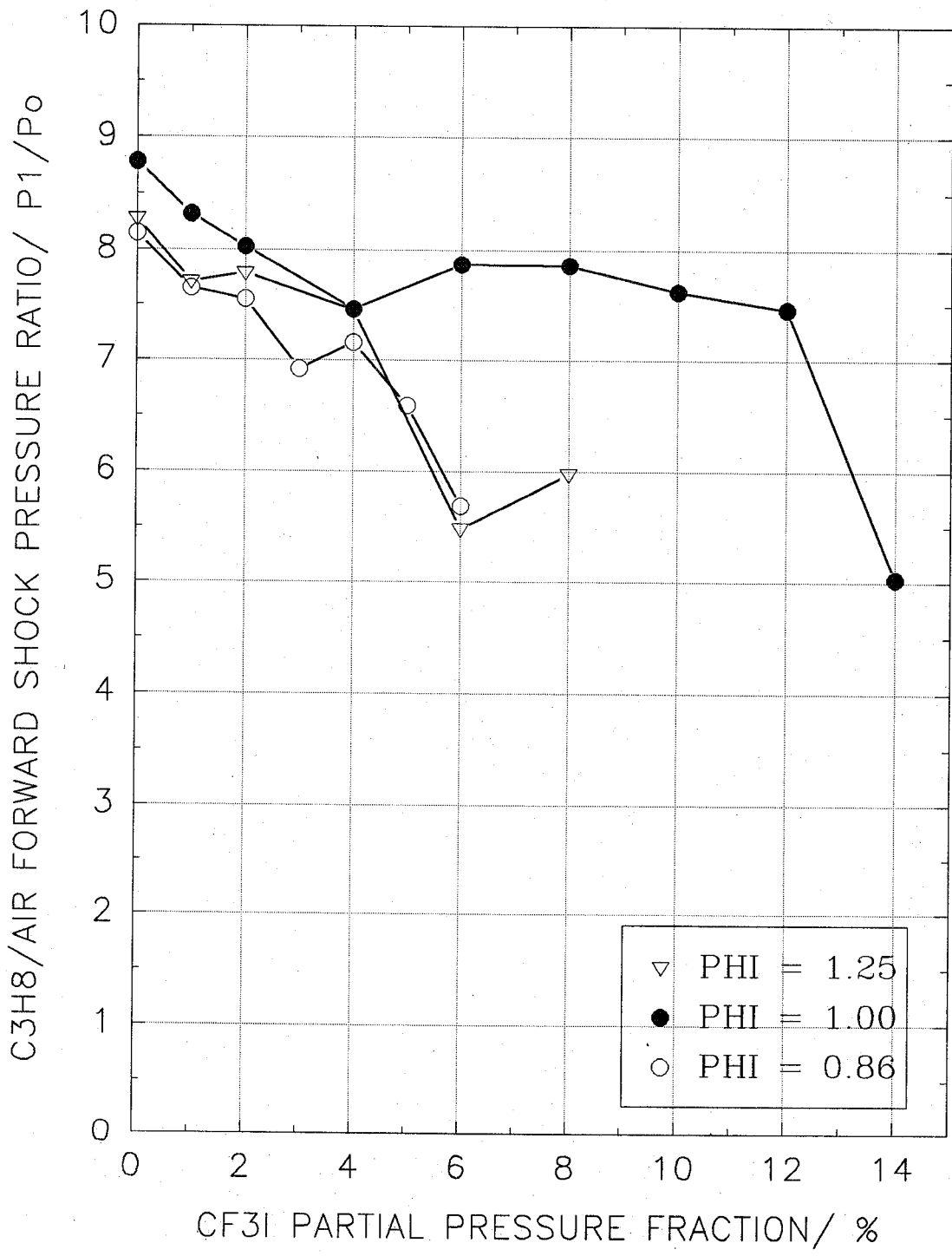


Figure 36. Shock pressure ratio in CF_3I/C_3H_8 /air mixtures (5 m, no spiral).

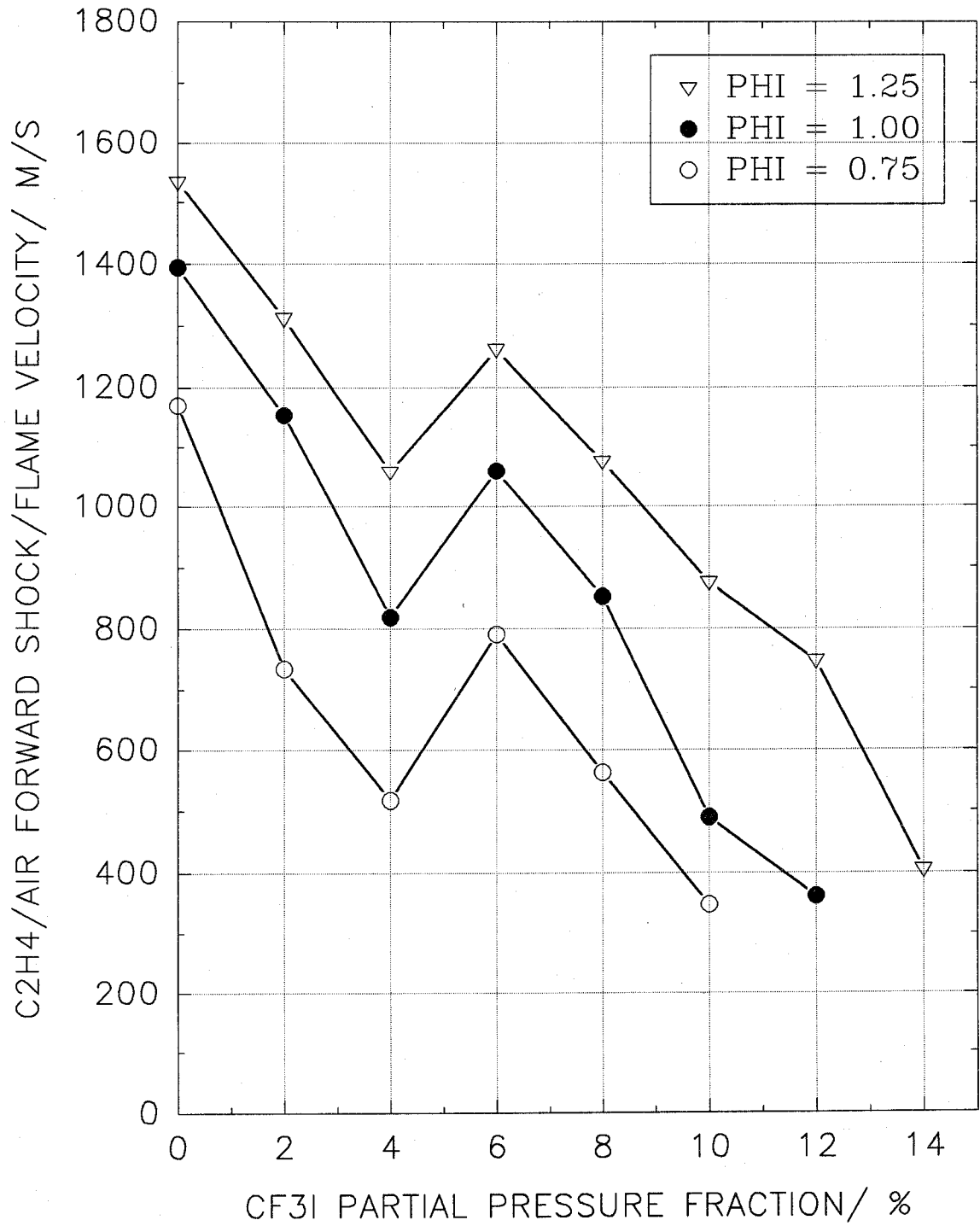


Figure 37. Shock/combustion wave speed in CF₃I/C₂H₄/air mixtures (2.5 m, spiral).

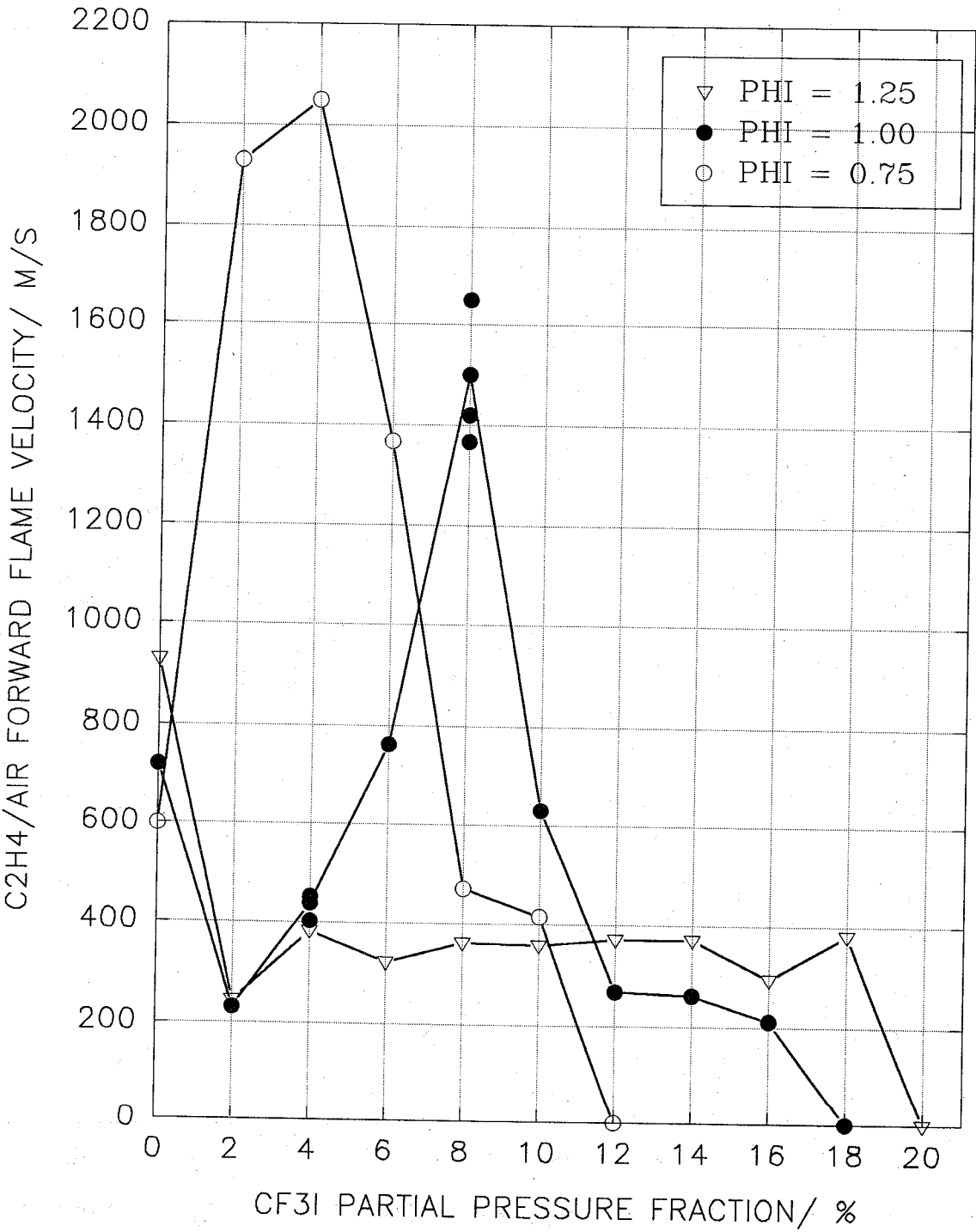


Figure 38. Combustion wave speed in CF₃I/C₂H₄/air mixtures (5 m, no spiral).

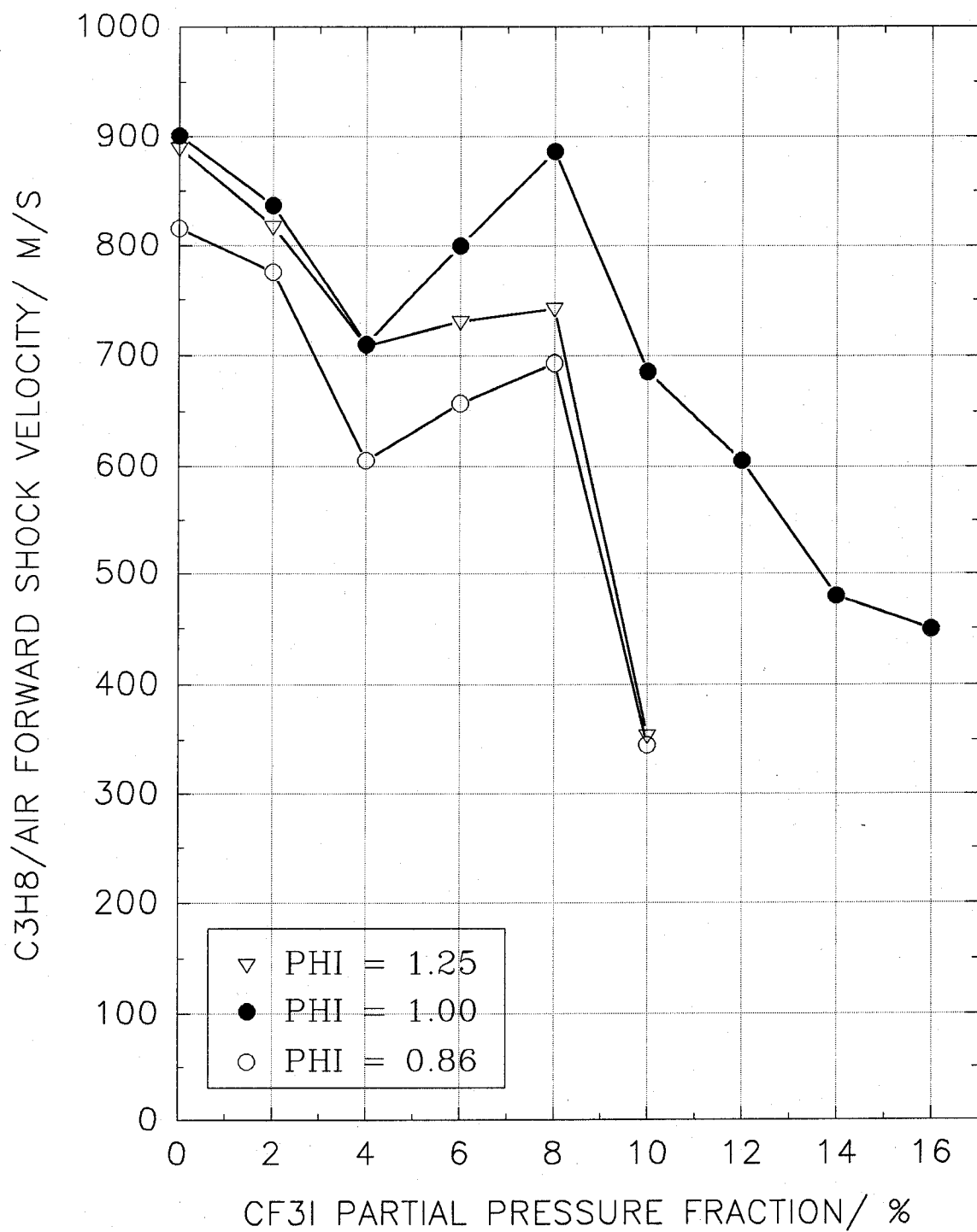


Figure 39. Shock/combustion wave speed in $\text{CF}_3\text{I}/\text{C}_3\text{H}_8/\text{air}$ mixtures (2.5 m, spiral).

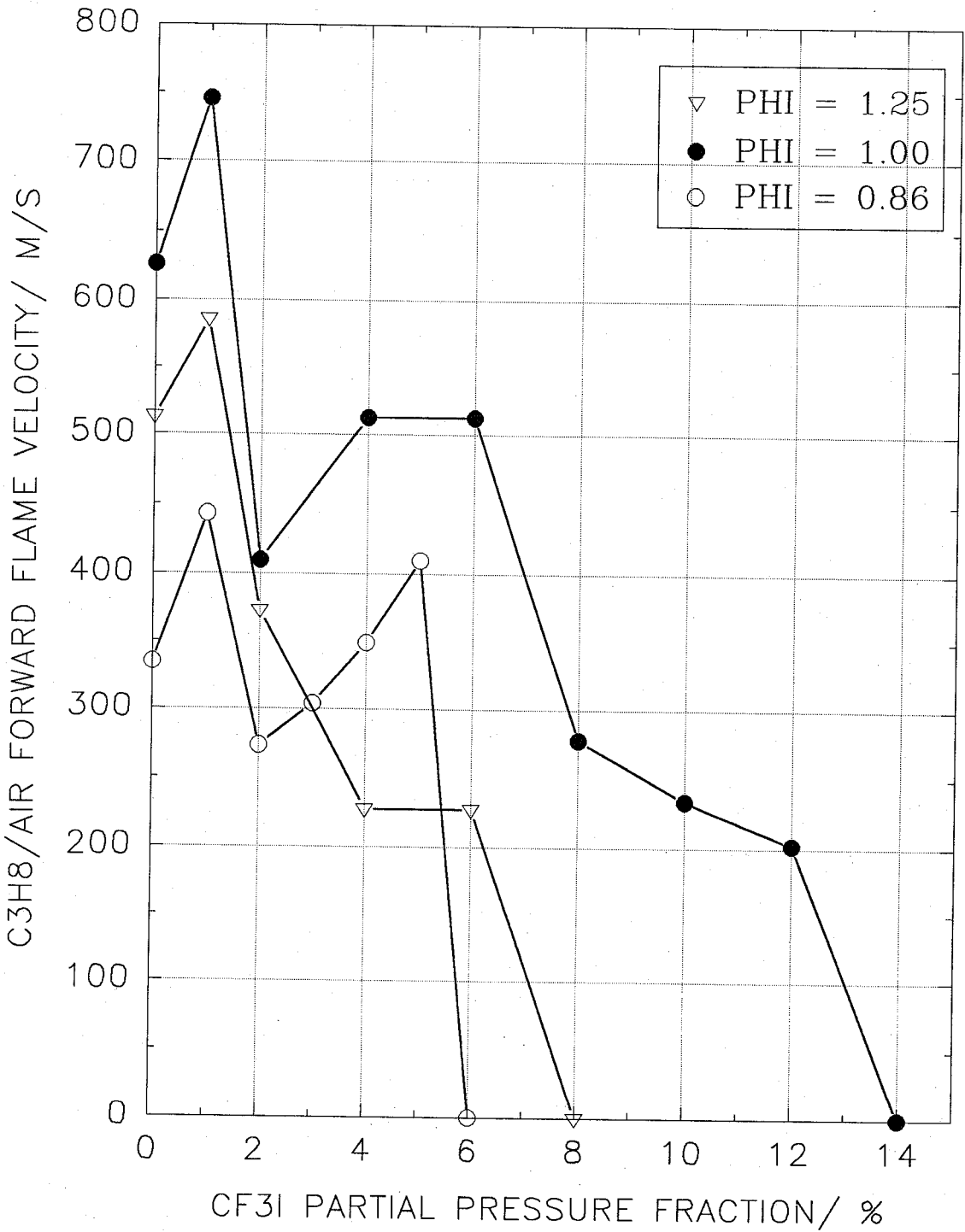


Figure 40. Combustion wave speed in CF₃I/C₃H₈/air mixtures (5 m, no spiral).

The wave speeds are congruent with the pressure ratio results. In Figure 37, the shock and combustion waves are merged. The local minimum in wave speed occurs at a partial pressure fraction of 4 %, which is slightly higher than the location of the minimum pressure ratio. The behavior of the combustion wave can be seen most clearly in Figure 38. Acceleration to a Chapman-Jouguet detonation is clearly observed for both the lean and stoichiometric C_2H_4 /air mixtures. The rich mixture requires 20 % CF_3I to quench the flame radiation, compared to 16 % and 18 % for the HFC-125 and FC-218, respectively.

Figures 39 and 40 show the shock and combustion wave speeds when C_3H_8 is the fuel. The stoichiometric mixture requires the most CF_3I to decelerate, but much less agent is required as compared to C_2H_4 combustion. Similar to C_2HF_5 and C_3F_8 , no C-J detonations are produced using CF_3I when propane is the fuel.

2.4.4.4 Relative Performance of C_2HF_5 , C_3F_8 , and CF_3I . Relative performance of the three compounds is compared as a function of the fuel and test section configuration in Figures 41 to 44. The stoichiometric mixture is chosen as representative. When ethene is the fuel and the spiral insert is in place, the uninhibited shock/combustion wave speed is 1400 m/s. Figure 41 shows that the CF_3I is the most efficient at reducing the wave speed for partial pressure fractions of 4 % and below. The FC-218 (C_3F_8) reduces the wave speed most effectively at higher concentrations, attaining a fully-suppressed condition of 400 m/s at less than 10 %. Removing the spiral reduces the initial condition to a high-speed deflagration traveling at 700 m/s (see Figure 42). The C_2HF_5 quenches the radiation completely with a partial pressure fraction of 10 %. The C_3F_8 is less efficient in suppressing a flame without the spiral insert, and actually enhances the flame when the partial pressure fraction is 8 %. The CF_3I causes a transition to a detonation at the same partial pressure fraction, producing a combustion wave that travels over 1400 m/s. A partial pressure fraction of 18 % is required for the CF_3I to fully suppress the flame.

The CF_3I reduces the shock wave velocity the best of the three agents for the propane/air mixture as long as the levels do not exceed 4 %, as seen in Figure 43. Beyond 7 %, the CF_3I is the poorest agent, requiring more than 16 % by partial pressure to attenuate the shock wave to less than 400 m/s. By contrast, C_3F_8 attains full suppression when the partial pressure fraction is only 6 %. HFC-125 is in between. The data plotted in Figure 44 are taken with stoichiometric C_3H_8 /air mixtures in the 5 m test section without the spiral. FC-218 causes the combustion wave speed to decrease in a monotonic manner, with suppression occurring when the partial pressure fraction is 8 %. Full suppression is attained with HFC-125 at a concentration of 10 %; however, 2 % and 6 % levels of C_2HF_5 strongly enhance the exothermic reaction. The CF_3I is relatively well behaved, but requires the largest amount (on both a molar and mass basis) of the three agents to fully quench the radiation.

2.4.5 Uncertainty Analysis. The measurement results are subject to experimental uncertainties. Because no generally applicable methods exist which would provide a measure of the reliability of the experimental data with absolute certainty, only an estimate of the magnitude of these uncertainties is undertaken. The estimate is affected by the uncertainty of the determination of the independent variables, such as partial pressures of the components constituting the mixtures under investigation, and the dependent variables, such as shock wave amplitudes, and shock/flame time differences serving to determine their velocities.

The uncertainty of the determination of the partial pressure of an agent is affected by the uncertainty of the static pressure transducer which is ± 0.15 % (combined non-linearity, hysteresis, repeatability, and temperature effects); the combined uncertainty of the digital display device which is ± 0.015 %; the uncertainty associated with the purity of the gases which is ± 0.5 %; and the uncertainty associated with the gas component losses due to leaks occurring in the circulation pump

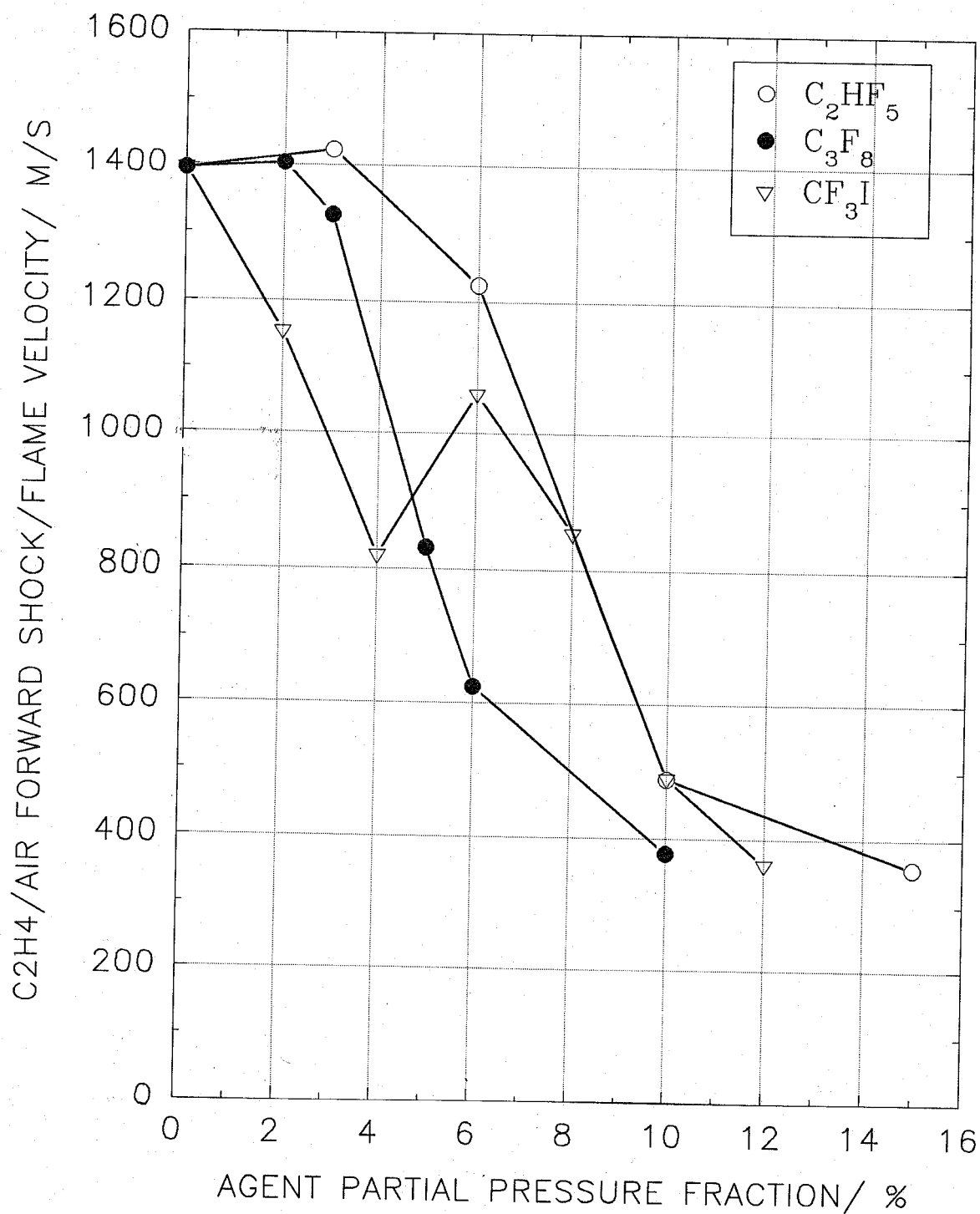


Figure 41. Shock/combustion wave speed in stoichiometric C₂H₄/air mixtures (2.5 m, spiral).

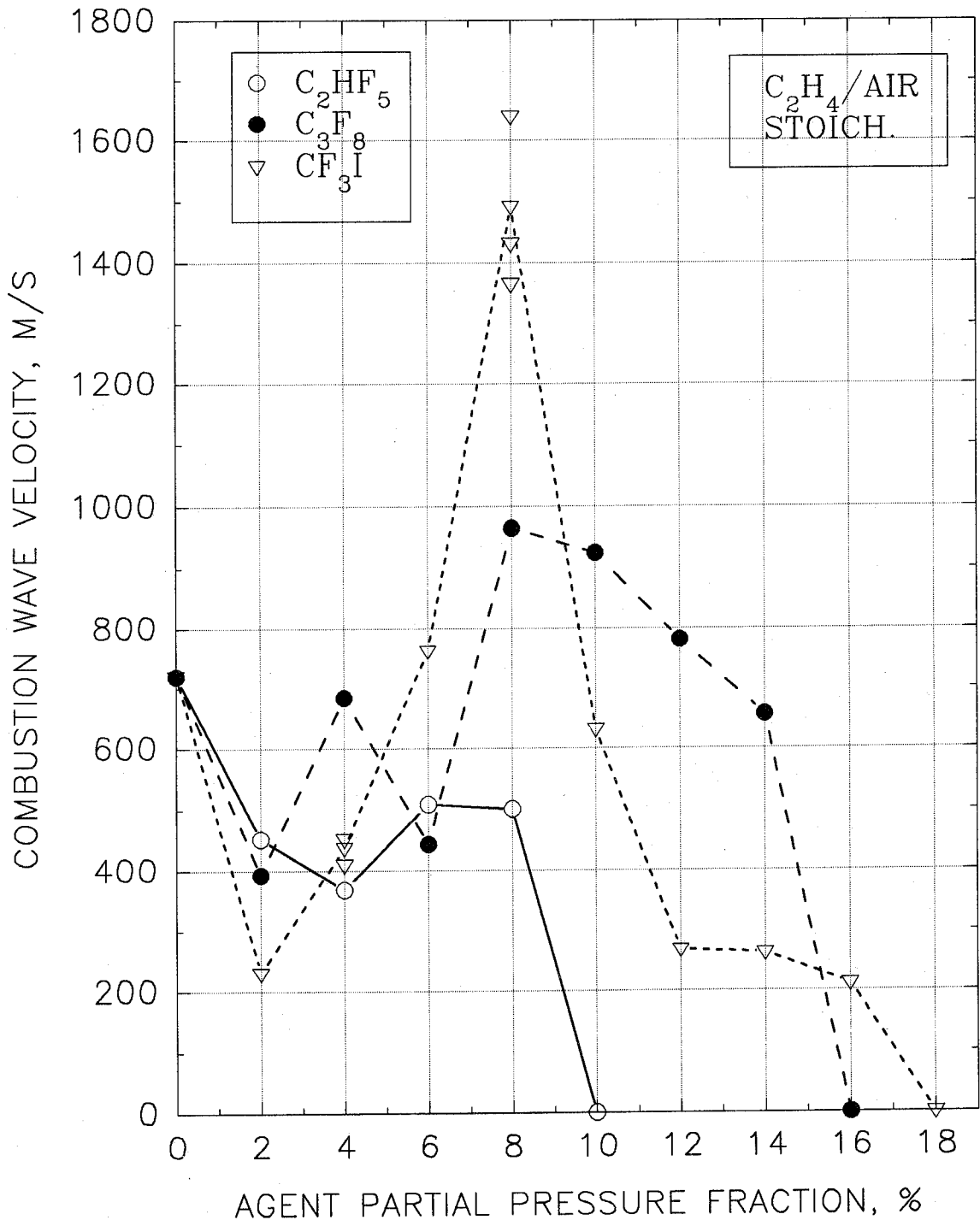


Figure 42. Combustion wave speed in stoichiometric C_2H_4 /air mixture (5 m, no spiral).

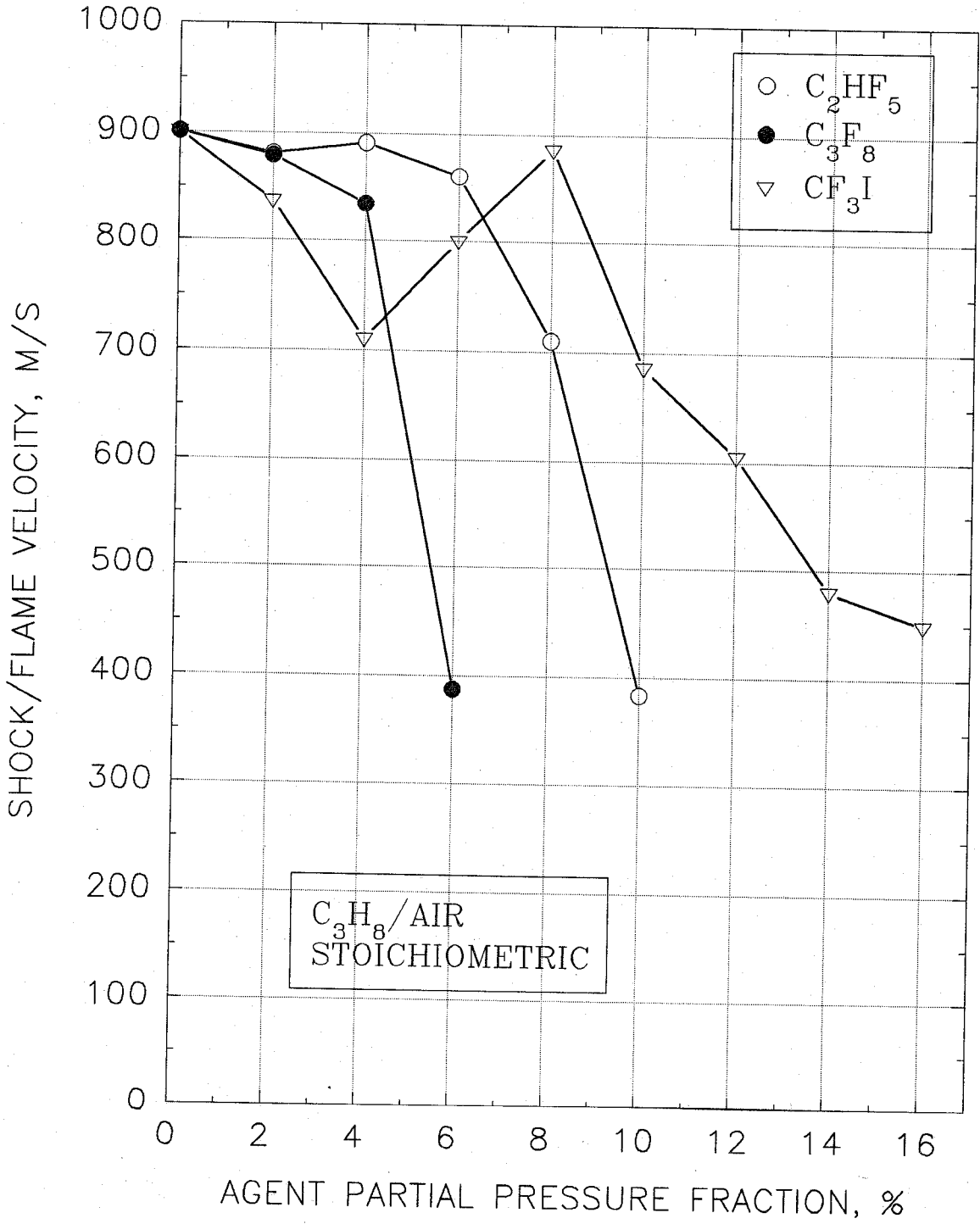


Figure 43. Shock/combustion wave speed in stoichiometric C_3H_8 /air mixtures (2.5 m, spiral).

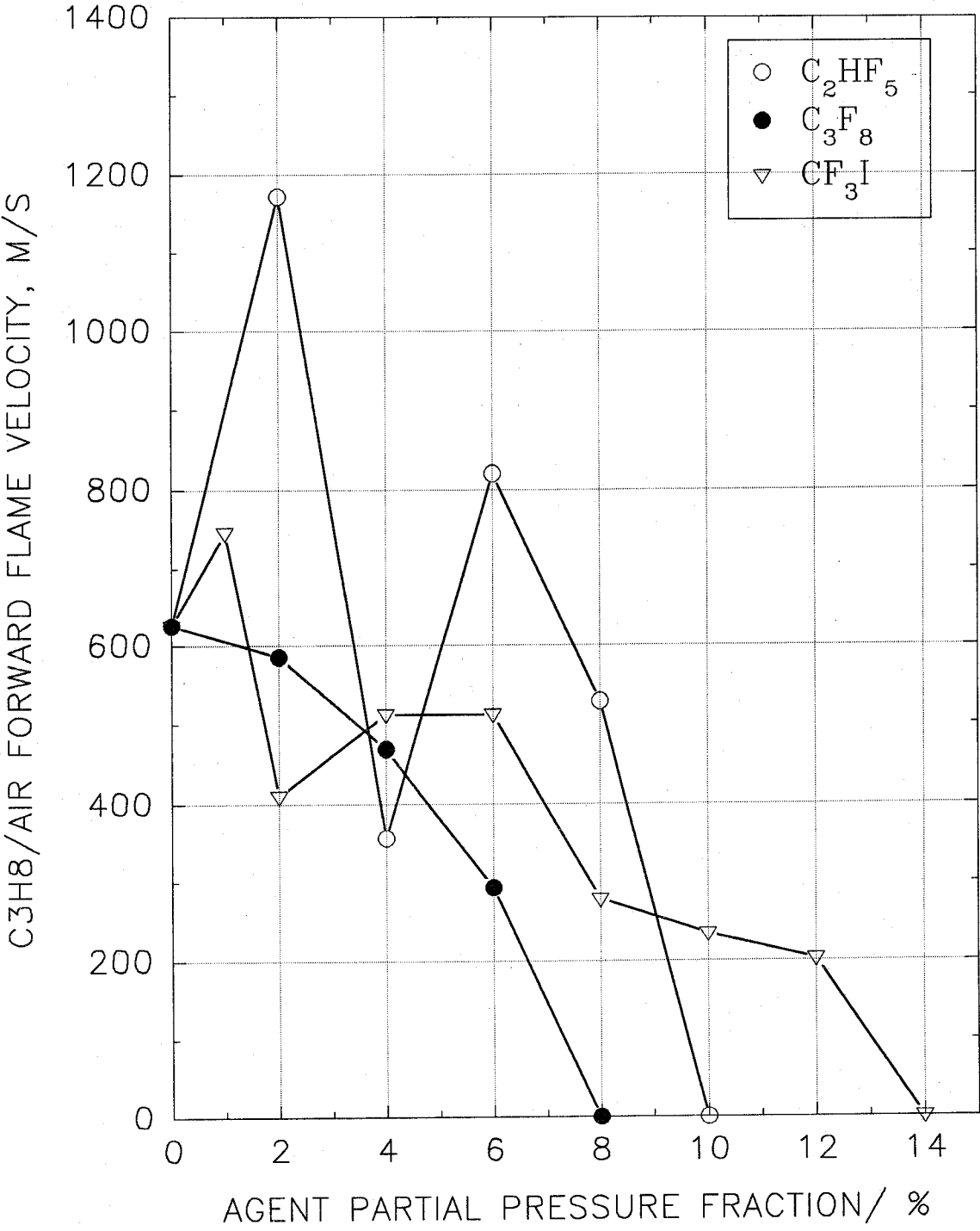


Figure 44. Combustion wave speed in stoichiometric C₃H₈/air mixture (5 m, no spiral).

under operation which is $\pm 0.3 \%$ (the worst case, assuming that only one component leaks). Combining the uncertainty components by root-sum-of-squares (Taylor and Kuyatt, 1994), the resultant expanded uncertainty of establishing the composition of the mixture is 1.2% of the reported value.

The determination of the shock wave amplitude is affected by the combined uncertainty of the dynamic pressure transducer, which is $\pm 1.0 \%$; the combined uncertainty of the transducer amplifier, which is $\pm 0.5 \%$; the combined uncertainty of the digital data acquisition system, which is $\pm 0.5 \%$; and the combined uncertainty of the digital readout device, which is $\pm 0.2 \%$. The root-sum-of-squares of these uncertainties results in an expanded uncertainty in determining the shock wave amplitude of 2.5% of the reported value. The uncertainty in the determination of the shock time differences is affected by the some of the same elements and, after considering the differential nature of the measurement and the uncertainty of the readout device ($\pm 0.1 \%$), can be estimated as $\pm 3.6 \%$.

The uncertainty of the determination of the flame time differences is affected by the following factors: the combined uncertainty of the photodiode which is $\pm 1.0 \%$; the combined uncertainty of the photodiode amplifier which is $\pm 0.5 \%$; the combined uncertainty of the digital data acquisition system which is $\pm 0.5 \%$; the combined uncertainty of the digital readout device which is $\pm 0.1 \%$. The resultant expanded relative uncertainty in the differential measurement of flame velocity is $\pm 3.5 \%$.

The precision of the experimental measurements can readily be determined by observing the agreement between the numerical values obtained in a series of measurements performed in exactly the same way and under the same conditions. Depending on the interpretation of experimental results, either the mean value and the standard deviation is of importance, or the mean value and the maximum absolute deviation is of interest. In the present study it seems that the latter is more meaningful because it indicates the worst possible case that could occur in reality. However, here, both the standard deviation and the maximum absolute deviation are presented as an illustration. The precision of the measurements in these experiments is affected by the following factors: preparation of the compositions of the mixtures; circulation/homogenization of the mixtures; opening of the gate valve; ignition event; formation/propagation of the flame/shock; vibrations of the spiral insert; and ambient temperature changes ($\pm 2^\circ\text{C}$). Ambient air pressure and humidity changes do not affect the results as air is supplied from a gas cylinder.

As an example experimental point, the 8% of CF_3I in the stoichiometric 6.5 percent ethene/air mixture without the spiral insert is analyzed in more detail. For this case, four experiments are taken into account (it is necessary to treat the analysis as very much approximate as from the statistical point of view it would be required to include more experimental points). The means of flame/shock velocities and pressure ratio are 1484 , 1635 m/s and 32.5 , respectively; the maximum absolute deviations of flame/shock velocities and pressure ratio are 157 , 15.2 m/s and 0.97 respectively; the maximum relative deviations of flame/shock velocities and pressure ratio are 10.6 , 0.9 and 3.0% respectively; the population standard deviations of flame/shock velocities and pressure ratio are 101 , 8.7 m/s and 0.61 respectively; and the sample standard deviations (as the number of experiments here is less than 20) of flame/shock velocities and pressure ratio are 117 , 10.1 m/s and 0.70 respectively (the expanded uncertainties are 233 , 20.2 m/s and 1.4). This gives an idea on the precision of the experimental results obtained with the detonation/deflagration tube facility.

2.5 Summary of Results

The fire threat discussed in this section results from a premixed, uninhibited turbulent flame accelerating into a quiescent, premixed, inhibited fuel/air mixture. The response of this highly dynamic situation to different suppressants is sensitive to the fuel, stoichiometry and geometry in the test

section, as well as to the amount of agent used. A successful agent mixture would quench the combustion wave, as evidenced by the disappearance of visible radiation, and diminish the speed and pressure build up across the incident shock wave. However, even with 100 % nitrogen in the test section, a residual shock wave will persist. Short of complete suppression, an agent which reduces the combustion and shock wave speeds and minimizes the pressure increase is desired.

Twelve alternative agents to halon 1301 for protection of aircraft dry bays were ranked previously according to how well each could suppress a laboratory turbulent spray flame and a quasi-detonation (Grosshandler *et al.*, 1994). The experiments were designed to cover the range of conditions that might occur following the penetration by an incendiary device of a fuel cell adjacent to a dry bay. High over-pressures (37:1) were measured when HFC-125 was used to suppress a lean C_2H_4 /air quasi-detonation. The range of initial conditions that lead to a worsening of the situation rather than a lessening of the threat has been investigated in the current study.

The detonation/deflagration tube facility was modified to operate over a less severe range of conditions. Pressure ratios below 9:1 were generated routinely for lean, stoichiometric and rich mixtures. These lower pressures were achieved by removing the spiral insert in the test section and by replacing the more reactive ethene with propane, which is also a better simulant of vaporized jet fuels. The flame speed was monitored close to the entrance of the test section to better assess the immediate impact of the suppressant on the flame. Previously, incident shock speeds over 1500 m/s were recorded. The current experiments with propane as fuel yielded uninhibited flame speeds between 300 m/s and 600 m/s, much closer to the hundreds of meters per second estimated to occur in the full-scale dry bay experiments. A further modification to the facility has been the doubling of the test section length, to 5 m, which has increased the time available for the incident shock to reflect back into the turbulent flame front. This arrangement has allowed the incident shock speed and pressure ratio, the turbulent flame speed, and the conditions behind the reflected shock wave all to be monitored. The reflected shock wave was always found to be stronger than the incident wave, and, with no agent present in the test section, led to a detonation for a range of initial stoichiometries. Thus, with a single shot, we were able to observe the performance of the suppressant under moderate and highly dynamic conditions.

Table 2 summarizes the results of all the detonation/deflagration experiments done with the three agents in this and the earlier NIST study. The suppression conditions are defined as the partial pressure of agent in the test section necessary to either totally quench the radiation from the reactants or to reduce the pressure ratio to the value had 100 % nitrogen been used. The peak pressure ratios and reaction wave speeds refer to the maximum in the plots of pressure ratios (or velocities) versus agent partial pressure fractions. The agent percent is the partial pressure fraction where the maximum is reached. In most cases, small amounts of agent increased the pressure and reaction wave velocity. A value of 0 % implies that the maximum is attained solely at the uninhibited condition. Generally speaking, the ethene quasi-detonation requires considerably more agent to extinguish than the turbulent propane flame; the stoichiometric mixtures require more agent than either rich or lean conditions; C_3F_8 (FC-218) requires the lowest partial pressure fraction to totally suppress both quasi-detonations and turbulent flames; C_2HF_5 (HFC-125) is the least effective suppressant of a quasi-detonation; and CF_3I is the least effective compound for total suppression of stoichiometric and rich turbulent propane flames. The highest pressure ratio observed was for the lean ethene quasi-detonation with 6 % C_2HF_5 added. HFC-125, when added to the stoichiometric turbulent propane flame at a partial pressure fraction of 2 %, greatly accelerated the speed of the reaction wave, but did little to enhance the pressure build up.

The exact conditions that are likely to exist in a dry bay prior to a fire or explosion are impossible to control. Unfortunately, the relative behavior of the three agents under investigation is strongly dependent upon the initial conditions, causing one chemical to be clearly superior under one arrangement and the same chemical to perform poorly in another. There are some general statements

Table 2. Summary of Experimental Results in Detonation/Deflagration Tube

Parameter	Agent	Fuel and Equivalence Ratio					
		Ethene ^a Φ = 0.75 Quasi- detonation	Ethene ^a Φ = 1 Quasi- detonation	Ethene ^a Φ = 1.25 Quasi- detonation	Propane ^b Φ = 0.86 Turbulent Flame	Propane ^b Φ = 1.0 Turbulent Flame	Propane ^b Φ = 1.25 Turbulent Flame
Maximum Pressure Ratio ^c (@ partial pressure %) ^d	none	18 (0%)	26 (0%)	35 (0%)	8.1 (0%)	8.8 (0%)	8.3 (0%)
	N ₂	2.5 (100%)	3.5 (100%)	g	4.5 (100%)	4.6 (100%)	4.5 (100%)
	C ₂ H ₂ F ₅	37 (6%)	29 (6%)	35 (0%)	8.5 (4%)	8.8 (2%)	8.3 (0%)
	C ₃ F ₈	24 (2%)	33 (2%)	37 (2%)	8.2 (2%)	9.5 (2%)	8.5 (2%)
	CF ₃ I	21 (6%)	27 (6%)	35 (6%)	8.1 (0%)	8.8 (0%)	8.3 (0%)
Maximum Reaction Wave Speed ^e , m/s (@ partial pressure %) ^d	none	1170 (0%)	1400 (0%)	1530 (0%)	330 (0%)	620 (0%)	510 (0%)
	N ₂	0 (100%)	0 (100%)	g	100 (100%)	100 (100%)	50 (100%)
	C ₂ H ₂ F ₅	1170 (0%)	1410 (3%)	1530 (0%)	510 (2%)	1180 (2%)	510 (0%)
	C ₃ F ₈	1250 (2%)	1400 (2%)	1530 (0%)	460 (2%)	620 (0%)	510 (0%)
	CF ₃ I	1170 (0%)	1400 (0%)	1530 (0%)	450 (1%)	740 (1%)	590 (1%)
Suppression Partial Pressure Per- cent ^f	N ₂	40%	g	g	g	g	g
	C ₂ H ₂ F ₅	13 to 15%	13 to 15%	13 to 15%	7.5 to 8%	9 to 10%	5 to 6%
	C ₃ F ₈	8 to 10%	> 10%	> 10%	5 to 6%	7 to 8%	3 to 4%
	CF ₃ I	> 10%	> 12%	13 to 14%	5.5 to 6%	13 to 14%	7 to 8%

^a 2.5 m test section, with spiral insert, measurement location 2.2 m into test section
^b 5.0 m test section, without spiral insert, measurement location 0.3 m into test section
^c ± 5% of value relative uncertainty
^d ± 1% absolute uncertainty, and note that 0% implies no enhancement over zero inhibitor conditions
^e ± 11% of value relative uncertainty
^f ± 1% absolute uncertainty, based upon no flame radiation or pressure ratio equal to value attained by 100% N₂
^g no data available

that can be made, though. For example, obstacles in the test section lead to higher shock pressure ratios and initial velocities; ethene/air mixtures lead to higher shock pressure ratios and initial velocities; a residual shock wave remains even when the combustion wave is extinguished; and the speed of the combustion wave without obstacles in the flow responds to the agents in a more chaotic manner than the shock pressure ratio.

The impact of these statements are reflected in Figures 45, 46 and 47 for HFC-125, FC-218 and CF_3I , respectively, in an attempt to identify the best overall chemical for an uncertain application. The response parameter, Ψ , is defined as

$$\Psi \equiv \frac{x - x^*}{x_0 - x^*}$$

where x_0 is the value of the parameter of interest (combustion wave speed, shock speed, or shock pressure ratio) when no agent is present and x^* is the corresponding value when extinction has occurred. A value of unity for Ψ means that the agent has no beneficial impact on the combustion process; $\Psi > 1$ implies the agent exacerbates the situation; a performance parameter near zero is desirable, indicating close to total suppression. The volume percents plotted on the abscissa in Figures 45 through 47 are identical to the partial pressure fractions for ideal gas mixtures. This is a reasonable approximation for the close-to-ideal mixtures under investigation in this work. The volume percent of agent is also a more conventional way to compare the performance of different compounds.

Each point in Figures 45 through 47 represents one measured parameter for an individual experiment. For most of the experiments, the normalized radiation wave speed (determined from the photodiodes) and the normalized shock speed and pressure ratio (measured with the piezoelectric transducers) are plotted. The averages of Ψ are shown as the dotted lines in Figures 45 through 47. The individual values exceed 2.5 (the maximum plotted) for a few of the experiments using C_2HF_5 and CF_3I . These data are not shown in the Figures but were included when the averages of Ψ were computed. By comparing the three curves one gets an indication of general trends, and where one agent is likely to out-perform another.

Examining Figure 45, one sees that the HFC-125, on average, cuts the magnitude of the deflagration/detonation threat in half when its volume fraction is greater than about 8 %. FC-218 (Figure 46) achieves the same level of protection for volume fractions greater than 5 %, while a volume fraction of almost 9.5 % is required of CF_3I to reduce the combustion activity to half (Figure 47). All three agents **increase** the threat for lesser levels. The HFC-125 leads to pressures and wave speeds higher by a factor of 1.8 at volume fractions near 5 %. The FC-218 and CF_3I produce close to a 50 % overshoot when the volume fractions are 2 % and 5 %, respectively. The CF_3I is much more chemically reactive than the other agents, undergoing three transitions between suppression and enhancement as its concentration is increased. A 90 % reduction in the threat requires 14 % CF_3I , 13 % FC-218, and 11 % HFC-125 by volume. Total extinction of the exothermic reaction under all conditions examined in this study requires volume percentages greater than 20 %, 18 % and 16 %, respectively, of CF_3I , FC-218 and HFC-125.

As a benchmark, about 6 % (vol.) of CF_3Br was required to reduce the pressure build-up by 90 % in the earlier NIST study (Grosshandler *et al.*, 1994). This implies that almost three and a half times as much liquid FC-218 is necessary for equivalent protection, while about two and one half times liquid CF_3I must be stored. With this measure of performance the HFC-125 appears to require the least liquid storage of the three halon alternatives tested, requiring just over twice the liquid volume of CF_3Br .

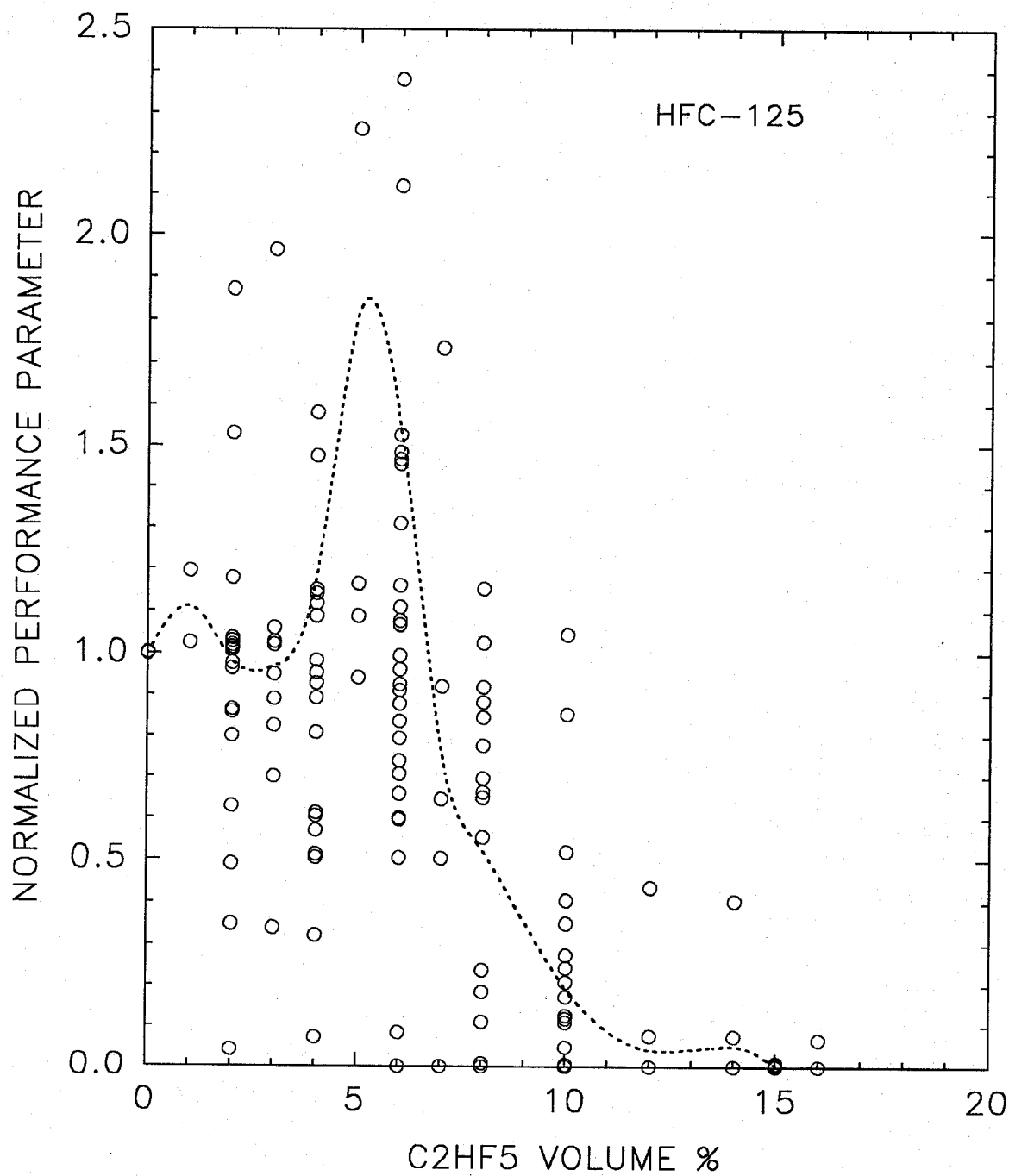


Figure 45. Performance parameter vs. volume fraction of HFC-125 (C₂HF₅).

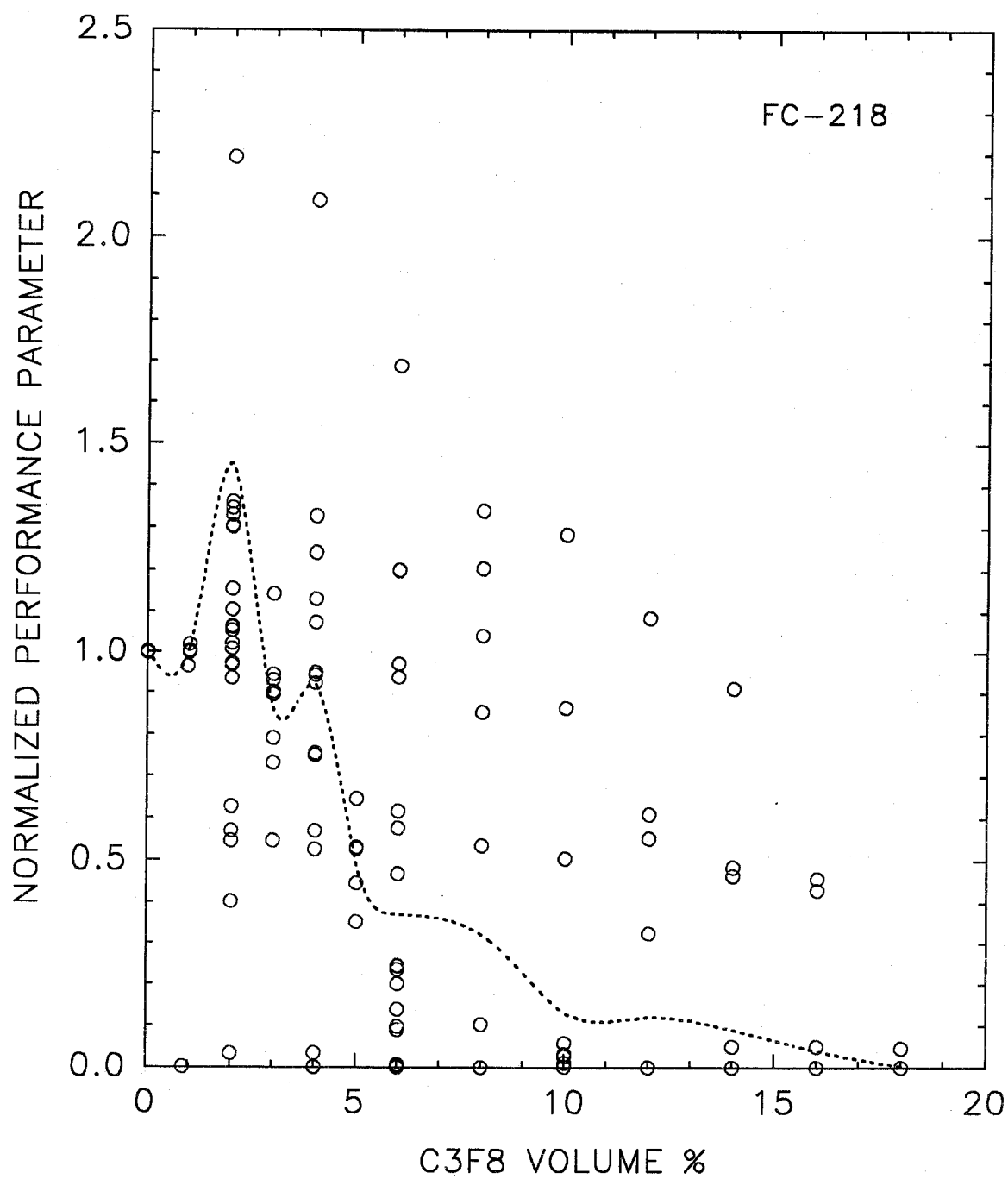


Figure 46. Performance parameter vs. volume fraction of FC-218 (C_3F_8).

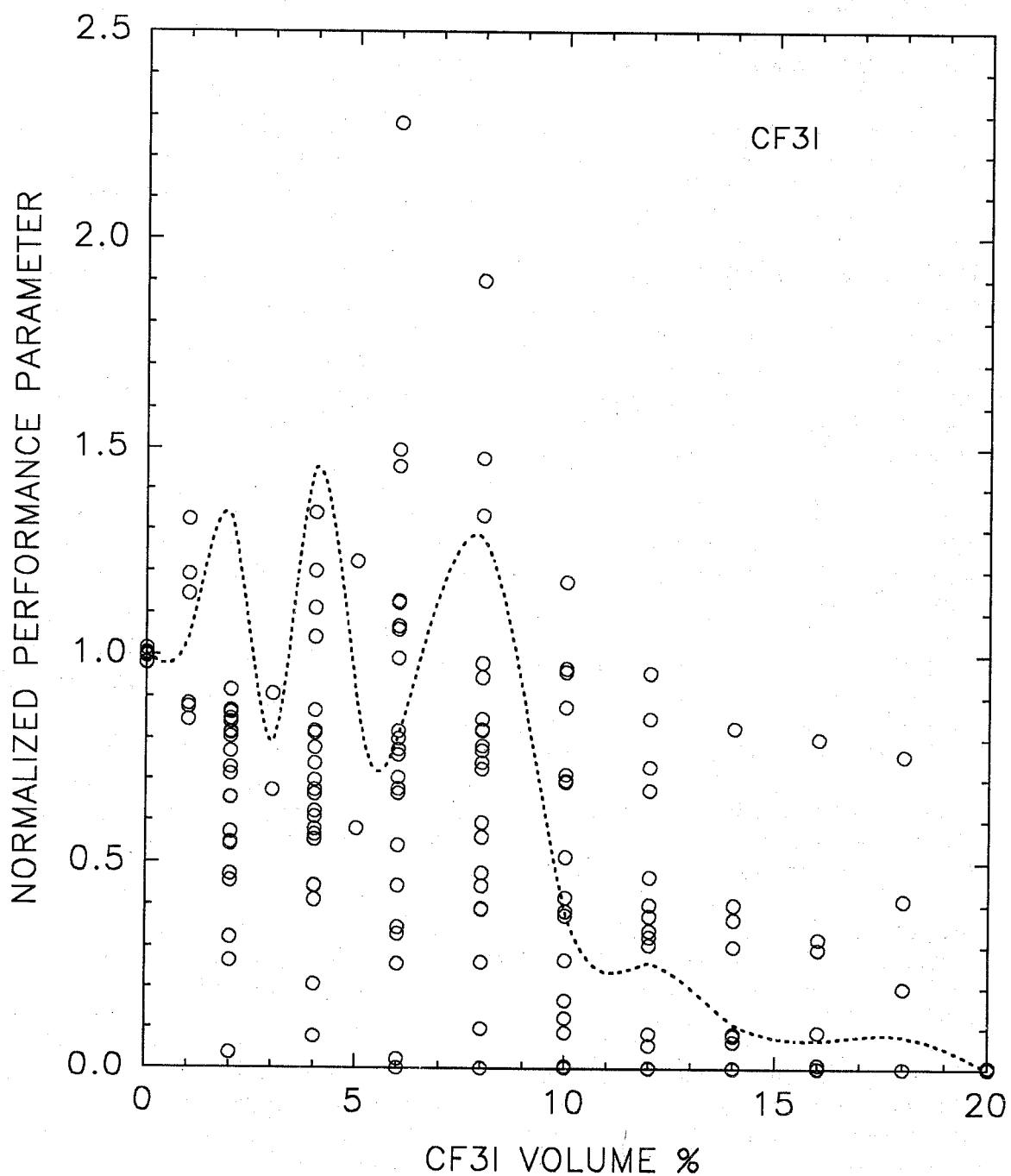


Figure 47. Performance parameter vs. volume fraction of CF₃I.

2.6 Conclusions

The following conclusions are made based on the results obtained:

- a. Combustion and suppression processes in premixed hydrocarbon/air systems under highly dynamic conditions can be more effectively studied in the **modified** two-sectional tube, permitting clear discrimination of the combustion modes and performance among various gaseous extinguishing compounds.
- b. There is a significant difference in combustion behavior between propane/air and ethene/air mixtures: the combustion modes at higher velocities overlap totally in the ethene/air mixture for the two geometric configurations while the propane/air mixture is characterized by a clear separation between the combustion modes for the two arrangements. Also, the regime of equivalence ratios for which combustion is detectable in the tube is much broader for the ethene/air mixture. Furthermore, a detonation was unable to develop in the propane/air mixture when the spiral insert was taken out of the tube.
- c. The ethene/air flame in the quasi-detonation wave under suppression very closely follows the shock wave with the same velocity. The distance between the flame and the shock increases with the amount of an extinguishing agent. At extinguishment, the flame disappears, while the residual shock still exists.
- d. The presence of a hydrogen-containing suppressant in the ethene/air mixture results in a significant increase in pressure ratio relative to that for the pure combustible mixture. The phenomenon occurs also for the compounds not containing hydrogen atoms at relatively lower concentrations. The impact is generally weaker for stoichiometric and rich mixtures than it is for lean mixtures.
- e. C_3F_8 is the most effective extinguishing compound in suppressing and attenuating flame/shock systems in the lean, stoichiometric, and rich ethene/air mixtures under highly dynamic conditions in the detonation/deflagration tube.
- f. Depending on their concentrations, the presence of the three extinguishing compounds in the propane/air mixtures causes the combustion either to be enhanced or suppressed, often with complex extrema exhibited. The behavior is diminished, however, when the mixture becomes richer in fuel content.
- g. CF_3I is the best agent for attenuating shock pressure ratio in the lean, stoichiometric and rich propane/air mixtures. Such performance may be attributed to the significant endothermicity of the decomposition process of CF_3I during the passage of the shock through the mixtures under investigation.

The bottom line is, the conclusions drawn from the previous NIST study have been confirmed. FC-218 provides the most consistent performance over the widest range of fuel/air mixtures and tube geometries. The CF_3I has the greatest positive impact at low partial pressure fractions, but exhibits non-monotonic behavior of flame speed and shock pressure ratio at increasing concentrations. The

dangerously high over-pressures previously exhibited by HFC-125 were not observed during suppression under more moderate (and likely) combustion conditions. Based upon the results from this section alone, none of the three agents can be eliminated from consideration as candidates for dry-bay applications.

2.7 Acknowledgments

This research was supported by the U.S. Naval Air Systems Command and the U.S. Air Force, Wright Laboratory. Wing Tsang, Anthony Hamins and Valeri Babushok of NIST are gratefully acknowledged for helpful discussions during the course of this work. The contribution of Wendy Chien to the experimental phase of this work is highly appreciated. Richard Thorpe, Science Applications International Corporation, is gratefully acknowledged for his editorial contribution.

2.8 References

- Baker, W.E., Cox, P.A., Westine, P.S., Kulesz, J.J. and Strehlow, R.A., *Explosion Hazards and Evaluation*, Elsevier, 1983.
- Bennett, M., Survivability Enhancement Branch, Wright-Patterson AFB, personal communication, 1993.
- Carbaugh, S.G., Survivability Enhancement Branch, Wright-Patterson AFB, Minutes of T2 Meeting, October 14, 1993.
- Chapman, W.R. and Wheeler, R.N.V., "The Propagations of Flame in Mixtures of Methane and Air. Part IV. The Effect of Restrictions in the Path of the Flame," *Journal of the Chemical Society*, London, p. 2139 (1926).
- Gmurczyk, G., Grosshandler, W., Peltz, M. and Lowe, D., "A Facility for Assessing Suppression Effectiveness in High Speed Turbulent Flames," *Eastern States Section Conference*, The Combustion Institute, Princeton, 1993.
- Gmurczyk, G.W., Grosshandler, W.L., and Lowe, D.L., "Suppression Effectiveness of Extinguishing Agents under Highly Dynamic Conditions," *Fire Safety Science - Proceedings of the Fourth International Symposium*, T. Kashiwagi, ed., International Association of Fire Safety Science, USA, pp. 925-936, 1994.
- Gmurczyk, G., and Grosshandler, W., "Suppression of High-Speed Flames with C₁-Halocarbons," *Twenty-fifth Symposium (International) on Combustion*, The Combustion Institute, in press, 1995.
- Grosshandler, W.L., Gann, R.G., and Pitts, W.M., editors, *Evaluation of Alternative In-flight Fire Suppressants for Full-scale Testing in Simulated Aircraft Engine Nacelles and Dry Bays*, NIST Special Publication 861, Gaithersburg, April 1984.
- Lee, J.H.S., "Fast Flames and Detonations," *Chemistry of Combustion Processes*, The American Chemical Society, 1984.
- Lee, J.H., Knystautas, R. and Chan, C.K., "Turbulent Flame Propagation in Obstacle-filled Tubes," *Twentieth Symposium (International) on Combustion*, The Combustion Institute, pp. 1663-1672, 1984.
- Lefebvre, M.H., Nzeyimana, E., Van Tiggelen, P.J., "Influence of Fluorocarbons on H₂/O₂/Ar Detonations Experiments and Modeling," *Progress in Astronautics and Aeronautics*, AIAA, 1992.
- Nettleton, M.A., *Gaseous Detonations: Their Nature, Effects and Control*, Chapman and Hall, 1987.

Peraldi, O., Knystautas, R. and Lee, J.H., "Criteria for Transition to Detonation in Tubes," *Twenty-first Symposium (International) on Combustion*, The Combustion Institute, pp. 1629-1637, 1986.

Sheinson, R.S., Penner-Hahn, J.E., and Indritz, D., 1989, "The Physical and Chemical Action of Fire Suppressants," *Fire Safety Journal* 15, pp. 437-450.

Taylor, B.N., and Kuyatt, C.E., *Guidelines for Evaluating and Expressing the Uncertainty of NIST Measurement Results*, NIST Technical Note 1297, Gaithersburg, September 1994.

Westbrook, C.K., "Chemical Kinetics of Hydrocarbon Oxidation in Gaseous Detonations," *Combustion and Flame* 46, 191 (1982).

3. PHOTODEGRADATION OF CF₃I

Marc R. Nyden
Building and Fire Research Laboratory

Contents

	Page
3. PHOTODEGRADATION OF CF ₃ I	77
3.1 Introduction	78
3.2 Experimental	78
3.3 Results	83
3.4 Conclusions	94
3.5 Acknowledgments	94
3.6 References	94

3.1 Introduction

CF₃I has been identified as a leading candidate for the replacement of halon fire extinguishing agents because of its high degree of effectiveness as a flame suppressant and its short tropospheric lifetime and low ozone depletion potential (Nyden, 1994). Although this compound is known to undergo rapid photolysis in the presence of sunlight, the byproducts of the photodegradation process have not been determined. It is also not known whether this agent will photolyze significantly when it is exposed to radiation from fluorescent lamps and other common sources of indoor light. This knowledge is essential to assess the stability of this agent and the risk of human exposure to it and its byproducts.

The ultraviolet absorption spectrum of CF₃I, which is displayed in Figure 1 (Fahr, 1994), exhibits a peak which is centered near 270 nm and extends beyond 350 nm. This is the so-called A band which is attributed to the superposition of electronic transitions from the ground state (X) to three low lying excited states which are designated, in order of increasing energy, ³Q₁, ³Q₀ and ¹Q₁ (Mulliken, 1935, 1940). These states correspond to the spin orbit couplings which arise from the promotion of an electron from a lone pair orbital (5 pπ) on the iodine to an antibonding orbital (σ*) which is localized in the region between the carbon and iodine nuclei.

Photoexcitation of the A band results in the dissociation of the C-I bond with unit quantum yield in accordance with Equation (1) (Felder, 1992; Van Veen, *et al.*, 1985).



The excited spin orbit state of the iodine (I*) correlates with the ³Q₀ state, whereas the ground state iodine (I) corresponds to the separated atom limit of the ¹Q₁ and ³Q₁ potential energy curves. The dissociation energy of the C-I bond is about 222 kJ/mole (Felder, 1992).

The spectrum of a fluorescent lamp, obtained in this laboratory (Figure 2), indicates a measurable radiative flux out to about 310 nm. The observation that this spectrum overlaps with the absorption spectrum of CF₃I suggests that this agent should undergo appreciable photolysis when it is exposed to radiation from fluorescent lights. The objectives of this study are to determine the extent of this degradation and the nature of the compounds which are likely to be produced when CF₃I is released in an indoor environment.

3.2 Experimental

The photodegradation experiments were conducted in a quartz cell which is transparent to ultraviolet and visible radiation with wavelengths longer than 200 nm. The cell was cylindrical in shape with a diameter of 5 cm. The long axis of the cell provided an optical path length of 10 cm for the spectroscopic measurements which were made before and after irradiation of the sample. The windows of the cell were made out of CaF₂ which is transparent from about 10000 nm (1000 cm⁻¹) in the infrared all the way to about 165 nm (60606 cm⁻¹) in the ultraviolet. Independent experiments were conducted using either a 1000 watt xenon arc or a 40 watt fluorescent lamp as the photolytic source. A schematic of the experimental setup is depicted in Figure 3.

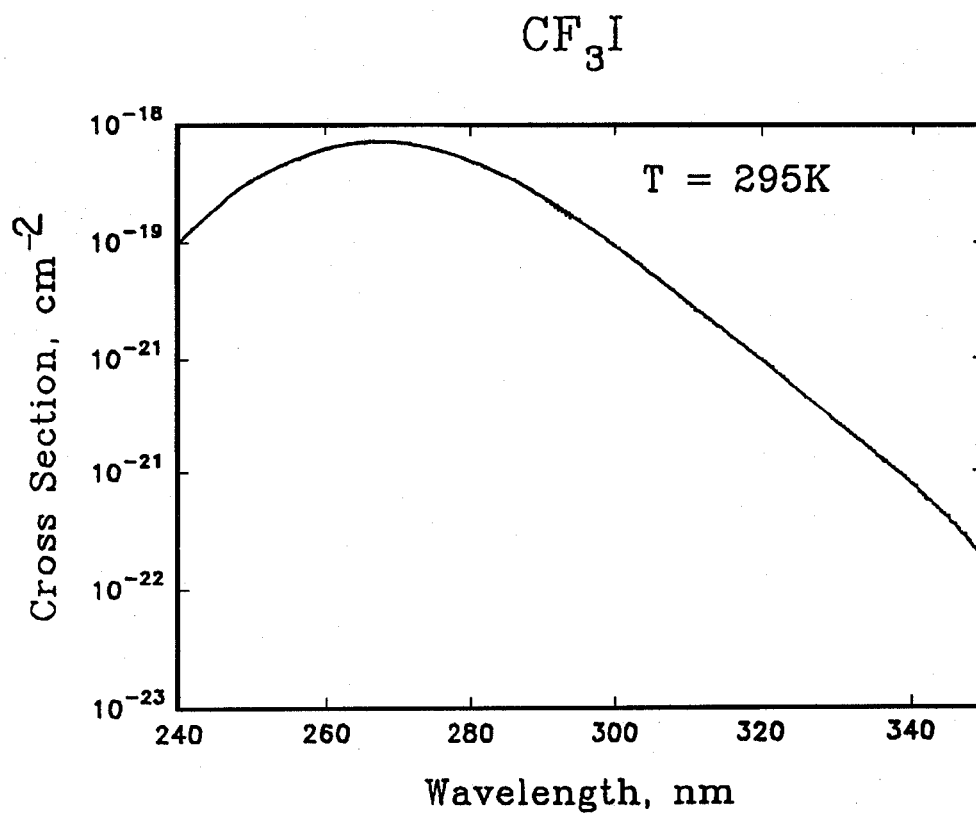


Figure 1. The UV spectrum of CF_3I at 295 K.

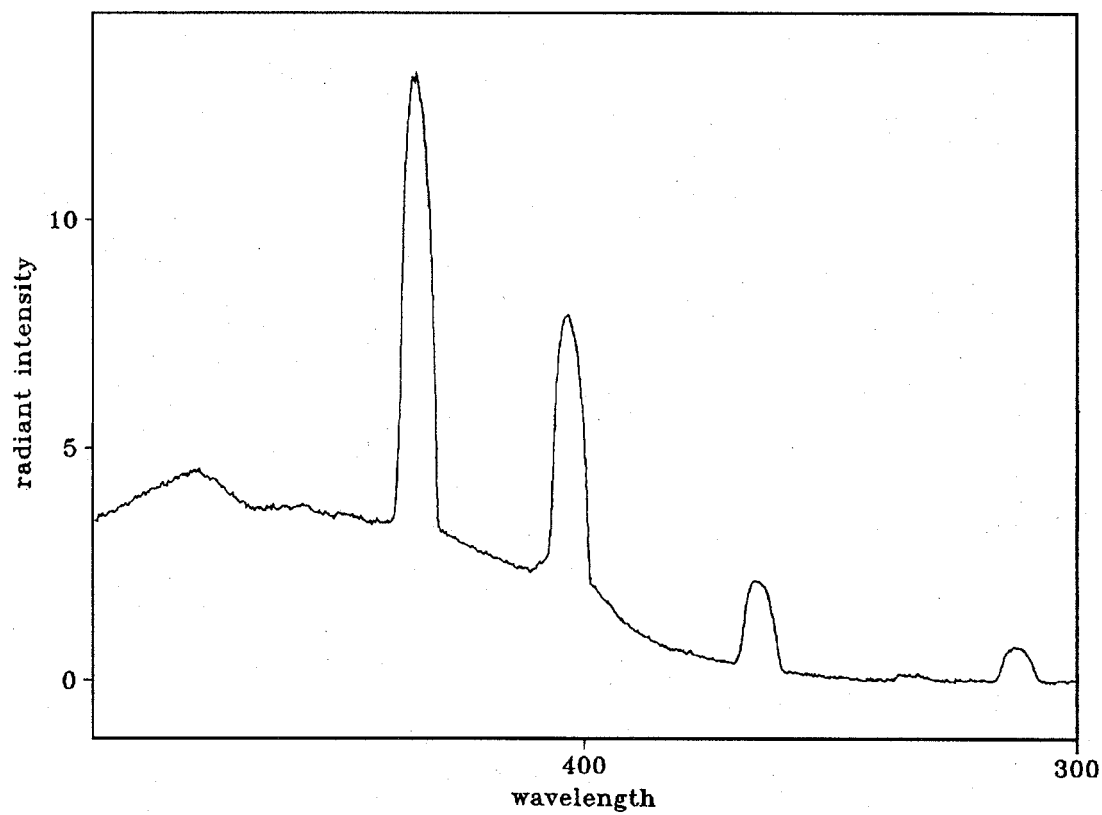


Figure 2. The near UV-VIS spectrum of a common fluorescent lamp.

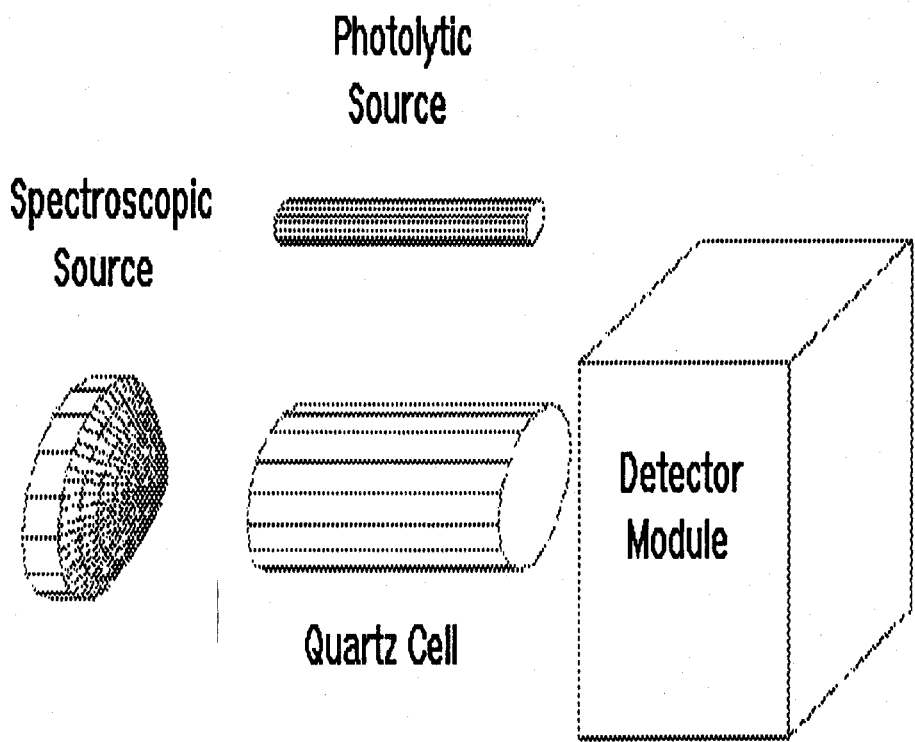


Figure 3. Schematic showing the experimental setup for the photodegradation experiments.

The CF₃I used in these experiments was obtained from PCR, Inc.¹ The stated purity was 99 % which was confirmed by GC/MS analyses performed on a Hewlett Packard 5710A gas chromatograph with an open split interface to a HP 5970 mass selective detector. Samples containing approximately 6.7 kPa of the agent, either by itself or mixed with a variety of other gases, were irradiated for 30 min with the high intensity Xe arc lamp. The experiments designed to measure the extent of degradation in the radiation field generated by the fluorescent lamp, however, were conducted over a much longer period of time (several days) because the rate of photolysis was much slower than it was with the Xe arc. The effects of adding various gases including O₂, Ar and air were also investigated.

The products of the photolysis of CF₃I were characterized by ultraviolet (UV), visible (VIS) and infrared (IR) spectroscopy. The UV/VIS spectra were measured over the range extending from about 250 nm to 850 nm using a fiber optic spectrometer manufactured by Ocean Optics, Inc. in conjunction with either a xenon flash (UV) or a tungsten halogen (VIS) source. The IR spectra, which were measured at 1 cm⁻¹ resolution and signal averaged over 64 scans, were obtained using a Midac open path Fourier transform infrared (FTIR) spectrometer.

Quantitative estimates of the fraction of unreacted agent (f) were obtained from least squares fits of the spectra of the original to the spectra of the photolyzed mixtures in accordance with Equation (2).

$$f = \frac{\int_{\nu} A_o(\nu) A_p(\nu) d\nu}{\int_{\nu} A_o(\nu)^2 d\nu}, \quad (2)$$

where A_o(ν) and A_p(ν) are the measured values of the IR absorbance of the original and photolyzed mixtures at the frequency, ν, and the integration is over the band in CF₃I which extends from 2272 - 2230 cm⁻¹. The extent of degradation is the fraction of reacted agent which is given by 1-f. The uncertainties in the spectroscopic measurements were computed as the standard error of the estimated concentration using Equation (3) (Haaland, 1980).

$$\Delta f = \sqrt{\frac{\int_{\nu} [f A_o(\nu) - A_p(\nu)]^2 d\nu}{(n - 1) \int_{\nu} A_o(\nu)^2 d\nu}}, \quad (3)$$

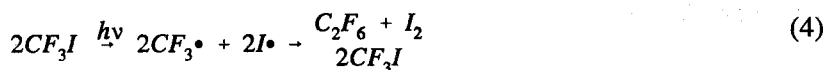
where n is the number of data points in the specified frequency range.

¹ Certain trade names and company products are mentioned in the text or identified in an illustration in order to specify adequately the experimental procedure and equipment used. In no case does such identification imply recommendation or endorsement by the National Institute of Standards and Technology, nor does it imply that the products are necessarily the best available for the purpose.

In addition, there were a number of sources of systematic error which might have affected the reproducibility of the experimental results. These include variations in the composition of the sample mixtures resulting from leaks and contamination of the photolytic cell, as well as variations in exposure times and in the intensity of the photolytic source which could have affected the amount of energy absorbed by the sample. The magnitudes of the resulting errors are difficult to quantify, however, past experience suggests that they can be as much as an order of magnitude larger than the uncertainties in the spectroscopic measurements calculated from Equation (3).

3.3 Results

The first set of experiments was designed to determine the extent of degradation of the pure agent in the presence of high intensity radiation from the Xe arc lamp. The expected reactions are summarized in Equation (4).



In fact, a comparison of the IR spectra measured before and after the irradiation (Figure 4) indicate that the net effect of the photolysis was minimal, presumably because the reverse reaction is favored over the reactions leading to the formation of new products. This is consistent with the entries in the NIST kinetic database which indicate that the rate constant for the formation of CF₃I from CF₃ + I is about twice as fast as the corresponding value for the formation of C₂F₆ + I₂ (Mallard, 1993). The observed extent of degradation, as estimated by least squares analysis over the region between 2230 cm⁻¹ - 2272 cm⁻¹, was only 5.5 % (Table 1). The formation of a small amount of C₂F₆, however, is apparent from the presence of a sharp peak centered at about 1250 cm⁻¹ in the difference spectrum displayed at the top of Figure 5. This assignment may be confirmed by comparing the spectrum in Figure 5 with the reference spectrum of C₂F₆ in Figure 6 (Sadler, 1993).

Additional measurements were performed to determine whether the presence of an inert gas would have an effect on the photolysis of CF₃I. In these experiments, a mixture consisting of 8.6 kPa of Ar and 6.7 kPa of CF₃I was exposed to the radiation from the Xe arc lamp for 30 min. The extent of degradation was about 4.1 % (Table 1); which is comparable to the value obtained in the photolysis of the pure agent. The small discrepancy in the extent of degradation (1.4 %) is indicative of the range of values obtained in repetitive experiments and is most likely due to the systematic errors delineated in the previous section. On this basis, it was concluded that the effect of the inert gas was minor.

The presence of even a small amount of O₂, however, has a dramatic effect on the photodegradation chemistry of CF₃I. This is apparent in the comparison of the UV spectra (Figure 7) of a mixture containing 6.7 kPa of CF₃I and 0.94 kPa of O₂ taken before (top) and after (bottom) irradiation for 30 min with the Xe arc lamp. A thick, white smoke formed almost immediately upon applying voltage to the arc. Shortly thereafter, a brown residue was observed to form in the crevices where the windows were joined to the cell. The IR spectra displayed in Figure 8 exhibit a significant loss of spectral intensity in the region between 2230 cm⁻¹ and 2272 cm⁻¹, which correlates with depletion of the agent, and a concomitant increase in absorbance in the region between 2300 cm⁻¹ and 2400 cm⁻¹, which is associated with the formation of CO₂. At the same time, the presence of I₂ was indicated by the appearance of a new feature centered at about 530 nm in the VIS spectrum which is

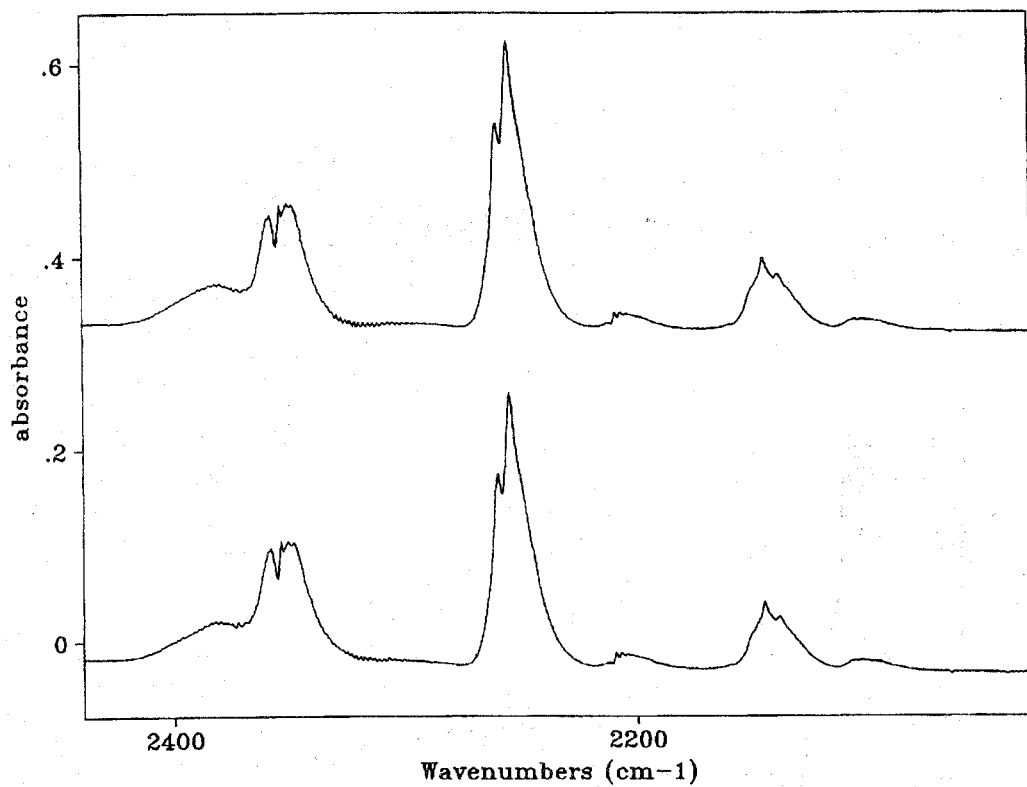


Figure 4. The IR spectra of CF_3I taken before (top) and after (bottom) irradiation for 30 min with the Xe arc lamp.

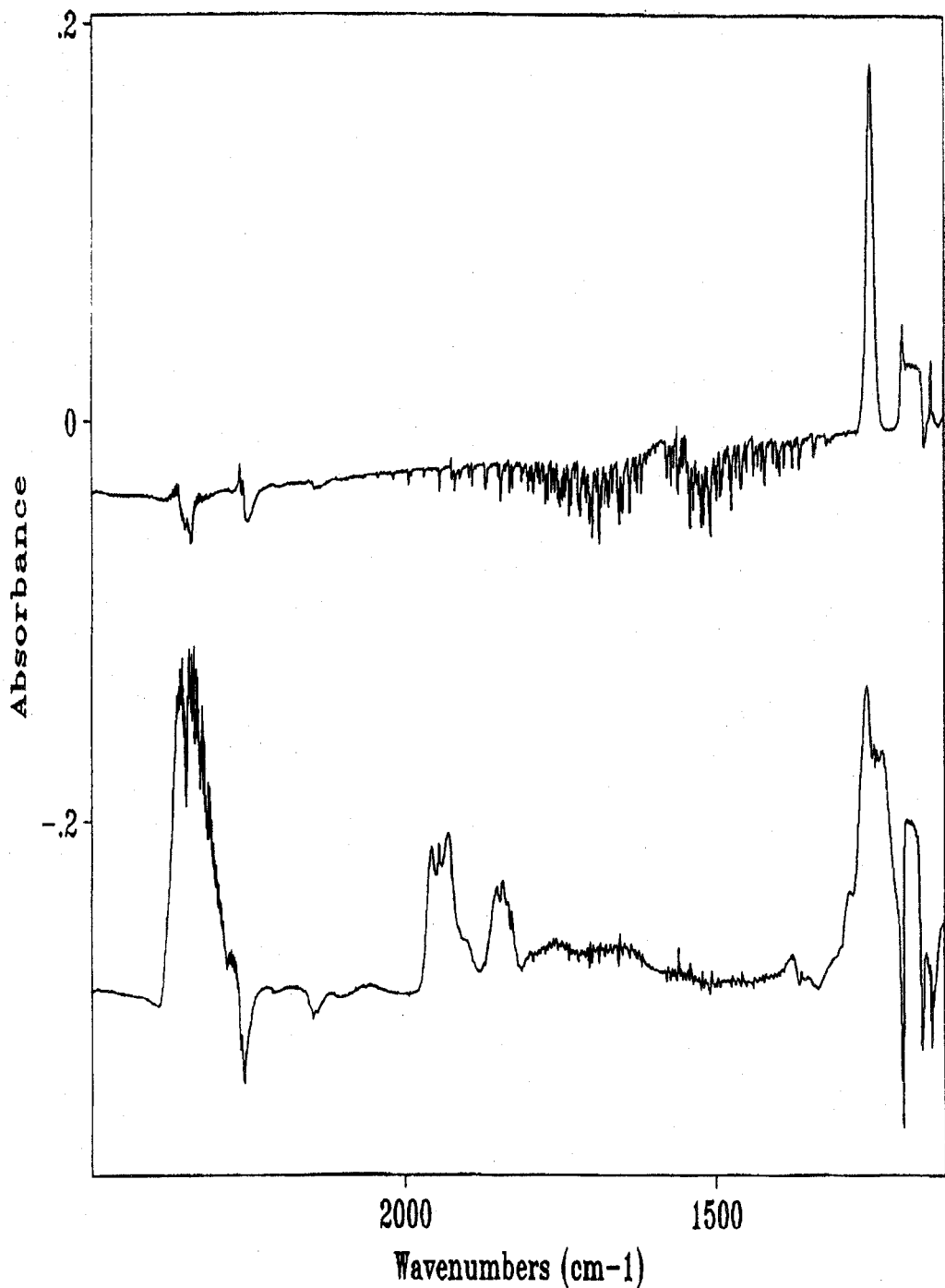


Figure 5. The differences in the IR spectra taken before and after irradiation with the Xe arc lamp of pure CF₃I (top) and a mixture of CF₃I and O₂ (bottom).

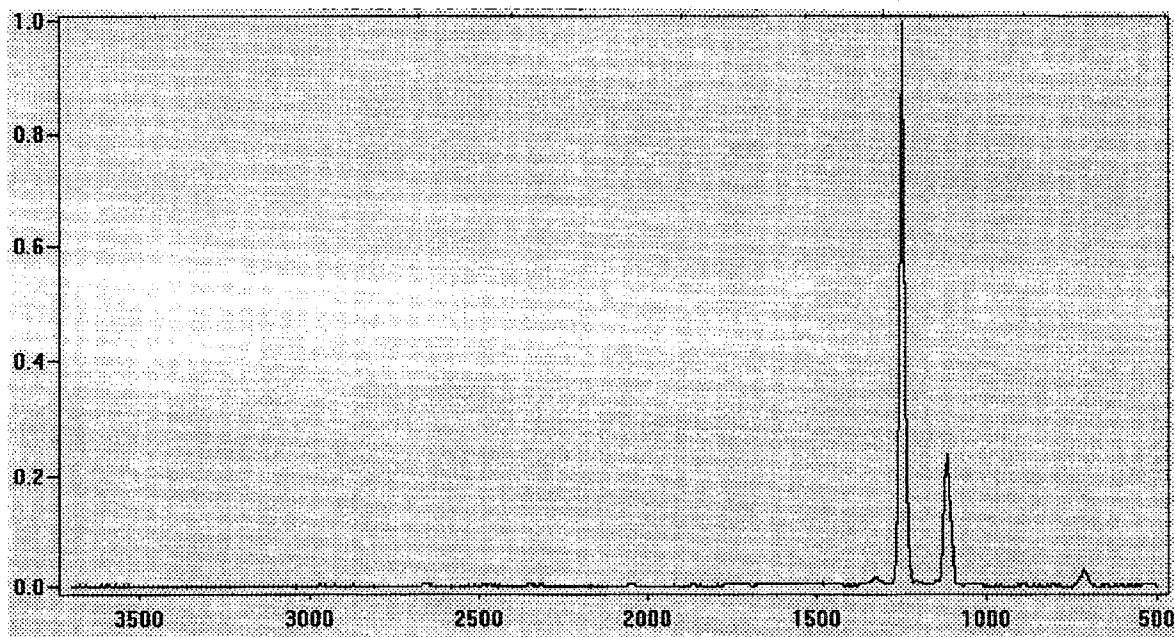


Figure 6. Library spectrum of C_2F_6 .

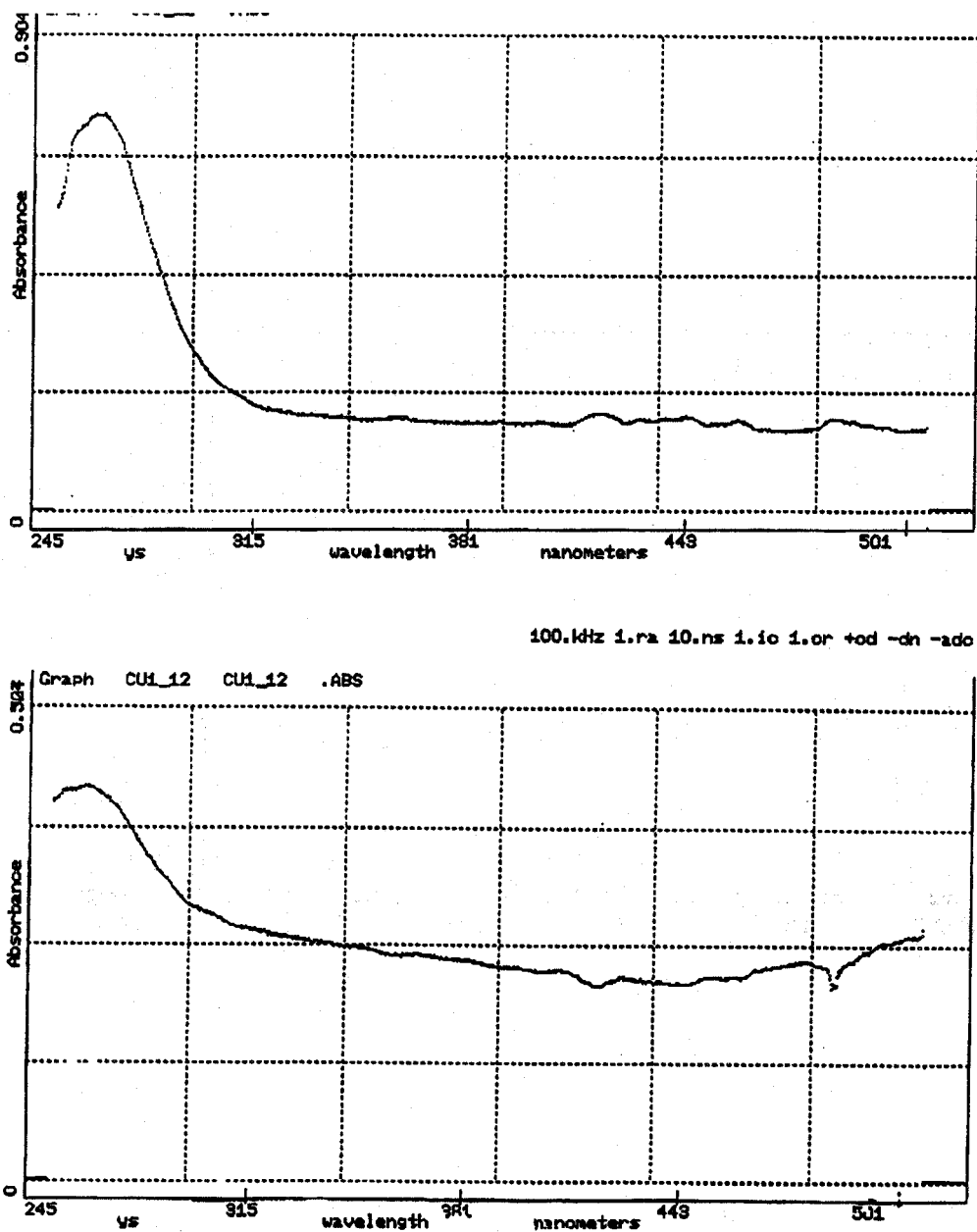


Figure 7. The UV spectra of a mixture of CF_3I and O_2 taken before (top) and after (bottom) irradiation for 30 min with the Xe arc lamp.

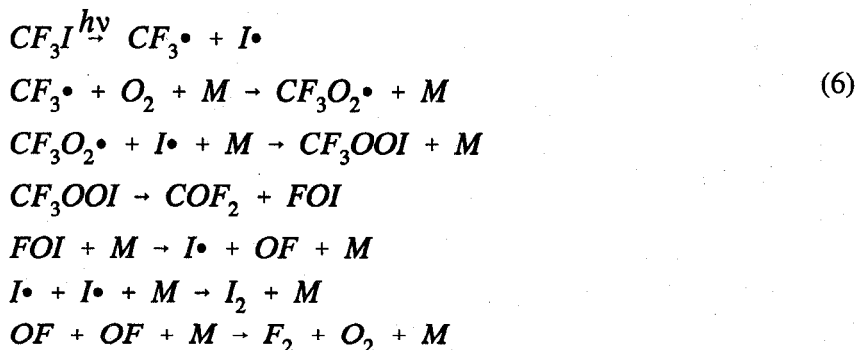
displayed in Figure 9. The extent of degradation, based on the change in optical density in the region between 2230 cm⁻¹ and 2272 cm⁻¹ in the spectra of the original and photolyzed mixtures in Figure 8, was approximately 32 %. This result implies that the stoichiometry of the photo-oxidation process is 2.3 mol of CF₃I per mole of O₂ (i.e., 6.7(.32)/0.94). A ratio of approximately 2:1 is obtained if the 5 % degradation of the agent, which would be expected to occur upon depletion of all of the available O₂, is taken into account.

The peak centered at 1950 cm⁻¹ in the difference spectrum displayed at the bottom of Figure 5 is attributable to COF₂. A spectrum of this compound, which was measured in this laboratory, is displayed in Figure 10. Carbonyl fluoride is an extremely toxic compound (Sax and Lewis, 1987) which can react further with H₂O to produce HF as summarized in Equation (5).



The smaller peak at about 1850 cm⁻¹ was not definitively assigned but it is consistent with the presence of compounds possessing a carbonyl group (C=O). There was an indication in the IR spectra that ethanol, which was used to clean the cell, was present as a contaminant during some of the photolytic experiments. It is possible, therefore, that this peak is associated with a product of a photochemical reaction involving the ethanol and that is not related to the photodegradation of the agent.

A mechanism for the photo-oxidation of CF₃I was put forward in a recent paper by Clemitshaw and Sodeau who used FTIR spectroscopy to measure the quantum yield of the formation of COF₂ in the photolysis of CF₃I at 253.7 nm (Clemitshaw and Sodeau, 1995). Their mechanism, which is consistent with the reaction stoichiometry of 2 mol of CF₃I to 1 mol of O₂ which was observed in this study, is summarized in Equation (6).



Another set of experiments were performed to determine the extent of degradation of CF₃I in the presence of radiation from a common fluorescent lamp. The photolysis of a mixture of 6.7 kPa of CF₃I and 82 kPa of O₂ was monitored for about 5 days. During this period of time, about 28 % of the CF₃I was transformed into products. The brown residue, which had been observed in the previous photo-oxidation measurements, formed after the first few hours of exposure to the lamp.

Table 1. Extent of Photodegradation Based on Eq.(2)

Conditions	$\int A_o(v)dv$	$\int A_p(v)dv$	% Degradation
Vacuum Xe arc lamp	4.55	4.32	5.5 ± 0.1
8.6 kPa Ar Xe arc lamp	5.80	5.53	4.1 ± 0.2
0.94 kPa O ₂ Xe arc lamp	3.59	2.37	31.7 ± 0.3
82 kPa O ₂ fluorescent lamp	3.20	2.30	28.1 ± 0.2
95 kPa air fluorescent lamp	4.33	3.34	23.2 ± 0.1

In the final experiment, the valve on the cell containing 6.7 kPa of CF₃I was opened to the atmosphere and allowed to equilibrate. The valve was closed after a few minutes and the resulting mixture of CF₃I and air was placed under the fluorescent lamp for approximately 24 hours. The idea was to simulate as closely as possible the environment inside of a building during a release of the agent. The IR spectra before (top) and after 24 hours of exposure to the radiation from the fluorescent lamp (bottom) are displayed in Figure 11. A comparison of these spectra indicate a 23 % reduction in optical density in the region between 2230 cm⁻¹ and 2272 cm⁻¹ which is attributable to the loss of CF₃I, and a concomitant increase in optical density in the region between 2300 cm⁻¹ and 2400 cm⁻¹ which is due to the formation of CO₂.

The first order rate constant obtained from the observation of a reduction of 23 % in the concentration of agent in 24 hours is $3 \times 10^{-6} \text{ s}^{-1}$. Not surprisingly, this is of the same order of magnitude as the value which was calculated for the rate constant of the photolysis of CF₃I in direct sunlight (Nyden, 1994).

It is then useful to estimate the extent of degradation of CF₃I and to assess the potential hazard to occupants should an accidental discharge take place. The magnitude of the threat to public safety will vary significantly depending on the ventilation and lighting in the vicinity of the release. Thus, for example, the rupture of a cylinder of CF₃I in a well-lit storage area will pose a more serious threat than a controlled release of the same agent into a dark dry bay.

As an example of the former, consider an accidental release into 100 m³ room which is uniformly lit with a series of 40 watt fluorescent fixtures. This is a conservative scenario as the mean photon flux incident on the agent in this room (at ground level) would be expected to be far lower than it was in the experiment where the photolytic cell was positioned only a few centimeters from the lamp. If the contents of a 5 kg storage cylinder were to be distributed uniformly throughout the space, the concentration of agent would be about 0.6 % by volume (assuming a ventilation rate of zero). The degree of degradation of the agent 5 min after the release, based on the value of the rate constant for

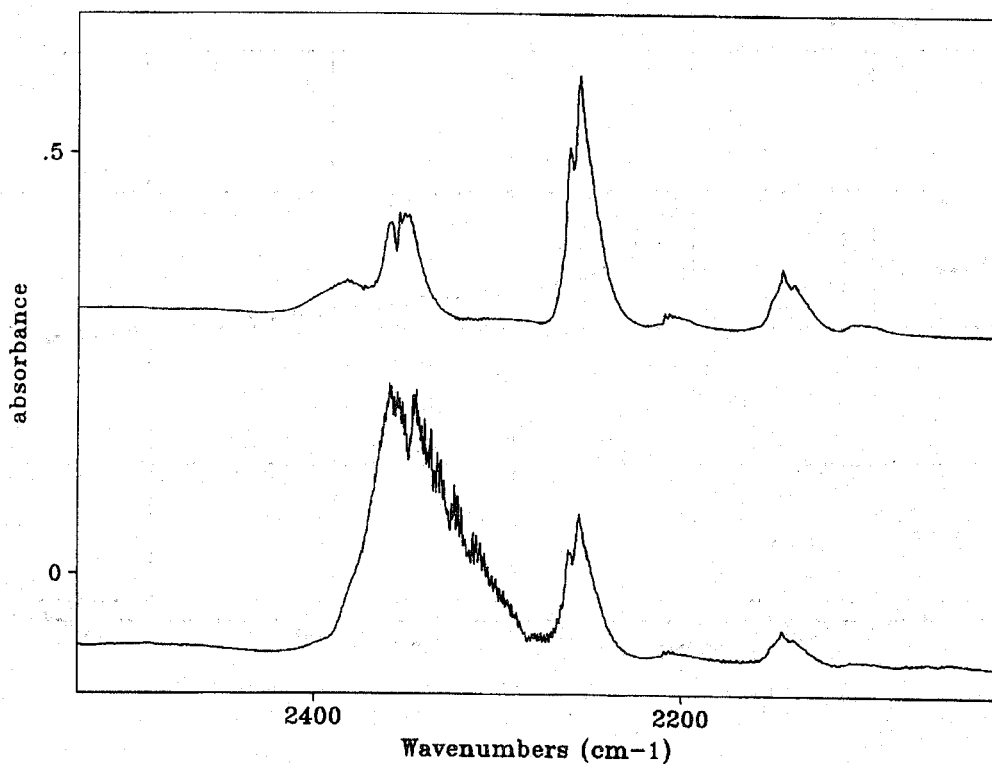


Figure 8. The IR spectra of a mixture of CF_3I and O_2 taken before (top) and after (bottom) irradiation for 30 min with the Xe arc lamp.

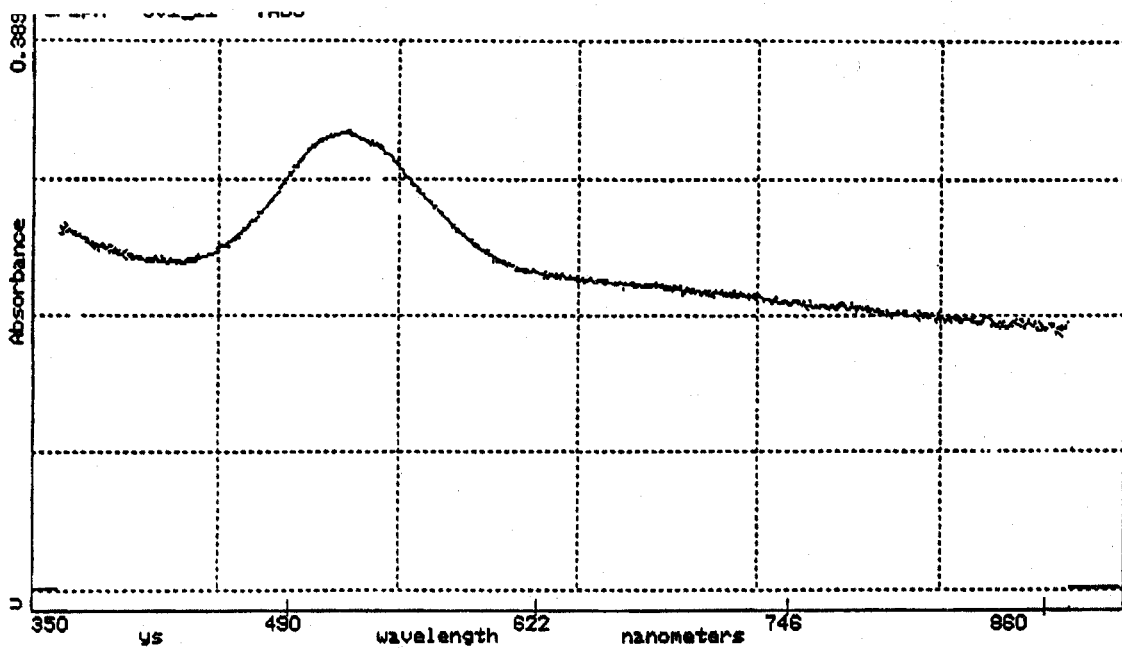


Figure 9. The VIS spectrum of a mixture of CF₃I and O₂ taken after irradiation for 30 min with the Xe arc lamp.

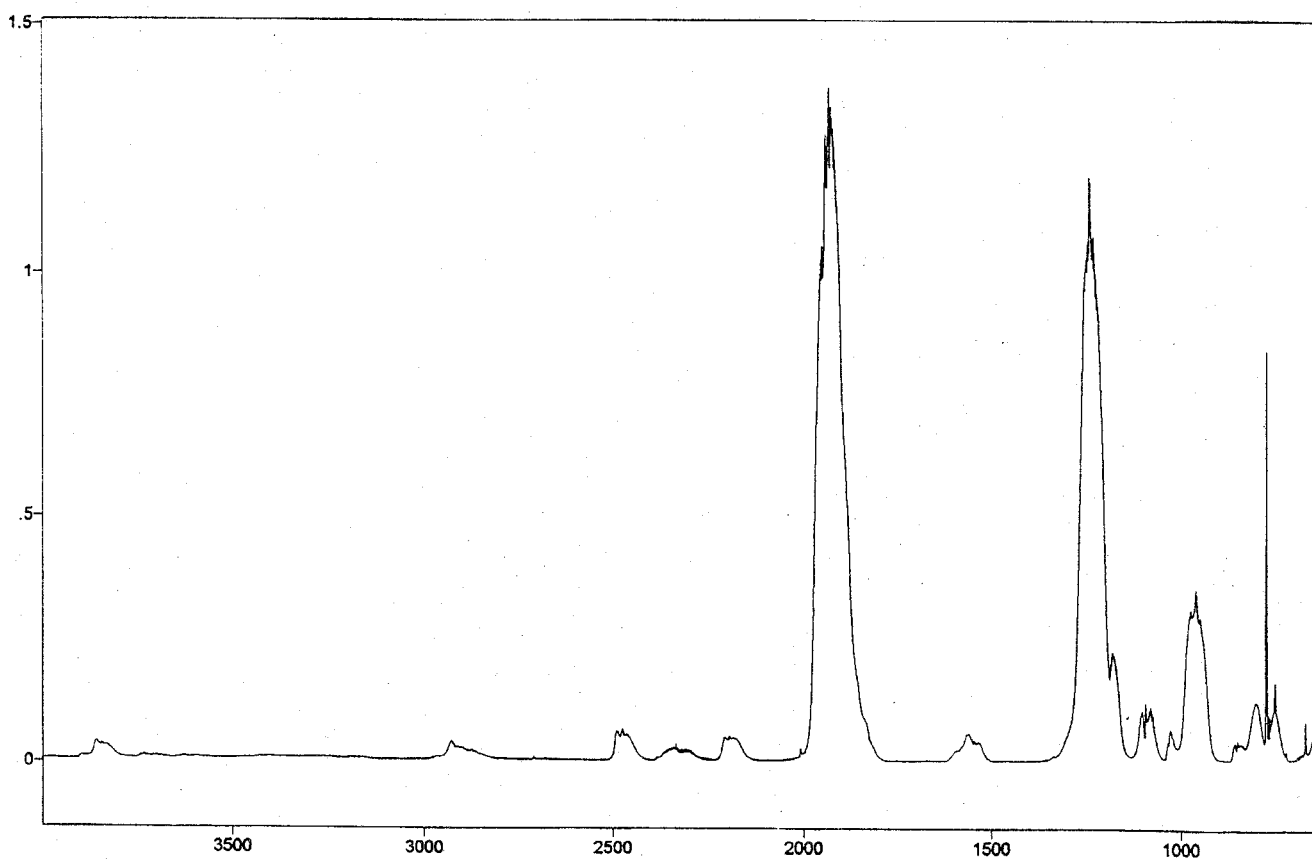


Figure 10. Spectrum of COF_2 .

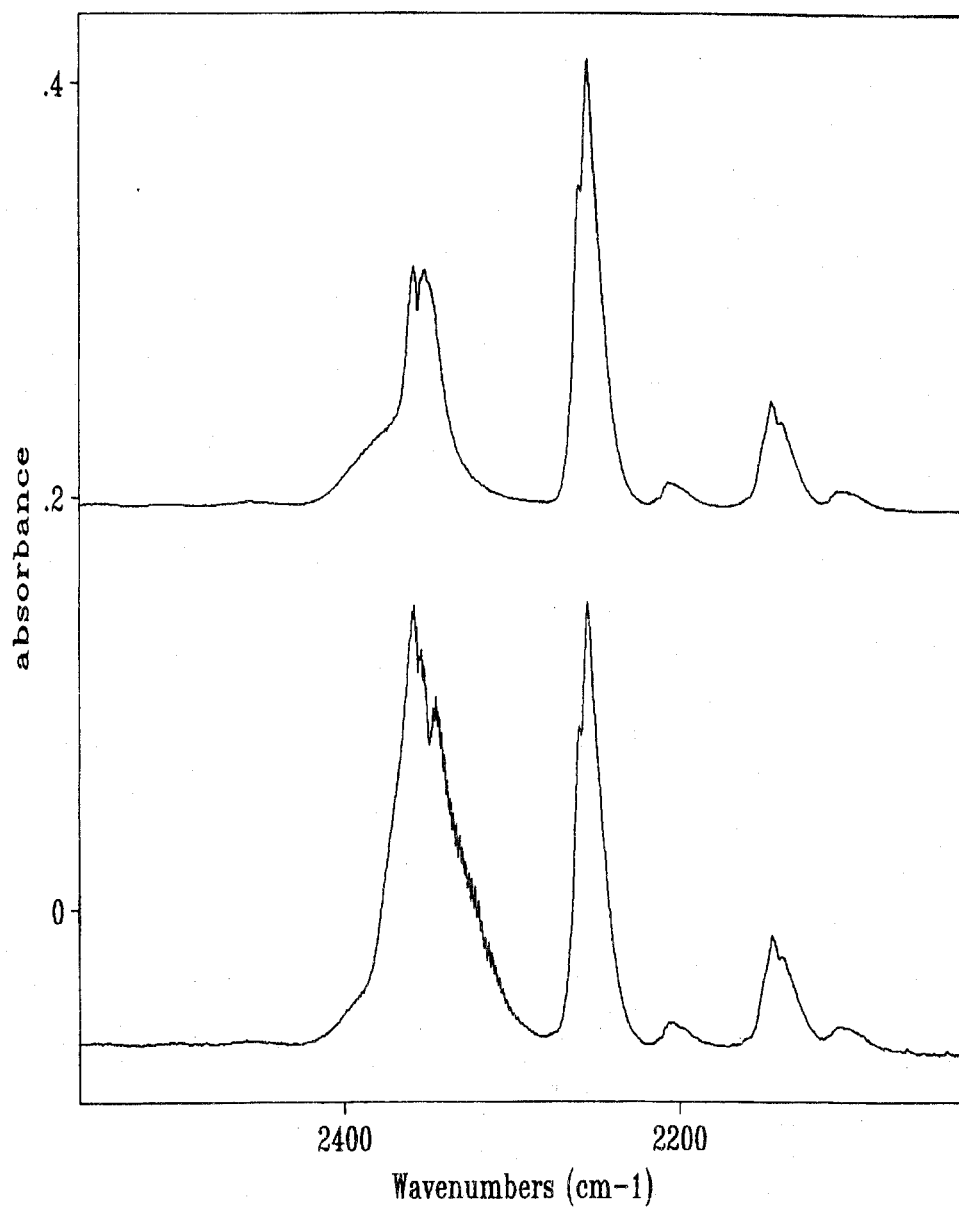


Figure 11. IR spectrum of a mixture of CF_3I and air after irradiation for 24 hours with a fluorescent lamp.

photodegradation given above, would then be only about 0.1 %. Even if all of the fluorine atoms were converted to HF (and none deposited on the walls), the concentration of HF would only be about 20 $\mu\text{L/L}$ by volume. Alternatively, a COF_2 concentration of about 5 $\mu\text{L/L}$ would be possible if all of the agent were to be converted to this compound (and none were to react further to form HF). Given the conservative assumptions used in this estimation, it seems unlikely that anyone who evacuated promptly would be seriously harmed by exposure to the degradation products. It would, however, be beneficial to assess the effect of exposure to low concentrations of HF on the integrity of sensitive electronic equipment in the vicinity of a release.

3.4 Conclusions

CF_3I photolyzes in the presence of radiation from common fluorescent lights with a rate constant which is comparable to that in photolysis in direct sunlight. The potential byproducts of this process include COF_2 and HF. The high level of toxicity associated with these compounds merits their inclusion when considering the impacts of accidental releases of CF_3I in well-lit, occupied spaces. However, the experiments performed as part of this study indicate that the indoor rate of photolytic decomposition is quite low, and a calculation based on conservative estimates further indicates that the resulting concentrations of the most hazardous degradation products (i.e., HF and COF_2) would also be expected to be quite low.

3.5 Acknowledgments

The GC/MS analyses were performed by Mr. Richard Harris of the Fire Science Division of NIST. The author also wishes to acknowledge the helpful advice and guidance offered Dr. Barna Laszlo and Dr. Robert Huie of the Chemical Kinetics and Thermodynamics Division of NIST.

3.6 References

- Clemetshaw, K.C. and Sodeau, J.R., "The quantum-yield of formation of CF_2O in the gas-phase photo-oxidation of CF_3I at 253.7 nm," *J. PhotoChem. and PhotoBio A:Chem.* **86**, 9-14 (1995).
- Fahr, A., Nayak, A.K., Huie, R.E., "Ultraviolet absorption Spectrum of CF_3I ," Halon Options Technical Conference: Albuquerque, NM, 465 (1994).
- Felder, P., "The influence of the molecular beam temperature on the photodissociation of CF_3I at 308 nm," *Chem. Phys. Letters* **197**, 425-432 (1992).
- Haaland, D.M. and Easterling, R.G., "Improved Sensitivity of Infrared Spectroscopy by the Application of Least Squares Methods," *Appl. Spectrosc.* **34**, 539-548 (1980).
- Mallard, W.G., Westley, F., Herron, J.T., Hampson, R.F. and Frizzell, D.H., "NIST Chemical Kinetics Database - Ver. 5.0," NIST Standard Reference Database **17**, (1993).
- Mulliken, R.S., "Electronic Structures of Polyatomic Molecules. VII. Amonia and water type molecules and their derivatives," *J. Chem. Phys.* **3**, 506-514 (1935).
- Mulliken, R.S., "Intensities in Molecular Electronic Spectra. X. Calculations on mixed-halogen, hydrogen halide, alkyl halide, and hydroxyl spectra," *J. Chem. Phys.* **8**, 382-395 (1940).

Nyden, M.R. "Flame Inhibition Chemistry and the Search for Additional Fire Fighting Chemicals," in *Evaluation of Alternative In-Flight Fire Suppressants for full-scale Testing in Simulated Aircraft Engine Nacelles and Dry Bays*, NIST SP 861, National Institute of Standards and Technology, Gaithersburg, MD, 467, 1994.

Sadtler Search Software, "IR Vapor Phase Library," Bio-Rad Laboratories, Inc. (1993).

Sax, N.I., Lewis, R.J., "Dangerous Properties of Industrial Materials," Van Norstrand Reinhold, New York (1987).

Van Veen, G.N.A., Baller, T., De Vries, A.E. and Shapiro, M., "Photofragmentation of CF₃I in the A band," *Chem. Phys.* **93**, 277-291 (1985).

4. EFFECT OF SUPPRESSANTS ON METAL FIRES

Thomas J. Ohlemiller and John R. Shields
Building and Fire Research Laboratory

Contents

	Page
4. EFFECT OF SUPPRESSANTS ON METAL FIRES	97
4.1 Introduction	98
4.2 Description of Apparatus	99
4.2.1 Burn Configuration	99
4.2.2 Combustion Chamber	99
4.2.3 Flow System	102
4.2.4 Sample Ignition	104
4.2.5 Test Materials	104
4.2.6 Data Acquisition	105
4.3 Results and Discussion	105
4.3.1 Magnesium	105
4.3.2 Titanium	108
4.4 Conclusions	117
4.5 References	118

4.1 Introduction

This study is focussed on two specific metals, magnesium and titanium. These metals, usually in the form of various alloys, are utilized in several locations in modern military aircraft. Magnesium is used extensively in structural areas of aircraft; titanium also has structural uses but is most commonly found in jet engines, for example, as compressor and turbine blades.

These metals, and alloys dominated by them, are flammable. Ignition of these metals requires that they be heated to near their melting points: *ca.* 650 °C for magnesium and *ca.* 1800 °C for titanium (somewhat lower for alloys). Their ease of ignition is much less than that of familiar solid organic materials such as polymers which typically ignite when heated to 300-400 °C. Bringing the metal surface to these temperatures is also more difficult than it is for organic materials (*i.e.*, it requires a higher heat flux) because the metals have much higher thermal inertia values, thus requiring more heat to achieve a given surface temperature (Elrod *et al.*, 1980).

Once ignited both metals are capable of intense, high temperature burning¹ as a result of the very high heats of formation of their oxides. Titanium requires more restrictive conditions for continued combustion than does magnesium, at least in part because its oxide accumulates in the molten metal surface region, slowing the rate of oxidation (Clark, Moulder and Runyan, 1975). As a result, continued combustion requires either a significant pre-heating of the metal, elevated oxygen partial pressure or shearing away of the molten oxide/metal layer (Clark, Moulder and Runyan, 1975; Rhein and Baldwin, 1980). All of these conditions can be found in jet engines; the shearing is provided by the high velocity of the gases and centrifugal forces (Fox, 1976; Anderson and Manty, 1978; Elrod and Lyon, 1979; Strobridge *et al.*, 1979; Rhein and Baldwin, 1980; Elrod *et al.*, 1982; Baldwin *et al.*, 1984).

The current study is directed toward the interaction of suppressants with these burning metals. Although it is possible for the metal alone to be the burning material in need of suppression, the concern here is broader. Military aircraft fires in general are most frequently suppressed with halons. A fire may start with a fuel or hydraulic fluid leak and spread, involving parts composed of magnesium or titanium. This fire will be manually or automatically flooded with halon compounds (or, in the future, their replacements). The use of halogen-containing suppressant agents on metal fires is considered hazardous and is not recommended (Andrews, 1981) but in the mixed materials environment of a military aircraft, where a fuel fire is the more likely threat, they are used, regardless of the possible involvement of metal aircraft components. Experience to date, based on halon suppressants, shows that this is an effective approach. The work here specifically addresses the concern of whether candidate halon replacements will pose any greater hazard in their interaction with a metal fire than do the currently used halons.

Halogens, particularly fluorine, can combine with magnesium or titanium with an evolution of more heat than is obtained from combining with oxygen. The heat of formation of magnesium fluoride is 83 % higher than that of magnesium oxide. For titanium there are several possible products but the most relevant comparison is probably titanium tetrafluoride which has a heat of formation that is 70 % higher than that of titanium dioxide. Simple calculations (below) suggest that under some conditions either of these metals might strip the halogens from a halon such as halon 1301 and evolve more heat than could be obtained from reaction with oxygen. Thus the suppressant could become an

¹In pure oxygen at one atmosphere pressure, the adiabatic combustion temperatures of magnesium and titanium are both approximately 3000 °C (Strobridge *et al.*, 1979).

accelerant. There are warnings in the literature regarding this (McCutchan, 1954; Maykuth, 1964; Kuchta *et al.*, 1965 & 1966; NASA, 1970; Rhein & Baldwin, 1980; Tapscott, *et al.*, 1986). Unfortunately, most of these references describe experiments in which the effect of a halogen-containing agent on a metal fire cannot be clearly quantified. The fires are qualitatively observed to "accelerate" or "flare-up" when sprayed with the halon agent from an extinguisher. The possible role of purely physical factors, such as intensification due to scattering of the burning metal by flash vaporization of liquid droplets of the halon, cannot be assessed.

Kuchta *et al.* (1966) did perform some more quantifiable experiments with heated titanium wires in hot gas streams containing the decomposition vapors of various halocarbons. Various halon vapors were heated to 450 °C and then passed over titanium wires at 600 °C; the increase in wire temperature was measured. This increase should be reflective of the heat release rate due to reaction of the halon vapors with the wire surface. Halon 1301 gave the least increase in wire temperature of any halon examined though it was still significant. This result does confirm that halons will chemically react with titanium in an exothermic manner (under these conditions). The variation of effect with halon type implies kinetic effects, perhaps both in extent of vapor decomposition and in rate of attack on the metal. The data are too limited to resolve such issues.

The present study is limited to examining the effect of the vapors of various halogen-containing suppressants on the burning of pure magnesium and titanium rods in a slow flow of oxygen-containing gas. The test configuration was instrumented to allow quantitation of the effect of the vapors on the rate of burning. As will be seen, the results were not as the literature leads one to expect in that the metal burning process was always either slowed or extinguished under the range of conditions examined.

The agents examined in the presence of burning magnesium included halon 1301 (the reference case), HFC-125, HFC-227ea, FC-218 and CF₃I. For titanium, time limitations narrowed the study to halon 1301, HFC-227ea² and HFC-125.

4.2 Description of Apparatus

4.2.1 Burn Configuration. For both metals, the burning configuration was upward propagation along a thin rod with the oxidant gas flowing in the same (upward) direction. This configuration was chosen so that gravity, by causing dripping of the molten metal in the case of titanium, would provide the necessary fresh metal surface to yield sustained combustion. It was not feasible, in the time allotted for this study, to set up the high speed, elevated temperature flows used previously to study titanium combustion propagation under jet engine conditions. Upward propagation was chosen because Sato *et al.* (1983) showed that downward propagation can produce much more erratic results (*i.e.*, highly variable propagation rates) due to the dripping molten metal haphazardly making contact with the rod as it flows/falls downward, causing spot ignition. Oxidant flow velocity levels were limited to low values by practical constraints on mass flows borne of the use of bottled gases.

4.2.2 Combustion Chamber. Figure 1 is a not-to-scale, cross-sectional sketch of the overall experiment; Figure 2 is a scaled, cross-sectional assembly drawing of the combustion chamber. The chamber is made of brass and consists of three sections, assembled in such a way as to allow relatively convenient cleaning and sample replacement. The bottom section accepts the incoming gas flow and

²HFC-227ea is referred to throughout the remainder of this discussion simply as HFC-227.

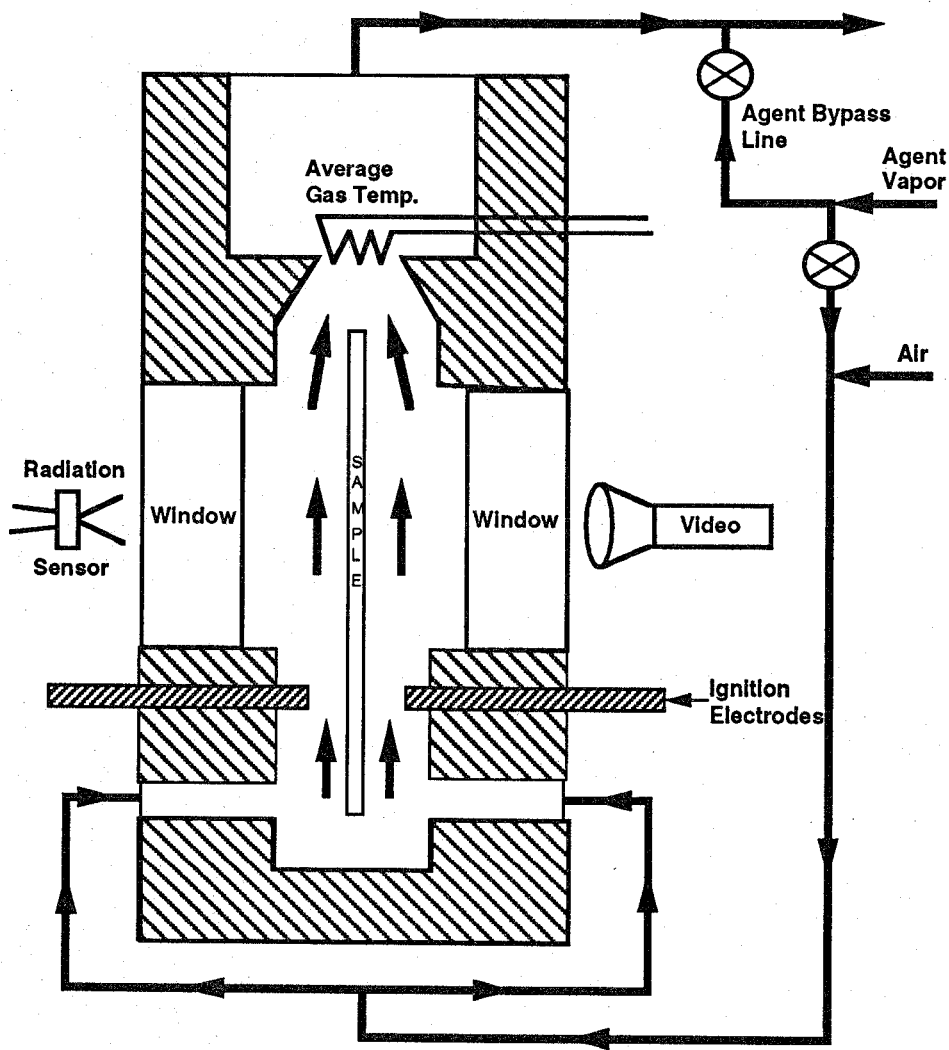


Figure 1. Schematic of metal combustion experiment.

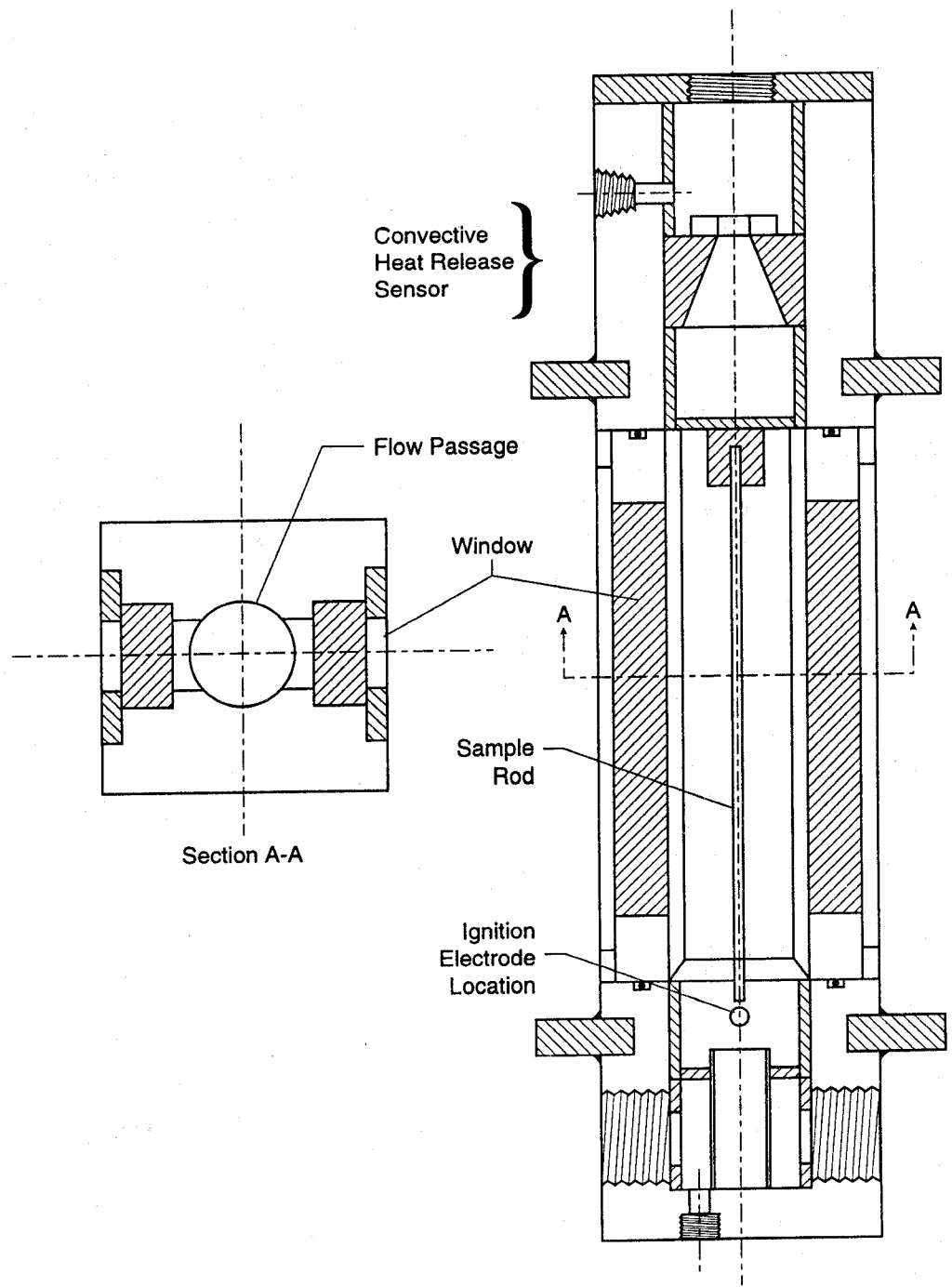


Figure 2. Scaled assembly drawing of combustion chamber.

directs it upward. This section also includes fittings for a pair of electrodes used in the metal ignition process. This section includes, as well, a small cup to catch and quench the drips of molten metal. The middle section contains the sample rod (16 cm long) suspended in the gas flow, between two windows for clear observation. The front window, through which a video camera records the burning process, is Pyrex. The rear window is Vycor which provides light transmission out to about 2.5 μm . A calibrated thermopile-type radiometer (Dexter Research Center, Model 2M-HS)³ views the burning rod through this latter window (a non-imaged view), providing a signal proportional to the radiative emissions of the burn zone. Early tests indicated that small burning particles emitted from the burning titanium rods could pit the windows (which are only about 2.5 cm from the burning rod). Thus the windows were lined with a thin (0.25 mm), reusable sheet of Kel-F polymer film which is essentially transparent to all of the radiation passing through the Vycor or Pyrex windows. The upper section of the chamber contains a bare wire thermopile consisting of four 0.125 mm diameter type S thermocouples wired in parallel; the four thermocouple junctions are arrayed in the flow. This thermopile samples the average temperature of the gases passing through the chamber downstream of the combustion process; it thus provides a measure of the convective heat output of the burning process. This measure could be made absolute by calibration with an electrical energy source in the sample burning region; this was not done here because only relative performance (to halon 1301 as a baseline) was of interest.

The chamber can be operated at pressures up to 1.48 MPa (200 psig). A burst disk is incorporated in the system because information on the possible flammability of mixtures of the candidate halon replacement agents in elevated oxygen atmospheres is not available. (It is known that some halogenated hydrocarbons are flammable in some oxygenated mixtures (Perlee, Martindill and Zabetakis, 1966).) A practical limit of 5 grams of incoming oxidant gas per second was imposed to accommodate the use of bottled gases and the limited supplies of some of the halon replacement agents. This fixed mass flow defines the outer envelope of achievable pressure and velocity conditions. The maximum oxidant flow velocity in the sample section thus varies from 3.7 m/s at 0.1 MPa (atmospheric pressure) to 0.27 m/s at 1.48 MPa.

4.2.3 Flow System. Figure 3 is a schematic of the flow system in its simplest configuration, used when the agent vapor pressure at room temperature was sufficient to supply the desired add-on level to the oxidant flow. All pressures were measured with gages rated by the manufacturer at $\pm 0.5\%$ accuracy. All flows were measured with rotameter-type flowmeters which had been calibrated with a dry test meter in the pressure and flow range of usage; flow accuracy is estimated to be $\pm 2-3\%$.

Figure 3 shows that the agent vapor could be added upstream or downstream of the combustion chamber. As will be described below, this bypass feature was necessary because the agent vapor tended to attack the sample ignition system. When the agent was introduced upstream of the chamber, a static mixer assured concentration uniformity in the oxidant flow prior to the chamber.

When flow of an oxidant stronger than air was needed, it was obtained by mixing air and pure oxygen. This was done using a two tube, mixing rotameter for which both tubes were calibrated as above. It should be noted that oxygen level data reported here are those prior to the agent vapor add-on.

In order to operate the chamber at pressures above the room temperature vapor pressure of the agent of interest, it is necessary to meter and introduce the agent as a liquid, mix it with the oxidant

³ Certain trade names and company products are mentioned in the text or identified in an illustration in order to specify adequately the experimental procedure and equipment used. In no case does such identification imply recommendation or endorsement by the National Institute of Standards and Technology, nor does it imply that the products are necessarily the best available for the purpose.

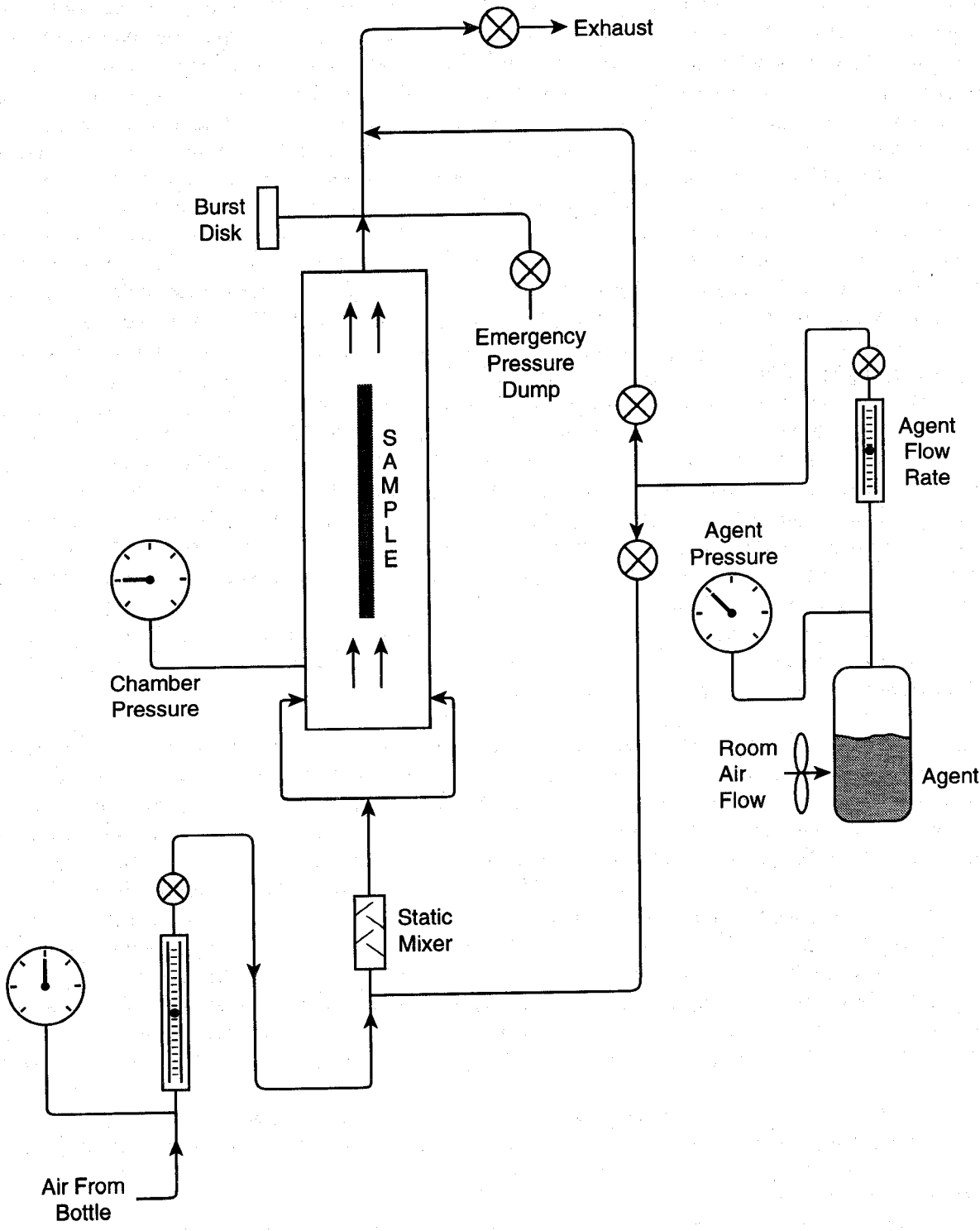


Figure 3. Flow system associated with combustion chamber.

gas in a heater section then cool the total flow back to room temperature. A system to achieve this was in fact built. However, when it was found that the agent vapors attacked the ignition system, this approach had to be discontinued. In the flow system shown in Figure 3, the agent vapor needs to be added a short distance upstream of the chamber so that the flow time to the chamber is short (compared to the sample burn time). The system required to vaporize the agent with heating and then cool the entire gas stream was several meters in length. In some conditions, the sample could have burned excessively before the agent vapor reached it. Thus all tests were confined to pressure conditions in which the desired agent level could be achieved using the vapors in the headspace above a liquid agent reservoir.

4.2.4 Sample Ignition. Ignition of the small diameter metal rods proved to be more problematical than expected. For magnesium, copper electrodes were used in the base of the combustion chamber to supply electrical current to a nichrome heating wire from a low voltage DC power supply. One end of a length (about 4 cm) of magnesium ribbon (0.25 mm thick by 3 mm wide) was wound around the bottom few mm of the sample rod; the other end was folded over the nichrome wire. Heating of the nichrome wire was to ignite the magnesium ribbon and the ribbon would ignite the rod. This was satisfactory as long as there was no agent vapor in the oxidant flow. When agent vapor was present, it attacked the nichrome wire, frequently causing it to break before the magnesium ribbon could ignite. This behavior necessitated the agent vapor bypass path shown in Figure 3. With this in place, the agent vapor was introduced into the chamber exhaust line during the sample ignition process; this allowed the agent flow system to achieve a steady-state condition. When the sample rod had clearly ignited and propagated combustion 1-2 cm, the agent vapor was switched into the chamber inlet line, reaching the sample burn zone a few seconds later.

Titanium, with its much higher melting point, could not be ignited in the above manner, even though the sample rod was only about 1 mm in diameter. An attempt was made to use an electric arc welder boosted by a high frequency, high voltage arc stabilizer in the manner of Baldwin, Beach and Rhein (1984). The arc welder itself was rated at 230 amperes AC; the arc stabilizer superimposed 3500 VAC of radio frequency oscillations to assist in arc formation and retention. The arc stabilizer proved to be totally ineffective for reasons which could not be established; it would not assist in arc formation even for atmospheric air gaps of a small fraction of a millimeter. Furthermore, it was very disruptive to the data acquisition system despite careful attempts at electromagnetic shielding. Ultimately, it was found that the titanium rods could be ignited by the contact resistance heating between tungsten electrodes and the surface of the sample rod. This required about 200 amperes and took as much as 20-30 seconds to yield ignition.

The combustion of the sample was recorded with a Hi-8 video camera which viewed the sample through a #12 welder's light filter. Progress of the propagation was also sensed by three blackened thermocouples (0.13 mm diameter; chromel/alumel) recessed into the sidewall of the middle section of the combustion chamber at intervals of 4.0 cm. Radiative heating of these was sufficient to yield a peak in voltage output as the combustion zone passed the thermocouple location.

4.2.5 Test Materials. The 1.6 mm diameter magnesium rod was 99.9 % pure. It appeared to have been extruded. The titanium rod was 1.14 mm in diameter; it was commercially pure grade, used for welding purposes. It appeared to be wire-drawn. The initial focus of the titanium work had been on alloy 6-2-4-2 (6 % aluminum, 2 % molybdenum, 4 % zirconium and 2 % tin) which is one of several forms in which titanium is frequently used in aircraft. However, it was found that ignition of the available 3 mm square rod required an atmosphere of more than 60 % oxygen. This alloy could not be obtained in the small diameter which the above ignition system could more readily handle. Thus the focus was shifted to the pure metal, obtainable in the smaller diameter form. The qualitative

conclusions of this work are believed to be applicable to high titanium alloys as well as the pure metal used here.

4.2.6 Data Acquisition. All data channels were hard-wired to a Strawberry Tree Workmate data acquisition board through an isothermal terminal board. Strawberry Tree Quicklog software was used as the data acquisition program. Data were acquired at 2 Hz with 14 bit resolution.

4.3 Results and Discussion

4.3.1 Magnesium. An initial short series of tests was conducted using pure air with no added agent to explore the possible sensitivity of the burning rate to other test parameters. Table 1 shows the results of varying both the chamber pressure and gas flow velocity in the test section. Chamber pressure was varied from 0.24 MPa (20 psig) to 0.79 MPa (100 psig); air flow velocity in the test section was varied from 13 to 42 cm/s. Note that the mass flow rate of air was held constant at one of two values which differed by 42 %.

Chamber pressure variation at a constant air mass flux will hold the mass transfer rate of oxygen to the burn zone constant while varying the gas phase chemical reaction rates between magnesium vapor and oxygen. This is done in the first four tests of Table 1. In the next three tests, the pressure (and thus the chemical reaction rate) is held constant but the mass flux is increased to enhance the oxygen mass transfer rate. Here the 42 % increase in mass flux will yield roughly a 20 % increase in mass transfer rate since the mass transfer coefficient is approximately proportional to the square root of Reynolds Number for this configuration (Bird, Stewart and Lightfoot, 1960).

No effect on burning rate from either of these changes clearly emerges from the data of Table 1. The average burning rate at the lower air mass flow rate is 3.9 ± 0.3 mm/s; at the higher mass flow rate it is 3.6 ± 0.4 mm/s. Here the uncertainties given are one standard deviation. The overlapping uncertainties preclude any inference of a trend. It is noteworthy, however, that the much larger percentage change in pressure (ca. 300 % for absolute pressure) did not clearly affect burning rate. This implies that the gas phase chemical reaction rate is not the controlling step here. The data are ambiguous on the possible control by oxygen mass transfer, but they are not inconsistent with this idea.

It is also noteworthy that the burning rate is not particularly sensitive to gas mass flow rate or to pressure so that the effects of any slight variations in these will not be confused with agent vapor effects in the results below. Unfortunately, one reason that no effects of these variables emerge in Table 1 is that the data are somewhat noisy. The source of the noise appears to have been the rather complex nature of the combustion zone. The magnesium oxide did not simply condense to an aerosol and float away in the gas flow. Rather, a large fraction of the oxide condensed locally around the immediate area where the magnesium vapors were emerging from the burning rod, ultimately leaving a rough replica of the rod behind, attached to the unburned portion. (This tendency for the oxide to form complex solid structures in the region of the burning zone has been noted in previous studies (Law and Williams, 1974).) Here, the condensation process seemed to interfere with the vaporization/burning process so that the burn zone was irregular and extended of the order of ten rod diameters. Varying heat transfer to the metal through the irregular oxide mass probably caused the burning rate to vary. This irregular burn zone also had the potential to fool the three sensor thermocouples in the side of the chamber, originally intended to provide burning rate information. Thus all of the burning rate information was obtained instead from the video tapes of the tests where the leading edge of the burn zone could be easily followed.

Table 1. Magnesium Burning in Pressurized Air

Test I.D.	Ambient gas	Mass flow rate of gas (g/s)	Gas flow velocity (cm/s)	Chamber pressure (MPa/psig)	Burn rate (mm/s)
Mg-24	AIR	1.33	42	0.24/20	3.66
Mg-21	"	"	22	0.44/50	4.23
Mg-4	"	"	13	0.79/100	4.14
Mg-5	"	"	"	"	3.75
Mg-50	"	1.89	36	0.27/25	4.14
Mg-52	"	"	"	"	3.45
Mg-53	"	"	"	"	3.33
Mg-16	AIR + NITROGEN (10 % ADD-ON)	1.46	13.9	0.79/100	3.75
Mg-19	"	"	"	"	3.53
Mg-20	"	"	"	"	3.57

Table 2 shows the result of adding on 5 or 10 weight percent of various agent vapors to the pressurized air flowing past the burning magnesium. Note that at least two replicates were run at each test condition. The surprising result in all cases was extinction of what was initially a vigorously propagating burning zone. (Recall that the sample rod was burning for about 2 cm before the agent vapor reached it.) Extinction typically occurred in 5-10 seconds, which is probably not much longer than the time to fully displace the agent-free atmosphere around the burning zone.⁴ Note that these add-on levels are low compared to those previously found necessary to extinguish various hydrocarbon flames (Hamins *et al.*, 1994) in a fairly similar situation (cup burner). For hydrocarbons, an add-on level of 25-30 % agent vapor to air was typically necessary. (Halon 1301 and CF_3I were exceptions, with the former requiring only 12-28 % add-on by weight and the latter, equally effective on a molar basis, about 25 % less than this on a mass basis.)

The reason for the present results is not clear. There is no obvious chemical basis for expecting the agents to act as suppressants here. Halon 1301 is believed to achieve its suppressant effect in hydrocarbon flames by trapping hydrogen radicals (Nyden and Linteris, 1994). Such radicals are not involved in magnesium burning (Tapscott *et al.*, 1986). Most, if not all, of the extinguishing

⁴Two tests, Mg-44 and Mg 45, with FC-218 were appreciably slower, with roughly 2/3 of the rod consumed before extinction occurred.

Table 2. Magnesium Burning in Pressurized Air with Agent Vapor^a

Test χI.D.	Agent (Add-on, wgt %)	Gas flow velocity (cm/s)	Chamber Pressure (MPa/psig)	Burn Rate (mm/s)
Mg-11,12,13,14	HALON-1301 (10 %)	13	0.79/100	EXTING.
Mg-25,26,27	"	37	0.27/25	EXTING.
Mg-47,48	HALON-1301 (5 %)	13	0.79/100	EXTING.
Mg-39,40	"	37	0.27/25	EXTING.
Mg-41,42	HFC-125 (5 %)	13	0.79/100	EXTING.
Mg-37,38	"	37	0.27/25	EXTING.
Mg-39,40	HFC-227 (5 %)	37	0.27/25	EXTING.
Mg-30,31	FC-218 (10 %)	37	0.27/25	EXTING.
Mg-43,44,45	FC-218 (5 %)	14	0.72/90	EXTING.
Mg-32,33	"	37	0.27/25	EXTING.
Mg-34,35,36	CF ₃ I (5 %)	37	0.27/25	EXTING.

^a Air mass flow rate held constant at 1.33 g/s for all tests.

effectiveness in hydrocarbon fires of the halon alternative agents examined here (except CF₃I) was attributed to the simple physical effect of thermal dilution (Hamins *et al.*, 1994). That is, these agents, by their heat capacity effects, simply reduce the flame temperature to the point of extinguishment. A similar effect may be responsible here but the substantially lower agent concentrations (<5 % by weight) make this less likely.

A few tests were run with nitrogen added-on at 10 weight percent to the air flow. Table 1 shows that this had no significant effect on the measured burning rate at 0.79 MPa (100 psig). This result is ambiguous, however, because nitrogen, which, of course, is the dominant gas in the air, may not be a passive diluent in this system. Magnesium nitride has a heat of formation that is 75 % of that of magnesium oxide. Thus magnesium can burn in pure nitrogen. Whether nitride formation is significant (and thus whether the add-on was a diluent or a reactant) in the present experiments

depends on its ability to compete with the oxygen/magnesium kinetics. Experiments in argon/oxygen mixtures could probably resolve the issue of whether an equivalent thermal capacitance⁵ of a truly inert diluent is capable of extinguishing the burning magnesium. There was insufficient time in the present study to pursue this issue further.

Some simple calculations, reported below with the titanium results, do, in fact, suggest a very weak slowing effect on the burning rate (not extinction) is possible for the conditions used here. As will be seen, the basis is oxygen dilution and retarded mass transfer of the alternative oxidant.

In spite of the incomplete picture as to the causes underlying the results in Table 2, those results do indicate that, at least down to the 5 % add-on level, there is no difference in the impact of the old and new agents. Halon 1301 and the four candidate agents tested here are equally prone to extinguishing the burning process in this configuration. Differences could exist in the minimum add-on level required for extinguishment. This would require substantially more testing to establish.

It should be noted that the burning configuration used here incorporates no radiative self-feedback of energy among surface elements of the fuel. Such feedback is stabilizing to the combustion of any solid fuel, making it more difficult to extinguish. Thus the present result indicating that 5 or 10 weight percent of these agent vapors can extinguish a burning magnesium rod does not necessarily carry over to more complex configurations, such as would be encountered in a burning aircraft structural fire.

4.3.2 Titanium. The test conditions and burning rate results for titanium are summarized in Table 3. The tests here are less extensive than with magnesium due to time constraints. Note that, in the tests done with no agent present, cutting the absolute pressure by greater than a factor of two (at a fixed mass flow rate) and increasing the ambient oxygen level by only 20 % yielded a roughly 30 % increase in the linear burning rate. This suggests (but does not prove) that mass transfer of oxygen is an important controlling factor. Since the oxidation reaction is evidently mainly heterogeneous here, within the molten oxide/metal mix (Clark *et al.*, 1975), it is likely to be largely uninfluenced by the noted pressure change.

Note that the no-agent burn velocities for titanium are generally significantly less than those for magnesium, despite that fact that the ambient oxygen level is considerably higher in the titanium cases. Burning rate models for metals such as that of Sato and Hirano (1988) should aid in explaining such differences but the requisite kinetic data on the oxidation reactions are not available. Thus the reasons for these differences are not clear at present but a wide variety of property differences between the two metals could be contributing.

In all of these tests (including those with agents present in the ambient atmosphere) the behavior of the burning metal was non-steady. A glow zone would progress up the metal rod several (up to about ten, depending on agent presence) diameters, sometimes seeming to proceed in steps of about one diameter. Surface tension in the elongated glowing zone behind the leading front would periodically cause this part or all of this zone to contract into a sphere. The extent of contraction to a sphere depended on the presence of agent vapors, as discussed below. This sphere would frequently begin to eject numerous fine, glowing particles. When the mass of the sphere exceeded the tensile strength of the glowing zone to which it was attached, it dropped off, taking much of the glowing material away below the propagation front. The front nevertheless continued and the cycle repeated itself. This occurred 3 to 6 times during the course of a typical full length burn.

⁵Thermal capacitance here means mass of the diluent times its heat capacity (J/g °C). Argon has less than half the heat capacity of nitrogen so its weight percent add-on would have to be increased accordingly.

Table 3. Titanium Burning in Elevated Oxygen Atmospheres

Test I.D.	Weight percent oxygen ^a	Chamber pressure (MPa/psig)	Gas flow velocity (cm/s)	Agent (add-on wgt %)	Burn rate (mm/s)
Ti-14 Ti-15	40	0.79/100	13	NONE	1.85 1.94
Ti-20 Ti-21	"	"	14	NITROGEN (10 %)	1.63 1.67
Ti-16 Ti-18 Ti-19	"	"	13	HALON-1301 (10 %)	1.11 EXTING. EXTING.
Ti-22 Ti-23 Ti-24 Ti-25	"	" 0.79-0.91 " 0.79-0.95	12	HFC-125 (10 %)	1.57 EXTING. EXTING. 1.92
Ti-39 Ti-40	50	0.31/30	33	NONE	2.53 2.59
Ti-37 Ti-38	"	"	34	HALON 1301 (15 %)	1.07 1.05
Ti-34 Ti-36	"	"	34	HFC-125 (15 %)	1.07 0.96
Ti-32 Ti-33	"	"	34	HFC-227 (15 %)	1.88 1.90
Ti-26 Ti-27	50	0.38/40	27	NONE	2.48 2.41
Ti-28 Ti-29	"	"	28	HALON 1301 (15 %)	1.24 1.20

^a This is the oxygen percentage by weight in the oxidant gas flow exclusive of the presence of the agent.

The enhanced heat release rate and/or heat transfer rate to the gas as the spheres developed and dropped was sometimes clearly visible in the output from the gas stream temperature sensor. Figure 4 shows such a case;⁶ this is for 50 % oxygen and 15 % halon 1301 vapor. Note the ambiguity in the preceding sentence as to the cause of the spikes; the shape changes and varying area available for convective heat transfer may be mimicking variations in heat release rate. A further source of ambiguity in the signal from this sensor, caused by the dripping phenomenon, is a possible erratic contribution from drips which hit and stuck to the ignition electrodes,⁷ continuing to burn for several seconds, rather than falling down into the quenching cup at the base of the chamber. Thus the output from this sensor has to be viewed with caution for the titanium tests; it cannot clearly differentiate heat release rate contributions from the primary burn zone from other sources of fluctuation. As a result, other data from this sensor are not reported here.

Figure 5 shows the simultaneous output (same test as Figure 4) from the radiation thermopile viewing the sample through the back window of the chamber. The timing of the molten metal drips is indicated. Note that the halon 1301 vapor control valve was switched 8 seconds after the initial ignition spike and would be arriving in the neighborhood of the sample about one second later (at about 14 seconds on the time scale of Figure 5). Except for the first drip, every drip is accompanied by a sharp drop in radiation output as the burning area shrinks sharply. As it builds up again, here in the form of a growing drop attached to the propagating front, the radiation again increases. However, each successive peak is smaller. It appears that the main reason for the monotonic peak shrinkage is erratic depositing of particles ejected from the burning zone on the rear chamber window, partially blocking some of the radiation. (The last peak is reduced by vignetting from the window frame.)

Figure 6 shows the radiation sensor output for a case at the same conditions as in Figure 5 except that there was no agent vapor present. The differing shape of the curve apparently corresponds to the different shape of the overall burning zone. When no agent was present, the burning zone consisted of several diameters of glowing rod, at the bottom of which the sphere of molten material accumulated before dropping off. When the sphere did drop off there was still an extensive glowing area that maintained the radiation signal at a fairly high level. When the agent vapors were present, as in Figure 5, the glowing rod section above the sphere was minimal in length leaving the sphere as the principal radiation source. When it dropped off the radiation signal dropped by a greater percentage. The mechanism whereby the agent vapors had this effect on the burning zone is not clear. One can speculate that it involves the relative rates of propagation (faster in the no-agent case) and of sphere formation.

In spite of these complications, there was a general tendency for the average radiation signal for the no-agent cases to be higher than for the cases with an agent vapor present. It is probable that this was due in part to the average temperature of the burning zone being hotter in the no-agent cases, but the confounding effects of shape changes and non-quantifiable window deposits make this unprovable with the available data. A lower burning zone temperature with the agent vapors present would, of course, be consistent with generally slower burning which Table 3 shows to occur in such cases, as compared to the no-agent cases.

Before proceeding to examine the titanium burning rate data further, it is of interest to make a simplified estimate of the potential effect on heat release rate from the burning metal due to participation of the agent vapors, if the burning process is taken to be mass-transfer limited. As was indicated

⁶Time zero is arbitrary in this Figure; ignition occurs when the sensor signal becomes non-zero.

⁷The chamber was tilted backwards slightly to minimize the occurrence of this phenomenon but it could not be avoided entirely.

TITANIUM ROD (TEST Ti-29)
AGENT: HALON 1301 (15%)
CHAMBER PRESSURE = 40 (psig)
OXIDANT GAS = AIR + O₂ (50% O₂ TOTAL)

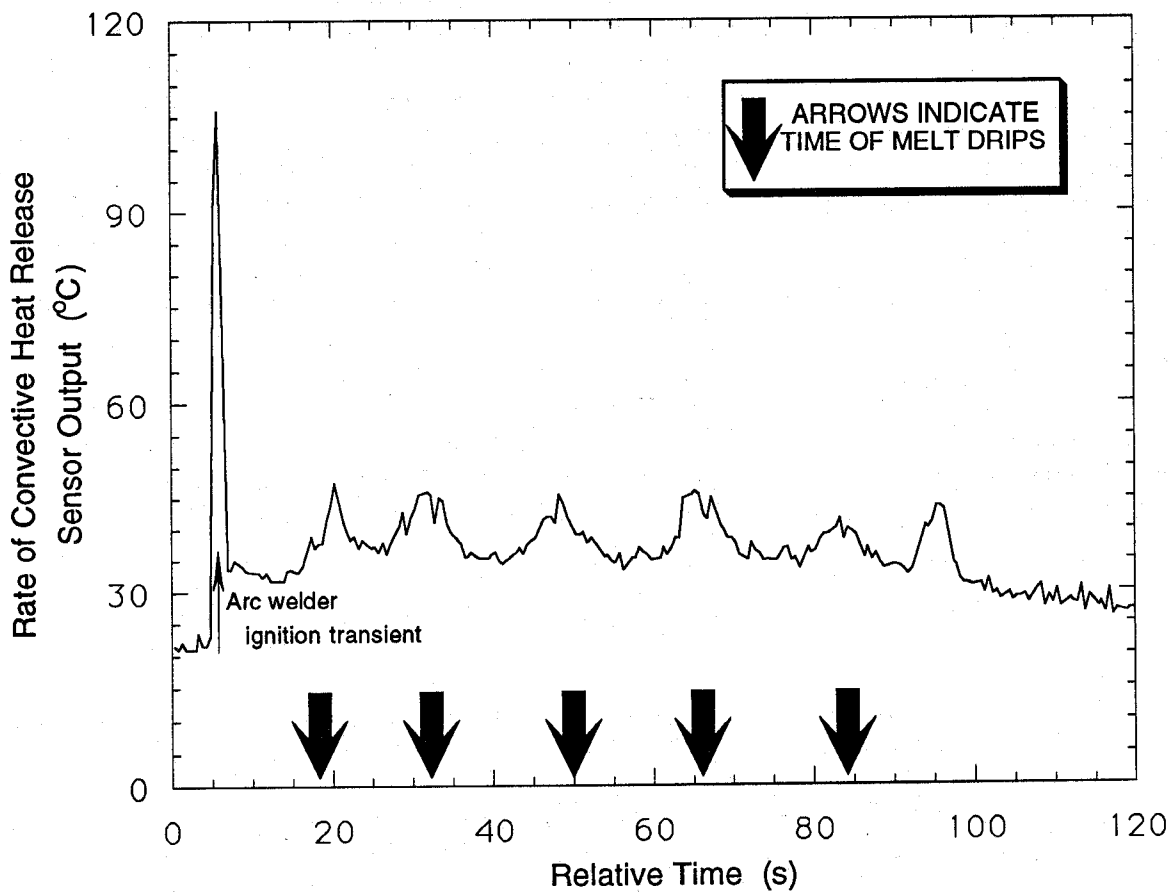


Figure 4. Output from convective heat release rate sensor.

TITANIUM ROD (TEST Ti-29)
AGENT: HALON 1301 (15%)
CHAMBER PRESSURE = 40 (psig)
OXIDANT GAS = AIR + O₂ (50% O₂ TOTAL)

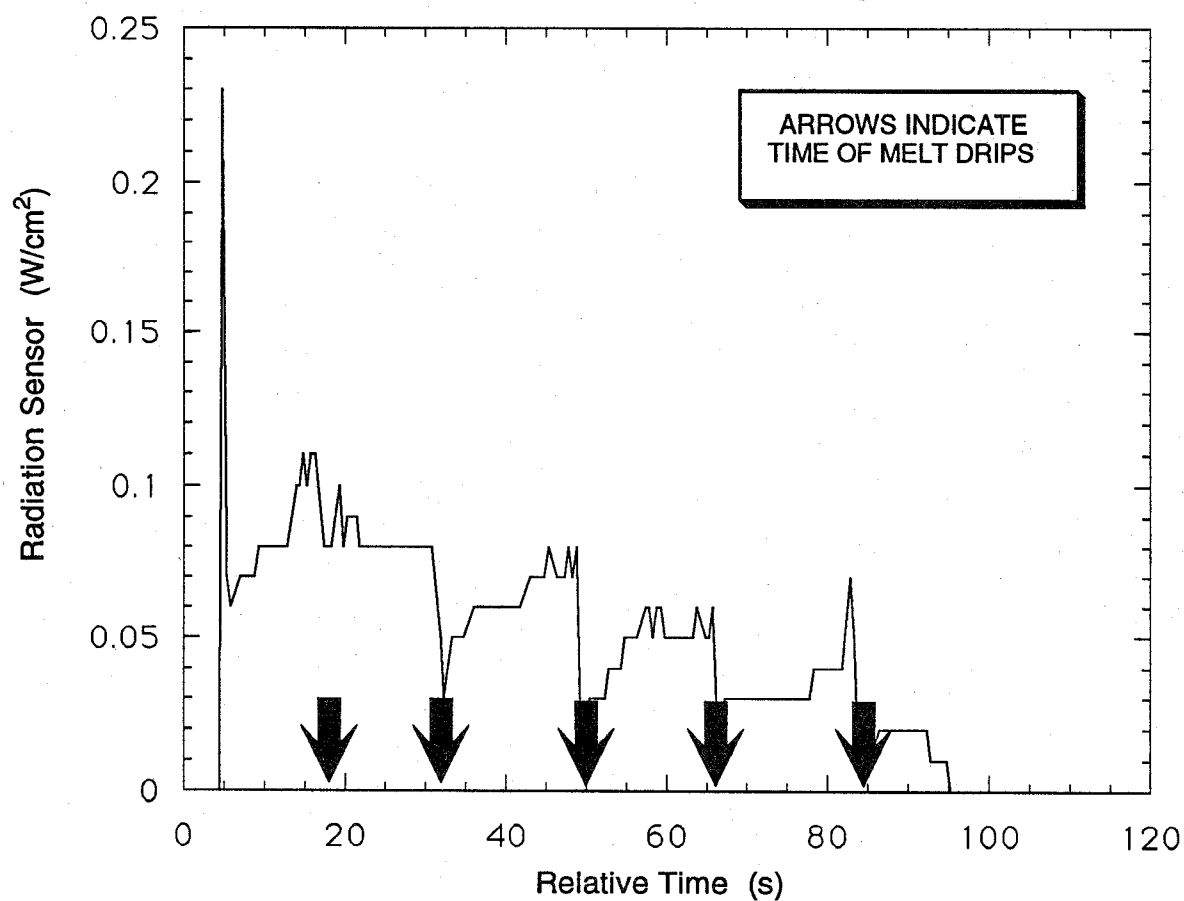


Figure 5. Output of radiation sensor for case with halon 1301 vapor present.

TITANIUM ROD (TEST Ti-26)
NO AGENT
CHAMBER PRESSURE = 40 (psig)
OXIDANT GAS = AIR + O₂ (50% O₂ TOTAL)

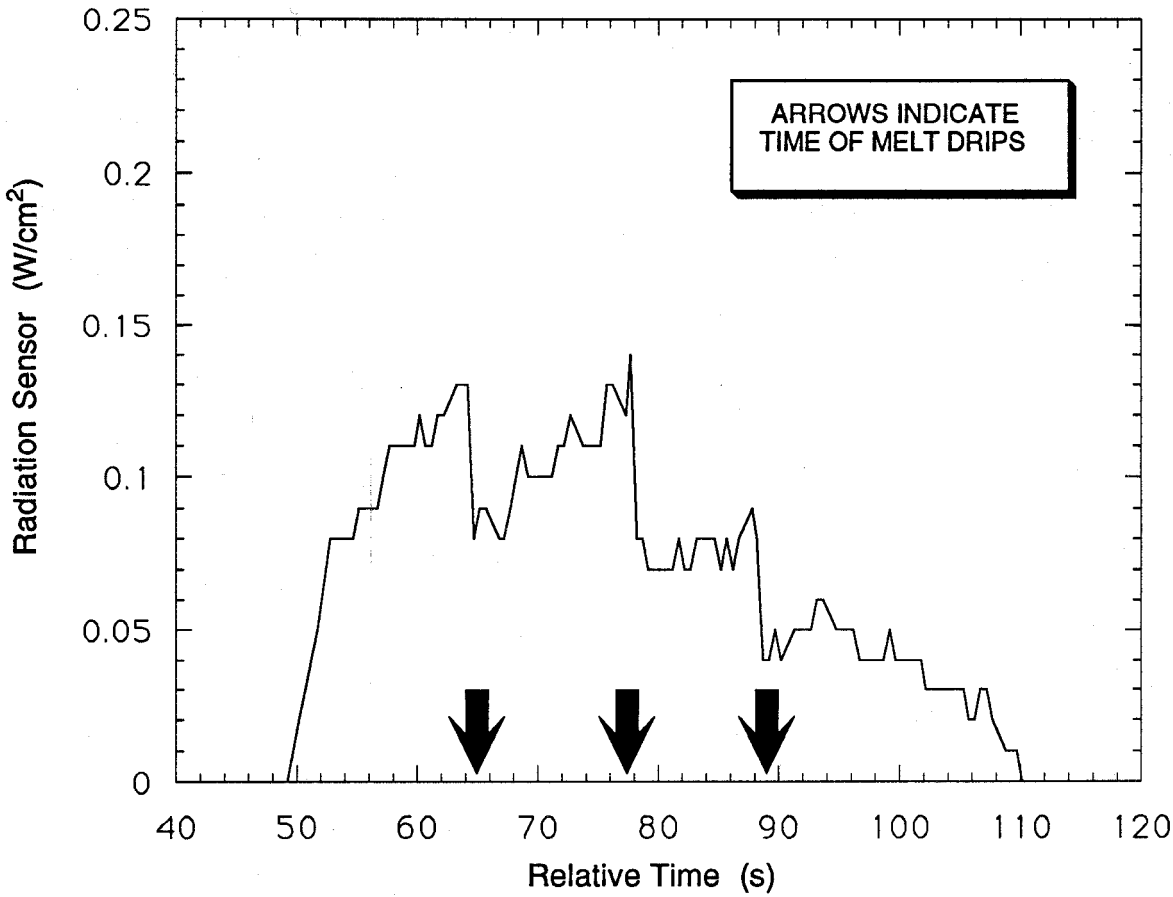


Figure 6. Output from radiation sensor for case with no agent vapor present.

previously, the data are not inconsistent with control by oxidant mass transfer through the boundary layer around the burn zone. The literature leads one to expect the impact of the agent to be burning rate enhancement. The source of such a potential burning rate or heat release rate enhancement is, of course, the higher heat of formation of the metal fluorides compared to the oxides.

Here we denote rate of heat release as RHR , where:

$$RHR = m_b H_o = k A_b (Y_{ox,gas} - Y_{ox,surf}) H_o / n_o \quad (1)$$

Here m_b is the mass burning rate of the metal (g/s); H_o is the heat of combustion of the metal by oxygen per unit weight of metal burned (J/g); n_o is the stoichiometric coefficient for oxidation (g O_2 /g metal burned); k is the overall mass transfer coefficient between the flowing ambient atmosphere and the burning metal surface (g/cm² s); A_b is the burning area of the metal; $Y_{ox,gas}$ is the mass fraction of oxygen in the ambient gas and $Y_{ox,surf}$ is the mass fraction of oxygen at the surface of the burning metal. Note that RHR and mass burning rate, m_b , are proportional; RHR is generally a more relevant measure of fire intensity. When the agent vapors are also present in the ambient gas they potentially comprise a second oxidizer which can attack the metal surface in parallel with the oxygen. However, note that they also displace some oxygen. Then one can write the total heat release rate as:

$$RHR' = A_b ((H_o k_o (Y'_{ox,gas} - Y'_{ox,surf}) / n_o + H_a k_a (Y_{a,gas} - Y_{a,surf}) / n_a)) \quad (2)$$

Here subscript "a" refers to the agent vapors. Note also that the prime on the oxygen mass fraction symbols indicates that they have been changed from their values in Equation 1 by the addition of the agent vapor. That is,

$$Y'_{ox,gas} = Y_{ox,gas} / (1 + Y_{a,gas}) \quad (3)$$

If the chemistry involving both of the oxidizers is fast compared to their mass transfer rates through the boundary layer, the surface values of both become very small and can be dropped. We can estimate the effect of the agent addition by taking the ratio of Equation 1 to Equation 2:

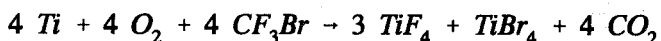
$$RHR/RHR' = (H_o k_o Y_{ox,gas} / n_o) / (H_o k_o Y'_{ox,gas} / n_o + H_a k_a Y_{a,gas} / n_a) \quad (4)$$

Note that the burn area parameter has been cancelled out on the assumption that it is unaffected by the agent vapor. The discussion above regarding the radiation output implies that the average burn area probably does decrease somewhat in the presence of the agent vapor but there is no way to quantify this at present. After dividing through, one obtains the following expression.

$$RHR/RHR' = Y_{ox, gas} / (Y_{ox, gas}' + (H_d/H_o)(k_d/k_o)(n_d/n_o)Y_{a, gas}) \quad (5)$$

Now it is possible to see that the effect of an add-on mass fraction of amount $Y_{a, gas}$ is modulated not only by the relative heat of reaction but also by the relative rate at which these new molecules can diffuse to the reaction zone and by the relative mass which must diffuse there (dictated by the reaction stoichiometry). The diffusion coefficients differ because the agent is typically a much bigger molecule than oxygen. Using diffusivity data for naphthalene and anthracene as molecules of appropriate weight, and a mid-temperature estimate in the boundary layer of 1500 °C, one finds that (k_d/k_o) is about 1/3. For halon 1301 versus oxygen, (n_d/n_o) is 0.216; for HFC-125 it is 0.335 (both based on the type of overall reaction indicated below).

An estimate of H_d requires that some estimate of the products be made for the interaction with the agent vapor. Lacking the requisite thermodynamic data to make detailed equilibrium calculations for this system, we assume the following plausible overall reaction scheme for halon 1301.



The evolved heat from this reaction is 1.06 MJ/g-mole of titanium, 16 % higher than that for titanium dioxide formation. A comparable calculation for HFC-125 yields an estimate that is about 50 % greater than for TiO_2 formation. (Necessary data on the heat of formation for HFC-227 could not be found so an estimate for this agent has not been made.) Note that the above overall reaction implies that there is some competition of the agent vapor for the oxygen that is diffusing to the metal surface, since the carbon in the agent is oxidized in the gas phase. Thus there is not a clean separation into two purely parallel, non-interacting paths of attack by the two oxidizing agents, as assumed in Equation 2. It seems likely that some of the carbon dioxide formed in the boundary layer would lose its oxygen to the titanium when it diffuses to the surface; this would somewhat lower the overall exotherm of the above reaction scheme and counter the effects of the neglected interaction. Any dissociation of the products would also lower the available heat.

With these caveats, one can use the preceding reaction heats in Equation 5 to estimate that the heat release rate effect for a 10 % add-on of halon 1301 is a net **decrease** of about 6 %.⁸ For a 10 % add-on of HFC-125, the estimated **decrease** in RHR is about 2 %. The estimated changes in mass burning rate are comparable. Given the various assumptions that went into these estimates they are probably accurate to no better than ± 50 %. (Furthermore, the model predictions cannot be any more accurate than the underlying assumptions allow them to be.) In any event, for the add-on levels of the order of 10 % they do predict a small **slow-down** of the burning process.

The reason that this prediction runs counter to the heat release enhancement one might expect is implicit in the main assumption behind the simplified model. Oxidant mass transfer is taken to be the rate controlling step. The large agent molecules cannot diffuse to the reaction zone at more than a fraction of the rate at which oxygen can. The displacement of some oxygen by the agent vapor reduces the titanium dioxide production rate and heat release; the halogen reactions, retarded by the

⁸A comparable calculation for magnesium and halon 1301 yields a 4 % decrease in RHR but one should note that the model assumptions are less appropriate here due to the gas phase chemistry, rather than heterogeneous chemistry.

relatively slow agent molecules, cannot proceed fast enough to make up the difference, in spite of their energetic advantage.

This simple model can make a prediction of what add-on level of agent would be needed to yield a net increase in heat release rate. This just implies that the denominator exceeds the numerator in Equation 5. Interestingly, the model says that for halon 1301 there is no add-on level of this agent which can achieve a greater heat release rate than one gets with oxygen as the sole oxidant gas; this holds for oxygen levels from that in air up to at least 50 %.⁹ For HFC-125 the model says that this agent will yield a RHR enhancement at add-ons above about 40 % if the starting gas is air; there is no add-on level capable of yielding enhancement when the starting gas has 40 % or 50 % oxygen.

The above estimates of the impact of agent addition stand in contrast to the actual observed behavior as shown in Table 3. As with magnesium, the actual effect of the agent vapors in all cases was strongly suppressive, not just slightly so. The reasons behind this are difficult to discern, given the limited data. The strong effect suggests a greater role for chemistry than the above model allows. Perhaps the oxidation reactions are more marginal (and thus more controlling) than has been assumed or there are suppressive chemical effects of the agent on the metal burning which are not known to the present authors.

In titanium burning, nitrogen is somewhat more akin to an inert diluent than it was with magnesium because the heat of formation of titanium nitride is one third that of titanium dioxide. Table 3 shows that a 10 % nitrogen add-on yields a 17 % reduction in burning rate (in 40 % oxygen at 0.79 MPa). A 10 % add-on of halon 1301 (with only about half of the thermal capacitance of the nitrogen add-on) yields either a much greater burning rate reduction or even extinction.¹⁰ A 10 % add-on of HFC-125 gave very erratic results under these same conditions, from no effect to extinction. (The pressure variation in these tests was the result of partial clogging of the downstream orifice by particles emitted from the burning titanium.) In terms of thermal capacitance or ability to lower temperature by pure dilution, a 10 % add-on of nitrogen is comparable to HFC-125 and about twice as effective as halon 1301. These results thus suggest that the apparent suppressive effects of the agents are beyond simple thermal dilution and well beyond the calculated effects if mass transfer was the controlling mechanism.

The ambient oxygen level was increased to 50 % so that the chamber pressure could be lowered to the point where HFC-227, with its comparatively low vapor pressure, could be tested alongside HFC-125 and halon 1301. Table 3 shows that the more vigorous burning that resulted from the oxygen enhancement resisted extinguishment by any of these agents. However, they again all slowed the burning process strongly. Here halon 1301 and HFC-125 appear about equally effective in slowing the burning. HFC-227 is distinctly less effective, though this inference is based on very limited data. One might cautiously extrapolate this result to infer that HFC-125 would produce a lesser hazard in aircraft applications than would HFC-227 but more data on this issue would certainly be desirable.

Again it is necessary to add the caveat noted previously with the magnesium results. The ability of these agent vapors to partially suppress the burning of titanium in the present experimental conditions does not mean that they will do so in a more complex burning configuration or at all

⁹For magnesium and halon 1301, this calculation says that agent add-on levels to air of nearly 80% are needed to yield an increase in heat release rate above that found in pure air.

¹⁰The extinction process here occurred after 50-80 % of the rod had burned and thus was much more marginal than in the case of magnesium. It occurred when the burn zone was in the contracted molten ball stage. A build-up of titanium dioxide near the ball surface (Clark *et al.*, 1975) could make this a slower reaction stage and thus a more vulnerable part of the burning cycle.

admixture levels. Also, any agent sprayed at a metal fire in liquid form has the potential to cause a flare-up due solely to droplet "explosions" which could enlarge the metal area exposed to oxidation.

4.4 Conclusions

Halon 1301 (the reference case), as well as the candidate replacement agents HFC-125, HFC-227, FC-218 and CF_3I , extinguished the strongly- established burning of thin rods of magnesium when added-on at the 5 % and 10 % level to pressurized air flowing past the burn zone. In nearly all cases the extinction occurred in a matter of seconds. FC-218 was appreciably slower in causing extinction in two replicate tests at one condition; this was the only differentiation among the various agents seen with burning magnesium. In this sense the candidate replacement agents, other than FC-218, have shown no greater tendency to interact with burning magnesium than does halon 1301.

The general suppressive effect on magnesium burning runs counter to the burning enhancement effects reported in the literature for halogen-containing compounds sprayed onto more complex magnesium burning configurations. A simplified calculation, based on the assumption of mass transfer control of the burning rate and an assumed reaction stoichiometry, suggests that a very weak suppressive effect could be expected here, largely as a result of oxygen dilution. The cause of the much stronger suppressive effects seen here is not clear at present. This same calculation suggests that enhancement of magnesium burning could occur at much higher agent add-on levels.

Halon 1301, HFC-125 and HFC-227 also showed substantial suppressive capabilities toward the burning of a thin titanium rod in elevated oxygen atmospheres. Here extinction was seen only in 40 % oxygen, not in 50 % oxygen. Nevertheless, even at the higher oxygen level, substantial reductions in burn propagation rate were seen. Here HFC-125 at a 15 % add-on level slowed the burn rate equally as much as did halon 1301 and much more than did HFC-227. This was the only differentiation among agents seen with titanium burning. It provides a very limited basis on which to infer that HFC-125 might be less reactive with titanium fires than HFC-227 (and comparable to halon 1301).

The simplified calculation, mentioned above but here done only for halon 1301 and HFC-125, again implies only a very weak suppressive effect of 10 to 15 % add-on levels of these agents, via oxygen dilution. The much stronger effect seen experimentally cannot be explained on the basis of the available information. This calculation implies that, at elevated oxygen levels, no add-on level of agent can yield burning enhancement. In air, according to this model, HFC-125 could yield enhancement of the burning rate at add-on levels above 40 %. This raises a note of caution about the relatively lower reactivity of HFC-125 compared to HFC-227 due to the limited number of hard facts available.

Since the results here for isolated, single metal rods run counter to the reported effects of halogen-containing agents on more massive magnesium and titanium fires, it appears that further experiments would be desirable, involving larger masses of burning metal, preferably in a linear burning mode as here, but incorporating radiative interchange among fuel elements. This would allow quantitation of the burning progress, allowing definitive determination of the impact of agent vapors and agent liquid/vapor sprays. Pre-heating and pressurization of the gas stream would also make it possible to adhere to oxygen levels closer to air with titanium so that one could determine more definitively the impact of halogen-containing agents under conditions most pertinent to jet aircraft fires.

4.5 References

- Anderson, V. and Manty, B., "Titanium Alloy Ignition and Combustion," Naval Air Development Center Report No. NADC 76083-30, Warminster, PA, January, 1978.
- Andrews, R., "Metals," Section 4, *National Fire Protection Handbook*, Fifteenth Edition, Chap. 10, Section 4, National Fire Protection Association, Quincy, MA, p. 4-98, (1981).
- Baldwin, J., Beach, C. and Rhein, R., "Extinction of Titanium Fires in Pressurized Flowing Air," Naval Weapons Center Report No. NWC TP 6439, China Lake, CA, Sept., 1984.
- Bird, B. Stewart, W. and Lightfoot, E., *Transport Phenomena*, Wiley, New York, p. 647 (1960).
- Clark, A., Moulder, J. and Runyan, C., "Combustion of Bulk Titanium in Oxygen," *Fifteenth Symposium (International) on Combustion*, The Combustion Institute, Pittsburgh, PA, p. 489 (1975)
- Elrod, C., Funkhauser, M. and Glickstein, M., "Compendium on Titanium Combustion," Air Force Wright Aeronautical Laboratories Report No. AFWAL-TR-82-2014, Wright-Patterson Air Force Base, OH, Nov., 1980.
- Elrod, C. and Lyon, S., "Self-Sustained Combustion Evaluation of Titanium 6Al-4V in an Aerodynamic Environment," Air Force Wright Aeronautical Laboratories Report No. AFAPL-TR-79-2047, Wright-Patterson Air Force Base, OH, August, 1976.
- Fox, D., "Investigation of Titanium Combustion Characteristics and Suppression Techniques," Air Force Wright Aeronautical Laboratories Report No. AFAPL-TR-75-73, Wright-Patterson Air Force Base, OH, July, 1975.
- Hamins, A., Gmurczyk, G., Grosshandler, W., Rehwoldt, G., Vazquez, I., Cleary, T., Presser, C. and Seshadri, K., "Flame Suppression Effectiveness," Chapter 4 in "Evaluation of Alternative Fire Suppressants for Full-Scale Testing in Simulated Aircraft Engine Nacelles and Dry Bays," National Institute of Standards and Technology Special Publication 861, April, 1994.
- Kuchta, J. Martindill, G. and Spolan, I., "Fire and Explosion Hazards of Flight Vehicle Combustibles," *Quarterly Progress*, U. S. Bureau of Mines, Pittsburgh, PA, June to August, 1965.
- ibid*, November to February, 1966.
- Law, C. and Williams, F., "Combustion of Magnesium Particles in Oxygen-Inert Atmospheres," *Combustion and Flame*, 22, p. 383 (1974).
- Maykuth, D., "Methods of Controlling and Extinguishing Titanium Fires," Defense Metals Information Institute Technical Note, Batelle Memorial Institute, Columbus, OH, July, 1964.
- McCutchan, R., "Investigation of Magnesium Fire-Extinguishing Agents," Wright Air Development Center Technical Report 54-5, Wright-Patterson Air Force Base, OH, Jan., 1954.
- National Aeronautics and Space Administration, "Detonation Hazards with 'Safe' Industrial Solvents," NASA Langley Research Center LAR-10299, Hampton, VA, 1970.
- Nyden, M., Linteris, G., Burgess, D., Westmoreland, P., Tsang, W. and Zachariah, M., "Flame Inhibition Chemistry and the Search for Additional Fire Fighting Chemicals," Chapter 5 in "Evaluation of Alternative Fire Suppressants for Full-Scale Testing in Simulated Aircraft Engine Nacelles and Dry Bays," National Institute of Standards and Technology Special Publication 861, April, 1994.
- Perlee, H., Martindill, G. and Zabetakis, M., "Flammability Characteristics of Selected Halogenated Hydrocarbons," U. S. Bureau of Mines TN23.U7, Pittsburgh, PA, 1966.
- Rhein, R. and Baldwin, J., "Literature Review on Titanium Combustion and Extinction," Naval Weapons Center Report No. NWC TP 6167, China Lake, CA, Jan., 1980.
- Sato, J. and Hirano, T., "Fire Spread Limits Along Metal Pieces in Oxygen," *Flammability and Sensitivity of Materials in Oxygen-Enriched Environments: Third Volume, ASTM STP 986*, D. Scroll (ed.), American Society for Testing and Materials, Philadelphia, PA, p. 158 (1988).

Sato, J., Sato, K. and Hirano, T., "Fire Spread Mechanisms along Steel Cylinders in High Pressure Oxygen," *Combustion and Flame*, 51, p. 279 (1983).

Strobridge, T., Moulder, J. and Clark, A., "Titanium Combustion in Turbine Engines," Federal Aviation Administration Report No.FAA-RD-79-51, Washington, DC, July, 1979.

Tapscott, R., Beeson, H., Lee, M., Plugge, M., Zallen, D., Walker, J. and Campbell, P., "Extinguishing Agent for Magnesium Fire: Phases I-IV," New Mexico Engineering Research Institute Report WA3-15, Albuquerque, NM, July, 1986.

5. COMPATIBILITY WITH METALS

Mark R. Stoudt, James L. Fink, James F. Dante and Richard E. Ricker
Metallurgy Division
Materials Science and Engineering Laboratory

Contents

Page

5. COMPATIBILITY WITH METALS	121
5.1 Introduction	122
5.2 Mass Change Exposure Tests	123
5.2.1 Materials	123
5.2.2 Experimental Procedure at 150 °C	123
5.2.3 Experimental Procedure at 20 °C	127
5.2.4 Results at 150 °C	127
5.2.5 Results at 20 °C	139
5.3 Environmentally Induced Fracture Experiments (Slow Strain Rate Tensile Tests)	152
5.3.1 Materials	152
5.3.2 Experimental Procedure at 150 °C	153
5.3.3 Experimental Procedure at 20 °C	153
5.3.4 Results at 150 °C	153
5.3.5 Results at 20 °C	161
5.4 Post Deployment Corrosion	168
5.4.1 Materials	172
5.4.2 Exposure Environment	172
5.4.3 Experimental Procedure	172
5.4.4 Results	172
5.5 Electrochemical Measurements	176
5.5.1 Materials	177
5.5.2 Experimental Procedure	177
5.5.3 Agent Resistivity	179
5.5.4 Defining a Reference Potential	180
5.5.5 $\text{Cp}_2\text{Fe}^{0/+}$ Electron Kinetics	183
5.5.6 Corrosion Rates of Storage Vessel Alloys in HCFC-124, HFC-125, and CF_3I	185
5.5.7 Corrosion Rates of Metals in Other Halon Replacement Agents	189
5.6 Conclusions	190
5.7 Acknowledgments	191
5.8 References	191
Appendix A. Mass Change Measurements at 150 °C	193
Appendix B. Mass Change Measurements at 20 °C	197

5.1 Introduction

Under current military practice, fire suppressants are stored for up to five years. Since the corrosivities of the chemicals currently under consideration as replacements for halon 1301 are not well known, there is a need for compatibility information between these chemicals and the array of materials used on high performance aircraft. As a result, experiments were conducted to assess the relative compatibility of the potential fire suppressants with the different metallic materials used for storage, distribution, and handling of aircraft fire suppressants.

On board an aircraft, the metallic materials will be exposed to fire suppressants during storage (storage vessels, rupture disks, etc.), deployment (distribution tubes, nozzles, etc.) and after deployment (structural and engine components exposed to combustion by-products). Of these possible exposures, the greatest concern for the safe operation of the aircraft lies in the possibility that the fire suppressant might cause attack of the storage vessels resulting in a loss of agent or prevention of proper operation of the deployment system.

In flight, the storage vessels, which are designed to contain the agent for up to five years, will experience pressure excursions up to 5.9 MPa at operational temperatures which will range from below ambient to those as high as 150 °C. At the maximum in-flight temperature, it is likely that the agent will surpass the critical temperature and will, therefore, be a single phase. At the lower in-flight and ground temperatures, the agent will be an equilibrium mixture of the liquid and vapor phases. Since corrosion behavior is a function of many variables and is also strongly dependent on temperature, it follows that the corrosion behavior at the ground conditions are likely to be very different from those in flight (Fontana, 1987).

Corrosion is defined as a degradation of the properties of a material resulting from a chemical reaction with the environment and can generally be classified into eight different categories based on the morphology of the corrosion damage. These eight forms are: general corrosion, pitting corrosion, crevice corrosion, intergranular corrosion, environmentally induced fracture, dealloying, galvanic corrosion, and erosion corrosion (Fontana, 1987). The definitions and descriptions of these forms of corrosion are detailed in an earlier report (Ricker, 1994). Of these eight corrosion failure modes, six are of potential concern for the storage, distribution, and post deployment corrosivity of fire suppressant agents on aircraft: general corrosion, pitting corrosion, crevice corrosion, intergranular corrosion, environmentally induced fracture, and dealloying (Ricker, 1994). Erosion corrosion may be a concern for nozzles, but the duration of the flow through the nozzle is very short and damage by this mechanism should be noted in the fire suppressant efficiency tests if it occurs. Galvanic coupling may influence corrosion damage accumulation, but due to the relatively low conductivity of these agents, galvanic effects should be minimal. As a result, the experiments were designed in a manner that would allow for the evaluation of the occurrence of the remaining six modes of damage (Ricker, 1994).

Very little is known about the corrosion behavior of the metals in these environments, and there is virtually no information available in the literature regarding the compatibility of these agents with the alloys used in the storage systems. As a result, corrosion experiments, which emulate these storage conditions, are a vital component in the selection of a replacement to halon 1301.

In the first phase of this investigation, a series of twelve possible replacements for halon 1301 were evaluated on the basis of a general ranking of the corrosivity with respect to storage vessel materials (Ricker, 1994). For the second phase, three candidates from the original list of twelve were selected for further study. These were: HFC-125, HFC-227ea, FC-218. An additional candidate, CF₃I, was also included in this corrosion study. The primary objective of the Phase II analysis was to assess the compatibility of this select group of replacement candidates over a broader range of environmental

conditions and longer exposure times. Since limited corrosion data is available for the selected alloys in 1301 in the literature, and the service performance record of this agent has been acceptable, this agent was included in Phase II as a reference environment.

The potential for corrosion damage to the structural materials of the aircraft by residual suppressant or by combustion by-products is also of great concern. These chemicals have been shown to form aggressive halide acids or salts during fire suppression (Nyden, 1994). Residual suppressant or the combustion by-products left on the surface of the structural components after deployment could result in extensive corrosion damage before they are cleaned.

This analysis was designed and conducted to further evaluate the compatibility of the replacement candidates selected for additional study under probable and potential service conditions. The experiments consisted of exposure tests which emulated the in-flight and on-the-ground conditions under which corrosion might occur followed by careful examination and evaluation of the resulting corrosion damage. Standard experimental techniques were employed to assess the potential for failure of the storage container alloys by the aforementioned six possible corrosion mechanisms in normal service. The techniques used for this evaluation consisted of immersion tests and slow strain rate tensile tests and were similar to those utilized in Phase I (Ricker, 1994). A new electrochemical technique was also developed to predict the corrosion behavior over a broader range of potential service conditions and incorporated into the analysis.

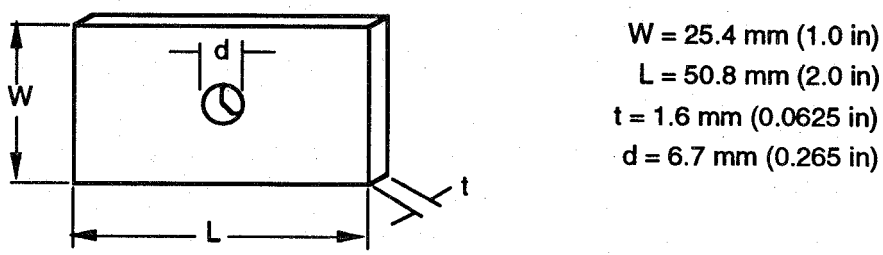
5.2 Mass Change Exposure Tests

Experiments were conducted to assess the changes in mass of container alloys as a result of a long term exposure to the replacements candidates. These measurements provided a basis to determine the rate of formation of surface scales or the rate of removal of metallic species due to the exposure to the replacement candidate. Also visual and optical microscopic examinations following the exposures allowed for further evaluation of the occurrence of pitting, intergranular corrosion, and dealloying.

5.2.1 Materials. The materials selected by the sponsors for evaluation in Phase II of this study represented the range of alloys currently in service as or under consideration for use as storage vessels. These were: 304 stainless steel, stainless steel alloy 21-6-9 (Nitronic 40)¹, titanium alloy 15-3-3-3 and 6061-T6 aluminum alloy. Shortly after the immersion tests began, a decision was made to include AISI 4130 alloy steel in the test matrix and the exposure times for this alloy were shortened appropriately. After HFC-125 was selected as the most likely candidate to replace halon 1301, several additional alloys were included for further testing in HFC-125 and halon 1301 in order to provide compatibility information over a broader range of materials. Those materials were: Inconel alloy 625, CDA-172 copper/beryllium alloy, CDA-110 copper alloy, 321 stainless steel, and AM-355 stainless steel. The compositions of these alloys are given in Table 1.

5.2.2 Experimental Procedure at 150 °C. All of the samples used for the weight loss immersion tests were flat coupons of the geometry shown in Figure 1 (ASTM G 01-93). The sample preparation

¹Certain trade names and company products are mentioned in the text or identified in an illustration in order to specify adequately the experimental procedure and equipment used. In no case does such identification imply recommendation or endorsement by the National Institute of Standards and Technology, nor does it imply that the products are necessarily the best available for the purpose.



General corrosion coupon design (ASTM G-01).

Figure 1. General corrosion coupon sample design (ASTM G 01-93).

Table 1. Composition of alloys tested in Phase II (mass fraction in percent)

Element	Nitronic 40	304 SS	Al 6061	Titanium 15-3-3-3	AISI 4130	Inconel 625	AM-355 SS	Cu-Be CDA 172	321 SS	Cu Alloy CDA 110
Al	--	--	bal	3.50	0.04	0.23	--	0.04	--	--
C	0.02	0.06	--	0.01	0.30	0.02	0.12	--	0.04	--
Cr	20.20	18.39	0.34	3.30	0.91	21.71	15.28	0.01	17.22	--
Cu	0.03	0.27	0.40	--	0.01	--	--	bal	0.10	99.95
Fe	bal	bal	0.70	0.11	bal	3.97	bal	0.06	bal	--
Mn	9.07	1.41	0.15	--	0.48	0.08	0.80	--	1.61	--
Mo	0.07	0.21	--	--	0.17	8.82	2.60	--	0.14	--
Ni	7.01	8.15	--	--	0.01	61.39	4.23	0.06	9.85	--
Ti	--	--	--	bal	--	--	--	--	0.43	--
V	--	--	--	14.70	--	--	--	--	--	--
Mg	--	--	1.20	--	--	--	--	--	--	--
Zn	--	--	0.25	--	--	--	--	--	--	--
B	--	--	--	--	--	--	--	--	--	--
N	0.31	0.03	--	0.01	--	--	0.12	--	0.02	--
Sn	--	--	--	3.00	--	--	--	--	--	--
Co	--	0.14	--	--	--	--	--	--	0.21	--
Nb	--	--	--	--	--	3.41	--	--	--	--
W	--	--	--	--	--	--	--	--	--	--
Be	--	--	--	--	--	--	--	1.94	--	--

technique used for these experiments was identical to that used for Phase I (Ricker, 1994). Three separate weighings were taken at approximately 30 s intervals and averaged. This average value was then referred to as the initial weight of the coupon. The balance used for these weight measurements was self-calibrating to maintain an accuracy to within $\pm 10 \times 10^{-6}$ g with a reproducibility of no less than $\pm 15.1 \times 10^{-6}$ g. Representative photographs of the surface of each alloy were also taken prior to the start of testing.

Prior to the start of each exposure test, three coupons of each alloy were mounted on a polytetrafluoroethylene (PTFE) rod with PTFE spacers between the samples. This was done (1) to separate and (2) to electrically isolate the samples so that the effects from galvanic couplings would be minimized. PTFE shields were also placed between the individual sets of alloys to protect them from contacting any corrosion products that may have formed on other alloy sets. The samples were next placed in a custom designed PTFE liner and placed into a 2 L pressure vessel, as shown in Figure 2, for exposure. The test vessel was sealed, connected to a mechanical vacuum pump and evacuated for a minimum of 45 min.

The mass of agent required to produce a nominal pressure of 5.9 MPa at 150 °C was determined with the same mass balance used for the elevated temperature tests in Phase I which is shown in the following equation: (Ricker, 1994)

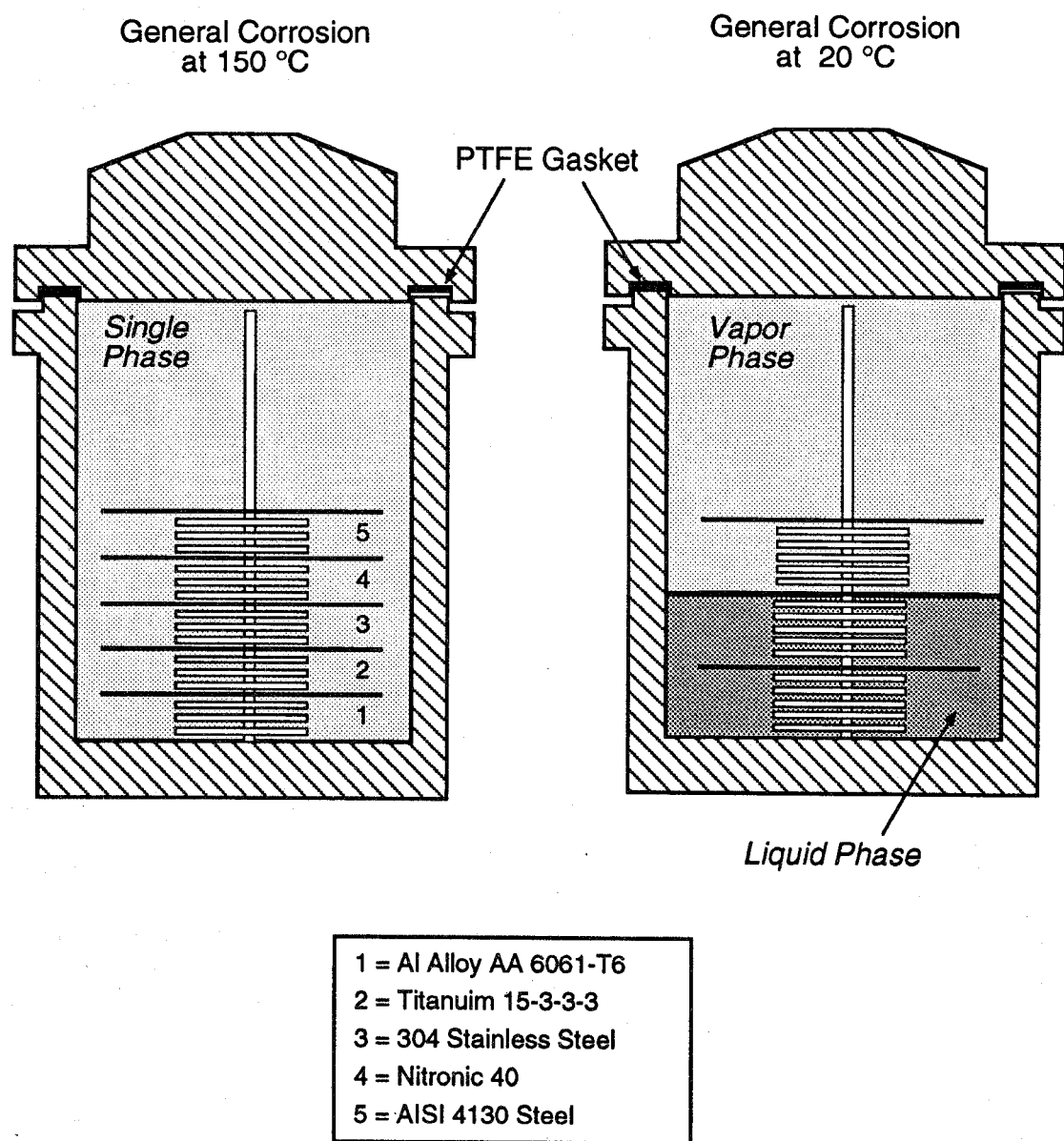


Figure 2. Schematic diagram of the immersion testing chamber used for general corrosion experiments.

$$M_T = \rho_l V_l + \rho_v V_v \quad (1)$$

where M_T is the total mass of the system, ρ_l is the density of the liquid agent at 20 °C, V_l is the volume of the liquid agent at 20 °C, ρ_v is the density of the vapor phase at 20 °C, and V_v is the volume of the vapor at 20 °C. To facilitate charging of the agents, the test vessels were chilled in a bath of either ice and water, or dry ice and alcohol, depending on the temperature necessary to maintain the liquid phase. The vessels were then placed on a balance so that the mass of the agent could be monitored during filling. Upon completion of the charging step, the vessels were placed in proportionally controlled, calrod-type heaters for the duration of the exposure period.

Mass-change measurements were performed on the coupons after one, two, four, eight, and twelve month elapsed times during the one year exposure. To minimize agent loss during the extraction process, the vessels were immersed in a bath of dry ice and alcohol for approximately three hours in order to condense as much of the agent as possible. The vessels were immediately sealed and returned to the cooling bath upon the extraction of the PTFE rod assemblies. After extraction, the samples were allowed to warm naturally to ambient temperature, promptly weighed using the standard weighing procedure, and then immediately returned to the test vessels.

At the end of the exposure tests, the agents were released, the coupons were extracted and immediately re-weighed, again using the standard weighing procedure. The average of the three weight measurements was then referred to as the final weight of the coupon. Representative photographs of the surfaces were again taken and compared to those of the initial condition.

A series of statistical analyses were performed on the weight loss coupon data. The results of these analyses were then used to evaluate the potential for general corrosion induced failure for each alloy in the replacement candidates.

5.2.3 Experimental Procedure at 20 °C. The sample charging procedure used for the ambient temperature experiments differed slightly from the one utilized for the tests at 150 °C. For these tests, the samples were not separated according to alloy type, but were stacked so that each set contained one coupon from each alloy. This sample arrangement was selected because it exposed two coupons from each alloy to the liquid phase, and one to the vapor phase as also shown in Figure 2. As with the tests conducted at 150 °C, each coupon was separated by a PTFE spacer and each alloy set was separated by a PTFE shield.

The agent filling procedure used for the ambient temperature tests was also slightly different from the high temperature test. For these tests, Equation (1) was used to determine an agent volume which located the interface region between the two phases near the midpoint of the vessel. The remainder of the procedure for these experiments was identical to the procedure used for the tests at 150 °C.

5.2.4 Results at 150 °C. The rate of mass change was calculated for each alloy/environment combination using the mass change measurements and the same relationship from Phase I (Ricker, 1994)

$$R = \frac{\Delta M}{A \tau} \quad (2)$$

where ΔM is the mass change, A is the total exposed area of the sample and t is the exposure time in days. These values are presented in Table 2. If the mass change rate is assumed to be essentially constant throughout the entire exposure period, then this relationship will provide a reasonable estimate of the average mass change rate for the duration of the exposure. While the magnitudes of these measurements are small they are larger than the minimum required to be statistically significant.

Linear regression analyses were also performed on the mass change rate values. Table 3 contains the results of a regression performed on mass change per unit area versus time basis (*i.e.*, $\Delta M/A$ vs t). In this table, the slope of the linear regression, m , corresponds to the estimated corrosion rate for each alloy/environment combination, R is the correlation coefficient for the linear regression, and the standard error is an estimate of the standard deviation of the estimated slope. In this table, it can be seen that the correlation coefficients reflect the high degree of scatter in the measurements. At this temperature, 4130 alloy steel in halon 1301 had the best correlation (R value > 0.9) and the 4130 alloy steel in HFC-125 was the worst ($R < 0.1$).

If the corrosion rates were indeed constant, then the weight changes would be linear and the regression slope would then equal the mass change rate for each exposure. However, in most cases the corrosion rate slows with time due to mass transport through the surface film thereby limiting the reaction rate. In this case, the corrosion rate should decrease with time following a square root of time dependence. As a result, a second regression was performed on the mass change data on a square root of time basis. If one assumes that transport through a surface film is rate limiting, then the rate of mass change would be inversely proportional to the thickness of the film according to the following relation:

$$\frac{\partial}{\partial t} \left(\frac{\Delta M}{A} \right) \propto \frac{1}{\ell} \quad (3)$$

where the film thickness, ℓ , is proportional to the mass change per unit area. Solving this differential equation yields the equation used for the second regression:

$$\left(\frac{\Delta M}{A} \right) = kt^{1/2} \quad (4)$$

The results of this regression are presented in Table 4. The correlation coefficients for this analysis also exhibited a wide scatter ranging from > 0.9 for Al-6061 in HFC-125 to ~ 0.1 for 4130 in the same agent. While the correlations of this regression were better in some cases, the overall fit was not much better than the simple linear regression. As a result, a third regression was also performed on this data. This analysis assumes that part of the samples surface is bare and exhibits linear reaction kinetics while part is filmed and exhibits square root of time behavior so that:

$$\left(\frac{\Delta M}{A} \right) = m_0 + m_1 t + m_2 t^{1/2} \quad (5)$$

This regression produced very good correlations for most of the environment/alloy combinations as shown in Table 5 and are also shown along with the raw mass change data as derived from the measurements made on the three samples of each of the alloys in each of the agents at 150 °C, (Figures 3-7). (The raw data used for these figures is presented in tabular form in Appendix A.)

Table 3. Mass change rate per unit area at 150 °C (g/meter² · day) estimated by the slope for a linear regression of mass change per unit area on exposure time (assumes constant, bare surface, reaction kinetics)

Alloy	HFC-125			HFC-227ea			Halon 1301		
	m	R	Std Err	m	R	Std Err	m	R	Std Err
Nit 40	0.00022	0.669	0.00006	0.00076	0.502	0.00036	0.00077	0.777	0.00016
Al 6061-T6	0.00233	0.800	0.00044	0.00474	0.861	0.00078	0.00237	0.681	0.00064
304 SS	0.00039	0.692	0.00010	0.00072	0.608	0.00026	0.00066	0.693	0.00017
Ti 15-3-3-3	0.00029	0.651	0.00009	0.00063	0.333	0.00049	0.00096	0.768	0.00020
AISI 4130	-0.00037	0.035	0.00407	-0.08934	0.413	0.07450	0.01737	0.937	0.00245
321 SS	‡	‡	‡	*	*	*	‡	‡	‡
CDA 110	‡	‡	‡	*	*	*	‡	‡	‡
CDA 172	‡	‡	‡	*	*	*	‡	‡	‡
AM 355	‡	‡	‡	*	*	*	‡	‡	‡
IN 625	‡	‡	‡	*	*	*	‡	‡	‡

Table 3. (continued)

Alloy	FC-218			CF ₃ I		
	m	R	Std Err	m	R	Std Err
Nit 40	0.02284	0.855	0.00384	0.07057	0.435	0.04622
Al 6061-T6	0.01996	0.454	0.01085	0.05121	0.864	0.00944
304 SS	0.00140	0.848	0.00024	0.19160	0.887	0.03156
Ti 15-3-3-3	0.00578	0.792	0.00124	0.00973	0.410	0.00819
AISI 4130	0.03982	0.804	0.01112	-0.45896	0.792	0.13382
321 SS	*	*	*	*	*	*
CDA 110	*	*	*	*	*	*
CDA 172	*	*	*	*	*	*
AM 355	*	*	*	*	*	*
IN 625	*	*	*	*	*	*

* No measurements were made in this alloy/environment combination

‡ Only one exposure time used for these measurements, see the average mass change rate table

m = estimated mass change rate for linear regression of mass change per unit area on exposure time (g/meter² · day)

R = correlation coefficient for regression

Std Error = estimated standard deviation for the mass change rate (regression slope)

Table 4. Mass change rate per unit area at 150 °C ($\text{g/meter}^2 \cdot \text{day}$) estimated by the slope for a linear regression of mass change per unit area on square root of the exposure time (assumes a uniformly filmed surface)

Alloy	HFC-125			HFC-227ea			Halon 1301		
	k	R	Std Err	k	R	Std Err	k	R	Std Err
Nit 40	0.00552	0.831	0.00092	0.01415	0.661	0.00446	0.01849	0.922	0.00194
Al 6061-T6	0.05442	0.923	0.00566	0.07080	0.922	0.00827	0.05913	0.839	0.00958
304 SS	0.00220	0.855	0.00147	0.01347	0.811	0.00269	0.00243	0.875	0.00232
Ti-15-3-3-3	0.00802	0.710	0.00221	0.01466	0.555	0.00609	0.02338	0.922	0.00246
AISI 4130	0.01836	0.140	0.49160	-1.10539	0.419	0.90484	0.22373	0.991	0.01171
321 SS	‡	‡	‡	*	*	*	‡	‡	‡
CDA 110	‡	‡	‡	*	*	*	‡	‡	‡
CDA 172	‡	‡	‡	*	*	*	‡	‡	‡
AM 355	‡	‡	‡	*	*	*	‡	‡	‡
IN 625	‡	‡	‡	*	*	*	‡	‡	‡

Table 4. (continued)

Alloy	FC-218			CF ₃ I		
	k	R	Std Err	k	R	Std Err
Nit 40	0.30768	0.818	0.06006	1.16426	0.657	0.42281
Al 6061-T6	0.26926	0.440	0.15261	0.53902	0.819	0.11951
304 SS	0.00450	0.783	0.00396	2.20300	0.918	0.30045
Ti-15-3-3-3	0.08392	0.824	0.01598	0.13561	0.343	0.14058
AISI 4130	0.48701	0.807	0.13449	-6.09099	0.862	1.35119
321 SS	*	*	*	*	*	*
CDA 110	*	*	*	*	*	*
CDA 172	*	*	*	*	*	*
AM 355	*	*	*	*	*	*
IN 625	*	*	*	*	*	*

* No measurements were made in this alloy/environment combination

‡ Only one exposure time used for these measurements, see the average mass change rate table

k = estimated mass change rate for linear regression of mass change per unit or square root of the exposure time ($\text{g/meter}^2 \cdot \text{day}^{1/2}$)

R = correlation coefficient for linear regression

Std Error = estimated standard deviation for the mass change rate (regression slope)

Table 5. Mass change rates at 150 °C estimated from a regression model that assumes mixed bare and filmed surface kinetics

HFC-125

Alloy	M_0	$M_0(\text{error})$	M_1	$M_1(\text{error})$	M_2	$M_2(\text{error})$	R
Nit 40	-0.00201	0.00986	-0.00038	0.00011	0.01282	0.00219	0.913
Al 6061-T6	-0.06235	0.06541	-0.00213	0.00072	0.09514	0.01452	0.952
304 SS	-0.00825	0.01503	-0.00065	0.00017	0.0220.	0.00334	0.931
Ti-15-3-3-3	-0.00179	0.01893	-0.00065	0.00021	0.02397	0.00420	0.920
AISI 4130	0.000	0.35385	-0.07341	0.03582	0.57720	0.26956	0.658
321 SS	‡	‡	‡	‡	‡	‡	‡
CDA 110	‡	‡	‡	‡	‡	‡	‡
CDA 172	‡	‡	‡	‡	‡	‡	‡
AM 355	‡	‡	‡	‡	‡	‡	‡
IN 625	‡	‡	‡	‡	‡	‡	‡

Table 5. (continued)

Halon 1301

Alloy	M_0	$M_0(\text{error})$	M_1	$M_1(\text{error})$	M_2	$M_2(\text{error})$	R
Nit 40	-0.01110	0.01654	-0.00095	0.00018	0.03665	0.00367	0.974
Al 6061-T6	-0.06996	0.10502	-0.00390	0.00115	0.13374	0.02331	0.912
304 SS	0.00554	0.01651	-0.00126	0.00018	0.04079	0.00366	0.972
Ti-15-3-3-3	-0.01031	0.01885	-0.00129	0.00021	0.04813	0.00418	0.979
AISI 4130	1.15e^{-10}	0.09515	0.00234	0.00964	0.33181	0.07258	0.993
321 SS	‡	‡	‡	‡	‡	‡	‡
CDA 110	‡	‡	‡	‡	‡	‡	‡
CDA 172	‡	‡	‡	‡	‡	‡	‡
AM 355	‡	‡	‡	‡	‡	‡	‡
IN 625	‡	‡	‡	‡	‡	‡	‡

Table 5. (continued)

FC-218

Alloy	M ₀	M ₀ (error)	M ₁	M ₁ (error)	M ₂	M ₂ (error)	R
Nit 40	-0.17990	0.56982	0.02352	0.01314	-0.00991	0.18321	0.855
Al 6061-T6	-0.14014	1.61140	0.01692	0.03715	0.04445	0.51810	0.455
304 SS	0.00294	0.03554	0.00182	0.00082	-0.00613	0.01143	0.852
Ti-15-3-3-3	-0.04398	0.17003	0.00050	0.00392	0.07724	0.05467	0.825
AISI 4130	0.00001	1.25580	0.08739	0.12758	0.10738	0.96200	0.813
321 SS	*	*	*	*	*	*	*
CDA 110	*	*	*	*	*	*	*
CDA 172	*	*	*	*	*	*	*
AM 355	*	*	*	*	*	*	*
IN 625	*	*	*	*	*	*	*

Table 5. (continued)

HFC-227ea

Alloy	M ₀	M ₀ (error)	M ₁	M ₁ (error)	M ₂	M ₂ (error)	R
Nit 40	-0.00571	0.04056	-0.00197	0.00094	0.03995	0.01304	0.762
Al 6061-T6	0.00940	0.08720	-0.00099	0.00201	0.08400	0.02804	0.923
304 SS	-0.00153	0.01084	-0.00212	0.00025	0.04168	0.00348	0.975
Ti-15-3-3-3	-0.00582	0.04084	-0.00402	0.00094	0.06807	0.01313	0.852
AISI 4130	0.000	8.55920	-0.15585	0.86606	-0.56139	6.52660	0.420
321 SS	*	*	*	*	*	*	*
CDA 110	*	*	*	*	*	*	*
CDA 172	*	*	*	*	*	*	*
AM 355	*	*	*	*	*	*	*
IN 625	*	*	*	*	*	*	*

Table 5. (continued)

CF₃I

Alloy	M ₀	M ₀ (error)	M ₁	M ₁ (error)	M ₂	M ₂ (error)	R
Nit 40	0.00119	1.4523	-0.35183	0.05306	4.9333	0.58918	0.953
Al 6061-T6	-0.06787	0.87966	0.05271	0.03214	-0.01757	0.35687	0.864
304 SS	-0.12567	2.5037	0.03099	0.09147	1.8759	1.0157	0.919
Ti-15-3-3-3	0.12893	0.55508	-0.04101	0.02028	0.88433	0.22519	0.915
AISI 4130	-2.12e10	12.199	0.50302	1.2265	-13.27	9.2174	0.876
321 SS	*	*	*	*	*	*	*
CDA 110	*	*	*	*	*	*	*
CDA 172	*	*	*	*	*	*	*
AM 355	*	*	*	*	*	*	*
IN 625	*	*	*	*	*	*	*

* No measurements were made in this alloy/environment combination

‡ Only one exposure time used for these measurements, see the average mass change rate table

 $m_0 = \text{g/meter}^2$ $m_1 = \text{g/meter}^2 \cdot \text{day}$ $m_2 = \text{g/meter}^2 \cdot \text{day}^{1/2}$

Figure 3 shows the mass change per unit exposed area for each sample in FC-218. The performances of the alloys in HFC-227ea, HFC-125 and in halon 1301 are shown in Figures 4, 5, and 6, respectively. Examination of these figures revealed that the majority of the observed changes were mass increases. Mass increases are not uncommon during immersion testing and are generally an indication of the formation and growth of a scale on the surface of the samples. Visual examinations confirmed the presence of such surface films; the samples were discolored in many cases. During immersion tests in aqueous solutions, the scales that form are usually oxide and/or hydroxide films. In the case of exposures to the replacement candidates, the films may be the result of reaction with the agent residual gasses, decomposition products, or just deposits of decomposition products. The large variations in mass exhibited in these figures could be due to cracking and/or spalling of these surface scales during the exposure period or during sample handling necessary for the measurements. Generally, the 4130 alloy steel exhibited the largest mass changes in every agent and the poorest correlation coefficients. Again, these were usually mass increases; however, the 4130 steel did exhibit significant mass decreases in the CF₃I (Figure 7). These decreases in mass are believed to be the result of active corrosion processes.

At this temperature, the CF₃I appeared to be substantially more aggressive than the other agents evaluated. The magnitudes of the mass changes observed in this agent were larger as a result of the formation of substantially thicker surface films. This hypothesis was supported by the results of the visual inspections performed on the coupons. While visual examination found that films were also present on the 4130 steel samples, they were layers of loose corrosion products. In general, the magnitudes of the mass changes for the 4130 steel were consistently higher than the other alloys tested in the same environments.

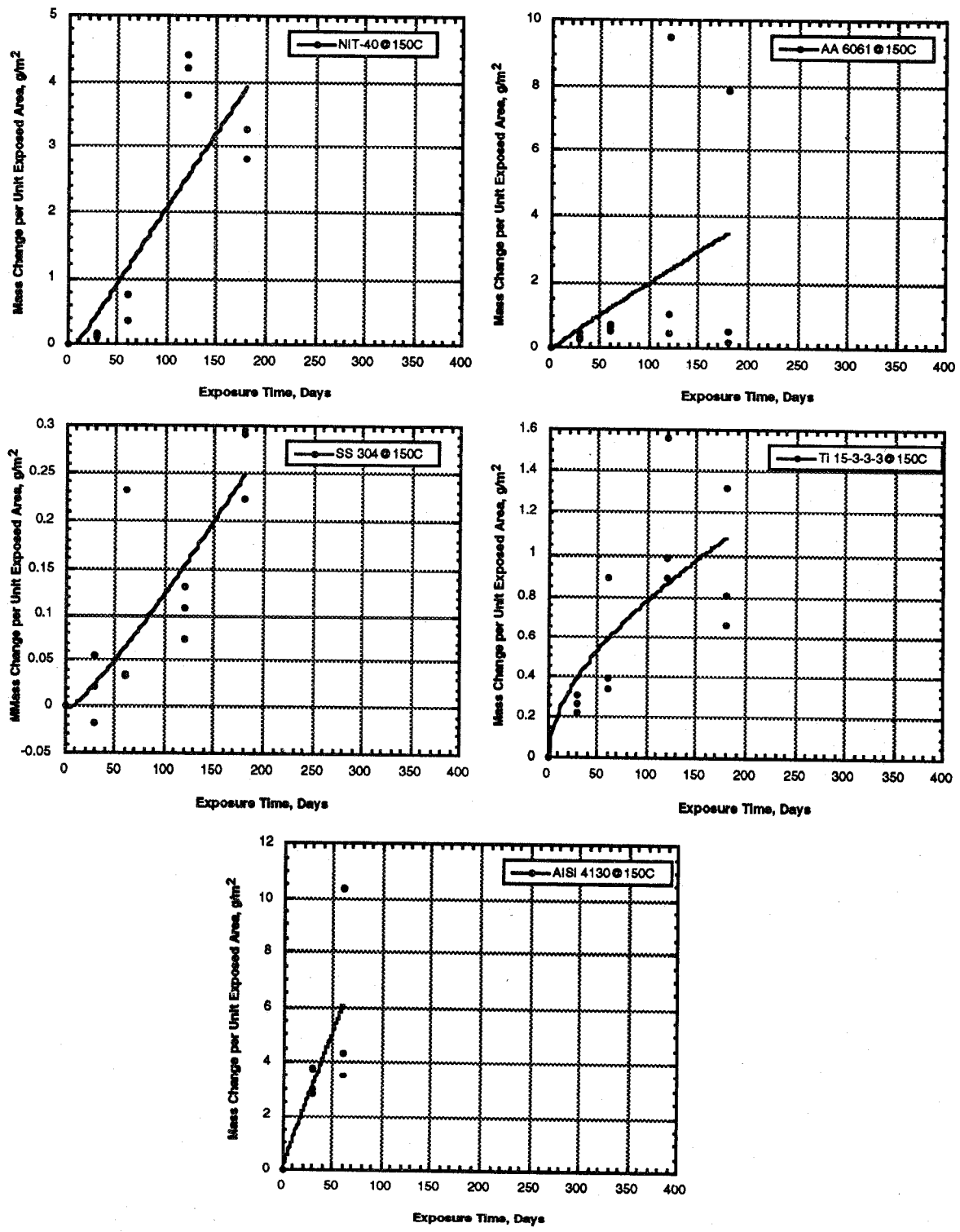


Figure 3. Mass change versus exposure time in FC-218 at 150 °C.

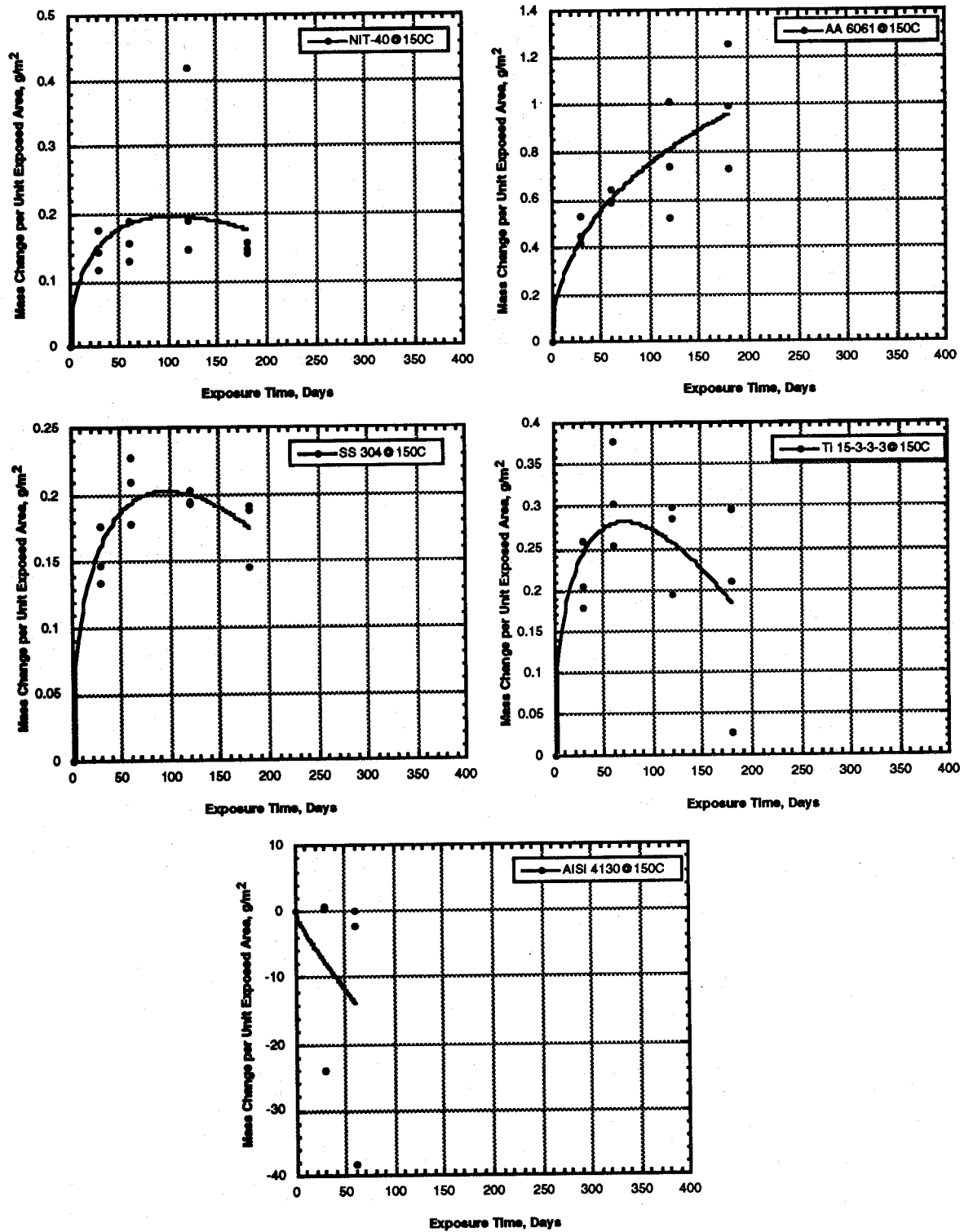


Figure 4. Mass change versus exposure time in HFC-227ea at 150 °C.

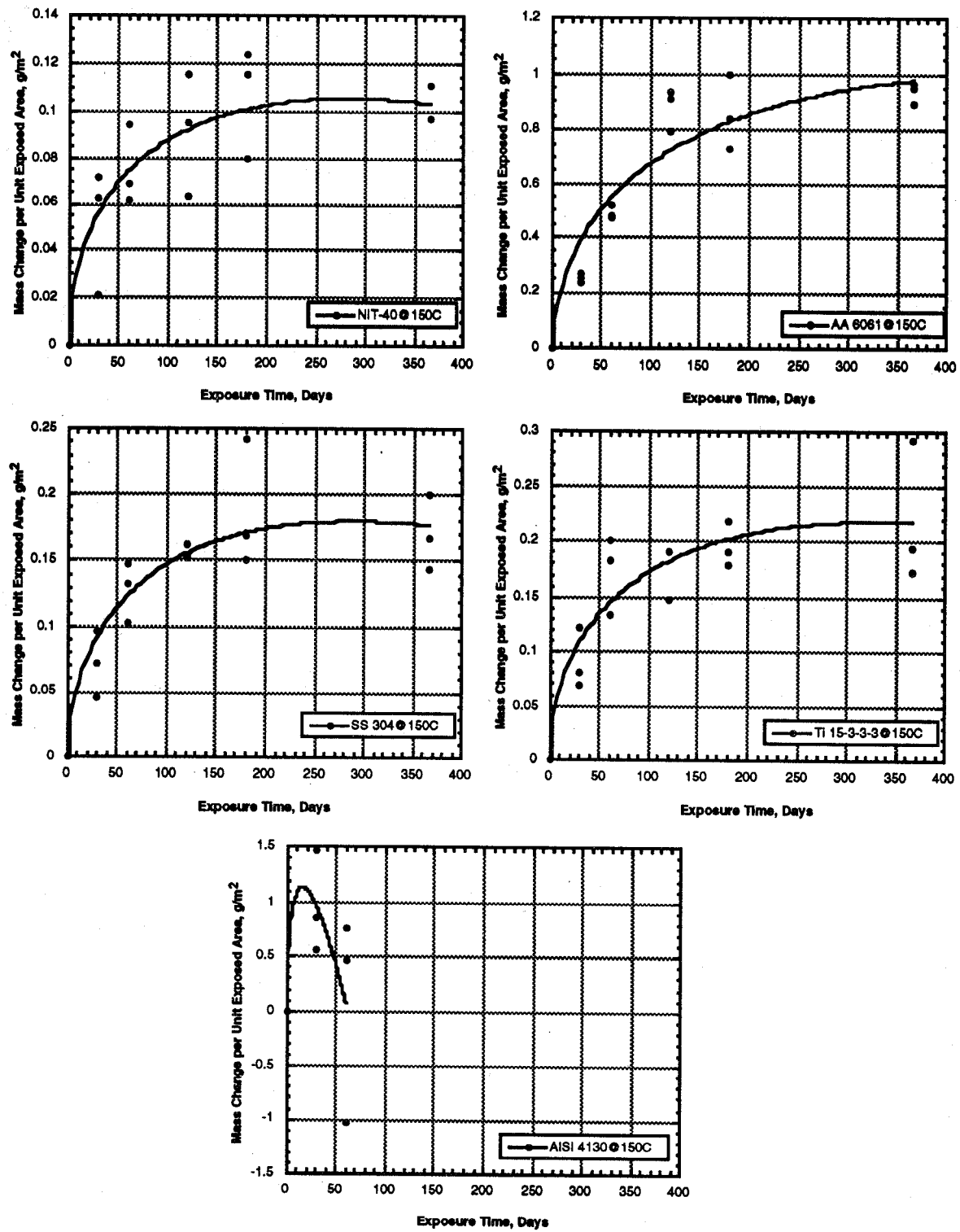


Figure 5. Mass change versus exposure time in HFC-125 at 150 °C.

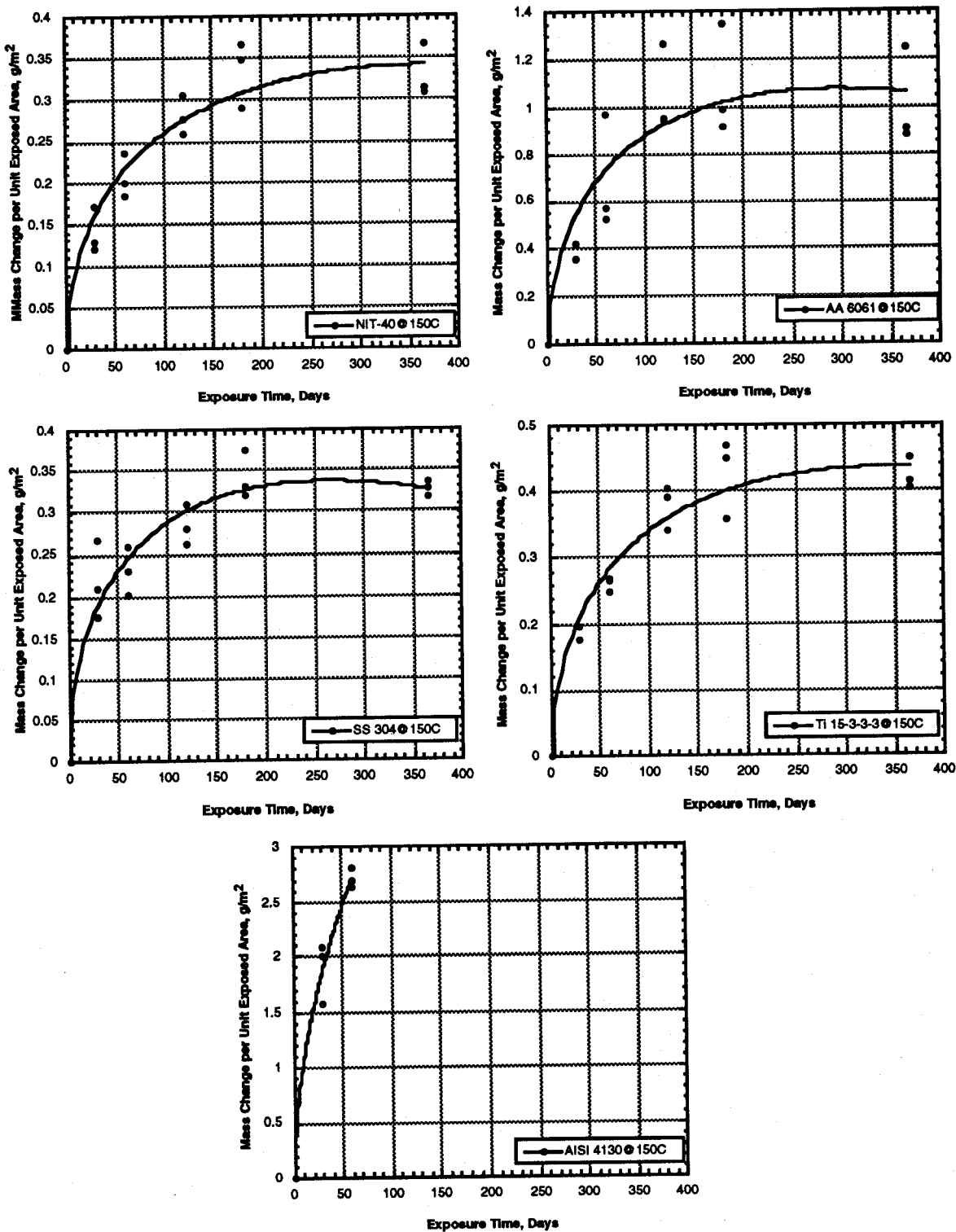


Figure 6. Mass change versus exposure time in halon 1301 at 150 °C.

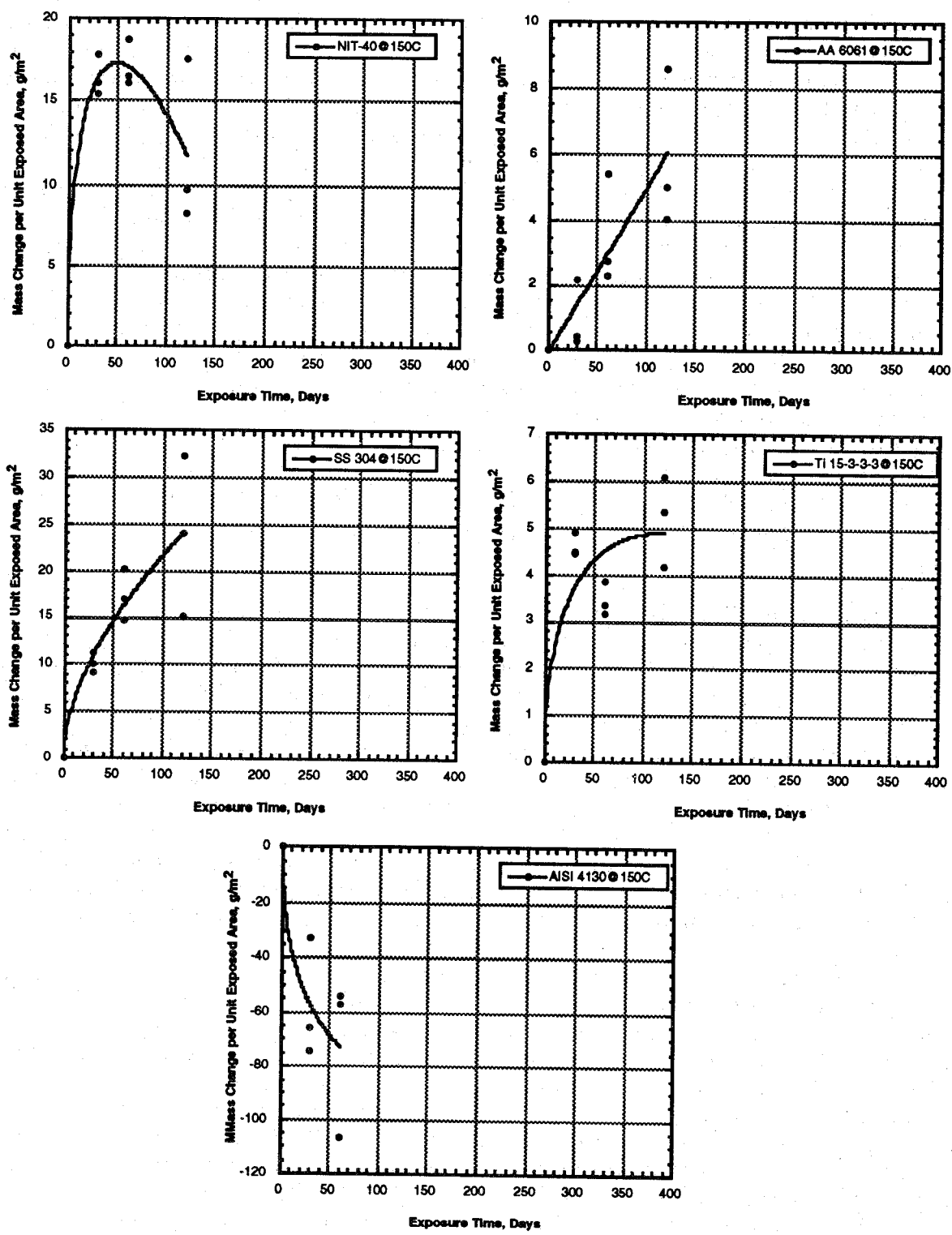


Figure 7. Mass change versus exposure time in CF_3I at 150°C .

As with the Phase I results, the evaluation of the relative performances of the alloy/agent combinations was hampered by the comparison of mass loss and mass gain measurements in the same environment. Typically, mass loss measurements are evaluated by assuming that all of the lost mass was the result of corrosion and that no corrosion products were left on the surface to generate errors in this determination. Then, the quantity of metal reacting and rate of the reactions can be calculated directly from the mass loss. Similarly, mass gain measurements can be evaluated if the reaction and the reaction product stoichiometry are known and it is assumed that none of the scale spalls off on the samples weighed before and after scale removal. For this study, descaling techniques were examined, but it was found that these techniques removed significant quantities of metal with respect to the magnitude of these measurements or did not remove the surface scales. For analysis of the relative corrosion behavior of the candidates, it is assumed that the relative magnitudes of the mass changes are proportional to the corrosion rates of the different alloy/agent combinations. It should be noted that the electrochemical measurements are the only means available for checking this assumption.

Visual inspections were also conducted on immersion test coupons. Those results are presented in Table 6. The attack observed on these coupons was relatively minor in nature and mainly consisted of staining and/or discolorations, but some pitting was observed. The observed staining may be an indication of general corrosion but this form of corrosion could not be distinguished from these measurements. CF_3I , again, appeared to be the most aggressive of the agents at 150 °C since pitting was observed in every alloy except for Nitronic 40 stainless steel. The 4130 alloy steel exhibited some slight pitting in every environment except for in the CF_3I where the most severe pitting was observed.

5.2.5 Results at 20 °C. The mass change rate, estimated for each alloy/environment combination using the same relationships from the 150 °C analyses, are presented in Table 7. As expected, the magnitudes of these values are much smaller at ambient temperature than at 150 °C. Similar linear regressions were also performed on these data. Table 8 shows the results of the mass versus simple time regression where m , the slope, is the estimated mass change rate, and R is the correlation coefficient. The standard error, again is the estimated standard deviation of the mass change rate values. The correlations at this temperature were somewhat better than those at 150 °C, but once again, the scatter resulting from the loss of surface films had a large influence. The worst value (< 0.1) occurred in the Al-6061 in CF_3I . The second regression, ($\Delta M/A = k(t)^{1/2}$) produced slightly better results (Table 9), but once again, the correlations were not encouraging. As in the case with the 150 °C data, the correlation coefficients of this regression demonstrate that the mass changes at 20 °C also followed a combined linear and $t^{1/2}$ dependence. The results of this regression are shown in Table 10.

The mass change data from the experiments performed at ambient temperatures are presented in similar fashion to those performed at 150 °C and the corresponding curves from the multiple regression are once again included with the data. The raw data used for these analyses are presented in Appendix B. Figures 8-12 are the mass change per unit exposed area for each alloy in FC-218, HFC-227ea, HFC-125, halon 1301 and CF_3I respectively. The magnitudes of the mass changes observed at ambient temperature were significantly smaller than those observed at 150 °C. These large variations are particularly evident in the aluminum data. The CF_3I did not appear to be as aggressive an environment at ambient temperature as it was at 150 °C. At this temperature, the mass changes appear to be due to the formation, growth and spalling of surface scales.

Visual inspections were also conducted on the coupons tested at 20 °C (Table 11). As in the case of the evaluation performed on the coupons tested at 150 °C, the attack observed on these coupons was relatively minor in nature and mainly consisted of staining. Some pitting was observed but, it was generally less severe at 20 °C. While the 6061-T6 aluminum alloy did not exhibit any

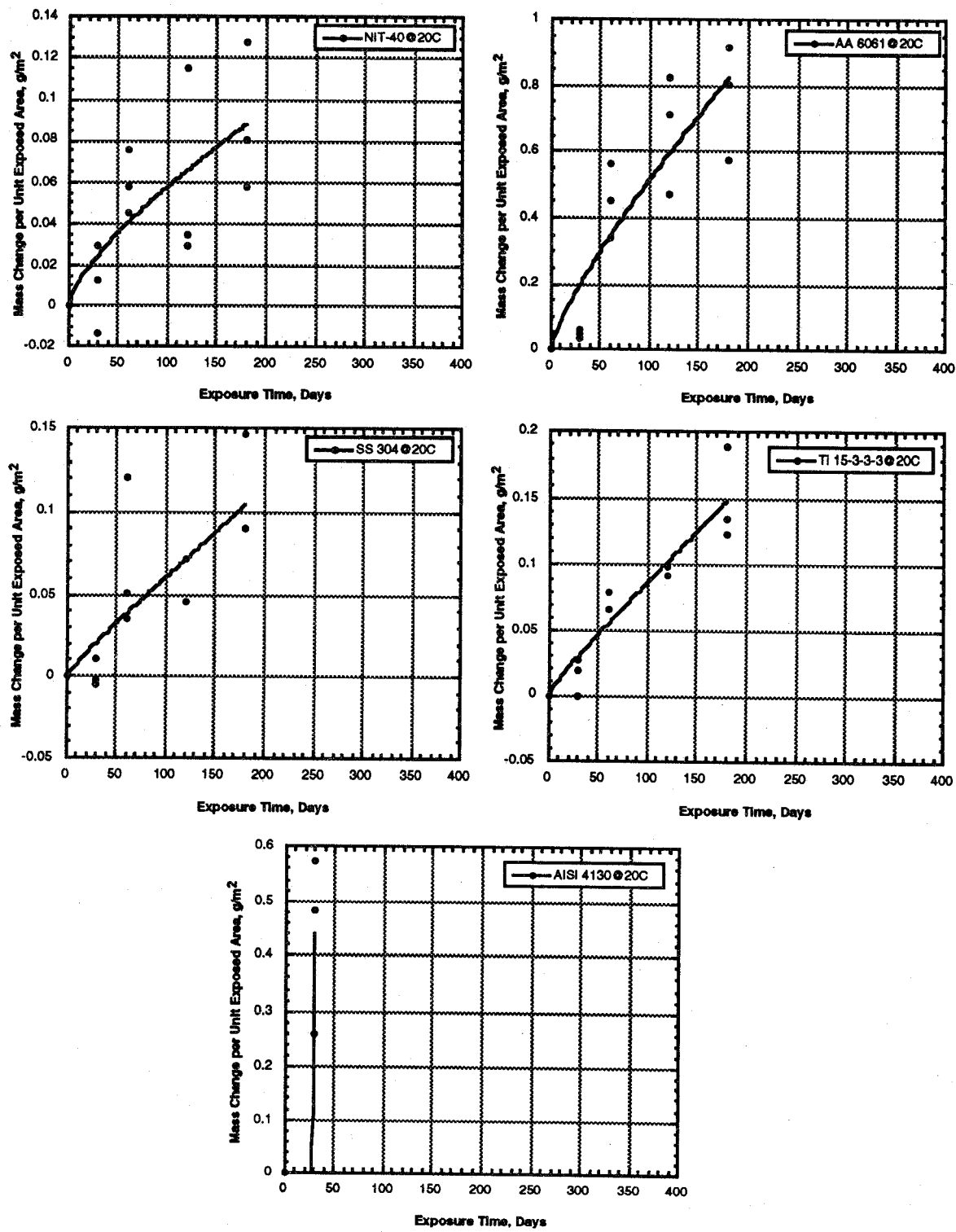


Figure 8. Mass change versus exposure time in FC-218 at 20 °C.

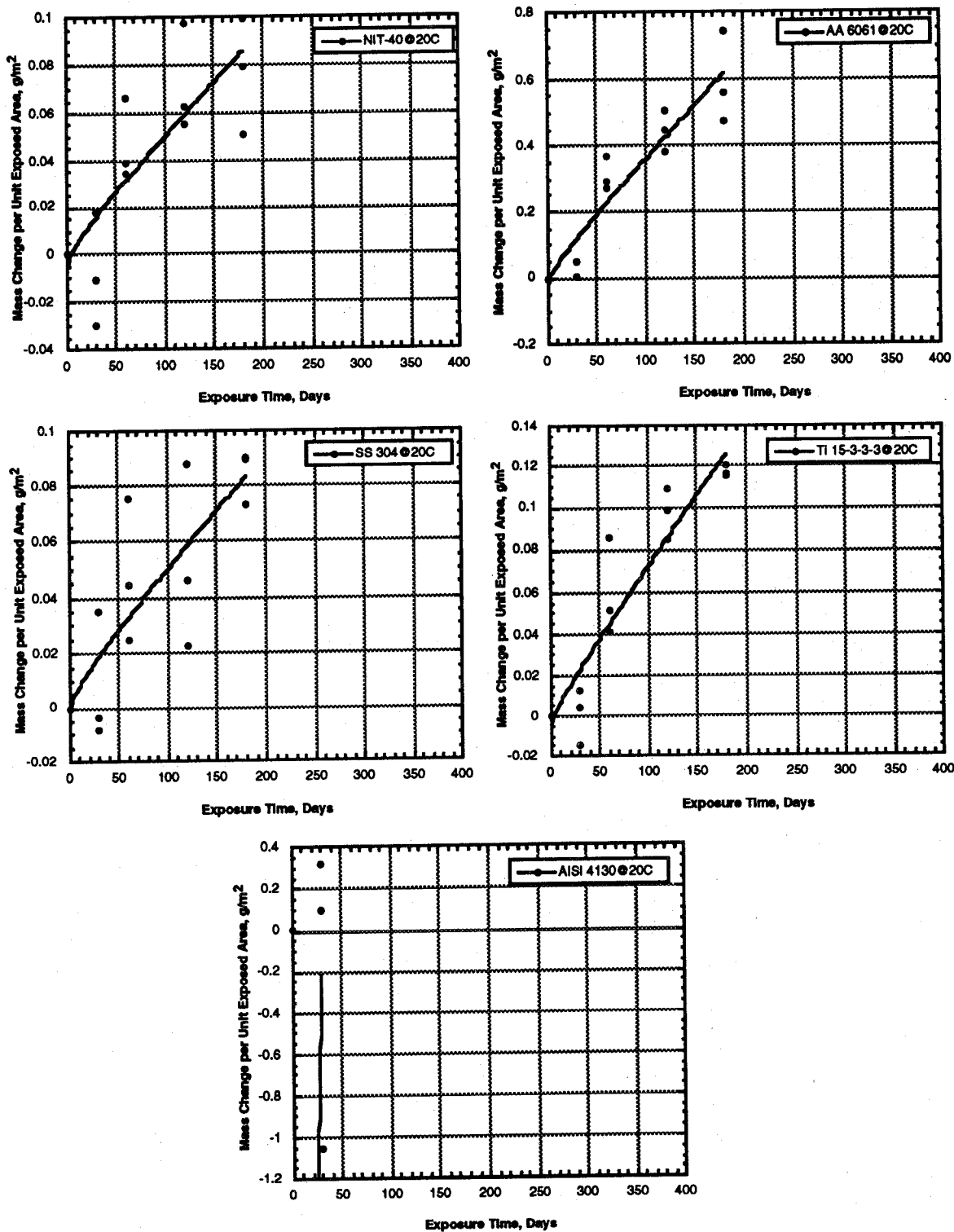


Figure 9. Mass change versus exposure time in HFC-227ea at 20 °C.

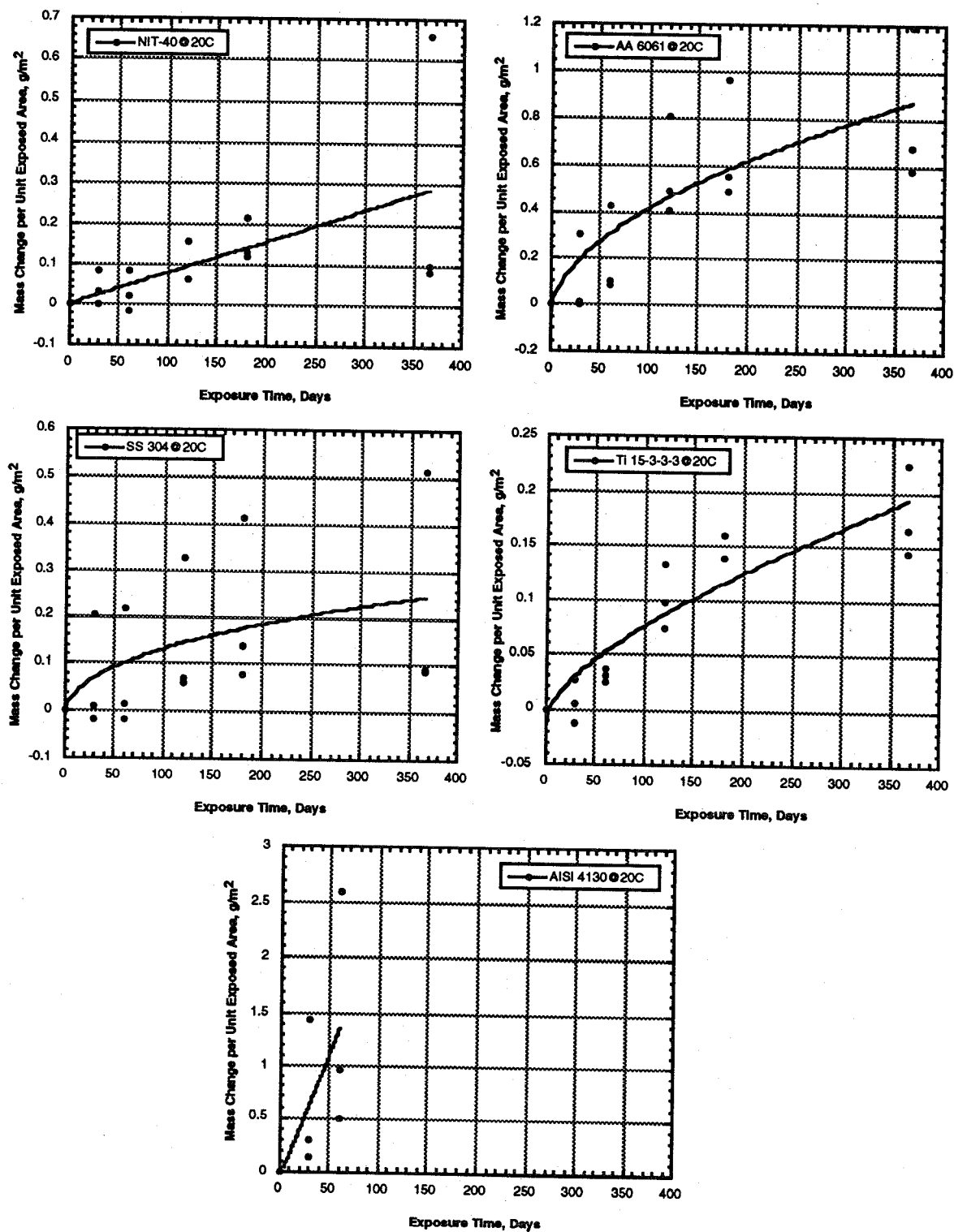


Figure 10. Mass change versus exposure time in HFC-125 at 20 °C.

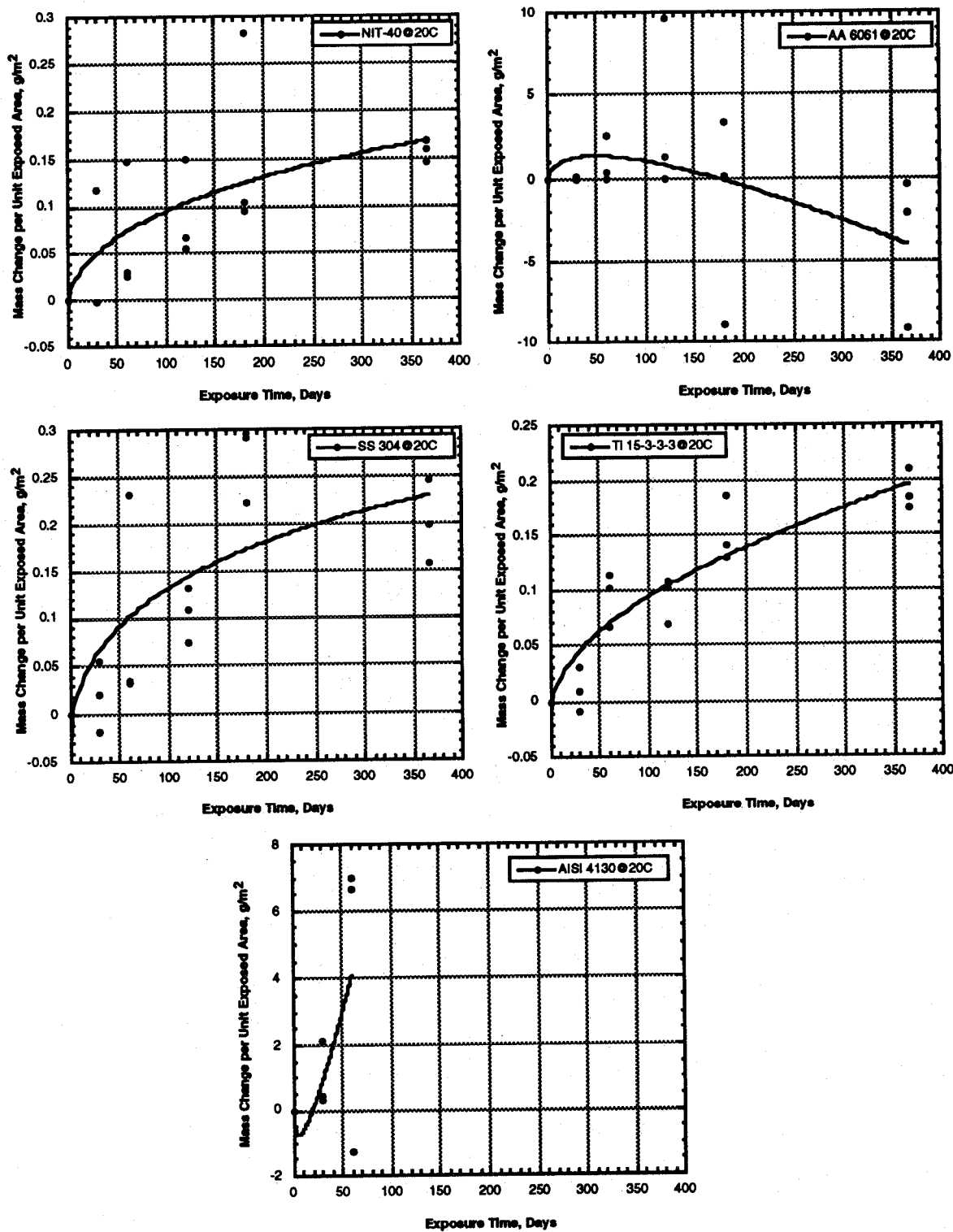


Figure 11. Mass change versus exposure time in halon 1301 at 20 °C.

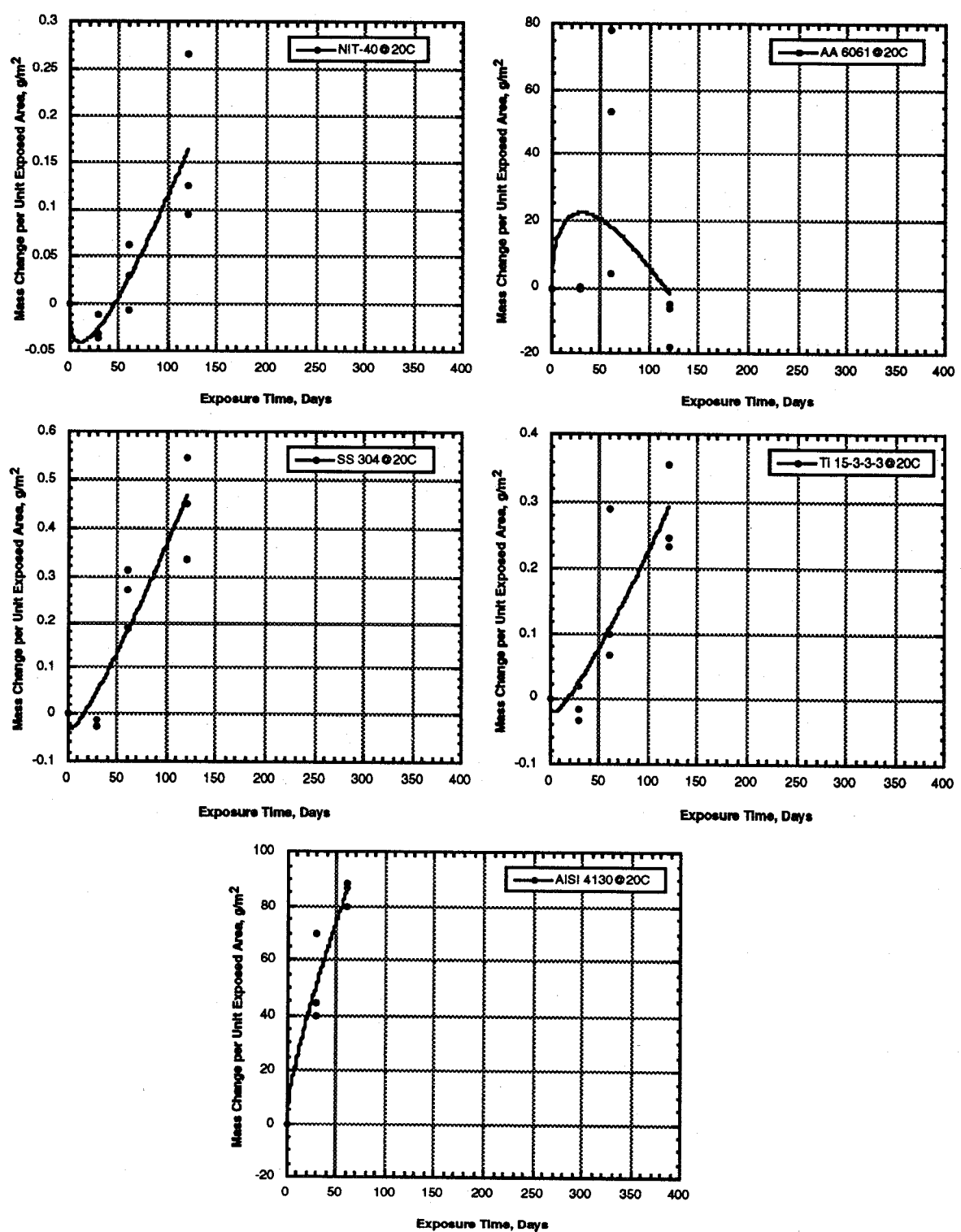


Figure 12. Mass change versus exposure time in CF₃I at 20 °C.

Table 6. Results of visual inspection of coupons tested at 150 °C

Alloy	HFC-125	HFC-227ea	Halon 1301	FC-218	CF ₃ I
Nit 40	0	0	0	0	0
Al 6061-T6	0	0	0	0	1
304 SS	0	0	0	0	2
Ti 15-3-3-3	0	0	0	0	1
AISI 4130	1	2	1	1	3
321 SS	0	*	0	*	*
CDA-110	0	*	0	*	*
CDA-172	0	*	0	*	*
AM 355	0	*	0	*	*
Inconel 615	0	*	0	*	*

- (0) No visual evidence attack
- (1) Average observed pit depth < 0.06 mm
- (2) Average observed pit depth between 0.06 mm and 0.1 mm
- (3) Average observed pit depth > 0.1 mm
- (*) Alloy not tested in this environment

Table 7. Mass change rate per unit area (g/meter² · day) at 20 °C estimated from the mass change measurements divided by the exposure time and sample area. This analysis assumes the reaction rate does not vary with time (bare surface kinetics)

Alloy	HFC-125		HFC-227ea		Halon 1301		FC-218		CF ₃ I	
	R	Std Dev	R	Std Dev	R	Std Dev	R	Std Dev	R	Std Dev
Nit 40	0.00084	0.00078	0.00039	0.00055	0.00090	0.00106	0.00057	0.00046	0.00031	0.00110
Al 6061-T6	0.00354	0.00277	0.00322	0.00183	0.00548	0.02867	0.00474	0.00253	0.22589	0.50962
304 SS	0.00128	0.00190	0.00049	0.00045	0.00104	0.00099	0.00056	0.00055	0.00248	0.00238
Ti 15-3-3-3	0.00058	0.00036	0.00062	0.00046	0.00080	0.00052	0.00084	0.00036	0.00149	0.00182
AISI 4130	0.00974	0.00884	-0.00352	0.01229	0.02156	0.02336	0.00731	0.00271	0.71189	0.23330
321 SS	0.00030	0.00027	*	*	0.00069	0.00010	*	*	*	*
CDA 110	0.00039	0.00073	*	*	0.00140	0.00078	*	*	*	*
CDA 172	0.00006	0.00058	*	*	-0.00020	0.00031	*	*	*	*
AM 355	-0.00001	0.00077	*	*	0.00022	0.00047	*	*	*	*
IN 625	0.00004	0.00012	*	*	0.00016	0.00015	*	*	*	*

(+) Values mean mass increase (scaling)
(-) Values mean mass decrease (corrosion)
* No measurement made in the agent for this alloy
R = Average mass change rate (g/meter² · day)

Table 8. Mass change rate per unit area ($\text{g/meter}^2 \cdot \text{day}$) at 20 °C estimated by the regression slope for a linear regression of mass change per unit area on exposure time (assumes constant, bare surface, reaction kinetics)

Alloy	HFC-125			HFC-227ea			Halon 1301		
	m	R	Std Err	m	R	Std Err	m	R	Std Err
Nit 40	0.00078	0.637	0.00023	0.00049	0.825	0.00009	0.00042	0.660	0.00012
Al 6061-T6	0.00229	0.791	0.00044	0.00348	0.934	0.00037	0.01262	0.389	0.00748
304 SS	0.00061	0.495	0.00027	0.00046	0.824	0.00009	0.00060	0.691	0.00016
Ti 15-3-3-3	0.00053	0.900	0.00006	0.00071	0.934	0.00008	0.00051	0.886	0.00007
AISI 4130	0.00894	0.664	0.00380	-0.00352	0.241	0.00709	0.02791	0.603	0.01395
321 SS	‡	‡	‡	*	*	*	‡	‡	‡
CDA 110	‡	‡	‡	*	*	*	‡	‡	‡
CDA 172	‡	‡	‡	*	*	*	‡	‡	‡
AM 355	‡	‡	‡	*	*	*	‡	‡	‡
IN 625	‡	‡	‡	*	*	*	‡	‡	‡

Table 8. (continued)

Alloy	FC-218			CF ₃ I		
	m	R	Std Err	m	R	Std Err
Nit 40	0.00048	0.753	0.00012	0.00149	0.798	0.00036
Al 6061-T6	0.00459	0.900	0.00062	0.03963	0.066	0.18881
304 SS	0.00058	0.800	0.00012	0.00409	0.919	0.00055
Ti-15-3-3-3	0.00082	0.944	0.00008	0.00257	0.860	0.00048
AISI 4130	0.00731	0.920	0.00156	0.55297	0.949	0.06940
321 SS	*	*	*	*	*	*
CDA 110	*	*	*	*	*	*
CDA 172	*	*	*	*	*	*
AM 355	*	*	*	*	*	*
IN 625	*	*	*	*	*	*

* No measurements were made in this alloy/environment combination

‡ Only one exposure time used for these measurements, see the average mass change rate table

m = estimated mass change rate for linear regression of mass change per unit area on exposure times ($\text{g/meter}^2 \cdot \text{day}$)

R = correlation coefficient for linear regression

Std Error = estimated standard deviation for the mass change rate (regression slope)

Table 9. Mass change rate per unit area ($\text{g}/\text{meter}^2 \cdot \text{day}$) at 20°C estimated by the slope for a linear regression of mass change per unit area on square root of the exposure time (assumes a uniformly filmed surface)

Alloy	HFC-125			HFC-227ea			Halon 1301		
	k	R	Std Err	k	R	Std Err	k	R	Std Err
Nit 40	0.01491	0.602	0.00494	0.00696	0.823	0.00133	0.00922	0.714	0.00226
Al 6061-T6	0.04856	0.829	0.00818	0.04711	0.907	0.00606	-0.18978	0.289	0.01570
304 SS	0.01331	0.530	0.00532	0.00622	0.809	0.00126	0.01327	0.761	0.02820
Ti 15-3-3-3	0.01084	0.913	0.00121	0.00965	0.904	0.00126	0.01078	0.925	0.00110
AISI 4130	0.10716	0.654	0.04691	-0.02725	0.241	0.05492	0.31117	0.552	0.17774
321 SS	‡	‡	‡	*	*	*	‡	‡	‡
CDA 110	‡	‡	‡	*	*	*	‡	‡	‡
CDA 172	‡	‡	‡	*	*	*	‡	‡	‡
AM 355	‡	‡	‡	*	*	*	‡	‡	‡
IN 625	‡	‡	‡	*	*	*	‡	‡	‡

Table 9. (continued)

Alloy	FC-218			CF ₃ I		
	k	R	Std Err	k	R	Std Err
Nit 40	0.00688	0.766	0.00160	0.01350	0.663	0.00483
Al 6061-T6	1.63021	0.894	1.63021	0.46755	0.070	2.09612
304 SS	0.00785	0.776	0.00177	0.04108	0.831	0.00869
Ti 15-3-3-3	0.01113	0.917	0.00135	0.02562	0.772	0.00668
AISI 4130	0.05658	0.920	0.01209	6.92014	0.975	0.59885
321 SS	*	*	*	*	*	*
CDA 110	*	*	*	*	*	*
CDA 172	*	*	*	*	*	*
AM 355	*	*	*	*	*	*
IN 625	*	*	*	*	*	*

* No measurements were made in this alloy/environment combination

‡ Only one exposure time used for these measurements, see the average mass change rate table

k = estimated mass change rate for linear regression of the mass change per unit area on square root of exposure time ($\text{g}/\text{meter}^2 \cdot \text{day}^{1/2}$)

R = correlation coefficient for linear regression

Std Error = estimated standard deviation for the mass change rate (regression slope)

Table 10. Mass change rates at 150 °C for a regression model that assumes mixed bare and filmed surface kinetics

HFC-125

Alloy	M ₀	M ₀ (error)	M ₁	M ₁ (error)	M ₂	M ₂ (error)	R
Nit 40	0.00035	0.06907	0.00075	0.00076	0.00047	0.01533	0.637
Al 6061-T6	-0.05633	0.11893	0.00014	0.00131	0.04588	0.02640	0.830
304 SS	-0.00965	0.07734	-9.53e-5	0.00085	0.01513	0.01716	0.531
Ti-15-3-3-3	-0.01411	0.01693	0.00020	0.00019	0.00700	0.00376	0.920
AISI 4130	1.05e-10	0.4376	0.02643	0.04432	-0.03015	0.33373	0.666
321 SS	‡	‡	‡	‡	‡	‡	‡
CDA 110	‡	‡	‡	‡	‡	‡	‡
CDA 172	‡	‡	‡	‡	‡	‡	‡
AM 355	‡	‡	‡	‡	‡	‡	‡
IN 625	‡	‡	‡	‡	‡	‡	‡

Table 10. (continued)

Halon 1301

Alloy	M ₀	M ₀ (error)	M ₁	M ₁ (error)	M ₂	M ₂ (error)	R
Nit 40	-0.00814	0.03247	-0.00012	0.00036	0.01154	0.00721	0.720
Al 6061-T6	-0.39446	2.1183	-0.03640	0.02326	0.50713	0.47012	0.461
304 SS	-0.02406	0.04067	-0.00026	0.00045	0.01815	0.00903	0.767
Ti-15-3-3-3	-0.00970	0.01602	5.18e-5	0.00018	0.00978	0.00355	0.926
AISI 4130	7.29e-15	1.593	0.15669	0.157	-0.68495	1.1102	0.614
321 SS	‡	‡	‡	‡	‡	‡	‡
CDA 110	‡	‡	‡	‡	‡	‡	‡
CDA 172	‡	‡	‡	‡	‡	‡	‡
AM 355	‡	‡	‡	‡	‡	‡	‡
IN 625	‡	‡	‡	‡	‡	‡	‡

Table 10. (continued)

FC-218

Alloy	M ₀	M ₀ (error)	M ₁	M ₁ (error)	M ₂	M ₂ (error)	R
Nit 40	-0.00226	0.01695	0.00022	0.00039	0.00378	0.00545	0.764
Al 6061-T6	-0.03239	0.08801	0.00268	0.00203	0.02799	0.02829	0.908
304 SS	-0.00210	0.01788	0.00047	0.00041	0.00154	0.00575	0.801
Ti-15-3-3-3	-0.00205	0.01165	0.00067	0.00027	0.00225	0.00374	0.946
AISI 4130	n/a	n/a	n/a	n/a	n/a	n/a	n/a
321 SS	*	*	*	*	*	*	*
CDA 110	*	*	*	*	*	*	*
CDA 172	*	*	*	*	*	*	*
AM 355	*	*	*	*	*	*	*
IN 625	*	*	*	*	*	*	*

Table 10. (continued)

HFC-227ea

Alloy	M ₀	M ₀ (error)	M ₁	M ₁ (error)	M ₂	M ₂ (error)	R
Nit 40	-0.00502	0.01389	0.00037	0.00032	0.00177	0.00447	0.827
Al 6061-T6	-0.01883	0.05417	0.00280	0.00125	0.00987	0.01742	0.936
304 SS	-0.00142	0.01276	0.00032	0.00030	0.00194	0.00410	0.828
Ti-15-3-3-3	-0.00467	0.01119	0.00060	0.00026	0.00172	0.00360	0.935
AISI 4130	n/a	n/a	n/a	n/a	n/a	n/a	n/a
321 SS	*	*	*	*	*	*	*
CDA 110	*	*	*	*	*	*	*
CDA 172	*	*	*	*	*	*	*
AM 355	*	*	*	*	*	*	*
IN 625	*	*	*	*	*	*	*

Table 10. (continued)

CF₃I

Alloy	M ₀	M ₀ (error)	M ₁	M ₁ (error)	M ₂	M ₂ (error)	R
Nit 40	-0.00019	0.0267	0.00353	0.00098	-0.02389	0.01083	0.874
Al 6061-T6	-3.2761	15.868	-0.83038	0.57971	9.2353	6.4376	0.436
304 SS	-0.00955	0.04828	0.00597	0.00176	-0.0220	0.01959	0.929
Ti-15-3-3-3	-0.00551	0.04308	0.00392	0.00157	-0.0159	0.01718	0.872
AISI 4130	1.21e-10	5.605	0.71758	0.56594	5.443	4.232	0.9706
321 SS	*	*	*	*	*	*	*
CDA 110	*	*	*	*	*	*	*
CDA 172	*	*	*	*	*	*	*
AM 355	*	*	*	*	*	*	*
IN 625	*	*	*	*	*	*	*

* No measurements were made in this alloy/environment combination
‡ Only one exposure time used for these measurements, see the average mass change rate table.
m₀ = g/meter²
m₁ = g/meter² · day
m₂ = g/meter² · day^{1/2}

Table 11. Results of visual inspection of coupons tested at 20 °C

Alloy	HFC-125	HFC-227ea	Halon 1301	FC-218	CF ₃ I
Nit 40	0	1	0	0	0
Al 6061-T6	1	1	3	0	0
304 SS	0	0	0	0	0
Ti 15-3-3-3	0	0	0	0	0
AISI 4130	3	1	1	1	3
321 SS	0	*	0	*	*
CDA-110	0	*	0	*	*
CDA-172	0	*	0	*	*
AM 355	0	*	0	*	*
Inconel 615	0	*	0	*	*

(0) No visual evidence attack observed

(1) Average observed pit depth < 0.06 mm

(2) Average observed pit depth between 0.06 mm and 0.1 mm

(3) Average observed pit depth > 0.1 mm

(*) Alloy not tested in this environment

pitting in the halon 1301 at 150 °C, it did however, exhibit some pitting in that agent at 20 °C. This result was unexpected and may be an indication that this alloy has some compatibility problems with the halon 1301. The 4130 alloy steel, once again, exhibited some pitting in every environment with the most severe pitting observed in the CF₃I.

5.3 Environmentally Induced Fracture Experiments (Slow Strain Rate Tensile Tests)

The environmentally induced fracture resistance of the alloys was evaluated by conducting exposure tests in each of the replacement candidates. This was accomplished by loading cylindrical tensile specimens of the alloys in tension, by a slow increase in the applied strain, until failure occurred by either a normal mechanical or an environmentally assisted means. Comparisons between the stresses and strains required to cause failure in an inert environment and in the agent at the same temperature provided a measure of the propensity for that agent to cause an environmentally induced failure.

5.3.1 Materials. The materials selected by the sponsors for Phase II were: 304 stainless steel, stainless steel alloy 21-6-9 (Nitronic 40), and beta-titanium alloy 15-3-3-3. These alloys were selected

because they are presently in service, or under consideration for future use, in the agent storage and distribution systems on board jet aircraft. The compositions of these alloys are also given in Table 1 (Section 5.2.1).

5.3.2 Experimental Procedure at 150 °C. The alloys were evaluated for stress corrosion cracking susceptibility in the replacement candidates by the slow strain rate (SSR) tensile test technique. This technique was selected because it generates intrinsic mechanical properties data for a given alloy and it also reveals any interactions that may have occurred between that alloy and the testing environment within a relatively short time frame (Ricker, 1994, Stoudt and Fink 1994, and Stoudt and Ricker, 1994).

All of the samples used for these experiments were machined with the tensile axis parallel to the rolling direction of the plate stock (Figure 13) and tested in the "as received" condition. The sample preparation consisted of a measurement of the appropriate quantities (e.g., gauge length) followed by degreasing in acetone and alcohol. The vessels used for these experiments were 250 ml volume autoclaves with a design similar to those used for the exposure testing, except that these vessels were modified so that load could be applied to the tensile specimen in-situ under constantly maintained environmental conditions as shown in Figure 14 (Ricker, 1994). The testing conditions used for this portion of the analysis were nominally 5.86 MPa at $150^{\circ} \pm 1^{\circ}\text{C}$.

The test vessels were evacuated and charged with agent in the same manner as the exposure test vessels, but due to the reduced capacity of the test vessels, the appropriate mass was obtained by a calculation based on the ideal gas law. This approach was selected over the mass balance shown in Equation (1) (Section 5.2.2) for two reasons. First, the number of moles of gas could be held constant allowing for a consistent agent concentration for each test. Second, this model generated a slightly lower pressure in the cells reducing the risk of a rupture.

The mechanical tests were conducted using a computer controlled SSR testing system which operated at a constant crosshead speed of 2.54×10^{-8} m/s (1.0×10^{-6} in/s). The computer was configured to sample and record the applied load, the crosshead displacement and the elapsed time at 90 s intervals. After failure, the agent was released, the vessels were then allowed to cool to ambient temperature, and the samples were removed from the vessel and stored in a desiccator until analyzed.

The fracture surfaces were sectioned from the broken samples and prepared for analysis. The influence of the agents on the ductility of the alloys was determined from reduction in area (RA) measurements performed on the fracture surfaces with an optical measuring microscope with a $\pm 0.5 \times 10^{-6}$ m resolution. All samples were examined visually and scanning electron microscopy was performed on selected samples to verify the presence of stress corrosion cracking. The results of these experiments were used to assess the potential for failure by stress corrosion cracking for each of the alloys in a replacement candidate.

5.3.3 Experimental Procedure at 20 °C. A second series of slow strain rate tests was conducted at ambient conditions in order to determine the possible influences of the liquid phase and/or the meniscus regions on the stress corrosion cracking resistance of these materials. To do this, Equation (1) was utilized to determine an appropriate mass of agent so as to locate the liquid/vapor meniscus region at the approximate midpoint of the gauge section of the tensile specimen. The resulting cell pressures varied according to the density of each agent, but were on the order of 1.38 MPa at $20 \pm 1^{\circ}\text{C}$. The remainder of the procedure was identical to the one outlined in the previous section.

5.3.4 Results at 150 °C. Environmentally induced fracture is the initiation and/or propagation of a crack at stresses well below those normally required to cause fracture resulting from simultaneous

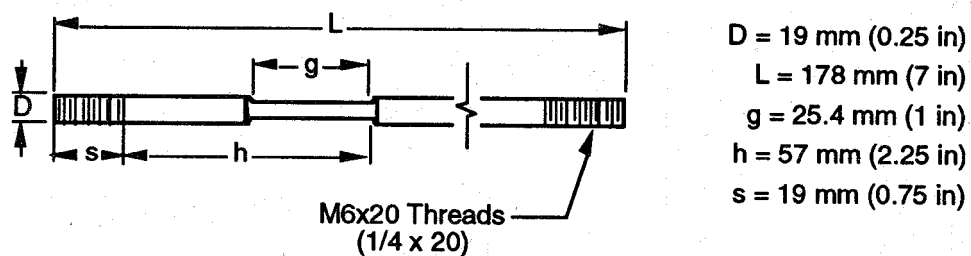


Figure 13. Slow strain rate tensile sample design (ASTM E-8, G-49).

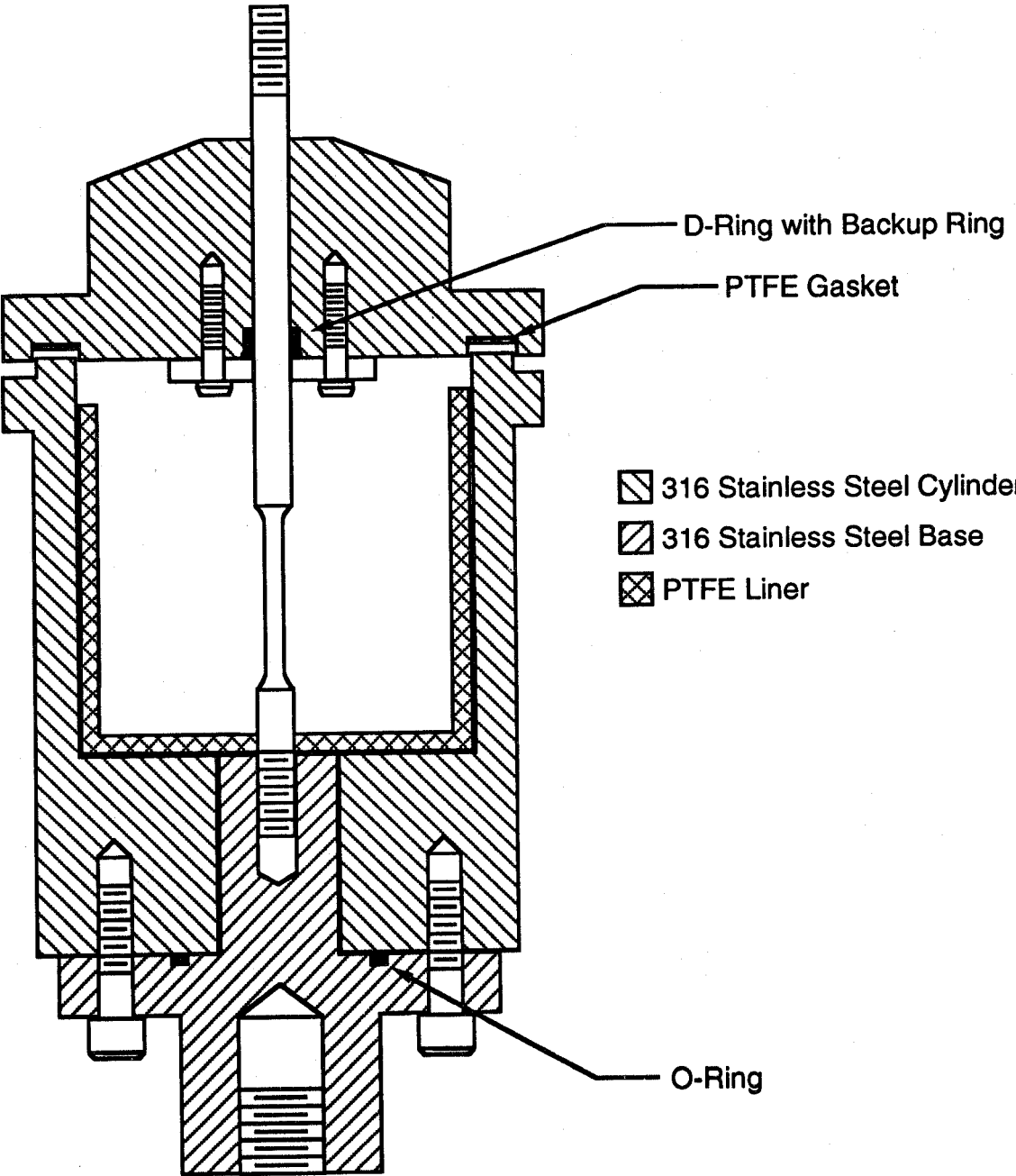


Figure 14. Schematic diagram of the slow strain rate test chamber.

exposure to a chemically reactive environment and a mechanical stress (Stoudt, 1995 and Stoudt, 1994). This particular form of corrosion occurs in specific material/environment combinations and while attack may not be readily apparent, failures can be sudden and catastrophic.

The same three parameters used to indicate the susceptibility of an alloy to environmentally induced failure used for Phase I were applied to the Phase II data. These are: the ultimate tensile strength (UTS), the strain to failure (ϵ_f), and the reduction in cross sectional area (RA) (Ricker, 1994).

The UTS is an indication of the fracture strength of the sample and it is determined from the maximum load observed during the tensile test according to the relationship:

$$\sigma_{UTS} = \frac{P_{max}}{A_o} \quad (6)$$

where P_{max} is the maximum load supported by the sample during the test and A_o is the initial cross-sectional area of the gauge section of the sample (Deiter, 1986). If cracking, or some other environmental interaction that promotes crack initiation or propagation at lower stresses, occurs, it will produce a noticeable change in this parameter (Stoudt, 1994). Environmental interactions can also alter deformation processes on the surfaces and at tips of cracks formed in the sample. One of the two parameters used to measure the ductility is the engineering strain to failure (ϵ_f) which can be determined from the relationship:

$$\epsilon_f = \frac{[L_f - L_o]}{L_o} \quad (7)$$

where L_f is the total change in sample length during the experiment and L_o is the initial gauge length (Deiter, 1986). This measurement includes both the elastic and plastic deformation components required to induce failure, which are measured by displacement gages located outside the environmental chamber increasing measurement errors. As a result, a ductility determination based solely on this quantity may contain significant experimental error. Another means for determining the ductility of a material is the reduction in area (RA). This quantity is obtained from physical measurements performed on the fracture surface after completion of the tensile test from the relationship:

$$RA = \frac{[A_f - A_o]}{A_o} \quad (8)$$

where A_f is the final cross-sectional area of the fracture surface and A_o is the initial gauge section cross-sectional area (Deiter, 1986). Unlike the strain to failure (STF), the RA measurement only includes the plastic deformation component required to induce failure and does not include measurement errors which may have occurred during the time the cell was ascending to the test temperature. Therefore, this is a better measure of the environmental interactions. Typically, all three of these parameters are analyzed by forming a ratio of the value observed in the environment to the value observed in an inert reference environment, argon (Ar), (Ricker, 1994 and Stoudt *et al.*, 1994).

Another approach for analysis of this data is to estimate the statistical significance of the difference between the mean determined for the parameter in the inert reference environment and the mean determined for the agent (Ricker, 1994). This analysis consisted of the calculation of Student's t-statistic for the significance of the difference between the mean determined in each environment and

the mean for the same parameter and alloy tested in argon at the same temperature. This statistic is calculated from the relationship:

$$t = \frac{(\bar{y}_{envir} - \bar{y}_{Ar})}{\sqrt{\left(\frac{S_{envir}^2}{n_{envir}} + \frac{S_{Ar}^2}{n_{Ar}} \right)}} \tag{9}$$

where: \bar{y}_{envir} is the mean of the tests in the agent, \bar{y}_{Ar} is the mean of the tests in argon, S_{envir} is the variance of the tests conducted in the agent, S_{Ar} is the variance of the tests conducted in argon, n_{envir} is the number of samples tested in the agent, and n_{Ar} is the number of samples tested in argon all at the same temperature (Mendenhall, 1992).

Table 12 gives the average UTS determined for each alloy in argon at 150 °C, and in each agent at 150 °C. The standard deviations for these calculated values are presented in Table 13. The ratio of the average UTS in each agent to the average UTS in argon at the same temperature is given in Table 14. In this table, it can be seen that 18 of the 20 agent/alloy combinations have a higher average UTS values in the agent than in argon.

Table 15 contains the results of a t-test estimate of the statistical significance of the observed differences using the alloy standard deviations. For a confidence level of 99.5 %, t determined in this manner (4 degrees of freedom) should be less than -4.60 to conclude that the environment significantly reduced the strength or ductility of the alloy. Similarly, a value greater than +4.60 would indicate a significant increase in strength or ductility caused by the environment. Values between -4.60 and +4.60 are considered statistically insignificant. A significant decrease in the average UTS may be an indication of cracking, but it could also be the result of corrosion reactions which reduced effective cross-section or otherwise assisting deformation. An increase in the average UTS is unusual and this may suggest that sample/environment interactions are inhibiting deformation and fracture, but it could also be an indication of an interference between the corrosion products being generated on the sample and the seal of the autoclave through which the sample must slide. The most important point is that no agent caused statistically significant changes in all of the alloys which demonstrates that suitable materials can be identified for the containment of any of these candidates (Ricker, 1994).

The ductility results for the 150 °C SSR tests are given in Tables 16 and 17. Table 16 gives the average strain to failure for each alloy/environment combination, and in argon at 150 °C. Table 17 shows the standard deviations for the STF calculations. The ratio of the average strain to failure for each alloy in each environment to that observed in the same alloy in argon at the same temperature is presented in Table 18. The significance of the difference is again presented as a function of the alloy standard deviations in Table 19. Environmental induced cracking, or stress corrosion cracking (SCC), is usually evidenced by a reduction in ductility. In Table 18, it can be seen that strain to failure ratio generally increased for Nitronic 40 and for 304 stainless for most of the alloy/environment combinations. The titanium 15-3-3-3 alloy demonstrated significant decreases in ductility for all of the environments. This is best reflected in the CF₃I data. The sharp decrease in the ductility was the result of severe cracking which was observed on two of the three specimens tested in this agent. However, these strain to failure measurements are based on load frame displacement measurements taken by a transducer positioned outside the autoclave during the experiment. As a result, the reduction in area measurements, which are based on measurements performed on the fracture surface with an optical microscope after the experiment, are a more reliable indication of changes in ductility.

Table 20 presents the RA data for each alloy in argon gas at 150 °C and each agent at 150 °C. Table 21 gives the standard deviations for these measurements. The ratio of the average reduction in

Table 12. Average ultimate tensile strength at 150 °C (MPa)

Environment	Nitronic 40	304 SS	Titanium 15-3-3-3
Argon	599	649	497
Halon 1301	603	671	497
FC-218	602	646	504
HFC-227ea	611	655	534
HFC-125	611	651	552
CF ₃ I	607	657	505

Table 13. Standard deviation of the ultimate tensile strength measurements at 150 °C (MPa)

Environment	Nitronic 40	304 SS	Titanium 15-3-3-3
Argon	1.5	0.6	6.0
Halon 1301	2.3	1.5	3.4
FC-218	3.7	0.8	4.7
HFC-227ea	4.8	2.0	5.7
HFC-125	3.6	2.4	2.0
CF ₃ I	0.9	2.0	2.2

Table 14. Ultimate tensile strength ratios at 150 °C [(UTS in Agent)/(UTS in Ar)]

Environment	Nitronic 40	304 SS	Titanium 15-3-3-3
Argon	*	*	*
Halon 1301	1.007	1.035	1.000
FC-218	1.006	0.996	1.015
HFC-227ea	1.021	1.010	1.076
HFC-125	1.020	1.003	1.112
CF ₃ I	1.013	1.012	1.017

Table 15. t-Test for significance in UTS change at 150 °C

Environment	Nitronic 40	304 SS	Titanium 15-3-3-3
Argon	*	*	*
Halon 1301	0.281	2.109	0.003
FC-218	0.226	-0.224	0.276
HFC-227ea	0.809	0.582	1.377
HFC-125	0.776	0.198	2.035
CF ₃ I	0.514	0.745	0.304

Table 16. Average strain to failure at 150 °C (%)

Environment	Nitronic 40	304 SS	Titanium 15-3-3-3
Argon	43.0	17.2	6.6
Halon 1301	44.9	18.1	5.7
FC-218	43.8	16.9	6.1
HFC-227ea	43.7	17.0	5.9
HFC-125	43.1	17.2	6.0
CF ₃ I	41.7	18.1	3.8

Table 17. Standard deviation of the strain to failure measurements at 150 °C (%)

Environment	Nitronic 40	304 SS	Titanium 15-3-3-3
Argon	0.5	2.3	1.9
Halon 1301	3.8	1.7	0.8
FC-218	2.6	1.5	0.8
HFC-227ea	2.1	0.6	0.6
HFC-125	1.0	0.4	0.6
CF ₃ I	1.0	4.0	2.5

Table 18. Strain to failure ratios at 150 °C [(STF in Agent)/(STF in Ar)]

Environment	Nitronic 40	304 SS	Titanium 15-3-3-3
Argon	*	*	*
Halon 1301	1.045	1.056	0.871
FC-218	1.019	0.986	0.927
HFC-227ea	1.018	0.991	0.899
HFC-125	1.004	1.000	0.912
CF ₃ I	0.972	1.056	0.571

Table 19. t-Test for significance in STF change at 150 °C

Environment	Nitronic 40	304 SS	Titanium 15-3-3-3
Argon	*	*	*
Halon 1301	1.119	0.619	-0.695
FC-218	0.464	-0.159	-0.394
HFC-227ea	0.457	-0.098	-0.543
HFC-125	0.098	-0.005	-0.472
CF ₃ I	-0.712	0.623	-2.312

Table 20. Average reduction in area at 150 °C (%)

Environment	Nitronic 40	304 SS	Titanium 15-3-3-3
Argon	77.6	75.0	54.8
Halon 1301	80.2	68.4	56.2
FC-218	80.5	68.4	58.5
HFC-227ea	79.2	68.2	55.7
HFC-125	68.2	80.9	54.0
CF ₃ I	79.4	66.6	44.9

Table 21. Standard deviation of the reduction in area measurements at 150 °C (%)

Environment	Nitronic 40	304 SS	Titanium 15-3-3-3
Argon	2.4	0.7	7.2
Halon 1301	1.2	0.7	3.2
FC-218	0.7	1.5	8.4
HFC-227ea	1.1	0.9	2.7
HFC-125	0.9	0.5	3.6
CF ₃ I	0.4	2.4	29.9

area measured for each alloy/agent combination to argon at 150 °C is presented in Table 22. The statistical significance of the difference is again presented as a function of the alloy standard deviations in Table 23. In Table 22, it can be seen that the reduction in area values for Nitronic 40 increase in every agent except for HFC-125, while 304 stainless has the opposite behavior. The titanium alloy performed well in halon 1301, FC-218 and HFC-227ea, but exhibited significantly lower values in HFC-125 and in CF₃I.

In general, each alloy performed well in one or more of the agents evaluated at 150 °C and the titanium alloy exhibited brittle cracking in two of the three samples tested in the CF₃I. Figure 15 is a low magnification scanning electron micrograph exhibiting the crack morphology observed in the titanium 15-3-3-3 samples tested in CF₃I at 150 °C. In this figure it can be seen that the entire fracture surface consists of brittle, transgranular cleavage cracks, which indicates this alloy has a strong sensitivity to this agent (Mills, 1987). Figure 16 is a higher magnification view of the observed cracking. This cracking could be the result of interactions between the titanium alloy and one or more of the decomposition products on the CF₃I. However, it is also possible that this cracking may have been due to an interaction with an impurity present in the CF₃I. Figures 17 and 18 are scanning electron micrographs of the alloy tested in argon at the same temperature included for comparison. In these figures, it can be seen that the fracture surfaces are entirely composed of microvoid coalescence which indicates the failures occurred by completely ductile processes. Figure 18 is a higher magnification view of the microvoid coalescence (Korb, 1987, Mills, 1987, and Boyer, 1987). These figures indicate that the titanium alloy may not be a suitable alloy for the containment of CF₃I.

5.3.5 Results at 20 °C. The slow strain rate data from the tests conducted at 20 °C are presented in a fashion similar to those used for the 150 °C tests. Table 24 gives the average UTS determined for each alloy in argon at 20 °C, and in each agent at 20 °C. The standard deviations for these calculated values are presented in Table 25. The ratio of the average UTS in each agent to the average UTS in argon at the same temperature is given in Table 26. In this table, it can be seen that all of the 20 agent/alloy combinations have a higher average UTS in the agent than in argon.

Tables 27 contains the results of an estimate of the significance of the differences. As before, a significant increase in the average UTS is unusual and this suggests that sample/environment interactions are inhibiting deformation and fracture, but it could also be an indication of an interference between the corrosion products being generated on the sample and the seal of the autoclave through which the sample must slide. The most important point is, once again, suitable materials can be identified for the containment and reliable distribution of any of these candidates (Ricker, 1994).

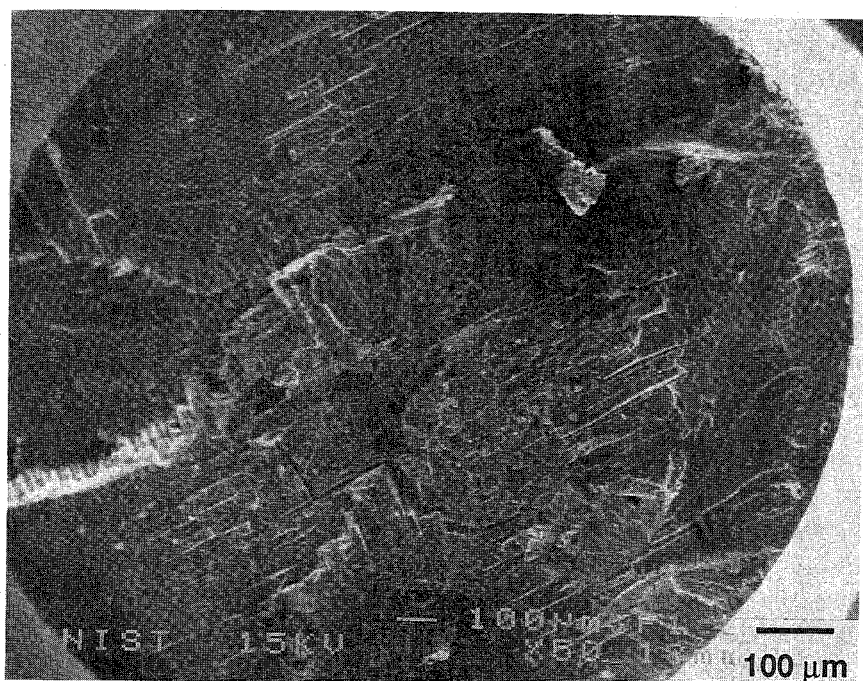


Figure 15. Scanning electron micrograph of the transgranular cleavage-like fracture observed in Ti 15-3-3-3 when tested in CF_3I at 150 °C.

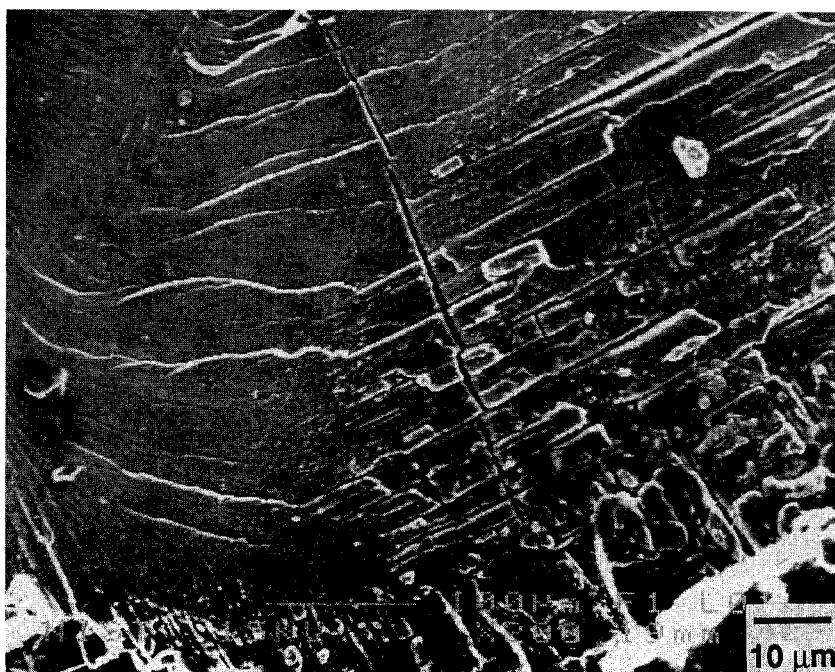


Figure 16. Higher magnification view of the transgranular cleavage-like crack morphology observed in titanium tensile specimen tested in CF_3I at 150 °C.

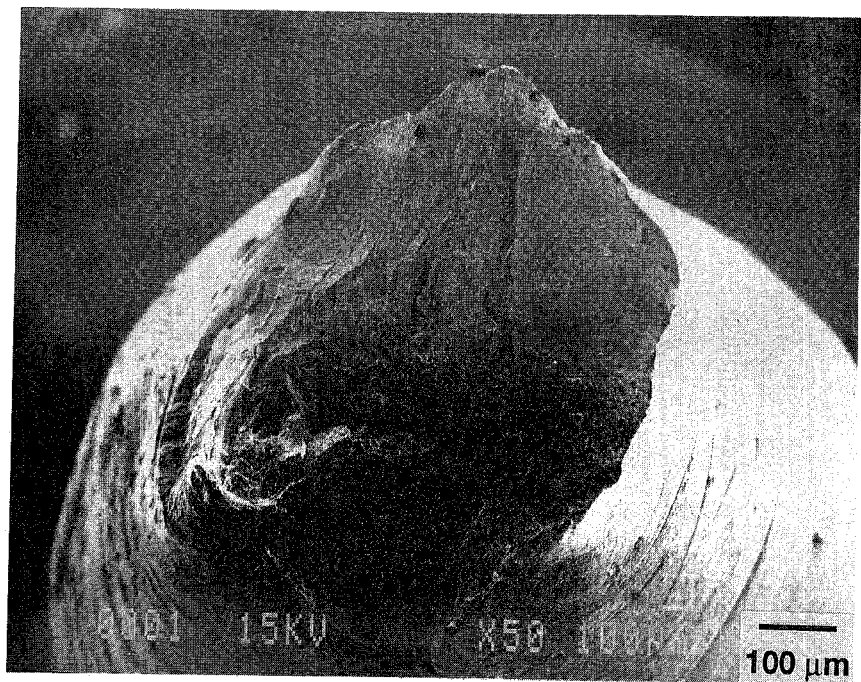


Figure 17. Scanning electron micrograph of the ductile microvoid coalescence type of fracture observed in Ti 15-3-3-3 when tested in argon at 150 °C.

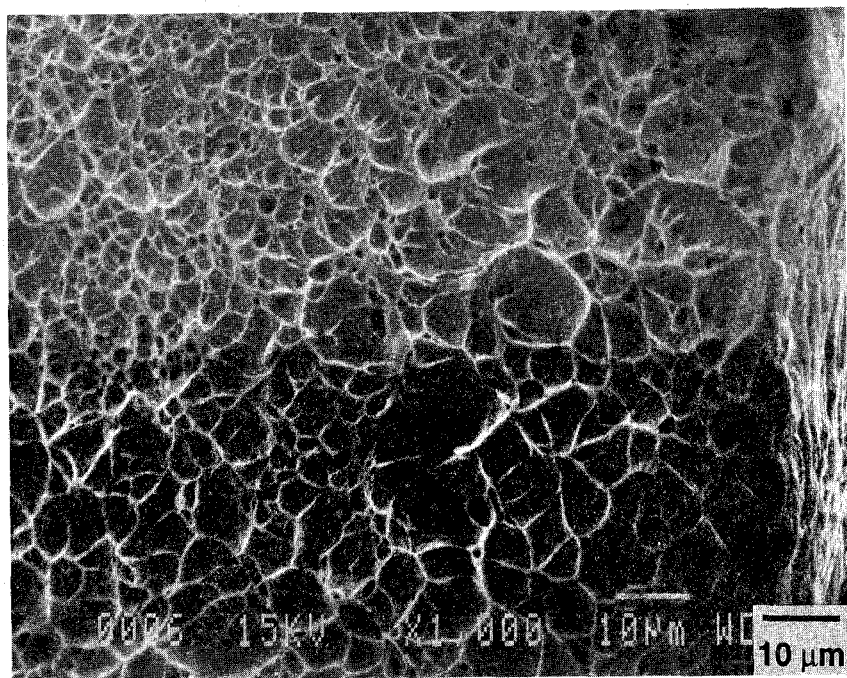


Figure 18. Higher magnification view exhibiting the microvoid coalescence observed on the titanium tensile specimens tested in argon at 150 °C.

Table 22. Reduction in area ratios at 150 °C [(RA in Agent)/(RA in Ar)]

Environment	Nitronic 40	304 SS	Titanium 15-3-3-3
Argon	*	*	*
Halon 1301	1.035	0.912	1.026
FC-218	1.038	0.912	1.068
HFC-227ea	1.021	0.909	1.015
HFC-125	0.879	1.078	0.985
CF ₃ I	1.024	0.888	0.820

Table 23. t-Test for significance in RA change at 150 °C

Environment	Nitronic 40	304 SS	Titanium 15-3-3-3
Argon	*	*	*
Halon 1301	0.699	-1.548	0.142
FC-218	0.768	-1.562	0.370
HFC-227ea	0.431	-1.615	0.084
HFC-125	-2.451	1.377	-0.084
CF ₃ I	0.476	-1.977	-0.983

Table 24. Average ultimate tensile strength at 20 °C (MPa)

Environment	Nitronic 40	304 SS	Titanium 15-3-3-3
Argon	718	793	579
Halon 1301	734	806	597
FC-218	735	805	627
HFC-227ea	726	799	633
HFC-125	746	803	606
CF ₃ I	724	803	603

Table 25. Standard deviation of the ultimate tensile strength measurements at 20 °C (MPa)

Environment	Nitronic 40	304 SS	Titanium 15-3-3-3
Argon	3.0	2.1	2.1
Halon 1301	3.0	2.5	2.4
FC-218	3.0	2.3	0.6
HFC-227ea	3.4	1.9	3.8
HFC-125	0.3	2.9	3.8
CF ₃ I	3.0	2.8	4.6

Table 26. Ultimate tensile strength ratios at 20 °C [(UTS in Agent)/(UTS in Ar)]

Environment	Nitronic 40	304 SS	Titanium 15-3-3-3
Argon	*	*	*
Halon 1301	1.023	1.016	1.031
FC-218	1.024	1.016	1.084
HFC-227ea	1.012	1.008	1.093
HFC-125	1.039	1.013	1.048
CF ₃ I	1.009	1.012	1.042

Table 27. t-Test for significance in UTS change at 20 °C

Environment	Nitronic 40	304 SS	Titanium 15-3-3-3
Argon	*	*	*
Halon 1301	1.072	1.076	0.840
FC-218	1.111	1.051	2.232
HFC-227ea	0.540	0.520	2.486
HFC-125	1.830	0.856	1.270
CF ₃ I	0.414	0.816	1.109

The ductility results for the 20 °C SSR tests are given in Tables 28-30. Table 28 gives the average strain to failure for each alloy/environment combination, and in argon at 20 °C. Table 29 shows the standard deviations for the STF calculations. The ratio of the average strain to failure for each alloy in each environment to that observed in the same alloy in argon at the same temperature is presented in Table 30. The significance of the difference is presented as a function of the alloy standard deviations, in Table 31. In Table 30, it can be seen that the STF ratios decreased for Nitronic 40 in all of the environments. However, both the 304 stainless steel and the titanium alloy exhibited increases in the STF ratio values in most of the environment/alloy combinations. This suggests that deformation may have been easier in these environments than in argon at this temperature.

Table 32 presents the RA data for each alloy in argon gas at 20 °C and each agent at 20 °C. Table 33 gives the standard deviations for these measurements and the ratio of the average reduction in area measured for each alloy/agent combination to argon at 20 °C is presented in Table 34. The statistical significance of the difference is again presented as a function of the alloy standard deviations in Table 35. In Table 34, it can be seen that the reduction in area values for Nitronic 40 increase in every agent. The 304 stainless steel alloy exhibited slight decreases in the RA values for all agents and the titanium alloy exhibited increases in every agent except for HFC-227ea, where it shows a significant decrease.

Based on these results, none of the alloys appear to be susceptible to environmentally induced fracture in these agents at 20 °C. Unlike the tests conducted at 150 °C, no evidence of environmentally induced cracking of any kind was observed on the fracture surface of any specimen tested at 20 °C. The values presented in these tables do not readily indicate any susceptibility to environmentally induced fracture at 20 °C.

5.4 Post Deployment Corrosion

When a fire suppressant is applied to a fire, the metals in the aircraft engine nacelle or the dry bays may become covered with deposits of the fire suppressant or fire suppressant combustion products. An additional evaluation of the relative corrosivity of the expected combustion products was included in the investigation. As a result, an evaluation of the relative corrosion behavior of representative structural materials with the combustion by-products was included in this investigation.

All of the potential replacements investigated in this study contain fluorine in their molecules and will produce fluoride ions and hydrofluoric acid (HF) during combustion. These ions are known to be aggressive when they contact certain alloy types. HF is commonly used to etch glasses and ceramics and will similarly attack the protective layer on the surface of passivated alloys. If the fluoride ion concentration in the combustion products deposited on the surface of an alloy exceeds some critical value, then pitting or crevice attack will result (Fontana, 1987, Zotikov, 1974, and Ricker, 1994). As a result, the post deployment corrosion damage to aircraft alloys will depend on the corrosivity of the surface films which contain these ions.

Most engineering alloys that exhibit good corrosion resistance do so because they form a protective surface film. This passive film is usually composed of metallic oxides or hydroxides (Fontana, 1987). Commercial aluminum alloys and stainless steels are examples of alloys which contain active elements, but behave in a relatively noble manner because of the formation of oxide films (Ricker, 1994). These protective surface films may be crystalline in form and may be precipitated from the solution adjacent to the bare metal surface, but it is widely believed that rapidly grown amorphous films are the most protective (Ricker, 1994). No matter what the structure of the surface

Table 28. Average strain to failure at 20 °C (%)

Environment	Nitronic 40	304 SS	Titanium 15-3-3-3
Argon	65.0	43.2	5.7
Halon 1301	63.1	44.4	6.9
FC-218	62.5	45.9	6.1
HFC-227ea	63.4	45.0	5.9
HFC-125	61.5	43.1	6.4
CF ₃ I	63.3	44.0	6.5

Table 29. Standard deviation of the strain to failure measurements at 20 °C (%)

Environment	Nitronic 40	304 SS	Titanium 15-3-3-3
Argon	0.9	2.5	0.7
Halon 1301	3.8	2.2	0.4
FC-218	3.7	2.7	0.2
HFC-227ea	2.1	1.3	3.5
HFC-125	1.4	3.2	1.0
CF ₃ I	1.1	3.0	0.1

Table 30. Strain to failure ratios at 20 °C [(STF in Agent)/(STF in Ar)]

Environment	Nitronic 40	304 SS	Titanium 15-3-3-3
Argon	*	*	*
Halon 1301	0.971	1.028	1.227
FC-218	0.962	1.062	1.073
HFC-227ea	0.975	1.041	1.045
HFC-125	0.947	0.999	1.139
CF ₃ I	0.974	1.020	1.154

Table 31. t-Test for significance in STF change at 20 °C

Environment	Nitronic 40	304 SS	Titanium 15-3-3-3
Argon	*	*	*
Halon 1301	-1.006	0.624	1.211
FC-218	-1.301	1.371	0.389
HFC-227ea	-0.861	0.902	0.240
HFC-125	-1.828	-0.030	0.741
CF ₃ I	-0.887	0.439	0.819

Table 32. Average reduction in area at 20 °C (%)

Environment	Nitronic 40	304 SS	Titanium 15-3-3-3
Argon	77.6	75.0	54.8
Halon 1301	78.7	74.3	60.3
FC-218	78.2	74.4	55.4
HFC-227ea	78.1	74.2	46.0
HFC-125	78.5	74.8	68.0
CF ₃ I	78.0	74.7	65.6

Table 33. Standard deviation of the reduction in area measurements at 20 °C (%)

Environment	Nitronic 40	304 SS	Titanium 15-3-3-3
Argon	1.2	0.4	6.9
Halon 1301	1.5	2.0	4.7
FC-218	0.7	0.6	4.9
HFC-227ea	1.3	0.3	23.9
HFC-125	0.9	1.0	25.4
CF ₃ I	0.4	0.5	3.1

Table 34. Reduction in area ratios at 20 °C [(RA in Agent)/(RA in Ar)]

Environment	Nitronic 40	304 SS	Titanium 15-3-3-3
Argon	*	*	*
Halon 1301	1.015	0.990	1.101
FC-218	1.008	0.991	1.011
HFC-227ea	1.007	0.989	0.839
HFC-125	1.012	0.997	1.241
CF ₃ I	1.005	0.996	1.197

Table 35. t-Test for significance in RA change at 20 °C

Environment	Nitronic 40	304 SS	Titanium 15-3-3-3
Argon	*	*	*
Halon 1301	1.433	-0.981	0.463
FC-218	0.740	-0.877	0.049
HFC-227ea	0.660	-1.154	-0.739
HFC-125	1.175	-0.262	1.110
CF ₃ I	0.474	-0.384	0.904

film, halogen ions generally tend to destabilize and/or reduce the protective nature of these films (Ricker, 1994).

Light weight alloys such as aluminum alloys are commonly used for aircraft applications. Unfortunately, these alloys are also susceptible to pitting corrosion in the presence of halide ions. Aluminum is a very active metal and alloys of this type will generally corrode as rapidly as mass transport kinetics will allow if the protective surface film is removed (Ricker, 1994). For this reason aluminum alloys are not used in environments where the passivity cannot be maintained (*i.e.*, pH<4 or pH>10). Other passivated materials such as titanium alloys and stainless steels are also susceptible to passivity breakdown.

In phase 1 of this study, the atmospheric corrosion behavior of representative aircraft alloys whose surfaces were contaminated with different chemical species expected to be produced by the combustion of different fire suppressants was investigated. In that investigation, three different surface pretreatments were used: (1) artificial seawater plus NaF, (2) artificial seawater plus NaHCO₃/Na₂CO₃, and (3) artificial seawater plus NaOH. The last two of these were used to represent surface conditions that may result from the use of NaHCO₃ as a fire suppressant and, therefore, are not relevant to this study. The first was used to represent surface conditions that may result from the combustion of fluoride or other halogen containing fire suppressants. When a surface film on a metal contains HF, the HF will react with the metal to form metal ions and hydrogen gas. This effectively

removes the hydrogen ion and increases the pH of the solution in the surface film. For NaF, the initial pH is higher, but the metal ions produced by corrosion will hydrolyze reducing the pH of the surface film. The end result is, whether the starting pH is low or high, the pH of the surface film will be determined by the chemical species present and the hydrolysis reaction. In Phase 1, it was decided to emulate the post deployment conditions by misting the surface of the samples. Because misting with HF would be a safety hazard and the steady state pH of the surface film is essentially independent of the initial pH, it was decided to sprinkle the surface with NaF instead of misting with HF. This resulted in questions about the difference that might result if the initial pH were lower. To resolve these questions, simple exposure experiments were conducted by dipping samples into different concentrations of HF and measuring their subsequent weight changes when exposed to humid air.

5.4.1 Materials. The materials selected by the sponsors for this study were designed to represent the broad range of aircraft structural materials which could be exposed to fire suppressant combustion by-products. The materials selected were: 6061-T6 aluminum alloy, Inconel alloy 718, Inconel alloy 903, 410 stainless steel, titanium alloy Ti-8-1-1-1, titanium grade 5 alloy, Haynes alloy 188 and a 3501-6/AS4 epoxy-graphite composite. The compositions of these alloys are shown in Table 36.

5.4.2 Exposure Environment. According to the current military specifications, combustion product layers could remain on component surfaces for up to one month before the surfaces are cleaned. The effects of humidity variations, corrosion by condensate droplets induced by thermal cycling and contamination of the surface by salts or particulate matter were not included in this study. Also, the combustion products themselves may form fine carbonaceous particulates which could then precipitate onto the metal surfaces and behave as cathodes stimulating corrosion.

5.4.3 Experimental Procedure. The sample geometry used for this analysis was identical to the one shown in Figure 1 (Section 5.2.2). After machining, the surfaces were glass bead blasted to remove any remaining surface oxides or scale and to provide a consistent smooth surface finish (120 grit, nominal). Additional preparation prior to the start of these tests consisted of an ultrasonic cleaning in acetone then in alcohol, drying with warm air and immediate weighing using the same procedure used for the weight loss experiment.

The purpose of these experiments was to evaluate the corrosion behavior of representative aircraft materials after a deployment of a fire suppressant. The results of a study conducted by Linteris *et al.*, revealed that the initial concentration of HF produced by combustion decomposition of these agents ranges between 1.0 % and 10.0 % by volume (Nyden, 1994 and Linteris, 1994). As a result, one complete set of samples was immersed in an aqueous solution containing 1.0 volume percent HF for 60 s and a second set was immersed in a similar solution containing 10.0 volume percent HF for the same time period. At the end of this exposure, the samples were extracted and hung on individual hooks inside a sealed chamber with a constant relative humidity for 30 days. The chamber used for this exposure was specially designed to maintain a near-saturation relative humidity through the use of wicks along each side of the chamber. Regular hygrometer measurements indicated that the relative humidity inside the chamber ranged between 98 % and 100 %. Mass change measurements were taken at regular intervals during the exposure using the same weighing technique outlined previously in this report (Section 5.2.2).

5.4.4 Results. The results of the post deployment tests are presented in Figures 19 and 20. Figure 20 is a plot of the mass change per unit exposed area as a function of the exposure time following a 60 s immersion in 1.0 % by volume HF. In this figure, it can be seen that after approximately four days of exposure at 100 % relative humidity, there is little change in the rate of

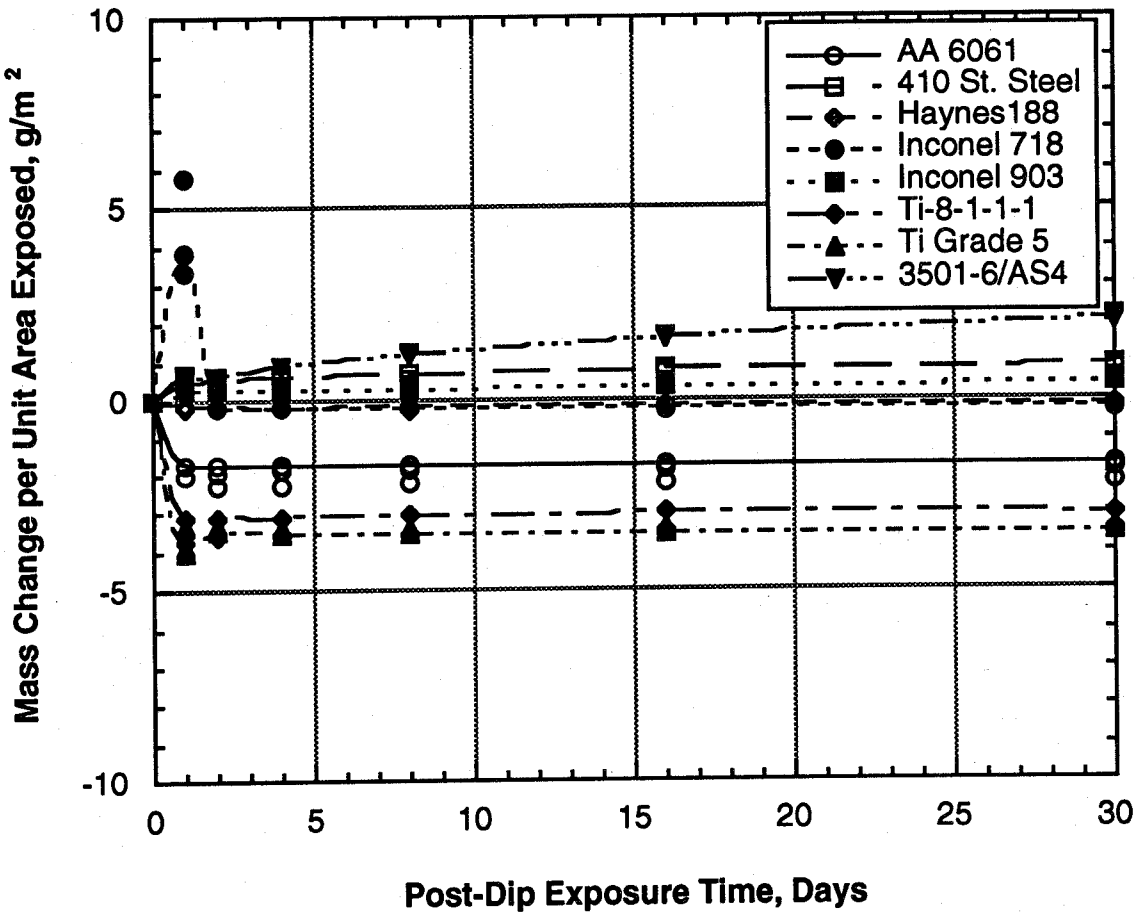


Figure 19. Mass change on exposure to saturated laboratory air following 60 s dip in 1 % HF.

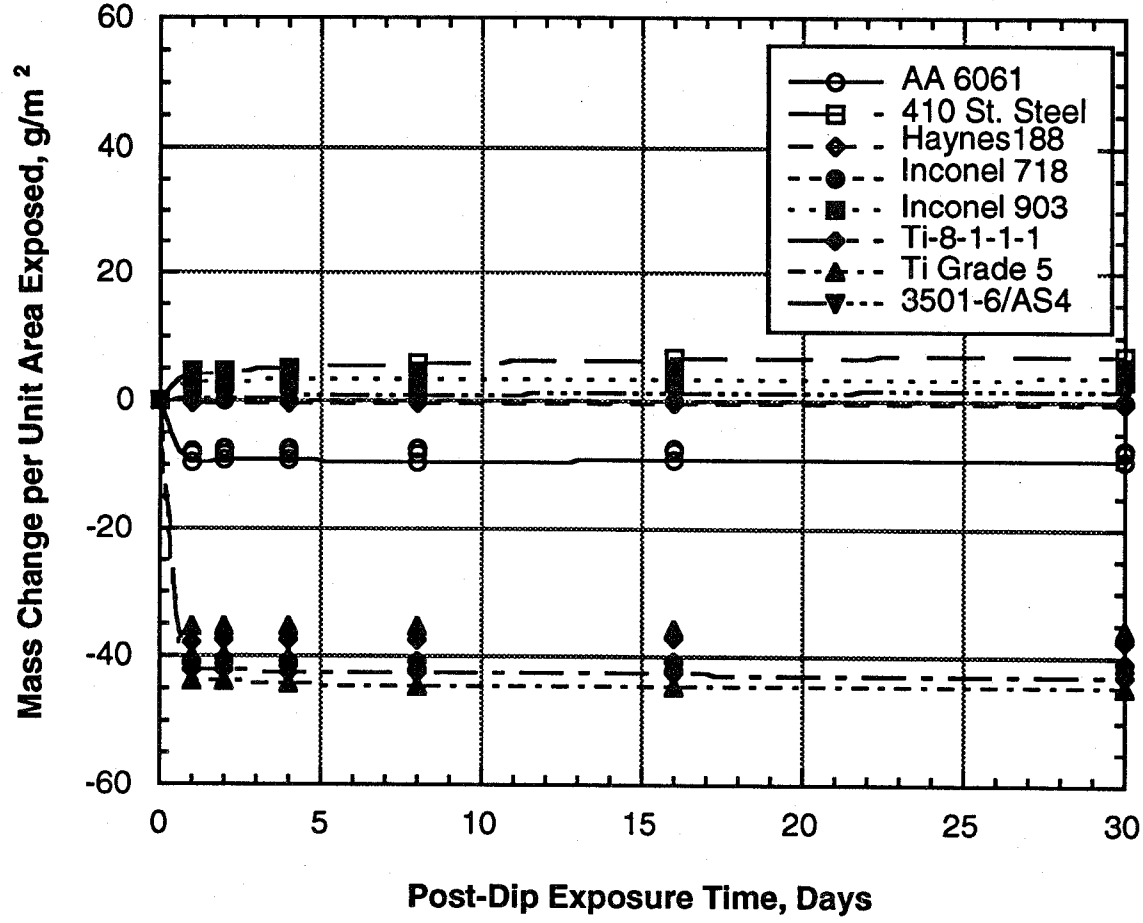


Figure 20. Mass change on exposure to saturated laboratory air following 60 s dip in 10.0 % HF.

Table 36. Composition of alloys used for post deployment testing (mass fraction in percent)

Element	Titanium 8-1-1	Inconel 718	410 SS	Haynes 188	Al 6061	Titanium Grade 5	Inconel 903
Al	7.60	0.51	--	--	bal	6.30	4.00
C	0.01	0.03	0.14	0.11	--	0.03	0.02
Cr	--	18.26	11.98	21.92	0.04	--	--
Cu	--	0.01	0.14	--	0.15	--	--
Fe	0.05	18.21	bal	2.47	0.70	0.18	41.90
Mn	--	0.05	0.31	0.86	0.15	--	0.12
Mo	1.00	2.87	0.02	--	--	--	--
Ni	--	54.01	0.20	22.53	--	--	37.96
Ti	bal	--	--	--	0.15	bal	--
V	1.00	--	--	--	--	4.00	--
Mg	--	--	--	--	1.20	--	--
Zn	--	--	--	--	0.25	--	--
OB	--	--	--	--	--	--	--
N	0.01	--	0.02	--	--	0.01	--
Co	--	0.02	--	bal	--	--	14.70
Nb	--	4.90	--	--	--	--	2.88
W	--	--	--	13.83	--	--	--

weight gain for the remainder of the thirty day exposure. The graphite/epoxy composite did continue to increase in mass, but this could be due to moisture uptake resulting from the high humidity. Research has shown that for these materials, moisture can be transported into the bulk by the wicking action of the fibers along the exposed edges and by solid state diffusion mechanisms (Stoudt, 1991).

Figure 20 is a similar plot showing the mass change as a function of exposure time after a 60 s immersion in 10.0 % by volume HF. During the immersion, the dissolution reactions were substantially more aggressive than those observed in the 1.0 % HF solution. As in Figure 19, the rate of mass change slowed shortly after the coupons were removed from the HF solution. The graphite/epoxy composite once again increased in mass, apparently the result of moisture uptake. In both cases, the decrease in the mass change rate can be attributed to the drying out of the corrosion products. Unlike the tests conducted in Phase I, the samples in this evaluation were not treated with any materials which could absorb and hold the water necessary to sustain the corrosion reactions. While the air in the exposure chamber was at saturation humidity, apparently, the corrosion products on the surface of the metal did not absorb water from the air otherwise corrosion and/or mass increases would have been observed. As a result, there was no liquid phase present to stimulate corrosion reactions. In essence, the layer of the corrosion products on the surface have an equilibrium vapor pressure for water that is greater than that of the air in the chamber so they stayed relatively dry. This may or may not be the case in actual service, since any kind of re-wetting of the corrosion product layer will re-establish the corrosion reactions (e.g., thermal transients causing condensation - fog, dew, rain, etc.)

and actual combustion product films will be composed of many more chemical species many of which may absorb water.

5.5 Electrochemical Measurements

There are a number of different electrochemical techniques that can be used to measure the corrosion rates of metals (Bard, 1980). However, because the fire suppression candidates have a high electrical resistivity, testing in these solutions becomes very difficult. For example, HCFC-124 (CF_3CHClF), has a resistivity of 1.5×10^9 ohms-cm. One technique that can be employed to enable electrochemical measurements in these environments is to add a salt to the environment which will dissolve and provide charge carriers to the electrolyte, but not alter the corrosivity of the environment (Sawyer, 1974). The choice of a salt for supporting the transfer of charge in these agents is complicated by their low dielectric constants. For example, the dielectric constant of HCFC-124 is about 6.73 (CRC Handbook, 1990). While the dielectric constant for the other compounds cannot be found in tables, examination of compounds with similar symmetry and bond strengths indicates that the dielectric constant for CF_3I and HFC-125 should be around 3.5 and 6, respectively, and even higher for FC-218, HFC-227ea and halon 1301. As a result, simple salts will not dissolve in these compounds. Several authors have shown (Pournaghi-Azar, 1994, Bond, 1988, Park, 1994 and Kadish, 1984), that quaternary ammonium salts, on the other hand, will dissolve in low dielectric constant media such as dichloromethane and chloroform where the dielectric constants are 9.08 and 4.81, respectively.

The behavior of the candidate compounds can essentially be characterized as aprotic in nature. As a result, their ability to ionize a supporting electrolyte is significantly reduced. The ability of a salt to be ionized in this type of medium is primarily a function of the anion (Sawyer, 1974). As the size of the anion increases and its electronegativity decreases, ionization becomes more probable (Sawyer, 1974). Furthermore, dissociation of the supporting salt is limited by the very low dielectric constant of the replacement candidates (Sawyer, 1974). This can be overcome, to a certain extent, by choosing a salt in which the cation and anion have a small charge to volume ratio. On the other hand, as the size of the cation and anion increase, their mobility, and hence the solution conductivity, is reduced (Ue, 1994). For a given charge on an ion, the size effect will have a larger effect on the dissociation constant of a salt than on the ionic mobility in a given medium. The molecular structure of the supporting salt will also affect its mobility in a solvent. The ionic mobility, and hence the solution conductivity, will decrease as the molecular interaction increases. Because of their small charge to volume ratio and their anions are of intermediate size, tetrabutylammonium hexafluorophosphate (TBAPF_6) and tetrabutylammonium trifluoromethanesulfonate (TBATFMS) were chosen as supporting salts (Ue, 1994).

As explained in a previous study, in order to define the potential axis for polarization measurements, a platinum quasi-reference electrode (Pt-QRE) referenced to the half wave potential ($E_{1/2}$) of the ferrocene/ferrocinium ($\text{Cp}_2\text{Fe}^{0/+}$) reduction-oxidation (redox) couple is necessary (Dante, 1994). The nonpolar character of this outer sphere redox couple facilitates its dissolution into compounds with a low dielectric constant.

Once the potential scale is established, three electrode slow scan measurements can be made and a Tafel extrapolation can be used to estimate the corrosion rate of the storage vessel alloys in the halon replacement candidates.

5.5.1 Materials. The alloys examined in this analysis were: 304 stainless steel, Nitronic 40 stainless steel, aluminum alloy 6061-T6, and Titanium alloy 15-3-3-3. The compositions of these alloys are given in Table 1, Section 5.2.2.

5.5.2 Experimental Procedure. The vapor pressure for HCFC-124, HFC-125, and CF_3I are $3.393 \text{ Pa} \times 10^5 \text{ Pa}$, $11.051 \text{ Pa} \times 10^5 \text{ Pa}$, and $4.390 \text{ Pa} \times 10^5 \text{ Pa}$, respectively, at room temperature. Therefore, electrochemical measurements of the corrosion rate in the liquid phase of these agents requires the experiments be conducted in a closed pressure chamber. A stainless steel pressure vessel was modified to allow for electrical feed-throughs, Figure 21. The vessel was constructed of 0.635 cm thick 316 stainless steel and was rated for pressures of $\sim 6.9 \text{ MPa}$. Four electrical feed-throughs were mounted through the head of the cell for performing two, three, or four electrode electrochemical tests. A pressure gauge was mounted on the cell to measure the vapor pressure in the cell. At higher temperatures, most of the gasses used in this study can reach very high vapor pressures so a rupture disc was incorporated to prevent accidental over pressurization. Temperature was monitored with the use of a thermocouple mounted in the head of the cell.

Electrochemical measurements were made using a commercial potentiostat. A commercial frequency response analyzer was used to make impedance measurements and the data was collected using commercially available software.

Before filling the electrochemical cell with one of the halon replacement candidates, $5 \times 10^{-2} \text{ mol/L}$ of one of the supporting salts, either TBATFMS or TBAPF_6 , was placed into the cell. Then, the cell was closed and purged with dry argon to remove water vapor. After 5 min, the fill valves were closed and the cell was chilled for 30 min to 60 min. Chilling facilitated filling the cell with agents. The agent was removed from the liquid phase in the storage bottle. Enough agent was transferred to the electrochemical cell to form a 3 cm deep (250 ml) liquid phase in the bottom of the cell, i.e., 352 g, 353 g, and 555 g of HCFC-124, HFC-125, and CF_3I , respectively. In all tests, a large area platinum-rhodium counter electrode and a platinum wire quasi-reference electrode (Pt-QRE) were used. The Pt-QRE electrode was placed between the counter and working electrodes approximately 2.5 cm from the working electrode. The electrodes were attached to the electrical feed-throughs using heat shrink tape. For the working electrodes, electrical contact was made using clips.

The effectiveness of both TBATFMS and TBAPF_6 in lowering the resistivity of HCFC-124, HFC-125, and CF_3I was measured using electrochemical impedance spectroscopy (EIS). The cell resistance was obtained by noting the value where the curve intersected the real impedance axis on the Nyquist plot. This value was converted to a resistivity by multiplying by the electrode area and subsequently dividing by the distance between the working and reference electrode. Unfortunately, it was not possible to get sufficient quantities of either of these salts to dissolve in either HFC-227ea or halon 1301 to enable electrochemical measurements.

Tests were run to elucidate the electron transfer kinetics of $\text{Cp}_2\text{Fe}^{0/+}$ in HCFC-124, HFC-125 and CF_3I . The tests were run at room temperature. A Pt disk working electrode (area = 0.00317 cm^2) was prepared by encapsulate a platinum wire in glass and polishing the electrode face to a 1 μm finish. The oxidation and reduction waves of ferrocene in each experiment were measured with respect to the Pt-QRE. The potential scale was then normalized to the half-wave potential of $\text{Cp}_2\text{Fe}^{0/+}$ redox couple.

In subsequent tests, the corrosion rate of 304 (area = 0.00785 cm^2) and Nitronic 40 (area = 0.01461 cm^2) stainless steels, aluminum 6061-T6 (area = 0.01954 cm^2), and Ti 15-3-3-3 were studied in the three agents using slow sweep voltammetry (scan rate = 0.5 mV/s) and Tafel extrapolations. In all cases, wires of each alloy were encapsulated in glass and the electrode surfaces were polished to a 1 μm finish. All of the alloys except 304 stainless steel were extruded and heat treated from stock samples. It should be noted that the encapsulation process involved temperature in excess of 500°C for short periods of time which may have modified the metallurgy of the wires slightly.

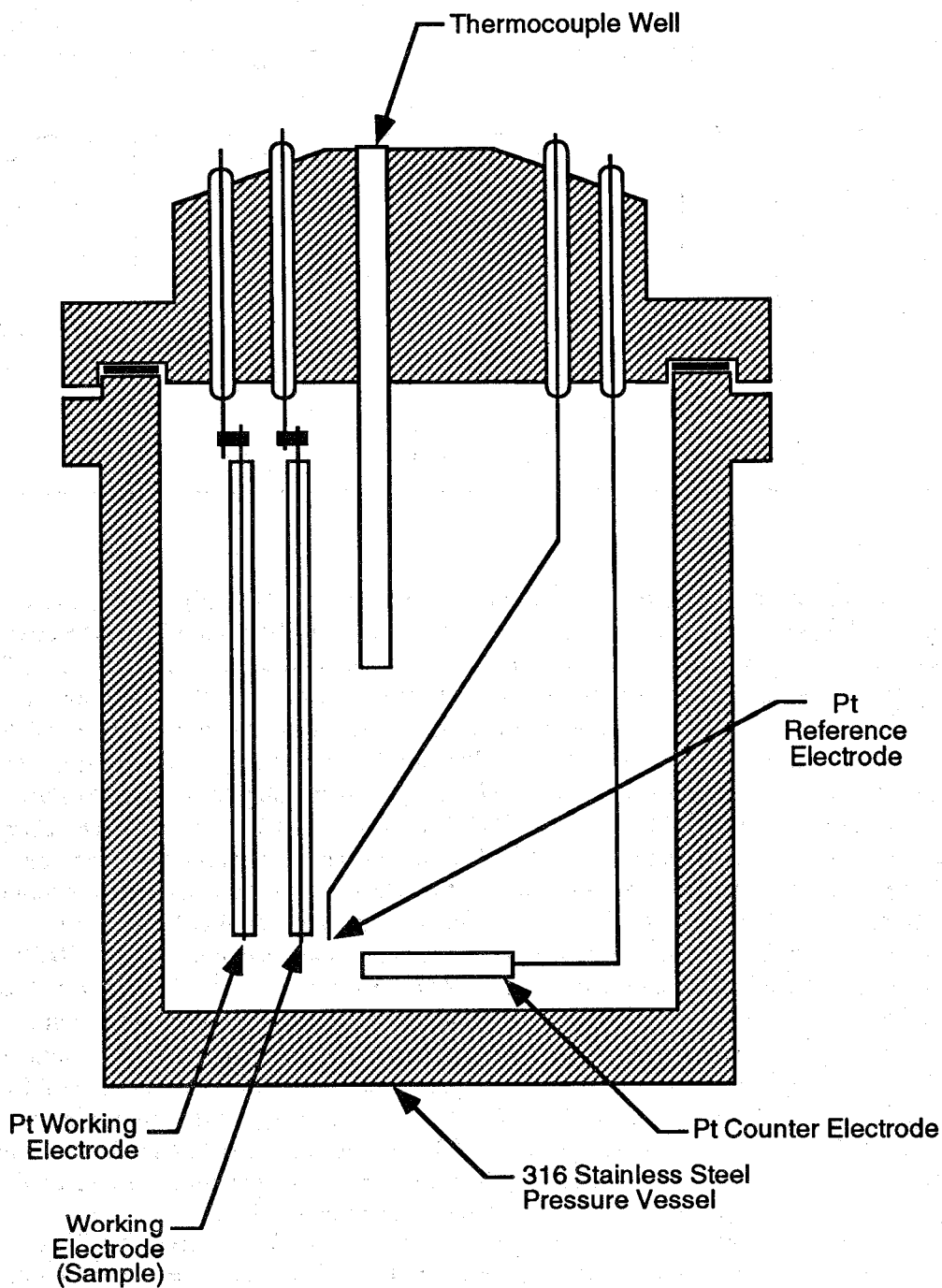


Figure 21. Electrochemical cell for making measurements in high vapor pressure low conductivity electrolytes.

Table 37. Resistivity and electron transfer rate constants of $\text{Cp}_2\text{Fe}^{0/+}$ and oxidation rates in various replacement candidates

Agent	Supporting Salt	Resistivity, ρ Ohms-cm	k^0 cm/s
HCFC-124	TBATFMS	80	0.0020
HCFC-124	TBAPF ₆	79	0.0013
HFC-125	TBATFMS	44	0.0024
HFC-125	TBAPF ₆	740	2.5×10^{-4}
CF ₃ I	TBATFMS	748	3.6×10^{-4}
CF ₃ I	TBAPF ₆	---	---

5.5.3 Agent Resistivity. Electrochemical impedance spectroscopy (EIS) was used to measure the resistivity of the agents as a function of added salt. Values for the resistivity of the agent/salt combinations are shown in Table 37. Several conclusions can be drawn from this data. The resistivity of the agent/supporting salt electrolyte is related to several factors *i.e.*, the ionization of the salt, the mobility of its ions and the dissociation constant of the salt in the medium which regulates the number of ions available as charge carriers from the solvated salt. Furthermore the size of the two salts is approximately the same (Ue, 1994) with the TFMS anion being slightly larger. Analysis of Table 37 reveals that the resistivity of TBAPF₆ and TBATFMS in HCFC-124 is similar. The charge to volume ratio of the TFMS anions are slightly smaller than that of the PF₆⁻ anions and hence dissociate to a slightly larger extent in HCFC-124. In order for the resistivity of the solutions containing the different salts to be similar, the mobility of the PF₆⁻ ions must be higher than that for the TFMS anions.

The situation in HFC-125, however, is very different. The resistivity of the TBAPF₆ electrolyte is an order of magnitude higher than that of the TBATFMS electrolyte. With the verified assumption that all of the salts are dissolved and knowing that the ions are of the same general size, the difference in resistivity must be attributed to a difference in the number and mobility of the charge carriers in HFC-125. The TFMS ion has a structure that more closely resembles the structure of HFC-125 than PF₆⁻ does, thus facilitating the ability of TBATFMS to move through the medium in response to an applied field. The charge to volume ratio of the TFMS anions are slightly smaller than that of the PF₆⁻ anions and hence dissociate to a slightly larger extent in this medium. These two effects combine to give a much lower resistivity for TBATFMS in HFC-125.

The TFMS ions more closely resemble the molecules of HFC-125 than HCFC-124 implying a weaker intermolecular force and hence a higher mobility in HFC-125. The dielectric constant of HFC-125 is slightly lower than that for HCFC-124. Thus, the number of charge carriers would be greater in HCFC-124. From Table 37, the resistivity of the TBATFMS solution is slightly lower in HFC-125 suggesting that the mobility of the charge carriers is the major factor contributing to the lower resistivity of TBATFMS in HFC-125. That is, even though the number of charge carriers is lower in HFC-125, they are more mobile than those in HCFC-124 and result in a lower resistivity in HFC-125. Table 37 illustrates the fact that the resistivity is an order of magnitude higher in HFC-125

relative to HCFC-124 containing TBAPF₆. The number of charge carriers in HCFC-124 would be greater than that in HFC-125 because of the higher dielectric constant of HCFC-124. This implies that the mobility of the charge carriers in HCFC-124 would be similar to or slightly higher than in HFC-125.

HCFC-124 and HFC-125 containing 5×10^{-2} mol/L of TBATFMS have similar resistivities. The resistivity in CF₃I, however is an order of magnitude higher. Since the dielectric constant of CF₃I is much lower than that in the other salts, the number of charge carriers in this medium are much less. This fact alone accounts for the much increased resistivity. TBAPF₆ does not dissolve in CF₃I. The slightly higher polarity of this molecule compared to TBATFMS is enough to prevent its dissolution.

5.5.4 Defining a Reference Potential. Figure 22 displays a 0.1 V/s CV scan from -2.5 V to 1 V versus a Pt-QRE in HCFC-124 and HFC-125 containing 5×10^{-4} mol/L of ferrocene and 5×10^{-2} mol/L of TBAPF₆. These scans represent a typical CV in the above environments. The current was measured at a glass encapsulated Pt electrode. The potential axis has been normalized to $E_{1/2}(\text{Cp}_2\text{Fe}^{0/+})$, which appeared at 0.234 V and 0.481 V (Pt-QRE) in HCFC-124 and HFC-125 respectively. It can be seen from the figure that a major reduction occurs in both environments at approximately -2.55 V ($\text{Cp}_2\text{Fe}^{0/+}$). This suggests that the peak at -2.55 V ($\text{Cp}_2\text{Fe}^{0/+}$) is a reduction process associated with the supporting salt. This peak is in the vicinity of the onset of reduction for the Bu_4N^+ cation in dimethylformamide and acetonitrile (Kadish, 1984). At approximately -1.50 V ($\text{Cp}_2\text{Fe}^{0/+}$) a slight change in the curve can be seen for both environments. In this figure, the peak height is small, but it varies in magnitude each time the test cell is reassembled. The peak is thought to be a result of water contamination. This is supported by other experiments that demonstrate that the magnitude of the peak changes when controlled amounts of H₂O are injected into the cell. In this study, there was no evidence of any oxidation occurring at 1.0 V (Pt-QRE) or 0.77 V ($\text{Cp}_2\text{Fe}^{0/+}$) leaving at least a 2.27 V window where no reactions occur on Pt. By averaging the peak separation between ferrocene and the Bu_4N^+ and ferrocene and the water peak for scan rates up to 0.5 V/s in each environment, the following results are obtained: $E_{1/2}(\text{Cp}_2\text{Fe}^{0/+}) - E(\text{Bu}_4\text{N}^+) = 2.55 \text{ V} \pm 0.002 \text{ V}$ and $2.56 \text{ V} \pm 0.014 \text{ V}$, respectively, $E_{1/2}(\text{Cp}_2\text{Fe}^{0/+}) - E_{\text{H}_2\text{O}} = 1.50 \text{ V}$ and 1.50 V for HCFC-124 and HFC-125 containing TBAPF₆, respectively.

Figure 23 displays a 0.1 V/s scan from -3 V to 1 V (Pt-QRE) in HCFC-124, HFC-125, and CF₃I containing 5×10^{-4} mol/L of ferrocene and 5×10^{-2} mol/L of TBATFMS. These are typical results for the above environments. As before, the current was measured at a glass encapsulated Pt electrode and the potential has been normalized to $E_{1/2}(\text{Cp}_2\text{Fe}^{0/+})$ which appeared at 0.19 V, 0.17 V, and 0.35 V (Pt-QRE) for HCFC-124, HFC-125, and CF₃I, respectively. At 2.48 V ($\text{Cp}_2\text{Fe}^{0/+}$) and 2.55 V ($\text{Cp}_2\text{Fe}^{0/+}$) for HCFC-124 and HFC-125, respectively, a major reduction peak can be seen. The peak separation between the ferrocene half wave and the major reduction peak is similar to the case in which TBAPF₆ was the supporting salt lending further credence to the belief that the major reduction peak is a result of the reduction of Bu_4N^+ . A second peak at 1.503 V ($\text{Cp}_2\text{Fe}^{0/+}$) and 1.458 V ($\text{Cp}_2\text{Fe}^{0/+}$) for HCFC-124 and HFC-125, respectively, is associated with water. This peak is much more pronounced for the curves in Figure 22 than for those in Figure 23. This may be a result of contamination of the TBATFMS. In several cases, the water peak masks the onset of the large reduction peak of the salt and care must be taken when determining the half wave potential of ferrocene in the situation where no ferrocene is present. Oxidation of the electrolyte was not seen for several hundred mV above the half wave potential of ferrocene yielding a usable potential window of at least 2.0 V anodic of the water peak. Peak separations for scans up to 0.5 V/s were averaged and the results are as follows: $E_{1/2}(\text{Cp}_2\text{Fe}^{0/+}) - E(\text{Bu}_4\text{N}^+) = 2.49 \text{ V} \pm 0.008 \text{ V}$ and $2.55 \text{ V} \pm 0.008 \text{ V}$ for

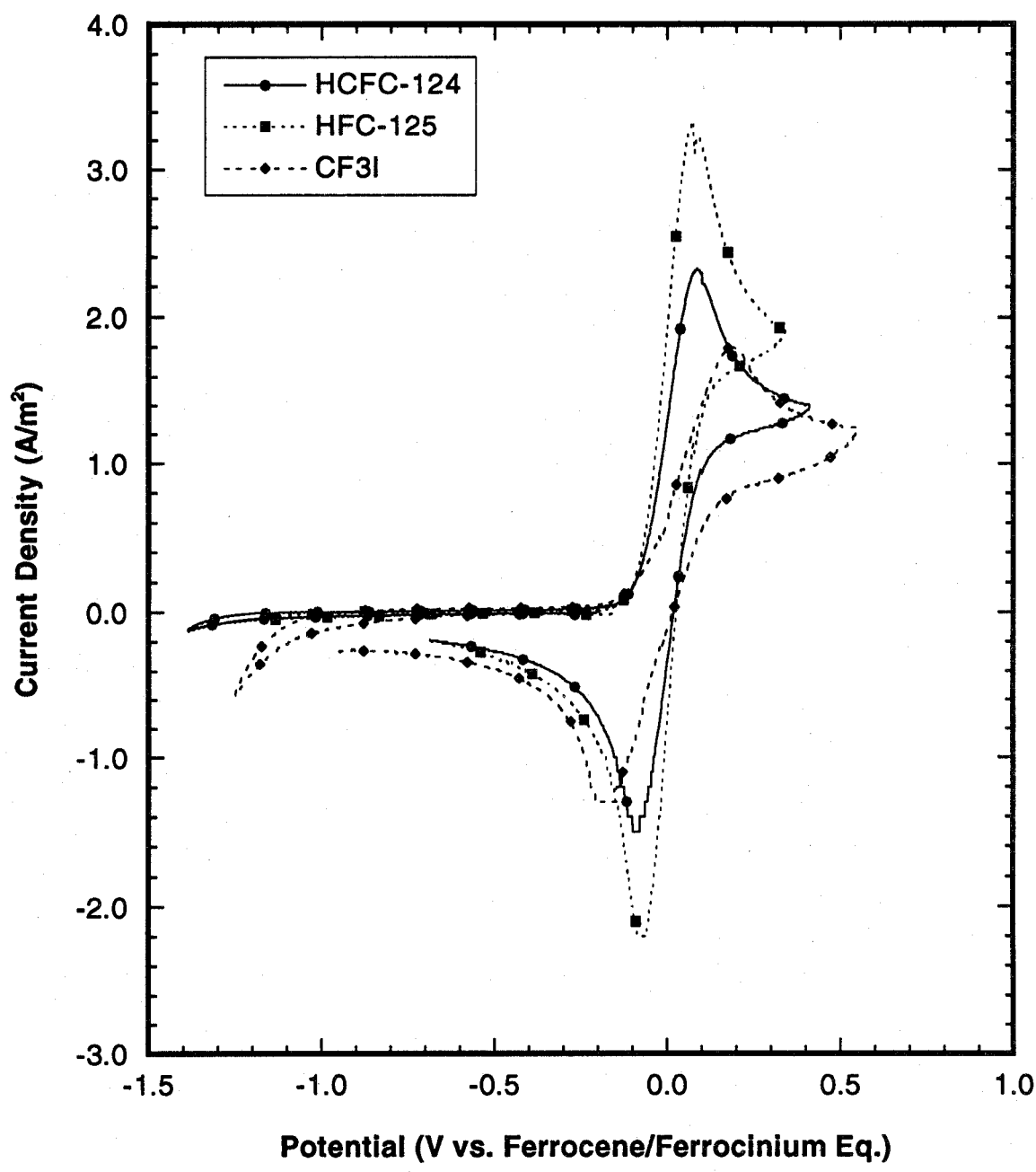


Figure 22. 0.1 V/s voltametric sweep on a Pt-QRE in HCFC-124 and HFC-125 using 5×10^{-4} mol/L of ferrocene and 5×10^{-2} mol/L of TBAPF₆ (1 out of 50 data points shown).

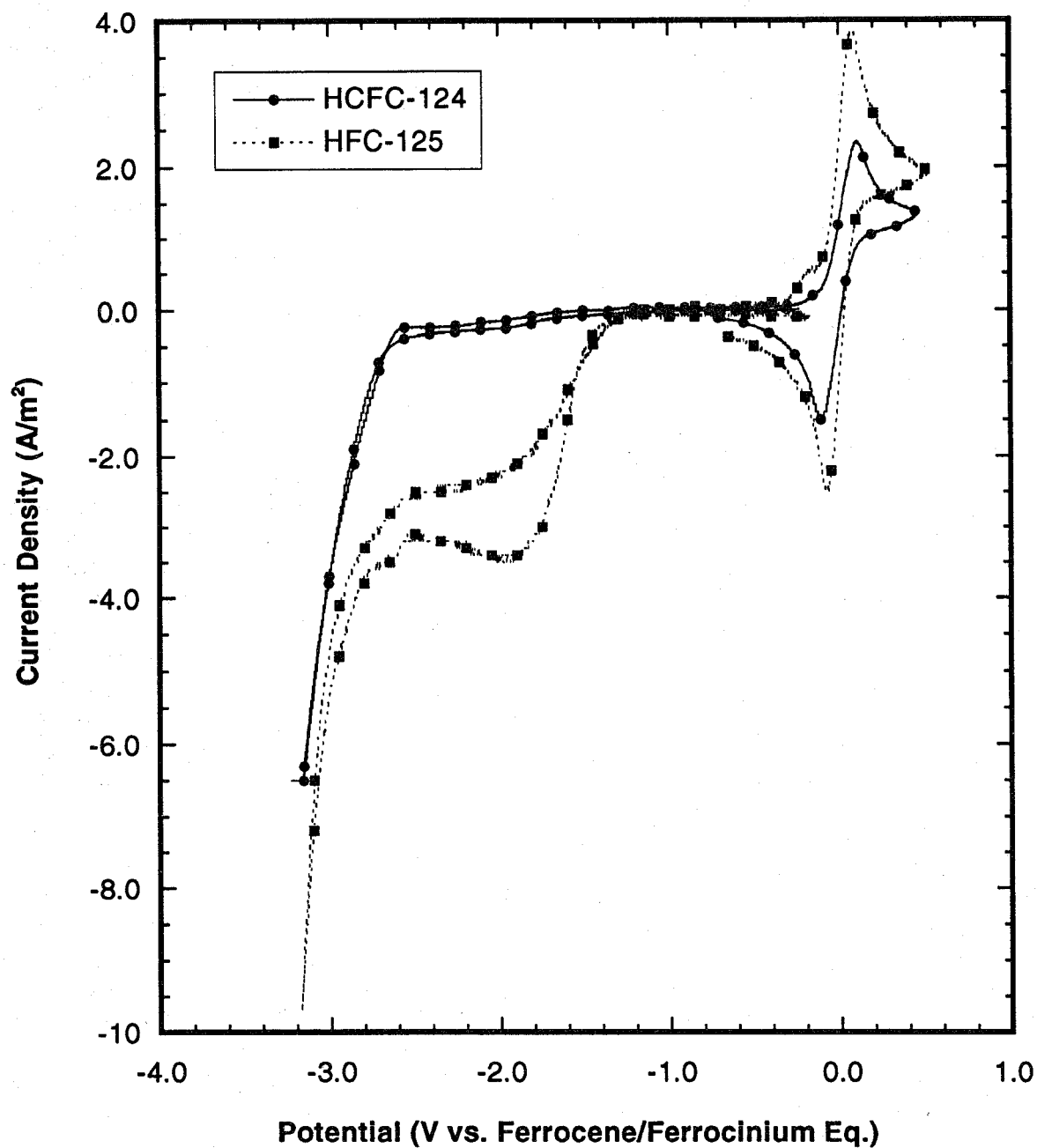


Figure 23. 0.1 V/s voltametric sweep on a Pt-QRE in HCFC-124, HFC-125, and CF_3I using 5×10^{-4} mol/L of ferrocene and 5×10^{-2} mol/L of TBATFMS (1 out of 50 data points shown).

HCFC-124 and HFC-125 respectively, $E_{1/2}(\text{Cp}_2\text{Fe}^{0/+}) - E_{\text{H}_2\text{O}} = 1.50 \text{ V} \pm 0.009 \text{ V}$ and $1.47 \text{ V} \pm 0.008 \text{ V}$ for HCFC-124 and HFC-125, respectively.

The situation with TBATFMS in CF_3I is different from this salt in the other two environments. As can be seen in Figure 24, only one major reduction peak is observed at 1.095 V ($\text{Cp}_2\text{Fe}^{0/+}$). The peak is very large and the peak maximum is never detected. The addition of water has no effect on the voltammograms. It can not be ruled out, however, that this large peak is a result of water contamination. It is known that water is often found as a contaminant of CF_3I . The usable window for CF_3I containing TBATFMS is at least 1.5 V . Peak separations for scans up to 0.5 V/s were averaged yielding $E_{1/2}(\text{Cp}_2\text{Fe}^{0/+}) - E_{\text{unknown}} = 1.103 \text{ V} \pm 0.008 \text{ V}$.

In subsequent experiments studying the corrosion of alloys in HCFC-124, HFC-125, and CF_3I , there was no ferrocene added to the cell. $E_{1/2}(\text{Cp}_2\text{Fe}^{0/+})$ was then defined by noting the position of the salt reduction, finding the appropriate value for the separation of the reduction peak and the ferrocene peak listed in Table 38, and realizing that ferrocene is this much more anodic than the Bu_4N^+ reduction peak. In several of these experiments, however, the reduction peak associated with H_2O masked the onset of reduction of the salt. In this case, $E_{1/2}(\text{Cp}_2\text{Fe}^{0/+})$ was defined with reference to the separation of ferrocene and the water peak. In the case of CF_3I , the half wave potential of ferrocene was measured using the peak separation of the large reduction peak and ferrocene, listed in Table 38, in all cases.

5.5.5 $\text{Cp}_2\text{Fe}^{0/+}$ Electron Kinetics. Cyclic voltammograms of $\text{Cp}_2\text{Fe}^{0/+}$ oxidation and reduction peaks on a Pt disk electrode in HCFC-124, HFC-125, and CF_3I at 0.1 V/s with TBATFMS as the supporting salt are shown in Figure 24. Using TBAPF_6 as the supporting salt resulted in similar scans. Peak separation ($E_a - E_c$) and the separation of the anodic peak potential and the half-wave potential of $\text{Cp}_2\text{Fe}^{0/+}$ ($E_a - E_{1/2}$) as a function of scan rate were used to estimate the electron transfer rate constant, k^0 (Bard, 1980). Values for k^0 in all of the agent/supporting salt combinations is shown in Table 37. k^0 was calculated assuming a diffusion coefficient of $1 \times 10^{-5} \text{ cm}^2/\text{s}$ and $\alpha = 0.5$. It should be noted that no IR compensation was used in the current experiments. The very large uncompensated resistance would thus result in a lowering of the k^0 values as the scan rate increased. Compensation for IR drop was attempted, but efforts to do so resulted in oscillations at entered resistance values that were much lower than their actual values.

The k^0 values found in the literature for $\text{Cp}_2\text{Fe}^{0/+}$ in acetonitrile, dichloromethane and chloroform using similar sized electrodes are $k^0 \sim 9 \times 10^{-2}$, 6×10^{-2} , and $3 \times 10^{-2} \text{ cm/s}$, respectively (Pournaghi-Azar, 1994 and Kadish, 1984). The k^0 values of $\text{Cp}_2\text{Fe}^{0/+}$ obtained in this study are approximately an order of magnitude lower, in the case of HCFC-124 with both salts and HFC-125 with TBATFMS. It should be mentioned that k^0 values for $\text{Cp}_2\text{Fe}^{0/+}$ of the magnitude seen in this study have been observed in electrolytes with similar dielectric constants using electrodes of similar proportions (Bond, 1988). In the case of HFC-125 with TBAPF_6 and CF_3I with TBATFMS, the k^0 values are about 1.5 orders of magnitude lower. In a study by Kadish *et al.*, there appears to be an inverse relationship between the solution resistivity and the value of k^0 that is not related to uncompensated resistance (Kadish, 1984). This trend is verified in the data for both TBATFMS and TBAPF_6 .

It is interesting to note that in HCFC-124, as is the case for the resistivity, the k^0 values appear to be unaffected by the salt used. In HCFC-124 with both salts and HFC-125 with TBATFMS, k^0 decreases slightly with scan rate, at higher scan rates, indicating that IR does play a minor role in the low k^0 values obtained in this study. It was also noted that the k^0 values decrease with scan rate to a greater extent in HFC-125 using TBAPF_6 and CF_3I using TBATFMS. This implies that the IR effect is much more noticeable in those two environments as would be expected given the values of the resistivity in Table 37.

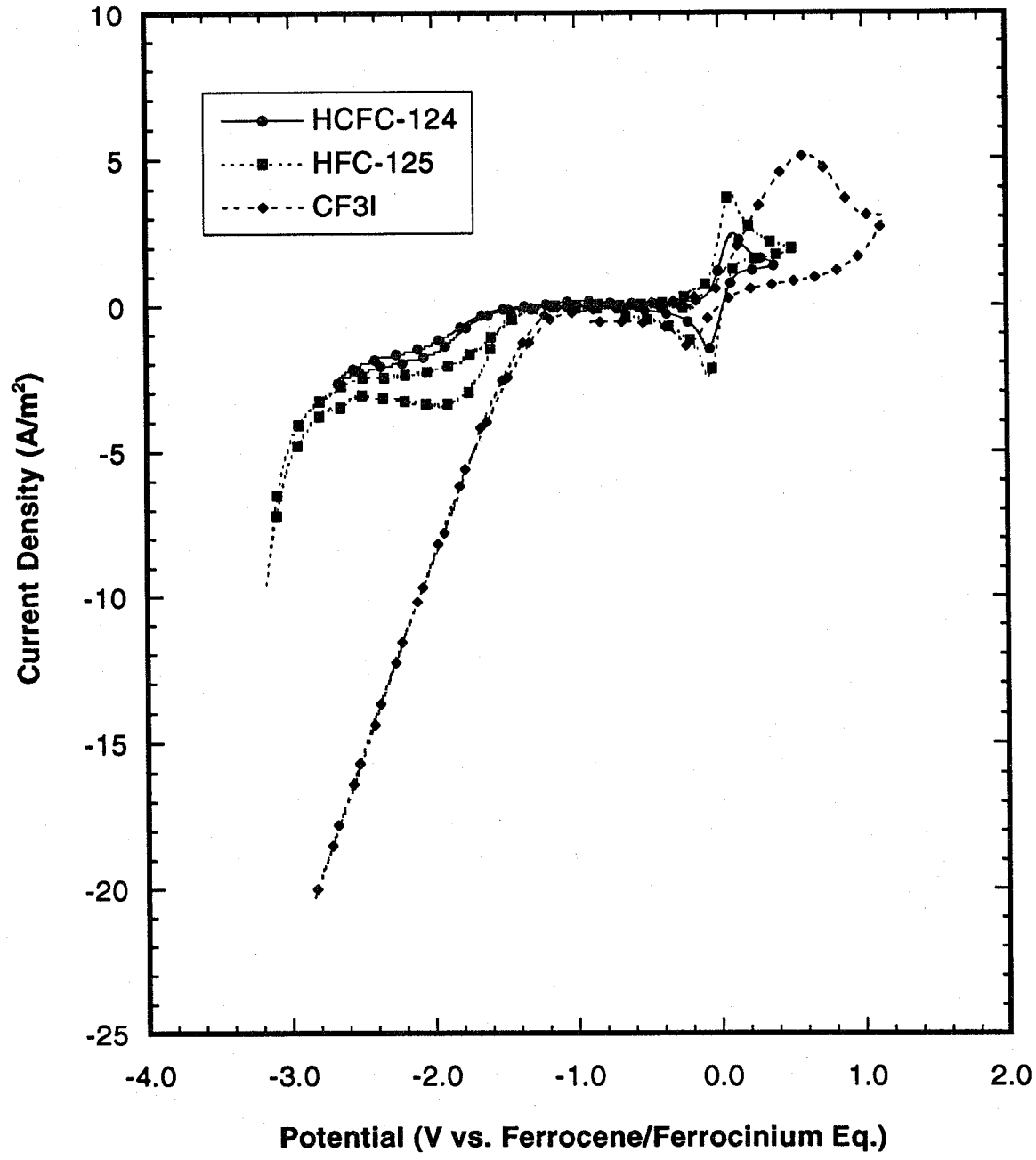


Figure 24. Ferrocene oxidation and reduction peaks on a Pt-QRE in HCFC-124, HFC-125, and CF₃I. (1 out of 50 data points shown).

Table 38. Reference peak values

Agent	Supporting Salt	$E_{1/2}(\text{CP}_2\text{Fe}^{0/+}) - E_{\text{lrp}}(\text{TBA})$ Volts	$E_{1/2}(\text{CP}_2\text{Fe}^{0/+}) - E_{\text{H}_2\text{O}}$ Volts
HCFC-124	TBTFMS	2.49 ± 0.008	-1.50 ± 0.009
HCFC-124	TBAPF ₆	2.55 ± 0.002	-1.50
HFC-125	TBTFMS	2.55 ± 0.009	1.47 ± 0.008
HFC-125	TBAPF ₆	2.56 ± 0.014	-1.50
CF ₃ I	TBTFMS	1.103 ± 0.008	---
CF ₃ I	TBAPF ₆	---	---

lrp = large reduction peak for tetrabutylammonium (TBA)

Based on solution resistivity and k^0 values in the various media, it appears that alternative fire suppressant solutions containing 5×10^{-2} mol/L of TBTFMS and 5×10^{-4} mol/L of ferrocene are the most appropriate systems for measuring corrosion rates of storage container alloys.

5.5.6 Corrosion Rates of Storage Vessel Alloys in HCFC-124, HFC-125, and CF₃I. Figures 25, 26, and 27 show Tafel plots of 304 stainless steel, Nitronic 40, Al 6061 T6, and Ti 15-3-3-3 in HCFC-124, HFC-125, and CF₃I, respectively. In all cases, the free corrosion potential (FCP) was very difficult to obtain and moved cathodically from a more or less stable value when potentiodynamic scans were performed. This cathodic movement was observed regardless of the direction of the scan. Fairly reproducible FCPs and scans were made by preconditioning the working electrode prior to a scan. A potential of -0.1 V was applied to the working electrode for 10 s prior to each scan. The potential was then allowed to return to a steady state over approximately 30 min. The sliding FCP was less severe in HFC-125. Therefore, scans were begun at -250 mV below the FCP and ended at 500 mV over the FCP. In the other two environments, where the FCP is less stable, potentiodynamic scans were begun at -100 mV below the FCP and terminated at 1.5 V of the FCP.

Table 39 shows the results of Tafel (Bard, 1980) extrapolations of the curves in Figures 25, 26, and 27. The extrapolation was based primarily on the anodic curves. It can be seen from the results that the corrosion current density in alternative fire suppressants is extremely low. The values are on the order of those obtained for passivated metals in aqueous solutions. No evidence of transpassive behavior was observed for any of the metals in any environment, even at high overpotentials. The low current densities may be a result of both a protective air formed oxide as well as the low dielectric constant of the environment. The presence of oxidation and reduction precursors and by products, *i.e.*, H^+ , OH^- , and metal ions, are highly unfavorable in the low dielectric constant media.

Corrosion rates of the four alloys are reported in the third column of Table 39. The estimated weight loss values were calculated assuming the current densities in Table 39 and that the major dissolution phases are Fe/Fe^{2+} for Nitronic 40 and 304 SS, Al/Al^{3+} for Al 6061, and Ti/Ti^{2+} for Ti 15-3-3-3. In the fourth column of Table 39, weight change data from 25 day immersion tests at 20 °C is presented. All but two of the weight change data are positive indicating that film formation had

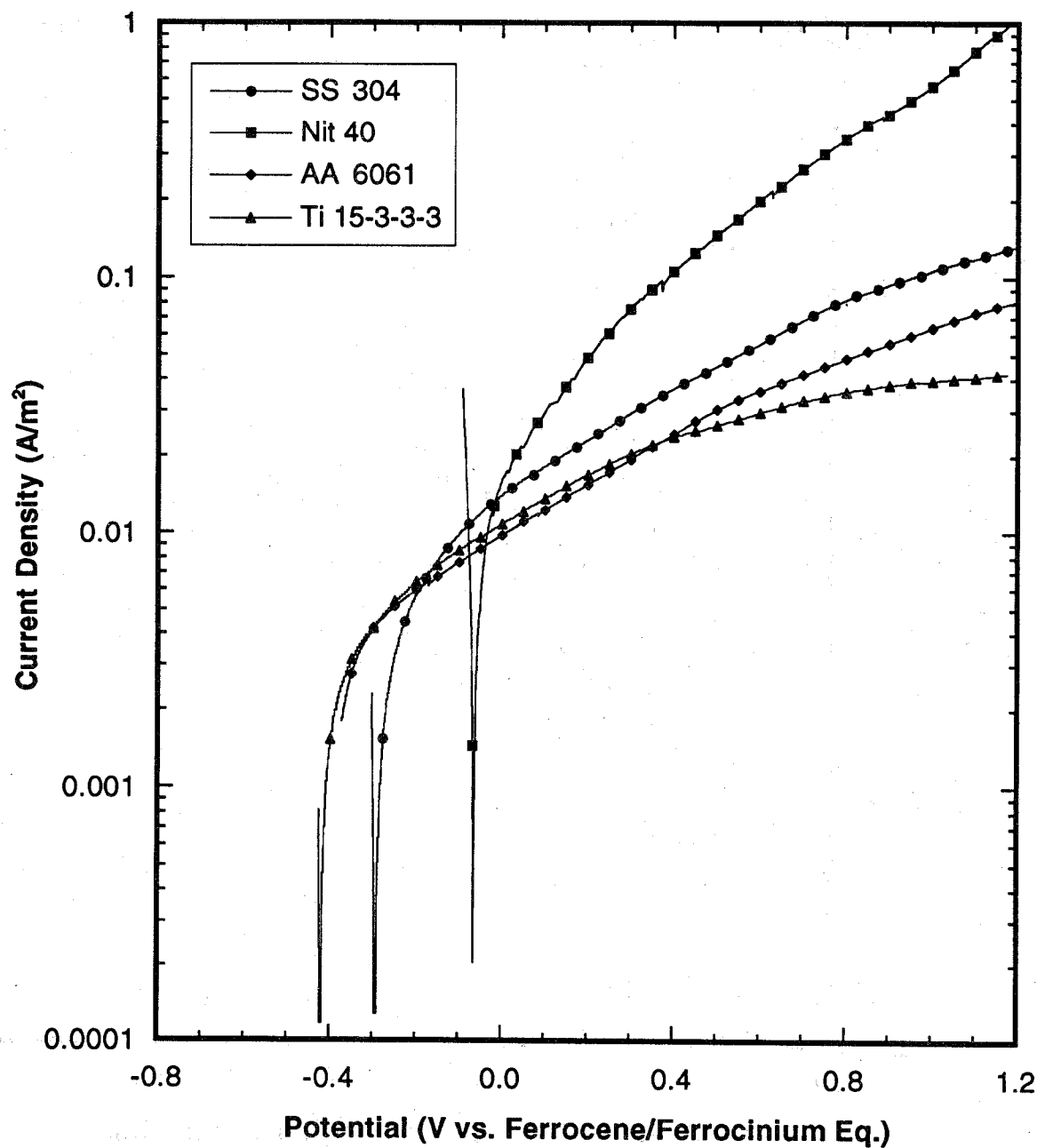


Figure 25. Potentiodynamic scans of 304SS, Nitronic 40, Al 6061-T6, and Ti 15-3-3-3 in HCFC-124 containing 5×10^{-2} mol/L of TBATFMS (1 out of 50 data points shown).

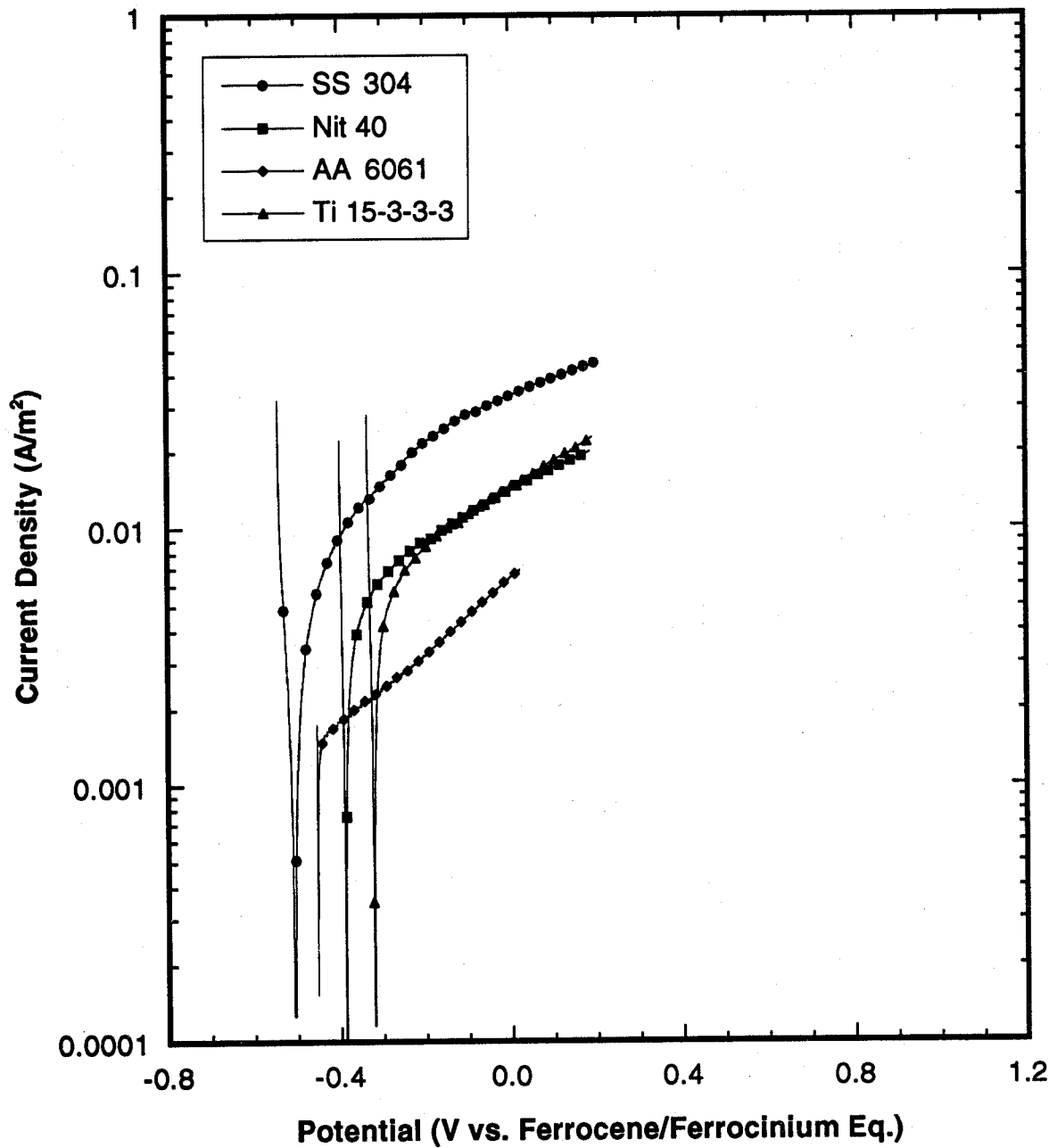


Figure 26. Potentiodynamic scans of 304SS, Nitronic 40, Al 6061-T6, and Ti 15-3-3-3 in HCFC-125 containing 5×10^{-2} mol/L of TBATFMS (1 out of 50 data points shown).

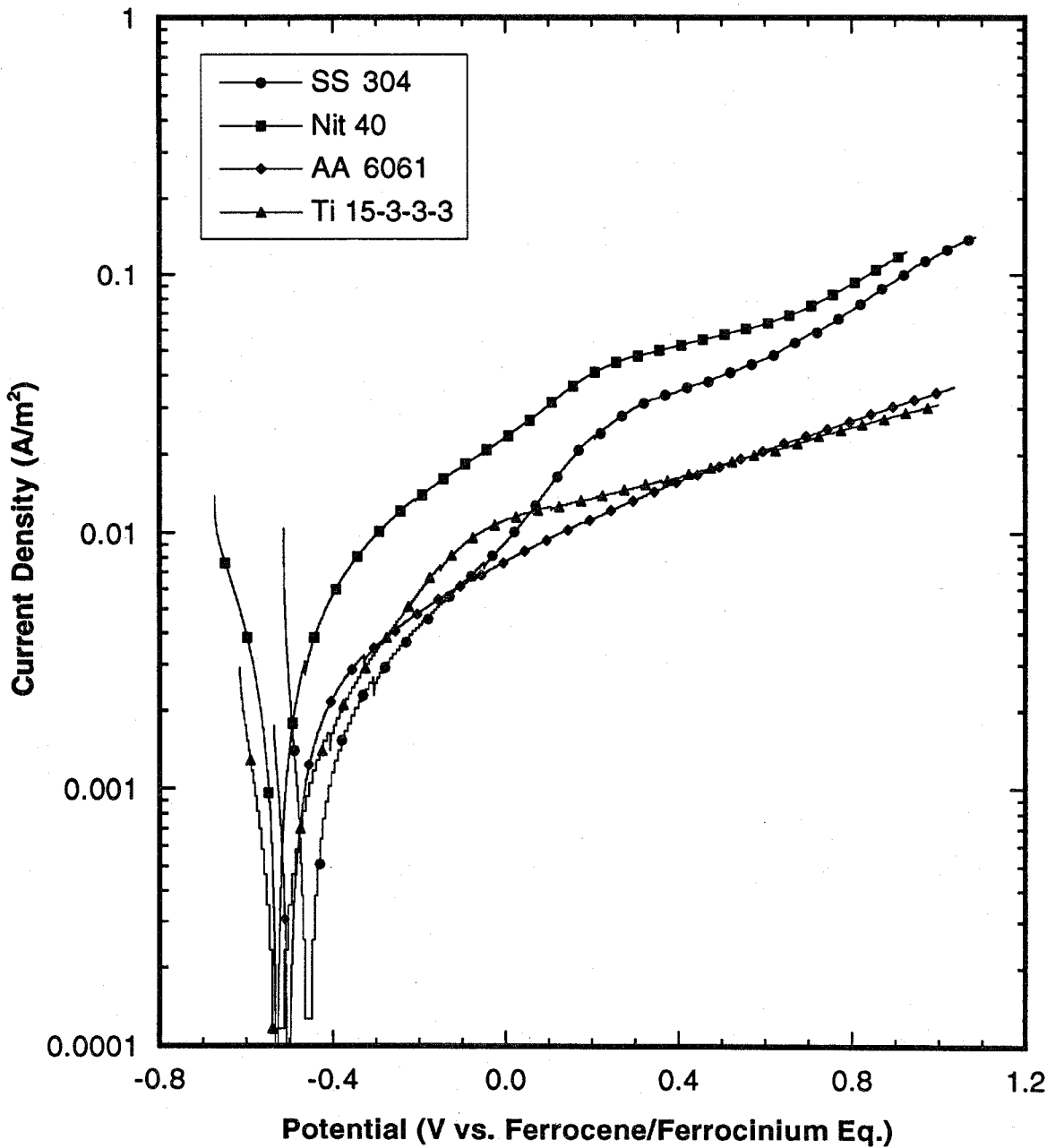


Figure 27. Potentiodynamic scans of 304SS, Nitronic 40, Al 6061-T6, and Ti 15-3-3-3 in CF_3I containing 5×10^{-2} mol/L of TBATFMS (1 out of 50 data points shown).

Table 39. Polarization for various alloys in replacement candidates as compared to weight change values after a 30 day immersion

Agent	Alloy	E_{Corr} (Volts)	I_{Corr} (A/cm ²)	Estimated $\Delta M/A$ (g/m ² · day)	Measured $\Delta M/A$ (g/m ² · day)
HCFC-124	Nitronic 40	-0.066	1.18×10^{-2}	-29.5×10^{-3}	---
HCFC-124	304 Stainless Steel	-0.314	3.97×10^{-3}	-9.93×10^{-3}	---
HCFC-124	Al 6061-T6	-0.401	3.67×10^{-3}	-2.96×10^{-3}	---
HCFC-124	Ti 15-3-3-3	-0.435	2.52×10^{-3}	-5.40×10^{-3}	---
HFC-125	Nitronic 40	-0.388	4.15×10^{-3}	-10.38×10^{-3}	2.79×10^{-3}
HFC-125	304 Stainless Steel	-0.508	4.73×10^{-3}	-11.82×10^{-3}	6.75×10^{-3}
HFC-125	Al 6061-T6	-0.453	1.50×10^{-3}	-1.21×10^{-3}	10.21×10^{-3}
HFC-125	Ti 15-3-3-3	-0.320	5.58×10^{-3}	-11.96×10^{-3}	0.89×10^{-3}
CF ₃ I	Nitronic 40	-0.532	3.72×10^{-3}	-9.30×10^{-3}	-1.01×10^{-3}
CF ₃ I	304 Stainless Steel	-0.460	1.16×10^{-3}	-2.90×10^{-3}	-0.39×10^{-3}
CF ₃ I	Al 6061-T6	-0.501	2.11×10^{-3}	-1.70×10^{-3}	1.09×10^{-3}
CF ₃ I	Ti 15-3-3-3	-0.531	6.63×10^{-4}	-1.42×10^{-3}	0.58×10^{-3}

occurred. Attempts to remove this film and measure an actual metal dissolution rate were unsuccessful. Therefore, the conclusions that can be drawn from comparisons of columns 3 and 4 in Table 39 are limited. However, it is interesting to note that all but one of the corrosion weight loss data values obtained using electrochemical techniques are within one order of magnitude of immersion test values. Furthermore, the absolute value of all but one of the electrochemical data are greater than the absolute values of the immersion test values. This would indicate that the electrochemical data would allow for a worse case design criteria based on the higher corrosion values. It is believed that the electrochemical data is more realistic in this study because a true dissolution rate was not obtained for the immersion tests. According to the electrochemical data, it appears that Al 6061-T6 has the best overall performance in the agents studied. It is interesting to note that the Al alloy has the highest weight gain in both HFC-125 and CF₃I. This is probably indicative of the formation and growth of a protective layer.

5.5.7 Corrosion Rates of Metals in Other Halon Replacement Agents. From the data in Table 39, it appears that, in general, the corrosion rates for the various metals are lower in CF₃I than for the other two replacement environment. The lower dielectric constant for this medium is believed to be the reason for this lower value. Typical charged species involved in corrosion have a low probability of being dissolved in a low dielectric constant media because of their low charge to volume ratio resulting in a lower corrosion rate.

The other halon replacement agents under consideration, FC-218 and HFC-227ea have lower dielectric constants than those examined in these electrochemical experiments. In support of this assumption, the salts used in this study did not dissolve in FC-218 or HFC-227ea. Thus, it is proposed that the corrosion rate of storage vessel alloys in these media will be less than those measured here because the solubility of aggressive species and corrosion products will be reduced.

5.6 Conclusions

The primary objective of this investigation was to determine whether any of the candidates selected as potential replacements for halon 1301 should be eliminated from further consideration because of unacceptable corrosion rates of the metals used in the fire suppressant storage and distribution systems on aircraft. In Phase II of this study, the remaining candidates from the screening process (Phase I) were examined for longer times and over a broader range of environmental conditions. In addition, this phase examined both the corrosivity of a representative post deployment deposit on aircraft structural materials and the use of supporting salts which resolved the resistivity of the suppressants thereby enabling electrochemical measurements of corrosion rates.

As in the first phase of this investigation, no single candidate was found to cause serious corrosion problems with all of the alloys and no serious concerns were raised for all of the alloys in any of the agents. However, some agents did consistently demonstrate poorer performance than others or yielded results which indicate further testing is warranted before they should be placed into service. In particular, CF_3I demonstrated higher mass change rates for most of the alloys than the other agents requiring a mass change scale at least one order of magnitude larger than halon 1301 to plot the results. The other agents demonstrated mass change rates that essentially the same or less than those observed for halon 1301. Visual examination of the samples after the exposure tests revealed that AISI 4130 developed small pits during exposure to HFC-227ea, FC-218, and CF_3I with the largest pits being observed in CF_3I . Small pits were also observed in Nitronic 40 and Al 6061 during exposure to HFC-227ea. The only agent to demonstrate any conclusive evidence of environmental induced fracture during the slow strain rate tensile tests was CF_3I which caused cracking of two of the three samples tested at 150 °C.

Electrochemical measurements could only be made in three of the agents: HCFC-124, HFC-125, and CF_3I . Presumably, the corrosion rates in the others would be lower than these three due the same factors that inhibit the measurement of corrosion rate (high resistivity and dielectric constant). Of these three, the lowest corrosion rates were observed in CF_3I which is in contrast to the immersion test results. This may be due to the formation of protective surface films that slow corrosion resulting in a lower average corrosion rate over the long exposure times in the other agents or it could be an indication that the corrosivity observed for CF_3I is the result of second phase contaminants present in the agent as supplied and the fact that the electrochemical experiments used smaller volumes of agent and very small area samples which would result in a much lower probability of contaminating the surface with an aggressive species such as a halogen acid. If contaminants are responsible for the poor performance of CF_3I in these tests, then removal of these impurities could make this agent acceptable for use.

The results of this investigation demonstrate that it may be possible to use any of these agents in aircraft fire suppression systems, but before CF_3I is used, a better understanding of the factors influencing its corrosivity will be needed. Also, this conclusion is based on the quality of the agents as supplied for testing and changes in the impurity content of any of the agents could result in dramatic shifts in the corrosivity. Assuming that the performance of the CF_3I was the result of trapped impurities, then the presence of similar impurities in any of the agents should result in similar levels of performance.

5.7 Acknowledgments

The authors would like to thank Dr. Thomas Moffat and Mr. Carlos Beauchamp of NIST for their technical assistance and helpful suggestions during the design and development of the electrochemical techniques. We also would like to thank Mr. George Hicho and Mr. Richard Harris, also of NIST, for their insightful reviews. We acknowledge Dr. Kumar Jata and Mr. Thomas Naguy of the Wright-Patterson Materials Laboratory for their assistance and recommendations in the selection of the alloys used in this study. The authors especially wish to thank Ms. Joan Teagle, also of NIST, for her dedication and invaluable help with the editing of this document.

5.8 References

- ASTM, Standard Test Methods of Tension Testing of Metallic Materials, *Annual Book of ASTM Standards, Section 3, Metals Test Methods and Analytical Procedures*, Philadelphia, PA, 1993.
- ASTM, Standard Practice for Preparation and Use of Direct Tension Stress-Corrosion Test Specimens, *Annual Book of ASTM Standards, Section 3, Metals Test Methods and Analytical Procedures*, Philadelphia, PA, 1993.
- ASTM, Standard Guide for Applying Statistics to Analysis of Corrosion Data, *Annual Book of ASTM Standards, Section 3, Metals Test Methods and Analytical Procedures*, Philadelphia, PA, 1993.
- ASTM, Standard Practice for Laboratory Immersion Corrosion Testing of Metals, *Annual Book of ASTM Standards, Section 3, Metals Test Methods and Analytical Procedures*, Philadelphia, PA, 1993.
- Bard, A. J., and Faulkner, L. R., *Electrochemical Methods, Fundamentals and Applications*, John Wiley and Sons, Inc., New York, 1980.
- Bond, A. M., Henderson, T. L. E., Mann, D. R., Thormann, W., and Zoski, C. G., (1988), "Fast Electron Transfer Rate for the Oxidation of Ferrocene in Acetonitrile or Dichloromethane at Pt Disk Ultramicroelectrodes," *Anal. Chem.* 60, D. R. Lide, ed., 1978.
- CRC Handbook of Chemistry and Physics* (71st ed.), W. Palm Beach, FL CRC Press, 1990.
- Dante, J. F., Stoudt, M. R., Fink, J. L., Beauchamp, C. R., Moffat, T. P., and Ricker, R. E., "Evaluation of the Corrosion Behavior of Storage Container Alloys in Halon 1301 Replacement Candidate Agents," Paper presented at the Tri-Service Conference on Corrosion, Orlando, FL 1994.
- Deiter, G. E., *Mechanical Metallurgy* (3rd ed.) McGraw-Hill Series in Materials Science and Engineering, 275-324, McGraw-Hill, New York, 1986.
- Fontana, M. G., and Greene, N. D., *Corrosion Engineering*, McGraw-Hill Series in Materials Science and Engineering, McGraw-Hill, New York, 1987.
- Kadish, K. M., Ding, J. Q., and Malinski, T., "Resistance of Nonaqueous Solvent Systems Containing Tetraalkylammonium Salts," *Anal. Chem.* 56, 1741, 1984.
- Linteris, G., Prediction of HF Formation During Suppression, 1994.
- Mendenhall, W., & Sincich, T., *Statistics for Engineering and the Sciences*, San Francisco, Dellen Publ. Co., 1992.
- Metals Handbook: Vol 12, Fractography*, K. Mills et al, eds. (9th ed.), Metals Park, OH, ASM International, 1987.
- Metals Handbook: Vol 9, Metallography and Microstructures*, H. E. Boyer, (8th ed.), Metals Park, OH, ASM International, 1987.
- Metals Handbook: Vol 13, Corrosion*, L. J. Korb et al., eds. (9th ed.), 669-706, Metals Park, OH, ASM International, 1987.

Nyden, M., Linteris, G., Burgess, D. R. F. Jr., Westmoreland, P. R., Tsang, W., and Zachariah, M. R., in *Evaluation of Alternative In-Flight Fire Suppressants for Full Scale Testing in Simulated Aircraft Engine Nacelles and Dry Bays*, NIST Special Publication 861, NIST, 1994.

Park, J., and Shaw, B. R., "Improved Performance of Unmodified and Cobalt Phthalocyanine-Modified Carbon-Kel F Composite Electrodes," *J. Electrochem. Soc.* 56, 1741, 1994.

Pournaghi-Azar, M. H., and Ojani, R., "Electrode Kinetic Parameters of the Ferrocene Oxidation at Pt, Au and Glassy Carbon Electrodes in Chloroform," *Electrochimica Acta* 39, 953, 1994.

Ricker, R. E., Stoudt, M. R., Dante, J. F., Fink, J. L., Beauchamp, C. R., and Moffat, T. P., in *Evaluation of Alternative In-Flight Fire Suppressants for Full Scale Testing in Simulated Aircraft Engine Nacelles and Dry Bays*, NIST Special Publication 861, NIST, 1994.

Sawyer, D. T., and Roberts, J. L., *Experimental Electrochemistry for Chemists*, John Wiley and Sons, Inc., New York, 1974.

Stoudt, M. R., Escalante, E., and Ricker, R. E., "The Influence of Moisture and Pressure on the Mechanical Properties of a Glass-Epoxy Matrix Composite and a Graphite-Epoxy Matrix Composite," *Environmental Effects on Advanced Materials*, San Diego, CA, 1991.

Stoudt, M. R., Fink, J. L., and Ricker, R. E., "The Environmentally-Induced Failure Susceptibility of Fire Suppressant Storage Container Alloys In Replacement Candidates for Halon 1301," In Press, 1995.

Stoudt, M. R., and Ricker, R. E., "Characterization of the Hydrogen Induced Cold Cracking Susceptibility at Simulated Weld Zones in HSLA-100 Steel," NISTIR 5408, NIST, 1994.

Stoudt, M. R., Fink, J. L., and Ricker, R. E., "Evaluation of the Stress Corrosion Cracking Susceptibility of Fire Suppressant Storage Container Alloys in Replacement Candidates for Halon 1301," Paper presented at the Tri-Service Conference on Corrosion, Orlando, FL, 1994.

Ue, M., "Mobility and Ionic Association of Li and Quaternary Ammonium Salts in Propylene Carbonate and -Butyrolactone," *J. Electrochem. Soc.* 141, 3336, 1994.

Zotikov, V. S., Bakmutova, G. B., Bocharova, N. A., and Semenyuk, E. Y., "Corrosion of Al and its Alloys in Hydrofluoric Acid," *Prot. Met.* 10, 2, 154-156, 1974.

Appendix A. Mass Change Measurements at 150 °C

Sample Number	Test Environ. 150 °C	$\Delta M/\text{Area}$ 30 Days g/m^2	$\Delta M/\text{Area}$ 60 Days g/m^2	$\Delta M/\text{Area}$ 120 Days g/m^2	$\Delta M/\text{Area}$ 180 Days g/m^2	$\Delta M/\text{Area}$ 365 Days g/m^2
NIT40/13	HFC-227ea	0.11681	0.15692	0.14866	0.14866	---
NIT40/14	HFC-227ea	0.17698	0.18878	0.42003	0.14040	---
NIT40/15	HFC-227ea	0.14394	0.13215	0.18878	0.15810	---
NIT40/16	FC-218	0.17934	0.75866	4.43396	3.26942	---
NIT40/17	FC-218	0.10855	0.35160	4.23220	3.28476	---
NIT40/18	FC-218	0.13804	0.35632	3.78267	2.80809	---
NIT40/19	halon 1301	0.17108	0.23479	0.30559	0.36694	0.31031
NIT40/20	halon 1301	0.12743	0.18288	0.27845	0.34924	0.36694
NIT40/21	halon 1301	0.12153	0.19822	0.26075	0.29143	0.31503
NIT40/22	HFC-125	0.02124	0.06135	0.06371	0.12389	0.09675
NIT40/23	HFC-125	0.07197	0.09439	0.11563	0.11563	0.11091
NIT40/24	HFC-125	0.06253	0.06843	0.09557	0.08023	0.09675
NIT40/25	CF ₃ I	16.16778	16.47808	17.56002	---	---
NIT40/26	CF ₃ I	15.40322	16.09344	8.26972	---	---
NIT40/27	CF ₃ I	17.85381	18.71158	9.64663	---	---

Sample Number	Test Environ. 150 °C	$\Delta M/\text{Area}$ 30 Days g/m^2	$\Delta M/\text{Area}$ 60 Days g/m^2	$\Delta M/\text{Area}$ 120 Days g/m^2	$\Delta M/\text{Area}$ 180 Days g/m^2	$\Delta M/\text{Area}$ 365 Days g/m^2
6061/13	HFC-227ea	0.42492	0.63796	1.00595	1.25245	---
6061/14	HFC-227ea	0.53056	0.58925	0.73011	0.98834	---
6061/15	HFC-227ea	0.44957	0.59629	0.52000	0.72658	---
6061/16	FC-218	0.47774	0.73363	9.49842	7.84688	---
6061/17	FC-218	0.35097	0.67846	0.49652	0.17607	---
6061/18	FC-218	0.29228	0.55051	1.04469	0.55990	---
6061/19	halon 1301	0.42609	0.97074	1.26419	1.34635	1.24775
6061/20	halon 1301	0.36153	0.56812	0.94609	0.98600	0.90852
6061/21	halon 1301	0.36153	0.52234	0.95665	0.92026	0.87801
6061/22	HFC-125	0.25472	0.47422	0.93317	0.99656	0.94961
6061/23	HFC-125	0.23711	0.48243	0.91087	0.84044	0.96839
6061/24	HFC-125	0.26411	0.51647	0.79232	0.72893	0.89444
6061/25	CF ₃ I	2.17389	5.46523	8.58872	---	---
6061/26	CF ₃ I	0.41201	2.32061	4.04376	---	---
6061/27	CF ₃ I	0.27584	2.76900	5.07201	---	---

Sample Number	Test Environ. 150 °C	$\Delta M/\text{Area}$ 30 Days g/m^2	$\Delta M/\text{Area}$ 60 Days g/m^2	$\Delta M/\text{Area}$ 120 Days g/m^2	$\Delta M/\text{Area}$ 180 Days g/m^2	$\Delta M/\text{Area}$ 365 Days g/m^2
304/13	HFC-227ea	0.17679	0.22831	0.19318	0.19201	---
304/14	HFC-227ea	0.14752	0.20957	0.20372	0.18850	---
304/15	HFC-227ea	0.13464	0.17913	0.19552	0.14518	---
304/16	FC-218	0.23182	0.49993	7.36548	4.32727	---
304/17	FC-218	0.14284	0.33953	7.80453	4.95715	---
304/18	FC-218	0.16625	0.30441	6.66301	4.37644	---
304/19	halon 1301	0.26811	0.25992	0.30909	0.37348	0.33602
304/20	halon 1301	0.20840	0.22948	0.28099	0.31846	0.32665
304/21	halon 1301	0.17445	0.20255	0.26109	0.33016	0.31612
304/22	HFC-125	0.04566	0.10303	0.16157	0.24235	0.19904
304/23	HFC-125	0.09601	0.14752	0.15455	0.15103	0.16625
304/24	HFC-125	0.07142	0.13230	0.15220	0.16859	0.14401
304/25	CF ₃ I	9.23290	14.76492	32.35966	---	---
304/26	CF ₃ I	11.33448	20.14005	24.00251	---	---
304/27	CF ₃ I	10.09344	16.99412	15.15245	---	---

Sample Number	Test Environ. 150 °C	$\Delta M/\text{Area}$ 30 Days g/m^2	$\Delta M/\text{Area}$ 60 Days g/m^2	$\Delta M/\text{Area}$ 120 Days g/m^2	$\Delta M/\text{Area}$ 180 Days g/m^2	$\Delta M/\text{Area}$ 365 Days g/m^2
Ti/13	HFC-227ea	0.25954	0.37657	0.28503	0.02665	---
Ti/14	HFC-227ea	0.17728	0.25491	0.19466	0.21088	---
Ti/15	HFC-227ea	0.20393	0.30357	0.29778	0.29546	---
Ti/16	FC-218	0.30705	0.88986	0.98603	0.80528	---
Ti/17	FC-218	0.26418	0.38468	0.89566	0.66392	---
Ti/18	FC-218	0.22478	0.33717	1.56074	1.32205	---
Ti/19	halon 1301	0.17728	0.26418	0.34181	0.35571	0.41249
Ti/20	halon 1301	0.19582	0.24796	0.38816	0.44957	0.40322
Ti/21	halon 1301	0.19813	0.26765	0.40438	0.46695	0.44957
Ti/22	HFC-125	0.08111	0.18307	0.19118	0.21899	0.29199
Ti/23	HFC-125	0.06836	0.13325	0.14715	0.17959	0.17264
Ti/24	HFC-125	0.12166	0.20045	0.19118	0.19118	0.19466
Ti/25	CF ₃ I	4.89308	3.14696	6.10969	---	---
Ti/26	CF ₃ I	4.51188	3.35089	4.15385	---	---
Ti/27	CF ₃ I	4.46322	3.86882	5.35540	---	---

Sample Number	Test Environ. 150 °C	$\Delta M/\text{Area}$ 60 Days g/m^2	$\Delta M/\text{Area}$ 150 Days g/m^2
4130/13	HFC-227ea	-24.06626	-38.42012
4130/14	HFC-227ea	0.32681	-2.49535
4130/15	HFC-227ea	0.48845	-0.18287
4130/16	FC-218	3.79199	4.33117
4130/17	FC-218	2.96846	3.53360
4130/18	FC-218	2.86936	10.36130
4130/19	halon 1301	1.58098	2.68766
4130/20	halon 1301	2.08241	2.81626
4130/21	halon 1301	1.99982	2.62867
4130/22	HFC-125	1.46181	-1.02528
4130/23	HFC-125	0.85538	0.75981
4130/24	HFC-125	0.56042	0.46485
4130/25	CF ₃ I	-65.49613	-106.61335
4130/26	CF ₃ I	-74.17617	-57.24083
4130/27	CF ₃ I	-33.08845	-53.94674

Sample Number	Test Environ. 150 °C	$\Delta M/\text{Area}$ 90 Days g/m^2
321/04	halon 1301	1.38949
321/05	halon 1301	2.78602
321/06	halon 1301	1.49176
321/10	HFC-125	0.01411
321/11	HFC-125	0.01411
321/12	HFC-125	0.00823

Sample Number	Test Environ. 150 °C	$\Delta M/\text{Area}$ 90 Days g/m^2
CDA110/04	halon 1301	1.52769
CDA110/05	halon 1301	1.77123
CDA110/06	halon 1301	1.43710
CDA110/10	HFC-125	0.05824
CDA110/11	HFC-125	0.12706
CDA110/12	HFC-125	0.02647

Sample Number	Test Environ. 150 °C	$\Delta M/\text{Area}$ 90 Days g/m^2
CDA172/04	halon 1301	5.89103
CDA172/05	halon 1301	2.10562
CDA172/06	halon 1301	3.28194
CDA172/10	HFC-125	2.47205
CDA172/11	HFC-125	2.35912
CDA172/12	HFC-125	2.45440

Sample Number	Test Environ. 150 °C	$\Delta M/\text{Area}$ 90 Days g/m^2
355/04	halon 1301	1.04301
355/05	halon 1301	1.42683
355/06	halon 1301	1.90702
355/10	HFC-125	0.00459
355/11	HFC-125	0.03901
355/12	HFC-125	0.01893

Sample Number	Test Environ. 150 °C	$\Delta M/\text{Area}$ 90 Days g/m^2
I625/04	halon 1301	0.62422
I625/05	halon 1301	0.67142
I625/06	halon 1301	0.68322
I625/10	HFC-125	-0.01534
I625/11	HFC-125	-0.03186
I625/14	HFC-125	-0.07434

Appendix B. Mass Change Measurements at 20 °C

Sample Number	Test Environ. 20 °C	$\Delta M/\text{Area}$ 30 Days g/m^2	$\Delta M/\text{Area}$ 60 Days g/m^2	$\Delta M/\text{Area}$ 120 Days g/m^2	$\Delta M/\text{Area}$ 180 Days g/m^2	$\Delta M/\text{Area}$ 365 Days g/m^2
NIT40/01	HFC-125	0.08377	0.08377	0.15928	0.21238	0.65955 0.08613
NIT40/02	HFC-125	0.03068	-0.01652	0.06371	0.12271 0.12979	0.09793
NIT40/03	HFC-125	0.00236	0.01888	0.06017		
NIT40/04	HFC-227ea	0.01770	0.06607	0.09793	0.09911 0.05073	---
NIT40/05	HFC-227ea	-0.01062	0.03894	0.05545	0.07905	---
NIT40/06	HFC-227ea	-0.02950	0.03422	0.06253		---
NIT40/07	halon 1301	0.11799	0.14748	0.14984	0.28199	0.15928 0.16872
NIT40/08	halon 1301	-0.00118	0.02596	0.05545	0.10265 0.09557	0.14394
NIT40/09	halon 1301	-0.00236	0.03068	0.06725		
NIT40/10	FC-218	0.01298	0.07551	0.11563	0.12743	---
NIT40/11	FC-218	0.02950	0.05781	0.02950	0.08023 0.05781	---
NIT40/12	FC-218	-0.01416	0.04484	0.03422		---
NIT40/28	CF ₃ I	-0.03068	-0.00708	0.26547	---	---
NIT40/29	CF ₃ I	-0.01180	0.06253	0.12507	---	---
NIT40/30	CF ₃ I	-0.03658	0.02950	0.09439	---	---

Sample Number	Test Environ. 20 °C	$\Delta M/\text{Area}$ 30 Days g/m^2	$\Delta M/\text{Area}$ 60 Days g/m^2	$\Delta M/\text{Area}$ 120 Days g/m^2	$\Delta M/\text{Area}$ 180 Days g/m^2	$\Delta M/\text{Area}$ 365 Days g/m^2
6061/01	HFC-125	0.30636	0.42609	0.80992	0.96487 0.49065	1.19376 0.57986
6061/02	HFC-125	0.01409	0.08686	0.40614	0.55638	0.68315
6061/03	HFC-125	0.00352	0.09860	0.48713		
6061/04	HFC-227ea	0.05165	0.36857	0.50474	0.55990 0.74419	---
6061/05	HFC-227ea	0.00587	0.28993	0.45074	0.47187	---
6061/06	HFC-227ea	0.00235	0.27467	0.38501		---
6061/07	halon 1301	0.11738	2.53072	9.66862	-8.98664	-9.22493
6061/08	halon 1301	0.02348	0.33219	0.02348	0.08569 3.35238	-0.44957
6061/09	halon 1301	0.03521	-0.00352	1.33109		-2.11285
6061/10	FC-218	0.03639	0.34392	0.46952	0.57869 0.91791	---
6061/11	FC-218	0.05986	0.56225	0.82284	0.80288	---
6061/12	FC-218	0.04343	0.45426	0.71485		---
6061/28	CF ₃ I	0.00352	4.36068	-4.69052	---	---
6061/29	CF ₃ I	0.03991	53.50903	-6.39019	---	---
6061/30	CF ₃ I	0.03287	78.45355	-17.90990	---	---

Sample Number	Test Environ. 20 °C	$\Delta M/\text{Area}$ 30 Days g/m^2	$\Delta M/\text{Area}$ 60 Days g/m^2	$\Delta M/\text{Area}$ 120 Days g/m^2	$\Delta M/\text{Area}$ 180 Days g/m^2	$\Delta M/\text{Area}$ 365 Days g/m^2
304/01	HFC-125	0.20255	0.21660	0.32548	0.41212 0.07844	0.51398 0.09249
304/02	HFC-125	-0.01756	-0.01756	0.06088	0.13815	0.08781
304/03	HFC-125	0.00937	0.01288	0.06791		
304/04	HFC-227ea	0.03512	0.07493	0.08781	0.09015 0.08898	---
304/05	HFC-227ea	-0.00351	0.02459	0.02225	0.07259	---
304/06	HFC-227ea	-0.00820	0.04449	0.04566		---
304/07	halon 1301	0.05503	0.23182	0.13113	0.29153 0.22245	0.19669 0.15572
304/08	halon 1301	0.02107	0.03161	0.07376	0.29504	0.24587
304/09	halon 1301	-0.01873	0.03512	0.10771		
304/10	FC-218	0.01054	0.12059	0.04566	0.14635 0.09015	---
304/11	FC-218	-0.00585	0.05034	0.07142	0.09015	---
304/12	FC-218	-0.00234	0.03512	0.04566		---
304/13	CF ₃ I	-0.01171	0.31143	0.54559	---	---
304/14	CF ₃ I	-0.02576	0.27162	0.33485	---	---
304/15	CF ₃ I	-0.01054	0.18850	0.44959	---	---

Sample Number	Test Environ. 20 °C	$\Delta M/\text{Area}$ 30 Days g/m^2	$\Delta M/\text{Area}$ 60 Days g/m^2	$\Delta M/\text{Area}$ 120 Days g/m^2	$\Delta M/\text{Area}$ 180 Days g/m^2	$\Delta M/\text{Area}$ 365 Days g/m^2
Ti/01	HFC-125	0.02665	0.03128	0.07300	0.13788 0.13904	0.22594 0.14368
Ti/02	HFC-125	0.00579	0.02549	0.09733	0.16106	0.16569
Ti/03	HFC-125	-0.01275	0.03592	0.13325		
Ti/04	HFC-227ea	0.01275	0.05098	0.10892	0.12050 0.11587	---
Ti/05	HFC-227ea	-0.01506	0.08574	0.08458	0.11471	---
Ti/06	HFC-227ea	0.00463	0.04055	0.09849		---
Ti/07	halon 1301	0.00927	0.10080	0.10196	0.14020 0.12861	0.18307 0.17496
Ti/08	halon 1301	-0.00811	0.06604	0.06720	0.18539	0.20856
Ti/09	halon 1301	0.03013	0.11239	0.10660		
Ti/10	FC-218	0.01854	0.07995	0.09269	0.18886 0.13556	---
Ti/11	FC-218	0.00000	0.06604	0.09269	0.12398	---
Ti/12	FC-218	0.02665	0.07995	0.09965		---
Ti/28	CF ₃ I	0.01738	0.29083	0.35571	---	---
Ti/29	CF ₃ I	-0.03476	0.06720	0.23405	---	---
Ti/30	CF ₃ I	-0.01854	0.10080	0.24680	---	---

Sample Number	Test Environ. 20 °C	$\Delta M/\text{Area}$ 60 Days g/m^2	$\Delta M/\text{Area}$ 150 Days g/m^2
4130/01	HFC-125	0.30558	0.49553
4130/02	HFC-125	0.13686	0.96156
4130/03	HFC-125	1.44058	2.59917
4130/04	HFC-227ea	0.09675	---
4130/05	HFC-227ea	0.32209	---
4130/06	HFC-227ea	-1.05241	---
4130/07	halon 1301	2.14140	-1.28838
4130/08	halon 1301	0.28906	6.95394
4130/09	halon 1301	0.41648	6.62123
4130/10	FC-218	0.48373	---
4130/11	FC-218	0.57340	---
4130/12	FC-218	0.25838	---
4130/30	CF_3I	69.90163	87.28177
4130/31	CF_3I	44.32047	88.18198
4130/32	CF_3I	39.79817	80.18507

Sample Number	Test Environ. 150 °C	$\Delta M/\text{Area}$ 90 Days g/m^2
321/01	halon 1301	0.06701
321/02	halon 1301	0.05172
321/03	halon 1301	0.06877
321/07	HFC-125	0.04702
321/08	HFC-125	0.00000
321/09	HFC-125	0.03409

Sample Number	Test Environ. 150 °C	$\Delta M/\text{Area}$ 90 Days g/m^2
CDA110/01	halon 1301	0.20589
CDA110/02	halon 1301	0.09883
CDA110/03	halon 1301	0.07412
CDA110/07	HFC-125	0.11059
CDA110/08	HFC-125	-0.00118
CDA110/09	HFC-125	-0.00471

Sample Number	Test Environ. 150 °C	$\Delta M/\text{Area}$ 90 Days g/m^2
CDA172/01	halon 1301	-0.05058
CDA172/02	halon 1301	0.00118
CDA172/03	halon 1301	-0.00588
CDA172/07	HFC-125	0.05646
CDA172/08	HFC-125	0.00706
CDA172/09	HFC-125	-0.04705

Sample Number	Test Environ. 150 °C	$\Delta M/\text{Area}$ 90 Days g/m^2
355/01	halon 1301	-0.02295
355/02	halon 1301	0.06196
355/03	halon 1301	0.02065
355/07	HFC-125	-0.07803
355/08	HFC-125	0.02065
355/09	HFC-125	0.05508

Sample Number	Test Environ. a150 °C	$\Delta M/\text{Area}$ 90 Days g/m^2
I625/01	halon 1301	0.00708
I625/02	halon 1301	0.00708
I625/03	halon 1301	0.03009
I625/07	HFC-125	-0.00354
I625/08	HFC-125	0.01593
I625/09	HFC-125	-0.00177

6. INTERACTIONS OF AGENTS WITH ELASTOMERS AND LUBRICANTS

Gregory B. McKenna, Ferenc Horkay, Peter H. Verdier and William K. Waldron Jr.
Polymers Division, Materials Science and Engineering Laboratory

Contents

	Page
6. INTERACTIONS OF AGENTS WITH ELASTOMERS AND LUBRICANTS	201
6.1 Introduction	202
6.2 Swelling Measurements	203
6.2.1 Theoretical Background	203
6.2.2 Experimental Materials and Methods	204
6.2.3 Results and Discussion of the Swelling Measurements	205
6.3 Mechanical Property Measurements	208
6.3.1 Compression Set	208
6.3.2 Tensile Testing	217
6.3.3 Extrapolating Results to Longer Times	219
6.3.3.1 Compression Set	219
6.3.3.2 Tensile Testing	225
6.4 Testing of Elastomers and Lubricants in CF_3I	234
6.4.1 Anomalous Testing Results with CF_3I	234
6.4.2 Swelling Measurements in CF_3I	235
6.4.3 Durability Test Results in CF_3I	235
6.5 Summary	235
6.5.1 Swelling measurements	239
6.5.2 Mechanical Property Measurements	240
6.5.3 Compression Set Measurements	240
6.5.4 Tensile Testing	241
6.6 References	246

6.1 Introduction

Elastomers and greases used in fire suppression systems serve to prevent container leakage and subsequent suppression system malfunction due to insufficient fire suppressant agent or container pressure. Excessive swelling or mechanical deterioration, particularly of the elastomeric seals, can lead to such leakage. The goal of the work undertaken in this part of the project was to obtain data on the compatibility of elastomeric seals and greases with candidate fire suppression agents. In the process a methodology was developed to obtain data that characterizes the swelling of elastomers and resistance of elastomers to mechanical degradation in the presence of the candidate elastomers.

In the first phase of the project short term exposure experiments were conducted to characterize the compatibilities of 11 agents with 6 commonly used elastomers and 3 lubricants (McKenna *et al.*, 1994). Two types of measurement techniques were developed and used:

(i) swelling measurements due to sorption of the agent into the elastomers (or lubricants) at four different temperatures from 35 °C to 150 °C, and

(ii) durability measurements, which produced data on residual mechanical (rheological) properties of the elastomers (and lubricants) after exposure to the agents at 150 °C and 5.86 MPa.

Based on the results of the swelling tests a rating system was proposed to characterize the compatibility of elastomers (and lubricants) with the different agents. In swelling measurements good compatibility (i.e., an elastomer or lubricant is acceptable for use with the fire suppressant) was defined as the value of the Flory-Huggins polymer-solvent interaction parameter (χ) determined at 35 °C being larger than 1.2. Bad compatibility ($\chi < 0.9$) corresponds to excessive swelling. For values of $0.9 < \chi < 1.2$, the agent was considered to have fair compatibility with the elastomer or lubricant and represents a marginally acceptable system.

In the measurements of the residual mechanical properties, compatibility ratings were to have been based on the results of compression set and tensile test data of the elastomers. The important conclusion to be drawn from the durability testing was that the 150 °C temperature was too high for reasonable evaluation of changes in the mechanical properties of candidate elastomers and greases and that the degradation resistance after long term exposure of the elastomeric materials could not be estimated from the results. Therefore, in the cases of the four agents selected for further testing (HFC-227ea, HFC-125, FC-218, and CF₃I (not considered in the first phase of the project)) measurements were performed at 50, 75 and 100 °C. The temperature 75 °C was chosen to conduct the long-term mechanical property measurements. Information from the sponsors indicated that all-metal storage containers are used for exposures above 70 °C. Further testing of the greases was not considered necessary.

This report summarizes the work performed in FY 1994-95 and is organized as follows: Section 6.2 describes the results of the swelling measurements for seven sets of crosslinked and uncrosslinked elastomers in the 3 selected fire suppressant agents. (Note that in the first phase of the project only six elastomers were investigated. The seventh elastomer, ethylene-propylene-diene (EPDM) terpolymer was suggested by NIST for completeness of the study because it is a widely-used, environmentally-inert elastomer.) The results are compared with those obtained for halon 1301 which serves as a baseline to compare the properties of the fluorocarbon alternatives. In Section 6.3 the results of the durability measurements are shown. A Kohlrausch-Williams-Watt (KWW) type stretched exponential function (Williams and Watt, 1970) is used to describe the compression set data. This function is used to predict the changes in the mechanical properties after long exposure times. In Section 6.4 the results obtained for iodotrifluoromethane (CF₃I) are presented. This chemical was not investigated in the first phase of the project. Later it was recommended for inclusion by the sponsor of the program because it was found to be as effective as halon 1301 in suppressing non-premixed

flames. Since testing in this agent was accompanied by several specific problems, the results of these investigations are discussed separately. In Section 6.5 the results of the thermodynamic (swelling) investigations in combination with the durability measurements are summarized.

6.2 Swelling Measurements

6.2.1 Theoretical Background. A polymer exposed to a thermodynamically compatible diluent absorbs solvent molecules. The driving force of the mixing process is mainly entropic. The Flory-Huggins lattice theory of polymer solutions (Flory, 1942; Huggins, 1943, Flory 1953) describes the free energy of mixing and allows the characterization of the affinity of the polymer (elastomer or lubricant) to the solvent (fire suppressant agent) by a single polymer-solvent interaction parameter χ .

In a swelling measurement the concentration of the polymer at equilibrium is measured as a function of solvent activity a_1 (Boyer, 1945; Gee *et al.*, 1965; Brotzman and Eichinger 1982 and 1983; Horkay and Zrinyi, 1982; McKenna *et al.*, 1989; Horkay *et al.*, 1989; McKenna *et al.*, 1990; McKenna and Crissmann 1993). According to the Flory-Huggins theory:

$$\ln a_1 = \ln(p/p^0) = \ln(1 - v_2) + (1 - 1/P)v_2 + \chi v_2^2 \quad (1)$$

where p is the equilibrium vapor pressure of the diluent, p^0 is its saturation vapor pressure, v_2 is the volume fraction of the polymer, P is the degree of polymerization and χ is the Flory-Huggins polymer-solvent interaction parameter. In general χ depends on the polymer volume fraction (Flory, 1970), *i.e.*, $\chi = \chi_0 + \chi_1 v_2 + \dots$, where χ_0 and χ_1 are constants.

From Equation (1) it follows that the measurement of the equilibrium polymer volume fraction as a function of the vapor pressure of the diluent allows the determination of the χ parameter, *i.e.*, the estimation of the solubility of elastomers in the fire suppressant agents. Small χ values ($\chi < 0.5$) correspond to solubility across the whole concentration range. In this case uncrosslinked polymers are completely dissolved and crosslinked polymers exhibit large swelling which can lead to seal failure in elastomeric o-ring based joints. High χ values are characteristic of polymer/solvent systems with limited miscibility.

Although the Flory-Huggins theory is formulated in terms of volume fractions (v_1 and v_2), the theory can also be expressed in terms of weight fractions (w_1 and w_2). This substitution does not change the functional form of Equation (1), *i.e.*,

$$\ln(p/p^0) = \ln(1 - w_2) + w_2 + \chi_0 w_2^2 + \chi_1 w_2^3, \quad (2)$$

where $\chi = \chi_0 + \chi_1 w_2$ has been substituted, and the term $(1 - 1/P)$ has become unity since P is large for polymeric materials and infinite in crosslinked networks. In this case the χ values differ from those calculated from the equilibrium volume fractions (v_1 and v_2). Throughout the present report weight fractions are used instead of volume fractions because they are directly measured quantities.

Table 1. Elastomers used in swelling experiments

Elastomer	Vendor	Designation
Silicone	Colonial Rubber	Si
55% Butadiene-45% Acrylonitrile	Goodyear	N206
Fluorosilicone	Colonial Rubber	FSi
Viton E-60 Fluorocarbon	Du Pont	FKM
Neoprene	Colonial Rubber	CR
85% Butadiene-15% Acrylonitrile	Goodyear	N926
Ethylene-Propylene-Diene	Exxon	EPDM

Table 2. Lubricants used in swelling experiments

Lubricant	Vendor	Designation
Krytox 240AC Fluorinated Grease	Du Pont	240AC
Braycote 600 Perfluoropolyether Grease, Low Volatility	Castrol	600
Braycote 807 Aircraft Grease MIL-G-27617, Type IV	Castrol	807

6.2.2 Experimental Materials and Methods. The elastomers and lubricants used in this study are shown in Tables 1 and 2, respectively.¹ Both crosslinked and uncrosslinked elastomers were investigated. The 85 % butadiene-15 % acrylonitrile crosslinked copolymer was prepared according to a method described earlier (McKenna et al., 1994). The silicone, fluorosilicone, neoprene, and ethylene-propylene-diene polymers were supplied crosslinked and uncrosslinked by the vendor. The fluorocarbon polymers were cured at NIST for one hour at 150 °C and post-cured at 240 °C for 24 hours.

The swelling measurements were performed in an apparatus (Figure 1) described earlier (McKenna et al., 1994). The pressure vessels were made of type 304 stainless steel and designed for a maximum working pressure of 5.86 MPa with two view ports 180° apart for viewing and backlighting purposes.

¹Certain trade names and company products are mentioned in the text or identified in an illustration in order to specify adequately the experimental procedure and equipment used. In no case does such identification imply recommendation or endorsement by the National Institute of Standards and Technology, nor does it imply that the products are necessarily the best available for the purpose.

Table 3. Saturation data for agents

Trade name	Formula	Chemical name	p^o @ 35°C - (MPa)	p^o @ 70 °C (MPa)	p^o @ 105°C (MPa)	T_c (°C)	p_c (MPa)
HFC-227ea	C_3HF_7	heptafluoropropane	0.615	1.49	--	101.7	2.91
HFC-125	CHF_2CF_3	pentafluoroethane	1.78	--	--	66.3	3.62
FC-218	C_3F_8	octafluoropropane	1.15	2.41	--	71.9	2.68
halon 1301	CF_3Br	bromotrifluoromethane	2.04	--	--	67	3.96

T_c : critical temperature

p_c : critical pressure

p^o : saturation vapor pressure

Samples weighing 25-50 mg were placed on quartz pans suspended from quartz springs (see Figure 1). The sensitivity of the springs was either 1 mg/mm or 1.25 mg/mm. The vessels were placed in a cylindrical Pyrex jar and completely immersed in silicone bath oil. Two rectangular holes were made so that the view ports were visible. The bath was heated using an immersion heater and stirred to maintain temperature uniformity. A pressure charging and recovery system was used for admission of the agent into the vessel and for recovery of it after each measurement.

The mass uptake by elastomers and lubricants was calculated from the displacement of the quartz spring measured by a cathetometer. Measurements were taken at 35, 70, 105 and 150 °C as a function of the vapor pressure. For each test temperature the agent vapor pressure was varied between the saturation pressure at the test temperature and that at the next (lower) temperature. In this way undesired saturation during cooling, which could ruin the samples, was avoided. Above the critical temperature T_c of the agent the upper limit of the pressure range was the maximum working pressure of the apparatus (5.86 MPa). Saturation pressures for each temperature were determined for agents HFC-125, FC-218, and halon 1301 using thermodynamic properties software (Gallagher *et al.*, 1991), and for agent HFC-227ea from vendor supplied data (Robin, 1992) and are shown in Table 3.

After measurements were performed for all temperatures considered, the vessel was evacuated and the spring displacements were checked for reversibility. Where appropriate, corrections for buoyancy effects were made (McKenna *et al.*, 1994).

6.2.3 Results and Discussion of the Swelling Measurements. In Figures 2-5, typical plots of solvent weight fraction w_1 vs. vapor pressure p are shown for different elastomer/agent systems. The fluid uptake of the elastomers considerably increases with the vapor pressure and decreases with increasing temperature (Figure 5). In Figures 6-8, the experimental data obtained at 35 °C are shown according to the Flory-Huggins representation. The curves are the least squares fits of Equation (2) to the data points. In Tables 4 and 5 are listed the values of the Flory-Huggins interaction parameters ($\chi = \chi_0 + \chi_1$) determined for the elastomers in the three selected agents and in halon 1301. (Similar data for the three agents and the six elastomers were given in the 1994 report (McKenna *et al.* 1994). In order to check the reproducibility of the swelling tests we repeated these measurements. The previous values of χ are given in parentheses in Tables 4 and 5. The results indicate that the repeatability of the χ data is, generally, better than 5 %.) In Table 6 the χ values are shown for the three lubricants. χ measures the solubilities (compatibilities) of the subcritical agents in various polymers. It is apparent from the data that the values of the interaction parameters for the crosslinked

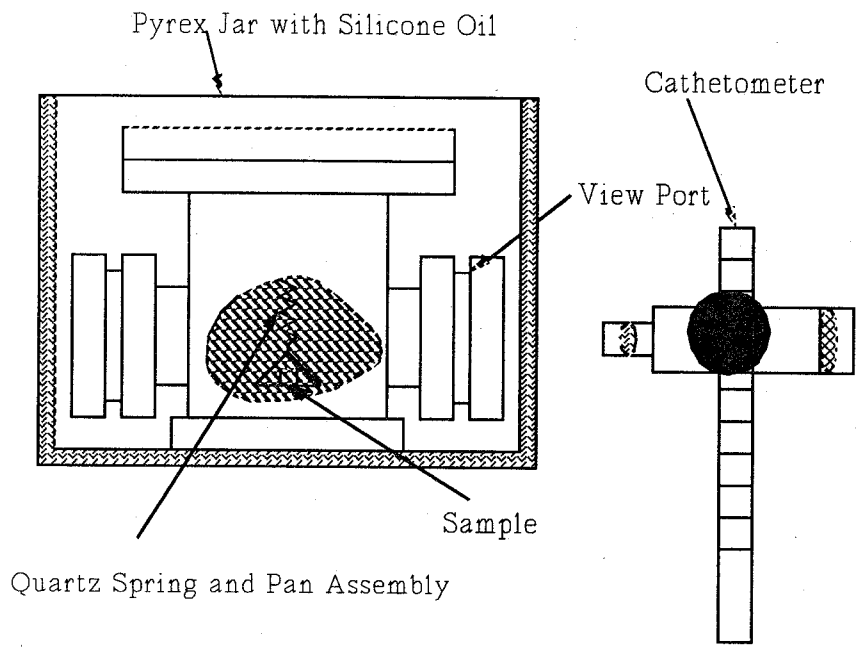


Figure 1. Schematic drawing of the experimental apparatus for isopiestic swelling measurements.

Table 4. Flory-Huggins interaction parameters χ for subcritical temperatures studied for different agent/elastomer systems

Agent (T °C)	u ^c CR	x ^d CR	u N926	x N926	u EPDM	x EPDM
227ea (35)	1.25 (1.25 ^b)	1.34 (1.33 ^a)	0.78 (0.80)	0.84 (0.84)	1.31	1.34
227ea (70)	1.29 (1.31)	1.44 (1.38)	0.85 (0.85)	0.88 (0.87)	1.35	1.37
125 (35)	1.99 (4.10 ^b)	2.03 (1.99)	1.22 (1.23)	1.26 (1.28)	1.98	2.02
218 (35)	1.64 (1.63)	1.70 (1.68)	1.62 (1.56 ^b)	1.71 (1.71)	1.53	1.58
218 (70)	1.74 (1.75)	1.77 (1.77)	1.67 (1.69)	1.74 (1.74)	1.62	1.70
halon 1301 (35)	1.98	2.08	1.25	1.12	1.06	1.12

^a12.5 < CV < 20% and 0.64 < χ < 1.5 (35 °C)^bCV > 20% (35 °C)^cuncrosslinked polymer^dcrosslinked polymer

polymers slightly exceed those of the corresponding uncrosslinked systems, i.e., the crosslinked polymer exhibits lower affinity to the solvent than its uncrosslinked counterpart. (Strictly speaking Equation (2) can only be applied for uncrosslinked polymers. The appropriate expression for a crosslinked polymer contains an additional term arising from the elasticity of the network (James and Guth, 1943; Flory and Rehner, 1943; Flory and Erman, 1982). For lightly crosslinked networks at high polymer concentration ($w_2 > 0.7$), however, this contribution is small in comparison to the mixing term.)

The rating system for characterizing the compatibility of the agents with the sealing materials was defined on the basis of the χ parameters determined at 35 °C. This temperature was chosen for several reasons. First, as shown in Figure 5, swelling is largest at 35 °C and gradually decreases with increasing temperature. Second, it is near the initial storage temperature of 25 °C. A good, bad, or fair rating is given for each agent/crosslinked elastomer system in Table 7.

The χ values shown in Tables 4-6 were calculated using a commercial software package. The curve fitter (SigmaPlot, Jandel, 1992) uses the Marquardt-Levenberg algorithm (Press *et al.*, 1986) to find the parameters which minimize the variance $s^2 (\ln p / p^0)$, i.e., the squared differences between the observed and predicted values of the dependent variable. The standard error or experimental standard deviation of the χ parameter, $s(\chi)$, and the coefficient of variation, $CV = 100s(\chi)/\chi$, were

Table 5. Flory-Huggins interaction parameters χ for subcritical temperatures studied for different agent/elastomer systems

Agent (T °C)	u ^c Si	x ^d Si	u N206	x N206	u FSi	x FSi	u FKM	x FKM
227ea (35)	0.89 (0.89)	0.91 (0.93 ^a)	1.33 (1.34 ^b)	1.43 (1.40 ^b)	0.98 (0.97)	1.04 (1.04 ^a)	1.00 (1.01)	1.07 (1.07 ^b)
227ea (70)	0.92 (0.94)	0.97 (0.96)	1.50 (1.48)	1.50 (1.50)	1.08 (1.10)	1.15 (1.13)	1.10 (1.09)	1.12 (1.13)
125 (35)	1.26 (1.29)	1.32 (1.30)	1.69 (1.69 ^b)	1.75 (1.72)	1.34 (1.33)	1.36 (1.35)	1.17 (1.18)	1.24 (1.21)
218 (35)	1.55 (1.55)	1.63 (1.62)	1.75 (1.77 ^b)	1.85 (1.84)	1.53 (1.56 ^b)	1.64 (1.64)	1.59 (1.65)	1.71 (1.65)
218 (70)	1.60 (1.64)	1.71 (1.69)	1.90 (2.04)	1.99 (1.99)	1.66 (1.67)	1.75 (1.74)	1.68 (1.66)	1.63 (1.67)
1301 (35)	0.92	0.97	2.15	2.16	1.04	1.11	1.69	1.71

^a12.5 < CV < 20% and 0.64 < χ < 1.5 (35 °C)

^bCV > 20% (35 °C)

^cuncrosslinked polymer

^dcrosslinked polymer

also calculated for each χ value. Thus, the standard uncertainty of the parameter χ is $u(\chi) = s(\chi)$ and the percentage of relative standard uncertainty is shown in Tables 4 and 5 with superscripts.

Estimated values of χ for which CV > 20 % are also shown with superscripts in Tables 4-6.

6.3 Mechanical Property Measurements

In order to characterize the long-term compatibility of the elastomers with the fire suppressant agents, mechanical property measurements (compression set and tensile testing) were performed after exposure times of 1, 2, 4, 8, 16, 32, 48 and 74 weeks. Exposure to the agents was carried out at 75 °C and 5.86 MPa, in pressure vessels similar to those used for the swelling measurements. Mechanical property measurements were also made after short term (1, 2 and 4 weeks) exposures at 50, 100, and 150 °C.

6.3.1 Compression Set. Measurements were carried out using standard test methods (ASTM, 1989 and 1990b). The o-rings used in this study were Parker No. 2-214 with a nominal cross section diameter (o-ring thickness) of 3.2 mm. The Parker compounds used are listed in Table 8. Specimens were prepared by cutting 52 mm sections from sample o-rings. The original thickness of each specimen was measured with a hand micrometer. Two specimens of each compound were placed in a

Table 6. Flory-Huggins interaction parameters χ for the subcritical temperatures studied for each agent/lubricant system considered

Agent (T °C)	Krytox 240AC	Braycote 600	Braycote 807
227ea (35)	1.14 ^a	0.93	0.93 ^b
227ea (70)	1.23	0.97	1.02
125 (35)	1.18	1.37	1.35
218 (35)	1.83 ^b	1.45	1.76
218 (70)	1.86	1.47	1.79
Halon (35)	1.36	1.50	1.57

^a12.5 < CV < 20% and 0.64 < χ < 1.5 (35 °C)

^bCV > 20% (35 °C)

compression set fixture. Each fixture consisted of two 18 cm diameter and 12.7 mm thick plates and seven spacers 2.65 ± 0.01 mm thick, 75 % of the measured mean value of the o-ring thicknesses. After removing from the fixture the specimens to be tested were kept at room temperature for a minimum of 30 minutes before measuring. Measurements were taken at four marked locations equally distributed around the circumference in the axial direction, both on the unexposed samples and after each exposure time. The average value was used for subsequent calculations.

The compression set C is defined as

$$C = \frac{w_o - w_i}{w_o - w_n} \times 100, \quad (3)$$

where w_o is the original average thickness of the o-ring, w_i is the o-ring thickness after exposure and w_n is the thickness of the fixture spacers.

In Table 9 are displayed the compression set results after each exposure time at 75 °C for all the elastomers in each fluorocarbon agent. As specified in Option 1 of the standards for compression set (ASTM, 1989 and 1990b), the value of compression set for each elastomer/agent system reported in Table 9 is the average of the compression set calculated from measurements of two samples. The sample standard deviation of the mean (sdm) of each pair of measurements was also calculated. The values of sdm obtained were 2 or less except for the fluorosilicone samples, for which the maximum value obtained was 4.4.

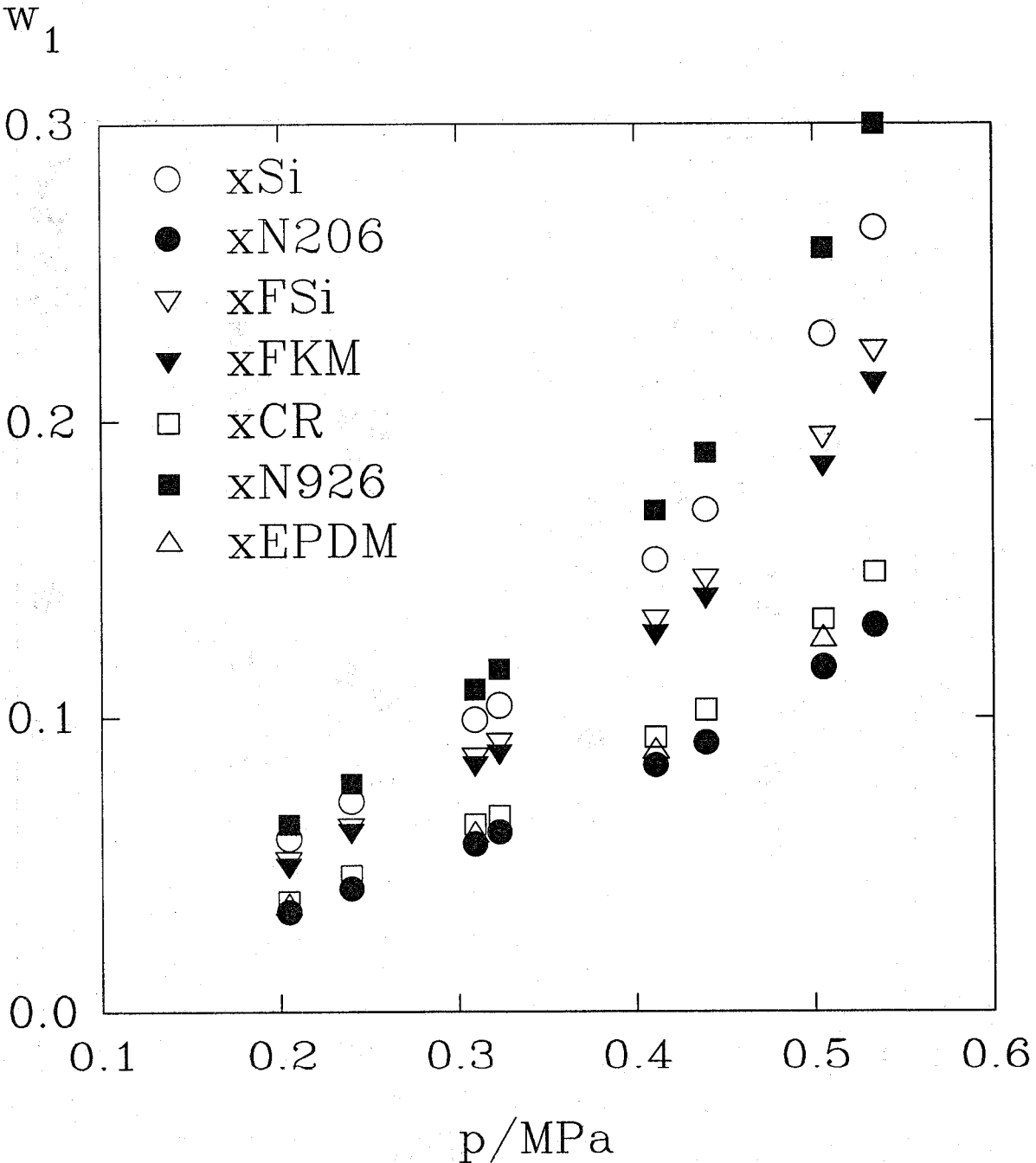


Figure 2. Weight fraction w_1 of HFC-227ea as a function of pressure for various crosslinked elastomers at 35 °C.

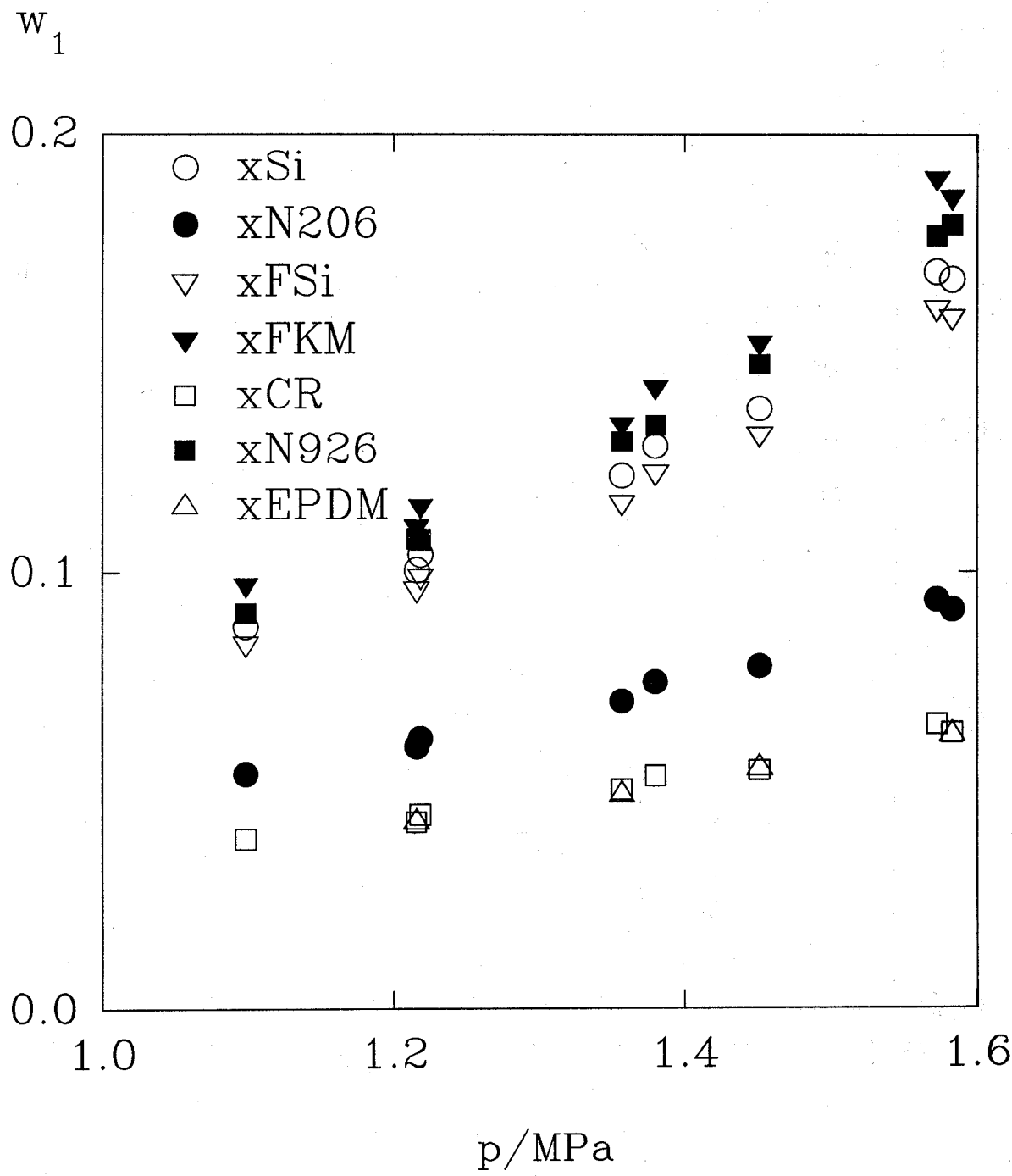


Figure 3. Weight fraction w_1 of HFC-125 as a function of pressure for various crosslinked elastomers at 35 °C.

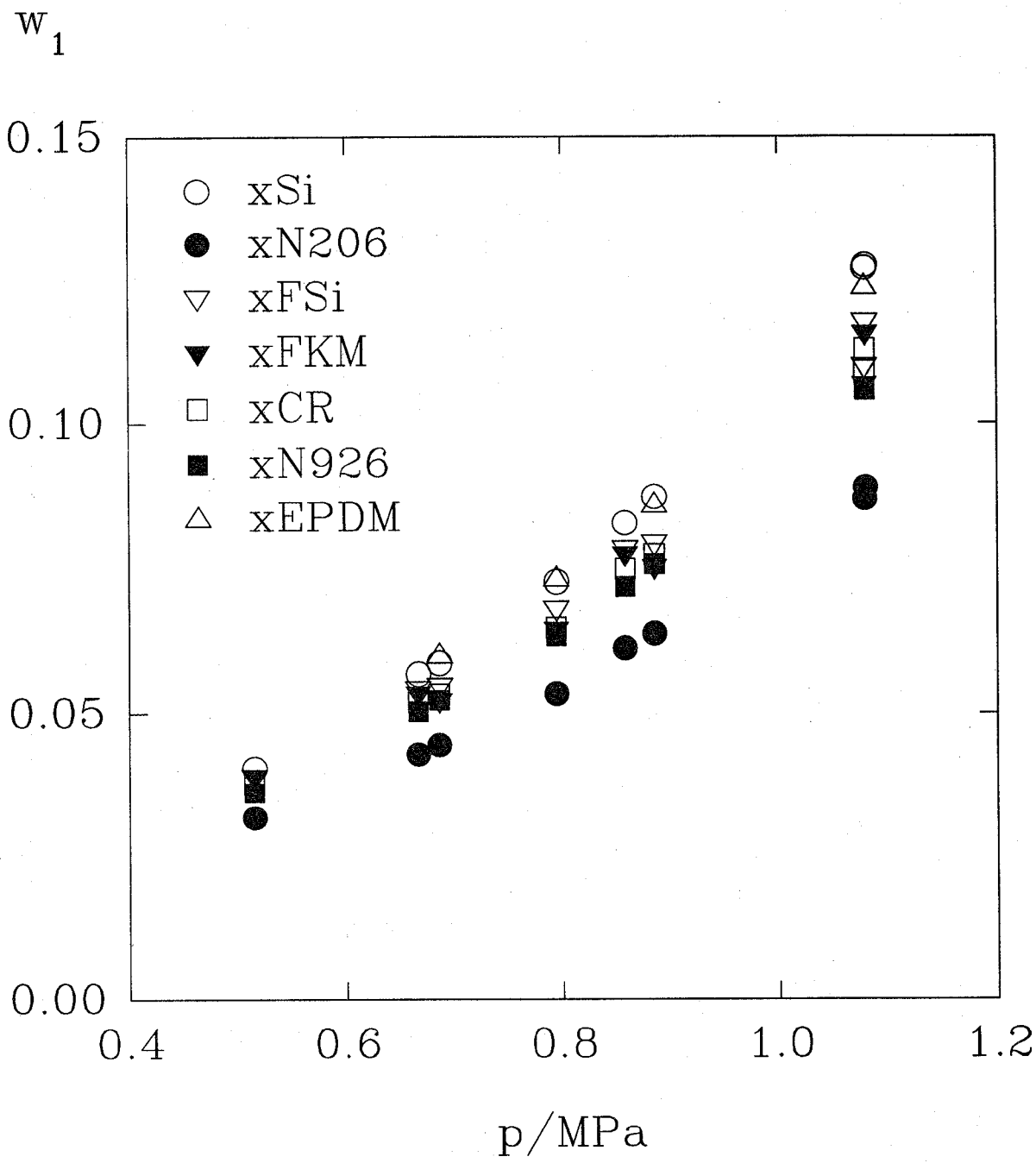


Figure 4. Weight fraction w_1 of FC-218 as a function of pressure for various crosslinked elastomers at 35 °C.

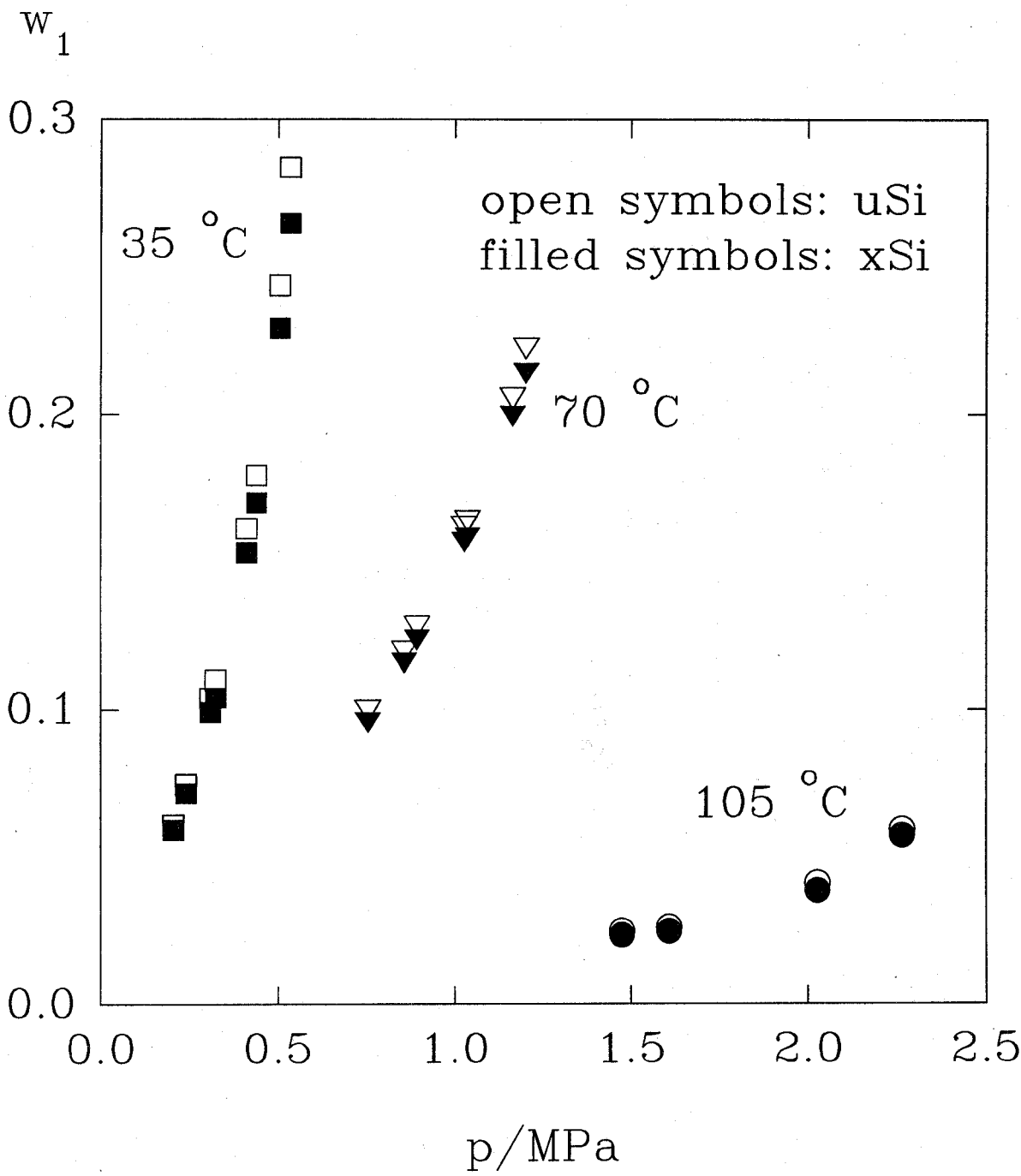


Figure 5. Weight fraction w_1 of HFC-227ea as a function of pressure in uncrosslinked and crosslinked silicone at various temperatures.

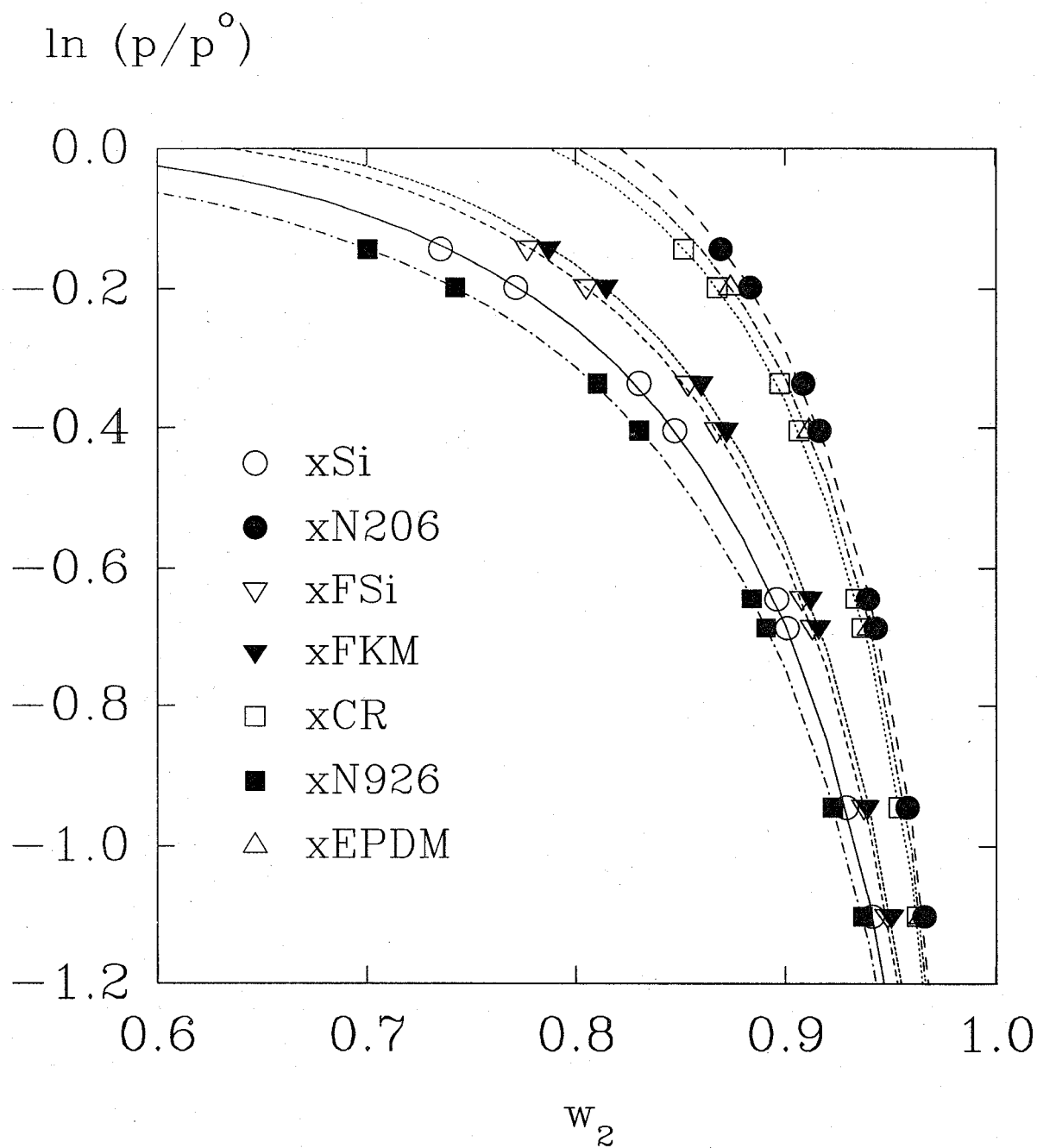


Figure 6. Solvent activity in various crosslinked elastomers in HFC-227ea as a function of polymer weight fraction w_2 at 35 °C. The curves show the least squares fits according to Equation (2).

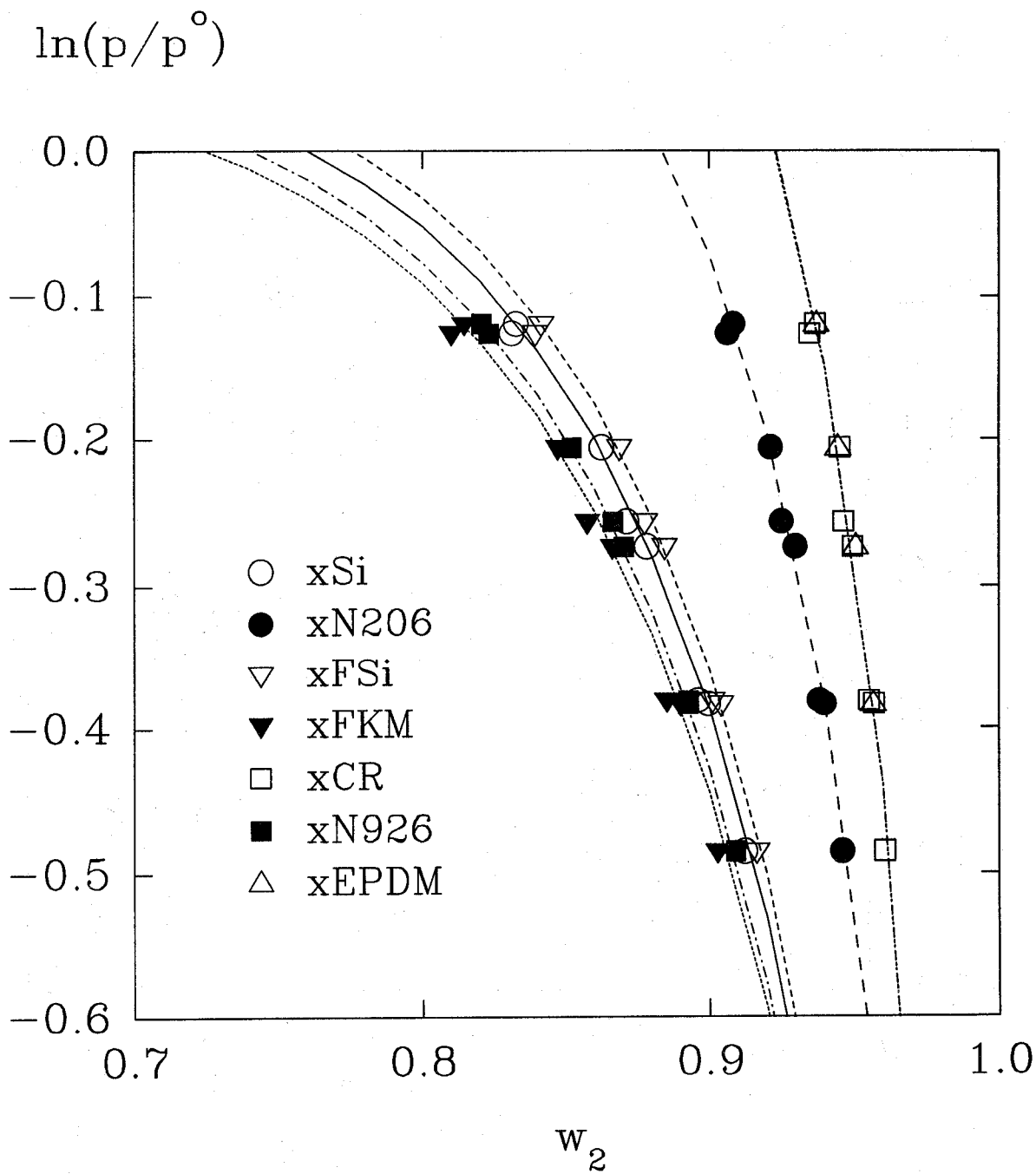


Figure 7. Solvent activity in various crosslinked elastomers in HFC-125 as a function of polymer weight fraction w_2 at 35 °C. The curves show the least squares fits according to Equation (2).

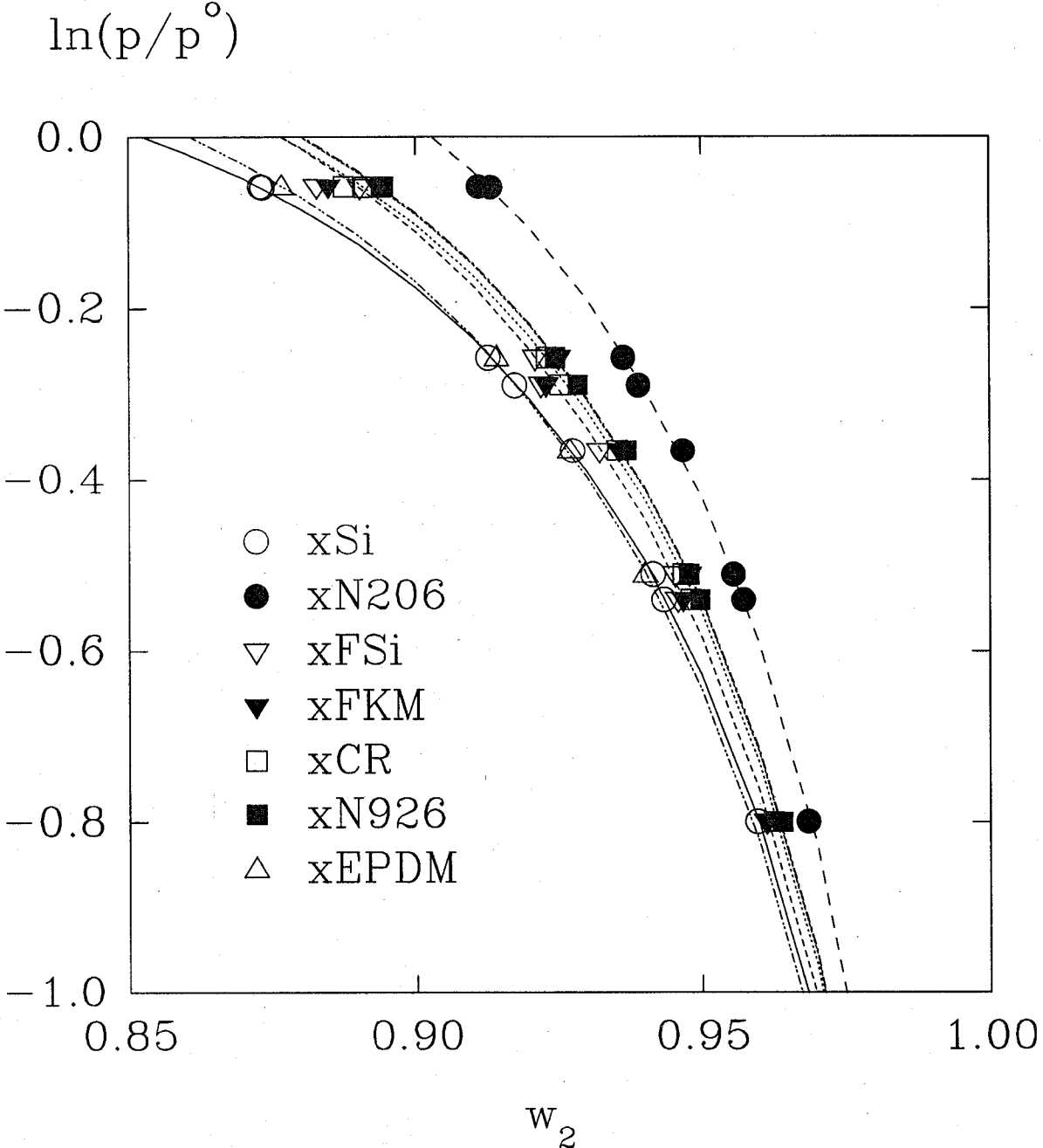


Figure 8. Solvent activity in various crosslinked elastomers in FC-218 as a function of polymer weight fraction w_2 at 35 °C. The curves show the least squares fits according to Equation (2).

Table 7. Compatibility of crosslinked elastomers based on swelling measurements in various fluorocarbon agents and halon 1301 at 35 °C.

Agent	Si	N206	FSi	FKM	CR	N926	EPDM
HFC-227ea	fair	good	fair	fair	good	bad	good
HFC-125	good	good	good	fair	good	good	good
FC-218	good	good	good	good	good	good	good
Halon 1301	fair	good	fair	good	good	good	fair

Table 8. Elastomers used in durability experiments

Elastomer	Vendor	Designation
Silicone	Parker	S604-70 ^a
Nitrile (standard industrial)	Parker	N674-70
Fluorosilicone	Parker	L1120-70
Fluorocarbon	Parker	V1164-75
Neoprene	Parker	C1185-70
Nitrile (low temperature industrial)	Parker	N103-70
Ethylene-propylene-diene	Parker	E0540-80

^aThe number following the dash in the designation (compound number) represents the Shore hardness of the elastomer.

6.3.2 Tensile Testing. Tensile tests were conducted using standard test methods (ASTM, 1990a and 1990b). The exposure was made in the same pressure vessels used for the compression set measurements. Ultimate elongation measurements were taken on sample o-rings after each exposure time. Elongation to failure and tensile strength were determined by stretching each sample at constant speed until it broke. The thickness of each specimen, *W*, was measured at four points equally distributed around the circumference in the radial and axial directions using a dial indicator with a contact force of 0.2 N. The average of all eight measurements was used for calculation. The internal diameter of the o-ring was measured using a stepped cone with diametric intervals of 0.50 mm.

An Instron type TT-B instrument was used for the testing. Grips for testing o-rings were designed and built from low carbon steel. The grips consisted of ball-bearing spools 8.9 mm in diameter. Stresses were minimized by lubricating the contact surfaces of the spools with Super-Lube

Table 9. Compression set after 1, 2, 4, 8, 15, 32, 48 and 74 week exposures at 5.86 MPa and 75 °C in the three fluorocarbon agents

Elastomer (agent)	weeks							
	1	2	4	8	15	32	48	74
S604-70 (227)	6	9	14	17	19	25	28	30
S604-70 (125)	7	8	14	31	33	35	36	39
S604-70 (218)	8	16	18	37	38	39	40	41
N674-70 (227)	12	19	28	26	31	35	38	50
N674-70 (125)	12	15	29	40	48	59	65	80
N674-70 (218)	15	18	30	35	49	59	68	79
L1120-70(227)	4	12	19	40	45	56	61	64
L1120-70(125)	15	25	41	62	68	71	74	73
L1120-70(218)	24	37	47	72	74	77	77	79
V1164-75(227)	-11	-11	-11	-4	-4	1	3	6
V1164-75(125)	-8	-6	0	6	13	14	18	20
V1164-75(218)	2	4	5	10	14	14	17	22
C1185-70(227)	12	15	22	35	52	60	66	74
C1185-70(125)	9	16	34	46	57	70	77	88
C1185-70(218)	11	20	30	35	50	65	76	85
N103-70 (227)	20	24	30	37	40	47	53	65
N103-70 (125)	21	26	41	49	60	73	80	89
N103-70 (218)	28	37	49	50	63	75	84	92
E0540-80(227)	12	14	17	15	21	24	26	43
E0540-80(125)	10	11	15	16	21	27	30	49
E0540-80(218)	9	11	17	15	24	25	30	46

o-ring lubricant. The crosshead speed was set to 50 cm/min, and a load cell with full scale load ranges of 2, 5, 10, 20, and 50 kg was used.

The ultimate elongation (U.E.) is expressed as a percentage of the original inside circumference as follows:

$$U.E. = \left[\frac{2D + G - C}{C} \right] \times 100, \quad (4)$$

where D is the distance between centers of the spool grips at the time of rupture, G is the circumference of a spool, and C is the inside circumference of the specimen.

The tensile strength T.S. is the tensile stress at rupture and is calculated as F/A , where F is the breaking force and A is twice the cross-sectional area, calculated from the thickness W as $\pi W^2/2$.

The median of three measurements was used. Tables 10 and 11 show the percent change in ultimate elongation and tensile strength for all the elastomers in each agent after different exposure times at 5.86 MPa and 75 °C.

6.3.3 Extrapolating Results to Longer Times. As discussed in Section 6.1, a major goal of this work is prediction of elastomer-agent compatibility at long times based on shorter-time measurements. We have employed two approaches here. In the first, we measure changes in mechanical properties as a function of time at fixed temperature, and fit the compression set C to a stretched exponential function $C_{\infty}\{1 - \exp[-(t/\tau)^{\beta}]\}$, where C_{∞} , τ , and β are adjustable parameters. If the fit is sufficiently good, the fitted functions may be used to predict results at longer times. In the second (activated process model), we seek to predict long-time behavior at lower temperatures from short-time behavior at higher temperatures by fitting the time required to achieve a given change in mechanical properties to the form $t' \exp(-\Delta H/RT)$, where t' and $\Delta H/R$ are adjustable parameters and T is absolute temperature.

6.3.3.1 Compression Set. Figures 9-11 show log-log plots of the compression set vs. exposure time data in Table 9 for elastomers in HFC-227ea, HFC-125, and FC-218 at 75 °C. (The data for elastomer V1164-75 are not shown for agents HFC-227ea and HFC-125 because the compression set values were small or negative due to swelling.) The lines show the result of fitting the measured values of compression set for exposure times from 1 to 48 weeks to a KWW type stretched exponential function

$$C = C_{\infty}\{1 - \exp[-(t/\tau)^{\beta}]\} \quad (5)$$

where C is the compression set, t is the exposure time, and C_{∞} , τ and β are the fitted parameters. The values of C_{∞} , τ and β so obtained are given in Table 12. The data obtained at exposure times of 74 weeks have not been used in the fitting. These 74-week values may be compared with the results predicted from measurements at shorter times to assess the reliability of the fit. It can be seen from Table 9 and Fig. 9-11 that the compression set for N674-70 in agents HFC-227ea and HFC-125, and for E0540-80 in all three agents, is markedly higher after 74 weeks exposure than would be predicted from extrapolations based on the behavior at shorter times.

Table 13 shows the values of compression set obtained for elastomers in HFC-227ea, HFC-125, and FC-218 after short-term exposures at 50, 100 and 150 °C. For the activated process model, times t_{10} and t_{20} required to obtain compression sets of 10 % and 20 %, respectively, were estimated for

Table 10. Percent change in tensile strength after 1, 2, 4, 8, 15, 32, 48 and 74 week exposures at 5.86 MPa and 75 °C in the three fluorocarbon agents

Elastomer (agent)	weeks							
	1	2	4	8	15	32	48	74
S604-70 (227)	14.4	10.9	21.5	0.3	-15.9	-6.7	-11.5	-4.6
S604-70 (125)	11.8	26.4	17.8	-8.9	-5.0	1.8	-10.3	-1.7
S604-70 (218)	12.7	14.4	12.7	-2.6	-5.8	-16.8	-0.9	-13.3
N674-70 (227)	4.6	10.7	-0.1	-65.5	-10.6	-33.4	-21.2	-42.4
N674-70 (125)	16.4	28.8	23.0	-68.6	-0.1	-25.8	-17.9	-41.8
N674-70 (218)	33.8	30.3	35.3	-66.5	-1.6	1.5	-1.6	-13.7
L1120-70(227)	17.7	-51.7	13.7	11.0	16.9	13.0	-0.1	-4.9
L1120-70(125)	28.5	7.4	40.9	-9.7	-0.1	-3.5	-0.7	-12.3
L1120-70(218)	14.1	30.2	20.8	-11.0	-4.9	1.2	-19.4	-7.8
V1164-75(227)	-6.0	-7.3	1.2	-7.7	-20.4	-44.4	-25.0	-42.6
V1164-75(125)	-38.7	-50.8	-71.9	-52.5	-75.6	-86.4	-72.5	-85.0
V1164-75(218)	12.3	28.6	10.0	-14.7	-28.6	-23.8	-15.6	-29.8
C1185-70(227)	13.8	18.9	24.2	-20.1	-23.0	-20.7	-13.4	-25.3
C1185-70(125)	18.9	20.6	15.5	-4.8	-20.7	-34.0	-20.7	-39.7
C1185-70(218)	-7.3	39.0	7.0	-12.5	-13.7	-17.0	-39.1	-44.7
N103-70 (227)	40.7	29.3	38.8	34.8	16.1	-1.2	-6.4	3.0
N103-70 (125)	33.0	51.3	46.4	27.3	15.8	-7.7	-0.3	-28.0
N103-70 (218)	55.0	59.2	40.2	16.2	10.3	3.0	1.1	-8.2
E0540-80(227)	13.0	13.0	19.9	-3.2	-4.5	-5.9	-47.7	-17.1
E0540-80(125)	13.7	19.9	9.1	-9.1	-6.8	-11.6	0.0	-7.7
E0540-80(218)	31.0	31.4	31.4	-3.2	-3.6	-14.7	-6.8	-17.1

Table 11. Percent change in ultimate elongation after 1, 2, 4, 8, 15, 32, 48 and 74 week exposures at 5.86 MPa and 75 °C in the three fluorocarbon agents

Elastomer (agent)	weeks							
	1	2	4	8	15	32	48	74
S604-70 (227)	3.2	-7.5	4.8	3.2	-3.8	-3.8	-10.8	3.2
S604-70 (125)	3.2	3.2	-5.9	-7.5	-0.5	6.5	-7.0	-3.8
S604-70 (218)	-2.2	-17.7	-11.3	-7.0	-3.8	-18.3	-1.6	-10.8
N674-70 (227)	-8.4	-3.0	-14.8	-12.3	-16.3	-28.3	-29.2	-44.0
N674-70 (125)	6.6	2.7	-6.3	-8.1	-18.4	-32.2	-38.3	-57.8
N674-70 (218)	1.8	-8.7	-8.7	-12.3	-20.2	-24.4	-36.1	-50.3
L1120-70(227)	8.1	-61.3	-4.4	7.5	11.9	20.0	6.3	3.8
L1120-70(125)	16.3	-20.6	15.6	-8.1	3.8	8.1	10.0	3.1
L1120-70(218)	-10.0	1.9	-24.4	-24.4	-16.3	-1.9	-38.8	-13.1
V1164-75(227)	6.1	7.8	15.1	21.8	11.2	-9.5	1.1	-8.9
V1164-75(125)	-29.6	-43.6	-59.8	-29.1	-56.4	-67.0	-50.8	-67.0
V1164-75(218)	16.8	24.6	15.1	18.4	7.8	18.4	18.4	7.8
C1185-70(227)	1.6	8.1	12.1	-17.0	-19.4	-11.7	-19.8	-24.7
C1185-70(125)	10.9	10.9	1.6	-3.6	-17.0	-22.3	-31.5	-45.7
C1185-70(218)	-8.9	10.1	-4.9	-6.5	-6.5	-8.9	-42.7	-44.9
N103-70 (227)	18.0	2.9	5.7	13.9	3.3	-13.9	-46.9	-27.3
N103-70 (125)	5.7	16.7	3.3	0.0	-13.9	-27.8	-20.4	-60.8
N103-70 (218)	13.9	2.9	-12.2	-5.7	-16.3	-30.6	-46.9	-58.0
E0540-80(227)	5.0	-1.5	6.4	-1.5	-5.0	1.5	-12.9	-14.4
E0540-80(125)	1.5	-3.0	-7.9	-7.9	-5.0	-2.0	-7.9	-11.4
E0540-80(218)	5.0	9.9	0.0	-5.0	-1.5	-5.0	-7.9	-11.4

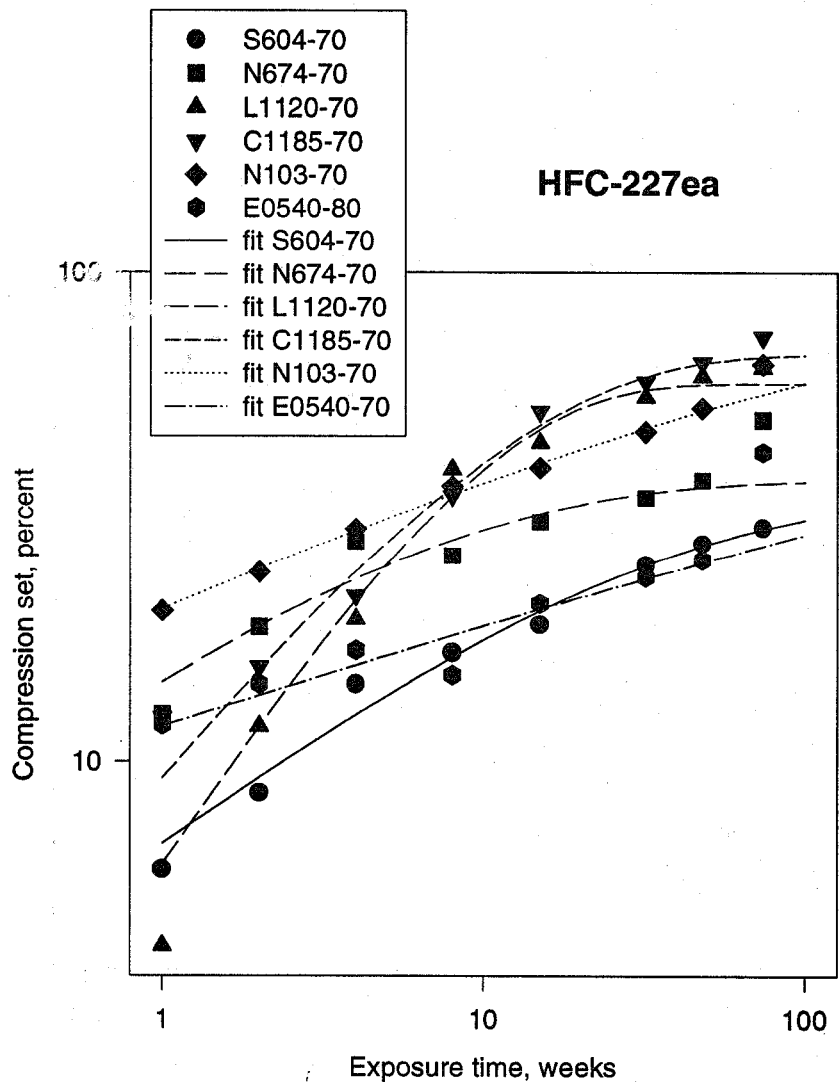


Figure 9. Compression set for various elastomers vs. exposure time to agent HFC-227ea at 5.86 MPa and 75 °C.

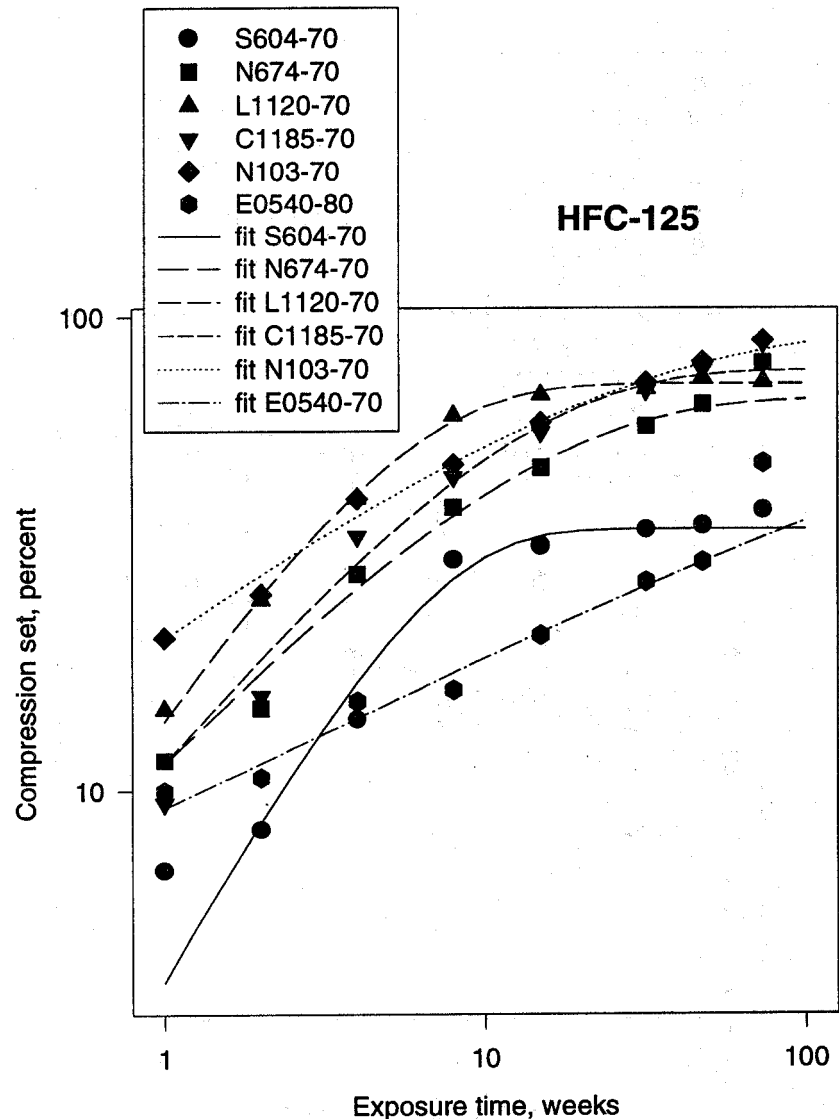


Figure 10. Compression set for various elastomers vs. exposure time to agent HFC-125 at 5.86 MPa and 75 °C.

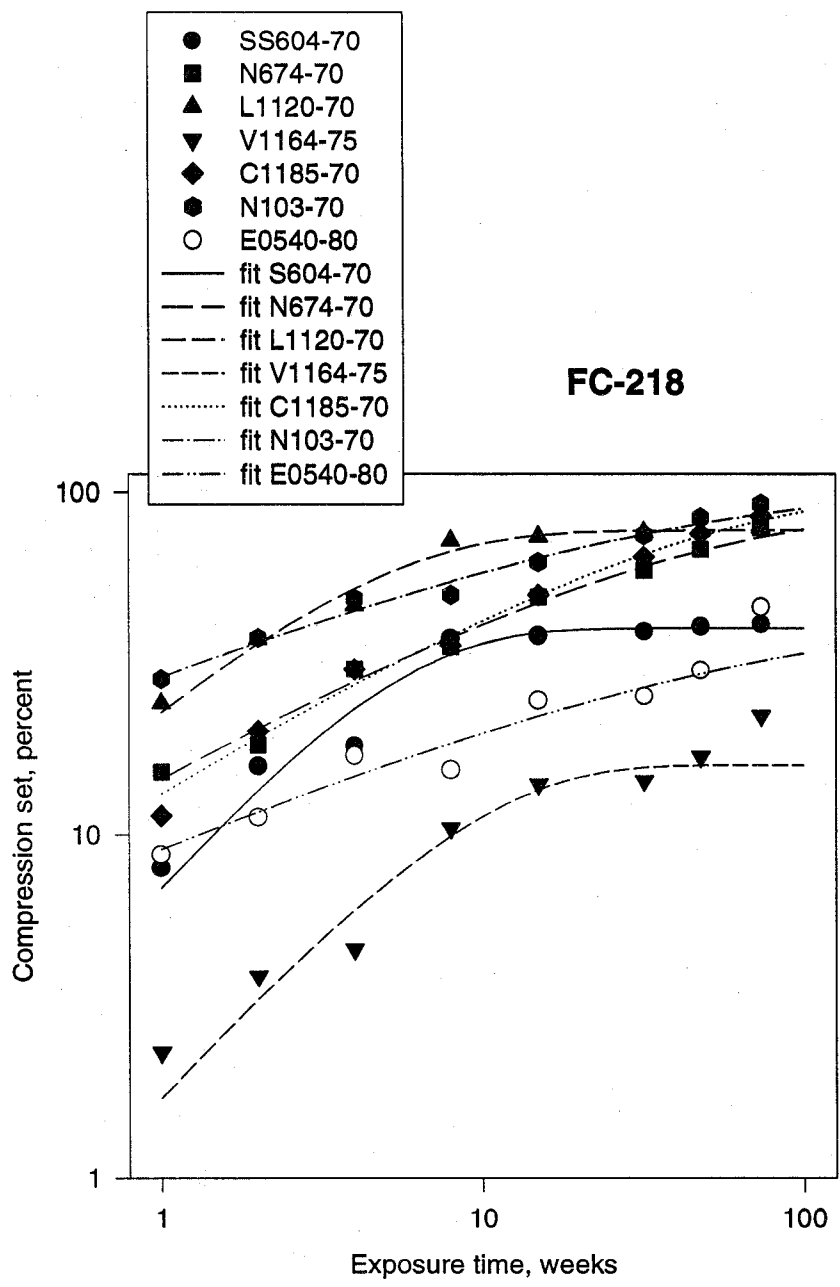


Figure 11. Compression set for various elastomers vs. exposure time to agent FC-218 at 5.86 MPa and 75 °C.

Table 12. Parameters C_∞ , τ (weeks), and β obtained by fitting compression set C vs exposure time t (weeks) to the KWW stretched exponential form of Equation (5).

agent	parameter	elastomer						
		S604-70	N674-70	L1120-70	V1164-75	C1185-70	N103-70	E540-80
227ea	C_∞	34.824	37.683	59.348	--	68.107	84.104	90.513
	τ	20.109	4.216	9.088	--	11.206	52.968	7245.738
	β	0.507	0.505	0.999	--	0.796	0.324	0.222
125	C_∞	35.548	67.433	72.261	15.828	77.22	94.216	100
	τ	5.67	10.394	4.51	12.011	9.581	14.397	953.701
	β	1.243	0.719	1.016	2.643	0.81	0.519	0.342
218	C_∞	39.854	88.16	77.387	15.803	100	100	42.19
	τ	4.6	24.164	3.483	8.102	28.241	13.98	32.139
	β	1.077	0.542	0.859	1.036	0.589	0.413	0.409
CF3I	C_∞	25.866	80.446	58.51	--	79.036	89.573	40.121
	τ	11.106	9.654	5.712	--	6.04	5.85	8.594
	β	0.867	1.359	0.715	--	1.056	1.061	0.927

each elastomer-agent pair from the compression sets measured at exposure times of 1, 2, and 4 weeks, and also at 6 weeks for 150 °C exposures. The compression set vs exposure time data for each agent, elastomer, and temperature were fitted to Equation (5) by unweighted least squares. Values of t_{10} and t_{20} were calculated from the parameters so determined; they are given in Table 14. For a few of the systems, the data did not allow meaningful estimates of t_{10} and/or t_{20} to be obtained; these are shown as dashes in Table 14. In other cases, especially at 150 °C, the estimates of t_{10} and/or t_{20} are too short to be used with the activated process model. Where the data permitted, values of t_{10} and t_{20} were fitted separately by least squares to the form $\ln(t_n) = \ln(t'_n) + (\Delta H/R)_n/T$, where n is 10 or 20, T is absolute temperature in Kelvins, and $\ln(t'_n)$ and $(\Delta H/R)_n$ are the fitted parameters, shown in Table 15. From the values of $\ln(t'_n)$ and $(\Delta H/R)_n$, estimates of t_n at other temperatures may be calculated. Table 15 shows estimated values of t_n in weeks at 70 °C obtained in this way.

6.3.3.2 Tensile Testing. The percent change in ultimate elongation vs. exposure time data in Table 10 are shown in Figures 12-14 for elastomers in HFC-227ea, HFC-125, and FC-218 at 75 °C. Since many of the values obtained were negative, a linear scale has been used for the change in ultimate elongation. The scatter in the data is much too large to allow meaningful fitting to stretched exponential or other relaxation functions.

Tables 16 and 17 show the percent change in ultimate elongation and tensile strength vs. exposure time data for all the elastomer-agent pairs for short-term exposures at 50, 100 and 150 °C. As with the longer-term data at 75 °C, there is too much scatter in the data to allow meaningful fits to activation process models.

Table 13. Compression set after short-term exposures at 5.86 MPa and 50, 100 and 150 °C.

Exposure temperature		50 °C			100 °C			150 °C			
Exposure time, weeks		1	2	4	1	2	4	1	2	4	6
Agent	Elastomer										
HFC-227ea	S604-70	4	7	9	17	23	30	25	34	48	57
	N674-70	7	10	17	34	38	47	77	84	93	97
	L1120-70	-2	1	9	39	46	52	51	56	72	83
	V1164-75	--	-13	-12	-4	-2	0	21	33	60	--
	C1185-70	9	12	15	37	42	50	66	75	81	84
	N103-70	16	19	26	47	52	57	79	87	91	94
	E0540-80	8	10	13	19	25	27	--	--	--	--
HFC-125	S604-70	3	5	9	16	21	24	33	36	50	58
	N674-70	3	6	12	29	36	56	70	84	91	96
	L1120-70	9	14	22	53	57	66	65	65	80	90
	V1164-75	--	-12	-12	4	6	15	35	46	72	90
	C1185-70	5	7	12	34	40	55	68	70	80	98
	N103-70	17	20	26	37	42	66	73	83	92	83
	E0540-80	8	11	13	18	22	26	--	--	--	--
FC-218	S604-70	3	6	10	22	24	27	41	48	50	52
	N674-70	11	14	18	39	49	60	77	88	92	95
	L1120-70	3	7	18	57	60	61	68	74	76	79
	V1164-75	--	6	8	4	7	7	25	39	56	58
	C1185-70	9	13	15	44	52	67	67	79	83	82
	N103-70	10	15	18	58	64	77	78	87	90	95
	E0540-80	7	13	15	22	24	28	--	--	--	--

Table 14. Times t_{10} and t_{20} , in weeks, to obtain compression sets of 10 % and 20 % at the exposure temperatures shown

Exposure temperature		50 °C		75 °C		100 °C		150 °C	
Agent	Elastomer	t_{10}	t_{20}	t_{10}	t_{20}	t_{10}	t_{20}	t_{10}	t_{20}
HFC-227ea	S604-70	6.9	--	2.3	6.9	0.3	1.4	0.2	0.7
	N674-70	1.9	5	0.7	2.2	0	0.1	0	0
	L1120-70	6.2	13.1	1.9	4.1	0	0.1	0	0.1
	V1164-75	0	--	--	--	--	--	0.5	1
	C1185-70	1.2	10.3	0.7	3.4	0	0.1	0	0
	N103-70	0.4	2.1	0.1	1	0	0	0	0
	E0540-80	2	13.2	0.6	11.8	0.4	1.1	--	--
HFC-125	S604-70	4.5	12.1	2.3	7.5	0.3	1.8	0.1	0.4
	N674-70	3.3	7	1	2.5	0.2	0.6	0	0
	L1120-70	1.2	3.4	0.6	1.5	0	0	0	0
	V1164-75	0	--	--	--	2.7	5.7	0.3	0.6
	C1185-70	3.1	8.6	1.1	2.2	0.1	0.3	0	0
	N103-70	0.2	1.8	0.3	1.1	0.1	0.4	0	0.1
	E0540-80	1.8	--	1.2	9.4	0.2	1.4	--	--
FC-218	S604-70	3.8	8.6	1.1	8.9	0	0.6	0.1	0.2
	N674-70	0.8	5.6	0.6	2	0	0.2	0	0
	L1120-70	2.3	4.9	0.3	0.8	0	0	0	0
	V1164-75	6.4	31.1	--	--	--	--	0.3	0.8
	C1185-70	1.3	--	0.9	2	0	0.1	0	0
	N103-70	1	--	0.1	0.5	0	0	0	0
	E0540-80	0	--	1.4	5.9	0	0.6	--	--

Table 15. Activated process parameters and predicted values at 70 °C for compression sets C of 10 % and 20 %. Values of $(\Delta H/R)_{10}$ and $(\Delta H/R)_{20}$ are in Kelvins; times are in weeks

Agent	Elastomer	C = 10			C = 20		
		$\ln(t'_{10})$	$(\Delta H/R)_{10}$	$t_{10}(70^\circ\text{C})$	$\ln(t'_{20})$	$(\Delta H/R)_{20}$	$t_{20}(70^\circ\text{C})$
HFC-227ea	S604-70	-14.28	5171	2.2	-10.73	4310	6.2
	N674-70	-13.26	4498	0.9	-24.11	8421	1.5
	L1120-70	-14.84	5386	2.3	-19.07	6926	3
	V1164-75	--	--	--	--	--	--
	C1185-70	-8.35	2770	0.8	-32.36	11359	2.1
	N103-70	-18.05	5496	0.1	-9.34	3256	1.2
	E0540-80	-12.06	4083	0.9	-15.26	5890	6.7
HFC-125	S604-70	-16.82	5979	1.8	-12.82	5028	6.3
	N674-70	-19.81	6820	1.1	-16.28	5921	2.6
	L1120-70	-8.72	2867	0.7	-10.45	3773	1.7
	V1164-75	-18.72	7357	15.1	-17.54	7196	30.9
	C1185-70	-26.32	8963	0.8	-22.11	7883	2.4
	N103-70	-5.34	1297	0.2	-11.63	3997	1
	E0540-80	-13.88	4740	0.9	-26.13	9878	14.2
FC-218	S604-70	-15.81	5542	1.4	-15.6	5865	4.5
	N674-70	-3.64	1088	0.6	-23.98	8388	1.6
	L1120-70	-25.86	8627	0.5	-24.05	8285	1.1
	V1164-75	-10.55	4010	3.1	-12.28	5080	12.5
	C1185-70	-5.16	1743	0.9	-39.25	13915	3.7
	N103-70	-30.96	10002	0.2	--	--	--
	E0540-80	--	--	--	-32.78	12031	9.8

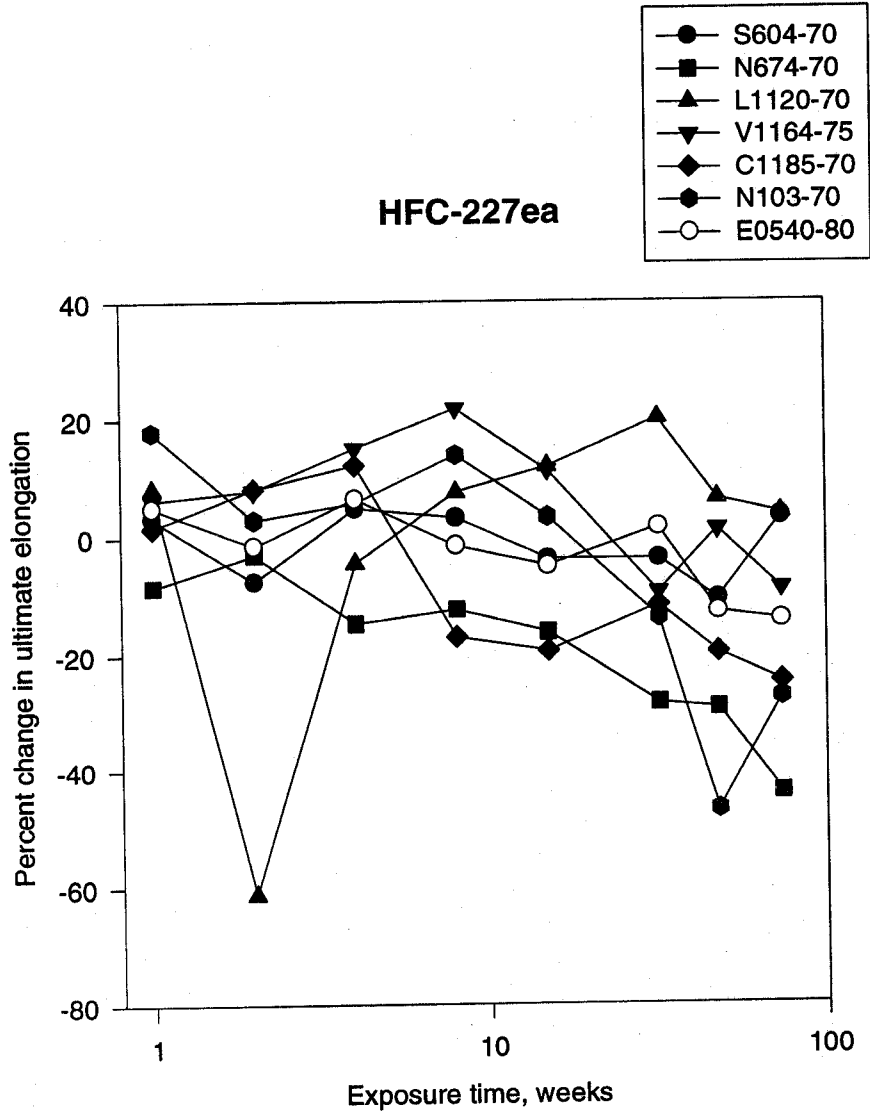


Figure 12. Percent change in ultimate elongation for various elastomers vs. exposure time to agent HFC-227ea at 5.86 MPa and 75 °C.

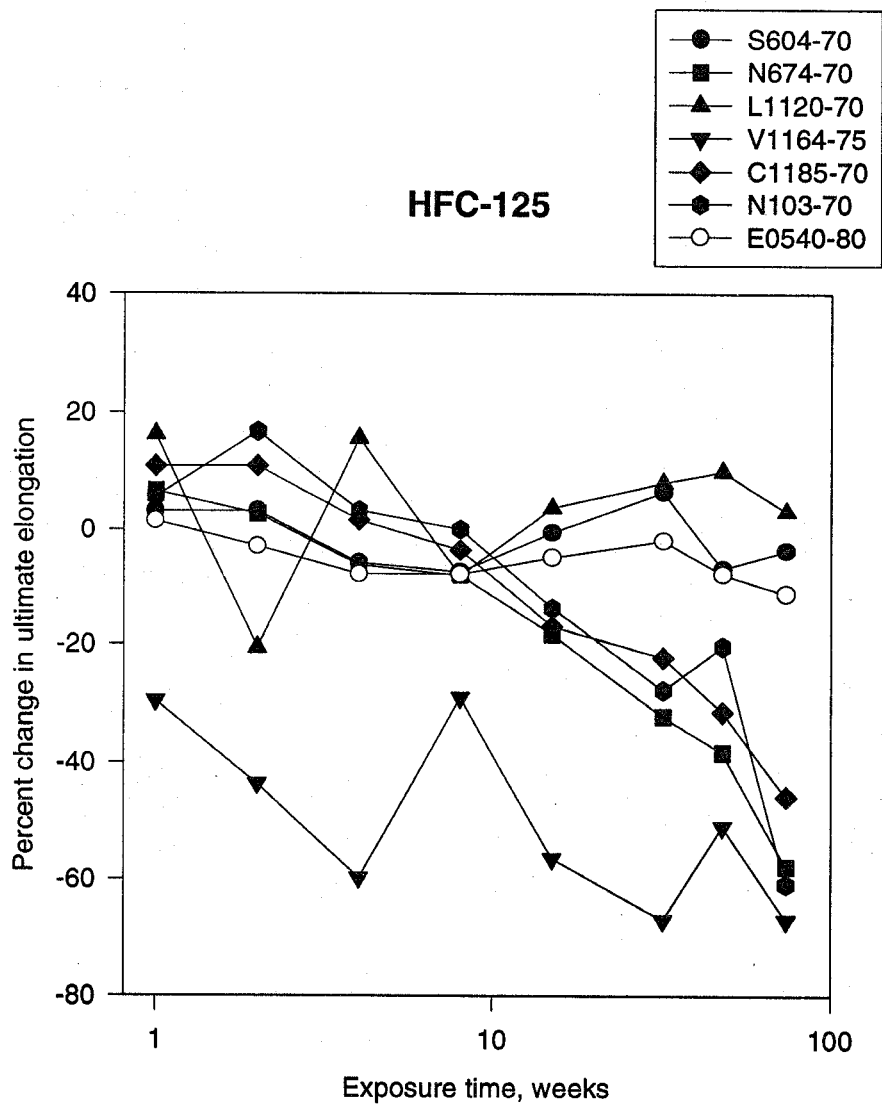


Figure 13. Percent change in ultimate elongation for various elastomers vs. exposure time to agent HFC-125 at 5.86 MPa and 75 °C.

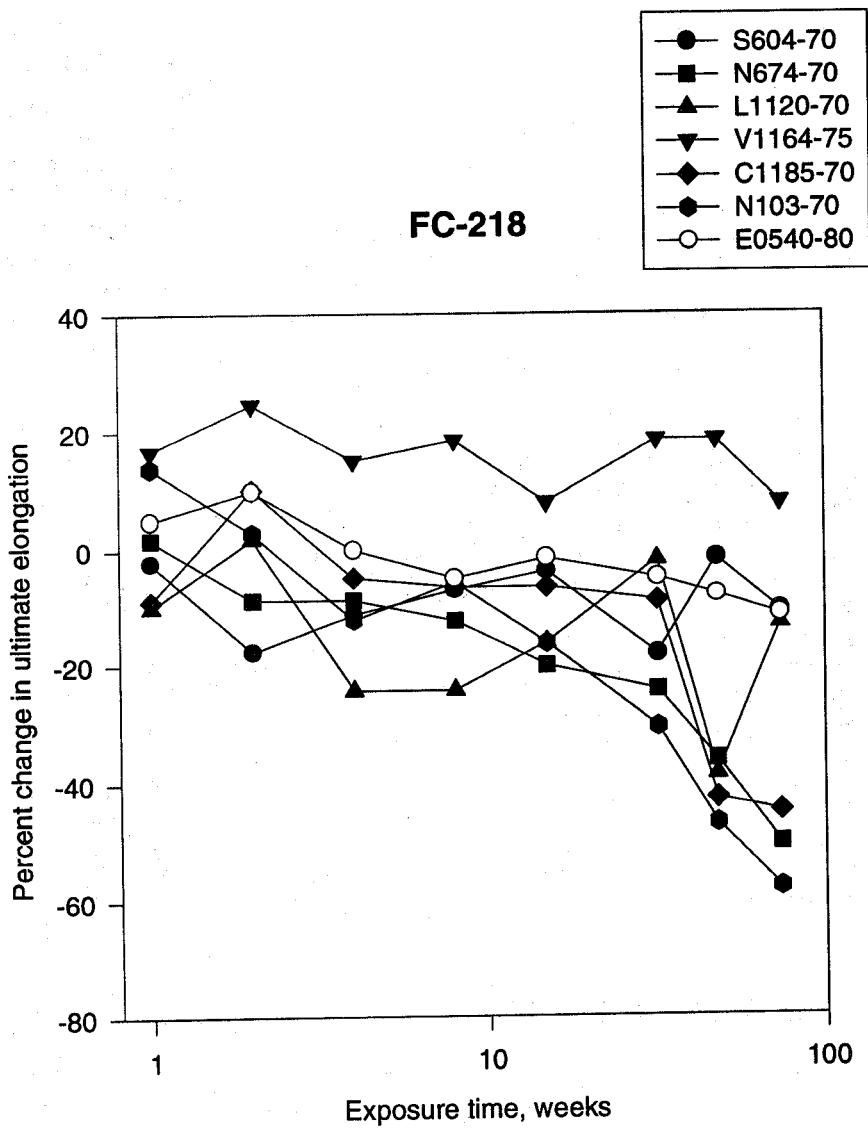


Figure 14. Percent change in ultimate elongation for various elastomers vs. exposure time to agent FC-218 at 5.86 MPa and 75 °C.

Table 16. Percent change in ultimate elongation after short-term exposures at 5.86 MPa and 50, 100 and 150 °C

Exposure temperature		50 °C			100 °C			150 °C			
Exposure time, weeks		1	2	4	1	2	4	1	2	4	6
Agent	Elastomer										
HFC-227ea	S604-70	-3.8	1.6	3.2	8.6	-11.3	6.5	-7.5	-10.6	1.8	6.2
	N674-70	-2.1	-7.2	-8.7	-23.2	-26.2	-40.4	-32.9	-80.7	-100	-99.8
	L1120-70	9.4	11.0	1.9	-13.1	-40.6	14.0	-17.8	-6.9	-41.4	-41.4
	V1164-75	--	6.1	7.8	0.6	13.0	-1.1	-53.9	-41.2	-62.5	-68.3
	C1185-70	4.0	-1.2	4.0	-7.7	-2.4	-27.5	-36.7	-63.9	-85.2	-95.9
	N103-70	-6.5	6.1	14.0	-6.5	-9.4	-27.8	-29.4	-79.9	-99.6	-100
	E0540-80	3.5	1.5	1.5	0.0	-5.0	1.5	--	--	--	--
HFC-125	S604-70	7.0	-3.8	-1.6	-10.8	-10.8	-8.6	-8.4	-7.1	-5.3	-10.6
	N674-70	4.8	2.7	-8.7	-20.5	-12.3	-45.2	-48.9	-74.6	-95.1	-98.7
	L1120-70	-0.6	-15.6	-0.6	41.0	33.0	14.0	-8.6	-22.4	-56.3	-75.1
	V1164-75	--	22.0	9.5	-58.1	-63.1	-58.1	-59.8	-69.6	-70.3	-87.7
	C1185-70	11.0	6.9	4.0	2.8	-8.9	-19.4	-23.8	-41.0	-63.9	-88.0
	N103-70	20.0	26.0	13.0	2.9	-18.0	-33.1	-60.8	-79.0	-94.4	-100
	E0540-80	5.0	1.5	3.5	5.0	-1.5	-3.0	--	--	--	--
FC-218	S604-70	3.2	3.2	3.2	-15.6	-3.8	8.6	1.3	-6.2	-9.3	-4.4
	N674-70	6.9	1.8	8.7	-6.3	-14.2	-32.2	-37.7	-59.1	-73.7	-81.6
	L1120-70	-8.1	-9.4	-12.5	-11.3	-19.4	-11.3	-47.9	-31.0	-43.2	-43.2
	V1164-75	--	6.1	7.8	2.2	13.0	-19.0	-50.9	-52.8	-72.2	-76.2
	C1185-70	11.0	6.9	-3.6	5.3	0.0	-11.7	-25.0	-41.4	-48.8	-58.6
	N103-70	22.0	-9.4	3.7	-4.1	-22.0	-33.5	-50.8	-72.9	-83.5	-89.0
	E0540-80	48.0	1.5	0.0	6.4	-6.4	0.0	--	--	--	--

Table 17. Percent change in tensile strength after short-term exposures at 5.86 MPa and 50, 100 and 150 °C

Exposure temperature		50 °C			100 °C			150 °C			
Exposure time, weeks		1	2	4	1	2	4	1	2	4	6
Agent	Elastomer										
HFC-227ea	S604-70	13.0	19.0	15.0	56.0	27.0	32.0	-4.6	-12.9	-15.8	-26.6
	N674-70	-1.5	-4.4	-1.5	9.2	9.2	-29.3	-8.6	-63.7	--	-92.1
	L1120-70	19.0	18.0	16.0	24.0	-20.1	13.0	131.0	-9.5	-39.9	-49.3
	V1164-75	--	-10.1	-10.4	4.5	15.0	-26.5	-51.7	-42.9	-55.0	-56.9
	C1185-70	8.7	-5.9	-1.2	26.0	6.9	-15.5	-19.6	-53.8	-74.3	-90.5
	N103-70	22.0	32.0	35.0	50.0	22.0	8.4	4.5	-51.3	-88.2	--
	E0540-80	--	--	-0.8	29.0	-4.5	4.6	--	--	--	--
HFC-125	S604-70	7.8	6.7	15.0	1.3	-3.2	1.3	-3.1	-6.7	-16.7	-32.3
	N674-70	7.5	9.0	6.1	-7.7	4.6	-36.4	-32.8	-51.5	-72.8	-87.9
	L1120-70	7.4	2.1	16.0	9.9	2.0	-2.0	-10.8	-25.9	-52.0	-76.1
	V1164-75	--	0.8	-7.7	-75.2	-80.5	-76.9	-68.5	-70.0	-54.5	-70.3
	C1185-70	5.5	3.6	0.7	0.0	-10.0	-17.5	-22.9	-32.3	-60.9	-82.6
	N103-70	31.0	39.0	29.0	20.0	12.0	1.1	-44.8	-52.7	-72.4	--
	E0540-80	--	--	-1.4	1.5	-3.2	-10.4	--	--	--	--
FC-218	S604-70	15.0	25.0	7.0	39.0	43.0	67.0	4.5	-0.9	1.5	-3.1
	N674-70	2.9	1.5	7.4	38.0	47.0	35.0	-16.0	-32.8	-42.0	-29.6
	L1120-70	13.0	21.0	3.8	27.0	26.0	42.0	-40.0	-18.1	-23.6	-28.3
	V1164-75	--	-3.1	-4.5	-7.7	6.1	-29.8	-59.1	-59.5	-67.9	-63.2
	C1185-70	7.2	-1.0	-1.2	26.0	29.0	14.0	-18.1	-33.2	-34.9	-45.0
	N103-70	15.0	-98.2	15.0	-83.9	48.0	44.0	-26.7	-45.5	-52.6	-55.0
	E0540-80	--	--	2.3	30.0	17.0	27.0	--	--	--	--

6.4 Testing of Elastomers and Lubricants in CF_3I

In this chapter the results of swelling measurements and mechanical property measurements obtained for CF_3I are reported. In the first phase of the project this agent was not investigated. It was included later in the testing programs because it was found to be very effective in suppressing non premixed flames. During the tests in this agent several anomalies were observed (the saturation vapor pressure at the test temperatures was not reproducible, oil-like residue was found in the pressure vessels after exposure, etc.). The details of the observed anomalies are described in 6.4.1.

6.4.1 Anomalous Testing Results with CF_3I . In the first lot of CF_3I both swelling and mechanical properties measurements were discontinued because of chemical purity problems. During the swelling measurements a slightly yellow solid residue developed on the Pyrex windows at 75 °C which changed from yellow to orange to a brownish red at 150 °C. Most of the elastomers were destroyed and even the stainless steel fixtures used for the compression set measurements were severely corroded after 1 week exposure at 100 °C. A high viscosity oil-like residue was found in the bottom of the pressure vessels. It was concluded CF_3I was degraded creating HI, HF and I_2 . Testing with a new lot of CF_3I (Deepwater Lot #224940901) has been repeated, but our observations indicate that the saturation vapor pressure of this chemical increases after exposures at elevated temperatures. This seems to be a consequence of chemical degradation, but to a much lesser degree than in the first lot.

We found that during the exposure at a given temperature the vapor pressure of the agent was constant. Then the CF_3I was removed from the pressure vessel to a storage vessel so that the samples (o-rings) could be withdrawn for mechanical testing. When the pressure vessel was refilled with the same amount of CF_3I , the vapor pressure was significantly higher than originally, i.e., the mass of CF_3I required to attain the original pressure was reduced. The details of our observations are outlined below.

The saturation vapor pressure of the new supply of CF_3I was observed to increase after 1 week exposure at both 75 °C and 100 °C. After filling a completely dark pressure vessel with approximately 0.9 kg of unused CF_3I , the initial vapor pressure of the agent was measured as 1.66 MPa at 76.9 °C. Approximately 0.9 kg of agent was recovered and stored in a previously empty and evacuated steel tank with brass fittings for approximately 3 hours. The pressure vessel was then refilled with approximately 0.3 kg of the previously used CF_3I and the vapor pressure increased to 2.02 MPa at 76.2 °C. After another week of exposure, the vapor pressure was 2.01 MPa at 76.2 °C and then approximately 0.3 kg was recovered from the pressure vessel. For the next time interval of 2 weeks, approximately 0.3 kg was filled and recovered from the pressure vessel and the vapor pressure was 1.94 MPa at 76.2 °C. It is possible that saturation was not achieved during this exposure. A black oil was removed from the bottom of the pressure vessel and 0.8 kg of unused (i.e., fresh) CF_3I was pumped into the vessel for the next exposure. The vapor pressure was measured as 1.68 MPa at 76.0 °C and approximately 0.6 kg was recovered.

Similarly for the 100 °C exposures, the vapor pressure increased from 2.46 MPa at 99.0 °C to 2.79 MPa at 98.8 °C after recovery in the same steel tank, but the filling mass was approximately constant. Note that the quantity of filling mass must be considered carefully because any mass in excess of the amount necessary for saturation will not increase the vapor pressure. Also, this pressure vessel did have glass windows (although "UV free" PMMA sheets were used for filtering purposes) and consequently some amount of blue and ultraviolet light may have reached the agent.

These observations during exposures at 75 and 100 °C indicate possible degradation of the CF₃I, and raise a flag about the chemical stability of the material. All swelling and mechanical measurements were made with Deepwater Lot #224940901.

6.4.2 Swelling Measurements in CF₃I. The experimental method has been described in 6.2.2. All seven sets of crosslinked and uncrosslinked elastomers and lubricants were exposed to CF₃I at temperatures 35, 70, and 105 °C.

In Figure 15 the solvent uptake of the elastomers is shown as a function of the vapor pressure at 35 °C. In Figure 16 the same data are displayed according to the Flory-Huggins representation. The curves in Figure 16 show the fit of equation (2) to the experimental points. The values of the χ parameters for all the elastomers and lubricants are displayed in Table 18.

6.4.3 Durability Test Results in CF₃I. Compression set and tensile measurements were made on samples exposed to CF₃I at 5.86 MPa and 75 °C, using the methods described in 6.3. The results are given in Tables 19-21.

Figure 17 shows log-log plots of the compression set vs. exposure time data in Table 19 for five elastomers in CF₃I. (The data for elastomers N674-70 and V1164-75 are not shown because the compression set values were small or negative due to swelling.) The lines show the result of fitting the measured values of compression set for exposure times from 1 to 32 weeks to eq. 5 by unweighted nonlinear least squares. As with the other three agents, the data obtained at the longest exposure time (58 weeks) have not been used in the fitting to allow comparison of the values measured at 58 weeks with the results predicted from measurements at shorter times. The values of C_{∞} , τ and β so obtained are given in Table 12. It is seen from Table 19 and Fig. 17 that the compression set for S604-70 and E0540-80 in CF₃I is markedly higher after 58 weeks exposure than would be predicted from extrapolations based on the behavior at shorter times. Figure 18 shows the data of Table 20, percent change in ultimate elongation vs. exposure time for all the elastomers.

The results of tensile tests of elastomers exposed to CF₃I at 5.86 MPa and 50 and 100 °C for 1, 2, and 4 weeks are shown in Tables 22 and 23. As with the other three agents, the results of tensile tests of elastomers exposed to CF₃I exhibited too much scatter to allow meaningful fitting for the extrapolation of either time (relaxation functions) or temperature (activated process models).

6.5 Summary

In order to characterize the compatibility of elastomeric o-rings in the fire suppressant storage system, swelling and mechanical property (compression set and tensile test) measurements were conducted and data were generated on the changes in the properties of seven sets of crosslinked and uncrosslinked elastomers (silicone, fluorosilicone, neoprene, fluorocarbon, two different butadiene-acrylonitrile copolymers, ethylene-propylene-diene terpolymer) after exposure to HFC-227, HFC-125 and FC-218. In CF₃I swelling measurements were conducted for the seven sets of elastomers plus three lubricants (Krytox 240AC, Braycote 600 and Braycote 807). Exposures at 75 °C and 5.86 MPa were carried out for 74 weeks (in the case of the CF₃I for 58 weeks) to provide estimates of the long term resistance of elastomers to in-service conditions.

The following sections summarize the swelling and mechanical property estimates of elastomer performance in the fire suppressant agents. In addition, swelling performance of the lubricants is summarized. The important conclusion to be derived from these summaries and the detailed data of

Table 18. Flory-Huggins interaction parameters χ for elastomers and lubricants in CF₃I

Elastomer/ Lubricant	χ (35 °C)	χ (70 °C)	compatibility
uSi	1.06	1.29	fair
xSi	1.11	1.40	fair
uN206	0.94	1.20	fair
xN206	1.00	1.25	fair
uFSi	1.20	1.41	good
xFSi	1.28	1.48	good
uFKM	1.43	1.67	good
xFKM	1.47	1.72	good
uCR	1.35	1.48	good
xCR	1.40	1.53	good
uN926	1.03	1.15	fair
xN926	0.95	1.21	fair
uEPDM	1.08	1.18	fair
xEPDM	1.13	1.25	fair
Krytox 240AC	2.11	2.12	good
Braycote 600	2.24	2.34	good
Braycote807	1.84	1.86	good

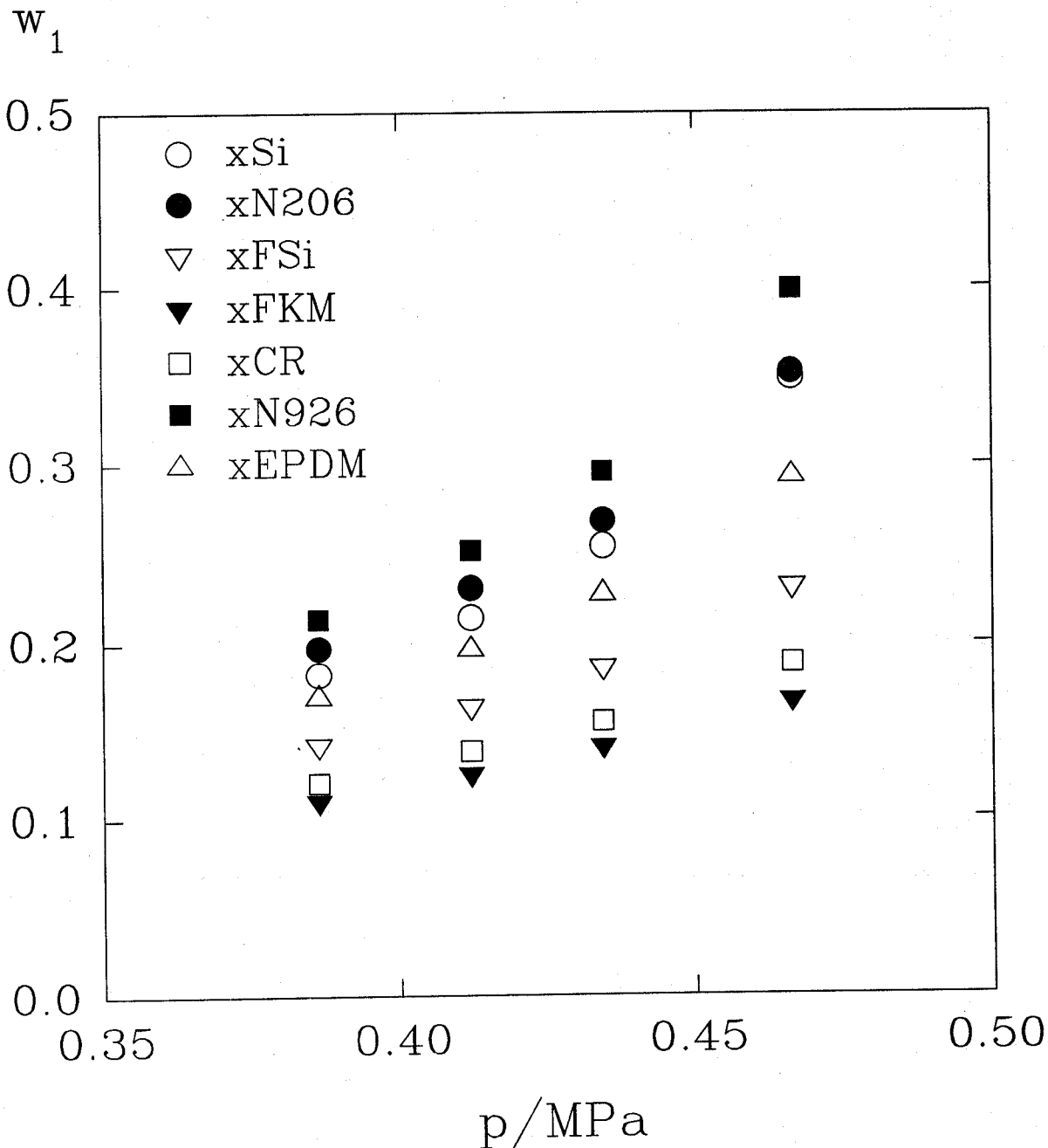


Figure 15. Weight fraction w_1 of CF_3I as a function of pressure for various crosslinked elastomers at 35 °C.

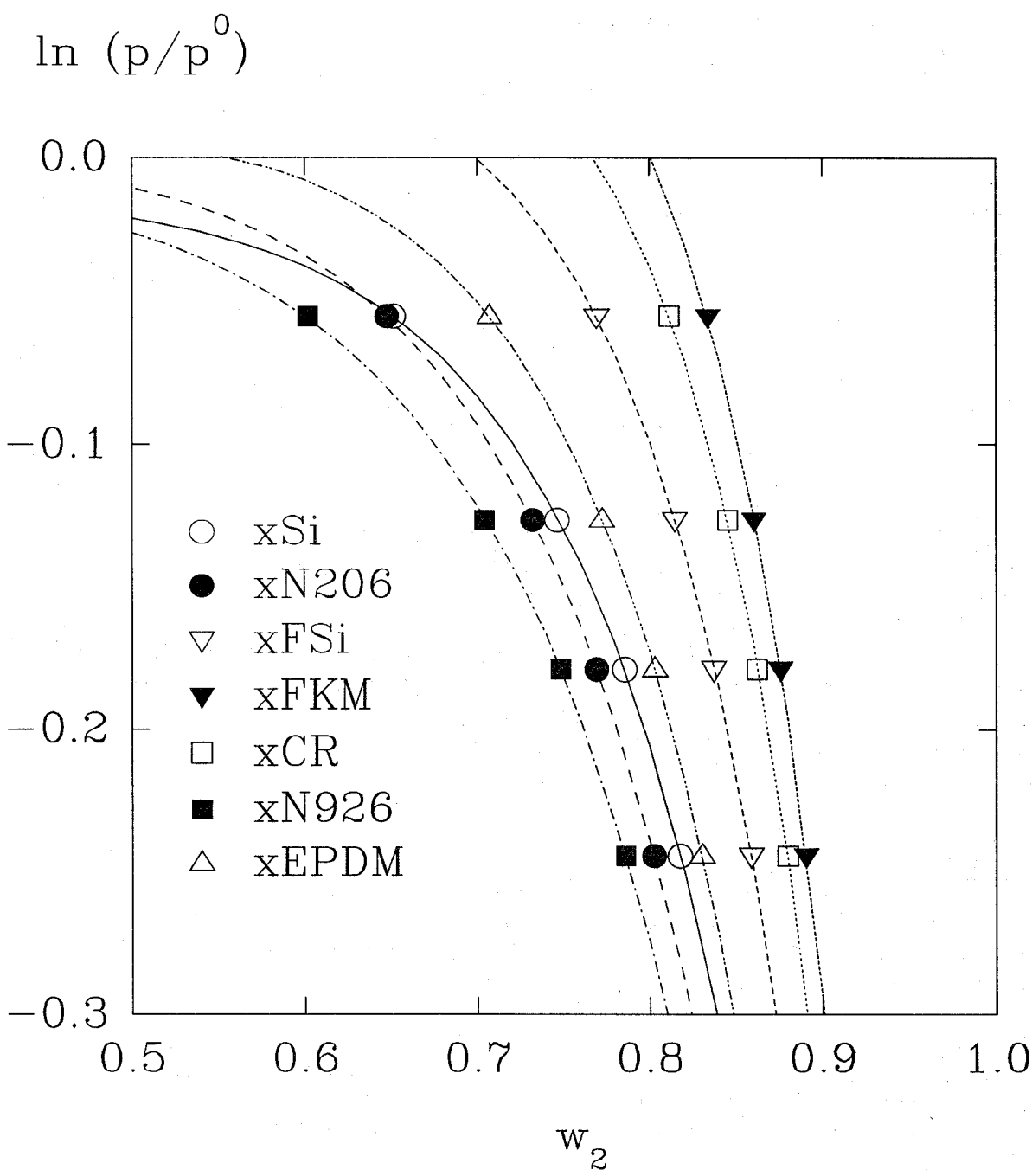


Figure 16. Solvent activity in various crosslinked elastomers in CF_3I as a function of polymer weight fraction w_2 at 35 °C. The curves show the least squares fits according to Equation (2).

Table 19. Compression set (C) after 1, 2, 4, 8, 16, 32 and 58 week exposures at 5.86 MPa and 75 °C in CF₃I

Elastomer	weeks						
	1	2	4	8	15	32	58
S604-70	2	6	8	14	18	24	33
N674-70	-3	12	24	35	70	80	81
L1120-70	13	20	36	40	48	58	65
V1164-75	-11	-5	-6	-6	-2	-1	2
C1185-70	9.1	20	43	50	76	78	81
N103-70	9	27	47	58	88	88	92
E0540-80	2	11	17	22	33	39	57

this and the prior reports (McKenna et al, 1994) is that for each of the final four agents, there exists at least one compatible elastomer and grease. It is up to the design engineer to make the appropriate selection.

6.5.1 Swelling measurements. The swelling measurements were used to make compatibility ratings based on the χ values determined for each polymer-agent system at 35 °C. Small χ values correspond to relatively high solubility or, for present purposes, bad compatibility. The results of the swelling measurements are summarized below for the four agents. An important finding is that for each agent there are several elastomers that show good compatibility, hence providing design flexibility for agent storage vessels.

HFC-227ea

55 % butadiene-45 % acrylonitrile (N206), neoprene and ethylene-propylene-diene have good compatibility, and silicone, fluorosilicone and fluorocarbon show fair compatibility. 85 % butadiene-15 % acrylonitrile (N926) has bad compatibility. Lubricants Braycote 600, Braycote 807, and Krytox 240AC are fairly compatible.

HFC-125

Silicon, 55 % butadiene-45 % acrylonitrile (N206), fluorosilicone, neoprene, 85 % butadiene-15 % acrylonitrile (N926) and ethylene-propylene-diene have good compatibility, and fluorocarbon has fair compatibility. Lubricants Braycote 600 and 807 have good compatibility, and Krytox 240AC is fairly compatible.

FC-218

All the elastomers have good compatibility. Lubricants Braycote 600, Braycote 807, and Krytox 240AC have good compatibility.

Table 20. Percent change in ultimate elongation after 1, 2, 4, 8, 16, 32 and 58 week exposures at 5.86 MPa and 75 °C in CF₃I

Elastomer	weeks						
	1	2	4	8	15	32	58
S604-70	0.0	10.2	17.2	6.5	31.7	-61.3	-17.2
N674-70	1.8	-2.4	-8.1	-8.1	-51.5	-56.6	-78.6
L1120-70	-20.6	-32.5	-21.9	-36.9	-21.9	3.8	-11.3
V1164-75	18.4	14.5	21.8	21.8	-10.1	11.2	-8.9
C1185-70	1.6	1.6	-27.5	-1.2	-14.2	-18.2	-32.3
N103-70	14.7	9.0	-2.4	3.3	-27.3	-67.8	-78.4
E0540-80	5.0	5.0	1.5	-5.0	1.5	12.9	11.4

CF₃I

Fluorosilicone, fluorocarbon and neoprene have good compatibility, and silicone 55 % butadiene-45 % acrylonitrile (N206), 85 % butadiene-15 % acrylonitrile (N926) and ethylene-propylene-diene have fair compatibility. Lubricants Krytox 240AC, Braycote 600 and Braycote 807 have good compatibility.

6.5.2 Mechanical Property Measurements. Two types of experiments were performed to produce data on residual mechanical properties of the elastomers: compression set and tensile test measurements. In order to study the effect of temperature short term (1,2 and 4 weeks) exposures to the four agents were performed at 50, 75 and 100 °C. An activation energy analysis was used to determine the temperature dependencies of the compression set data. The results of long-term exposures for 8, 16, 32, 48, and 74 weeks (58 weeks for CF₃I) carried out at 75 °C and 5.86 MPa have been analyzed using a KWW stretched exponential creep function. This analysis allows extrapolation to longer exposure times.

6.5.3 Compression Set Measurements. The compression set measurements showed significant differentiation between the results obtained for the elastomers in each agent after exposure at 5.86 MPa and 75 °C.

HFC-227ea

After 74 weeks exposure the compression set was small for silicone (30 %), moderate for ethylene-propylene-diene and standard nitrile (43 % and 50 %), and large for fluorosilicone, low-temperature nitrile and neoprene (64, 65 and 74 %). In the case of fluorocarbon swelling was observed.

Table 21. Percent change in tensile strength after 1, 2, 4, 8, 16, 32 and 58 week exposures at 5.86 MPa and 75 °C in CF₃I

Elastomer	weeks						
	1	2	4	8	15	32	58
S604-70	-1.1	-0.9	5.8	-9.4	1.8	-74.2	-34.6
N674-70	4.5	3.0	3.0	-68.8	-48.5	-34.3	-69.4
L1120-70	-28.4	-40.9	-30.9	-44.1	-33.5	-6.4	-15.8
V1164-75	-20.4	-26.2	-22.8	-22.8	-50.0	-30.7	-49.2
C1185-70	-1.2	0.2	-32.0	-2.0	-30.3	-23.6	-45.5
N103-70	25.4	12.4	17.9	23.5	-14.5	-51.3	-60.0
E0540-80	1.5	-5.5	-0.8	-13.6	-21.4	-13.6	-7.4

HFC-125

After 74 weeks exposure the compression set was small for fluorocarbon (20 %), moderate for silicone and ethylene-propylene-diene (39 % and 49 %), and large for fluorosilicone, standard nitrile, neoprene and low-temperature nitrile (73, 80, 88 and 89 %).

FC-218

After 74 weeks exposure the compression set was small for fluorocarbon (22 %), moderate for silicone and ethylene-propylene-diene (41 % and 46 %), and large for fluorosilicone, standard nitrile, neoprene and low-temperature nitrile (79, 79, 85 and 92 %).

CF₃I

After 58 weeks exposure the compression set was moderate for silicone and ethylene-propylene-diene (33 % and 57 %) and large for fluorosilicone, neoprene and low-temperature nitrile (65, 81 and 92 %) In the cases of standard nitrile and fluorocarbon swelling was observed.

As a note of caution, the silicone, standard nitrile and ethylene-propylene-diene elastomers exhibited abrupt increases in compression set between 48 and 74 week exposures in some of the agents. The reader is referred to Tables 9 and 19 and Figures 9-11 and 17 for details. This indicates the difficulty of extrapolating the results to longer times than the measurements.

6.5.4 Tensile Testing. The ultimate elongation data showed very large scatter with the exposure time at all temperatures. As a result, such standard test results are not very amenable to reliable interpretation of the agent-elastomer compatibility.

Table 22. Percent change in ultimate elongation after short-term exposures to CF₃I at 50 and 100 °C.

Exposure temperature	50 °C			100 °C		
Exposure time, weeks	1	2	4	1	2	4
Elastomer						
S604-70	14.0	17.0	12.0	24.0	6.5	28.0
N674-70	4.8	4.8	6.9	-10.2	-16.3	-46.1
L1120-70	12.0	16.0	1.9	12.0	12.0	12.0
V1164-70	--	13.0	17.0	11.0	7.3	7.8
C1185-70	11.0	9.3	9.3	-27.5	-11.7	-27.5
N103-70	8.2	18.0	16.0	-2.4	-8.2	-41.2
E0540-80	7.9	9.4	11.0	15.0	15.0	7.9

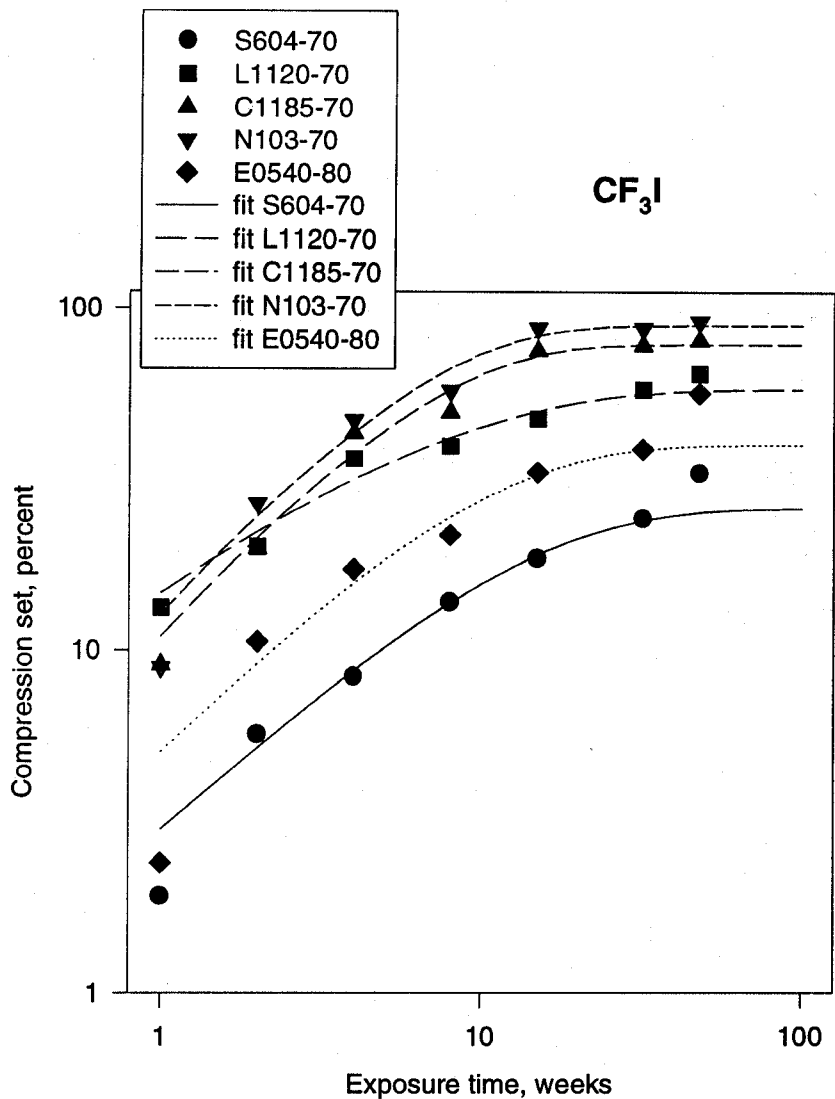
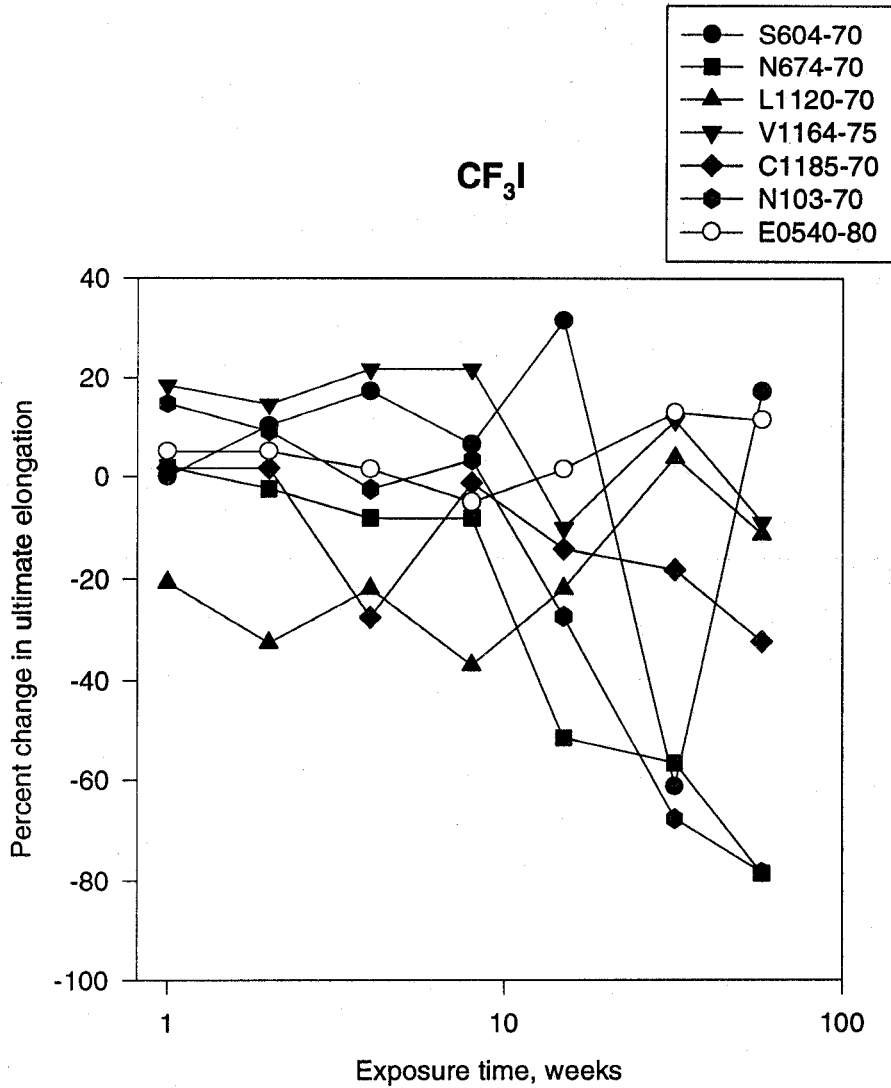


Figure 17. Compression set for various elastomers vs. exposure time to agent CF₃I at 5.86 MPa and 75 °C.

Table 23. Percent change in tensile strength after short-term exposures to CF_3I at 50 and 100 °C.

Exposure temperature	50 °C			100 °C		
Exposure time, weeks	1	2	4	1	2	4
Elastomer						
S604-70	25.0	27.0	21.0	3.9	-10.3	4.2
N674-70	6.0	3.0	7.5	4.6	-1.6	-26.6
L1120-70	15.0	13.0	3.6	-10.1	-9.5	-3.6
V1164-70	--	-9.1	-4.5	-26.2	-32.1	-29.8
C1185-70	5.8	7.2	5.2	-6.9	-10.8	-27.6
N103-70	7.5	16.0	22.0	18.0	16.0	-8.8
E0540-80	--	--	9.1	12.0	-0.8	-5.5



6.6 References

- ASTM, Designation D 395-89, "Standard Test Methods for Rubber Property - Compression Set," *Annual Book of ASTM Standards*, **09.01**, 24 (1989).
- ASTM, Designation D 412-87, "Standard Test Methods for Rubber Properties in Tensions," *Annual Book of ASTM Standards*, **09.02**, 100 (1990a).
- ASTM, Designation D 1414-90, "Standard Test Methods for Rubber O-Rings," *Annual Book of ASTM Standards*, **09.02**, 181 (1990b).
- Boyer, R.F., "Deswelling of Gels by High Polymer Solutions," *J.Chem.Phys.*, **13**, 363 (1945).
- Brotzman, R.W. and Eichinger, B.E., "Volume Dependence of the Elastic Equation of State. 3. Bulk-Cured Poly(dimethylsiloxane)," *Macromolecules* **15**, 531 (1982).
- Brotzman, R.W. and Eichinger, B.E., "Swelling of Model Poly(dimethylsiloxane) Networks," *Macromolecules*, **16**, 1131 (1983).
- Flory, P.J., "Thermodynamics of High Polymer Solutions," *J. Chem. Phys.*, **10**, 51 (1942).
- Flory, P.J., *Principles of Polymer Chemistry*, Cornell University Press, Ithaca, New York (1953).
- Flory, P.J., "Thermodynamics of Polymer Solutions," *Disc. Faraday. Soc.*, **49**, 7 (1970).
- Flory, P.J. and Erman, B., "Theory of Elasticity of Polymer Networks 3.," *Macromolecules* **15**, 800 (1982).
- Flory, P.J. and Rehner, J., Jr., "Statistical Mechanics of Cross-Linked Polymer Networks," *J.Chem.Phys.*, **11**, 521 (1943).
- Gallagher J., McLinden, M., Huber, M., and Ely, J., *NIST Standard Reference Database 23: Thermodynamic Properties of Refrigerants and Refrigerant Mixtures Database (REFPROP)*, Version 3.0, U.S. Department of Commerce, Washington, DC (1991).
- Gee, G., Herbert, J.B.M. and Roberts, R.C., "The Vapor Pressure of a Swollen Cross-Linked Elastomer," *Polymer* **6**, 51 (1965).
- Horkay, F. and Zrinyi, M., "Studies on Mechanical and Swelling Behavior of Polymer Networks on the Basis of the Scaling Concept. 4. Extension of the Scaling Approach to Gels Swollen to Equilibrium in a Diluent of Arbitrary Activity," *Macromolecules* **15**, 1306 (1982).
- Horkay, F., Hecht, A.-M. and Geissler, E., "The Effects of Cross-Linking on the Equation of State of a Polymer Solution," *J. Chem. Phys.*, **91**, 2706 (1989).
- Huggins, M.L., "Some Properties of Solutions of Long-Chain Compounds," *J. Phys. Chem.*, **46**, 151 (1942).
- James, H.M. and Guth, E., "Theory of Elastic Properties of Rubber," *J. Chem. Phys.*, **11**, 455 (1943).
- Jandel Scientific, *SigmaPlot Scientific Graphing Software*, Version 5.0, (1992).
- McKenna, G.B., Waldron, W.K. and Horkay, F., "Elastomer Seal Compatibility," in *Evaluation of Alternative In-Flight Fire Suppressants for Full-Scale Testing in Simulated Aircraft Engine Nacelles and Dry Bays*, Eds. W.L. Grosshandler, R.G. Gann and W.M. Pitts, U.S. Department of Commerce, NIST SP 861, pp 729-763 (1994).
- McKenna, G.B. and Crissmann, J.M., "Thermodynamics of Crosslinked Polymer Networks: The Anomalous Peak in Swelling Activity Measurements," *Macromolecules* 1992, ed by J. Kahovec, VSP, Utrecht, The Netherlands, pp. 67-81 (1993).
- McKenna, G.B., Flynn, K.M. and Chen, Y., "Experiments on the Elasticity of Dry and Swollen Networks: Implications for the Frenkel-Flory-Rehner Hypothesis," *Macromolecules* **22**, 4507 (1989).

McKenna, G.B., Flynn, K.M. and Chen, Y., "Swelling in Crosslinked Natural Rubber: Experimental Evidence of the Crosslink Density Dependence of χ ," *Polymer* **31**,1937 (1990).

Press, W.H., Flannery, B.P., Teukolsky, S.A., and Vetterling, W.T., "Numerical Recipes," Cambridge University Press (1986).

Robin, M.L., *Thermodynamic and Transport Properties of FM-200*, Great Lakes Corporation (1992).

Williams, G., and Watts, D.C. *Trans. Faraday Soc.* **66**, 80 (1970).

7. AGENT STABILITY UNDER STORAGE

Richard H. Harris, Jr.
Building and Fire Research Laboratory

Contents

	Page
7. AGENT STABILITY UNDER STORAGE	249
7.1 Introduction	250
7.2 Experimental	251
7.2.1 Test Matrix	251
7.2.2 Materials	251
7.2.3 Preparation of Cylinders for Testing	252
7.2.4 Spectral Analysis Equipment and Procedure	256
7.2.5 Use of the FTIR Spectra to Determine Agent Degradation	256
7.2.6 Determination of Uncertainty	266
7.3 Results	269
7.3.1 FC-218	269
7.3.2 HFC-125	269
7.3.3 HFC-227ea	281
7.3.4 Summary of Fluorocarbon Area Data	281
7.3.5 Iodotrifluoromethane (CF ₃ I)	282
7.3.5.1 Changes in the Agent Peak Area of CF ₃ I in the 53.3 Pa Spectra for the Different Conditions	290
7.3.5.2 Changes in the Impurity Peak Areas Appearing in the 5330 Pa Spectra	304
7.3.6 Summary of the CF ₃ I Area Data	305
7.4 Conclusions	338
7.5 Acknowledgments	338
7.6 References	338
Appendix A. Initial and Final FTIR Spectra for HFC-125	340
Appendix B. Initial and Final FTIR Spectra of HFC-227ea	349
Appendix C. Initial and Final FTIR Spectra of CF ₃ I Tested in the Dry Condition without Copper	362
Appendix D. Initial and Final FTIR Spectra of CF ₃ I Tested in the Dry Condition with Copper	378
Appendix E. Initial and Final FTIR Spectra of CF ₃ I Tested in the Moist Condition without Copper	390
Appendix F. Initial and final FTIR Spectra of CF ₃ I Tested in the Moist Condition with Copper	397

7.1 Introduction

Significant losses in fire suppression effectiveness and increases in toxicity are possible if a fire extinguishing agent degrades during multi-year storage. Halon 1301 is known to be stable in metal containers for many years, and any trace degradation products do not affect its fire suppression effectiveness. For candidate replacement agents, comparable data are needed, reflecting the storage conditions of elevated temperature and pressure.

The storage environment fosters conditions which may have an adverse effect on the stability of halon replacements. Stored chemicals may engage in oxidation-reduction reactions, hydrolysis, and other corrosive interactions with metal cylinders. They are also subject to unimolecular decomposition and attack by reactive impurities in the agent. Water and oxygen, for example, will sorb to surfaces of cylinders and transfer lines and can never be completely excluded. These sources of instability, along with the possibility of catalytic interactions with the cylinder walls, can promote the evolution of undesirable products and a concomitant loss of fire suppression effectiveness. Toxicity and corrosiveness are particularly important concerns with respect to halogenated compounds, due to the tendency to liberate hydrogen halide in the process of degradation.

Section 6 of NIST Special Publication 861 (Peacock *et al.*, 1994) detailed a screening test for the stability of thirteen agents and eight metals, with the purity of the agent determined by infrared spectral analysis. This test involved storing the agents in PTFE-lined cylinders for one month at a temperature of 150 °C (300 °F). The infrared spectra of the original and "aged" samples were compared. The results of the aging study in combination with other studies of the thirteen agents resulted in the selection of four agents for continued study. These agents were HFC-125, FC-218, HFC-227ea, and CF₃I. Also, in Section 7 of the above publication (Ricker *et al.*, 1994) three of the eight metals studied were chosen as being the best with respect to corrosion. Additionally, the sponsors requested a titanium alloy as a candidate storage metal and copper as an additive for CF₃I be investigated in this study.

Although the screening test was an appropriate method for short-term evaluation, the promising candidate agents need a more rigorous examination. A more comprehensive, long-term evaluation is needed to give stability and degradation information as a function of time and temperature. The information obtained in this study, in combination with information obtained in the studies described in Sections 5 and 6, can then be used in selecting the most thermally stable agents and/or appropriate storage materials.

In this study, samples of the four candidate agents with each of the four storage metal candidates and the copper additive in CF₃I were evaluated in pressurized cylinders at various temperatures and conditions. In order to allow for potential interactions analogous to actual storage conditions, a measured amount of metal (with separate tests for each candidate cylinder metal) was introduced into the containers prior to the experiments. The vessel and its contents were stored at ambient conditions or in ovens at elevated temperatures for as many as 52 weeks as the project time allowed. After specified aging times the cylinders were removed from their respective environments, cooled to ambient conditions, and an infrared (IR) spectrum of the aged sample was collected. Degradation of the sample would be indicated by a systematic decrease in the absorbance of peaks attributable to the agent and/or the appearance of new peaks in the IR spectrum of the aged agent.

This report gives the details of the test procedure and a comparison of agent absorbance band areas from low concentration spectra. Also, presented are a comparison of absorbance bands in high density spectra for impurities present in the agents or produced as a result of degradation. These data provide a quantification of any degradation of the agents during long-term storage.

7.2 Experimental

7.2.1 Test Matrix. Table 1 shows the test matrix. This matrix was designed to utilize oven space, increase the number of exposure temperatures, and expand the exposure conditions to include moisture and addition of copper to CF_3I . The sponsors designed this test matrix to include all agents, all metals, and the various exposure temperatures. The resulting test matrix required 68 sample cylinders. This test procedure was agreed to by NIST.

Since the agents might interact with the metal storage cylinder during long term storage, it was important to evaluate the selected agents in the best metals found in the previous screening study. Containers constructed of each metal would have been ideal for this study, but the cost and availability of cylinders necessitated using metal coupons inside an inert cylinder. In this approach, an amount of metal with the surface area roughly equal to the storage cylinder was introduced into PTFE-lined stainless steel cylinders.

The manufacturers of organoiodide compounds have routinely stored these compounds in the presence of copper (Dierdorf, 1995.) Iodine, if formed during storage, will react with copper to produce cuprous iodide, which is virtually insoluble in most solvents. The sponsors requested that copper be tested as an inhibitor in the CF_3I agent. With this in mind, the test matrix incorporated the addition of copper coupons in certain cylinders, in addition to the test metals.

Since CF_3I appeared to be the least stable agent in the previous screening study, the addition of small amounts of water to some of the test cylinders was incorporated into the test matrix for this agent. In any realistic filling method of storage containers, the presence of residual water in lines and other components of a filling apparatus can be expected. The sponsors requested that the study include the addition of microliter quantities of water into certain cylinders to determine what affect, if any, water has on the degradation of CF_3I .

The temperature dependence of the degradation was also incorporated into the test matrix. This temperature dependence can be dramatic, especially for catalytic degradation. If by-products do form then knowledge of the amounts produced from degradation at different temperatures can be used extrapolate to longer storage times.

7.2.2 Materials. The four agents that were tested for their long-term storage stability are listed in Table 2. They were typical of production grade rather than ultra-pure research samples. All agents were used as received from the manufacturers. Different lots of FC-218 (R-218¹), HFC-227ea (FM-200), and CF_3I (Triiodide) were used in the study. The lots of each agent were compared to each other by comparing their high density Fourier transform infrared (FTIR) spectra (5330 Pa). No differences were found in the lots of FC-218 or HFC-227ea. However, CO_2 was found in the lot of HFC-125. CO_2 and CF_3H were found in the lots of CF_3I . More detail on the amounts of impurities in the lots will be given in 7.2.5.

The five metals that were exposed to each of the agents were the same as those used in the study described in Section 5, Table 1. They were Nitronic 40 (N40), Ti-15-3-3-3 (Ti), C4130 alloy steel (C4130), Inconel 625 (I625), and CDA 110. The metals were supplied by Metal Samples Co., Inc. as coupons 10.2 cm long, 0.8 cm wide, and 0.2 cm thick. In this study, the C4130 alloy steel coupons had a small hole drilled into one end. They were then sent to Walter Kidde Aerospace for phosphate

¹Certain trade names and company products are mentioned in the text or identified in an illustration in order to specify adequately the experimental procedure and equipment used. In no case does such identification imply recommendation or endorsement by the National Institute of Standards and Technology, nor does it imply that the products are necessarily the best available for the purpose.

Table 1. Test matrix

Agent/Test Condition	Metal/Temperature				
	Blank	Nitronic-40	Ti-15-3-3-3	C4130	Inconel 625
FC-218	1T	1T	1T	1T	1T
HFC-125	2T	2T	2T	2T	2T
HFC-227ea	3T	3T	3T	3T	3T
CF ₃ I/a ₁	3T*	3T*	3T*	3T*	3T*
CF ₃ I/b ₁	3T*	2T	2T	2T	2T
CF ₃ I/a ₂	2T*	1T	1T	1T	1T
CF ₃ I/b ₂	2T*	1T	1T	1T	1T

Key:

a = w/o Cu	T ₁ = 23 °C	1T = T ₄
b = w/Cu	T ₂ = 100 °C	2T = T ₁ , T ₄
₁ = dry	T ₃ = 125 °C	2T* = T ₂ , T ₄
₂ = moist	T ₄ = 150 °C	3T = T ₁ , T ₃ , T ₄
		3T* = T ₁ , T ₂ , T ₄

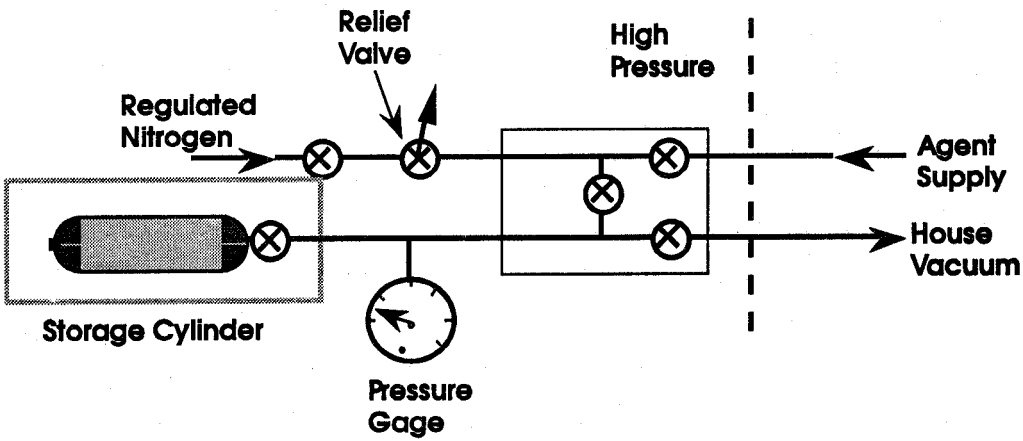
Table 2. Agents used in agent stability study

Agent	Supplier	Lot Numbers
R-218 (FC-218)	3M Chemolite Center 10	L-12677, L-13201
HFC-125	Allied Signal Chemicals	835
FM-200 (HFC-227ea)	Great Lakes Chemical Corp.	92-002-356, 93-200-278
Triiodide (CF ₃ I)	Deepwater	224940901, 226941712, 226941891

treatment prior to being introduced into the cylinders. The phosphate treatment renders the C4130 alloy steel less susceptible to rusting.

The storage cylinders were constructed of stainless steel, lined with polytetrafluoroethylene (PTFE), and had a 1000 ml capacity. All new cylinders were assembled with high temperature/high pressure stainless steel valves and end plugs, then heated to 150 °C (300 °F) for at least 48 hours with the valves completely open. For re-used cylinders, the heating time was cut to 24 hours.

7.2.3 Preparation of Cylinders for Testing. Each agent/metal combination was exposed to the various temperatures specified in the test matrix. Testing conditions dictated that the maximum exposure temperature be no higher than 150 °C, and that the room temperature fill pressure be



4.13 MPa (600 psia). In order to assure that the storage cylinder pressure not exceed the pressure rating on the cylinder or valve when exposed to the elevated temperature, a conservatively low amount of agent was placed in each cylinder. The cylinders were filled with agent up to a maximum pressure of the saturation vapor pressure of the agent at room temperature. Nitrogen was then added to achieve the final pressure. Since small amounts of additional liquid would vaporize at the elevated temperature only a single phase would exist anyway, though a significant pressure increase would be observed. The effect of the system pressure on degradation was not explored, but is thought to be small.

To assure that the metal coupons were free of oil and markings, they were immersed and stirred in dichloromethane solvent. The coupons were removed from the solvent, stripped with clean paper towels, and dried at room temperature. The phosphate-treated C4130 alloy steel coupons were used as received from Walter Kidde Aerospace. After cleaning, care was taken to handle the coupons with gloved hands only.

A filling procedure was designed to insure low levels of contaminants (including room air) and a reasonably accurate measurement of the amounts of material introduced into the cylinder. Highly accurate measurement of amounts of agent and/or nitrogen were not required in this method, since it is the change in spectra that was desired. Figure 1 is a schematic of the filling apparatus. It consisted of a three-valve manifold, an absolute pressure gage, and filling lines, all constructed from stainless steel and capable of handling high pressures. The lines to the agent supply tank and the house vacuum were not high pressure rated and were isolated by valves. The following steps outline the filling procedure.

1. Thirty pieces of each metal were weighed and placed into their respective cylinders. The number of coupons was fixed at 30 for each cylinder because that amount is approximately the surface area of the interior of the cylinder. Overlapping of the coupons in the cylinder effectively decreased the exposed surface area, but this decrease, though not calculated, should be similar for all tests, except those containing the additional copper coupons. The end plug threads were wrapped with PTFE tape and tightened. The cylinder valves were opened and the cylinders were heated for at least 12 hours at 150 °C. Immediately, the cylinder valves were closed. When the cylinders were cool enough to be handled with gloves, they were attached to the sampling system used for the FTIR analyses shown in Figure 2. The cylinders were purged with N₂, then evacuated to an absolute pressure of less than 1.3 Pa (0.01 torr). Each evacuated cylinder was weighed.
2. The evacuated storage cylinder was attached to the filling apparatus.
3. Certain cylinders required the addition of water (Table 1). A fitting was designed with a rubber septum. The fitting was attached to the cylinder with N₂ purging the connection. After the fitting was tightened, the cylinder valve was opened. A syringe containing 100 µL of distilled H₂O was inserted through the septum and injected. The cylinder valve was closed and the "evacuated" cylinder was then attached to the filling apparatus.
4. The filling apparatus was evacuated with the house vacuum which was capable of reduced pressures near 34 Kpa. Then the valve to the house vacuum was closed.
5. The filling apparatus was pressurized with nitrogen in excess of 1.4 Mpa. The pressure was released through the relief valve.

6. The filling apparatus was then evacuated again with the house vacuum. The residual room air in the apparatus was less than 1 % of the original amount.
7. The agent inlet valve was opened slowly until the pressure in the filling apparatus reached the vapor pressure of the agent at ambient temperature (the agent inlet line was pre-charged with agent). The agent inlet valve was closed. This dilutes any residual air again. The house vacuum was opened to remove the agent and any remaining residual air. The agent inlet valve was opened slowly until the pressure again reached the agent's vapor pressure. The valve to the evacuated storage cylinder was slowly opened and agent flowed in. Both the inlet valve and the cylinder valve must be opened slowly to avoid the possibility of drawing liquid agent into the apparatus. The system was allowed to equilibrate for one to two minutes, the pressure recorded, and the agent inlet valve closed.
8. The mass of agent in the storage cylinder was determined by removing the first cylinder filled in a series for a given agent and weighing it. The cylinder was then reattached to the filling apparatus. With the cylinder valve closed, the filling apparatus was again evacuated and purged with N_2 . Then the cylinder valve was opened and the cylinder was filled to nominally 4.2 Mpa with N_2 . This pressure was slightly higher than the prescribed target pressure of 4.13 Mpa. This allowed a small amount of the agent/ N_2 mixture to be removed from the cylinder for the initial FTIR analysis. The total pressure was recorded and the valve to the storage cylinder closed.
9. Proceeding with this method for each cylinder was time consuming and introduced the chance of contamination from air. Since the exact amount of agent in each cylinder at the start of aging was not considered critical, each succeeding storage cylinder filled in a series was attached only once and filled with both agent and N_2 . The agent pressure was recorded for all cylinders prior to introducing the N_2 .
10. The high pressure gas was bled from the filling apparatus and the cylinder disconnected and weighed. At this point, a new cylinder was connected and filled starting with Step 1 above.
11. After FTIR analyses were completed for a series of storage cylinders, they were placed in their proper storage environment as specified in the test matrix. Ambient cylinders were placed on laboratory benches where the temperature remains at 23 ± 1 °C. Cylinders at elevated temperature conditions were placed in laboratory/production ovens with forced convection airflow. The ovens were capable of maintaining a temperature uniformity of ± 1 °C at 100 °C and ± 2 °C at 200 °C.
12. When a series of aged cylinders required analysis, they were removed from their respective storage environment. Cylinders at elevated temperature storage were cooled to ambient temperature (at least 2 hours for those at 150 °C). While the cylinders were cooling, the FTIR was prepared for the analyses. After analyses, the cylinders were weighed and the weights recorded. Before being put back into storage, the cylinders were checked for leaks around the valves and endcaps.
13. The cylinders remain in their respective environments pending the desire for longer-term results.

Tables 3-9 list for each cylinder the metal mass, the agent pressure, initial agent/ N_2 pressure, and the mass before and after storage for all of the agents as well as for all the different environments of

the CF_3I . As mentioned above (steps 8 and 9), only the first cylinder in a given series of agent was actually weighed to see if the agent weight was approximating what was expected from the ideal gas law. For the remaining cylinders in a series the agent mass can be estimated from the agent density at the recorded agent pressure and ambient temperature (along with the fixed 1000 MI volume of the cylinders. The error in this calculated value is the combination of the uncertainty in the agent pressure reading which is estimated to be ± 0.02 Mpa (± 2.5 psia), deviations of the agent temperature from ambient temperature (at least two minutes were allowed for the system to equilibrate), and the error associated with the equation of state. Here, generalized compressibility charts were used (Balzhiser *et al.*, 1972). Where the tables have a mass value in parentheses the weight was calculated from the measured vapor pressure. The mass before storage was the cylinder weight after the initial spectrum had been taken and the cylinder was ready to go into storage. The mass after storage was the weight of the cylinder after the final spectra were obtained. The difference in the above two masses is thus the amount of agent/ N_2 lost as a result of analyses and leakage. Leakage was a problem over the course of the study for roughly 17 of the 68 cylinders in the study. The leakage resulted primarily from cylinders that were reused. The overall validity of the test results was not affected.

7.2.4 Spectral Analysis Equipment and Procedure. The IR analyses were done with a Galaxy Series 7000 FTIR Spectrometer fitted with a KBr beamsplitter and a narrow band mercury cadmium telluride (MCT) detector. The spectral range was from 600 to 4000 cm^{-1} with a resolution of 1 cm^{-1} . A variable path 20-meter gas cell with a volume of 5.4 L and a path length of 10 m was used. A diagram of the sampling system used for the FTIR analyses is shown in Figure 2. All cylinders were analyzed after cooling to ambient temperature. The gas cell was at 105 ± 1 °C for all analyses. The cylinders were connected to the inlet of the gas cell on the FTIR spectrometer. The lines and gas cell were purged with gaseous N_2 from a liquid nitrogen cylinder. A vacuum of less than 1.3 Pa (0.01 torr) was drawn on the gas cell and inlet line up to the cylinder valve. A positive shutoff toggle valve and a micro-metering valve were placed in line between the cylinder valve and the gas cell to accurately control the flow of the agent into the gas cell. The micro-metering valve allowed precise filling of the gas cell and provided reproducible filling of the gas cell. The agent/ N_2 was introduced into the gas cell to an absolute pressure of 53.3 ± 0.1 Pa ($0.400 \pm .001$ torr). A spectrum was taken, then the cell was emptied. Two more replicates were done in the same manner. After the third replicate additional agent/ N_2 was added to fill the gas cell to 5333 ± 13 Pa (40.0 ± 0.1 torr). A spectrum was taken. The cylinder valve was closed tightly. Then the gas cell and lines were emptied with vacuum and N_2 purging. The cylinders were then removed, the end caps fastened tightly, and weighed. Each cylinder was then checked for leaks before being put back into its aging temperature environment.

The fluorocarbon agents were analyzed every 8 weeks, unless the results indicated no changes were occurring. The CF_3I samples were analyzed every 4 weeks, unless the results indicated no changes were occurring. Samples that were not changing (e.g., those at ambient conditions) were analyzed every 16 or 8 weeks for fluorocarbon and CF_3I cylinders, respectively.

7.2.5 Use of the FTIR Spectra to Determine Agent Degradation. The FTIR spectra of the agents were used as both quantitative and qualitative tools to determine if there was degradation of the agent. As a quantitative tool, an absorbance band for each agent was selected in the 53.3 Pa spectra and the area under this absorbance band was determined for each 4 or 8 week interval. Chemical analysis by IR spectroscopy is based on the assumption that the IR spectrum of a compound is sufficiently unique to identify it. An IR spectrum is obtained by measuring the ratio of the intensity of IR radiation which passes through the sample, I , to the intensity of the incident radiation, I_0 , as a

Table 3. Agent and metal amounts in storage cylinders for FC-218

Metal	Temp. (°C)	Metal mass (±0.1 g)	Agent		Agent/N ₂		
			Pressure (± 0.02 Mpa)	Mass (g)	Pressure (± 0.02 Mpa)	Mass before storage (± 0.1 g)	Mass after storage (± 0.1 g)
Blank	150	--	0.85	79.9	4.20	122.2	95.6
N40	150	344.4	0.84	(82.3)	4.20	120.5	107.5
Ti	150	188.3	0.83	(81.3)	4.24	113.8	76.9
C4130	150	304.5	0.76*	(74.5)	4.20	113.0	106.2
I625	150	326.9	0.83	71.9	4.24	118.1	108.7

* Storage tank was almost empty when this cylinder was filled.

Table 4. Agent and metal amounts in storage cylinders for HFC-125

Metal	Temp. (°C)	Metal mass (±0.1 g)	Agent		Agent/N ₂		
			Pressure (± 0.02 Mpa)	Mass (g)	Pressure (± 0.02 Mpa)	Mass before storage (± 0.1 g)	Mass after storage (± 0.1 g)
Blank	23	--	1.28	80.2	4.24	119.7	116.0
N40	23	345.1	1.28	(76.8)	4.24	115.5	109.5
Ti	23	187.5	1.28	(76.8)	4.24	119.2	114.4
C4130	23	304.4	1.28	(76.8)	4.20	121.2	115.2
I625	23	327.0	1.31	78.6	4.27	121.7	114.7
Blank	150	--	1.28	(76.8)	4.27	119.8	111.9
N40	150	343.3	1.28	(76.8)	1.28	117.9	94.6
Ti	150	188.0	1.28	(76.8)	4.27	121.0	105.4
C4130	150	304.2	1.28	78.8	4.24	122.3	114.1
I625	150	327.0	1.28	(76.8)	4.27	118.2	109.0

Table 5. Agent and metal amounts in storage cylinders for HFC-227ea

Metal	Temp. (°C)	Metal mass (±0.1 g)	Agent		Agent/N ₂		
			Pressure (± 0.02 Mpa)	Mass (g)	Pressure (± 0.02 Mpa)	Mass before storage (± 0.1 g)	Mass after storage (± 0.1 g)
Blank	23	--	0.41	31.8	4.20	77.3	74.6
N40	23	343.7	0.41	(31.8)	4.20	73.7	71.4
Ti	23	187.3	0.41	(31.8)	4.20	76.0	73.2
C4130	23	304.3	0.41	(31.8)	4.20	72.1	68.9
I625	23	327.0	0.41	30.6	4.20	72.0	67.4
Blank	125	--	0.41	32.9	4.20	80.7	74.7
N40	125	344.5	0.41	(31.8)	4.20	74.3	63.1
Ti	125	187.7	0.41	(31.8)	4.20	74.9	64.4
C4130	125	303.9	0.41	(31.8)	4.20	74.6	67.4
I625	125	327.2	0.41	(31.8)	4.20	73.1	68.1
Blank	150	--	0.41	(31.8)	4.20	76.5	71.7
N40	150	344.6	0.41	(31.8)	4.20	72.9	66.1
Ti	150	187.3	0.41	(31.8)	4.20	78.1	70.3
C4130	150	304.4	0.41	(31.8)	4.20	73.9	66.3
I625	150	327.0	0.43	(33.4)	4.20	58.7	42.9

Table 6. Agent and metal amounts in storage cylinders for dry CF₃I samples w/o copper

Metal	Temp. (°C)	Metal mass (±0.01 g)	Agent		Agent/N ₂		
			Pressure (± 0.02 Mpa)	Mass (g)	Pressure (± 0.02 Mpa)	Mass before storage (± 0.1 g)	Mass after storage (± 0.1 g)
Blank	23	--	0.45	37.4	4.24	85.4	70.4
N40	23	345.7	0.45	(40.2)	4.24	82.5	71.4
Ti	23	188.3	0.45	(40.2)	4.24	80.1	72.0
C4130	23	304.3	0.45	36.9	4.20	81.4	72.9
I625	23	326.8	0.48	36.8	4.20	79.9	72.4
Blank	100	--	0.48	36.9	4.20	83.3	35.3
N40	100	343.7	0.48	(42.9)	4.20	80.9	--
Ti	100	187.3	0.48	(42.9)	4.20	78.1	70.2
C4130	100	304.3	0.45	(40.2)	4.20	79.1	54.2
I625	100	327.5	0.45	(40.2)	4.20	78.0	71.5
Blank	150	--	0.47	40.1	4.20	87.3	33.8
N40	150	345.1	0.47	(42.0)	4.20	80.9	55.8
Ti	150	187.5	0.47	(42.0)	4.20	84.8	30.1
C4130	150	304.5	0.45	(40.2)	4.20	79.1	32.8
I625	150	327.0	0.48	(42.9)	4.20	80.4	66.3

Table 7. Agent and metal amounts in storage cylinders for dry CF₃I samples with copper

Metal	Temp. (°C)	Cu(CDA110)/ metal mass (±0.1 g)	Agent		Agent/N ₂		
			Pressure (± 0.02 Mpa)	Mass (g)	Pressure (± 0.02 Mpa)	Mass before storage (± 0.1 g)	Mass after storage (± 0.1 g)
Blank	23	353.9/--	0.45	(40.2)	4.24	80.4	72.3
N40	23	354.5/342.6	0.45	(40.2)	4.24	77.7	68.1
Ti	23	354.5/187.1	0.45	(40.2)	4.24	78.7	70.6
C4130	23	354.6/304.2	0.45	(40.2)	4.20	74.8	68.6
I625	23	354.1/327.0	0.48	(42.9)	4.20	75.2	25.7
Blank	100	355.1/--	0.48	(42.9)	4.20	80.5	--
Blank	150	352.9/--	0.47	(42.0)	4.20	84.0	71.8
N40	150	352.7/343.5	0.47	(42.0)	4.20	80.2	60.0
Ti	150	352.5/188.2	0.47	(42.0)	4.20	78.5	67.6
C4130	150	354.1/304.2	0.45	(40.2)	4.20	74.8	49.2
I625	150	353.6/327.0	0.48	(42.9)	4.20	77.1	65.3

Table 8. Agent and metal amounts in storage cylinders for moist CF₃I samples w/o copper

Metal	Temp. (°C)	Metal mass (±0.01 g)	Agent		Agent/N ₂		
			Pressure (± 0.02 Mpa)	Mass (g)	Pressure (± 0.02 Mpa)	Mass before storage (± 0.1 g)	Mass after storage (± 0.1 g)
Blank	100	--	0.48	(42.9)	4.20	81.8	73.4
Blank	150	--	0.47	39.1	4.20	86.0	60.1
N40	150	345.5	0.47	(42.0)	4.20	82.4	63.9
Ti	150	188.1	0.47	(42.0)	4.20	80.6	60.7
C4130	150	304.1	0.45	(40.2)	4.20	77.1	63.7
I625	150	327.0	0.48	(42.9)	4.20	80.7	70.5

Table 9. Agent and metal amounts in storage cylinders for moist CF₃I samples with copper

Metal	Temp. (°C)	Cu(CDA110)/ metal mass (±0.1 g)	Agent		Agent/N ₂		
			Pressure (± 0.02 Mpa)	Mass (g)	Pressure (± 0.02 Mpa)	Mass before storage (± 0.1 g)	Mass after storage (± 0.1 g)
Blank	100	354.2/--	0.48	(42.9)	4.20	79.1	70.7
Blank	150	354.4/--	0.47	(42.0)	4.20	80.0	54.9
N40	150	353.7/344.4	0.47	(42.0)	4.20	76.6	64.9
Ti	150	352.6/187.4	0.47	(42.0)	4.20	75.4	64.5
C4130	150	353.5/304.3	0.45	(40.2)	4.20	73.0	59.1
I625	150	352.7/319.1	0.45	(40.2)	4.20	73.9	61.9

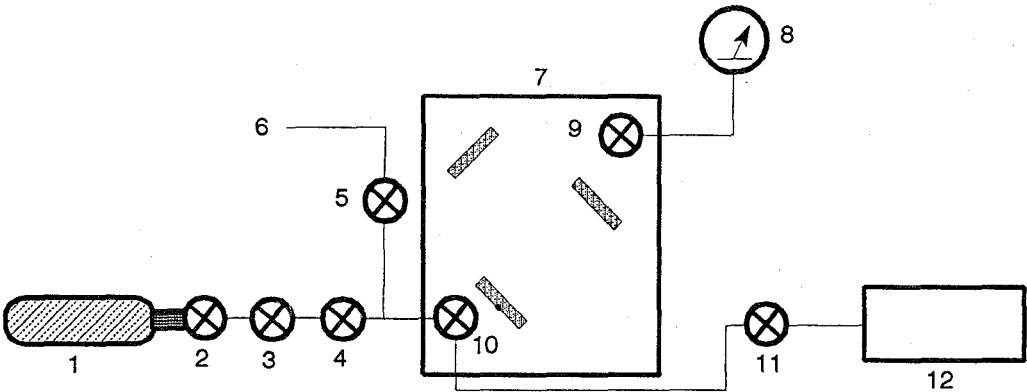
function of frequency (ν). Concentrations of individual components are quantified by applications of Beer's law

$$C_i = \left(\frac{A_i(\nu)}{A_r(\nu)} \right) C_r, \quad A(\nu) = -\log \frac{I(\nu)}{I_0(\nu)}. \quad (1)$$

where subscript r indicates known values obtained from a reference sample. IR spectroscopy is extremely versatile in the sense that almost all compounds, with the notable exception of single atoms and homonuclear diatomics, are IR active. In principle, IR analysis makes it possible to monitor the degradation of each candidate and identify the corresponding products from a sample before and after comparison of the spectra. In practice, IR analysis can suffer from overlapping peaks in a spectrum similar to matrix effects with other analytical methods. In addition, quantitative determination of degradation products require either pre-existing spectra for comparison (libraries of spectra for common materials are commercially available) or available reference samples. The criteria for choosing an agent absorbance band for integration were the following: an absorbance band representing the weakest bond in the molecule; a small band with maximum absorbance less than 0.6 so that if a reduction in area occurred as a result of degradation the change would be detected; assumed to obey Beer's law at lower concentrations if the absorbance is less than 0.6 at higher concentrations; and well resolved with respect to the baseline noise.

FC-218 is a symmetrical molecule with 2 C-C and 8 C-F bonds. The well resolved peak at 731 cm⁻¹ was chosen for integration. Both HFC-125 and HFC-227ea contain C-C, C-H and C-F bonds. The C-H stretch absorbance band near 3000 cm⁻¹ for each of these agents was chosen. All of these chosen agent absorbance bands satisfied the above criteria. The spectra for these agents are shown in Figures 3-5 with the absorbance band that was integrated noted.

For CF₃I, the ideal absorbance band to have integrated would have been that for the C-I stretch. The fundamental vibrational frequency for the C-I stretch from the literature (McGee, 1952) is 539 cm⁻¹. However, the current detector is only sensitive from 4,000 to 600 wavenumbers. As shown in the lower spectrum in Figure 6, a small, but well resolved peak appears at 2255 cm⁻¹. This peak



- 1. Agent Storage Cylinder
- 2. Cylinder Valve
- 3. Toggle Valve
- 4. Micro-Metering Valve
- 5. Toggle Valve
- 6. N₂ Purge Line
- 7. Variable Path Length Gas Cell @ 10 m Path Length
- 8. Pressure Gauge
- 9. Gas Cell Pressure Gauge Valve
- 10. Gas Cell Filling Valve
- 11. Main Vacuum Valve
- 12. Two-Stage Vacuum Pump

Figure 2. Diagram of the equipment for the FTIR spectral analyses.

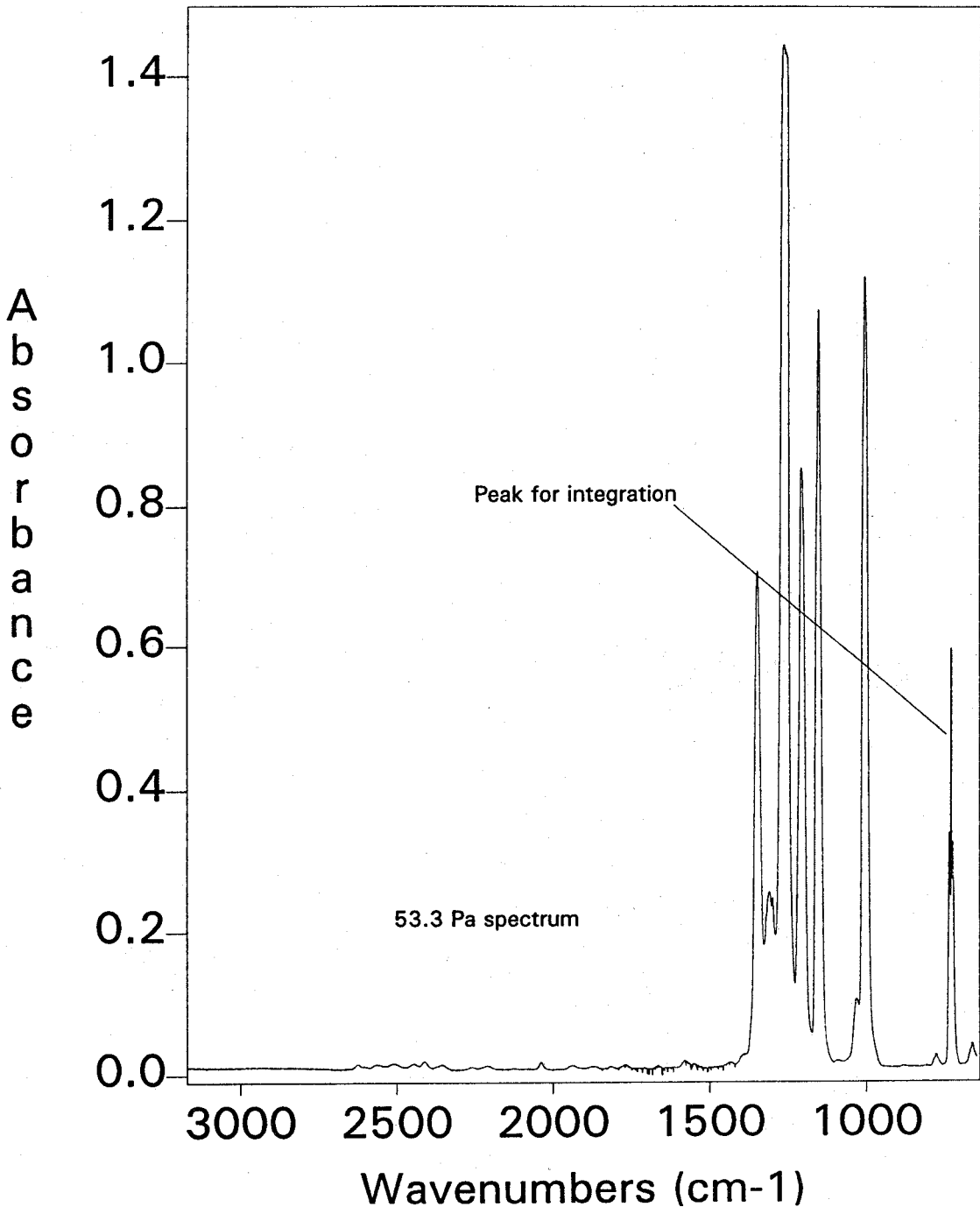


Figure 3. Agent absorbance band in the 53.3 Pa IR spectrum of FC-218 that was integrated.

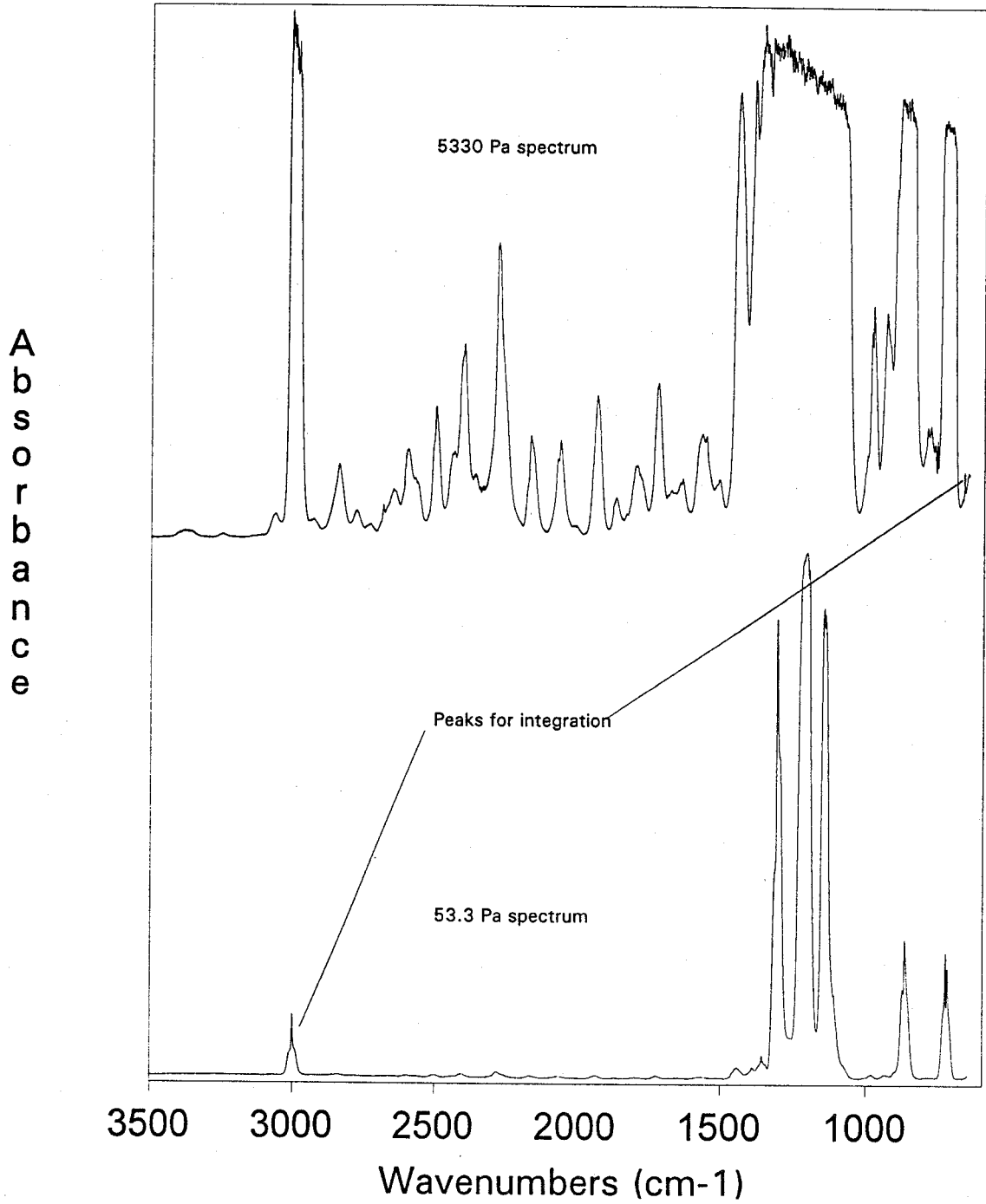


Figure 4. Agent absorbance band in the 53.3 Pa IR spectrum and CO₂ absorbance band in the 5330 Pa IR spectrum of HFC-125 that were integrated.

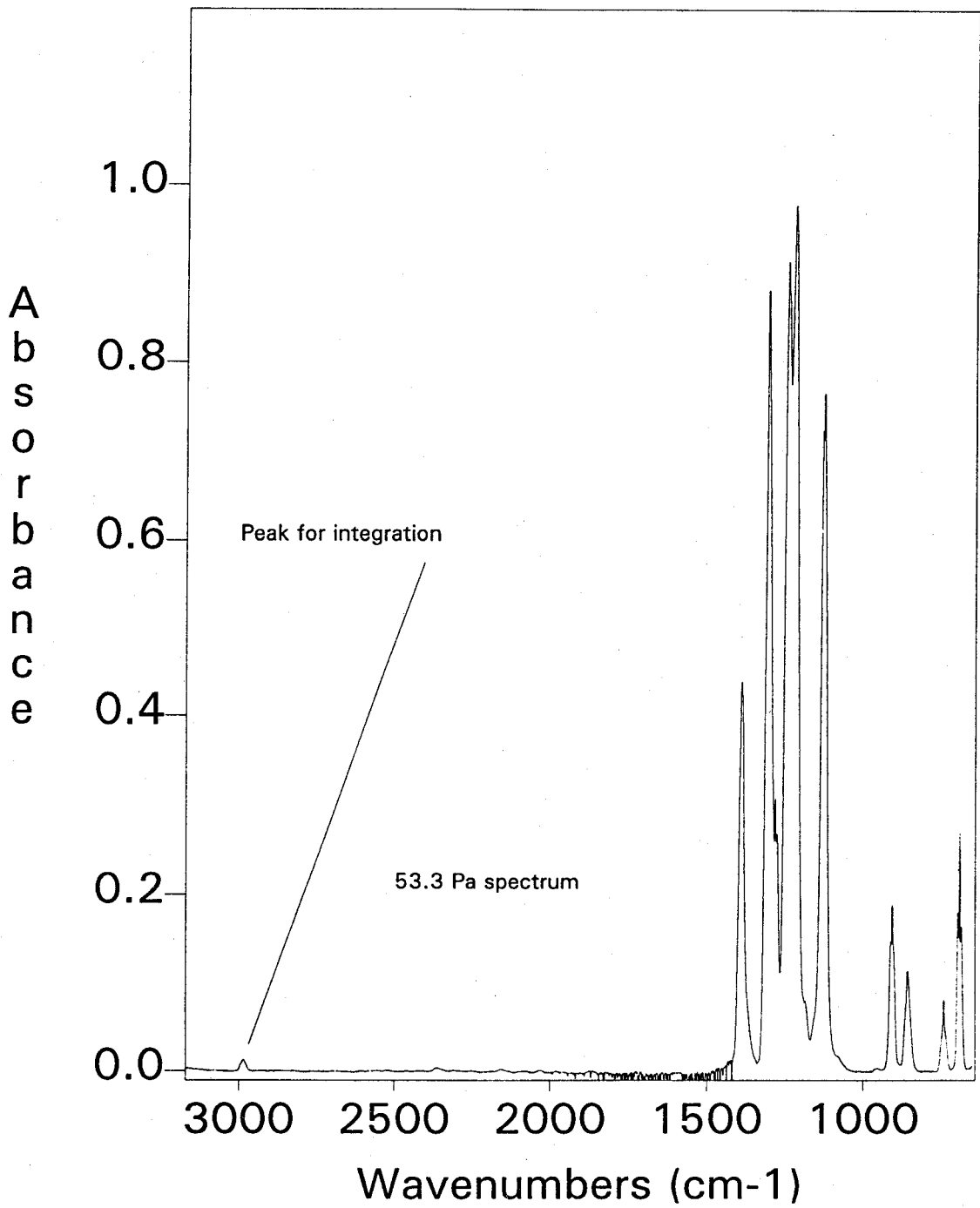


Figure 5. Agent absorbance band in the 53.3 Pa IR spectrum of HFC-227 that was integrated.

corresponds to a combination mode of two larger peaks that correspond to the fundamental stretching frequency of C-F bonds and are labelled peaks 1 and 2 in Figure 6. The small peak thus results from both the stretching and bending of symmetrical C-F bonds. If only a small fraction of CF_3I molecules in the cylinder are degrading, then a reduction in area under this small band will be more easily detected because the low intensity band is more likely to follow Beer's law. Therefore, we used the 2255 cm^{-1} absorbance band.

As a qualitative tool, higher concentration spectra were used. If degradation of the agent were to occur, then the degradation products should begin to form and impurity bands in the aged IR spectrum from each cylinder should appear. Since the amount of degradation products might be small in comparison to the amount of agent, aged spectra at 5330 Pa (or 100 times as dense as the quantitative spectra) were obtained for each cylinder at each testing interval. The baselines of these higher concentration, "qualitative spectra" were examined closely to determine if new absorbance bands were appearing.

In addition to any new bands appearing, bands from impurities already present in the agents could be determined from the higher concentration spectrum. Impurity bands from CO_2 were found in all of the initial spectra at 5330 Pa for both the HFC-125 and CF_3I samples. CO_2 might have been present in FC-218 and HFC-227ea, however, this could not be determined because both agents have strongly absorbing bands in the 670 and 2360 wavenumber regions which obscures the absorption spectra of CO_2 . Also detected in the initial spectra for the CF_3I cylinders was CF_3H . Since different lots of some agents were used, Table 10 shows the initial areas for the impurity absorbance bands for each lot of agent determined from the initial 5330 Pa FTIR spectrum.

The only agent to show a new absorbance band appearing in the spectra at elevated temperatures was CF_3I . This new absorbance band will be discussed in 7.3.5.2.

Figures 4 and 6 also show the absorbance bands in the higher concentration spectra that were integrated.

As the study progressed, it became obvious that the 5330 Pa spectra for samples stored at 150°C were changing, especially for the CF_3I samples. A software program (Mattson Instruments, Inc., 1992) generates a correlation coefficient comparison (Mendenhall *et al.*, 1992) report of sample data (aged spectrum) and reference data (initial spectrum). This spectral comparison takes into account changes that are occurring in a spectrum as a result of changes in existing peaks and the appearance of new absorbance peaks. The more a spectral comparison decreases from 1.000 (the value obtained when a spectrum is compared to itself) represents the magnitude of the changes taking place. Thus the value of the spectral comparison for an aged spectrum compared to its initial spectrum allowed a quantitative value to be assigned to the changing spectra as a function of temperatures and conditions of aging.

7.2.6 Determination of Uncertainty. A Type A evaluation of the standard uncertainty (Taylor, 1995) was used in this study. The samples kept at ambient conditions (23°C) were not changing with time. This was evident by seeing no pattern in the measured integrated peak areas as a function of time. For each agent and metal combination at 23°C , the peak area measurements obtained over the study period were averaged and a standard deviation was determined. As a worst-case scenario,

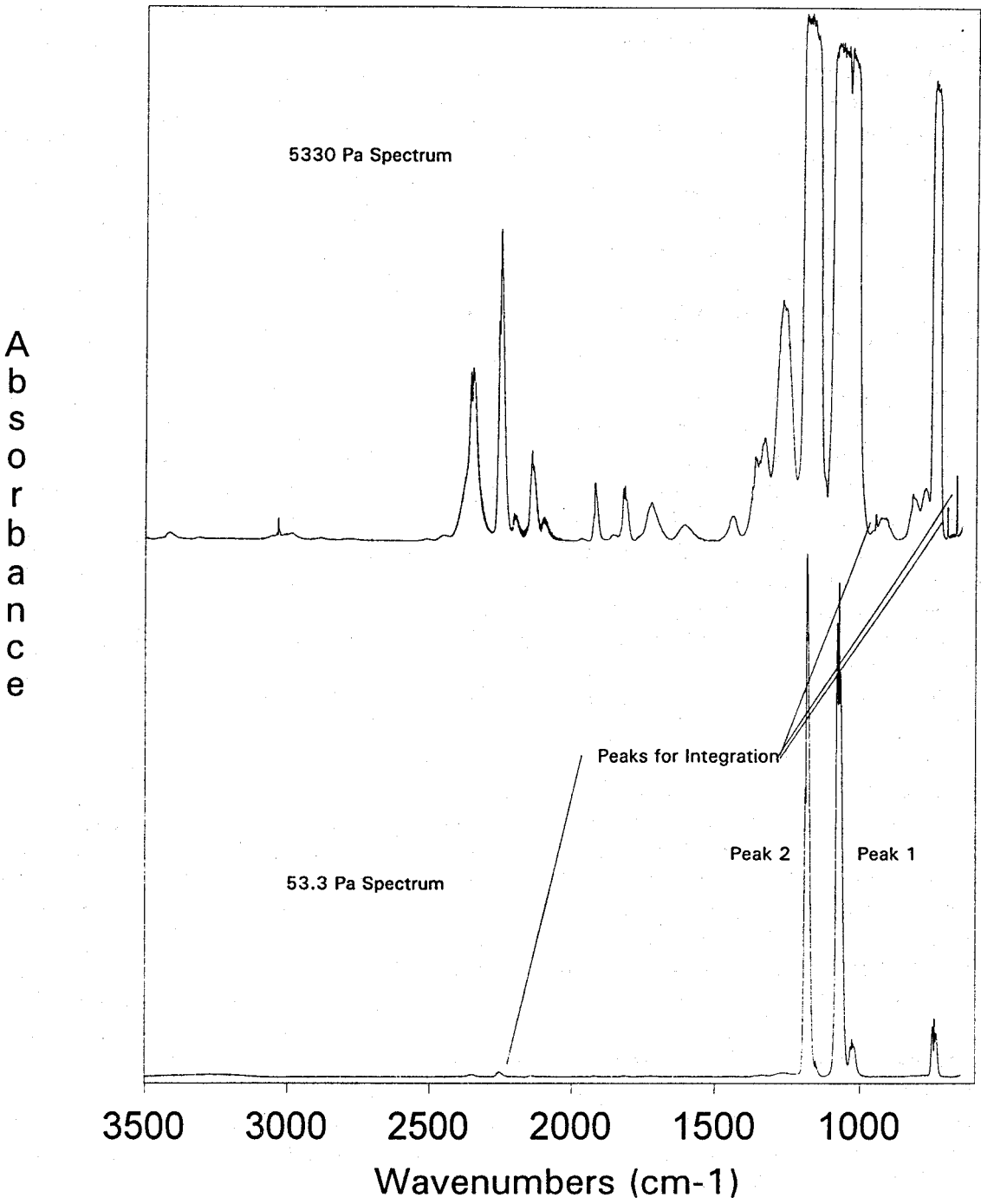


Figure 6. Agent absorbance band in the 53.3 Pa IR spectrum and impurity absorbance bands in the 5330 Pa IR spectrum of CF₃I that were integrated.

Table 10. Impurity levels in the lots of agents at the start of the study

Agent	Lot numbers	Integrated area	
		Impurity compound	
		CO ₂	CF ₃ H
FC-218	L-12677	ND ^a	ND
HFC-125	835	0.01	ND
HFC-227ea	92-002-356	ND	ND
HFC-227ea	93-200-278	ND	ND
CF ₃ I	224940901 ^b	0.09	0.01
CF ₃ I	226941712 ^c	0.18	0.04
CF ₃ I	226941891 ^d	0.01	ND

^a Not detected^b Storage tank was roughly half full when analyzed^c Storage tank was full when analyzed^d Storage tank was nearly empty when analyzed.

the largest standard deviation for a given agent and condition was used for the uncertainty. Agents FC-218 and CF₃I in the moist condition were exceptions. Neither of these samples had ambient cylinders specified in the test matrix. The uncertainty reported for FC-218 was made from the 150 °C peak area data as stated above, based on the fact that no changes in the 5330 Pa spectra were occurring. The uncertainty for the moist CF₃I samples was assigned the same as that for the dry condition. Table 11 lists the wavenumber ranges over which integration was performed for each agent and impurity band along with the uncertainty in the area measurements and the number of observations (N). Note the relatively high uncertainties for the FC-218 and HFC-125. These were the two strongest absorbance bands in the 53.3 Pa spectra of these agents.

The uncertainty in the spectral comparison values was determined in the same manner as described above for the change in area. For each agent and metal combination at 23 °C, each aged spectrum was compared to its respective initial spectrum. These values were averaged and a standard deviation was determined. Once again the largest standard deviation was chosen as the standard uncertainty. The spectral comparisons and uncertainties are reported below in the tables of agent absorbance band areas for each agent and metal combination at 23 °C, along with the number of observations (N).

In some cases the impurity bands for CO₂ and CF₃H in the initial spectra were very small. To ascertain whether these bands could be measured reliably, a measure of the uncertainty in the detection of these peaks was determined. Examination of the baseline of a typical FTIR spectrum in the expanded axis mode reveals a baseline that is sinusoidal in nature. One of these very small "sinusoidal" peaks where no absorbance was occurring as a result of agent, and near the impurity absorbance band of interest was integrated. One of the smallest areas for absorbance reported (0.01) was three times larger than one of the largest baseline absorbance areas. The changes in the agent absorbance bands and impurity bands are described below for the individual agents.

Table 11. Wavenumber ranges for integrated areas of agent and extraneous peaks

Agent	Wavenumber range for integrated area (cm^{-1})	Uncertainty in measured area/N
FC-218	710 - 750	0.15/6
HFC-125	2963 - 3038 (Agent)	0.042/4
	667 - 671 (CO_2)	0.0023/4
HFC-227ea	2966 - 3006 (Agent)	0.0095/4
	2219 - 2274 (Agent)	0.011/9
	667 - 671 (CO_2)	0.0048/9
CF_3I	698 - 701 (CF_3H)	0.0011/9
	944 - 953 (F-alkene)	0.011/9

Because of the large number of samples, the time required to obtain all materials and equipment, and the time required for initial analyses, the introduction of cylinders into the test matrix took several months. Thus, not all metals in a given agent or test condition of CF_3I received the same time of aging. In the tables of integrated data area, the last column to have data reported was the extent of aging. Because the agents, especially CF_3I , were in short supply at the beginning of this study and other studies had to get underway, it was not possible to retain a particular lot of any agent. When a series of cylinders was filled, the agent storage tank was passed to other researchers. By the time that agent was needed again in this study, all of the lot was sometimes used. Therefore, getting all of the cylinders started required the use of different lot numbers of agents. These factors added to the uncertainty of the data analyses. Operator experience and care in performing the analyses also affected the spectral comparisons. For this reason, an attempt to establish Type B evaluations of standard uncertainty (Taylor, 1995) were not done.

7.3 Results

7.3.1 FC-218. At the onset of this investigation, FC-218 was considered to be the most stable of the four agents. Therefore, the test matrix (Table 1) specified this agent to be tested only at 150 °C. Figures 7-11 show the overlaid spectra of the initial and final aged spectra at 5330 Pa for each metal and blank. Visual examination of these spectra indicated no changes occurred. Table 12 shows the integrated area for the agent absorbance band with time and the spectral comparison for the samples. The initial area value for C4130 is an outlier known to result from improper filling of the IR gas cell. Figure 12 shows the integrated areas in Table 12 graphically represented. The areas tended to drift upward over the 48 week period. This was the only agent for which the integrated area for the absorbance band of an agent showed the slight upward drift. The data for this agent had more scatter than any of the other agents. However, the spectral comparison values in the last column of Table 12 indicate the spectra are unchanged.

7.3.2 HFC-125. Because of the weaker C-H bond in this molecule, the test matrix (Table 1) specified two test temperatures. A typical initial and aged spectra at 5330 Pa and at 23 and 150 °C for the

Table 12. Integrated peak areas for a C-F absorbance band in the 53.3 Pa spectra for FC-218 at 150 °C and the spectral comparisons

	Integrated area from 710 to 750 cm ⁻¹ (± 0.15)							Spectral comparison (± 0.00070) ^a
	Week number							
Metal	0	8	16	24	32	40	48	
Blank	6.2	6.3	NM ^b	6.4	6.4	6.5	6.5	0.996
N40	6.6	6.8	NM	6.9	6.8	7.0	7.0	0.996
Ti	6.6	6.7	NM	6.8	6.7	6.8	6.7	0.996
C4130	5.7 ^c	6.5	6.4	6.5	6.5	6.5	NM	0.999
I625	6.5	6.5	6.7	6.6	6.6	6.7	6.9	0.998

^a Number of observations was 5

^b Not measured

^c Outlier from improper gas cell filling.

blank for HFC-125 are shown in Figures 13 and 14, respectively. Visual examination of the initial and final spectra for the cylinder at 23 °C (Figure 13) showed no change in the absorbance and no new peaks. Visual examination of the initial and final spectra for the cylinder tested at 150 °C (Figure 14) did show a small increase in the absorbance band for CO₂ in the 670 cm⁻¹ region. The samples containing each of the four metals gave similar results. Their spectra are shown in Appendix A for reference.

Table 13 lists the integrated areas under the C-H stretch absorbance band with time and temperature for each metal and temperature. Figure 15 is a graphic representation of this data. In all cases the peak areas randomly varied from 2.7 to 2.9. The graphs showed some scatter of the areas, but no upward or downward drift with time. All of the areas reported for the aged samples were within three standard deviations of its initial area. At the 99 % confidence interval, the spectral comparisons did not change significantly either.

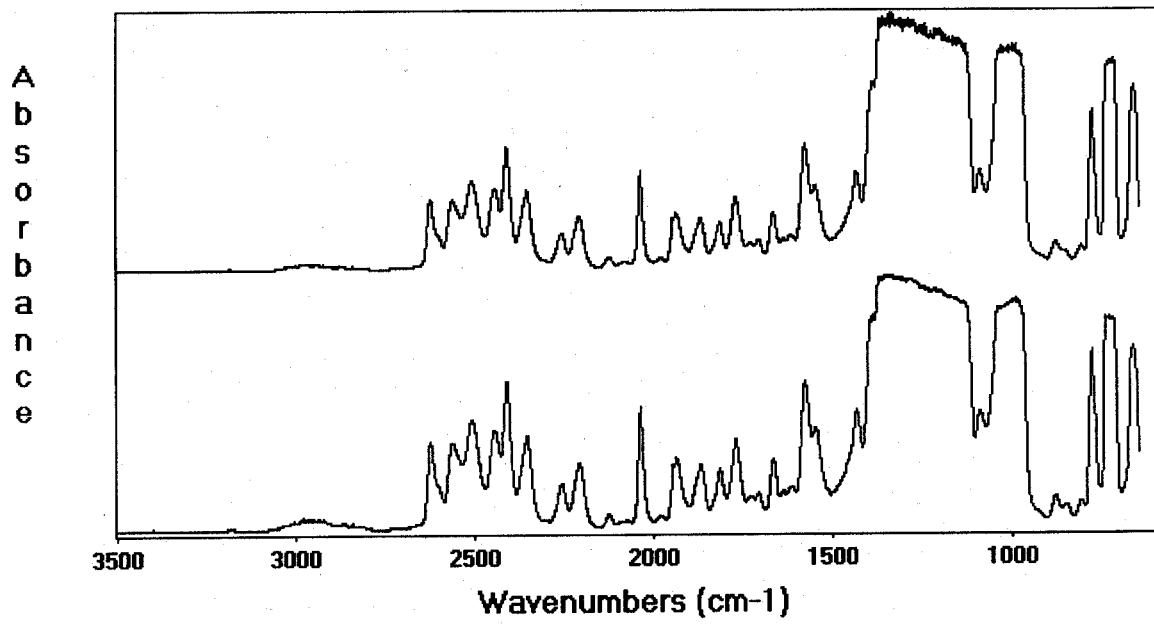


Figure 7. Initial (lower) and 48 week (upper) 5330 Pa spectra for the blank for FC-218 at 150 °C.

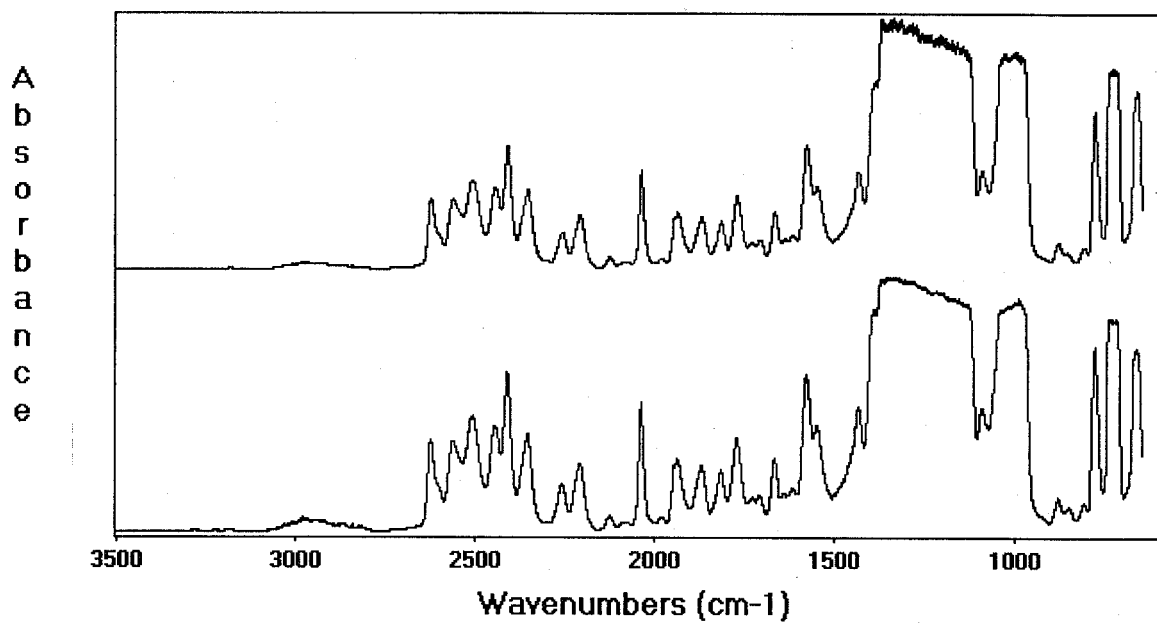


Figure 8. Initial (lower) and 48 week (upper) 5330 Pa spectra for nitronic 40 in FC-218 at 150 °C.

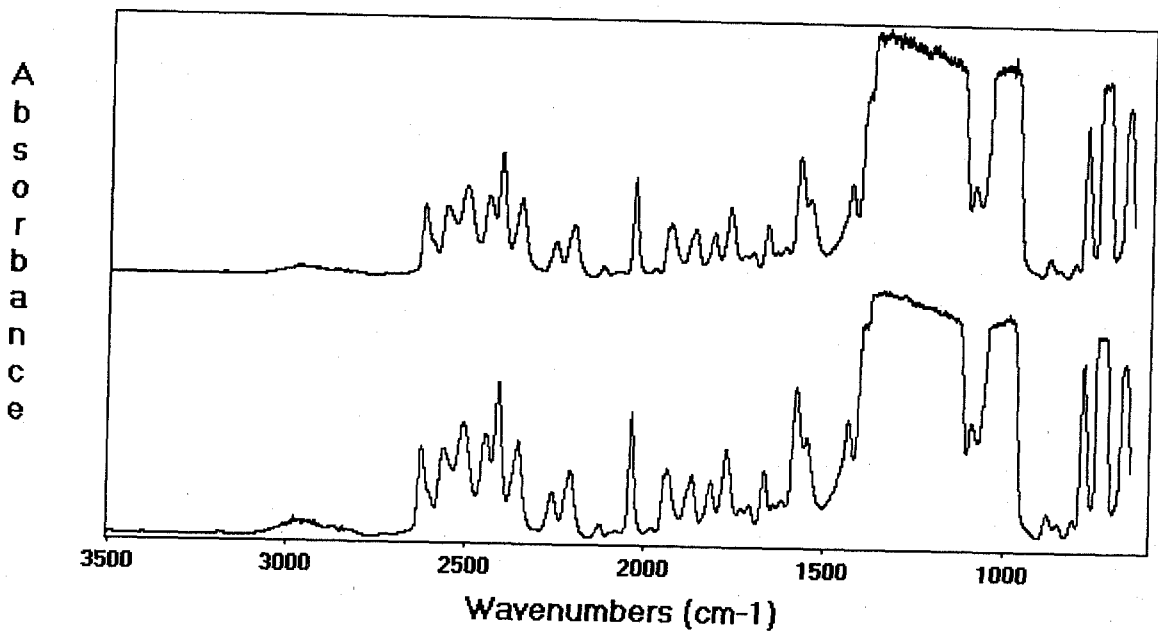


Figure 9. Initial (lower) and 48 week (upper) 5330 Pa spectra for Ti-15-3-3-3 in FC-218 at 150 °C.

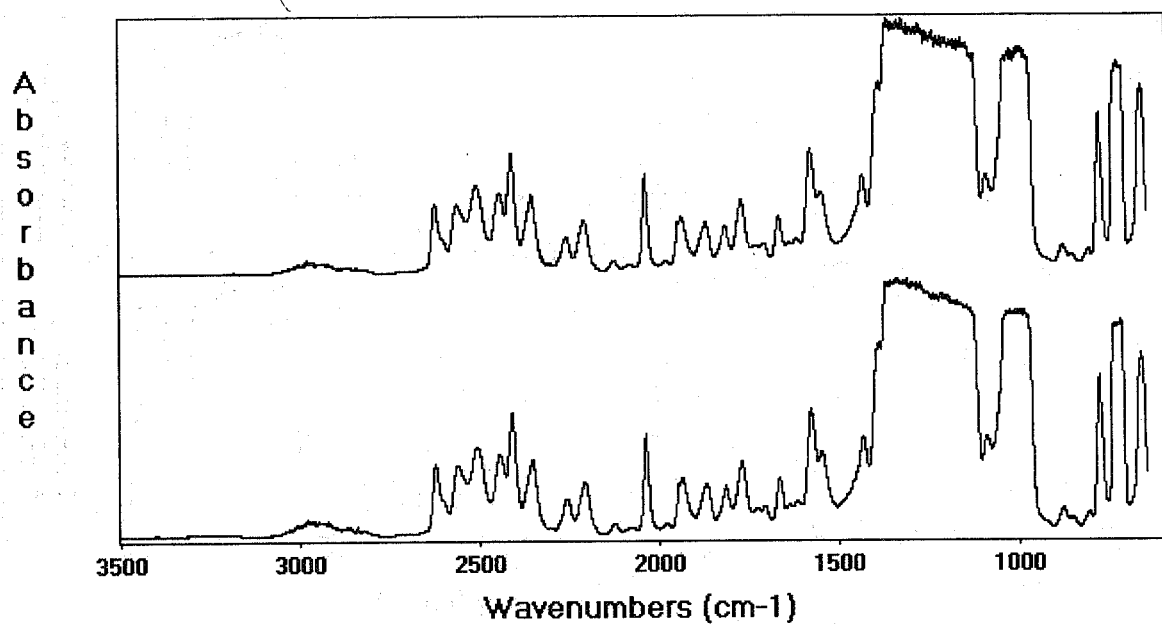


Figure 10. Initial (lower) and 40 week (upper) 5330 Pa spectra for C4130 in FC-218 at 150 °C.

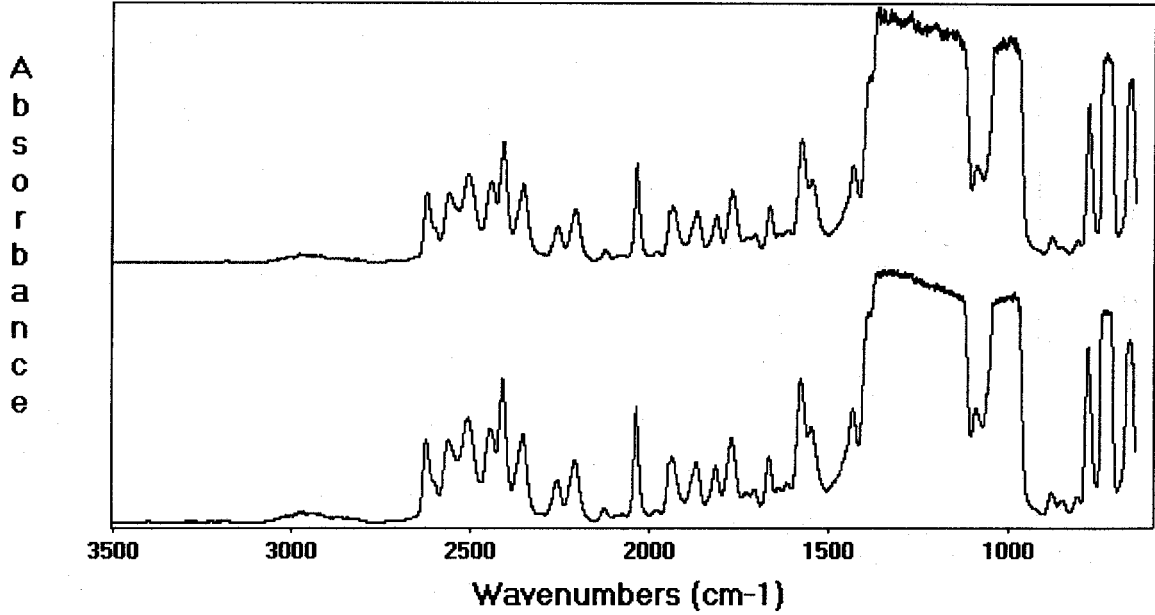


Figure 11. Initial (lower) and 48 week (upper) 5330 Pa spectra for I625 in FC-218 at 150 °C.

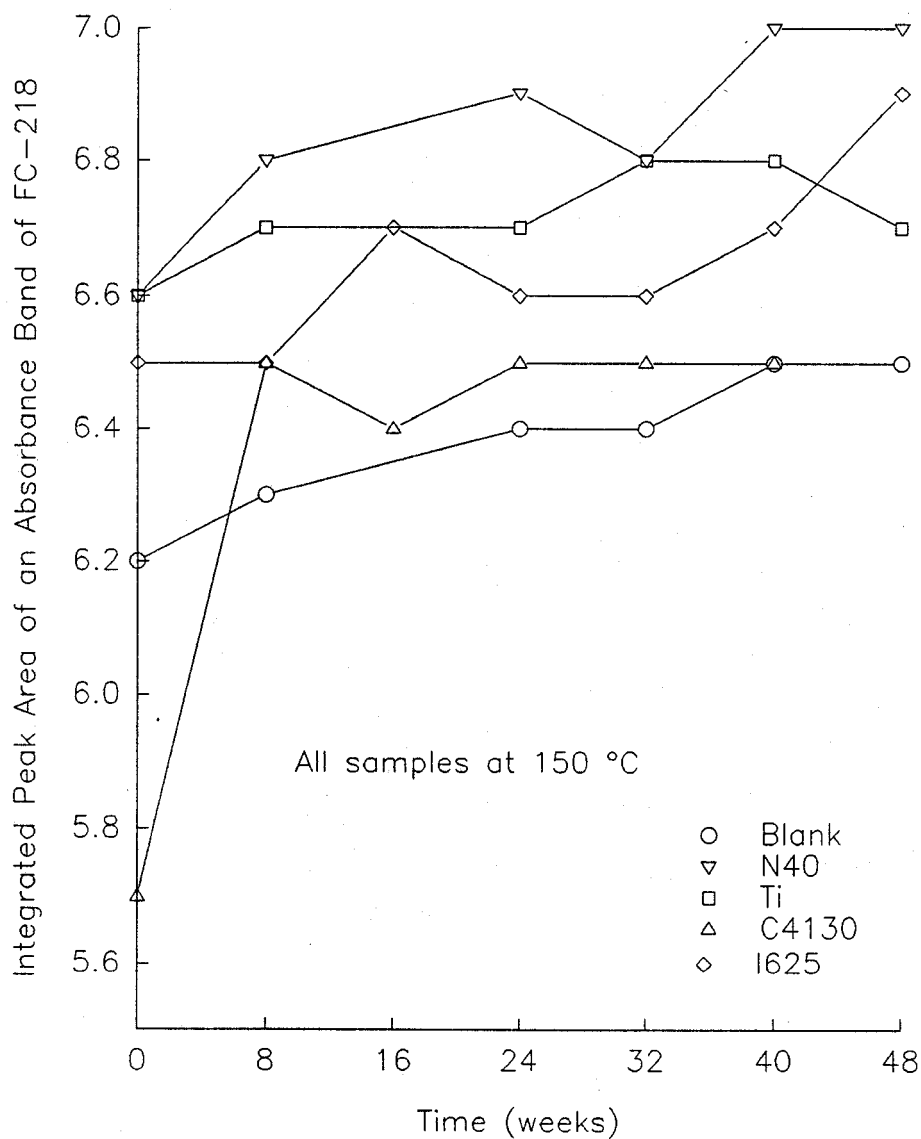


Figure 12. Integrated peak areas for all samples of FC-218 at 150 °C plotted as a function of time.

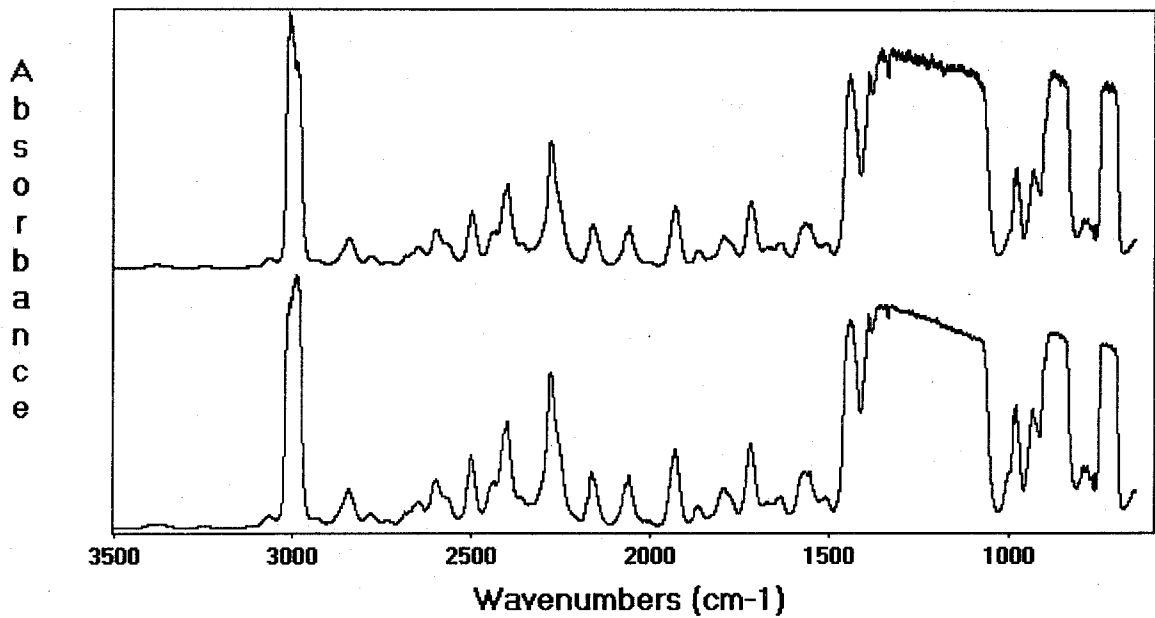


Figure 13. Initial (lower) and 48 week (upper) 5330 Pa spectra for the blank for HFC-125 at 23 °C.

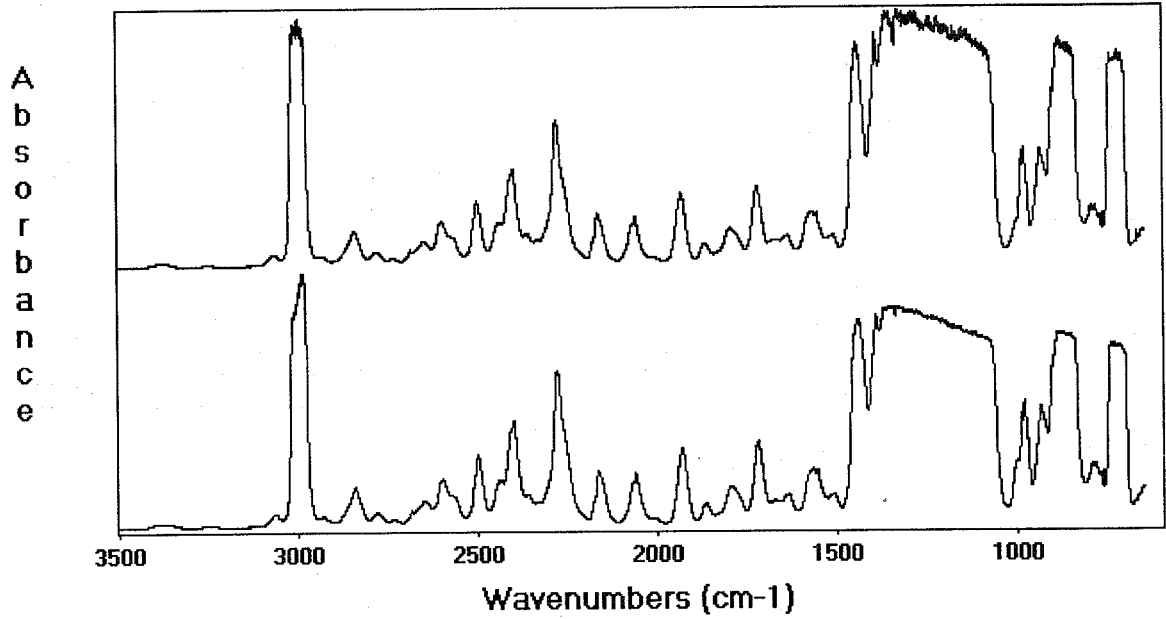


Figure 14. Initial (lower) and 48 week (upper) 5330 Pa spectra for the blank in HFC-125 at 150 °C.

Table 13. Integrated peak areas for the C-H stretch absorbance band in the 53.3 Pa spectra for HFC-125 at 23 and 150 °C and the spectral comparisons

		Integrated Area from 2963 to 3038 cm ⁻¹ (± 0.042)							Spectral Comparison (± 0.00095) ^a
		Week Number							
Metal	Temp. (°C)	0	8	16	24	32	40	48	
Blank	23	2.8	NM ^b	NM	2.7	NM	2.8	2.7	0.996
N40	23	2.7	NM	NM	2.7	NM	2.7	2.7	0.997
Ti	23	2.8	NM	NM	2.8	NM	2.8	2.8	0.996
C4130	23	2.8	2.8	2.8	2.9	2.8	NM	NM	0.998
I625	23	2.8	NM	2.8	2.8	2.8	2.8	2.9	0.998
Blank	150	2.8	2.8	NM	2.8	2.7	2.8	2.8	0.995
N40	150	2.8	2.8	NM	2.8	2.7	2.8	2.8	0.995
Ti	150	2.8	2.8	NM	2.8	2.7	2.8	2.8	0.996
C4130	150	2.8	2.9	2.8	2.8	2.9	2.9	NM	0.998
I625	150	2.8	2.9	2.8	2.8	2.8	2.8	2.9	0.998

^a Number of observations was 3

^b Not measured

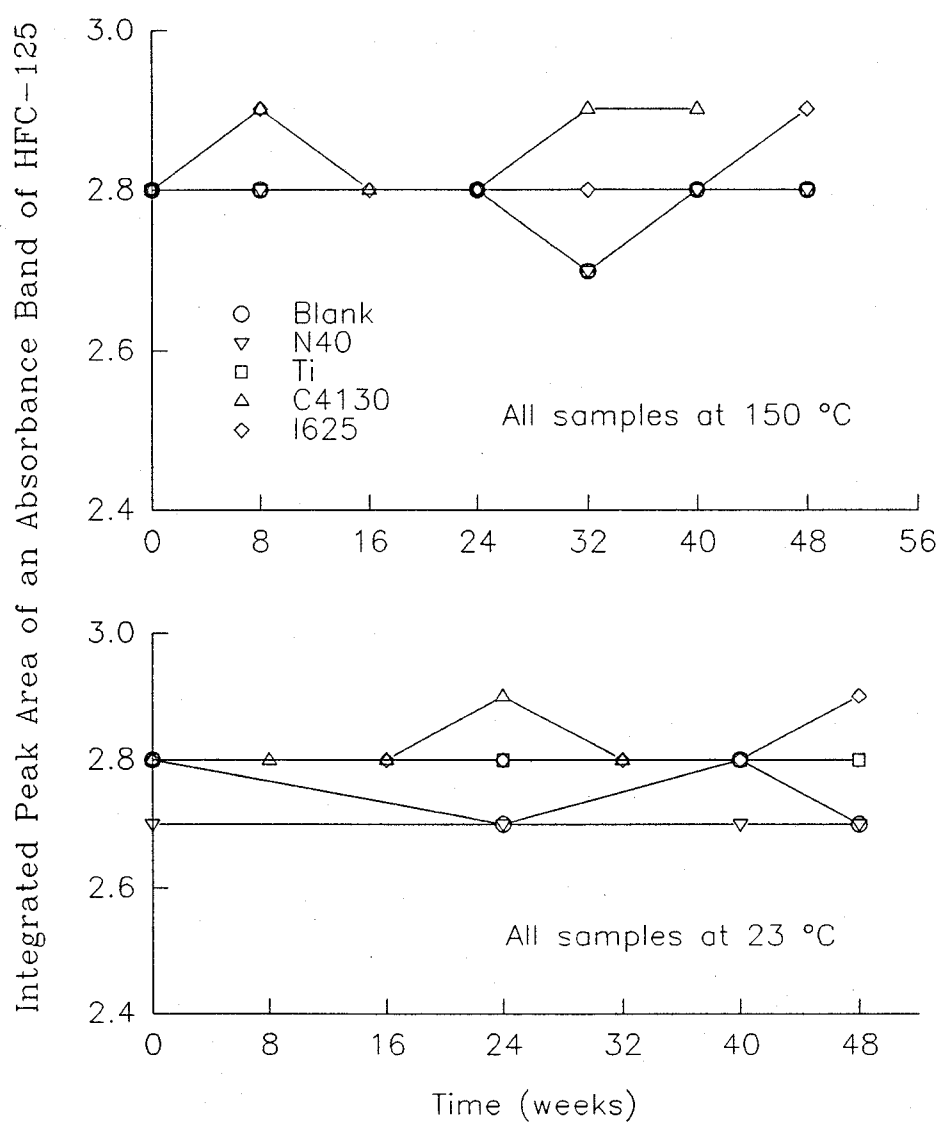


Figure 15. Integrated peak areas for all samples of HFC-125 at 23 °C and 150 °C plotted as a function of time.

In the 5330 Pa spectrum of HFC-125 a small amount of CO_2 ($<100 \mu\text{L/L}$) was detected in all of the initial analyses. Table 14 shows the integrated areas under the absorbance band at 670 cm^{-1} for CO_2 for all samples and temperatures. Figure 16 is the graphic representation of this data. At 23°C no changes in the amount of CO_2 were seen. At 150°C the CO_2 content in the samples increased anywhere from three and a half to a twelve times after 32 weeks. Beyond 32 weeks the CO_2 concentration remained constant. These data confirm the visual observations of an increase in the CO_2 content with time and temperature. The CO_2 could be from outgassing or from agent decomposition in air, which would also yield H_2O , HF, HI, or other compounds. These would be measurable if they didn't sorb to or react with the cylinder walls or metal coupons. There were no hints from the spectra of the above compounds forming, so the CO_2 increase was probably from outgassing. It should be noted that the increase in this peak is not sufficient to change the spectral comparisons.

There are no other apparent changes in the initial and final spectra of any of the cylinders at 23°C or 150°C .

7.3.3 HFC-227ea. HFC-227ea is a three carbon chain molecule with C-C and C-F bonds and a C-H bond. Of the three fluorocarbon agents this agent was thought to be the most likely to undergo degradation at elevated temperatures. The test matrix (Table 1) specifies that this agent was to be tested at 23 , 125 , and 150°C to see if thermal degradation would result. Figures 17-19 show the initial and final spectra at 5330 Pa for the blank at the three temperatures, respectively. Visual examination of the baselines and comparison of the spectra at 5330 Pa show no additional absorbance bands appearing in any of the spectra at any temperature. This is true for all of the metal samples at all three temperatures. The initial and final spectra for all of these samples are shown in Appendix B for reference.

Table 15 shows the integrated peak areas for the C-H absorbance band and the spectral comparisons for each metal and blank at each temperature. The integrated area for I625 at 150°C is half that for the other cylinders. This is a result of incomplete filling at the outset. Figure 20 is the graphical representation of the data in Table 15. As with the HFC-125, there was little if any change in the peak areas with time or temperature. Also the data show no tendencies to drift either up or down. All of the reported aged data areas fall within two standard deviations of their respective means. The spectral comparisons are all 0.997 or greater. The blank, Nitronic 40, and Ti at 125°C all had spectral comparisons higher than their respective 23°C controls. The 125°C samples were prepared and analyzed later in the study. By this time the analytical technique had become more efficient and quite routine, leading to better spectral comparisons.

7.3.4 Summary of Fluorocarbon Area Data. The above graphs of the agent peak areas suggested that no changes were occurring in the agents. Table 16 is a summary of the area data from Tables 12, 13 and 15. This table shows only the initial and final peak areas along with the number of weeks each sample was aged. The last column shows whether the final data areas changed significantly at the 99 % confidence interval. None of the final peak areas were significantly less for any agent. All of the final areas for the FC-218 were actually higher than their original peak areas. For a peak to increase, the change has to be in the analysis. As such, the "increase" may set a level of uncertainty.

Table 17 summarizes the spectral comparisons for all agents tested at 150°C . Since there were no ambient controls for FC-218, the spectral comparisons listed for this agent are simply the final spectra compared to the initial spectra. These spectral comparisons suggest that little change in any of the samples occurred. For the other two agents, the spectral comparisons are amazingly similar. With the exception of the blank and Nitronic 40 in HFC-125, which showed a slight decrease, but not statistically less at the 99 % confidence interval, there were no changes in the spectral comparisons for

Table 14. Integrated peak areas for an absorbance band of CO₂ in the 5330 Pa spectra of HFC-125 at 23 and 150 °C

		Integrated Area from 667 to 671 cm ⁻¹ (± 0.0023)						
		Week Number						
		0	8	16	24	32	40	48
Metal	Temp. (°C)							
Blank	23	0.01	NM ^a	NM	0.01	NM	0.01	0.01
N40	23	0.01	NM	NM	0.01	NM	0.01	0.01
Ti	23	0.01	NM	NM	0.01	NM	0.01	0.01
C4130	23	0.02	0.01	0.01	0.01	0.01	NM	NM
I625	23	0.01	NM	0.01	0.01	0.01	0.01	0.01
Blank	150	0.01	0.06	NM	0.08	0.09	0.09	0.09
N40	150	0.01	0.08	NM	0.10	0.12	0.12	0.12
Ti	150	0.01	0.06	NM	0.07	0.08	0.08	0.08
C4130	150	0.01	0.06	0.08	0.09	0.09	0.10	NM
I625	150	0.02	0.04	0.06	0.07	0.07	0.08	0.09

^a Not measured

samples aged at elevated temperatures. The summary data presented in Tables 16 and 17 indicate the fluorocarbon agents are stable at elevated temperatures for as long as 48 weeks.

7.3.5 Iodotrifluoromethane (CF₃I). This agent contains C-F bonds and a C-I bond. The C-I bond in this molecule is very weak, about 223 kJ/mole (Felder, 1992). This suggests that degradation, particularly at elevated temperatures, may be a factor. Additionally, the presence of moisture in the storage vessels at elevated temperatures was investigated, since water was hypothesized to be an accelerator of degradation. Finally, the possibility that the addition of copper to the cylinders might inhibit degradation was investigated. Therefore, this agent was tested not only at three temperatures, but also at four different conditions of copper and moisture content (Table 1).

The initial spectroscopic analyses of the three lots of CF₃I that were tested indicated that they contained CO₂ and CF₃H. These could have been left from the synthesis or they may be an indication that some degradation of the agent has already occurred. The amount of these impurities depended in large part to the amount of agent still remaining in the storage container when the test cylinders were filled. Since the boiling points of both CO₂ and CF₃H are lower than that of CF₃I, the vapor that is removed from a storage tank is richer in these impurities. Table 10 shows the starting impurity levels of CO₂ and CF₃H for each of the lots used. Notice in the footnotes the amount of agent remaining in the storage tanks when they were analyzed. Lot number 226941712 was analyzed before any of the agent had been used and the CO₂ and CF₃H were the highest. Lot number 226941891 was nearly empty when it was analyzed and it contained little CO₂ and undetectable CF₃H (probably present, but below the detection limit of the method.) In the forthcoming graphical presentations of the data for these impurities, the initial areas vary up and down the y-axis, generally, as a function of which lot of CF₃I was used and when the cylinder was filled (higher areas as a result of fuller tanks.)

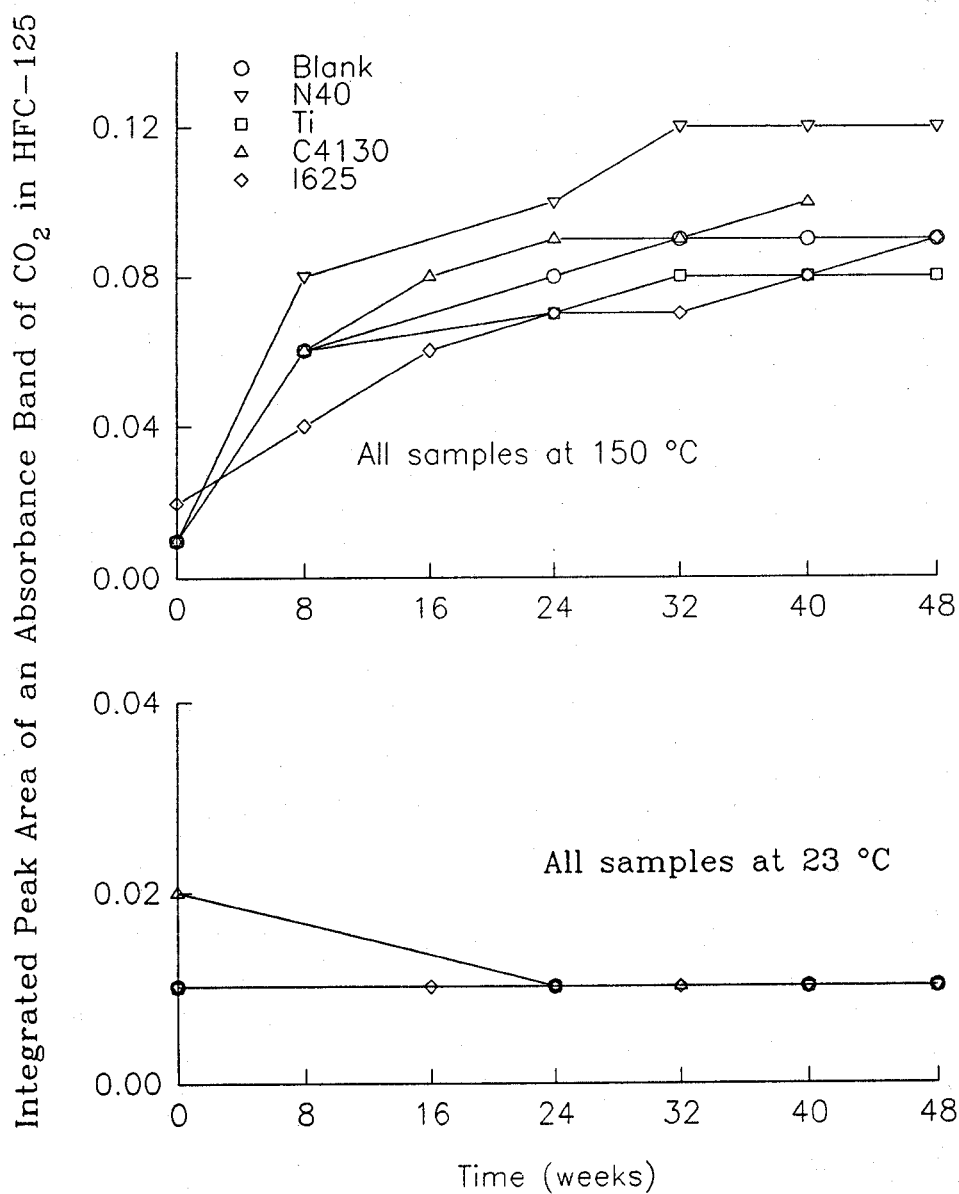


Figure 16. Integrated peak areas for the CO₂ absorbance band at 670 cm⁻¹ for all samples of HFC-125 at 23 °C and 150 °C plotted as a function of time.

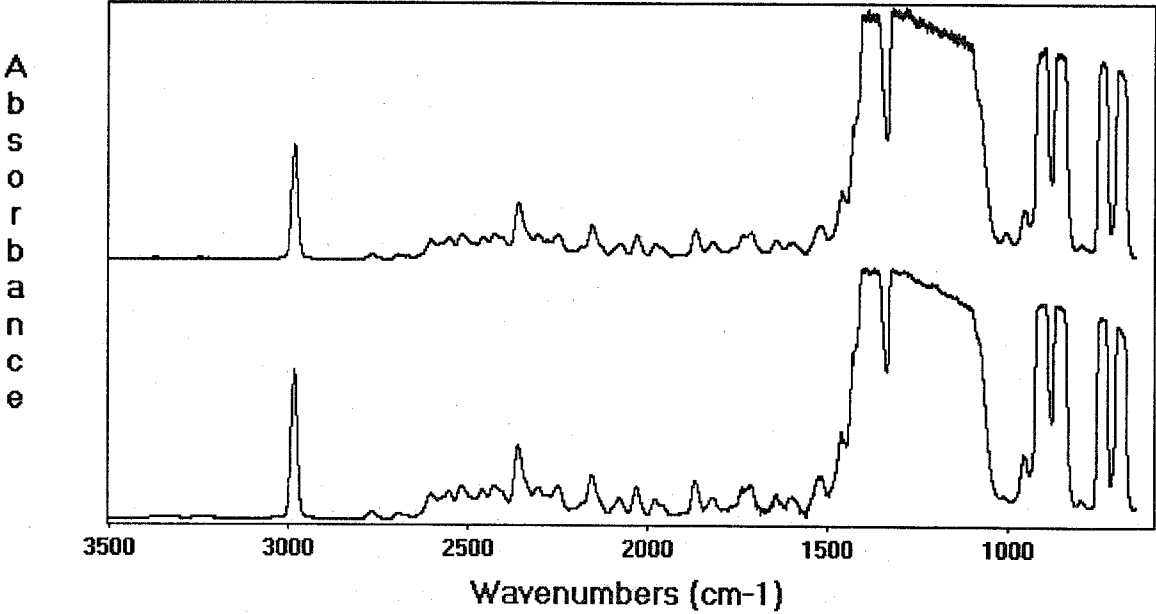


Figure 17. Initial (lower) and 48 week (upper) 5330 Pa spectra of the blank in HFC-227ea at 23 °C.

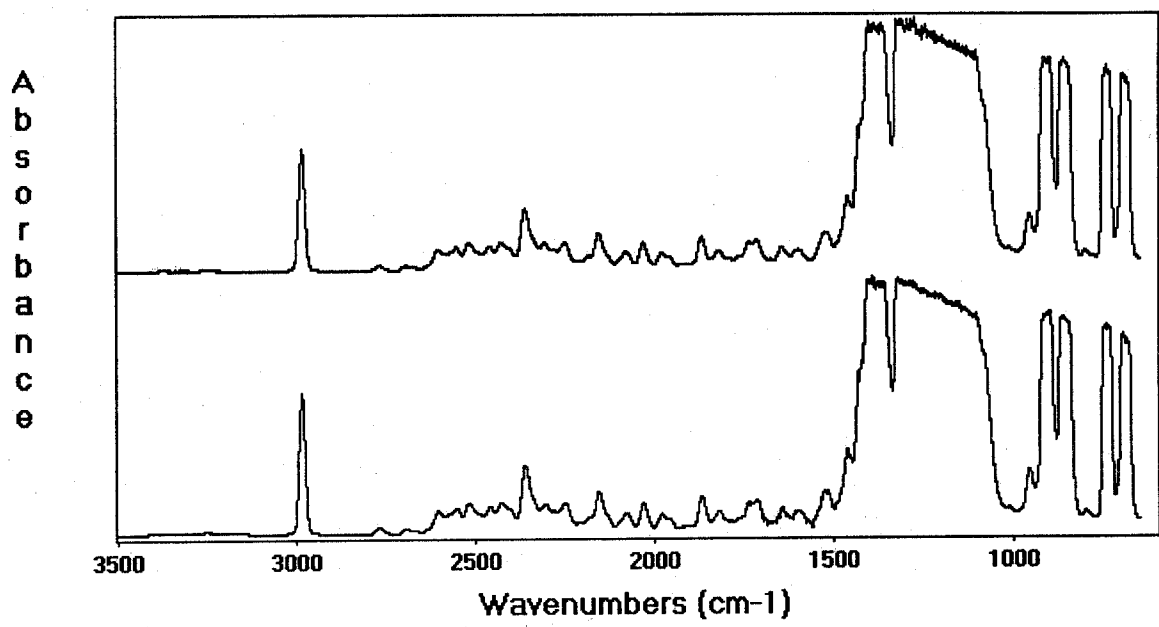


Figure 18. Initial (lower) and 40 week (upper) 5330 Pa spectra for the blank in HFC-227ea at 125 °C.

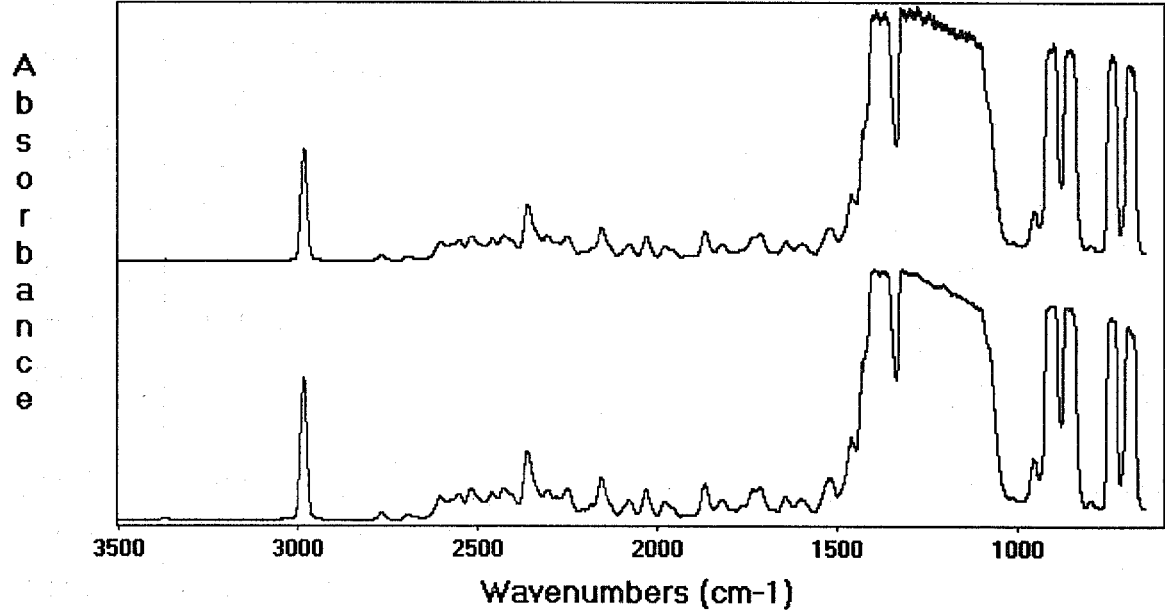


Figure 19. Initial (lower) and 48 week (upper) 5330 Pa spectra of the blank in HFC-227ea at 150 °C.

Table 15. Integrated peak areas for the C-H stretch absorbance band in the 53.3 Pa spectra of HFC-227ea at 23, 125, and 150 °C and the spectral comparisons

		Integrated area from 2966 to 3006 cm ⁻¹ (± 0.0095)							Spectral comparison (± 0.00044) ^a
		Week number							
Metal	Temp. (°C)	0	8	16	24	32	40	48	
Blank	23	0.22	NM ^b	NM	0.21	NM	0.20	0.21	0.997
N40	23	0.21	NM	NM	0.20	NM	0.19	0.20	0.997
Ti	23	0.21	NM	NM	0.20	NM	0.20	0.20	0.997
C4130	23	0.19	0.19	0.19	0.18	0.20	NM	NM	0.999
I625	23	0.18	NM	0.19	0.18	0.19	0.19	0.19	0.999
Blank	125	0.21	0.22	0.21	0.21	0.23	0.20	NM	0.999
N40	125	0.19	0.20	0.20	0.20	0.21	0.18	NM	0.999
Ti	125	0.19	0.19	0.19	0.19	0.20	0.18	NM	0.999
C4130	125	0.20	0.20	0.19	0.20	0.21	0.20	NM	0.999
I625	125	0.20	0.20	0.20	0.20	0.20	0.20	NM	0.999
Blank	150	0.20	0.20	NM	0.20	0.19	0.19	0.19	0.997
N40	150	0.20	0.20	NM	0.21	0.18	0.20	0.19	0.997
Ti	150	0.23	0.23	NM	0.23	0.21	0.23	0.22	0.997
C4130	150	0.20	0.19	0.19	0.19	0.21	0.20	NM	0.999
I625	150	0.10 ^c	0.11	0.12	0.10	0.11	0.10	0.11	0.999

^a Number of observations was three^b Not measured^c Improper filling of cylinder at outset of test.

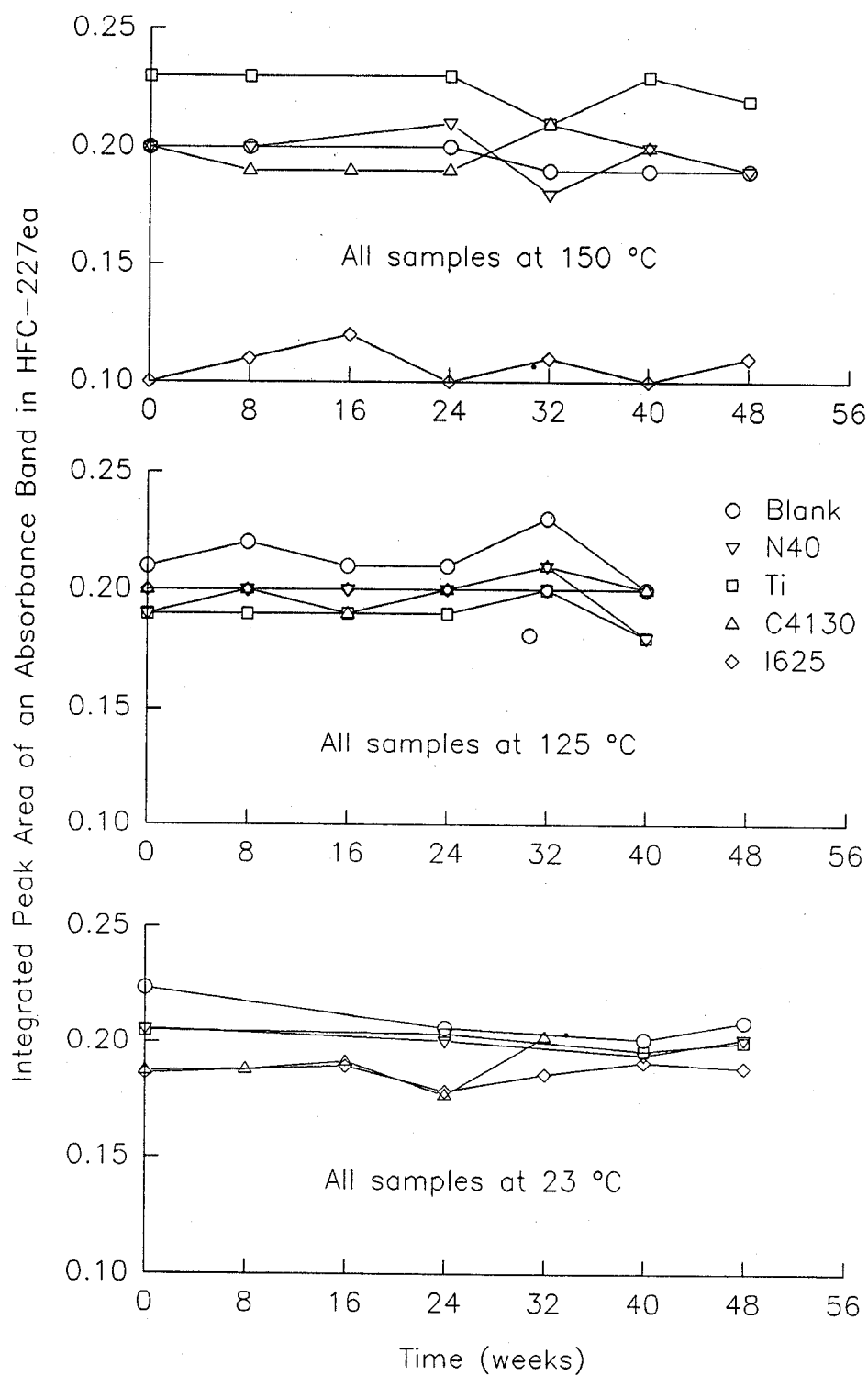


Figure 20. Integrated peak areas for all samples of HFC-227ea at 23 °C, 125 °C, and 150 °C plotted as a function of time.

Table 16. Summary of the initial and final peak areas for the fluorocarbon agents at all temperatures

Metal	Number of weeks	Temp (°C)	Initial	Final	Significant @ 3x uncertainty
FC-218:			area \pm (0.15)		
Blank	48	150	6.2	6.5	no
N40	48	150	6.6	7.0	no
Ti	48	150	6.6	6.7	no
C4130	40	150	5.7 ^a	6.5	--
I625	48	150	6.5	6.9	no
HFC-125:			area \pm (0.042)		
Blank	48	23	2.8	2.7	no
N40	48	23	2.7	2.7	no
Ti	48	23	2.8	2.8	no
C4130	32	23	2.8	2.8	no
I625	48	23	2.8	2.9	no
Blank	48	150	2.8	2.8	no
N40	48	150	2.8	2.8	no
Ti	48	150	2.8	2.8	no
C4130	40	150	2.8	2.9	no
I625	48	150	2.8	2.9	no
HFC-227ea:			area \pm (0.0095)		
Blank	48	23	0.22	0.21	no
N40	48	23	0.21	0.20	no
Ti	40	23	0.21	0.20	no
C4130	32	23	0.19	0.20	no
I625	48	23	0.18	0.19	no
Blank	40	125	0.21	0.20	no
N40	40	125	0.19	0.18	no
Ti	40	125	0.19	0.18	no
C4130	40	125	0.20	0.20	no
I625	40	125	0.20	0.20	no
Blank	48	150	0.20	0.19	no
N40	48	150	0.20	0.19	no
Ti	48	150	0.23	0.22	no
C4130	40	150	0.20	0.20	no
I625	48	150	0.10 ^b	0.11	no

^a Improperly filled gas cell during analysis^b Cylinder did not fill completely at outset of test.

Table 17. Spectral comparisons of the initial and aged fluorocarbon agents

Agent		FC-218	HFC-125 (± 0.00095)		HFC-227ea (± 0.00044)		
Temp. ($^{\circ}\text{C}$)		150	23	150	23	125	150
Metal	Weeks tested						
Blank	48	0.996	0.996	0.995	0.997	0.997	0.997
N40	48	0.996	0.997	0.995	0.997	0.997	0.997
Ti	48	0.996	0.996	0.996	0.997	0.997	0.997
C4130	40	0.999	0.998	0.998	0.999	0.999	0.999
I625	48	0.998	0.998	0.998	0.999	0.999	0.999

As mentioned earlier, an absorbance band in the 5330 Pa spectra of CF_3I tested at 100 and 150°C began to appear around 950 cm^{-1} after 4 weeks of aging. This absorbance was looked for in reference spectra of C_2F_6 , COF_2 , and CH_3F , but does not appear in any of these compounds. This absorbance band is in the region of $\text{C}=\text{C}$ bond stretch frequencies. The absorbance band has not been definitely assigned, but may correspond to the presence of ethylene or a fluorinated alkene. Since the corresponding $\text{C}-\text{H}$ stretch band for ethylene is absent (or below the detection limit at this concentration), it is suspected that the absorbance band might correspond to a fluorinated alkene. Reference spectra for double bonded fluorinated compounds such as C_2F_4 , $\text{C}_2\text{H}_2\text{F}_2$ (the 1,1 compound), and $\text{C}_2\text{H}_3\text{F}$ did not have an absorbance band in this region of the spectrum. Not all of the spectra for the fluorinated alkenes are present in our library, so positive identification still remains unresolved. This fluorinated alkene peak and the increase in the impurity peaks are shown in Figure 21. The lower spectrum is the initial, 5330 Pa spectrum of a moist sample without copper and containing phosphate-treated C4130. This is one of the samples that initially had no detectable CF_3H or CO_2 . The upper spectrum is that of the corresponding aged sample after 20 weeks at 150°C . The small peak at 670 cm^{-1} is an absorbance band of CO_2 , the peaks at 700, 1400, and 3000 cm^{-1} are from CF_3H , and the absorbance band at 950 cm^{-1} for the fluorinated alkene. This spectrum illustrates quite well the changes that occurred in the CF_3I at elevated temperatures.

The spectrum in Figure 22 shows a spectrum that results from the subtraction of the spectra shown in Figure 21. This subtracted spectrum not only shows the peaks mentioned in Figure 21, but also shows the characteristic peak at 2150 cm^{-1} for carbon monoxide and the other characteristic peak at 2360 cm^{-1} for CO_2 . The peaks in the 1200 cm^{-1} region correspond to agent peaks that did not completely subtract out because of their high intensity.

The following data for CF_3I are presented for the dry and moist conditions and with or without the presence of copper. Changes in peak areas for agent, CO_2 , CF_3H , and fluorinated alkene are the order of presentation for each test condition.

7.3.5.1 Changes in the Agent Peak Area of CF_3I in the 53.3 Pa Spectra for the Different Conditions. Tables 18-21 show the integrated areas for the absorbance band in the agent and the spectral comparisons. The data presented in these tables are an average of the three replicate gas cell fillings. Figures 23-26 show the respective graphical representations of the data. Figure 23 shows the

data for the dry condition without copper. At 23 °C, with the exception of the outlier for Nitronic 40 (a result of improper filling of the gas cell), the data are closely bunched and remain relatively constant. The same was true for the data at 100 °C. The data for 150 °C were more spread out but generally seem to equilibrate after a slight decrease.

Figure 24 shows the peak area data for the dry condition with copper. At 23 °C, the areas tended to drift downward slightly, then equilibrated. Overall, there is not much change in the data for any of the metals over the course of the study. The blank at 100 °C was scattered but also unchanged. The areas at 150 °C were drifting downward consistently. This suggests that copper is not inhibiting the degradation of CF_3I at the elevated temperature.

Figure 25 shows the peak area data for the moist condition without copper. There were no 23 °C controls for this condition. The areas for the blank at 100 °C remained fairly constant over the study. The peak areas at 150 °C drifted downward slightly, but reached a minimum at about 32 weeks and started to equilibrate. All of the H_2O may have been consumed by this time. The areas at 150 °C were more scattered than the previous areas at 150 °C for the dry condition.

Figure 26 shows the peak area data for the moist condition with copper. Once again there were no controls at 23 °C for this condition. The areas were changing similarly to the moist condition without copper shown in Figure 25.

The above graphs suggest that small decreases in agent peak area were occurring, especially at 150 °C and in the moist condition more so than the dry condition. It appears that copper is not inhibiting the degradation, H_2O causes accelerated degradation, and both combined cause about the same amount, all at 150 °C. The other metals seem to have no effect. Since the samples at 100 °C showed no effect, it may be that at ≤ 100 °C there is little loss of CF_3I .

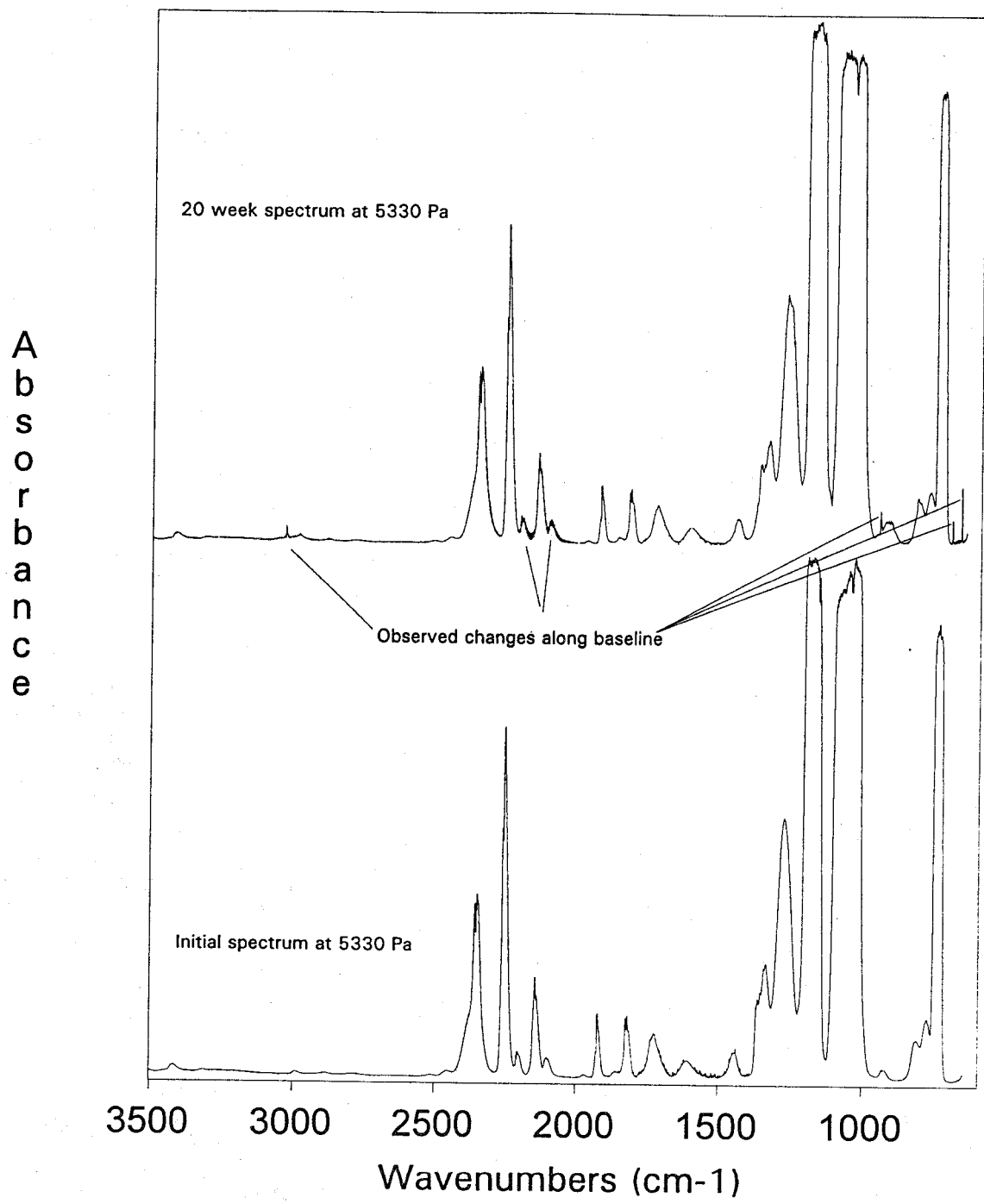


Figure 21. Illustration of the changes taking place in CF_3I samples at elevated temperatures.

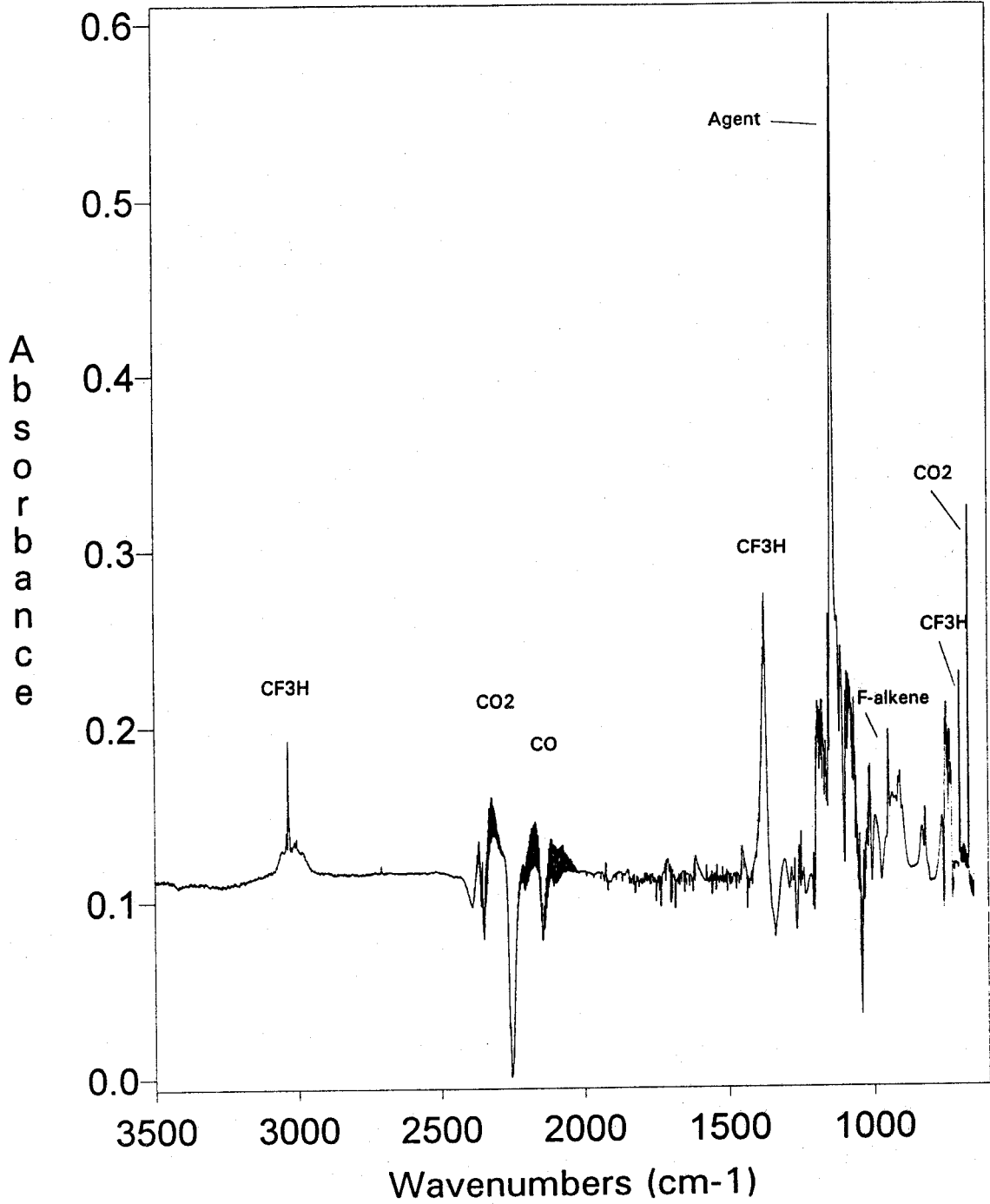


Figure 22. The subtracted spectrum at 5330 Pa for CF_3I in the presence of C4130 alloy and moisture at 150 °C after 20 weeks.

Table 18. Integrated peak areas for an absorbance band of CF_3I in the 53.3 Pa spectra tested in the dry condition without copper and the spectral comparisons

		Integrated area from 2219 to 2274 cm^{-1} (± 0.011)								
		Week number								
Metal	Temp. ($^{\circ}\text{C}$)	0	4	8	16	20	24	28	32	36
Blank	23	0.25	0.25	0.24	0.24	0.25	0.22	NM ^a	0.24	NM
N40	23	0.19	0.27	0.25	0.25	0.25	0.24	NM	0.26	NM
Ti	23	0.26	0.25	0.25	0.25	0.23	0.23	NM	0.24	NM
C4130	23	0.24	0.25	0.26	0.24	0.22	0.24	NM	0.23	NM
I625	23	0.27	0.26	0.24	0.24	0.24	0.24	NM	0.24	0.24
Blank	100	0.25	0.24	0.25	0.25	0.24	0.25	0.24	0.25	0.21
N40	100	0.24	0.25	0.25	0.24	0.24	0.24	0.23	0.25	-- ^b
Ti	100	0.25	0.25	0.24	0.24	0.24	0.23	0.24	0.25	0.24
C4130	100	0.25	0.25	0.24	0.25	0.24	0.23	NM	0.25	0.24
I625	100	0.25	0.26	0.25	0.25	0.25	0.22	NM	0.23	0.24
Blank	150	0.28	0.28	0.28	0.27	0.26	0.25	0.25	0.25	0.25
N40	150	0.27	0.26	0.27	0.25	0.25	0.24	0.24	0.23	0.24
Ti	150	0.28	0.27	0.27	0.26	0.25	0.25	0.26	0.25	0.25
C4130	150	0.29 ^c	0.24	0.24	0.24	0.26	0.21	NM	0.21	0.23
I625	150	0.25	0.25	0.24	0.23	0.22	0.23	NM	0.22	0.22

Table 18 (cont.). Integrated peak areas for an absorbance band of CF_3I in the 53.3 Pa spectra tested in the dry condition without copper and the spectral comparisons

		Integrated area from 2219 to 2274 cm ⁻¹ (± 0.011)				Spectral comparison (0.0018) ^d
		Week number				
		40	44	48	52	
Metal	Temp. (°C)					
Blank	23	0.23	NM	0.23	NM	0.996
N40	23	0.25	NM	0.24	NM	0.998
Ti	23	0.24	NM	0.23	NM	0.998
C4130	23	0.25	NM	NM	NM	0.999
I625	23	0.25	0.24	NM	NM	0.998
Blank	100	0.25	0.25	NM	NM	0.999
N40	100	-- ^b	-- ^b	-- ^b	-- ^b	0.997
Ti	100	0.24	0.24	NM	NM	0.998
C4130	100	0.24	NM	NM	NM	0.999
I625	100	0.24	NM	NM	NM	0.999
Blank	150	0.25	0.25	0.24	0.25	0.991
N40	150	0.24	0.23	0.23	0.25	0.995
Ti	150	0.26	0.25	0.25	0.25	0.996
C4130	150	0.23	NM	NM	NM	0.994
I625	150	0.22	0.22	NM	NM	0.988

^a Not measured^b Cylinder emptied after 32 weeks as a result of leak^b Suspected to be an outlier because of improper gas cell filling^c Number of observations was eight.

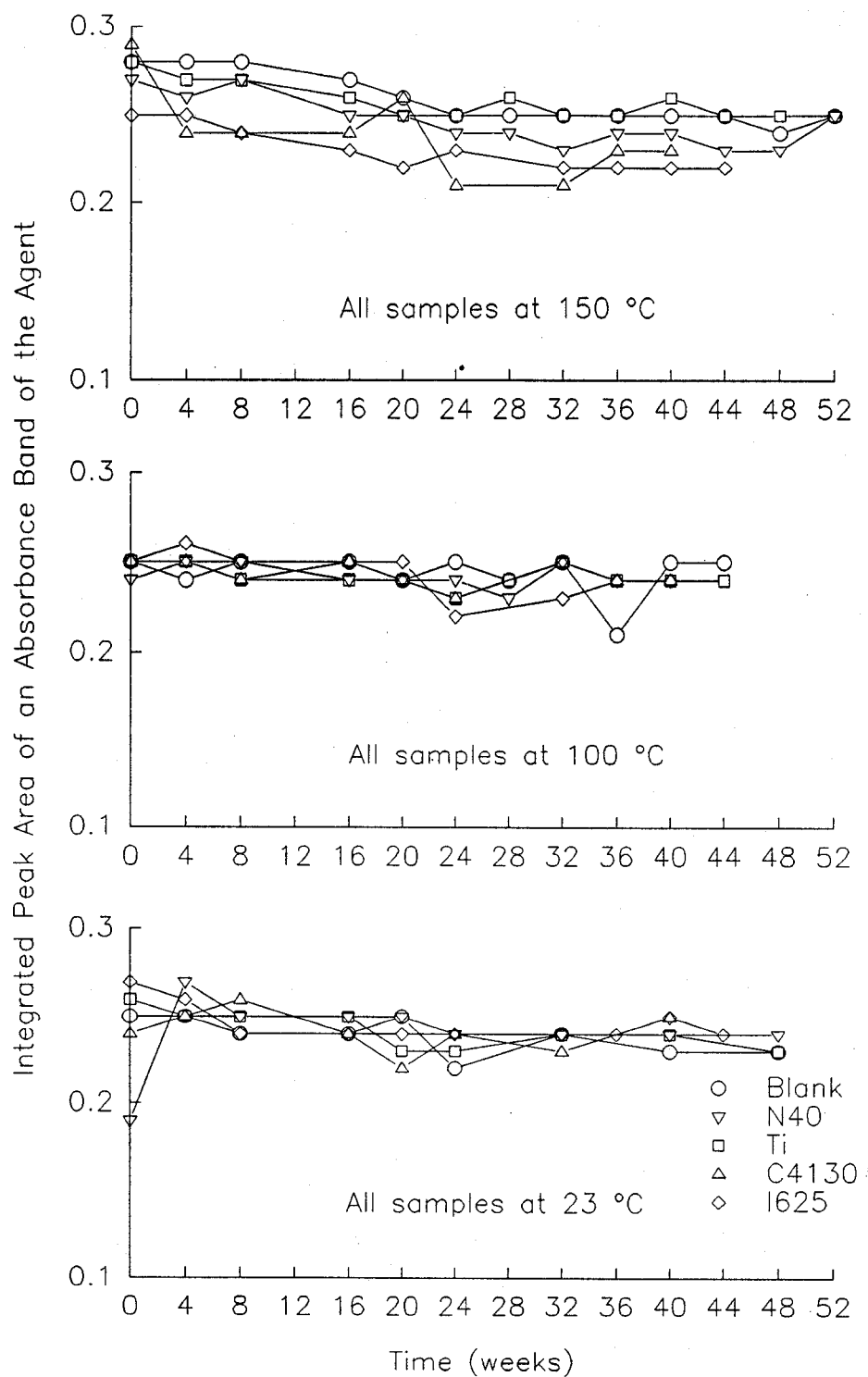


Figure 23. Integrated agent peak areas for all samples of CF_3I tested in the dry condition without copper at 23 °C, 100 °C, and 150 °C plotted as a function of time.

Table 19. Integrated peak areas for an absorbance band of CF_3I in the 53.3 Pa spectra tested in the dry condition with copper and the spectral comparisons

		Integrated area from 2219 to 2274 cm^{-1} (± 0.011)								
		Week number								
Metal	Temp. ($^{\circ}\text{C}$)	0	4	8	16	20	24	28	32	36
CDA 110 Blank	23	0.26	0.25	0.24	0.25	0.23	0.24	NM ^a	0.24	NM
CDA 110 N40	23	0.26	0.25	0.24	0.23	0.23	0.24	NM	0.24	NM
CDA 110 Ti	23	0.27	0.26	0.25	0.24	0.24	0.24	NM	0.24	NM
CDA 110 C4130	23	0.23	0.25	0.24	0.23	0.23	0.24	NM	0.21	NM
CDA 110 I625	23	0.26	0.25	0.25	0.23	0.24	0.23	NM	0.24	0.24
CDA 110 Blank	100	0.25	0.25	0.23	0.23	0.25	0.23	0.25	0.26	-- ^b
CDA 110 Blank	150	0.29	0.26	0.26	0.26	0.25	0.24	0.25	0.23	0.24
CDA 110 N40	150	0.26	0.27	0.27	0.25	0.24	0.23	0.23	0.23	0.23
CDA 110 Ti	150	0.28	0.26	0.27	0.26	0.24	0.24	0.24	0.24	0.24
CDA 110 C4130	150	0.24	0.25	0.25	0.25	0.23	0.22	NM	0.23	0.25
CDA 110 I625	150	0.25	0.24	0.25	0.22	0.22	0.23	NM	0.23	0.23

Table 19 (cont.). Integrated peak areas for an absorbance band of CF_3I in the 53.3 Pa spectra tested in the dry condition with copper and the spectral comparisons

		Integrated area from 2219 to 2274 cm ⁻¹ (±0.011)				Spectral comparison (±0.0018) ^c
		Week number				
		Metal	Temp. (°C)	40	44	
CDA 110 Blank	23	0.25	NM	0.23	NM	0.997
CDA 110 N40	23	0.23	NM	0.24	NM	0.997
CDA 110 Ti	23	0.24	NM	0.25	NM	0.997
CDA 110 C4130	23	0.24	NM	NM	NM	0.999
CDA 110 I625	23	0.24	0.23	NM	NM	0.999
CDA 110 Blank	100	-- ^b	-- ^b	-- ^b	-- ^b	0.999
CDA 110 Blank	150	0.24	0.23	0.22	0.23	0.980
CDA 110 N40	150	0.21	0.22	0.20	0.19	0.875
CDA 110 Ti	150	0.23	0.24	0.23	0.23	0.985
CDA 110 C4130	150	0.22	NM	NM	NM	0.997
CDA 110 I625	150	0.22	0.23	NM	NM	0.994

^a Not measured

^b Cylinder emptied after 32 weeks as a result of leak

^c Number of measurements was eight.

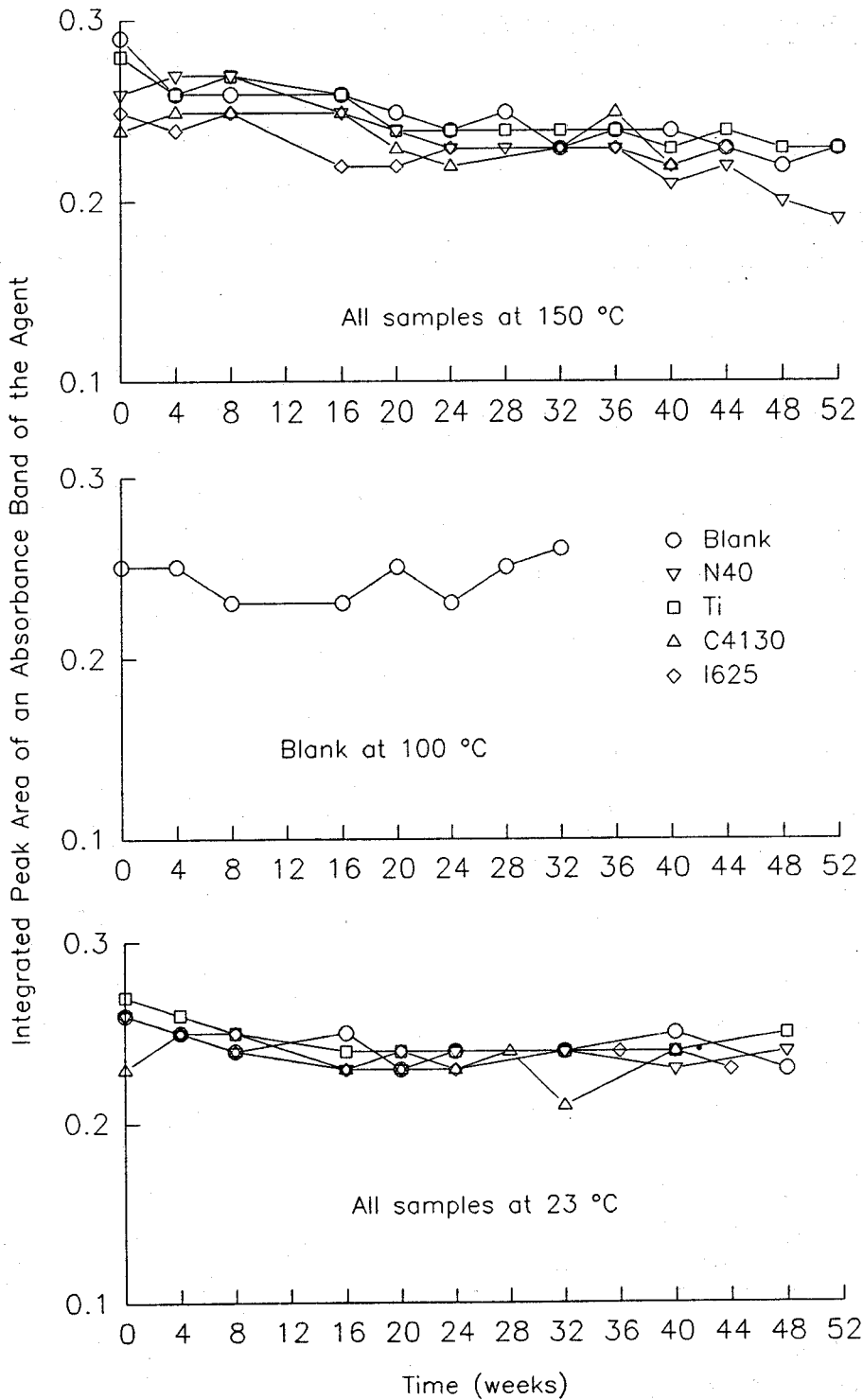


Figure 24. Integrated agent peak areas for all samples of CF_3I tested in the dry condition with copper at 23 °C, 100 °C, and 150 °C plotted as a function of time.

Table 20. Integrated peak areas for an absorbance band in the 53.3 Pa spectra of CF₃I tested in the moist condition without copper and the spectral comparisons

		Integrated area from 2219 to 2274 cm ⁻¹ (±0.011)								
		Week number								
		0	4	8	16	20	24	28	32	36
Metal	Temp. (°C)									
Blank	100	0.25	0.24	0.24	0.24	0.23	0.23	0.24	0.22	0.23
Blank	150	0.27	0.25	0.27	0.25	0.24	0.24	0.24	0.24	0.23
N40	150	0.27	0.25	0.27	0.25	0.24	0.24	0.25	0.24	0.20
Ti	150	0.28	0.25	0.27	0.27	0.24	0.24	0.24	0.24	0.24
C4130	150	0.24	0.25	0.23	0.23	0.22	0.21	NM ^a	0.20	0.22
I625	150	0.25	0.24	0.24	0.22	0.22	0.22	NM	0.21	0.21

Table 20 (cont.). Integrated peak areas for an absorbance band in the 53.3 Pa spectra of CF₃I tested in the moist condition without copper and the spectral comparisons

		Integrated area from 2219 to 2274 cm ⁻¹ (±0.011)				Spectral Comparison (±0.0018) ^b
		Week number				
Metal	Temp. (°C)	40	44	48	52	
Blank	100	0.23	0.24	NM	NM	0.999
Blank	150	0.24	0.23	0.24	0.23	0.984
N40	150	0.25	0.25	0.25	0.23	0.992
Ti	150	0.24	0.24	0.23	0.23	0.990
C4130	150	0.21	NM	NM	NM	0.990
I625	150	0.22	0.21	NM	NM	0.983

^a Not measured
^b Number of observations was eight.

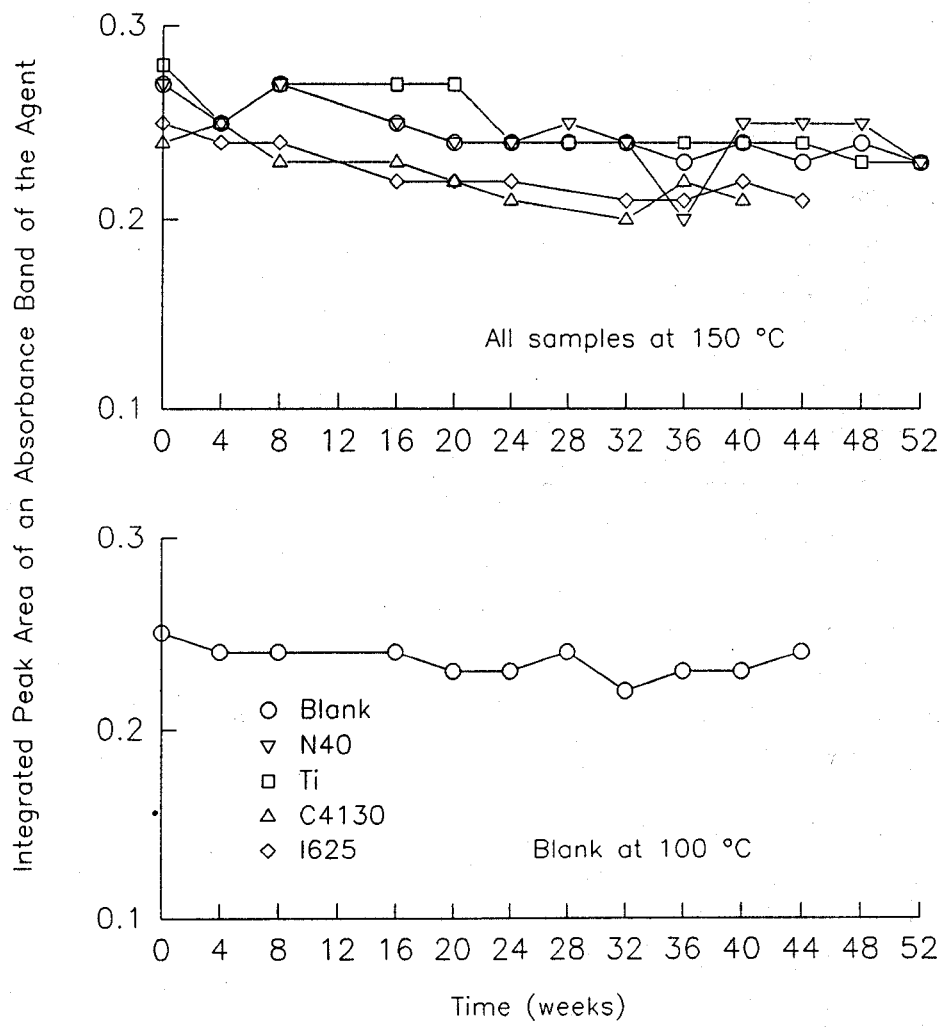


Figure 25. Integrated agent peak areas for all samples of CF_3I tested in the moist condition without copper at 100 °C and 150 °C plotted as a function of time.

Table 21. Integrated peak areas for an absorbance band in the 53.3 Pa spectra of CF_3I tested in the moist condition without copper and the spectral comparisons

		Integrated area from 2219 to 2274 cm^{-1} (± 0.011)								
		Week number								
		0	4	8	16	20	24	28	32	36
Metal	Temp. ($^{\circ}\text{C}$)									
CDA 110 Blank	100	0.25	0.24	0.23	0.24	0.22	0.22	0.23	0.23	0.23
CDA 110 Blank	150	0.27	0.25	0.26	0.25	0.25	0.22	0.23	0.22	0.22
CDA 110 N40	150	0.27	0.25	0.26	0.24	0.25	0.21	0.22	0.22	0.21
CDA 110 Ti	150	0.28	0.26	0.27	0.25	0.26	0.23	0.23	0.23	0.24
CDA 110 C4130	150	0.23	0.24	0.22	0.23	0.22	0.23	NM ^a	0.21	0.23
CDA 110 I625	150	0.23	0.23	0.23	0.23	0.21	0.22	NM	0.22	0.22

Table 21 (cont.). Integrated peak areas for an absorbance band in the 53.3 Pa spectra of CF_3I tested in the moist condition without copper and the spectral comparisons

		Integrated area from 2219 to 2274 cm ⁻¹ (±0.011)				Spectral comparison (±0.0018) ^a
		Week number				
		40	44	48	52	
Metal	Temp. (°C)	40	44	48	52	
CDA 110 Blank	100	0.23	0.24	NM	NM	0.998
CDA 110 Blank	150	0.23	0.22	0.22	0.22	0.981
CDA 110 N40	150	0.21	0.21	0.20	0.19	0.949
CDA 110 Ti	150	0.23	0.23	0.22	0.24	0.990
CDA 110 C4130	150	0.21	NM	NM	NM	0.998
CDA 110 I625	150	0.21	NM	NM	NM	0.994

^a Not measured

^b Number of observations was eight.

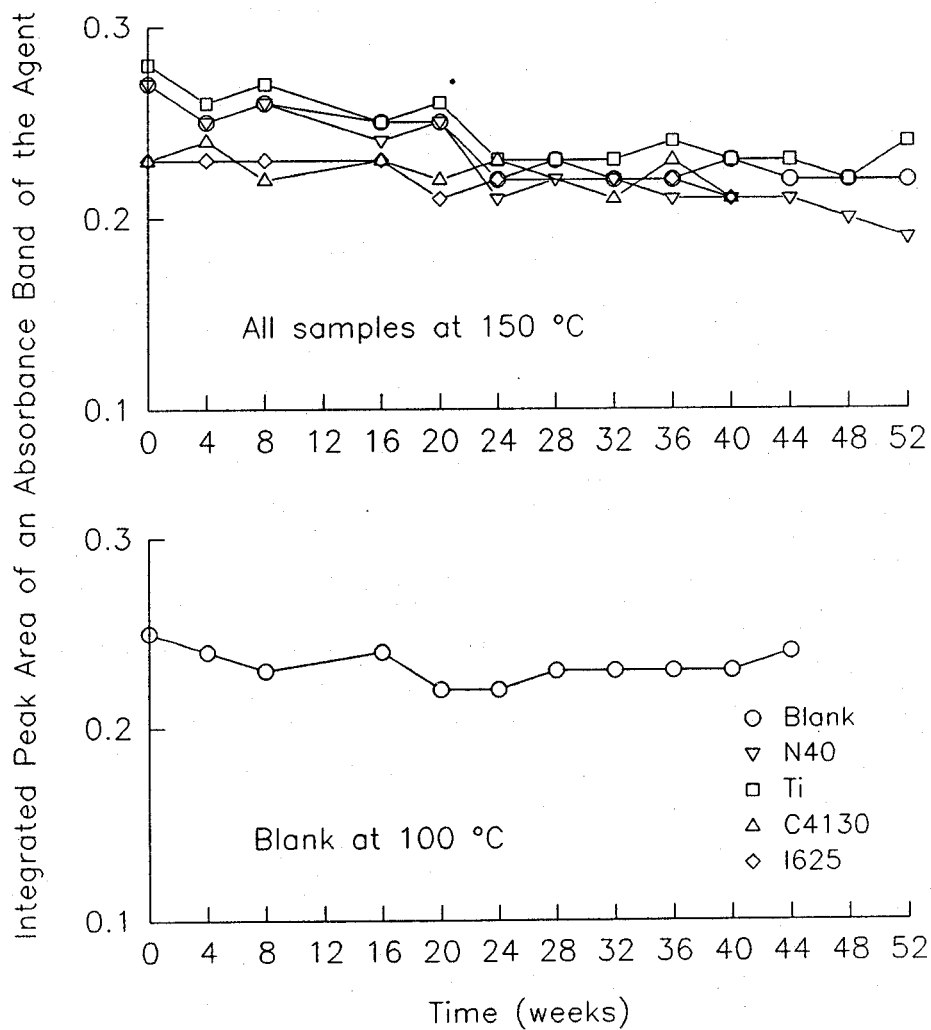


Figure 26. Integrated agent peak areas for all samples of CF_3I tested in the moist condition with copper at 100 °C and 150 °C plotted as a function of time.

7.3.5.2 Changes in the Impurity Peak Areas Appearing in the 5330 Pa Spectra. The peak area data in the remaining tables represent a single value for each analysis obtained over the course of the study. Tables 22-25 show the integrated peak areas for the absorbance band at 670 cm^{-1} for CO_2 for all temperatures and test conditions of CF_3I . Figures 27-30 are the respective graphical representations of the data. In both of the test conditions where ambient samples were tested (Figures 27 and 28), no changes in the peak areas were noted. The CO_2 concentration in the initial cylinders ranged from 26 to $460\text{ }\mu\text{L/L}$ (based on a 0.1 % by volume standard of CO_2 in N_2 .) However, all samples tested at elevated temperatures showed an increase in the CO_2 peak area. Even samples that initially contained CO_2 as low as $26\text{ }\mu\text{L/L}$ (C4130 and I625) experienced an increase in CO_2 concentration to roughly $900\text{ }\mu\text{L/L}$. The CO_2 concentration in the cylinder containing I625 metal in the dry condition with and without copper and the moist condition without copper increased from $400\text{ }\mu\text{L/L}$ to nearly $1900\text{ }\mu\text{L/L}$. The dramatic increase in the CO_2 did not occur for the I625 in the moist condition with copper, but the initial CO_2 content in this cylinder was only $26\text{ }\mu\text{L/L}$. The CO_2 content in the cylinders with the other metals only increased about half this amount. The CO_2 production continued to increase after 52 weeks. Also, all samples tested at $100\text{ }^\circ\text{C}$ showed an increase in the CO_2 peak area. The actual concentration was about half that in the $150\text{ }^\circ\text{C}$ cylinders, except for C4130 and I625 in the dry condition without copper, which had very little CO_2 present at the outset of testing.

Tables 26-29 show the integrated peak areas for the absorbance band at 700 cm^{-1} in the 5330 Pa spectrum for the CF_3H impurity. Figures 31-34 show the graphs for the respective data. There was no increase in the CF_3H peak area for any of the conditions at $23\text{ }^\circ\text{C}$ or $100\text{ }^\circ\text{C}$. However, at $150\text{ }^\circ\text{C}$ the generation of CF_3H was increasing with time and, like the CO_2 , was still increasing after 52 weeks. Noticeably different for the CF_3H increase was a longer time before the slope started to show an increase. I625 in both the dry and moist conditions without copper (Figures 31 and 33, respectively) showed a more rapid increase than the other metals. In the dry condition with copper (Figure 32) it was the Nitronic 40 metal that showed a more rapid increase.

Tables 30-33 show the integrated peak areas for the absorbance band at 950 cm^{-1} of the fluorinated alkene. Figures 35-38 show the graphs for the respective data. In this case, none of the initial samples showed any absorbance in the 950 cm^{-1} band and at $23\text{ }^\circ\text{C}$ for as long as 48 weeks there was no evidence of formation. After about 8 weeks at $100\text{ }^\circ\text{C}$, a small but easily resolved peak started to appear. In both the dry and moist condition without copper (Figures 35 and 37, respectively), the concentration was still increasing after 8 weeks. In both the dry and moist condition with copper (Figures 36 and 38, respectively), the concentration increased then equilibrated. However, after only 4 weeks at $150\text{ }^\circ\text{C}$, the concentration of the fluorinated alkene increased rapidly then began to equilibrate after 20 weeks. In the dry condition without copper at $150\text{ }^\circ\text{C}$ (Figure 35), the fluorinated alkene content maximized around 20 weeks, then equilibrated. There may have been some differentiation of the other metals with copper present at $150\text{ }^\circ\text{C}$ (Figures 36 and 38). The blank containing only copper strips, and the Ti-15-3-3-3 with copper strips in the dry condition (Figure 36) maximized in about 8 weeks, then started to drop and after 52 weeks was approaching a very low level. The Nitronic 40 and I625 metals with the copper caused more of the fluorinated alkene to appear and the decline was even more gradual. The C4130 in combination with copper resulted in the most fluorinated alkene appearing and there was no decline in the compound.

Figure 38 shows the data for the moist condition with copper. Note the similarity of this data to Figure 36 with respect to the alkene content and metal, but equilibration occurred after 20 weeks. Also of note is that the blank, which contains only copper strips, did not produce detectable amounts of the alkene at $150\text{ }^\circ\text{C}$. However, the blank at $100\text{ }^\circ\text{C}$ showed the presence of detectable fluorinated alkene; the peak area did appear to equilibrate with time. A possible explanation is that the copper is causing the double bond to break, and a higher temperature is needed to activate the reaction.

Although the characteristic band at 2150 cm^{-1} for CO appears in all of the elevated temperature samples for CF_3I , this absorbance peak was not integrated as a function of time as with the other impurity peaks. It is reasonable to expect the presence of CO along with CO_2 .

The initial and final spectra for all samples of CF_3I are found in appendixes C, D, E, and F. These spectra are included for reference in order of dry condition, without copper (Appendix C); dry condition, with copper (Appendix D); moist condition, without copper (Appendix E) and moist condition, with copper (Appendix F).

7.3.6 Summary of the CF_3I Area Data. The peak area data for an absorbance band of the CF_3I presented in the above graphs (Figures 23-26) suggest that the areas are decreasing slightly as a function of time at elevated temperatures, especially with moisture present. Table 34 is a summary of the data in Tables 18-21 showing only the initial and final peak areas along with the time of aging at all temperatures and conditions. The last column shows whether the final area was significantly decreased at the 99 % confidence interval. None of the samples at 23 or 100°C showed a statistically significant change. However, some samples at 150°C aging started to show statistically significant decreases, especially those that aged for 52 weeks. In the dry condition without copper at 150°C none of the final areas were significantly decreased (the initial area for this sample was higher than expected and might be an outlier.) In the dry condition with copper, three of the areas decreased significantly and the other two which did not age as long appear to be decreasing and in time will become significantly lower. In the moist condition without copper, four of the five samples show a significant decrease, the other sample appears to be going down, also. Finally, in the moist condition with copper, three of the samples show a significant decrease. The other two samples are decreasing and at longer time might become significant. Even though some of the areas at 150°C are showing "statistically significant" differences, the actual loss in agent is probably quite small and poses no problem to the fire extinguishing capability of the CF_3I .

The data presented in Table 35 show the spectral comparisons for all of the CF_3I samples aged at 150°C compared to their respective samples maintained at 23°C . Keep in mind that the spectral comparisons for the elevated temperature samples were for the longest aged sample compared to its initial spectrum and represents a single value, whereas the spectral comparisons for the 23°C samples are an average of each aged spectrum compared to its respective initial spectrum. Although not all samples have been aged the same length of time, these data do suggest some significant changes in the aged spectra with time. Also one should keep in mind that the impurity peaks are small in comparison to the agent peaks, so the increase in the areas of all combined peaks resulted in significant changes. Since the agent concentration in the cylinders is greater than $100\,000\text{ }\mu\text{L/L}$, and the highest measured concentration of CO_2 impurity was only $1900\text{ }\mu\text{L/L}$, the amount of impurity from all sources is probably not enough to have an affect on the overall performance of the CF_3I . Some fluorinated alkenes are highly toxic, and if the peak at 950 cm^{-1} is a result of an alkene, the only question is whether enough is being generated to form a harmful mixture.

The data for CF_3I suggested that the weak C-I bond in CF_3I was indeed breaking at the 100 and 150°C temperatures. Once the bond broke the radical was free to recombine with another CF_3 radical, an H atom or other radicals in the matrix. Since the CF_3H concentration in the cylinders continued to increase with time and the CF_3I agent peak continued to show slight decreases, the CF_3 radical combined with a hydrogen atom to form a more stable CF_3H molecule. The presence of moisture in the sample probably provided an increased source of hydrogen atoms, therefore the degradation process was accelerated.

Table 22. Integrated peak areas for an absorbance band of CO₂ in the 5330 Pa spectra of CF₃I in the dry condition without copper

		Integrated area from 667 to 671 cm ⁻¹ (±0.0048)								
		Week number								
Metal	Temp. (°C)	0	4	8	16	20	24	28	32	36
Blank	23	0.09	0.09	0.09	0.09	0.09	0.09	NM ^a	0.09	NM
N40	23	0.08	0.08	0.08	0.08	0.08	0.07	NM	0.08	NM
Ti	23	-- ^b	0.08	0.09	0.08	0.09	0.08	NM	0.08	NM
C4130	23	0.01	0.01	0.01	0.01	0.01	0.01	NM	0.01	NM
I625	23	0.18	0.17	0.16	0.16	0.16	0.17	NM	0.16	0.17
Blank	100	0.14	0.15	0.14	0.15	0.16	0.16	0.17	0.17	0.16
N40	100	0.14	0.14	0.14	0.16	0.16	0.16	0.17	0.17	-- ^c
Ti	100	0.14	0.14	0.14	0.15	0.15	0.16	0.17	0.16	0.16
C4130	100	0.01	0.01	0.02	0.02	0.03	0.03	NM	0.04	0.05
I625	100	0.01	0.01	0.01	0.02	0.02	0.02	NM	0.03	0.04
Blank	150	0.18	0.24	0.25	0.27	0.30	0.30	0.31	0.35	0.36
N40	150	0.17	0.26	0.27	0.28	0.30	0.29	0.30	0.31	0.32
Ti	150	0.17	0.20	0.22	0.24	0.28	0.25	0.26	0.29	0.30
C4130	150	0.01	0.09	0.12	0.16	0.20	0.23	NM	0.27	0.32
I625	150	0.17	0.68	0.66	0.69	0.68	0.72	NM	0.69	0.72

Table 22 (cont.). Integrated peak areas for an absorbance band of CO₂ in the 5330 Pa spectra of CF₃I in the dry condition without copper

		Integrated area from 667 to 671 cm ⁻¹ (±0.0048)			
		Week number			
Metal	Temp. (°C)	40	44	48	52
Blank	23	0.08	NM	0.09	NM
N40	23	0.07	NM	0.08	NM
Ti	23	0.08	NM	0.09	NM
C4130	23	0.01	NM	NM	NM
I625	23	0.16	0.17	NM	NM
Blank	100	0.18	0.19	NM	NM
N40	100	-- ^c	-- ^c	-- ^c	-- ^c
Ti	100	0.18	0.19	NM	NM
C4130	100	0.05	NM	NM	NM
I625	100	0.04	NM	NM	NM
Blank	150	0.38	0.41	0.39	0.42
N40	150	0.32	0.32	0.31	0.33
Ti	150	0.32	0.34	0.35	0.40
C4130	150	0.36	NM	NM	NM
I625	150	0.73	0.75	NM	NM

^a Not measured^b Lost spectrum file^c Cylinder emptied after 32 weeks from a leak.

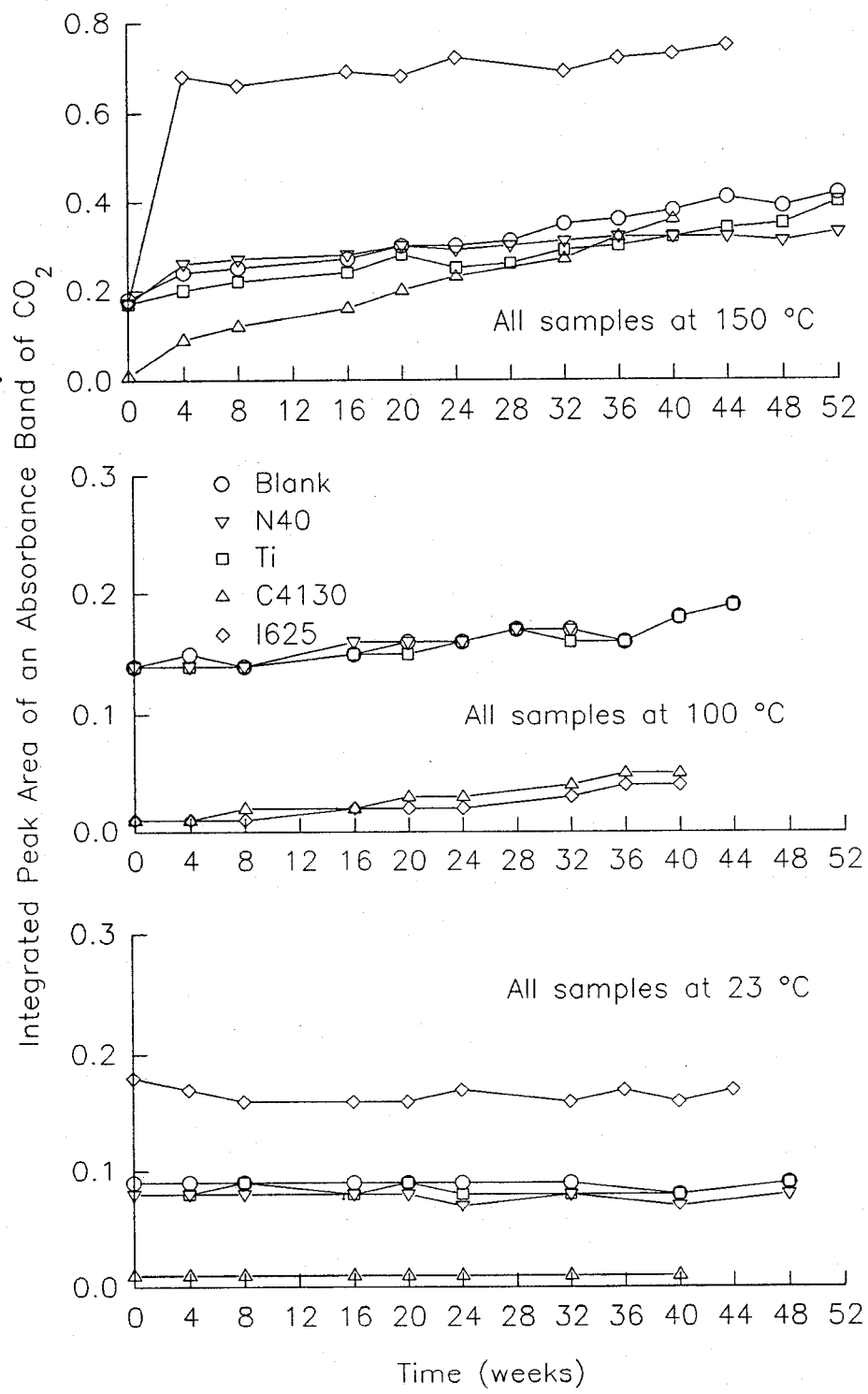


Figure 27. Integrated peak areas for CO₂ for all samples of CF₃I tested in the dry condition without copper at 23 °C, 100 °C, and 150 °C plotted as a function of time.

Table 23. Integrated peak areas of an absorbance band of CO₂ in the 5330 Pa spectra of CF₃I tested in the dry condition with copper

		Integrated area from 667 to 671 cm ⁻¹ (±0.0048)								
		Week number								
		0	4	8	16	20	24	28	32	36
Metal	Temp. (°C)									
CDA 110 Blank	23	0.09	0.08	0.08	0.08	0.09	0.08	NM ^a	0.08	NM
CDA 110 N40	23	0.08	0.08	0.08	0.08	0.08	0.08	NM	0.08	NM
CDA 110 Ti	23	0.08	0.08	0.08	0.08	0.08	0.07	NM	0.08	NM
CDA 110 C4130	23	0.01	0.01	0.01	0.01	0.01	0.01	NM	0.01	NM
CDA 110 I625	23	0.17	0.16	0.15	0.15	0.15	0.16	NM	0.15	0.16
CDA 110 Blank	100	0.14	0.14	0.14	0.15	0.15	0.16	0.17	0.18	-- ^b
CDA 110 Blank	150	0.17	0.23	0.25	0.27	0.30	0.27	0.28	0.30	0.30
CDA 110 N40	150	0.16	0.23	0.25	0.26	0.29	0.27	0.27	0.29	0.29
CDA 110 Ti	150	0.16	0.22	0.24	0.25	0.28	0.26	0.26	0.27	0.28
CDA 110 C4130	150	0.01	0.12	0.15	0.19	0.20	0.22	NM	0.23	0.26
CDA 110 I625	150	0.17	0.33	0.40	0.48	0.50	0.54	NM	0.54	0.57

Table 23 (cont.). Integrated peak areas of an absorbance band of CO₂ in the 5330 Pa spectra of CF₃I tested in the dry condition with copper

		Integrated area from 667 to 671 cm ⁻¹ (±0.0048)			
		Week number			
Metal	Temp. (°C)	40	44	48	52
CDA 110 Blank	23	0.08	NM	0.08	NM
CDA 110 N40	23	0.08	NM	0.08	NM
CDA 110 Ti	23	0.08	NM	0.08	NM
CDA 110 C4130	23	0.01	NM	NM	NM
CDA 110 I625	23	0.16	0.16	NM	NM
CDA 110 Blank	100	-- ^b	-- ^b	-- ^b	-- ^b
CDA 110 Blank	150	0.30	0.30	0.30	0.32
CDA 110 N40	150	0.30	0.30	0.30	0.32
CDA 110 Ti	150	0.27	0.25	0.27	0.29
CDA 110 C4130	150	0.28	NM	NM	NM
CDA 110 I625	150	0.58	0.59	NM	NM

^a Not measured

^b Cylinder emptied after 32 weeks from a leak

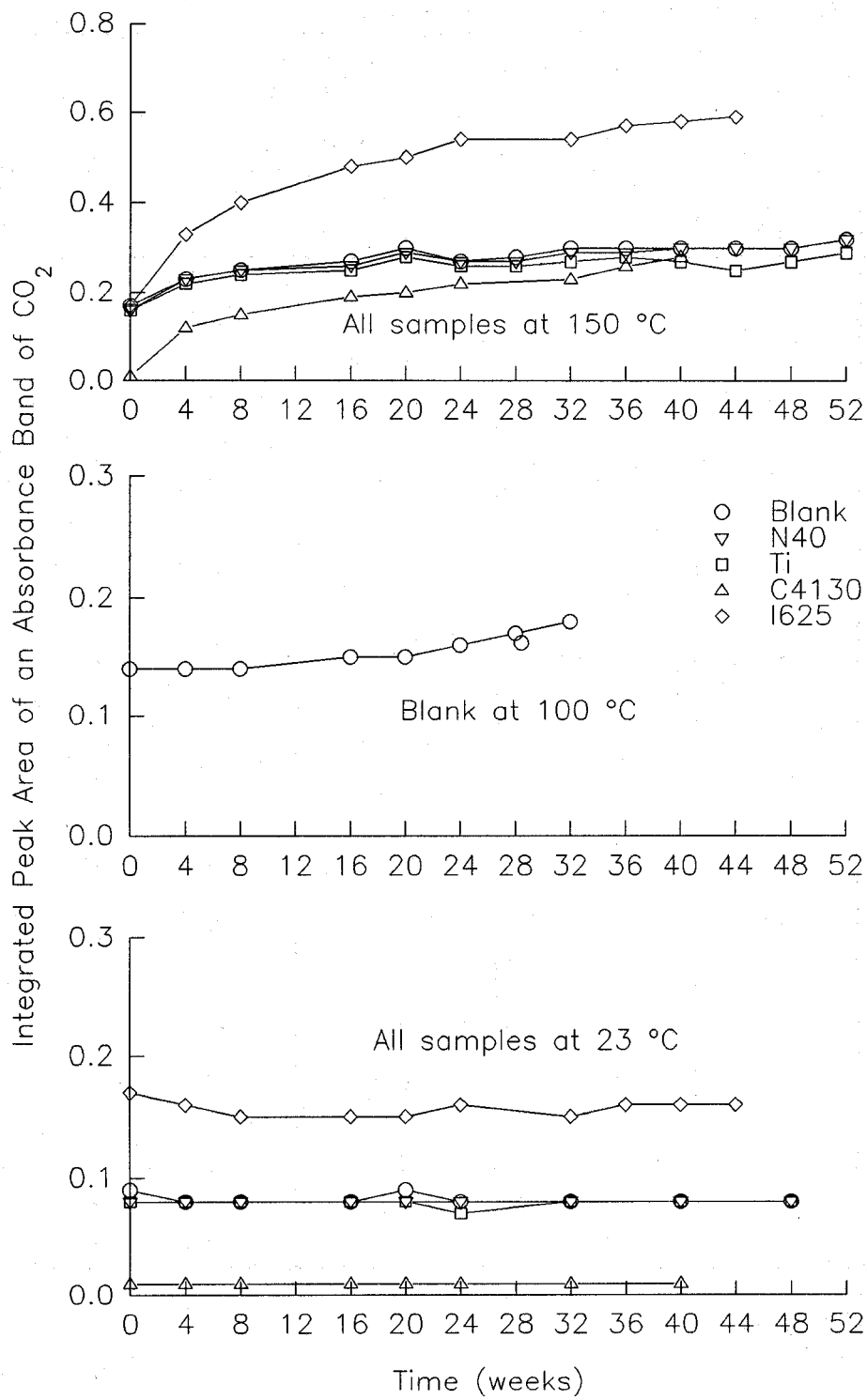


Figure 28. Integrated peak areas for CO₂ for all samples of CF₃I tested in the dry condition with copper at 23 °C, 100 °C, and 150 °C plotted as a function of time.

Table 24. Integrated peak areas for an absorbance band of CO₂ in the 5330 Pa spectra of CF₃I tested in the moist condition without copper

		Integrated area from 667 to 671 cm ⁻¹ (±0.0048)								
		Week number								
Metal	Temp. (°C)	0	4	8	16	20	24	28	32	36
Blank	100	0.13	0.15	0.16	0.17	0.18	0.18	0.18	0.19	0.18
Blank	150	0.14	0.23	0.26	0.28	0.34	0.37	0.40	0.44	0.43
N40	150	0.14	0.21	0.23	0.23	0.25	0.25	0.25	0.27	0.27
Ti	150	0.13	0.22	0.24	0.25	0.28	0.28	0.29	0.32	0.30
C4130	150	0.01	0.10	0.13	0.20	0.23	0.27	NM ^a	0.29	0.33
I625	150	0.16	0.68	0.66	0.66	0.67	0.70	NM	0.68	0.71

Table 24 (cont.). Integrated peak areas for an absorbance band of CO₂ in the 5330 Pa spectra of CF₃I tested in the moist condition without copper

		Integrated area from 667 to 671 cm ⁻¹ (±0.0048)			
		Week number			
Metal	Temp. (°C)	40	44	48	52
Blank	100	0.20	0.21	NM	NM
Blank	150	0.45	0.46	0.45	0.49
N40	150	0.27	0.27	0.27	0.29
Ti	150	0.34	0.34	0.34	0.37
C4130	150	0.35	NM	NM	NM
I625	150	0.71	0.75	NM	NM

^a Not measured.

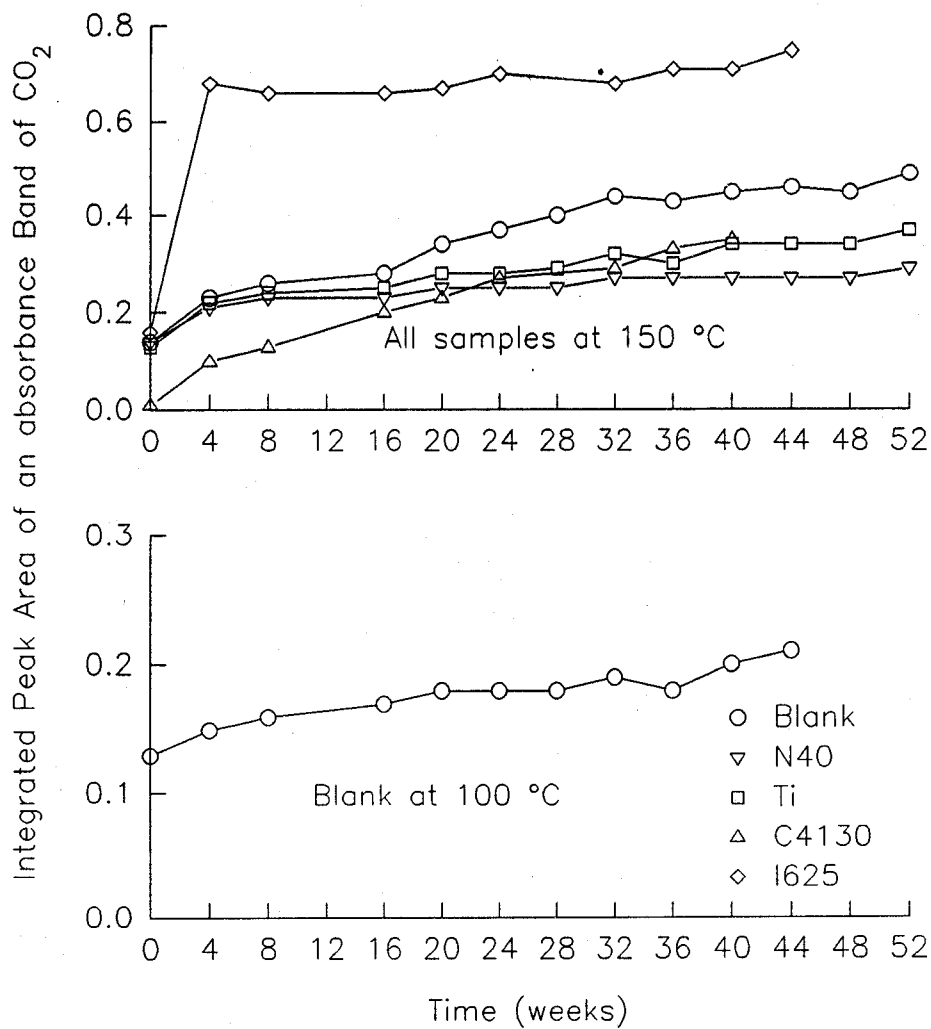


Figure 29. Integrated peak areas for CO₂ for all samples of CF₃I tested in the moist condition without copper at 100 °C and 150 °C plotted as a function of time.

Table 25. Integrated peak areas of an absorbance band of CO₂ in the 5330 Pa spectra of CF₃I tested in the moist condition with copper

		Integrated area from 667 to 671 cm ⁻¹ (±0.0048)								
		Week number								
		0	4	8	16	20	24	28	32	36
Metal	Temp. (°C)									
CDA 110 Blank	100	0.13	0.16	0.17	0.18	0.19	0.19	0.19	0.20	0.20
CDA 110 Blank	150	0.13	0.23	0.26	0.28	0.31	0.30	0.32	0.34	0.34
CDA 110 N40	150	0.13	0.22	0.25	0.29	0.33	0.33	0.35	0.37	0.37
CDA 110 Ti	150	0.13	0.20	0.22	0.26	0.29	0.29	0.33	0.36	0.38
CDA 110 C4130	150	0.01	0.13	0.16	0.21	0.22	0.25	NM ^a	0.27	0.30
CDA 110 I625	150	0.01	0.14	0.18	0.25	0.28	0.30	NM	0.32	0.35

Table 25 (cont.). Integrated peak areas of an absorbance band of CO₂ in the 5330 Pa spectra of CF₃I tested in the moist condition with copper

		Integrated area from 667 to 671 cm ⁻¹ (±0.0048)			
		Week number			
		40	44	48	52
Metal	Temp. (°C)				
CDA 110 Blank	100	0.21	0.23	NM	NM
CDA 110 Blank	150	0.35	0.34	0.33	0.36
CDA 110 N40	150	0.37	0.38	0.36	0.39
CDA 110 Ti	150	0.39	0.41	0.39	0.43
CDA 110 C4130	150	0.33	NM	NM	NM
CDA 110 I625	150	0.37	NM	NM	NM

^a Not measured

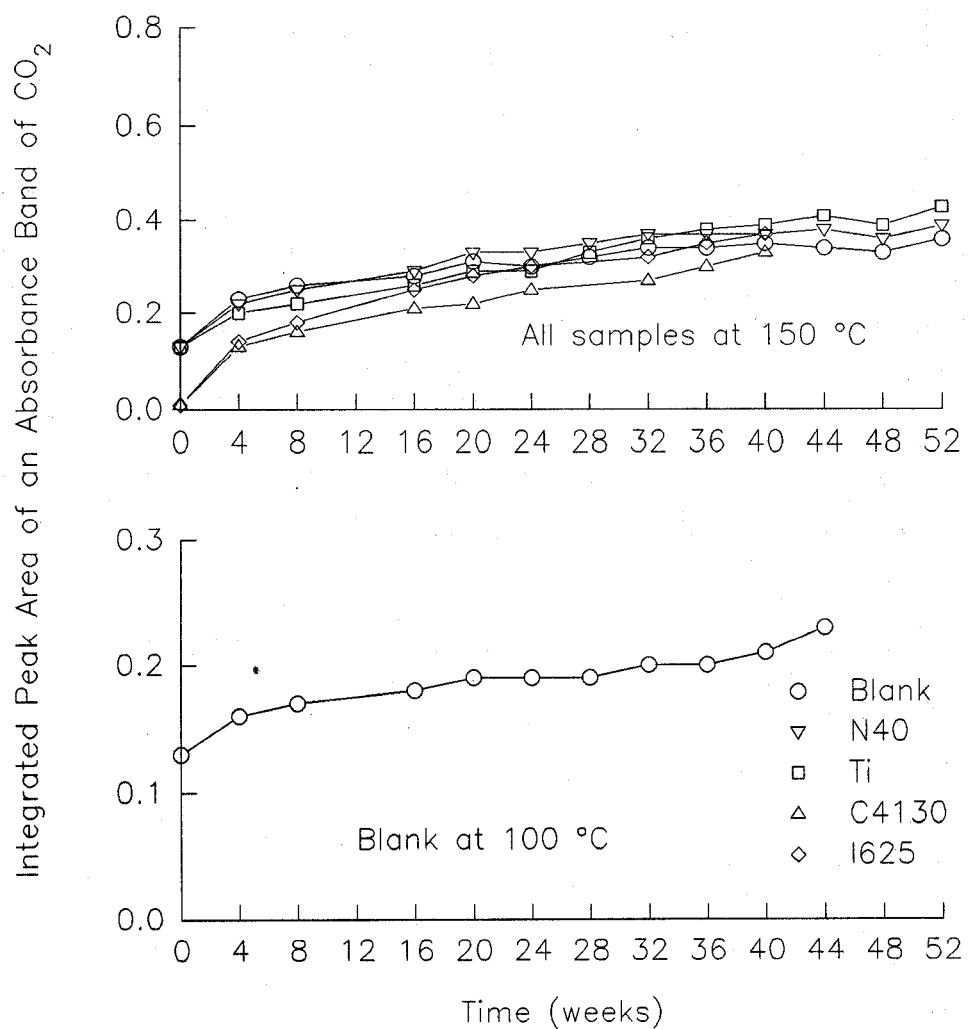


Figure 30. Integrated peak areas for CO₂ for all samples of CF₃I tested in the moist condition with copper at 100 °C and 150 °C plotted as a function of time.

Table 26. Integrated peak areas of an absorbance band for CF_3H in the 5330 Pa spectra of CF_3I tested in the dry condition without copper

		Integrated area from 698 to 701 cm^{-1} (± 0.0011)								
		Week number								
		0	4	8	16	20	24	28	32	36
Metal	Temp. ($^{\circ}\text{C}$)									
Blank	23	0.01	0.01	0.01	0.01	0.01	0.01	NM ^a	0.01	NM
N40	23	0.01	0.01	0.01	0.01	0.01	0.01	NM	0.01	NM
Ti	23	-- ^b	0.01	0.01	0.01	0.01	0.01	NM	0.01	NM
C4130	23	ND ^c	ND	ND	ND	ND	ND	NM	ND	NM
I625	23	0.04	0.04	0.04	0.04	0.04	0.04	NM	0.04	0.04
Blank	100	0.03	0.03	0.03	0.03	0.03	0.03	0.03	0.03	0.03
N40	100	0.03	0.03	0.03	0.03	0.03	0.03	0.03	0.03	-- ^d
Ti	100	0.03	0.03	0.03	0.03	0.03	0.03	0.03	0.03	0.03
C4130	100	ND	ND	ND	ND	ND	ND	NM	ND	ND
I625	100	ND	ND	ND	ND	ND	ND	NM	ND	ND
Blank	150	0.02	0.02	0.03	0.04	0.05	0.06	0.08	0.11	0.15
N40	150	0.02	0.03	0.04	0.06	0.07	0.09	0.10	0.11	0.12
Ti	150	0.02	0.02	0.03	0.03	0.03	0.03	0.04	0.04	0.05
C4130	150	ND	<0.01	0.01	0.03	0.04	0.06	NM	0.12	0.15
I625	150	0.04	0.06	0.10	0.22	0.26	0.30	NM	0.35	0.37

Table 26 (cont.). Integrated peak areas of an absorbance band for CF_3H in the 5330 Pa spectra of CF_3I tested in the dry condition without copper

		Integrated area from 698 to 701 cm^{-1} (± 0.0011)			
		Week number			
Metal	Temp. ($^{\circ}\text{C}$)	40	44	48	52
Blank	23	0.01	NM	0.01	NM
N40	23	0.01	NM	0.01	NM
Ti	23	0.01	NM	0.01	NM
C4130	23	ND	NM	NM	NM
I625	23	0.04	0.04	NM	NM
Blank	100	0.03	0.04	NM	NM
N40	100	-- ^d	-- ^d	-- ^d	-- ^d
Ti	100	0.03	0.04	NM	NM
C4130	100	ND	NM	NM	NM
I625	100	ND	NM	NM	NM
Blank	150	0.19	0.24	0.28	0.32
N40	150	0.12	0.13	0.14	0.15
Ti	150	0.06	0.07	0.10	0.12
C4130	150	0.19	NM	NM	NM
I625	150	0.39	0.41	NM	NM

^a Not measured^b Lost spectrum file^c Not detected^d Cylinder emptied after 32 weeks from a leak.

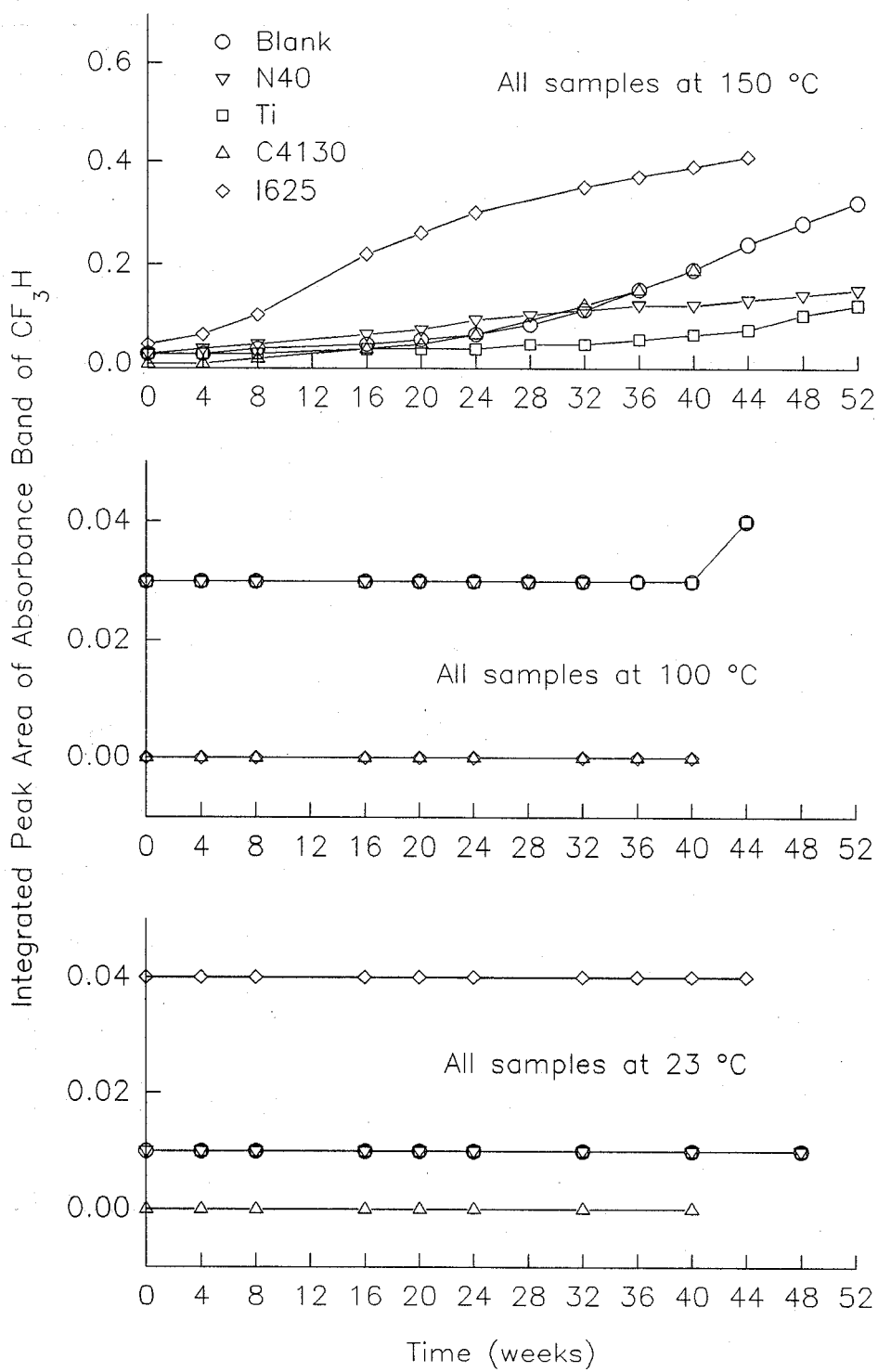


Figure 31. Integrated peak areas for CF_3H for all samples of CF_3I tested in the dry condition without copper at 23 °C, 100 °C, and 150 °C plotted as a function of time.

Table 27. Integrated peak areas of an absorbance band for CF_3H in the 5330 Pa spectra of CF_3I tested in the dry condition with copper

		Integrated area from 698 to 701 cm^{-1} (± 0.0011)								
		Week number								
		0	4	8	16	20	24	28	32	36
Metal	Temp. ($^{\circ}\text{C}$)									
CDA 110 Blank	23	0.01	0.01	0.01	0.01	0.01	0.01	NM	0.01	NM
CDA 110 N40	23	0.01	0.01	0.01	0.01	0.01	0.01	NM ^a	0.01	NM
CDA 110 Ti	23	0.01	0.01	0.01	0.01	0.01	0.01	NM	0.01	NM
CDA 110 C4130	23	ND ^b	ND	ND	ND	ND	ND	NM	ND	NM
CDA 110 I625	23	0.04	0.04	0.04	0.04	0.04	0.04	NM	0.04	0.04
CDA 110 Blank	100	0.03	0.03	0.03	0.03	0.03	0.03	0.03	0.03	-- ^c
CDA 110 Blank	150	0.02	0.02	0.03	0.06	0.07	0.09	0.12	0.15	0.19
CDA 110 N40	150	0.02	0.03	0.05	0.16	0.22	0.27	0.32	0.37	0.39
CDA 110 Ti	150	0.02	0.02	0.03	0.05	0.07	0.09	0.10	0.12	0.14
CDA 110 C4130	150	ND	0.01	0.02	0.03	0.05	0.05	NM	0.07	0.09
CDA 110 I625	150	0.04	0.04	0.04	0.05	0.07	0.08	NM	0.13	0.16

Table 27 (cont.). Integrated peak areas of an absorbance band for CF_3H in the 5330 Pa spectra of CF_3I tested in the dry condition with copper

		Integrated area from 698 to 701 cm^{-1} (± 0.0011)			
		Week number			
Metal	Temp. ($^{\circ}\text{C}$)	40	44	48	52
CDA 110 Blank	23	0.01	NM	0.01	NM
CDA 110 N40	23	0.01	NM	0.01	NM
CDA 110 Ti	23	0.01	NM	0.01	NM
CDA 110 C4130	23	ND	NM	NM	NM
CDA 110 I625	23	0.04	0.04	NM	NM
CDA 110 Blank	100	-- ^c	-- ^c	-- ^c	-- ^c
CDA 110 Blank	150	0.23	0.28	0.33	0.37
CDA 110 N40	150	0.41	0.45	0.47	0.49
CDA 110 Ti	150	0.16	0.18	0.20	0.22
CDA 110 C4130	150	0.11	NM	NM	NM
CDA 110 I625	150	0.21	0.23	NM	NM

^a Cylinder emptied after 32 weeks from a leak

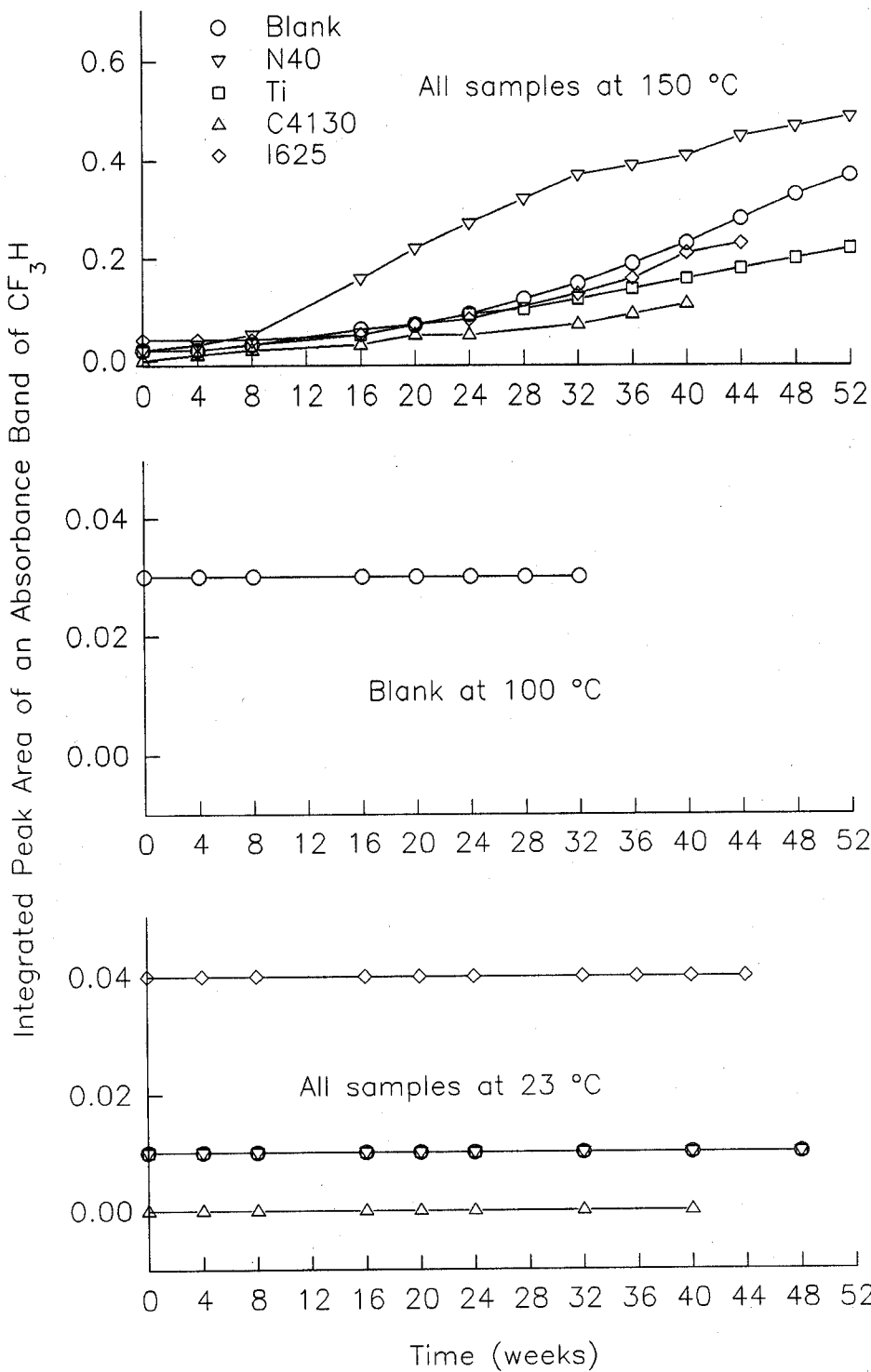


Figure 32. Integrated peak areas for CF₃H for all samples of CF₃I tested in the dry condition with copper at 23 °C, 100 °C, and 150 °C plotted as a function of time.

Table 28. Integrated peak areas of an absorbance band for CF₃H in the 5330 Pa spectra of CF₃I tested in the moist condition without copper

		Integrated area from 698 to 701 cm ⁻¹ (±0.0011)								
		Week number								
Metal	Temp. (°C)	0	4	8	16	20	24	28	32	36
Blank	100	0.03	0.03	0.03	0.03	0.03	0.03	0.03	0.03	0.03
Blank	150	0.01	0.02	0.03	0.07	0.11	0.18	0.24	0.29	0.34
N40	150	0.01	0.03	0.05	0.08	0.10	0.12	0.14	0.15	0.16
Ti	150	0.02	0.02	0.03	0.05	0.07	0.09	0.12	0.14	0.17
C4130	150	ND ^a	0.01	0.01	0.05	0.08	0.11	NM ^b	0.18	0.22
I625	150	0.04	0.12	0.25	0.36	0.38	0.41	NM	0.44	0.46

Table 28 (cont.). Integrated peak areas of an absorbance band for CF₃H in the 5330 Pa spectra of CF₃I tested in the moist condition without copper

		Integrated area from 698 to 701 cm ⁻¹ (±0.0011)			
		Week number			
Metal	Temp. (°C)	40	44	48	52
Blank	100	0.03	0.03	NM	NM
Blank	150	0.37	0.40	0.42	0.45
N40	150	0.17	0.19	0.20	0.21
Ti	150	0.19	0.22	0.24	0.27
C4130	150	0.27	NM	NM	NM
I625	150	0.48	0.51	NM	NM

^a Not detected
^b Not measured.

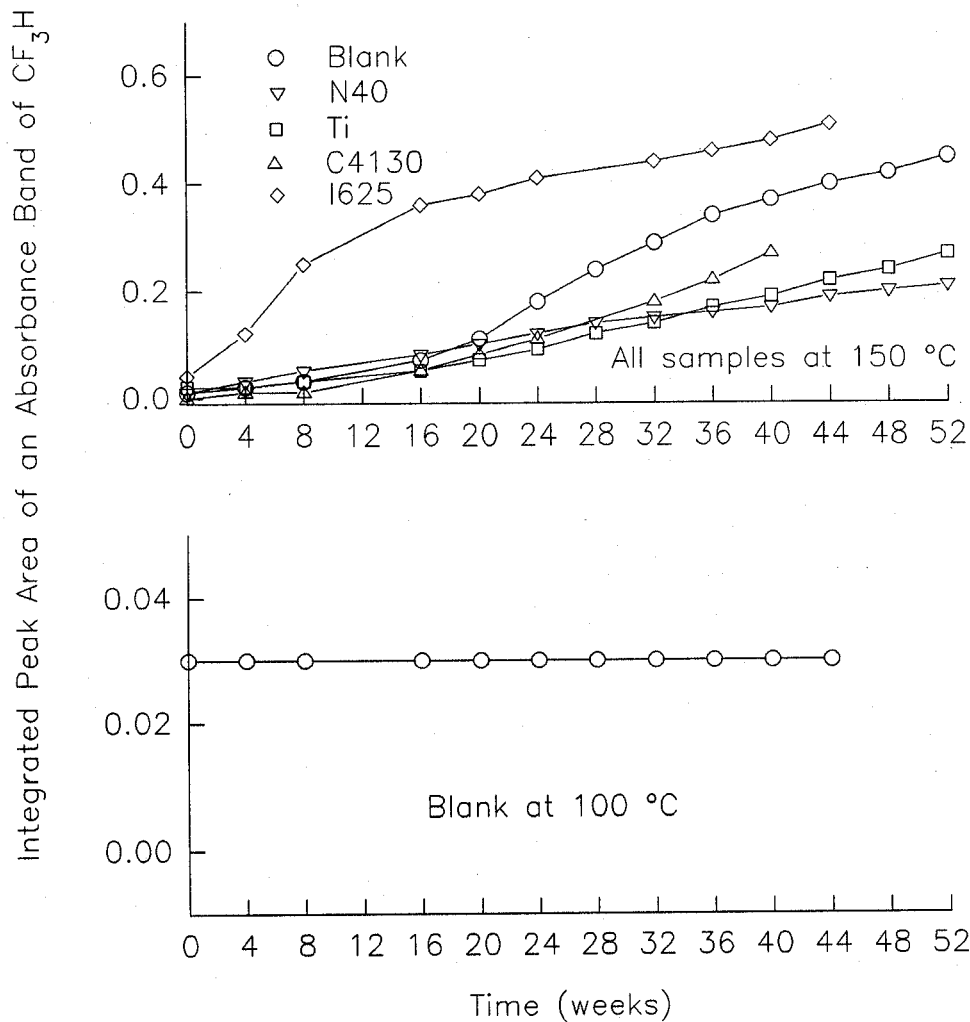


Figure 33. Integrated peak areas for CF₃H for all samples of CF₃I tested in the moist condition without copper at 100 °C and 150 °C plotted as a function of time.

Table 29. Integrated peak areas of an absorbance band for CF₃H in the 5330 Pa spectra of CF₃I tested in the moist condition with copper

		Integrated area from 698 to 701 cm ⁻¹ (±0.0011)								
		Week number								
		0	4	8	16	20	24	28	32	36
Metal	Temp. (°C)									
CDA 110 Blank	100	0.03	0.03	0.03	0.03	0.03	0.03	0.03	0.03	0.03
CDA 110 Blank	150	0.01	0.02	0.02	0.06	0.09	0.14	0.19	0.24	0.29
CDA 110 N40	150	0.01	0.02	0.03	0.07	0.10	0.14	0.19	0.26	0.35
CDA 110 Ti	150	0.01	0.02	0.05	0.09	0.11	0.13	0.15	0.16	0.18
CDA 110 C4130	150	<0.01	0.01	0.02	0.04	0.05	0.05	NM ^a	0.06	0.07
CDA 110 I625	150	0.03	0.01	0.01	0.03	0.05	0.07	NM	0.13	0.16

Table 29 (cont.). Integrated Peak Areas of an Absorbance Band for CF₃H in the 5330 Pa Spectra of CF₃I tested in the Moist Condition with Copper

		Integrated Area from 698 to 701 cm ⁻¹ (±0.0011)			
		Week Number			
		40	44	48	52
Metal	Temp. (°C)				
CDA 110 Blank	100	0.03	0.03	NM	NM
CDA 110 Blank	150	0.34	0.37	0.40	0.44
CDA 110 N40	150	0.41	0.50	0.55	0.63
CDA 110 Ti	150	0.19	0.20	0.22	0.24
CDA 110 C4130	150	0.08	NM	NM	NM
CDA 110 I625	150	0.21	NM	NM	NM

^a Not measured

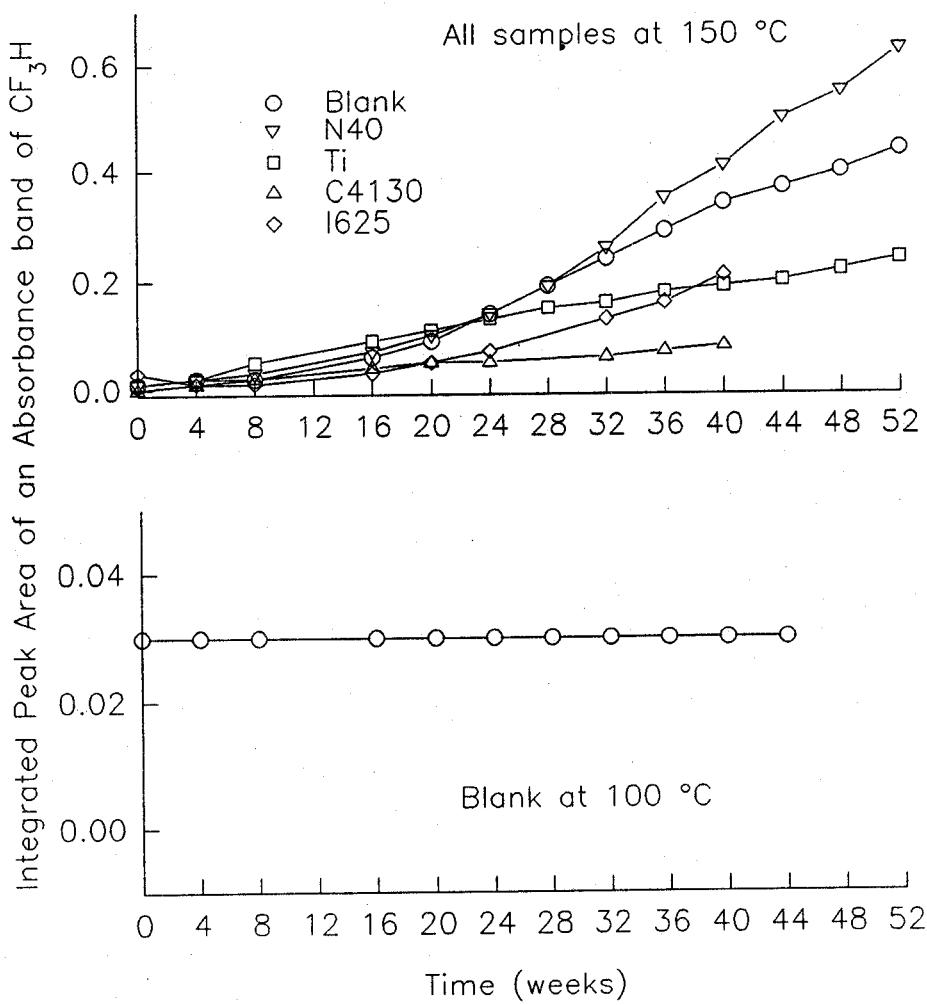


Figure 34. Integrated peak areas for CF₃H for all samples of CF₃I tested in the moist condition with copper at 100 °C and 150 °C plotted as a function of time.

Table 30. Integrated peak areas for an absorbance band of the fluorinated alkene in the 5330 Pa spectra of CF₃I tested in the dry condition without copper

		Integrated area from 944 to 953 cm ⁻¹ (±0.011)								
		Week number								
Metal	Temp. (°C)	0	4	8	16	20	24	28	32	36
Blank	23	ND ^a	ND	ND	ND	ND	ND	NM ^b	ND	NM
N40	23	ND	ND	ND	ND	ND	ND	NM	ND	NM
Ti	23	-- ^c	ND	ND	ND	ND	ND	NM	ND	NM
C4130	23	ND	ND	ND	ND	ND	ND	NM	ND	NM
I625	23	ND	ND	ND	ND	ND	ND	NM	ND	ND
Blank	100	ND	ND	ND	0.01	0.01	0.01	.02	.02	0.02
N40	100	ND	<0.01	0.01	0.02	0.03	0.03	.03	.04	-- ^d
Ti	100	ND	ND	0.01	0.02	0.02	0.03	.04	.04	0.05
C4130	100	ND	<0.01	0.01	0.04	0.05	0.06	NM	0.06	0.07
I625	100	ND	ND	0.01	0.02	0.03	0.03	NM	0.06	0.07
Blank	150	ND	0.06	0.09	0.10	0.10	0.11	0.10	0.11	0.11
N40	150	ND	0.01	0.10	0.10	0.11	0.11	0.11	0.11	0.11
Ti	150	ND	0.03	0.06	0.07	0.12	0.08	0.08	0.09	0.09
C4130	150	ND	0.06	0.09	0.11	0.11	0.12	NM	0.11	0.12
I625	150	ND	0.06	0.06	0.12	0.17	0.12	NM	0.15	0.13

Table 30 (cont.). Integrated peak areas for an absorbance band of the fluorinated alkene in the 5330 Pa spectra of CF₃I tested in the dry condition without copper

		Integrated area from 944 to 953 cm ⁻¹ (±0.011)			
		Week number			
Metal	Temp. (°C)	40	44	48	52
Blank	23	ND	NM	ND	NM
N40	23	ND	NM	ND	NM
Ti	23	ND	NM	ND	NM
C4130	23	ND	NM	NM	NM
I625	23	ND	ND	NM	NM
Blank	100	0.02	0.03	NM	NM
N40	100	-- ^d	-- ^d	-- ^d	-- ^d
Ti	100	0.05	0.06	NM	NM
C4130	100	0.07	NM	NM	NM
I625	100	0.08	NM	NM	NM
Blank	150	0.11	0.11	0.11	0.11
N40	150	0.12	0.12	0.12	0.12
Ti	150	0.10	0.10	0.10	0.10
C4130	150	0.14	NM	NM	NM
I625	150	0.12	0.12	NM	NM

^a Not detected^b Not measured^c Lost spectrum file^d Cylinder emptied after 32 weeks from a leak.

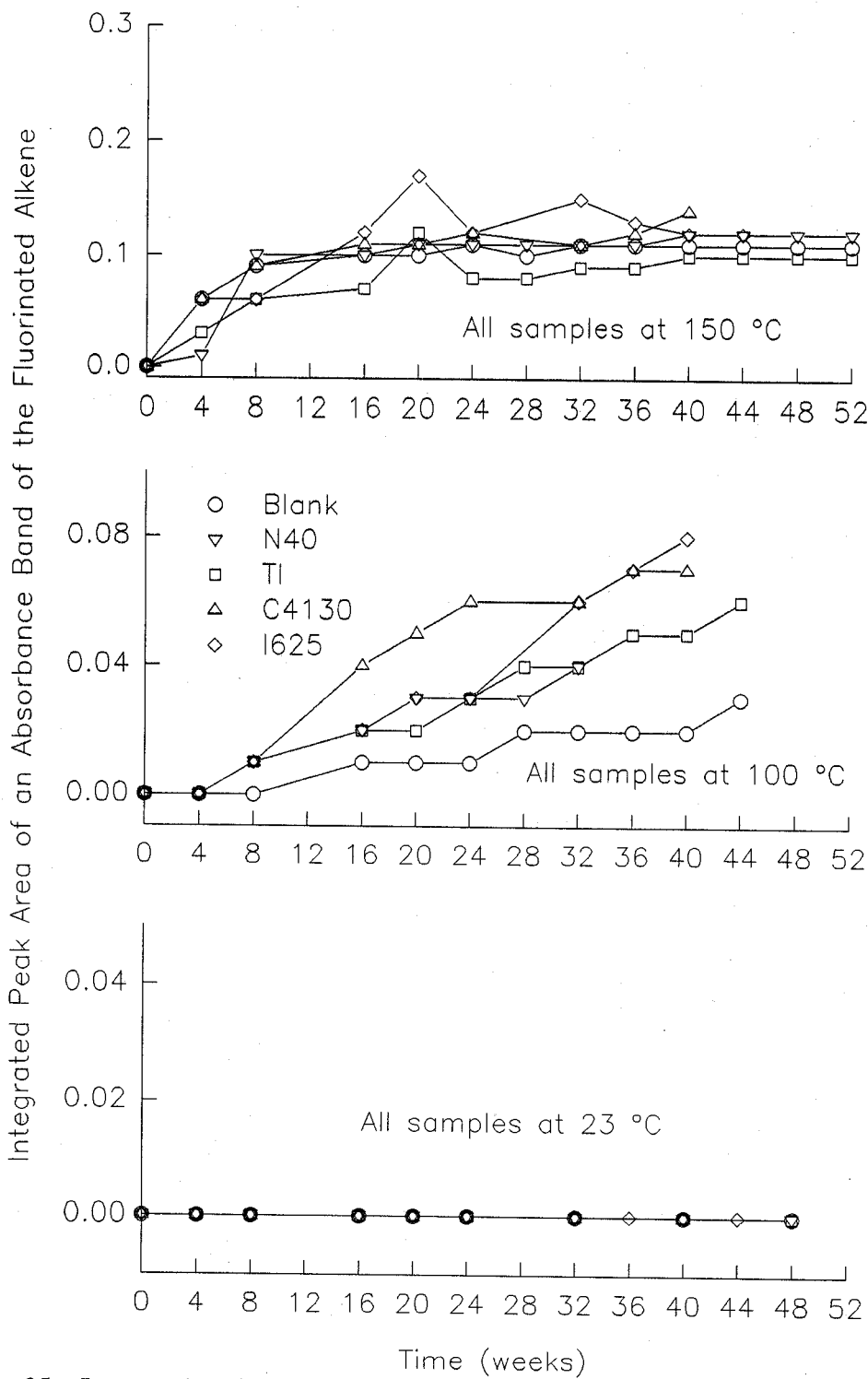


Figure 35. Integrated peak areas for the fluorinated alkene for all samples of CF₃I tested in the dry condition without copper at 23 °C, 100 °C, and 150 °C plotted as a function of time.

Table 31. Integrated peak areas for an absorbance band of the fluorinated alkene in the 5330 Pa spectra of CF_3I tested in the dry condition with copper

		Integrated area from 944 to 953 cm^{-1} (± 0.011)								
		Week number								
Metal	Temp. (°C)	0	4	8	16	20	24	28	32	36
CDA 110 Blank	23	ND ^a	ND	ND	ND	ND	ND	NM ^b	ND	NM
CDA 110 N40	23	ND	ND	ND	ND	ND	ND	NM	ND	NM
CDA 110 Ti	23	ND	ND	ND	ND	ND	ND	NM	ND	NM
CDA 110 C4130	23	ND	ND	ND	ND	ND	ND	NM	ND	NM
CDA 110 I625	23	ND	ND	ND	ND	ND	ND	NM	ND	ND
CDA 110 Blank	100	ND	ND	ND	0.01	0.01	0.01	.02	.02	-- ^c
CDA 110 Blank	150	ND	0.11	0.14	0.08	0.08	0.06	0.06	0.06	0.05
CDA 110 N40	150	ND	0.13	0.14	0.13	0.14	0.12	0.12	0.12	0.10
CDA 110 Ti	150	ND	0.10	0.12	0.10	0.09	0.07	0.06	0.05	0.04
CDA 110 C4130	150	ND	0.11	0.14	0.18	0.19	0.19	NM	0.19	0.19
CDA 110 I625	150	ND	0.04	0.10	0.14	0.16	0.14	NM	0.14	0.12

Table 31 (cont.). Integrated peak areas for an absorbance band of the fluorinated alkene in the 5330 Pa spectra of CF_3I tested in the dry condition with copper

		Integrated area from 944 to 953 cm^{-1} (± 0.011)			
		Week number			
Metal	Temp. ($^{\circ}\text{C}$)	40	44	48	52
CDA 110 Blank	23	ND	NM	ND	NM
CDA 110 N40	23	ND	NM	ND	NM
CDA 110 Ti	23	ND	NM	ND	NM
CDA 110 C4130	23	ND	NM	NM	NM
CDA 110 I625	23	ND	ND	NM	NM
CDA 110 Blank	100	-- ^c	-- ^c	-- ^c	-- ^c
CDA 110 Blank	150	0.05	0.04	0.04	0.03
CDA 110 N40	150	0.10	0.10	0.09	0.08
CDA 110 Ti	150	0.03	0.03	0.02	0.02
CDA 110 C4130	150	0.19	NM	NM	NM
CDA 110 I625	150	0.12	0.12	NM	NM

^a Not detected

^b Not measured

^c Cylinder emptied after 32 weeks from a leak.

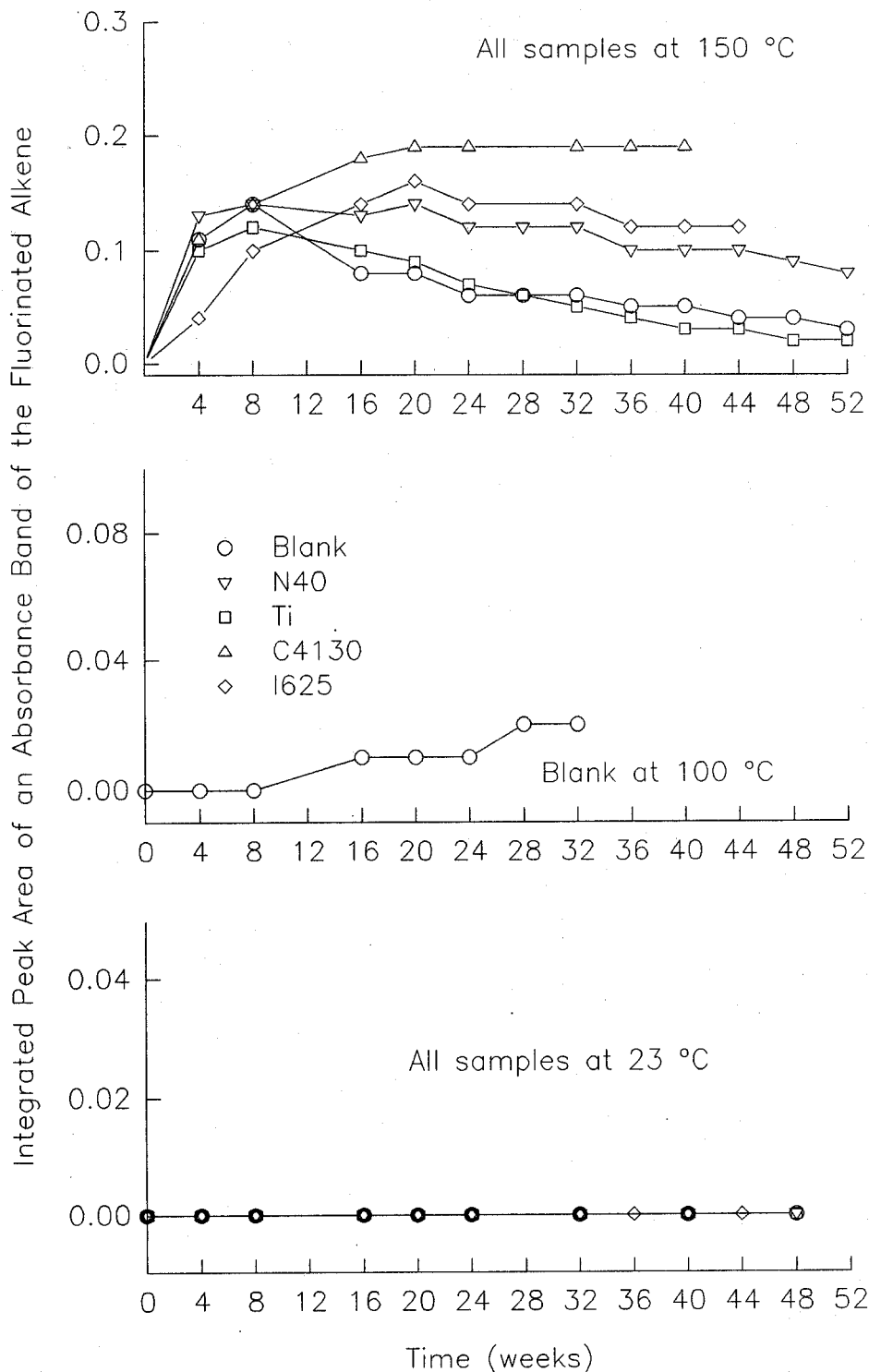


Figure 36. Integrated peak areas for the fluorinated alkene for all samples of CF_3I tested in the dry condition with copper at 23 °C, 100 °C, and 150 °C plotted as a function of time.

Table 32. Integrated peak areas of an absorbance band of the fluorinated alkene in the 5330 Pa spectra of CF₃I tested in the moist condition without copper

		Integrated area from 944 to 953 cm ⁻¹ (±0.011)								
		Week number								
Metal	Temp. (°C)	0	4	8	16	20	24	28	32	36
Blank	100	ND ^a	ND	0.01	0.02	0.03	0.03	0.04	0.04	0.04
Blank	150	ND	0.08	0.10	0.16	0.20	0.18	0.17	0.18	0.18
N40	150	ND	0.09	0.10	0.10	0.11	0.12	0.11	0.12	0.12
Ti	150	ND	0.08	0.07	0.10	0.10	0.10	0.09	0.09	0.09
C4130	150	ND	0.11	0.13	0.23	0.24	0.19	NM ^b	0.19	0.18
I625	150	ND	0.12	0.14	0.12	0.13	0.12	NM	0.12	0.12

Table 32 (cont.). Integrated peak areas of an absorbance band of the fluorinated alkene in the 5330 Pa spectra of CF₃I tested in the moist condition without copper

		Integrated area from 944 to 953 cm ⁻¹ (±0.011)			
		Week number			
Metal	Temp. (°C)	40	44	48	52
Blank	100	0.04	0.05	NM	NM
Blank	150	0.17	0.18	0.18	0.19
N40	150	0.12	0.12	0.12	0.12
Ti	150	0.09	0.08	0.09	0.09
C4130	150	0.20	NM	NM	NM
I625	150	0.12	0.13	NM	NM

^a Not detected

^b Not measured.

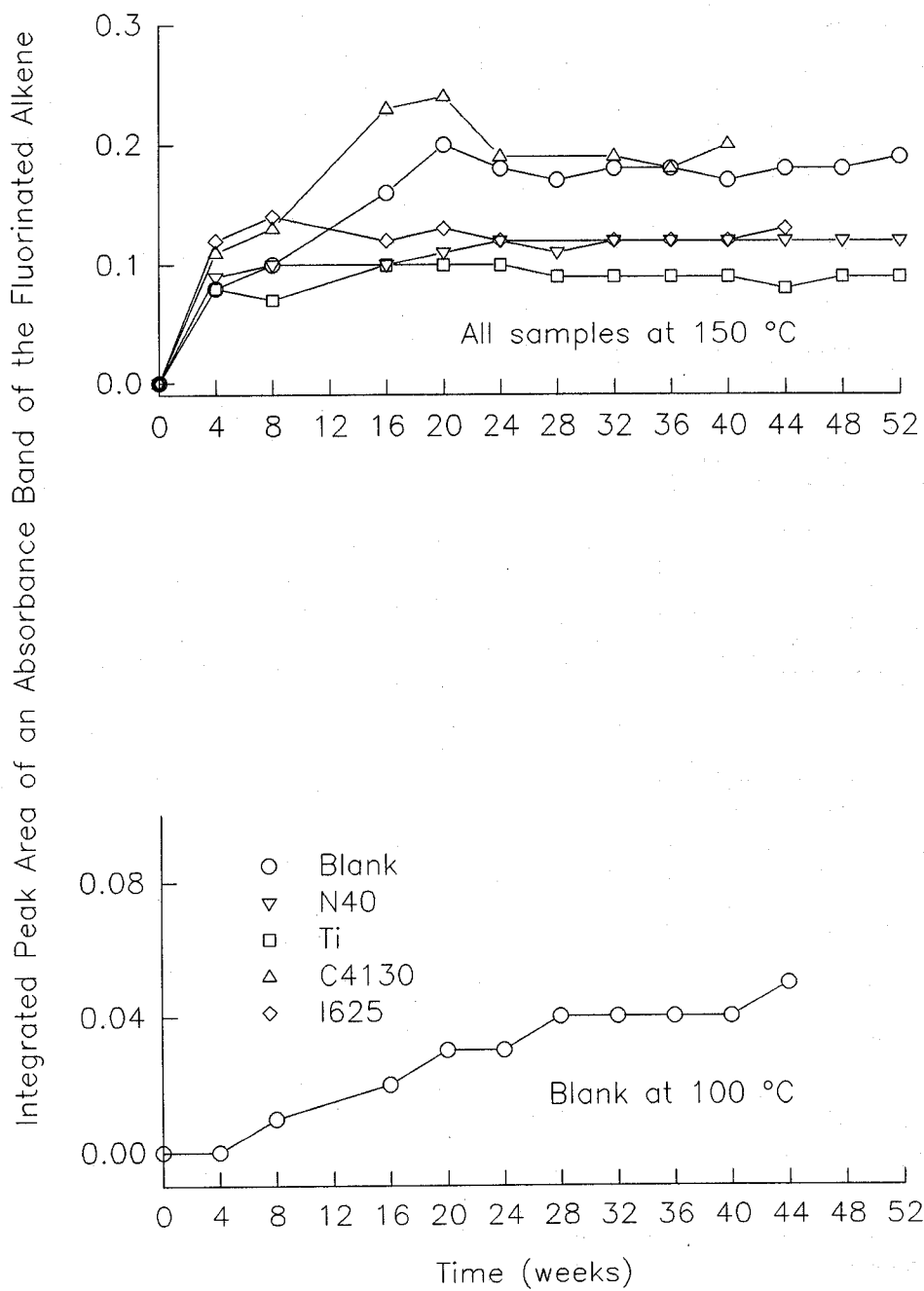


Figure 37. Integrated peak areas for the fluorinated alkene for all samples of CF_3I tested in the moist condition without copper at 100 °C and 150 °C plotted as a function of time.

Table 33. Integrated peak areas of an absorbance band of the fluorinated alkene in the 5330 Pa spectra of CF_3I tested in the moist condition with copper

		Integrated area from 944 to 953 cm^{-1} (± 0.011)								
		Week number								
		0	4	8	16	20	24	28	32	36
Metal	Temp. ($^{\circ}\text{C}$)									
CDA 110 Blank	100	ND ^a	ND	0.01	0.01	0.02	0.02	0.02	0.02	0.03
CDA 110 Blank	150	ND	ND	ND	ND	ND	ND	ND	ND	ND
CDA 110 N40	150	ND	0.02	0.04	0.11	0.12	0.12	0.12	0.12	0.12
CDA 110 Ti	150	ND	0.04	0.07	0.04	0.03	0.03	0.03	0.03	0.03
CDA 110 C4130	150	ND	0.12	0.18	0.22	0.23	0.17	NM ^b	0.18	0.17
CDA 110 I625	150	ND	0.11	0.04	0.06	0.04	0.03	NM	0.03	0.03

Table 33 (cont.). Integrated peak areas of an absorbance band of the fluorinated alkene in the 5330 Pa spectra of CF_3I tested in the moist condition with copper

		Integrated area from 944 to 953 cm^{-1} (± 0.011)			
		Week number			
		40	44	48	52
Metal	Temp. ($^{\circ}\text{C}$)				
CDA 110 Blank	100	0.03	0.03	NM	NM
CDA 110 Blank	150	ND	ND	ND	ND
CDA 110 N40	150	0.12	0.12	0.12	0.12
CDA 110 Ti	150	0.03	0.03	0.03	0.03
CDA 110 C4130	150	0.18	NM	NM	NM
CDA 110 I625	150	0.04	NM	NM	NM

^a Not detected

^b Not measured.

Table 34. Summary of the initial and final peak areas of CF₃I at all temperatures and conditions

Metal	Number of weeks	Temp. (°C)	Area (± 0.011)		Significant @ 3 x uncertainty
			Init.	Final	
Condition: Dry without Copper					
blank	48	23	0.25	0.23	no
N40	48	23	0.19 ^a	0.24	--
Ti	48	23	0.26	0.23	no
C4130	40	23	0.24	0.25	no
I625	44	23	0.27	0.24	no
blank	44	100	0.25	0.25	no
N40	32	100	0.24	0.24	no
Ti	44	100	0.25	0.24	no
C4130	40	100	0.25	0.24	no
I625	40	100	0.25	0.24	no
blank	52	150	0.28	0.25	no
N40	52	150	0.27	0.25	no
Ti	52	150	0.28	0.25	no
C4130	40	150	0.29 ^a	0.23	--
I625	44	150	0.25	0.22	no
Condition: Dry with Copper					
blank	48	23	0.26	0.23	no
N40	48	23	0.26	0.24	no
Ti	48	23	0.27	0.25	no
C4130	40	23	0.23	0.24	no
I625	44	23	0.26	0.23	no
blank	32	100	0.25	0.26	no
blank	52	150	0.29	0.23	yes
N40	52	150	0.26	0.19	yes
Ti	52	150	0.28	0.23	yes
C4130	40	150	0.24	0.22	no
I625	44	150	0.25	0.23	no

Table 34. (continued) Summary of the initial and final peak areas of CF₃I at all temperatures and conditions

Metal	Number of weeks	Temp. °C	Area (± 0.011)		Significant @ 3 x uncertainty
			Init.	Final	
Condition: Moist without copper					
blank	44	100	0.25	0.24	no
blank	52	150	0.27	0.23	yes
N40	52	150	0.28	0.23	yes
Ti	52	150	0.28	0.23	yes
C4130	40	150	0.24	0.21	no
I625	44	150	0.25	0.21	yes
Condition: Moist with copper					
blank	44	100	0.25	0.24	no
blank	52	150	0.27	0.22	yes
N40	52	150	0.27	0.19	yes
Ti	52	150	0.28	0.21	yes
C4130	40	150	0.23	0.21	no
I625	40	150	0.23	0.21	no

^a Suspected to be an outlier because of improper gas cell filling.

Table 35. Spectral comparisons of initial and aged CF₃I samples

Condition		Without copper (± 0.0018)			With copper (± 0.0018)		
Metal	Weeks tested	Dry at 23 °C	Dry at 150 °C	Moist at 150 °C	Dry at 23 °C	Dry at 150 °C	Moist at 150 °C
Blank	52	0.996	0.991	0.984	0.997	0.980	0.981
N40	52	0.998	0.995	0.992	0.997	0.875	0.949
Ti	52	0.998	0.996	0.990	0.997	0.985	0.990
C4130	40	0.999	0.994	0.990	0.999	0.997	0.998
I625	44	0.998	0.988	0.983	0.999	0.994	0.994

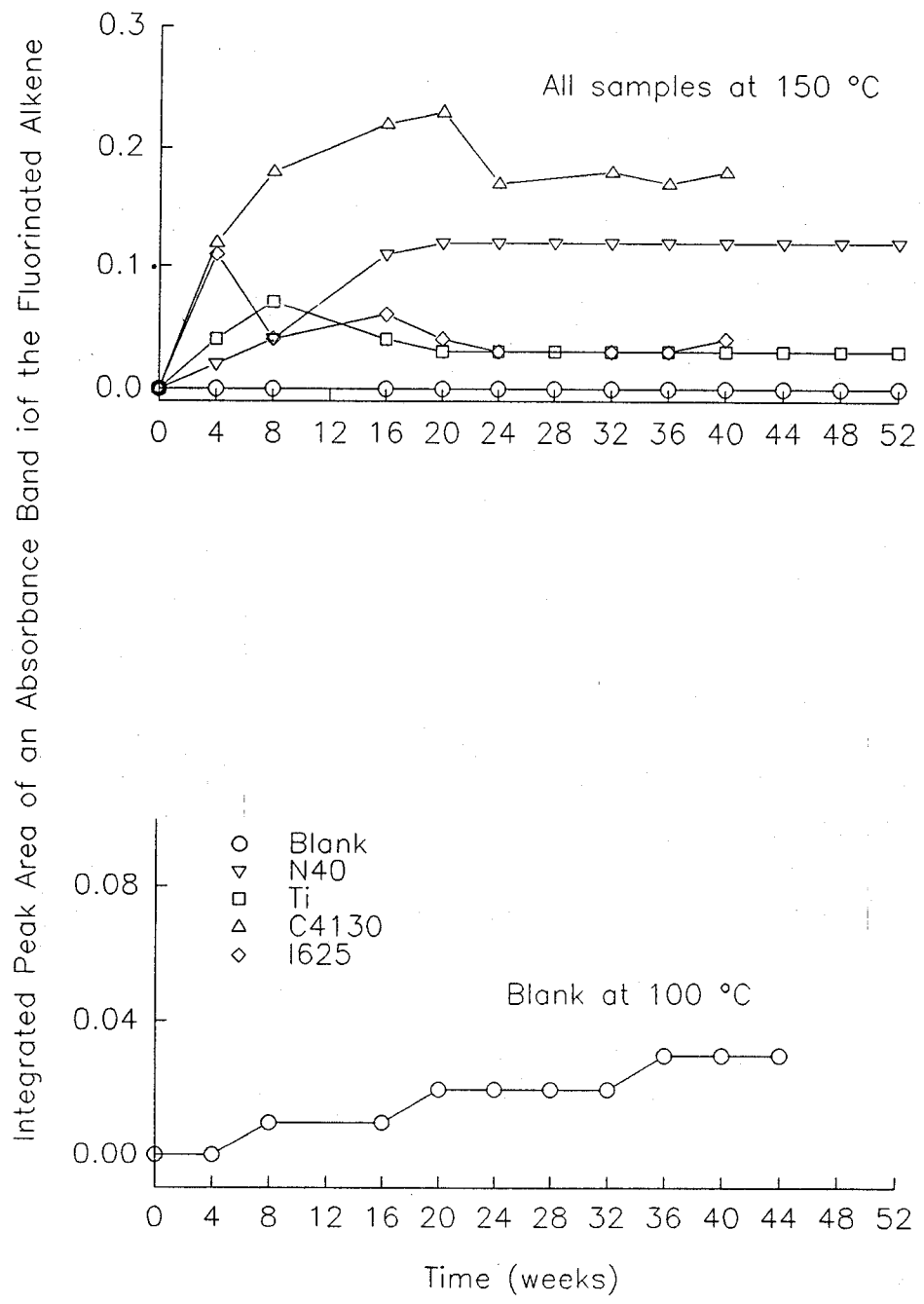


Figure 38. Integrated peak areas for the fluorinated alkene for all samples of CF_3I tested in the moist condition with copper at 100 °C and 150 °C plotted as a function of time.

7.4 Conclusions

The long-term stability project showed the following:

- the fluorocarbon agents FC-218, HFC-125, and HFC-227ea were stable at temperatures as high as 150 °C for as long as 48 weeks. No by-products were formed.
- CF_3I degraded at 100 °C and was accelerated at 150 °C.
- CF_3H , CO_2 , and CO were produced in low levels as degradation products of CF_3I .
- the presence of moisture accelerates the degradation of CF_3I .
- the presence of copper accelerates the degradation of CF_3I .
- the presence of copper and moisture accelerate the degradation of CF_3I .
- an absorbance band at 950 cm^{-1} was generated in the CF_3I samples that may be from a fluorinated alkene; the presence of copper at 150 °C caused the double bond to break.
- storage at ambient conditions of any of the four agents is feasible, but storage at elevated temperatures for CF_3I needs more study.

7.5 Acknowledgments

The author wishes to acknowledge a number of additional NIST staff members who made contributions to this section. These include Mr. Richard Peacock, Dr. Marc Nyden, Mr. Thomas Cleary, Dr. Takashi Kashiwagi, Dr. Richard Gann, and Mr. Darren Lowe for providing their technical expertise. Also, Ms. Paula Garrett for organizing and editing the section.

In addition the author wishes to acknowledge Mr. Richard Sears of Walter Kidde Aerospace for coordinating the treatment of the C4130 alloy steel and Mr. Larry Braden of Metal Samples Co., Inc. for assistance in providing the numerous metal coupons used. Dr. Douglas Dierdorf of Pacific Scientific helped to try and identify and confirm the presence of a fluorinated alkene in aged CF_3I samples. Mr. Thomas Austin of Washington Valve and Fitting Co. recommended equipment that made the FTIR analyses procedure very precise.

7.6 References

- Balzhiser, R.E., Samuels, M.R., and Eliassen, J.D., *Chemical Engineering Thermodynamics, The Study of Energy, Entropy, and Equilibrium*, Prentice-Hall, Englewood Cliffs, NJ, 1972.
- Dierdorf, D., personal communication, 1995.
- Felder, P., "The influence of the molecular beam temperature on the photodissociation of CF_3I at 308 nm," *Chem. Phys. Lett.* **197**, 425 (1992).
- Fourier Infrared Software Tools for Microsoft Windows, User's Reference Guide, Mattson Instruments, Inc., 1992.
- McGee, P. R., Cleveland, F. F., Meister, A. G., Decker, C. E., and Miller, S. I., "Substituted Methanes.X. Infrared Spectral Data, Assignments, Potential Constants, and Calculated Thermodynamic Properties for CF_3Br and CF_3I ," *J. of Chem. Phys.*, **21**, 2, 1948.

Mendenhall, W. and Sincich, T., *Statistics for Engineering and the Sciences*, Dellen Publishing Co., p. 213, 214, 1992.

Peacock, R.D., Cleary, T.G., and Harris, Jr., R.H., "Agent Stability under Storage and Discharge Residue," Section 6 in *Evaluation of Alternative In-Flight Fire Suppressants for Full-Scale Testing in Simulated Aircraft Engine Nacelles and Dry Bays*, NIST Special Publication 861, Grosshandler, W. L., Gann, R. G., and Pitts, W. M., eds, U.S. Department of Commerce, Washington, DC 1994. 643-668.

Ricker, R.E., Stoudt, M.R., Dante, J.F., Fink, J.L., Beauchamp, C.R., and Moffat, T.P., "Corrosion of Metals," Section 7 in *Evaluation of Alternative In-Flight Fire Suppressants for Full-Scale Testing in Simulated Aircraft Engine Nacelles and Dry Bays*, NIST Special Publication 861, Grosshandler, W. L., Gann, R. G., and Pitts, W. M., eds, U.S. Department of Commerce, Washington, DC 1994. 643-668.

Taylor, B.N., Kuyatt, C.E., *Guidelines for Evaluating and Expressing the Uncertainty of NIST Measurement Results*, NIST Technical Note 1297, U.S. Department of Commerce, Washington DC. 1994.

Appendix A. Initial and Final FTIR Spectra for HFC-125

The spectra in Appendix A are those of the HFC-125. The gas cell pressure for all was 5330 Pa. The lower spectrum is for the initial analysis; the upper spectrum is for the final aged analysis. The blanks for this agent appear in Figures 13 and 14.

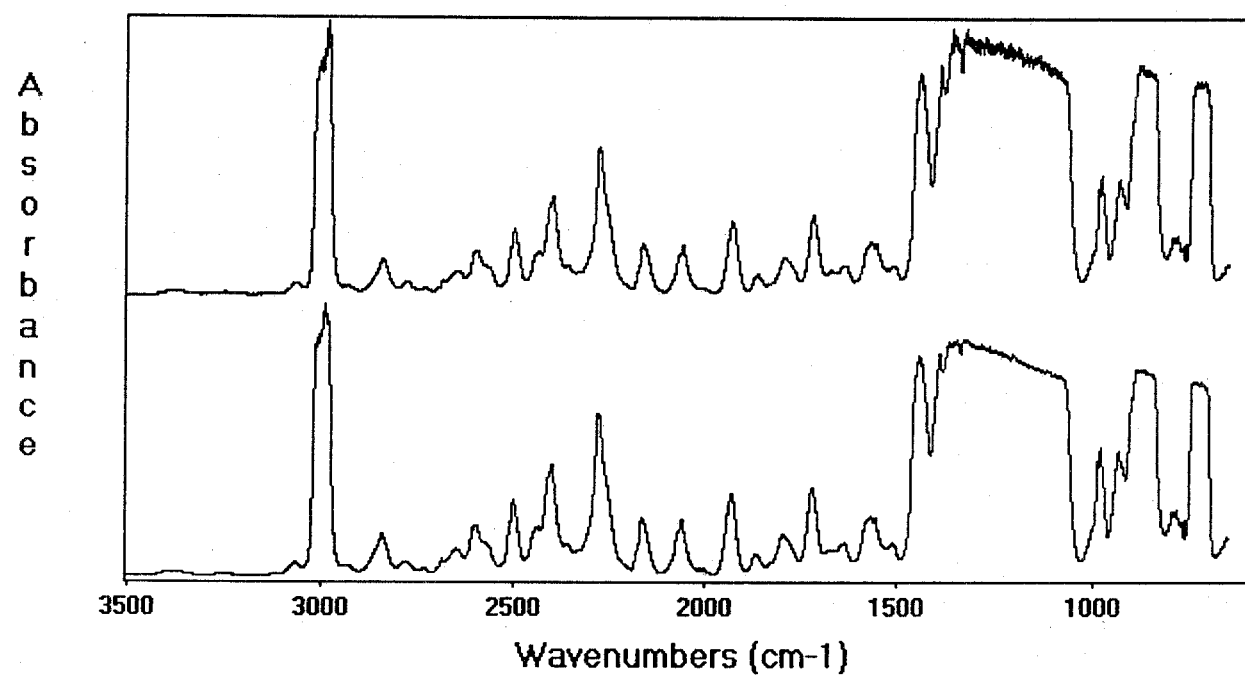


Figure A-1. Initial (lower) and 48 week (upper) spectra for Nitronic 40 in HFC-125 at 23 °C.

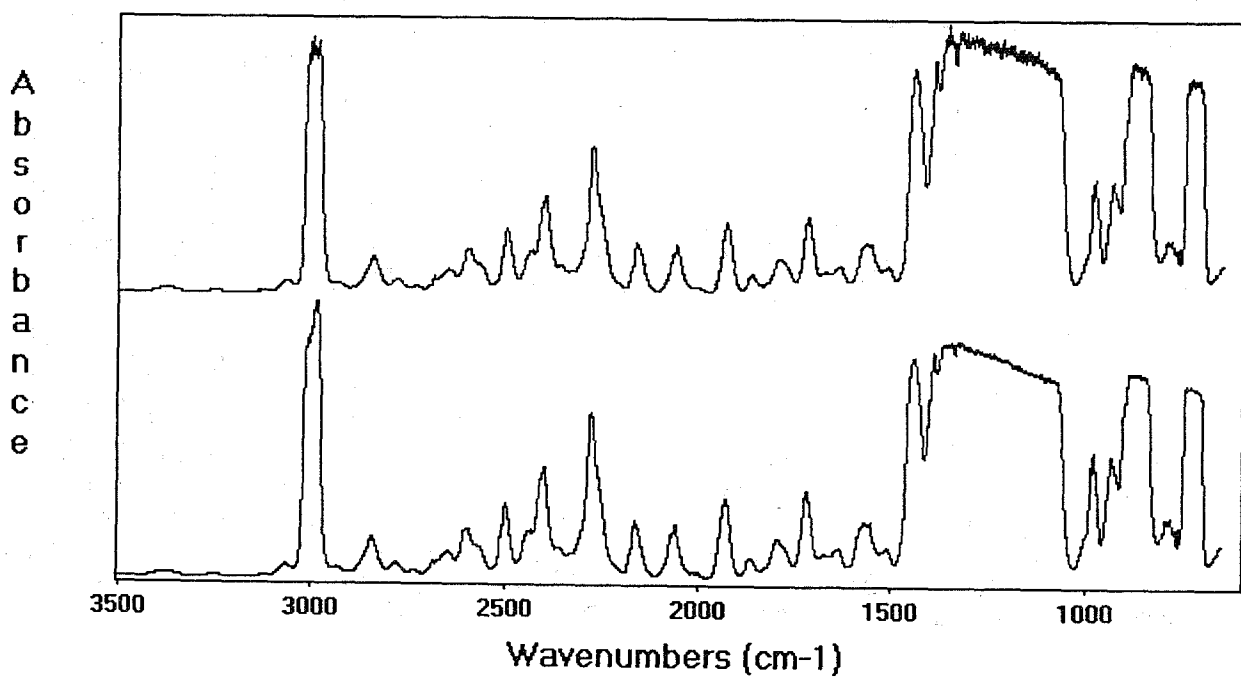


Figure A-2. Initial (lower) and 48 week (upper) spectra for Ti-15-3-3-3 in HFC-125 at 23 °C.

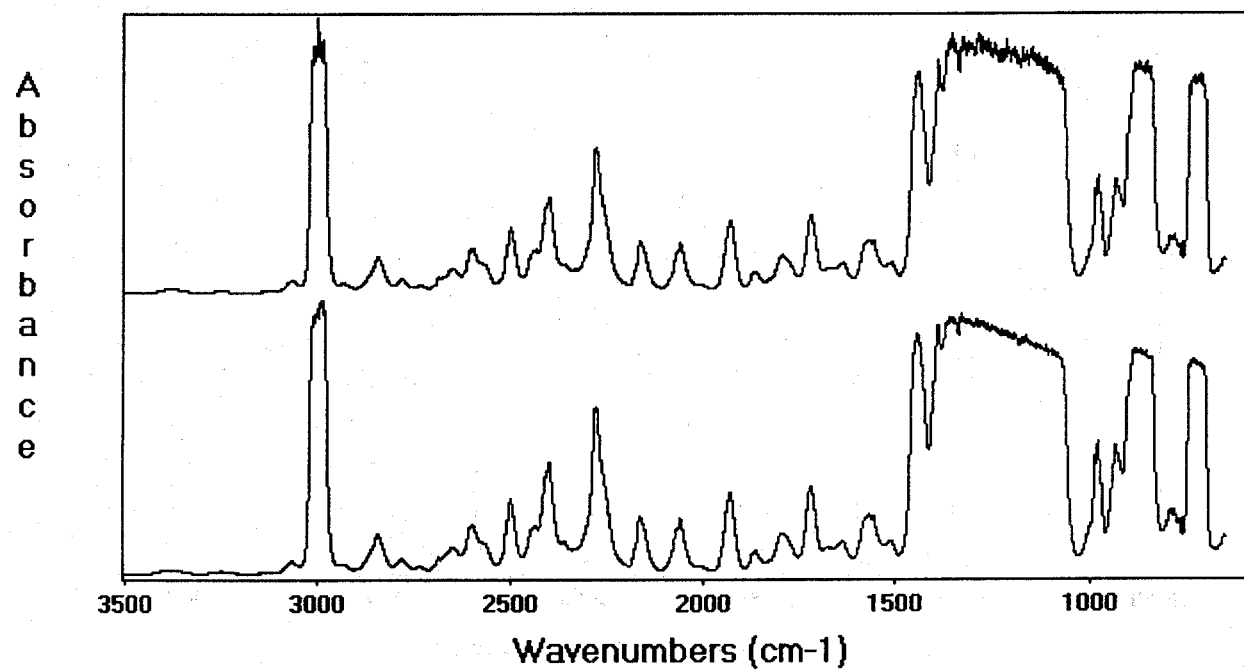


Figure A-3. Initial (lower) and 32 week (upper) spectra for C4130 in HFC-125 at 23 °C.

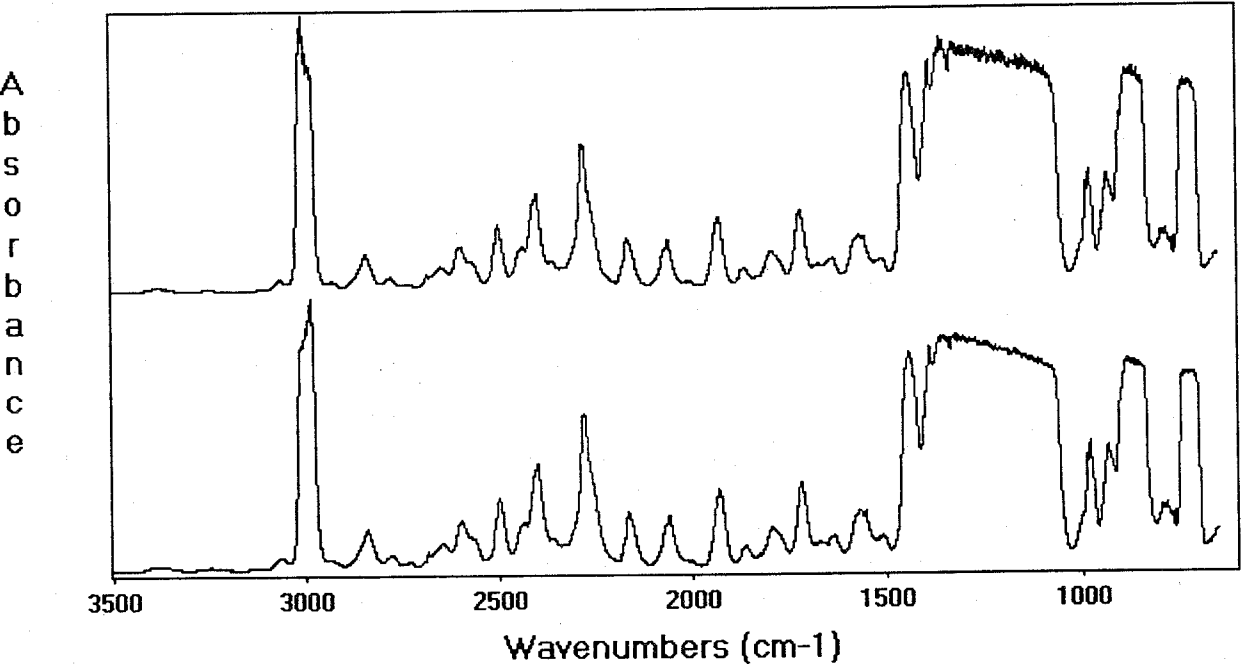


Figure A-4. Initial (lower) and 48 week (upper) spectra for I625 in HFC-125 at 23 °C.

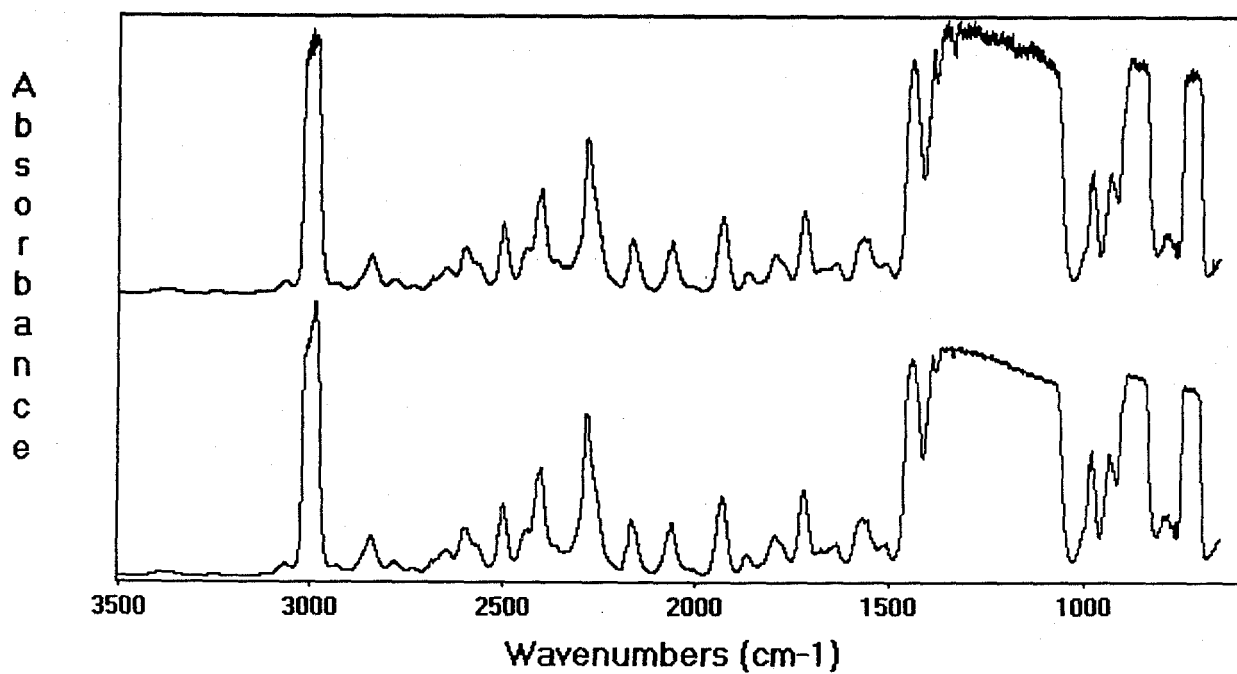


Figure A-5. Initial (lower) and 48 week (upper) spectra for nitronic 40 in HFC-125 at 150 °C.

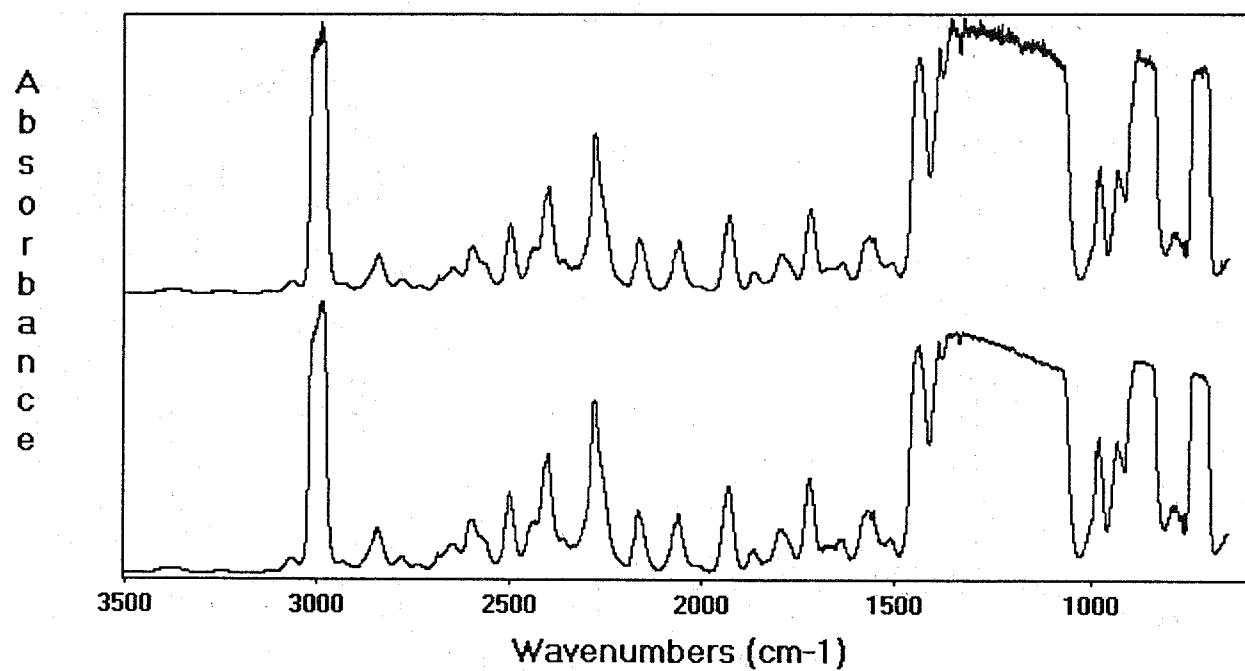


Figure A-6. Initial (lower) and 48 week (upper) spectra for Ti-15-3-3-3 in HFC-125 at 150 °C.

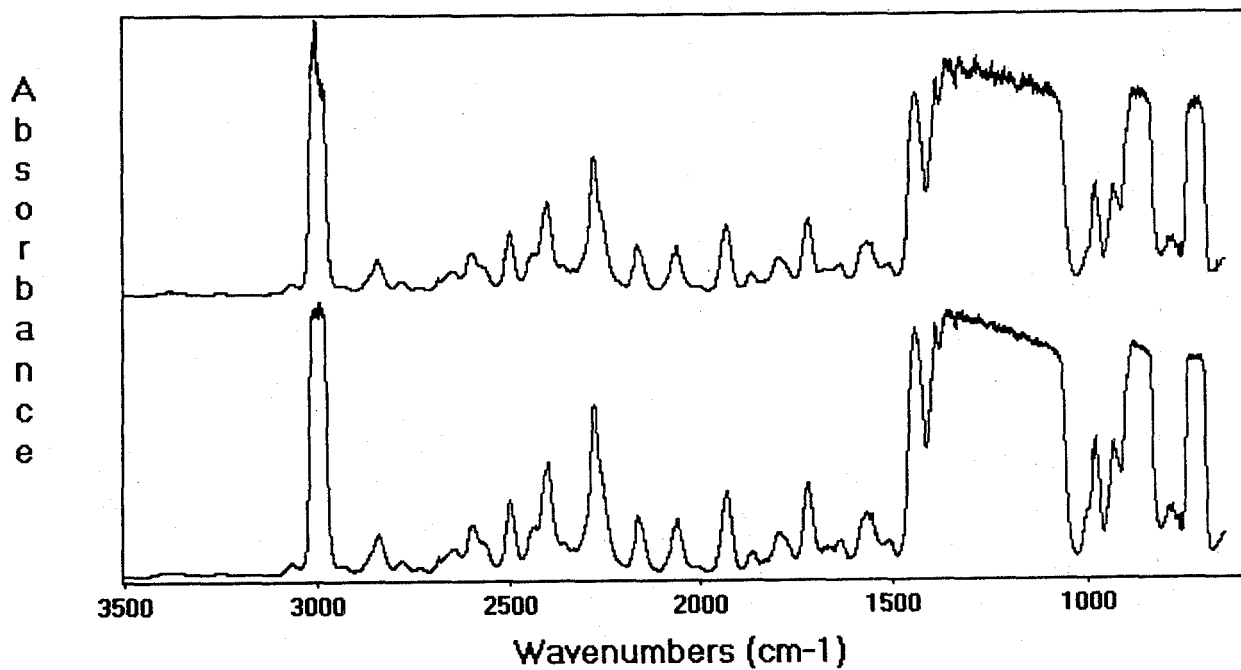


Figure A-7. Initial (lower) and 40 week (upper) spectra for C4130 in HFC-125 at 150 °C.

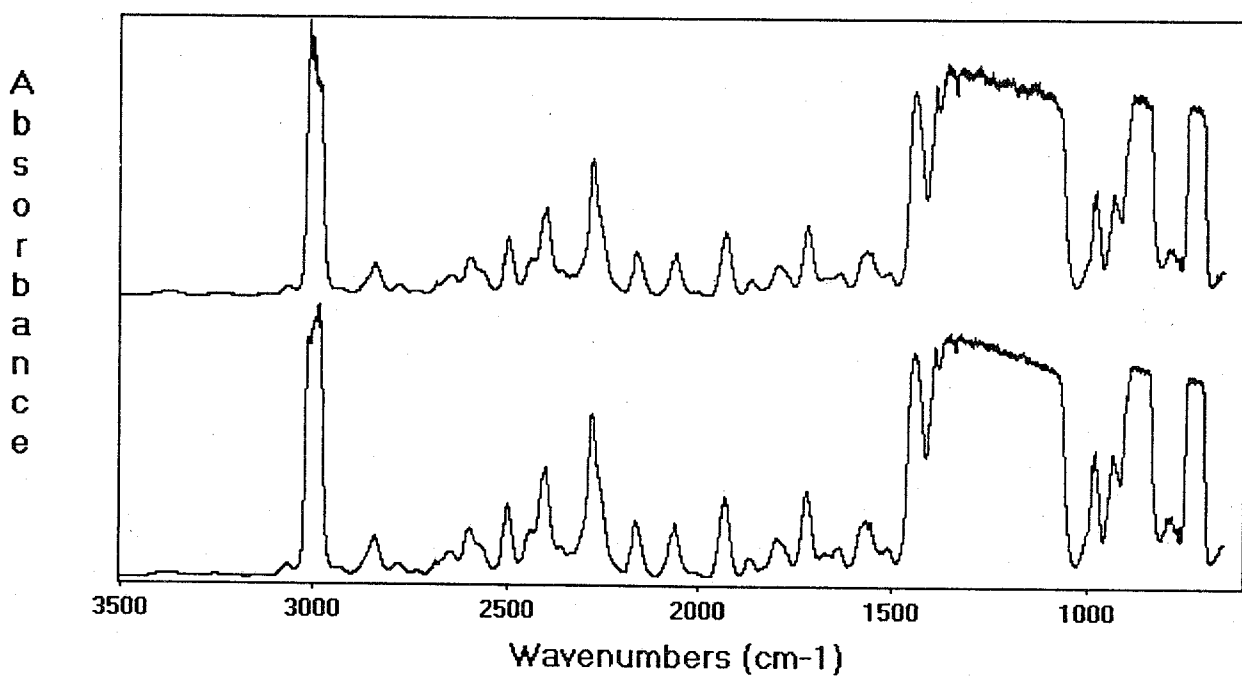


Figure A-8. Initial (lower) and 48 week (upper) spectra for I625 in HFC-125 at 150 °C.

Appendix B. Initial and Final FTIR Spectra of HFC-227ea

The spectra in Appendix B are those of the HFC-227ea. The gas cell pressure for all was 5330 Pa. The lower spectrum is for the initial analysis; the upper spectrum is for the final aged analysis. The blanks for this agent appear in Figures 17-19.

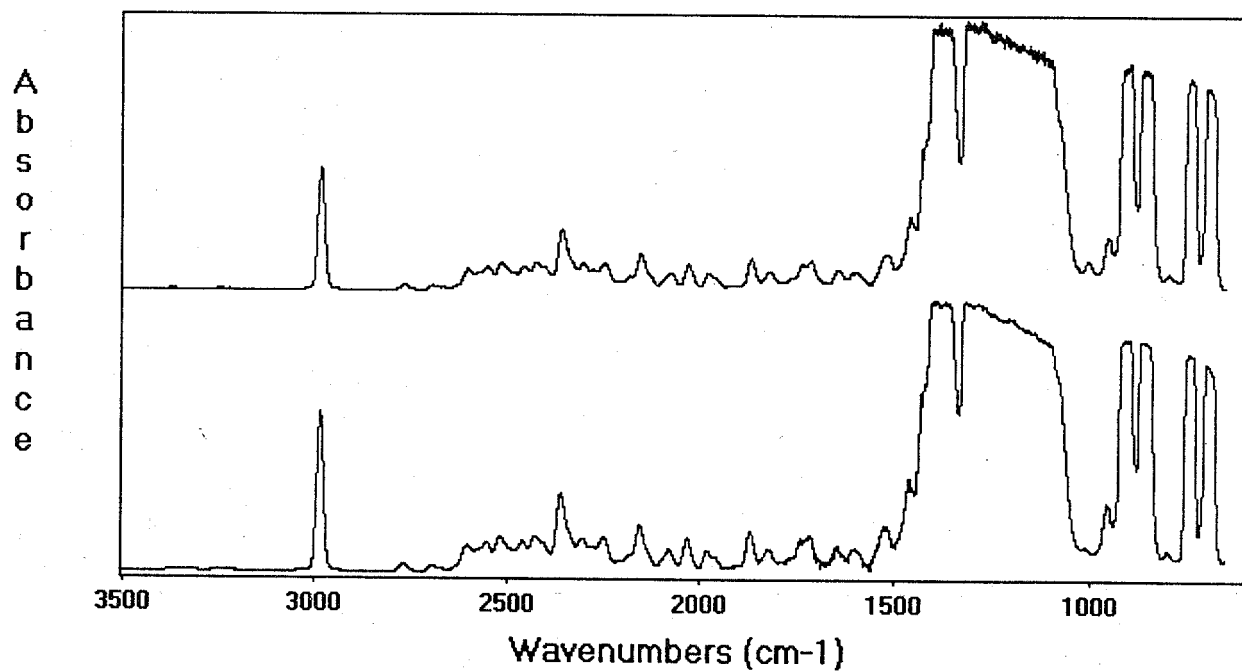


Figure B-1. Initial (lower) and 48 week (upper) spectra for nitronic 40 in HFC-227ea at 23 °C.

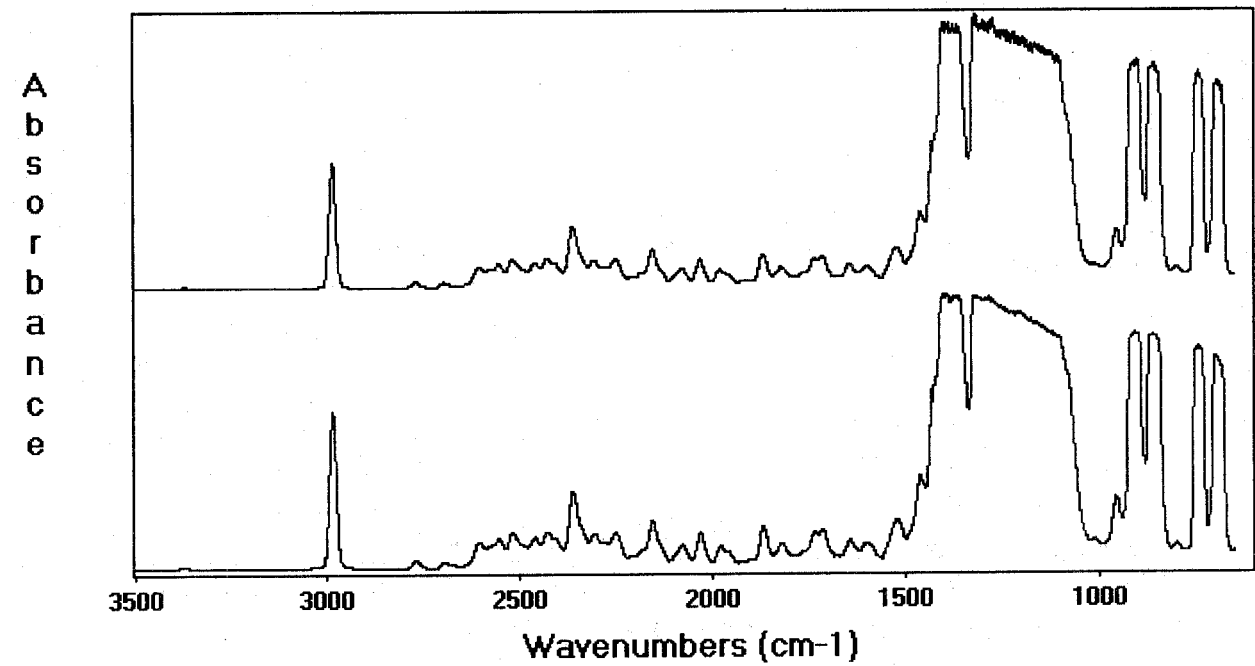


Figure B-2. Initial (lower) and 40 week (upper) spectra for Ti-15-3-3-3 in HFC-227ea at 23 °C.

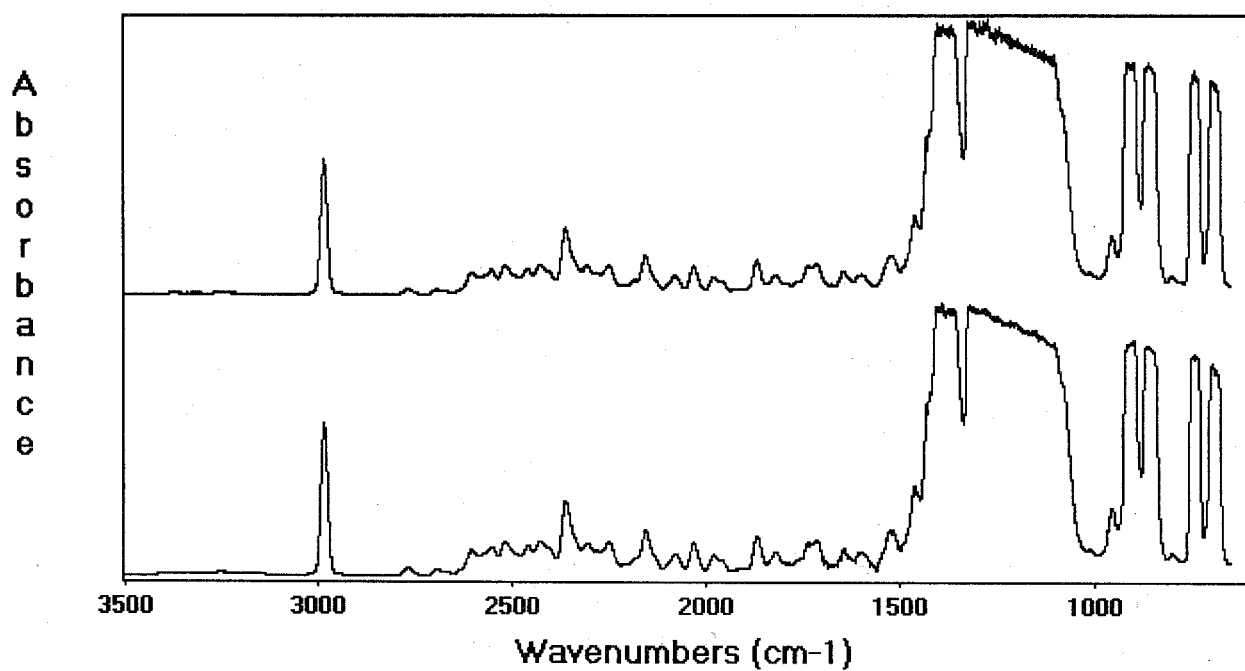


Figure B-3. Initial (lower) and 32 week (upper) spectra for C4130 in HFC-227ea at 23 °C.

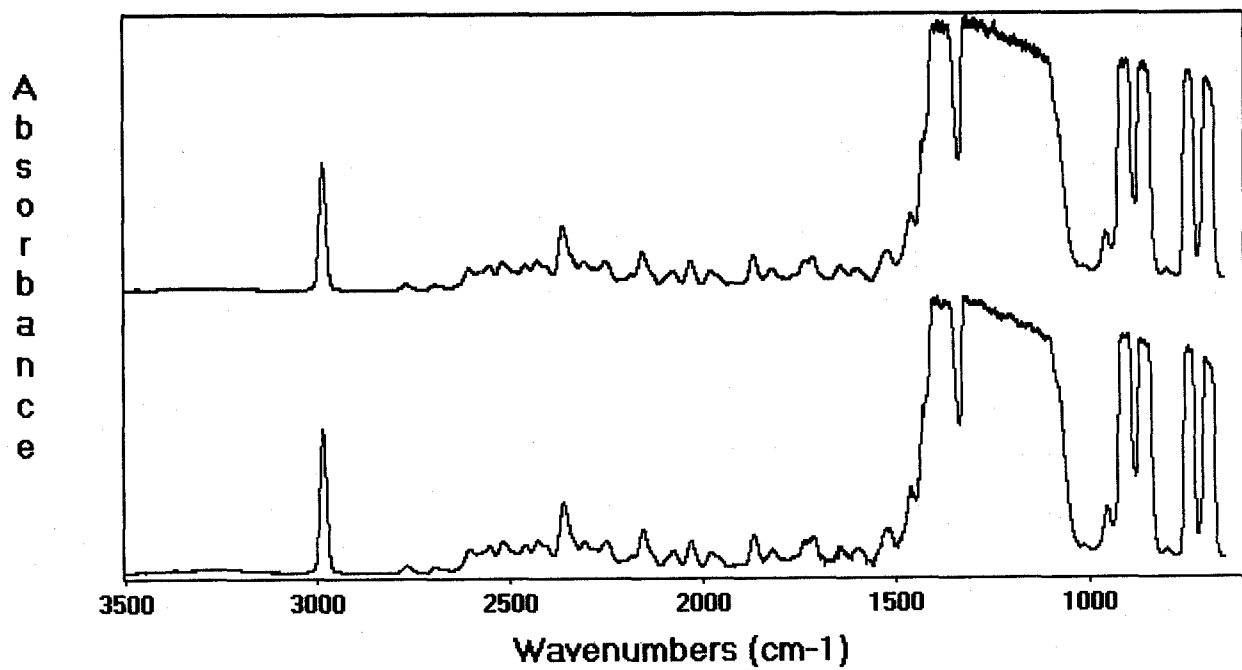


Figure B-4. Initial (lower) and 48 week (upper) spectra for I625 in HFC-227ea at 23 °C.

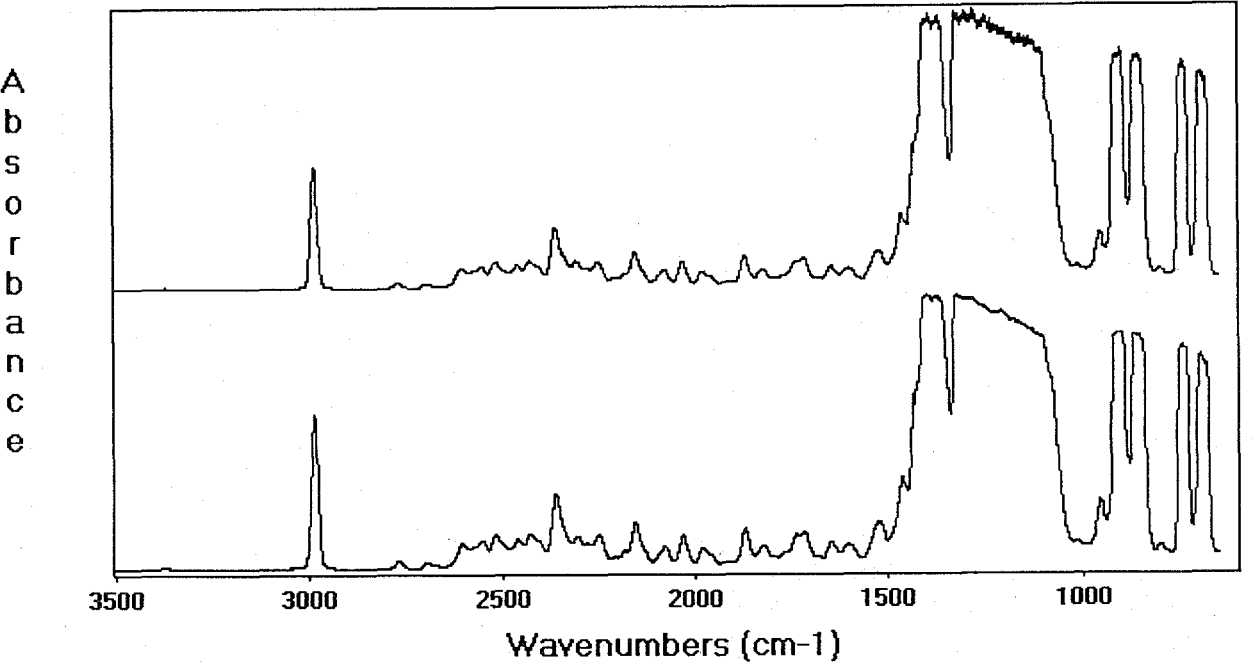


Figure B-5. Initial (lower) and 40 week (upper) spectra for nitronic 40 in HFC-227ea at 125 °C.

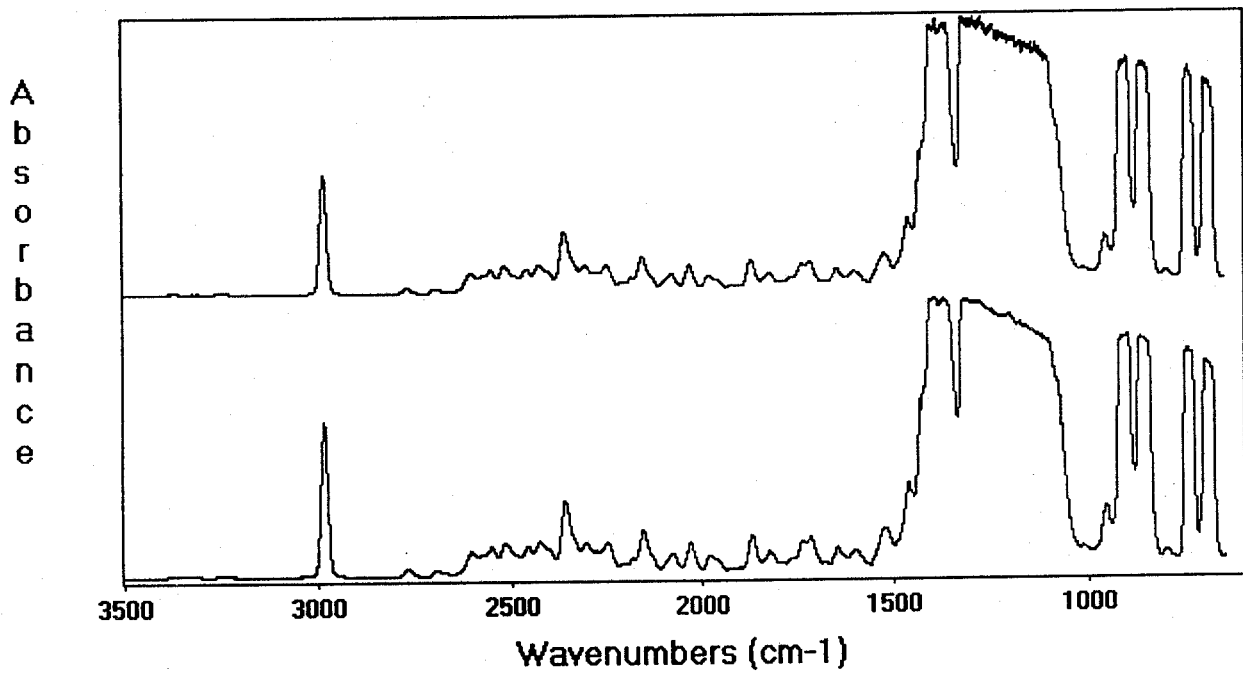


Figure B-6. Initial (lower) and 40 week (upper) spectra for Ti-15-3-3-3 in HFC-227ea at 125 °C.

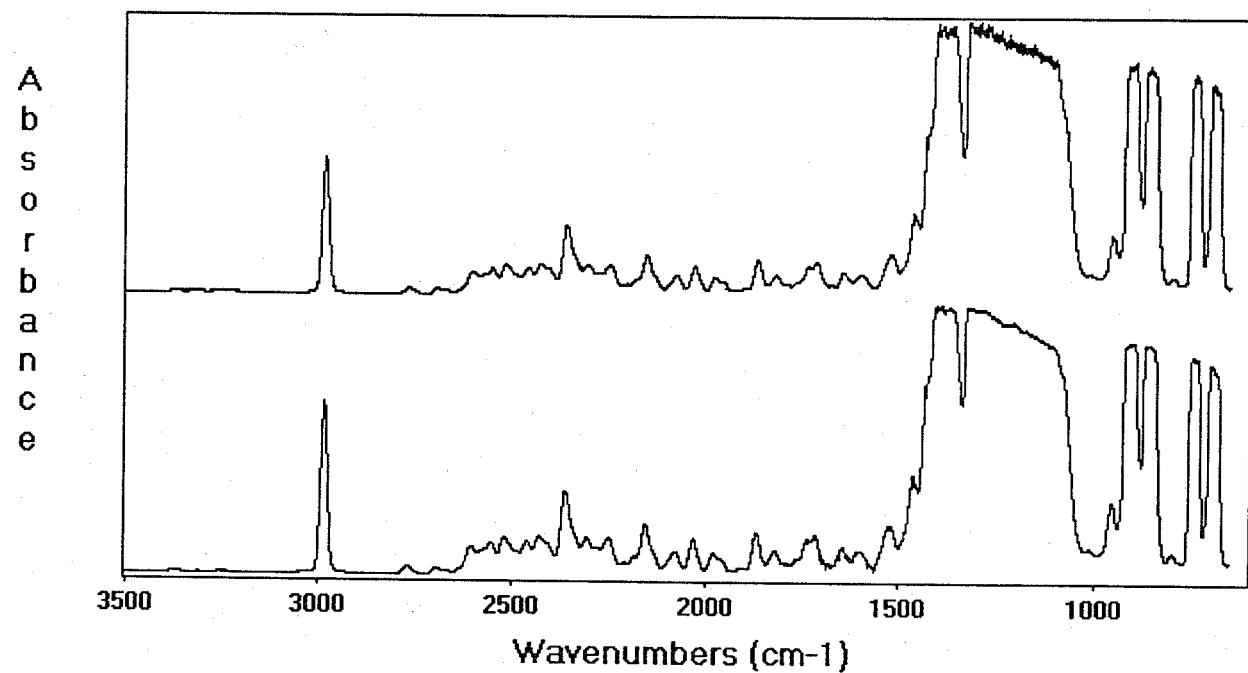


Figure B-7. Initial (lower) and 40 week (upper) spectra for C4130 in HFC-227ea at 125 °C.

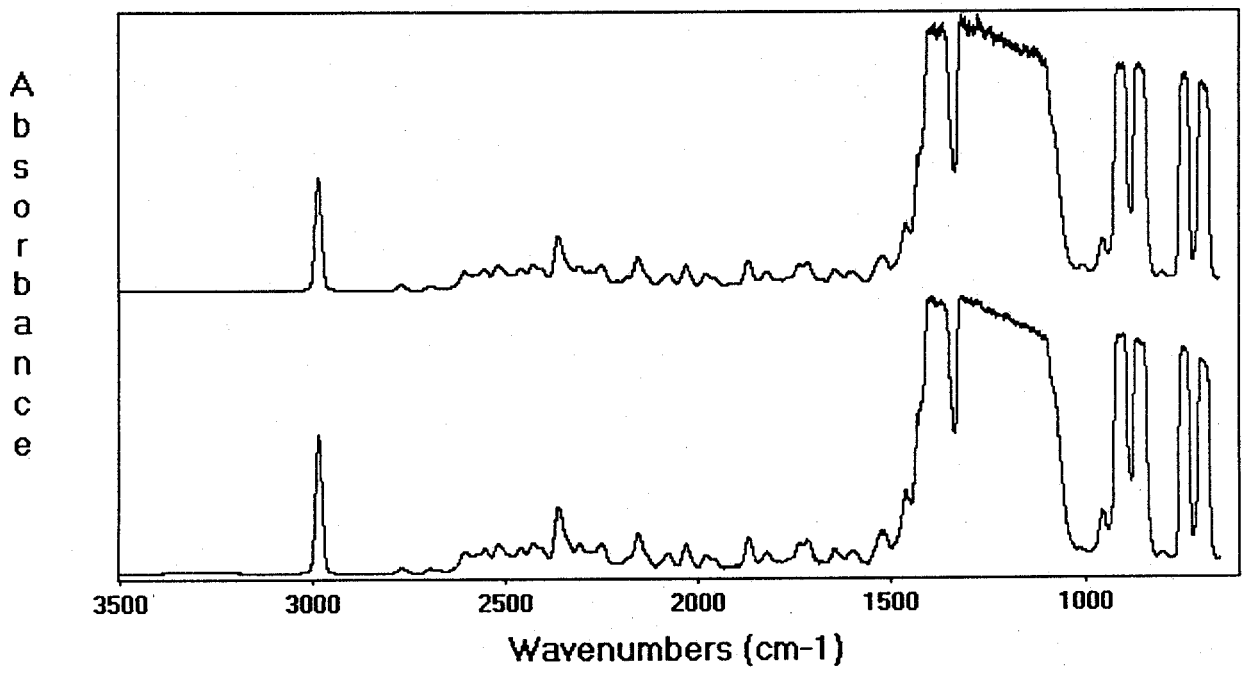


Figure B-8. Initial (lower) and 40 week (upper) spectra for I625 in HFC-227ea at 125 °C.

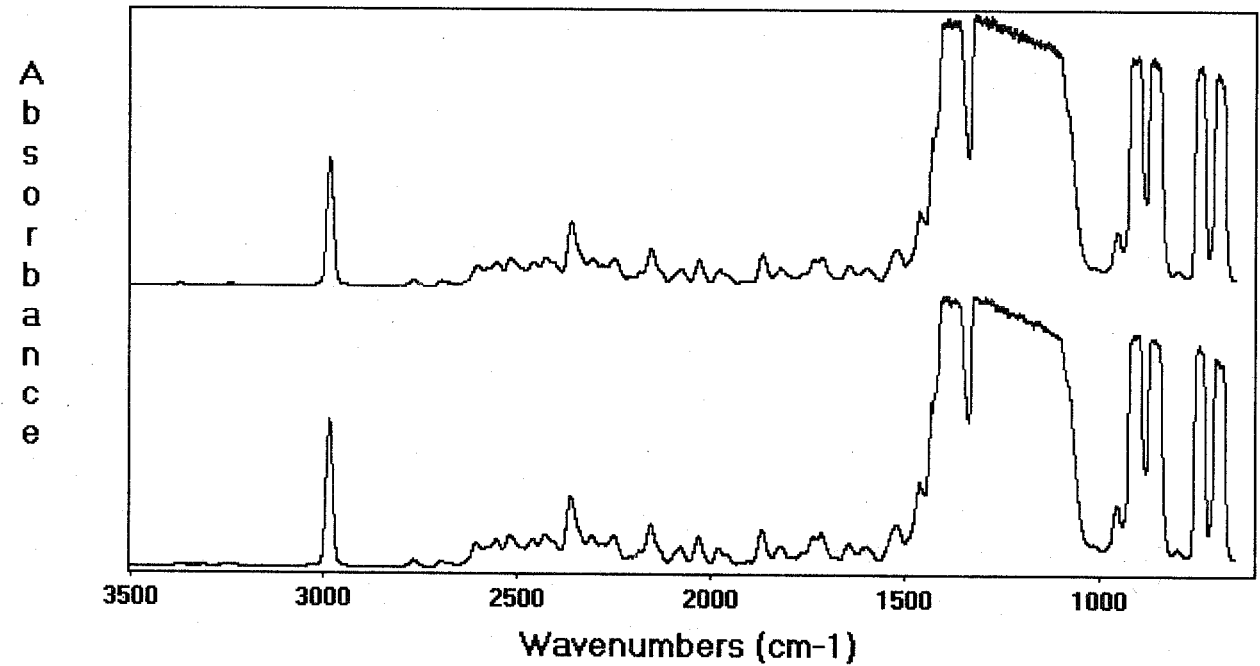


Figure B-9. Initial (lower) and 48 week (upper) spectra for nitronic 40 in HFC-227ea at 150 °C.

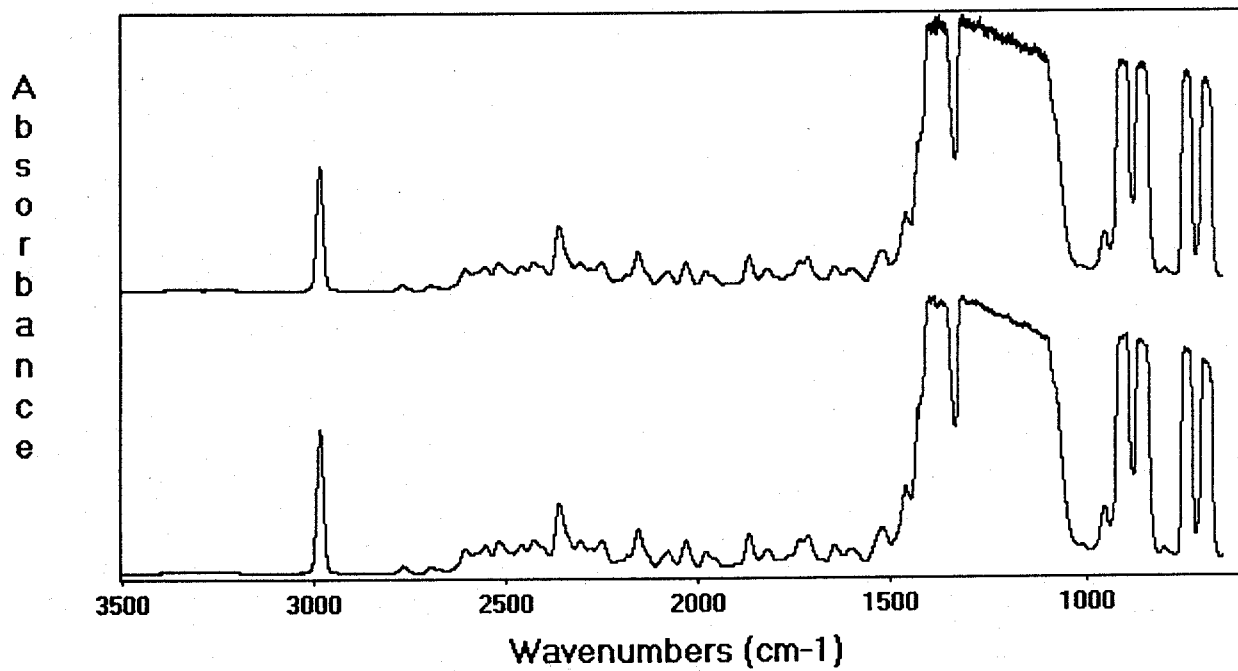


Figure B-10. Initial (lower) and 48 week (upper) spectra for Ti-15-3-3-3 in HFC-227ea at 150 °C.

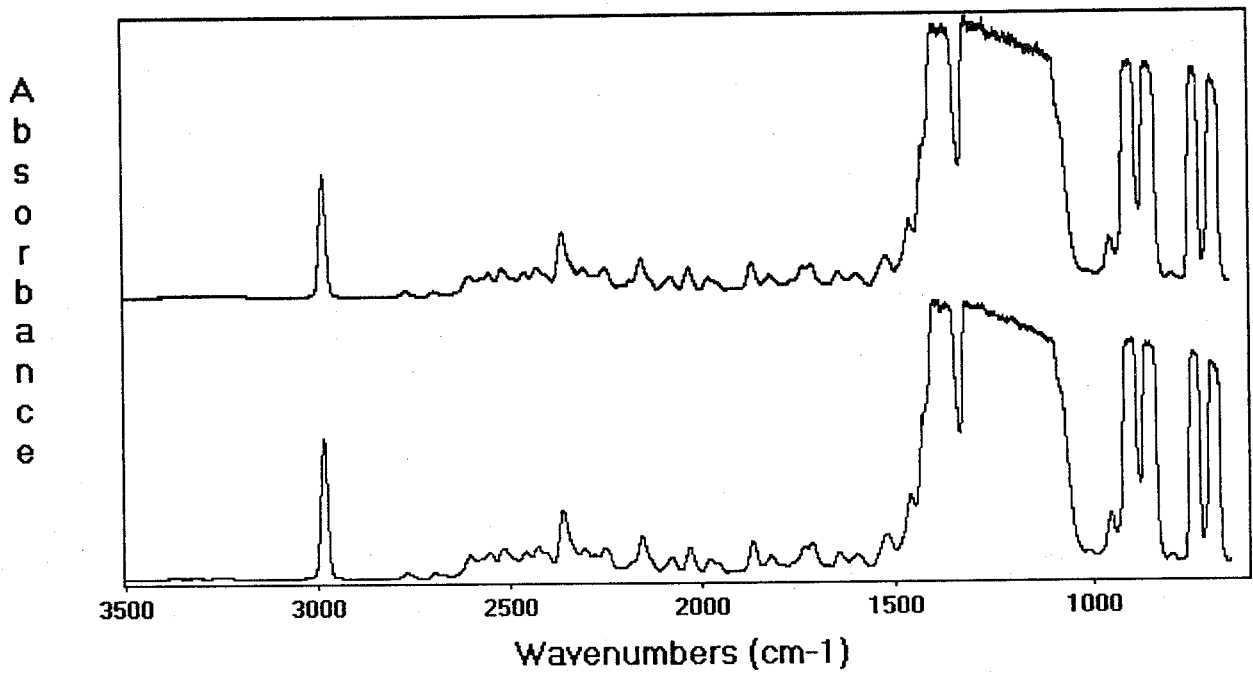


Figure B-11. Initial (lower) and 40 week (upper) spectra for C4130 in HFC-227ea at 150 °C.

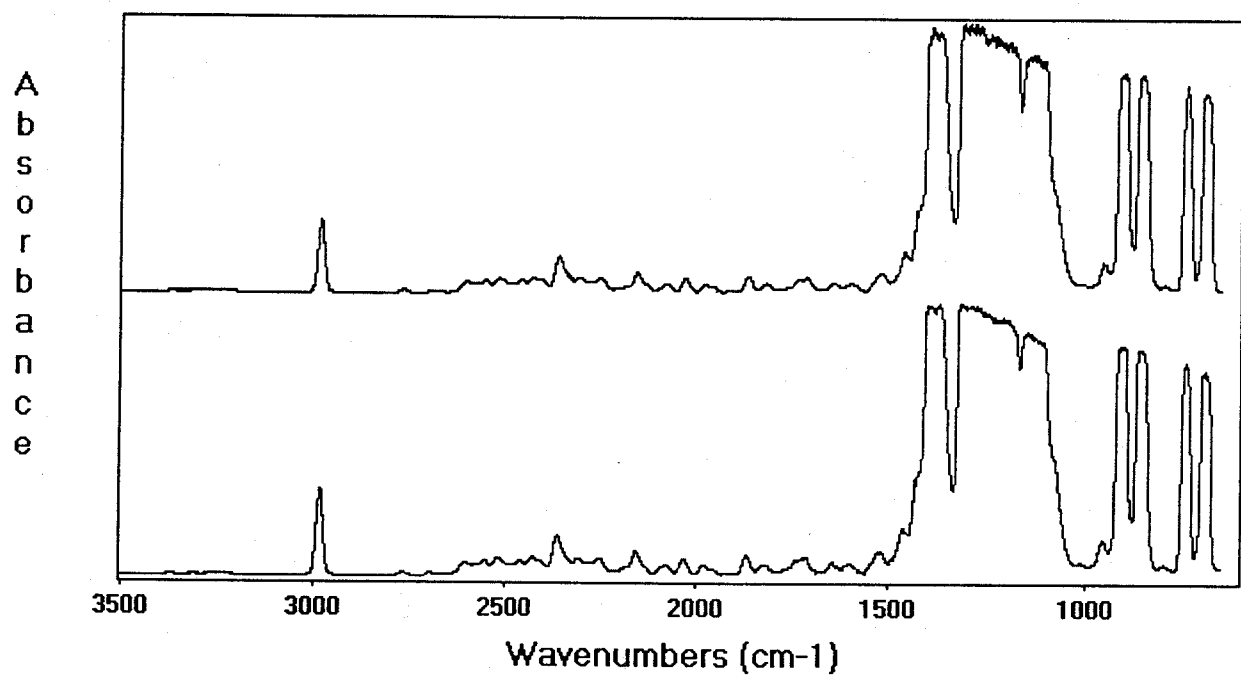


Figure B-12. Initial (lower) and 48 week (upper) spectra for I625 in HFC-227ea at 150 °C.

Appendix C. Initial and Final FTIR Spectra of CF₃I Tested in the Dry Condition without Copper

The spectra in Appendix C are those of the CF₃I. The gas cell pressure for all was 5330 Pa. The lower spectrum is for the initial analysis; the upper spectrum is for the final aged analysis.

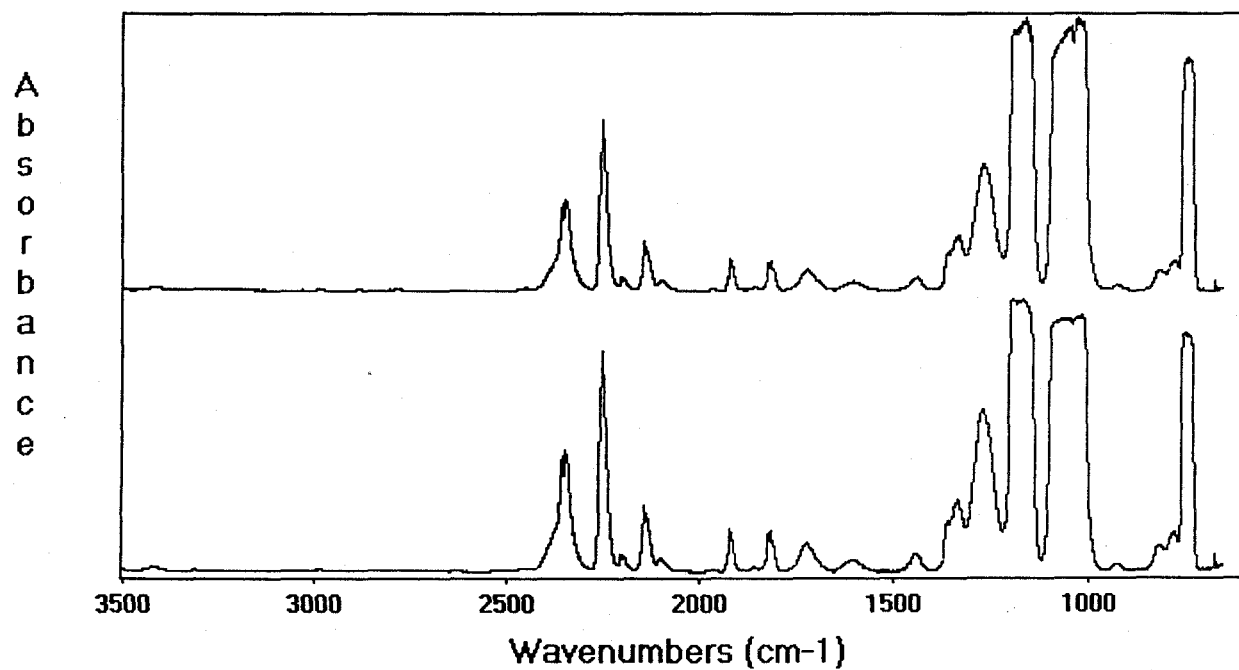


Figure C-1. Initial (lower) and 48 week (upper) spectra for the blank in CF_3I tested in the dry condition without copper at 23 °C.

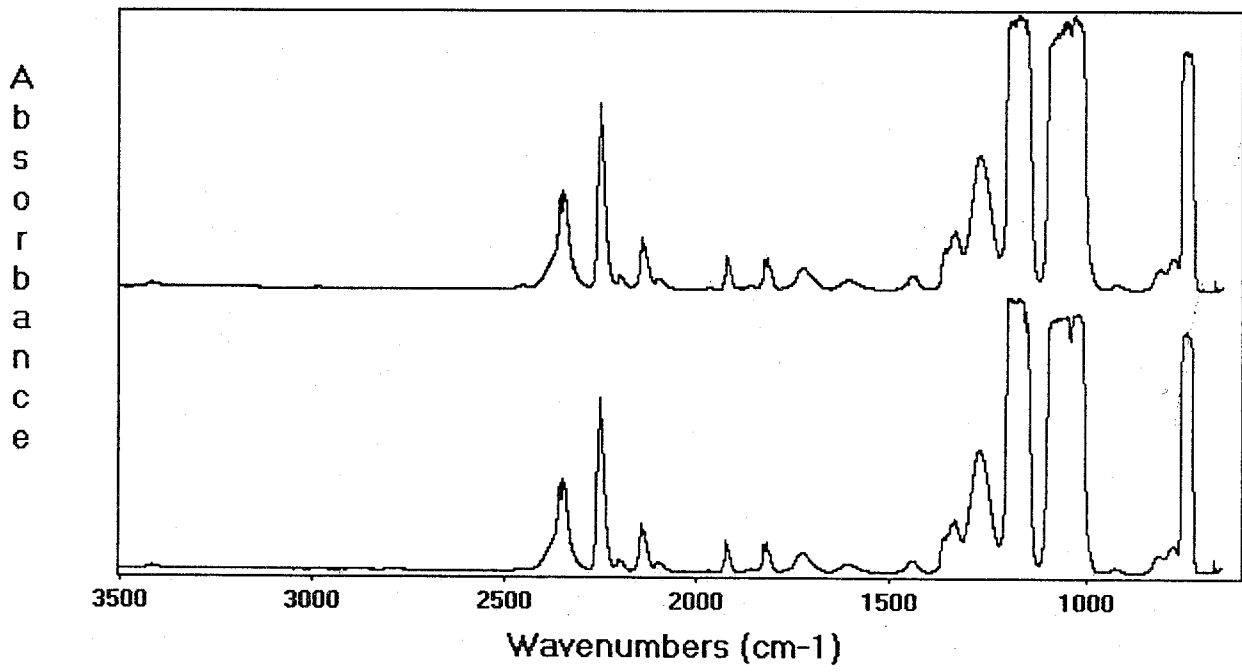


Figure C-2. Initial (lower) and 48 week (upper) spectra for nitronic 40 in CF₃I tested in the dry condition without copper at 23 °C.

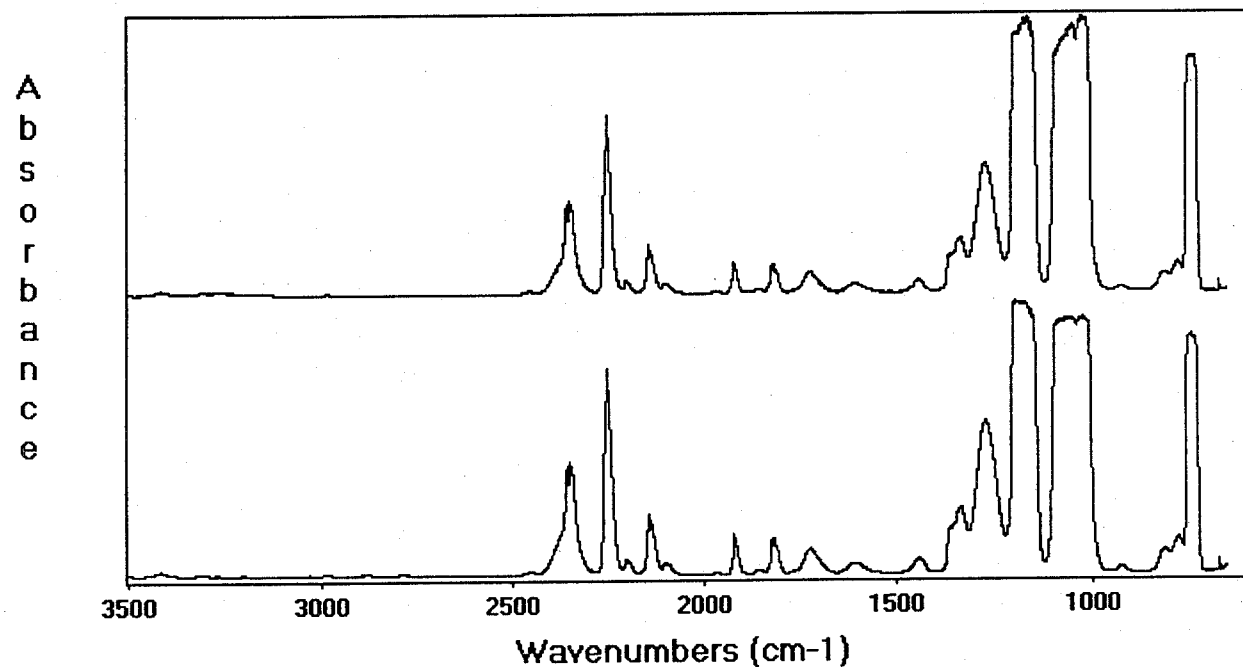


Figure C-3. Initial (lower) and 48 week (upper) spectra for Ti-15-3-3-3 in CF₃I tested in the dry condition without copper at 23 °C.

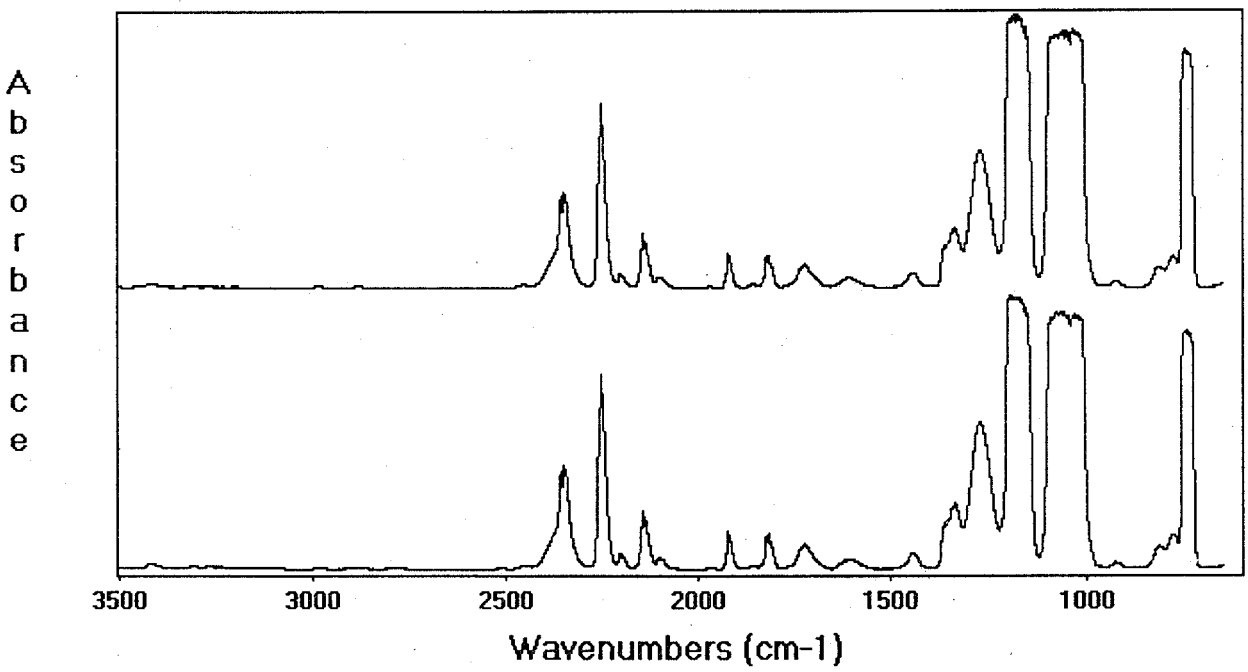


Figure C-4. Initial (lower) and 40 week (upper) spectra for C4130 in CF₃I tested in the dry condition without copper at 23 °C.

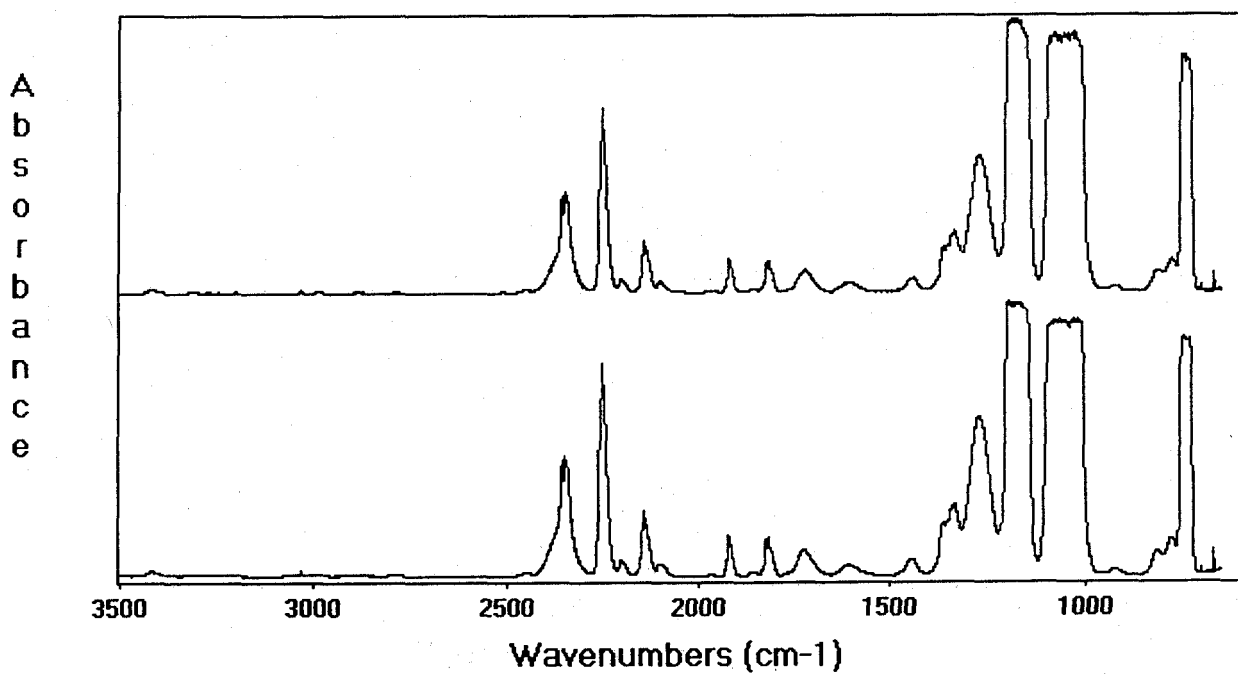


Figure C-5. Initial (lower) and 44 week (upper) spectra for I625 in CF_3I tested in the dry condition without copper at 23 °C.

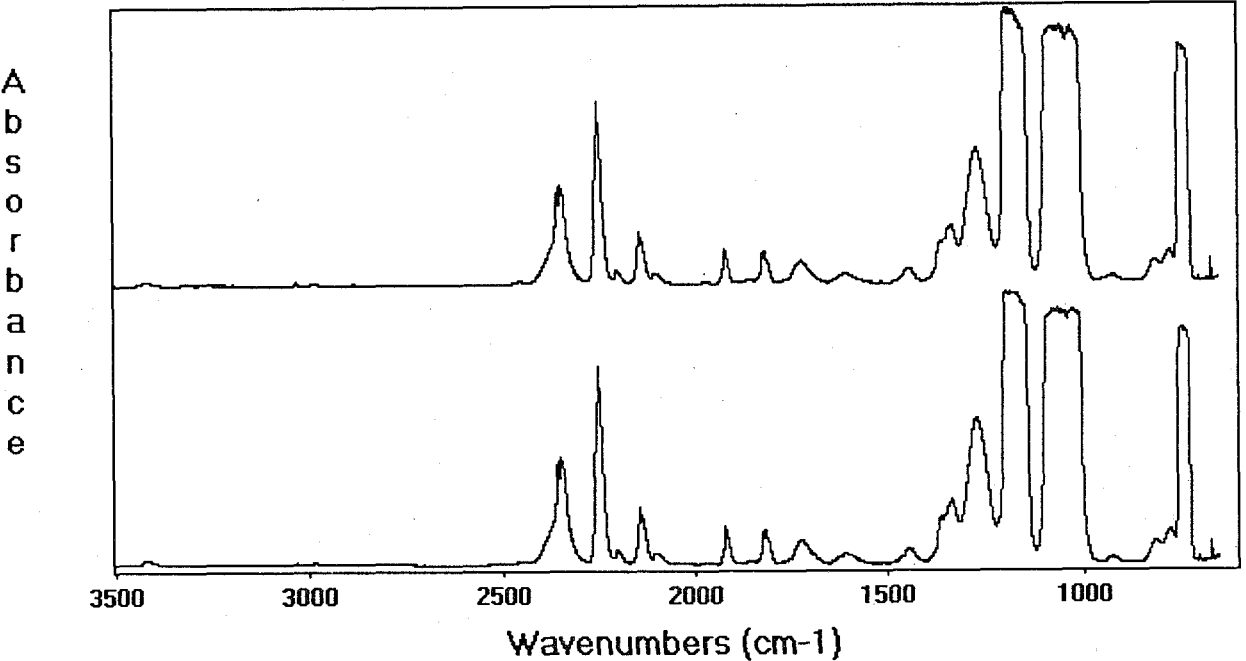


Figure C-6. Initial (lower) and 44 week (upper) spectra for the blank in CF₃I tested in the dry condition without copper at 100 °C.

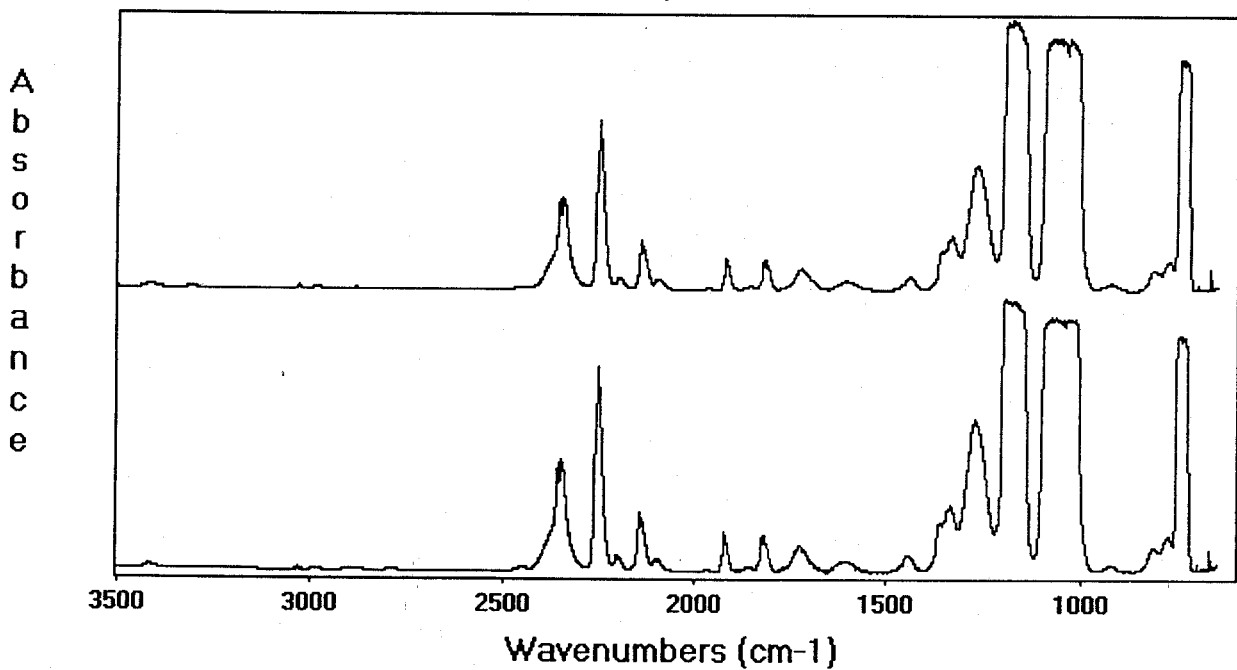


Figure C-7. Initial (lower) and 32 week (upper) spectra for nitronic 40 in CF_3I tested in the dry condition without copper at 100 °C.

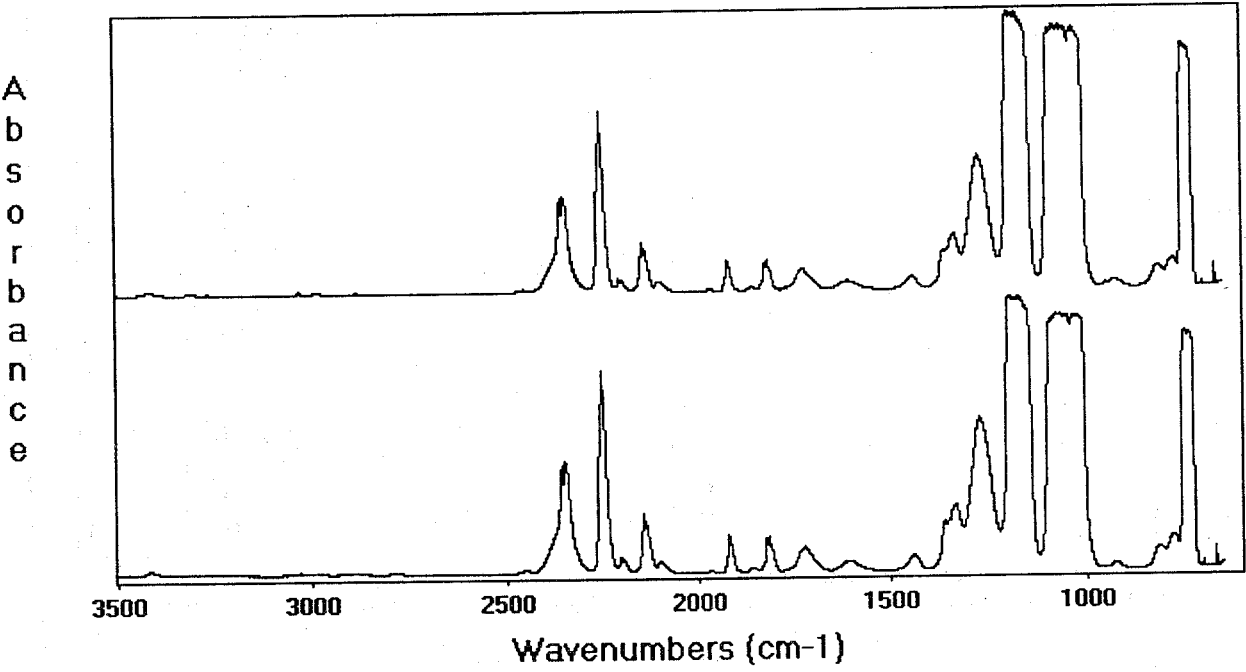


Figure C-8. Initial (lower) and 44 week (upper) spectra for Ti-15-3-3-3 in CF₃I tested in the dry condition without copper at 100 °C.

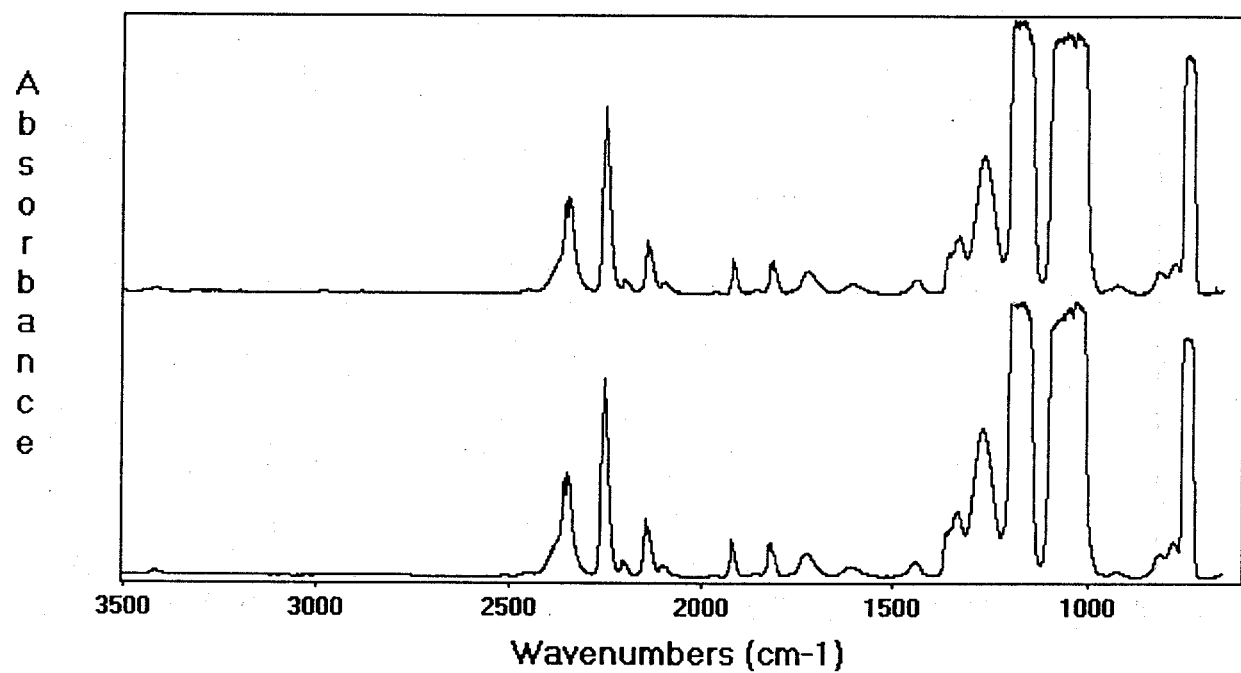


Figure C-9. Initial (lower) and 40 week (upper) spectra for C4130 in CF_3I tested in the dry condition without copper at 100 °C.

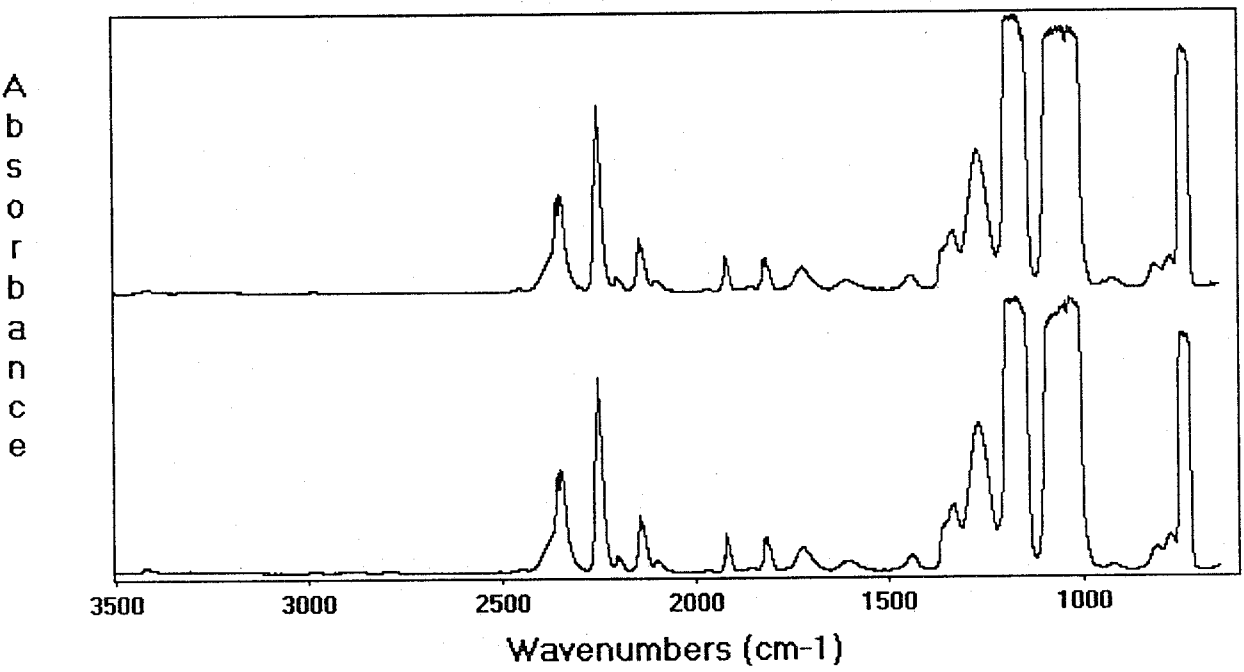


Figure C-10. Initial (lower) and 40 week (upper) spectra for I625 in CF₃I tested in the dry condition without copper at 100 °C.

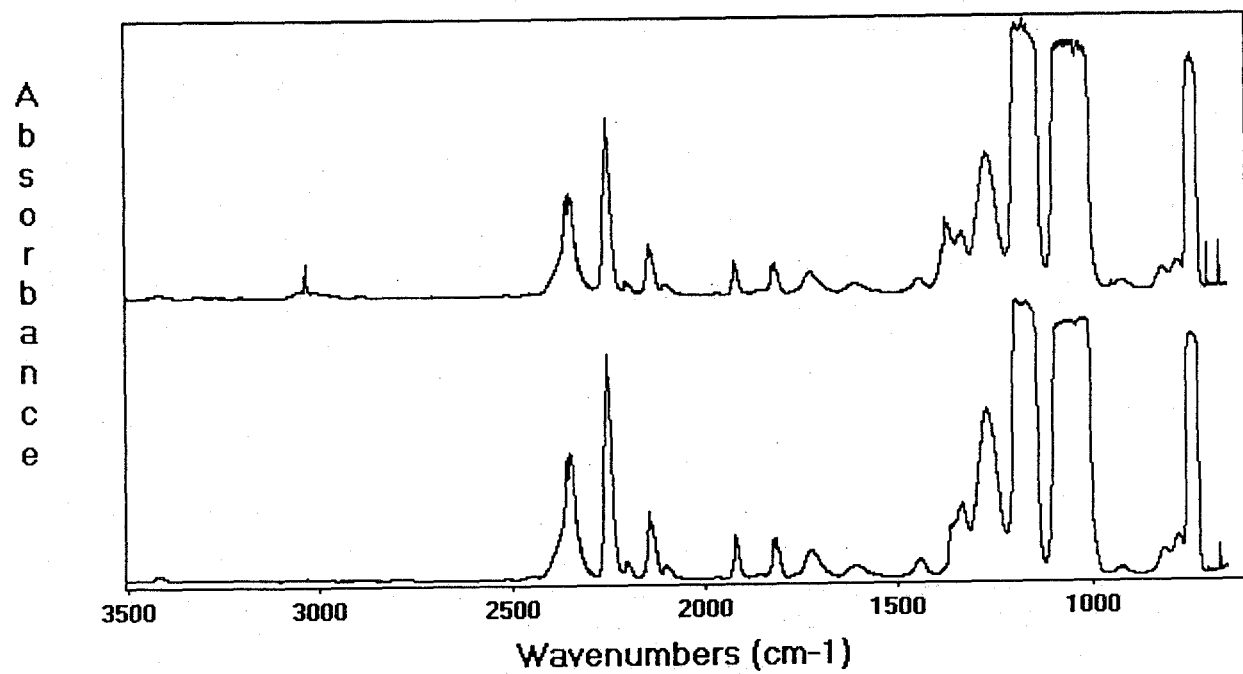


Figure C-11.

Initial (lower) and 52 week (upper) spectra for the blank in CF_3I tested in the dry condition without copper at 150 °C.

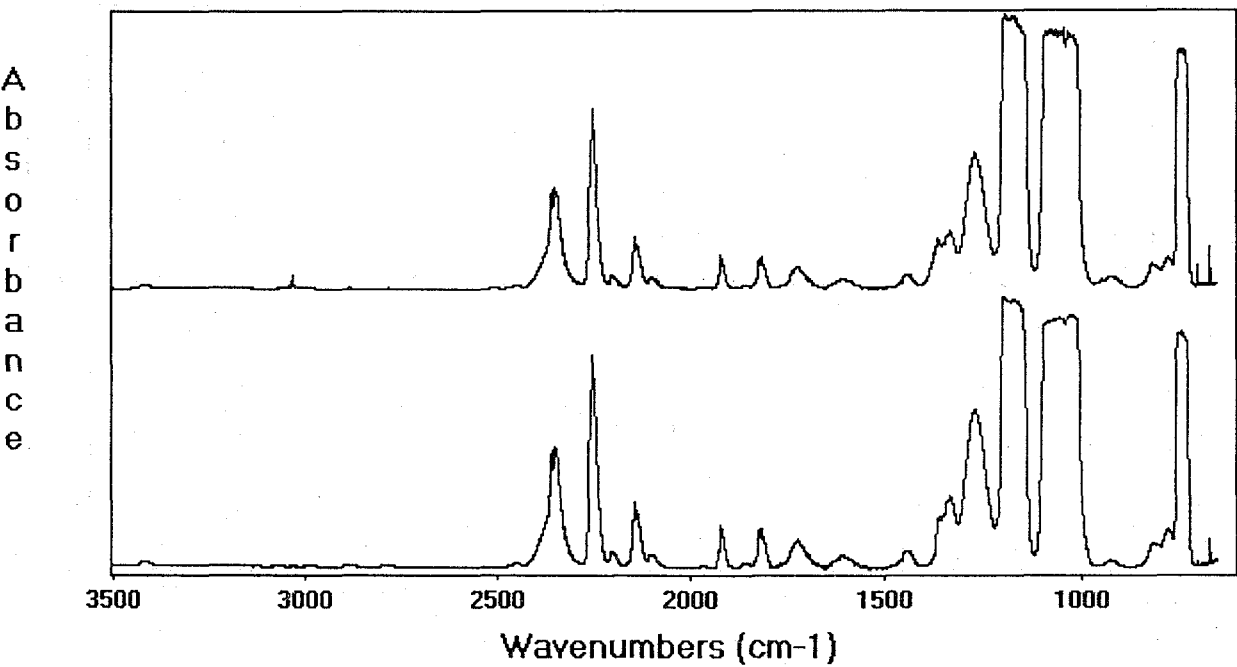


Figure C-12. Initial (lower) and 52 week (upper) spectra for nitronic 40 in CF₃I tested in the dry condition without copper at 150 °C.

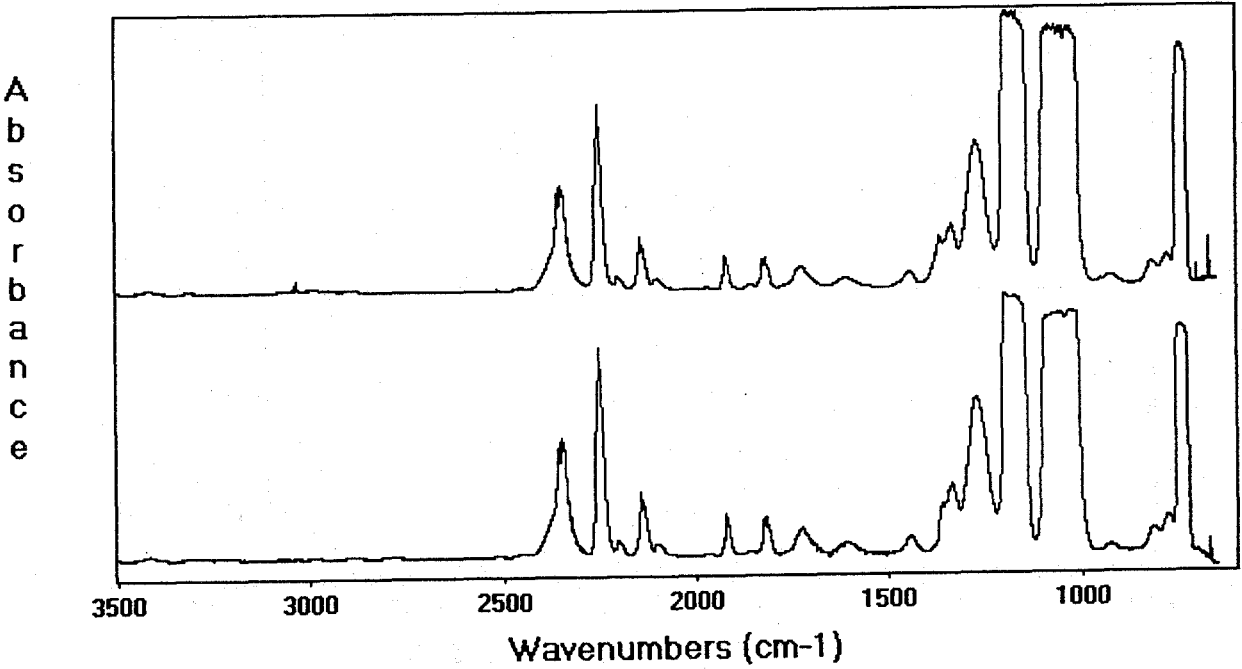


Figure C-13. Initial (lower) and 52 week (upper) spectra for Ti-15-3-3-3 in CF₃I tested in the dry condition without copper at 150 °C.

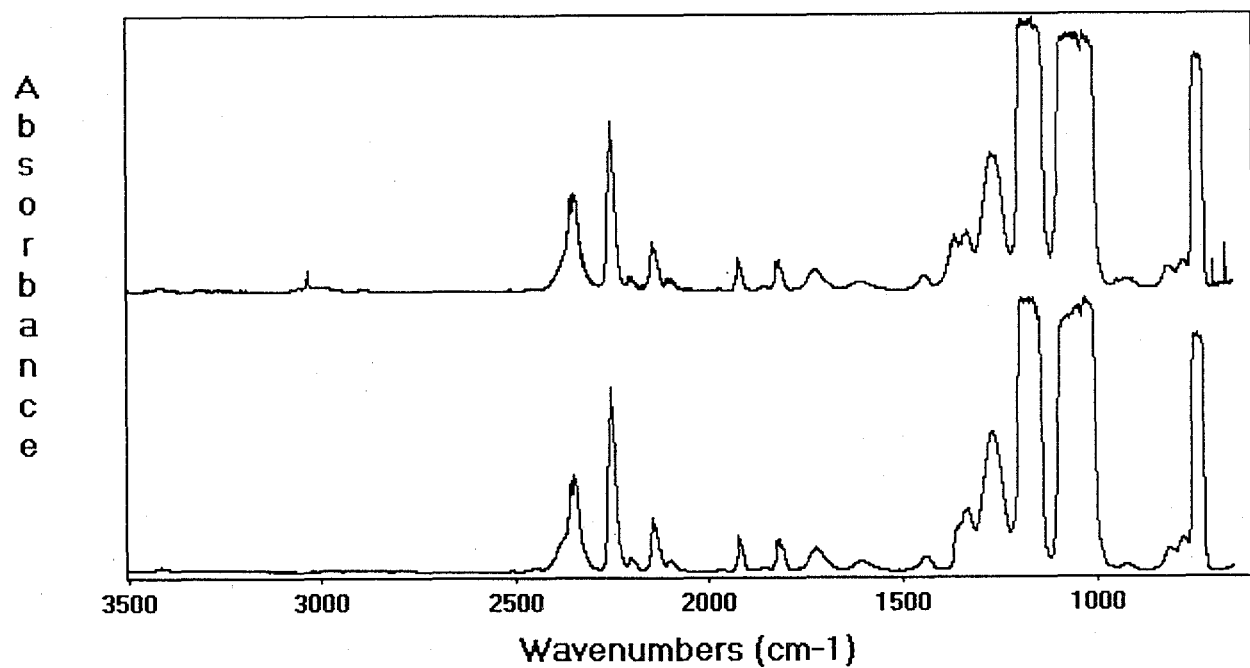


Figure C-14.

Initial (lower) and 40 week (upper) spectra for C4130 in CF_3I tested in the dry condition without copper at 150 °C.

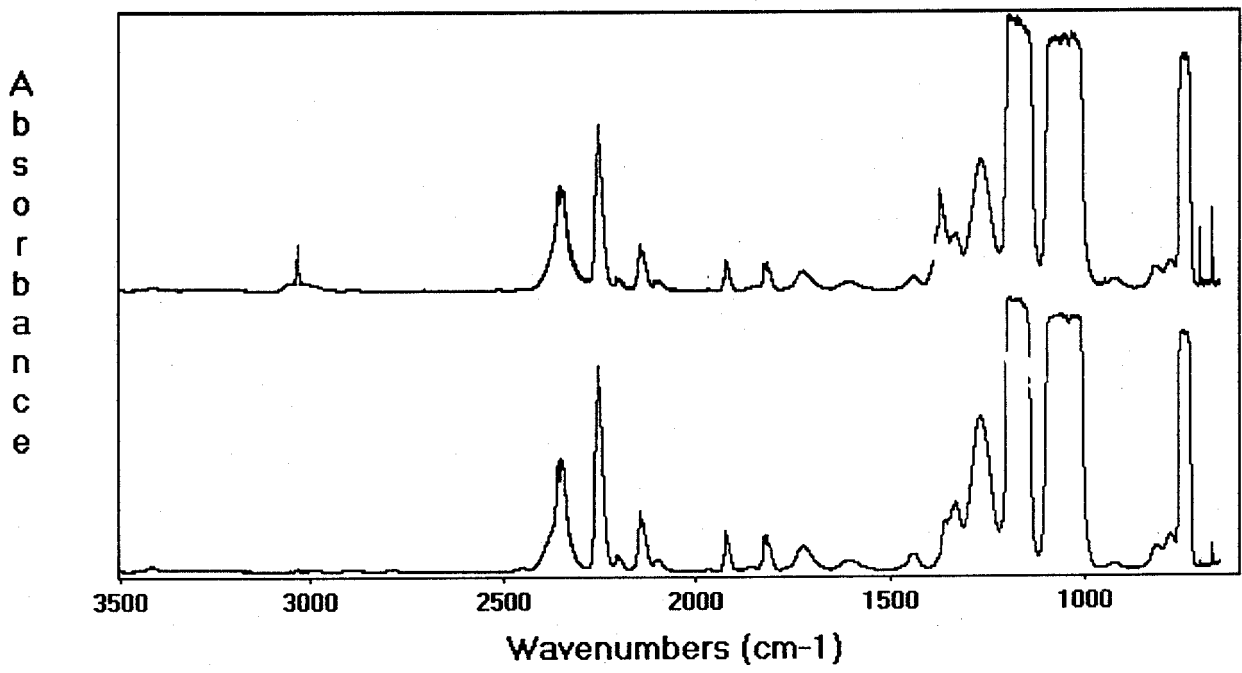


Figure C-15. Initial (lower) and 44 week (upper) spectra for I625 in CF₃I tested in the dry condition without copper at 150 °C.

Appendix D. Initial and Final FTIR Spectra of CF₃I Tested in the Dry Condition with Copper

The spectra in Appendix D are those of the CF₃I. The gas cell pressure for all was 5330 Pa. The lower spectrum is for the initial analysis; the upper spectrum is for the final aged analysis.

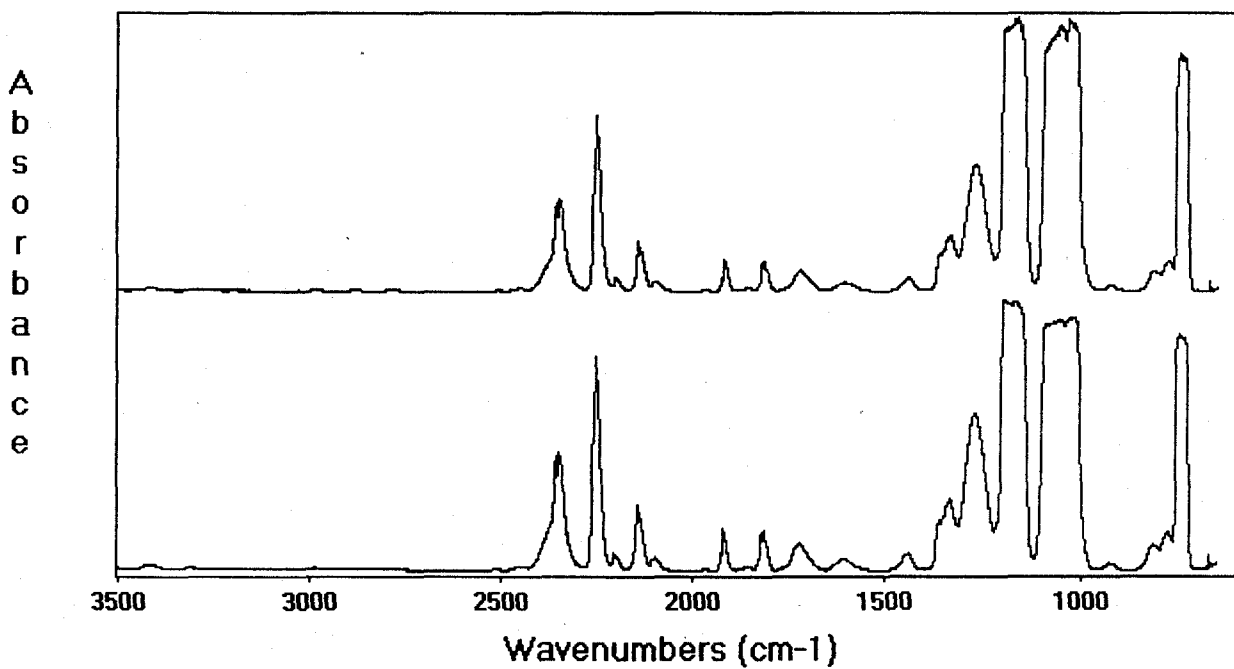


Figure D-1. Initial (lower) and 48 week (upper) spectra for the blank in CF_3I tested in the dry condition with copper at 23 °C.

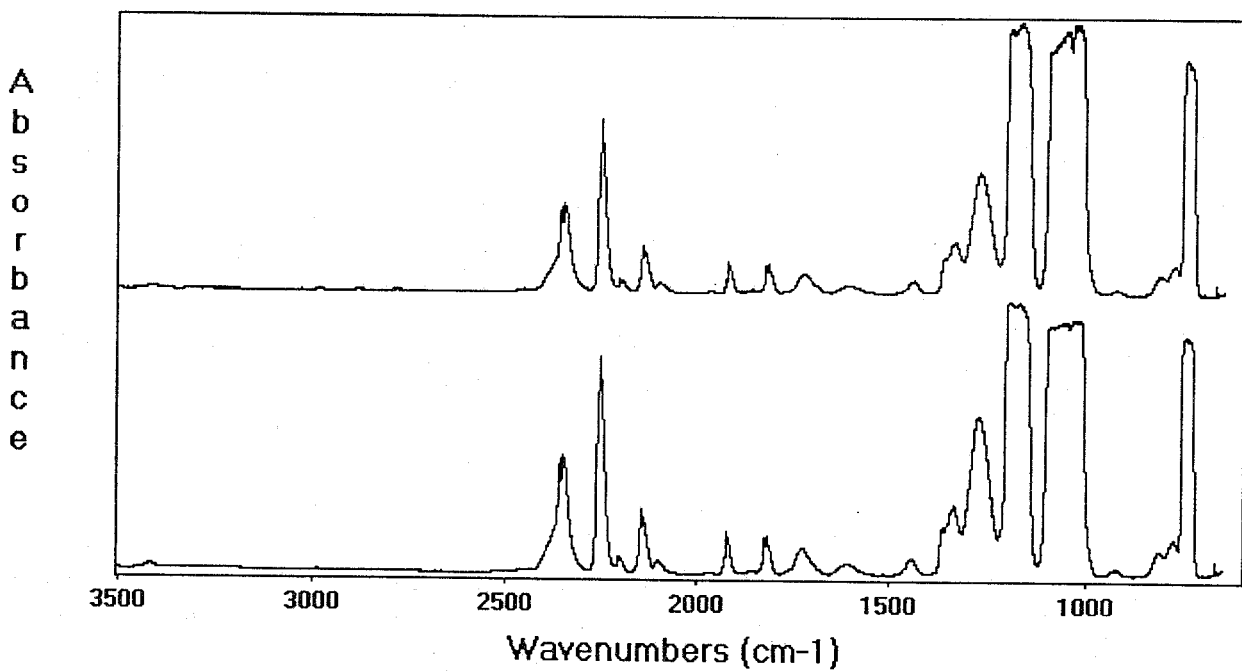


Figure D-2.

Initial (lower) and 48 week (upper) spectra for nitronic 40 in CF_3I tested in the dry condition with copper at 23 °C.

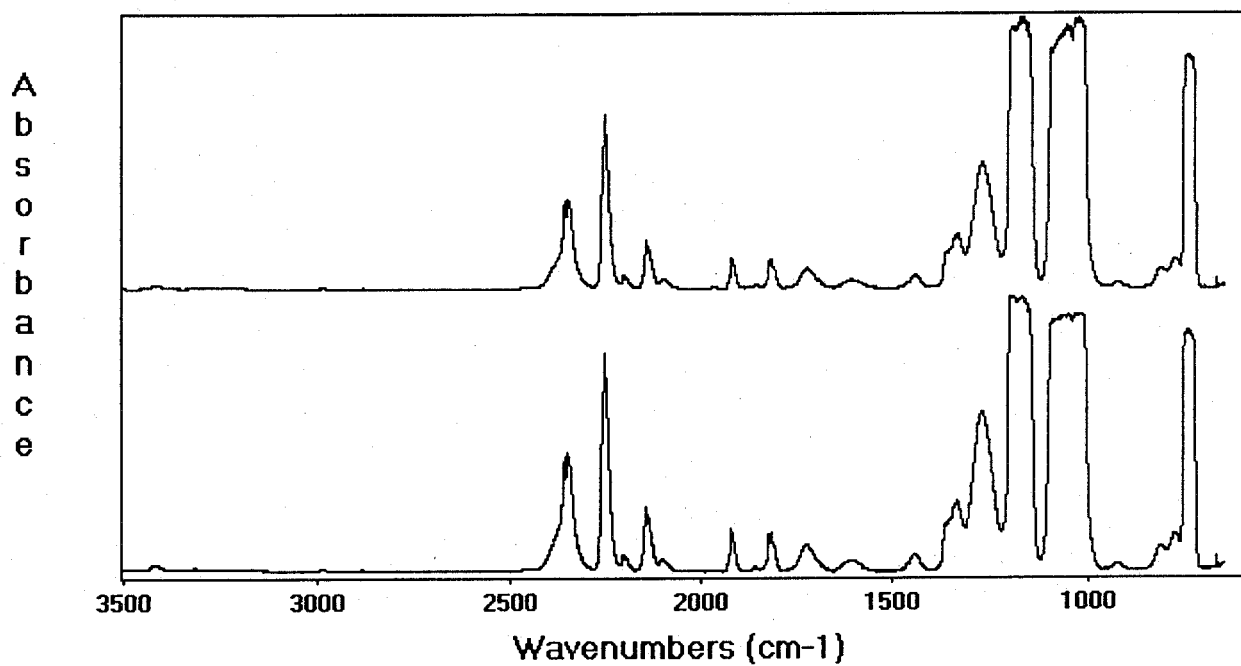


Figure D-3.

Initial (lower) and 48 week (upper) spectra for Ti-15-3-3-3 in CF_3I tested in the dry condition with copper at 23 °C.

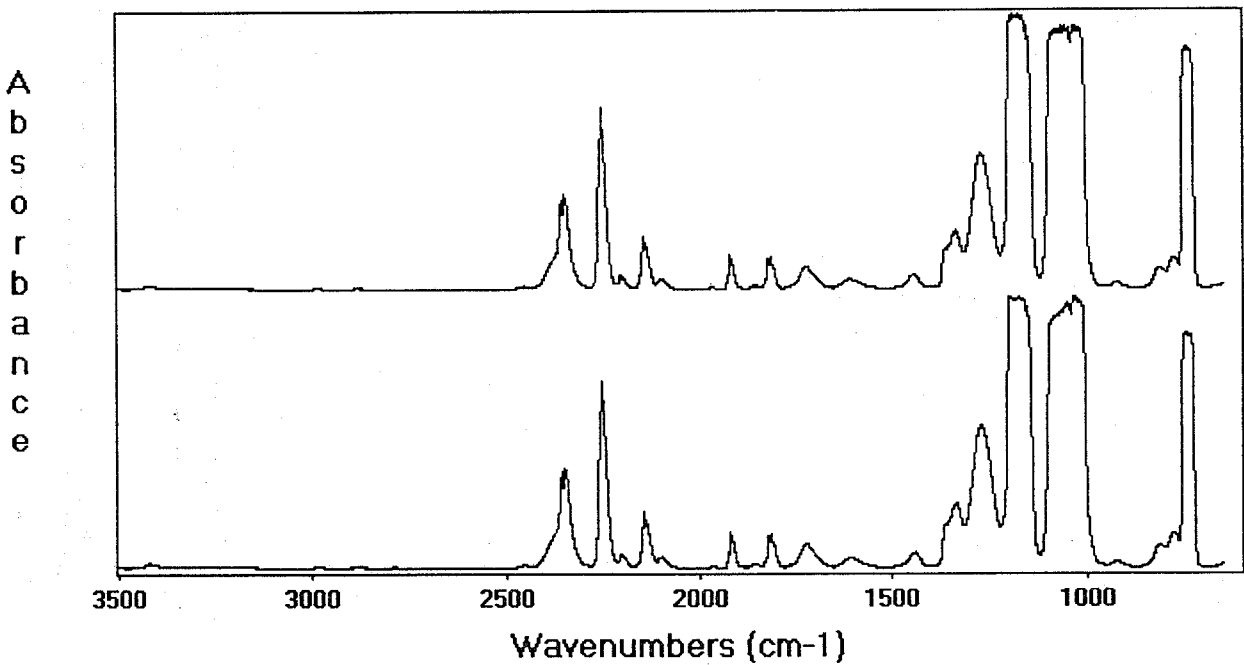


Figure D-4. Initial (lower) and 40 week (upper) spectra for C4130 in CF₃I tested in the dry condition with copper at 23 °C.

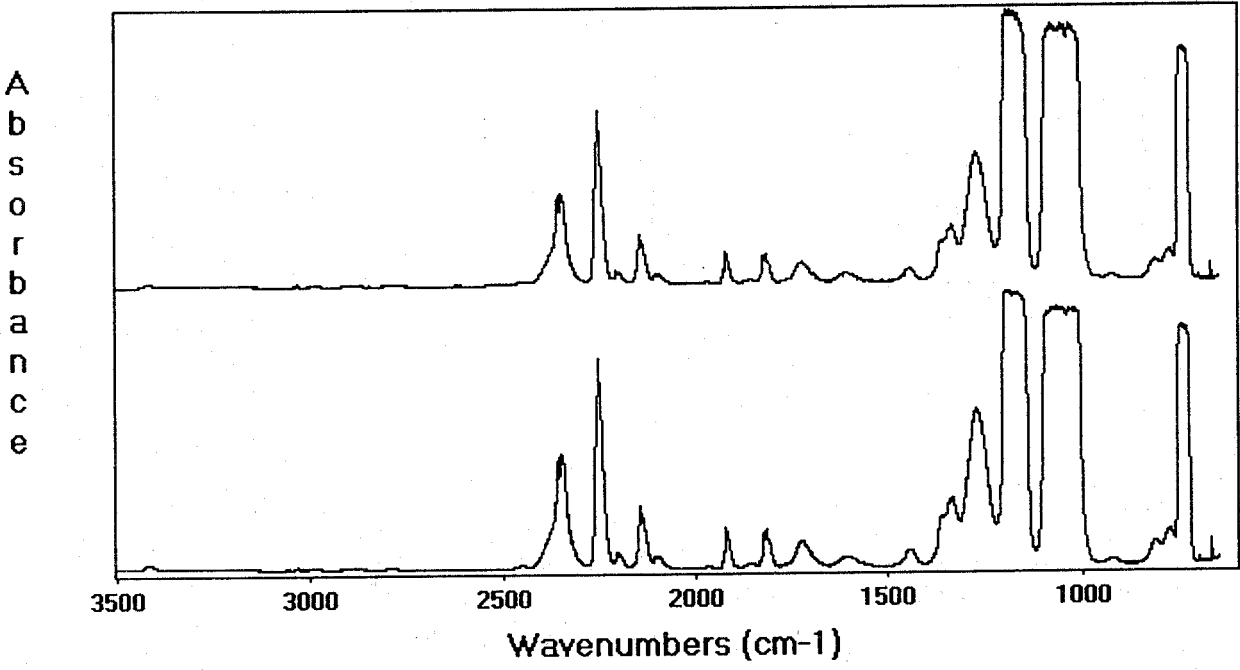


Figure D-5. Initial (lower) and 44 week (upper) spectra for I625 in CF₃I tested in the dry condition with copper at 23 °C.

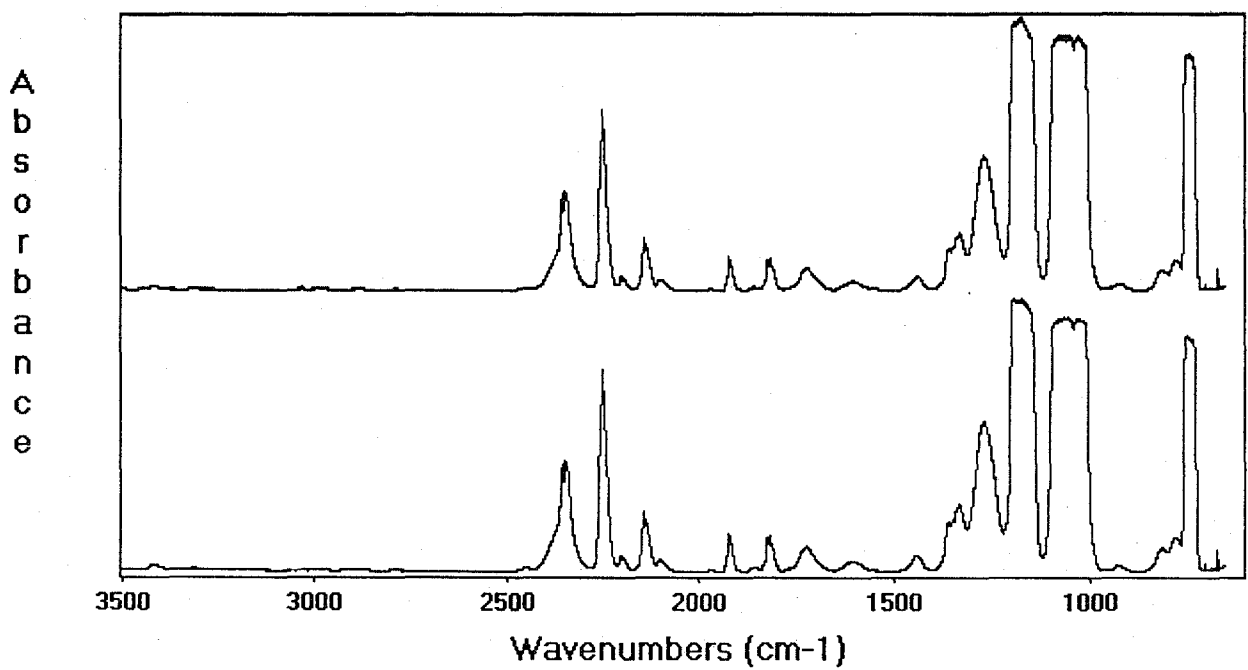


Figure D-6. Initial (lower) and 32 week (upper) spectra for the blank in CF₃I tested in the dry condition with copper at 100 °C.

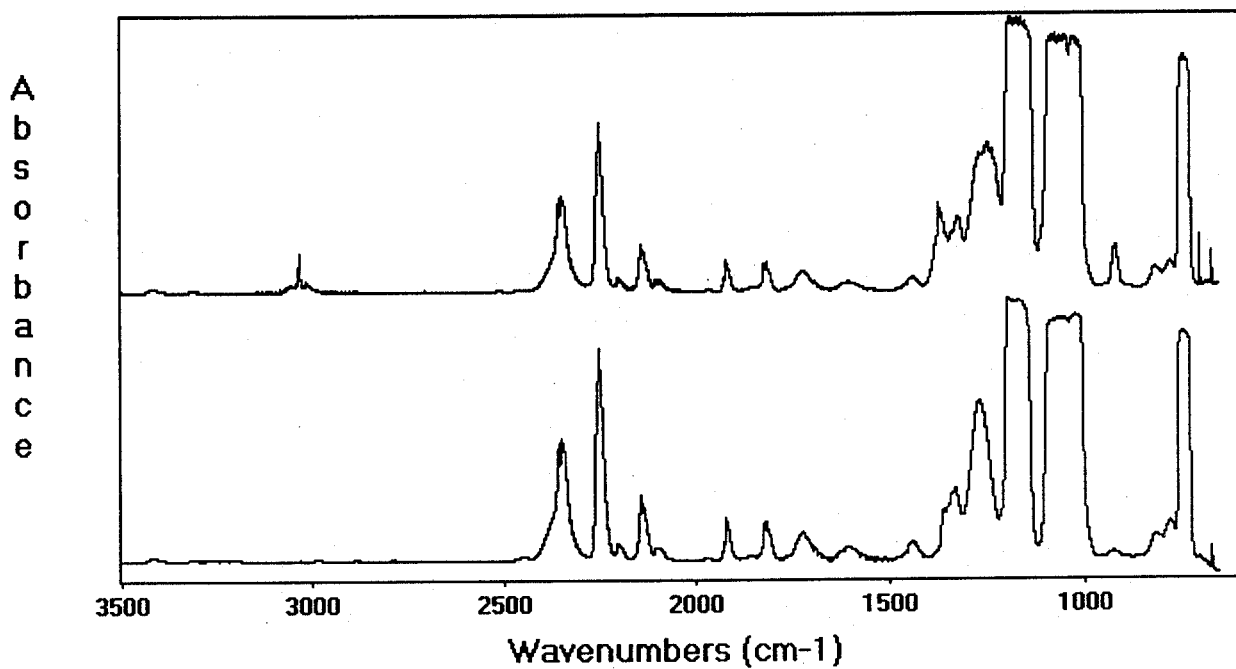


Figure D-7.

Initial (lower) and 52 week (upper) spectra for the blank in CF_3I tested in the dry condition with copper at 150 °C.

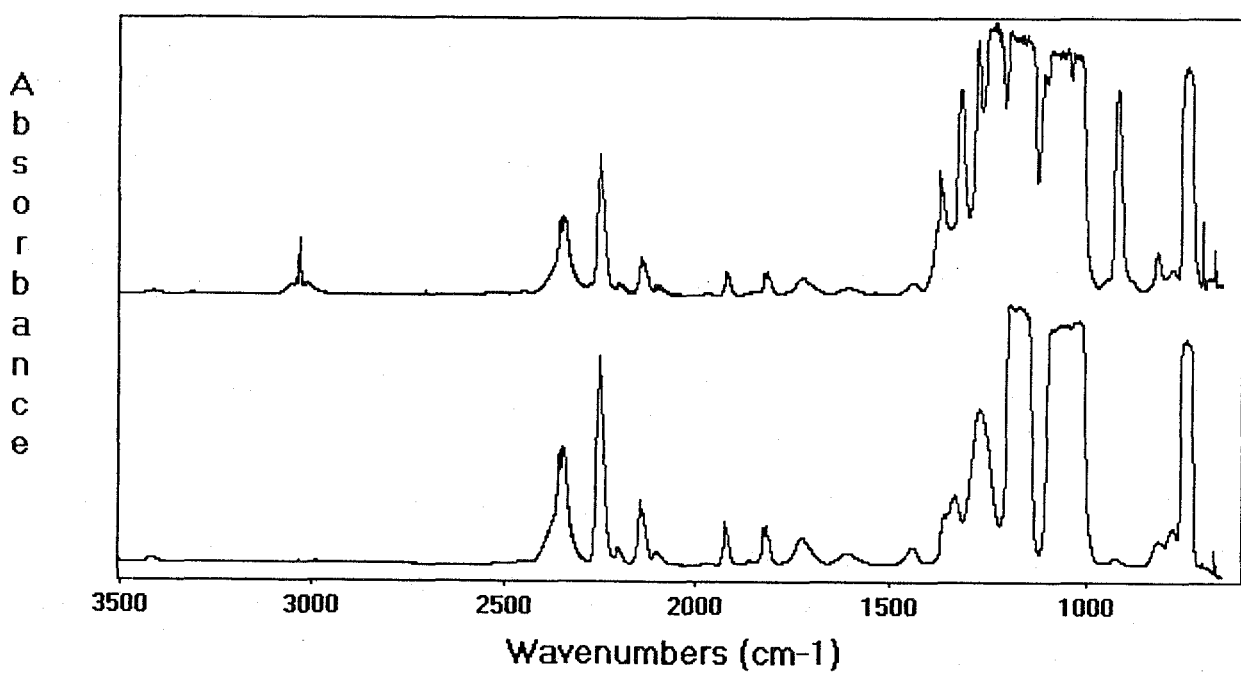


Figure D-8.

Initial (lower) and 52 week (upper) spectra for nitronic 40 in CF_3I tested in the dry condition with copper at 150 °C.

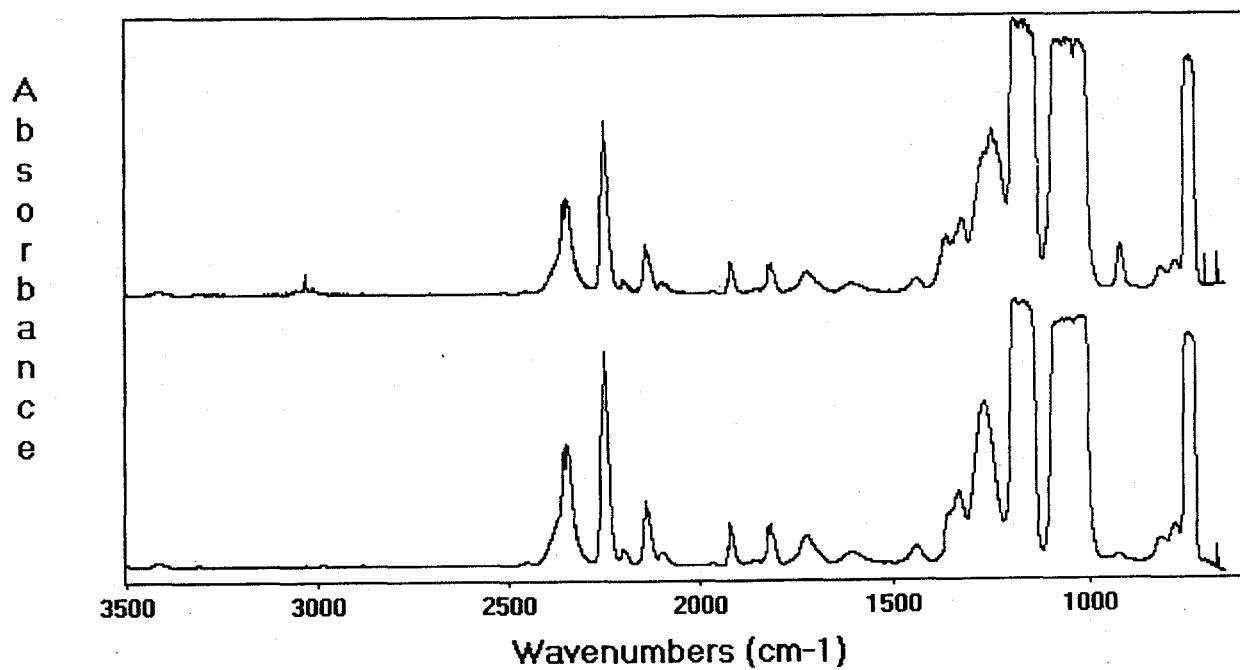


Figure D-9. Initial (lower) and 52 week (upper) spectra for Ti-15-3-3-3 in CF_3I tested in the dry condition with copper at 150 °C.

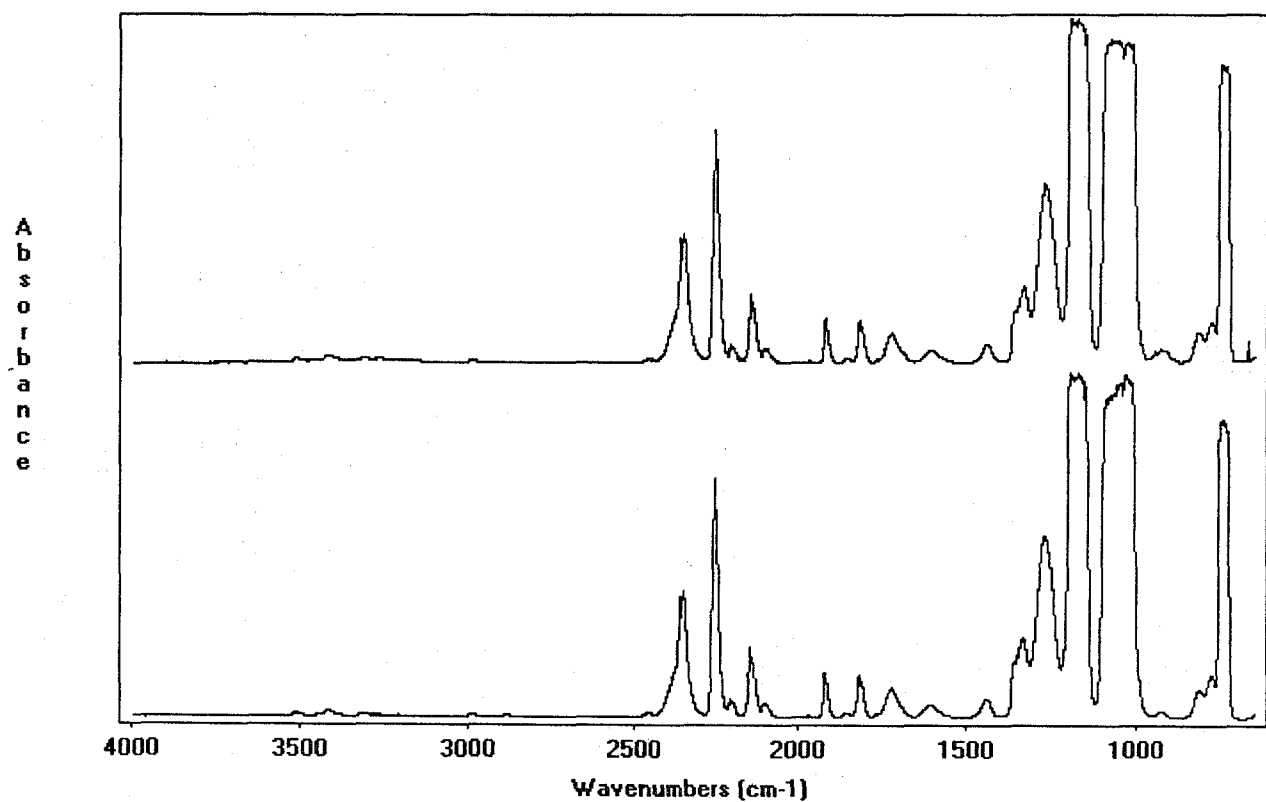


Figure D-10.

Initial (lower) and 40 week (upper) spectra for C4130 in CF₃I tested in the dry condition with copper at 150 °C.

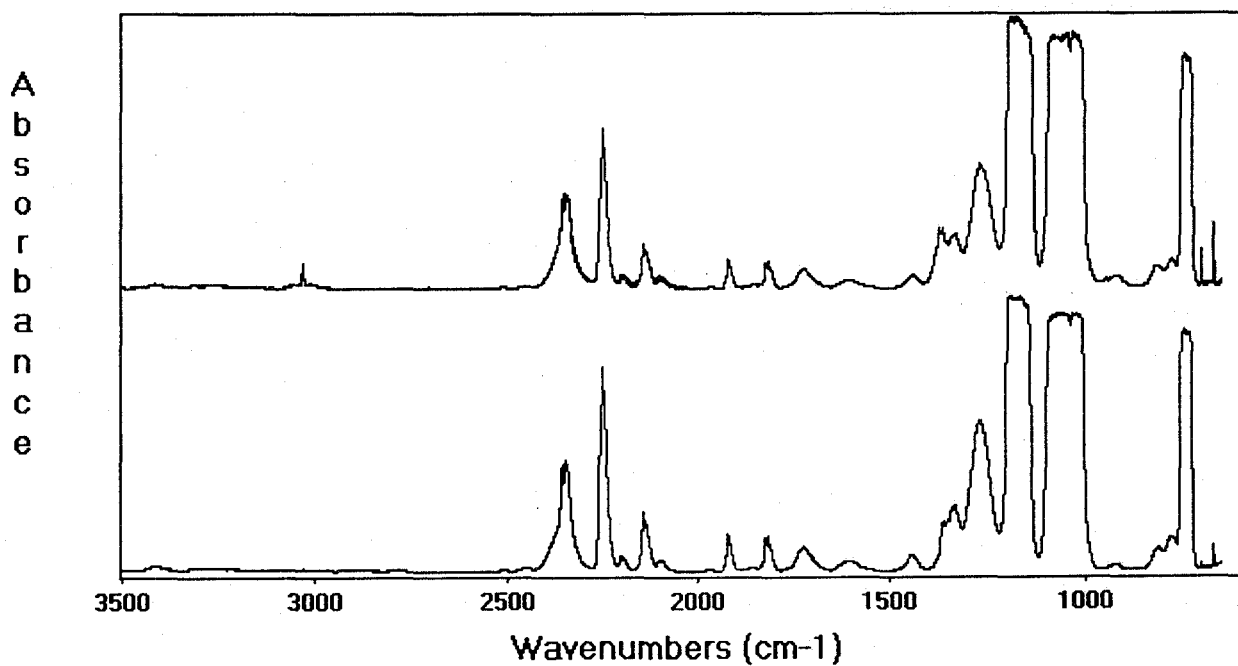


Figure D-11. Initial (lower) and 44 week (upper) spectra for I625 in CF_3I tested in the dry condition with copper at 150 °C.

Appendix E. Initial and Final FTIR Spectra of CF₃I Tested in the Moist Condition without Copper

The spectra in Appendix E are those of the CF₃I. The gas cell pressure for all was 5330 Pa. The lower spectrum is for the initial analysis; the upper spectrum is for the final aged analysis.

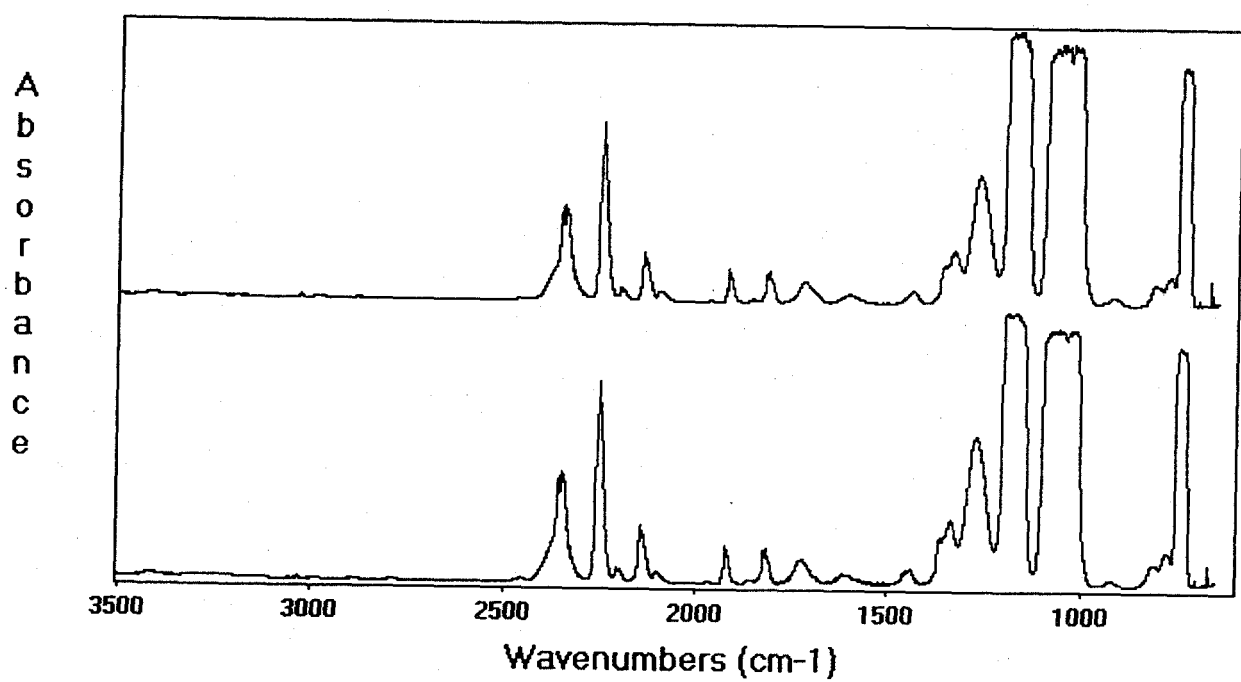


Figure E-1. Initial (lower) and 44 week (upper) spectra for the blank in CF_3I tested in the moist condition without copper at 100 °C.

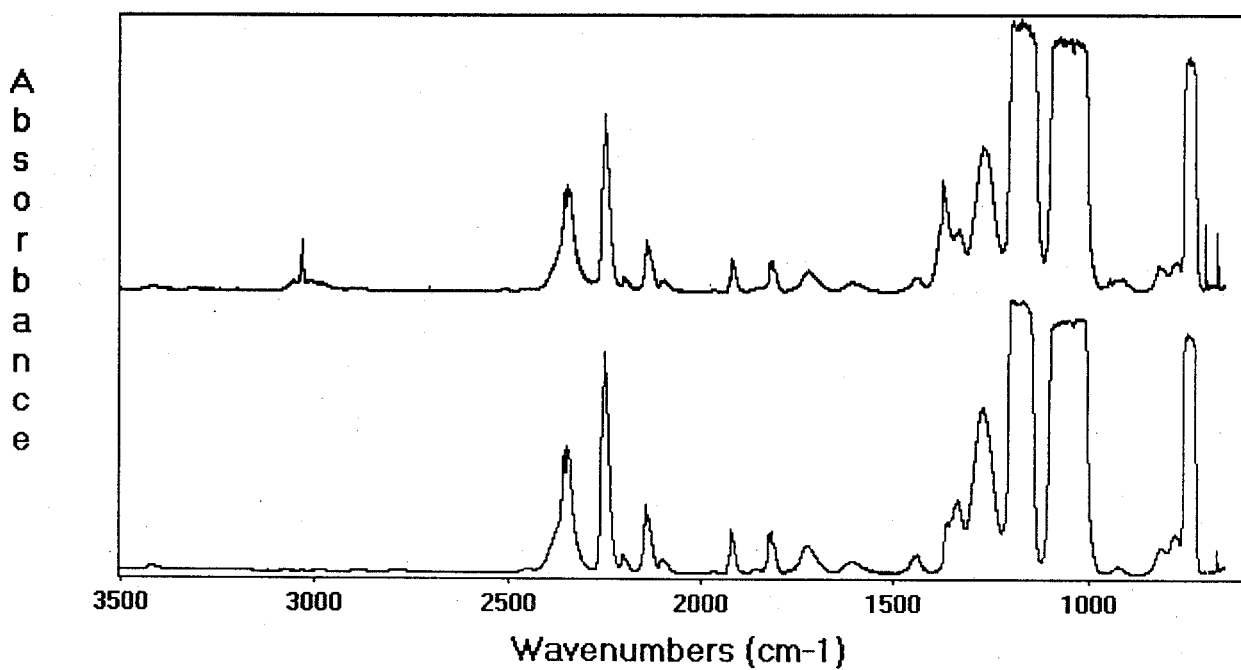


Figure E-2. Initial (lower) and 52 week (upper) spectra for the blank in CF_3I tested in the moist condition without copper at 150 °C.

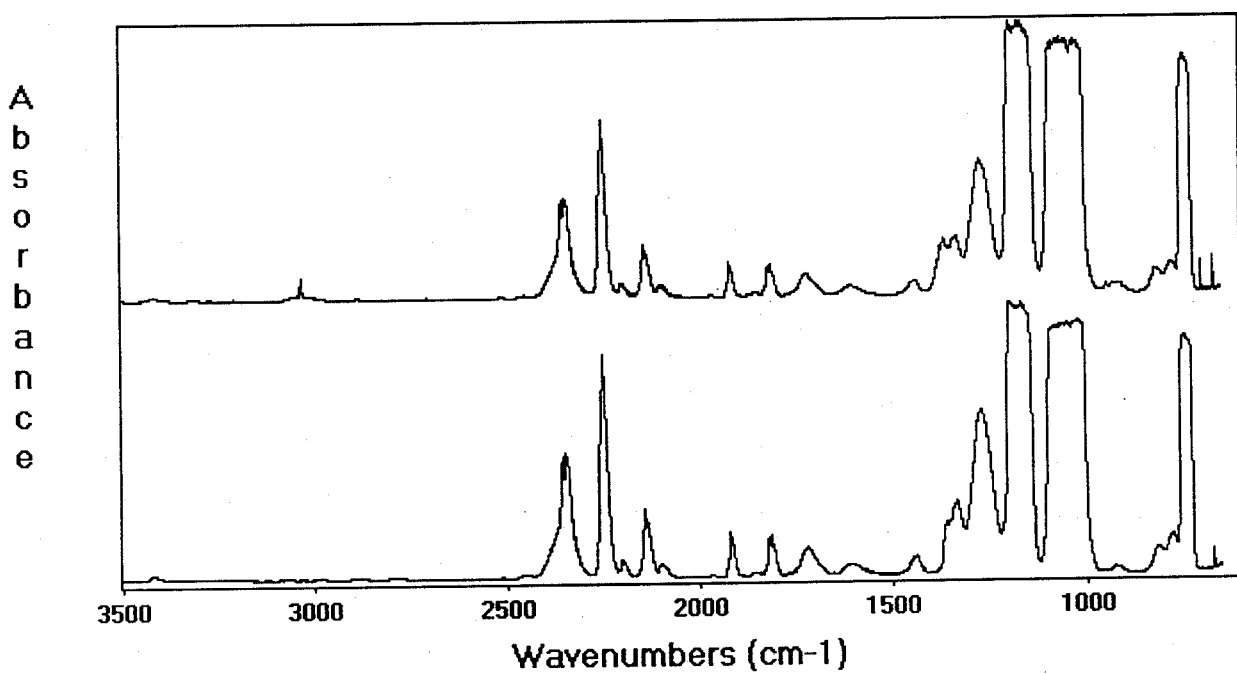


Figure E-3. Initial (lower) and 52 week (upper) spectra for nitronic 40 in CF_3I tested in the moist condition without copper at 150 °C.

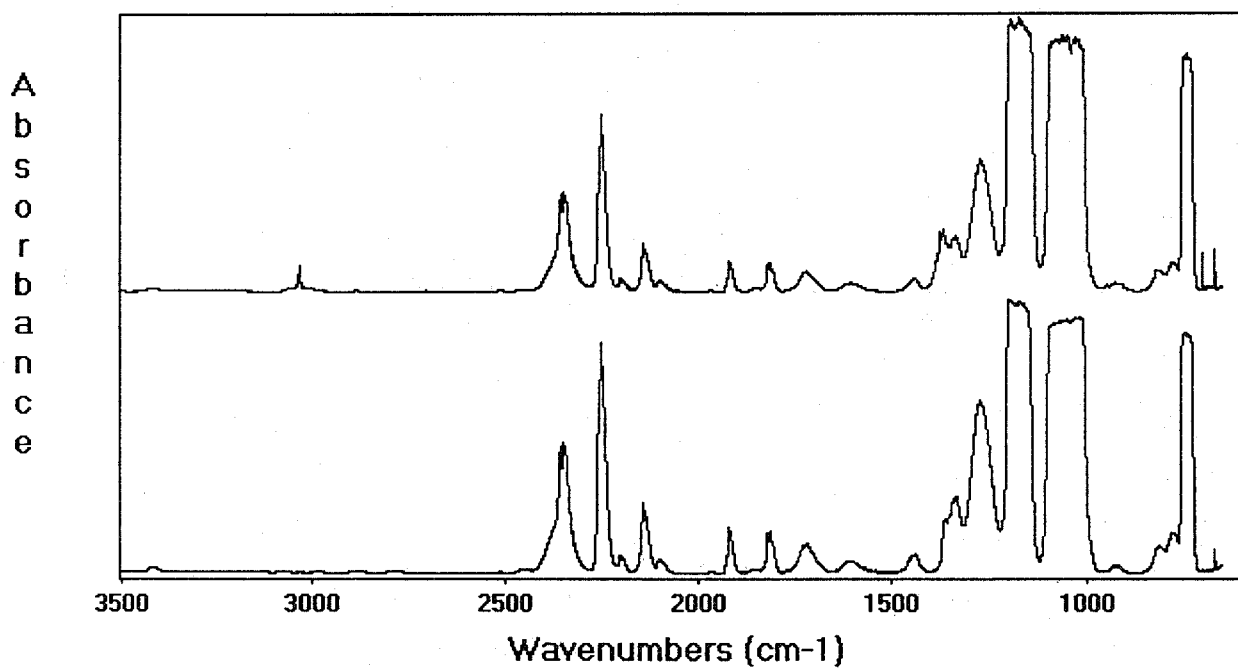


Figure E-4. Initial (lower) and 52 week (upper) spectra for Ti-15-3-3-3 in CF_3I tested in the moist condition without copper at 150 °C.

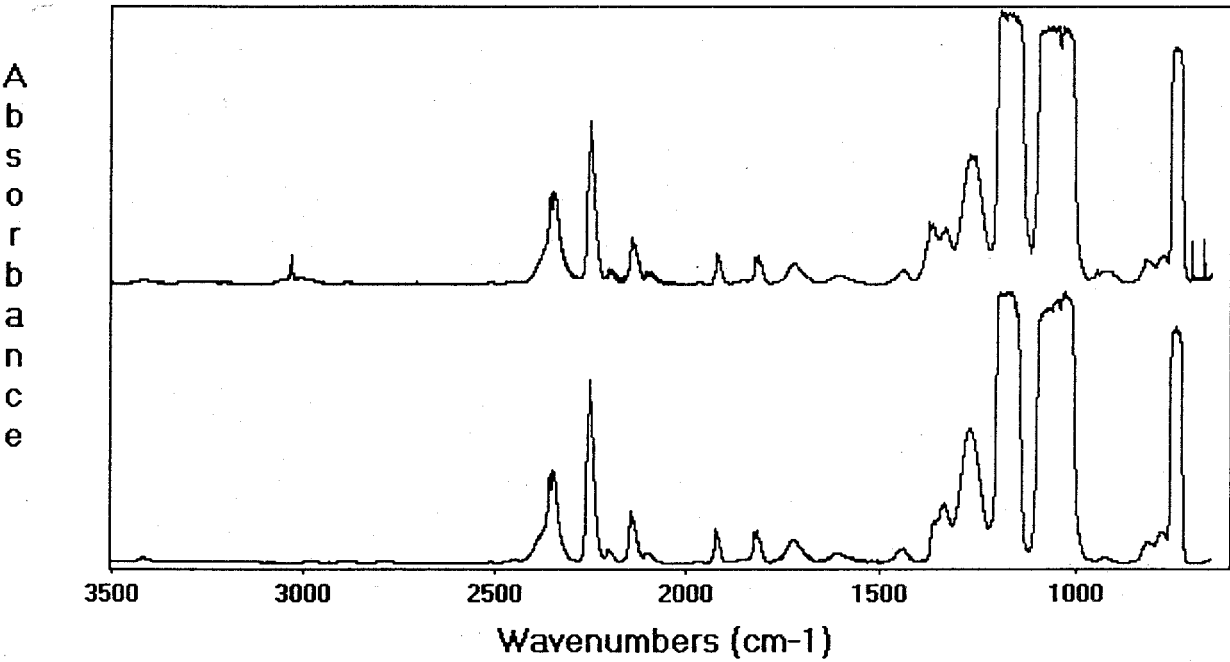


Figure E-5. Initial (lower) and 40 week (upper) spectra for C4130 in CF₃I tested in the moist condition without copper at 150 °C.

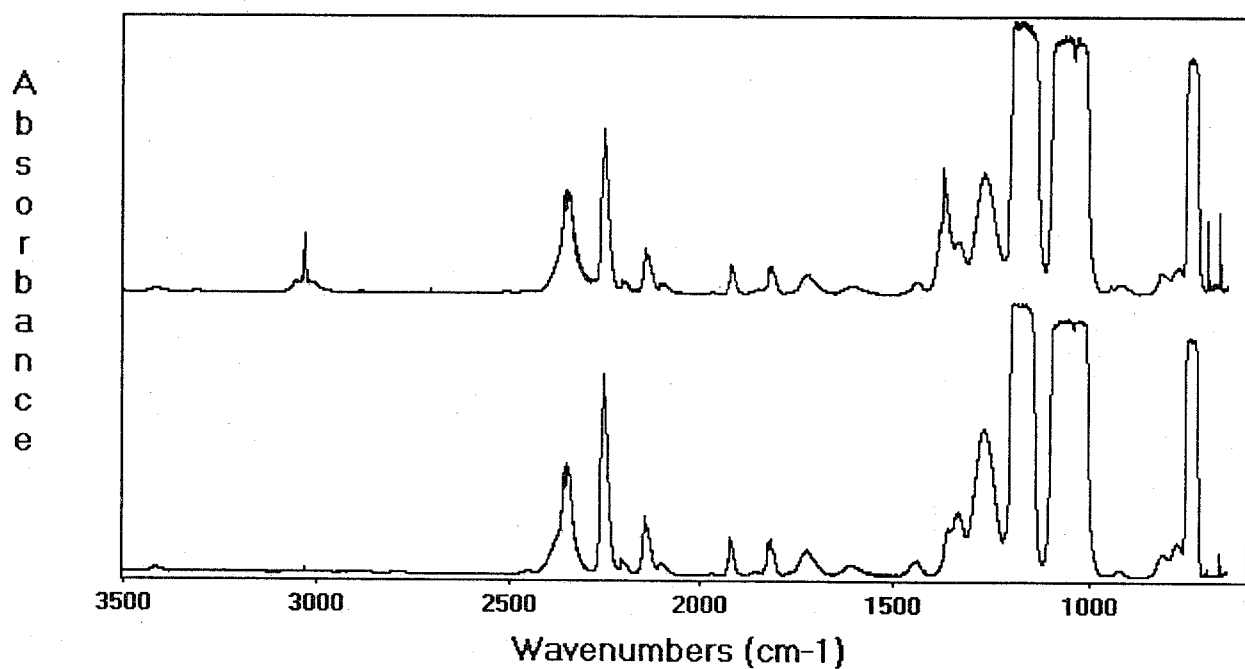


Figure E-6. Initial (lower) and 44 week (upper) spectra for I625 in CF_3I tested in the moist condition without copper at 150 °C.

Appendix F. Initial and final FTIR Spectra of CF₃I Tested in the Moist Condition with Copper

The spectra in Appendix F are those of the CF₃I. The gas cell pressure for all was 5330 Pa. The lower spectrum is for the initial analysis; the upper spectrum is for the final aged analysis.

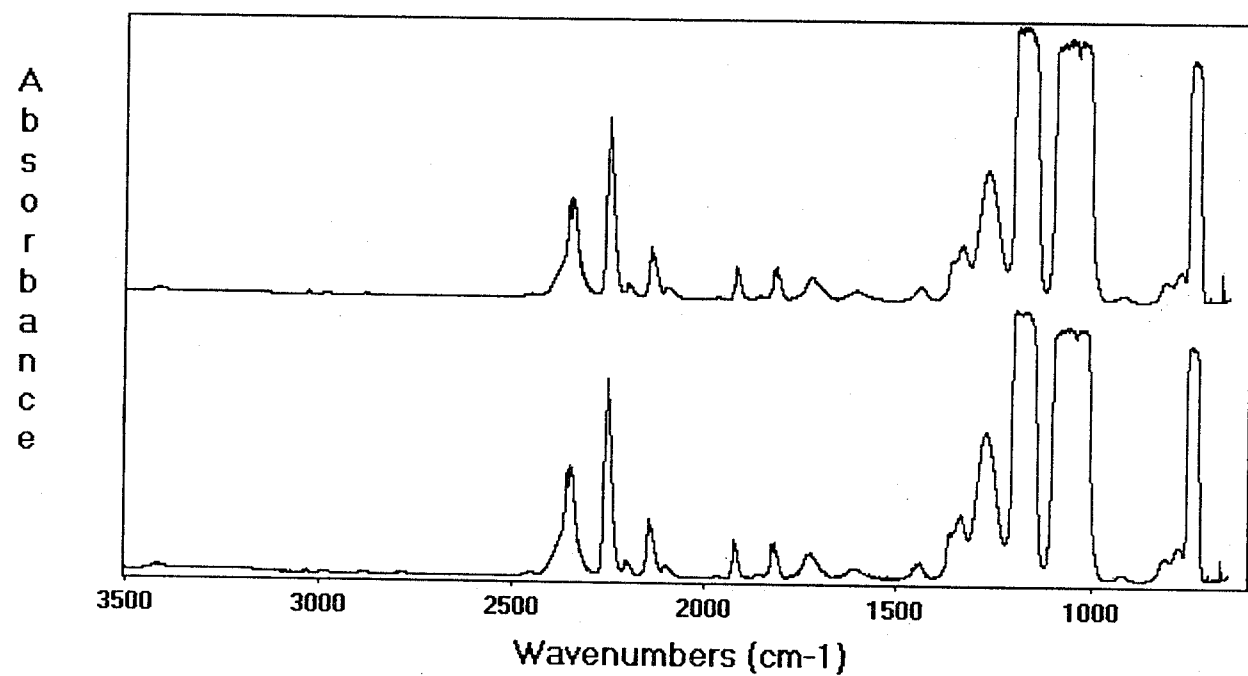


Figure F-1. Initial (lower) and 44 week (upper) spectra for the blank in CF₃I tested in the moist condition with copper at 100 °C.

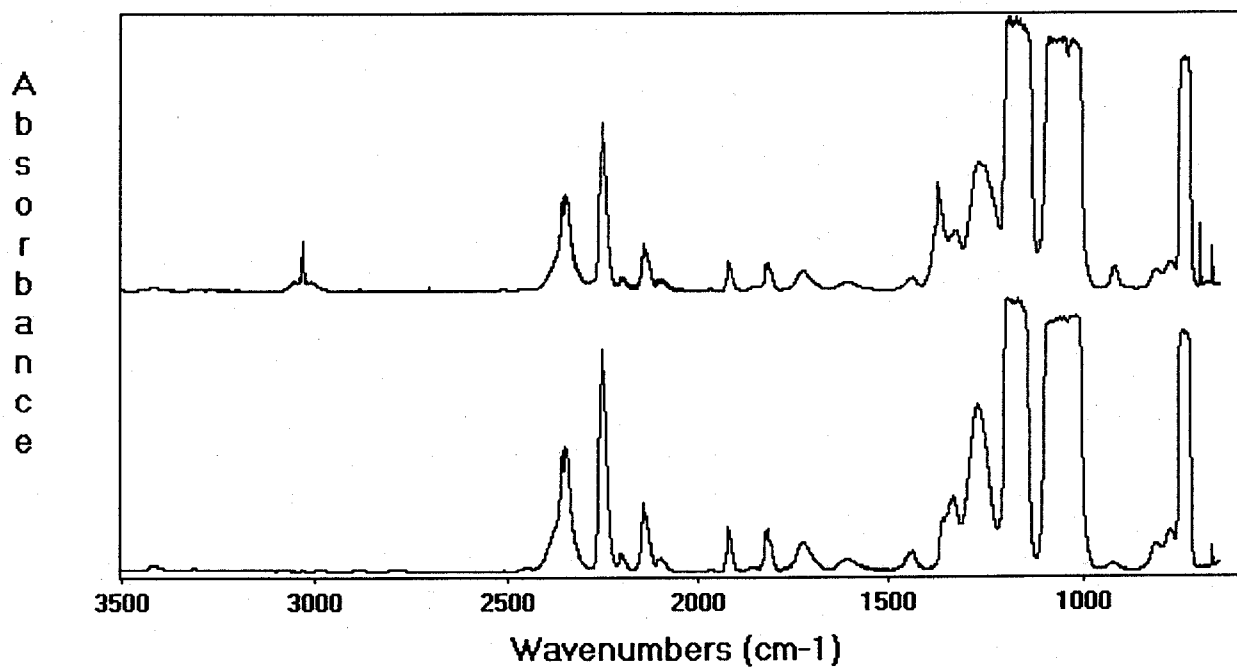


Figure F-2. Initial (lower) and 52 week (upper) spectra for the blank in CF_3I tested in the moist condition with copper at 150 °C.

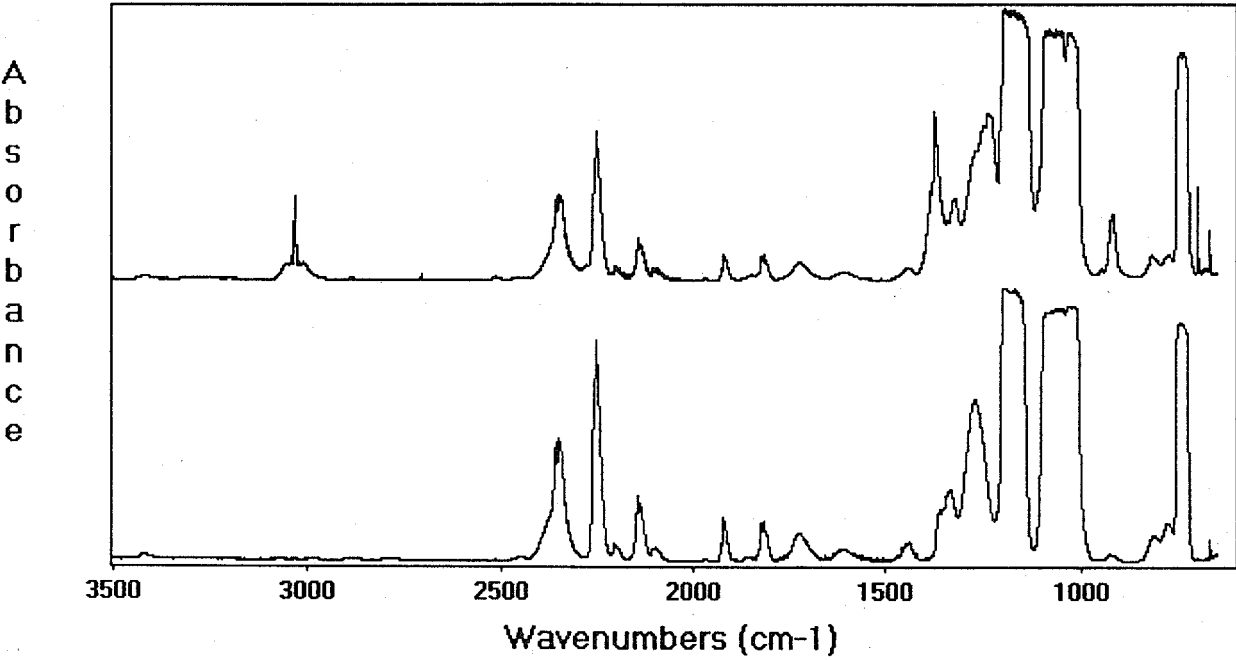


Figure F-3. Initial (lower) and 52 week (upper) spectra for nitronic 40 in CF₃I tested in the moist condition with copper at 150 °C.

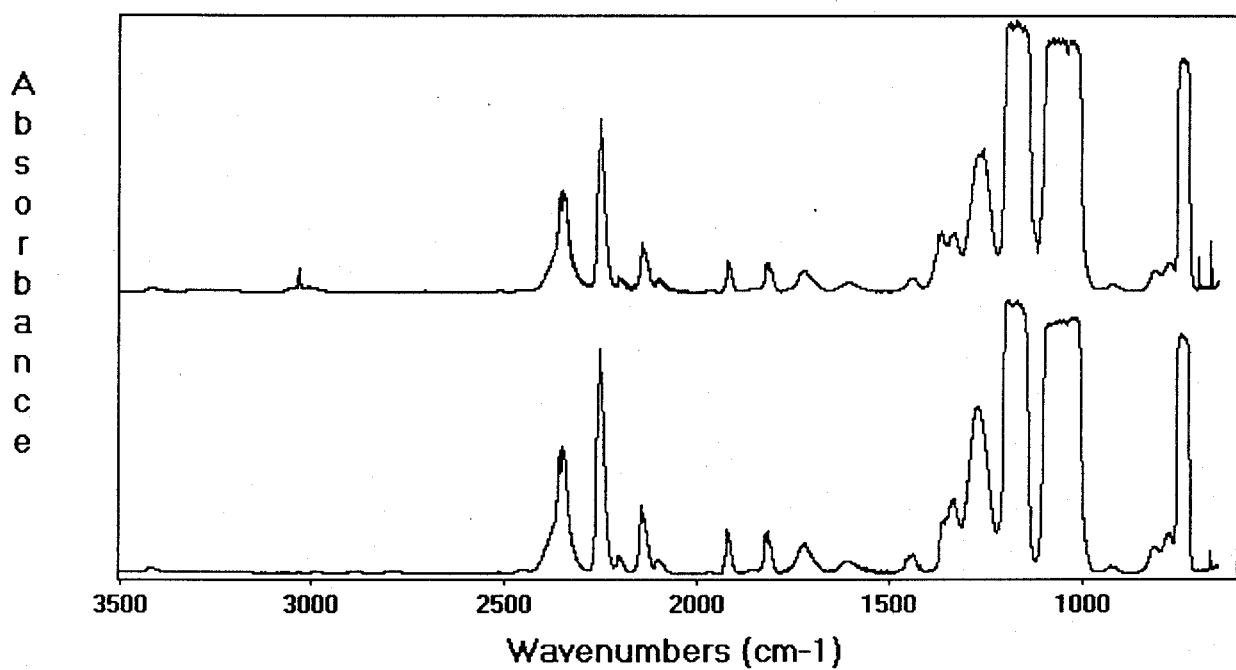


Figure F-4. Initial (lower) and 52 week (upper) spectra for Ti-15-3-3-3 in CF_3I tested in the moist condition with copper at 150 °C.

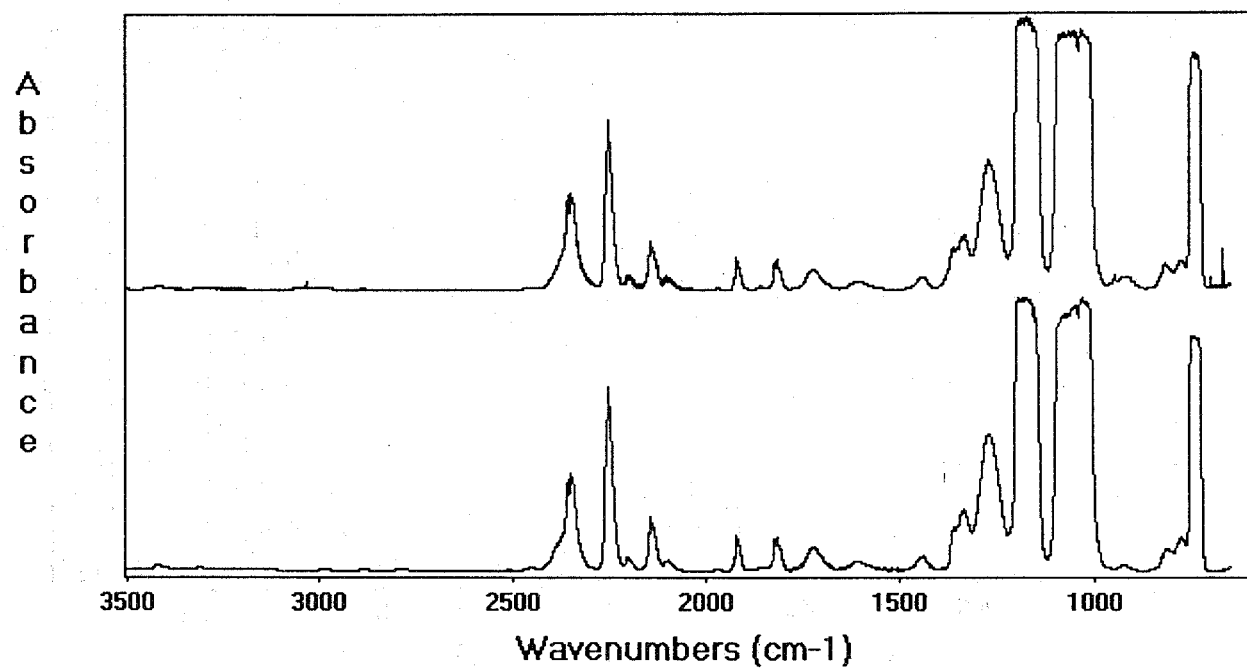


Figure F-5. Initial (lower) and 40 week (upper) spectra for C4130 in CF₃I tested in the moist condition with copper at 150 °C.

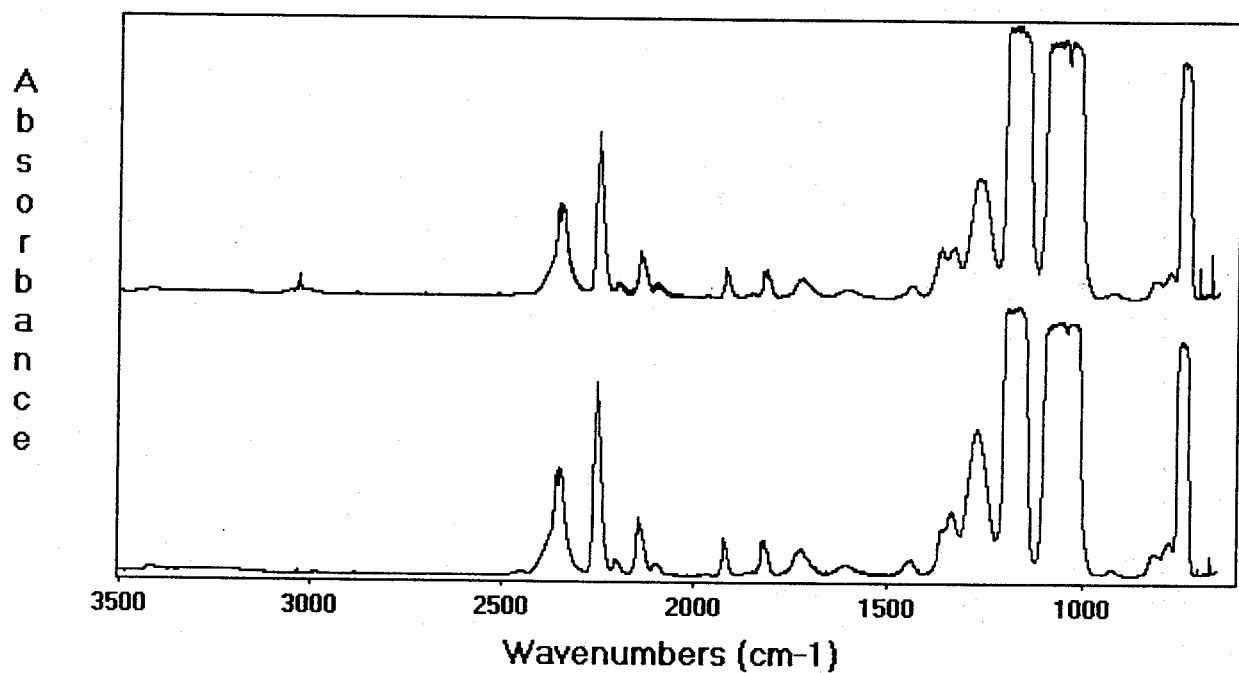


Figure F-6. Initial (lower) and 40 week (upper) spectra for I625 in CF₃I tested in the moist condition with copper at 150 °C.

PART 2

ENGINEERING DESIGN CRITERIA

8. OPTIMIZATION OF SYSTEM DISCHARGE

Jiann C. Yang, Thomas G. Cleary, Isaura Vázquez, Charles I. Boyer, Michelle D. King,
Brett D. Breuel, Carole Womeldorf, and William L. Grosshandler
Building and Fire Research Laboratory

Marcia L. Huber and Lloyd Weber
Chemical Science and Technology Laboratory

Grzegorz Gmurczyk
Science Applications International Corporation

Contents

	Page
8. OPTIMIZATION OF SYSTEM DISCHARGE	407
8.1 Overview	410
8.2 System Constraints	410
8.3 Thermophysical Properties of Selected Agents and Agent/Nitrogen Mixtures	413
8.3.1 Introduction	413
8.3.2 Experimental Apparatus and Procedures	414
8.3.2.1 Agent Filling Calculations.	414
8.3.2.2 Agent Preparation	416
8.3.2.3 Pure Agent Measurements	416
8.3.2.4 Nitrogen Solubility in Agents	421
8.3.2.5 Agent/Nitrogen Mixture Measurements	421
8.3.3 Modeling Thermodynamic Properties of Agent/Nitrogen Mixtures	423
8.3.3.1 Introduction	423
8.3.3.2 Extended Corresponding States Model	423
8.3.3.3 Calculation Procedure	427
8.3.4 Results and Discussion	427
8.3.4.1 Pure Agents	427
8.3.4.2 Solubility of Nitrogen in Agents	429
8.3.4.3 Agent/Nitrogen Mixtures	432
8.3.5 Summary and Conclusions	438
8.4 Discharge of Agent/Nitrogen Mixtures in a Simulated Dry Bay	438
8.4.1 Introduction	438
8.4.2 Experimental Methods	439
8.4.3 Results and Discussion	447
8.4.3.1 General Visual Observations	447

- 8.4.3.2 Marotta Solenoid Valve 448
 - 8.4.3.3 HTL Solenoid Valve 467
 - 8.4.3.4 Kidde-Graviner Valve 468
 - 8.4.3.5 HTL Squibs 471
 - 8.4.3.6 Effect of an Orifice Plate 471
 - 8.4.3.7 Effect of Fill Density 476
 - 8.4.3.8 Effect of Initial Nitrogen Charge Pressure 476
 - 8.4.3.9 Effect of Initial Vessel Temperature. 494
 - 8.4.3.10 Effect of Vessel Orientation 500
 - 8.4.3.11 Effect of Partial Nitrogen Saturation 502
 - 8.4.3.12 Effect of Vessel Geometry 509
 - 8.4.3.13 Model Predictions 509
- 8.4.4 Summary and Conclusions 531
- 8.5 Computer Simulation of Agent Dispersion 531
 - 8.5.1 Introduction 531
 - 8.5.2 Modeling of Agent Dispersion Process 532
 - 8.5.3 Solution Method 533
 - 8.5.4 Numerical Results and Discussion 533
 - 8.5.5 Conclusions 562
- 8.6 Pipe Flow Characteristics of Alternative Agents 563
 - 8.6.1 Introduction 563
 - 8.6.2 Agent Discharge in Piping 563
 - 8.6.3 Single-Phase Flow 564
 - 8.6.4 Two-Phase Flow 565
 - 8.6.5 Experimental Apparatus 566
 - 8.6.5.1 Discharge Vessel and Piping Design 566
 - 8.6.5.2 Experimental Measurements 568
 - 8.6.5.3 Test Matrix 572
 - 8.6.6 Results and Discussion 574
 - 8.6.6.1 Constant-Head Discharge 576
 - 8.6.6.2 Transient Discharge 579
 - 8.6.6.3 Straight Pipe Configuration 583
 - 8.6.6.4 Piping with a 90° Angle Bend 584
 - 8.6.6.5 Straight Pipe with a Sudden Expansion 584
 - 8.6.6.6 Straight Pipe with a Sudden Contraction 585
 - 8.6.6.7 Tee Configuration 588
 - 8.6.6.8 Cooled Agent Discharge 588
 - 8.6.6.9 Heated Agent Discharge 588
 - 8.6.6.10 Visual Observations 596
 - 8.6.7 Transient Discharge Model 596
 - 8.6.7.1 Model Equations 598
 - 8.6.7.2 Fill Conditions and Thermodynamic Inputs 604
 - 8.6.7.3 Friction Factor 604
 - 8.6.8 Model Calculations 613
 - 8.6.8.1 Constant-Head Conditions 613
 - 8.6.8.2 Transient Conditions 613
 - 8.6.9 Hardware Design Scheme 627
 - 8.6.10 Conclusions and Recommendations 639

8. OPTIMIZATION OF SYSTEM DISCHARGE	409
8.7 Concluding Remarks	643
8.8 Acknowledgments	645
8.9 References	645
Appendix A. A User's Guide to PROFISSY	649
Appendix B. Tabulated fill Conditions and Pressure Traces for All Pipe Flow Discharge Tests	668
Appendix C. Thermodynamic and Transport Properties of Agent/Nitrogen Mixtures	773

8.1 Overview

Current aircraft fire suppression bottles for dry bay and engine nacelle applications, which are designed to meet Military Specification MIL-C-22284A (proof pressure of 9.62 MPa and minimum burst pressure of 12.37 MPa), are normally filled with liquid halon 1301 (CF_3Br) to about half of the bottle volume, and the bottle is then pressurized with nitrogen to a specified equilibrium pressure (typically 4.1 MPa) at room temperature. The purpose of using the pressurization gas is to expedite the discharge of the agent and to facilitate the dispersion of the agent. Without nitrogen pressurization, the bottle pressure, which is simply the vapor pressure of the agent, can be so low (even sub-atmospheric) at extremely cold ambience that there is virtually no driving force to expel the agent from the bottle in case of a fire, thus hindering a rapid release of the mixture.

From the above description, three important issues have emerged and need be considered when using a halon alternative as an in-flight fire suppressant: (1) the system hardware, (2) the thermophysical properties of the agent/nitrogen mixture, and (3) the agent/nitrogen mixture behavior during a discharge.

In this section, the last two issues which are pertinent to agent storage and its subsequent discharge will be addressed in detail. With respect to the first issue, a survey of the system constraints on existing in-flight halon 1301 fire protection systems will be given. This survey is also used to provide guidelines for identifying important experimental parameters for subsequent agent/nitrogen storage and discharge studies. The information on system constraints consists of bottle size, percent liquid-fill, nitrogen pressurization, range of operating temperatures, and proof and burst pressures of the vessel. In addition, the information on piping systems used to distribute halon 1301 for engine nacelle fire protection applications will be discussed. The thermophysical properties of selected agents and agent/nitrogen mixtures are presented under conditions commensurate with those identified in the system constraint studies. This information is also relevant to the establishment of the initial conditions of the vessel before the discharge of the mixture. Finally, parametric studies on the discharges of agent/nitrogen mixtures without (to simulate dry bay applications) and with (to simulate engine nacelle applications) a piping system will be discussed. Numerical calculations using CONCHAS-SPRAY and KIVA II were also performed in order to explore the feasibility of applying such complex codes to the study of a flashing discharge into an enclosure. This section focuses on the four selected agents (HFC-125, FC-218, CF_3I , and HFC-227ea) for dry bay (HFC-125, FC-218, and CF_3I) and engine nacelle (HFC-125, CF_3I , and HFC-227ea) applications.

The results obtained from this study provide important technical information on bottle design and agent discharge for new generation aircraft that may use the halon alternatives, for the existing aircraft that may undergo retrofitting, or simply for possible "drop-in" replacements.

8.2 System Constraints

This section describes a survey summarizing the current in-flight halon 1301 systems. This work was conducted with the cooperation of several aircraft fire extinguisher manufacturers, aircraft and airframe manufacturers, defense contractors, the three branches of the U.S. Military Service, and the Federal Aviation Administration (FAA). This survey is the result of examining the halon 1301 system specifications for over fifty types of aircraft (both military and commercial). The halon 1301 systems included in this survey are used for fire protection in engine nacelles, dry bays, and auxiliary power units (APU). Table 1 lists the participants in the survey and the acquired information. Since some of the information obtained was considered proprietary, it was not possible to tabulate the system

Table 1. Names of the participants in the survey and the acquired information on current halon 1301 system constraints

Participant	Acquired information
Boeing	Piping
Booz-Allen & Hamilton, Inc.	Bottle sizes, agent fill volumes, operating temperatures, vessel growth potential, nitrogen pressurization
Federal Aviation Administration	Bottle sizes and agent fill volumes
Lockheed Martin	Piping, and bottle sizes
McDonnell Douglas	Vessel growth potential
Northrop Grumman	Vessel growth potential
Pacific Scientific	Bottle sizes, agent fill volumes, operating temperatures, and nitrogen pressurization
Systron-Donner	Bottle sizes, agent fill volumes, operating temperatures, and nitrogen pressurization
Walter Kidde	Bottle sizes, agent fill volumes, operating temperatures, and nitrogen pressurization
U.S. Air Force	Bottle sizes, agent fill volumes, operating temperatures, and nitrogen pressurization
U.S. Army	Bottle sizes, agent fill volumes, operating temperatures, and nitrogen pressurization
U.S. Navy	Bottle sizes, agent fill volumes, operating temperatures, and nitrogen pressurization

specifications for each individual aircraft in detail. Only the minimum and maximum operating ranges of the parameters were compiled in this study. Note that no differentiation among the areas of application were made in identifying the parameters. The survey is summarized in Table 2. The percent of liquid fill was calculated based on the total amount and liquid density of *pure* agent at 25 °C. In *most* applications, the bottle specifications closely conform to Military Specification MIL-C-22284A. The vessel growth potential is defined as the allowable percent increase in the original vessel size. However, it is not clear from the literature whether the growth potential refers to the increase in vessel size at the same mounting location of the vessel or different, new location when rerouting of agent distribution is feasible.

Based on the volume factor, it is not possible, in most cases, to use the existing containers for the selected halon alternatives as "drop-in" replacements because the containers may not be large enough to hold the amount of agent required for fire extinguishment or may encounter the so-called liquid-full condition (Grosshandler *et al.*, 1994) sooner even at moderately high ambient temperatures due to an initial small ullage as a result of an increased initial fill volume of the liquid halon alternative. The volume factor is defined as a measure of the liquid agent volume in the storage vessel *normalized* by the liquid volume of halon 1301 required to suppress a flame under identical conditions (Grosshandler *et al.*, 1994). The following calculations, using HFC-125 as an example, illustrate how the system constraints on the bottle size can be assessed based only on thermodynamic considerations. Note that

Table 2. Summary of current halon 1301 system specifications for engine nacelle, dry bay, and auxiliary power unit applications

Property	Range
Bottle size (cm ³)	650 to 23000
Percent liquid fill (%)	25 to 70
Operating temperature (°C)	- 54 to 160
Nitrogen pressurization (MPa)	1.4 to 5.7
Proof pressure (MPa)	6.4 to 24.7
Burst pressure (MPa)	11.3 to 37.1
Vessel growth potential (%)	0 to 400

other constraints (*e.g.*, mechanical properties of the vessel, discharge time) have to be taken into account in the overall system constraint evaluation. The intent here is not to provide a comprehensive methodology for system constraint evaluation, but rather to provide system designers a set of engineering tools to perform design calculations (in this case, on bottle size).

Assuming the original halon 1301 bottle is a military standard CF-6 type vessel with an internal volume of $3.67 \times 10^{-3} \text{ m}^3$ and contains 2.96 kg of halon 1301 pressurized to 4.12 MPa with nitrogen at 21 °C, the percent of liquid fill at this condition is calculated to be 49.7 % using the computer code PROFISSY (to be discussed in detail in Section 8.3). The volume of liquid HFC-125 required is $5.47 \times 10^{-3} \text{ m}^3$, based on an average volume factor of 3 as reported in Grosshandler *et al.* (1994). If there is no vessel growth potential, then the original halon 1301 vessel can not be used for HFC-125 because the liquid volume of the agent is greater than the vessel volume. Table 3 summarizes the system constraint evaluation based on other vessel growth potentials. It is clear that even with a growth potential of 500 %, which results in 24.9 % liquid fill, the pressure at 150 °C is still very close to the burst pressure of a standard CF-6 vessel. In the calculations, a temperature of 150 °C was assumed to be the extreme operating temperature of the vessel. Similar calculations were also performed for the other three agents, and the results are given in Tables 4, 5, and 6.

To the best of our knowledge, no military specifications exist for storage and delivery systems for dry bay discharge applications. Since the events typically occurring in a dry bay are on the order of milliseconds, it is expected that the discharge will be directly from the vessel without going through any piping systems. For engine nacelle applications, piping systems are required to transport halon from the bottles (normally located outside the engine nacelle) to the point of application in the nacelle. The design of the piping system centers around Military Specification MIL-E-22285 (1959) and its amendment (1960). According to these documents, the discharge time, defined as the time measured from the instant the agent (halon 1301) starts to leave the tubing ends to the time the required amount of agent has been discharged, should be 1 second or less. The initial amount of agent in the container(s) should be able to provide an agent concentration of at least 6 % by volume in all parts of the affected zone for at least 0.5 second at normal cruising condition. The pipe lines should be less than 3.1 m (10 ft) long, where practicable, and be straight if possible. The fittings and turns in the piping system should be kept to a minimum. Discharge piping should terminate in open ends without

Table 3. Sample calculations showing vessel size constraint for HFC-125 based on an average volume factor of 3 and various vessel growth potentials

Vessel growth potential (%)	New vessel volume (m ³)	Percent liquid fill (%)	Vessel pressure @ 150 °C (MPa)
0	3.67×10^{-3}	Not possible	Not calculated
50	5.51×10^{-3}	99.4	> 41.23
100	7.34×10^{-3}	74.6	26.65
200	11.01×10^{-3}	49.7	16.77
300	14.68×10^{-3}	37.3	14.01
400	18.35×10^{-3}	29.8	12.61
500	22.02×10^{-3}	24.9	11.73

nozzles, and tubing and fittings should have a minimum burst pressure of 10.3 MPa. Tubing sizes are determined based on the desired discharge rates and on system-volume considerations (*i.e.*, minimizing the system volumes). It is likely that any system employing a halon replacement agent would, at least, have to meet similar performance criteria and system constraints.

8.3 Thermophysical Properties of Selected Agents and Agent/Nitrogen Mixtures

8.3.1 Introduction. The total pressure in the bottle is a complex function of ambient temperature because of the temperature dependence of the agent vapor pressure, the partial pressure of nitrogen in the gas ullage, and the solubility of nitrogen in the liquid agent. For halon 1301, the bottle pressure-temperature relationship and the solubility of nitrogen in halon 1301 have been well characterized. By contrast, such a relationship and solubility data are scarce or do not exist for some of the halon alternatives.

The major objectives of this study are very similar to those reported in the previous work (Grosshandler *et al.*, 1994), the only difference being the initial liquid agent fill conditions at room temperature and the number of agents used. The present study expands the temperature-pressure database for the four selected agents (HFC-125, FC-218, CF₃I, and HFC-227ea) using two additional initial fill conditions and an experimental apparatus that can accommodate much higher final pressures at elevated temperatures than the earlier study.

The first subtask of this study was to determine the solubility of nitrogen in the four selected agents at room temperature. Halon 1301 was also included in this study for the purposes of reference and comparison with the alternative agents. Specifically, the objective was to measure the amount of nitrogen that was needed to pressurize the bottle to a specified equilibrium pressure.

In the second subtask, the thermodynamic properties of the four selected agents together with halon 1301 were measured. The objective was to determine the final pressure of the bottle when the bottle, filled with either a pre-determined amount of pure agent or with agent pressurized with nitrogen, was exposed to two extreme temperatures (– 60 °C and 150 °C). Experiments on pure

Table 4. Sample calculations showing vessel size constraint for FC-218 based on an average volume factor of 2.8 and various vessel growth potentials

Vessel growth potential (%)	New vessel volume (m ³)	Percent liquid fill (%)	Vessel pressure @ 150 °C (MPa)
0	3.67×10^{-3}	Not possible	Not calculated
50	5.51×10^{-3}	92.8	30.81
100	7.34×10^{-3}	69.6	18.43
200	11.01×10^{-3}	46.4	12.88
300	14.68×10^{-3}	34.8	11.22
400	18.35×10^{-3}	27.9	10.38
500	22.02×10^{-3}	23.2	9.83

agents were performed in order to obtain pressure-temperature relationships for some of the agents (especially CF₃I) where documented data were not readily available.

Furthermore, in order to assimilate the results obtained from the two aforementioned subtasks into useful engineering correlations that could be easily used by the bottle designers, the third subtask was to develop a computer code that could facilitate such calculations.

For the purpose of reference, selected thermophysical properties of the four selected agents are tabulated in Table 7 where MW is the molecular weight, T_b is the normal boiling point (at 0.101 MPa), \tilde{T}_c is the critical temperature, P_{sat} is the saturation vapor pressure at 25 °C, P_c is the critical pressure, ρ_c is the critical density, ρ_l is the saturated liquid density at 25 °C, C_{pl} is the isobaric liquid heat capacity at T_b , C_{p2} is the isobaric liquid heat capacity at 25 °C, and h_{fg} is the latent heat of vaporization at T_b . The references from which these data were taken are also given in the table.

8.3.2 Experimental Apparatus and Procedures. This section describes the experimental techniques used to measure the amount of nitrogen required to pressurize the vessel initially filled with a fixed amount of agent to a specified equilibrium pressure at room temperature and the pressure-temperature relationship for pure agents and agent/nitrogen mixtures. The initial amounts of liquid agent dispensed in the vessel before nitrogen pressurization corresponded to approximately half and two-thirds of the vessel volume at room temperature. For agent/nitrogen mixtures, two initial equilibrium nitrogen charge pressures (2.75 MPa and 4.12 MPa) at room temperature were used in this study. The amount of nitrogen required to pressurize the vessel with agent to 2.75 MPa or 4.12 MPa, were measured only at room temperature. To determine the final vessel pressure as a function of temperature, experiments were performed at - 60 °C, 22 °C, and 150 °C.

8.3.2.1 Agent Filling Calculations. This sub-section describes the method used to calculate the total amount of agent needed such that the liquid volume fraction corresponds to the amount that is one-half or two-thirds of the vessel volume at room temperature. The calculation procedure is as follows.

Since two phases (liquid-vapor) exist in equilibrium for all the four selected agents at room temperature, the total mass ($m_{a,t}$) of agent in the vessel with a total volume V_t is equal to the sum of the masses of agent in both vapor and liquid phases.

Table 5. Sample calculations showing vessel size constraint for CF₃I based on an average volume factor of 0.8 and various vessel growth potentials

Vessel growth potential (%)	New vessel volume (m ³)	Percent liquid fill (%)	Vessel pressure @ 150 °C (MPa)
0	3.67 x 10 ⁻³	39.8	11.53
50	5.51 x 10 ⁻³	26.5	10.46
100	7.34 x 10 ⁻³	19.9	9.85
200	11.01 x 10 ⁻³	13.3	9.04
300	14.68 x 10 ⁻³	10.0	8.52
400	18.35 x 10 ⁻³	8.0	8.18
500	22.02 x 10 ⁻³	6.6	7.93

$$m_{a,t} = m_{a,v} + m_{a,l} = \rho_{a,v}V_v + \rho_{a,l}V_l$$

(1)

where *m* is the mass, *ρ* is the saturation density of the agent, *V* is the volume, subscripts *t*, *a*, *v*, and *l* represents total, agent, vapor phase, and liquid phase respectively. For a given agent at room temperature, *ρ_{a,v}* and *ρ_{a,l}* are known or can be estimated. If the vessel is half filled with liquid agent,

$$V_l = V_v = \frac{V_t}{2}$$

(2)

Similarly, for a two-thirds liquid full vessel,

$$V_l = \frac{2V_t}{3}$$

(3)

$$V_v = \frac{V_t}{3}$$

(4)

With *V_l* and *V_v* calculated by the method shown above, *m_{a,t}* can then be determined from Equation (1). In the calculations for HFC-227ea, FC-218, HFC-125, and halon 1301, *ρ_{a,v}* and *ρ_{a,l}* were obtained from the database developed by Gallagher *et al.* (1993). For CF₃I, *ρ_{a,l}* was estimated by the modified Rackett method (Reid *et al.*, 1987), and *ρ_{a,v}* was calculated by using the vapor pressure at room temperature and assuming an ideal vapor phase.

Table 6. Sample calculations showing vessel size constraint for HFC-227ea based on an average volume factor of 2.5 and various vessel growth potentials

Vessel growth potential (%)	New vessel volume (m ³)	Percent liquid fill (%)	Vessel pressure @ 150 °C (MPa)
0	3.67×10^{-3}	Not possible	Not calculated
50	5.51×10^{-3}	82.9	26.65
100	7.34×10^{-3}	62.2	15.74
200	11.01×10^{-3}	41.4	11.80
300	14.68×10^{-3}	31.1	10.71
400	18.35×10^{-3}	24.9	10.07
500	22.02×10^{-3}	20.7	9.62

8.3.2.2 Agent Preparation. Before the agent was dispensed into the test vessel, it was degassed to remove any dissolved noncondensable gases which might be present in the agent. Figure 1 is a schematic of the degassing apparatus. The entire apparatus was first evacuated to 1.33 Pa for at least half an hour before agent vapor was condensed in the sublimizer which was chilled in a dry ice bath. The sublimizer was a stainless steel vessel with a re-entrant well at the center. After sufficient liquid had been condensed, liquid nitrogen was poured into the well. The liquid agent in the sublimizer was then made to boil by applying vacuum. As the liquid boiled, it would give off its own vapor and the noncondensable gases. Because the wall of the well was very cold due to the presence of liquid nitrogen, the agent vapor was condensed on the wall, and the condensate then dripped back to the boiling liquid agent. In this way, only the noncondensable gases and a very small amount of agent vapor were removed from the sublimizer by the vacuum pump. Depending on the initial amount of liquid agent in the sublimizer, this degassing process normally went on for at least half an hour.

Because the initial batch of CF₃I was found to contain trace amounts of HI, CO₂, H₂O, and I₂, a purification system was constructed in order to remove impurities which might be present in other batches. The purification system is shown schematically in Figure 2. After the entire system was evacuated, the agent vapor passed through a column packed with potassium hydroxide whose main function was to remove HI, then through a molecular sieve filter to remove water vapor and carbon dioxide, and finally through a stainless steel coil which was immersed in an ice bath to remove I₂. The purified vapor was then retrieved by condensation in a stainless steel container. The collected agent was again subjected to boiling using a vacuum at dry-ice temperature for about half an hour to further remove noncondensable gases.

8.3.2.3 Pure Agent Measurements. For low temperature (– 60 °C) measurements of the pure agents, the experimental set-up, which is similar to the one used in the previous agent screening project (Grosshandler *et al.*, 1994), is shown in Figure 3. It consists of a stainless steel (SS 304)

Table 7. Selected thermophysical properties of agents

Agent	MW (kg/mol)	T_b	T_c	P_c	P_{sat}	ρ_c	ρ_l	C_{p1}	C_{p2}	h_{fg} (kJ/kg)
		(°C)		(MPa)		(kg/m ³)		(kJ/kg K)		
HFC-227ea	0.170	−16.4 ^a	101.9 ^a	2.95 ^a	0.46 ^a	621 ^b	1389 ^a	1.074 ^a	1.177 ^a	126 ^a
CF ₃ I	0.196	−22.0 ^c	122.0 ^d	4.04 ^d	0.49 ^e	871 ^d	2106 ^f	0.542 ^g	0.592 ^g	106 ^h
FC-218	0.188	−36.8 ^a	72.0 ^a	2.68 ^a	0.87 ^a	629 ⁱ	1251 ^a	0.977 ^a	1.190 ^a	101 ^a
HFC-125	0.120	−48.6 ^a	66.2 ^a	3.63 ^a	1.38 ^a	571 ^j	1190 ^a	1.126 ^a	1.426 ^a	164 ^a
CF ₃ Br	0.149	−57.8 ^a	67.0 ^a	4.02 ^a	1.61 ^a	745 ^k	1551 ^a	0.670 ^a	0.881 ^a	111 ^a

^aFrom Gallagher et al. (1993)^bFrom Great Lakes Chemical Corporation (1993)^cFrom Kudchadker et al. (1979)^dFrom Sladkov and Bogacheva (1992)^eEstimated by the method of Lee and Kesler (Reid et al., 1987)^fEstimated by the modified Rackett method (Reid et al., 1987)^gEstimated by the method of Rowlinson (Reid et al., 1987)^hEstimated by Pitzer acentric factor correlation (Reid et al., 1987)ⁱFrom Braker and Mossman (1980)^jFrom Allied Signal Inc. (1990)^kFrom ASHRAE Inc. (1969)

vessel (tested hydrostatically to 20.6 MPa), a needle valve (Whitey SS-ORS2)¹ for dispensing the agent and nitrogen, a K-type thermocouple (Omega TJ36-CASS-116U-12), and a pressure transducer (Druck Model PDCR 330) with an uncertainty of 6.9 kPa. The volume of the whole system was determined by filling the system with nitrogen to various specified pressures at room temperature and weighing the pressurized system on an electronic scale with an uncertainty of 0.1 g. With the mass of nitrogen, temperature, and pressure known, the volume was calculated by using a generalized correlation for the compressibility factor (Smith and Van Ness, 1975). The total volume of the apparatus was determined to have a mean of 52.2 cm³ with a standard deviation of 0.3 cm³.

The experimental procedure was as follows. The apparatus was evacuated to 1.33 Pa for at least ten minutes. The set-up was then connected to the agent supply bottle (not shown in Figure 3). The vessel was placed in a Dewar flask and chilled by using dry ice before gaseous agent was dispensed through the needle valve into the vessel. Liquid agent was obtained by condensing the agent vapor, and the total amount was metered by placing the vessel and the Dewar flask on an electronic balance. When the amount of agent reached the target mass, the needle valve was closed. The vessel was then removed from the Dewar flask, warmed back to room temperature, and weighed on an electronic balance with an uncertainty of 0.1 g to determine the actual mass in the system.

The filled vessel was then immersed in a heat transfer fluid (Dow Corning Syltherm XLT) which was chilled by two immersion coolers (NESLAB Models IBC-4A and CC100-II) to - 60 °C. The

¹Certain commercial products are identified in this report in order to specify adequately the equipment used. Such identification does not imply recommendation by the National Institute of Standards and Technology, nor does it imply that this equipment is the best available for the purpose.

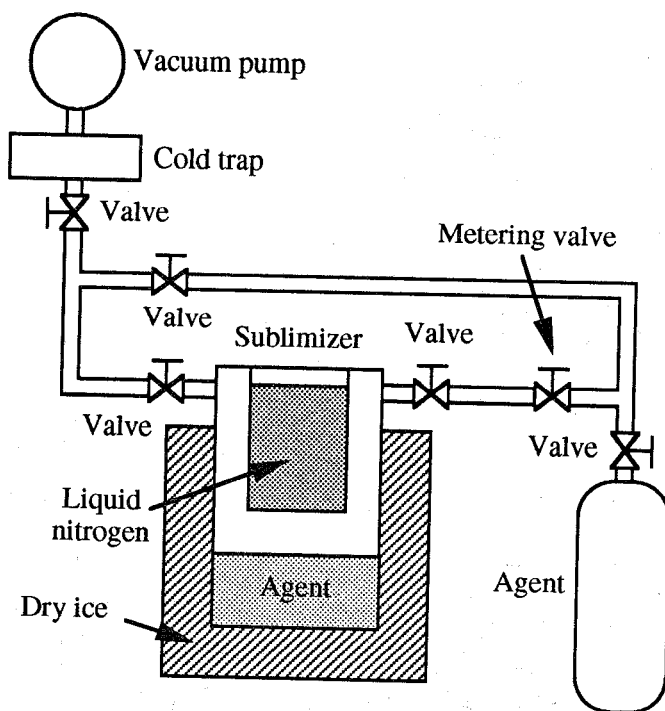


Figure 1. Schematic of the degassing apparatus.

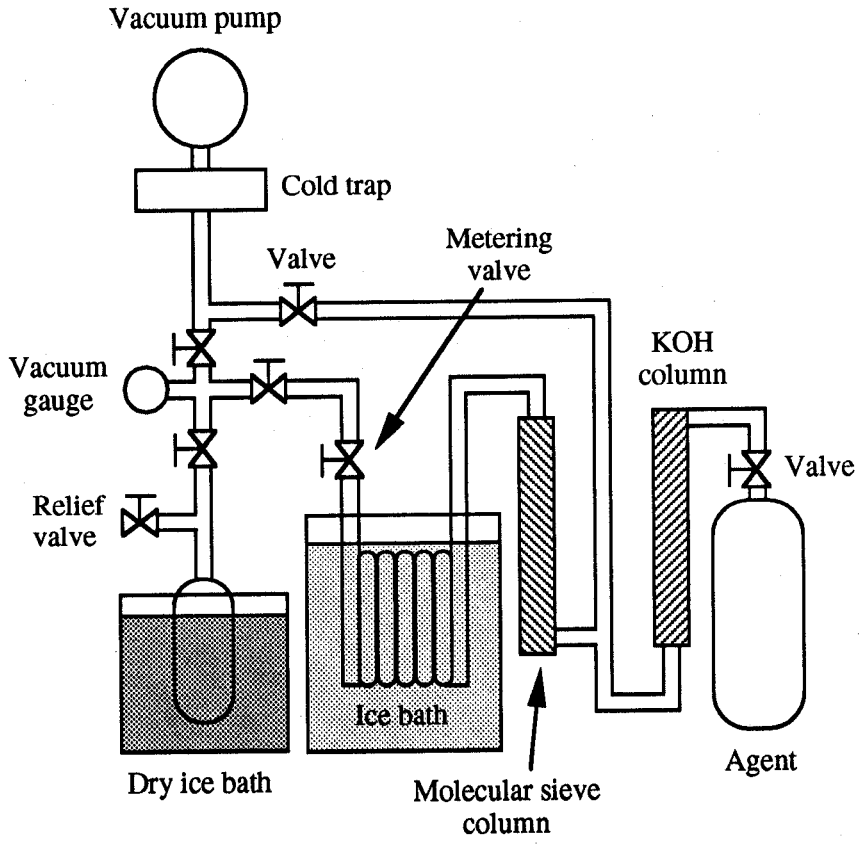


Figure 2. Schematic of CF₃I purification system.

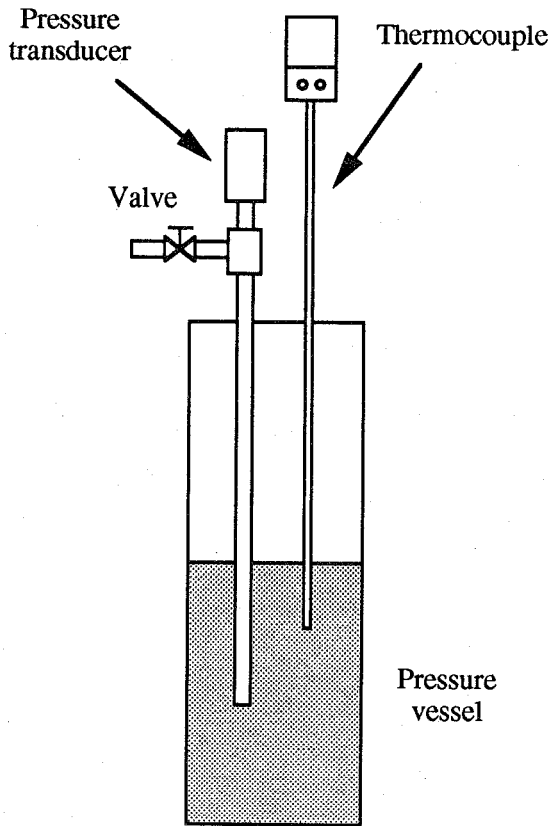


Figure 3. Experimental set-up for cold temperature measurements.

final vessel pressure was recorded from the pressure transducer read-out at least an hour later, after the internal temperature had reached thermal equilibrium with the bath temperature.

For high temperature (150 °C) measurements, a different set-up was constructed because the vessel used in the cold temperature experiments could not withstand the pressure that resulted from the high temperature condition. The apparatus is shown schematically in Figure 4. It consisted of a stainless steel (SS 316) high pressure vessel with a working pressure rated for 68.7 MPa at 204 °C (Jerguson Series 51 liquid level sight gage), a magnetic pump/mixer, a pressure transducer (Druck Model PDCR 330), and taper seal high pressure valves (HiP Company). Heating was achieved by placing the test apparatus in a temperature controlled oven. The internal volume of the entire system with the valves to the vacuum pump, vent, nitrogen bottle, and sublimizer closed was determined by evacuating the system followed by sucking distilled water into the system from a beaker. The amount of water required to fill the system was then determined from the loss of weight of the beaker. Knowing the mass of water and its density at room temperature, the internal system volume was calculated to have an average of 42.6 cm³ with a standard deviation of 0.2 cm³. Each window on the pressure vessel was also calibrated in terms of the volume percent of liquid filled to facilitate the filling process. The calibration was conducted by measuring the amount of water required to fill up to each window. In order to minimize photolysis of CF₃I, agent filling was performed under a darkroom safelight. In addition, when CF₃I was used in a test, extreme caution was taken to prevent any stray room light from getting into the oven.

The experimental procedure was as follows. The entire system was evacuated for at least half an hour before liquid agent was dispensed from the sublimizer. The exact amount of agent in the system was determined by weighing the sublimizer. The oven was then turned on, and the test apparatus was heated to the desired temperature. Because of space limitation, it was not possible to insert a thermocouple into the vessel to monitor the internal temperature. To ensure that thermal equilibrium had been reached, two thermocouples were placed at two different locations on the vessel wall, and the final pressure was recorded only when the two thermocouple readings were within 1.0 °C of the set temperature of the oven and the final pressure maintained a steady reading for at least half an hour.

8.3.2.4 Nitrogen Solubility in Agents. To measure the total amount of nitrogen required to pressurize the vessel to a specified equilibrium pressure at room temperature, the set-up for the cold temperature experiments was used. The agent filling procedure was the same as in the cold temperature studies. After a pure liquid agent was dispensed in the vessel, the nitrogen gas supply line (not shown in Figure 3) was connected to the vessel. The supply line was evacuated for at least five minutes before initiating a slow flow of nitrogen. The needle valve was then opened to allow nitrogen to bubble slowly through the liquid agent until an equilibrium pressure of approximately 2.8 MPa was reached. Shaking the vessel intermittently and vigorously and repetitive bubbling of nitrogen was required before the final equilibrium pressure was attained. The amount of nitrogen needed to pressurize the vessel was obtained by weighing the apparatus. This amount corresponded to the sum of the mass of nitrogen in the gas ullage of the vessel and that dissolved in the liquid agent. The charged vessel was then ready for the cold temperature experiments, as described in Section 8.3.2.5. When the cold experiments were completed, the charged vessel was warmed back to room temperature and was pressurized again with nitrogen to approximately 4.1 MPa. The amount of nitrogen was then determined, and the vessel was ready for another cold temperature experiment.

8.3.2.5 Agent/Nitrogen Mixture Measurements. The same two apparatus (see Figures 3 and 4) used for pure agent studies were also utilized to perform agent/nitrogen mixture experiments. In fact, since the experimental procedure for the solubility studies was equivalent to the preparation of the vessel at room temperature for subsequent pressure-temperature measurements, cold temperature

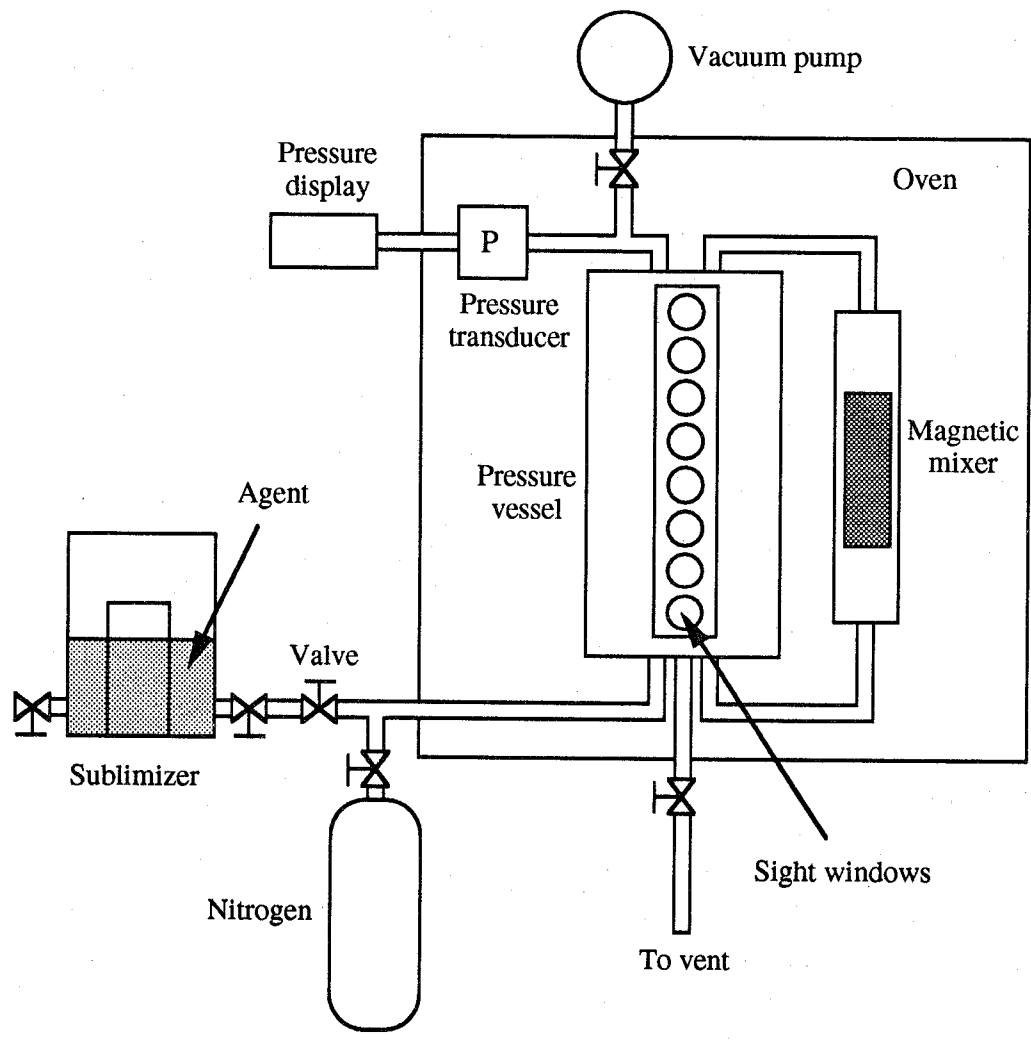


Figure 4. Apparatus for high temperature experiments.

experiments were therefore performed immediately after the solubility measurements were made by simply immersing the same vessel in the chilled heat transfer fluid.

For high temperature measurements, the experimental procedure was as follows. The same agent filling procedure in the pure agent studies was used. After the agent was dispensed, the pressurization of the vessel with nitrogen to a specified equilibrium pressure (approximately 2.8 MPa) at room temperature was initiated with the magnetic pump running to facilitate the mixing of nitrogen with the agent. After pressurization, the apparatus was heated to the final temperature (150 °C), and the final pressure of the vessel was recorded the same way as in the pure agent experiments. The apparatus was then cooled back to room temperature, pressurized with nitrogen to approximately 4.1 MPa, and heated to the final temperature (150 °C), where the equilibrium pressure was recorded.

8.3.3 Modeling Thermodynamic Properties of Agent/Nitrogen Mixtures

8.3.3.1 Introduction. The thermodynamic properties of agent/nitrogen mixtures are modeled using a computer program PROFISSY (acronym for Properties Of Fire Suppression Systems). The program incorporates a model known as "extended corresponding states" (ECS). This model has been quite successful in modeling the thermodynamic and transport properties of fluids. An early model of this type, known as the TRAPP model (Ely and Hanley, 1981a, 1981b, and 1983), has been successful in the prediction of hydrocarbon transport properties, including LNG (McCarty, 1982). Much of the development of TRAPP occurred in the early 1980's at the National Institute of Standards and Technology. Since that time, the model has been revised, improved, and used successfully to predict the properties of hydrocarbon mixtures (Ely, 1982; Huber and Ely, 1990; Friend, 1992), air (Ely, 1990), and CO₂-rich hydrocarbon mixtures (Sherman *et al.*, 1989), and forms the basis of two current Standard Reference Data Products (Huber and Ely, 1990; Friend, 1992). ECS has been used successfully to predict equilibrium properties such as density, heat capacity, speed of sound, entropy, enthalpy, Joule-Thomson coefficient, viscosity, and thermal conductivity. It is a powerful method, applicable to the entire range of fluid states, from dense liquid to dilute gas, as well as to the supercritical fluid regime. It may be used with only minimal information on a fluid: the critical point, the normal boiling point, and the molecular weight. Additional information on a fluid, such as vapor pressures, saturated liquid densities, and liquid viscosities can be used to refine the model predictions.

Recently ECS models have been used to model thermophysical properties of alternative refrigerants and their mixtures (Huber and Ely, 1992; Huber *et al.*, 1992; Gallagher *et al.*, 1995). In this work, we extended the model to calculate the thermodynamic properties of agent/nitrogen mixtures.

8.3.3.2 Extended Corresponding States Model. The central idea of extended corresponding states is that all points on the *PVT* surface of any fluid may be represented by scaling the *PVT* surface of a reference substance. These "scale factors" involve the critical properties of the fluid of interest and the reference fluid and may also be functions of temperature and density.

The basic equation in the extended corresponding states theory relates the dimensionless residual Helmholtz free energy of a pure fluid, denoted by subscript *j*, to that of a reference fluid, denoted by subscript *o*, whose thermodynamic properties are known, in principle, with great accuracy:

$$a_j^r(\rho_j, T_j) = a_o^r(\rho_o, T_o) \quad (5)$$

where the residual Helmholtz free energy is defined as

$$a^r = \frac{A(\rho, T) - A^*(\rho, T)}{RT} \quad (6)$$

In the above two equations, A is the Helmholtz free energy, the asterisk indicates an ideal gas state value, ρ is the molar density, T is the absolute temperature, and R is the universal gas constant. The temperature and molar density of the fluid j are scaled with the corresponding values for the reference fluid o according to the following two equations:

$$T_o = \frac{T_j}{f_j} \quad (7)$$

$$\rho_o = \rho_j h_j \quad (8)$$

where the scale factors f_j and h_j are called the equivalent substance reducing ratios. In extended corresponding states between two pure fluids j and o , they are related to the critical parameters of the two fluids, namely

$$f_j = \frac{T_{c,j}}{T_{c,o}} \theta_j(\rho_j, T_j) \quad (9)$$

$$h_j = \frac{\rho_{c,o}}{\rho_{c,j}} \phi_j(\rho_j, T_j) \quad (10)$$

where the functions θ_j and ϕ_j are called shape factors, and subscript c denotes a critical property. In addition, the condition that the compressibility factors of the fluids be equal, $Z_j^r = Z_o^r$, is imposed. Other dimensionless residual thermodynamic properties of a fluid can be derived from differentiation of Equation (5) and can be found in Huber and Ely (1994).

To calculate properties of mixtures using extended corresponding states, we use what is known as a "one-fluid" mixture model. The properties of a mixture are found by first assuming the mixture to be a single hypothetical pure fluid (subscript x) through the use of some mixing and combining rules. In this way, the properties of the hypothetical pure fluid are then found by scaling with a single reference fluid o .

$$a_{mix}^r(\rho, T, [x_j]) = a_x^r(\rho_x, T_x) = a_o^r(\rho_o, T_o) \quad (11)$$

In order to obtain the equivalent substance reducing ratios, f_x and h_x , for the hypothetical pure fluid, we use the van der Waals one-fluid mixing rules,

$$h_x = \sum_{i=1}^n \sum_{j=1}^n x_i x_j h_{ij} \quad (12)$$

$$f_x h_x = \sum_{i=1}^n \sum_{j=1}^n x_i x_j f_{ij} h_{ij} \quad (13)$$

and the combining rules,

$$f_{ij} = \sqrt{f_i f_j} (1 - k_{ij}) \quad (14)$$

$$h_{ij} = \frac{(h_i^{1/3} + h_j^{1/3})^3 (1 - l_{ij})}{8} \quad (15)$$

where x is the mole fraction, n is the number of components, subscripts i and j refer to component i and j respectively, k_{ij} and l_{ij} are the binary interaction parameters that may be non-zero when $i \neq j$ and k_{ii} and l_{ii} are defined to be zero. The parameters are generally found empirically by fitting experimental data. However, in order to test the robustness of the ECS model without resorting to the experimental data which have to be obtained *a priori*, the binary interaction parameters are set equal to zero in the model.

Several factors contribute to the ability of the ECS model to accurately predict thermophysical properties. Two important factors are the choice of the reference fluid and the determination of the shape factors. It is important to have a very well characterized empirical reference fluid equation of state. The reference fluid used in this work is HFC-134a (1,1,1,2-tetrafluoroethane) which is represented by the Jacobsen-Stewart (1973) modified 32 term Benedict-Webb-Rubin equation of state (MBWR-32) with coefficients as determined by Huber and McLinden (1992). This equation has been used extensively to represent the properties of hydrocarbons, common inorganics, and most recently refrigerants. Its functional form is essentially a polynomial in density and temperature and is given by

$$p = \sum_{n=1}^9 a_n(T) \rho^n + e^{-(\rho/\rho_c)^2} \sum_{n=10}^{15} a_n(T) \rho^{2n-17} \quad (16)$$

The temperature dependence of the $a_n(T)$ is summarized in Table 8. The 32 coefficients (b_1 to b_{32}) for the reference fluid HFC-134a are tabulated in Huber and Ely (1994). Equation (16), when applied to HFC-134a, typically reproduces the pressures within 0.4 % and the density within 0.2 %. Exceptions are large density deviations in the near critical region, and large pressure errors in the low-temperature compressed liquid region near the saturation boundary.

Table 8. Temperature dependence of the MBWR-32 coefficients

$a_1 = RT$	$a_9 = b_{19} / T^2$
$a_2 = b_1 T + b_2 T^{1/2} + b_3 + b_4 / T + b_5 / T^2$	$a_{10} = b_{20} / T^2 + b_{21} / T^3$
$a_3 = b_6 T + b_7 + b_8 / T + b_9 / T^2$	$a_{11} = b_{22} / T^2 + b_{23} / T^4$
$a_4 = b_{10} T + b_{11} + b_{12} / T$	$a_{12} = b_{24} / T^2 + b_{25} / T^3$
$a_5 = b_{13}$	$a_{13} = b_{26} / T^2 + b_{27} / T^4$
$a_6 = b_{14} / T + b_{15} / T^2$	$a_{14} = b_{28} / T^2 + b_{29} / T^3$
$a_7 = b_{16} / T$	$a_{15} = b_{30} / T^2 + b_{31} / T^3 + b_{32} / T^4$
$a_8 = b_{17} / T + b_{18} / T^2$	

The accuracy one obtains from ECS models also depends on how well the shape factors are determined. The shape factors are functions of both density and temperature. In principle, if one has accurate, analytical equations of state for the two fluids, the exact shape factors relating them can be found, as discussed by Ely (1990). However, often only one fluid (the reference) has an accurate, analytical equation of state available. In this situation, one usually assumes an empirical form for the shape factors. Leach *et al.* (1968) expressed the shape factors as weak functions of temperature and density using the acentric factor as a third correlating parameter. Since the shape factors are much stronger functions of temperature than density and most of the data which are available for refrigerants are for the saturation boundary, we have chosen a different approach utilizing information along the saturation boundary of the fluids (Huber and Ely, 1994) which results in density independent shape factors. It can be shown (Huber and Ely, 1994) that the vapor pressures and the saturated liquid densities of a fluid can be related to the reference fluid properties through the following equations

$$p_{sat, j}(T_j) = p_{sat, o} \left(\frac{T_j}{f_j} \right) \frac{f_j}{h_j} \quad (17)$$

$$\rho_{sat, j}(T_j) = \rho_{sat, o} \left(\frac{T_j}{f_j} \right) \frac{1}{h_j} \quad (18)$$

where subscript *sat* refers to a property of a fluid along the saturation boundary. Equations (17) and (18) are simultaneously solved to obtain f_j and h_j along the saturation boundary. Vapor pressures and saturated liquid densities are provided from empirical correlations of data, if available, or from estimations (Reid *et al.*, 1987). Additional information on the procedure for obtaining shape factors can be found in Huber and Ely (1994).

We do not yet have extensive results on the performance of the ECS model for predicting the density of agent/nitrogen mixtures; however, our experience with hydrocarbon mixtures and with refrigerant mixtures gives us confidence that generally the densities of the liquid phase are accurate to within 3 %. This number can be improved with the use of the binary interaction parameters.

8.3.3.3 Calculation Procedure. The computer code PROFISSY was developed with the primary purpose of helping fire suppression bottle designers or users to obtain temperature-pressure characteristics of the bottle. In other words, given a vessel (V_f) charged with agent and nitrogen at room temperature, one would like to know what the final vessel pressure will be when the vessel is exposed to a different temperature. In this aspect, only the information which is pertinent to the problem is provided in the output although the computer program can perform other thermodynamic property calculations.

The first step in the calculation is to determine the initial conditions of the vessel, that is to determine the compositions of the liquid and vapor phases, the fraction of the mixture (agent/nitrogen) that will be in the vapor phase, and the amount of nitrogen required to pressurize the vessel or the initial total pressure of the vessel given an initial amount of nitrogen. To perform such calculations, it is required that the amount of agent, the fill temperature, the vessel size, and the total pressure of the vessel or the amount of nitrogen in the vessel be known. The calculation is essentially a flash calculation at fixed T and P . The flash calculation can be generally stated as follows:

Given a mixture, in this case agent/nitrogen, whose bulk compositions (z_i) are known at T and P , determine x_i , y_i , and fraction vaporized (α), where x is the liquid mole fraction and y is the vapor mole fraction. The solution of the problem requires mass balance and vapor-liquid equilibrium calculations. A detailed computational procedure can be found in Prausnitz *et al.* (1980) and Walas (1985). In our case, the calculation is slightly different depending on whether (1) the amount of nitrogen ($n_{g,t}$) or (2) the total initial charge pressure (P_i) is given.

In Case (1), with V_f , T_f , $n_{a,t}$, and $n_{g,t}$ given, we calculate P_i , x_g , y_g , and α , where n is the number of moles and subscripts, t , g , and a represent total, nitrogen, and agent respectively. Note that for a binary system x_a and y_a are known once x_g and y_g are determined. In Case (2), knowing V_f , T_f , $n_{t,a}$, and P_i , then $n_{g,t}$, x_g , y_g , and α are calculated. Irrespective of Case (1) or (2), bubble point and dew point calculations (see *e.g.*, Prausnitz *et al.*, 1980) need be carried out to ensure that the flash calculations are performed in the two-phase region. Flash calculations are feasible only when the vessel conditions are above the bubble point and below the dew point. Below the bubble point, the mixture is a subcooled liquid; in this case, $x_i = z_i$. Above the dew point, the mixture is a superheated vapor; in this case $y_i = z_i$.

Once the initial conditions of the vessel are established, calculations of temperature-pressure characteristics can proceed. In this case, given V_f , $n_{a,t}$, and $n_{g,t}$, we want to calculate P_f , x_g , y_g , and α at T_f if the resulting condition is in a two-phase region. The computational procedure is similar to Case (1) above. If the resulting condition in the vessel is in a single-phase region, then straightforward PVT calculations will provide P_f given V_f , T_f , and $z_i (= x_i \text{ or } y_i)$.

Only four pieces of information are required to run the program: (1) agent mass, (2) vessel volume, (3) fill temperature, and (4) either nitrogen mass needed to pressurize the vessel, or the fill pressure of the vessel. **Appendix A** provides a typical session showing how to run the computer program. The current version of the program only supports the agents used in this study although other agents can be incorporated into the program by modifying the property data base.

8.3.4 Results and Discussion

8.3.4.1 Pure Agents. The results of the temperature-pressure measurements for pure agents are summarized in Table 9. In all cases, the combined standard uncertainty of the measurement was estimated to be less than 0.2 MPa based on the law of propagation of uncertainty with the sensitivity coefficients calculated using the ideal gas law. The total agent mass in the second column corresponds to the initial liquid agents whose volumes in the two cases measured approximate one-half or two-

Table 9. Comparison of measured pressures of pure agents at 150 °C ± 2 °C with predicted values

Agent	Agent, $m_{a,t}$ (g)	P_f (measured) (MPa)	P_f (predicted) (MPa)	error ^a (%)
HFC-227ea	28.3	6.83	6.47	5.3
	30.3	7.10	6.74	5.1
	40.7	10.82	10.33	4.5
	38.2	10.09	9.32	7.6
CF ₃ I	43.0	6.51	6.62	1.7
	43.0	6.77	6.77	0.0
	57.3	8.84	9.23	4.4
	58.6	9.52	9.85	3.5
FC-218	28.9	8.33	8.01	3.8
	29.1	8.32	8.01	3.7
	37.4	11.90	11.72	1.5
	37.3	11.85	11.74	0.9
HFC-125	26.1	11.57	11.29	2.4
	34.6	16.61	16.01	3.6
	32.3	15.21	14.83	2.5
CF ₃ Br	34.9	11.98	11.50	4.0
	33.8	11.68	11.21	4.0
	44.4	16.28	15.55	4.5
	45.6	16.97	16.26	4.2

$$^a \text{error (\%)} = | P_f(\text{measured}) - P_f(\text{predicted}) | \times 100 / P_f(\text{measured})$$

thirds of the system volume at room temperature. The measurements were obtained at ~ 150 °C. Only the high temperature results are reported here because at low temperature (– 60 °C) the pressures for all the agents were found to be below 0.1 MPa, which was the lowest value that could be measured from the pressure transducer.

For all the tests with liquid agent initially half filling the vessel, the final pressures at 150 °C were found to be less than 12.5 MPa. For an initially two-thirds filled vessel, the final pressures at 150 °C were measured to be less than 17.5 MPa.

The predicted final pressures obtained using PROFISSY are also tabulated in Table 9. Note that PROFISSY was developed specifically for agent/nitrogen mixtures with no intention to duplicate the function of the REFPROP computer program (Gallagher *et al.*, 1993) (which is designed to estimate thermophysical properties of pure and mixed refrigerants). An attempt to use REFPROP for the pure agents proved to be unfruitful because the final conditions attained in the experiments exceeded the calculational range of REFPROP. To use PROFISSY for the estimation, 0.00001 g of nitrogen was

artificially input into the program to simulate the calculations for a pure agent. This procedure was found to be justifiable because the calculated initial charge pressures at the initial fill temperatures were very close to the measured agent vapor pressures at the same temperatures. In most cases except CF_3I , PROFISSY tended to underestimate the final pressures. Overall, the predictions were found to be within 7.6 % or less of the measured values.

Since very few previous studies related to CF_3I vapor pressure measurements have been reported in the literature (Smith and Srivastava, 1986), temperature-pressure relationships for CF_3I were also measured over a temperature range from -20°C to 150°C . From these measurements, the vapor pressure as a function of temperature was determined. Figure 5 shows three sets of PT measurements using initial liquid agent volumes corresponding to one-third, half, and two-thirds of the vessel volume at room temperature, respectively. The trend in Figure 5 can be explained based on a comparison between the fill density, defined as the ratio of the total agent mass to vessel volume, and the critical density of CF_3I (Grosshandler *et al.*, 1994). Irrespective of the fill conditions at room temperature, if the vessel is chilled to a lower temperature, the measured pressure will correspond to the vapor pressure at that temperature. On the contrary, if the vessel is heated to a higher temperature, the pressure that one measures depends on whether the liquid and vapor phases still coexist at that temperature. To determine whether the two phases are still present at the temperature of interest, one has to find out whether the fill density lies between the saturated vapor and liquid densities at that temperature (Smith and Van Ness, 1975). Using the same reasoning, vapor pressures that were extracted from Figure 5 in the temperature range between -20°C and 70°C are shown in Figure 6. The data were fitted in the form of $\log P_{\text{sat}} = A - (B/T)$ where A and B have values of 3.186 and 1037 respectively, P_{sat} is in MPa and T is in K. Note that the above equation should only be used within the stated temperature range.

8.3.4.2 Solubility of Nitrogen in Agents. Table 10 summarizes the experimental results obtained under an initial total pressure (P_i) of approximately 2.8 MPa or 4.1 MPa at room temperature ($T_i = 23^\circ\text{C} \pm 1^\circ\text{C}$) and with an initial amount of liquid agent corresponding to one-half of the vessel volume. For all the agents evaluated, the amounts of nitrogen ($m_{g,i}$) required to pressurize the vessel to ~ 2.8 MPa and ~ 4.1 MPa were found experimentally to be less than 4 % and 6 % of the total mass of the agent ($m_{a,i}$), respectively. The predicted nitrogen mass in the fifth column and the predicted solubilities of nitrogen ($x_{g,i}$) in the agent under T_i and P_i in the last column of Table 9 were obtained using PROFISSY. The calculations were performed with $m_{a,i}$, P_i , $V_i (= 52.2 \text{ cm}^3)$, and T_i as input and the two binary interaction parameters (k_{ij} and l_{ij}) set equal to zero. The solubility is defined as the mole fraction of dissolved nitrogen in the liquid agent/nitrogen mixture at pressure P_i . The predicted nitrogen mass compares favorably with the measured value even without taking k_{ij} and l_{ij} into consideration. The solubility of nitrogen in FC-218 was found to be the highest compared to the other four agents, whereas nitrogen exhibited the lowest solubility in CF_3Br when P_i was ~ 2.8 MPa and in CF_3I when P_i was ~ 4.1 MPa.

Table 11 tabulates the experimental results as well as the predictions obtained under similar experimental conditions as in Table 10, except that the initial amount of liquid agent corresponded to two-thirds of the vessel volume. The predicted nitrogen mass also compares favorably with the measured value. For all the agents evaluated, the amount of nitrogen required to pressurize the vessel was found experimentally to be less than 3 % to 4 % of the total mass of the agent. Note that the calculated solubilities in Table 11 are very close to those tabulated in Table 10. This is not surprising because the solubility depends only on P_i and T_i and does not depend on the amount of liquid agent. Again, FC-218 was found to have the highest nitrogen solubility compared to the other four agents, irrespective of P_i . At low P_i (~ 2.8 MPa), the solubility of nitrogen in CF_3Br was calculated to be the

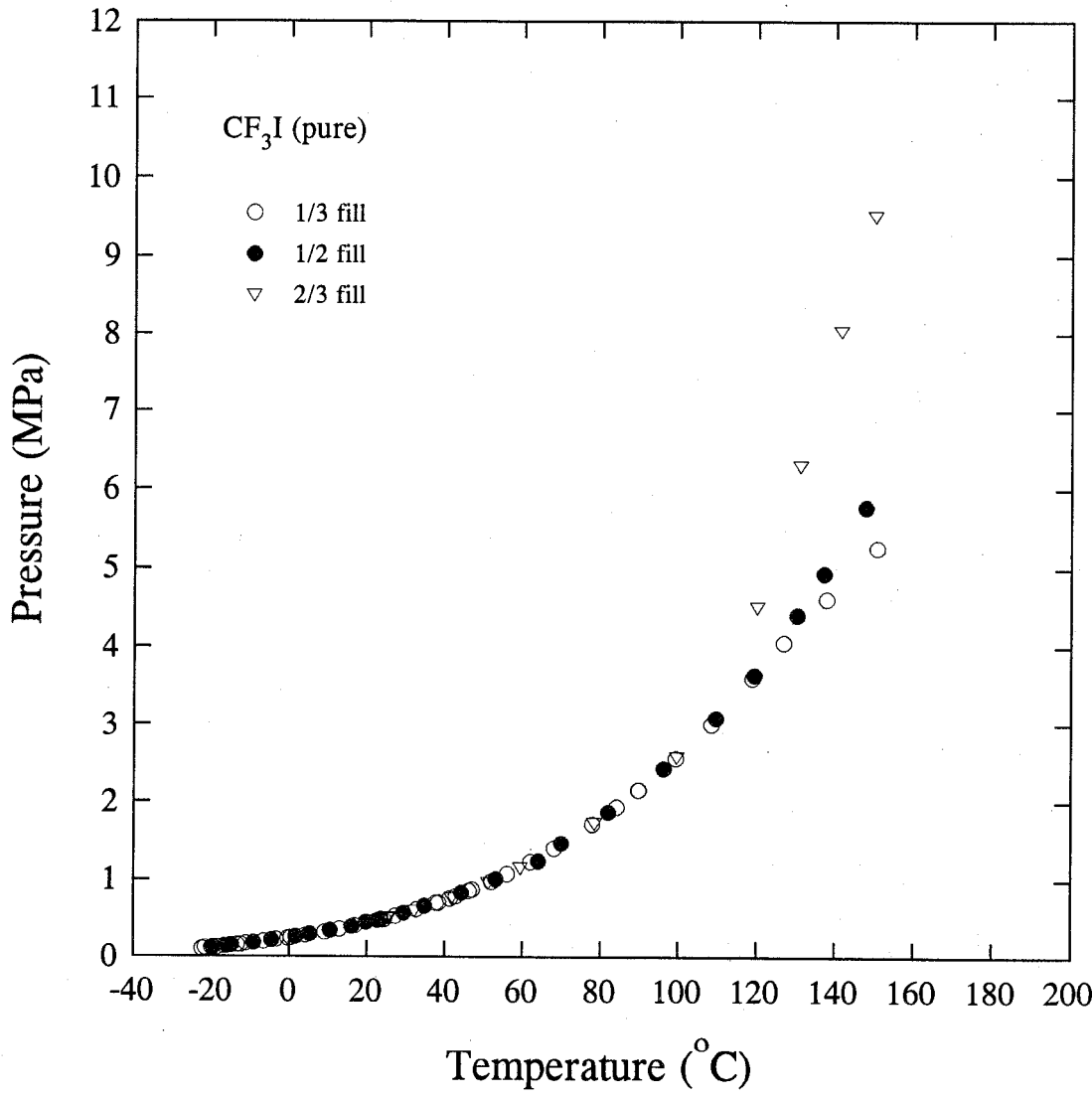


Figure 5. Pressure-temperature measurements of pure CF₃I.

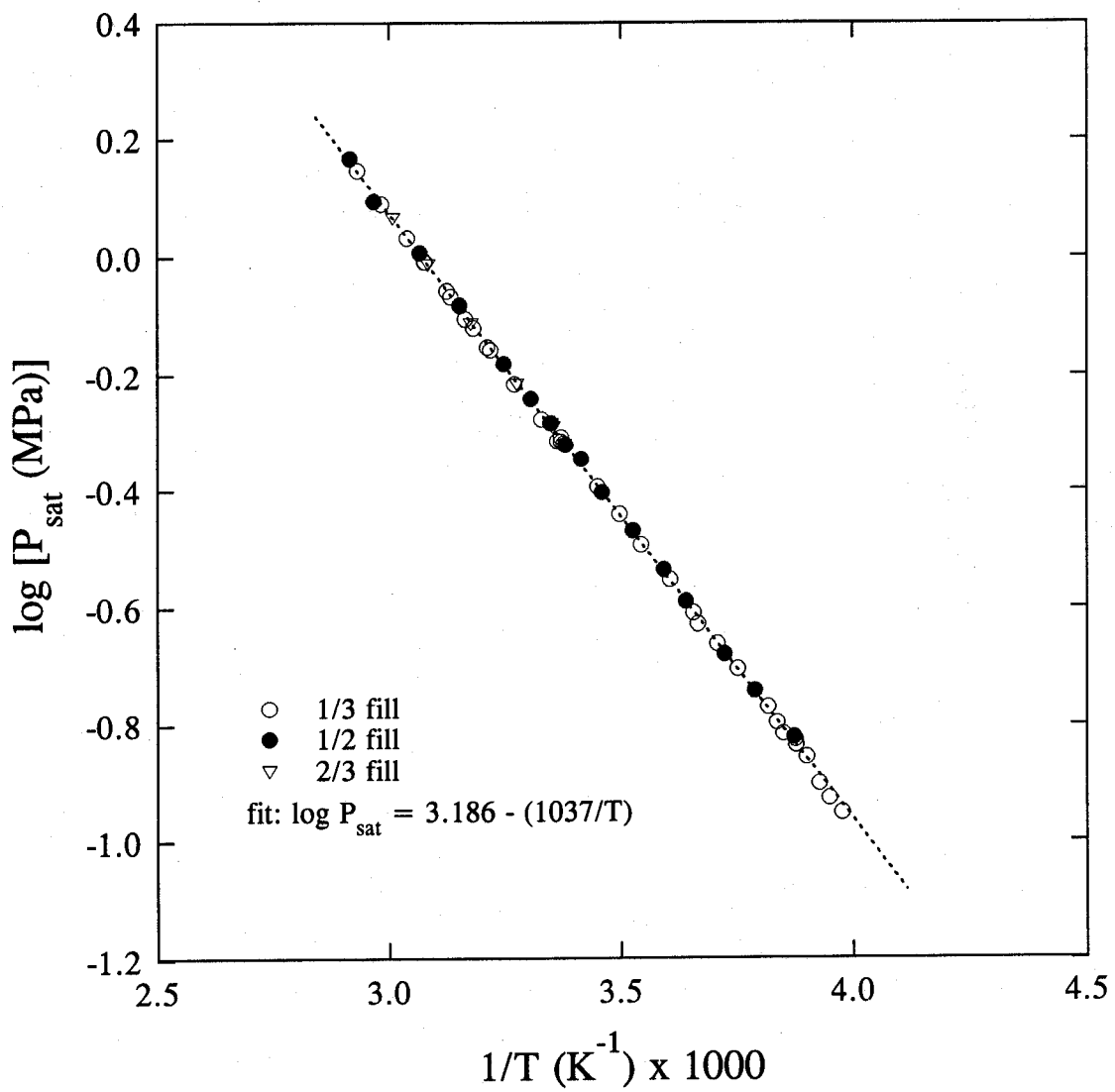


Figure 6. Vapor pressure of CF₃I as a function of temperature.

Table 10. Amount of nitrogen ($m_{g,t}$) required to pressurize mixture to P_i at $T_i = 23\text{ }^{\circ}\text{C} \pm 1\text{ }^{\circ}\text{C}$ with an initial amount of liquid agent corresponding to half of the vessel volume

Agent	Agent, $m_{a,t}$ (g)	P_i (MPa)	Nitrogen, $m_{g,t}$ (g)	Predicted $m_{g,t}$ (g)	Solubility, $x_{g,l}$ (predicted)
HFC-227ea	36.5	2.90	1.2	1.24	0.083
	36.6	2.93	1.2	1.26	0.084
	36.5	4.29	1.9	1.95	0.129
	36.6	4.28	1.9	1.94	0.128
CF ₃ I	54.9	2.87	1.0	1.15	0.056
	54.8	2.87	1.1	1.15	0.056
	54.9	4.21	1.6	1.79	0.087
	54.8	4.21	1.7	1.78	0.087
FC-218	33.2	2.89	1.0	1.07	0.090
	33.1	2.89	1.1	1.07	0.090
	33.2	4.27	1.8	1.77	0.152
	33.1	4.31	1.8	1.80	0.154
HFC-125	31.3	2.78	0.9	0.81	0.053
	31.1	2.79	0.8	0.81	0.053
	31.3	4.24	1.6	1.62	0.106
	31.1	4.23	1.6	1.61	0.106
CF ₃ Br	40.9	2.89	0.7	0.75	0.046
	40.7	2.87	0.6	0.75	0.046
	40.9	4.29	1.4	1.53	0.095
	40.7	4.29	1.4	1.53	0.095

lowest, whereas the solubility of nitrogen in CF₃I was found to be the lowest at high P_i (~ 4.1 MPa). This is quite explainable by the great difference in the vapor pressures of these two agents, as noted in Table 7.

8.3.4.3 Agent/Nitrogen Mixtures. The experimental results for agent/nitrogen mixtures at $-60\text{ }^{\circ}\text{C}$ with an initial volume of liquid agent corresponding to half of the vessel volume are shown in Table 12. In all cases, the combined standard uncertainty of the measurement was found to be less than 0.1 MPa. The sensitivity coefficients in the uncertainty estimation were calculated based on PROFISSY. Comparing to the vapor pressure of a pure agent at $-60\text{ }^{\circ}\text{C}$, the measurements showed that there were still significant residual pressures in the vessel. These residual pressures are deemed necessary to expel the cold liquid agents if the vessels are discharged under such extremely low temperature. The fifth column in the table tabulates the predicted final pressures using PROFISSY.

Table 11. Amount of nitrogen ($m_{g,t}$) required to pressurize mixture to P_i at T_i ($= 23\text{ }^{\circ}\text{C} \pm 1\text{ }^{\circ}\text{C}$) with an initial amount of liquid agent corresponding to two-thirds of the vessel volume

Agent	Agent, $m_{a,t}$ (g)	P_i (MPa)	Nitrogen, $m_{g,t}$ (g)	Predicted $m_{g,t}$ (g)	Solubility, $x_{g,t}$ (predicted)
HFC-227ea	48.7	2.87	1.1	1.16	0.082
	48.7	2.98	1.2	1.21	0.086
	48.7	4.25	1.8	1.81	0.127
	48.7	4.25	1.8	1.82	0.127
CF ₃ I	72.8	2.77	0.9	1.02	0.054
	72.7	2.79	0.9	1.02	0.054
	72.8	4.14	1.4	1.62	0.086
	72.7	4.16	1.4	1.63	0.086
FC-218	44.1	2.94	1.0	1.07	0.096
	44.2	2.93	1.0	1.06	0.096
	44.1	4.36	1.6	1.81	0.161
	44.2	4.29	1.6	1.75	0.157
HFC-125	41.9	2.70	0.8	0.79	0.051
	41.8	2.85	0.8	0.83	0.055
	41.9	4.18	1.5	1.56	0.104
	41.8	4.18	1.5	1.51	0.102
CF ₃ Br	54.9	2.92	0.7	0.76	0.048
	54.8	2.87	0.7	0.74	0.046
	54.9	4.25	1.4	1.48	0.094
	54.8	4.25	1.4	1.49	0.094

The calculations were performed with k_{ij} and l_{ij} set equal to zero, $V_t = 52.2\text{ cm}^3$, and the initial conditions given in the table. In general, the predicted values were all found to be within 6 % of the measured values.

Table 13 summarizes the results obtained from experiments at $-60\text{ }^{\circ}\text{C}$ using an initial liquid agent volume equivalent to two-thirds of the vessel volume. Considerable final pressures in the vessel were also noted at $-60\text{ }^{\circ}\text{C}$. Predictions using PROFISSY with k_{ij} and l_{ij} set equal to zero and $V_t = 52.2\text{ cm}^3$ were also carried out, and the comparisons between predicted and measured final pressures indicate that overall the errors were within 8 % for all the agents.

Table 12. Initial conditions at $T_i = 23\text{ }^{\circ}\text{C} \pm 1\text{ }^{\circ}\text{C}$ and final pressures ($P_{f,c}$) at $-60\text{ }^{\circ}\text{C} \pm 1\text{ }^{\circ}\text{C}$ for agent/nitrogen mixtures (half filled volume)

Agent	$m_{a,i}$ (g)	P_i (MPa)	$P_{f,c}$ (MPa) (measured)	$P_{f,c}$ (MPa) (predicted)	error ^a (%)
HFC-227ea	36.5	2.90	1.69	1.70	0.6
	36.6	2.93	1.72	1.71	0.6
	36.5	4.29	2.59	2.60	0.4
	36.6	4.28	2.58	2.61	1.2
CF ₃ I	54.9	2.87	1.71	1.61	5.9
	54.8	2.87	1.71	1.62	5.3
	54.9	4.21	2.62	2.49	5.0
	54.8	4.21	2.61	2.47	5.4
FC-218	33.2	2.89	1.44	1.39	3.5
	33.1	2.89	1.43	1.38	3.5
	33.2	4.27	2.34	2.23	4.7
	33.1	4.31	2.38	2.27	4.6
HFC-125	31.3	2.78	1.11	1.07	3.6
	31.1	2.79	1.11	1.08	2.7
	31.3	4.24	2.10	2.04	2.9
	31.1	4.23	2.09	2.03	2.9
CF ₃ Br	40.9	2.89	1.04	1.02	1.9
	40.7	2.87	1.00	1.02	2.0
	40.9	4.29	1.95	1.94	0.5
	40.7	4.29	1.99	1.97	1.0

$$^a\text{error (\%)} = | P_{f,c}(\text{measured}) - P_{f,c}(\text{predicted}) | \times 100 / P_{f,c}(\text{measured})$$

The results for high temperature (150 °C) measurements are shown in Tables 14 and 15 for initial conditions corresponding to half and two-thirds filled volumes, respectively. The combined standard uncertainty, in all cases, was estimated to be less than 0.2 MPa, and the sensitivity coefficients were calculated based on an ideal gas mixture model. The predictions were obtained by using PROFISSY. In the calculations, k_{ij} and l_{ij} were again assumed to be zero and $V_i = 42.6\text{ cm}^3$ was used. For these two experimental conditions, the errors between the predicted and measured final pressures were found to be within 10 %.

Table 13. Initial conditions at $T_i = 23\text{ }^{\circ}\text{C} \pm 1\text{ }^{\circ}\text{C}$ and final pressures ($P_{f,c}$) at $-60\text{ }^{\circ}\text{C} \pm 1\text{ }^{\circ}\text{C}$ for agent/nitrogen mixtures (two-thirds filled volume)

Agent	$m_{a,i}$ (g)	P_i (MPa)	$P_{f,c}$ (MPa) (measured)	$P_{f,c}$ (MPa) (predicted)	error ^a (%)
HFC-227ea	48.7	2.87	1.66	1.67	0.6
	48.7	2.98	1.70	1.73	1.8
	48.7	4.25	2.55	2.57	0.8
	48.7	4.25	2.51	2.59	3.2
CF ₃ I	72.8	2.77	1.60	1.52	5.0
	72.7	2.79	1.64	1.53	6.7
	72.8	4.14	2.49	2.43	2.4
	72.7	4.16	2.62	2.41	8.0
FC-218	44.1	2.94	1.41	1.41	0.0
	44.2	2.93	1.39	1.38	0.7
	44.1	4.36	2.32	2.32	0.0
	44.2	4.29	2.30	2.27	1.3
HFC-125	41.9	2.70	1.08	1.06	1.9
	41.8	2.85	1.10	1.11	0.9
	41.9	4.18	2.06	2.05	0.5
	41.8	4.18	2.02	1.99	1.5
CF ₃ Br	54.9	2.92	1.05	1.04	1.0
	54.8	2.87	1.02	1.02	0.0
	54.9	4.25	1.94	1.94	0.0
	54.8	4.25	1.90	1.96	3.2

^aerror (%) = $| P_{f,c}(\text{measured}) - P_{f,c}(\text{predicted}) | \times 100 / P_{f,c}(\text{measured})$

Table 14. Initial conditions at $T_i = 23\text{ }^{\circ}\text{C} \pm 1\text{ }^{\circ}\text{C}$ and final pressures ($P_{f,h}$) at $150\text{ }^{\circ}\text{C} \pm 2\text{ }^{\circ}\text{C}$ for agent/nitrogen mixtures (half filled volume)

Agent	$m_{a,t}$ (g)	P_i (MPa)	$P_{f,h}$ (MPa) (measured)	$P_{f,h}$ (MPa) (predicted)	error ^a (%)
HFC-227ea	28.3	2.76	10.70	10.39	2.9
	30.3	2.81	11.25	10.95	2.7
	28.3	4.29	13.58	13.25	2.4
	30.3	4.19	14.43	14.00	3.0
CF ₃ I	43.2	2.75	10.38	10.55	1.6
	43.2	2.74	10.22	10.35	1.3
	43.2	4.13	12.71	13.03	2.5
	43.2	4.16	12.92	13.05	1.0
FC-218	28.9	2.85	12.13	11.90	1.9
	29.1	2.76	11.84	11.76	0.7
	28.9	4.16	14.64	14.44	1.4
	29.1	4.25	14.73	14.59	1.0
HFC-125	26.4	2.79	14.45	14.43	0.1
	26.1	2.78	14.35	14.41	0.4
	26.4	4.18	17.32	17.56	1.4
	26.1	4.21	17.20	17.36	0.9
CF ₃ Br	34.9	2.80	14.32	14.04	2.0
	34.9	4.22	17.11	16.90	1.2

^aerror (%) = $| P_{f,h}(\text{measured}) - P_{f,h}(\text{predicted}) | \times 100 / P_{f,h}(\text{measured})$

Table 15. Initial conditions at $T_i = 23\text{ }^{\circ}\text{C} \pm 1\text{ }^{\circ}\text{C}$ and final pressures ($P_{f,h}$) at $150\text{ }^{\circ}\text{C} \pm 1\text{ }^{\circ}\text{C}$ for agent/nitrogen mixtures (two-thirds filled volume)

Agent	$m_{a,t}$ (g)	P_i (MPa)	$P_{f,h}$ (MPa) (measured)	$P_{f,h}$ (MPa) (predicted)	error ^a (%)
HFC-227ea	38.4	2.80	15.56	14.57	6.4
	39.7	2.78	16.77	15.34	8.5
	38.4	4.14	19.19	17.71	7.7
	39.7	4.29	20.54	18.87	8.1
CF ₃ I	57.3	2.76	13.79	14.34	4.0
	58.6	2.79	14.42	15.08	4.6
	57.3	4.23	17.62	18.38	4.3
	58.6	4.10	18.25	18.41	0.9
FC-218	37.4	2.88	16.39	16.24	0.9
	37.3	2.78	16.51	16.68	1.0
	37.4	4.16	20.03	20.01	0.1
	37.3	4.23	19.99	19.94	0.3
HFC-125	34.6	2.76	20.13	20.37	1.2
	32.3	2.86	18.87	18.94	0.4
	34.6	4.16	24.25	24.71	1.9
	32.3	4.18	22.39	22.87	2.1
CF ₃ Br	44.4	2.76	18.92	18.68	1.3
	45.6	2.76	20.19	19.69	2.5
	44.4	4.18	22.91	22.82	0.4
	45.6	4.21	23.22	23.31	0.4

$$^a \text{error (\%)} = | P_{f,h}(\text{measured}) - P_{f,h}(\text{predicted}) | \times 100 / P_{f,h}(\text{measured})$$

8.3.5 Summary and Conclusions. For all the pure agents studied under two fill conditions (1/2 and 2/3 filled), the final pressure that the vessel experienced when it was heated to 150 °C was found to be less than 17.5 MPa. Irrespective of the initial fill conditions, the final pressures were all below 0.1 MPa when the vessel was chilled to - 60 °C and pure agents were used.

For an initial fill condition corresponding to approximately half of the vessel volume, the amount of nitrogen required to pressurize the vessel up to 4.4 MPa was measured to be less than 6 % of the total agent mass in the vessel in all cases. Under an initial condition of two-thirds liquid fill, the required nitrogen mass was found to be less than 4 % of the total agent mass. Independent of the initial amount of liquid agent in the vessel, the mole fractions of nitrogen in the liquid agents (solubilities) at room temperature were calculated to be less than 0.10 and 0.17, respectively, at 2.8 MPa and 4.1 MPa.

For agent/nitrogen mixtures with an initial liquid agent fill condition of one half or two-thirds and initial total pressures of approximately 2.8 MPa and 4.1 MPa at room temperature, the final pressures measured at - 60 °C were found to be higher than 0.9 MPa and 1.8 MPa respectively in all cases. Compared to the vapor pressures of the pure agents, significant residual pressures were still present in the vessel at - 60 °C. These residual pressures, as the result of the initial nitrogen pressurization, are vital to agent discharges at cold ambience.

For agent/mixtures with an initially half full condition and initial charge pressures of approximately 2.8 MPa and 4.1 MPa, the resulting pressures at 150 °C were measured to be less than 15 MPa and 18 MPa respectively. For the two-thirds condition under similar initial charge pressures, the final pressures were found to be less than 21 MPa and 25 MPa respectively. Comparisons of the measurements among the four selected agents showed that HFC-125 exhibited the highest final pressures at 150 °C under all the experimental conditions used in this study.

The thermodynamic properties of agent/nitrogen mixtures were calculated using the computer code PROFISSY which is based on an extended corresponding states model. The code was developed to help fire suppression bottle designers to facilitate the calculations of bottle temperature-pressure relationships. Comparing to the experimental measurements, the predictions from PROFISSY were generally found to be within 10 % or less of the measured values.

Based on the experimental results from this study, the following conclusions are made:

1. Under the current pressure vessel design criteria in military specification MIL-C-22284A (proof pressure of 9.62 MPa and minimum burst pressure of 12.37 MPa), the structural integrity of the vessel will be severely compromised by the resulting high pressure if the vessel, when used with the four selected agents, is exposed to ambient temperatures up to 150 °C.
2. When using the computer code PROFISSY, extreme care should be taken because PROFISSY tends to *underestimate* the final pressures at elevated temperatures by about 10 % in some cases.

8.4 Discharge of Agent/Nitrogen Mixtures in a Simulated Dry Bay

8.4.1 Introduction. Currently, CF₃Br (halon 1301) is used for in-flight dry bay fire protection applications. It is normally stored under pressure above its vapor pressure at room temperature by using nitrogen. Due to nitrogen pressurization, nitrogen is dissolved in the liquid agent, and the presence of dissolved nitrogen complicates the discharge process in that the fluid leaving the vessel is

not pure halon but a mixture of halon and nitrogen and that degassing of the dissolved nitrogen (*i.e.*, the dissolved nitrogen coming out of the liquid in the form of bubbles) occurs inside the vessel during discharge (depressurization).

The search for halon alternatives has resulted in three potential agents, HFC-125, FC-218, and CF_3I , for dry bay fire protection applications from a list of more than ten candidates (Grosshandler *et al.*, 1994). This task is an extension of the study of agent discharge fluid dynamics previously reported as a part of the agent screening work in Grosshandler *et al.* (1994). In the previous study, the agent was only pressurized with nitrogen a few minutes before the initiation of a test. Given such a short contact time of nitrogen with agent, it was not possible to have an appreciable amount of nitrogen dissolved in the agent. The experimental protocol was dictated by an *idealized* discharge mechanism (a rupture disc). Rupture discs, which offered simple flow geometry and quick action and also facilitated the agent screening process, were chosen as the result of a compromise between a simulated and a real discharge event. Furthermore, it was believed that the effect of dissolved nitrogen on the discharge process was similar among all the agents evaluated because the nitrogen solubilities in all the agents were measured to be very similar (Grosshandler *et al.*, 1994) and that any observable differences in the discharge dynamics among the agents studied were attributable to the agents themselves rather than the dissolved nitrogen.

In this study, the role of dissolved nitrogen in the agent discharge dynamics was examined in a systematic way. Actual discharge mechanisms (solenoid valves and squibs) were used to simulate discharge processes. The main objective of this task was to study the discharge characteristics of the three selected agents (CF_3Br was also included as a reference) in an unconfined space to simulate a dry bay (without airflow and obstacles) under various experimental conditions in greater detail than the previous screening project. In particular, the parameters of interest include size of valve opening, fill density, nitrogen charge pressure, initial agent temperature, discharge orientation, and the degree of nitrogen saturation in liquid agent.

8.4.2 Experimental Methods. This section describes the experimental hardware and procedures used to performed the dry bay discharge tests. The simulated dry bay was essentially a room with dimensions of 3 m (width) x 3 m (length) x 3.4 m (height). No clutter or obstacles, except a pressure transducer located about 1.4 m downstream from the vessel outlet, were placed in the flow path of the flashing spray. Depending on the release mechanism used and discharge orientation, the vessel was centrally located either on one side of the room, near the ceiling, or near the floor. There were two major components in the experimental set-up: (1) the pressure vessel and (2) the release mechanism.

Three pressure vessels, a cylindrical, a spherical, and a cylindrical with sight gages, were used in this study. The choice of the vessel was dictated by the release mechanism. The cylindrical vessel, which was also used in the previous study (Grosshandler *et al.*, 1994), was made from a stainless steel SS 304 tube with an internal diameter of 50.8 mm and a wall thickness of 6.4 mm. One end of the tube was welded with an end cap in which four holes were drilled and tapped to provide access for mounting a piezoelectric dynamic pressure transducer (Kistler Model 603B1), a pressure gage, two K-type thermocouples (Omega CASS-18E-12 and KMQSS-125U-6), and a needle valve (Whitey SS-1RS4) for agent filling and subsequent nitrogen pressurization. Occasionally, a fast response static pressure transducer (Druck Model PDCR 330) was also mounted to the vessel in order to validate the readings from the dynamic pressure transducer. A flange for mounting the release mechanism was welded to the other end of the tube. The internal volume of the vessel without the release mechanism in place was found to be $4.97 \times 10^{-4} \text{ m}^3$, determined by the volume of water required to fill the vessel. Although the vessel was hydrostatically tested to 17.2 MPa, it was never operated above 11 MPa for safety reasons. A schematic of the vessel is shown in Figure 7.

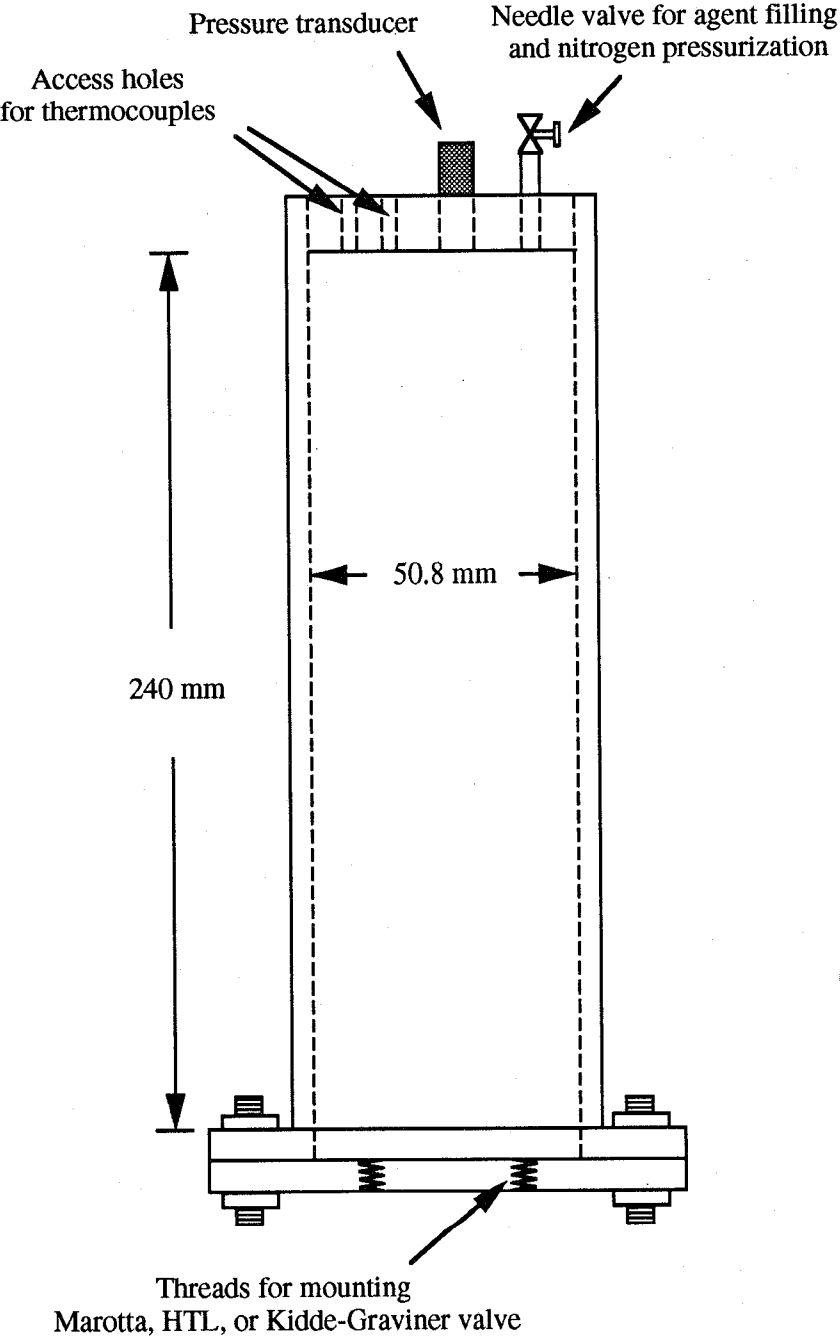


Figure 7. Schematic of the cylindrical vessel.

The spherical vessel was custom-made for the National Institute of Standards and Technology by Pacific Scientific HTL Kin-Tech Division. The vessel was made of metal alloy with an internal volume of $5.38 \times 10^{-4} \text{ m}^3$. There was a three-outlet manifold welded to the top of the vessel. The three access holes were for mounting a K-type thermocouple to monitor the liquid temperature, a dynamic or static pressure transducer, and a needle valve. The vessel was also equipped with a one-way fill valve (not used in this study). At 21 °C, the vessel had a proof pressure of 12.4 MPa and a burst pressure of 18.6 MPa. Figure 8 shows the schematic of the spherical vessel.

The cylindrical vessel with sight gages was an industrial liquid level gage (Jerguson 14TL10). It was made of stainless steel SS 316 and had two opposing slots on the side wall of the vessel. The slots were machined to provide plane seats for the gaskets and the glass assemblies. The gage glasses were specially processed, heat treated, and tempered. The glass assemblies were secured in place with steel covers and specially designed bolts. There were a 3/4 NPT top end connection for mounting instrumentation and a 600# RF slip-on flanged bottom connection for mounting the release mechanism. A cross was attached to the top end connection to provide three access holes for a dynamic pressure transducer, a pressure gage, and a needle valve. The vessel was hydrostatically tested by the manufacturer to 10.2 MPa at 38 °C. The internal volume of the vessel without the release mechanism was estimated to be $6.10 \times 10^{-4} \text{ m}^3$. The schematic of the vessel is shown in Figure 9.

Four types of release mechanisms were used in this study: two solenoid valves (from Marotta Scientific Model MV121KJ-2 and HTL Pacific Scientific PN 36400036), a pyrotechnic piston-actuated valve (Kidde-Graviner, Jordan Crew Bay System), and a squib (HTL Pacific Scientific). There are some slight differences in the operating procedures for the two solenoid valves. Upon activation, the Marotta valve with an outlet of 4.45 cm remains open and requires re-arming if it is to be used again, whereas the HTL valve, which has an outlet size similar to the Marotta valve, will close automatically and no re-arming of the valve is needed. Note that both valves have a smaller passage upstream of the outlet. The activation of the Kidde-Graviner valve with a straight-through opening of 4 cm is achieved by using a fast acting beam assembly held initially in position by a spindle. A pyrotechnic piston actuator, when it is energized, causes the spindle to rotate and free the beam assembly. Re-arming of the valve is also required. The squib assembly consists of an explosive cartridge (HTL PN 30903827), a rupture disc, and a discharge outlet port (Military Standard MS33649-08) with a diameter of 2 cm. Opening of the rupture disc is initiated by the explosive cartridge. The squib was used *solely* with the spherical vessel. A DC power source was used to activate the release mechanism. Approximately 25 V and 10 A were required for the Marotta and HTL solenoid valves, approximately 10 V and 1 A for the piston-actuated Kidde-Graviner valve, and approximately 20 V and 3.5 A for the HTL squib. The response times of all the release mechanisms were on the order of 10 ms.

The experimental preparation involved the following steps. The vessel was filled approximately two-thirds full (by volume); in some experiments a half-filled condition was used. The total mass of the agent dispensed to the vessel was obtained by weighing on an electronic scale with an uncertainty of 1 g. The vessel was then pressurized with nitrogen to a specified *equilibrium* pressure at room temperature. The attainment of the final equilibrium pressure could be facilitated by shaking the vessel intermittently and vigorously and by repetitive nitrogen pressurization. The vessel was then mounted and was ready to be discharged at room temperature.

Figure 10 shows the experimental set-up for the vessel with a Marotta or HTL solenoid valve. Because of the configuration of the valve outlet, the normal discharge orientation is horizontal in this case. For the Kidde-Graviner valve and the HTL squib, the normal discharge direction is vertically downward. The five lasers and photodiode detectors shown in Figure 10 were used to measure the average dispersion velocities of the leading edge of the evaporating spray propagating downstream from the vessel exit. The measurement technique was based on the principle of laser attenuation, details of which can be found in the previous report by Grosshandler *et al.* (1994). A piezoelectric

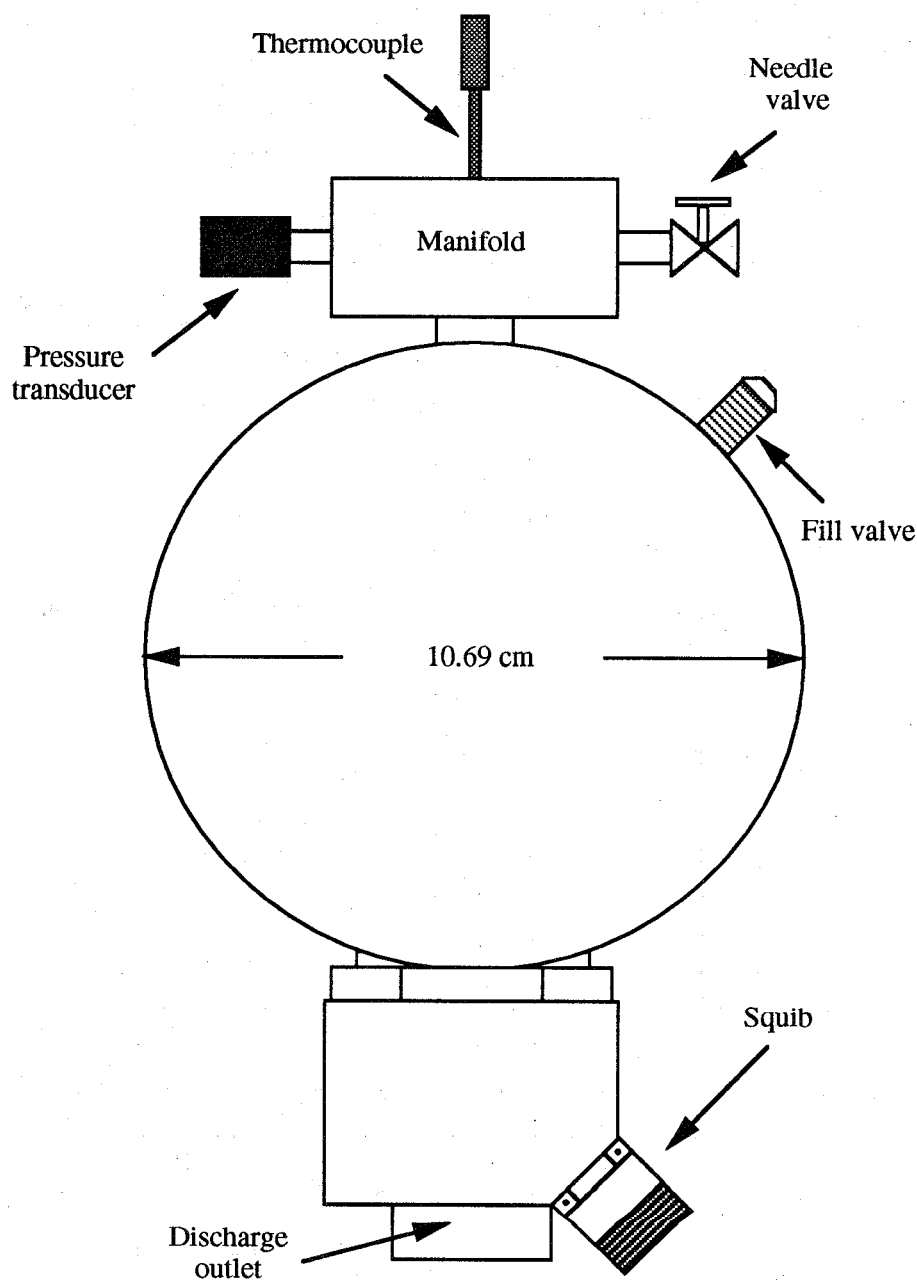


Figure 8. Schematic of the spherical vessel.

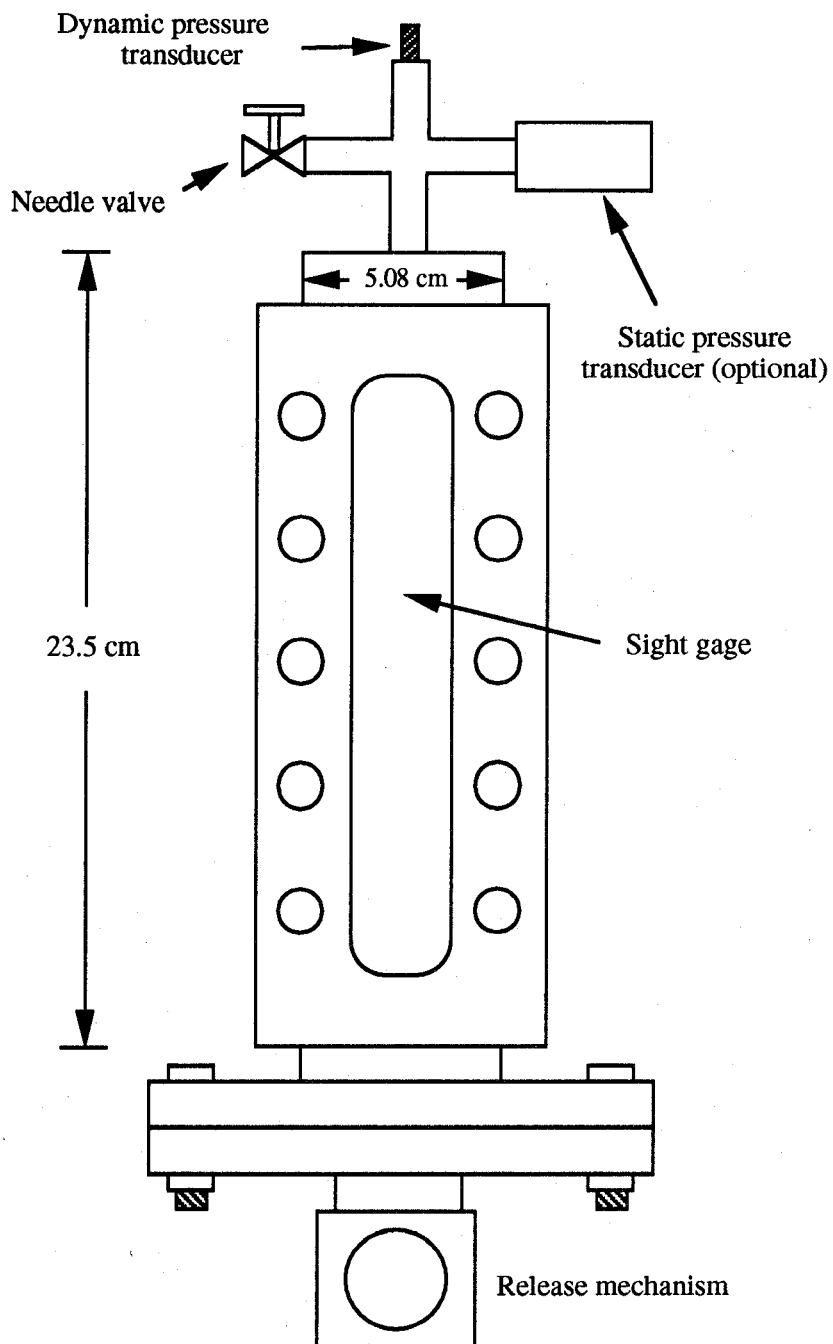


Figure 9. Schematic of the cylindrical vessel with sight gages.

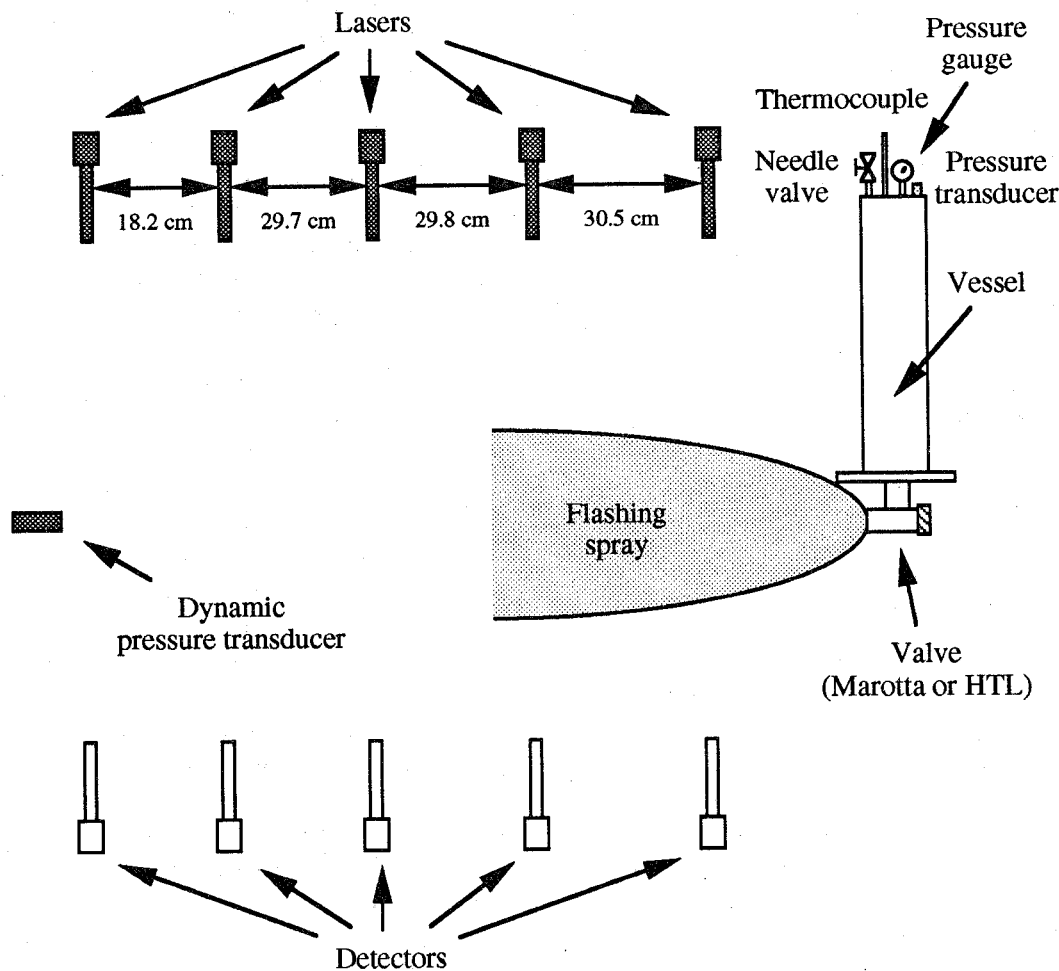


Figure 10. A schematic of the experimental set-up.

dynamic pressure transducer (Kistler Model 603B1) oriented normal to the flow direction was placed along the centerline of the valve outlet at a downstream position of approximately 1.4 m and was used to measure the impact pressure and to obtain some qualitative two-phase behavior of the flashing spray. The mounting of the pressure transducer was also discussed in detail in Grosshandler *et al.* (1994).

All the piezoelectric dynamic pressure transducers were regulated by dual mode charge amplifiers (Kistler Model 5004) with 180 kHz frequency filters. The amplifiers were operated in the "long" time constant mode in order to track the temporal variation of pressure over the relatively long discharge time interval (on the order of 100 ms).

The outputs from the amplifiers, the static pressure transducer (when used), and the photodiode detectors were recorded using a 16 channel, 12 bit, high-speed data acquisition board (Strawberry Tree FLASH-12TM Model 1) at a rate of 25 kHz per channel for 0.6 s. The total number of samples collected per channel was 15000. Because of the speed and memory size, a 1 Mbyte daughter board was required for direct memory access. The data acquisition system was controlled by menu-driven software (WorkBench 4.0), and the data obtained were stored in a personal computer (PC-486) for subsequent data analysis.

A high-speed movie camera (Photec IV) operating at 2000 frames per second was used to document the flashing behavior of agent/nitrogen mixtures at the exit of the vessel and the events occurring inside the vessel during discharge when the cylindrical vessel with sight gages was used. Kodak Ektachrome high-speed daylight films (ASA 400) together with two flood lights for front lighting and an intense flood light for backlighting were used.

The experimental sequence was controlled by a timing circuit. At the initiation of the timing sequence, the high-speed camera was first triggered to ensure that the full framing rate had been attained before photographing the discharge process, and the camera was on for 2 s. At 0.8 s, the data acquisition was initiated for a duration of 0.6 s. At 1 s, the timing circuit sent a control signal to turn on the DC power supply for 0.2 s to activate the release mechanism.

In this section, unless otherwise stated, all the discharge experiments were conducted at room temperature with a nitrogen charge pressure of ~ 4.12 MPa. The vessel was initially filled with an amount of pure liquid agent equivalent to approximately two-thirds of the vessel volume. The discharge orientation was the normal configuration of the release mechanism, as discussed above. This condition is termed *standard discharge* in the discussion.

The effects of several experimental parameters on the discharge characteristics were also examined. These parameters included: (1) discharge orifice size, (2) initial amount of agent, (3) nitrogen charge pressure, (4) initial temperature of agent, (5) discharge orientation, and (6) degree of nitrogen saturation in the liquid agent. Table 16 shows the experimental matrix.

The effect of the orifice size on the standard discharge process was evaluated by mounting a stainless steel orifice plate at the Marotta or HTL solenoid valve outlet. The orifice diameter (2.38 cm) used in this work was about half of the valve outlet diameter.

The initial amount of agent in the vessel was also varied from two-thirds fill (used in all the standard discharge tests) to half fill. Only two agents (CF_3I and HFC-125) were used in this part of the parametric studies.

The effect of initial nitrogen charge pressure on the discharge was examined by performing a series of experiments at room temperature with ~ 2.75 MPa, 4.12 MPa, and 5.50 MPa nitrogen pressures. Because the operating pressures of the Marotta and HTL valves were rated to be less than 5.50 MPa, only two charge pressures (2.75 MPa and 4.12 MPa) were used, whereas all three pressures were evaluated using the spherical vessel equipped with a squib.

Some experiments were performed to determine the effect of initial agent temperature on the discharge characteristics. In the low temperature experiments, the vessel was initially filled with agent,

Table 16. Test matrix for discharge experiments

	CF ₃ I	FC-218	HFC-125	CF ₃ Br
HTL valve ^a	✓ ^b	✓	✓ ^{‡c}	✓
HTL valve ^d	---	✓	✓	✓
HTL valve ^{a,e}	---	✓	✓	✓
Marotta valve ^a	✓ [‡]	✓	✓ [‡]	✓
Marotta valve ^d	✓	✓	✓	✓
Marotta valve ^{a,e}	✓	✓	✓	✓
Marotta valve ^{a,f}	✓	✓	✓	✓
Marotta valve ^{d,f}	✓	✓	✓	✓
KG valve ^a	✓	✓	✓	✓
KG valve ^g	✓	✓	✓	✓
Squib ^a	✓	✓	✓	✓
Squib ^d	✓	✓	✓	✓
Squib ^h	✓	---	✓	---
Squib ⁱ	✓	✓	✓	✓
Squib ^a	---	---	†bj	---

^ainitial nitrogen charge pressure ~ 4.12 MPa

^btwo-third fill condition

^chalf fill condition

^dinitial nitrogen charge pressure ~ 2.75 MPa

^ewith an orifice plate at the valve outlet

^fcylindrical vessel with sight gages

^ghigh temperature experiments

^hinitial nitrogen charge pressure ~ 5.50 MPa

ⁱcold temperature experiments

^jeffect of discharge orientation

pressurized with nitrogen to ~ 4.12 MPa at room temperature, and then cooled with dry ice to below - 50 °C before a discharge was initiated. Due to the large thermal inertia of the cylindrical vessel and the limitations for the operating temperatures of the Marotta and HTL solenoid valves, only the spherical vessel with a squib was used in this set of experiments. In the high temperature experiments, the vessel was heated with a heating tape wrapped around it after it was filled with agent and pressurized with nitrogen to ~ 4.12 MPa at room temperature. Depending on which agent was used in the test, the vessel was heated to a temperature (90 °C for CF₃I) at which the corresponding pressure inside the vessel did not go beyond 9.62 MPa; this was considered to be the maximum operating pressure of the closed cylindrical vessel. Because of the limitation of the operating pressure, the cylindrical vessel with sight gages and the spherical vessel were not used in this study. In addition, only the Kidde-Graviner valve was used due to the fact that the final attainable pressure at the elevated temperature was above the operating pressure of the Marotta and HTL solenoid valves. Note that, since no shaking or agitating of the vessel was performed during the cooling or heating process, the

liquid and gas phases might not be in equilibrium before discharge. This condition is similar to that of an actual fire extinguishing vessel in which no mixing mechanism to maintain equilibrium between the liquid and vapor phases exists at cold or hot ambience.

The study of the effect of orientation on the discharge dynamics was conducted at room temperature with a nitrogen charge pressure of ~ 4.12 MPa by using the spherical vessel and varying the discharge direction from vertically downward (standard discharge) to vertically upward, horizontal, and downward with an angle of 30° or 45° with the vertical. The spherical vessel was chosen because it was lightweight and easy to mount. Only HFC-125 was used in this parametric study.

In order to shed some light on the effect of the degree of nitrogen saturation on the discharge process, a limited set of experiments was performed by partially saturating the liquid agent with nitrogen. Partial saturation was achieved by simply bubbling nitrogen through the liquid agent to a specified pressure without attaining the final equilibrium pressure and without agitating the vessel. In other words, if one were to agitate the vessel, an equilibrium pressure lower than the specified pressure would be obtained because more nitrogen would be dissolved in the liquid agent.

8.4.3 Results and Discussion

8.4.3.1 General Visual Observations. The events occurring *inside* the vessel during a discharge of CF_3Br were *conceptually* described by Elliot *et al.* (1984) without any confirmation from visual observations. Based on the experimental pressure decay curves during discharge and a simple theoretical flow model, he suggested that there were several sequential events occurring inside the vessel. When the release mechanism was activated, there was a short duration during which the pressure continuously decreased, and the liquid agent/nitrogen mixture was expelled as a superheated liquid through the valve exit. Nitrogen remained dissolved in the liquid agent as a non-equilibrium supersaturated solution, and the liquid/nitrogen mixture remained a clear solution. As the pressure inside the vessel dropped further, degassing of nitrogen in the solution occurred, and nitrogen bubbles started to form. Once the bubbles nucleated, the dissolved nitrogen quickly came out of the solution into the bubbles causing the bubbles to grow. Due to rapid bubble expansion, the liquid level swelled, and the ullage was compressed to a higher pressure which was noted as a short transient pressure recovery in the pressure decay history. The pressure then began to decrease again until an inflection point in the pressure decay curve was reached. A low quality (defined as the fraction of the mass flow rate which is gas) bubbly two-phase CF_3Br /nitrogen mixture was assumed to be discharged from the vessel during this time interval. The inflection point signified the depletion of the low quality two-phase mixture and the initiation of the discharge of the ullage gas mixture (CF_3Br vapor and nitrogen) from the vessel. The rate of pressure decay increased because the gas mixture was less dense than the low quality bubbly two-phase mixture and experienced a higher volumetric discharge rate.

The visual observations made in this study by using the cylindrical vessel with sight gages and high-speed photography revealed the following phenomena which were slightly different from the description given by Elliot *et al.* (1984). For CF_3Br , HFC-125, and FC-218, the liquid agent/nitrogen mixture remained clear for a short duration (~ 5 ms) after the initiation of the discharge. This duration was found to be agent dependent, with CF_3Br the shortest and FC-218 the longest. During this period, the receding liquid/vapor interface was clearly visible. The interior of the vessel as seen through the sight gages then became completely foggy, and the liquid/vapor interface was no longer visible. It was not possible to determine from the movies whether the fogginess prevented the observation of the liquid/vapor interface or the degassing of the dissolved nitrogen induced frothing of the liquid mixture throughout the vessel, thus causing the liquid/vapor interface to disappear. The fogginess was sustained for a period of time during which the liquid mixture was assumed to be completely

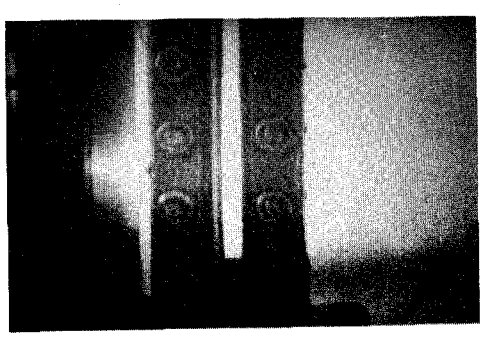
discharged. The sight gages on the vessel then became clear once again. This fogginess is *conjectured* to be due both to vapor condensation as a result of cooling by the adiabatic expansion of the ullage vapor, and the evolution of the dissolved nitrogen as bubbles in the liquid mixture. The existence of the nitrogen bubbles could not be visually confirmed from the high speed movies due to the limited spatial resolution of the pictures. For CF_3I , the receding liquid/vapor interface and the liquid mixture remained clear for a relatively long time (at least half of the liquid had been depleted) after the initiation of the discharge. The fogginess then appeared throughout the vessel, and the liquid/vapor interface vanished. The interior of the vessel became clear again after a period of fogginess. It was postulated that nitrogen degassing did not occur in the CF_3I /nitrogen mixture (see discussion in Section 8.4.3.2). Selected photographic sequences of events for CF_3Br , HFC-125, FC-218, and CF_3I are given in Figures 11, 12, 13, and 14 respectively.

The flashing behavior of CF_3Br external to the vessel was also noted by Elliot *et al.* (1984). They reported that to the eye the discharge was a puff of white vapor. Their high speed movies showed an opaque white plume that steadily diminished in size but did not change in density. The appearance of the plume did not seem to change, with either front lighting or back lighting, even when the vapor mixture discharge began because a white cloud continued to form due to vapor condensation. The observations obtained in the current study were very similar to those made by Elliot *et al.* (1984) although the visualization of the process using the naked eye was almost impossible because the discharge time was much shorter in this work. Due to the difficulty in discerning the transition from the liquid discharge to the remaining vapor discharge from the appearance of the spray at the valve exit, the time for the depletion of the liquid from the vessel could not be determined with great certainty from the high-speed movies. In addition, even when the vessel with sight gages was used, the fact that the liquid/vapor interface inside the vessel was not visible during the course of the discharge also hindered the determination of the liquid depletion time. Figures 15, 16, 17, and 18, respectively, show individual photographic shots taken at the same instant (5 ms after the first appearance of the spray at the valve exit) during discharges of CF_3Br , HFC-125, FC-218, and CF_3I from the cylindrical vessel equipped with a Marotta solenoid valve. When other release mechanisms were used, the general appearances of the flashing sprays (other than the spray angles) were also observed to be very similar to Figures 15 to 18.

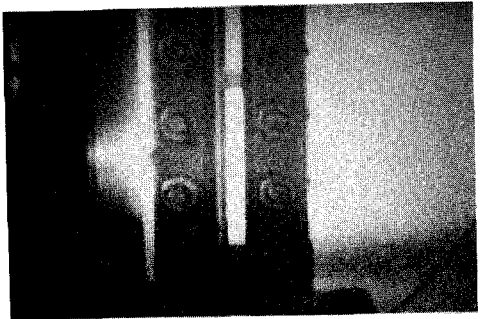
8.4.3.2 Marotta Solenoid Valve. This subsection discusses the experimental results obtained using a Marotta solenoid valve. Figure 19 through Figure 22 show respectively the pressure decay curves obtained inside the vessel during *standard* discharges of CF_3Br , HFC-125, FC-218, and CF_3I . Pressures reported in the figures are gauge pressures. The pressure is nondimensionalized by the initial pressure (P_i) in the vessel before the initiation of a discharge. The time $t = 0$ s is defined as the time when the solenoid valve is first opened partially. This time, with an estimated uncertainty of 0.08 ms, is inferred from the instant when the initial vessel pressure starts to decrease by 34 kPa and continues to decrease. Note that the baseline fluctuation of the initial vessel pressure is less than 34 kPa peak-to-peak.

For the CF_3Br (Figure 19) standard discharges, the pressure decay curves show four regions as suggested by Elliot *et al.* (1984). The first corresponds to the discharge of metastable liquid agent/dissolved nitrogen mixture, followed by a sudden pressure recovery which presumably implies the degassing of nitrogen from the liquid mixture. The third region corresponds to the discharge of a low quality two-phase bubbly mixture, and the last region signifies the discharge of the remaining vapor mixture from the vessel. In Figure 19, the transition from the third to the fourth region in one case ($P_i = 4.05$ MPa) is not very distinct.

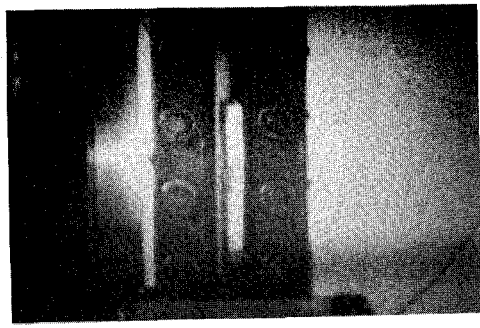
For the HFC-125 and FC-218 tests, the aforementioned four regions are clearly shown in Figures 20 and 21 respectively. However, it is unclear, at present, why the rate of pressure decay in



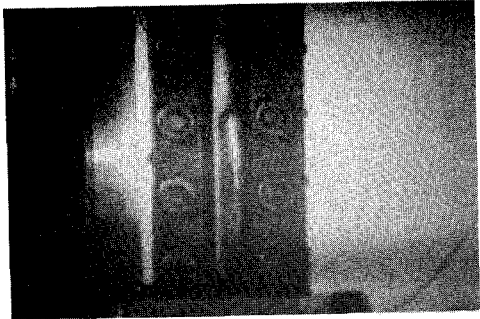
$t = 0$ ms



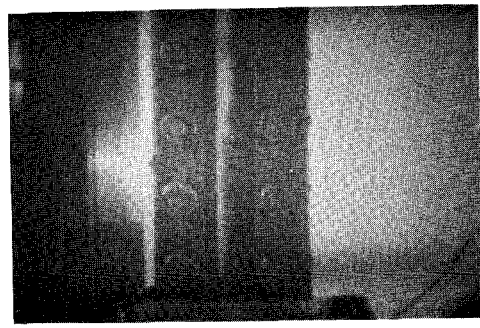
$t = 1.5$ ms



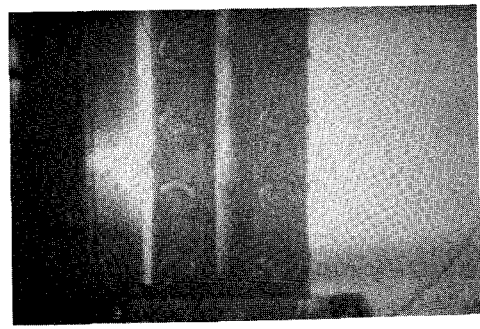
$t = 2.5$ ms



$t = 3.5$ ms



$t = 5.0$ ms



$t = 7.5$ ms

Figure 11. Photographic sequence of events as seen through the sight gages of the cylindrical vessel during a discharge of CF_3Br .

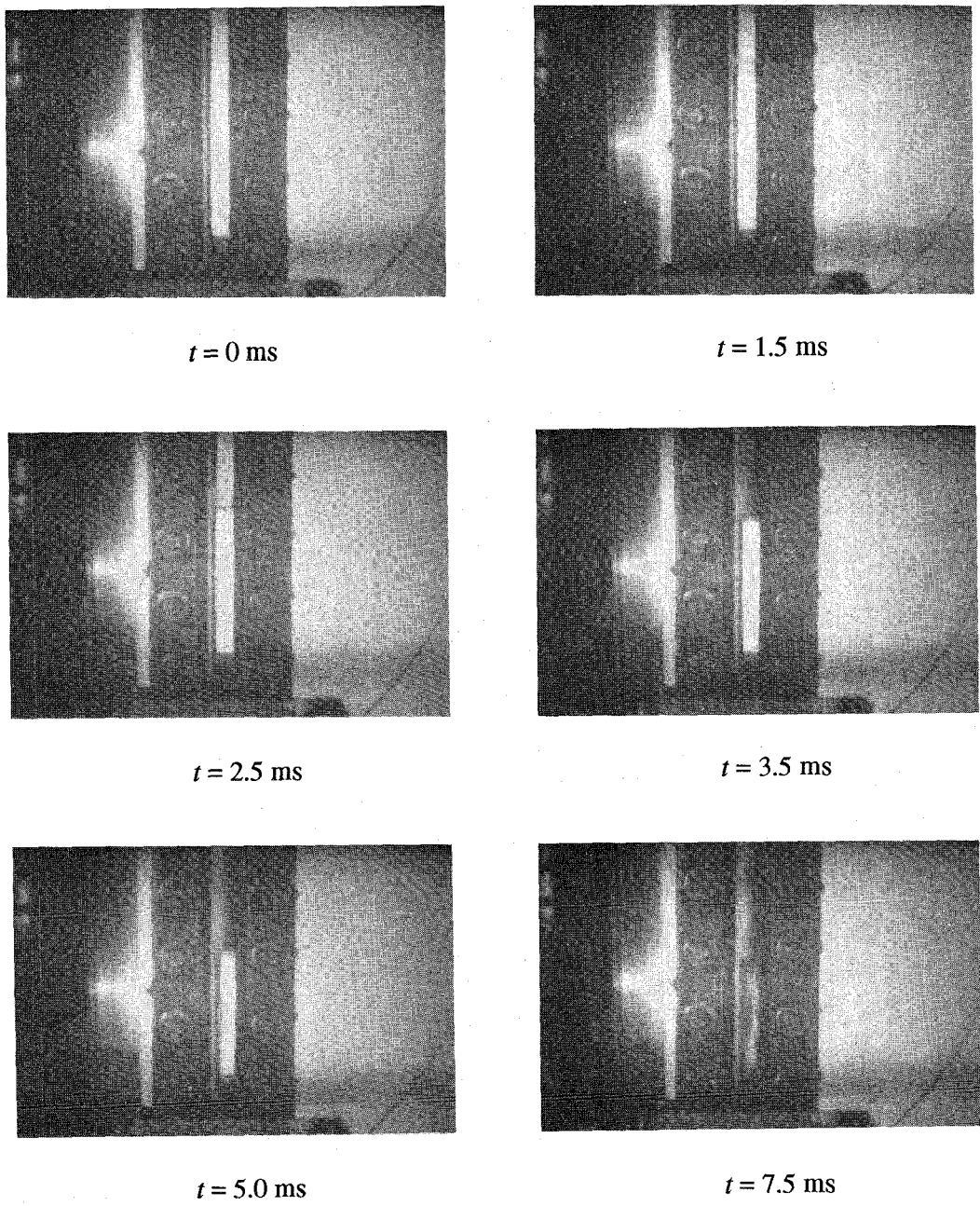
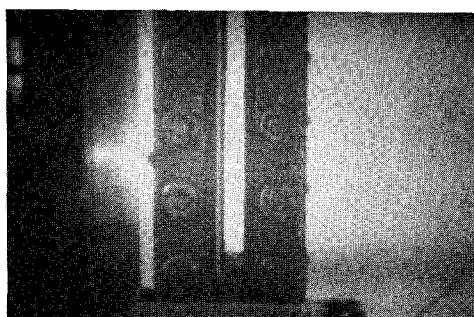
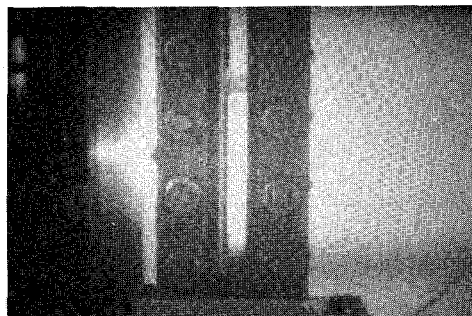


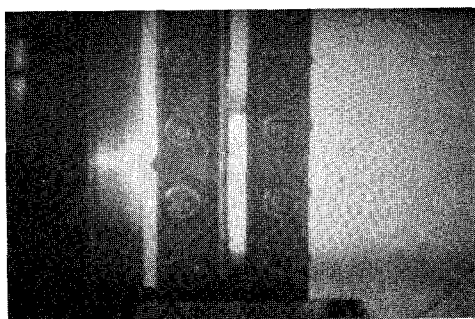
Figure 12. Photographic sequence of events as seen through the sight gages of the cylindrical vessel during a discharge of HFC-125.



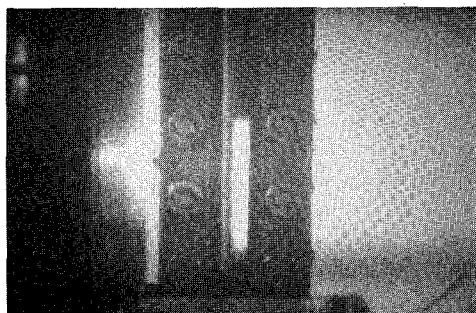
$t = 0 \text{ ms}$



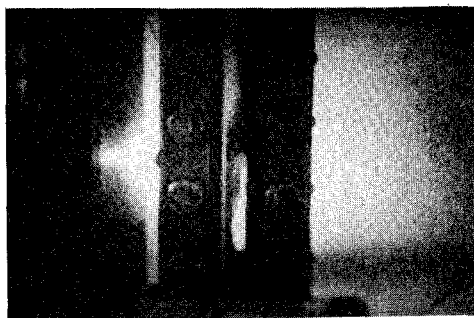
$t = 1.5 \text{ ms}$



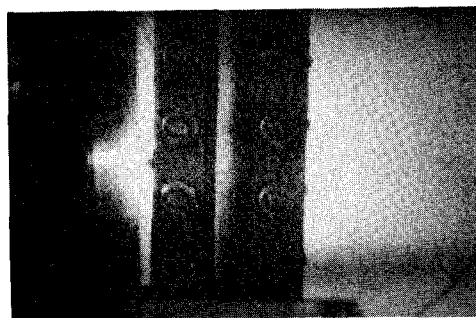
$t = 2.5 \text{ ms}$



$t = 3.5 \text{ ms}$

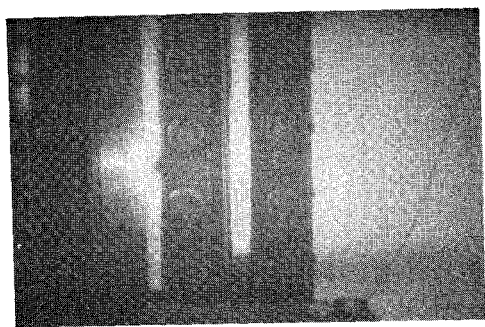


$t = 5.0 \text{ ms}$

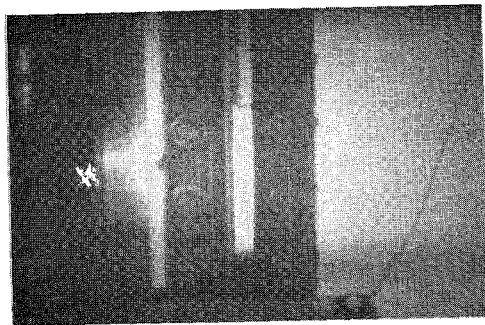


$t = 7.5 \text{ ms}$

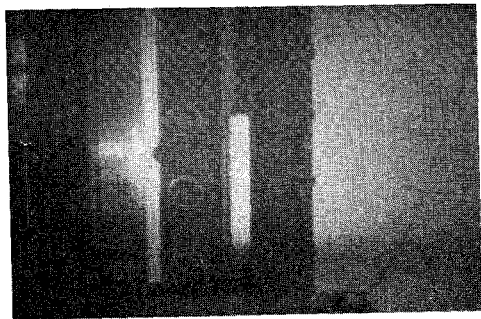
Figure 13. Photographic sequence of events as seen through the sight gages of the cylindrical vessel during a discharge of FC-218.



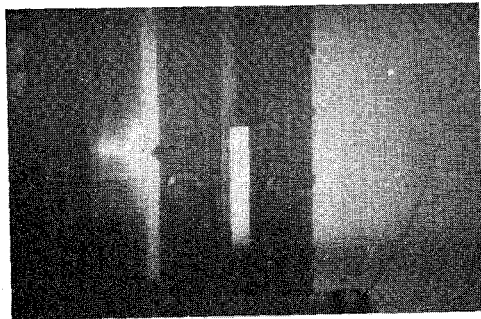
$t = 0 \text{ ms}$



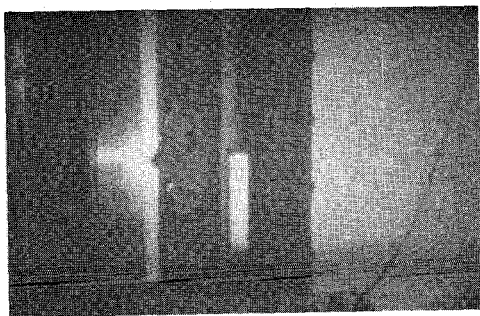
$t = 1.5 \text{ ms}$



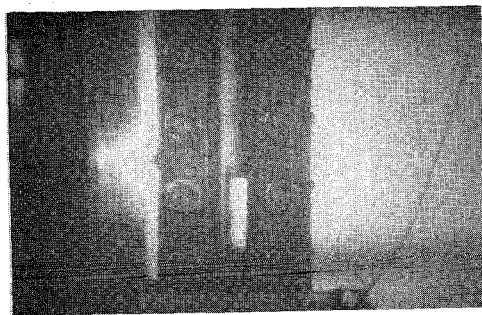
$t = 2.5 \text{ ms}$



$t = 3.5 \text{ ms}$



$t = 5.0 \text{ ms}$



$t = 7.5 \text{ ms}$

Figure 14. Photographic sequence of events as seen through the sight gages of the cylindrical vessel during a discharge of CF_3I .

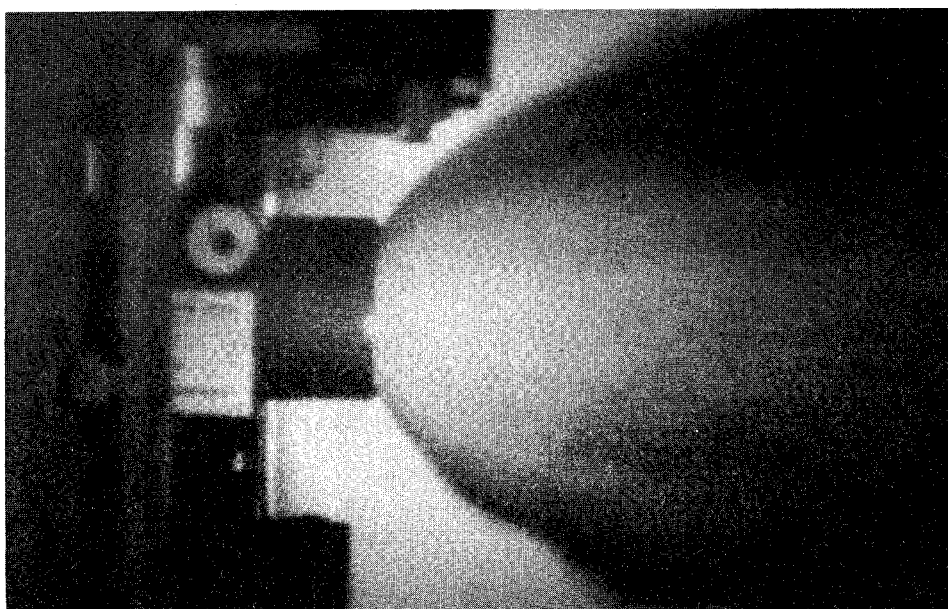


Figure 15. A snapshot of CF_3Br discharge (taken 5 ms after the first appearance of the spray at the valve exit).

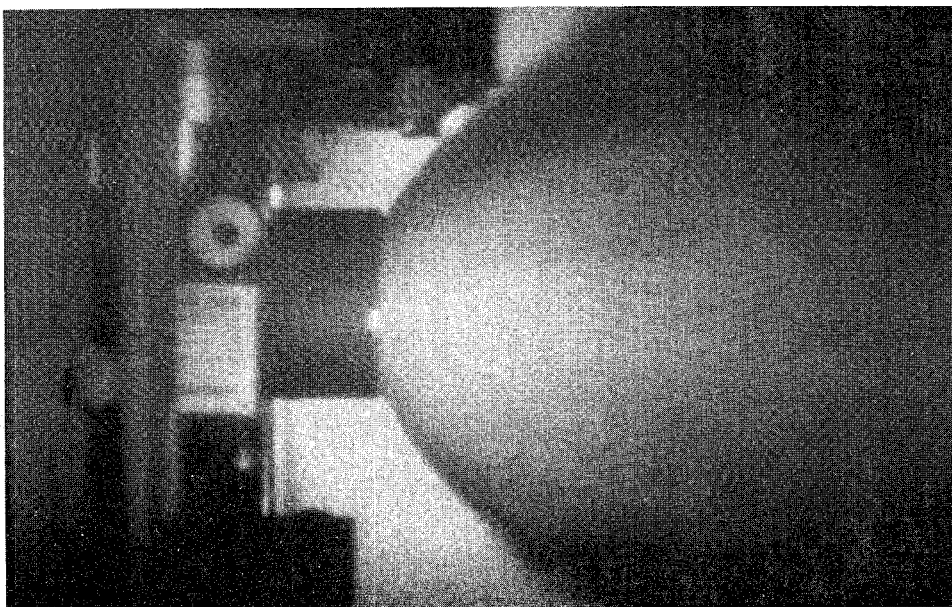


Figure 16. A snapshot of HFC-125 discharge (taken 5 ms after the first appearance of the spray at the valve exit).

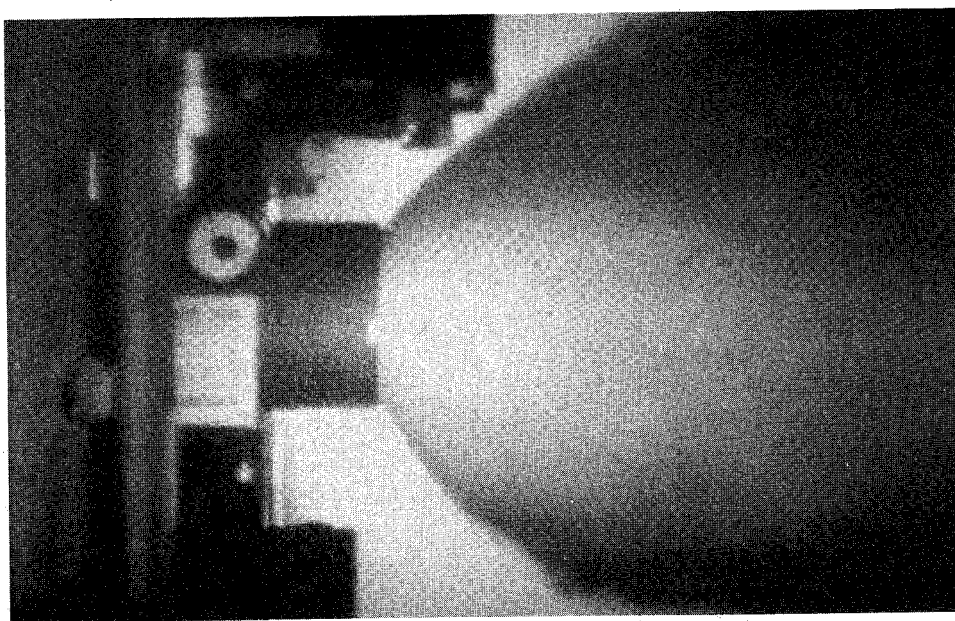


Figure 17. A snapshot of FC-218 discharge (taken 5 ms after the first appearance of the spray at the valve exit).

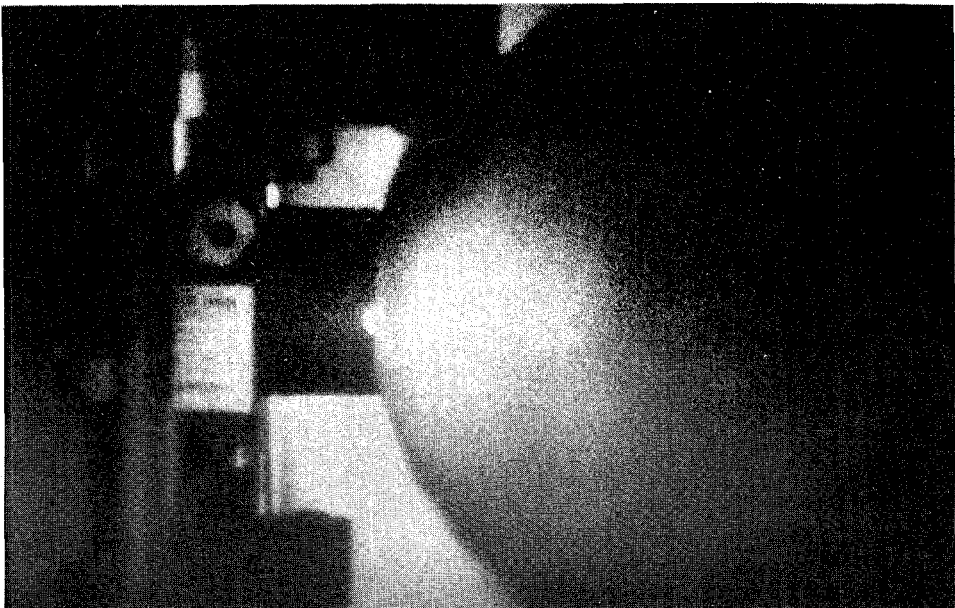


Figure 18. A snapshot of CF₃I discharge (taken 5 ms after the first appearance of the spray at the valve exit).

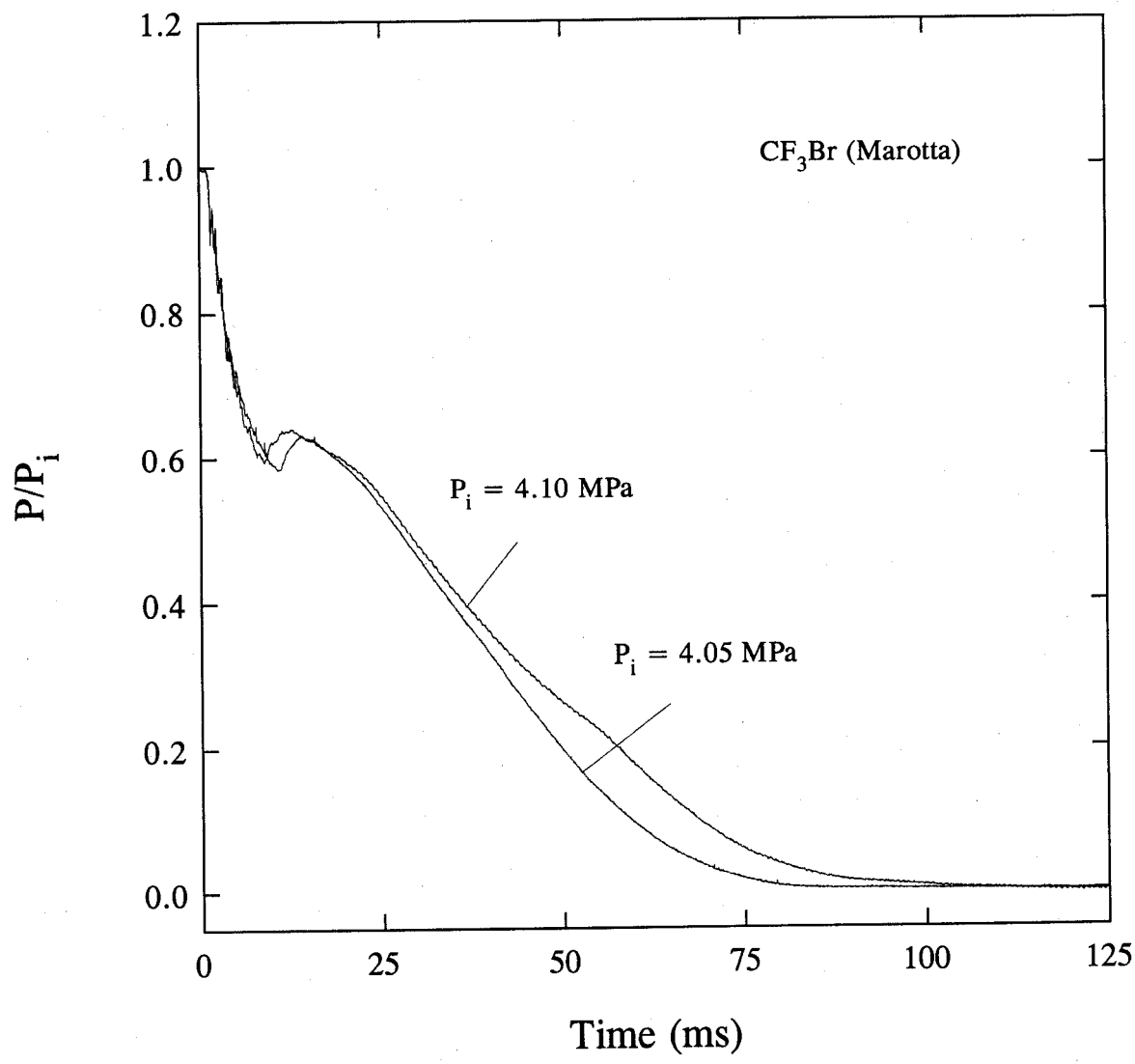


Figure 19. Pressure decay curves during standard discharges of CF_3Br using a Marotta valve.

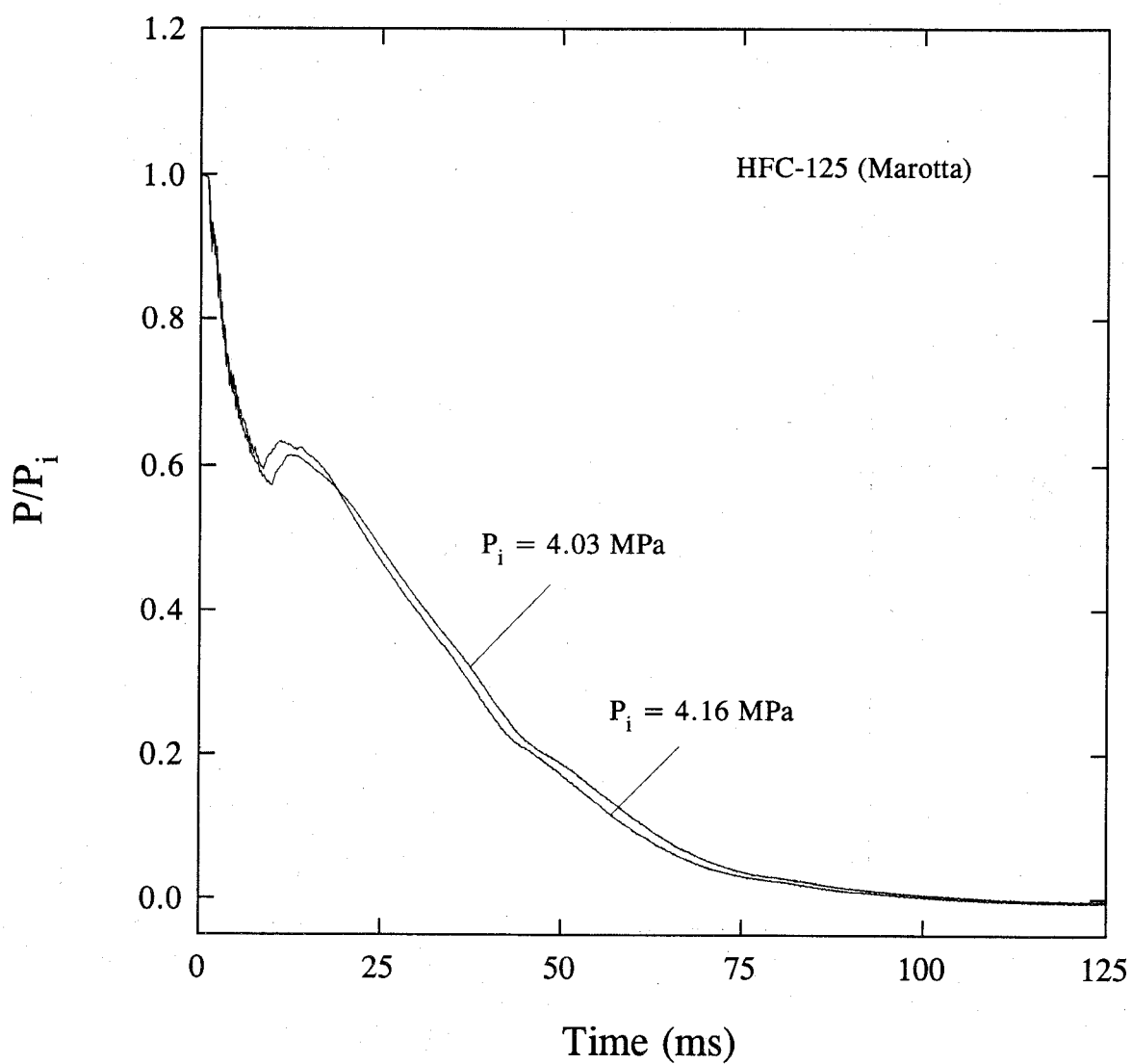


Figure 20. Pressure decay curves during standard discharges of HFC-125 using a Marotta valve.

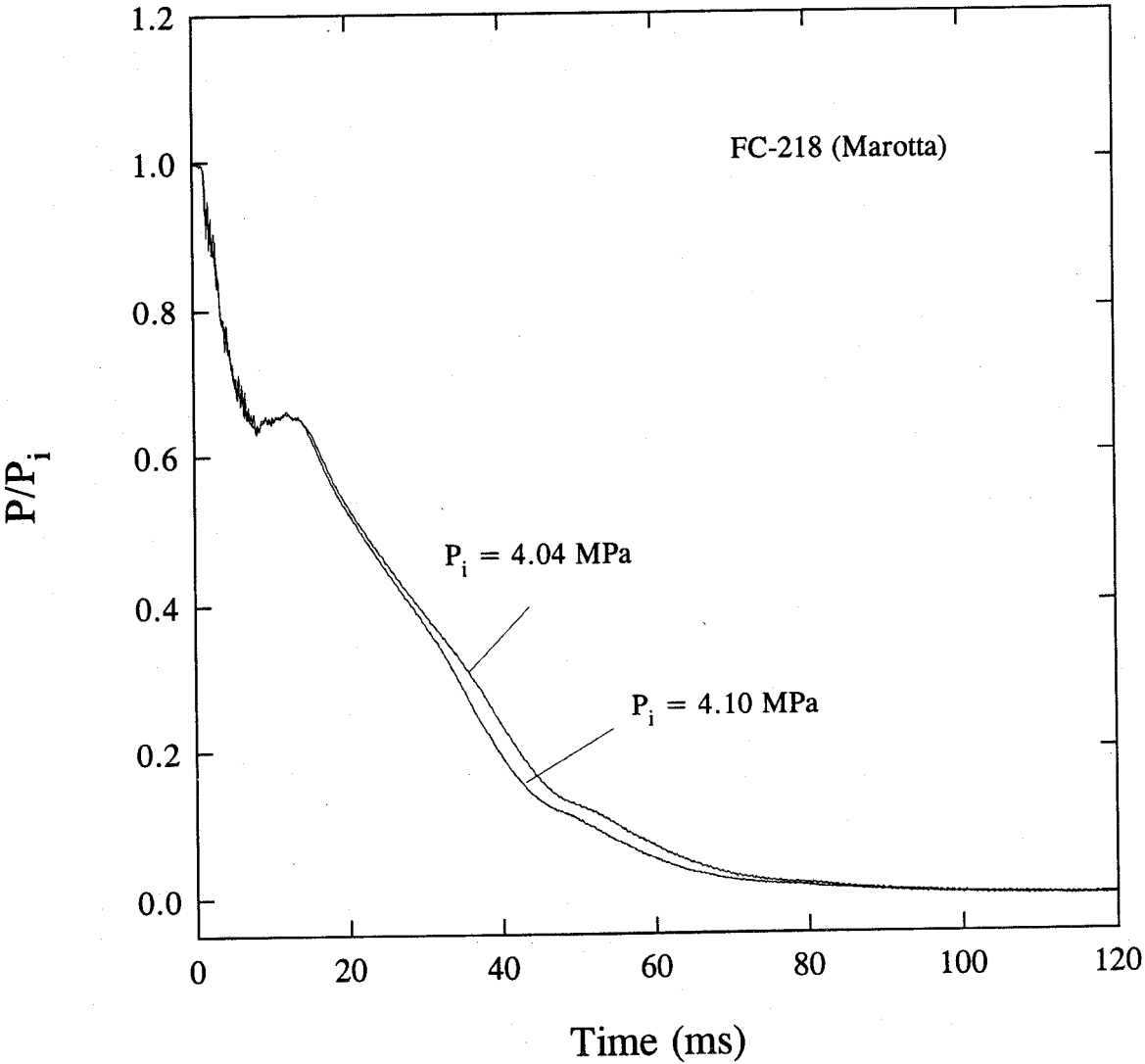


Figure 21. Pressure decay curves during standard discharges of FC-218 using a Marotta valve.

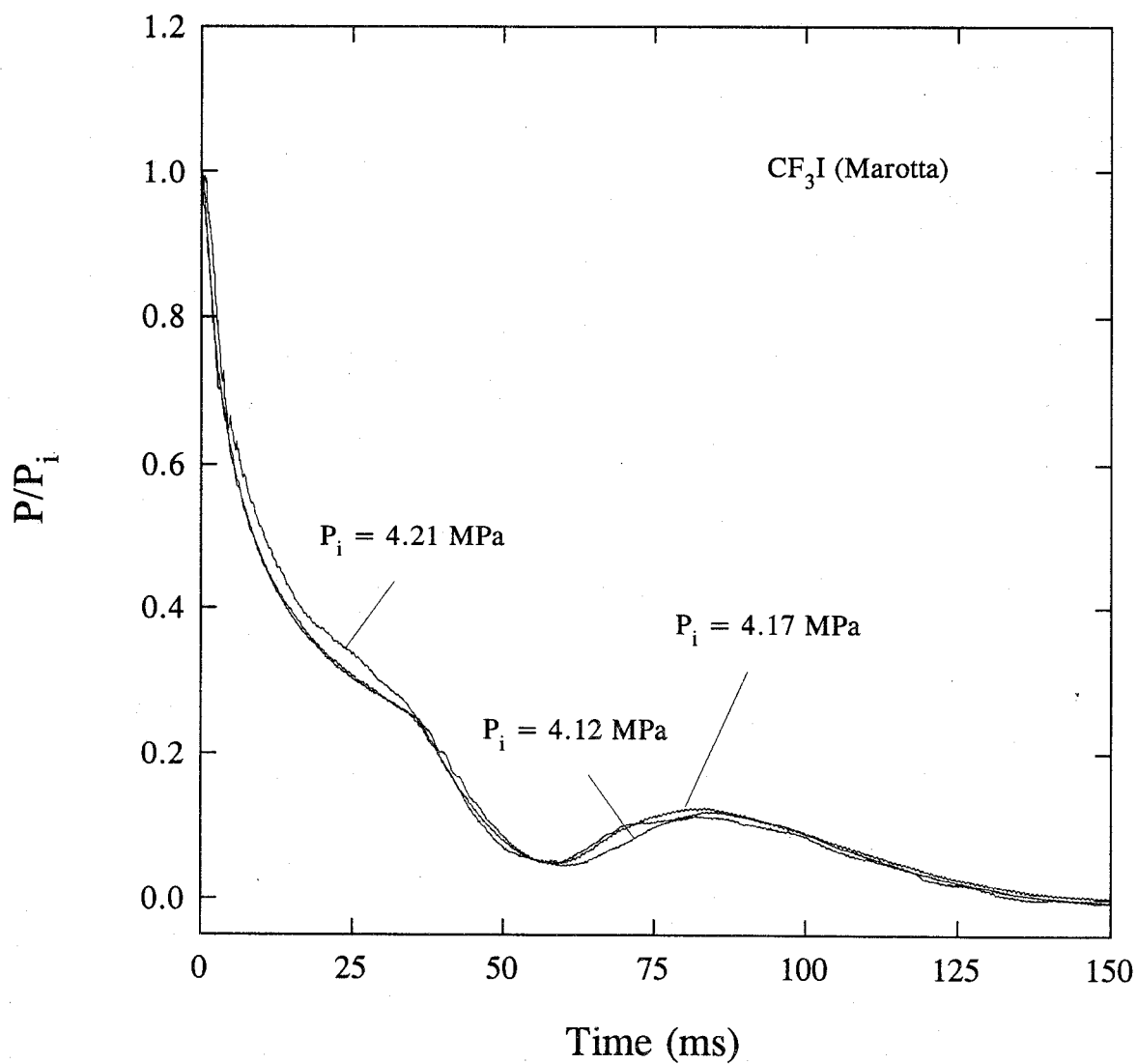


Figure 22. Pressure decay curves during standard discharges of CF_3I using a Marotta valve.

the fourth region is slower than that in the third region, which is opposite to the trend observed in the CF_3Br tests.

For the CF_3I experiments, the pressure recovery before the third region is not noted in Figure 22. In addition, there is a pressure recovery in the fourth region. This pressure recovery was subsequently found to be caused by some artifact from the dynamic pressure transducer. This is substantiated by Figure 23 which compares the two pressure decay curves obtained using two different pressure transducers, one static and one dynamic, in the same test. Note that this pressure recovery artifact was only observed in the CF_3I tests.

If the pressure recovery is assumed to be related to the degassing of the dissolved nitrogen in the liquid agent and if the degassing process can presumably be explained in terms of homogeneous nucleation theory and can be modeled by an isothermal decompression process, then the homogeneous nucleation pressure, according to the work by Forest and Ward (1977), should depend on the initial pressure, the surface tension of the liquid mixture, and the vapor pressure of the agent and the solubility of nitrogen in the liquid agent at the temperature of interest. The homogeneous nucleation pressure, which is the pressure at which homogeneous nucleation occurs, can be estimated by the following set of equations whose derivations were given in detail by Forest and Ward (1977). To simplify the analysis, it is further assumed that the effect of pressure and concentration of the dissolved nitrogen on the vapor pressure of the liquid is negligible and that the gas mixture inside the bubble is ideal. It is expected that under the experimental conditions used in this study, a very good estimate of the homogeneous nucleation pressure can be obtained by invoking the above assumptions and without resorting to the detailed calculations. The homogeneous nucleation pressure (P_h) is given by

$$P_h = P_{sat} + \frac{CP_h}{C_s} - \left[\frac{16\pi\sigma^3}{3kT\ln(Z/J)} \right]^{1/2} \quad (19)$$

with

$$\ln \left[\frac{f_n^o(1 + C_s)}{C_s} \right] = \ln H + \frac{v_n P_h}{RT} \quad (20)$$

and

$$f_n^o = P_h \exp \left(\frac{P_h B_{nn}}{RT} \right) \quad (21)$$

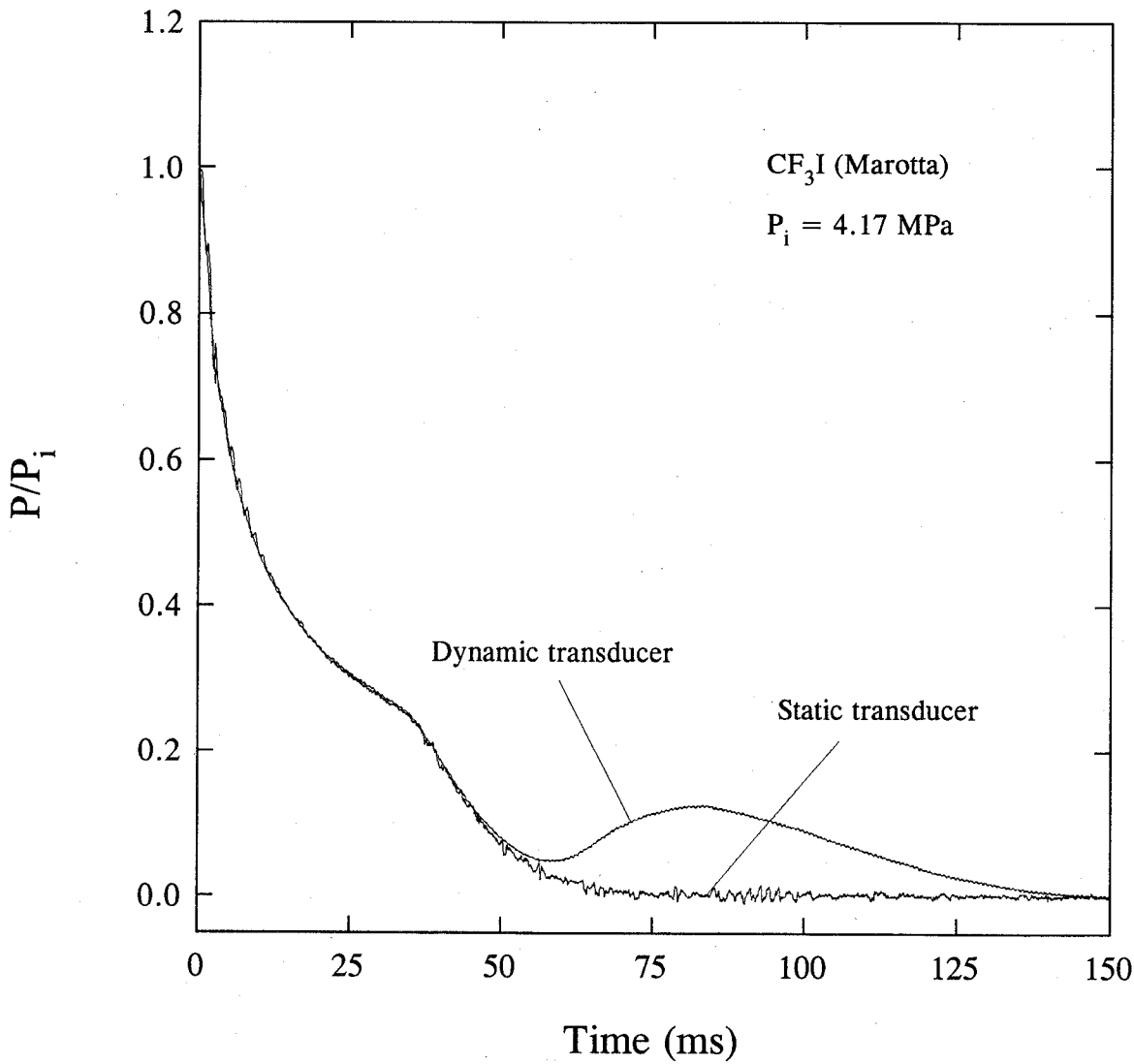


Figure 23. Comparison of the pressure decay curve obtained by a dynamic pressure transducer with that obtained by a static pressure transducer.

where P_{sat} is the vapor pressure of the agent at temperature T , C is the ratio of moles of nitrogen dissolved to moles of liquid agent, C_s is the concentration of nitrogen which would be present in the liquid agent if the pressure of the gas above the liquid were at the total pressure P_h , σ is the surface tension, Z ($\text{cm}^{-3} \text{s}^{-1}$) is the rate constant, J ($\text{nuclei s}^{-1} \text{cm}^{-3}$) is the nucleation rate per volume, k is the Boltzmann constant ($= 1.38048 \times 10^{-16} \text{ dyne cm K}^{-1}$), f_n^o is the fugacity of the pure gas, H is the Henry's constant, v_n is the partial molar volume of the dissolved nitrogen, B_{nn} is the second virial coefficient, and R is the universal gas constant.

The mole ratio C can be determined from the solubility (mole fraction) of nitrogen in the liquid agent at T and P_i by the following equation:

$$C = \frac{x_n}{1 - x_n} \quad (22)$$

where x_n is the solubility of nitrogen and can be calculated using the vapor-liquid equilibrium computer code (PROFISSY).

Following the procedure outlined in Forest and Ward (1977), Henry's constant H can be estimated using Equation (19) without the last term and Equations (20) and (21), with P_h replaced by P_i in all three equations.

The surface tension for pure agent was estimated by the method of Brock and Bird (Reid *et al.*, 1987); the effect of the dissolved nitrogen on the surface tension was assumed to be negligible. The vapor pressure was estimated by the method proposed by Gomez-Nieto and Thodos (Reid *et al.*, 1987). The partial molar volume of the dissolved nitrogen was calculated using the method in Chueh and Prausnitz (1967). The second virial coefficient B_{nn} was obtained from the tabulation in Dymond and Smith (1969). For all the agents used in this study, the rate constant Z was estimated by the method described in Volmer (1945) and found to be on the order of $10^{32} \text{ cm}^{-3} \text{s}^{-1}$. For the nucleation rate J , a value of $10^4 \text{ nuclei s}^{-1} \text{cm}^{-3}$ was used. The value of the pressure determined was found to be very insensitive to the value of J chosen because J is in the logarithmic term in Equation (19). The determination of P_h requires an iteration procedure because of the nonlinear nature of Equation (19). The Newton-Raphson numerical scheme (Carnahan *et al.*, 1969) was used to obtain P_h . The initial pressure P_i was used as an initial guess for P_h in the iteration. Table 17 shows the calculated results based on the experimental conditions used to obtain Figures 19 to 22. The calculated homogeneous nucleation pressures for CF_3I /nitrogen mixtures were found to be negative (*i.e.*, in tension); negative homogeneous nucleation pressures are possible according to Reid (1976) although at present no experimental data on CF_3I /nitrogen mixtures are available to substantiate the predictions.

The pressure ratio (P/P_i) at which the degassing of nitrogen initiates or not can now be qualitatively explained in terms of the aforementioned, simplified homogeneous nucleation theory. Based on the calculated homogeneous nucleation pressures in Table 17, the degassing of nitrogen from CF_3I /nitrogen liquid mixtures, which was not observed experimentally as shown in Figure 22, was predicted not to occur under the same experimental conditions. No attempt was made to compare quantitatively the calculated homogeneous nucleation pressures to the experimental degassing pressures because of the uncertainties associated with the thermophysical property predictions used in the calculations. It should be noted that although homogeneous nucleation theory appears to provide some qualitative explanations with regard to the degassing process, heterogeneous bubble nucleation (a more complicated process) from the nucleation sites on the vessel wall could also play a role. However, it can be argued that the ease with which the agents wet the inner surface of the container due to their small contact angles (low surface tensions) during vessel filling favors homogeneous nucleation

Table 17. Calculated homogeneous nucleation pressure (P_h) at T

Agent	Mass (g)	T (K)	P_i (MPa)	P_h (MPa)	P_h/P_i
CF ₃ Br	591	295	4.10	1.90	0.46
CF ₃ Br	564	295	4.05	1.85	0.46
HFC-125	438	294	4.03	1.63	0.41
HFC-125	428	294	4.16	1.76	0.42
FC-218	450	295	4.04	2.12	0.53
FC-218	435	294	4.10	2.11	0.52
CF ₃ I	723	294	4.12	---	---
CF ₃ I	719	294	4.21	---	---
CF ₃ I	755	294	4.17	---	---

because less effective vapor trapping in the irregular cavities on the imperfect container wall surface will be expected (Carey, 1992).

A comparison of the pressure decay curves for all the agents is made in Figure 24. It is clear that different agents exhibit different discharge rate and degassing characteristics. Based on the pressure decay curves, CF₃I discharges the fastest and CF₃Br the slowest under similar initial conditions. These observations were also confirmed qualitatively by the high-speed movies.

The average dispersion velocities of the spray obtained by the laser attenuation technique are summarized in Figure 25. The dispersion of CF₃I has the slowest average downstream velocities. All the other agents have similar but higher spray dispersion velocities than CF₃I.

The measurements from the downstream dynamic pressure transducer can be used to provide a qualitative description of the two-phase behavior of the spray downstream. According to Whalley (1990), if the two-phase flow is assumed to be homogeneous, then the momentum flux M , which in this case is the measured dynamic pressure, is given by

$$M = \frac{G^2}{\rho_h} = \rho_h u^2 \quad (23)$$

with

$$\rho_h = \alpha \rho_g + (1 - \alpha) \rho_l \quad (24)$$

where G is the mass flux, u is the average velocity, α is the void fraction, ρ_h is the homogeneous mixture density, and ρ_g and ρ_l are the saturated vapor and liquid densities. The void fraction is defined

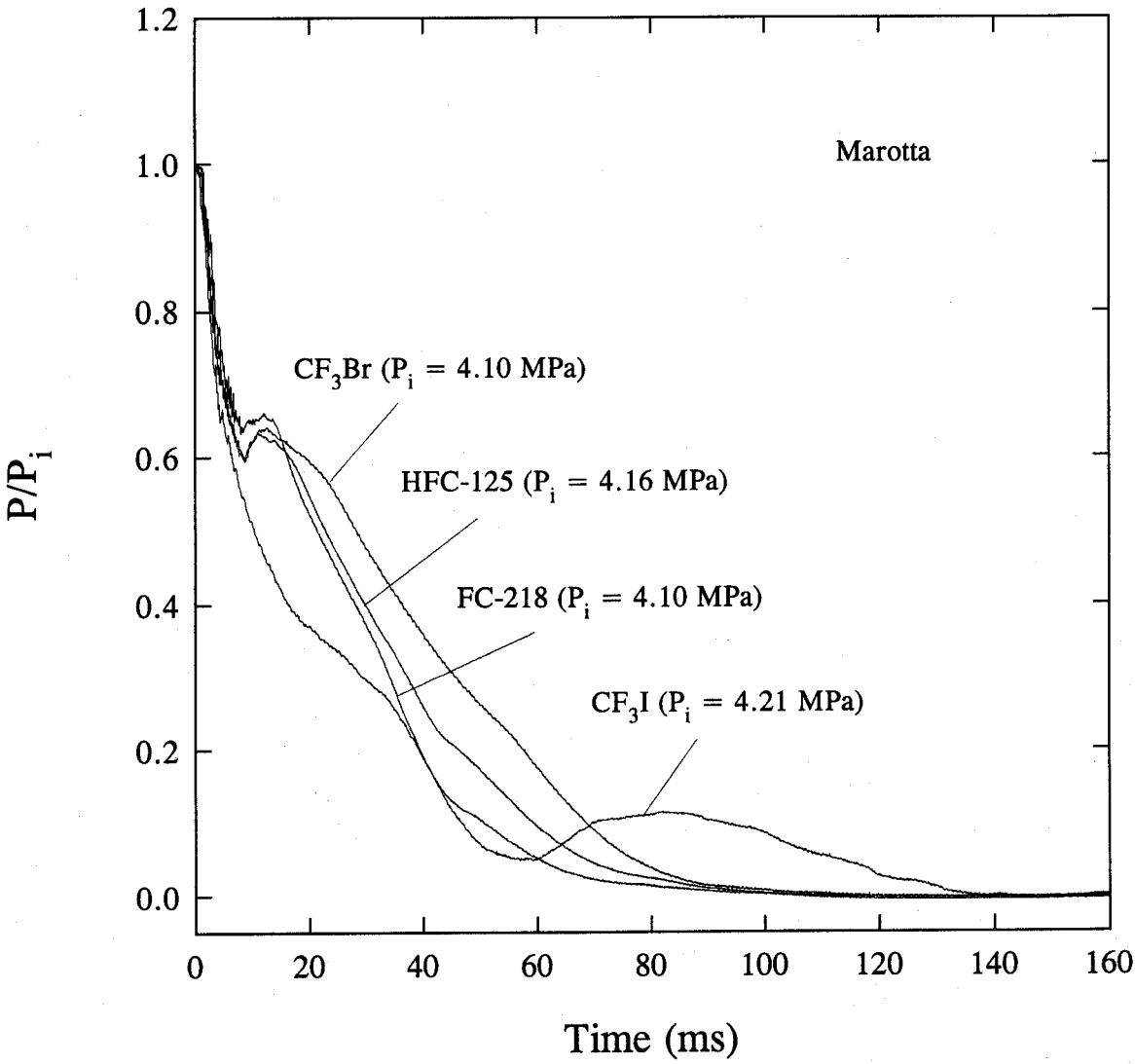


Figure 24. Comparison of pressure decay curves during standard discharges using a Marotta valve.

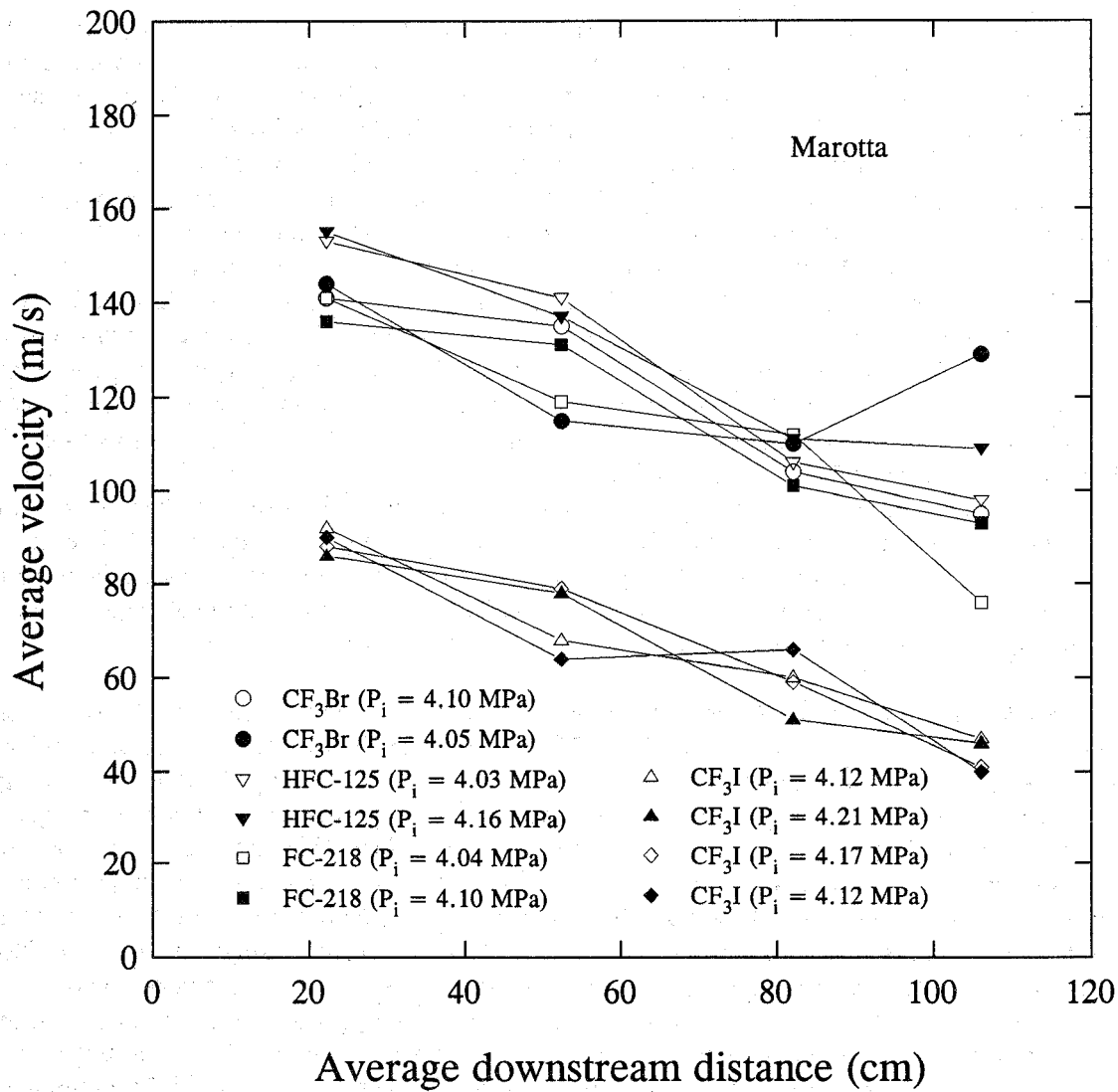


Figure 25. Average downstream velocities during standard discharges using a Marotta valve.

as the average fraction of the volume which is occupied by the gas phase. Using Equations (23) and (24), one can solve for α ,

$$\alpha = \frac{\left(\rho_l - \frac{M}{u^2} \right)}{\rho_l - \rho_g} \quad (25)$$

Since M and u were measured in the experiments, an estimate of α could be made. Table 18 summarizes the calculated results. The saturated vapor and liquid densities were assumed to be those of the pure agents at their normal boiling points. For CF₃Br, HFC-125, and FC-218, the saturated densities were obtained from the REFPROP database (Gallagher *et al.*, 1993). For CF₃I, the saturated liquid density was estimated using the modified Rackett method described in Reid *et al.* (1987), and the vapor density was calculated by assuming the vapor was ideal. The average velocities u were obtained by taking the ratio of the distance between the transducer and the valve exit to the time when the spray hit the transducer. The dynamic pressures (M) used in the calculations corresponded to the maximum pressures recorded in the experiments. Among all the agents, CF₃I has the lowest estimated void fraction, which implies that a fair amount of CF₃I has not been evaporated at this downstream location. The low Jakob number (see Grosshandler *et al.*, 1994) of CF₃I and its high normal boiling point also provide some qualitative support of the calculated low void fraction. Since the other three agents have higher Jakob numbers and lower boiling points than CF₃I, it is not surprising to find higher calculated void fractions for all three agents.

The maximum angles sustained by the sprays at the valve exit during discharges were also measured and are tabulated in Table 18. Note that the spray angle is a function of time during discharge. Since it was very difficult to define clearly the boundaries of the sprays because of their flashing characteristics, an uncertainty of 4° was typical. Compared to the other agents, the maximum spray angles in the selected CF₃I tests were found to be the largest.

8.4.3.3 HTL Solenoid Valve. For comparison purposes, selected pressure decay curves obtained during standard discharges of CF₃Br, HFC-125, FC-218, and CF₃I using the HTL solenoid valve are shown in Figure 26. The initial, relatively flat plateaus in the figure suggest that the opening times of the solenoid valve are slow and differ, depending on which agent is used. However, no general trends were observed when all of the experimental data were examined although Figure 26 shows the opening time of the valve for CF₃I is the slowest. The initial, slow, and *continuous* decrease in pressure could not be attributed to the drift of the baseline initial pressure P_i before the opening of the valve because the baseline value for P_i remained relatively constant except for some small fluctuations. Note that such initial slow pressure decays were not observed in all the tests using a Marotta valve.

Similar to the CF₃I discharges using a Marotta valve, the pressure recovery artifact in the CF₃I pressure trace caused by the dynamic transducer is also noted in Figure 26, and no degassing of CF₃I is suggested. If the opening time of the valve were to be ignored, CF₃I would discharge the fastest, and CF₃Br the slowest under similar initial conditions.

Figure 27 summarizes the average downstream dispersion velocities of the sprays for all the agents. Similar to the observations made using a Marotta valve, the dispersion of CF₃I exhibits the slowest downstream velocities. All the other agents have similar but higher spray dispersion velocities than CF₃I.

Table 18. Calculated void fractions and measured maximum spray angles (standard discharges using a Marotta valve)

Agent	Mass (g)	u (m/s)	M_{max} (MPa)	α	Maximum spray angle
CF ₃ Br	591	103	0.30	0.99	100°
CF ₃ Br	564	---	---	---	---
HFC-125	438	114	0.84	0.96	110°
HFC-125	428	104	0.41	0.98	---
FC-218	450	102	0.43	0.98	108°
FC-218	435	94	0.25	0.99	---
CF ₃ I	723	64	1.58	0.84	142°
CF ₃ I	719	64	1.65	0.83	141°
CF ₃ I	755	61	1.68	0.81	---

* not recorded

Table 19 tabulates the calculated void fractions at the location of the downstream dynamic pressure transducer. Similar to the results for the Marotta valve, the void fraction for CF₃I is estimated to be the smallest, whereas all the other agents show comparable and higher void fraction values. The measured maximum spray angles are also summarized in Table 19. The CF₃I spray angles still appear to be the largest.

8.4.3.4 Kidde-Graviner Valve The results of the standard discharges of all the agents for this valve are shown in Figure 28. The pressure recovery artifact occurring close to the end of the discharge in the CF₃I measurements is again noted in the figure. According to the pressure decay curves, the discharge rate of CF₃I is the fastest and CF₃Br the slowest. The pressure trace also suggests that the degassing of dissolved nitrogen does not occur in the CF₃I test, consistent with the prediction using the homogeneous nucleation theory (see Table 17). For the other three agents, the pressure recoveries due to the degassing of dissolved nitrogen are not very pronounced, that is the pressures do not rebound significantly. Since this valve has a bigger opening, one possible explanation for these flat pressure plateaus is that the rate of the ullage compression due to the degassing is offset by the rate of ullage expansion resulting from the faster liquid discharge.

The average downstream dispersion velocities are summarized in Figure 29. Once again, the dispersion velocities of CF₃I are the slowest among the other three agents. The high temperature results in the figure will be discussed later in Section 8.4.3.9.

The calculated void fractions at the location of the downstream pressure transducer, together with the measured maximum spray angles, are tabulated in Table 20. Care should be exercised in interpreting the calculated void fraction for HFC-125 because the unusual high M , which results in a low void fraction, could have been caused by the accidental impact of the flying debris (from the actuation of the pyrotechnic piston) on the pressure transducer; the debris was frequently observed coming from the valve exit in the high-speed movies. Excluding the result of HFC-125, CF₃I again

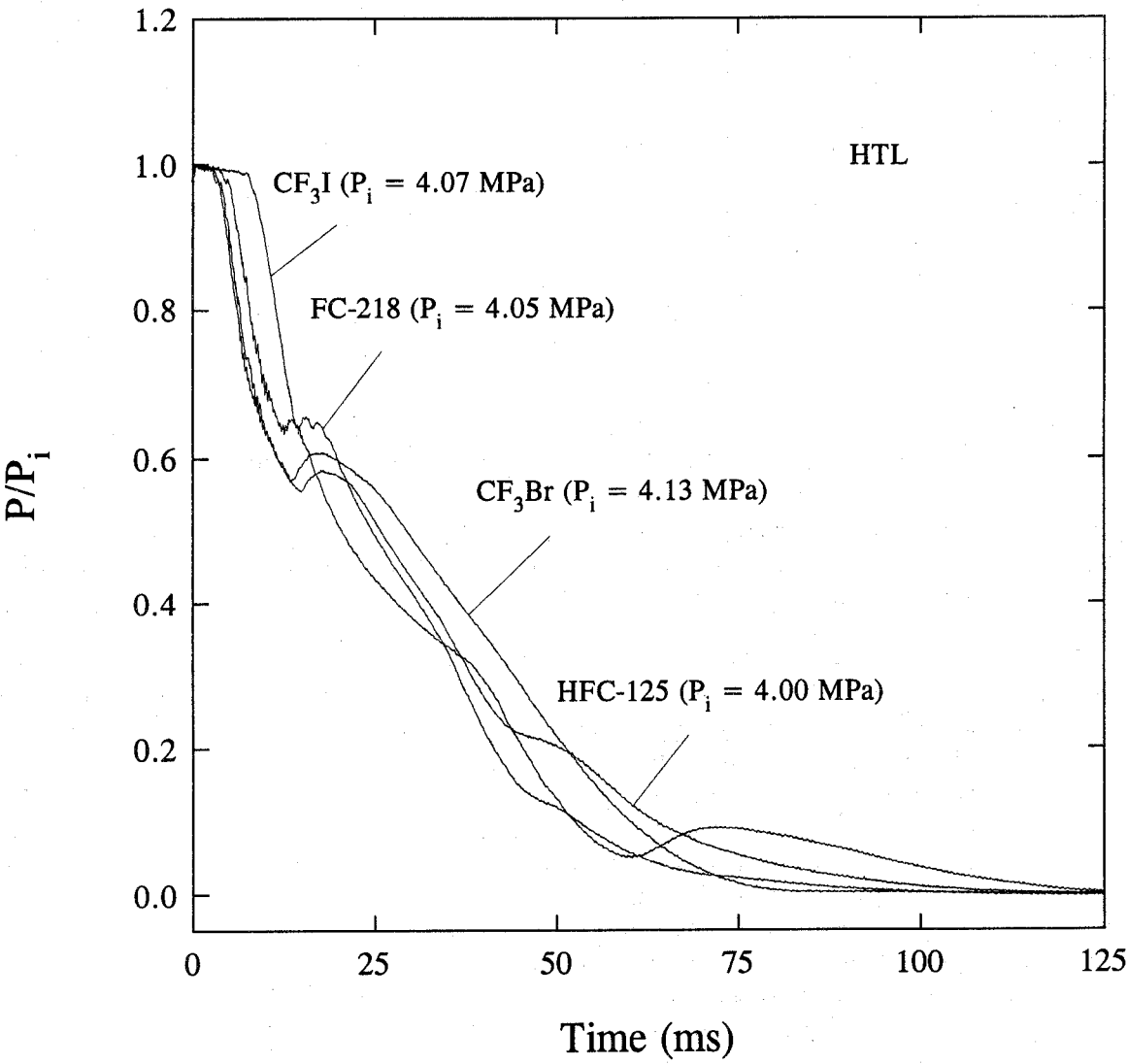


Figure 26. Comparison of pressure decay curves during standard discharges using a HTL solenoid valve.

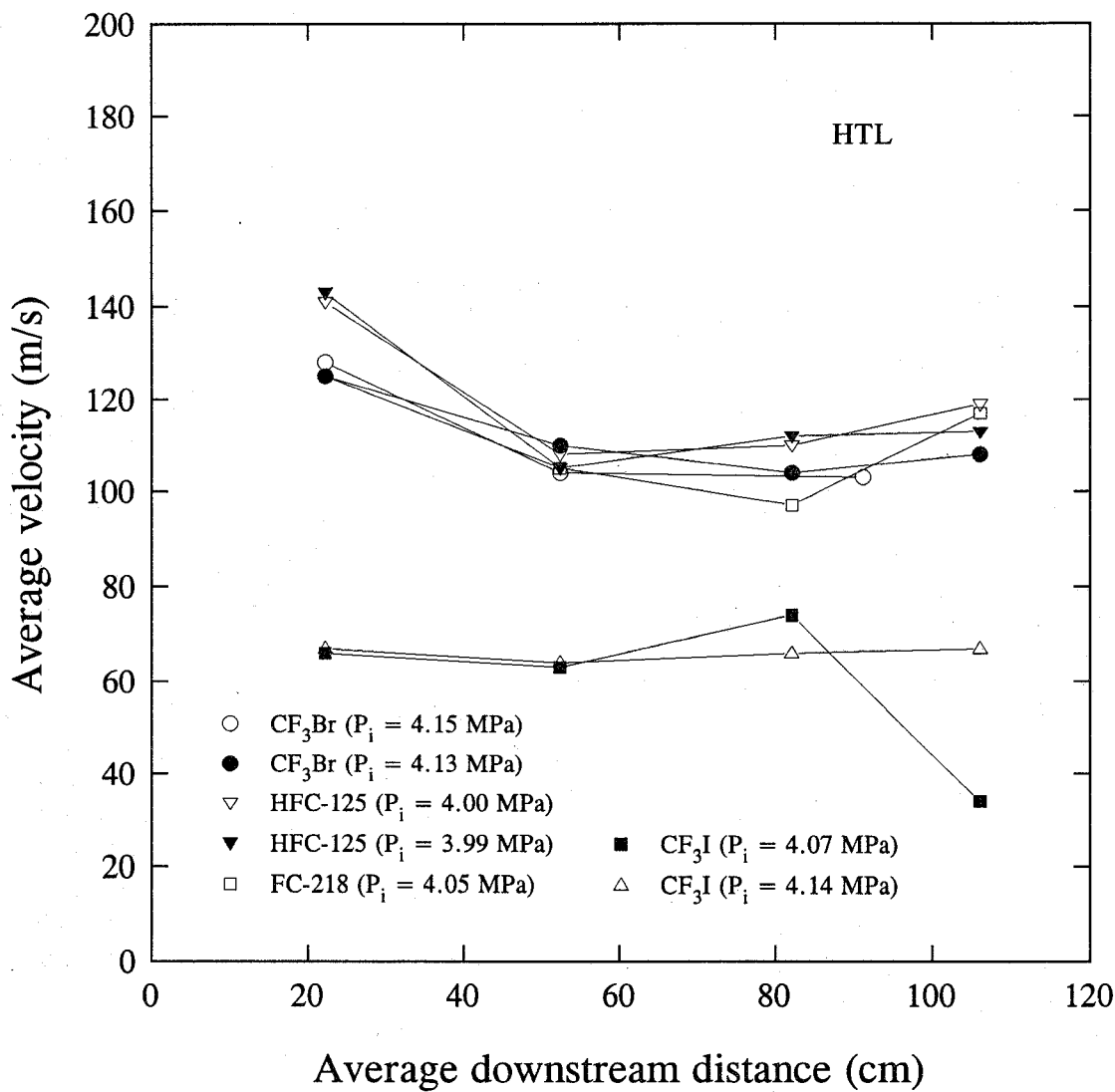


Figure 27. Average downstream velocities during standard discharges using a HTL valve.

Table 19. Calculated void fractions and measured maximum spray angles (standard discharges using a HTL valve)

Agent	Mass (g)	u (m/s)	M_{max} (MPa)	α	Maximum spray angle
CF ₃ Br	586	91	0.83	0.95	103°
HFC-125	431	98	0.58	0.97	105°
HFC-125	426	98	0.65	0.96	105°
FC-218	444	83	0.55	0.95	108°
CF ₃ I	707	46	1.65	0.67	115°
CF ₃ I	713	51	1.67	0.73	120°

shows the lowest calculated void fraction at a fixed downstream location. In addition, CF₃I spray has the largest maximum spray angle at the valve exit.

8.4.3.5 HTL Squibs. Figure 30 summarizes the results of the standard discharges using HTL squibs. Three salient points are noted in the figure. First, no degassing of the dissolved nitrogen in CF₃I is suggested. Second, the inflection points in the pressure decay curves of CF₃Br, HFC-125, and FC-218 are barely distinguishable. Third, the initial CF₃I discharge rate is the fastest, and CF₃Br has the slowest discharge rate. The dynamic pressure transducer still caused a pressure recovery artifact close to the end of the discharge in some of the CF₃I tests; however, the pressure rebound was not as pronounced as in the tests using Marotta, HTL, and Kidde-Graviner valves. All of the pressure curves have much more fluctuation during the initial discharge period; this could be the result of the violent vibration caused by the activation of the explosive cartridge.

The measurements of average spray dispersion velocities could not be carried out because the brightness of the flash caused by the explosion of the cartridge completely saturated the laser detectors. However, estimates of the average velocities could still be made using the time at which the downstream pressure transducer detected the arrival of the spray. Table 21 summarizes the average velocities, the calculated void fractions, and the measured maximum spray angles. The average dispersion velocity u of the CF₃I spray is still the slowest. In Table 21, the unusual high values of M could again be due to the flying debris (resulting from the action of the explosive cartridge) hitting the pressure transducer. The measured maximum spray angles of all the agents are very similar within the measurement uncertainty. Based on the discussion so far, the spray angle appears to be dependent not only on the agent considered but also on the release mechanism used.

8.4.3.6 Effect of an Orifice Plate. The pressure decay curves obtained using an orifice plate and a Marotta valve during standard discharges are respectively shown in Figures 31, 32, 33, and 34 for CF₃Br, HFC-125, FC-218, and CF₃I. The low P_i and half-fill measurements in the figures will be discussed in later sections. There are three important features in these figures.

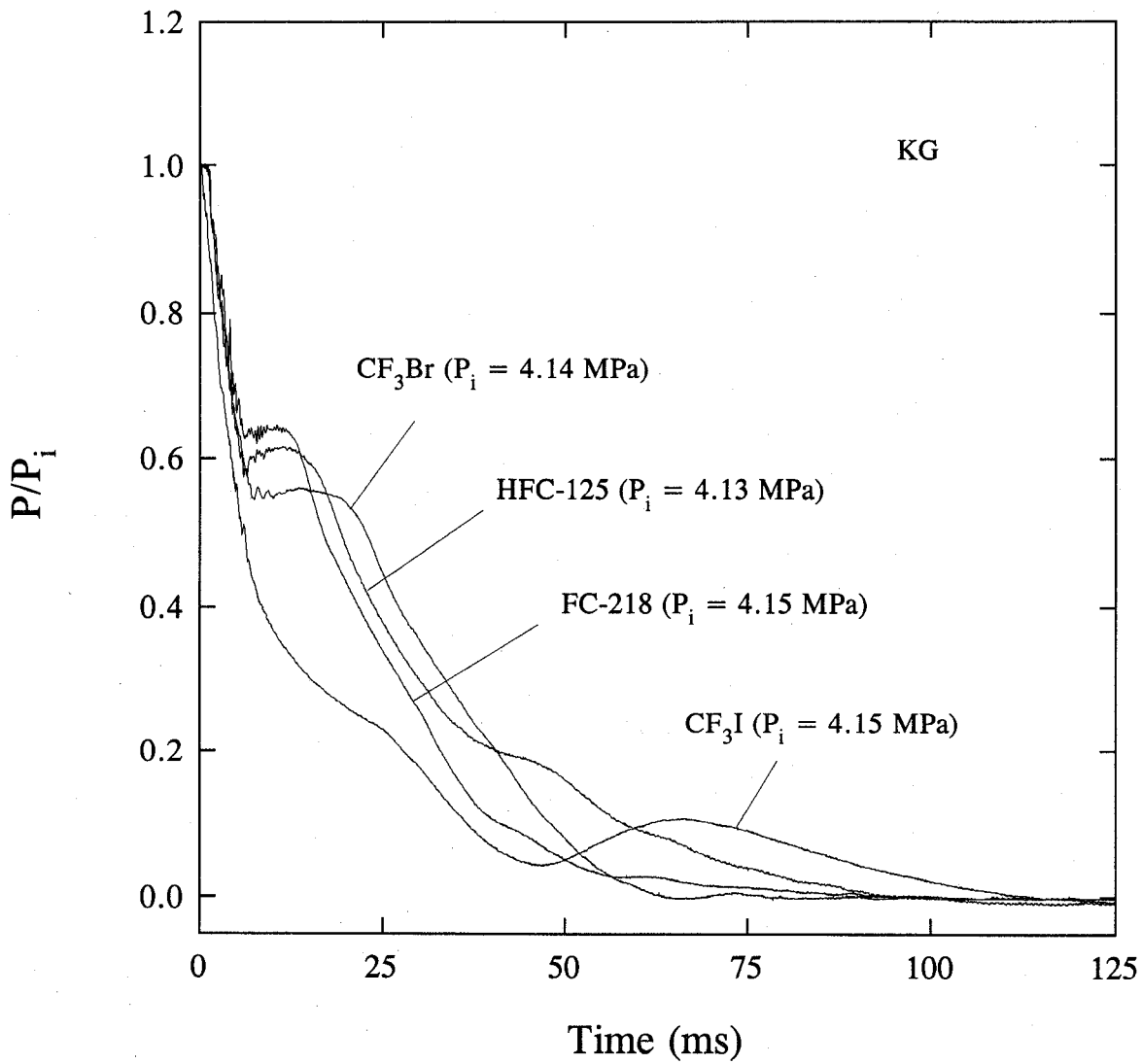


Figure 28. Comparison of pressure decay curves during standard discharges using a Kidde-Graviner (KG) valve.

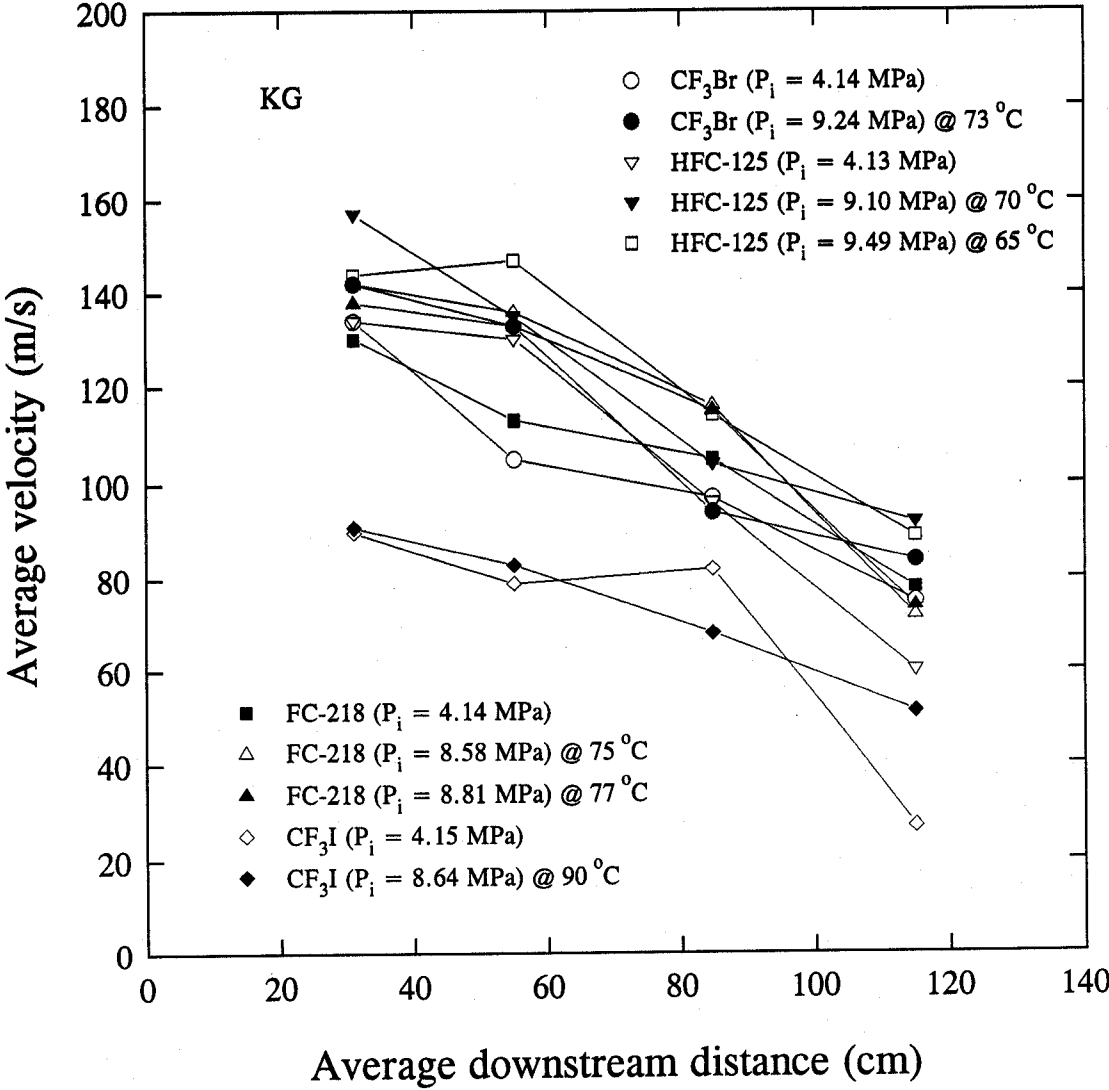


Figure 29. Average downstream velocities during standard discharges using a Kidde-Graviner valve.

Table 20. Calculated void fractions and measured maximum spray angles (standard discharges using a Kidde-Graviner valve)

Agent	Mass (g)	u (m/s)	M_{max} (MPa)	α	Maximum spray angle
CF ₃ Br	625	89	1.28	0.92	132°
HFC-125	497	92	2.20	0.83	145°
FC-218	492	75	1.18	0.87	134°
CF ₃ I	800	54	1.21	0.83	152°

1. The pressures at which the degassing occurs (see Figures 31, 32, and 33) do not appear to depend on the presence or absence of the orifice plate under similar initial conditions of the vessel. This is consistent with the calculations of the homogeneous nucleation pressures which depend only on the initial conditions of the vessel (see Section 8.4.3.2).
2. No degassing is noticeable in the CF₃I pressure decay curves. In Figure 34, the pressure rebound at the end of the pressure decay curves is due to the artifact of the pressure transducer.
3. Compared to the standard discharges, the discharge rates are much slower when a restricted orifice plate is present.

Figure 35 compares the results of all the agents under similar initial conditions. The tendency to degas also conforms qualitatively with the predictions using homogeneous nucleation theory. The initial discharge rate of CF₃I is the fastest, whereas CF₃Br again shows the slowest discharge rate. Figure 36 summarizes the results obtained from the HTL solenoid valve with the same orifice plate. Note that CF₃I was not used in this parametric study. The results are very similar to those obtained using the Marotta valve; this is not surprising because both valves are geometrically similar. In Figure 36, it is unclear why the pressure traces of all the CF₃Br runs show jagged appearances when an orifice plate is used.

Figures 37, 38, 39, and 40 show the average spray dispersion velocities of individual agents using the Marotta valve under various experimental conditions. Only the standard discharges with and without an orifice plate will be discussed here. The other parametric effects will be considered in subsequent sections. In the presence of the orifice plate, the measured average velocities closest to the exit (*i.e.*, at 20 cm downstream) are comparable to or lower than those observed in the standard discharges. Similar trends are noted in Figures 41, 42, and 43 when using the HTL solenoid valve. Figure 44 compares the average velocities obtained in the standard Marotta discharges of all the agents with the orifice plate. The average dispersion velocities of CF₃I again are the slowest among all the other agents.

Table 22 tabulates the calculated void fractions and the measured maximum spray angles. There are no significant differences in the spray angles for the different cases. However, CF₃I still has the lowest calculated void fraction at the specified downstream location.

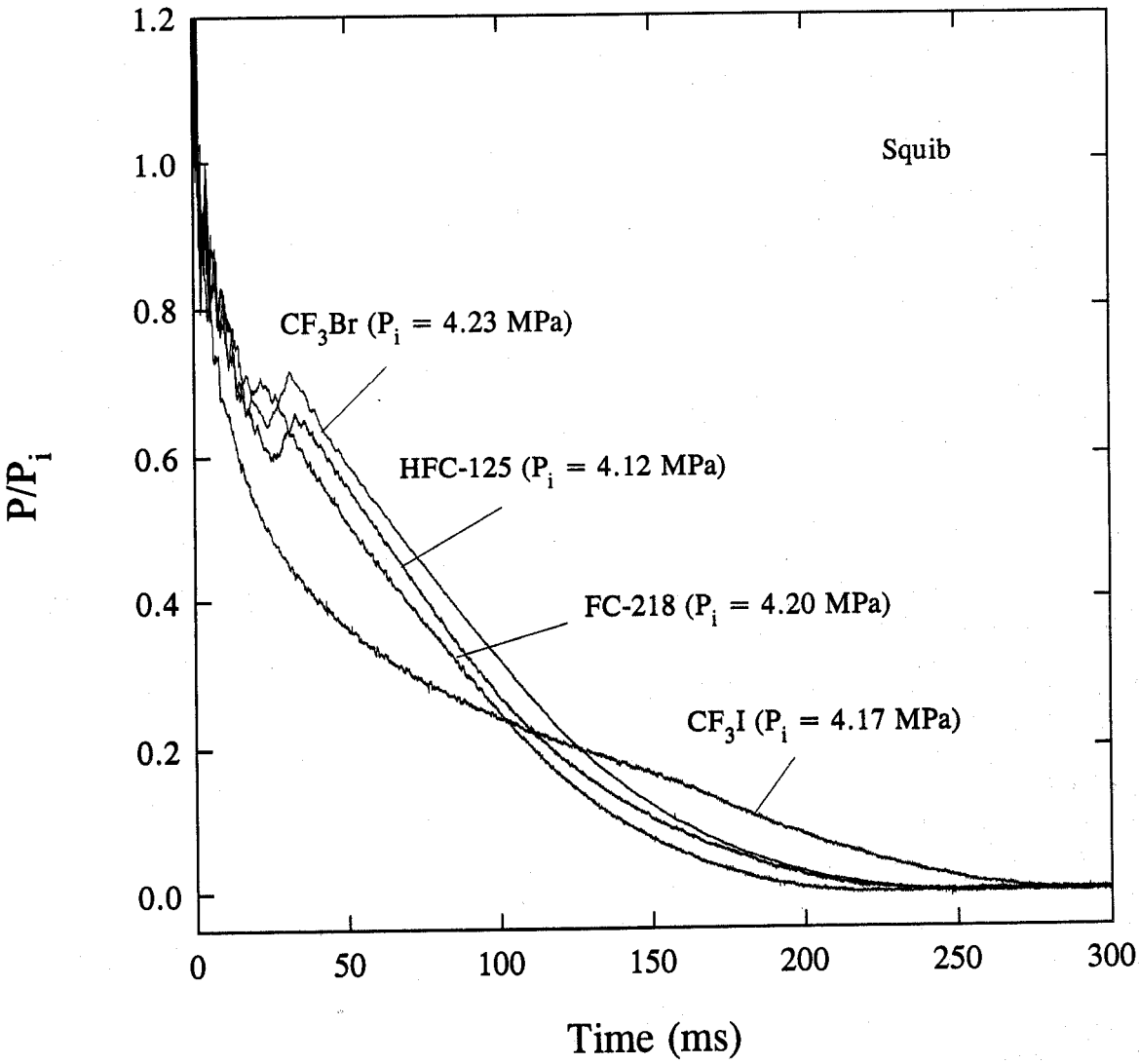


Figure 30. Comparison of pressure decay curves during standard discharges using HTL squibs.

Table 21. Calculated void fractions and measured maximum spray angles (standard discharges using HTL squibs)

Agent	Mass (g)	u (m/s)	M_{max} (MPa)	α	Maximum spray angle
CF ₃ Br	581	93	2.03	0.89	140°
HFC-125	454	89	2.37	0.81	131°
HFC-125	453	95	2.61	0.81	146°
FC-218	476	83	1.72	0.84	144°
CF ₃ I	773	62	1.52	0.84	136°

8.4.3.7 Effect of Fill Density. Figures 32 and 34 also compare respectively the discharge characteristics of HFC-125 and CF₃I under two fill conditions, the standard (2/3) *versus* one-half, using the Marotta valve. Notice the pressure rebound, an artifact, at the end of the CF₃I discharge, and the pressure decay curves of CF₃I do not suggest any degassing of the dissolved nitrogen, an observation consistent with homogeneous nucleation theory. Figure 45 shows the results for HFC-125 from the HTL valve tests. The pressures at which the degassing occurs under two different fill conditions with similar initial nitrogen charge pressures at the same temperature appear to be not significantly different from each other although the results in Figure 45 show some scatter. This observation can also be explained qualitatively by homogeneous nucleation theory. According to the theory, the bubble nucleation pressure only depends on the initial total pressure and temperature. Since the amount of agent required is less under one-half fill condition, the overall discharge rates, based on the inflection points in the curves, are faster than the discharges under two-thirds fill condition.

The calculated void fractions and the measured spray angles are summarized in Table 23. The calculated void fractions of CF₃I are still the lowest irrespective of the fill conditions. The average spray dispersion velocities under one-half fill conditions are also shown in Figures 38, 40, and 42. Comparing Figures 38 and 40 for the one-half fill condition, CF₃I still has lower average velocities than HFC-125. However, no general conclusions can be made when the average velocities under the two fill conditions are compared at various downstream locations because of the scatter in the results.

8.4.3.8 Effect of Initial Nitrogen Charge Pressure. Visual observations of the behavior of the agent/nitrogen mixtures inside a vessel were also made using the cylindrical vessel with sight gages and the low initial charge pressure (~ 2.75 MPa). For the same agent, the high-speed movies revealed similar phenomena as observed in the standard discharges, except that the liquid/vapor interface remained visible and clear for a much longer duration.

Figures 31, 32, 33, and 34 compare the discharge characteristics of individual agents using the Marotta valve under two initial nitrogen charge pressures. At the low initial nitrogen charge pressure, there is no indication of degassing from the pressure decay curves using any of the agents. The homogeneous nucleation theory, discussed above, also predicts that the degassing does not occur. Table 24 shows the calculated homogeneous nucleation pressures of all the agents based on the experimental conditions used in the Marotta valve tests. The nucleation pressure of CF₃I is not shown in the table because it is calculated to be negative (*i.e.*, in tension). It is clear from the pressure decay

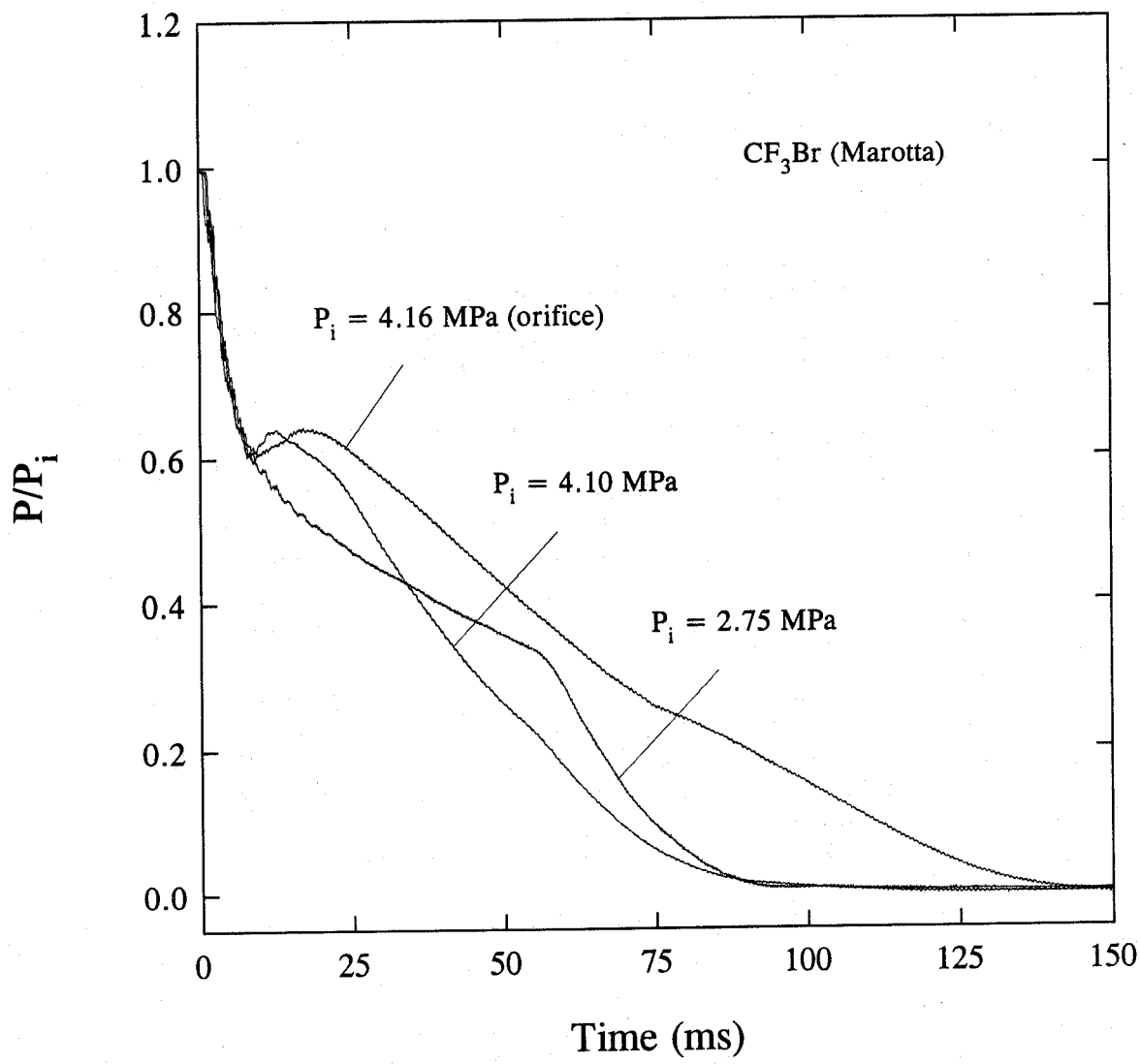


Figure 31. Pressure decay curves during discharges of CF_3Br using a Marotta valve under various conditions.

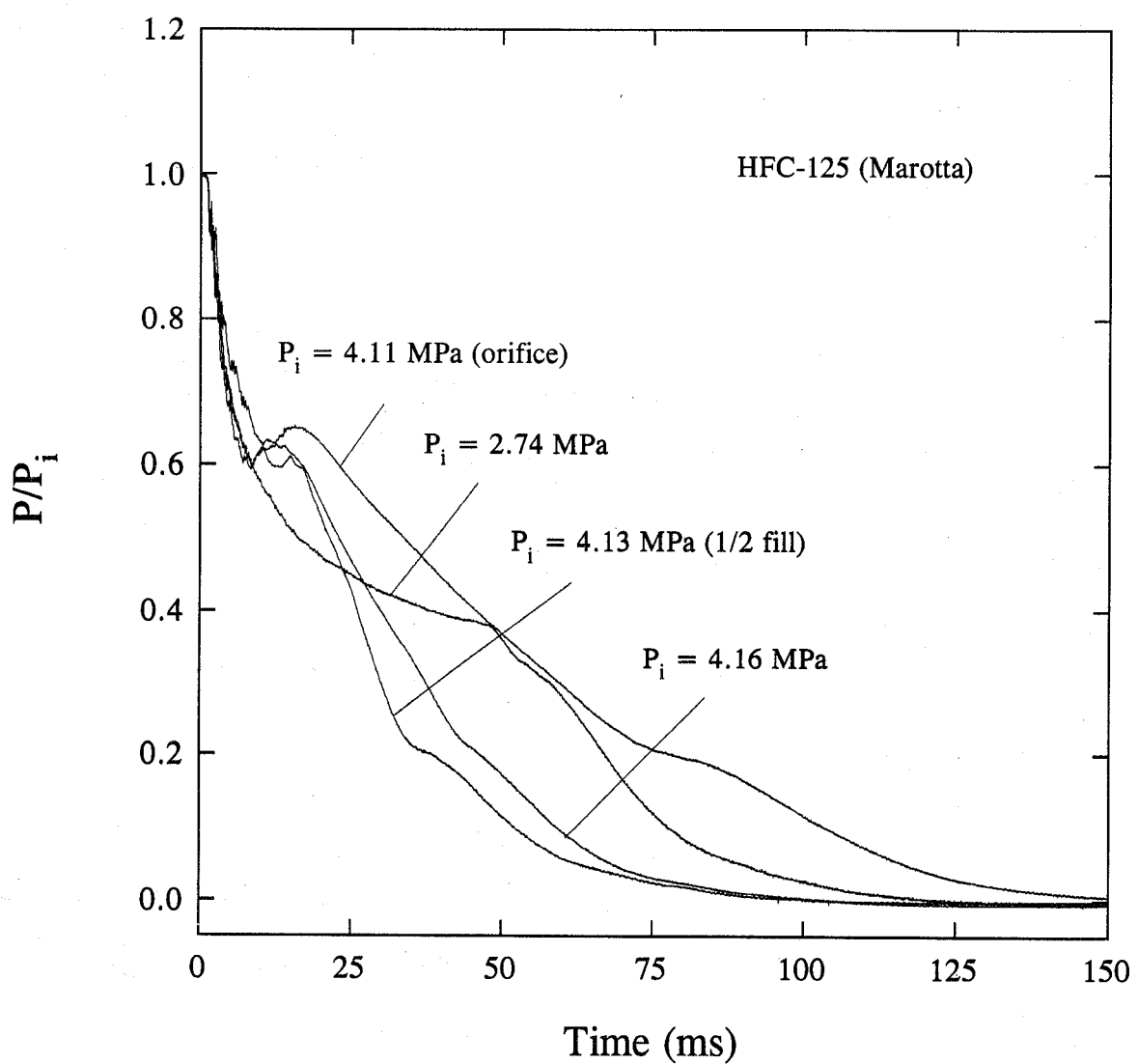


Figure 32. Pressure decay curves during discharges of HFC-125 using a Marotta valve under various conditions.

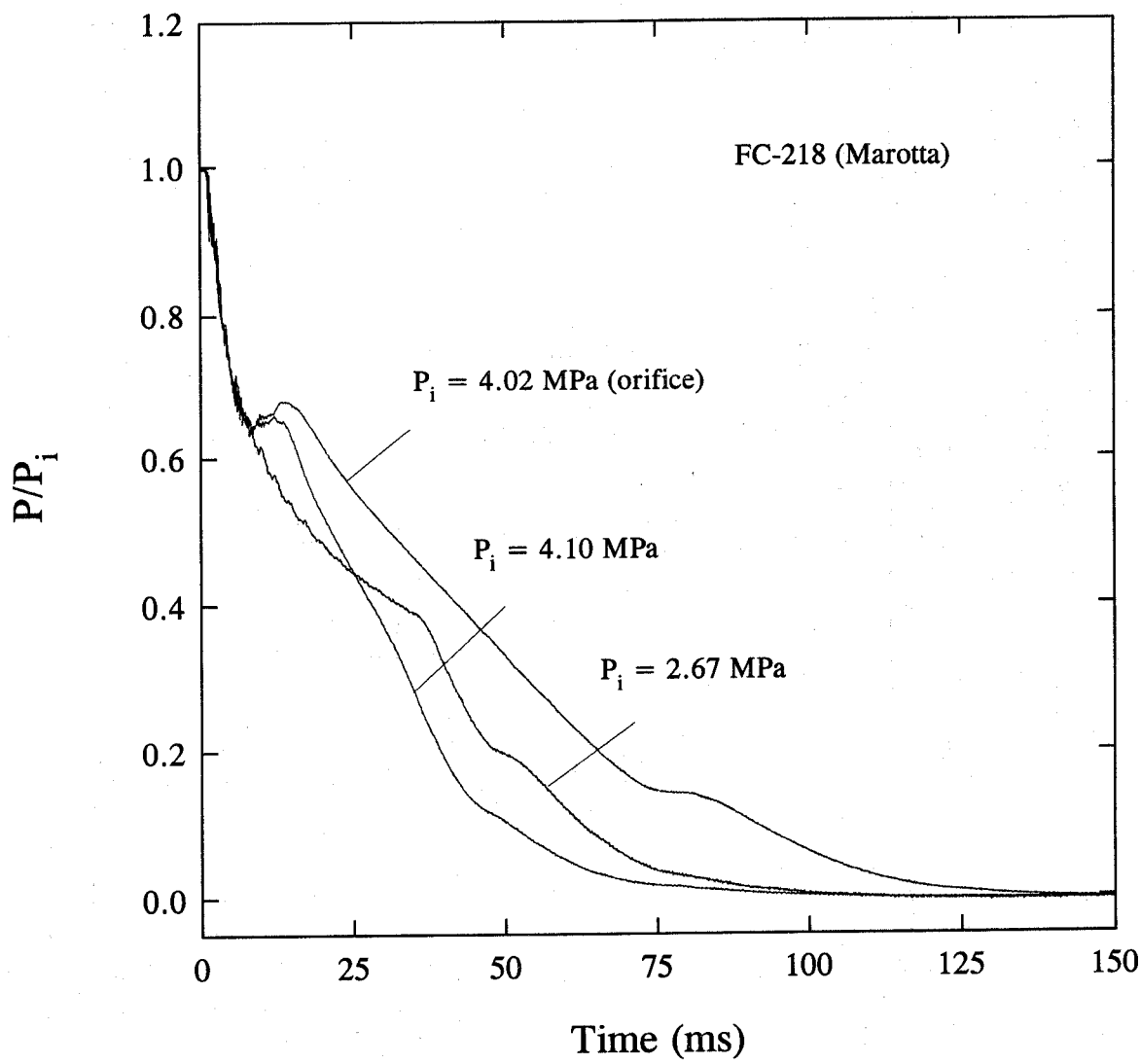


Figure 33. Pressure decay curves during discharges of FC-218 using a Marotta valve under various conditions.

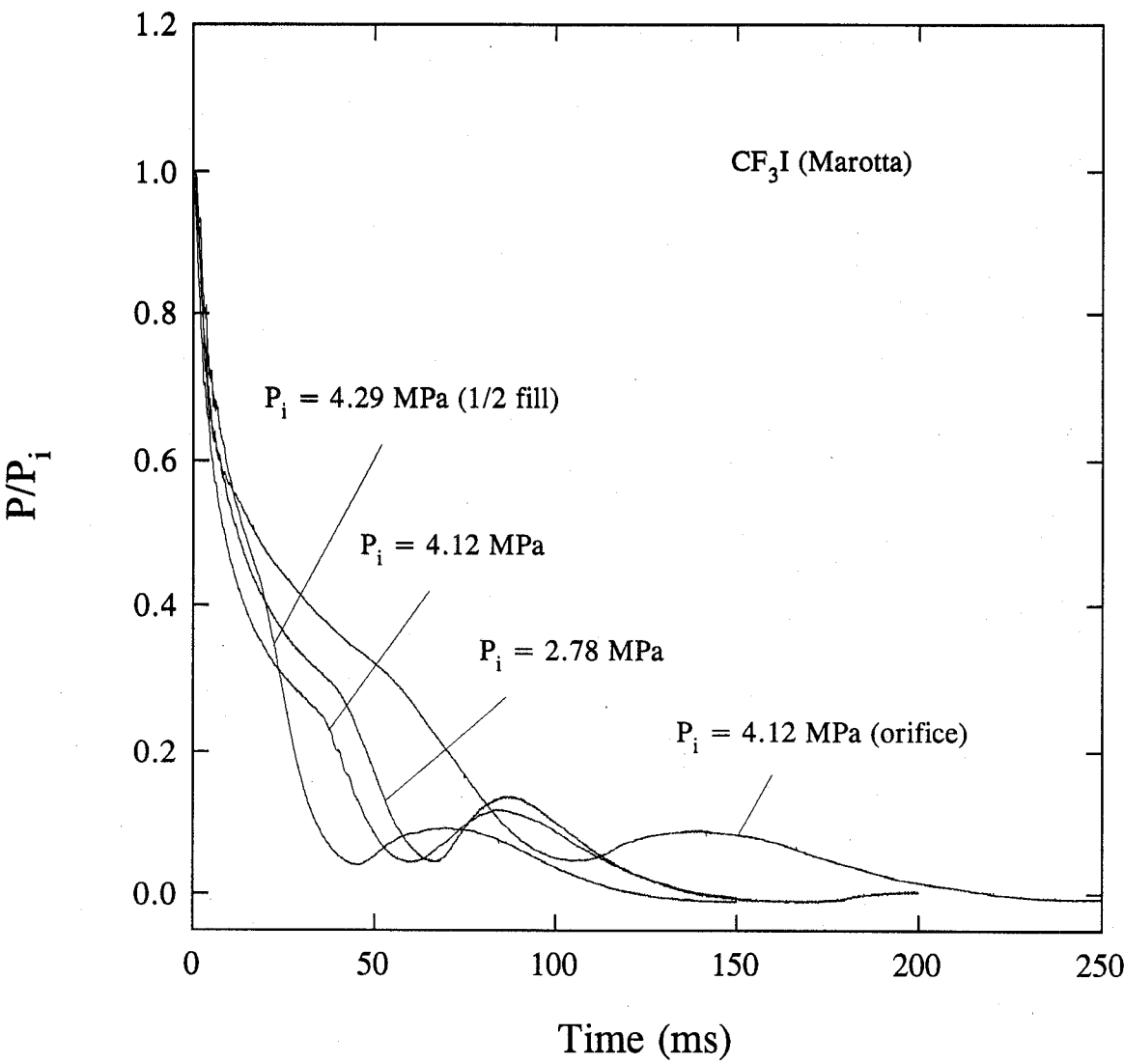


Figure 34. Pressure decay curves during discharges of CF_3I using a Marotta valve under various conditions.

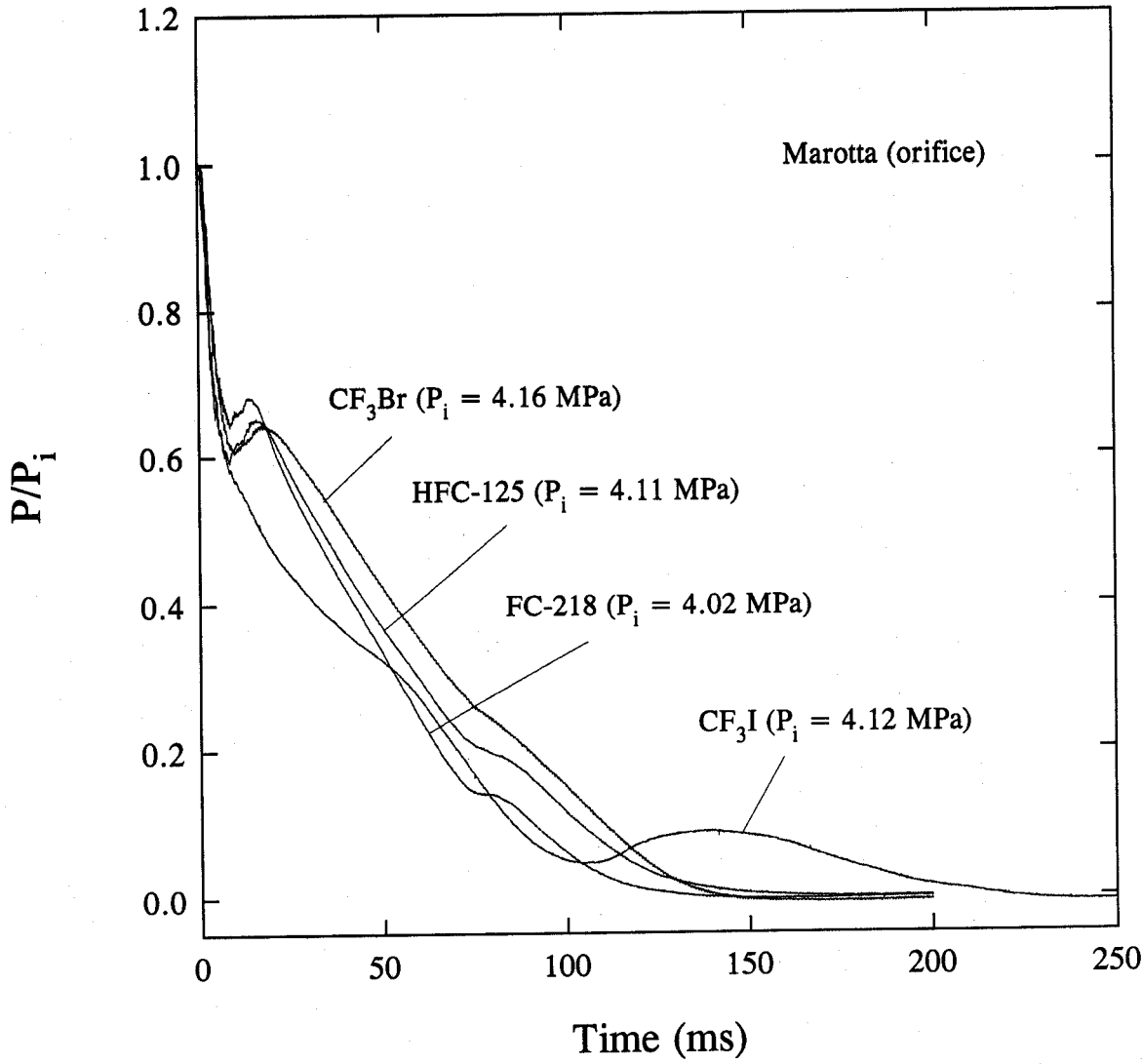


Figure 35. Comparison of pressure decay curves during standard discharges using a Marotta valve with an orifice plate.

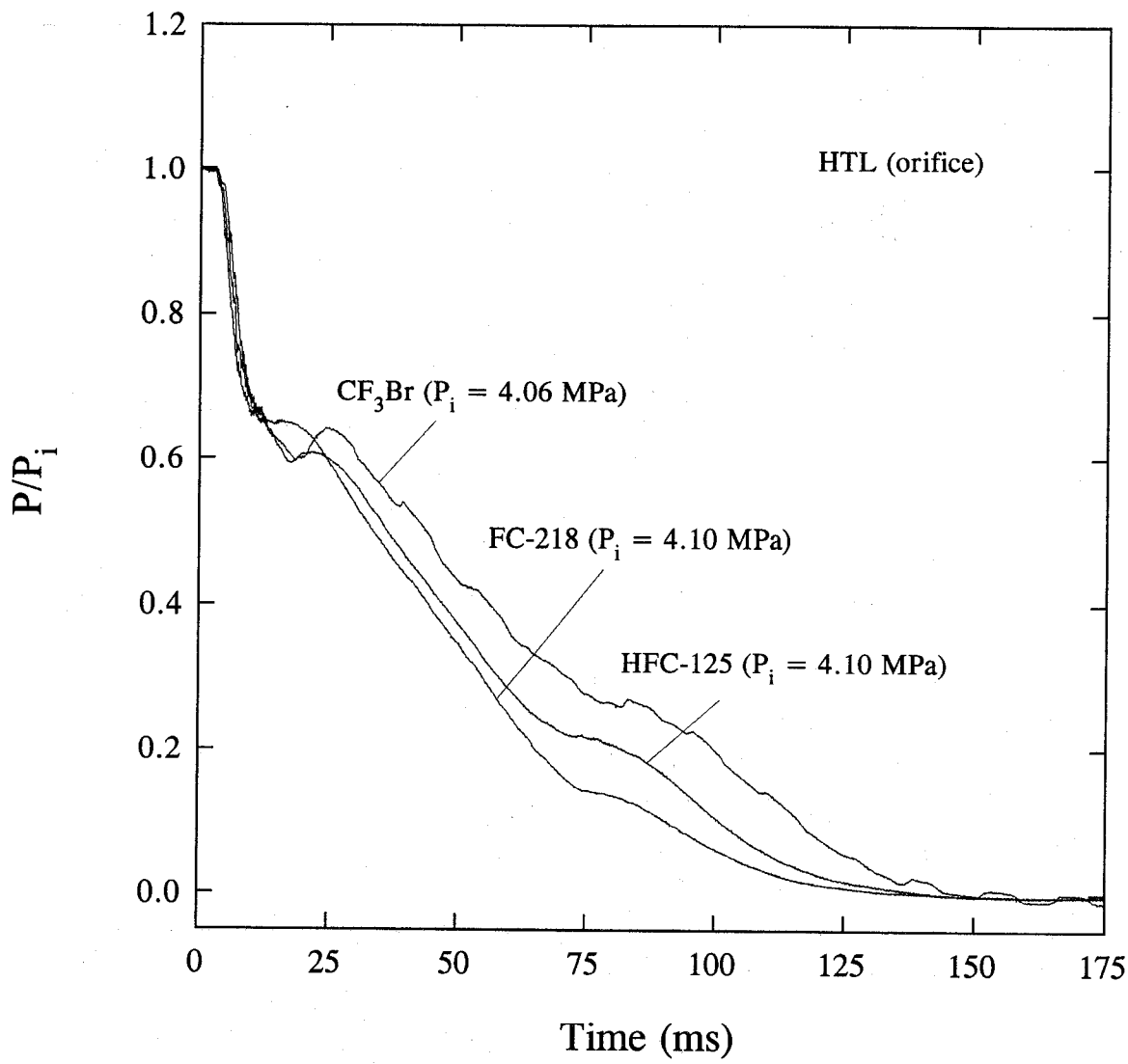


Figure 36. Comparison of pressure decay curves during standard discharges using a HTL valve with an orifice plate.

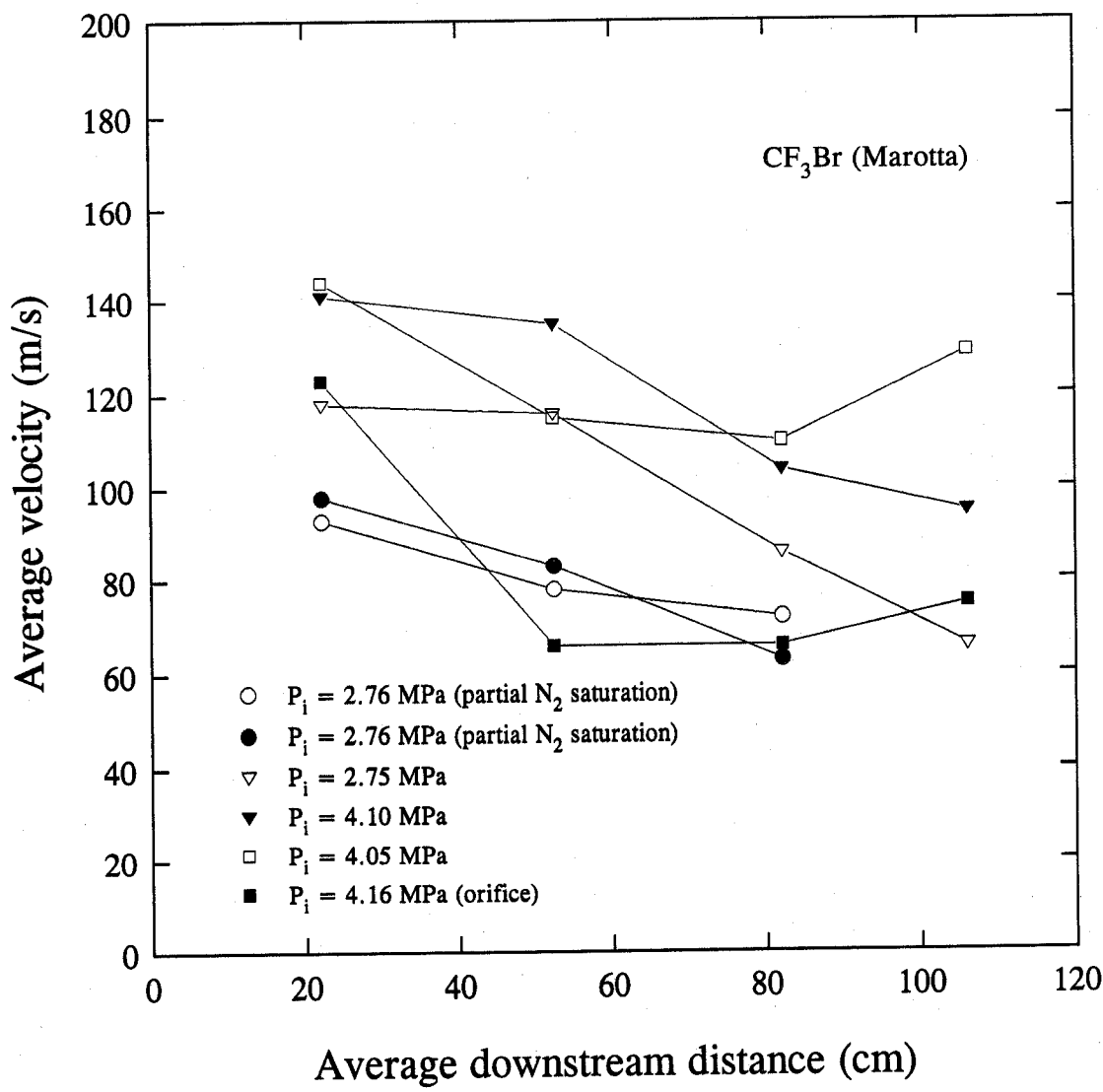


Figure 37. Average downstream velocities during discharges of CF_3Br using a Marotta valve under various conditions.

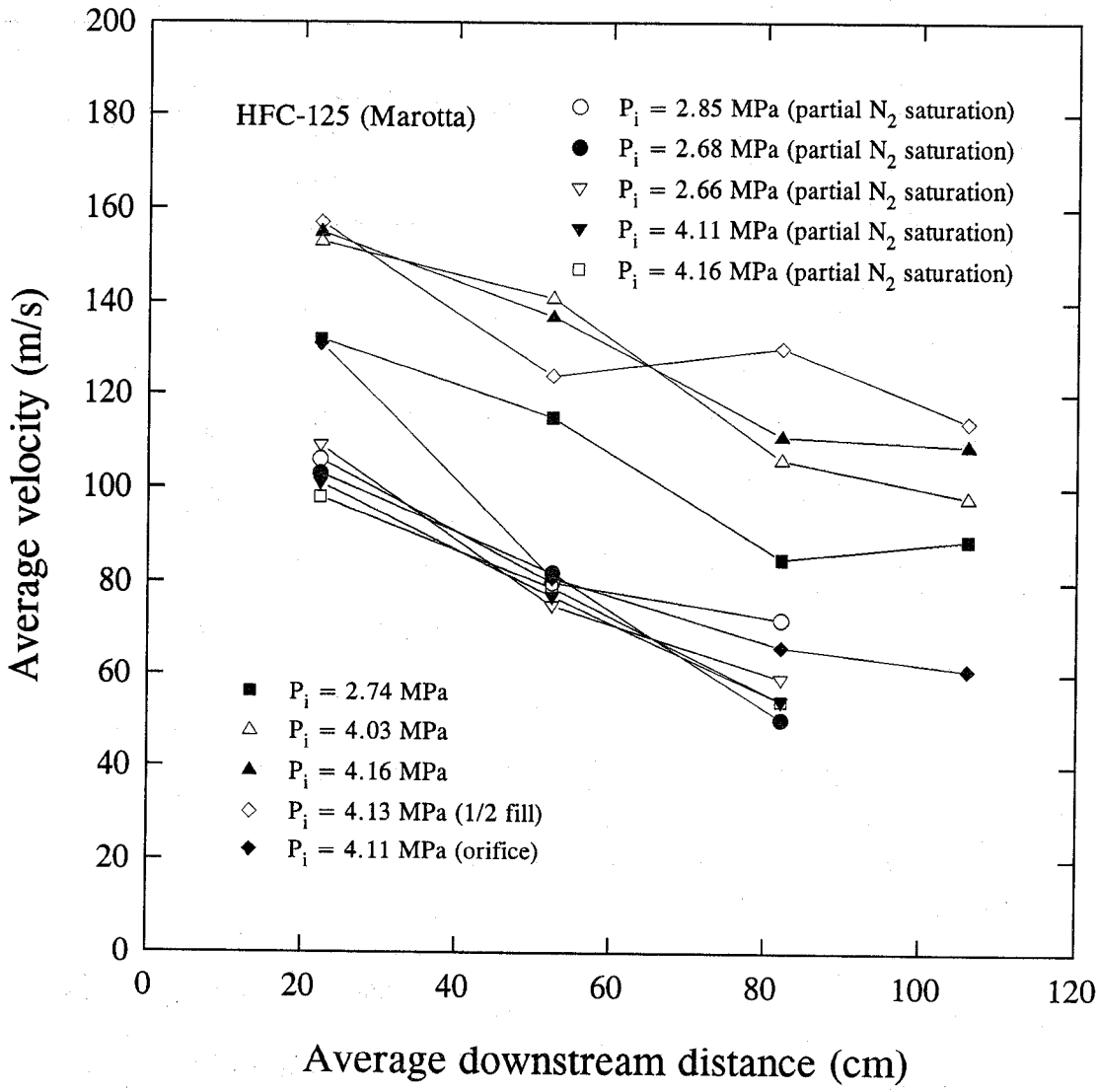


Figure 38. Average downstream velocities during discharges of HFC-125 using a Marotta valve under various conditions.

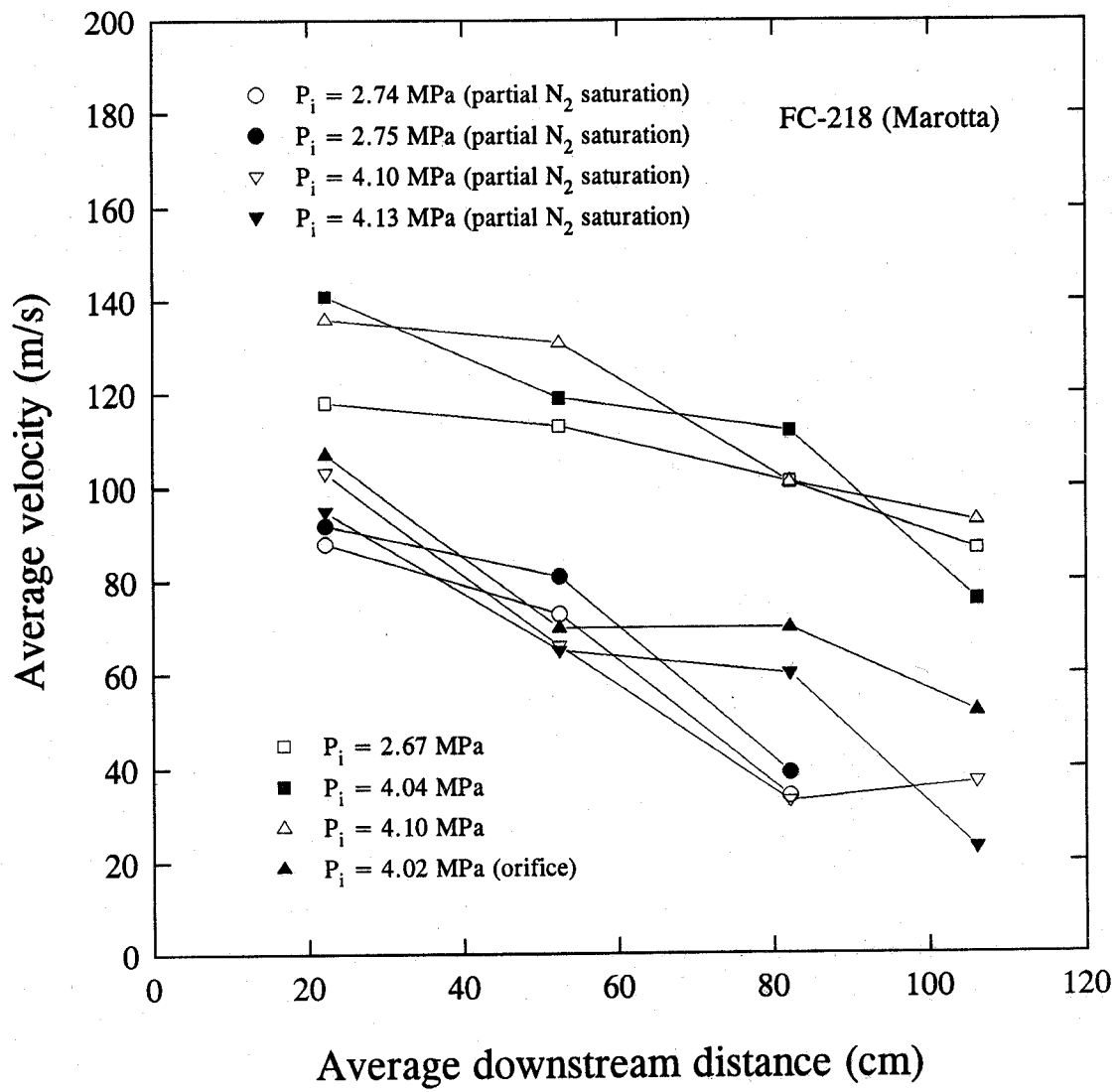


Figure 39. Average downstream velocities during discharges of FC-218 using a Marotta valve under various conditions.

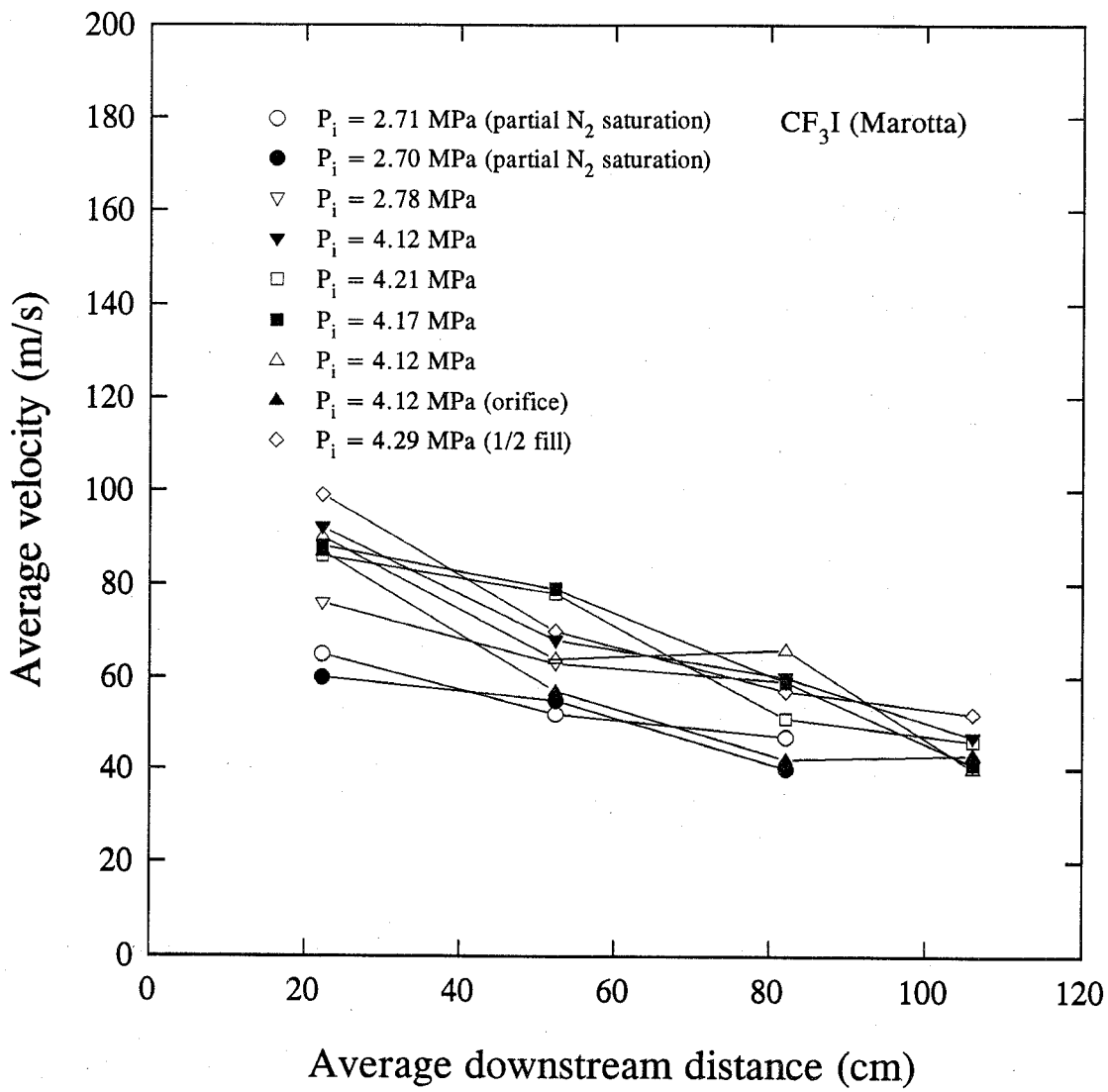


Figure 40. Average downstream velocities during discharges of CF₃I using a Marotta valve under various conditions.

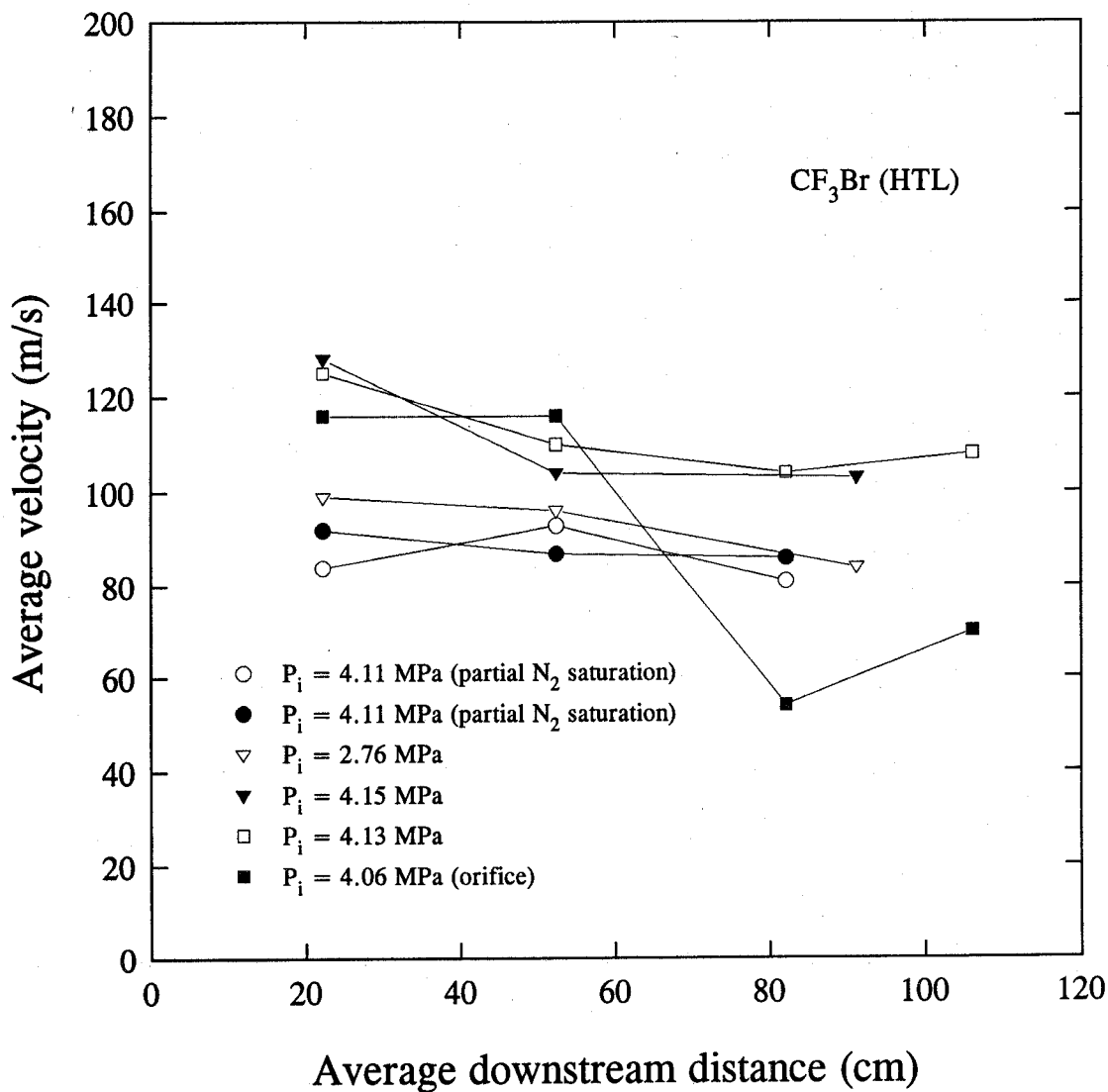


Figure 41. Average downstream velocities during discharges of CF₃Br using a HTL valve under various conditions.

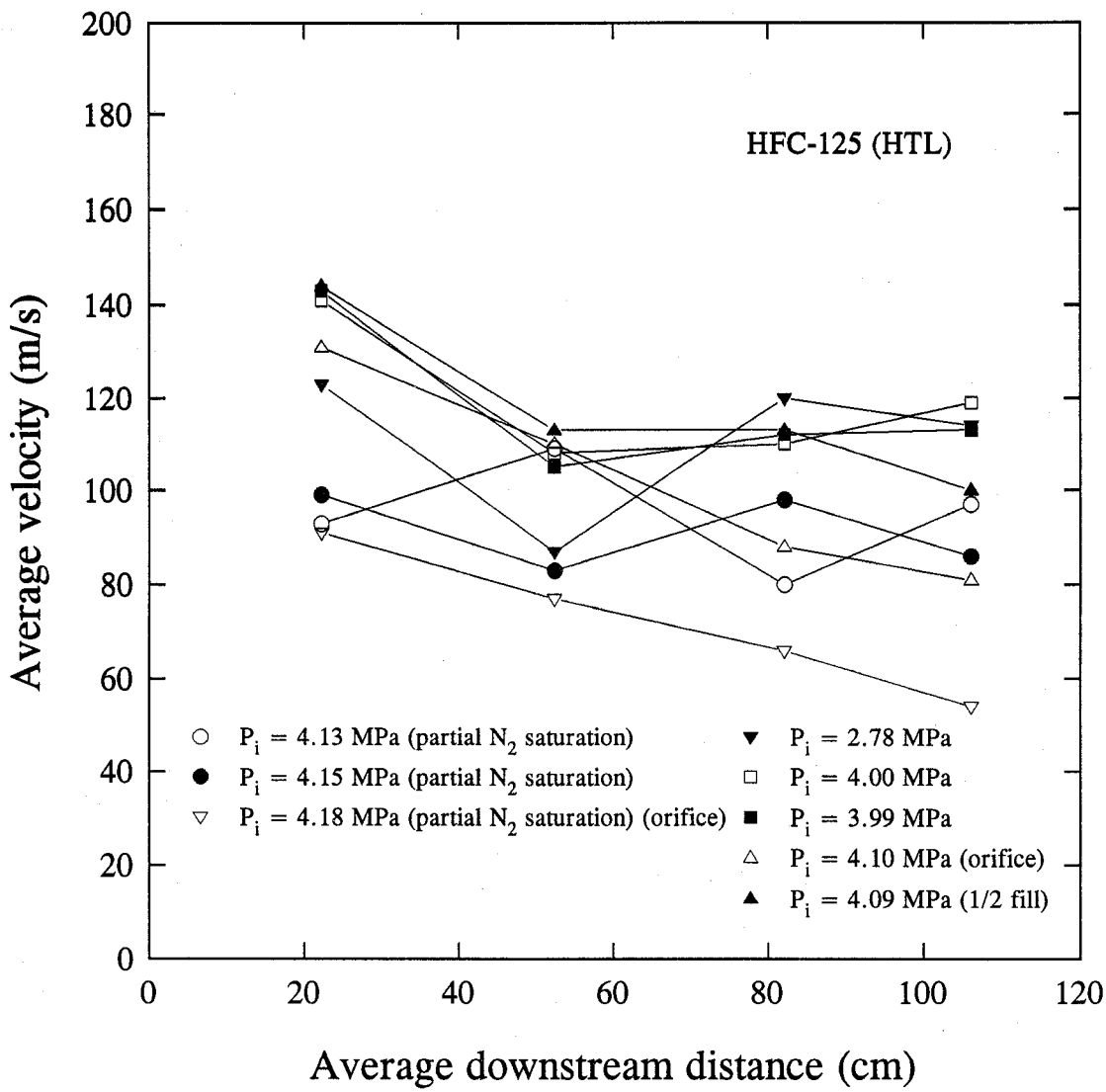


Figure 42. Average downstream velocities during discharges of HFC-125 using a HTL valve under various conditions.

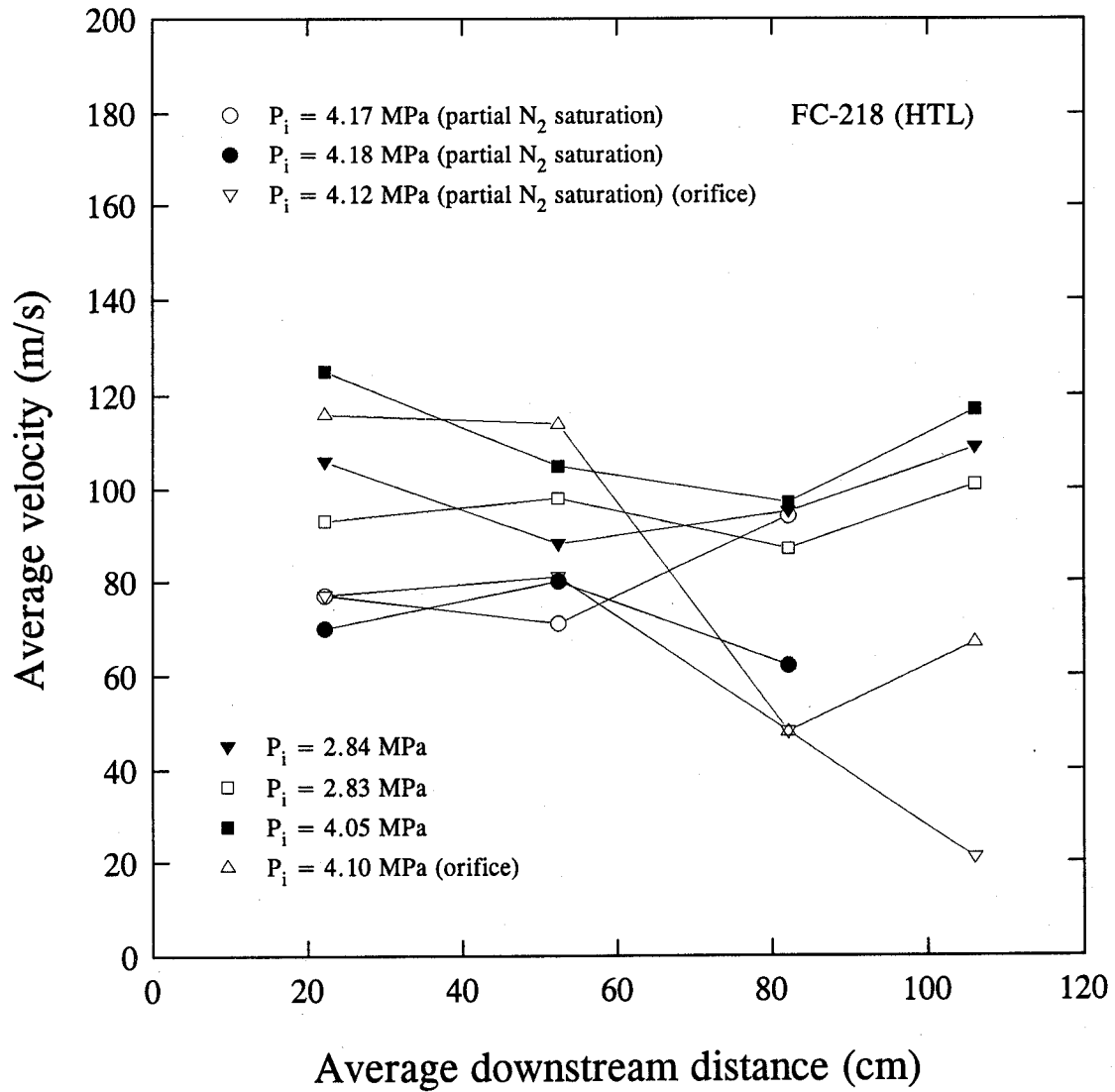


Figure 43. Average downstream velocities during discharges of FC-218 using a HTL valve under various conditions.

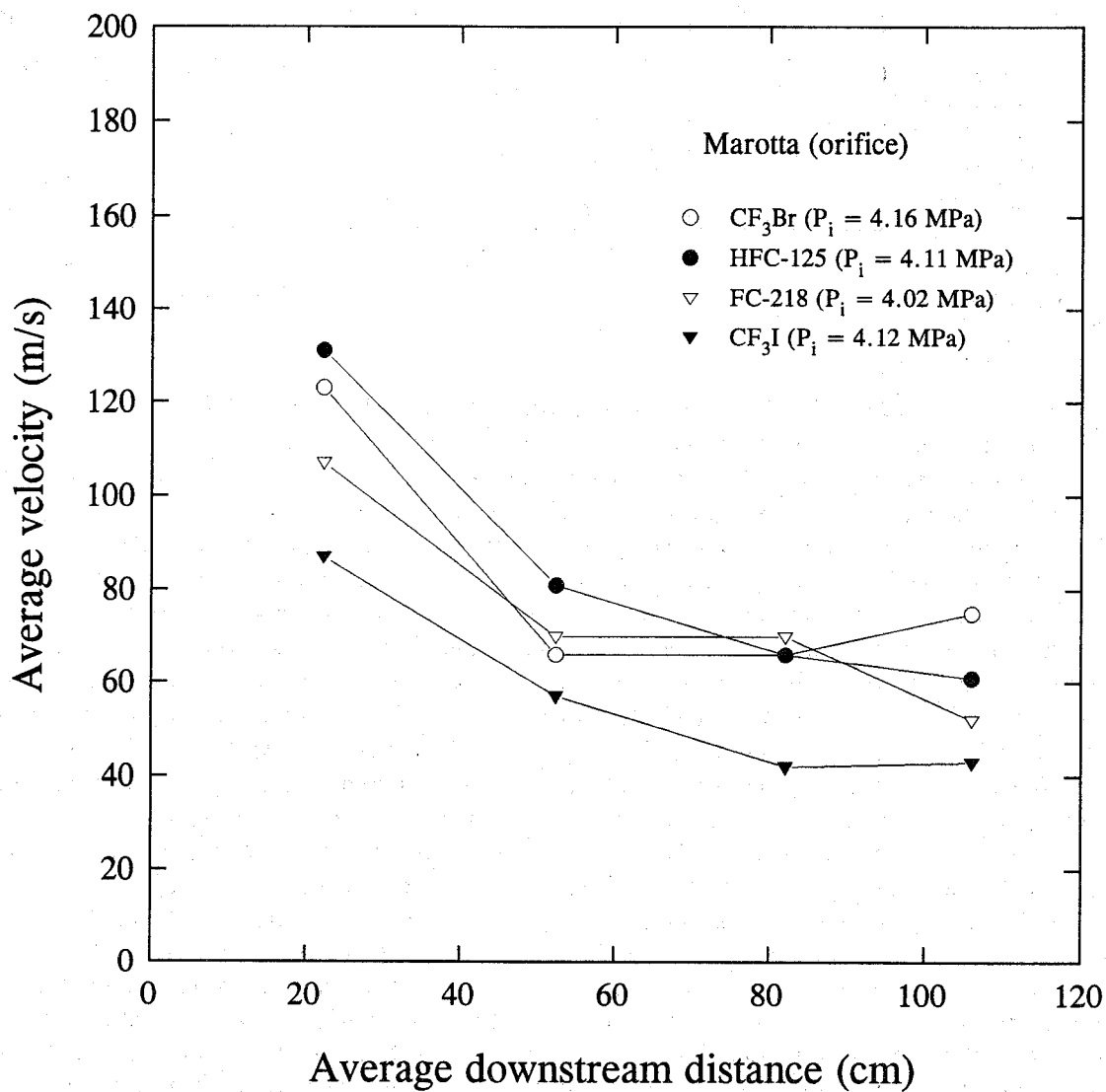


Figure 44. Average downstream velocities during standard discharges using a Marotta valve with an orifice plate.

Table 22. Calculated void fractions and measured maximum spray angles (discharges with orifice plate)

Agent	Mass (g)	u (m/s)	M_{max} (MPa)	α	Maximum spray angle
CF ₃ Br*	577	66	0.19	0.98	143°
HFC-125*	452	76	0.41	0.96	142°
FC-218*	442	68	0.21	0.98	145°
CF ₃ I*	695	54	1.32	0.81	147°
CF ₃ Br**	577	59	0.35	0.95	---
HFC-125**	425	61	---	---	145°
FC-218**	447	58	0.34	0.94	145°

* Marotta valve

** HTL valve

curves that by the time the P_H/P_i ratio is reached, all the liquid has been discharged from the vessel; therefore, no homogeneous nucleation or degassing is possible.

The discharge rates, based on the inflection points, are slower for a lower initial nitrogen charge pressure. The results obtained by using the HTL valve were very similar. Figures 46 and 47 compare the discharge characteristics among the agents. Note that CF₃I was not used in the HTL valve tests. In Figure 46, the discharge rate of CF₃I is the fastest, and CF₃Br the slowest.

The comparisons of the average dispersion velocities of the leading edges of the sprays between the low initial charge pressure tests and the standard discharges are also shown in Figures 37 to 43 for individual agents. In general, the velocities near the valve exit are higher in the standard discharges than in the low pressure tests. The comparisons of the velocities among the four agents in the low pressure tests are given in Figure 48. Note again that CF₃I has the lowest dispersion velocities.

Table 25 tabulates the calculated void fractions and maximum spray angles from the tests using low initial charge pressure. For CF₃I, the calculated void fraction is the lowest.

A set of experiments using HFC-125 and the Marotta valve was performed in order to examine the effect of a range of initial charge pressures. The results are summarized in Figure 49. In the figure, "pure" refers to no nitrogen pressurization. Curve *e* in the figure was obtained using the static pressure transducer which, in general, exhibited more noise than the dynamic transducer in the transient pressure measurements. From the figure, degassing appears to occur only for the two highest initial charge pressures. These two runs have the abrupt pressure recovery associated with the degassing of dissolved nitrogen. This observation can also be explained qualitatively in terms of the homogeneous nucleation theory. Table 26 shows the calculated homogeneous nucleation pressures for various initial charge pressures. At pressures below 2.74 MPa, the calculated homogeneous nucleation pressures are negative (*i.e.*, in tension). In other words, homogeneous nucleation is predicted not to occur under the experimental conditions used in this study. The prediction agrees with the observations in Figure 49. Although homogeneous nucleation is predicted for $P_i = 2.74$ MPa, the nucleation pressure is so low by the time this pressure is reached that all the liquid in the vessel has been depleted; this prediction is in agreement with the observation for $P_i = 2.74$ MPa in Figure 49 that degassing is not indicated. The dependence of discharge rate on initial charge pressure can also be

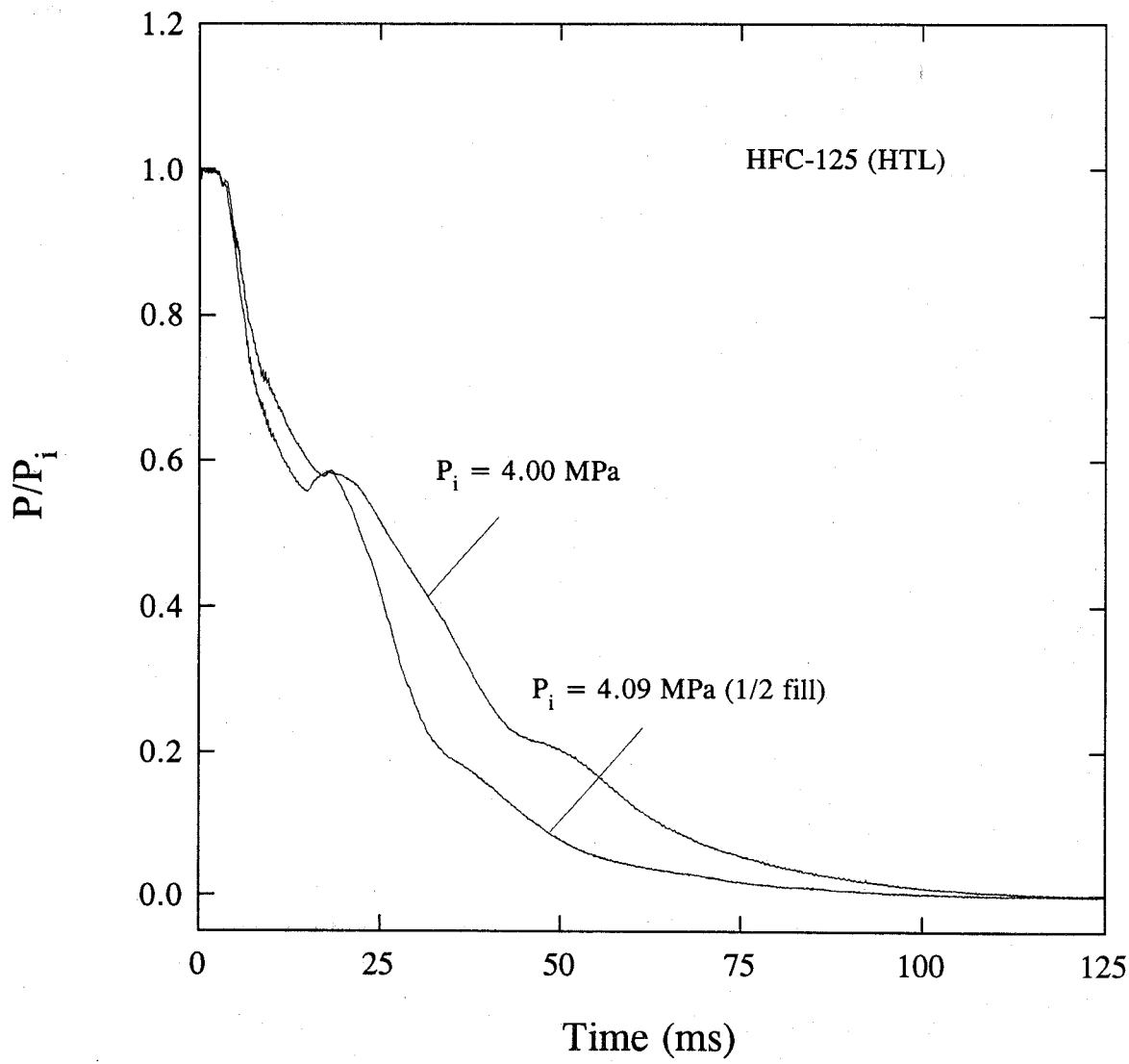


Figure 45. Pressure decay curves during discharges of HFC-125 using a HTL valve under two fill conditions.

Table 23. Calculated void fractions and measured maximum spray angles (discharges with different fill densities)

Agent	Mass (g)	u (m/s)	M_{max} (MPa)	α	Maximum spray angle
HFC-125*	428	104	0.41	0.98	---
HFC-125*	354**	114	0.33	0.99	114°
CF ₃ I*	719	64	1.65	0.83	141°
CF ₃ I*	547**	57	1.20	0.85	133°
HFC-125§	431	98	0.58	0.97	105°
HFC-125§	342**	94	1.07	0.92	108°

* Marotta valve

** one-half fill condition

§ HTL valve

seen in Figure 49. Based on the inflection points of the curves for similar fill densities, higher initial charge pressures result in higher discharge rates.

Figure 50 summarizes the average spray dispersion velocities of HFC-125 for various initial charge pressures. At the location closest to the valve exit (*i.e.*, 20 cm in the figure), it appears that the velocity is slower for lower initial charge pressures. The estimated void fractions and the measured maximum spray angles are given in Table 27. The maximum spray angle initially increases with increasing initial charge pressure, reaches a maximum, and then decreases with increasing initial charge pressures. Despite the scatter in the measured average velocities and momentum fluxes, the calculated void fractions appear to be higher at high initial charge pressures than at low charge pressures. This implies that the high initial charge pressure facilitates the dispersion and evaporation of the agent *downstream*.

The effect of initial charge pressure was also studied using HTL squibs. Figures 51, 52, 53, and 54 show the discharges of CF₃Br, HFC-125, FC-218, and CF₃I respectively. The low temperature condition in the figures will be discussed later. In all the figures, it is clear that there is no indication that degassing occurs at low initial charge pressures. At the highest initial pressure ($P_i \sim 5.48$ MPa), the initial fluctuation in the pressure traces in Figures 52 and 53 due to the initiation of the explosive cartridge could have masked the pressure recovery during degassing; there is no apparent reason why degassing should not occur in HFC-125/nitrogen and FC-218/nitrogen liquid mixtures at higher initial charge pressures. Once again for CF₃I, no degassing is indicated in Figure 54 even at the highest initial charge pressure. Figure 55 compares the results of all the agents at low initial charge pressures. The overall discharge rate of CF₃I is the fastest and that of CF₃Br the slowest. Figure 56 compares the results of HFC-125 and CF₃I at high initial charge pressure. Although the two pressure decay curves cross over at $P/P_i < 0.3$, the overall discharge rate of CF₃I is still faster than that of HFC-125 because for $P/P_i < 0.3$, most of the liquid should have been expelled.

Table 28 compares the calculated void fractions and measured maximum spray angles under various initial charge pressures for all the agents. Note that the scatter in the velocities and momentum flux measurements could have been caused by the flying debris from the explosive cartridge. It appears that the initial charge pressure has little or no effect on the maximum spray angle and that high initial charge pressures result in high average velocities and *vice versa*.

Table 24. Calculated homogeneous nucleation pressure (P_h) at T

Agent	Mass (g)	T (K)	P_i (MPa)	P_h (MPa)	P_h/P_i
CF ₃ Br	586	294	2.75	0.51	0.19
HFC-125	448	294	2.74	0.39	0.14
FC-218	442	295	2.67	0.69	0.26
CF ₃ I	725	294	2.78	---	---

8.4.3.9 Effect of Initial Vessel Temperature. Except the spray angles, visual observations from high-speed movies reveal a similarity in the appearance of the spray between the standard discharges and the discharges where an agent is initially chilled before discharging into the simulated dry bay which is at room temperature. However, after most of the agent/nitrogen mixture had been discharged, large liquid drops were observed dripping out of the vessel outlet.

Figures 51, 52, 53, and 54 also show the pressure decay curves of individual agents obtained at cold temperatures. Figure 57 summarizes the results of all the cold agent discharges. Irrespective of agent, degassing is not noted in the discharges of cold agents. The discharge rates are slower in cold discharges than in standard discharges because the initial pressures are lower.

In Table 29, the calculated void fractions and measured maximum spray angles and average velocities are compared to those obtained from standard discharges. Despite the potentially inaccurate measurements of M_{max} and u caused by the flying debris from the explosive cartridges, the very low calculated void fractions based on the release of a cold agent, when compared to the standard discharges, indicate that the liquid phase still constitutes a significant volume fraction at a location ~ 1.4 m downstream from the vessel exit. This appears to be consistent with the fact, based on droplet evaporation theory (Kanury, 1977), that the liquid agent droplets, formed as a result of flashing, vaporize much slower when the initial droplet temperature is much closer to or lower than its normal boiling point than the droplets whose initial temperature is much higher than its normal boiling point, as in the case of a standard discharge. The average velocities of cold agent discharges are much slower than those of standard discharges, and there is also a significant, in some cases a factor of two, reduction in the maximum spray angle for cold agent discharges. The observations are very similar to the critical discharges of a pure liquid under different degrees of subcooling (Celata *et al.*, 1982, 1983) in that the spray angle decreases with increasing liquid subcooling.

From the high-speed movies, the spray appearance, other than the spray angle, of a hot-agent discharge is similar to that of a standard discharge spray. Figures 58, 59, 60, and 61 compare the internal pressure traces for standard discharges of CF₃Br, HFC-125, FC-218, and CF₃I to high temperature discharges using a Kidde-Graviner valve. Note that the temperatures in these figures are the measurements from the thermocouple initially located in the liquid phase. In Figures 58 and 59, the high temperature curves suggest the occurrence of degassing, thus implying that the critical points of the agent/nitrogen mixtures may not have been reached; otherwise smooth pressure decay curves of supercritical fluid discharges should have been observed, as in Figure 60 for FC-218. Note that the calculated mixture critical points from the PROFISSY code are very close to (slightly lower than) the two high temperatures used in Figures 58 and 59. However, since there is no mixing to ensure thermal equilibration between the liquid and vapor phases during heating, a temperature gradient in the vessel exists. Therefore, it is not possible to know precisely the temperatures of the mixtures inside

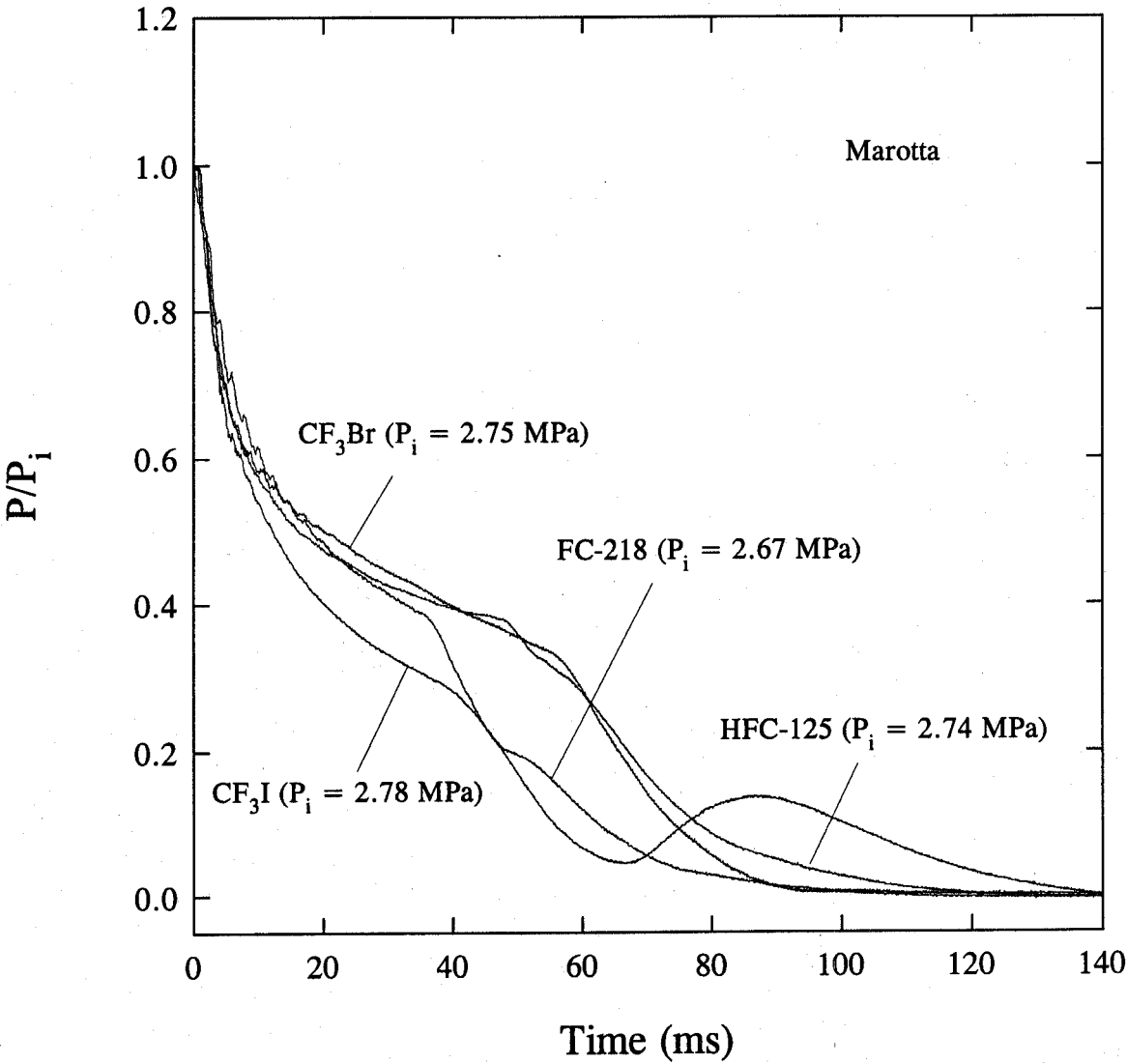


Figure 46. Comparison of the pressure decay curves during discharges using a Marotta valve under low initial charge pressures.

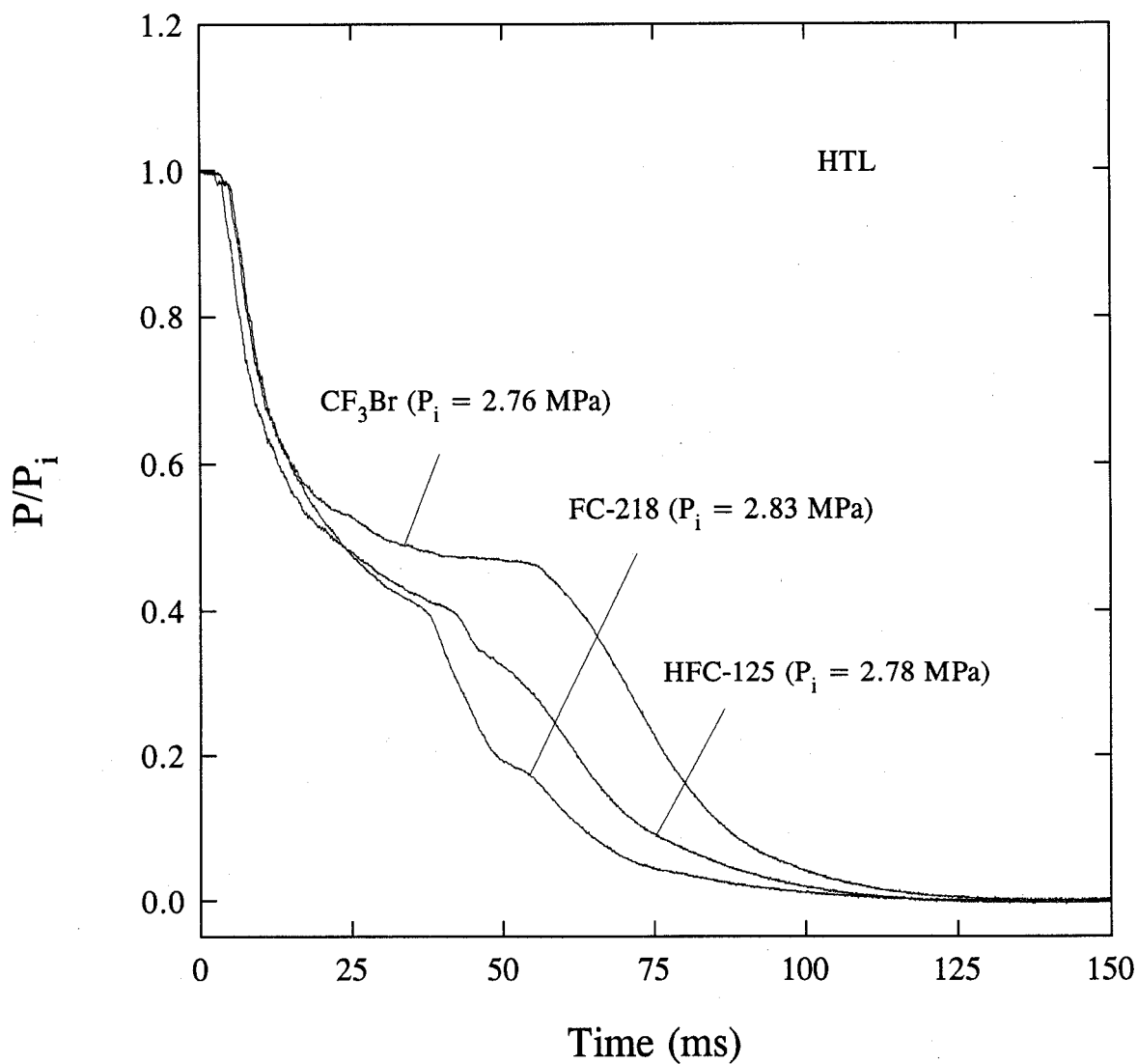


Figure 47. Comparison of pressure decay curves during discharges using a HTL valve under low initial charge pressures.

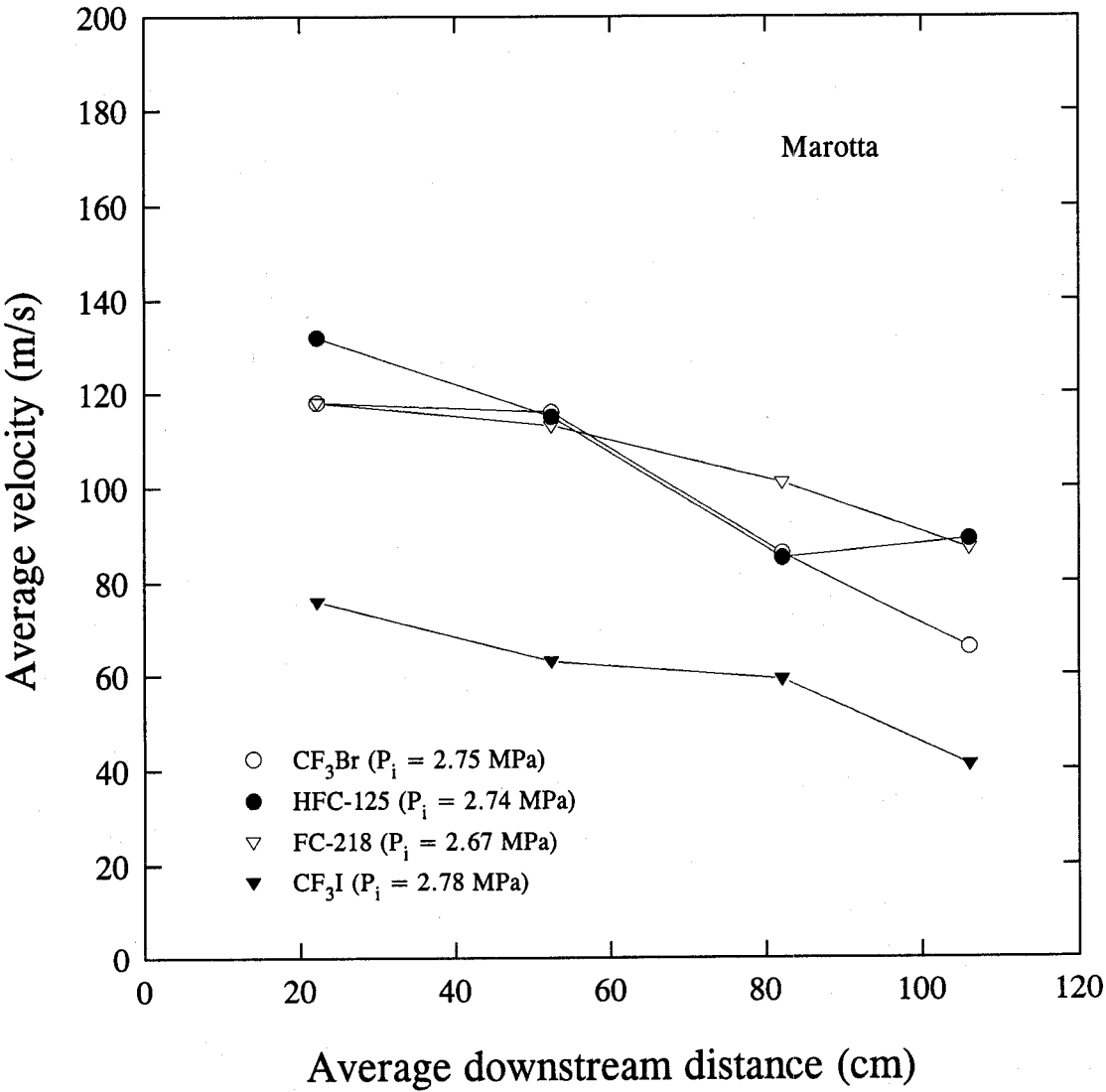


Figure 48. Average downstream velocities during discharges using a Marotta valve under low initial charge pressures.

Table 25. Calculated void fractions and measured maximum spray angles (discharges with $P_i \sim 2.75$ MPa)

Agent	Mass (g)	u (m/s)	M_{max} (MPa)	α	Maximum spray angle
CF_3Br^*	586	75	1.19	0.90	135°
HFC-125*	448	73	1.37	0.83	140°
FC-218*	442	85	0.22	0.99	136°
CF_3I^*	725	47	1.80	0.66	127°
CF_3Br^{**}	586	77	1.14	0.91	107°
HFC-125**	433	88	2.41	0.80	140°
FC-218**	438	78	0.58	0.94	123°
FC-218**	450	77	0.69	0.93	115°

* Marotta valve

** HTL valve

the vessel. On the contrary, in the case of FC-218, the achievable temperature, dictated by the working pressure of the vessel, in the experiment is much higher (at least 20 °C) than the calculated mixture critical point. Despite the existence of a temperature gradient, it is reasonable to expect that the condition inside the vessel in this case may still reach supercritical.

In Figures 58 and 59, the degassing process can be partly explained using homogeneous nucleation theory. The differences in the nucleation pressures (at which the plateaus occur) observed in the standard and high temperature cases can be attributed to differences in the thermodynamic pathways that lead to the metastable states (at which homogeneous nucleation occurs) of the mixtures from their initial states. In the standard discharges, the pathways are likely to be isothermal depressurization, whereas in the high temperature discharges, due to the temperature gradients inside the vessel the pathways are very complicated. For the purpose of illustration, if one assumes the pathways in the high temperature cases to be isentropic (not an unrealistic assumption), then the homogeneous nucleation pressures can be lower (possibly in this case) or higher than those observed during isothermal decompression, depending on the initial entropies of the mixture (Kim-E and Reid, 1983). The occurrence of a plateau instead of an observable pressure recovery in the figures could be due to the resultant effect of the rate of degassing and the rapid discharge rate.

Contrary to the standard discharges, the high temperature result of CF_3I in Figure 61 indicates some degree of degassing, evident from the occurrence of a plateau in the pressure trace. Note that the temperature used in the test is still below the calculated mixture critical point. If one recalls that the homogeneous nucleation pressure under standard discharge conditions was calculated to be negative (*i.e.*, in tension), no degassing was observed in the standard discharges of CF_3I . The occurrence of degassing in the high temperature discharge can be explained based on the different thermodynamic pathways leading to the metastable states as discussed above in the cases of CF_3Br and HFC-125. That is, in this case, the homogeneous nucleation pressure of a high temperature discharge is higher (positive) than that (negative) of a standard discharge. Note also that the *disappearance* of the pressure rebound, an artifact, at the end of the high temperature discharge in Figure 61, implying that temperature has an important role in the performance of the dynamic pressure transducer.

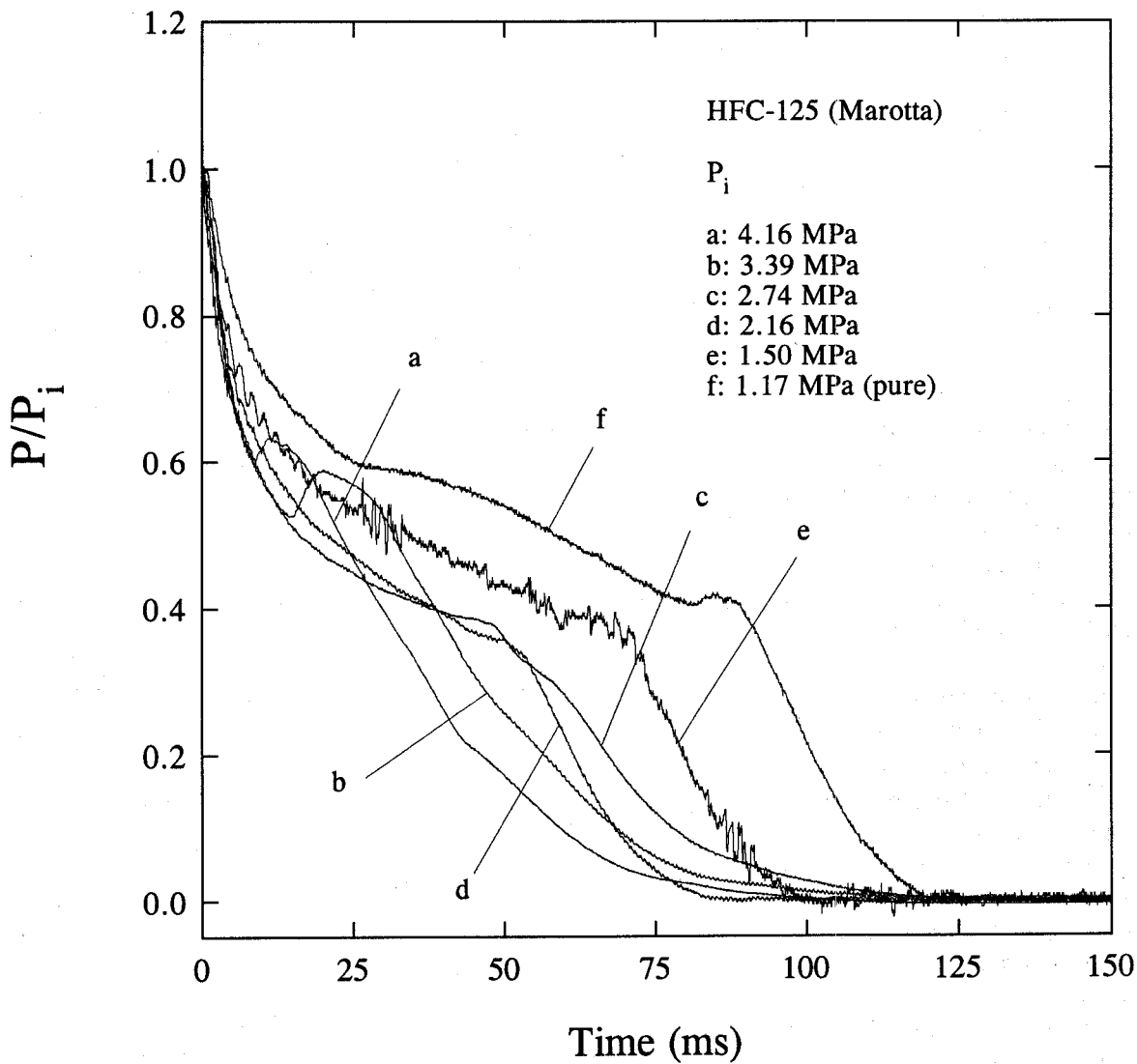


Figure 49. Comparison of pressure decay curves during discharges of HFC-125 using a Marotta valve under various initial charge pressures.

Table 26. Calculated homogeneous nucleation pressure (P_h) at T under various initial charge pressures for HFC-125

Mass (g)	T (K)	P_i (MPa)	P_h (MPa)	P_h/P_i
428	294	4.16	1.76	0.42
456	294	3.39	1.02	0.30
448	294	2.74	0.39	0.14
454	294	2.16	---	---
454	294	1.50	---	---
453	294	1.17	---	---

A comparison of the average spray dispersion velocities for all the agents studied in the standard and high temperature discharges is given in Figure 29, and CF_3I again exhibits the slowest velocities. For the same agent, the measured dispersion velocities *nearest* to the valve exit are higher due to higher initial vessel pressure as a result of higher temperature than those measured in the standard discharges.

The measured maximum spray angles of standard and high temperature discharges using a Kidde-Graviner valve are compared in Table 30. The void fractions are not calculated and are not listed in Table 30 because an estimate of a representative downstream temperature cannot be made in the high temperature discharges. For the same agent, the maximum spray angle is smaller in the standard discharges than in the high temperature discharges. The very low values of the maximum downstream dynamic pressures in the case of high temperature discharges of FC-218 also provide some evidence that FC-218 was discharged as a supercritical fluid (gas) at the temperature of interest.

8.4.3.10 Effect of Vessel Orientation. Based on visual observations from the high-speed movies, the direction of vessel discharge does not generally seem to affect the spray appearance *at* the squib exit although the sprays resulted from vertically upward discharges are narrower downstream. Figures 62, 63, and 64 show snapshots taken at the same instant (5 ms after the activation of the squib) of vertically downward and upward, and horizontal discharges of HFC-125 using HTL squibs. Figure 65 compares the pressure decay curves during discharges of HFC-125 using HTL squibs under various discharge orientations. Two important features are noted in the figure. First, irrespective of the discharge orientation and as long as the initial conditions (*i.e.*, total pressure, initial temperature, amount of agent) remain the same in all cases, the degassing occurs approximately at the same P/P_i although the time to reach P/P_i differs. This is not surprising because bubble nucleation should be independent of any direction relative to the gravitation vector. Second, the discharge rates do not seem to depend strongly on the orientation of the vessel, a contrast to the observations made in Grosshandler *et al.* (1994). In that study, nitrogen was in contact with the agent for a very short time before the agent was discharged; however, in this work nitrogen was fully saturated with the agent before the experiments began. The dissolved nitrogen clearly plays an important role in the situation where the discharge orientation is a limiting factor in the application. However, extreme care should be exercised when one tries to extrapolate this observation to other fill conditions. For example, in the situation where the initial liquid level is very low (a case which may not be encountered in practical applications) and the discharge orientation is upwards, the maximum swelling of the liquid level may

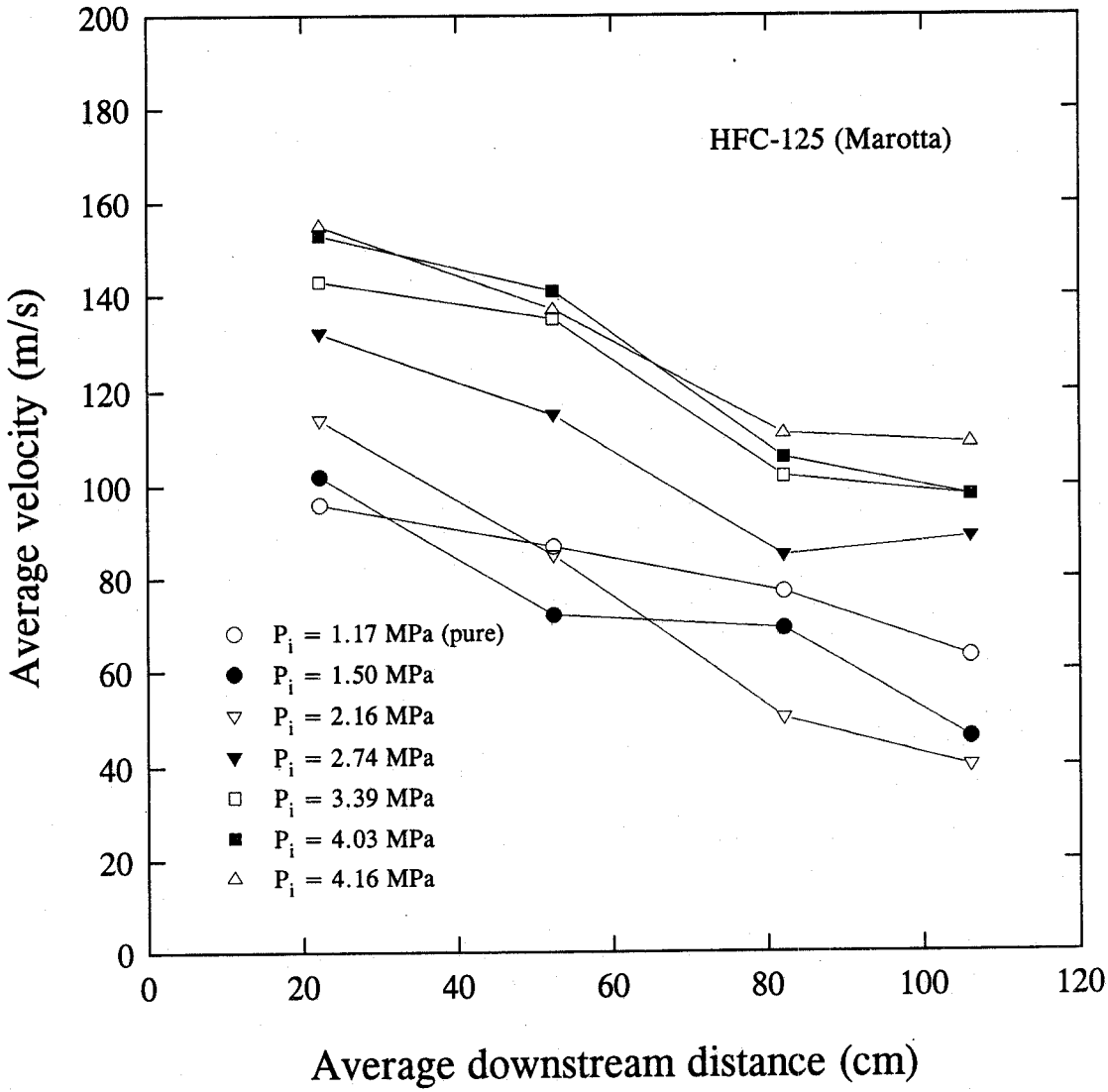


Figure 50. Average downstream velocities during discharges of HFC-125 using a Marotta valve under various initial charge pressures.

Table 27. Calculated void fractions and measured maximum spray angles of HFC-125 discharges under various initial charge pressures (using a Marotta valve)

Mass (g)	P_i (MPa)	u (m/s)	M_{max} (MPa)	α	Maximum spray angle
438	4.03	114	0.84	0.96	110°
428	4.16	104	0.41	0.98	---
456	3.39	121	2.41	0.90	124°
448	2.74	73	1.50	0.83	140°
454	2.16	60	2.34	0.57	133°
454	1.50	67	2.30	0.67	115°
453	1.17	65	2.30	0.64	102°

not reach the top of the vessel during depressurization. In this case, a very *high* quality two-phase mixture is expected to be discharged from the vessel. Therefore, it is recommended that irrespective of the fill conditions, the discharge orientation should be downwards so that a very low quality two-phase mixture can be obtained.

Table 31 summarizes the measured maximum spray angles and the calculated void fractions. Because of the flying debris resulted from the cartridge explosion, it is very difficult to make any reasonably meaningful conclusions in the calculated void fractions. Within the uncertainty, the measured maximum spray angles appear to be similar in all cases; however, the overall appearance of the vertically upward discharge spray is different (less dispersed) from that of the standard discharge spray (*cf.* Figures 62 and 63).

8.4.3.11 Effect of Partial Nitrogen Saturation. Figures 66 and 67 compare respectively the discharge characteristics of complete nitrogen saturation (standard discharge) to partial nitrogen saturation for HFC-125 and FC-218 at $P_i \sim 4.12$ MPa and room temperature using a Marotta valve. In the two figures, the degassing of nitrogen is not noted when it is only partially saturated with the agent. Another interesting observation is that the discharge rate is *slower* when the agent is completely saturated with nitrogen.

Figures 68, 69, 70, and 71 compare the two cases under a lower initial total pressure ($P_i \sim 2.75$ MPa) for CF_3Br , HFC-125, FC-218, and CF_3I respectively. No degassing is noted in either case, and the discharge rate is again slower in the case of complete nitrogen saturation. Note that in Figure 71, the pressure rebound at the end of the discharge is an artifact from the pressure transducer, as discussed above. The reason for not recording such pressure rebound in one of the runs is not known. When a HTL valve was used for similar tests (complete *versus* partial), similar trends were observed with regard to the degassing and the discharge rates.

Figures 37, 38, 39, 40, 41, 42, and 43 also display the average downstream spray velocities for the various agents studied when nitrogen is partially saturated with the agent. Compared to the case of complete nitrogen saturation, the average spray velocities *nearest* to the valve exit are consistently slower.

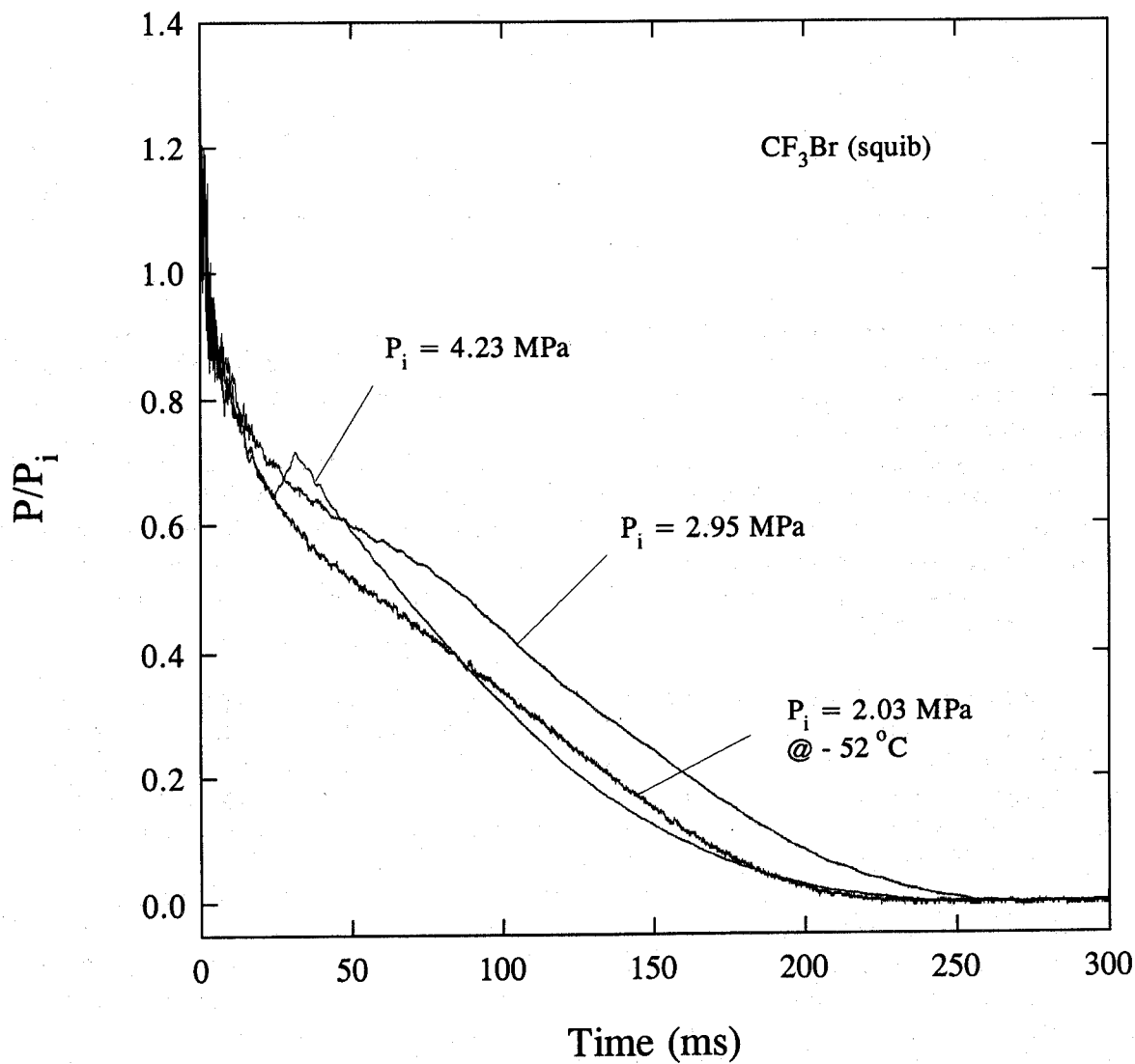


Figure 51. Comparison of pressure decay curves during discharges of CF₃Br using HTL squibs under various initial conditions.

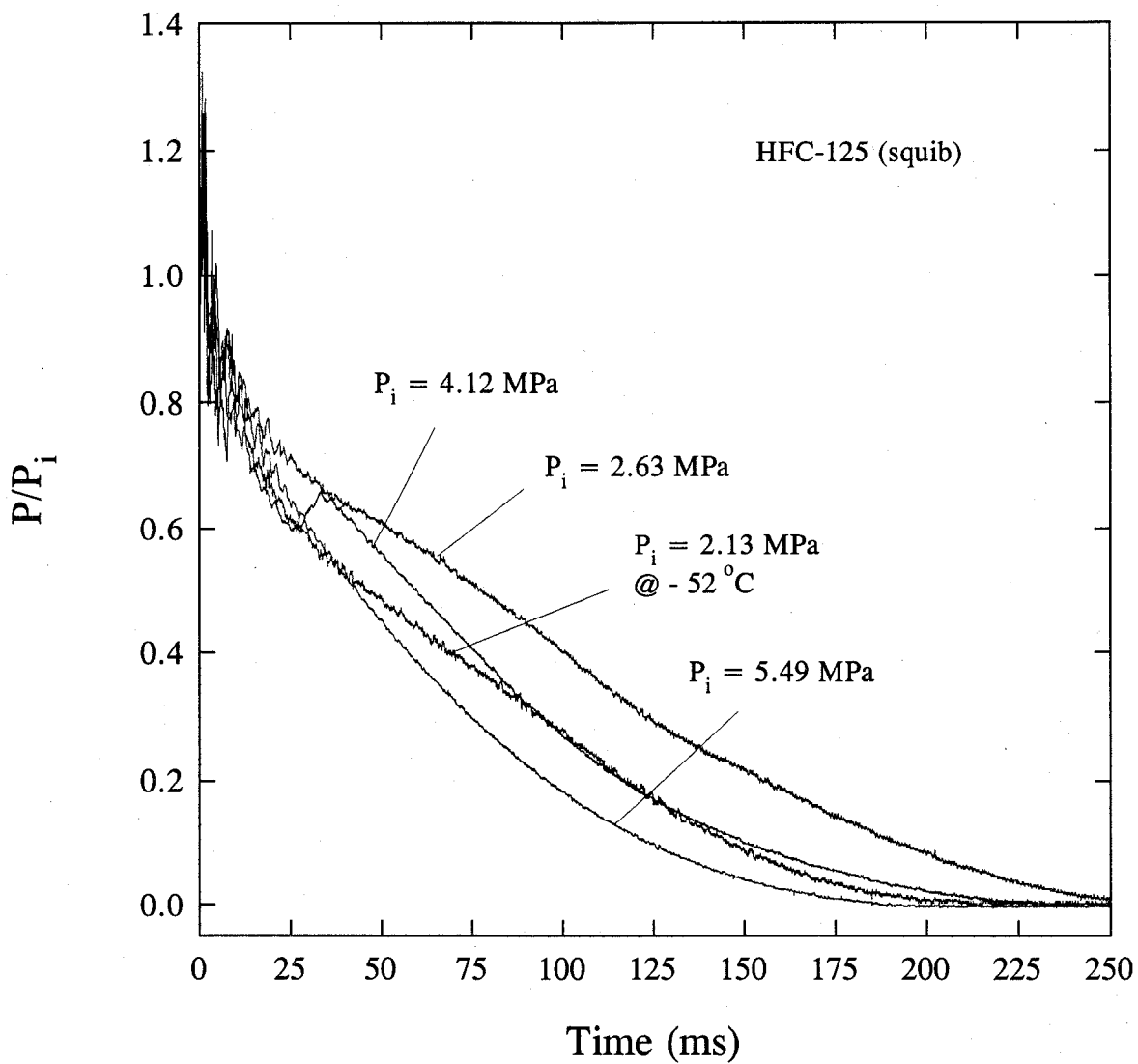


Figure 52. Comparison of pressure decay curves during discharges of HFC-125 using HTL squibs under various initial conditions.

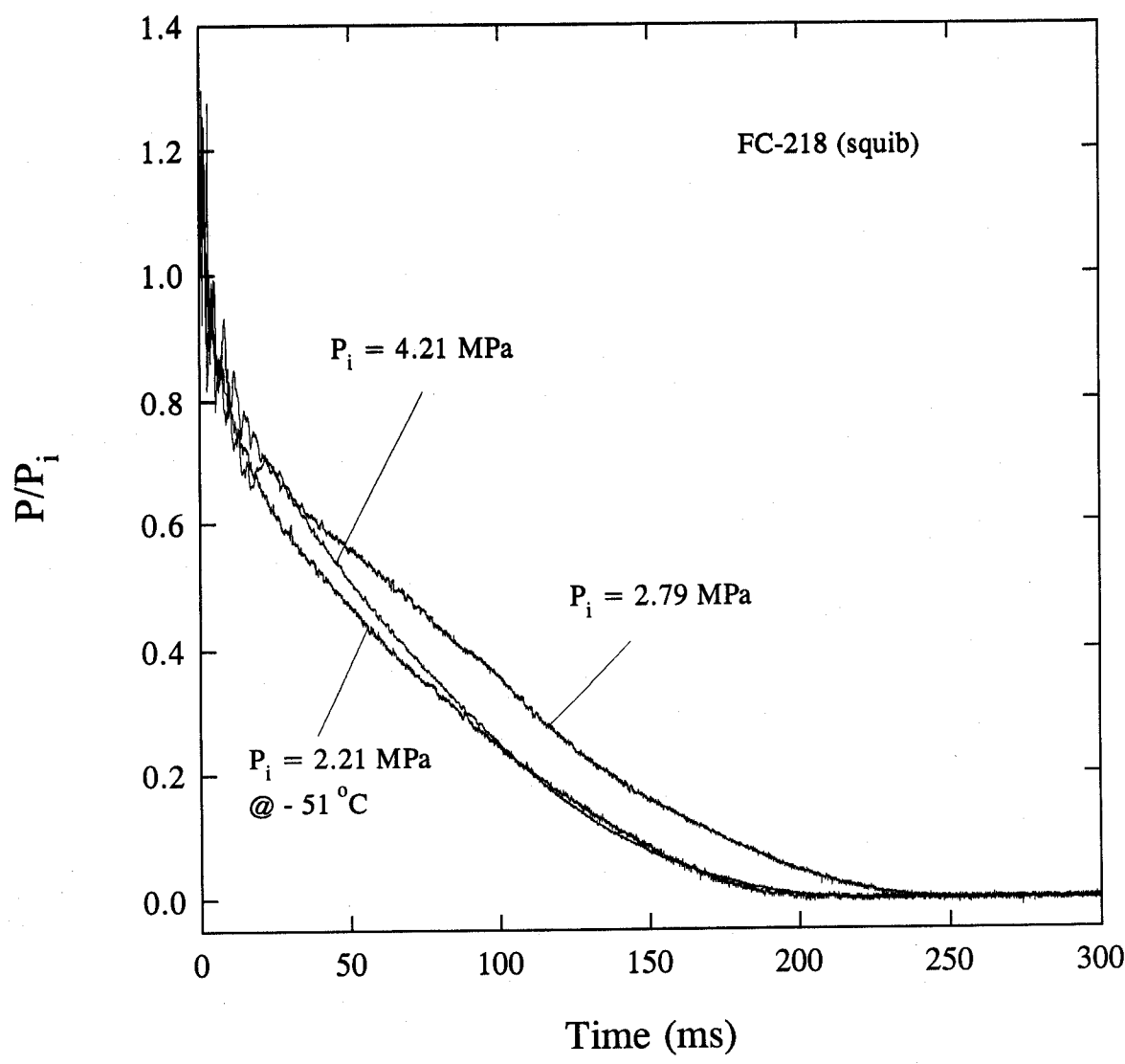


Figure 53. Comparison of pressure decay curves during discharges of FC-218 using HTL squibs under various initial conditions.

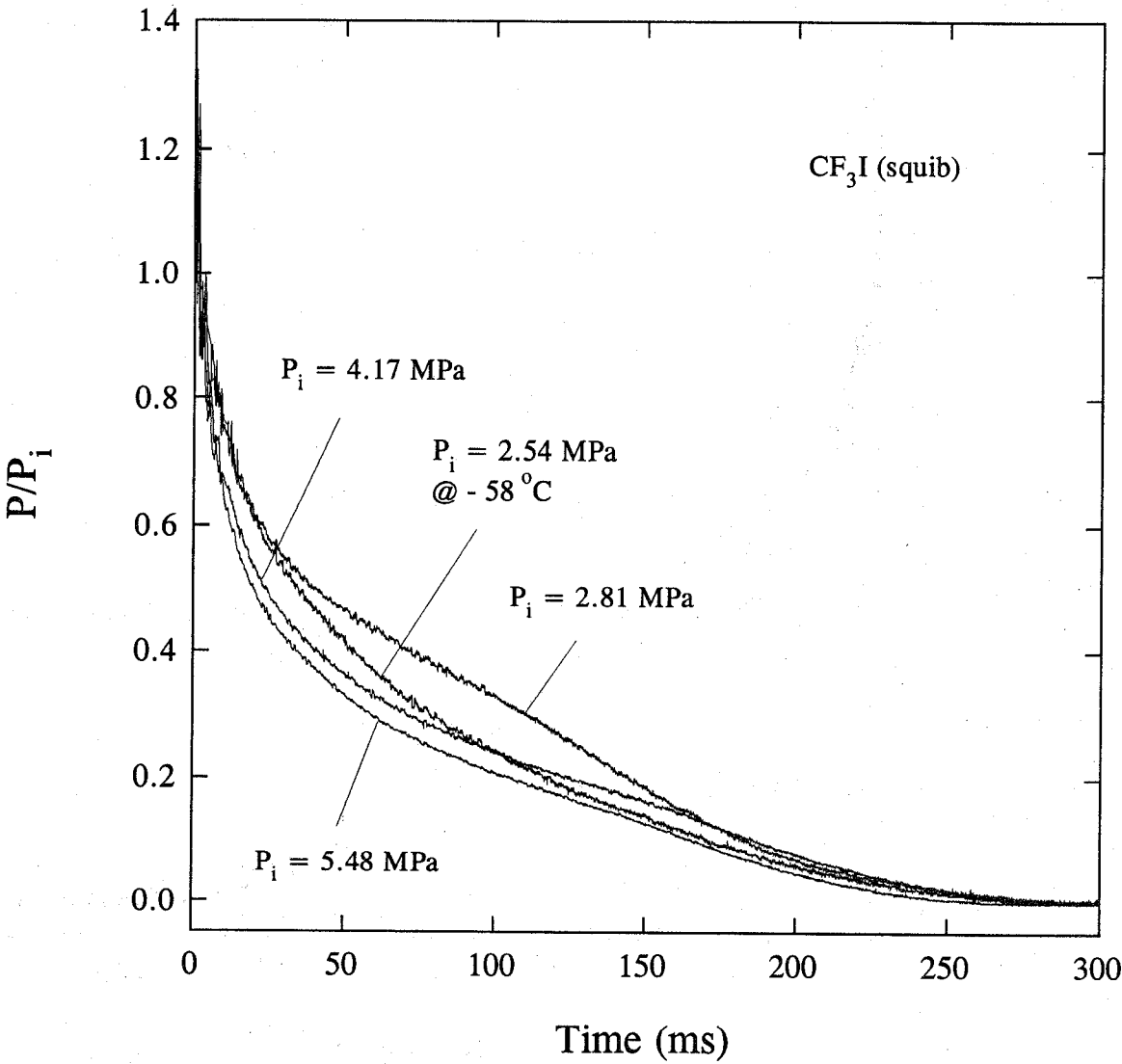


Figure 54. Comparison of pressure decay curves during discharges of CF_3I using HTL squibs under various initial conditions.

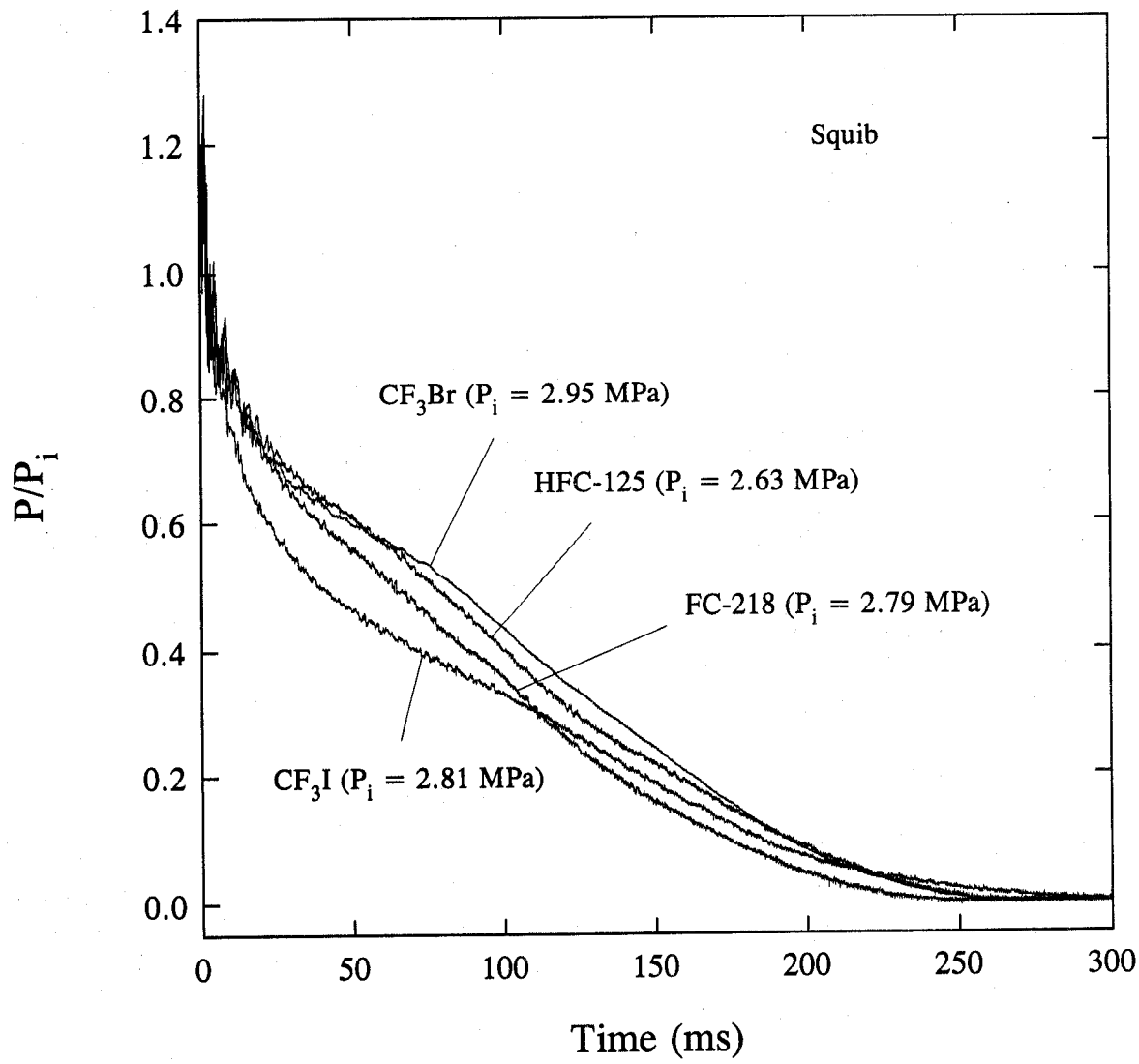


Figure 55. Comparison of pressure decay curves during discharges using HTL squibs at low initial charge pressure.

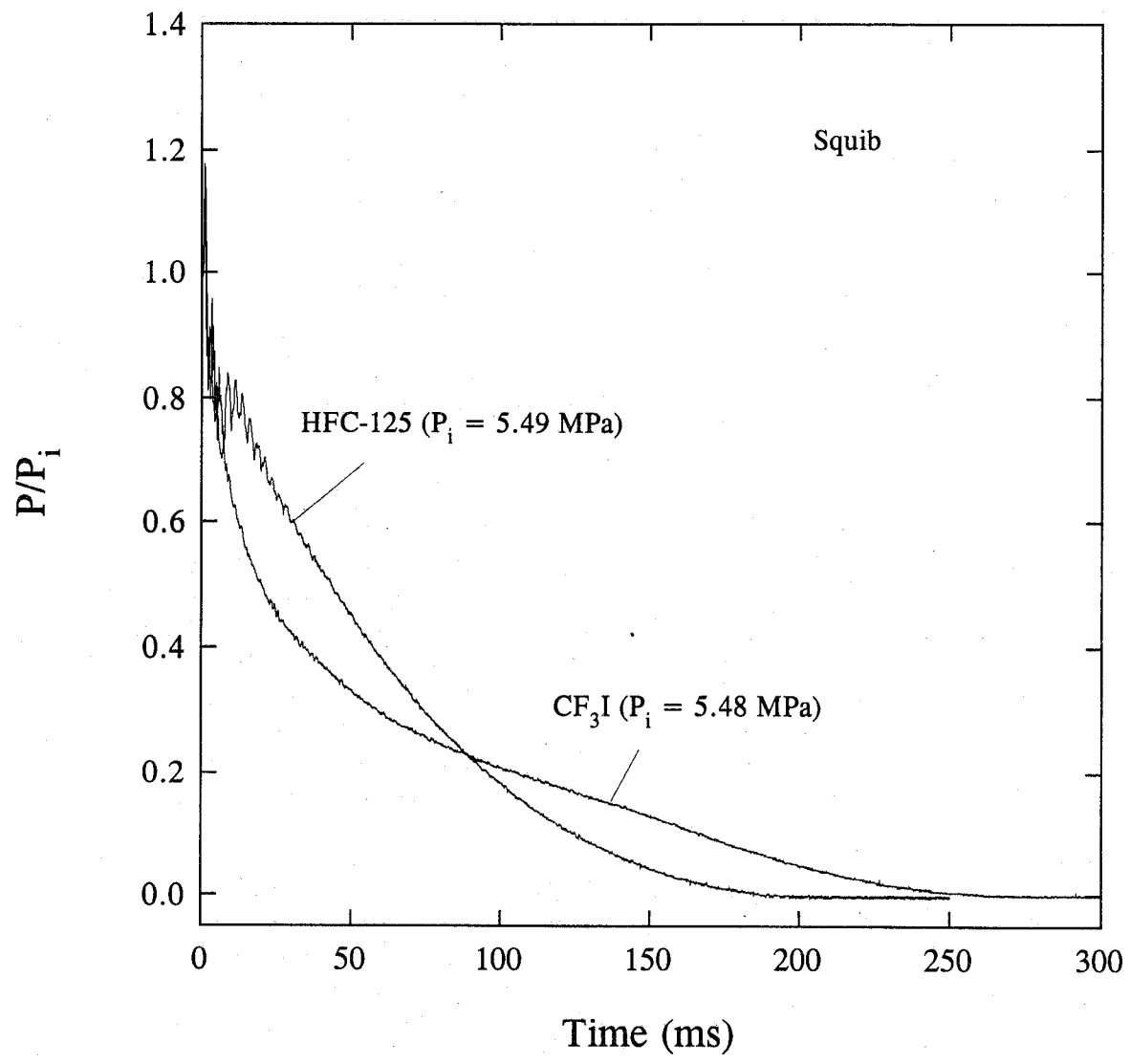


Figure 56. Comparison of pressure decay curves during discharges using HTL squibs at high initial charge pressure.

Table 28. Calculated void fractions and measured maximum spray angles under various initial charge pressures (using HTL squibs)

Agent	Mass (g)	P_i (MPa)	u (m/s)	M_{max} (MPa)	α	Maximum spray angle
CF ₃ Br	581	4.23	93	2.03	0.89	140°
CF ₃ Br	586	2.95	71	2.63	0.74	136°
HFC-125	458	5.49	93	2.22	0.83	145°
HFC-125	454	4.12	89	2.37	0.81	131°
HFC-125	453	4.14	95	2.61	0.81	146°
HFC-125	454	2.63	69	2.24	0.69	140°
FC-218	476	4.21	83	1.72	0.84	144°
FC-218	458	2.79	69	1.68	0.77	147°
CF ₃ I	773	5.48	79	1.49	0.90	---
CF ₃ I	773	4.17	62	1.52	0.84	136°
CF ₃ I	753	2.81	47	1.39	0.74	130°

8.4.3.12 Effect of Vessel Geometry. In all the tests conducted, no qualitative differences in the discharge behaviors were observed when the cylindrical vessel equipped with a Marotta, HTL, or Kidde-Graviner valve or a spherical vessel equipped with a HTL squib was used. Although no experiments have been performed using cylindrical and spherical bottles with *identical* internal volumes due to logistics in the experimental hardware design, it is expected that the discharge behaviors should also be strikingly similar, based on the following arguments. First, nitrogen degassing should be independent of the vessel geometry assuming that the process can be explained according to homogeneous nucleation theories. As discussed above, the homogeneous nucleation theories seem to provide a reasonably good, qualitative prediction of the occurrence of the degassing process. Second, the discharge characteristics of all the agents studied, using a cylindrical or spherical vessel with a slightly different internal volume and different release mechanism, are very similar. Third, the discharge process depends mainly on the ullage pressure, and pressure is an intensive variable and independent of the shape of the vessel; therefore, the effect of vessel geometry will likely have an insignificant effect on the discharge rate. It should be pointed out that the *final* drainage of the remaining liquid through a valve attached to the bottom of one of the two flat heads of a cylindrical vessel and from a spherical vessel will be different. However, in practical vessel design, a cylindrical pressure vessel does not normally have two flat heads, but rather has two hemispherical heads. Consequently, the final drainage problem is expected to be dynamically similar to that of a spherical vessel.

8.4.3.13 Model Predictions. Based on the above discussion and experimental observations, a model that predicts the discharge times of an agent under various experimental conditions is proposed. The intent here is to determine whether the proposed model can provide similar qualitative trends when compared to the experimental observations. The major difference between the proposed model

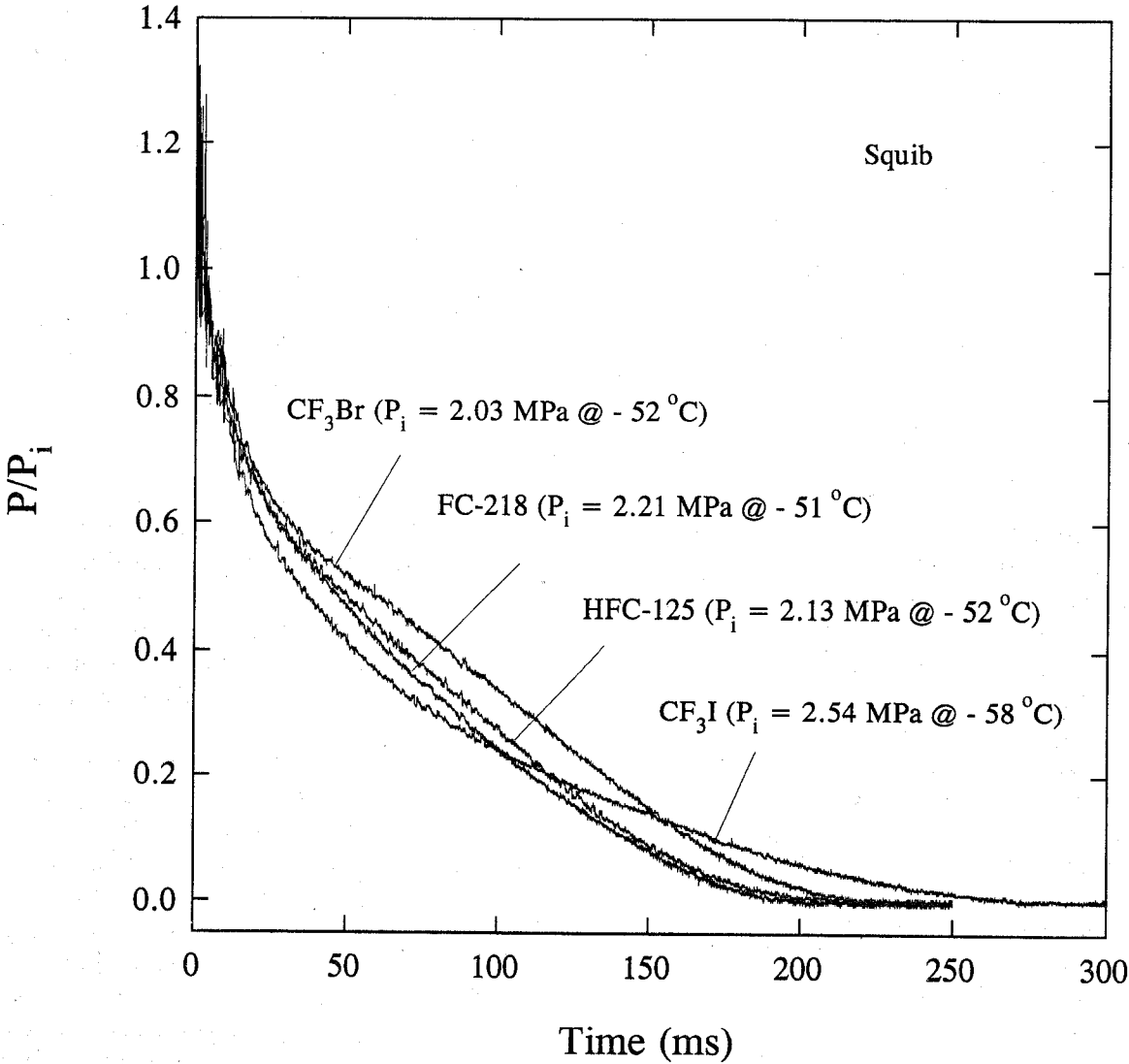


Figure 57. Comparison of pressure decay curves during cold agent discharges using HTL squibs.

Table 29. Calculated void fractions and measured maximum spray angles of standard and cold agent discharges using HTL squibs

Agent	Mass (g)	T (°C)	P_i (MPa)	u (m/s)	M_{max} (MPa)	α	Maximum spray angle
CF ₃ Br	581	21	4.23	93	2.03	0.89	140°
CF ₃ Br	584	-52	2.03	43	2.25	0.39	82°
HFC-125	454	21	4.12	89	2.37	0.81	131°
HFC-125	453	22	4.14	95	2.61	0.81	146°
HFC-125	457	-52	2.13	47	2.45	0.27	73°
HFC-125	455	-55	2.05	---	---	---	85°
FC-218	476	22	4.21	83	1.72	0.84	144°
FC-218	475	-51	2.21	47	2.00	0.41	70°
CF ₃ I	773	21	4.17	62	1.52	0.84	136°
CF ₃ I	771	-58	2.54	48	1.74	0.68	51°

and the model developed by Elliot *et al.* (1984) is how the process of degassing of dissolved nitrogen is treated. In Elliot's model (for CF₃Br discharge), there is no provision to determine whether degassing will or will not occur. The degassing of dissolved nitrogen is always assumed to occur, and the critical bubble size is fixed at 15 nm. Degassing may not occur when CF₃I is used or when the initial vessel pressure is below 4.12 MPa, as discussed above. Note that in Elliot's experiments, the total initial vessel pressures all exceeded 4.1 MPa. The proposed model, under certain assumptions, can predict the occurrence or the non-occurrence of degassing. In the following, the assumptions and the equations used in the model are presented.

The discharge configuration of the vessel is assumed to be vertically downward, *i.e.*, the liquid mixture will be discharged first, followed by the ullage vapor mixture. During discharge, no heat and mass transfer between the liquid and the vapor phases is assumed to occur. As discussed in Grosshandler *et al.* (1994), the liquid is assumed to undergo an isothermal depressurization during discharge, and the degassing of dissolved nitrogen is modeled by homogeneous nucleation theory, as described in Forest and Ward (1977). The occurrence of degassing is determined by comparing the ullage pressure to the calculated homogeneous bubble nucleation pressure during the liquid discharge period. If the ullage pressure at some instant in this time interval is equal to or less than the homogeneous nucleation pressure, degassing is assumed to occur. When no degassing is predicted by the homogeneous nucleation theory, *i.e.*, during the liquid discharge period the ullage pressure never goes below the homogeneous nucleation pressure, the discharge is modeled as a two-step process, a superheated liquid discharge followed by an emptying of ullage vapor. When degassing occurs, the model is formulated as a four-step process, a superheated liquid discharge followed by swelling of the liquid level due to degassing, a two-phase mixture discharge, and finally a vapor discharge.

The control volume under consideration is the ullage above the liquid. Since no heat and mass transfer is assumed to occur between the liquid and the vapor phases, the control volume is an adiabatic closed system. Furthermore, due to the rapidity of the discharge, the ullage expansion or

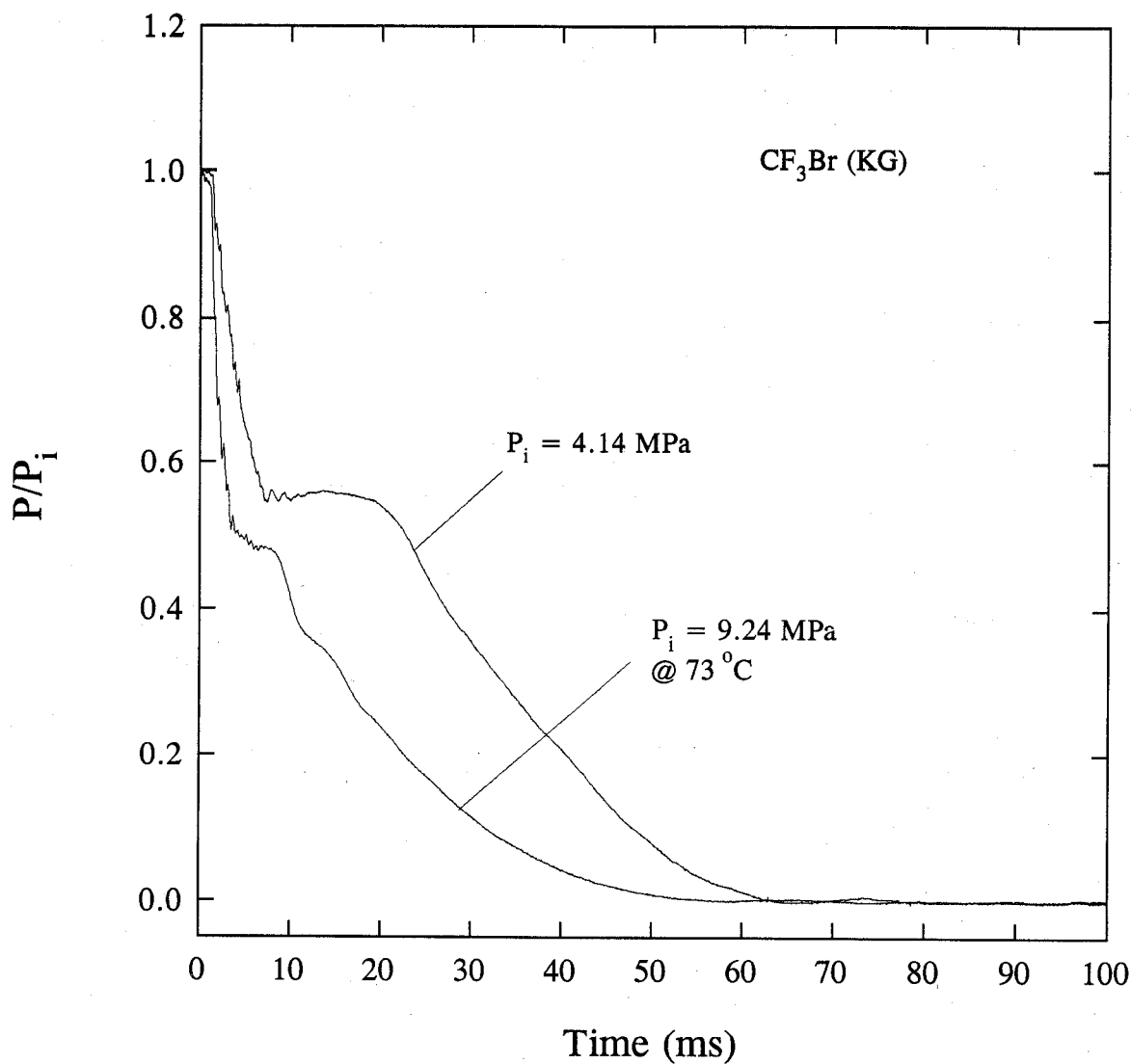


Figure 58. Comparison of pressure decay curves during discharges of CF_3Br using a Kidde-Graviner valve under two initial agent temperatures.

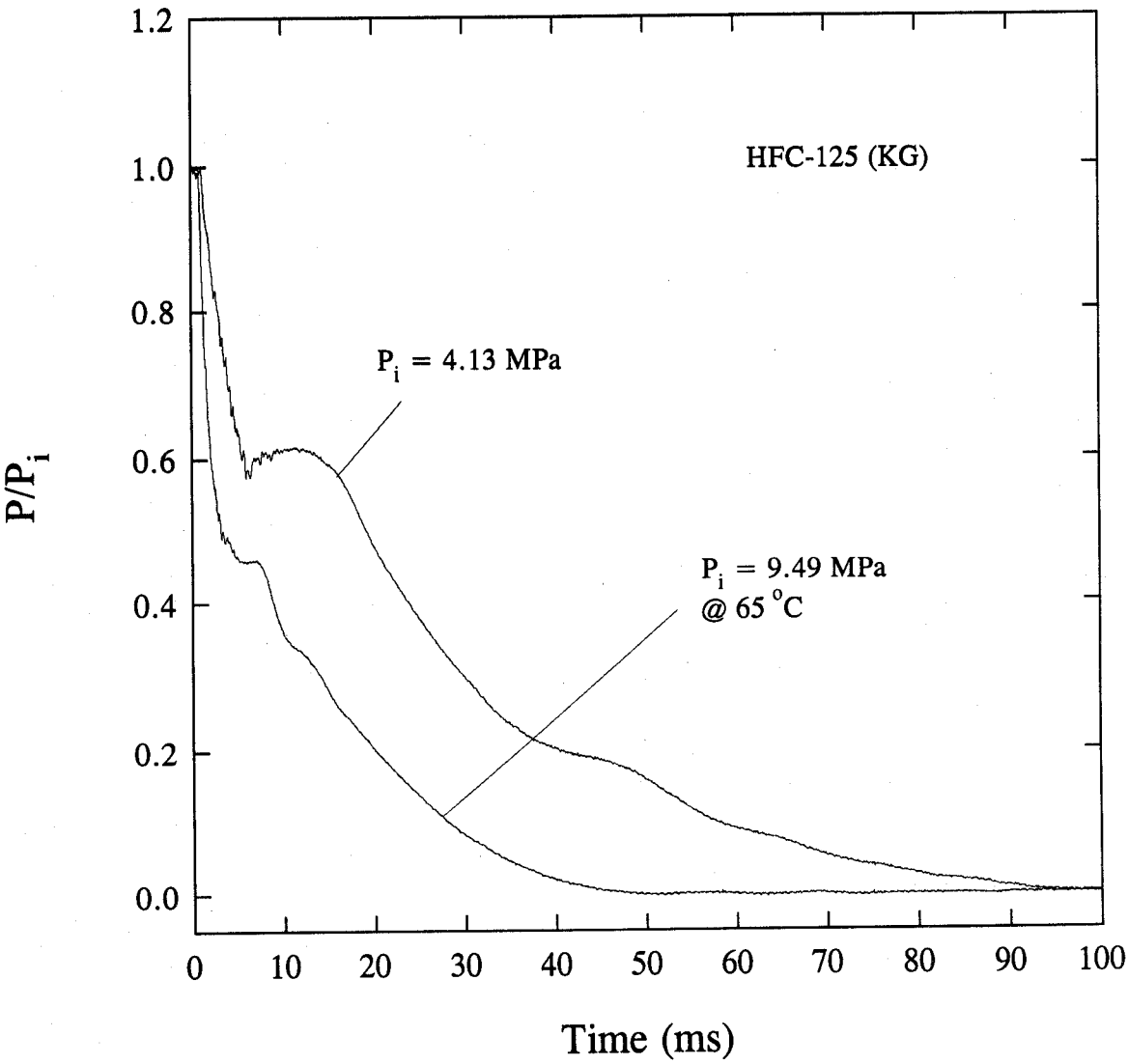


Figure 59. Comparison of pressure decay curves during discharges of HFC-125 using a Kidde-Graviner valve under two initial agent temperatures.

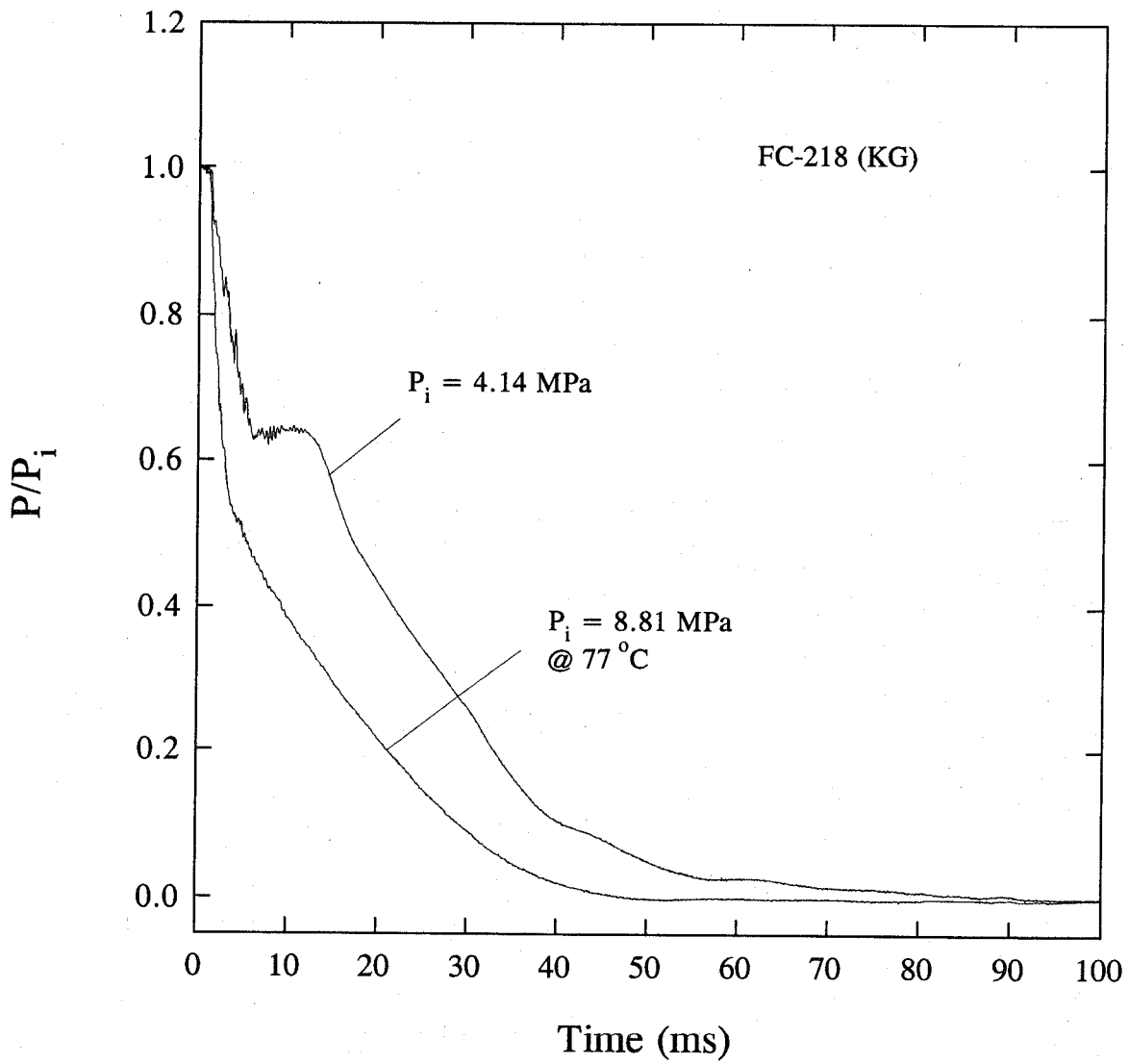


Figure 60. Comparison of pressure decay curves during discharges of FC-218 using a Kidde-Graviner valve under two initial agent temperatures.

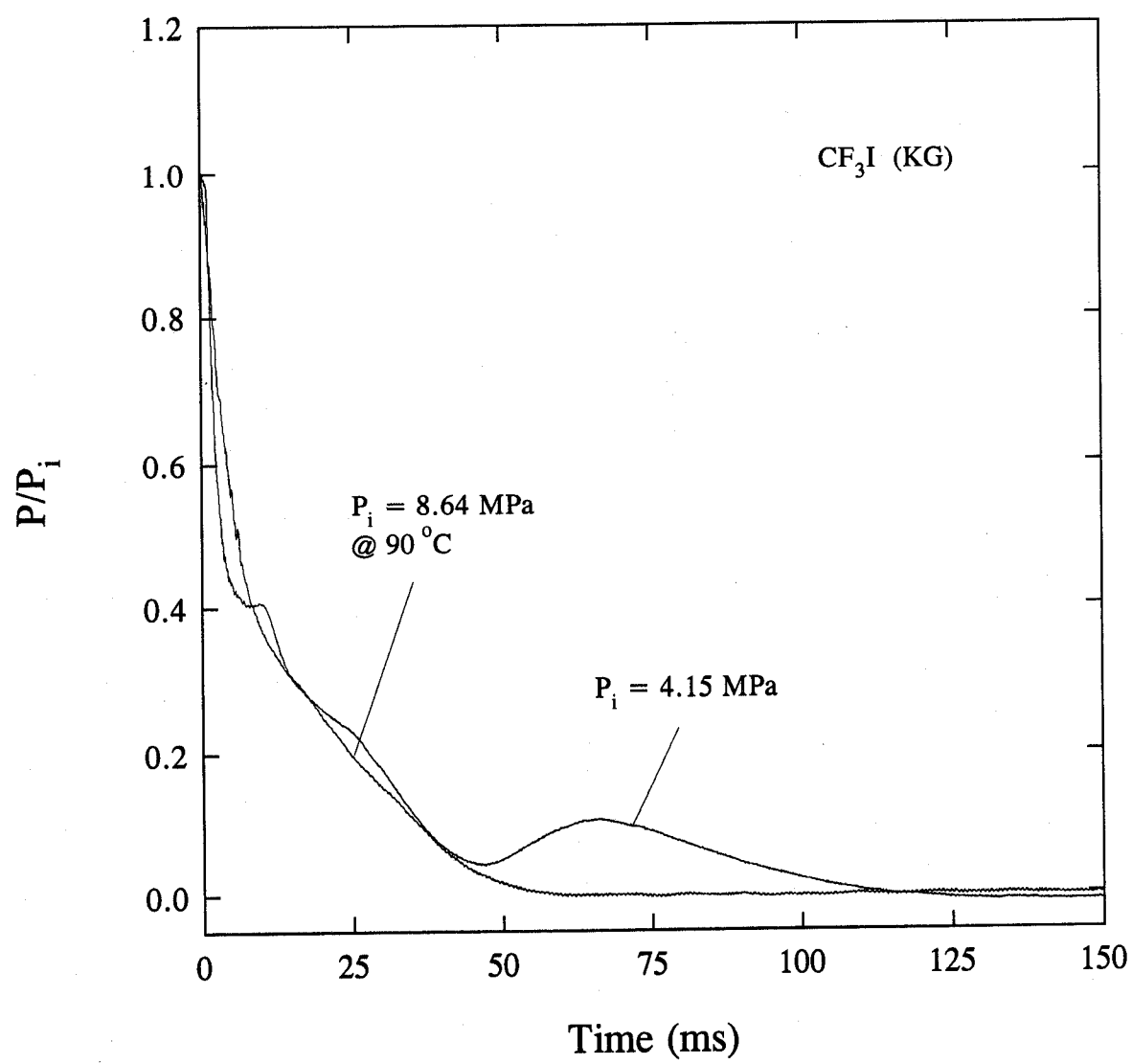


Figure 61. Comparison of pressure decay curves during discharges of CF_3I using a Kidde-Graviner valve under two initial agent temperatures.

Table 30. Comparison of measured maximum spray angles under standard and high temperature conditions using a Kidde-Graviner valve

Agent	Mass (g)	T (°C)	P_i (MPa)	u (m/s)	M_{max} (MPa)	Maximum spray angle
CF ₃ Br	625	21	4.14	89	1.28	132°
CF ₃ Br	620	73	9.24	106	1.84	167°
HFC-125	477	21	4.13	92	2.20	145°
HFC-125	481	70	9.10	114	1.05	180°
HFC-125	484	65	9.49	117	1.66	176°
FC-218	492	21	4.14	75	1.18	134°
FC-218	505	75	8.58	111	0.08	170°
FC-218	508	77	8.81	115	0.12	168°
CF ₃ I	800	21	4.15	54	1.21	152°
CF ₃ I	817	90	8.64	68	1.56	161°

momentary compression (caused by degassing) is assumed to be reversible. Therefore, the processes occurring in the ullage can be assumed to be *isentropic*. From the first law of thermodynamics for an isentropic process and assuming an ideal vapor phase,

$$PV^\gamma = constant \quad , \tag{26}$$

where γ is the ratio of the constant pressure and volume heat capacities of the vapor mixture, P is the ullage pressure, and V is the ullage volume. Since nitrogen is the dominant species in the vapor phase, the γ of nitrogen with a value of 1.4 is used in the model calculations. If a time derivative of Equation (26) is performed, then

$$\frac{dP}{dt} + \frac{P\gamma}{V} \frac{dV}{dt} = 0 \quad . \tag{27}$$

Before degassing, the initial saturated liquid agent/dissolved nitrogen mixture discharging through a sharp-edged orifice behaves in a completely metastable manner (Henry, 1979), and the discharge rate can be predicted using incompressible flow formulation. Assuming that the flow through the discharge

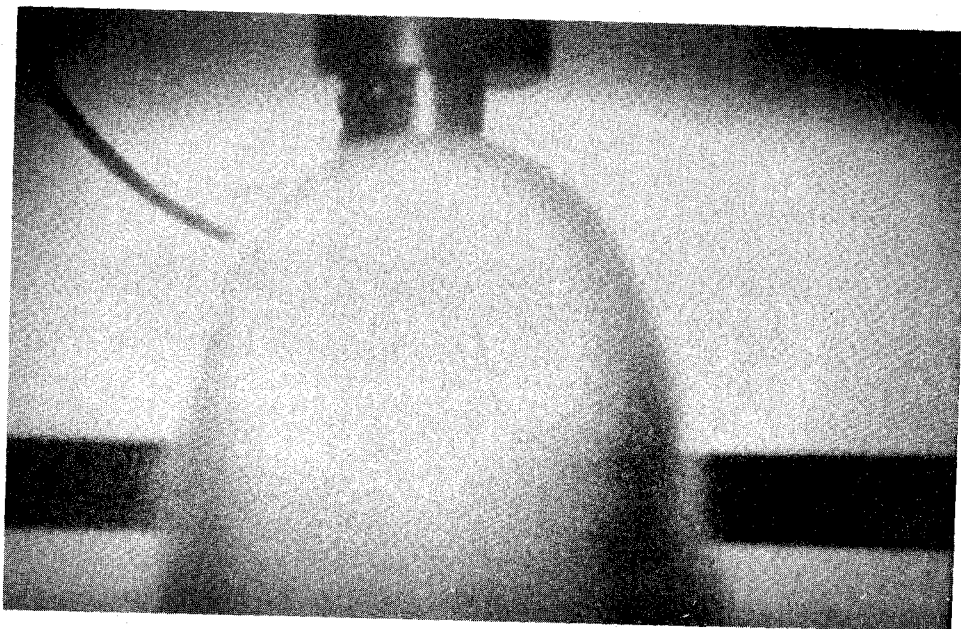


Figure 62. A snapshot of vertically downward discharge of HFC-125 (taken 5 ms after the activation of the squib).

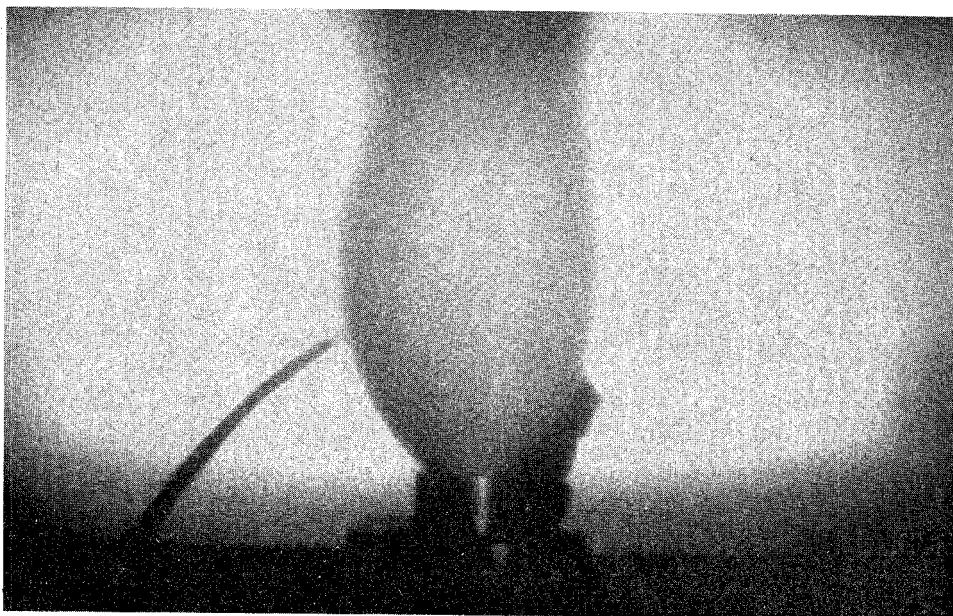


Figure 63. A snapshot of vertically upward discharge of HFC-125 (taken 5 ms after the activation of the squib).

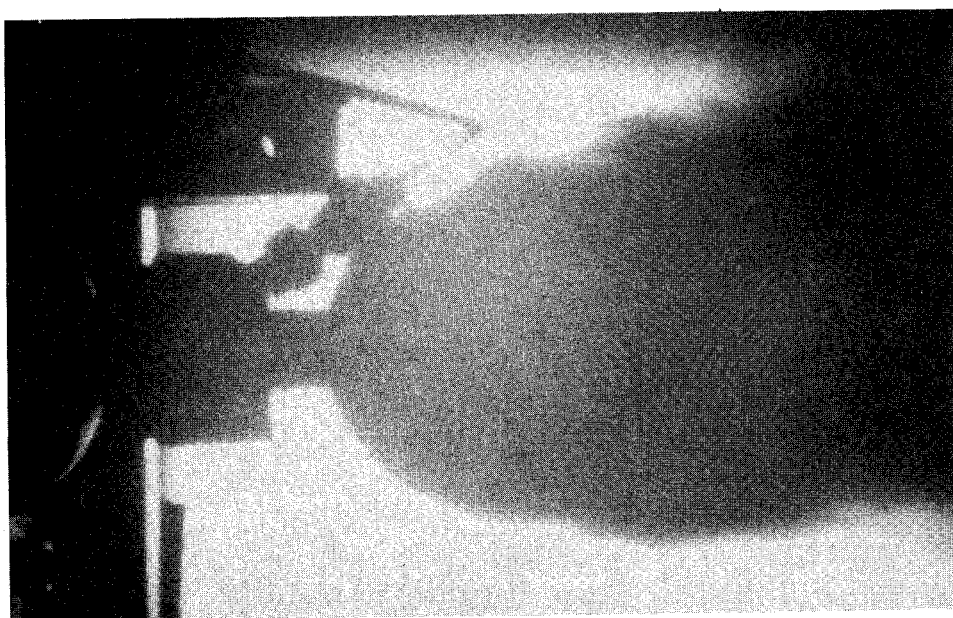


Figure 64. A snapshot of horizontal discharge of HFC-125 (taken 5 ms after the activation of the squib).

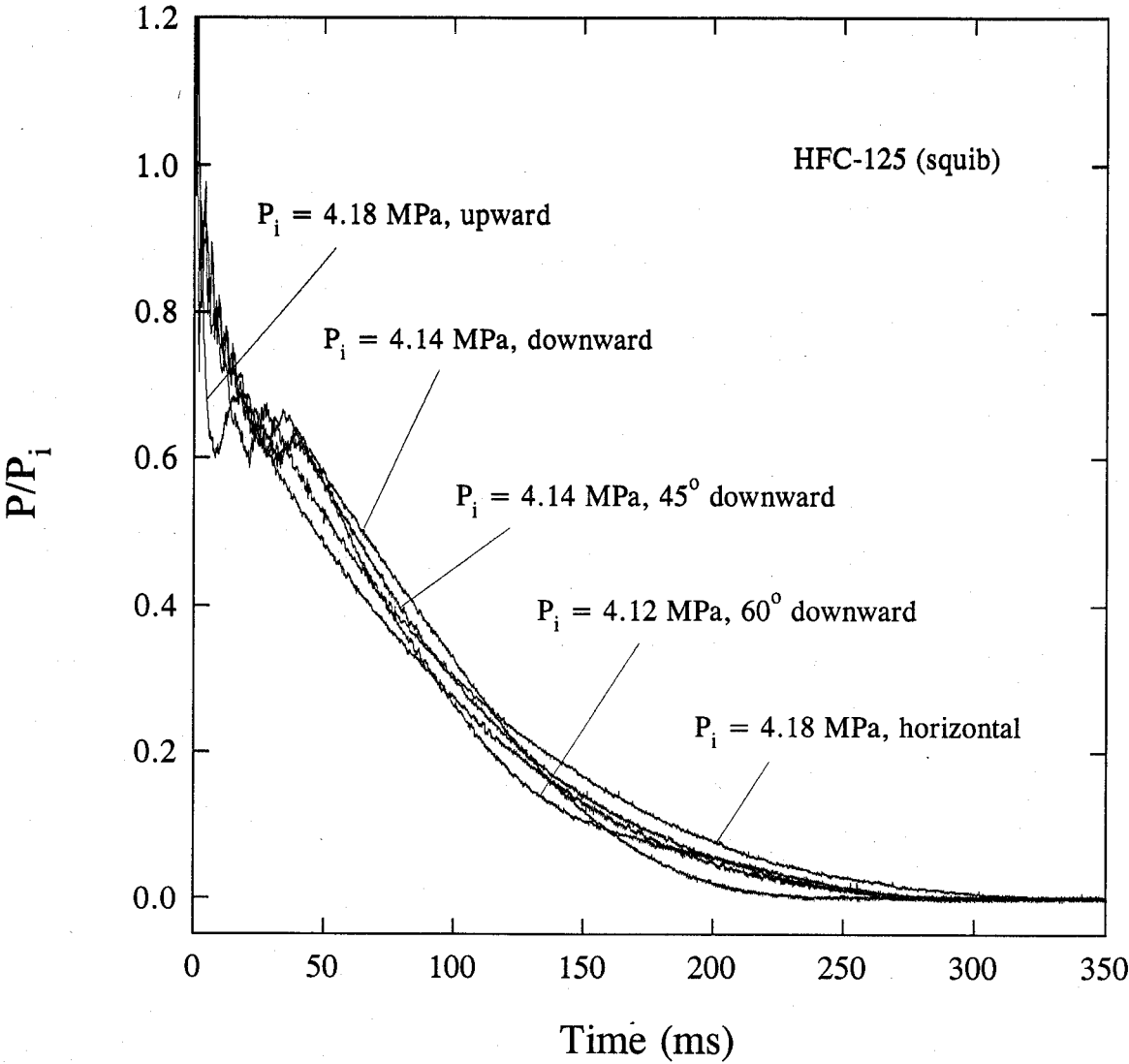


Figure 65. Comparison of pressure decay curves during discharges of HFC-125 using HTL squibs under various discharge orientations.

Table 31. Calculated void fractions and measured maximum spray angles of discharges of HFC-125 using HTL squibs at room temperature, $P_i \sim 4.12$ MPa, and different discharge orientations

Orientation	Mass (g)	u (m/s)	M_{max} (MPa)	α	Maximum spray angle
Vertically downward	454	89	2.37	0.81	131°
"	453	95	2.61	0.81	146°
Vertically upward	453	83	2.49	0.77	137°
Downward 45°	449	---	---	---	146°
Downward 60°	456	---	---	---	---
Horizontal	450	99	0.70	0.96	145°

valve can be approximated by an orifice flow of a superheated liquid, the rate of change of the ullage volume can be expressed in terms of the volumetric flow rate of the liquid as

$$\frac{dV}{dt} = C_d A \sqrt{\frac{2(P - P_a)}{\rho_{l,m}}} \quad (28)$$

where C_d is the discharge coefficient for the liquid, with the measured value found to be 0.61 in the literature (Henry, 1979), A is the opening of the orifice, P_a is the ambient pressure, and $\rho_{l,m}$ is the liquid mixture density. In writing Equation (28), quasi-steadiness is implicitly assumed, that is the discharge is treated as a steady-state process at any instant in time. In the calculations, the value of 0.61 was used for C_d , and the liquid mixture density was obtained from the computer program PROFISSY. Equations (27) and (28) were solved numerically using a fourth-order Runge-Kutta method (Carnahan *et al.*, 1969) to obtain the ullage pressure and volume as a function of time. At each time step, the calculated pressure was compared to the calculated homogeneous nucleation pressure in order to determine whether degassing occurred or not. In the case of degassing, the swelling of the liquid level is treated with the following simple model. At the onset of bubble nucleation, all the dissolved nitrogen is assumed to form bubbles with a critical radius, and any subsequent bubble growth and rise to the liquid surface is not considered in the formulation. That is all the bubbles, once formed, stay in the liquid. This approach was also taken by Elliot *et al.* (1984). According to Forest and Ward (1977) who assumed negligible effects of pressure and concentration of the dissolved nitrogen on the vapor pressure of the liquid and an ideal gas mixture inside the bubble, the critical bubble radius can be calculated as

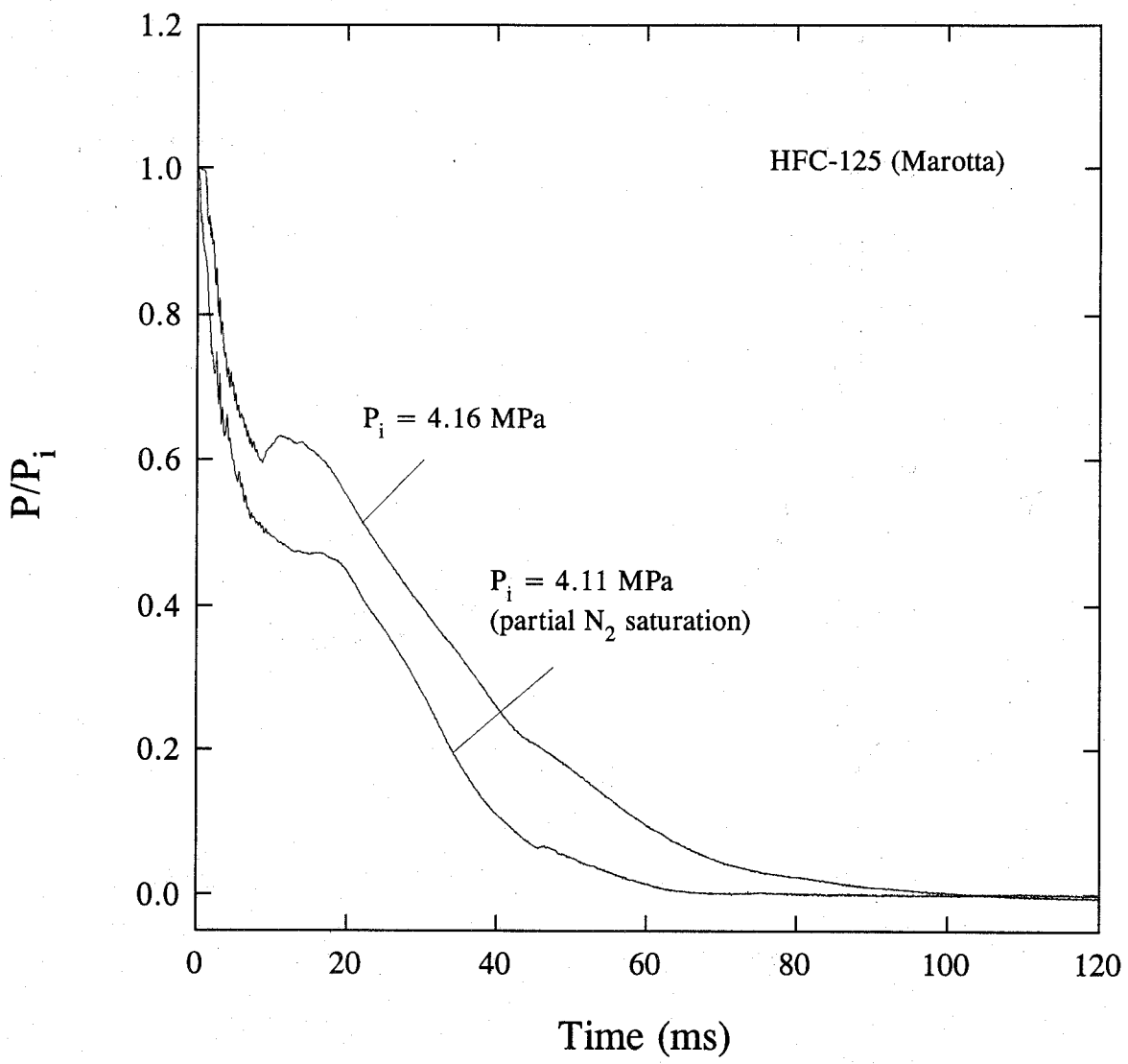


Figure 66. Comparison of pressure decay curves during discharges of HFC-125 using a Marotta valve at $P_i \sim 4.12 \text{ MPa}$ under complete and partial nitrogen saturation.

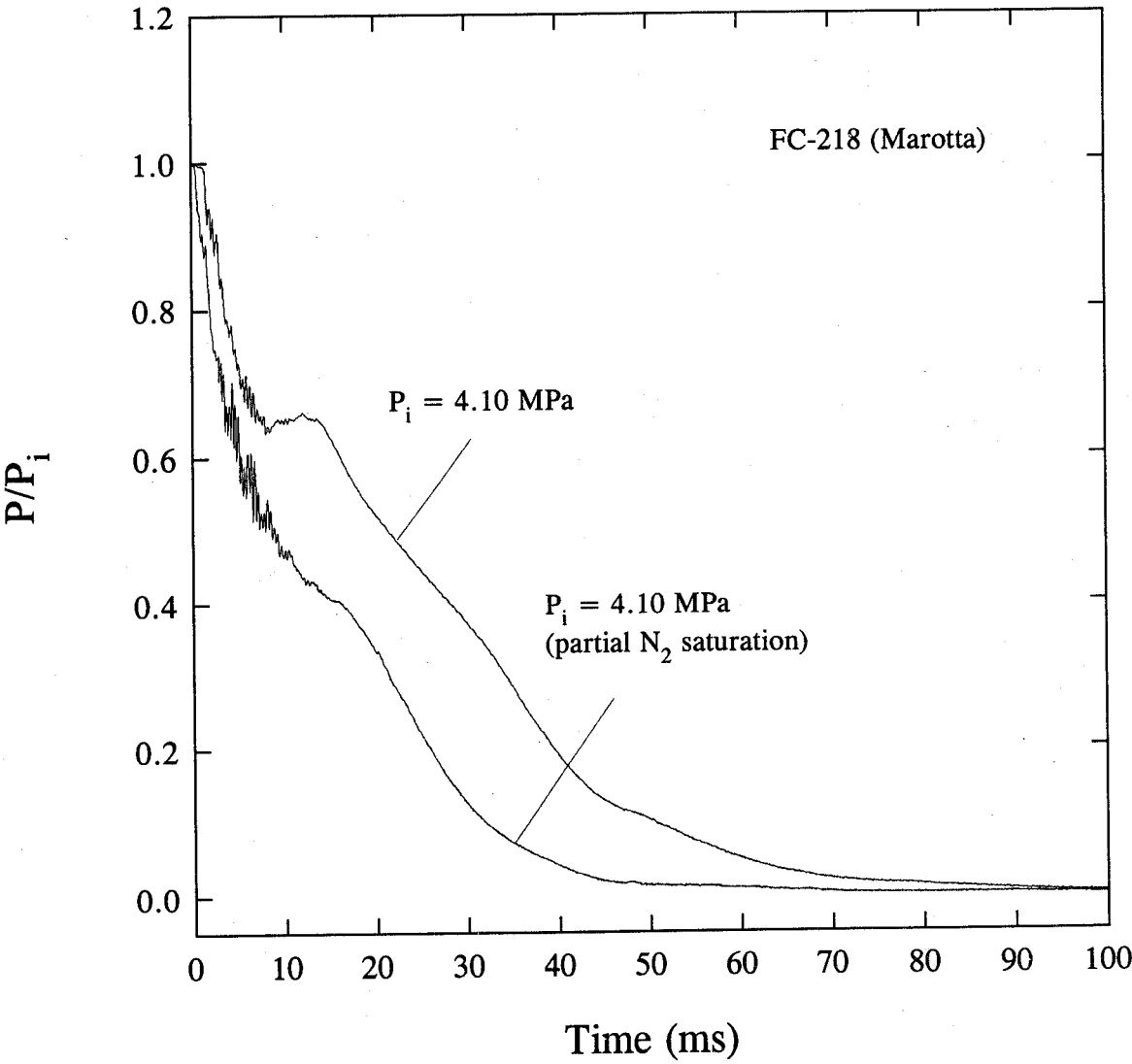


Figure 67. Comparison of pressure decay curves during discharges of FC-218 using a Marotta valve at $P_i \sim 4.12$ MPa under complete and partial nitrogen saturation.

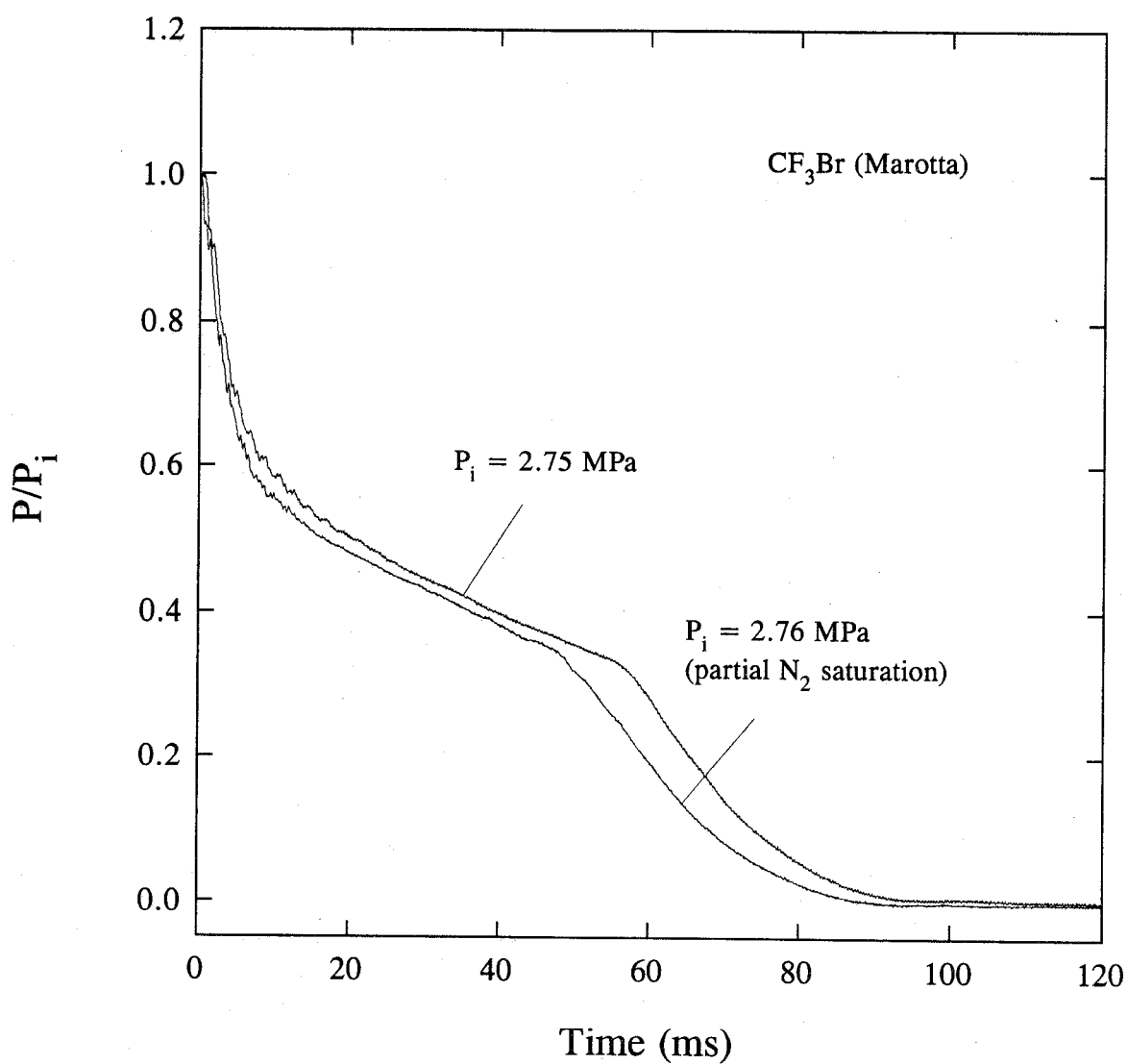


Figure 68. Comparison of pressure decay curves during discharges of CF_3Br using a Marotta valve at $P_i \sim 2.75 \text{ MPa}$ under complete and partial nitrogen saturation.

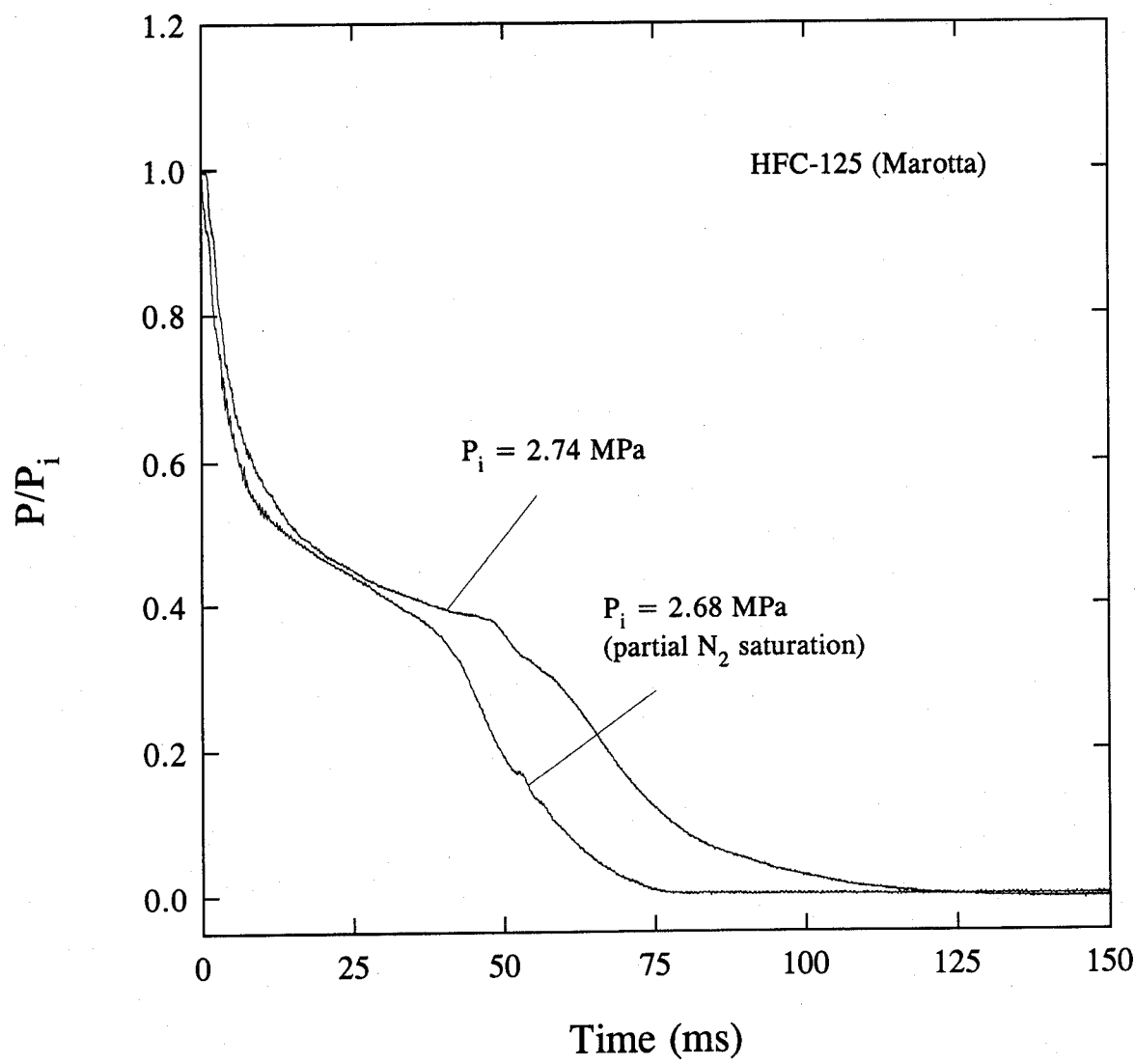


Figure 69. Comparison of pressure decay curves during discharges of HFC-125 using a Marotta valve at $P_i \sim 2.75 \text{ MPa}$ under complete and partial nitrogen saturation.

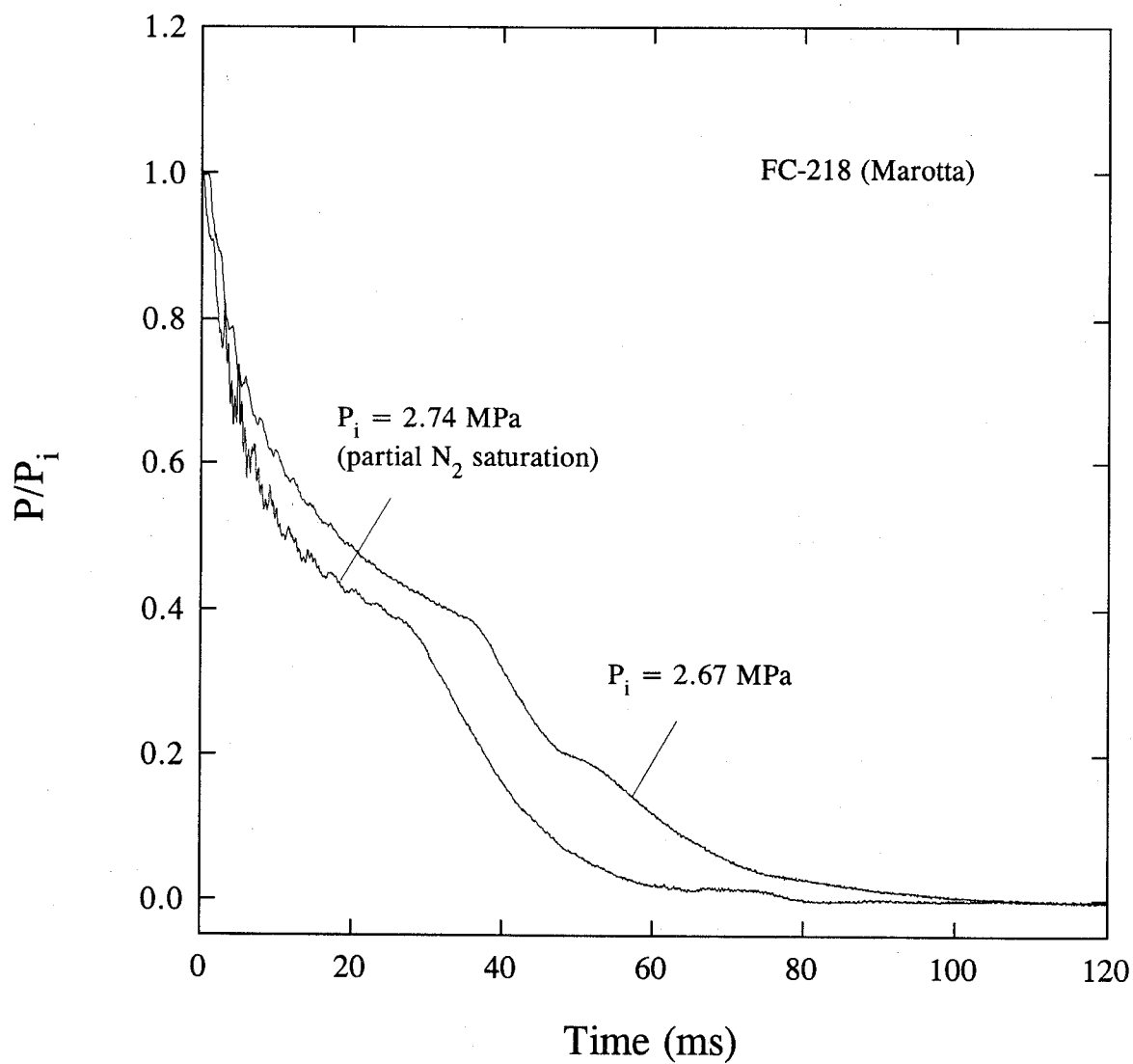


Figure 70. Comparison of pressure decay curves during discharges of FC-218 using a Marotta valve at $P_i \sim 2.75 \text{ MPa}$ under complete and partial nitrogen saturation.

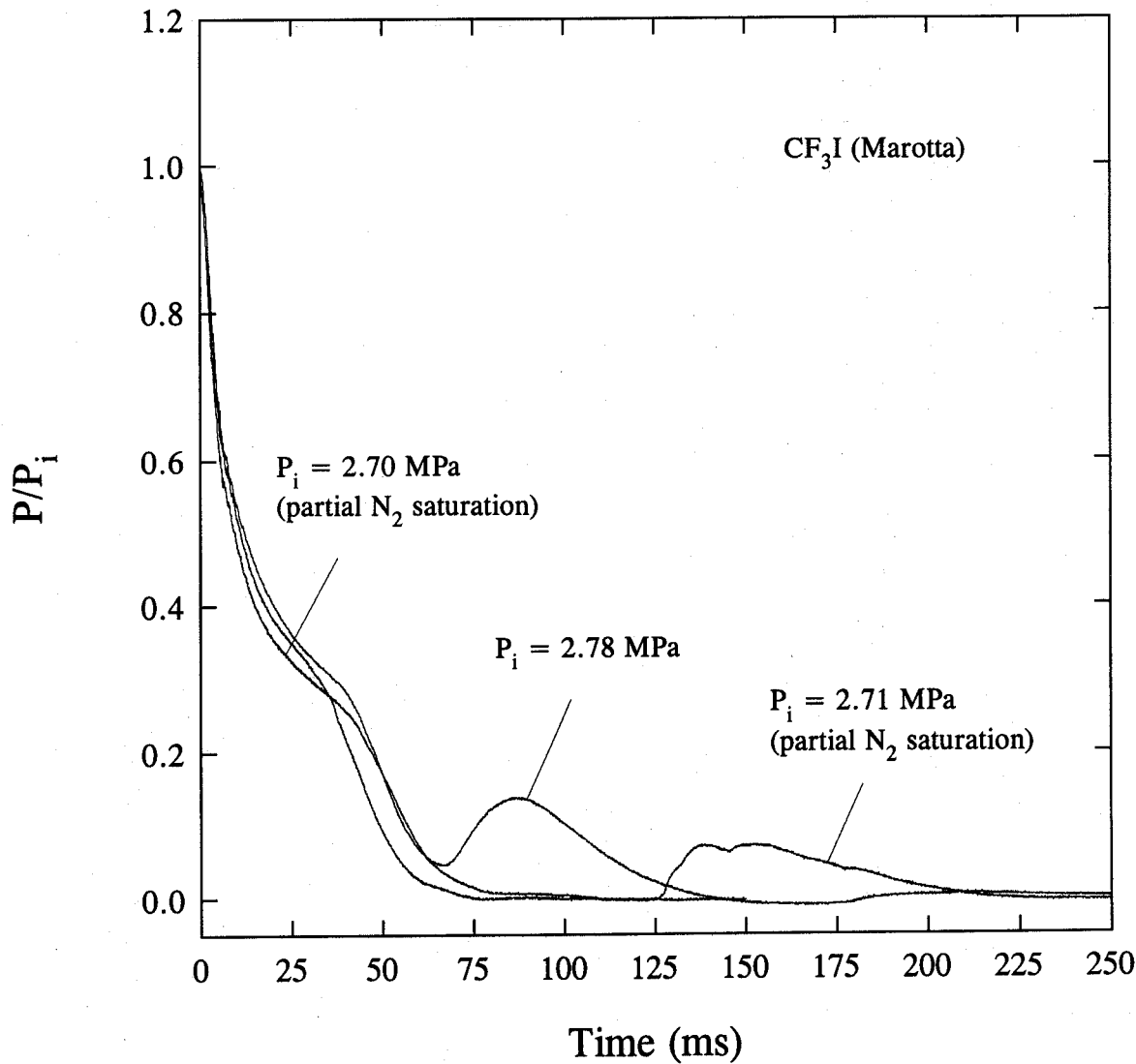


Figure 71. Comparison of pressure decay curves during discharges of CF_3I using a Marotta valve at $P_i \sim 2.75 \text{ MPa}$ under complete and partial nitrogen saturation.

$$R_c = 2\sigma \left(P_{sat} + \frac{CP_h}{C_s} - P_h \right) \quad (29)$$

where R_c is the critical bubble radius. The volume of each bubble (V_{bubble}) can then be calculated as

$$V_{bubble} = \frac{4}{3} \pi R_c^3. \quad (30)$$

The pressure inside the bubble can be obtained from the Young-Laplace equation (Carey, 1992):

$$P_{bubble} - P_h = \frac{2\sigma}{R_c}. \quad (31)$$

The amount of nitrogen mass in each bubble can be calculated assuming an ideal gas. The temperature used in the calculations is the initial temperature of the liquid because the thermodynamic path is isothermal depressurization. The total number of nitrogen bubbles formed (N_{bubble}) can be obtained from the ratio of the remaining mass of dissolved nitrogen before degassing, which can be calculated from Equations (27) and (28), to the amount of nitrogen vapor in a bubble. The swelling of the liquid level, which is assumed to be primarily due to the volume displacement of the nitrogen bubbles, can now be estimated by

$$V_{l,swell} = N_{bubble} V_{bubble} \quad (32)$$

where $V_{l,swell}$ is the increase in liquid volume due to swelling. The expansion of the liquid level causes compression of and reduction in the ullage volume. If the process is assumed to be isentropic, the pressure ($P_{recovery}$) in the compressed ullage volume ($V_{compress}$) can be calculated using

$$P_{recovery} = P_{bd} \left(\frac{V_{bd}}{V_{compress}} \right)^\gamma \quad (33)$$

where P_{bd} and V_{bd} are the immediate pressure and ullage volume before degassing respectively, which can be obtained in solving Equations (27) and (28). The above approach used to estimate the pressure recovery in the pressure decay curves will result in an abrupt rise in pressure rather than a smooth recovery as noted in the experimental results. The smooth pressure rebound is probably due to the combined effects of bubble inception and growth, bubble coalescence, bubble rise to the liquid surface, disengagement of rising bubbles from the liquid surface, and the discharge of the agent during the degassing period. Because of their complexity, all these effects have not been taken into account in the present model.

To simulate the two-phase (vapor/liquid) discharge after degassing, a homogeneous frozen flow model (Whalley, 1990) is assumed. That is, the two-phase mixture is assumed to be homogeneous, and the quality, defined as the mass fraction of gaseous nitrogen in the mixture, is assumed to be constant during the flow through the orifice. The liquid is assumed not to vaporize. Furthermore, no heat transfer between the gas and the liquid is assumed to occur, and the two-phase mixture is treated as incompressible, a reasonable assumption for a low quality two-phase flow. Under these assumptions, Equation (28) can be used as an approximation to describe the homogeneous two-phase flow with $\rho_{l,m}$ being the homogeneous two-phase mixture density in this case. This density can be estimated using the volume and the mass of the two-phase mixture immediately after degassing. A discharge coefficient with a value of 0.61 was assumed in the calculations. The initial pressure during the two-phase discharge period is $P_{recovery}$.

After complete depletion of liquid (in the case of no degassing) or two-phase mixture (in the case of degassing), the remaining ullage vapor discharge can be modeled using the following equation (Kim-E and Reid 1983):

$$\frac{P}{P_{el}} = \left[1 - \frac{C_a A}{V_t} \left(\frac{RT_{el} \gamma^3 K}{m} \right)^{1/2} \left(\frac{1 - \gamma}{2\gamma} \right) t \right]^{\frac{2\gamma}{1 - \gamma}}, \quad (34)$$

with

$$K = \left(\frac{2}{\gamma + 1} \right)^{\left(\frac{\gamma + 1}{\gamma - 1} \right)} \quad (35)$$

where C_a is the discharge coefficient, m is the molecular weight of the vapor (assuming to be nitrogen), P_{el} and T_{el} are the pressure and temperature in the vessel at the instant of complete depletion of liquid or two-phase mixture, respectively, and V_t is the vessel volume. A value of 0.61 was also used for C_a in the calculations. T_{el} can be calculated by

$$T_{el} = T \left(\frac{V_{ullage}}{V_t} \right)^{\gamma - 1} \quad (36)$$

where V_{ullage} and T are the initial vapor ullage volume and temperature, respectively.

If the initial vessel temperature is above the critical temperature of the agent/nitrogen mixture, the discharge of the supercritical fluid may simply be modeled using Equations (34) and (35) with T_{el} and P_{el} being the initial vessel temperature and pressure.

Table 32 summarizes the predicted and observed complete discharge times for all the agents under the standard discharge conditions. Although the time corresponding to the inflection point in the pressure trace could be used to indicate the end of *liquid* discharge, this approach was not used due to

Table 32. Comparison between predicted and observed discharge times for standard discharges

Agent	Mass (g)	Observed discharge time (ms) \pm 5 ms	Predicted discharge time (ms)
CF ₃ Br*	591	89	55
CF ₃ Br*	564	---	54
CF ₃ Br [§]	625	72	21
CF ₃ Br [¶]	581	265	79
HFC-125*	438	77	51
HFC-125*	428	---	50
HFC-125 [§]	477	64	20
HFC-125 [¶]	454	257	75
FC-218*	450	73	50
FC-218*	435	---	49
FC-218 [§]	492	60	19
FC-218 [¶]	476	250	74
CF ₃ I*	723	75	56
CF ₃ I*	719	75	56
CF ₃ I*	755	---	59
CF ₃ I [§]	800	78	22
CF ₃ I [¶]	773	295	86

*Marotta valve

§Kidde-Graviner valve

¶HTL squibs

the uncertainties in discerning the inflection points in most of the pressure traces. Instead, the *complete* discharge times were used in the comparison.

In Table 32, the observed *complete* discharge times were measured from the high-speed movies. These times are defined as the interval between the instant when the flashing spray first appears at the vessel exit and the time when the spray can no longer be observed. Using this definition, the discharge times for CF₃I are the longest, which seems to contradict the observations from the measured pressure decay curves. However, the high-speed movies show that the denseness of the flashing CF₃I spray diminishes much sooner than those of the other agents, implying that the bulk of CF₃I discharges faster. The calculated discharge times do not show such a distinct trend among agents. This is probably due to the assumptions used in the model. When *all* the dissolved nitrogen is assumed to degas, it will cause an artificially high liquid swelling level, resulting in an artificially high pressure recovery in the ullage and an overall faster discharge rate. Therefore, the agent/nitrogen mixtures with a tendency to degas will have shorter discharge times. In addition, the calculated homogeneous nucleation pressures in the model agree only qualitatively with the observed degassing pressures. Although one can use the experimentally determined degassing pressures as input

parameters in the model and good predictions can be obtained if the *measured* degassing pressures and the pressure recoveries are used as input in the model, it is better to predict these pressures using homogeneous nucleation theories so that no *a priori* information is required and the versatility of the model can be demonstrated. Despite these simplified descriptions of the liquid swelling process and nitrogen degassing, the discharge times can still be estimated within a factor of four (usually better when a solenoid valve was used) by the model. It is conjectured that the action of a squib or pyrotechnic device could render some of the assumptions used in the model invalid.

8.4.4 Summary and Conclusions. Experiments have been conducted in order to delineate the effects of various parameters on agent discharge into an enclosure. The major experimental observations are summarized in the following.

1. Irrespective of the release mechanisms (two solenoid valves, one piston-actuated valve, and a squib), CF_3I exhibits the fastest volumetric discharge rate from the pressure vessel at room temperature; however, the average dispersion velocity of the spray is the slowest once the agent leaves the vessel. All the other agents have comparable volumetric discharge rates and spray dispersion velocities.
2. For a given initial vessel pressure, reducing the orifice opening prolongs the discharge time. Based on the experimental results, the discharge time is approximately inversely proportional to the area of the orifice opening. Reducing the liquid fill volume decreases the discharge time because less agent mass is available in the vessel. For a given fill condition, increasing initial nitrogen charge pressure decreases the discharge time and *vice versa*. However, due to the dependence of the degassing process on the initial charge pressure, no simple, empirical correlation between the discharge time and the initial vessel pressure was apparent from the experimental data.
3. The average dispersion velocities of cold agent discharges are much slower than those of discharges at room temperature. In addition, the discharge rates of cold agents are slower, and the spray angles are narrower.
4. Based on the results of nitrogen saturated HFC-125 discharges (*2/3 liquid fill*), the vessel orientation does not affect the discharge rate significantly. The dissolved nitrogen in the liquid agent plays an important role.
5. When the agent is partially saturated with nitrogen, instead of complete nitrogen saturation, the volumetric discharge rate is much faster.
6. A discharge model incorporating homogeneous nucleation theories to account for nitrogen degassing predicts all qualitative aspects of the discharge process and the discharge times within a factor of four.

8.5 Computer Simulation of Agent Dispersion

8.5.1 Introduction. The objective of this study is to explore a computational tool which will provide detailed analysis on the dispersion process of a flashing spray in a simulated dry bay. Since the

discharge process under this scenario is extremely rapid (events typically lasting less than 100 ms), detailed spatial and temporal measurements of temperatures, velocities and concentrations of the flashing spray are very difficult. Therefore, numerical simulation may prove valuable for studying such a highly transient process. This work was conducted in connection with the experimental studies on the agent discharge and dispersion processes described in Section 8.4.

8.5.2 Modeling of Agent Dispersion Process. The computer codes KIVA-II and CONCHAS-SPRAY developed at the Los Alamos National Laboratory (LANL) (Amsden *et al.*, 1989; Cloutman *et al.*, 1982) were used to simulate the agent dispersion of a flashing spray which was obtained from a liquid agent being discharged from a nitrogen-pressurized vessel through a simple, nozzle/orifice-like exit. The system under consideration involves a vessel volume of the order of 10^{-3} m^3 , with a discharge time of the order of 10^{-2} s . To achieve such a rapid discharge, the pre-pressurization level is typically on the order of several megapascals.

The dispersion of a flashing spray into a confined space is a complicated process which involves many physical phenomena occurring simultaneously and interacting with one another. As the agent exits from the vessel, thermodynamic and fluid-dynamic instabilities lead to flashing and break-up of the agent into a two-phase gaseous/droplet jet mixture. This occurs in a relatively short transition region which starts at the vessel exit and ends at a section of the two-phase jet where thermodynamic and fluid-dynamic instabilities have ceased.

Downstream of this section, called the "initial section," the flow begins to develop as a mixed, two-phase agent/air jet. Beyond the initial section, thermodynamic equilibrium is maintained and droplet collision and agglomeration do not play an important role in either the ensuing jet dynamics or the dispersion of the agent throughout the protected space. Within the initial section, the spray consists of a mixture of liquid-agent fragments of various shapes and sizes and gaseous agent. The spray begins to entrain initially quiescent air from the surrounding environment as it moves away from the bottle exit. Because the temperature of the discharged liquid agent is far above its normal boiling point, it very quickly evaporates and creates a cloud of agent vapor surrounding the moving spray. The entrainment, mixing and evaporation continue as the spray is dispersed throughout the space. The above processes are included in the present analysis.

The dispersion process is described as a two-phase, three-component, turbulent, compressible, dissipative flow. It is assumed that the gas phase consists of the following three components: agent vapor, nitrogen, and oxygen. The liquid phase only consists of pure liquid agent. The vapor pressure equation is a highly non-linear function of temperature. Heat conduction and convection, diffusive and convective mass transfer, momentum transport, and turbulent flow are taken into account in the gas-phase formulations. In addition, the interphase transport processes, such as momentum exchange in the form of Stokes forces and aerodynamic drag between the droplets and the gas phase, heat exchange in the form of forced convection, and mass exchange in the form of evaporation, are considered. It is assumed that the spray droplets can be represented by a Sauter mean diameter. The droplet evaporation process is assumed to be quasi-steady. The effect of turbulence on droplet motion within the spray is also included, and the turbulence in the gas phase is described by relating the velocity gradients to the turbulent viscosity.

The transport coefficients (heat conductivity, mass diffusivity, and viscosity) and the specific heats are temperature dependent. The effect of the gravitational field is also included. No chemical reactions and their associated thermal effects (*e.g.*, heat release) are assumed in the formulation.

The governing equations are the conservation equations of mass, momentum and energy for the medium under investigation. This set of equations constitutes an initial/boundary value problem within a region bounded by the initial section and the far-field boundaries of the protected space. The set of

time-dependent equations is expressed in a three-dimensional form although the discharges were assumed to be axisymmetric.

The total mass density of the fluid, excluding the mass of the spray droplets, is defined in terms of a partial mass density of the component species. The mass balance equates the change in species concentration with time to the sum of the advection, diffusion and source terms due to evaporation of that particular component. The total fluid density satisfies the total mass balance equation, recognizing that the net diffusion must sum to zero.

The axial and radial momentum balance equations for the fluid mixture equate the time rate of change of momentum to the sum of the advection, pressure, viscous stress, droplet drag, and body force terms. The energy equation for the gas phase accounts for the local change in specific internal energy from the sum of the net advection of sensible heat, heat conduction, enthalpy transport accompanying the diffusion of individual species, flow work, viscous heating, and energy transfer between the two phases. The state relations are assumed to be those of an ideal gas mixture. The transport coefficients include the laminar and turbulent contributions to the momentum, heat, and mass transfer. The turbulent viscosity is broken into a constant uniform background term and a variable turbulent viscosity. The thermal and mass turbulent diffusivity are related to the viscosity through the local Prandtl and Schmidt numbers of the gas mixture.

The motion of the droplets in the spray is governed by ordinary differential equations in Lagrangian form. It is assumed that the spray is sufficiently thin, and, as a consequence, the volume displaced by the droplets may be neglected. Velocity components in the axial, radial and swirl directions are tracked, and the transport between phases is dependent upon the Reynolds number computed from the slip velocity and the film temperature and composition. Internal droplet motion is ignored, leading to uniform droplet temperatures.

The model developed by Dukowicz (1979) was used to calculate droplet mass loss due to evaporation. The particle velocity is computed from the drag associated with the slip velocity. The latent heat cools the droplet during evaporation, and the heat transfer between the drop and the environment is determined using the Ranz-Marshall correlation (1952), modified to account for mass leaving the surface. The fluid-particle interactions are all two-way coupled to ensure overall conservation of mass, momentum and energy.

8.5.3 Solution Method. The gas-phase solution procedure is based on a finite volume method called the ALE (Arbitrary Lagrangian-Eulerian) method. Spatial differences are formed on a finite-difference mesh that subdivides the computational region into a number of small cells that are hexahedrons. The corners of the cells are called vertices, and the positions of the vertices may be arbitrarily specified functions of time, thereby allowing a Lagrangian, Eulerian, or mixed description. The arbitrary mesh can conform to curved boundaries and can move to follow allowable changes in geometry. An advantage of the method is that the mesh need not be orthogonal. The transient solution is marched out in a sequence of finite time increments called cycles or time steps. In each cycle the values of the dependent variables are calculated from those in the previous cycle.

8.5.4 Numerical Results and Discussion. Computations using the two-dimensional axisymmetric approach were performed using the LANL CONCHAS-SPRAY and KIVA-II codes. CONVEX and CRAY supercomputers with the UNIX operating system at NIST were used for the calculations.

The results for a generic agent simulant with thermophysical properties very similar to HCFC-22 are presented graphically as contours of constant velocity, density, pressure, temperature, species concentration, vorticity, kinematic viscosity, mass flux, and liquid phase. The only difference in thermophysical properties between the simulant and HCFC-22 is the vapor pressure curves. As will be discussed below, the actual vapor pressure curve of HCFC-22 could not be used in the calculations

because of convergence problems. The shape of the curve was modified slightly so that calculations could be performed. The rationale for selecting this generic simulant is that its thermophysical properties lie within those of the selected agents.

The performance of the two codes, CONCHAS-SPRAY and KIVA-II, were compared. It was found that in one test case, CONCHAS-SPRAY and KIVA-II gave essentially the same results. Since CONCHAS-SPRAY requires less computing time, the computational results reported herein were obtained using CONCHAS-SPRAY. It should be emphasized that the original codes were designed for the use with the LANL computer facility. In addition, the codes employed graphics libraries installed in that system. To apply the codes using the NIST computing facility, it was necessary to configure them to the NIST operating system. The codes have also been modified to write their output into organized ASCII files. The output files were transferred onto a PC computer where they were further graphically processed with a graphics program written in the C language. The program converted the numerical output into postscript files.

The configuration investigated is the discharge of a droplet spray, with properties similar to one of the halon alternatives, into a totally enclosed space. The transitional region between the nozzle exit and a fully-developed spray was not considered but has been discussed by Cooper (1994). Therefore, it is assumed that the spray has been already established at the discharge orifice exit and is injected into the area at a prescribed rate.

Computational parcels representing the droplets are introduced at the injector with an axial velocity of 61.4 m/s, directed at an angle of 0° relative to the symmetry axis. A zero azimuthal component of velocity is assumed for the droplets at the injector. All the gas and liquid parameters are assumed to be uniform across the orifice exit. All the parameters within the compartment are also assumed to be uniform initially.

The surrounding walls of the compartment are treated as solid boundaries maintained at a constant temperature of 21°C . Free-slip conditions are assumed on the walls for the velocities. Thus the subsequent penetration and shape of the spray result solely from the interactions of the liquid droplets with the ambient air. The numerical solution of the balance equations associated with the initial and boundary conditions and the material properties provides the time evolution of the spray in the compartment.

The nozzle is located on the centerline of the 0.42 m diameter cylindrically shaped volume. The length of the compartment is either 1.0 m or 2.5 m. Agent inflow boundary conditions, including temperature, density, and velocity are estimated from the results of the discharge vessel experiments and specified in the calculation. The ambient temperature is either 21°C or -30°C . The ambient pressure is 1×10^5 kPa. The liquid spray mean diameter is either 200 μm or 600 μm . Table 33 lists the set of the input data used as initial parameters in the computations and the figure numbers corresponding to the figures showing the computational results.

Figures 72 to 76x illustrate the computational mesh used in the calculations and the temporal variations of liquid spray outline, agent vapor density, temperature, pressure and gas density contour under the following conditions: initial droplet diameter of 200 μm , enclosure length of 1 m, and initial ambient temperature equal to the 21°C .

The effect of droplet diameter is demonstrated in Figures 77 to 80, where the initial droplet size varies from 200 μm to 600 μm ; all other parameters remained constant.

Figures 81 to 84 illustrate the evolution of the spray with an initial Sauter mean diameter of 200 μm and an initial ambient temperature of -30°C . Figures 85 to 88 show the results for the larger initial mean diameter (600 μm) at -30°C .

Figures 89 to 92 show the calculated results using a Sauter mean diameter of 200 μm and a different compartment length (2.5 m) at 21°C . Figures 93 to 96 display the results for a Sauter mean diameter of 600 μm under the same initial ambient temperature.

Table 33. Input data used in the computations

Figure number	Spray mean diameter (μm)	Ambient temperature ($^{\circ}\text{C}$)	Compartment height (m)
72-76	200	21	1.0
77-80	600	21	1.0
81-84	200	-30	1.0
85-88	600	-30	1.0
89-92	200	21	2.5
93-96	600	21	2.5

Based on the computational results, the penetration distance of the spray (around 0.9 m after 14 ms, which roughly corresponds to the values measured in the totally open discharge apparatus) is about the same for the 200 μm and 600 μm drops; however, the spray structure and thickness differ significantly. For the small droplet diameter, the spray is clearly thicker, especially in the head of the spray, the distribution of the parameters within the spray is more uniform, and the higher density area of the gas phase (containing agent vapor) is much larger.

An additional aerodynamic effect is the tendency to form a vortex in the vicinity of the head of the spray with the small droplet mean diameter. This phenomenon enhances the area filled with the agent vapor. The spray with the large droplet mean diameter is significantly narrower and without the fat head.

An unexpected effect is the generation of local temperatures which exceed the initial ambient temperature. This is caused by the strong shock waves created during the discharge process which compress the gas. The possibility of creating such waves is indicated by Thompson *et al.* (1986) and Kurschat *et al.* (1992). Although the vaporization of the agent cools the chamber, it is possible that some local temperature rise due to compression of the strong shock waves can offset the temperature decrease due to evaporation. The maximum gas phase temperature is significantly higher for the spray with the small droplet mean diameter (there is an increase of 40 K relative to the initial ambient temperature), whereas for the large droplet mean diameter, the temperature only increases 10 K. This influences the interphase heat transfer, which depends on the surface area and temperature difference. Similar observations, with one exception, were made at a lower initial ambient temperature (-30°C). For the small droplet diameter, the maximum gas-phase temperature is just slightly higher than the ambient value, but for the large droplet diameter, it is lower than the ambient value and nearly equal to the liquid phase temperature (boiling point).

Similar observations were also made when a longer compartment was used in the simulation. Again, there is one exception in the gas-phase temperature behavior. For the large droplet mean diameter, the maximum gas-phase temperature is slightly higher than the ambient value. For the small droplet diameter, the temperature is lower by 51° relative to the ambient value. The conclusion is that the dynamics of the interphase heat exchange phenomena depends strongly on the spray Sauter mean diameter, ambient temperature, and geometry.

The effect of compartment geometry on the dispersion process can be assessed by comparing the results obtained using two different compartment heights. In the case of a 1.0 m high compartment, a pressure wave is generated by the fast moving agent just after 1 ms of the process. The pressure wave reflects alternately from the bottom and top walls of the compartment, thereby influencing the spray

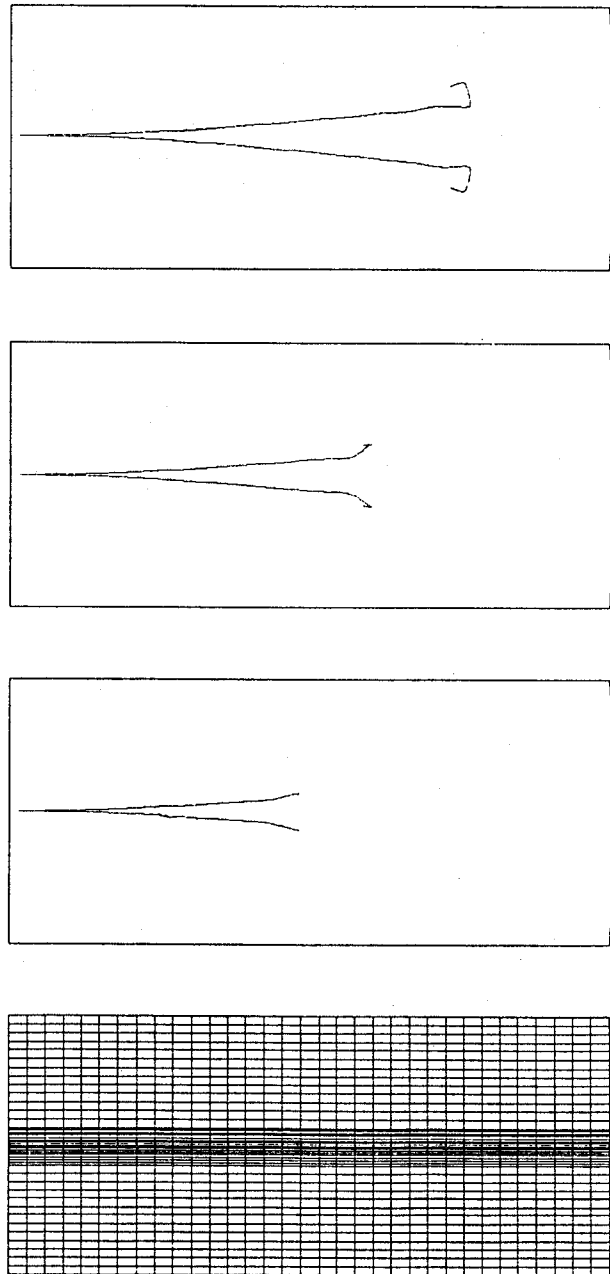


Figure 72. Agent discharge. Computational mesh and liquid phase outlines at: 8.3 ms, 10.7 ms, and 14.3 ms (upward). Initial spray angle 0° . Spray mean diameter $200\text{ }\mu\text{m}$. Ambient $T = 294\text{ K}$ and $P = 101\text{ kPa}$. Compartment $1\text{ m} \times 0.42\text{ m}$.

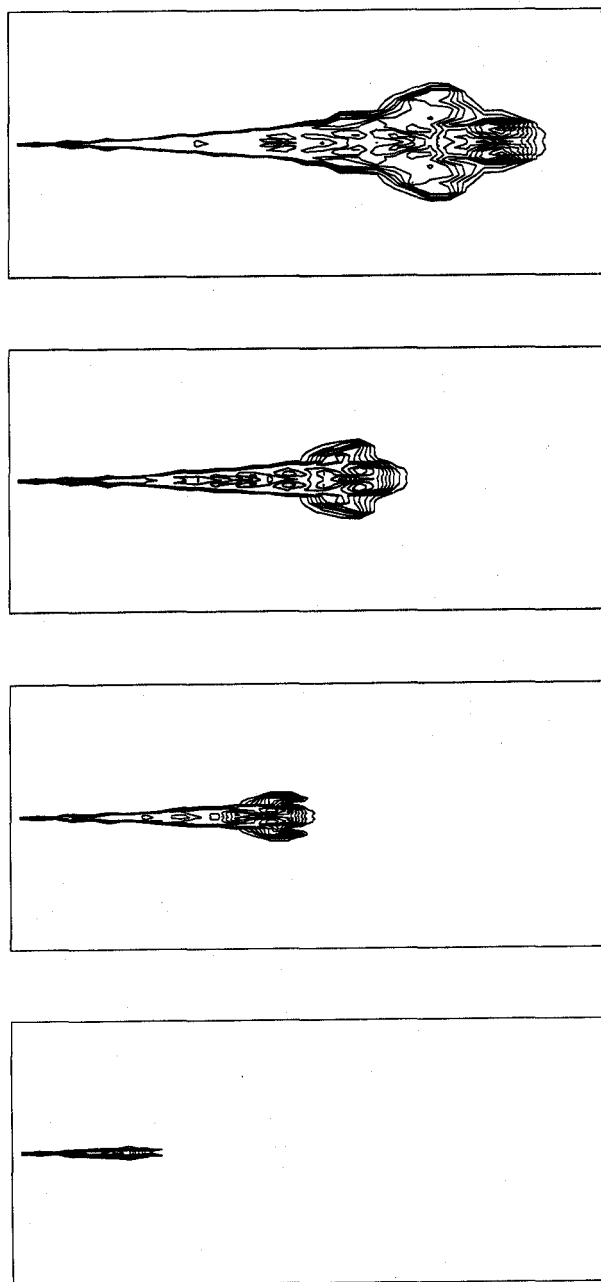


Figure 73. Vapor density maps at: (3.5, 8.3, 10.7, 14.3) ms (upward); the outline value 0.032 kg/m^3 . Initial spray angle 0° . Spray mean diameter $200 \text{ }\mu\text{m}$. Ambient $T = 294 \text{ K}$ and $P = 101 \text{ kPa}$. Compartment $1 \text{ m} \times 0.42 \text{ m}$.

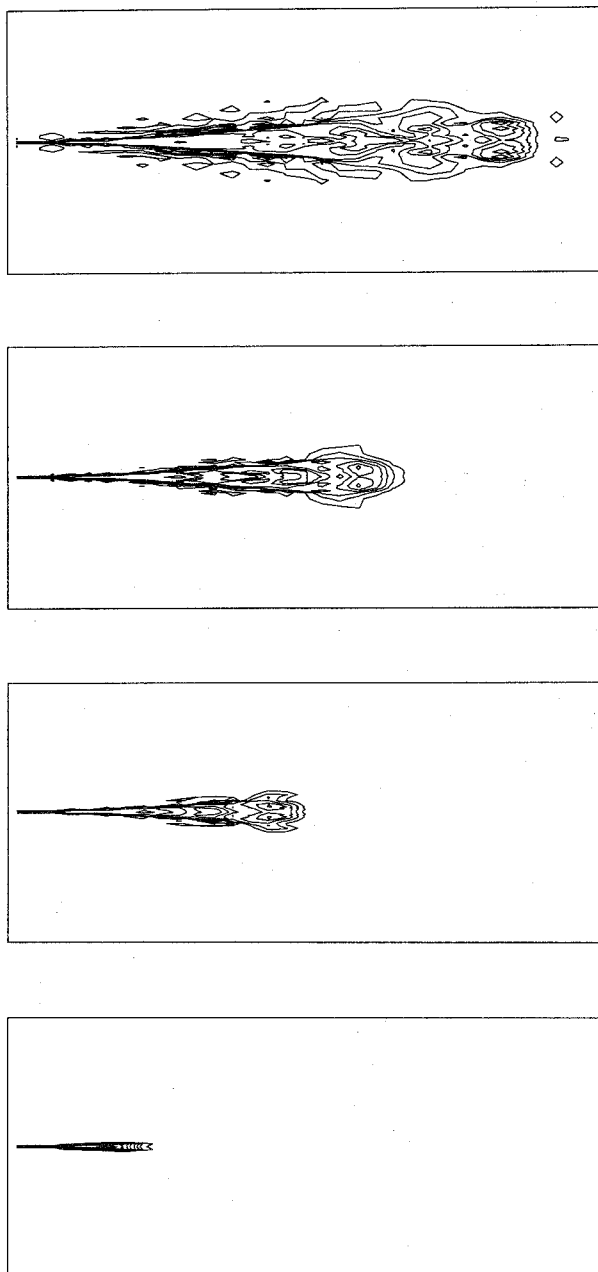


Figure 74. Gas phase temperature maps at: (3.5, 8.3, 10.7, 14.3) ms (upward); the maximum value 335 K. Initial spray angle 0° . Spray mean diameter $200\text{ }\mu\text{m}$. Ambient $T = 294\text{ K}$ and $P = 101\text{ kPa}$. Compartment $1\text{ m} \times 0.42\text{ m}$.

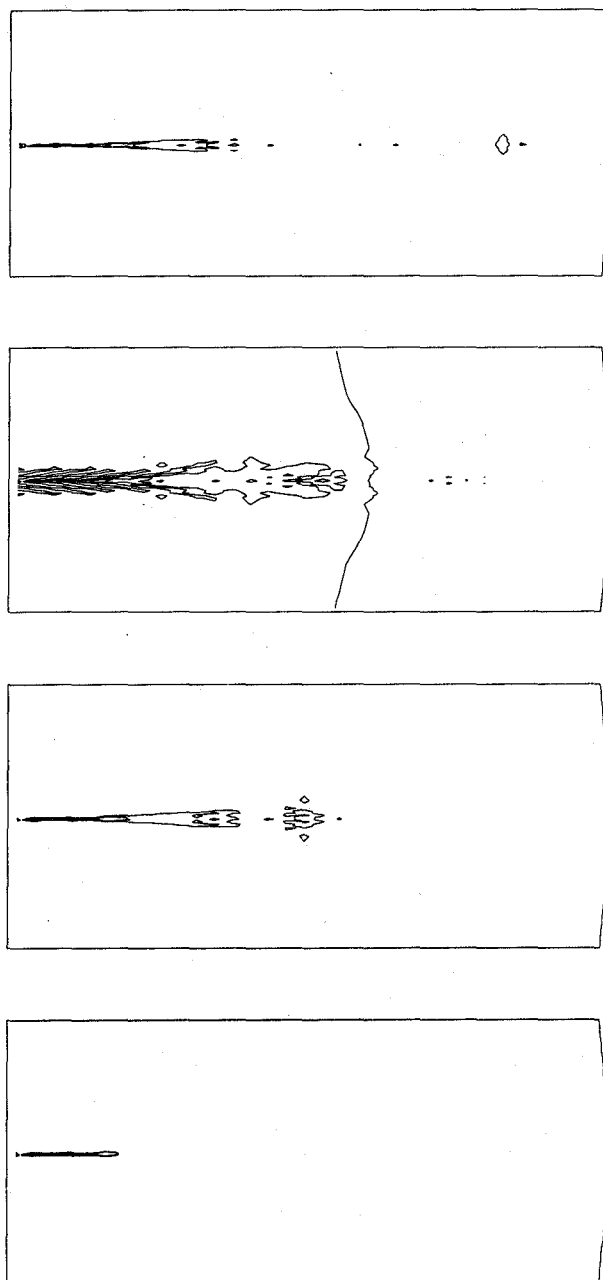


Figure 75. Gas phase pressure maps at: (3.5, 8.3, 10.7, 14.3) ms (upward); the outline value 105 kPa. Initial spray angle 0° . Spray mean diameter $200\ \mu\text{m}$. Ambient $T = 294\ \text{K}$ and $P = 101\ \text{kPa}$. Compartment $1\ \text{m} \times 0.42\ \text{m}$.

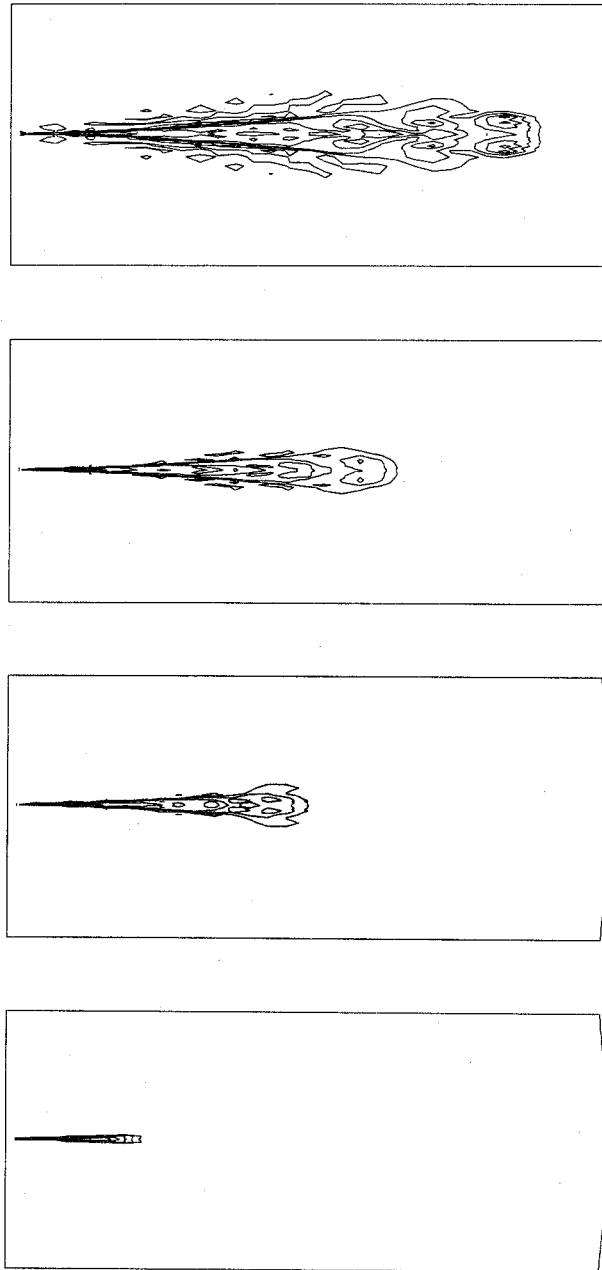


Figure 76. Gas phase density maps at: (3.5, 8.3, 10.7, 14.3) ms (upward); the outline value 1.27 kg/m^3 . Initial spray angle 0° . Spray mean diameter $200 \text{ }\mu\text{m}$. Ambient $T = 294 \text{ K}$ and $P = 101 \text{ kPa}$. Compartment $1 \text{ m} \times 0.42 \text{ m}$.

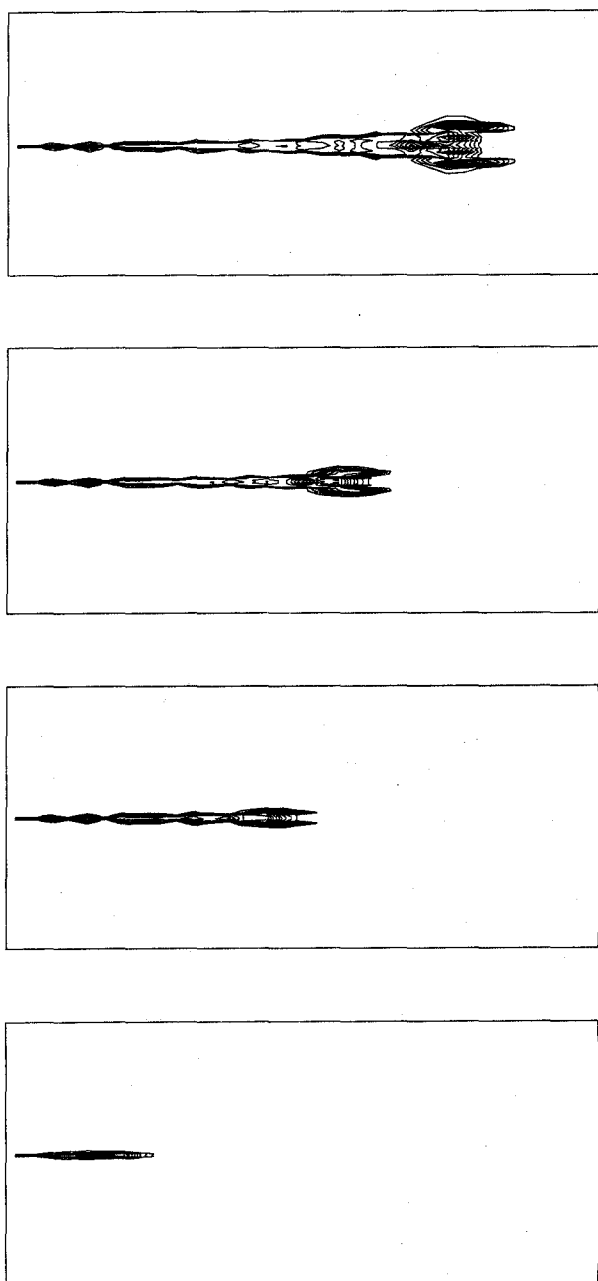


Figure 77. Vapor density maps at: (3.5, 8.3, 10.7, 14.3) ms (upward); the outline value 0.026 kg/m^3 . Initial spray angle 0° . Spray mean diameter $600 \mu\text{m}$. Ambient $T = 294 \text{ K}$ and $P = 101 \text{ kPa}$. Compartment $1 \text{ m} \times 0.42 \text{ m}$.

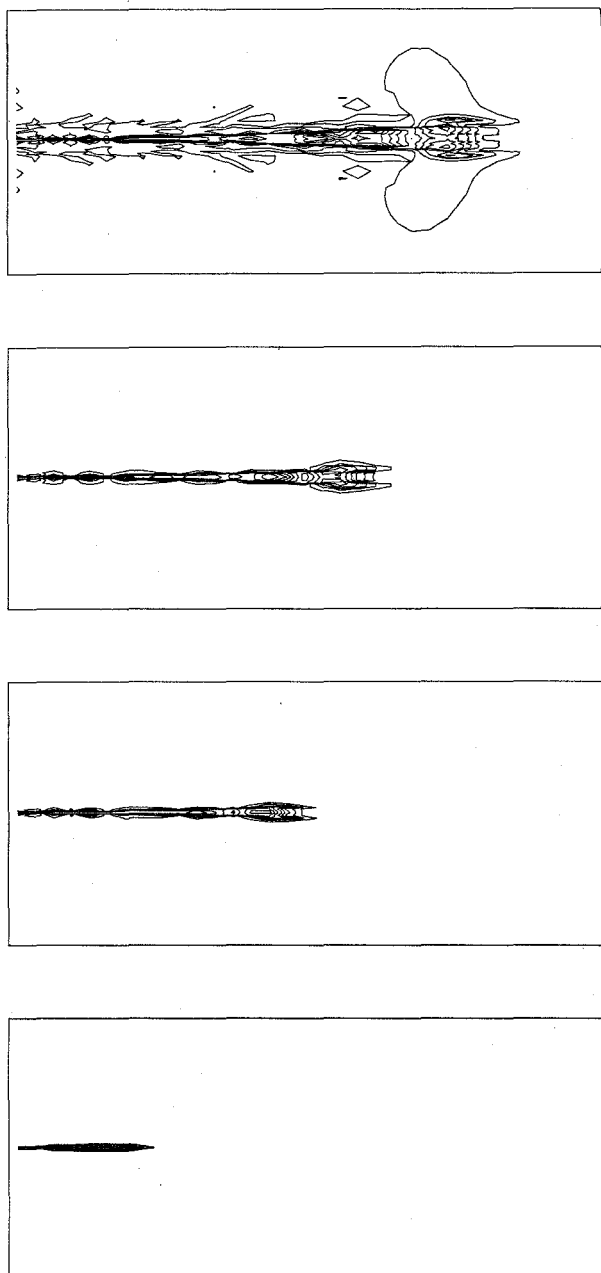


Figure 78. Gas phase temperature maps at: (3.5, 8.3, 10.7, 14.3) ms (upward); the maximum value 304 K. Initial spray angle 0° . Spray mean diameter $600\ \mu\text{m}$. Ambient $T = 294\ \text{K}$ and $P = 101\ \text{kPa}$. Compartment $1\ \text{m} \times 0.42\ \text{m}$.

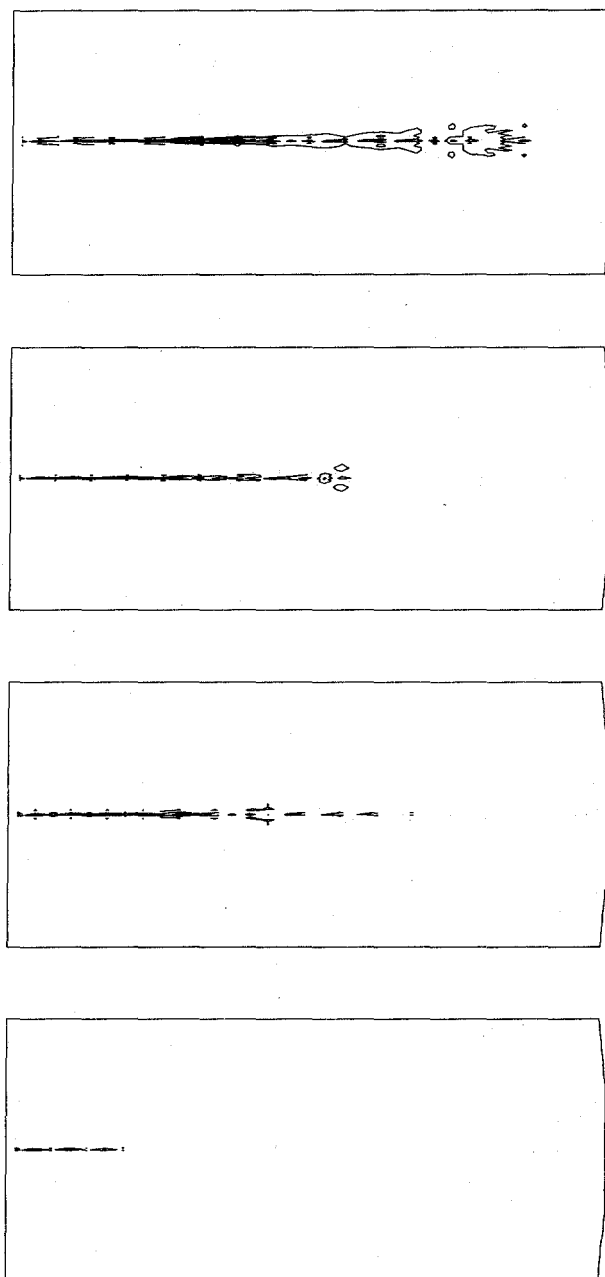


Figure 79. Gas phase pressure maps at: (3.5, 8.3, 10.7, 14.3) ms (upward); the outline value 113 kPa. Initial spray angle 0° . Spray mean diameter $600\text{ }\mu\text{m}$. Ambient $T = 294\text{ K}$ and $P = 101\text{ kPa}$. Compartment $1\text{ m} \times 0.42\text{ m}$.

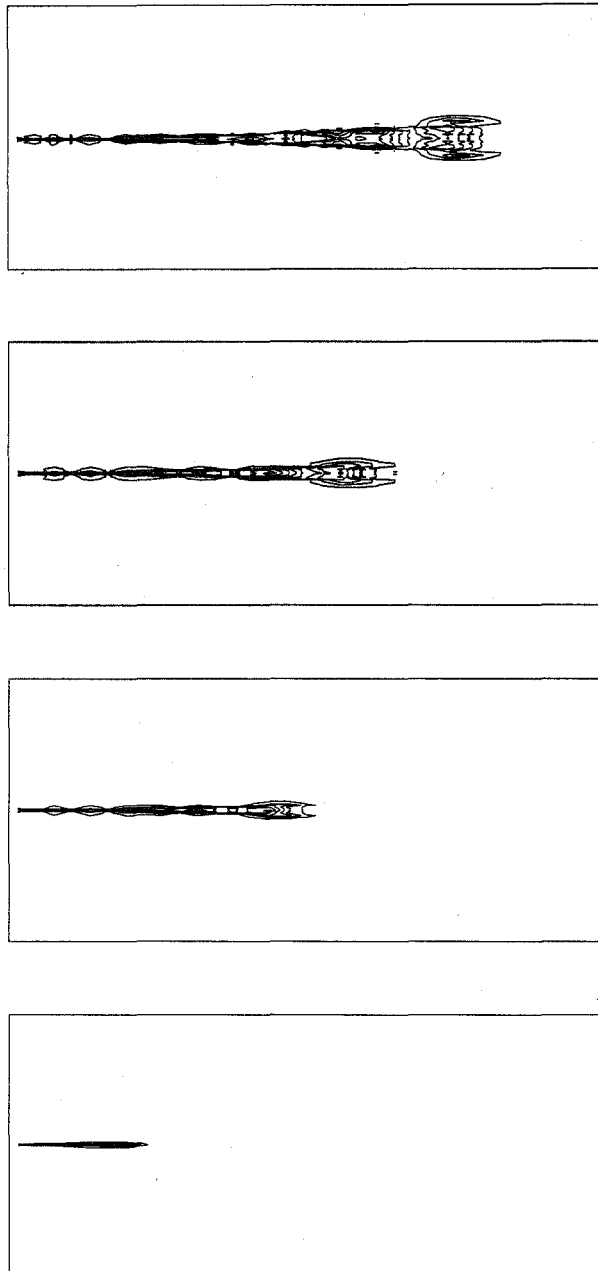


Figure 80. Gas phase density maps at: (3.5, 8.3, 10.7, 14.3) ms (upward); the outline value 1.37 kg/m^3 . Initial spray angle 0° . Spray mean diameter $600 \text{ }\mu\text{m}$. Ambient $T = 294 \text{ K}$ and $P = 101 \text{ kPa}$. Compartment $1 \text{ m} \times 0.42 \text{ m}$.

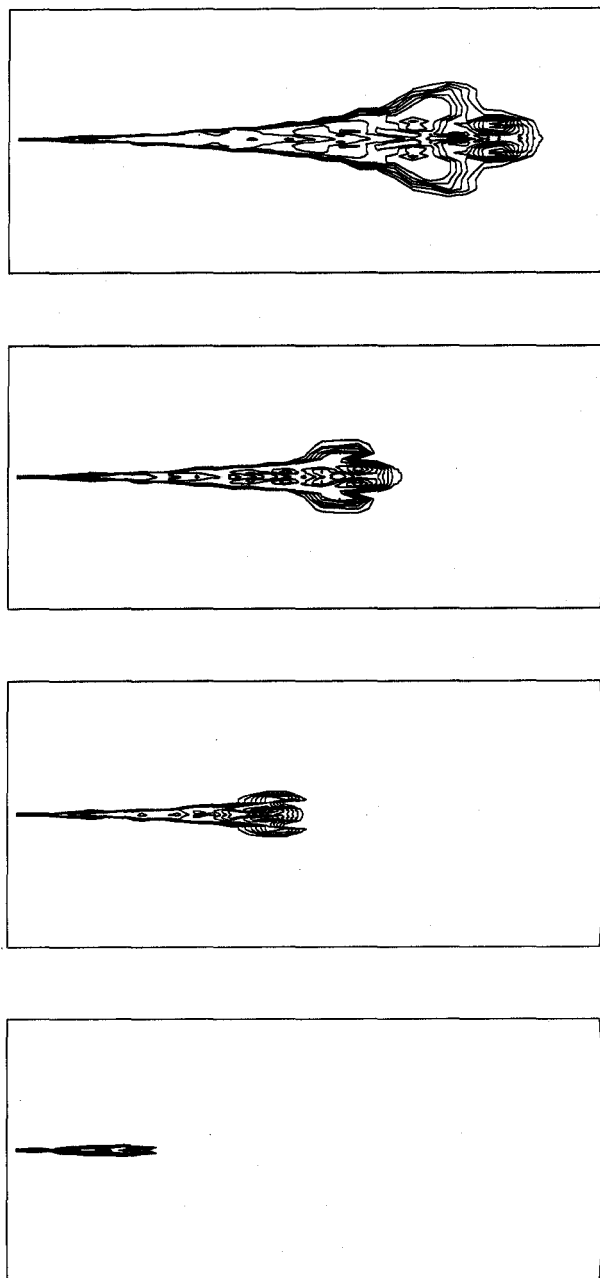


Figure 81. Vapor density maps at: (3.5, 8.3, 10.7, 14.3) ms (upward); the outline value 0.036 kg/m^3 . Initial spray angle 0° . Spray mean diameter $200 \mu\text{m}$. Ambient $T = 243 \text{ K}$ and $P = 101 \text{ kPa}$. Compartment $1 \text{ m} \times 0.42 \text{ m}$.

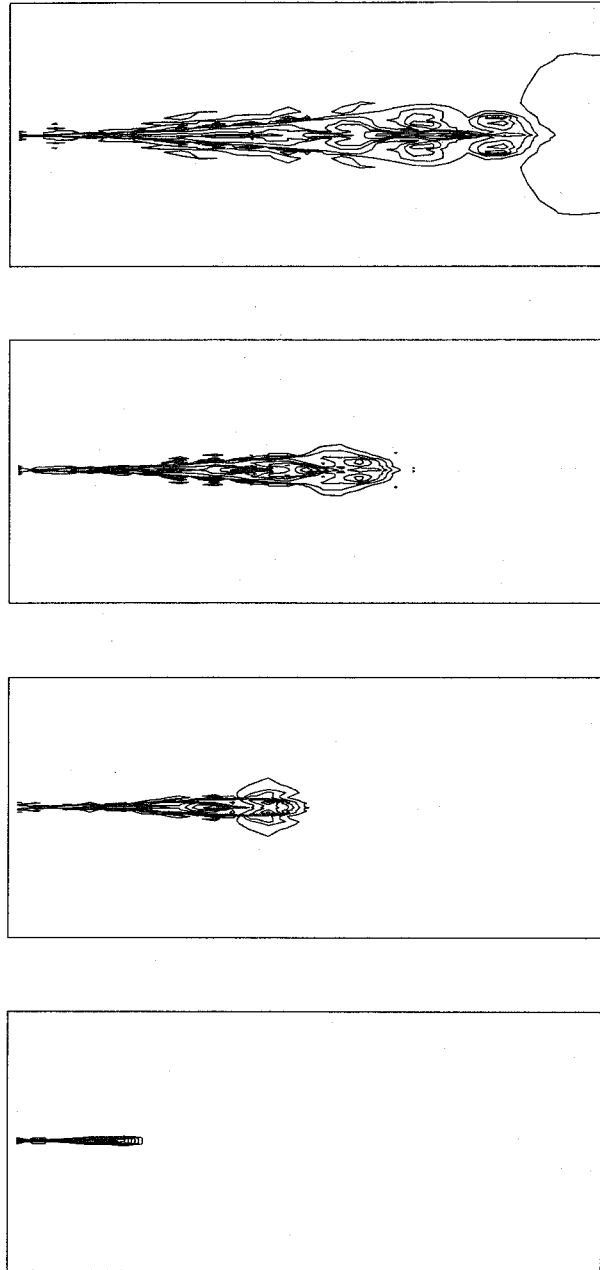


Figure 82. Gas phase temperature maps at: (3.5, 8.3, 10.7, 14.3) ms (upward); the maximum value 249 K. Initial spray angle 0° . Spray mean diameter $200\text{ }\mu\text{m}$. Ambient $T = 243\text{ K}$ and $P = 101\text{ kPa}$. Compartment $1\text{ m} \times 0.42\text{ m}$.

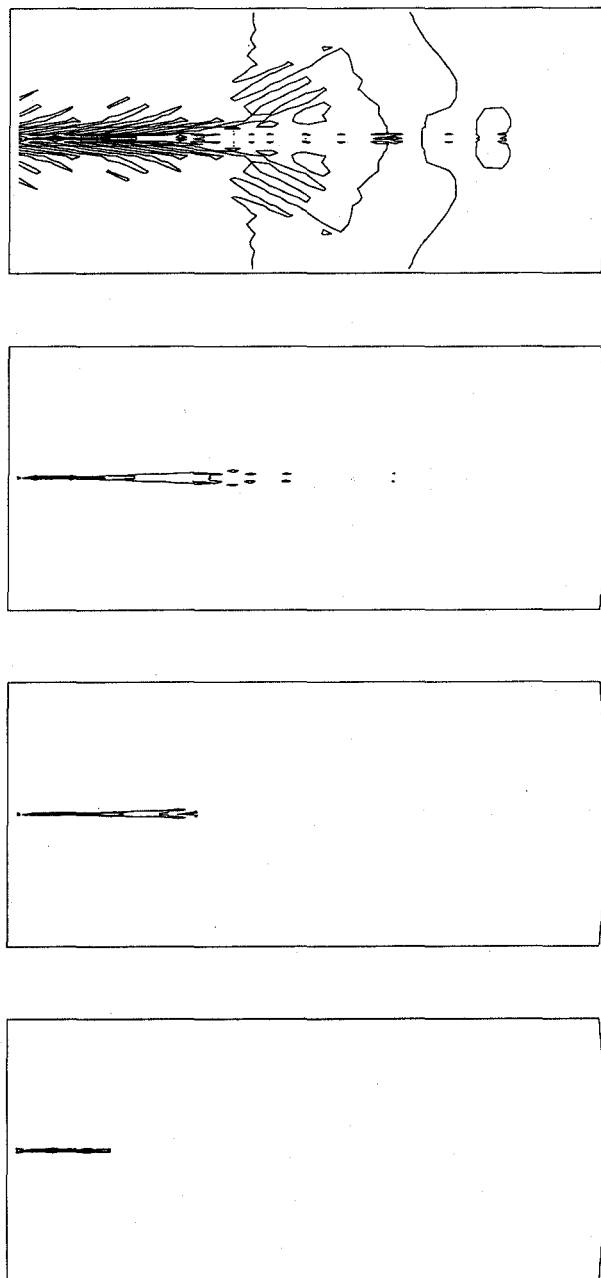


Figure 83. Gas phase pressure maps at: (3.5, 8.3, 10.7, 14.3) ms (upward); the outline value 89 kPa. Initial spray angle 0° . Spray mean diameter $200\text{ }\mu\text{m}$. Ambient $T = 243\text{ K}$ and $P = 101\text{ kPa}$. Compartment $1\text{ m} \times 0.42\text{ m}$.

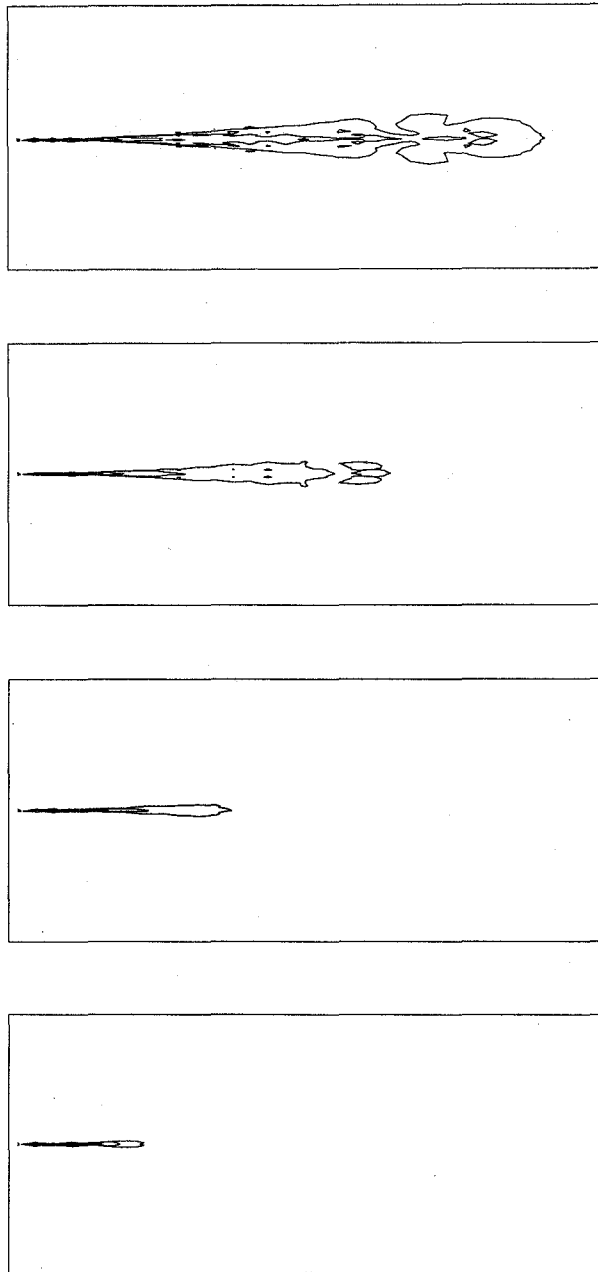


Figure 84. Gas phase density maps at: (3.5, 8.3, 10.7, 14.3) ms (upward); the outline value 1.29 kg/m^3 . Initial spray angle 0° . Spray mean diameter $200 \text{ }\mu\text{m}$. Ambient $T = 243 \text{ K}$ and $P = 101 \text{ kPa}$. Compartment $1 \text{ m} \times 0.42 \text{ m}$.

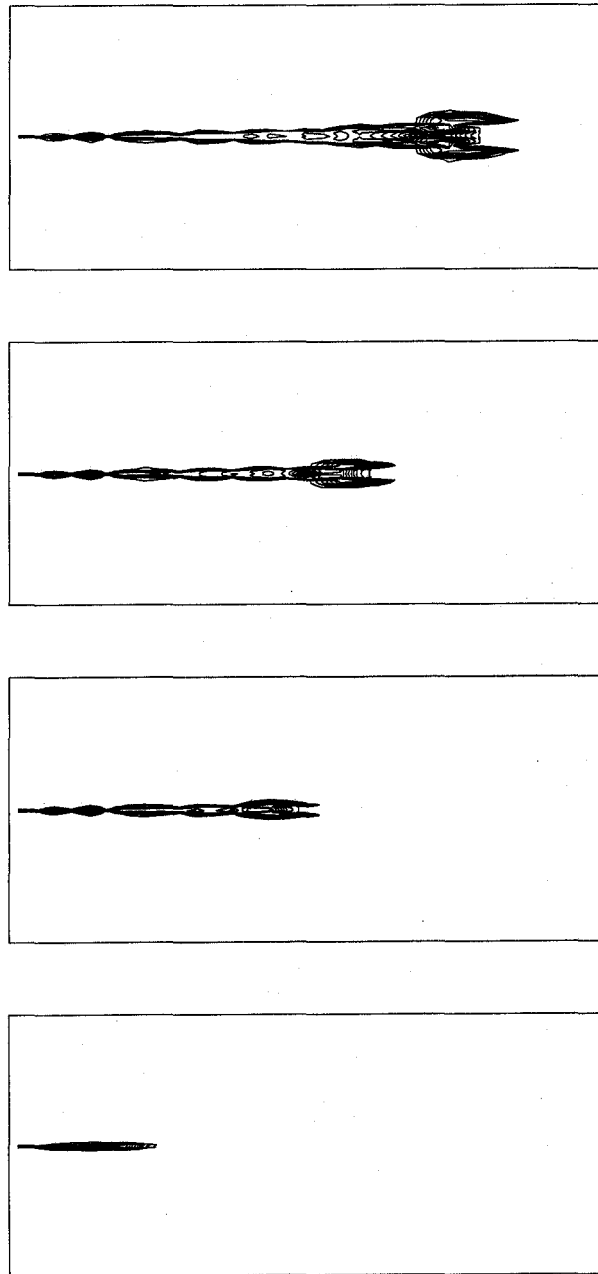


Figure 85. Vapor density maps at: (3.5, 8.3, 10.7, 14.3) ms (upward); the outline value 0.029 kg/m^3 . Initial spray angle 0° . Spray mean diameter $600 \text{ }\mu\text{m}$. Ambient $T = 243 \text{ K}$ and $P = 101 \text{ kPa}$. Compartment $1 \text{ m} \times 0.42 \text{ m}$.

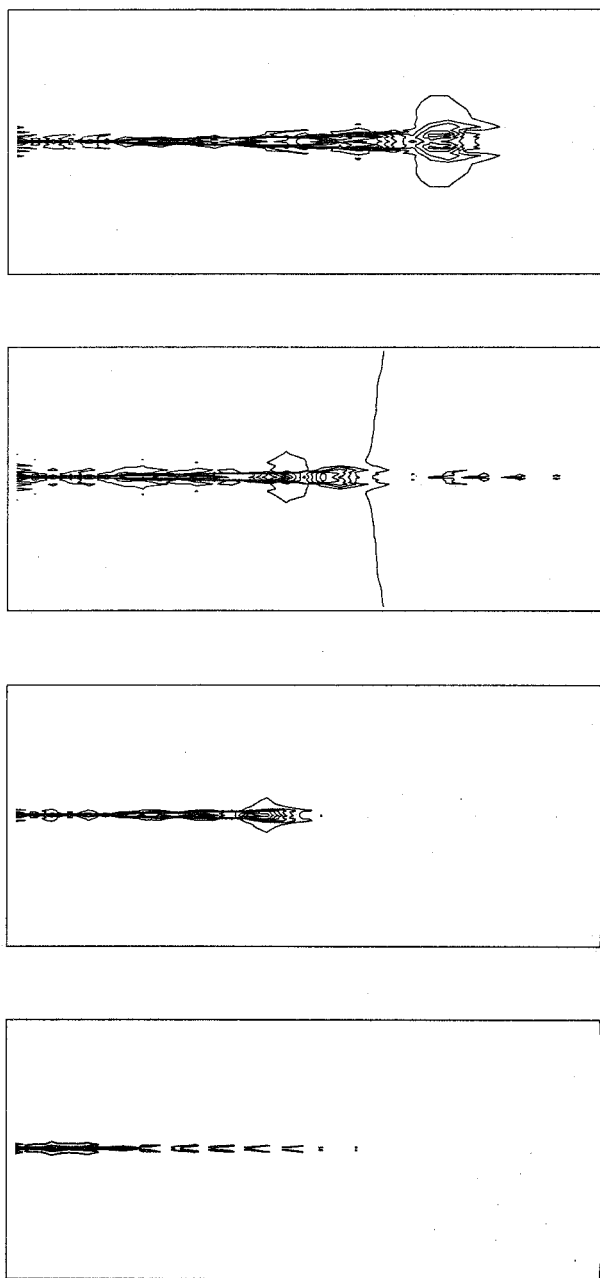


Figure 86. Gas phase temperature maps at: (3.5, 8.3, 10.7, 14.3) ms (upward); the maximum value 233 K. Initial spray angle 0° . Spray mean diameter $600\ \mu\text{m}$. Ambient $T = 243\ \text{K}$ and $P = 101\ \text{kPa}$. Compartment $1\ \text{m} \times 0.42\ \text{m}$.

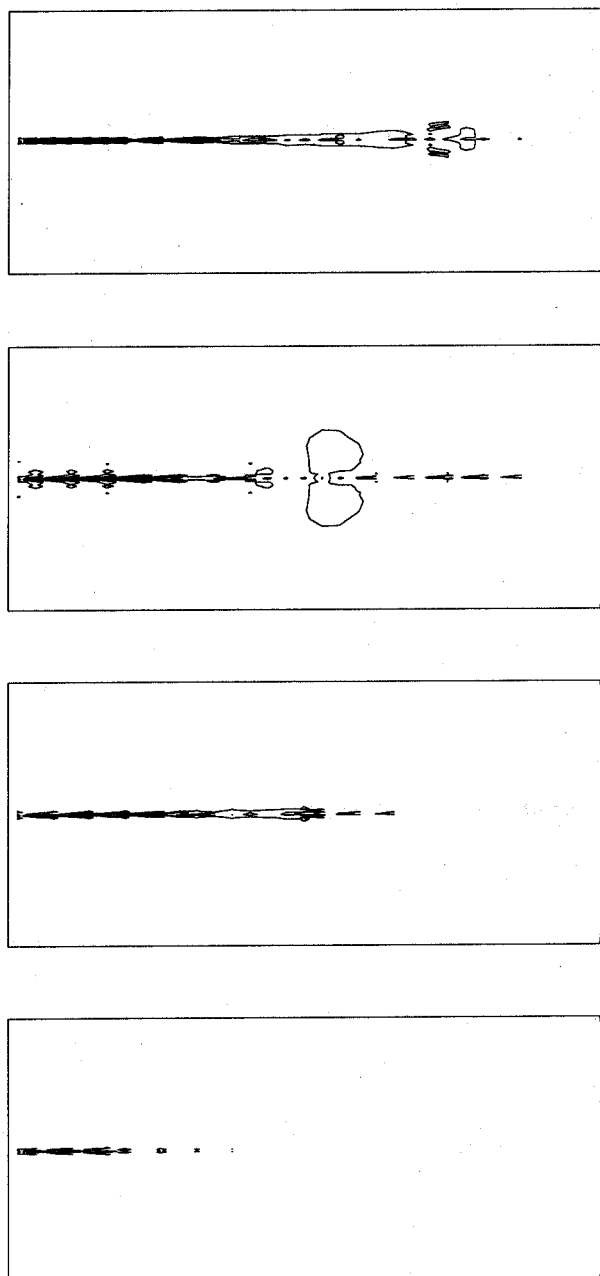


Figure 87. Gas phase pressure maps at: (3.5, 8.3, 10.7, 14.3) ms (upward); the outline value 0.93 kPa. Initial spray angle 0° . Spray mean diameter $600\ \mu\text{m}$. Ambient $T = 243\ \text{K}$ and $P = 101\ \text{kPa}$. Compartment $1\ \text{m} \times 0.42\ \text{m}$.

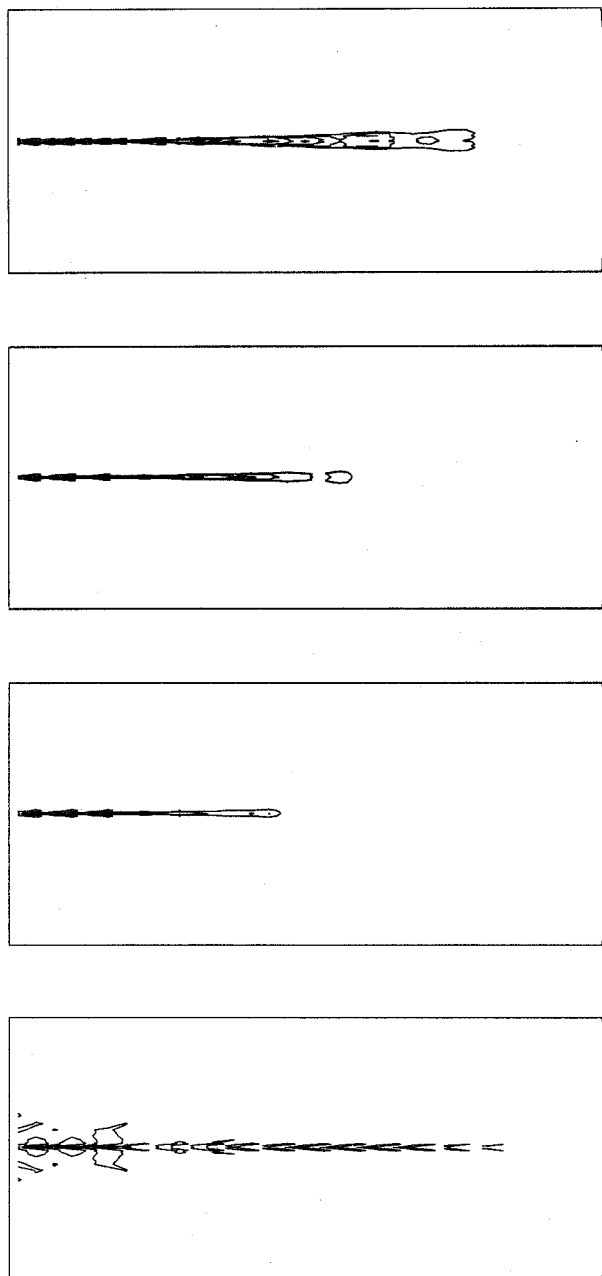


Figure 88. Gas phase density maps at: (3.5, 8.3, 10.7, 14.3) ms (upward); the outline value 1.35 kg/m^3 . Initial spray angle 0° . Spray mean diameter $600 \text{ }\mu\text{m}$. Ambient $T = 243 \text{ K}$ and $P = 101 \text{ kPa}$. Compartment $1 \text{ m} \times 0.42 \text{ m}$.

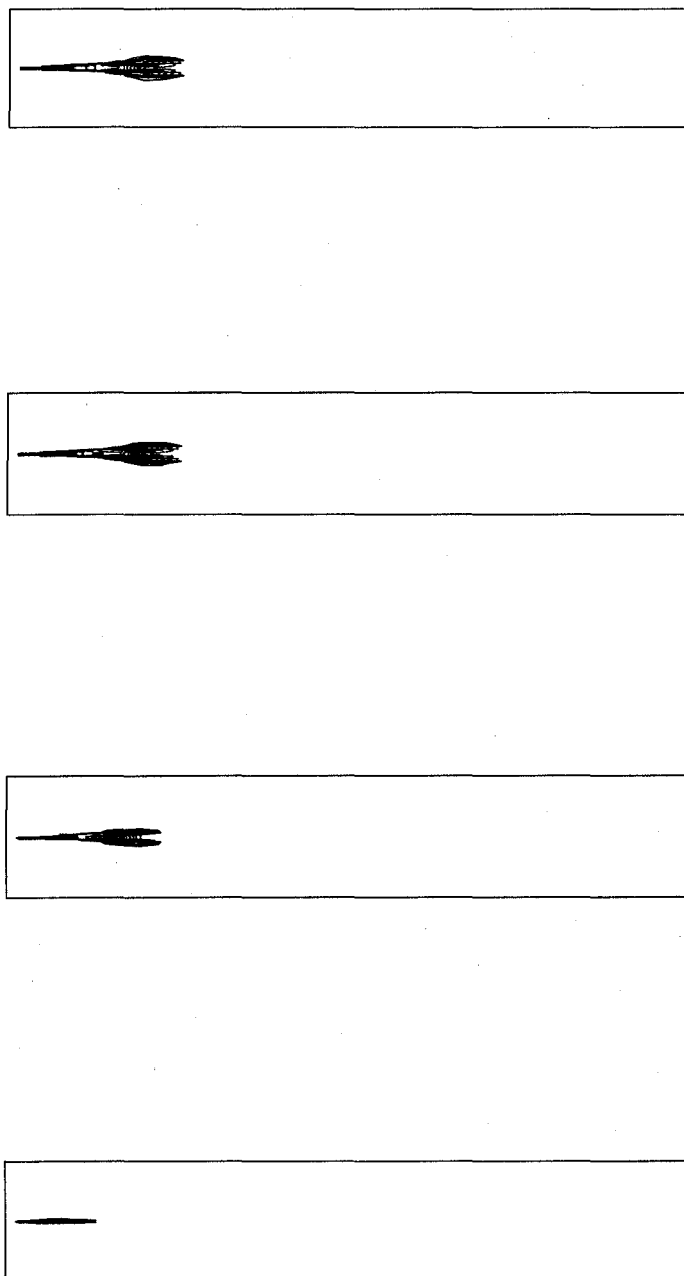


Figure 89. Vapor density maps at: (3.5, 8.3, 9.4, 9.5) ms (upward); the outline value 0.024 kg/m^3 . Initial spray angle 0° . Spray mean diameter $200 \text{ }\mu\text{m}$. Ambient $T = 294 \text{ K}$ and $P = 101 \text{ kPa}$. Compartment $2.25 \text{ m} \times 0.42 \text{ m}$.

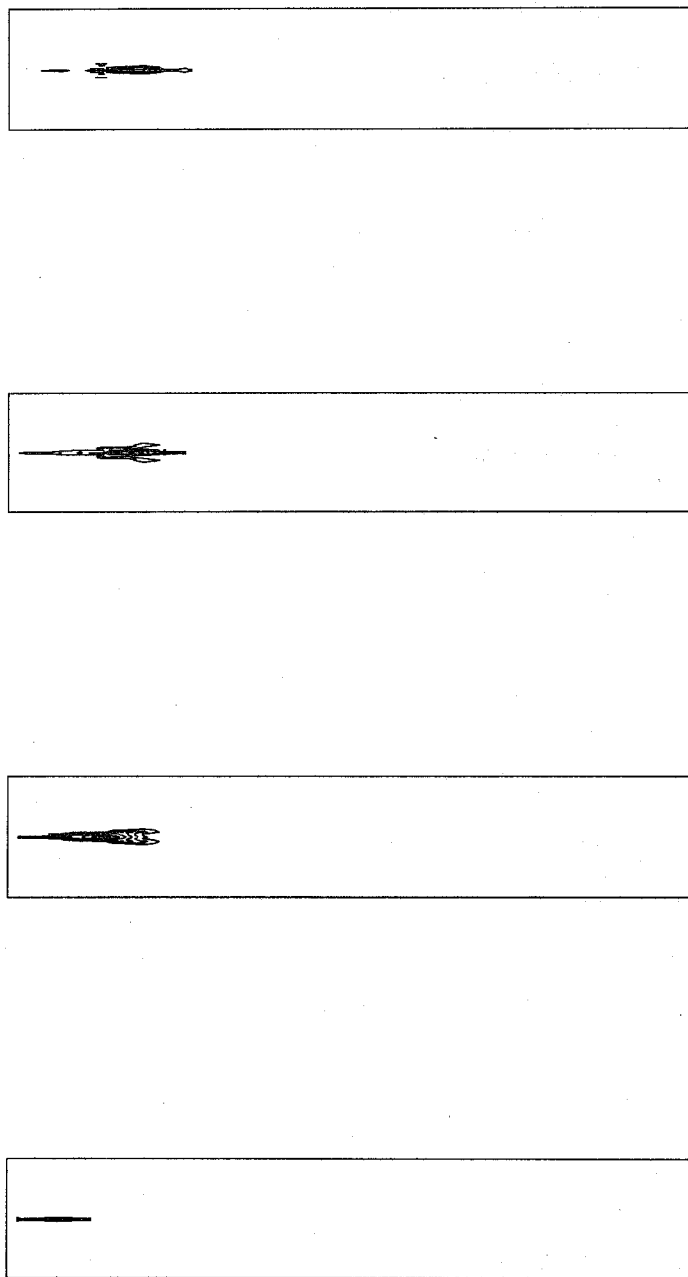


Figure 90. Gas phase temperature maps at: (3.5, 8.3, 9.4, 9.5) ms (upward); the maximum value 243 K. Initial spray angle 0° . Spray mean diameter $200\text{ }\mu\text{m}$. Ambient $T = 294\text{ K}$ and $P = 101\text{ kPa}$. Compartment $2.25\text{ m} \times 0.42\text{ m}$.

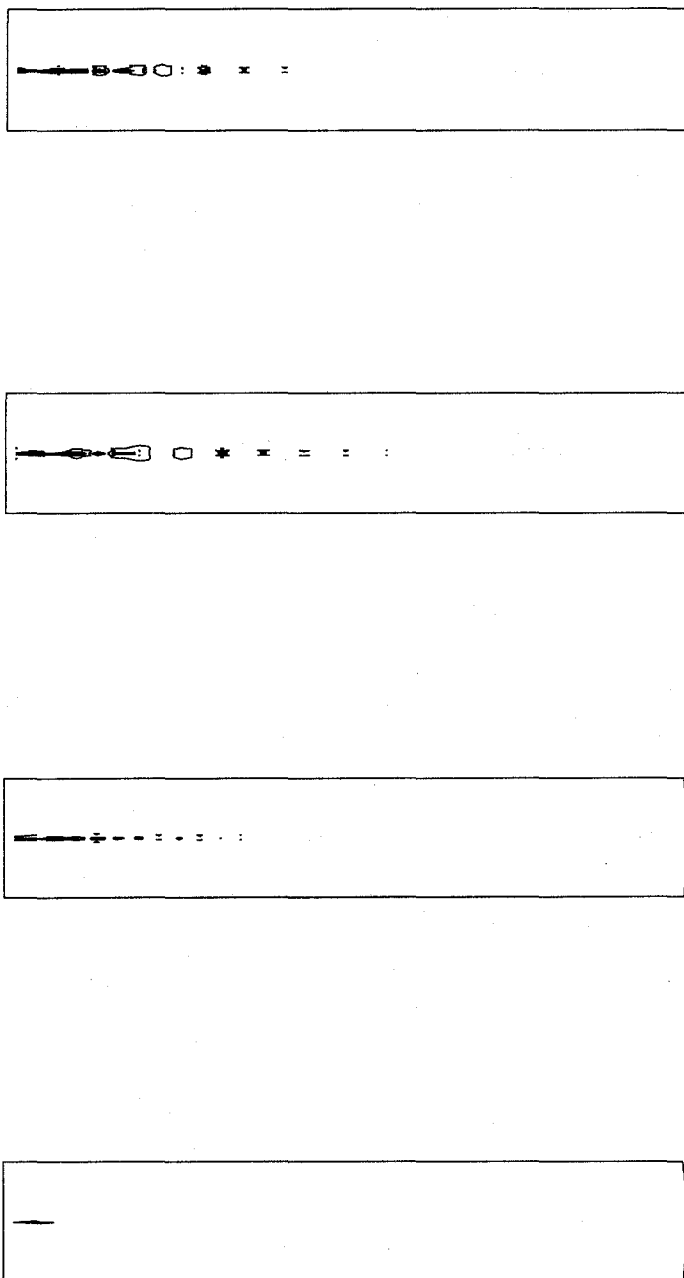


Figure 91. Gas phase pressure maps at: (3.5, 8.3, 9.4, 9.5) ms (upward); the maximum value 121 kPa. Initial spray angle 0° . Spray mean diameter $200\text{ }\mu\text{m}$. Ambient $T = 294\text{ K}$ and $P = 101\text{ kPa}$. Compartment $2.5\text{ m} \times 0.42\text{ m}$.

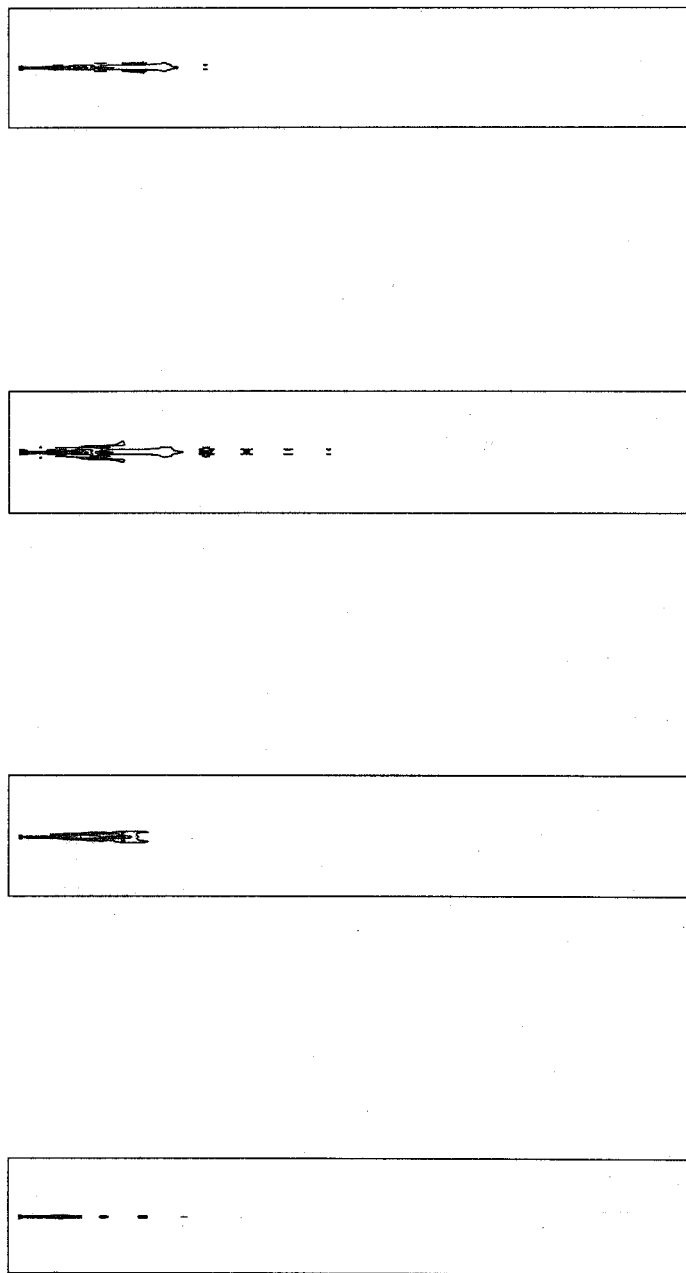


Figure 92. Gas phase density maps at: (3.5, 8.3, 9.4, 9.5) ms (upward); the outline value 1.39 kg/m^3 . Initial spray angle 0° . Spray mean diameter $200 \text{ }\mu\text{m}$. Ambient $T = 294 \text{ K}$ and $P = 101 \text{ kPa}$. Compartment $2.25 \text{ m} \times 0.42 \text{ m}$.

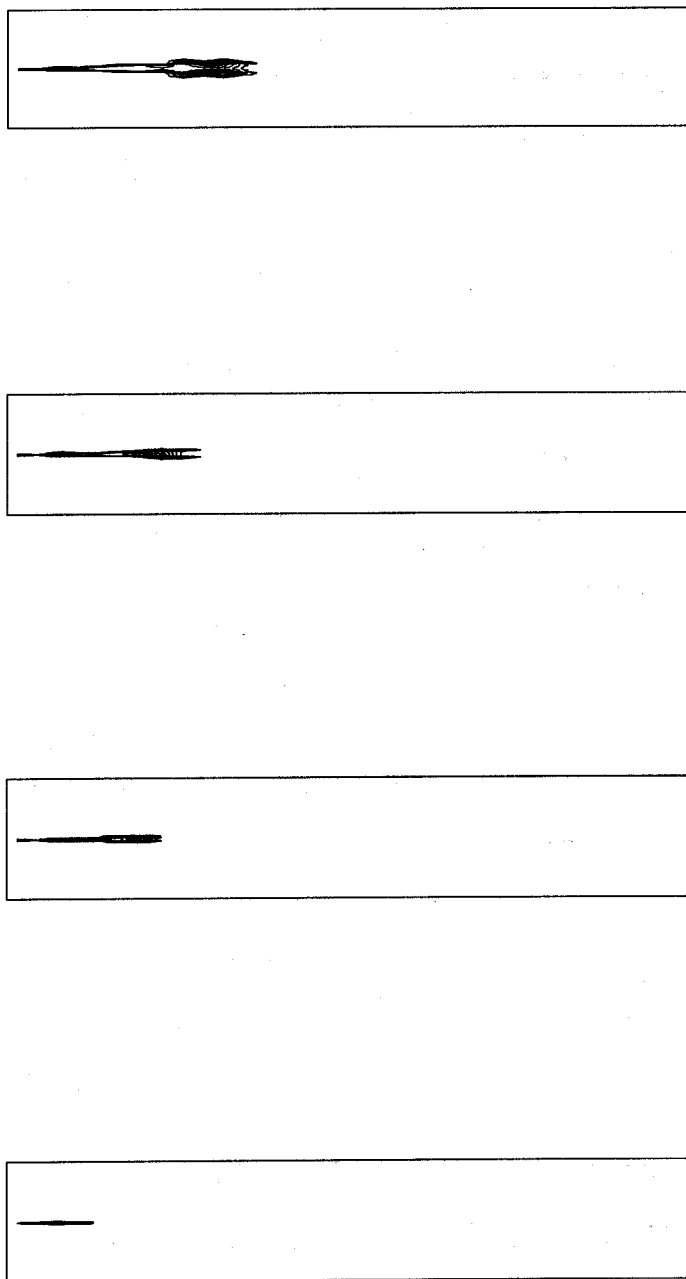


Figure 93. Vapor density maps at: (3.5, 8.3, 10.7, 13.8) ms (upward); the outline value 0.024 kg/m^3 . Initial spray angle 0° . Spray mean diameter $600 \text{ }\mu\text{m}$. Ambient $T = 294 \text{ K}$ and $P = 101 \text{ kPa}$. Compartment $2.5 \text{ m} \times 0.42 \text{ m}$.

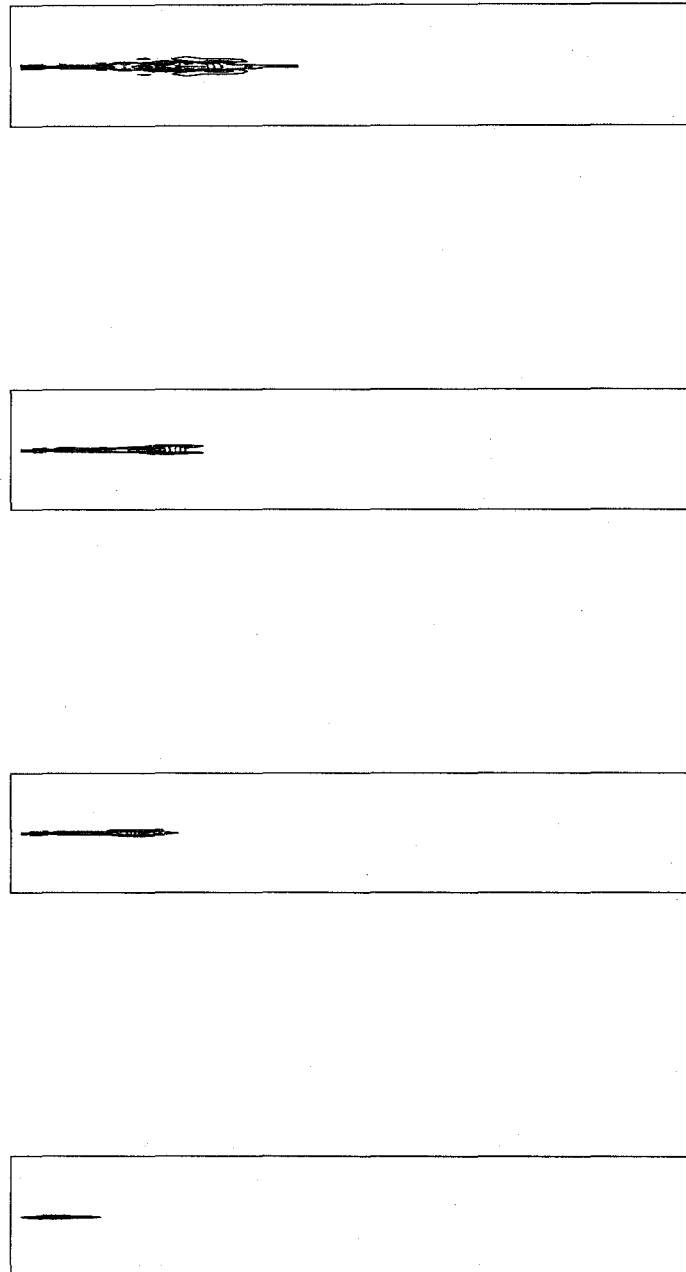


Figure 94. Gas phase temperature maps at: (3.5, 8.3, 10.7, 13.8) ms (upward); the maximum value 298 K. Initial spray angle 0° . Spray mean diameter $600\ \mu\text{m}$. Ambient $T = 294\ \text{K}$ and $P = 101\ \text{kPa}$. Compartment $2.5\ \text{m} \times 0.42\ \text{m}$.

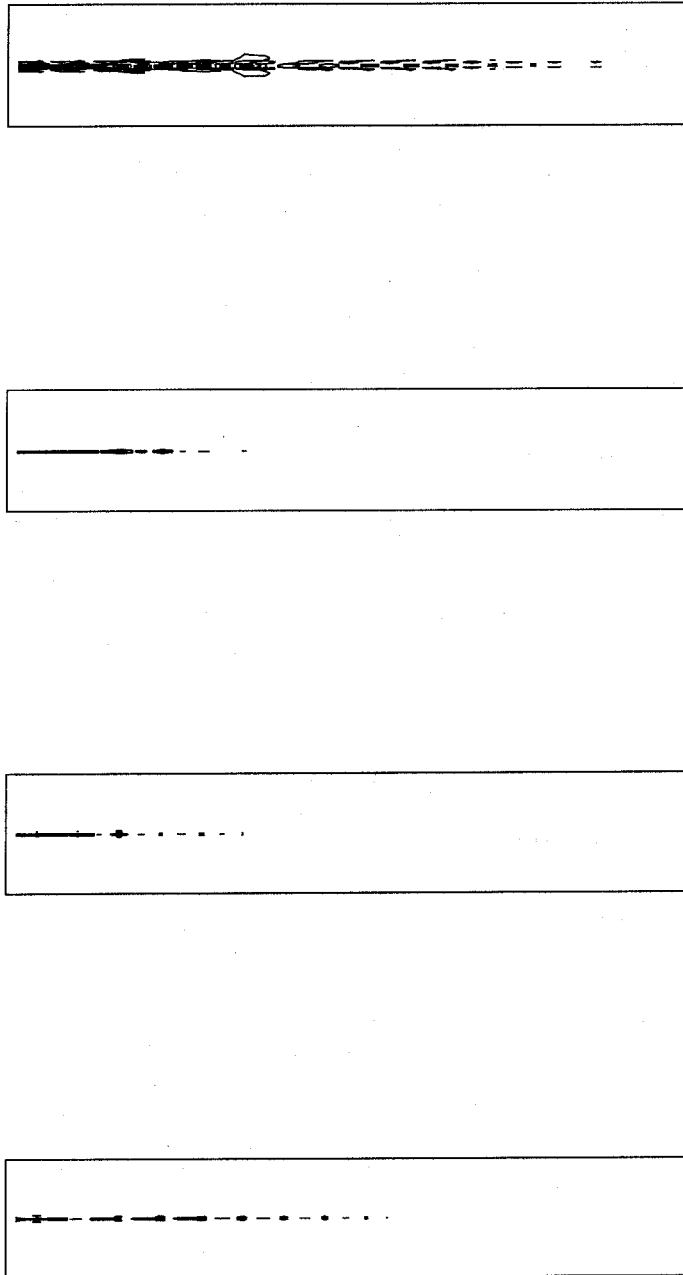


Figure 95. Gas phase pressure maps at: (3.5, 8.3, 10.7, 13.8) ms (upward); the outline value 102 kPa. Initial spray angle 0° . Spray mean diameter $600\ \mu\text{m}$. Ambient $T = 294\ \text{K}$ and $P = 101\ \text{kPa}$. Compartment $2.5\ \text{m} \times 0.42\ \text{m}$.

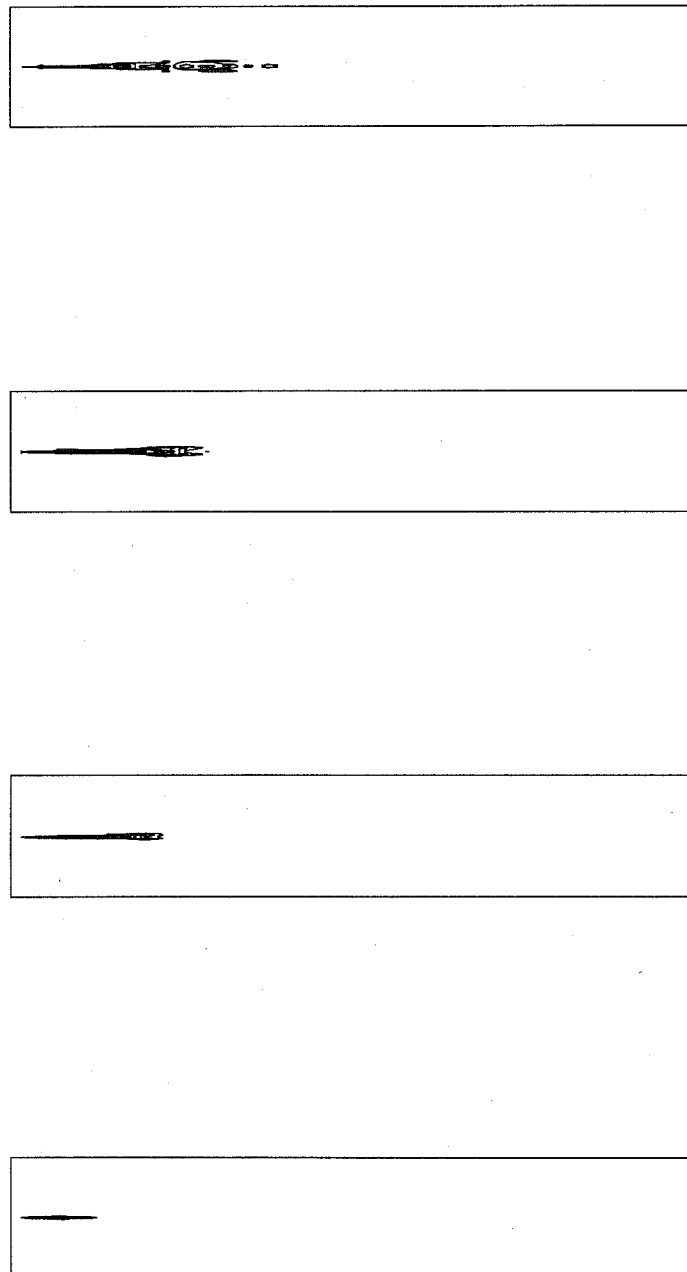


Figure 96. Gas phase density maps at: (3.5, 8.3, 10.7, 13.8) ms (upward); the outline value 1.19 kg/m^3 . Initial spray angle 0° . Spray mean diameter $600 \text{ }\mu\text{m}$. Ambient $T = 294 \text{ K}$ and $P = 101 \text{ kPa}$. Compartment $2.5 \text{ m} \times 0.42 \text{ m}$.

structure and dynamics. The spray becomes thicker and slower. In the case of a 2.5 m long compartment, the spray penetration is greater, but at the same time the spray and its head are thinner. After 1 ms, the wave generated by the spray still travels downward, approaching the bottom wall. It eventually reaches the wall at a later moment and becomes weaker due to dissipation and collision with the head of the spray. The speed of the pressure wave for the two different compartment heights is about the same. Because of the difference in the compartment height, the pressure wave influences the spray structure 2.5 times more frequently in the short compartment. Moreover, the interactions are shifted in time, thereby affecting the spray dynamics and structure. A similar effect was observed when a different initial droplet mean diameter was used.

By comparing the results for the two different ambient temperatures (with the spray mean diameter fixed at 200 μm), the penetration of the spray is about the same; however, the spray structures differ significantly. This is evident especially in the temperature, pressure, and density fields. At an ambient temperature of 21 $^{\circ}\text{C}$, the density outlines of the gaseous phase are significantly broader. The maximum temperature of the gas phase is higher than the initial ambient temperature by about 40 $^{\circ}\text{C}$, thereby enhancing the interphase heat exchange process. At - 30 $^{\circ}\text{C}$, the maximum temperature is about the same as the ambient one. This phenomenon may be associated with the much faster evaporation process, which depends on the interphase heat exchange rate and the compressibility effect in the gas phase. To further substantiate these observations, the behavior of the reflected pressure waves from the walls is examined. In the case of the higher ambient temperature, the pressure wave travels faster. After 10.7 ms in the 1.0 m long compartment, the pressure wave interacts with the spray, while in the other case the pressure wave reaches the spray only after 14.3 ms. Thus, the evaporation process affects the phenomena associated with the compressibility effects.

The effect of initial ambient temperature depends, to some extent, on the spray mean diameter. For the 600 μm diameter, all the phenomena described above occur, with the exception of the maximum gas-phase temperature. In this case, the peak temperature is only slightly higher than the ambient value. This indicates that the process of cooling via evaporation dominates the compression heating.

In all cases, the maximum values of the velocities in the gas phase are between 80 m/s and 290 m/s, the lower values being comparable to those measured in the discharge experiments (refer to Section 8.4). In the computations, the initial velocity of the agent droplets was assumed to be 61.4 m/s, and the ambient air was initially stagnant. In the near-field, momentum is transferred to the air, increasing the air velocity at the expense of the droplets. In the far-field, the velocities of both phases would be close to each other if vaporization were not present. However, the velocity of the gas phase increases dramatically. Under certain conditions the agent evaporation process becomes so fast that the vapor leaving the droplet surface contributes to the resultant gas velocity. The phenomenon occurs in the vicinity of the injector orifice and also downstream, well beyond the injector area. The maximum values occur first in the vicinity of the injector orifice during the first 3 ms of the process, and then in a later stage, between 10 ms (smaller diameter) and 14 ms (bigger diameter) downstream. Such high velocities lead to the creation of pressure waves, reflecting further between the walls. When the local temperature of the gas phase approaches the agent boiling point, the Mach number may exceed the sonic condition because the speed of sound decreases with the square root of absolute temperature. This means that a weak shock wave is created. The wave initially appears close to the injector exit and then travels downstream toward the end wall. It is also stronger in the area downstream, where higher gas velocities occur. A typical maximum increase of pressure at the wave is about 20 %.

It is necessary to remember that the dynamics of the dispersion process depends on the initial conditions in the transitional region where we have no experimental data to use as input for the

calculations. In the above simulations, the droplets were assumed to have a specific size and the temperature was set equal to the agent boiling point, -41°C . In reality, the droplet size distribution is unknown, and the theories leading to droplet formation under such dynamic conditions have not yet been established. Likewise, the temperature may be higher in the transition zone. Because the evaporation model approximates the agent vapor pressure as an exponential function of the surrounding temperature, small changes in temperature have a large impact on the spray dynamics.

It should be emphasized that realistic results from such models as CONCHAS-SPRAY/KIVA-II will be dependent on the validity of the transition-region concept and on the ability to provide reasonable estimates of the state of the spray at the initial section (*i.e.*, the boundary conditions). In spite of the fact that the initial droplet size distribution may play an important role in the agent dispersion process, a method for estimating such a distribution does not seem to be forthcoming. In the present calculations, the droplet size distribution could only be hypothesized.

A numerical problem was encountered when solving the set of equations describing the droplet evaporation process. The problem arises when the agent vapor pressure equation is described by an exponential function of temperature and when the temperature difference between the liquid and gas phases is over 10°C ; this problem becomes worse with increasing temperature difference between the two phases. Under such conditions, the required time step to obtain stable computation is on the order of 10^{-12} s when the original vapor pressure equation is used. If the vapor pressure equation is analytically modified in such a way to mitigate the sharp pressure increase, the time step is increased by six orders of magnitude to 10^{-6} s. However, this modification is associated with the change of the original thermophysical properties of the compound. Therefore, it is impossible at the present time to compare the computational results with the dispersion characteristics determined experimentally. Note that the LANL codes are originally designed for applications to internal combustion engines, where liquid hydrocarbons are used. It is possible that a separate subroutine could be written to solve the vapor pressure equation with a numerical method appropriate for this highly non-linear behavior. One possible solution to this problem is to adopt the numerical techniques that are used in solving exponential chemical kinetics equations.

A further comparison between KIVA-II and CONCHAS-SPRAY for the same set of conditions is needed to determine the impact of the turbulence and droplet breakup model on the results. If the outcome is independent of the code, additional analyses with CONCHAS-SPRAY could be conducted. If the turbulence and droplet models influence the results, KIVA-II or preferably KIVA-III (Amsden *et al.*, 1993) should be used for future calculations.

The KIVA codes have the additional advantage that fully three-dimensional spaces can be handled. Extended resources on a CRAY computer will be required for these investigations. The spectrum of parameters influencing the spray dynamics should be broadened to include additional compartment geometries, discharge orifice geometry, thermodynamic and gas dynamic parameters of the agent and ambient air, agent injection and atomization parameters, as well as the conditions of the transition region of spray.

8.5.5 Conclusions. Numerical simulation was carried out using the LANL CONCHAS-SPRAY and KIVA-II computer codes in an attempt to better understand agent dispersion processes. The following conclusions can be drawn based on the computational results obtained so far:

1. CONCHAS-SPRAY is at least an order of magnitude more efficient, in terms of the computational time, than KIVA-II when applied to the dispersion process of a simulated halon alternative. Both codes give the same qualitative and quantitative results using the same input data.

2. It was found from the calculations that the geometry of a compartment into which the agent was released is an important parameter governing the spray dynamics. The propagation of pressure waves generated by the fast moving agent affects the shape and penetration of the spray and eventually affects the agent vapor mass fraction field due to pressure wave reflections. The smaller the compartment, the thicker the spray, the lesser the spray penetrates, and the broader the agent density field.
3. The liquid agent atomization process, expressed in terms of Sauter mean diameter, influences the spray structure significantly. The smaller the spray mean diameter, the better the agent disperses.
4. For a higher ambient temperature, the spray is broader, and the penetration of the spray is farther.
5. The occurrence of higher gas velocities corresponds to the presence of pressure waves. The phenomenon may be associated with the enhanced evaporation process which contributes to the total gas velocity.

8.6 Pipe Flow Characteristics of Alternative Agents

8.6.1 Introduction. Three potential near-term halon alternatives for engine nacelle fire protection applications have been identified by the Technology Transition Team (Grosshandler *et al.*, 1994): HFC-227ea, CF_3I , and HFC-125. In engine nacelle applications, the fire suppression agent is located remotely from the nacelle, and a piping system delivers the agent to the nacelle injection location(s). It is crucial to deliver the proper amount of agent in a timely manner to achieve the desired agent concentration in the nacelle for the required time interval. The flow regime in the piping is characteristically a two-phase, two-component gas/liquid system. Since no universally accepted flow prediction method is available for two-phase flows, an experimental study was undertaken to investigate the effects of selected parameters on the flow of alternative agents. The work here focused on the performance of alternative agents based on flow time through piping systems. Rapid transport to, and effective mixing in the nacelle are important for an efficient design utilizing an alternative agent.

The initial selection criteria of the alternative agents included more than just environmental concerns and suppression efficiency. NIST Special Publication 861 (Grosshandler *et al.*, 1994) details the measurements and analyses performed by NIST that assisted in the selection of a reduced list of alternatives. Detailed studies of pipe flow characteristics were not included, primarily because it represents a portion of the overall system performance which does not, to some extent, depend only on the chemical properties of the agent. However, design parameters such as pipe diameter, length, and storage conditions play a significant role in the system's discharge performance. In this study, the effects of the following design parameters were examined: bottle fill condition and temperature, pipe diameter, length, elbows, tees, contractions, and expansions. Steady pipe flow experiments were performed by adding make-up nitrogen to the storage bottle as the agent was discharged. From these experiments, mass flow rate and pipe pressure drop as functions of fixed bottle pressure were obtained. Optical access to the flowing agent in the pipe verified the nature of the flow.

8.6.2 Agent Discharge in Piping. The fact that there is two-phase flow of halon or of alternative agents stems from the "optimized design" of a generic suppression system, expressed as the desire to

get most of the agent to the nacelle very quickly, while minimizing the storage space. First, the bulk of the agent is in the liquid phase in the storage bottle which drastically cuts down on the storage volume. The liquid phase is subject to flashing during depressurization. The portion of the bottle volume that contains vapor is referred to as the ullage. Second, nitrogen gas is added to the storage bottle, raising the ullage pressure above the saturation vapor pressure of the agent; the ullage pressure is the main driving force for the expulsion of the agent from the bottle. Nitrogen dissolves in each of the agents to some extent and can come out of solution during depressurization, initiating two-phase flow.

At this point, a qualitative description of halon or alternative agent pipe flow sets the stage for the more detailed discussion to follow. For now consider that the bottle is very large relative to the piping so that conditions in the bottle do not change during the ensuing pipe flow. Thus, upstream conditions are given by stagnation properties and the pipe flow is steady. Traversing down the long horizontal pipe (with no significant entrance effects, valves, etc.) the pressure is dropping due to wall friction losses and acceleration of the expanding fluid. If the agent is originally saturated with nitrogen, a pressure decrease results in a supersaturated liquid and bubbles can form. Ignoring the effects of bubble inception (nucleation) and growth, a differential amount of nitrogen will come out of solution after a differential drop in pressure from the stagnation conditions (assuming an isothermal liquid phase, so that Henry's law constant does not change). These bubbles will contain both nitrogen and agent vapor even though the total pressure may still be above the saturation vapor pressure of the agent. The quality of the flow (defined as the mass fraction in the gas phase) increases as the pressure drops along the pipe. The two-phase flow is compressible; thus it is possible to exhibit choking. In gaseous flows, choking is the realization of a thermodynamic limit on the mass flux as the flow achieves its sonic velocity; critical flow and choked flow have the same meaning. In two-phase gas/liquid flows choking may be realized at velocities below that of the gas-phase sonic velocity. If the flow is choked, the mass flow rate is independent of the discharge pressure (here, the pressure of the ambience).

An actual bottle discharge exhibits highly transient flow. At first, as the pipe is filling up with agent, the pipe pressure at any point is rising rapidly while the bottle pressure is falling rapidly. The pipe pressure achieves a maximum when the pipe just fills, then starts to fall along with the bottle pressure. As the bottle pressure drops, the dissolved nitrogen in the liquid phase may not come out of solution immediately, resulting in a metastable, supersaturated solution. After some time delay, degassing of the dissolved nitrogen can produce a net pressure rise inside the bottle due to the expansion of a bubbly two-phase fluid. The bottle pressure may reach a local maximum then start to drop again as this two-phase fluid continues to empty. At the point where the last of the two-phase mixture is being expelled from the bottle, a pressure rise is observed in the piping for a short period of time. The fluid in the piping is changing from a low quality (mostly liquid) fluid to a high quality (mostly gaseous) fluid, which exhibits a different pressure drop in the piping. At that point, most of the agent has been discharged from the bottle and piping. The pressure in the piping starts dropping again as the ullage contents discharge.

8.6.3 Single-Phase Flow. Single-phase steady pipe flows are well understood, and accurate flow calculations can be readily performed. Single-phase flows are treated as either incompressible (*i.e.*, liquids) or compressible (*i.e.*, gases). As a rule of thumb, if the change in fluid density is greater than 10 % over the flow section of interest, the flow is treated as compressible. Incompressible flow is the simplest case and is described below to illustrate the significant parameters affecting the flow characteristics.

As is characteristic of all fluid flows, the driving force is the pressure gradient. The pressure force is needed to overcome the resistance to flow arising from fluid drag at the pipe walls. For both laminar and turbulent flow, the following equation holds for flow in a straight horizontal pipe.

$$\frac{\Delta P}{L} = \frac{2f\rho u^2}{D} \quad (37)$$

ΔP is the pressure drop over the pipe length of interest. L is the pipe length, D is the diameter, ρ is the fluid density, u is the mean velocity and f is the Fanning friction factor. The friction factor is a parameter that describes the fluid-wall interaction; it is possible to calculate the friction factor for laminar flow from pipe geometry, flow conditions and fluid properties. For turbulent flow, the friction factor is treated empirically and is correlated with pipe geometry, flow conditions and fluid properties. Correlations for the friction factor are cast in terms of the Reynolds number (a dimensionless group formed by the ratio of the inertia force to the viscous force) and the relative roughness of the pipe, ϵ/D where ϵ is the surface roughness and has been measured for many typical piping materials. The Reynolds number also is indicative of the flow regime with laminar flow existing below $Re \sim 2300$ and turbulent flow above $Re \sim 4000$ with a transition region between 2300 and 4000 for pipe flows. The concept of equivalent length is very useful in determining flow rates or pressure drops in realistic piping systems with fittings, bends, valves, etc. Simply put, the concept is to equate the observed pressure drop in a pipe fitting with an equivalent length of pipe (L_{eq}) with the same diameter and friction factor as the piping of interest. A complicated piping system is reduced to an equivalent (fictitious) total pipe length. L_{eq}/D can be obtained from head loss coefficients tabulated for many different pipe fittings (SFPE Handbook, 1988). A loss coefficient divided by $(2f)$ yields L_{eq}/D .

If the fluid is compressible, the density is a function of pressure, and the equation above is not appropriate. The flow depends on the thermodynamic path the fluid follows. Usually, to simplify analysis, a compressible flow is assumed to be either isothermal, adiabatic isentropic or adiabatic isenthalpic, which fixes the thermodynamic path. The same friction factor correlations hold for compressible flow as those for incompressible flow, though the friction factor may change locally as the flow progresses.

8.6.4 Two-Phase Flow. Two-phase gas/liquid flows are common in the chemical process industries and in electric power plants (steam/water system). Design calculations for many steady two-phase flow conditions are readily available, although the accuracy of two-phase flow correlations can be poor (Olujć, 1985); all two-phase flow correlations rely on some empiricism. The lack of a generalized physical model stems in part from the number of flow regimes possible in two-phase gas/liquid flows. These flow regimes are descriptive of the phase separation and include bubbly, annular, wavy, slug and mist flows. A correlation which is reasonable for wavy flow may be extremely poor for bubbly flow, etc. A flow map, which is a graphical depiction of the conditions giving rise to the various flow regimes, can be used to assist in selecting the best correlation equations, though it is best to have direct knowledge of the flow regime if the conditions are uncertain. Depending on the flow regime, a particular model may be preferred to describe the flow. The homogeneous flow model assumes that the two phases are well mixed and traveling with the same velocity which is reasonable for bubbly flows. There are equilibrium and non-equilibrium homogeneous flow approximations. Separated flow models, where the liquid and gas phases are not well mixed and may be travelling at different speeds, characterize the rest of the cases. A good discussion of two-phase gas/liquid flow is presented by Whalley (1990).

The literature on transient two-phase flows mainly involves the high-pressure water/steam system. This is due to the importance of nuclear reactor safety assurance during a loss-of-coolant-accident (LOCA). Most of the literature on halon 1301 systems deals with design of systems for total flooding applications with agent discharge times which are an order of magnitude longer than that required for engine nacelle fire protection application. A review of halon discharge testing and system design for total flooding applications is presented by DiNenno and Budnick (1988). They also include an extensive bibliography on two-phase flow in general and halon systems in particular. The most comprehensive study detailing transient discharge of halon 1301 through piping systems reported in the literature is by Elliot *et al.* (1984).

Design calculation schemes for halon systems are for the most part proprietary. System designers only have to provide a design that works for a given case, meaning design concentrations of agent are maintained for the appropriate times. This requires an experimental test to verify a specific design. Three models of halon 1301 pipe flow described in the literature are mentioned below. The National Fire Protection Association's Standard 12A "Halon 1301 Fire Extinguishing Systems" (National Fire Codes, 1995), gives a simplified design method for systems that should meet the performance criteria for extended discharge into enclosed spaces. The pipe flow equation is an application of the steady-state mechanical energy and mass balances with a specified friction factor and data specific to halon 1301 inserted; homogeneous, equilibrium two-phase flow is assumed. Pipe flow calculations are based on a fixed average bottle pressure condition and adiabatic, isenthalpic flow. DiNenno and Budnick (1988) point out potential accuracy and uncertainty problems in this method. This method was designed for extended discharges (discharge times of about 10 s). Elliot *et al.* (1984) use a homogeneous, equilibrium model of two-phase flow to solve for transient pipe and nozzle flow in halon systems. They also examined a Los Alamos National Laboratory code "Sola-Loop" developed for the steam/water system which uses the "drift-flux model," a separated flow model, to predict the transient discharge of halon. Both of their calculations compare favorably to some limited halon 1301 tests.

These documented flow calculations do well for certain situations, but rely on data explicit to halon 1301, and make various assumptions about the flow. The observations and data from this study verify some of the assumptions made, and their validity for the alternative agents. Here, a model that simulates the transient discharge of an agent through piping has been developed. It is similar to the NFPA 12A methodology and Elliot's model in that it is based on a homogeneous, equilibrium two-phase flow description. Thermodynamic properties and fill conditions are obtained from a separate vapor-liquid equilibrium computer program called "PROFISSY" (see Section 8.3).

8.6.5 Experimental Apparatus. A range of test conditions was examined to better understand the nature of the alternative agent flows under conditions that may be encountered in suppression system piping. Both transient and quasi-steady flow cases were investigated. The quasi-steady flow experiments were performed to obtain the mass flow rate and steady pipe pressure drop for a fixed discharge pressure.

The experimental apparatus was designed so that different configurations and conditions could be studied. A schematic diagram of the experimental apparatus is shown in Figure 97 and each of its components is described below. System constraints, specific to engine nacelle applications, limited the range of conditions investigated. Pipe diameters and lengths were selected based on a review of military aircraft specifications. Also the fill condition and nitrogen pressurization were selected based on knowledge of typical halon 1301 engine nacelle systems.

8.6.5.1 Discharge Vessel and Piping Design. The discharge vessel was constructed from a cylindrical tube of stainless steel with an internal diameter of 100 mm and a wall thickness of

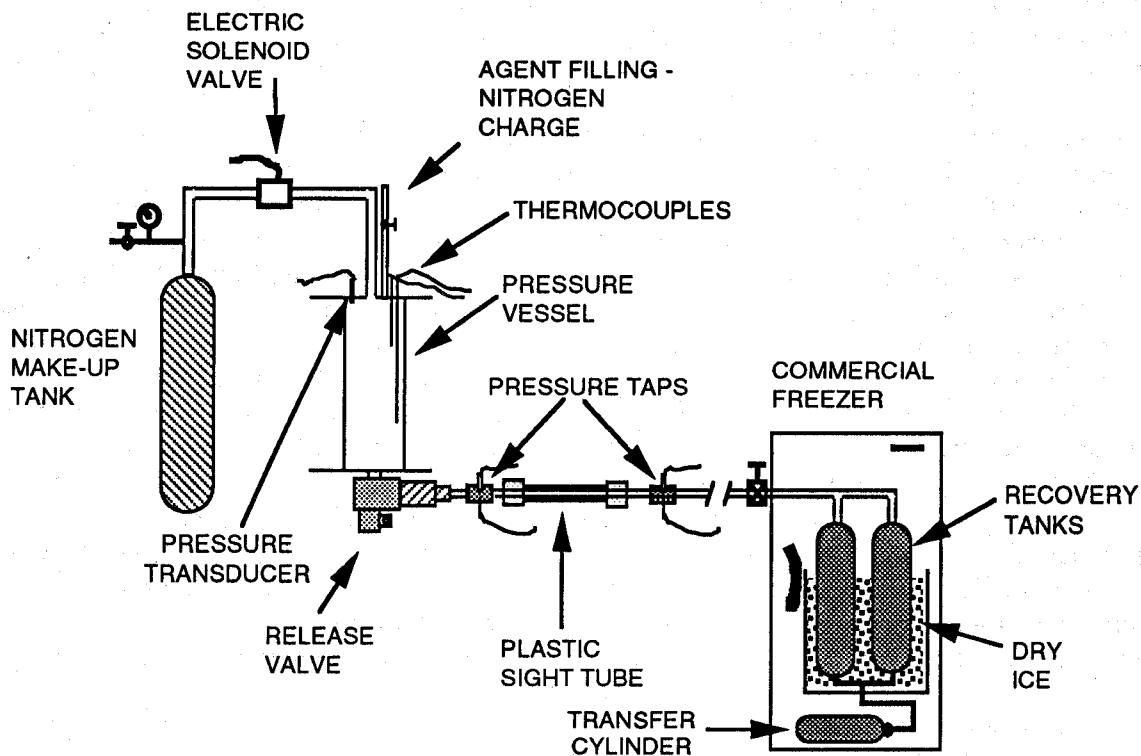


Figure 97. Schematic of the apparatus for pipe flow experiments.

12.7 mm. Flanges were welded to the two ends of the tube so that top and bottom plates, 19.1 mm thick, could be attached with bolts (Figure 98). The seal between a flange and plate was made with an O-ring. The vessel volume with the flanges attached is $4.06 \times 10^{-3} \text{ m}^3$. This volume was verified by water displacement. The combined standard uncertainty in the volume measurement is estimated to be less than $\pm 10 \text{ cm}^3$. The top plate had five threaded access holes for agent filling, two thermocouples, a pressure transducer, and make-up nitrogen. The bottom plate had one threaded access hole for the release mechanism. The vessel was designed to operate at pressures up to 14 MPa. There was a pressure relief valve connected to the filling port to protect the vessel from unexpected high pressure conditions.

The agent release mechanism was a quick-opening solenoid valve (Marotta Scientific Controls Inc., Model MV121KJ-2) with an inlet diameter of 31.8 mm and an exit diameter of 44.5 mm. The valve exit is at a 90° angle to the inlet. This valve can be easily re-armed for quick turn-around of tests. The valve was activated by a DC power source of approximately 25 V and 10 A; the opening time was on the order of 10 ms. Since the valve exit was much larger than the internal pipe diameters used in this study, a smooth tapered connector was fabricated to make the internal diameter transition from 44.5 mm to 15.9 mm (Figure 99).

The nitrogen make-up tanks were two standard high-pressure gas cylinders with a combined internal volume of $88 \times 10^{-3} \text{ m}^3$. The cylinder valves were removed and 19.1 mm I.D. tubing leading to a large-orifice solenoid valve was used to deliver the make-up nitrogen. The valve was a piston-plunger type solenoid valve which required a pressure difference of 30 kPa to open after the solenoid was activated. The opening time is on the order of 50 ms for nitrogen flow at test condition pressures. The make-up nitrogen entered the vessel from an access hole in the top flange. There were two reasons for using a solenoid valve here: first, the bottle contents must be separated from the nitrogen make-up tanks or else agent vapor will mix with the nitrogen, and second, it was desired to shut down the nitrogen flow after the agent discharge to avoid losing most of the make-up nitrogen and pressurizing the entire system.

The piping was drawn stainless steel tubing. Two diameters were investigated, 15.9 mm and 9.5 mm inner diameter with tube wall thicknesses of 3.2 mm. Brass pressure taps were constructed with the same inner diameter as each of the pipes (Figure 100). These taps allowed the pipe pressure transducers to be installed flush to the tube wall. The transducers were mounted and maintained in the horizontal orientation. An extra access port was provided for thermocouple installation. The piping sections were connected with threaded fittings for easy reconfiguration, and rigidly attached to a bench to limit motion during agent discharge.

The recovery tanks contained the agent after it flowed through the piping. They consisted of four separate high pressure sample cylinders with a combined volume of $15 \times 10^{-3} \text{ m}^3$, located in a commercial freezer and surrounded by dry ice. This allowed most of the agent to condense in the sample cylinders after a test. Piping connected to the bottom of the cylinders led to a transfer cylinder which was used to transfer the agent back to the discharge vessel for subsequent tests. Usually, 80 % to 90 % of the agent was recovered with this system after a given test. This significantly reduced the total amount of agent required to perform the series of tests.

8.6.5.2 Experimental Measurements. The liquid and gas temperatures in the vessel were recorded by type E sheathed thermocouples prior to a test. Temperatures were not taken during tests because the thermal time lag through the sheath was longer than the discharge time. Attempts to measure the temperature of the fluid in the piping during discharge were unsuccessful because the unsheathed fine wire (13 μm diameter) thermocouple probes would break in the flow.

The pressure in the storage vessel was recorded with a strain-gage-type transducer (Druck Model 330) with a total accuracy of 0.75 % and an operating and compensated temperature range of

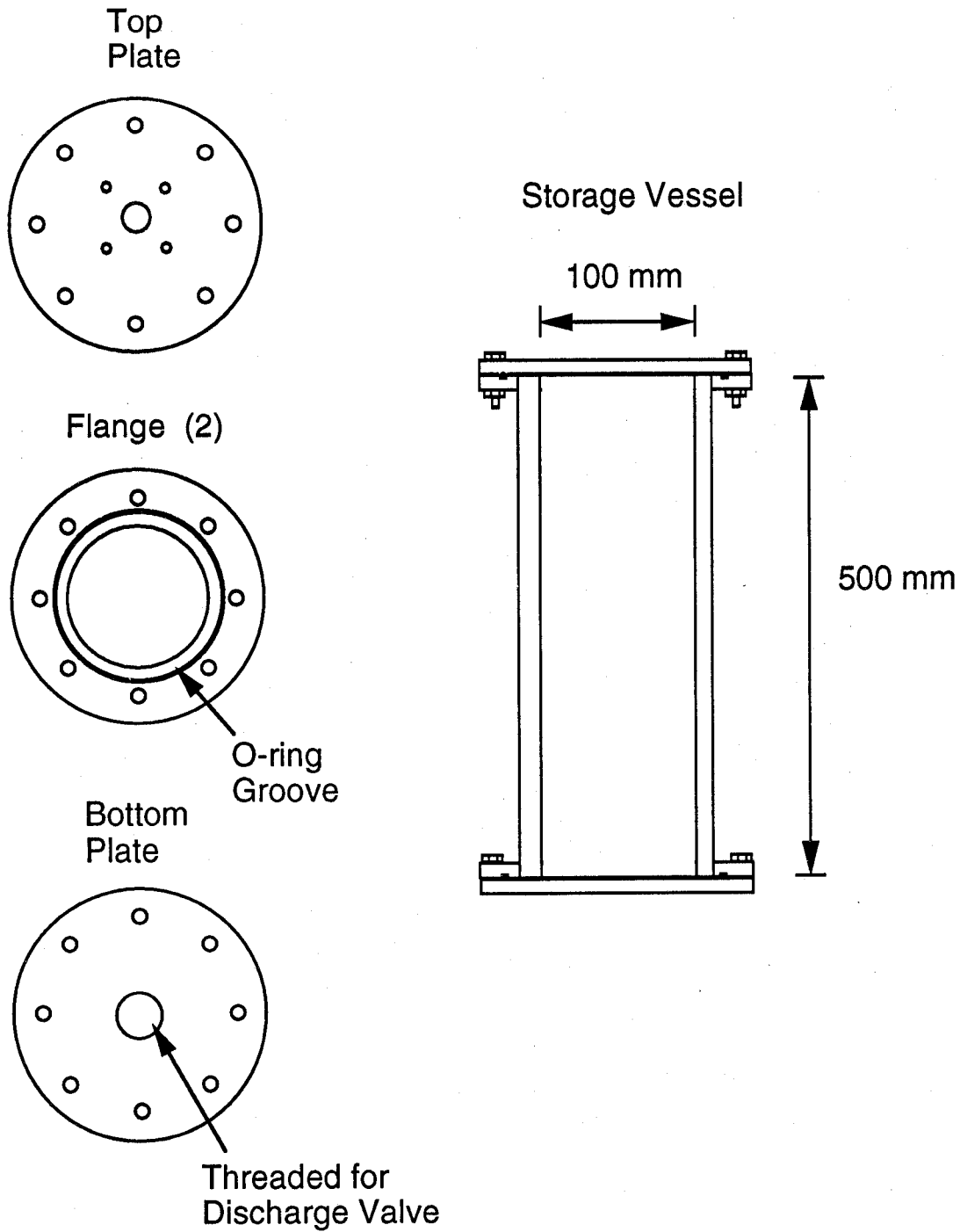


Figure 98. Schematic of the pressure vessel.

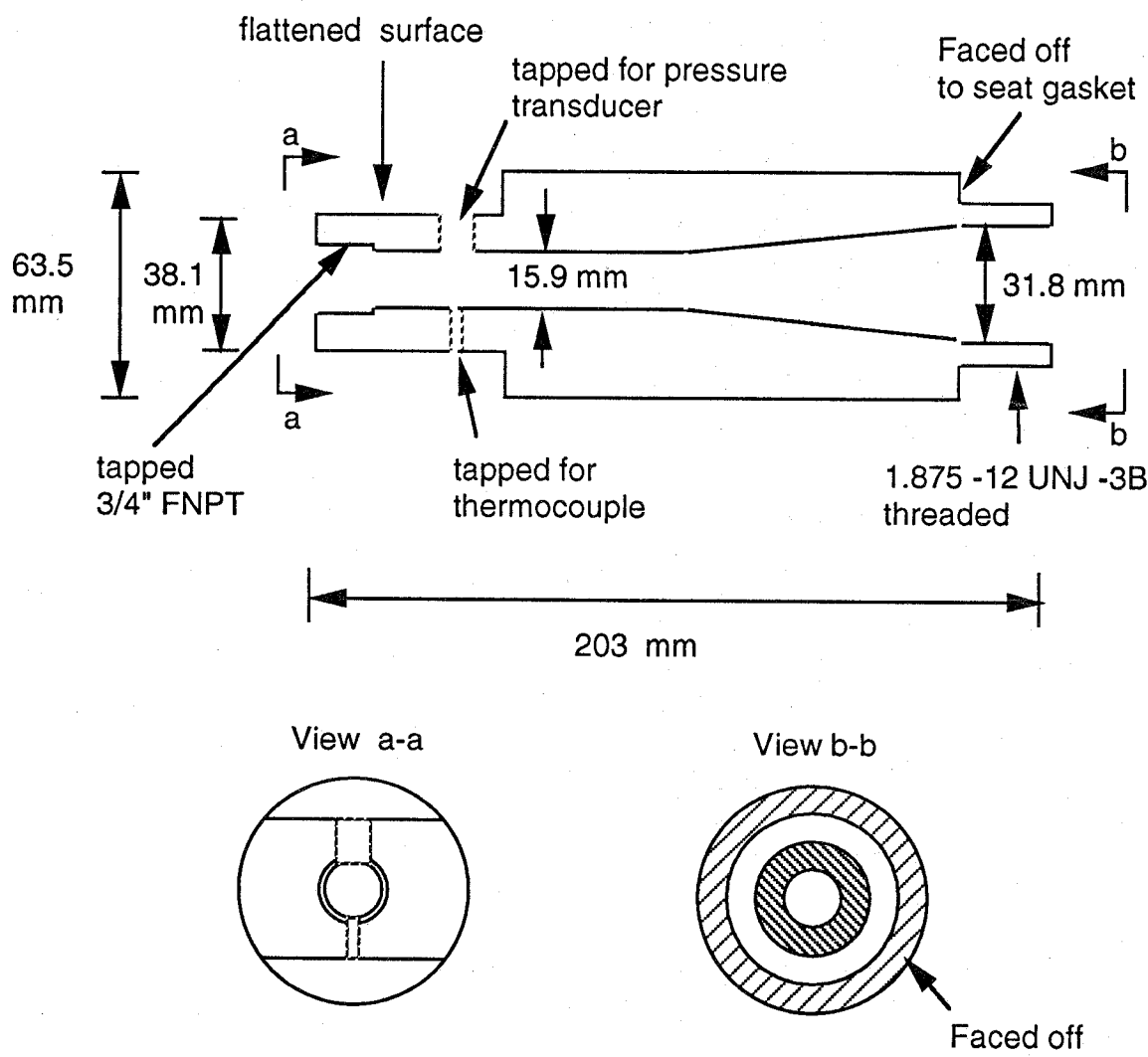


Figure 99. Schematic of valve reducer.

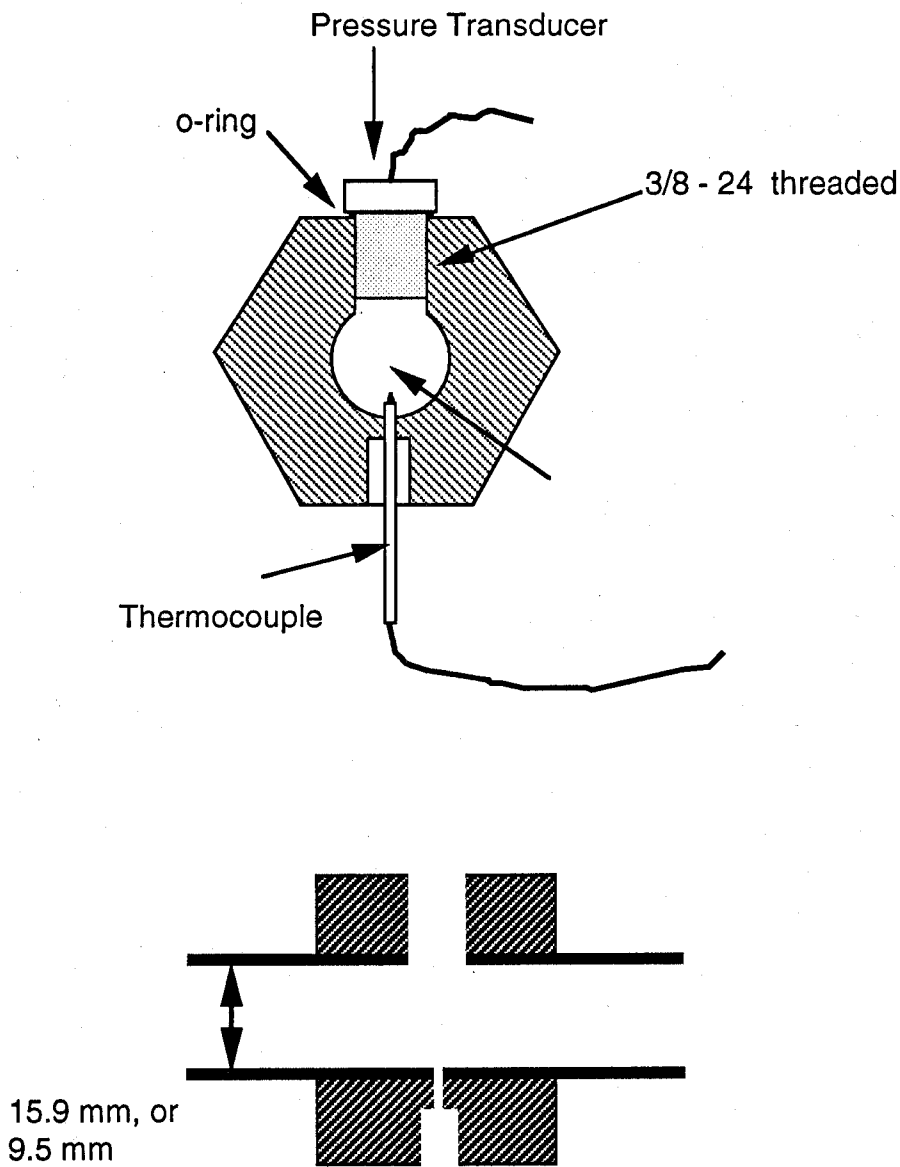


Figure 100. Schematic of pipe tap for pressure transducer and thermocouple.

– 54 °C to 150 °C. The transducer's pressure range was 0 MPa to 14 MPa with a response time on the order of 1 ms. Pressure in the piping was recorded by strain-gage type, flush-mount pressure transducers (Omega Model PX-600) with a diaphragm face diameter of 7.9 mm. The transducers had a nominal range of 0 MPa to 3.4 MPa or 0 MPa to 6.9 MPa, depending on the gage. The stated accuracy was 1 % over the compensated temperature range of 16 °C to 71 °C. The operable temperature range was – 54 °C to 150 °C; a temperature correction must be applied to achieve the nominal accuracy outside the compensated temperature range. The gage response time was on the order of 1 ms. A fast-response (2 kHz) signal conditioner/amplifier provided the boosted voltage signal that was recorded by the data acquisition system. In early trial experiments, piezoelectric-type dynamic transducers were used in the piping. Pipe pressure traces from the dynamic transducers and the strain-gage type transducers were essentially the same for nitrogen flow, but for agent flow the results deviated near the end of the liquid two-phase expulsion. The deviation was attributed to a significant non-compensated temperature effect experienced by the dynamic transducers. That problem eliminated dynamic transducers from consideration for use.

Initially, the pipe pressure transducers were calibrated against the more accurate and stable storage vessel transducer. This was done by filling the vessel and the piping with nitrogen to a number of pressures and recording the output from each pipe transducer and comparing it to the vessel transducer output. Periodic re-calibrations indicated zero shifts for the pipe pressure transducers on the order of ± 30 kPa, though very little change in calibration-line slopes was evident. The pipe pressure transducers were subjected to water-hammer-type shock waves during flow start-up, which can sometimes cause a zero-shift. Therefore, the pipe pressure traces are offset to initial values of 0.101 MPa in the reported results.

Transparent acrylic tube test sections with the same inner diameter as the larger diameter pipe (15.9 mm) were fabricated and one transparent test section was hydrostatically tested to failure at a pressure of 11 MPa. A section was connected to the piping at the upstream location right after the valve reducer and was replaced after one or two tests. A high speed movie camera (Photec IV) operating at 500 frames per second recorded the flow through the transparent section. Kodak Ektachrome high-speed daylight film with intense lighting at a 90° angle to the camera was used. The camera was turned on approximately 1 second before the discharge valve was activated to allow the camera motor to come up to the stated framing rate. The liquid two-phase flow portions of selected tests were filmed and analyzed.

Data were acquired with a Strawberry Tree Flash-12 Model 1 data acquisition board installed in a DOS-based personal computer. This board can scan a single channel at a rate of 1 MHz. Here the multiple channels were scanned at 1 kHz since the response time of the pressure transducers is only 1 ms. A timing circuit triggered the data acquisition and sent signals to solid state relays to activate the valves and movie camera if a high speed movie was taken. The raw data were stored in the computer for subsequent analysis.

8.6.5.3 Test Matrix. The series of tests included a number of transient discharges with various initial vessel conditions. The effects of agent temperature, fill volume, and vessel pressure were investigated. Piping configurations included 3.5 m of straight pipe, straight pipe with a 90° angle bend, tee, pipe expansion, and pipe contraction. Figure 101 details the piping configurations. Constant-head tests were performed with fixed 3.5 m of piping at 3 constant vessel pressures: 3.0 MPa, 2.5 MPa, and 2.0 MPa. Table 34 details the nominal conditions for the separate tests. A total of 21 different tests were performed for each agent. A limited number of repeated tests at slightly different fill conditions were also performed. The initial pipe and recovery tanks pressure were at atmospheric pressure except for one test where the pipe and recovery tanks were evacuated.

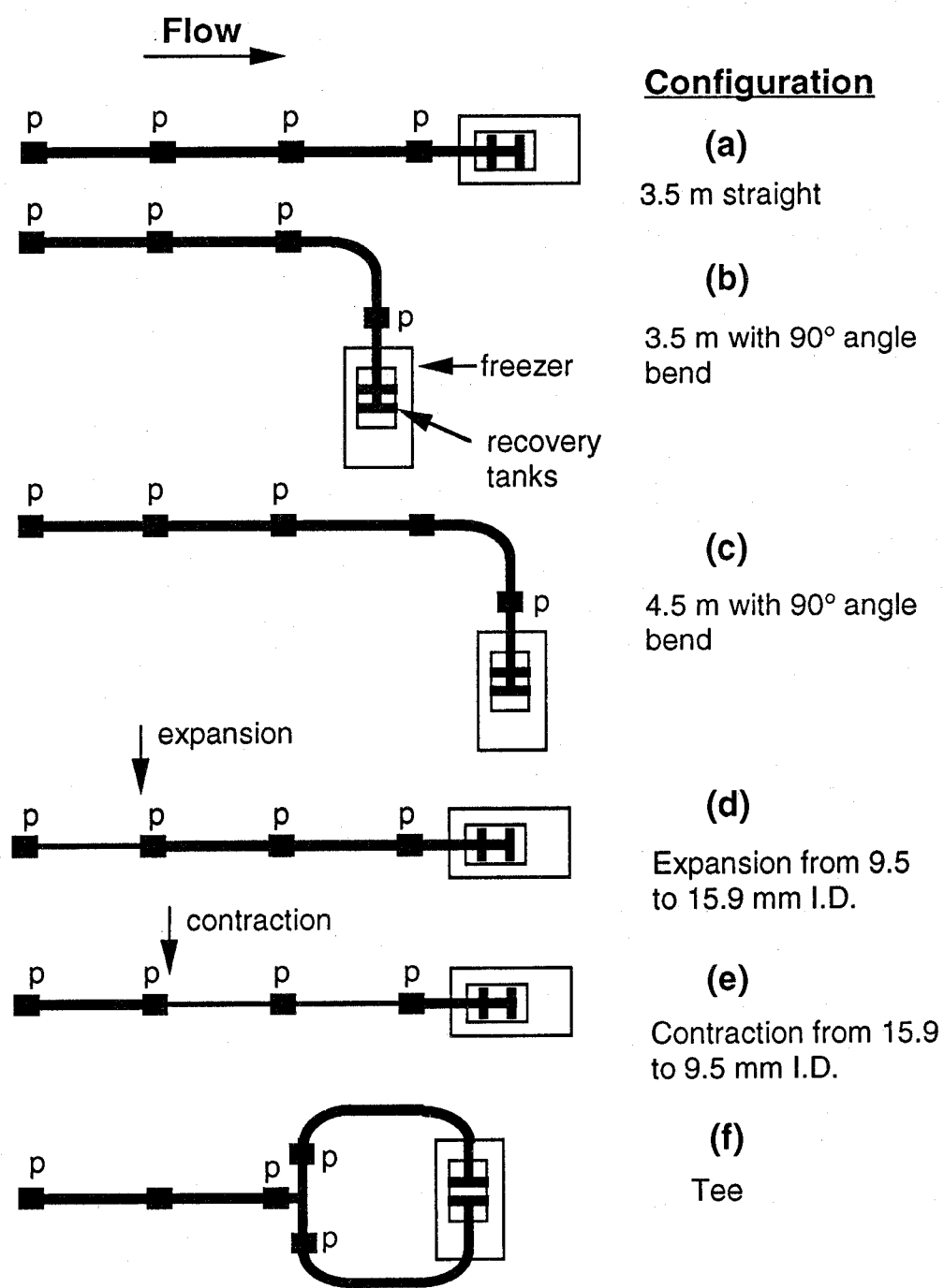


Figure 101. Piping configurations. Pressures were recorded at tap locations marked with a "p".

Table 34. Test Matrix

Parameter tested	Pipe geometry		Initial storage vessel conditions		
	Diameter (mm)	Nominal length (m)	Pressure (MPa)	Liquid fill volume (%)	Temperature (°C)
Constant-head	9.5 and 15.9	3.0	2.0, 2.5 and 3.0	N.A.	23
Straight pipe	9.5 and 15.9	3.0	2.75 and 4.12	50 and 67	23
Storage temperature	15.9	3.0	4.12	50	- 45 and 71
90° Bend	9.5 and 15.9	3.0 and 4.0	4.12	50	23
Tee	15.9	4.0	4.12	50	23
Expansion	9.5 to 15.9	3.0	4.12	50	23
Contraction	15.9 to 9.5	3.0	4.12	50	23

Pressure taps with installed transducers were placed at four locations in the piping. The first pipe pressure tap was in the 15.9 mm diameter section of the valve reducer. For straight piping the pressure was recorded at 1.00 m intervals from the valve reducer. Since the distance from the valve reducer to the flow split in the recovery tanks was 3.50 m, the last pressure recording was at the 3.00 m location. For the 3.50 m of piping with a 90° angle bend, the taps were located at 1.00 m intervals starting from the valve reducer. For the 4.50 m of piping with a 90° angle bend, the taps were located at the valve reducer, and 1.00 m, 2.00 m, and 4.00 m downstream. For the flow-splitting tee experiments, the taps were located at the valve reducer and at 2.00 m downstream before the tee. The tee was located 2.10 m downstream, and the last two taps were placed in the opposing pipes 0.50 m from the tee. Pressure in the recovery tanks was monitored in about half of the tests.

Cold storage vessel tests were performed with the large diameter straight piping configuration. An insulated sheet-metal sleeve was placed around the vessel and filled with dry ice to cool the liquid contents to about - 45 °C (Figure 102). First the vessel was filled to 1/2 liquid volume at 23 °C and pressurized with nitrogen to a total pressure of 4.12 MPa, then dry ice was added to the cooling jacket. When the temperature of the liquid reached about - 45 °C, the agent was discharged.

High storage vessel temperature tests were also performed with the large diameter straight piping configuration. Electrical heating tape was wrapped around the vessel to heat up the vessel and contents (Figure 102). First, the vessel was filled to 1/2 liquid fill volume at 23 °C and pressurized with nitrogen to 4.12 MPa, then power was supplied to the heating tape. When the temperature of the liquid reached about 70 °C, the agent was discharged. Pipe pressures were recorded at the valve reducer section and the last pressure tap 3.00 m downstream. The pipe pressure transducers for the elevated temperature discharge have a nominal range of 0 MPa to 6.9 MPa.

8.6.6 Results and Discussion. The initial fill conditions for each test are given in Tables B-1 to B-5 (see **Appendix B**). The temperatures of the liquid and gas phase in the storage vessel were between 21 °C and 23 °C (23 °C being the ambient room temperature) for the room temperature fill conditions. The mass of agent and pressure were recorded prior to each test. The combined standard uncertainty in the mass determination is estimated as ± 0.01 kg based on the load cell uncertainty of ± 0.005 kg

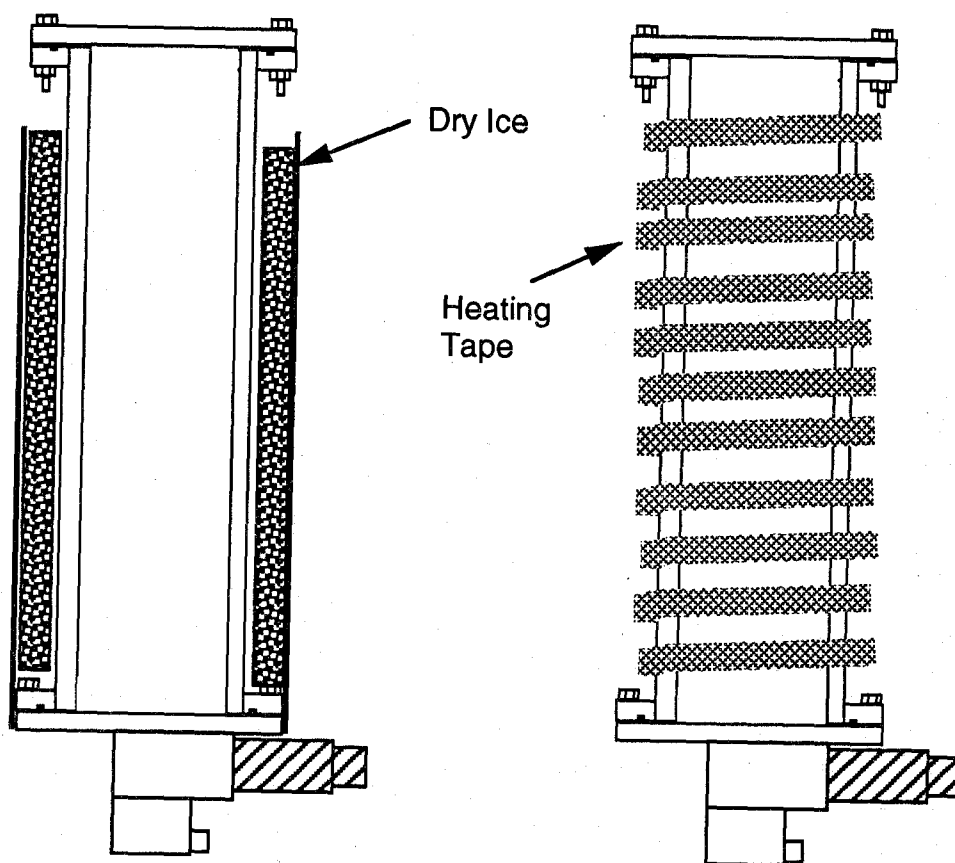


Figure 102. Agent cooling and heating techniques for the cooled and heated agent discharge tests.

and the fact that typically three agent transfers were required to fill the storage vessel. The combined standard uncertainty in the tabulated pressures is ± 0.005 MPa due to rounding off the third digit past the decimal and not due to the stated uncertainty of the transducer. The computer program "PROFISSY" was used to estimate the fill condition and mass of the liquid and gas phase assuming equilibrium conditions were achieved at a temperature of 23 °C.

Temperature equilibration was normally achieved in about 1 hour. Slow bubbling of the nitrogen through the liquid phase (typically 30 min in duration) greatly facilitated nitrogen dissolution. For some storage vessel fills, the agent/nitrogen mixture was allowed to sit for 60 h or longer. The pressure drop over such a long time is indicative of the level of nitrogen saturation achieved by the bubbling technique. Two equilibrium calculations (using PROFISSY) were performed based on the agent mass and the pressure achieved just after bubbling and after a long time storage. Assuming the system had equilibrated after the long storage, the nitrogen saturation level achieved from bubbling alone was approximately (90 ± 5) % of the mass required for saturation. HFC-125 achieved the lowest level of nitrogen saturation from the bubbling technique, while HFC-227ea and CF_3I nearly achieved nitrogen saturation from bubbling alone. The test results did not appear to be strongly influenced by differences in nitrogen saturation level on the order of 10 %.

Pressure traces for all tests are shown in **Appendix B**. The results from the different configurations are discussed below.

8.6.6.1 Constant-Head Discharge. The three selected pressures (3.0 MPa, 2.5 MPa and 2.0 MPa) cover the bottle pressure range where most of the liquid would be discharged from the bottle for a typical transient discharge. Figure 103 (Figure B-2 in **Appendix B**) is a typical constant-head pressure trace for the small diameter piping. The agent was halon 1301 with the vessel pressure fixed at 2.5 MPa, and the pipe pressure was initially atmospheric. At approximately 1000 ms the discharge valve opened. The vessel pressure dropped sharply then recovered due to the nitrogen flow from the make-up tanks. The make-up tank solenoid valve was set to open 20 ms after the discharge valve opened (the solenoid valve requires a pressure difference to open). The make-up tanks were filled to the initial vessel pressure and quickly re-pressurized the vessel. The vessel pressure remained nearly constant until the make-up nitrogen valve was closed about 2.5 s after it was opened. The pipe pressure traces rose sharply after the discharge valve opened, reaching a maximum about 100 ms later and remained nearly constant until the liquid ran out of the vessel. As the liquid runs out of the vessel, the pressure starts to rise in the pipe, then falls as the pipe empties the two-phase fluid contents. After the make-up tank valve was closed, the bottle and pipe pressures continue to drop until the pressure equilibrated about 3.5 s after the beginning of the discharge.

Figure 104 (Figure B-14 in **Appendix B**) is a typical constant-head pressure trace for the large diameter piping. The agent was halon 1301 with a vessel pressure fixed at 2.0 MPa, and the initial pipe pressure was atmospheric. The pipe pressure traces rise fast and take about 300 ms to reach steady values. The crossover of the third pressure tap's trace with that of the fourth tap's trace is due most likely to an incorrect time response of the gage at the third tap during the transient pipe filling period. The recovery tank pressure starts to climb much slower than the pipe pressures and ends up at the final pressure. Notice that the increasing recovery pressure has no noticeable effect on the pipe pressure trace until after the two-phase fluid runs out of the bottle and gas is being discharged. The pressure equilibrated at about 2.0 MPa.

Experimental time-averaged mass flow rates were estimated by dividing the initial liquid-phase mass (calculated by PROFISSY) by the time increment from the initial rise in the pipe pressure to the first indication that the liquid has run out of the vessel. The combined standard uncertainty in the experimental mass flow rate was estimated by the RSS method (root-sum-of-the-squares) for the standard uncertainty of the time increment and the liquid mass. Here the standard uncertainty of the

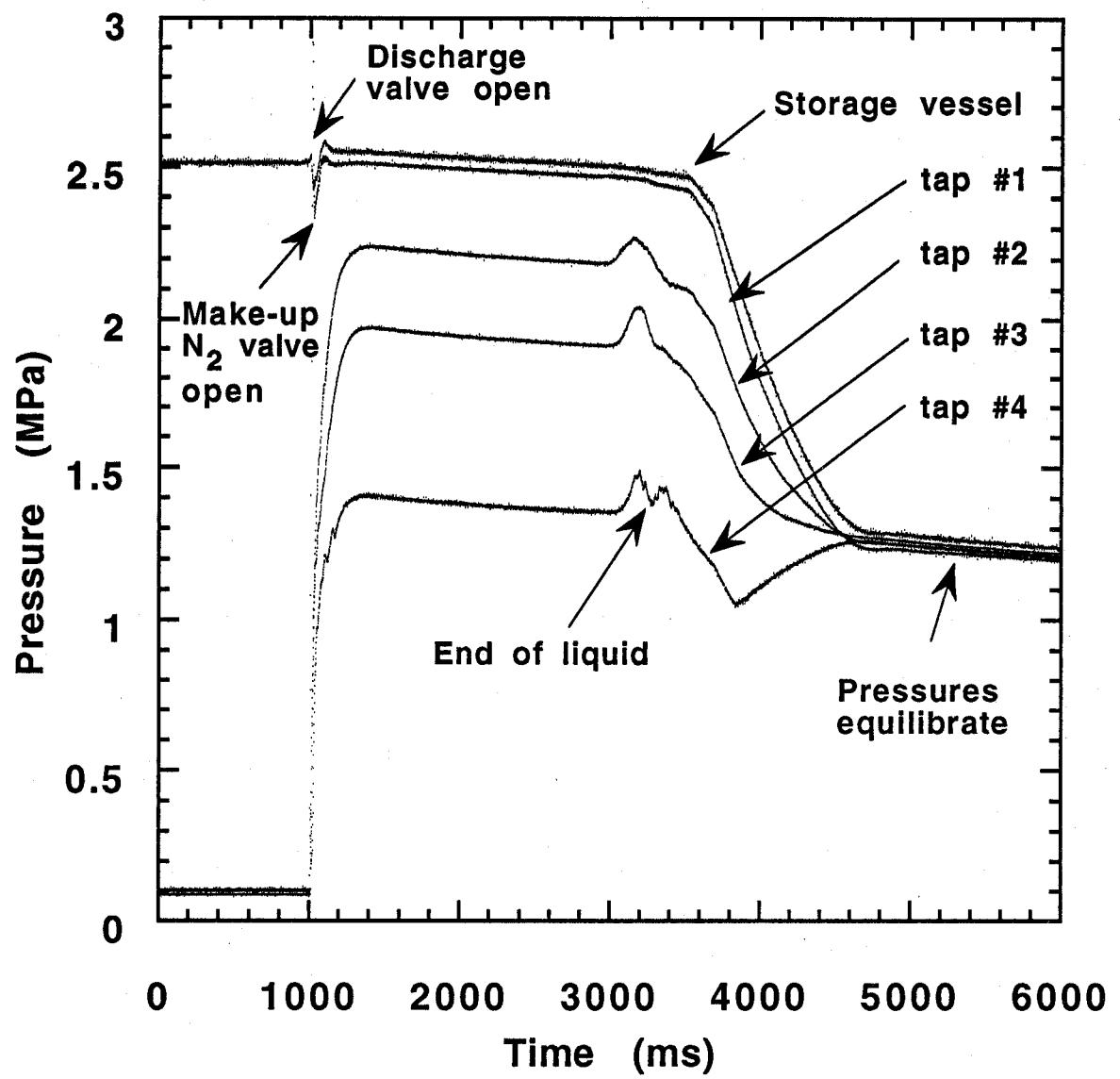


Figure 103. Small diameter piping (9.5 mm I.D.) constant-head discharge test. The agent was halon 1301 with a vessel pressure of 2.5 MPa, and piping initially at atmospheric.

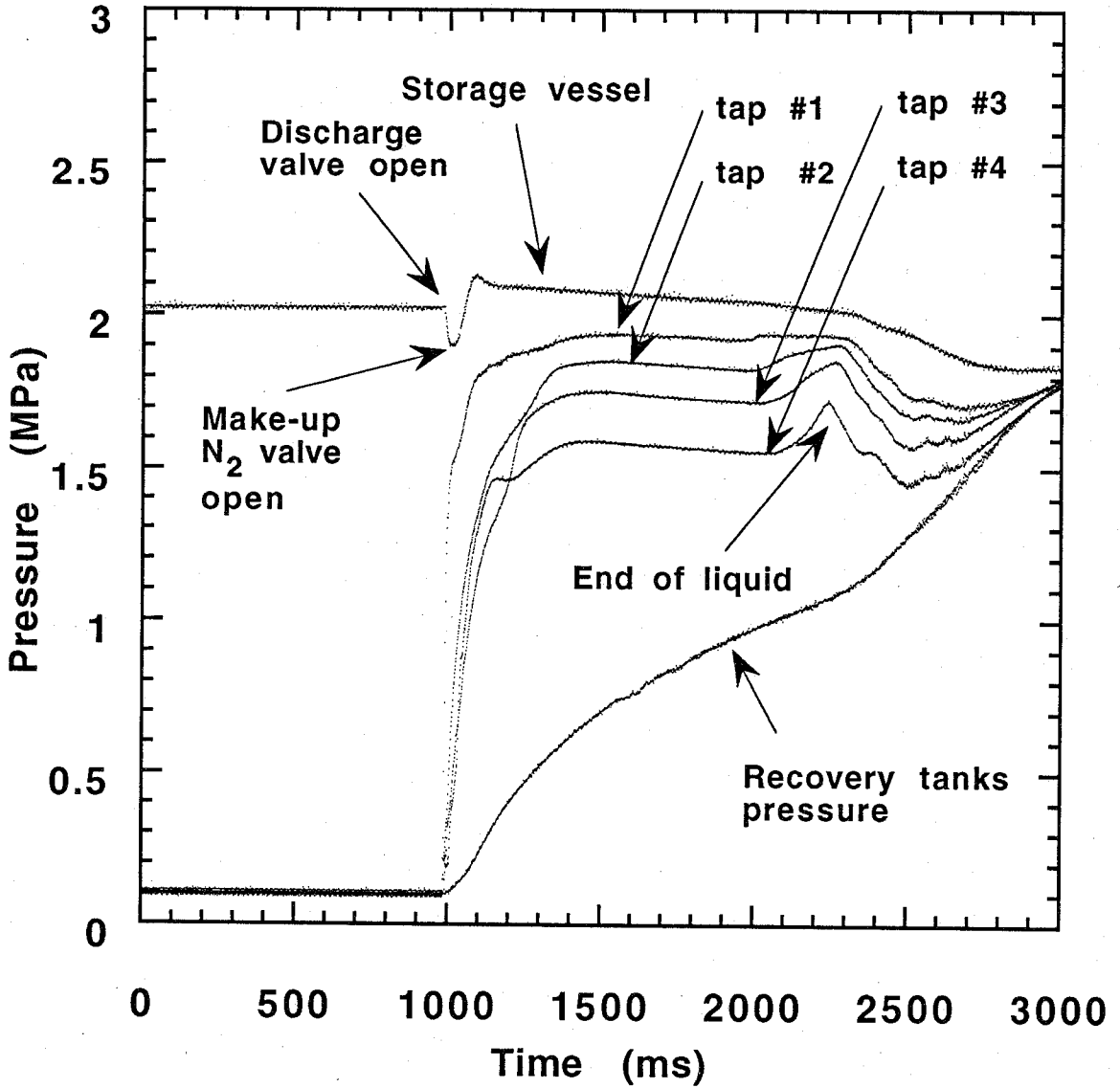


Figure 104. Large diameter piping (15.9 mm I.D.) constant-head discharge test. The agent was halon 1301 with a vessel pressure of 2.0 MPa, and piping initially at atmospheric.

liquid-phase mass is estimated to be equal to the standard uncertainty of the total agent mass. The results, including the uncertainty estimates are reported in Table 35.

The large diameter pipe mass flow rates are 3 to 4 times greater than the small diameter pipe results. Theoretically, during the filling and emptying of the pipe, the mass flow rate should be higher than the steady value; there is a shorter length of pipe for the contents to flow through. Since the filling and emptying times of the large pipe tests are a significant fraction of the total flow time, the estimated average flow rate over the entire test will be higher than the flow rate during the steady-flow portion of the test.

The constant-head discharge tests yield steady pipe flow conditions from 0.5 s to over 4 s, depending on the fill condition and pipe diameter. There are no observed effects of the recovery tanks pressure on the two-phase flow during the tests. The flatness of the pressure traces suggests that transient heat transfer from the pipe walls to the two-phase fluid was not significant. Nonlinearity of the pressure drop in the piping is indicated by the variation in the pressure difference between the equally spaced pipe taps, which implies compressible flow. Another indication that the flow is compressible is that if the flow is assumed to be incompressible, calculated mass flow rates from Equation (37) using the initial densities are on the order of 2-3 times greater than the experimentally determined mass flow rates.

8.6.6.2 Transient Discharge. The transient discharge tests simulated two-phase pipe flow of realistic systems. A typical ambient temperature, straight piping test result is shown in Figure 105 (Figure B-41 in **Appendix B**). Initially, the vessel was filled with HFC-125 to 1/2 liquid fill volume, pressurized to 4.12 MPa with the pipe (0.0159 m I.D.) and recovery tanks at atmospheric pressure. At approximately 1000 ms the discharge valve was opened, and the vessel pressure started to drop while the pipe and recovery tanks pressures started to rise. The pipe pressures peak, then start to fall with the vessel pressure. Notice that one trace, representing the second transducer, crossed over the third and fourth traces. As stated above, this effect is most likely due to that transducer's incorrect response to the highly transient conditions; it is apparent in the large diameter tests, though not apparent in the small pipe diameter tests. The vessel and pipe pressures stop decreasing after about 1400 ms, achieve a local maximum, and then resume decreasing. This pressure recovery is thought to be due to degassing of nitrogen in the storage bottle. At about 1800 ms the vessel pressure starts decreasing at a faster rate, which is attributed to the discharge of the ullage contents after the two-phase mixture leaves the vessel. At the same time, pipe pressures start to increase, peak, then decrease at a much faster rate which is indicative of the two-phase mixture leaving the piping followed by discharge of the ullage contents. All pressure traces equilibrate to about 1.2 MPa. The final equilibrated pressure for the transient tests ranged from 0.5 MPa to 1.5 MPa, depending on the agent, fill conditions, and piping configuration.

Experimental liquid discharge times were estimated for each test as the time interval from the initial vessel pressure drop to the final hump in the last pipe pressure trace. There is some uncertainty in the liquid discharge time since the last amount of liquid draining from the vessel will not flow out as a plug, but will be entrained into the discharging ullage gas. The bracketed time is estimated to represent lower and upper limits of the liquid discharge time, with the best estimate given by the mean value, and the standard uncertainty given by the half width of the time interval divided by the square root of 3 (Taylor and Kuyatt, 1994). The results for the experimental liquid discharge times are presented in Tables 36-39. The discharge times for the large diameter pipe were approximately 2.5 times shorter than the small diameter pipe.

The effects of the increasing recovery tanks pressure on the transient flow are identifiable, given the pipe and recovery tanks pressure traces. If the pipe exit pressure is above the discharge pressure (recovery tanks pressure), the flow remains choked, and the flow rate is independent of the discharge

Table 35. Constant-head mass flow rates

Agent/ figure number	Pressure (± 0.005 MPa)	Pipe I.D. (mm)	Liquid phase mass (± 0.01 kg)	Flow time (± 0.025 s)	Mass flow rate* (kg/s)	Calculated mass flow rate (kg/s)
CF ₃ Br/B1	2.00	9.5	3.00	2.95	1.02 (0.01)	1.09
CF ₃ Br/B2	2.50	9.5	3.15	2.50	1.26 (0.01)	1.28
CF ₃ Br/B3	3.00	9.5	3.09	2.00	1.55 (0.02)	1.50
CF ₃ Br/B14	2.00	15.9	3.87	1.00	3.89 (0.10)	3.39
CF ₃ Br/B15	2.50	15.9	3.57	0.85	4.20 (0.12)	3.92
CF ₃ Br/B16	3.00	15.9	4.23	0.93	4.55 (0.12)	4.51
HFC 125/B26	2.00	9.5	2.31	2.05	1.13 (0.01)	1.06
HFC 125/B27	2.50	9.5	2.75	2.50	1.10 (0.01)	1.14
HFC 125/B28	3.00	9.5	2.32	1.80	1.29 (0.02)	1.33
HFC 125/B37	2.00	15.9	2.54	0.77	3.30 (0.11)	3.07
HFC 125/B38	2.55	15.9	3.15	0.70	4.50 (0.16)	3.51
HFC 125/B39	3.00	15.9	2.63	0.60	4.38 (0.18)	3.98
HFC 227ea/B51	2.00	9.5	3.24	2.45	1.32 (0.01)	1.36
HFC 227ea/B52	2.50	9.5	3.10	2.05	1.51 (0.02)	1.51
HFC 227ea/B53	3.00	9.5	3.16	2.00	1.58 (0.02)	1.70
HFC 227ea/B62	2.00	15.9	3.68	0.70	5.25 (0.19)	4.25
HFC 227ea/B64	2.50	15.9	3.59	0.70	5.13 (0.18)	4.81
HFC 227ea/B65	3.00	15.9	3.49	0.65	5.37 (0.21)	4.93
CF ₃ I/B77	2.00	9.5	5.32	3.50	1.52 (0.01)	1.61
CF ₃ I/B78	2.50	9.5	5.50	3.00	1.83 (0.02)	1.95
CF ₃ I/B79	3.00	9.5	5.13	2.60	1.97 (0.02)	2.11
CF ₃ I/B88	2.00	15.9	3.92	0.60	6.53 (0.27)	5.16
CF ₃ I/B89	2.50	15.9	4.10	0.60	6.83 (0.29)	5.94
CF ₃ I/B91	3.00	15.9	4.20	0.60	7.00 (0.29)	6.45

*Bracketed numbers are combined standard uncertainties (2σ) for experimental mass flow rates.

pressure. If, however, the pipe exit pressure is equal to the discharge pressure, then the flow rate depends on the discharge pressure, and it will not achieve the maximum choked value. For these tests, the pipe exit pressure is somewhat lower than that recorded by the last pressure tap (the pipe terminates at the recovery tanks some distance downstream from the last pressure tap), so if that trace follows the trend of the recovery tanks pressure it is evidence that the flow is not choked at the exit.

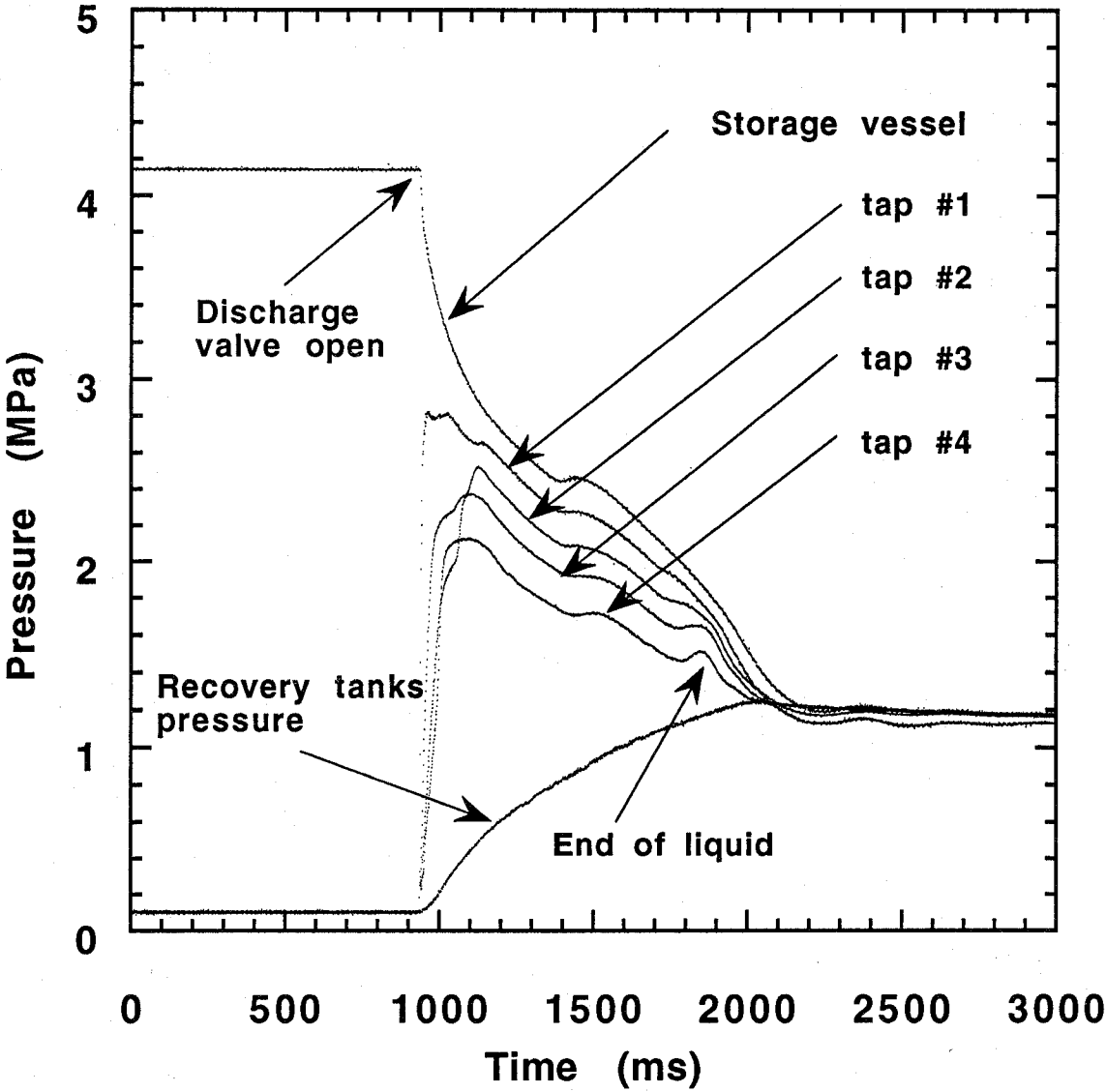


Figure 105. Large diameter piping (15.9 mm I.D.) transient discharge test. The configuration was straight piping. The vessel was filled to 1/2 liquid fill volume with HFC-125 and pressurized to 4.12 MPa.

Table 36. Liquid discharge times for halon 1301

Pipe geometry		Fill conditions		Figure number	t_d (exp.) (s)	t_d (calc.) (s)	
Piping config.	Diameter (mm)	Pressure (MPa)	Liquid fill vol. (%)			Equil.	Non-Eq.
Straight	9.5	2.77	46.6	B-4*	3.3 - 3.7	3.41	3.41
	15.9	2.75	51.1	B-17*	1.4 - 1.7	1.46	1.46
	9.5	4.12	50.4	B-8*	2.5 - 2.8	2.79	3.02
	15.9	4.12	49.6	B-19	1.0 - 1.2	1.03	1.08
	9.5	4.12	65.7	B-9*	3.6 - 4.0	4.23	4.48
	15.9	4.12	65.5	B-20*	1.4 - 1.6	1.55	1.66
3.5 m, 90° Bend	9.5	4.12	48.9	B-10*	2.9 - 3.1	2.75	2.95
	15.9	4.12	48.7	B-21	1.1 - 1.3	1.02	1.05
4.5 m, 90° Bend	9.5	4.12	49.1	B-11*	3.0 - 3.4	3.09	3.32
	15.9	4.12	48.7	B-22	1.1 - 1.3	1.14	1.16
Expansion	9.5/15.9	4.12	48.3	B-13	2.1 - 2.4	1.84	1.98
Contraction	15.9/9.5	4.12	48.3	B-12	2.4 - 2.8	2.30	2.43
tee	15.9	4.12	47.9	B-23	1.0 - 1.2	1.00	1.05
straight	15.9	2.20 [†]	41.8	B-24	1.4 - 1.5	1.09	1.10

*Two-phase flow appears effected by recovery tanks pressure

[†]Cold temperature discharge

To simulate the flow of the two-phase mixture discharging to the atmosphere, it is only necessary to delay the effect of the recovery tanks pressure increase until the ullage contents start to discharge, ensuring that the two-phase flow is always choked. In some cases it appears that the recovery tanks pressure is high enough to affect the two-phase flow from the piping, occurring at the later stage of the two-phase discharge. Figure 106 (Figure B-54 in **Appendix B**) is an example of this effect. The agent is HFC-227ea and the fill conditions are 1/2 liquid fill volume, pressurized to 2.75 MPa. The configuration was straight, small diameter piping. The pressure trace for the last tap location shows a gradual pressure increase starting at about 4500 ms. This behavior is most evident for the following conditions: high fill volume, small diameter piping and agents with lower saturation vapor pressures (HFC-227ea and CF₃I). If the flow is not always choked at the pipe exit, the flow time will be slightly longer than the flow time for an atmospheric discharge. The tests that appear to be affected by the finite size of the recovery tanks are indicated in Tables 36-39. This effect probably results in not more than a 10 % increase in flow time for any affected test.

In some experiments, like the one described in Figure 105, the storage vessel pressure experiences a recovery to a local maximum. It is most pronounced for halon 1301 and HFC-125 2/3 fill

Table 37. Liquid discharge times for HFC-125

Pipe geometry		Fill conditions		Figure number	t_d (exp.) (s)	t_d (calc.) (s)	
Piping config.	Diameter (mm)	Pressure (MPa)	Liquid fill vol. (%)			Equil.	Non-Eq.
Straight	9.5	2.76	50.4	B-30*	3.1 - 3.3	3.35	3.48
	15.9	2.75	54.2	B-40	1.3 - 1.5	1.40	1.43
	9.5	4.13	56.4	B-31*	2.7 - 2.9	2.79	3.34
	15.9	4.12	52.7	B-42	0.9 - 1.1	0.99	1.08
	9.5	4.12	69.8	B-32	3.4 - 3.7	4.19	4.65
	15.9	4.12	65.9	B-44*	1.4 - 1.5	1.39	1.59
3.5 m, 90° Bend	9.5	4.12	47.1	B-33	2.6 - 2.8	2.28	2.53
	15.9	4.12	48.8	B-46	0.9 - 1.0	0.90	0.99
4.5 m, 90° Bend	9.5	4.12	48.1	B-34	2.6 - 2.8	2.63	2.92
	15.9	4.12	46.6	B-47	0.9 - 1.0	0.95	1.02
Expansion	9.5/15.9	4.12	49.6	B-35	1.9 - 2.1	1.67	1.91
Contraction	15.9/9.5	4.12	49.8	B-36	2.2 - 2.4	2.10	2.34
tee	15.9	4.12	54.4	B-48	0.9 - 1.0	1.04	1.18
straight	15.9	2.55†	39.1	B-49	0.9 - 1.0	0.80	0.82

*Two-phase flow appears effected by recovery tanks pressure

†Cold temperature discharge

conditions. It is not strong for HFC-227ea and CF_3I and is only indicated in one trace each for those agents. No visual observations of the fluid inside the vessel were made during these tests. It has been surmised that the pressure recovery is due to nitrogen coming out of a supersaturated solution, which in turn increases the liquid two-phase volume compressing the ullage gas and raising the vessel pressure. The exact mechanism(s) for bubble formation is not known and it is possibly a combination of heterogeneous and homogenous nucleation. There is scatter in the lowest pressure reached before the pressure rise for any agent. It appears to depend on the fill volume, vessel pressure and pipe diameter. If it was purely homogenous nucleation, it should only depend on the initial pressure. This degassing phenomenon has implications for the discharge time and is explored in the model calculations to follow.

8.6.6.3 Straight Pipe Configuration. The straight pipe configuration was the baseline for the tests at different fill conditions and vessel pressures. Figure 101(a) shows the configuration. Typical results are shown in Figures 105 and 106. Two fill conditions (nominally 1/2 and 2/3 liquid filled) at 4.12 MPa and two vessel pressures (4.12 MPa and 2.75 MPa) at 1/2 liquid filled were examined. The liquid discharge time was always longer for the 2/3 liquid filled condition compared to the 1/2 liquid

Table 38. Liquid discharge times for HFC-227ea

Pipe geometry		Fill conditions		Figure number	t_d (exp.) (s)	t_d (calc.) (s)	
Piping config.	Diameter (mm)	Pressure (MPa)	Liquid fill vol. (%)			Equil.	Non-Eq.
Straight	9.5	2.75	56.4	B-54*	4.2 - 4.4	3.44	3.81
	15.9	2.75	54.1	B-66	1.2 - 1.4	1.19	1.27
	9.5	4.12	53.7	B-55*	2.9 - 3.1	2.43	2.63
	15.9	4.12	49.4	B-68	0.8 - 0.9	0.80	0.84
	9.5	4.12	70.0	B-57*	4.1 - 4.4	3.90	4.80
	15.9	4.12	69.4	B-70*	1.7 - 1.9	1.40	1.64
3.5 m, 90° Bend	9.5	4.12	49.2	B-58	2.5 - 2.7	2.19	2.31
	15.9	4.12	49.4	B-71	0.8 - 1.0	0.82	0.86
4.5 m, 90° Bend	9.5	4.12	49.2	B-59	2.6 - 2.9	2.47	2.61
	15.9	4.12	48.8	B-72	0.9 - 1.0	0.90	0.94
Expansion	9.5/15.9	4.12	49.0	B-61	1.8 - 2.0	1.46	1.55
Contraction	15.9/9.5	4.12	49.0	B-60	2.1 - 2.3	1.81	1.90
tee	15.9	4.12	48.4	B-73	0.8 - 0.9	0.79	0.82
straight	15.9	3.00 [†]	43.5	B-74	0.9 - 1.0	0.75	0.76
	15.9	5.95 [‡]	59.8	B-76	0.8 - 0.9	0.90	1.03

*Two-phase flow appears effected by recovery tanks pressure

[†]Cold temperature discharge[‡]Hot temperature discharge

filled condition. The relative increase depends on the particular agent. The liquid discharge times for the 2.75 MPa charge pressures were 30 % to 50 % greater than the 4.12 MPa charge pressures

8.6.6.4 Piping with a 90° Angle Bend. Tests with 3.5 m of piping with a smooth-bend-radius 90° angle bend located 2.5 m downstream, and 4.5 m of piping with a smooth-bend-radius 90° angle bend located 3.5 m downstream (see Figures 101(b) and (c)) were performed. Comparing the straight piping results to the 3.5 m piping with a 90° angle bend, the liquid discharge times and the pressure drops are longer and lower, respectively, for the configurations with the elbow compared to the straight piping results. The 4.5 m piping with a 90° angle bend displayed still longer liquid discharge times, due to the effects of the bend and the extra 1.00 m of piping.

8.6.6.5 Straight Pipe with a Sudden Expansion. The sudden expansion configuration consisted of 1.00 m of straight 9.5 mm I.D. piping connected to 2.5 m of straight 15.9 mm I.D. piping (see Figure 101(d)). Figure 107 (Figure B-13 in **Appendix B**) is a typical pressure trace. Following the

Table 39. Liquid discharge times for CF₃I

Pipe geometry		Fill conditions		Figure number	t_d (exp.) (s)	t_d (calc.) (s)	
Piping config.	Diameter (mm)	Pressure (MPa)	Liquid fill vol. (%)			Equil.	Non-Eq.
Straight	9.5	2.75	49.7	B-80*	4.1 - 4.3	3.35	3.57
	15.9	2.80	49.6	B-92	1.3 - 1.4	1.26	1.32
	9.5	4.13	50.2	B-81*	3.4 - 3.6	2.61	2.76
	15.9	4.12	48.7	B-93	1.0 - 1.1	0.94	0.98
	9.5	4.12	67.9	B-83*	5.1 - 5.3	4.38	5.10
	15.9	4.12	68.2	B-94*	1.9 - 2.1	1.62	1.84
3.5 m, 90° Bend	9.5	4.12	52.0	B-84*	3.6 - 3.8	2.84	3.02
	15.9	4.12	49.4	B-95	1.0 - 1.1	0.98	1.02
4.5 m, 90° Bend	9.5	4.12	51.2	B-85*	3.8 - 4.0	3.12	3.29
	15.9	4.12	55.1	B-96	1.2 - 1.4	1.29	1.35
Expansion	9.5/15.9	4.12	53.8	B-87	2.5 - 2.6	2.01	2.15
Contraction	15.9/9.5	4.12	52.4	B-86	2.9 - 3.1	2.40	2.53
tee	15.9	4.12	49.9	B-97	0.8 - 1.0	0.98	1.02
straight	15.9	3.05 [†]	44.2	B-98	1.1 - 1.2	0.95	0.96
	15.9	5.70 [‡]	56.7	B-99	0.9 - 1.0	1.00	1.09

*Two-phase flow appears effected by recovery tanks pressure

[†]Cold temperature discharge[‡]Hot temperature discharge

first pipe tap's pressure trace, after it initially rises, it tracks the vessel pressure trace very closely, with a small pressure difference between the two. This is common to all tests where a section of small piping follows the valve reducer. The reason these two pressure traces track so closely is because the first pressure tap is located in the valve reducer where the inner diameter is 15.9 mm and most of the flow resistance occurs in the small diameter piping located 0.05 m downstream. There is a large pressure drop from the valve reducer to the next pressure tap 1.00 m downstream. The next two pressure records 2.00 m and 3.00 m downstream are only slightly different, and after some time they follow the recovery tanks pressure trace. These observations suggest that the flow does not choke at the recovery tanks entrance, but at the expansion point. This implies that liquid discharge time to the end of the first 1.00 m of piping would be equivalent to the liquid discharge time through a 1.00 m section of piping discharging to atmosphere.

8.6.6.6 Straight Pipe with a Sudden Contraction. The sudden contraction configuration consisted of 1.00 m of straight 15.9 mm I.D. piping connected to 2.00 m of straight 9.5 mm I.D.

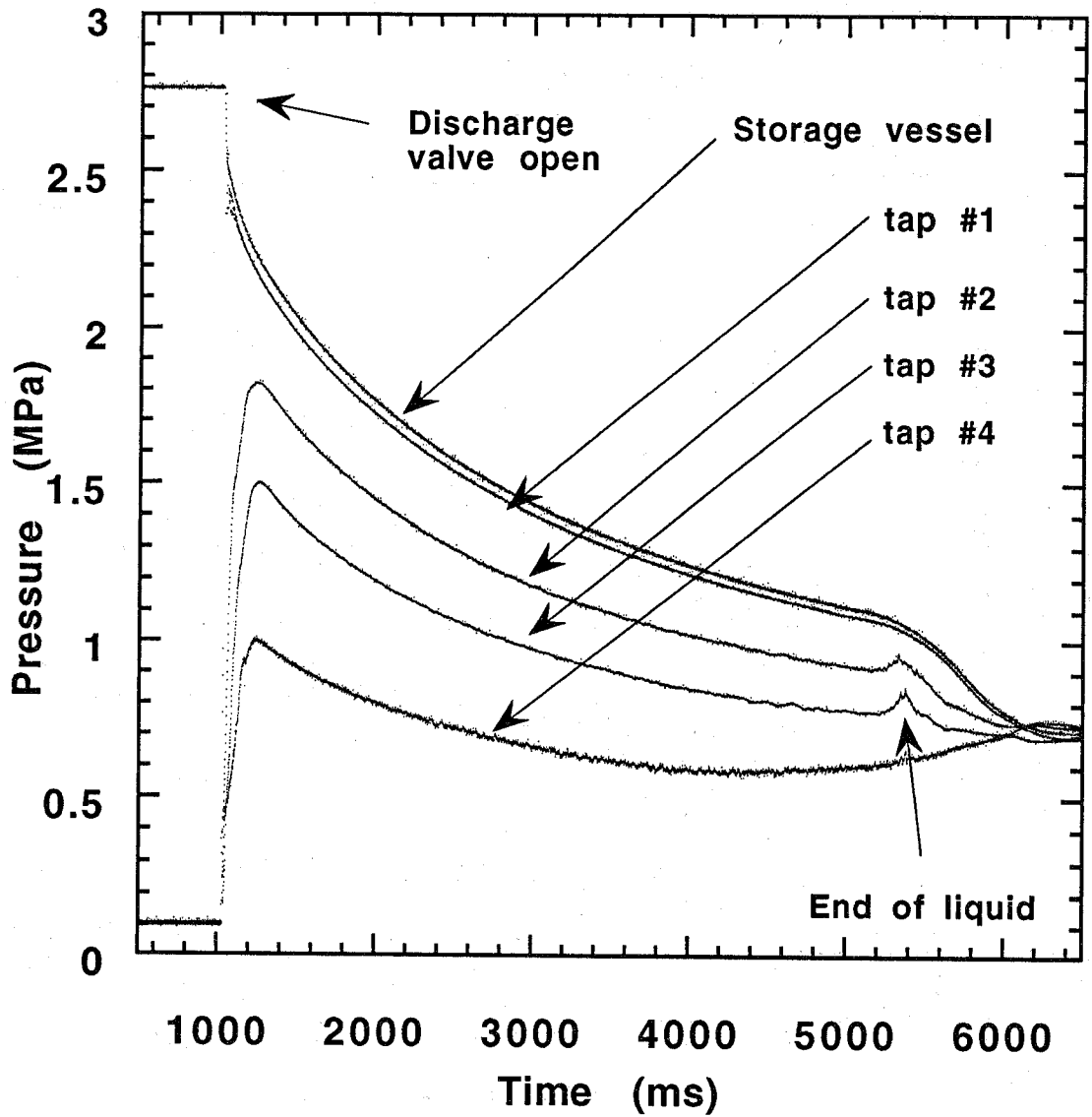


Figure 106. Small diameter piping (9.5 mm I.D.) transient discharge test. The configuration was straight piping. The vessel was filled to 1/2 liquid fill volume with HFC-227ea and pressurized to 2.75 MPa.

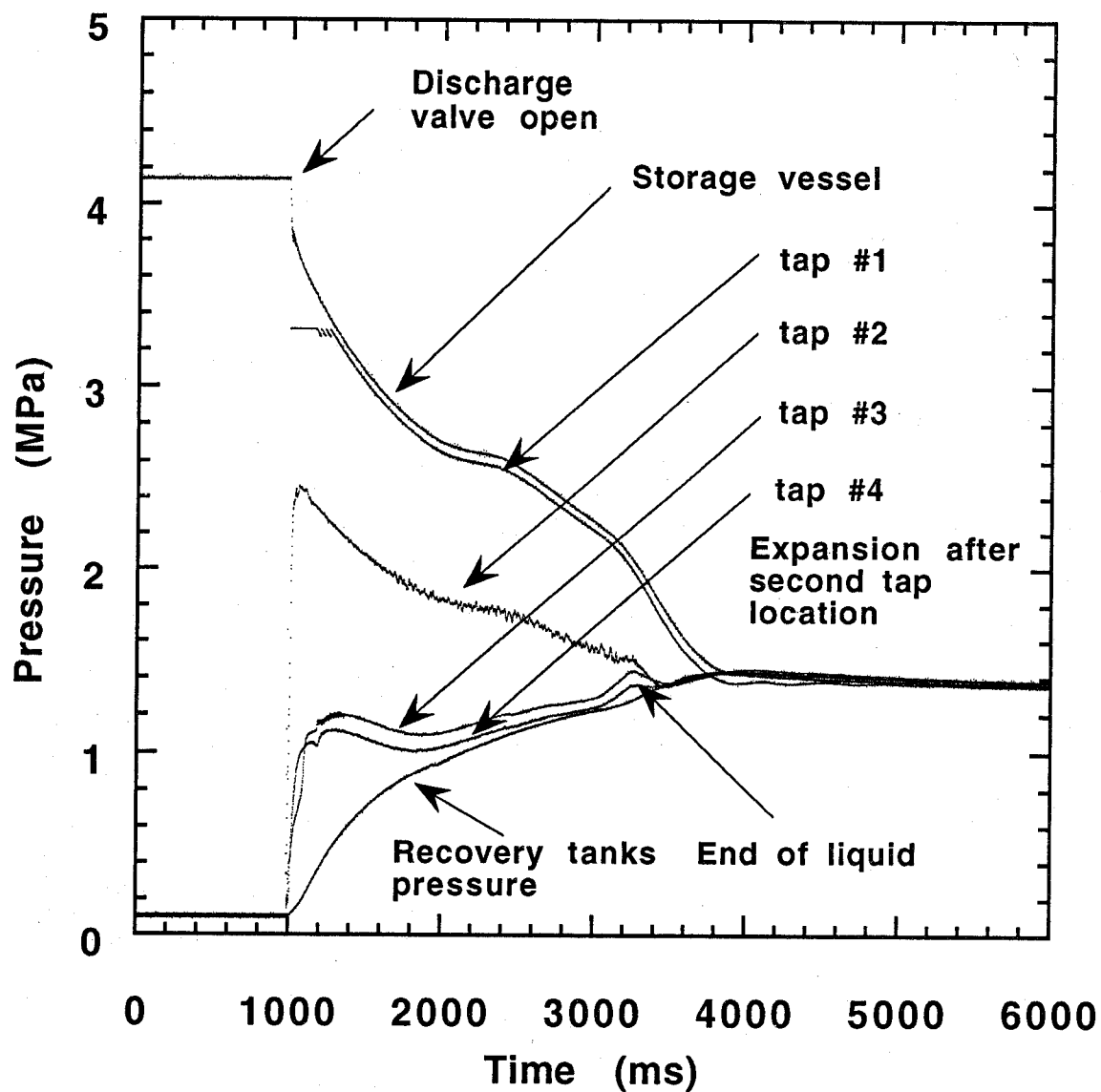


Figure 107. Transient discharge test; straight pipe with a sudden expansion. The vessel was filled to 1/2 liquid fill volume with halon 1301 and pressurized to 4.12 MPa.

piping, then connected back to 0.5 m of 15.9 mm I.D. piping leading to the recovery tanks (see Figure 101(e)). Figure 108 (Figure B-35 in **Appendix B**) is a typical trace. The first two pipe tap pressure traces rapidly rise to just below the bottle pressure; they then track the bottle pressure for the rest of the test. The first two traces follow the bottle pressure because the taps are located in the 15.9 mm I.D. valve reducer and piping which are before the contraction. The next two traces show significant pressure drop from the bottle pressure. These traces are for the taps 2.00 m and 3.00 m downstream located in the 9.5 mm I.D. piping. The liquid discharge time for this configuration should be approximately equivalent to the discharge time for a 2.00 m section of 9.5 mm I.D. piping leading from the vessel to the atmosphere.

8.6.6.7 Tee Configuration. The tee configuration consisted of 2.10 m of 15.9 mm I.D. piping leading to a tee fitting, connected to two legs, one 1.80 m long and the other 2.05 m long, both with 2 smooth radius 90° angle bends leading to the recovery tanks (see Figure 101(f)). Figure 109 (Figure B-73 in **Appendix B**) is a typical example. The first pipe tap's pressure trace rises quickly then follows the vessel pressure with some pressure difference. The second pipe tap's pressure trace (the tap is located just before the tee) rises quickly, then falls much slower than the vessel or the first tap's pressure trace until the hump signifying the liquid emptying from the pipe. The pressure traces for the taps located in the tee legs 0.50 m downstream of the tee essentially follow the second pipe tap's trace with some pressure drop. The slight difference in the two tee leg traces is most likely due to the slight difference in length to the recovery tanks.

8.6.6.8 Cooled Agent Discharge. Cooled agent discharges were performed with 3.5 m of straight 15.9 mm I.D. piping (Figure 101(a)). Table B-1 details the initial fill conditions, final test pressures, and the equilibrium conditions. Thermal equilibrium was never achieved between the liquid and gas phases due to conduction of heat from the gas phase. Liquid phase temperatures ranged from -44 °C to -50 °C, while gas phase temperatures were around 4 °C. Though thermal equilibrium was not achieved, the final pressures were only approximately 10 % higher than predicted equilibrium pressures based on the liquid-phase temperature for all of the agents. Figure 110 (Figure B-98 in **Appendix B**) is a typical trace. The pressure trace results appear similar to ambient temperature discharges at low storage vessel pressure. The longer liquid discharge times for the cooled agent discharge appear to be due to the lower initial vessel pressure.

The first pipe tap's pressure trace shows a temperature effect. The pressure tap is located in the valve reducer which is in contact with the vessel via the discharge valve. Cold ambient temperature affects the zero and the slope of the pressure transducer calibration. (Calibration of the gage recording the recovery tanks pressure was done at the cold ambient temperature). The other pressure taps are located far downstream and do not appear to be cooled below ambient conditions appreciably during the agent chilling period.

8.6.6.9 Heated Agent Discharge. High temperature agent discharges were performed with 3.5 m of straight piping 15.9 mm I.D. (Figure 101(a)). Table B-1 details the initial fill conditions, the final temperatures and pressures, and calculated equilibrium conditions based on the final temperature. The final temperature achieved in all of the tests was approximately 70 °C. PROFISSY calculations indicate that two of the agents (halon 1301 and HFC-125) are single-phase fluids at this elevated temperature: the bottle conditions are given in Table B-1. The temperatures inside the bottle as measured with the two installed thermocouples were within 5 °C. Temperature differences could be due to non-equilibrated gas and liquid phases or a temperature gradient in the fluid. The results are shown in Figures 111-114 (Figures B-25, B-50, B-75 and B-99 in **Appendix B**) for halon 1301, HFC-125, HFC-227ea and CF₃I respectively. The pipe pressure traces for halon 1301 and HFC-125

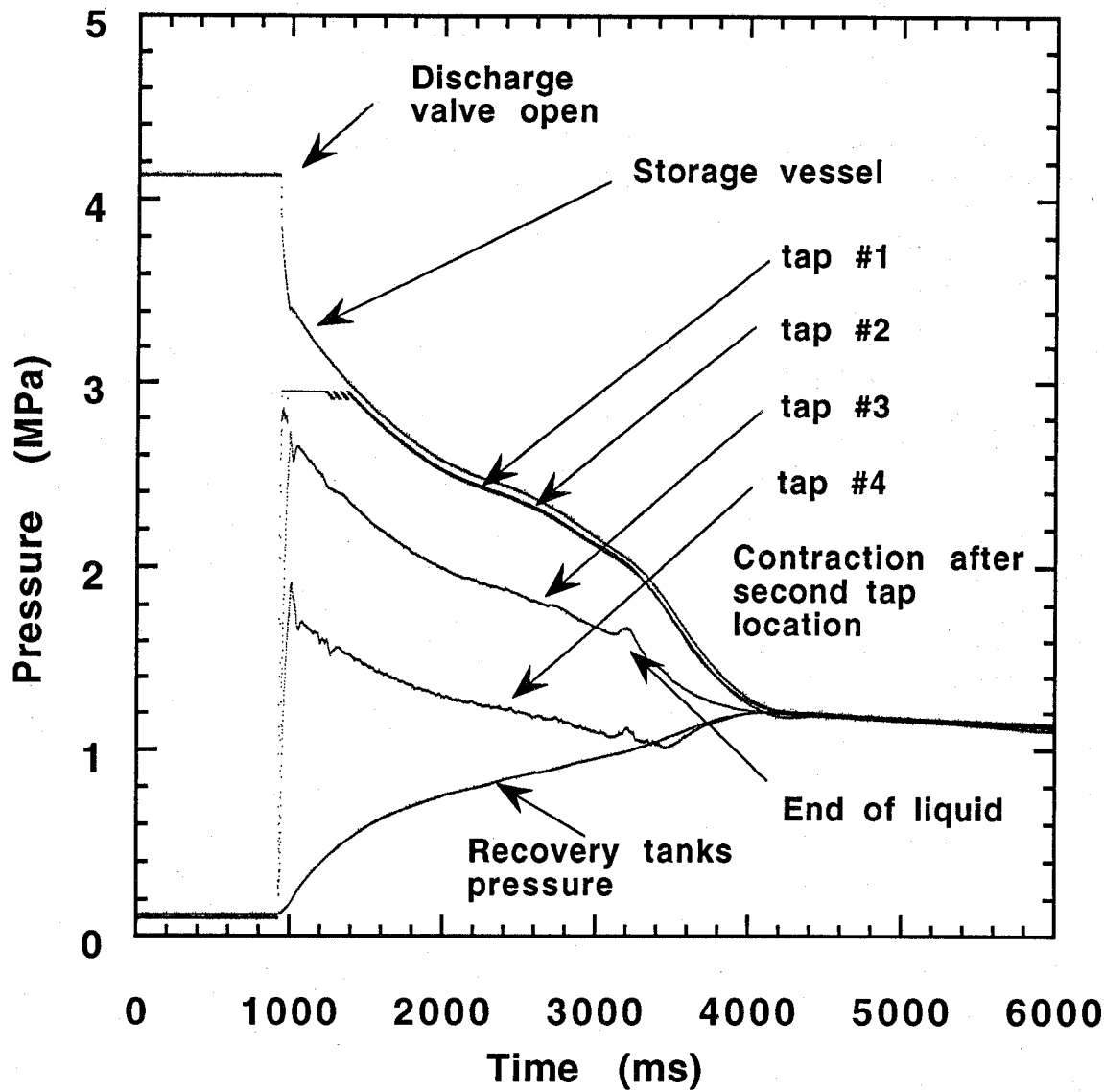


Figure 108. Transient discharge test; straight pipe with a sudden contraction. The vessel was filled to 1/2 liquid fill volume with HFC-125 and pressurized to 4.12 MPa.

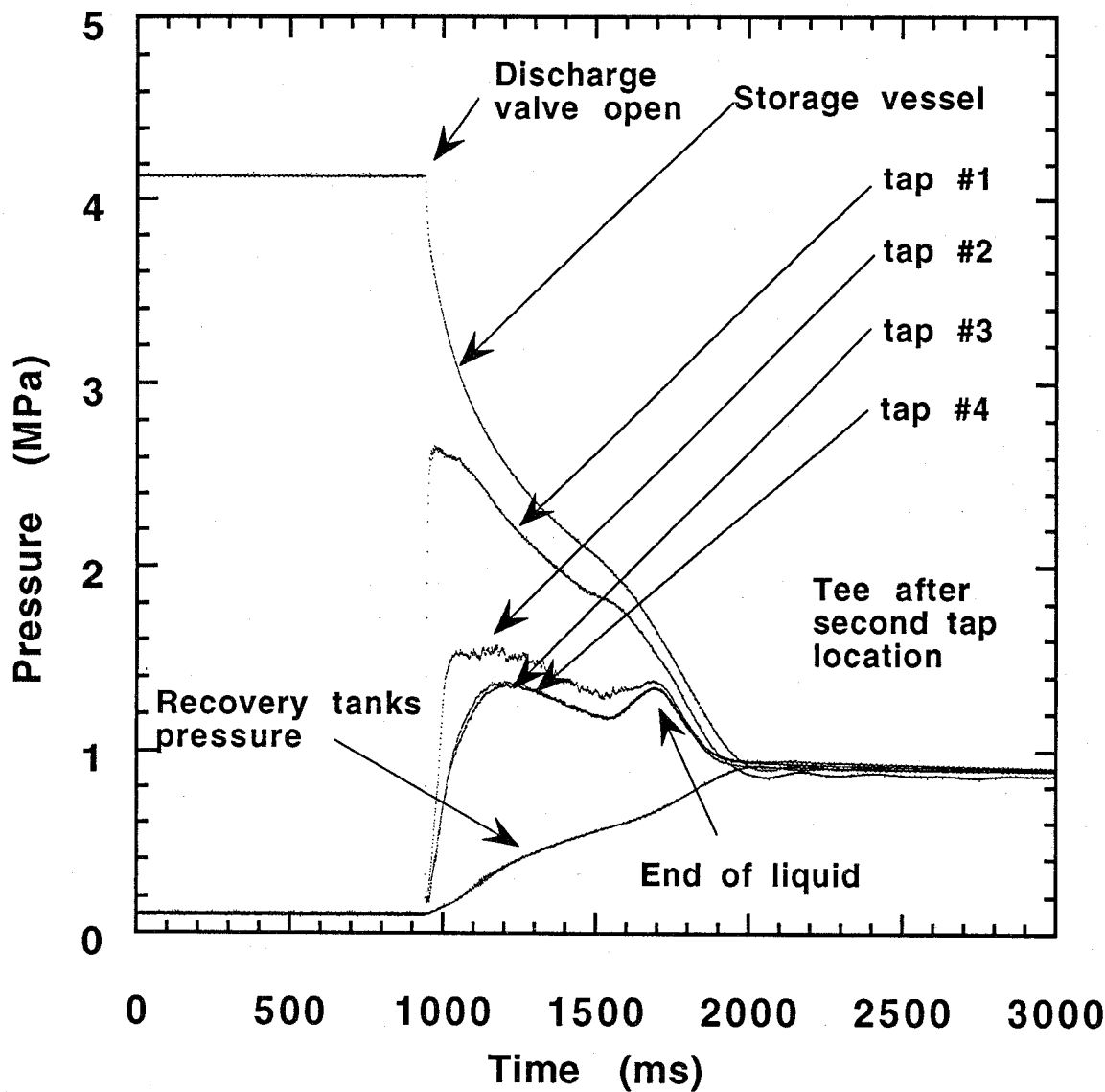


Figure 109. Transient discharge test; tee configuration. The vessel was filled to 1/2 liquid fill volume with HFC-227ea and pressurized to 4.12 MPa.

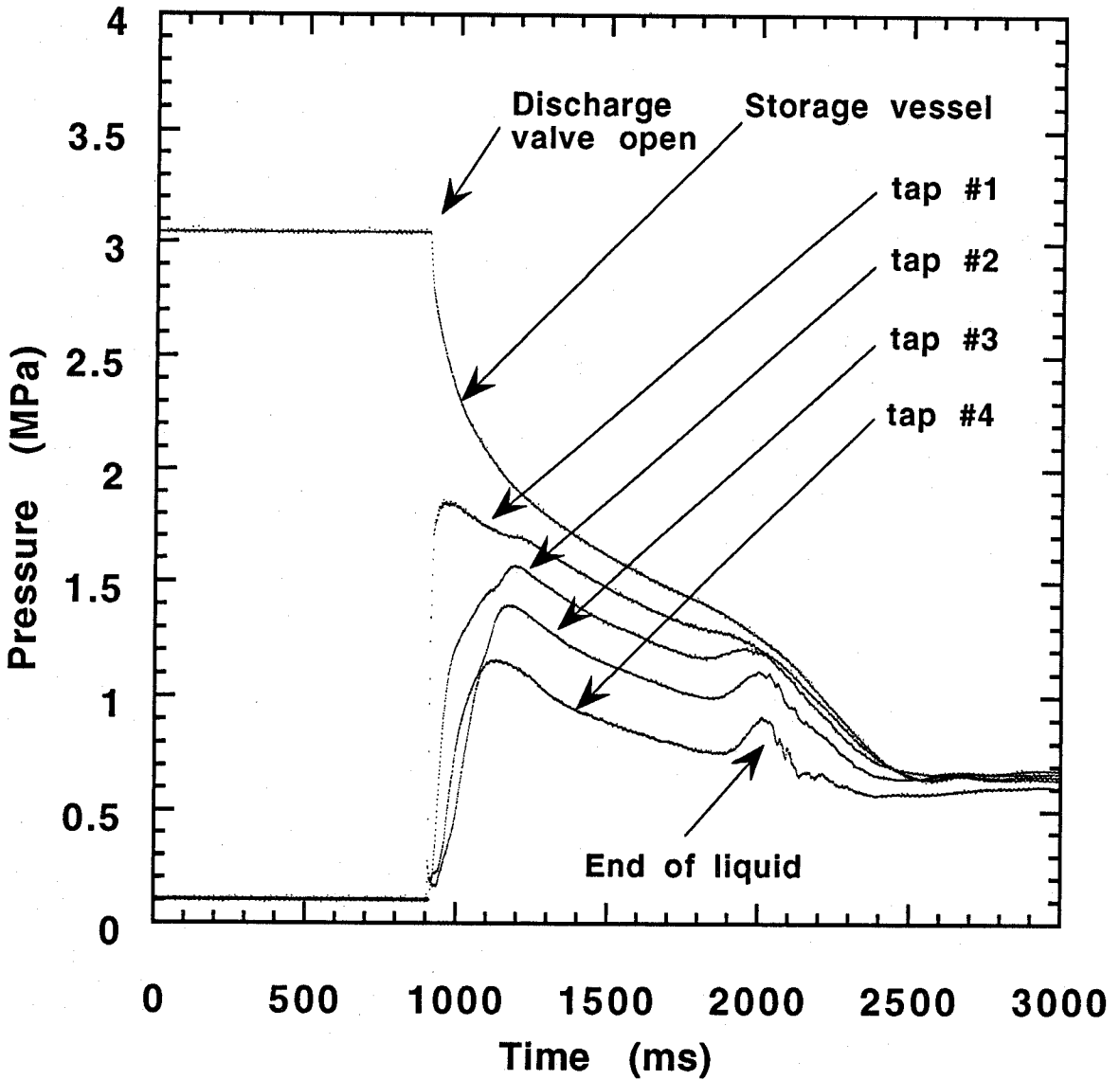


Figure 110. Transient cooled agent discharge test; straight piping. The vessel was filled to 1/2 liquid fill volume with CF_3I , pressurized to 4.12 MPa, then cooled to -45°C or less prior to discharge.

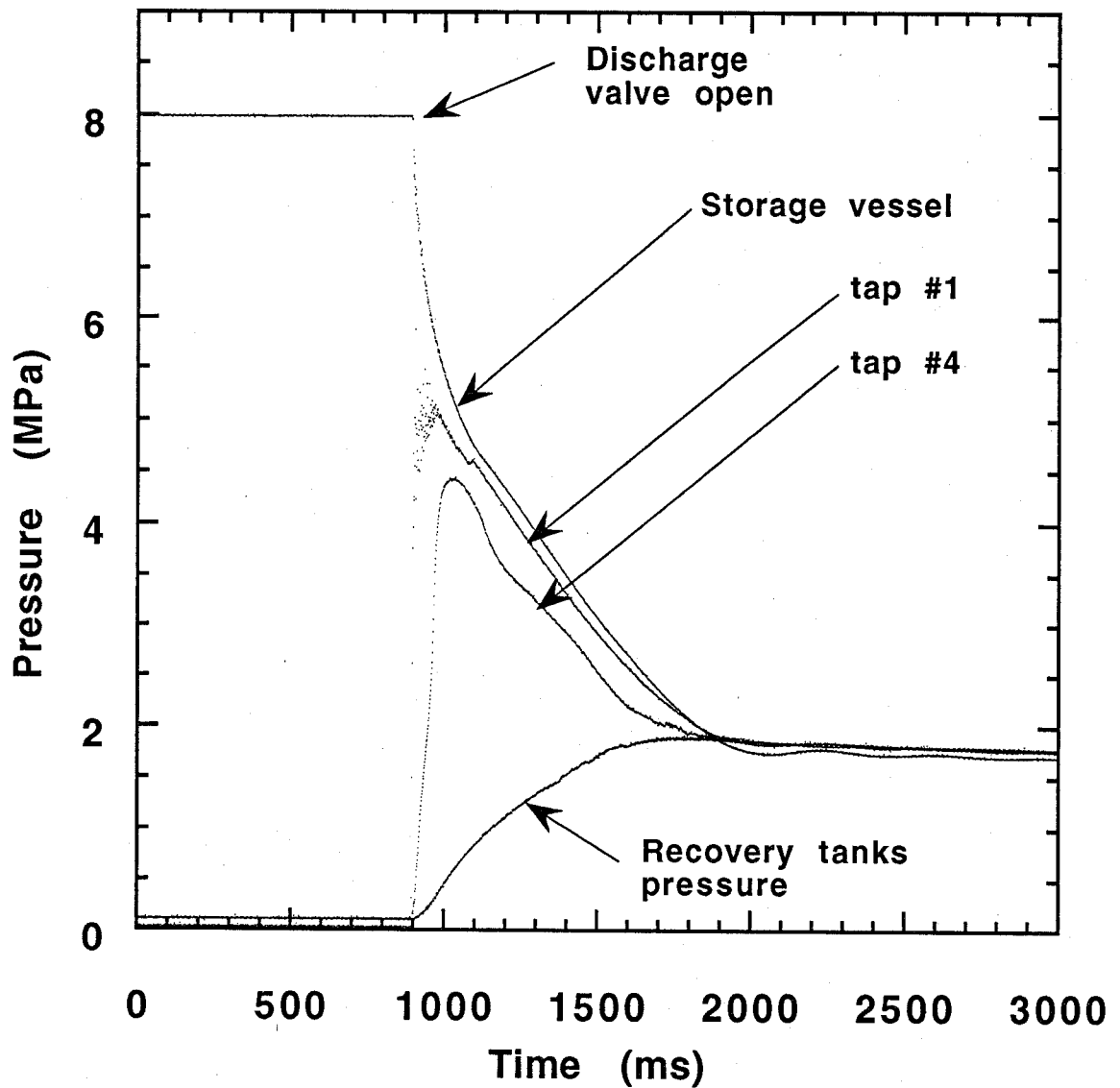


Figure 111. Transient heated agent discharge test; straight piping. The vessel was filled to 1/2 liquid fill volume with halon 1301, pressurized to 4.12 MPa, then heated to 70 °C prior to discharge.

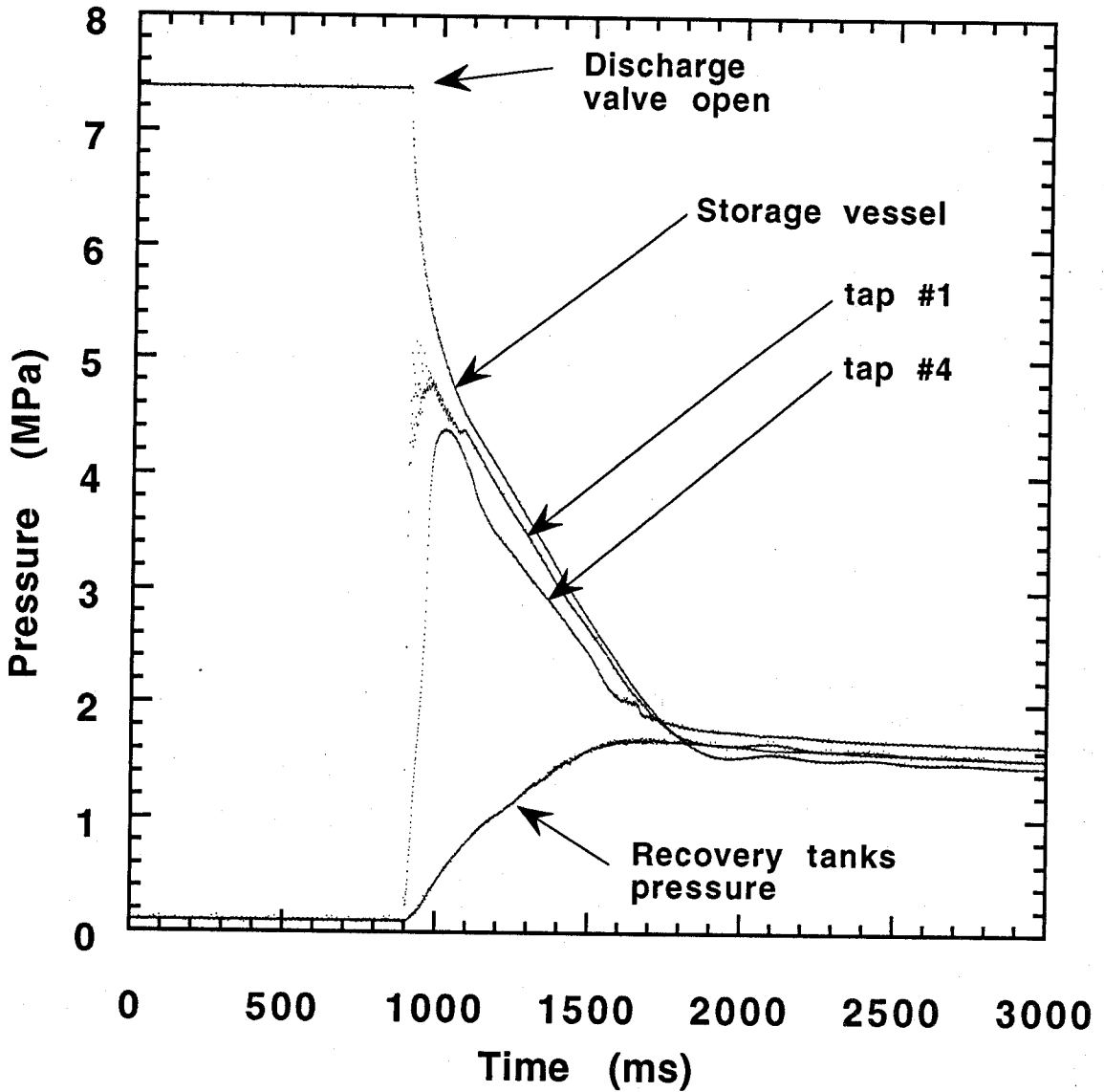


Figure 112. Transient heated agent discharge test; straight piping. The vessel was filled to 1/2 liquid fill volume with HFC-125, pressurized to 4.12 MPa, then heated to 70 °C prior to discharge.

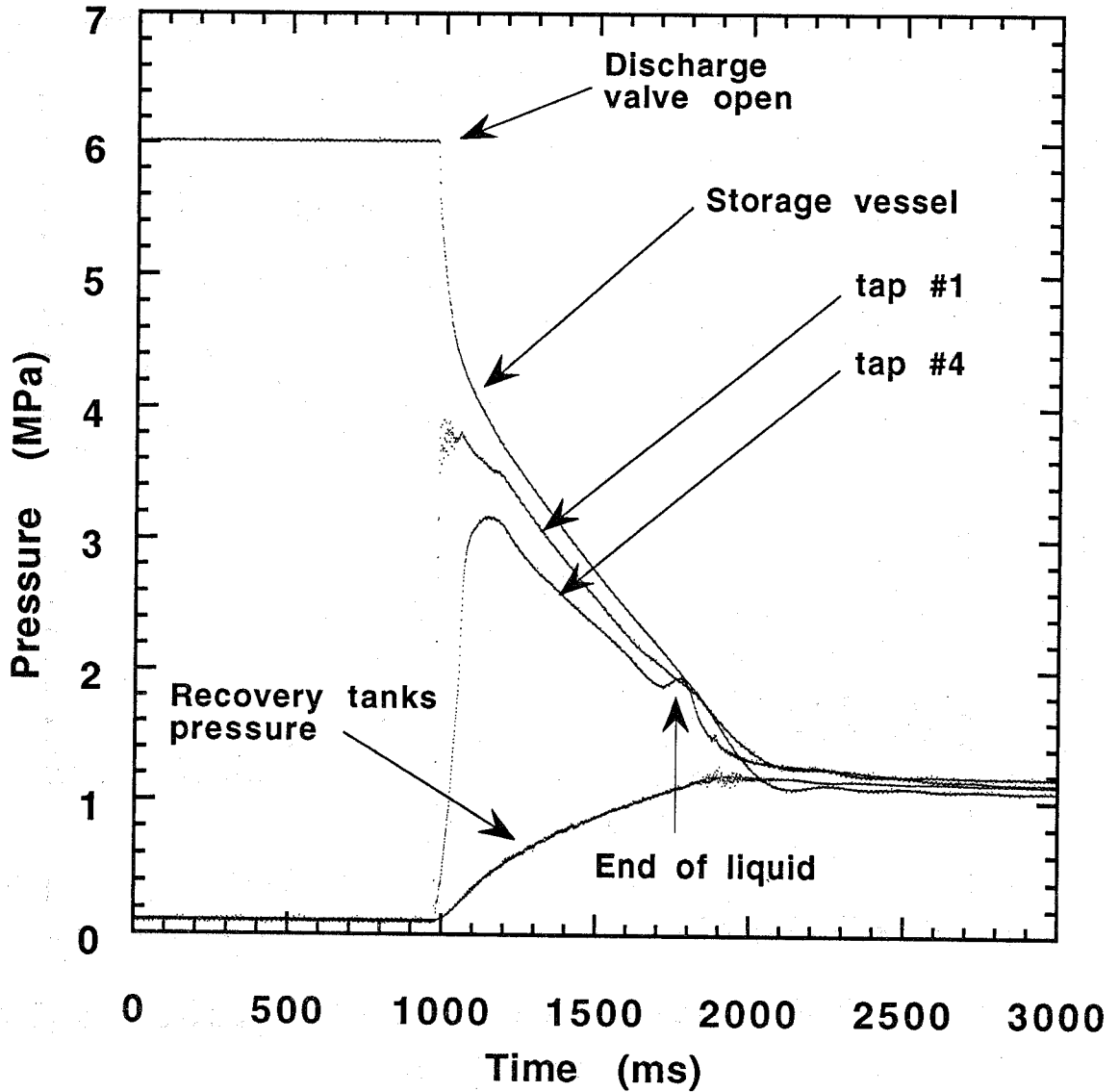


Figure 113. Transient heated agent discharge test; straight piping. The vessel was filled to 1/2 liquid fill volume with HFC-227ea, pressurized to 4.12 MPa, then heated to 70 °C prior to discharge.

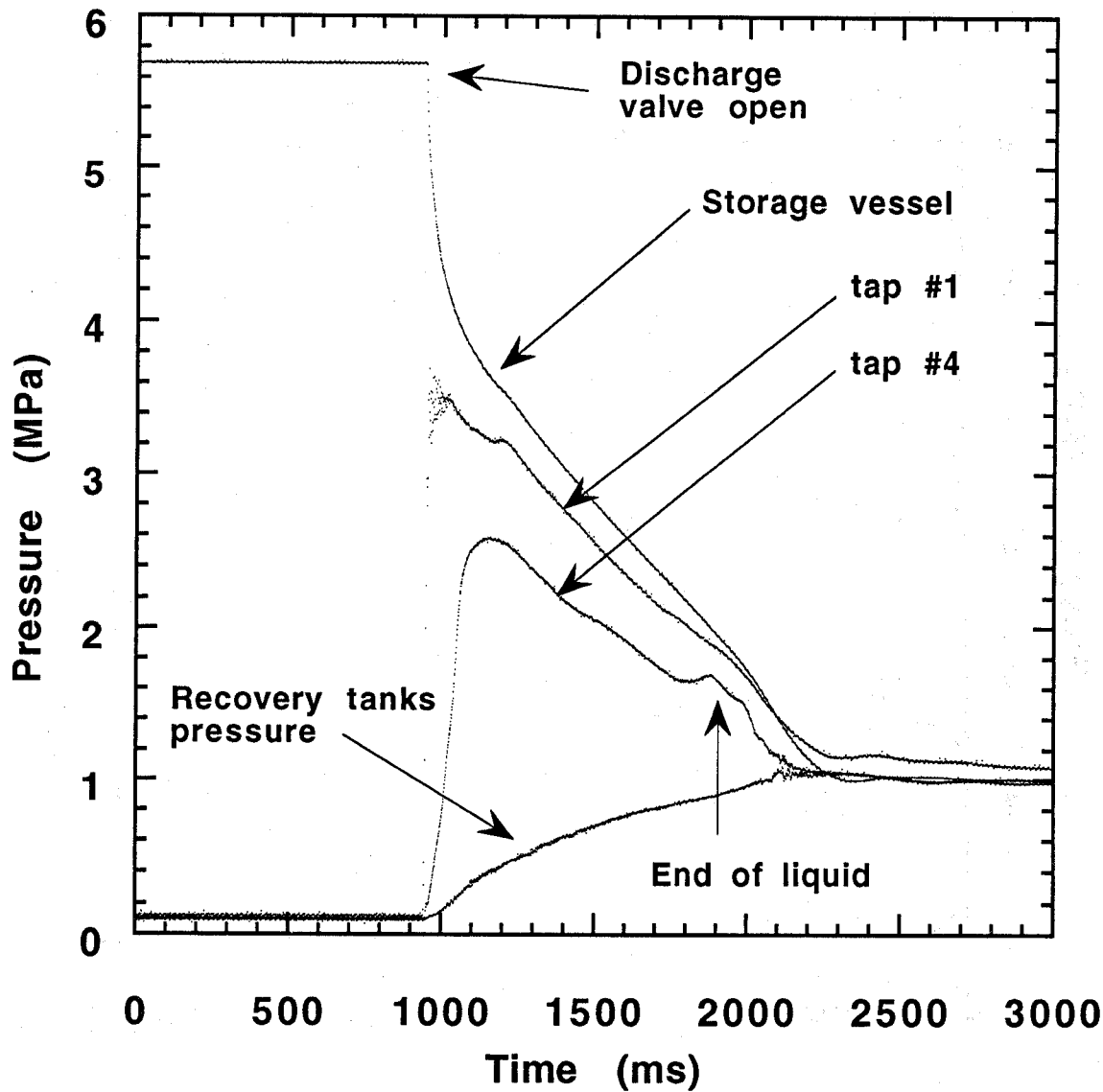


Figure 114. Transient heated agent discharge test; straight piping. The vessel was filled to 1/2 liquid fill volume with CF_3I , pressurized to 4.12 MPa, then heated to 70 °C prior to discharge.

do not show characteristic signs of liquid run out. This observation can be explained by the prediction of single-phase halon 1301/nitrogen and HFC-125/nitrogen mixtures at the recorded elevated temperatures. A single-phase compressible fluid is discharging in those cases. HFC-227ea and CF_3I pipe pressure traces do show liquid run out. These liquid discharge times are not significantly less than the discharge times if the agents had been discharged at 23 °C at the lower initial bottle pressures. One effect that compensates for the higher discharge pressure is the increase in the initial liquid-phase volume in the storage vessel and consequently a decrease in the ullage volume.

8.6.6.10 Visual Observations. The transparent test section was installed and high speed movies taken of a limited number of experiments. CF_3I attacked the plastic pipe strongly and would probably shatter the tube consistently, and therefore, it was the only agent not filmed. Although the test section was hydrostatically tested to failure at 11 MPa, during testing a number of tube failures occurred at around 1 MPa. These failures were attributed to temperature induced failure and/or chemical attack on the plastic tube. All failures occurred at the end of the test after the pressures had equilibrated.

The location of the sight tube was at the exit of the vessel just after the valve reducer section. The initial vessel conditions were ambient temperature, 4.12 MPa charge pressure, and 1/2 liquid fill volume. In addition, one HFC-227ea test with the same fill conditions had the sight tube located 2.8 m downstream from the valve reducer. One constant-head test of HFC-227ea at 2.5 MPa was filmed with the sight tube located just downstream from the valve reducer. The most important observation for all of these tests was that a cloudy two-phase fluid was observed immediately after the vessel valve was opened, and it persisted until essentially all of the liquid contents of the vessel had emptied. This implies that bubbles nucleate somewhere before this location, and two-phase flow is always present during the liquid discharge period. Figure 115 shows four frames of the movie taken of the HFC-125 discharge. The first picture is of the frame just before the arrival of the agent. The next picture is of the very next frame 2 ms later. The cloudy section indicates the two-phase flow. The third picture is of the flow during the middle of the two-phase flow time and is indicative of the frames throughout the two-phase flow period. The last picture is of a frame near the end of the two-phase flow time. The tube is noticeably clearing up.

The time interval between the initial cloudy flow and until it starts to clear up is indicative of the liquid discharge time and it roughly corresponds to the time from the initial pipe pressure rise to the end of the hump in the pipe pressure traces. Table 40 gives the time interval from the first cloudy frame to the point where the flow is clearing up.

8.6.7 Transient Discharge Model. The experimental study yielded a great deal of quantitative information on the flow characteristics of the alternative agents and halon. The effects of piping configuration and initial fill conditions were shown to have significant impact on the flow characteristics. Even though a number of tests were performed, a very limited range of conditions and piping configurations were explored. Modeling the pipe flow would allow other configurations and conditions to be examined. With this in mind, a computer model was developed that predicts the transient discharge of an alternative agent superpressurized with nitrogen from a storage bottle through piping. The model assumptions and equations are presented below.

The model assumes homogeneous, equilibrium two-phase compressible flow. The homogeneous assumption specifies that the gas and liquid phase are well mixed and traveling at the same velocity. This is a good assumption for bubbly flow at low void fractions. Bubbles tend to coalesce at higher void fractions; the transition from bubbly flow to plug flow occurs around a void fraction of 0.3 (Whalley, 1990). At high liquid flow rates though, large bubbles tend to be broken up. The fluid is assumed to be in thermodynamic equilibrium at all locations. Adiabatic, isenthalpic flow is assumed, greatly simplifying the analysis. The change in entropy is attributed to lost work due to frictional

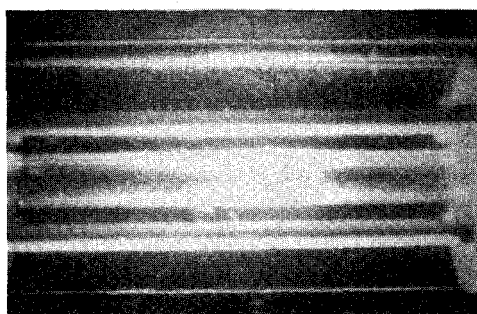
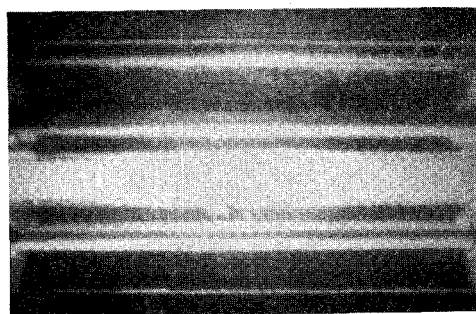
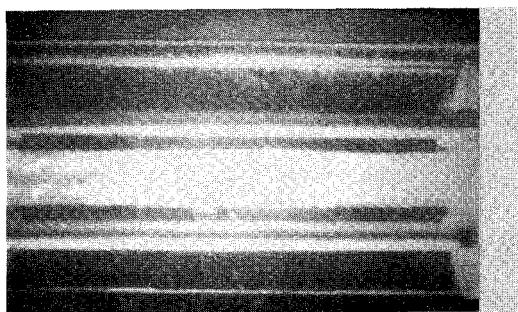
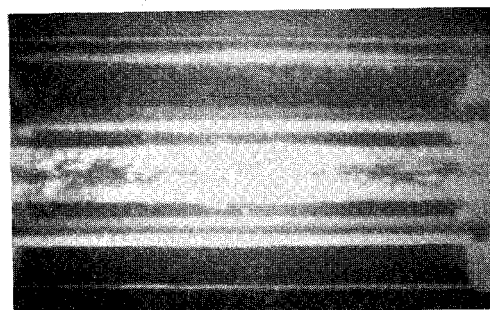
 $t = 0 \text{ ms}$  $t = 2 \text{ ms}$  $t = 1200 \text{ ms}$  $t = 1400 \text{ ms}$

Figure 115. A sequence from a high-speed movie (500 frames/s) of the flow of HFC-125 in 15.9 mm I.D. piping just after the valve reducer.

Table 40. Two-phase time interval from high speed movies

Agent	Figure number	Pressure (MPa)	Cloudy flow interval (± 0.05 s)	t_d (exp.) (s)
Halon 1301	B-18	4.12	1.2	1.0 - 1.2
HFC-125	B-41	4.12	1.2	0.9 - 1.0
HFC-227ea	B-67	4.12	1.1	0.8 - 0.9
HFC-227ea	B-68	4.13	0.9	0.8 - 0.9
HFC-227ea	B-63	2.5	1.1	0.6 - 0.7

losses. The agent flow in the piping is always assumed to be two-phase flow for initially nitrogen-saturated bottle conditions. If the liquid agent is not saturated with nitrogen, the flowing agent is a single-phase liquid until the pipe pressure drops to the equilibrium nitrogen saturation pressure, and at that point degassing occurs. The liquid in the bottle can either follow the isenthalpic pressure/density path, or be frozen (constant density, single-phase liquid) until a critical pressure is reached. There is no mass transfer across the initial liquid-gas boundary in the bottle; bubbles that form in the liquid phase are assumed to stay in the liquid phase. The ullage gas expands adiabatically and isentropically, and is treated as an ideal gas. The ratio of specific heats $C_p/C_v = \gamma$ is a constant value.

Figure 116 shows schematically the bottle and pipe fluid contents for the modeled conditions. Pipe filling and emptying, and ullage discharge are calculated differently than the pipe full case.

8.6.7.1 Model Equations. The foundation for the flow prediction is an application of the steady-state mechanical energy balance and continuity equation for pipe flow. An important assumption is that the process is quasi-steady, *i.e.*, the upstream stagnation properties (the bottle conditions) are fixed over a time increment, and a steady mass flow rate is calculated. The small out-flow of mass changes the bottle conditions for the next time increment. The steady-state differential mechanical energy balance is

$$u \, du + \frac{dP}{\rho} + \delta LW = 0 \quad (38)$$

where δLW , the lost work term for pipe flow is given by

$$\delta LW = \frac{2fu^2}{D} dL \quad (39)$$

The equation of continuity for steady flow is

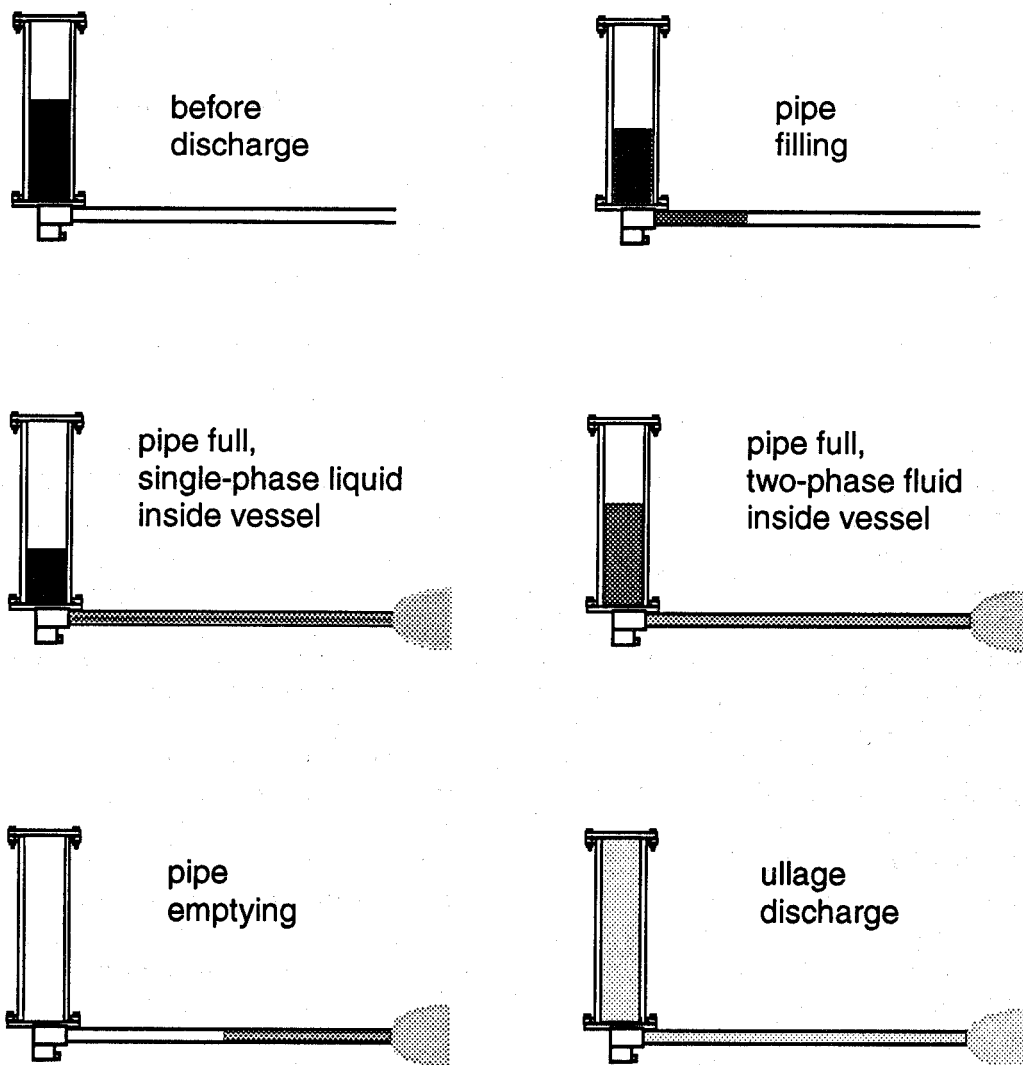


Figure 116. Schematic showing stages of agent discharge. The model calculation scheme is different for the various stages.

$$\rho u = G = \text{const.} \quad (40)$$

where G is the mass velocity.

Equation (38) can be re-arranged, substituting for u with the continuity equation, and integrated over the pipe length to yield

$$\int_{P_1}^{P_2} \rho dP + G^2 \ln\left(\frac{\rho_1}{\rho_2}\right) + \frac{2fG^2 L}{D} = 0 \quad (41)$$

States 1 and 2 are the initial (upstream) and final (exit) states respectively. This equation is applicable to steady compressible flow in pipes with diameter D . If the pipe length is known, G can be calculated, though the calculation is not explicit since the pipe exit pressure is not specified and the flow may be choked. The solution is the pipe exit pressure that maximizes the value of G in Equation (41). Re-arranging Equation (41) so that it is explicit in G , a one-dimensional search is performed to obtain the value of the exit pressure that maximizes G .

If the discharge pressure (the pressure of the receiving vessel, or atmospheric pressure if discharged to the open) is above some critical value, the pipe exit pressure is at the discharge pressure for G to be maximized. If the discharge pressure is below some critical value, the flow in the pipe is choked, and the pipe exit pressure is higher than the discharge pressure.

In the above formulation, it is necessary to have the density of the two-phase mixture expressed explicitly as a function of pressure. Recall that the two-phase flow is assumed to expand adiabatically at constant enthalpy. The Gibbs phase rule for non-reacting systems is

$$F = c - \phi + 2 \quad (42)$$

where F is the degrees of freedom, c is the number of components, and ϕ is the number of phases. In a two-phase, two-component mixture, there are two degrees of freedom. Therefore, with enthalpy fixed, density can be expressed as a function of pressure. An appropriate equation of state is all that is needed to generate the functional relationship between density and pressure.

For any upstream condition, the mass velocity and pipe exit pressure can be calculated. This alone is not enough though for a prediction of the transient bottle discharge. Over each time increment, some mass exits the bottle and the pipe (after the pipe has filled). The difference between the mass leaving the bottle and that leaving the pipe is the change in the mass of the pipe contents. A mass balance must be applied to ensure that the mass exiting the pipe and the change in the mass of the pipe contents is equal to the mass leaving the bottle. This allows for a time increment to be calculated. The calculation scheme is described below.

Assuming the pipe is already filled at a given bottle pressure, a mass velocity and pipe exit pressure are calculated. From the mass velocity a mass flow rate is obtained; this is the mass flow rate leaving the bottle over a short time period. The mass in the pipe at that time is obtained by using a variation of Equation (41) and solving for pressure as a function of distance along the pipe. Since density is a known function of pressure, the density along the pipe is known. Therefore, the mass in the pipe is given by

$$Mp = \frac{\pi}{4} D^2 \sum_{x=0}^L \rho_{avg}(x) \Delta L \quad (43)$$

where Mp is the mass in the pipe, the sum of ΔL is the total length L , and $\rho_{avg}(x)$ is the mean density at the pipe location (x). The mass lost from the pipe is given by the following "liquid" mass balance, (a mass balance applied to the original liquid phase contents)

$$Mlp = (Mvl_t + Mp_t) - (Mvl_{t+\Delta t} + Mp_{t+\Delta t}) \quad (44)$$

where Mlp is the mass lost from the pipe over the time increment Δt . Mvl is the liquid mass in the vessel. The liquid mass is obtained from the liquid volume multiplied by the liquid density at the vessel pressure. The liquid volume is the difference between the total volume and the ullage volume. The ullage expands isentropically and is assumed to behave as an ideal gas so the following relationship holds

$$P \left(\frac{V_u}{M_g} \right)^\gamma = \text{Const.} \quad (45)$$

where P is the bottle pressure, V_u is the ullage volume and M_g is the mass of the ullage contents.

The time increment (Δt) over which the pressure in the bottle drops from P_t to $P_{t+\Delta t}$ is calculated from

$$\Delta t = \frac{Mlp}{(W_t + W_{t+\Delta t})/2} \quad (46)$$

where W_t and $W_{t+\Delta t}$ are the mass flow rates at times (t) and ($t+\Delta t$) respectively. The bottle pressure is then stepped down and the process repeated. A pressure increment of 5 kPa was found to be sufficient for calculation accuracy.

The filling and emptying of the pipe with the two-phase mixture is approximated using a different method. In each case, the effective pipe length is segmented, and the calculation proceeds by the filling or emptying of the segments. Eight segments provided sufficient accuracy for the calculations described here.

In the filling case, the addition of each segment represents an increase in the pipe length for the calculation of pipe end pressure and mass velocity. The flow is assumed to be two-phase and choked at the "liquid front" which is located at the end of the particular segment of interest. For the first time increment, the pipe length is equal to the length of a segment. At this point, the bottle pressure, pipe end pressure, mass velocity and mass in the pipe are all unknown. The solution is obtained by guessing a bottle pressure, solving for the remaining unknowns and then comparing the "liquid" mass balance equation to that solution. The "liquid" mass balance reduces to

$$Mv l_t = Mv l_0 + Mp_t \quad (47)$$

during the pipe filling stage. $Mv l_0$ is the initial liquid-phase mass. Once the exit pressure and mass velocity are obtained for the guessed bottle pressure, the mass in the pipe can be calculated. The value of $Mv l_t$ is used to calculate a new liquid volume in the bottle, and an ullage volume is obtained by difference. This ullage volume is compared to the ullage volume calculated from the isentropic expansion relationship using the initial bottle pressure guess. Successive guesses of bottle pressure are required until the ullage volumes converge. The time to fill the first section of pipe is estimated as the mass in the pipe divided by the mass flow rate. The time to fill the pipe up to the j th segment is estimated by

$$t_{fill, j} = \sum_{i=1}^j \frac{Mp_i - Mp_{i-1}}{W_i} \quad (48)$$

When the bottle is emptied of its originally liquid contents, a calculation similar to the one above is performed. To start, the first segment is empty of the two-phase mixture, and the bottle pressure is calculated from the isentropic expansion relationship, with the ullage volume equal to the bottle volume plus the empty pipe segment volume. Isentropic expansion of the ullage gas into the pipe is justified due to the relatively slow velocity of the two-phase mixture/gas front which acts as a slow-moving piston allowing the gas to expand essentially reversibly. The pipe length is equal to the effective length minus the segment. The pipe exit pressure is solved using Equation (41) and maximizing the mass velocity. The mass in the pipe is then calculated. The time increment for the liquid two-phase/gas front to travel to the end of the j th segment is estimated by

$$t_{empty, j} = \sum_{i=1}^j \frac{Mp_{i-1} - Mp_i}{W_i} \quad (49)$$

Emptying of the ullage contents (assumed to behave as an ideal gas) is calculated in a similar quasi-steady fashion. Assuming adiabatic flow of an ideal gas, the following relation holds (Balzhiser *et al.*, 1972)

$$G^2 = \frac{0.5(1 - \frac{\rho_2^2}{\rho_1^2})}{\frac{\gamma-1}{4\gamma}(\frac{\rho_2^2}{\rho_1^2} - 1) + (\frac{\gamma-1}{2\gamma} - 1)\ln \frac{\rho_2}{\rho_1} + \frac{2fL}{D}} \quad (50)$$

After the two-phase slug leaves the pipe, the gas in the pipe accelerates to its maximum mass velocity given by the vessel pressure, assuming no ullage mass has left the piping. This creates a discontinuous step down to the exit pressure for the gas flow as a result of the approximation that the gas isentropically expands into the piping while the two-phase mixture is leaving the piping. In reality, there is a smooth, steep decrease in the exit pressure as the two-phase mixture leaves and the ullage begins to discharge.

The calculation proceeds in the following manner. The mass flow rate of the gas exiting the piping is multiplied by a small time increment. This mass is subtracted from the mass balance for the next time step. Successive guesses of the vessel pressure are made until the guessed pressure and the calculated pressure from isentropic expansion of the vessel contents converge. A new mass flow rate is obtained, and the process is repeated.

The pressure recovery in the bottle is thought to be due to nitrogen coming out of solution from the supersaturated liquid. In these tests there was no direct visual confirmation (*i.e.*, visualization of the formation of bubbles in the vessel liquid) proving that to be the case, but it is assumed to be the correct interpretation. For some agents and fill conditions the pressure recovery is more pronounced, whereas in others it is not evident. Pipe flow visualization with high speed movies does confirm the two-phase nature of the fluid exiting the valve. To simulate the retardation of the nitrogen degassing in the bottle, the calculation initially proceeds with the bottle liquid phase density fixed at the initial density. When the bottle pressure drops below a critical degassing pressure, nitrogen comes out of solution. The critical degassing pressure used is an experimentally inferred value for a particular agent and fill condition, and it is the lowest pressure achieved before the observed pressure rise. There is a lot of scatter in these data for a given agent; a mean value was selected. For HFC-227ea and CF₃I the calculation assumes no degassing in the bottle, since no characteristic pressure recovery was noticed for these agents (except one HFC-227ea and CF₃I test at 2/3 fill volume). When the bottle pressure drops below the degassing pressure, the liquid density decreases due to bubble formation. The liquid (two-phase) mass is fixed, thus its volume must increase. The increase in the liquid (two-phase) volume compresses the ullage gas, and the pressure rises. The mass velocity at the pipe exit does not instantaneously increase to a value given by an elevated bottle pressure. There must be a pressure wave moving down the length of the pipe (similar to the pipe filling case), since after the bottle pressure rises, more mass can be stored in the pipe. This transient is approximated in the following manner. Over the transient time Δt_{trans} , the mass lost from the pipe is

$$Mlp = W_t \Delta t_{trans} \quad (51)$$

Time (t) is at the beginning of the transient. The transient time is equal to the sum of the mass lost from the pipe and the change in the pipe mass divided by an average mass flow rate as shown below. The average mass flow rate is the mean value of the mass flow rate after the transient and the mass flow rate before the transient.

$$\Delta t_{trans} = \frac{Mp_{t+\Delta t} - Mp_t + Mlp}{(W_{t+\Delta t} + W_t)/2} \quad (52)$$

or substituting for Mlp

$$\Delta t_{trans} = \frac{Mp_{t+\Delta t} - Mp_t}{(W_{t+\Delta t} - W_t)/2} \quad (53)$$

To calculate Δt_{trans} , a bottle pressure at the end of the transient is guessed, $W_{t+\Delta t}$ and $Mp_{t+\Delta t}$ are calculated, then Δt_{trans} is calculated from above. The bottle liquid content mass at the end of the transient is

$$Mvl_{t+\Delta t} = Mvl_t + Mp_t - Mp_{t+\Delta t} - Mlp \quad (54)$$

From this bottle two-phase mass and the two-phase density based on the guessed pressure, the liquid volume and then the ullage volume is calculated. Bottle pressure is calculated from the isentropic relationship of the ullage gas, compared to the initial guessed pressure and, subsequently, new guesses are made until the two pressures converge.

8.6.7.2 Fill Conditions and Thermodynamic Inputs. Specific fill conditions, *i.e.*, mass in the liquid and gas phase and fill volume are calculated by the program PROFISSY. The thermodynamic relationships are obtained from a variation of the program PROFISSY that performs isentropic or isenthalpic expansion calculations. While the process for obtaining the thermodynamic inputs is not automatic, the inputs are valid for any fill condition at a given charge pressure and temperature. First, PROFISSY is used to calculate the mass of agent and nitrogen in the liquid and gas phases for a given fill condition and temperature. An isenthalpic expansion of the liquid phase and an isentropic expansion of the gas phase calculation is performed. For the isenthalpic expansion, at the initial storage pressure a single phase exists. During the expansion a two-phase gas/liquid mixture is formed. The average density, temperature, and mass fraction in the liquid phase are obtained at each pressure step. These results are fitted to third or fourth order polynomial functions of pressure. **Appendix C** shows some plotted results. The coefficients for the pressure/density for each of the agents at various pressures are given in Table C-1. The isentropic expansion of the gas phase begins with initially gaseous agent and nitrogen; upon expanding, some agent condenses. The mean density is plotted as a function of pressure, then fitted by a power law equation. The inverse of the exponent is defined as the ideal γ coefficient. Results are shown in **Appendix C** for agent/nitrogen mixtures initially at 4.12 MPa. The power-law exponent was insensitive to initial pressure, so γ was fixed for each agent/nitrogen mixture.

8.6.7.3 Friction Factor. Since the flow is described as a homogeneous two-phase flow, the friction factor analysis will follow the method for established for single phase flows. The Colebrook equation (see Perry *et al.*, 1984), shown below, relates the Fanning friction factor to pipe diameter, roughness, and Reynolds number (Re) for turbulent flows as

$$\frac{1}{\sqrt{f}} = -4 \log_{10} \left(\frac{\epsilon}{3.7D} + \frac{1.256}{Re \sqrt{f}} \right) \quad (55)$$

which requires an iterative scheme to solve for f . The Reynolds number is defined as

$$Re = \frac{uD\rho}{\mu} \quad (56)$$

At high Re , Equation (55) reduces to von Kármán's equation (see Perry *et al.*, 1984)

$$\frac{1}{\sqrt{f}} = -4 \log_{10} \left(\frac{\epsilon}{3.7D} \right) \quad (57)$$

Haaland (see Welty *et al.*, 1984) has shown that for $4 \times 10^4 \leq Re \leq 10^8$ and $\epsilon/D \leq .05$ the friction factor can be expressed (within $\pm 1.5\%$) as

$$\frac{1}{\sqrt{f}} = -3.6 \log_{10} \left[\frac{6.9}{Re} + \left(\frac{\epsilon}{3.7D} \right)^{\frac{10}{9}} \right] \quad (58)$$

which allows explicit calculation of f . Moody (see Perry *et al.*, 1984) reports the value of surface roughness for drawn tubing as 0.00152 mm, and it is the value used here.

For the flows encountered in this study, the density and viscosity of the mixture are functions of pressure and temperature. Therefore the Reynolds number, and thus the friction factor, is a function of pipe position, and in addition, a function of time for the transient discharge. In the model, the friction factor is assumed to be constant. The validity of this assumption is demonstrated by the following analysis.

The NIST program REFPROP (Gallagher *et al.*, 1993) was used to obtain the viscosity of the liquid and gas phase for halon 1301, HFC-125, and HFC-227ea as a function of temperature; nitrogen viscosity as a function of temperature was also obtained. The viscosity of the homogeneous two-phase mixture was estimated from the functional form suggested by Dukler *et al.* (1964).

$$\mu_h = \mu_g \frac{y \rho_h}{\rho_g} + \mu_l \frac{(1-y) \rho_h}{\rho_l} \quad (59)$$

where y is the mass fraction of the gas phase, and the subscripts l , g and h stand for liquid, gas, and homogeneous respectively. The gas phase mixture viscosity at a given temperature was estimated as the sum of the agent and nitrogen gas viscosities multiplied by their respective volume fractions in the gas phase. Table C-2 in **Appendix C** gives the calculated results, expressed as polynomial fits, at initial pressures of 2.75 MPa and 4.12 MPa at 20 °C. The first step in the analysis was to calculate a

friction factor from the von Kármán equation, then simulate the flow. From the calculations, the velocity, density, and viscosity are known for any location and time in the pipe, thus local Reynolds numbers are calculated, and Equation (58) is used to obtain the local friction factor. The mean friction factor at a specified time is given by

$$f_m = \frac{1}{L} \sum_{i=1}^L \frac{f_i + f_{i-1}}{2} (x_i - x_{i-1}) \quad (60)$$

where f_m is the mean friction factor, and x is a particular pipe location. Plots of the Reynolds number and mean friction factor versus time for a 4.1 m straight pipe with two different internal piping diameters (15.9 mm and 9.5 mm) are shown in Figures 117 to 122. In these figures, the thick dashed lines are the high Reynolds number limits for the friction factors given by the von Kármán equation. The mean Reynolds number is shown along with two curves representing $\pm 2\sigma$. The standard deviation of the mean friction factor is on the order of 10^{-6} and is not shown on the plots. Although the Reynolds number decreases over the flow time, the mean friction factor rises only slightly. The mean friction factor and the friction factor calculated from the von Kármán equation differ by 3 % for the larger pipe and 6 % for the small pipe. The main conclusion is that for the conditions here, the Reynolds number is high enough that for all practical purposes viscous effects can be ignored, allowing the von Kármán equation to be used.

Pressure drops across bends, valves, and other piping elements can be included by treating those items in terms of an effective pipe length. This technique is well established in hydraulic calculations. Here the flow elements of interest are the discharge valve and the reducer, 90° angle bends, expansions, contractions, and tees. The effective lengths for the discharge valve and valve reducer section were determined from the experimental pressure drops. The effective length was varied until the calculated pressure drop from the bottle pressure to the first pressure tap reproduced the experimental pressure drop. For the large diameter piping, an effective length equivalent to the open volume of the valve and the reducer ($1.25 \times 10^{-4} \text{ m}^3 \pm 2.5 \text{ cm}^3$) divided by the pipe cross-sectional area gives 0.63 m and approximates the experimental pressure drop. For the small pipe, the pressure drop across the valve and reducer was very small (most of the pressure drop occurs in the piping), and the effective length was estimated to be 0.1 m for the constant head tests. For the transient tests the pressure drop across the valve and reducer was ignored, and the open volume of the valve and reducer was added to the vessel volume. When the valve opens, it is assumed the fluid fills that volume and the ullage isentropically expands. The effective bottle volume becomes the bottle volume plus the valve and reducer volume.

The effective length for smooth bends in the piping was estimated from the following equation (SFPE, 1988)

$$\frac{2fL_{eff}}{D} = [0.13 + 1.85 \left(\frac{r}{R}\right)^{3.5}] \left(\frac{\alpha^\circ}{180^\circ}\right)^{0.5} \quad (61)$$

where α° is the bend angle, R is the bend radius, and r is the pipe inner radius. With the friction factor given by the von Kármán equation, the equivalent length for the small pipe with a 50 mm radius bend was 0.25 m and for the large pipe with a 150 mm radius bend was 0.47 m.

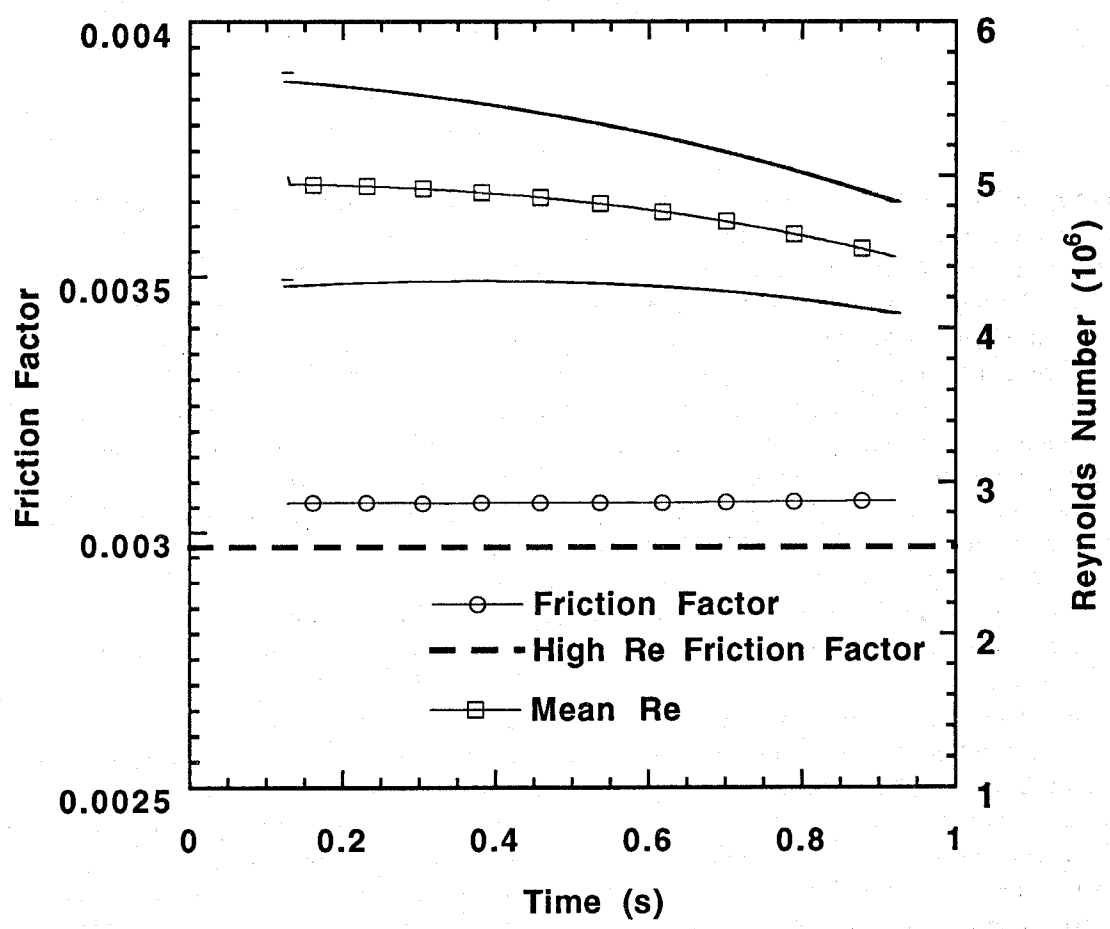


Figure 117. Mean friction factor and Reynolds number as a function of time for a simulated transient discharge of halon 1301: 15.9 mm I.D. piping was specified, and the vessel was at 1/2 liquid fill volume and pressurized to 4.12 MPa.

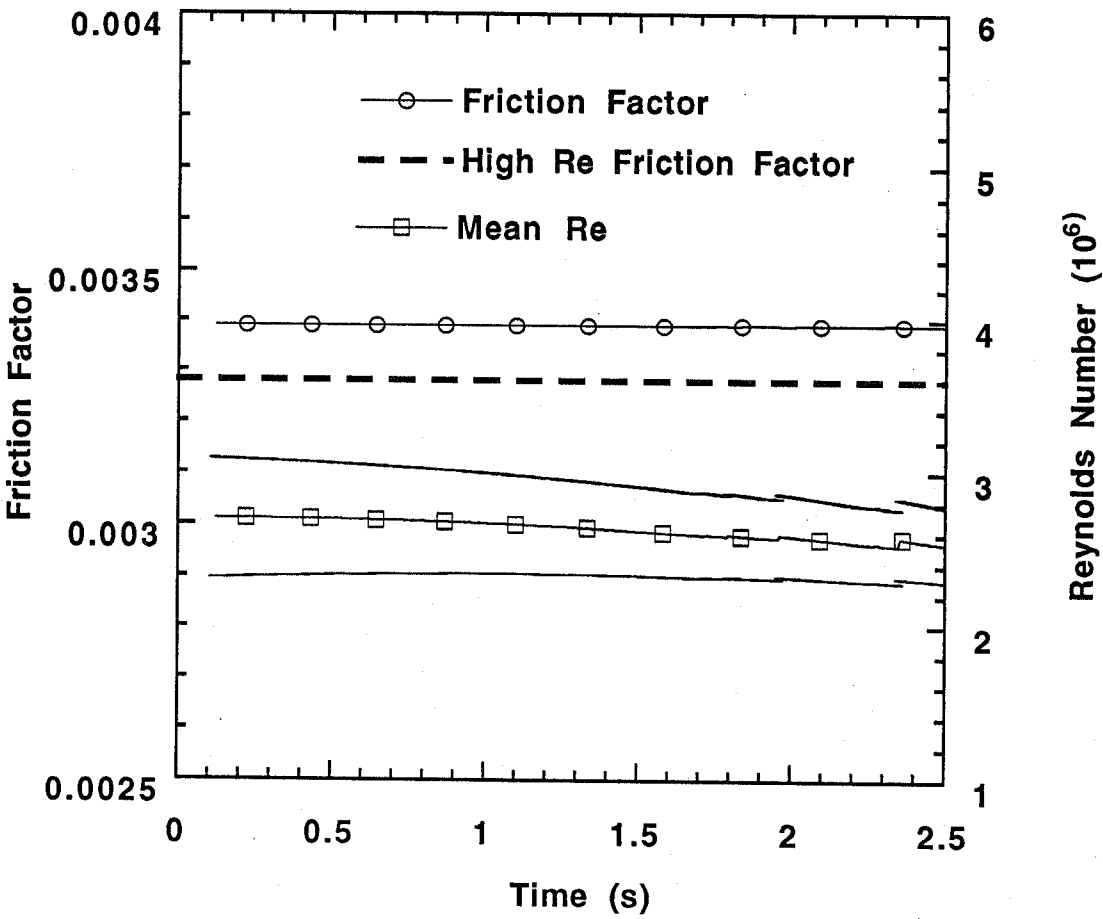


Figure 118. Mean friction factor and Reynolds number as a function of time for a simulated transient discharge of halon 1301: 9.5 mm I.D. piping was specified, and the vessel was at 1/2 liquid fill volume and pressurized to 4.12 MPa.

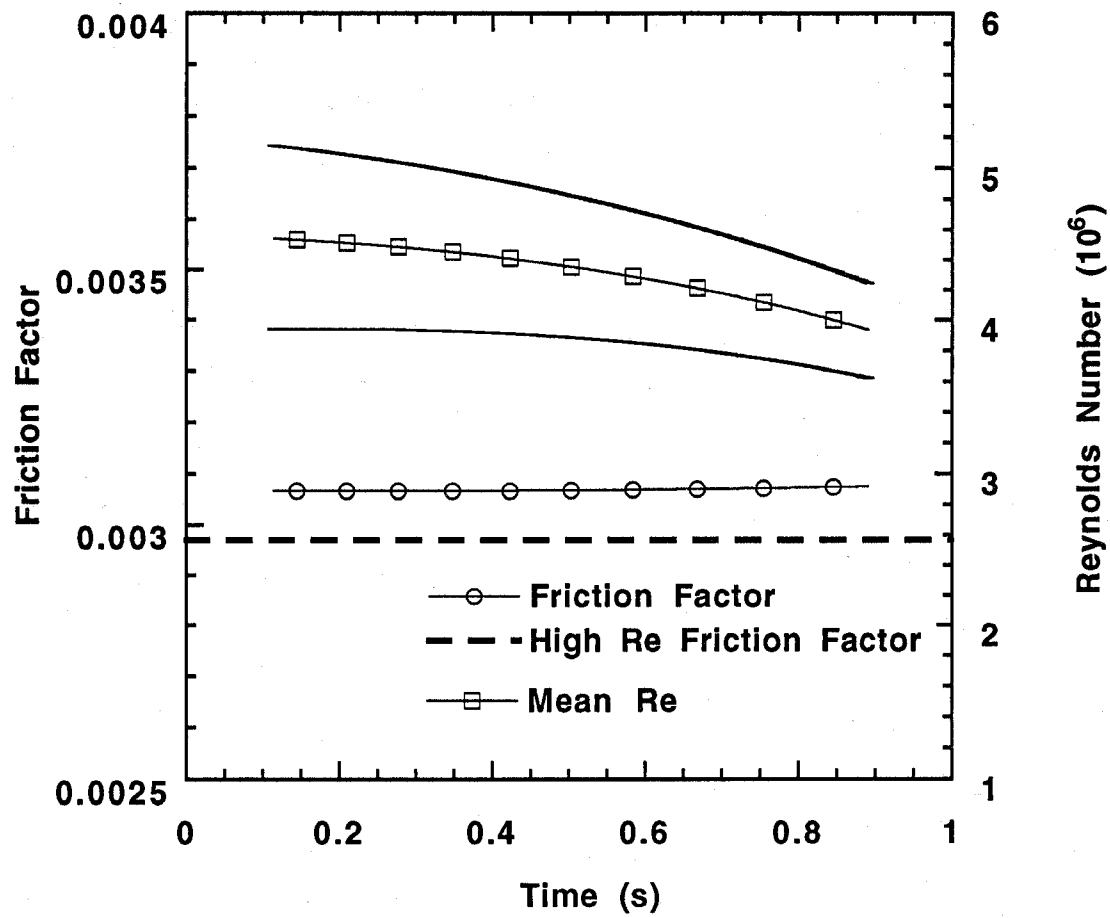


Figure 119. Mean friction factor and Reynolds number as a function of time for a simulated transient discharge of HFC-125: 15.9 mm I.D. piping was specified, and the vessel was at 1/2 liquid fill volume and pressurized to 4.12 MPa.

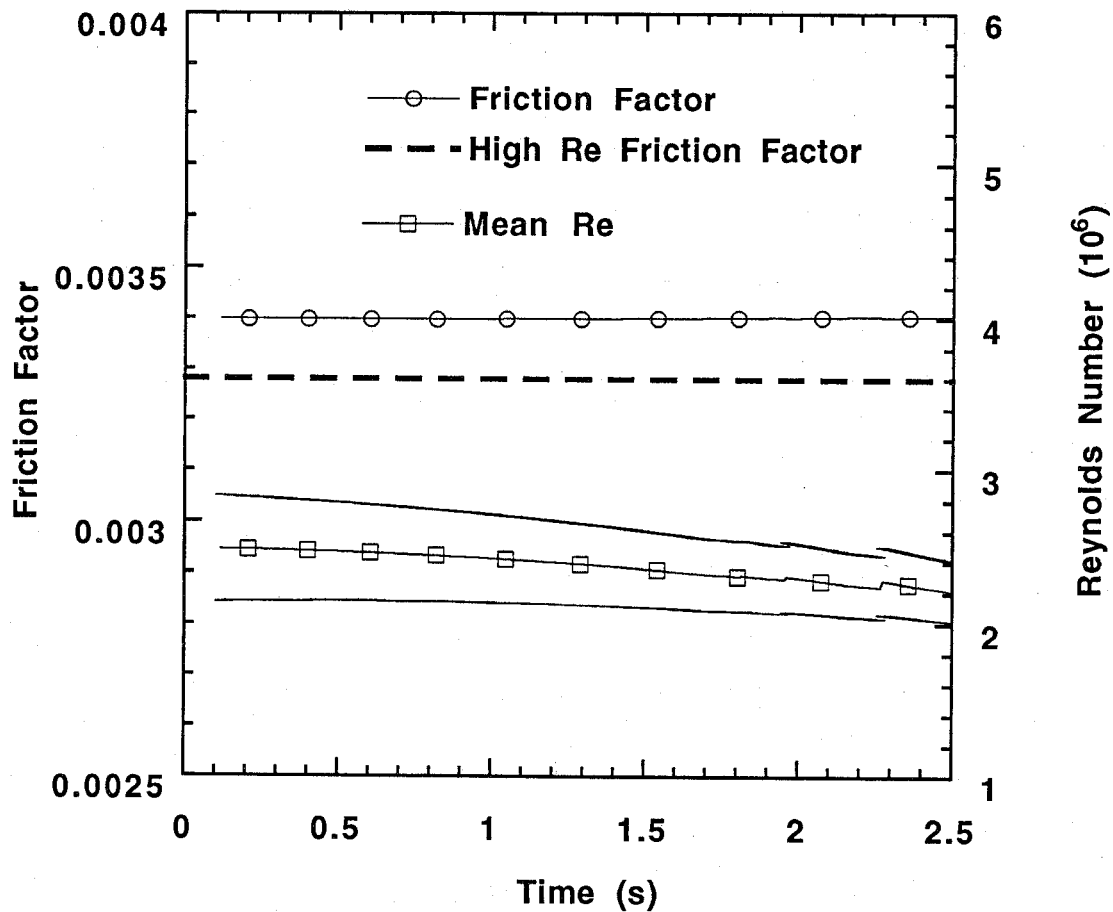


Figure 120. Mean friction factor and Reynolds number as a function of time for a simulated transient discharge of HFC-125: 9.5 mm I.D. piping was specified, and the vessel was at 1/2 liquid fill volume and pressurized to 4.12 MPa.

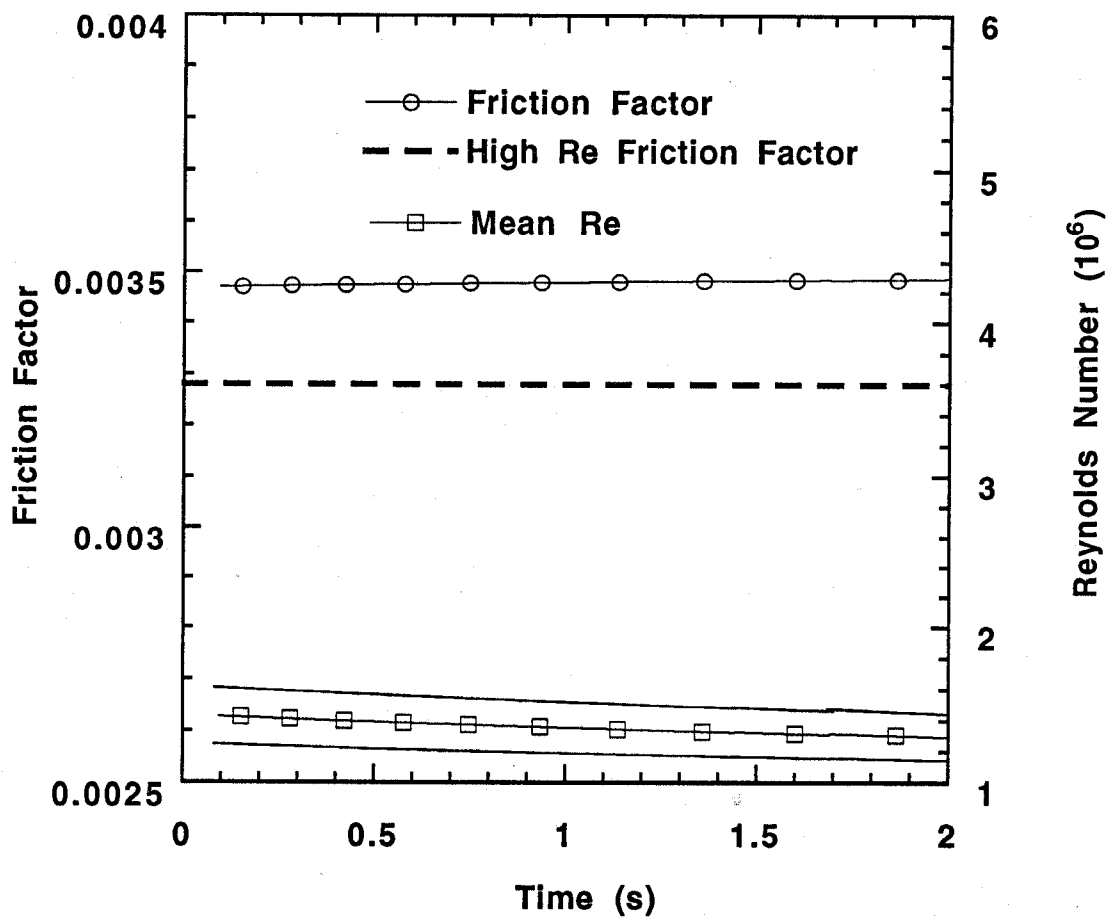


Figure 121. Mean friction factor and Reynolds number as a function of time for a simulated transient discharge of HFC-227ea: 15.9 mm I.D. piping was specified, and the vessel was at 1/2 liquid fill volume and pressurized to 4.12 MPa.

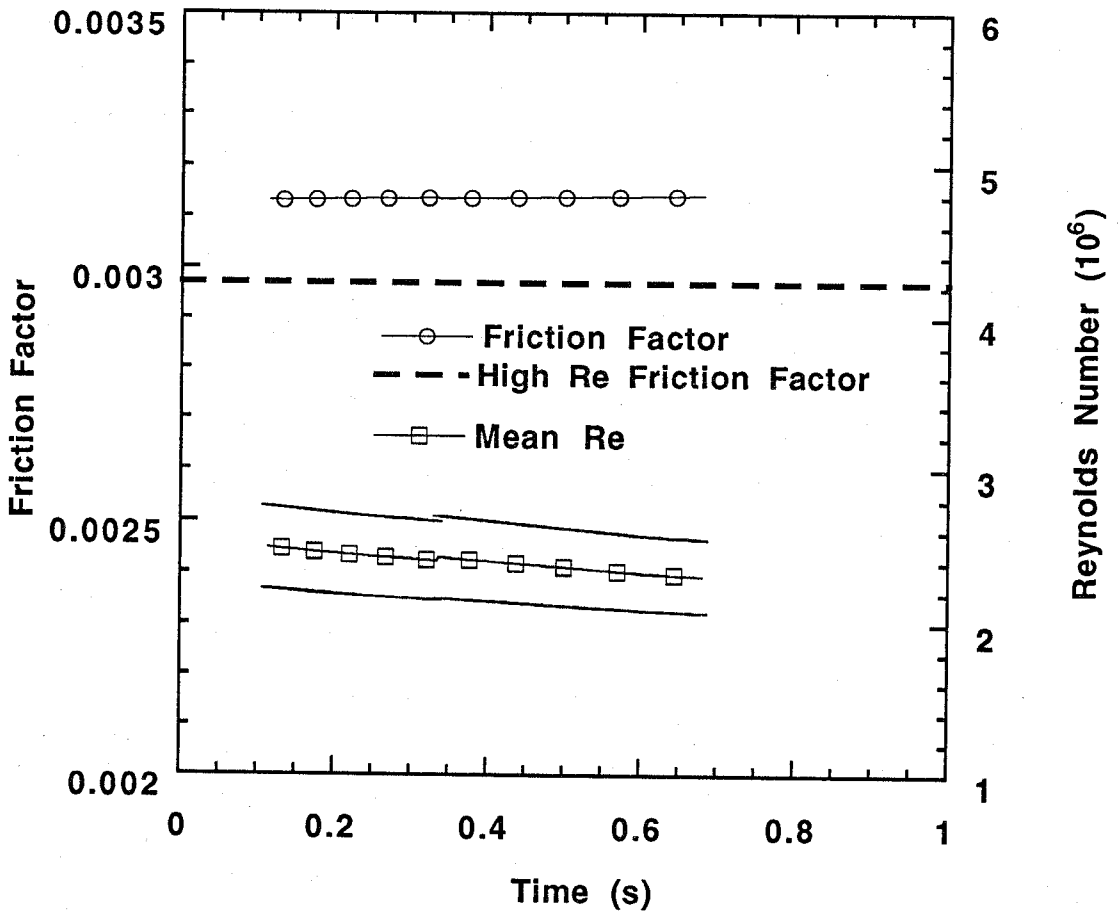


Figure 122. Mean friction factor and Reynolds number as a function of time for a simulated transient discharge of HFC-227ea: 9.5 mm I.D. piping was specified, and the vessel was at 1/2 liquid fill volume and pressurized to 4.12 MPa.

For the contraction run, the pressure drop in the first 1.00 m of large piping was very small, therefore, the pipe volume was added to the valve and reducer volume which increased the effective bottle volume. For the expansion run, the flow was assumed to be choked at the expansion, therefore, the downstream pressure does not affect the mass flow rate. The calculations assume a 1.00 m length of small piping.

The effective length for the tee configuration was the sum of the effective length of the valve and reducer (0.63 m) plus the length of piping to the tee (2.1 m), plus the effective length of the tee element (0.9 m), plus the length of one leg to the recovery tanks (1.2 m).

The input requirements for a piping element are the effective length and the location of the piping element. The location of the piping element is important because the mass in the pipe is based on the sum of the mass in a number of small portions of the physical pipe. At a piping element with an effective pipe length, a step change in the density is required for the pipe mass calculation.

8.6.8 Model Calculations

8.6.8.1 Constant-Head Conditions. The constant-head tests were simulated by fixing the upstream conditions and calculating the steady mass flow rate and the pipe pressures at the tap locations. The effective length of the 15.9 mm diameter pipe was specified as 4.13 m, 3.50 meters of pipe from the valve reducer to the recovery tanks plus a 0.63 m effective length for the valve and valve reducer section (which essentially reproduces the experimental pressure drop from the bottle to the first pressure tap location). For the 9.5 mm pipe an effective length of 3.10 m was specified. There are 3.00 m of physical pipe length until the expansion to the larger pipe diameter which leads to the recovery tanks, and 0.10 m was chosen as an effective pipe length for the valve and reducer.

Table 35 compares the calculated steady mass flow rate with the experimentally determined average mass flow rate. Figure 123 is a plot of experimentally determined flow rates versus the calculated flow rates for all of the tests. The calculated results for the small diameter tests are within 10 % of the mean experimental value. For the large diameter tests, the experimental values are larger than the calculated values. Given the uncertainty in the experimental values and the probability that the calculated steady values should underestimate the large diameter values, the results compare favorably.

Calculated pipe pressures are shown in Figures 124-131. The pressure predictions show good agreement with the experimental pressures and illustrate the validity of the flow assumptions. Deviations from the experimental values may be due to metastable flow, heat transfer, and/or departures from the assumed homogeneous flow condition.

8.6.8.2 Transient Conditions. Each transient test was simulated by the model. Experimental fill conditions were used. It was assumed that the mass of dissolved nitrogen was the equilibrium amount. Calculations were performed for the cases with the bottle liquid contents in thermodynamic equilibrium and repeated with a specified degassing pressure for each agent at the given storage pressure.

Figures 132 and 133 are the simulated pressure traces for one test (halon 1301 at 1/2 liquid fill volume and 4.12 MPa storage pressure flowing through 3.5 m of straight piping). The results from Figure 132 are for equilibrium bottle conditions, while the results for Figure 133 are for "frozen" non-equilibrium bottle conditions until the critical degassing pressure (in this case 2.5 MPa) is reached. Figures 134 and 135 compare selected calculated pressure traces to experimental pressure traces. The

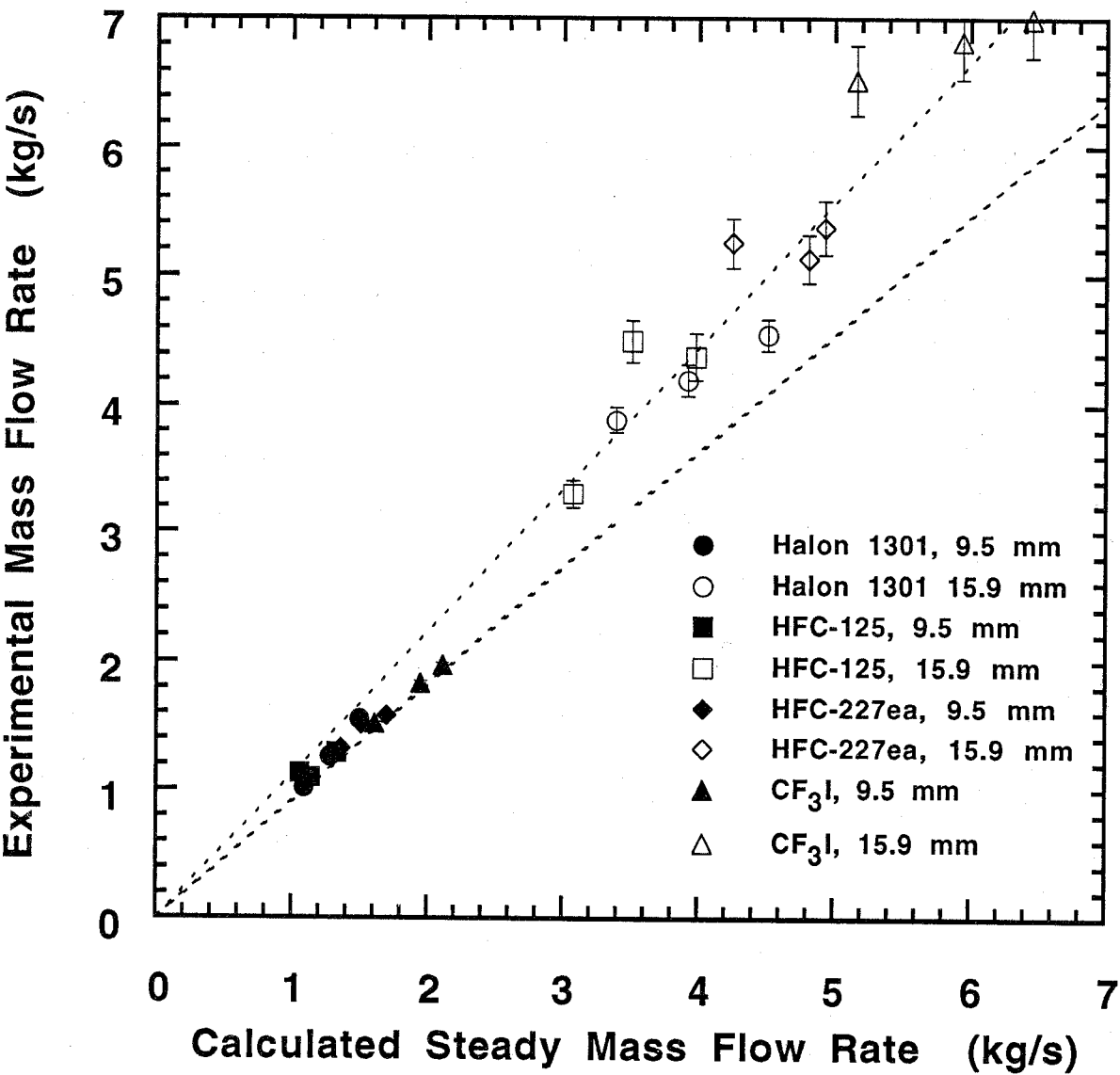


Figure 123. Constant-head mass flow rate. The dashed lines represent $\pm 10\%$ deviation of predictions. Estimated measurement errors are indicated by error bars.

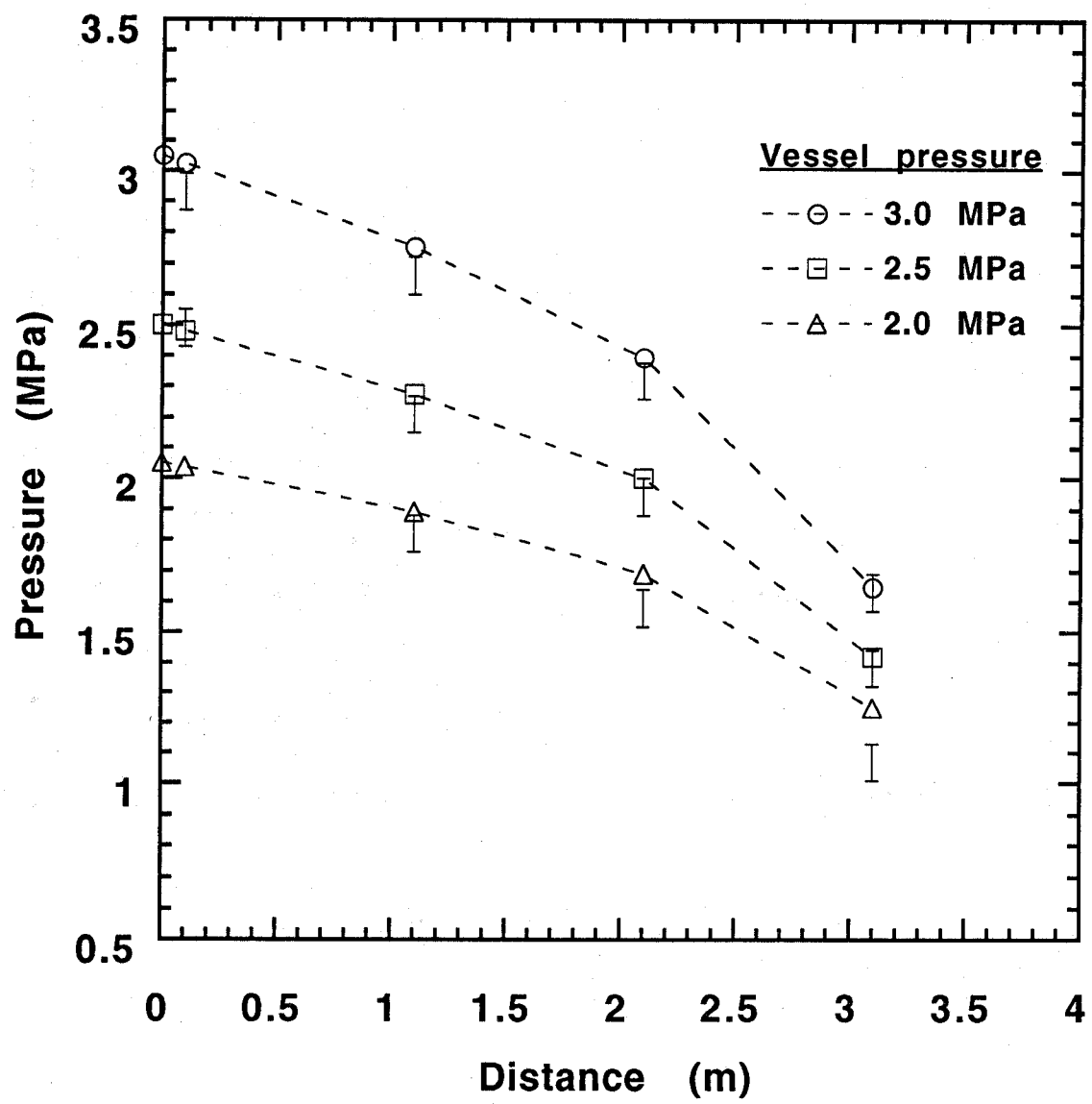


Figure 124. Pipe pressures for constant-head tests: halon 1301 and 3.1 m effective length of 9.5 mm I.D. piping. Symbols: calculations, and vertical lines with error bars: mean experimental pressures $\pm 2\sigma$ uncertainty.

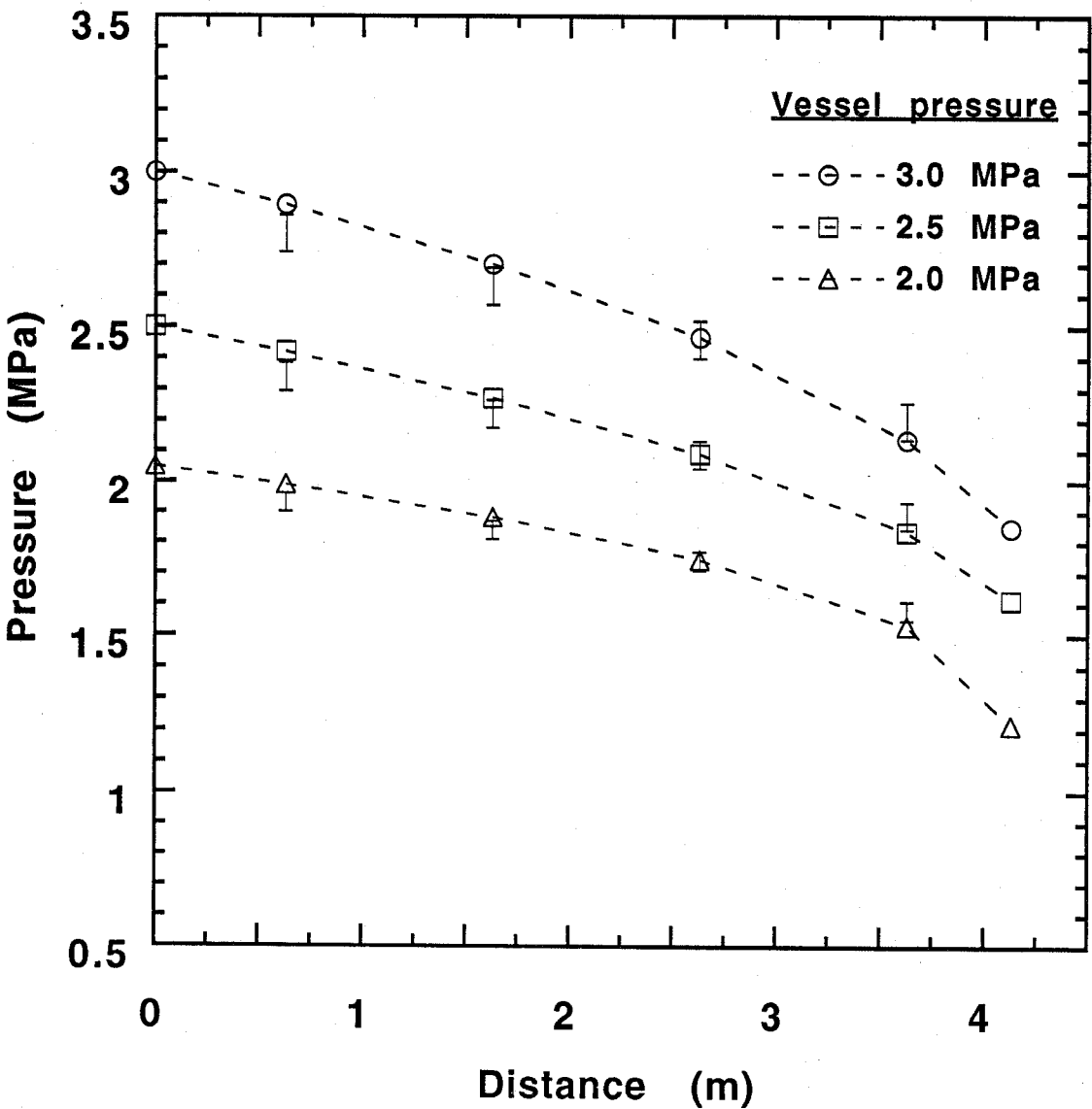


Figure 125. Pipe pressures for constant-head tests: halon 1301 and 4.13 m effective length of 15.9 mm I.D. piping. Symbols: calculations, and vertical lines with error bars: mean experimental pressures $\pm 2\sigma$ uncertainty.

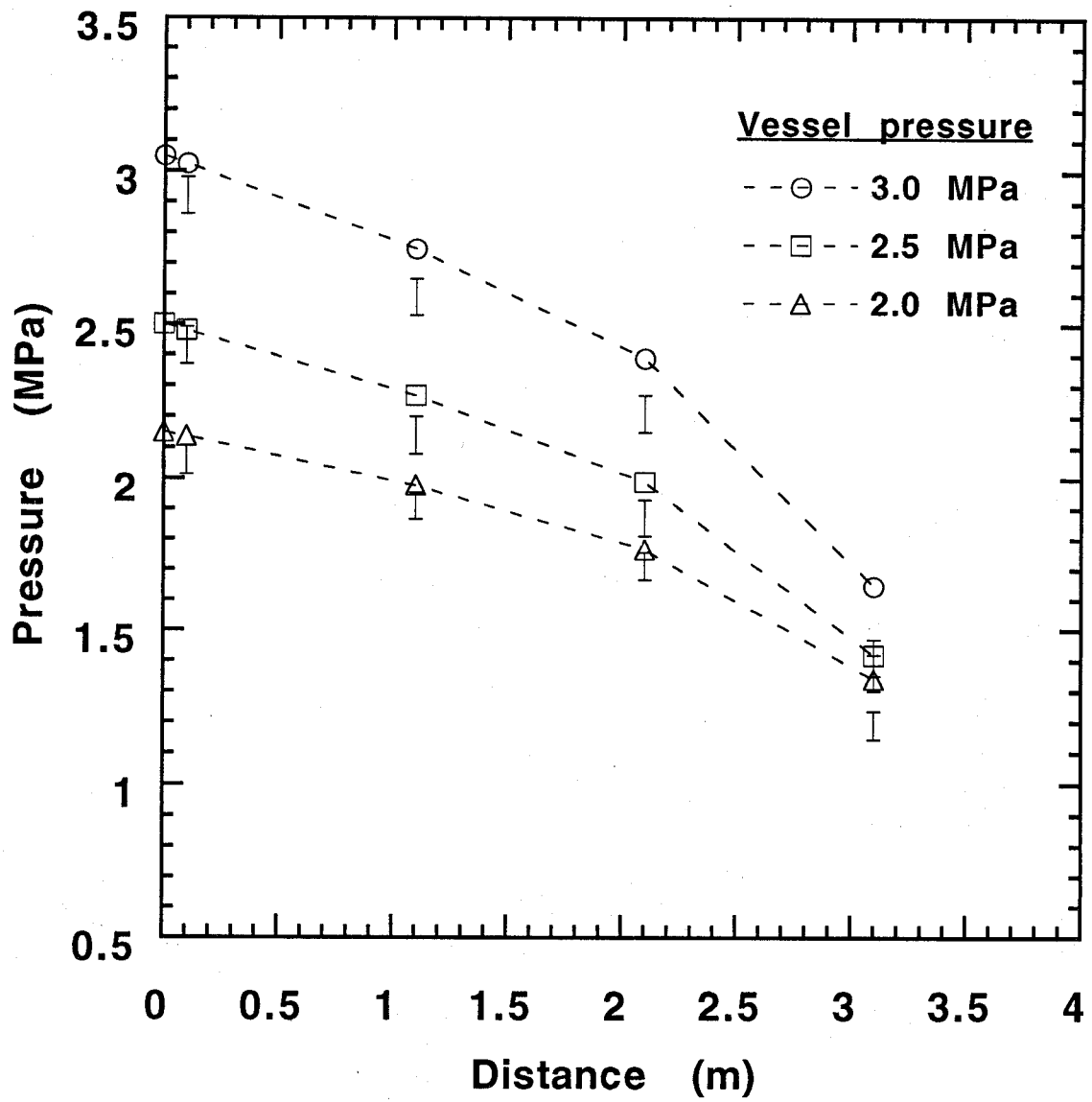


Figure 126. Pipe pressures for constant-head tests: HFC-125 and 3.1 m effective length of 9.5 mm I.D. piping. Symbols: calculations, and vertical lines with error bars: mean experimental pressures $\pm 2\sigma$ uncertainty.

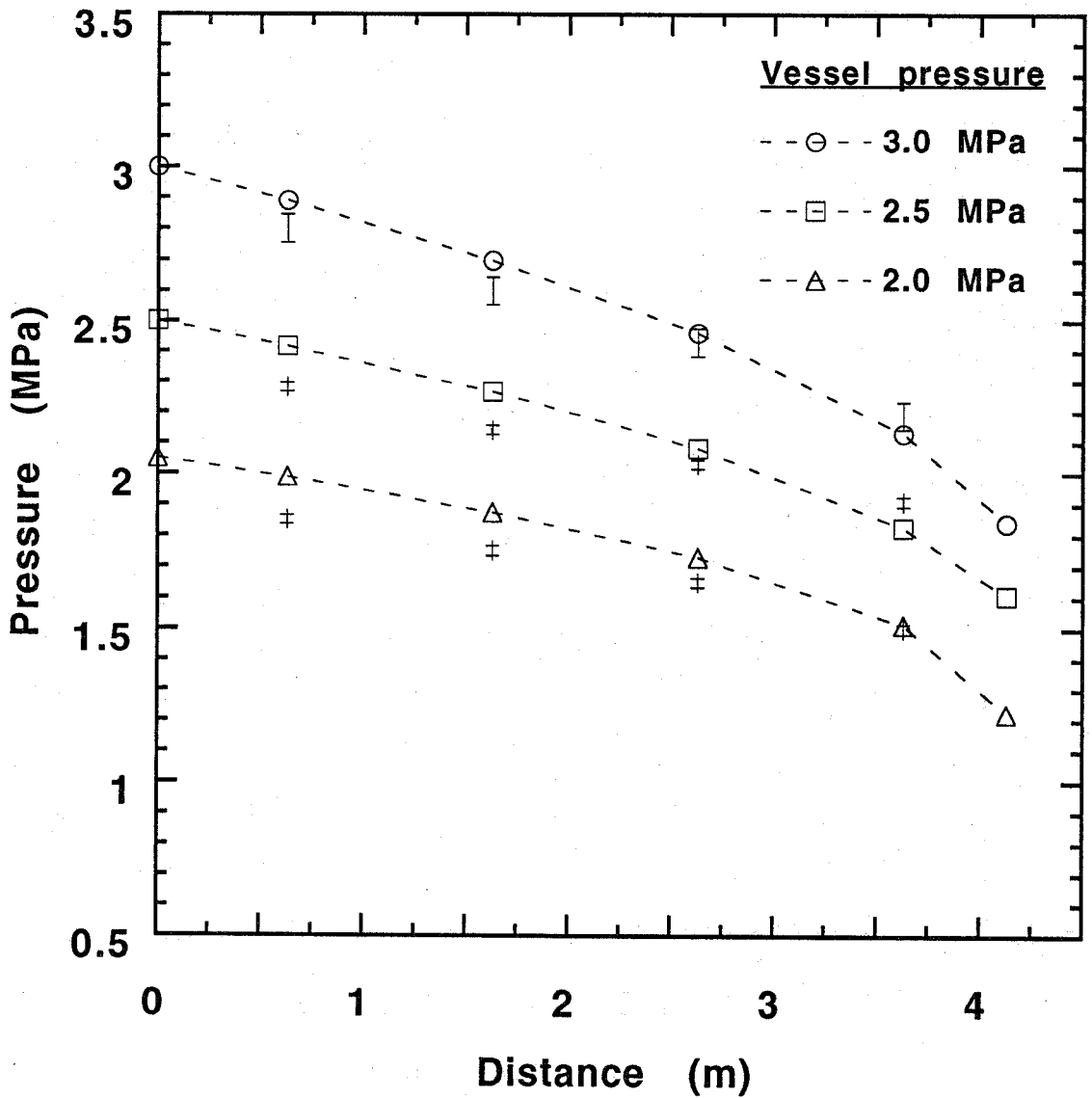


Figure 127. Pipe pressures for constant-head tests: HFC-125 and 4.13 m effective length of 15.9 mm I.D. piping. Symbols: calculations, and vertical lines with error bars: mean experimental pressures $\pm 2\sigma$ uncertainty.

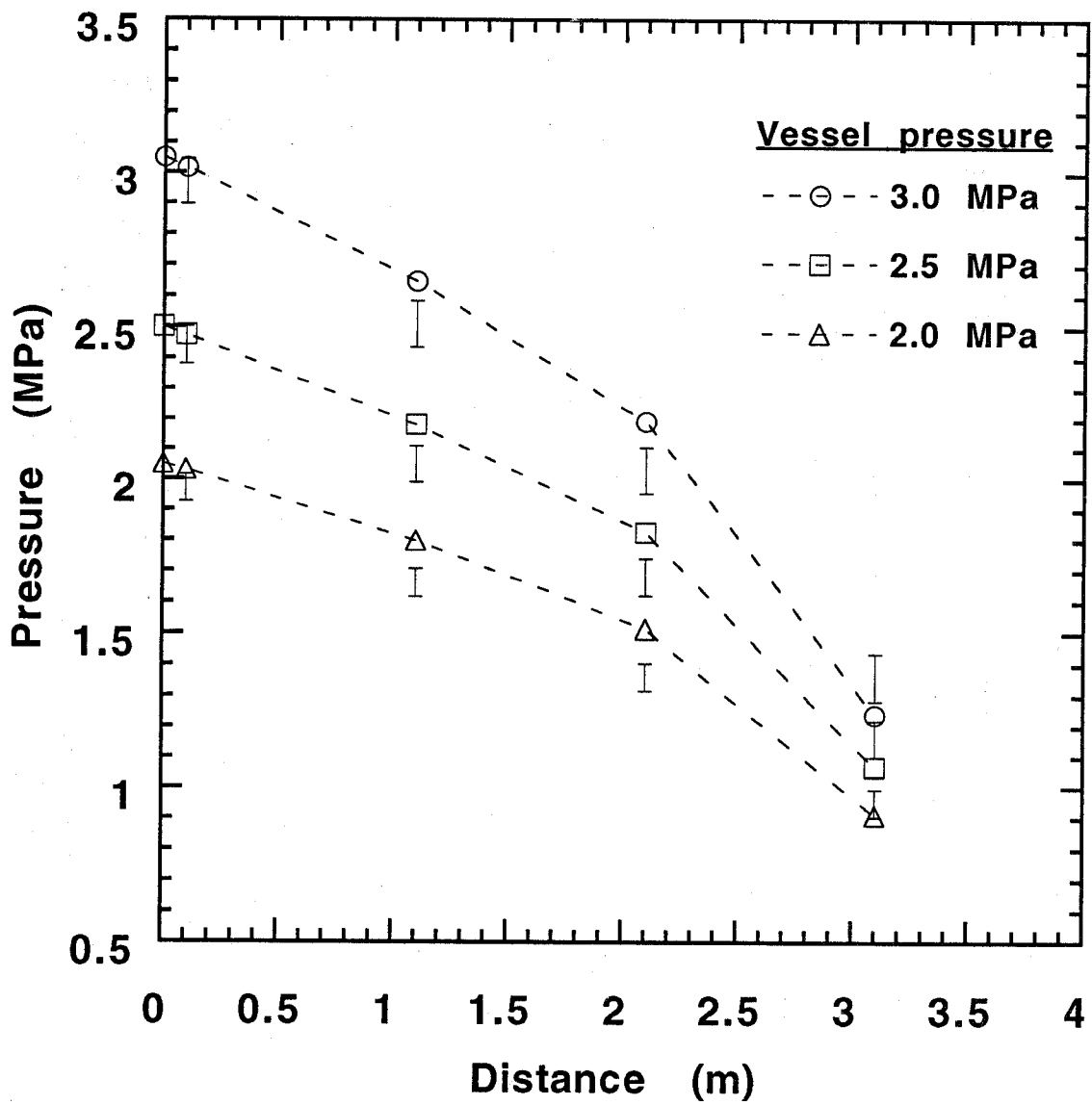


Figure 128. Pipe pressures for constant-head tests: HFC-227ea and 3.1 m effective length of 9.5 mm I.D. piping. Symbols: calculations, and vertical lines with error bars: mean experimental pressures $\pm 2\sigma$ uncertainty.

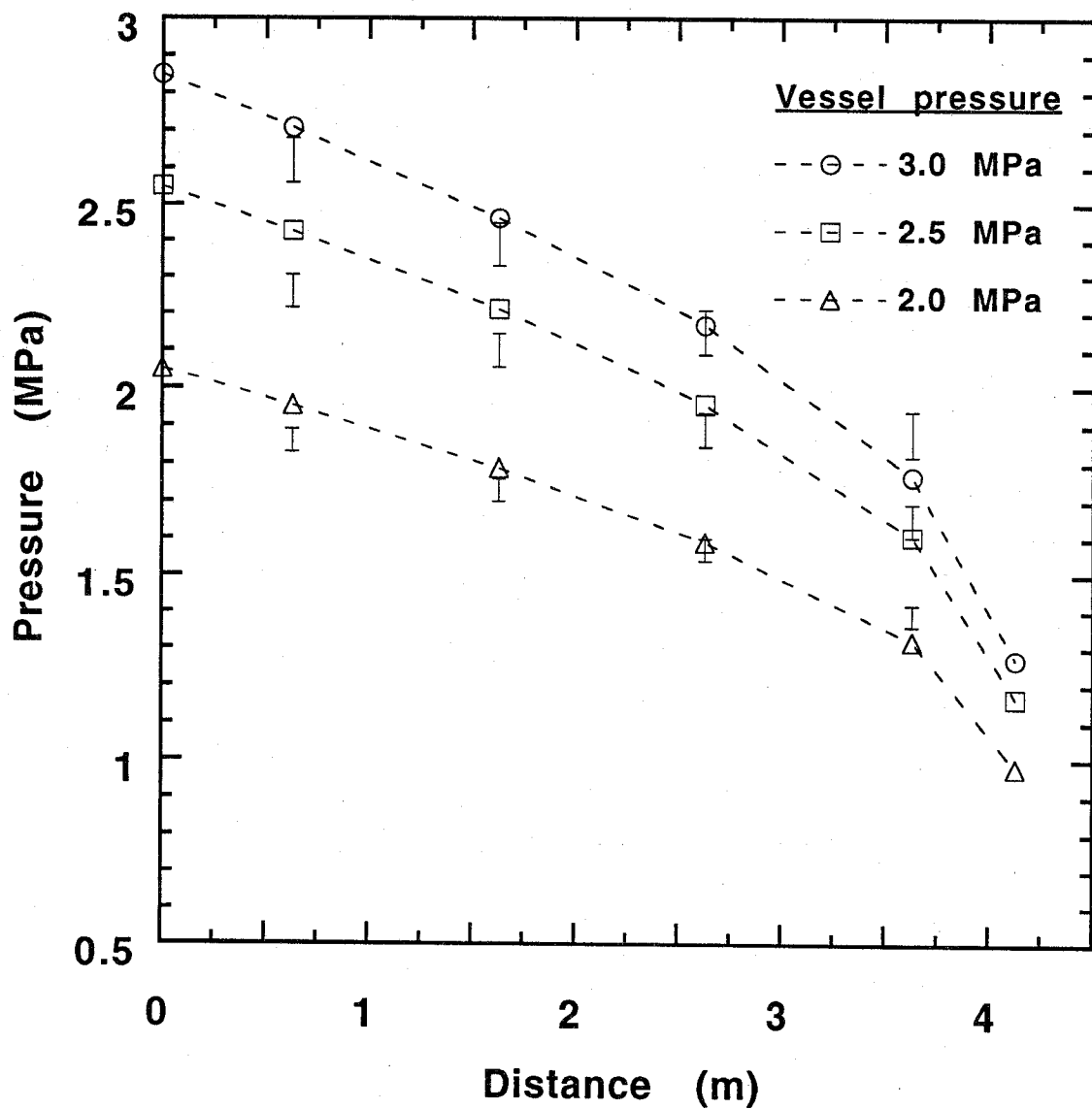


Figure 129. Pipe pressures for constant-head tests: HFC-227ea and 4.13 m effective length of 15.9 mm I.D. piping. Symbols: calculations, and vertical lines with error bars: mean experimental pressures $\pm 2\sigma$ uncertainty.

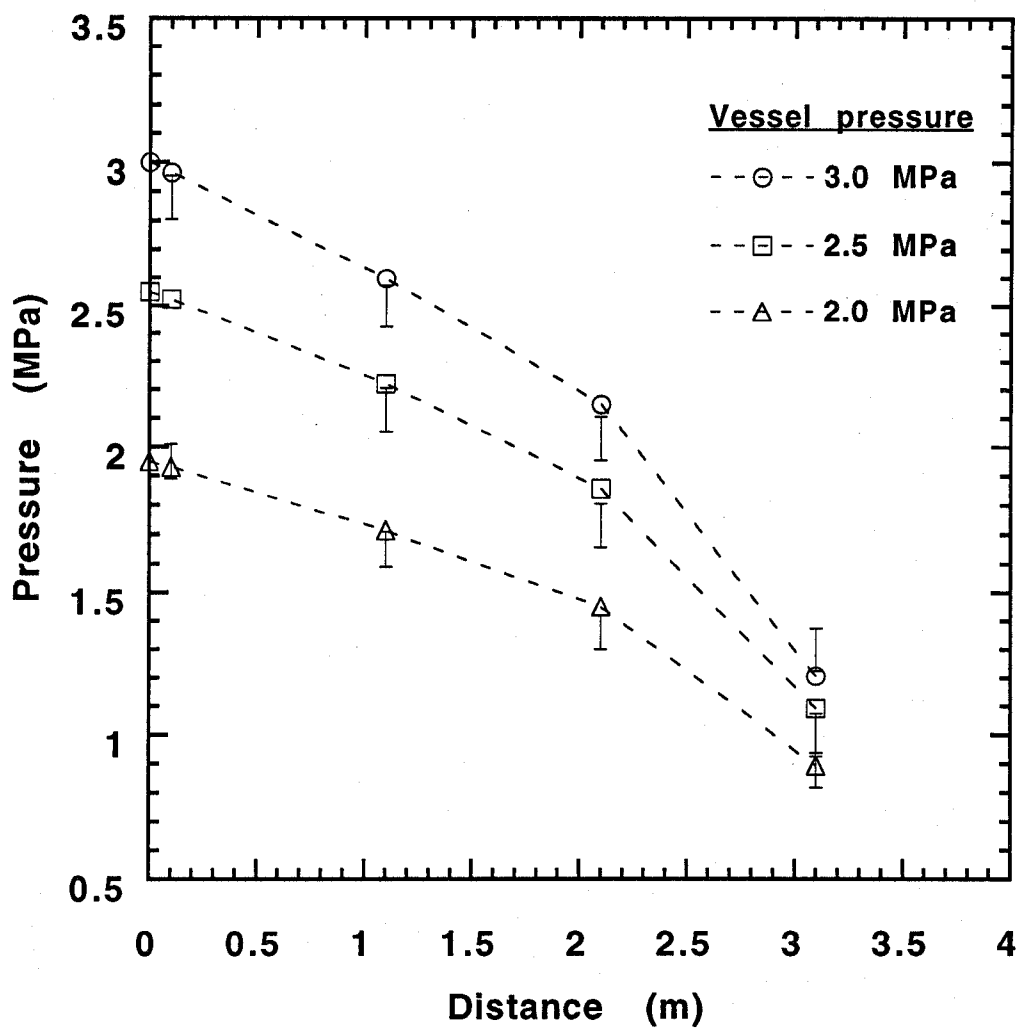


Figure 130. Pipe pressures for constant-head tests: CF_3I and 3.1 m effective length of 9.5 mm I.D. piping. Symbols: calculations, and vertical lines with error bars: mean experimental pressures $\pm 2\sigma$ uncertainty.

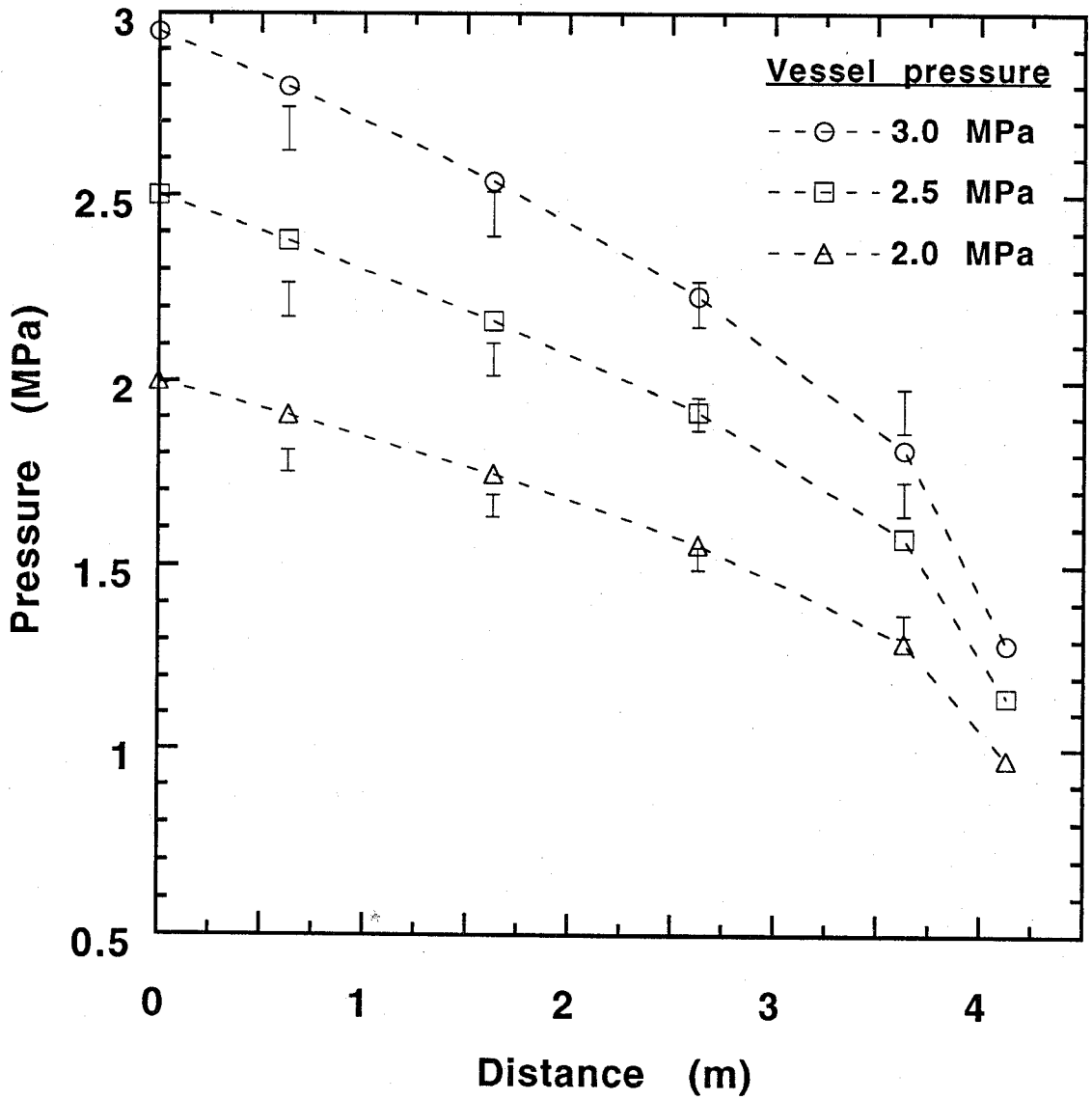


Figure 131. Pipe pressures for constant-head tests: CF_3I and 4.13 m effective length of 15.9 mm I.D. piping. Symbols: calculations, and vertical lines with error bars: mean experimental pressures $\pm 2\sigma$ uncertainty.

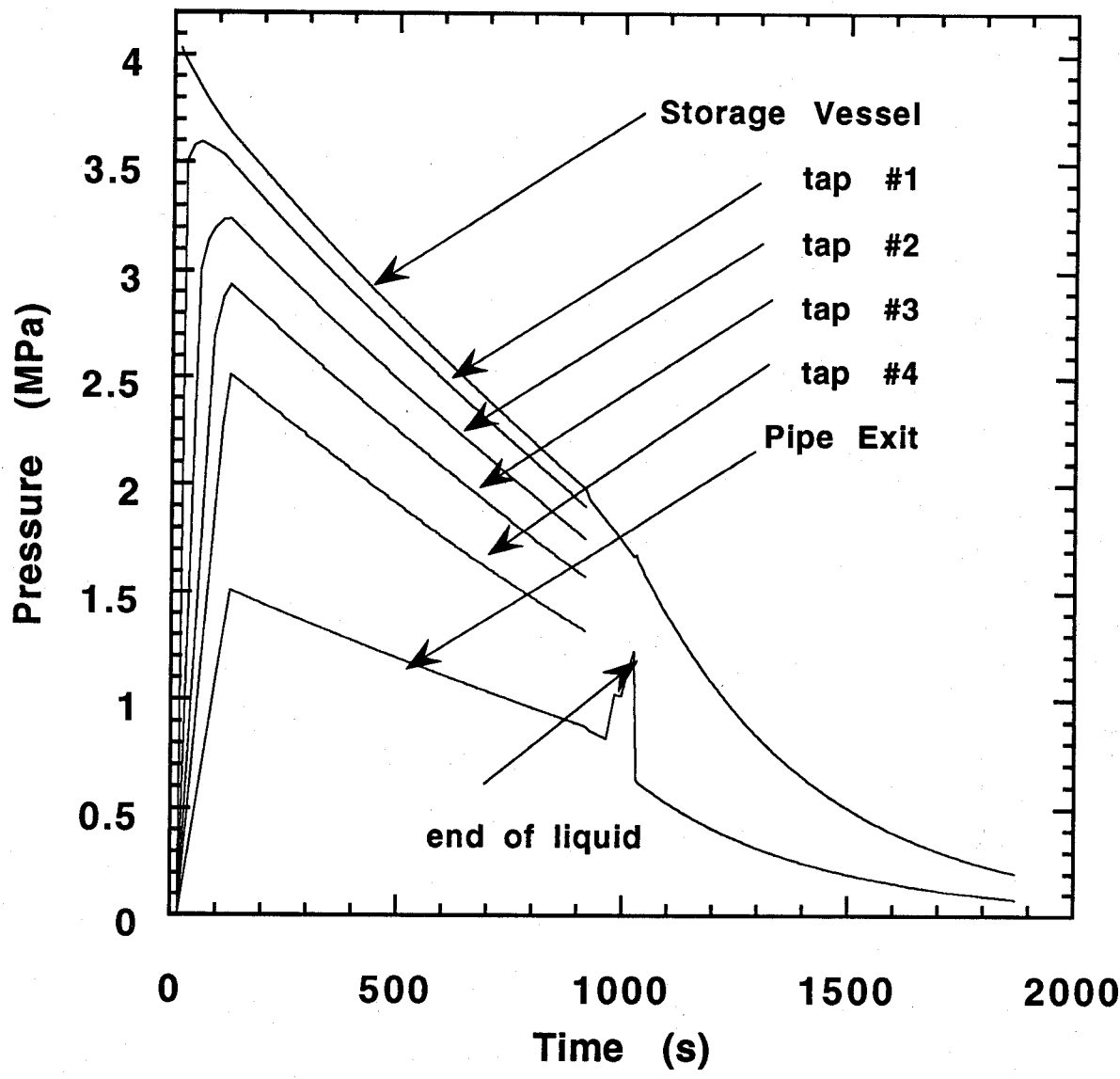


Figure 132. Simulated pressure traces for transient halon 1301 discharge: 1/2 liquid fill volume, pressurized to 4.12 MPa, and 3.5 m of 15.9 mm I.D. piping. Vessel liquid contents are assumed to be in equilibrium at all times.

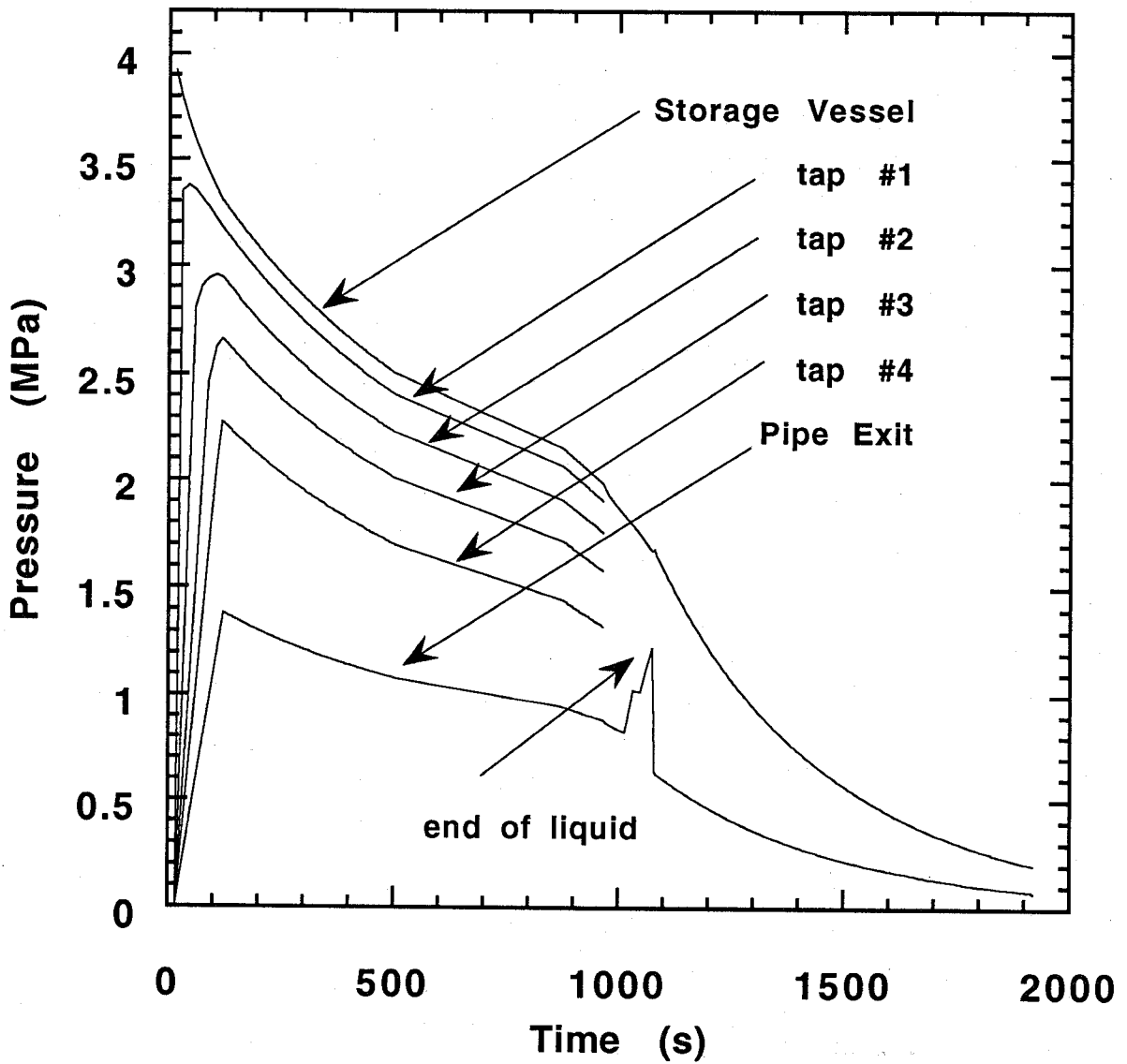


Figure 133. Simulated pressure traces for transient halon 1301 discharge: 1/2 liquid fill volume, pressurized to 4.12 MPa, and 3.5 m of 15.9 mm I.D. piping. Vessel liquid contents are in a frozen, non-equilibrium state until degassing occurs.

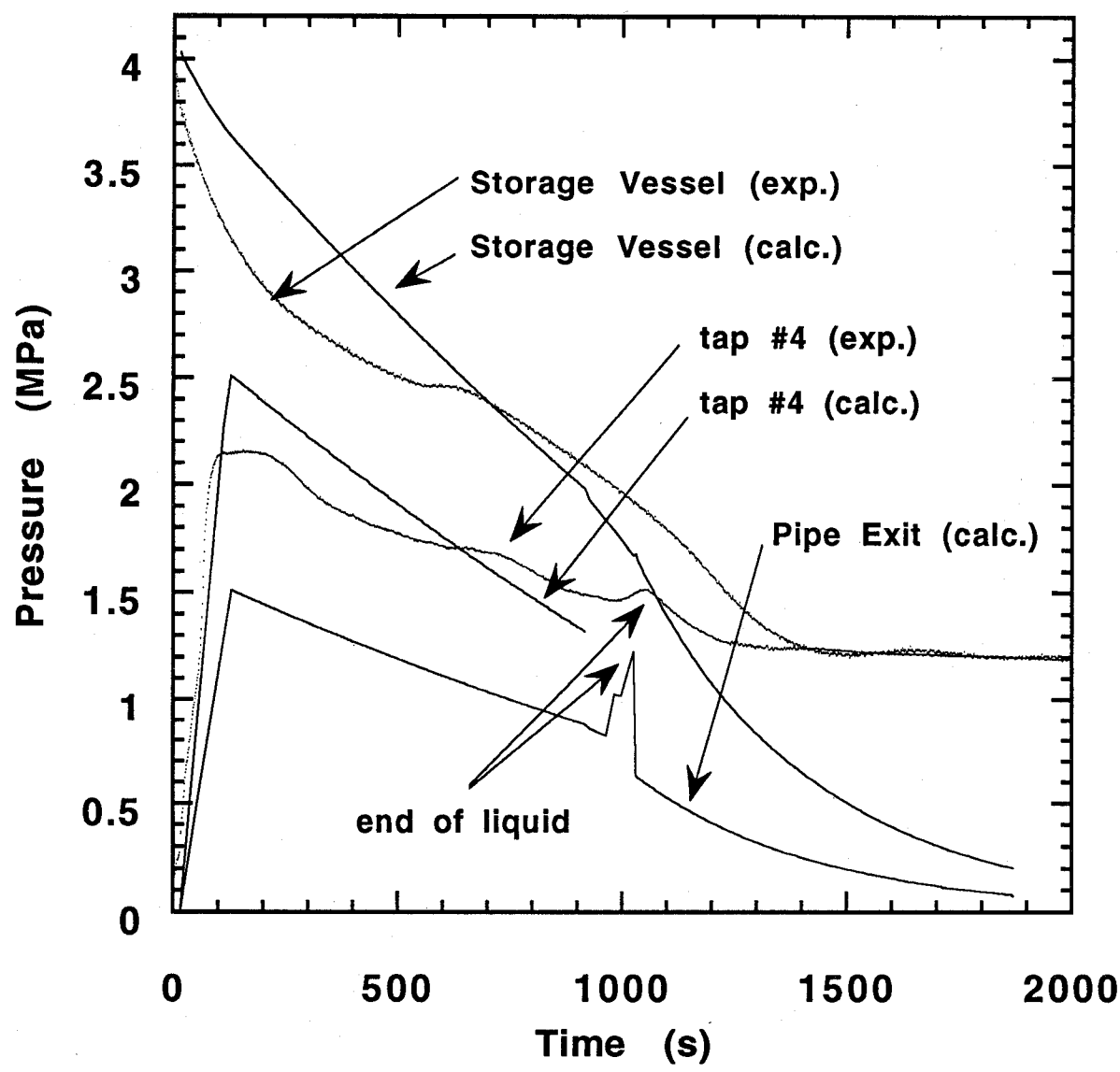


Figure 134. Selected simulated pressure traces from Figure 132 compared to the experimental data presented in Figure B-19.

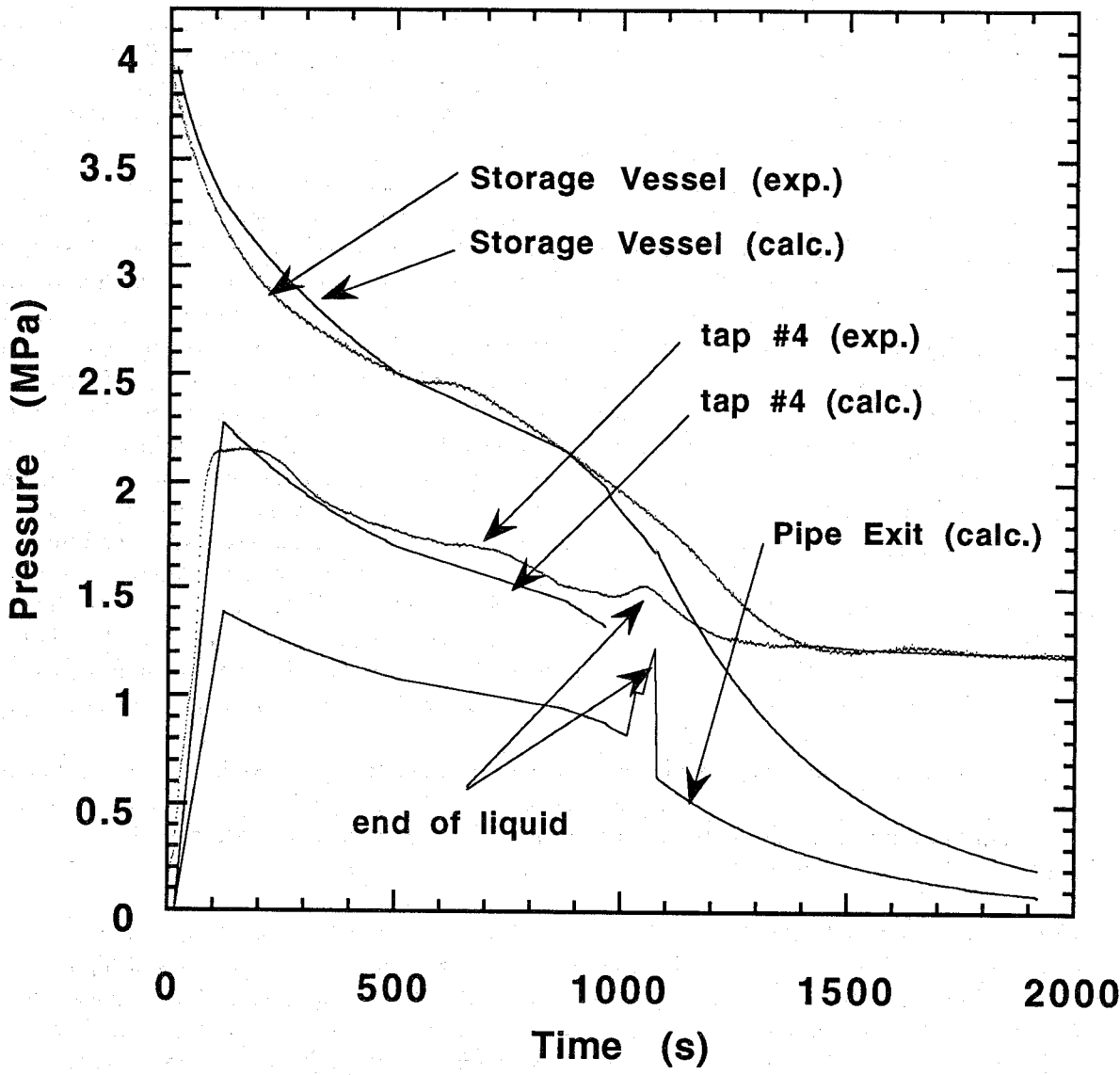


Figure 135. Selected simulated pressure traces from Figure 133 compared to the experimental data presented in Figure B-19.

non-equilibrium bottle condition calculations yield vessel and pipe pressure results that compare more favorably to experiments than do the equilibrium bottle condition calculations.

The model describes flow conditions which may be of interest. Figure 136 is a plot of the mean density of the fluid at the pipe exit (or at the liquid two-phase front before the pipe is filled). Figure 137 is the mass flow rate. Figure 138 is the exit velocity for the two-phase mixture. Figure 139 is the exit temperature of the two-phase mixture. Figure 140 is the exit quality of the two-phase mixture. Figure 141 is the mass fraction discharged from the pipe.

The results for the calculated and the experimental liquid discharge times are presented in Tables 36-38. Figures 142-145 show the experimental liquid discharge times versus the calculated discharge times. In these figures, the dashed lines represent $\pm 10\%$ deviation from the experimental discharge times, and the error bars indicate 2σ uncertainty in the experimental values. The liquid flow time calculations based on equilibrium bottle conditions tend to be shorter than the calculations based on a fixed degassing pressure or no bottle degassing. For HFC-227ea and CF_3I , there appears to be a systematic trend for the cases with the small diameter piping. For most cases, the calculated liquid discharge time is less than 90 % of the experimental discharge time. These deviations may be due to the recovery tanks pressure build-up during those tests which decreases the flow rate below the choked condition for a period of time. Another systematic trend appears to be an overprediction in the liquid discharge time for the 2/3 fill, small piping cases. One possible explanation may be that significant heat transfer to the ullage contents may raise the pressure above the isentropic expansion condition. Since the ullage can expand by a factor of 3 before the liquid runs out, the adiabatic temperature of the ullage will be lower than the 1/2 fill case, which favors heat transfer from the vessel walls. The two-phase flow time is the longest for these tests which also favors heat transfer. The cold temperature discharge simulation of halon 1301 significantly underpredicts the liquid discharge time, which suggests that heat transfer from the pipe walls may be increasing the fluid expansion which slows the flow down.

There is no obvious reason why the model cannot be extended to higher bottle pressure and larger pipe diameter predictions. Testing at higher bottle pressures and larger pipe diameters would confirm the model's ability to predict liquid discharge times under those conditions and add confidence to extending the predictive capabilities.

8.6.9 Hardware Design Scheme. Since the model predicts the experimental discharge times within $\pm 10\%$, it is assumed that the model can be used to calculate the liquid discharge times at higher pressures and larger pipe diameters, though it should be validated for those cases. A design exercise for hardware and fill specifications for each of the three alternative agents is detailed below. The exercise illustrates the model's potential usefulness in selecting hardware for a replacement agent.

Assume that a given halon fire suppression system is designed to protect an engine nacelle and meets the following specifications: 3.37 kg of halon 1301 superpressurized with nitrogen to 4.12 MPa at 23 °C in a 0.0042 m³ bottle, and 4 m of 0.016 m diameter piping from the bottle to the injection port. The calculated liquid discharge time is 1.0 s which meets the duration of discharge criterion in MIL-E-22285 section 3.9 which states "The period of time required to discharge the calculated amount of agent shall be one second or less, measured from the time the agent starts to leave the tubing ends until the required amount of agent has been discharged." The "calculated amount" means the mass stored in the liquid phase which is 90 % of the total agent mass in this case; the discharge time of the agent vapor in the ullage would take another second for this configuration. For a given alternative agent, the mass of agent, bottle size, storage pressure, fill condition, and pipe diameter that fulfills the discharge requirement of a one second liquid discharge time needs to be determined.

Realizing that a number of conditions may meet the discharge requirement, an "optimized" system requires knowledge of the economics of specific configurations and the space limitations for a given

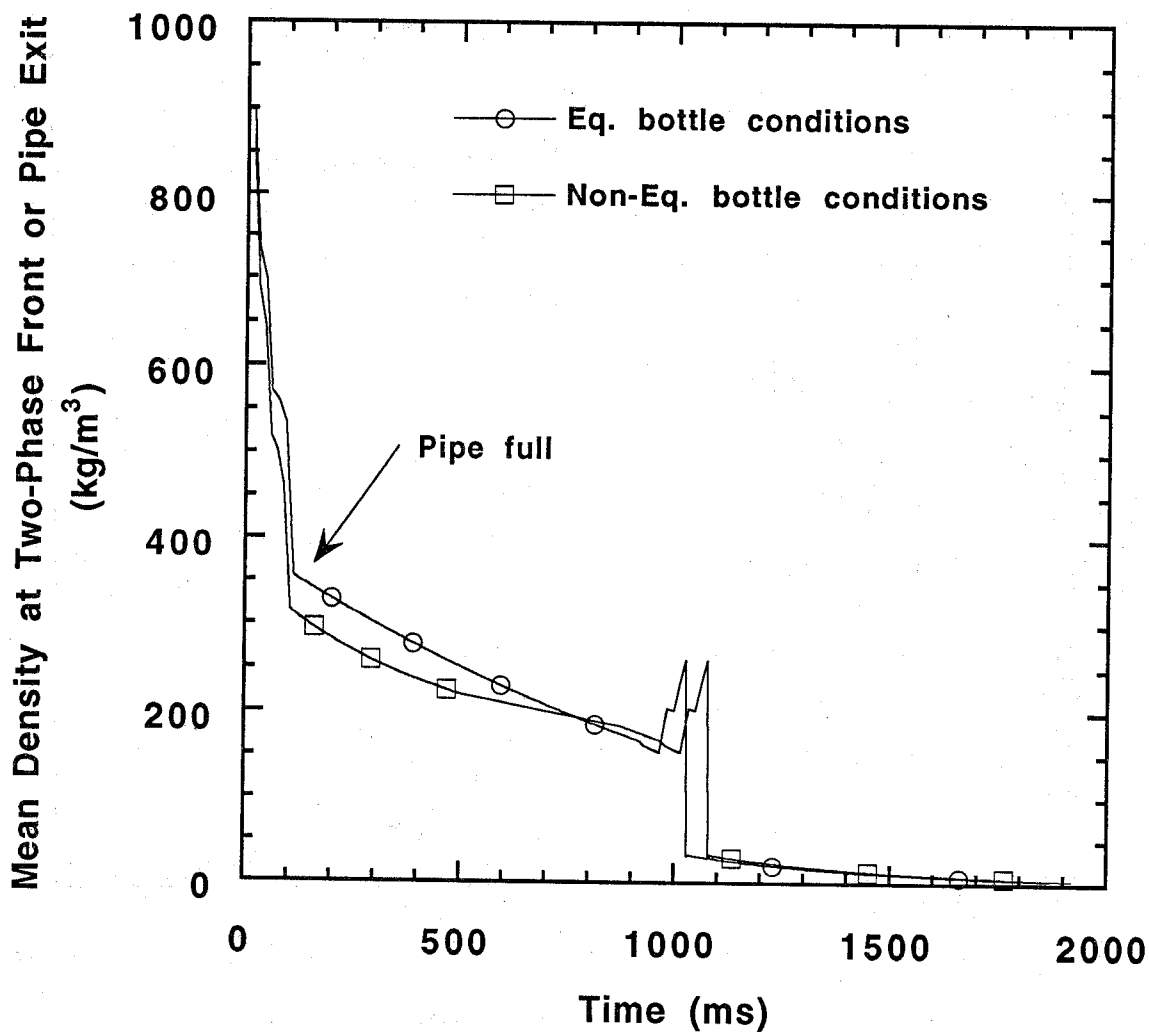


Figure 136. Calculated mean density of the two-phase fluid at the pipe exit (or at the two-phase front if it has not reached the pipe exit): halon 1301, 1/2 liquid fill volume, pressurized to 4.12 MPa, and 3.5 m of straight 15.9 mm I.D. piping.

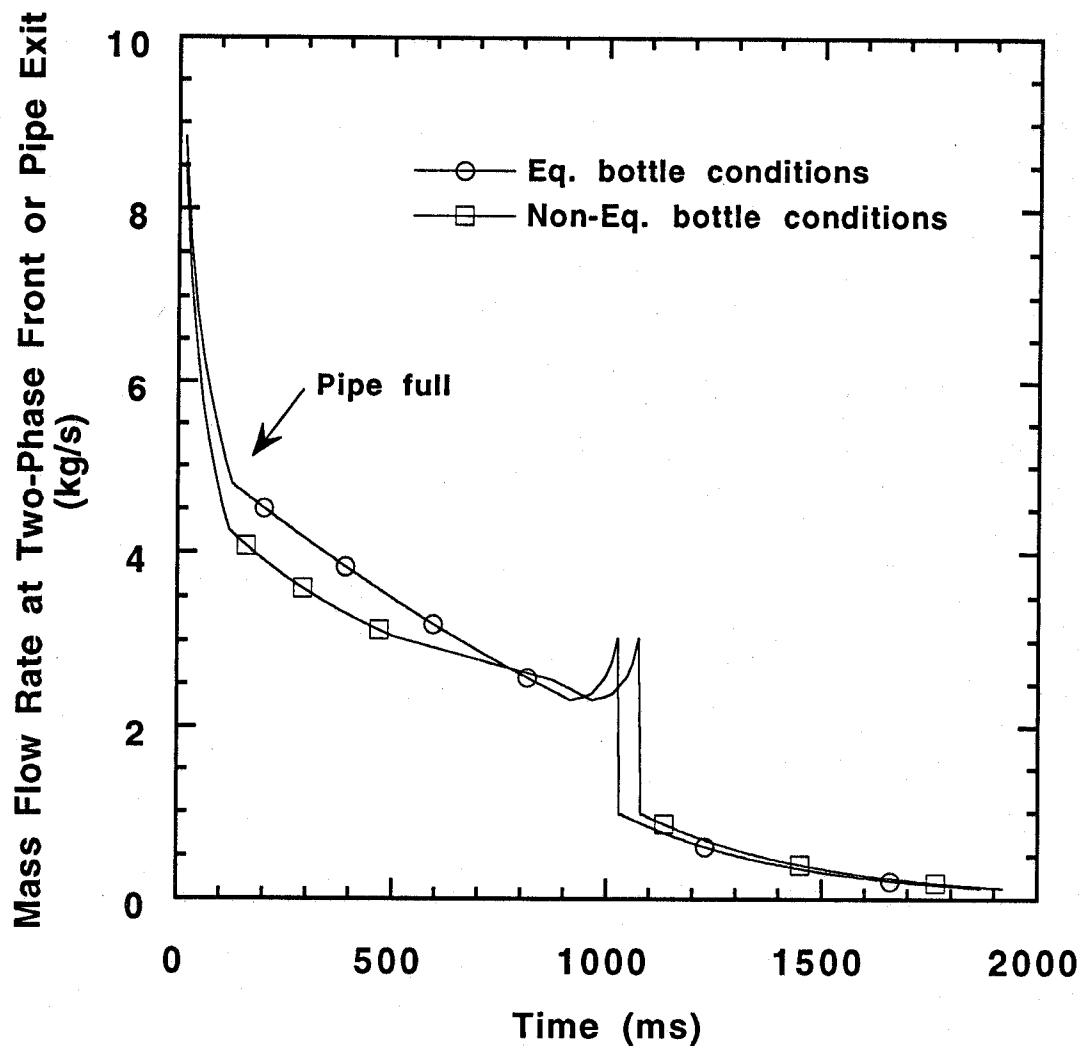


Figure 137. Calculated mass flow rate of the two-phase fluid: halon 1301, 1/2 liquid fill volume, pressurized to 4.12 MPa, and 3.5 m of straight 15.9 mm I.D. piping.

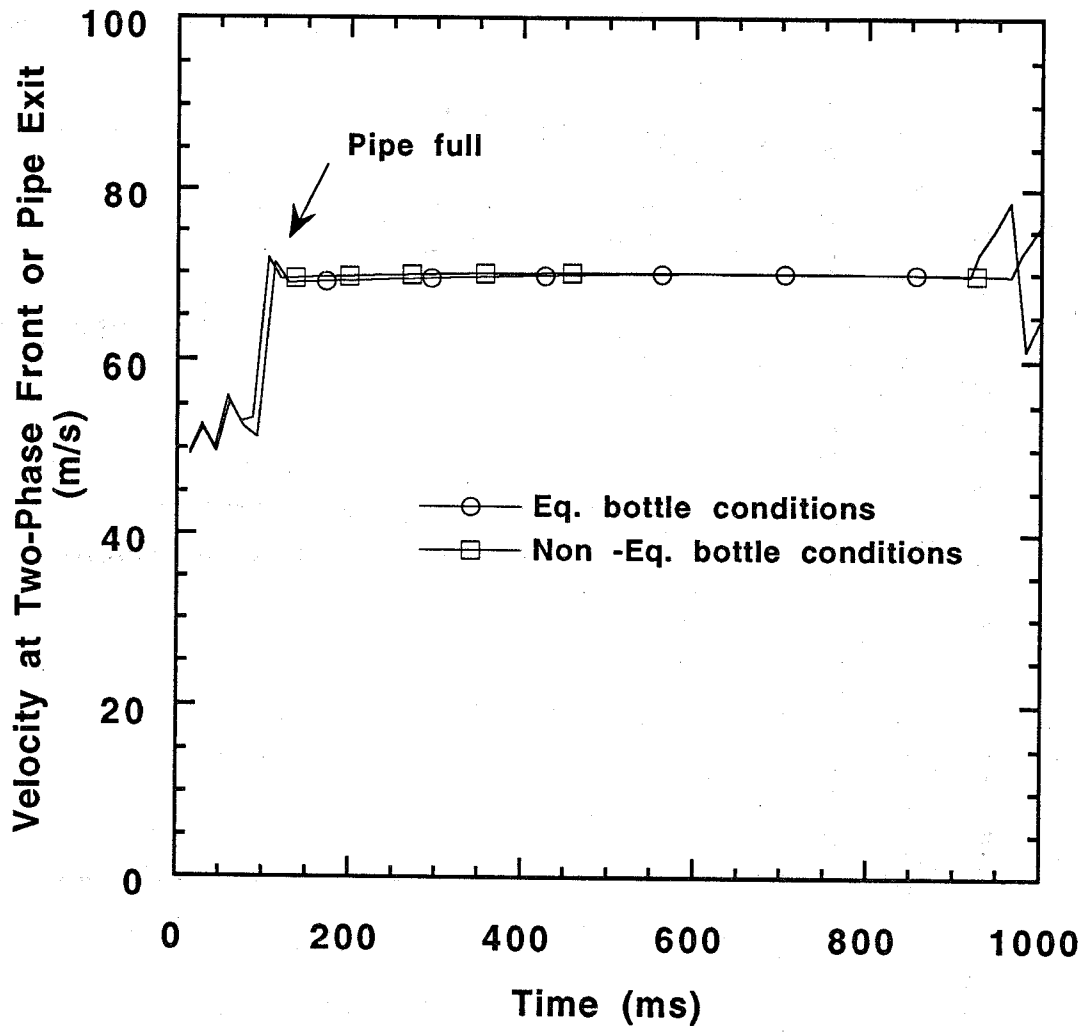


Figure 138. Calculated exit velocity of the two-phase fluid: halon 1301, 1/2 liquid fill volume, pressurized to 4.12 MPa, and 3.5 m of straight 15.9 mm I.D. piping.

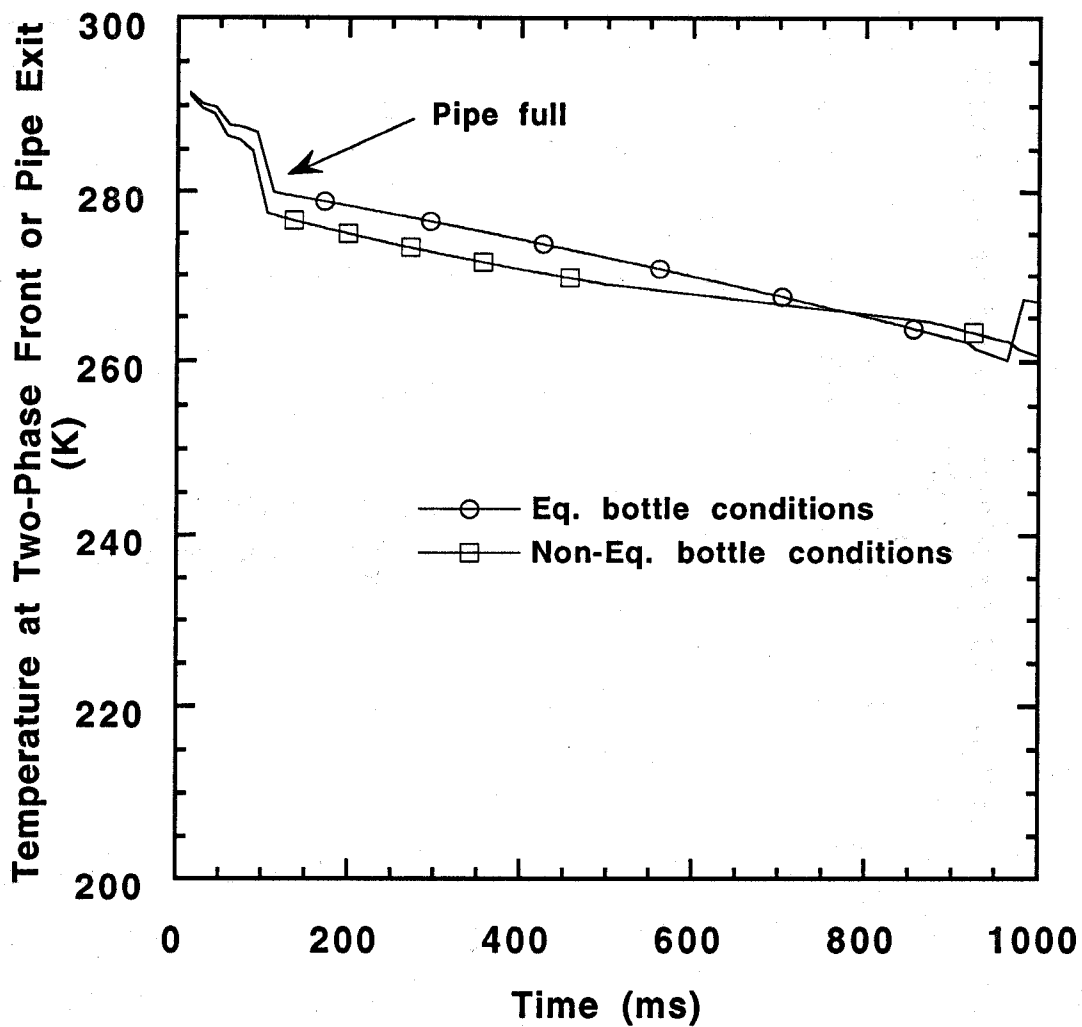


Figure 139. Calculated exit temperature of the two-phase fluid: halon 1301, 1/2 liquid fill volume, pressurized to 4.12 MPa, and 3.5 m of straight 15.9 mm I.D. piping.

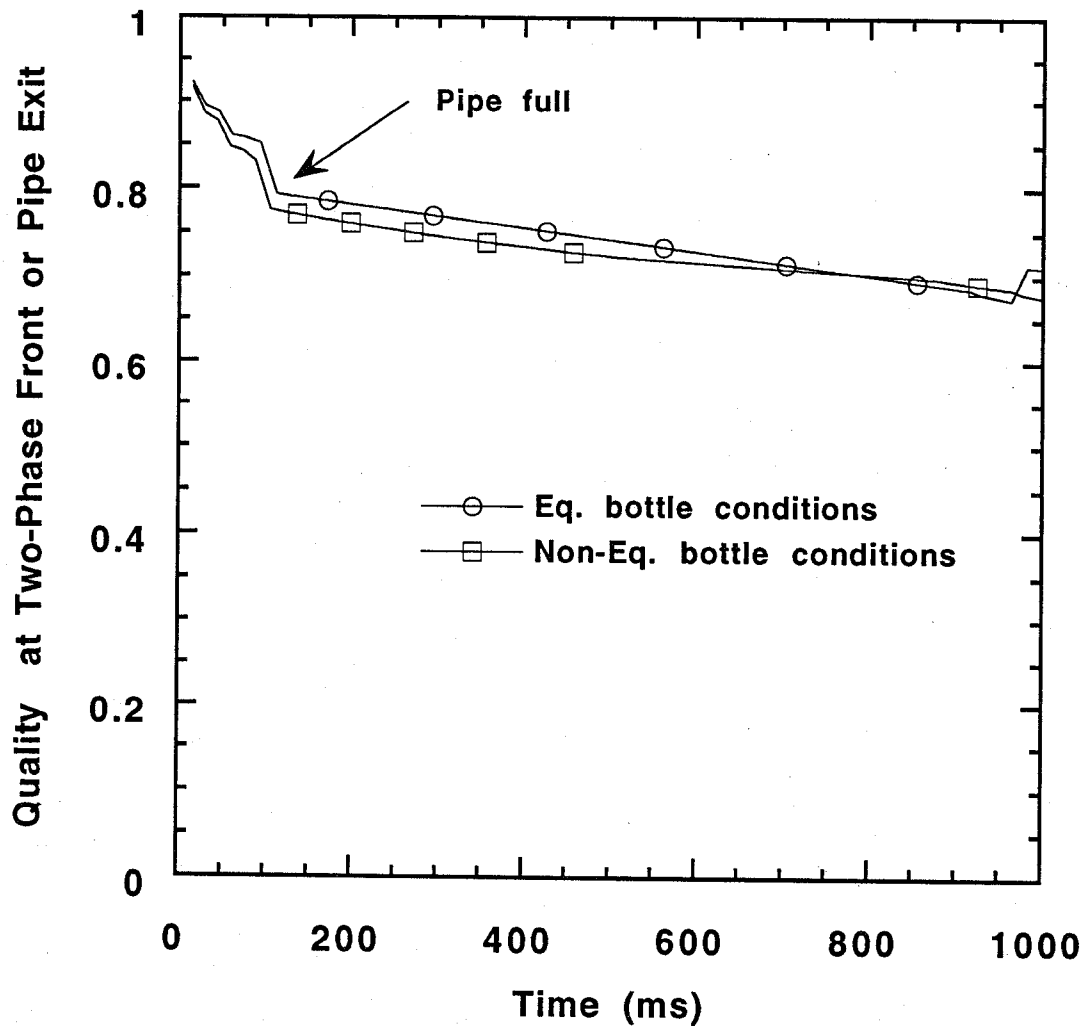


Figure 140. Calculated exit flow quality of the two-phase fluid: halon 1301, 1/2 liquid fill volume, pressurized to 4.12 MPa, and 3.5 m of straight 15.9 mm I.D. piping.

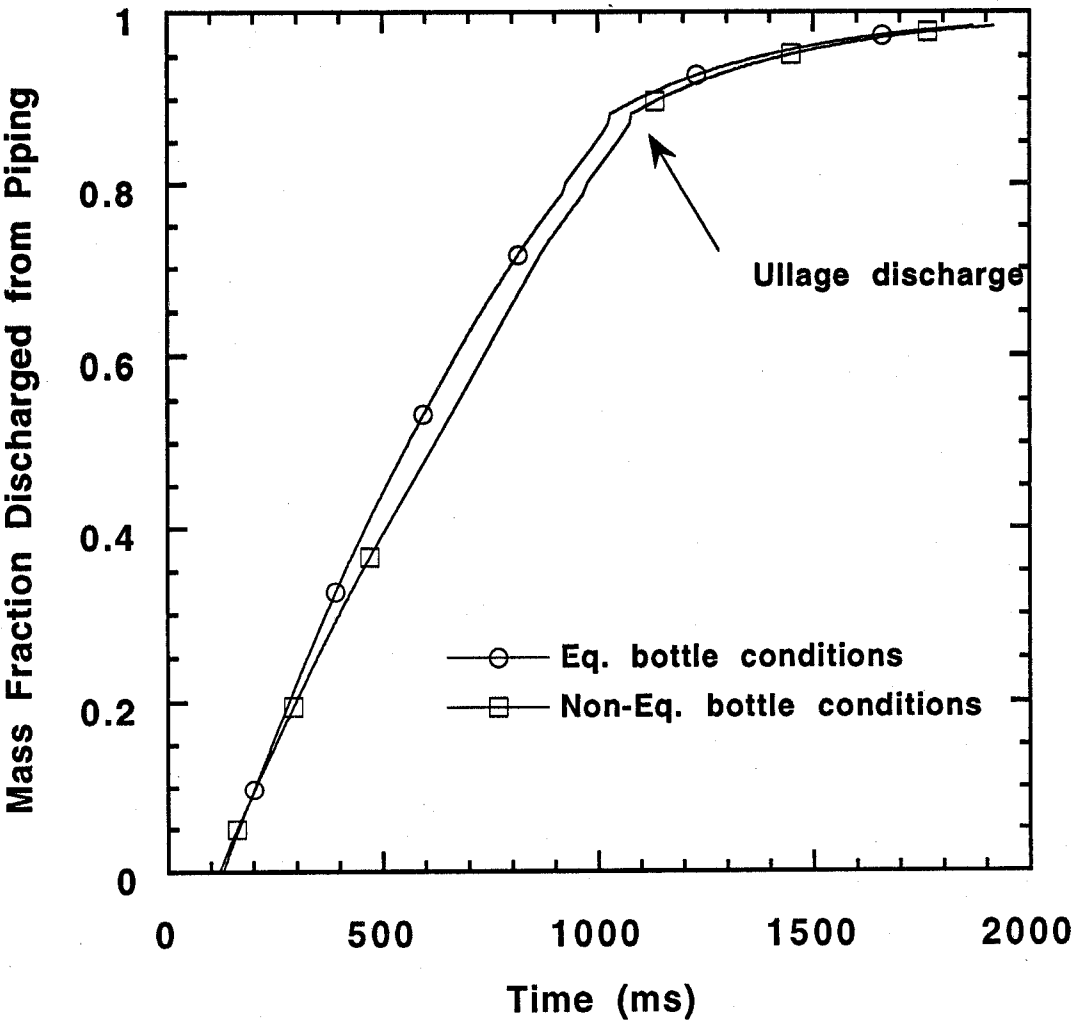


Figure 141. Calculated mass fraction discharged from the vessel: halon 1301, 1/2 liquid fill volume, pressurized to 4.12 MPa, and 3.5 m of straight 15.9 mm I.D. piping.

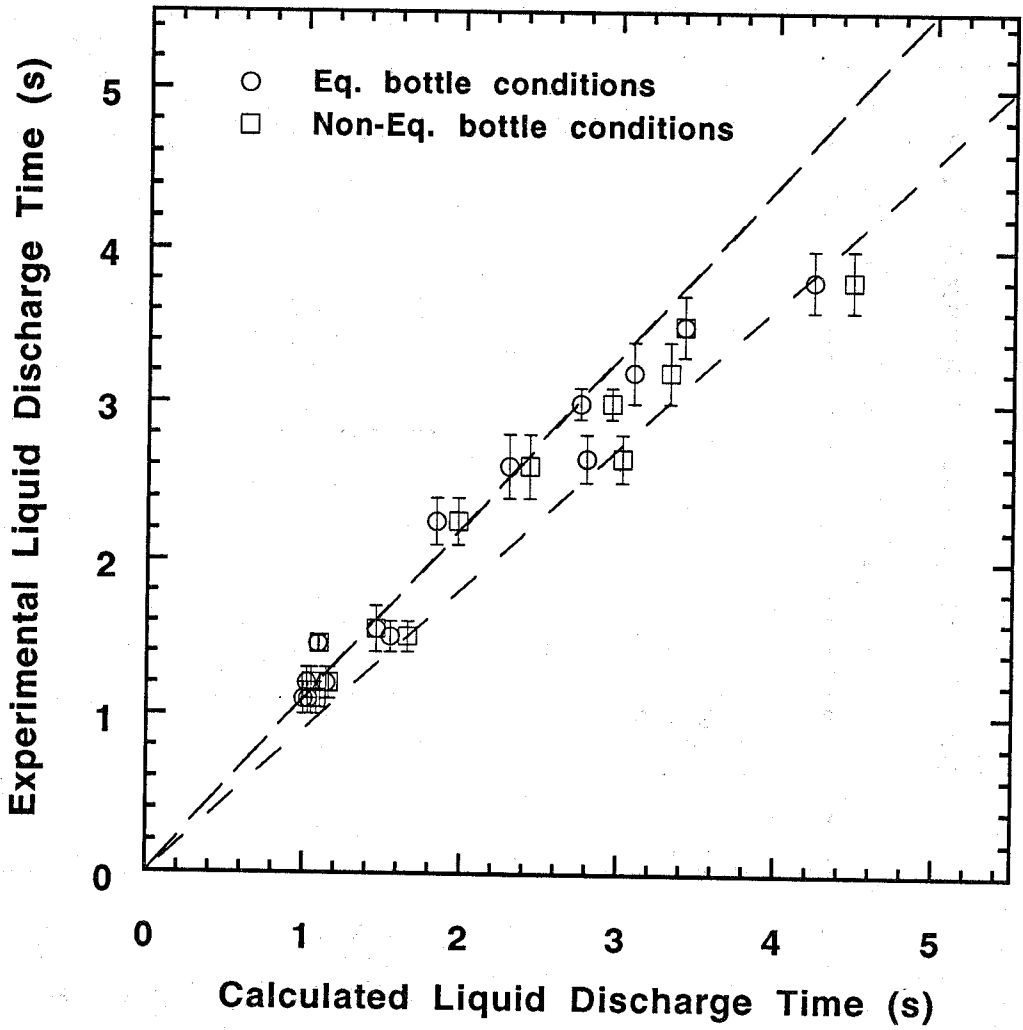


Figure 142. Experimental and calculated liquid discharge times for halon 1301. Calculations assuming equilibrium and non-equilibrium bottle conditions.

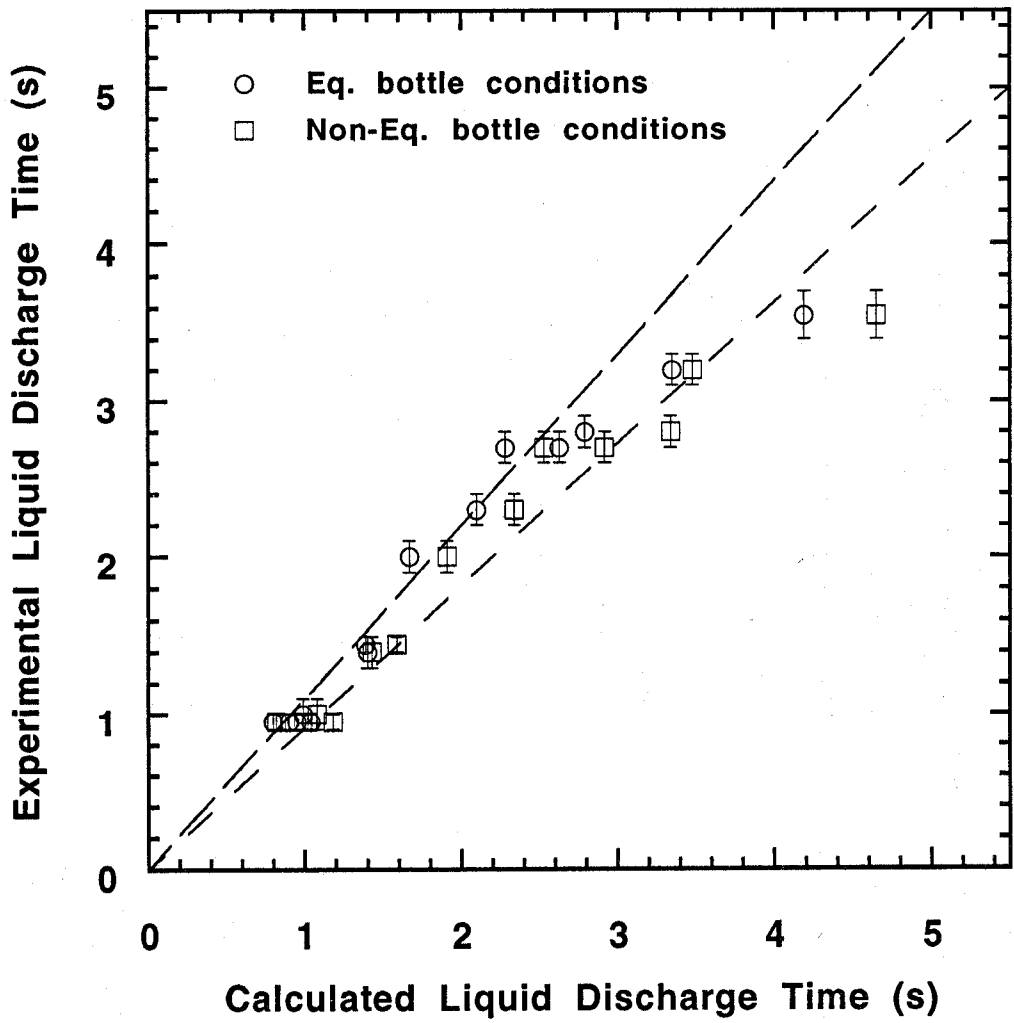


Figure 143. Experimental and calculated liquid discharge times for HFC-125. Calculations assuming equilibrium and non-equilibrium bottle conditions.

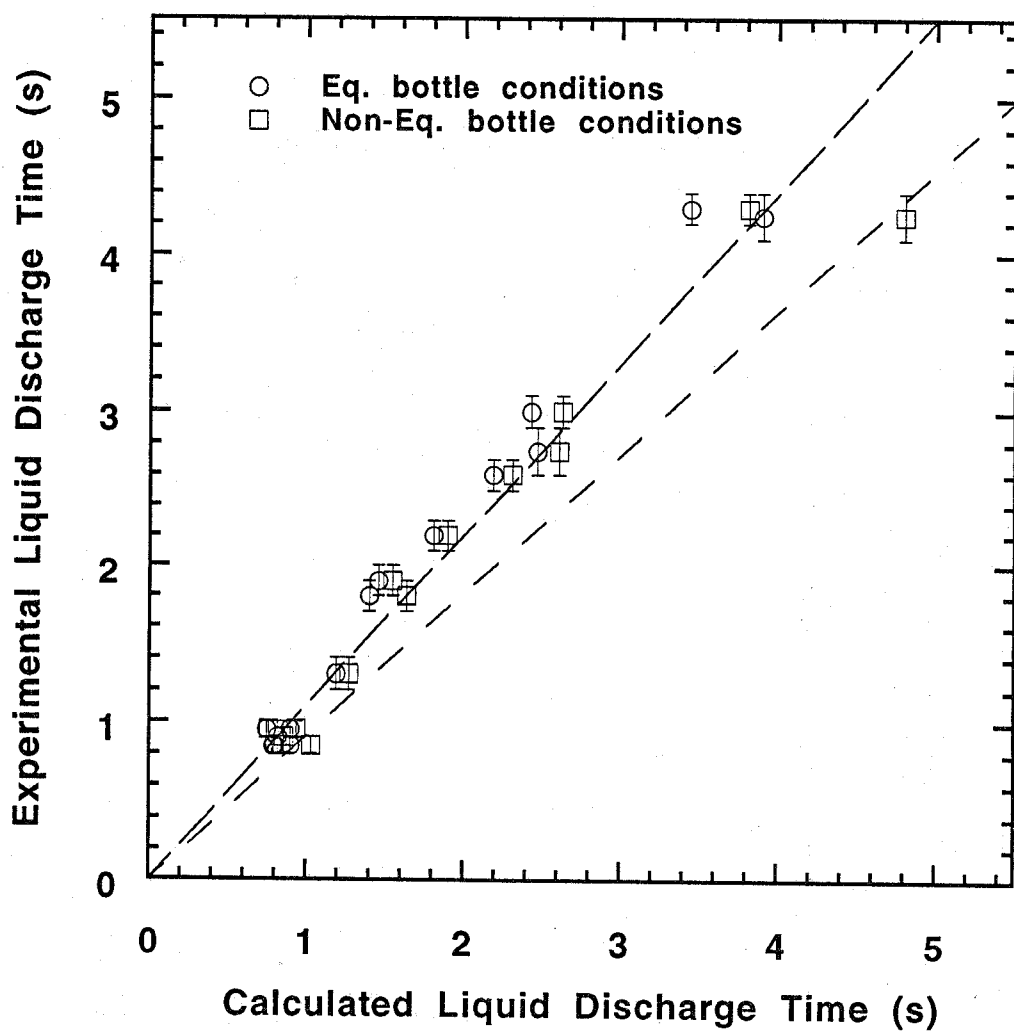


Figure 144. Experimental and calculated liquid discharge times for HFC-227ea. Calculations assuming equilibrium and non-equilibrium bottle conditions.

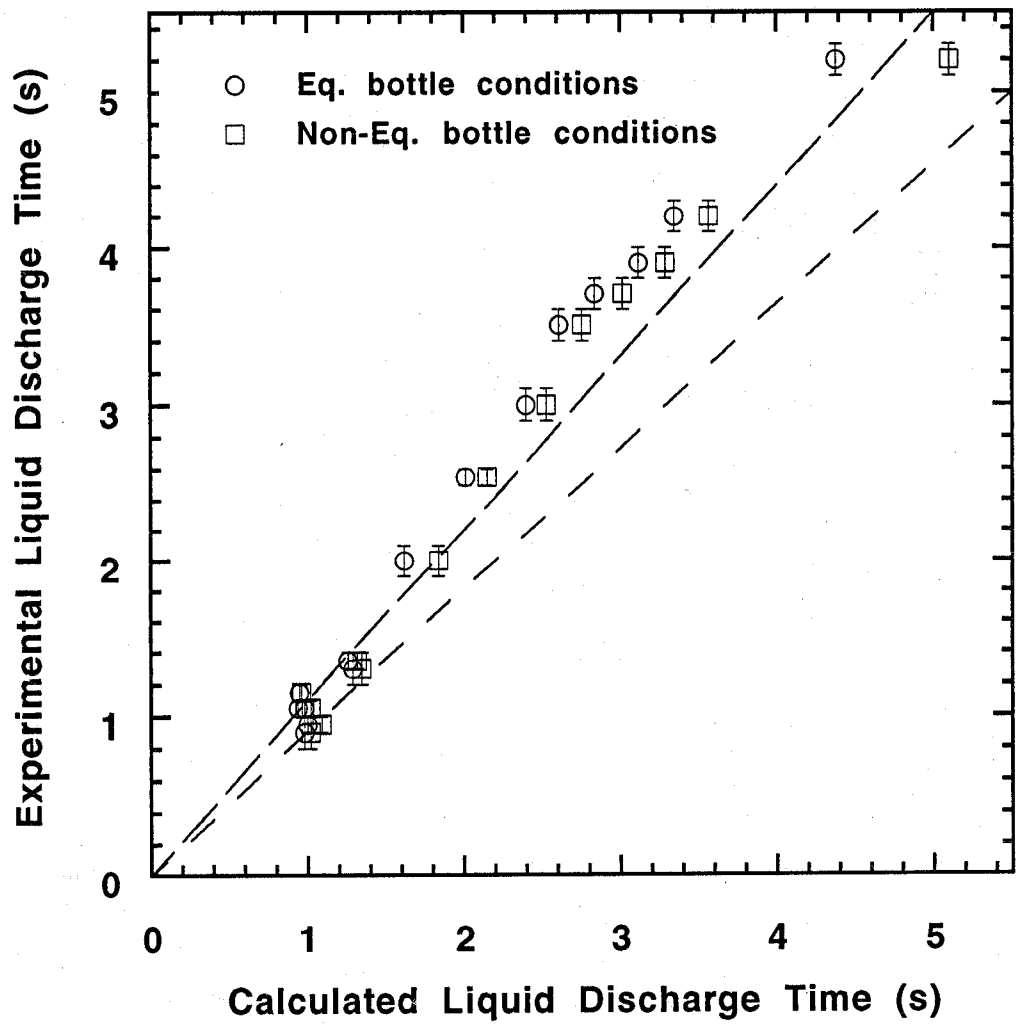


Figure 145. Experimental and calculated liquid discharge times for CF_3I . Calculations assuming equilibrium and non-equilibrium bottle conditions.

Table 41. Agent mass requirements for a retro-fit system

Agent	Mean volume factor	Liquid density at 25 °C (kg/m ³)	Equivalent mass stored in liquid phase (kg)
Halon 1301	1	1538	3.02
HFC-125	3.0	1190	7.02
HFC-227ea	2.5	1395	6.86
CF ₃ I	0.8	2016	3.31

bottle location. Such a design optimization is well beyond the scope of this study, but for the sake of this exercise, the following considerations are probably close to an actual optimal design scheme. First, assume that the preferred case would be if the original bottle size and pressure could be used and that the piping remains the same for an alternative agent. This would represent a "drop-in" replacement for halon 1301. The next best case would be if the only change was an increase in the storage pressure. This implies that the bottle can withstand the elevated pressure. If the discharge time cannot be achieved with the original bottle size, a larger bottle size and increased storage pressure then is checked. Finally, the piping can be replaced with larger diameter piping to achieve the desired discharge time.

The pressure range searched was from 4.12 MPa to 8.24 MPa in increments of 1.37 MPa. Three liquid fill volumes were included; 1/3, 1/2, and 2/3 filled, as were piping diameters of 15.9 mm and 25.4 mm. The calculations assume equilibrium bottle conditions. The specific amount of each alternative agent equivalent in suppression capability to halon 1301 for engine nacelle protection was estimated from the results reported in NIST SP 861 (Grosshandler *et al.*, 1994) on the volume factor. The volume factor (VF) is a measure of the liquid volume of the agent in the storage vessel normalized by the liquid volume of halon 1301 required to suppress a flame under identical conditions. The average value of the volume factors for the opposed flow diffusion burner, cup burner, spray burner, and deflagration tube was used. Table 41 shows the average volume factor and the required amount of agent for equivalent protection. A major assumption here is that this average volume factor prescribes the proper amount of alternative agent for the engine nacelle case. This must be validated by actual engine nacelle testing, or a more appropriate relationship should be used (see Section 9).

From the replacement agent liquid densities and the mass in the liquid phase required, only CF₃I has a chance to fit in the original bottle and therefore is a candidate for "drop-in" replacement. From PROFISSY, 3.5 kg of CF₃I in a 0.0042 m³ liter vessel pressurized to 4.12 MPa will yield 3.34 kg of agent in the liquid phase with a liquid fill volume of 40.1 % at 23 °C. The liquid discharge time through 4 m of 15.9 mm diameter piping is calculated to be 0.71 s. So, CF₃I can be used as a direct replacement of halon 1301. No more calculations with CF₃I were performed.

HFC-125 and HFC-227ea will require a larger bottle size than the 0.0042 m³ halon bottle. Since the search includes 3 liquid fill volumes and 4 pressures, a total of 12 bottle conditions were examined. The exact bottle size is fixed by the liquid fill volume and pressure for each of the agents. If bottle sizes are limited to off-the-shelf items, then a search of bottle size and pressure could be performed. The bottle size and the total agent mass tends to increase as the pressure increases for a fixed liquid fill volume. Tables 42 and 43 give the fill conditions for the various pressures and liquid fill volumes and the calculated liquid discharge times for the simulations with the two pipe diameters.

Table 42. Fill conditions and liquid discharge times for HFC-125

Storage pressure (MPa)	Total mass of agent (kg)	Mass of agent in liquid phase (kg)	Fill volume (%)	Storage vessel volume (m ³)	Liquid discharge time (s)	
					pipe I.D. 15.9 mm	pipe I.D. 25.4 mm
4.12	8.60	7.10	32.5 (1/3)	0.0200	2.00	0.75
4.12	7.80	7.08	49.9 (1/2)	0.0130	2.37	0.90
4.12	7.30	6.95	67.1 (2/3)	0.0095	2.86	1.10
5.49	8.75	6.97	33.0 (1/3)	0.0205	1.66	0.62
5.49	7.85	6.98	50.3 (1/2)	0.0135	1.98	0.74
5.49	7.40	6.98	67.9 (2/3)	0.0100	2.46	0.94
6.87	9.30	7.05	33.3 (1/3)	0.0220	1.52	0.56
6.87	8.20	7.02	48.7 (1/2)	0.0150	1.75	0.66
6.87	7.60	7.04	66.5 (2/3)	0.0110	2.18	0.82
8.24	9.95	7.01	32.9 (1/3)	0.0240	1.40	0.52
8.24	8.50	7.02	49.4 (1/2)	0.0160	1.65	0.61
8.24	7.80	7.06	66.3 (2/3)	0.0120	2.03	0.77

The liquid discharge times are also plotted against bottle pressure for the different fill conditions in Figures 146 and 147. A lower liquid fill volume and higher bottle pressure decrease the liquid discharge time for a given pipe diameter. The rate of decrease in the liquid discharge time slows as the bottle pressure is increased at any one fill condition.

The liquid discharge times for HFC-125 through the 15.9 mm diameter piping are not under one second for any fill condition and pressure, which necessitates an increase in piping diameter. At a piping diameter of 25.4 mm, all liquid discharges are under 1 s except for the highest liquid fill volume and lowest bottle pressure (2/3 fill and 4.12 MPa). For HFC-227ea, the liquid discharge times through the 15.9 mm diameter piping also are not under 1 s, but at the lowest liquid fill volume and highest pressure, (1/3 filled and 8.24 MPa) the discharge time is nearly 1 s, which might warrant a closer look. The penalty for the high pressure and low liquid fill volume is a relatively large bottle volume. Discharge times through the 25.4 mm diameter piping are all below 1 s for HFC-227ea.

The above exercise illustrates the vastly different hardware requirements for HFC-125 and HFC-227ea versus halon 1301 and CF₃I. The results are indicative only of this particular case; other cases require separate study, hence the importance of a general calculation scheme. Once the particular alternative agent is selected and the design agent mass specified (using the volume factor approach, or other suitable approach), this design scheme can be repeated for any number of retro-fits or new systems.

8.6.10 Conclusions and Recommendations. The experimental study and modeling effort of the transient discharge of agent through piping presented here should assist in the design of engine nacelle

Table 43. Fill conditions and liquid discharge times for HFC-227ea

Storage pressure (MPa)	Total mass of agent (kg)	Mass of agent in liquid phase (kg)	Fill volume (%)	Storage vessel volume (m ³)	Liquid discharge time (s)	
					pipe I.D. 15.9 mm	pipe I.D. 25.4 mm
4.12	7.40	6.88	33.9 (1/3)	0.0150	1.46	0.56
4.12	7.15	6.88	50.0 (1/2)	0.0105	1.73	0.67
4.12	7.00	6.86	66.3 (2/3)	0.0079	2.13	0.84
5.49	7.50	6.87	33.6 (1/3)	0.0160	1.27	0.48
5.49	7.25	6.92	49.2 (1/2)	0.0110	1.48	0.57
5.49	7.05	6.89	66.6 (2/3)	0.0081	1.84	0.72
6.87	7.70	6.90	32.7 (1/3)	0.0170	1.14	0.43
6.87	7.30	6.90	49.7 (1/2)	0.0112	1.33	0.51
6.87	7.10	6.91	67.0 (2/3)	0.0083	1.66	0.65
8.24	7.85	6.88	32.9 (1/3)	0.0175	1.07	0.40
8.24	7.35	6.88	50.0 (1/2)	0.0115	1.25	0.48
8.24	7.10	6.87	67.6 (2/3)	0.0085	1.55	0.60

fire protection hardware systems which specify a replacement candidate. The observed flow characteristics for all of the replacement candidates are similar to halon 1301. Non-linear pressure drop versus pipe length increment indicates the high compressibility of the flows, while high speed movies of transparent piping sections validate the two-phase nature of the flow after it leaves the storage bottle. Discharge times for the initially liquid phase in the bottle for fixed fill volume, pressure, and piping condition did not vary widely for the three alternative agents and halon 1301. The amount of mass discharged did vary from agent to agent due mostly to the density differences. Liquid flow times from the small pipe diameters were approximately a factor of 2.5 greater than those for the large pipe diameter. There was significant scatter in the observed bottle pressure where the pressure recovery occurred (the lowest bottle pressure achieved before it began to rise) for any given agent. In most cases, model calculations of the steady-state mass flow rates and transient discharge times are within $\pm 10\%$ of the experimental values, suggesting that the model can be used as a design tool for hardware selection of an alternative agent fire suppression system. A hardware design scheme for retro-fitting a halon 1301 system illustrated the model's utility.

Some areas of further research for transient discharge would include the behavior of a squib activated discharge, its interaction with nitrogen degassing, and the degassing phenomena in general. Discharges at elevated bottle pressure and larger piping diameters should be performed to validate the model for those conditions. Unbalanced flow networks should be studied if they are important for engine nacelle application.

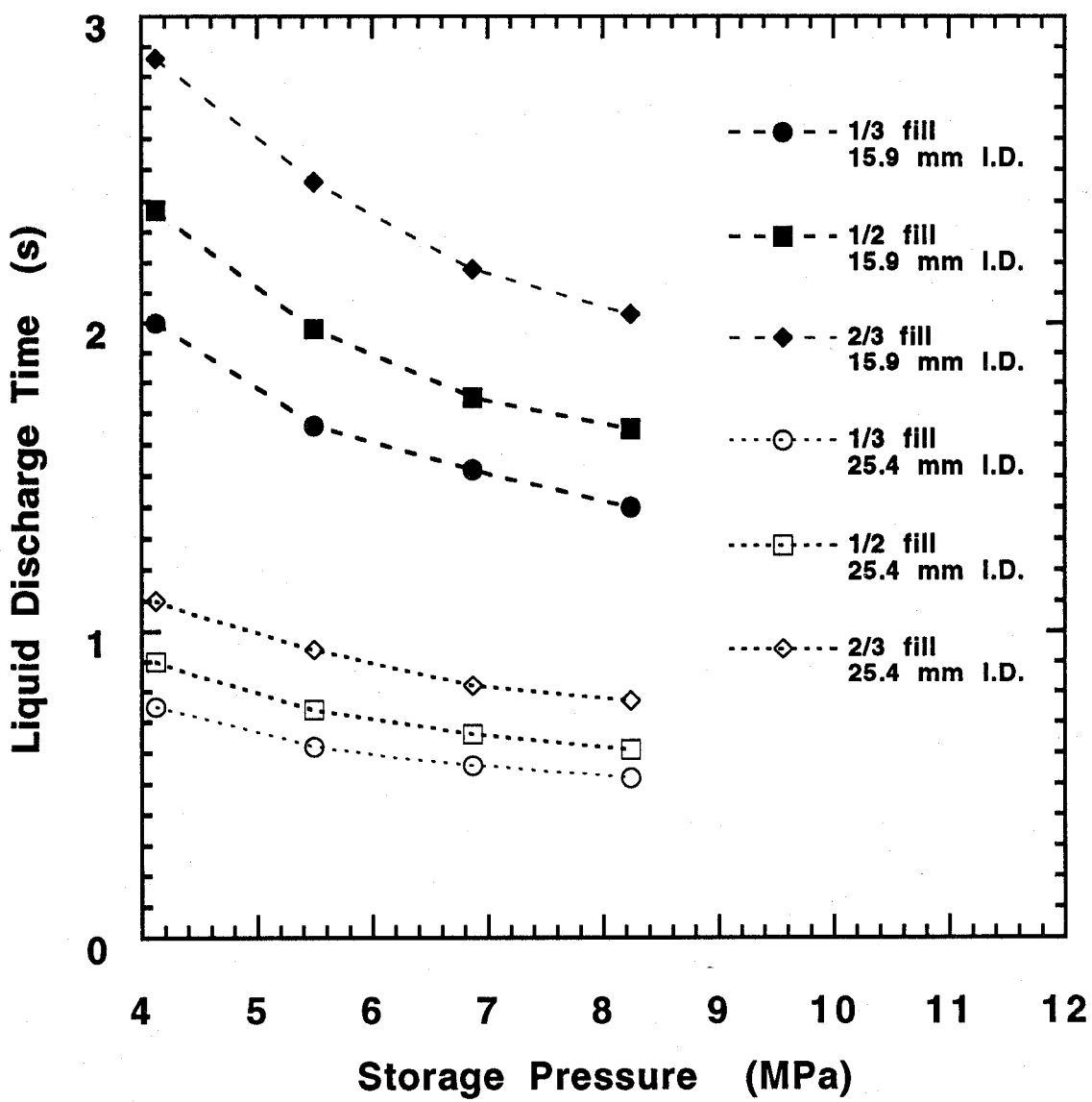


Figure 146. Calculated liquid discharge times for HFC-125 for a various liquid fill volumes and storage pressures. The mass in the liquid-phase was held constant. Calculations assume equilibrium bottle conditions.

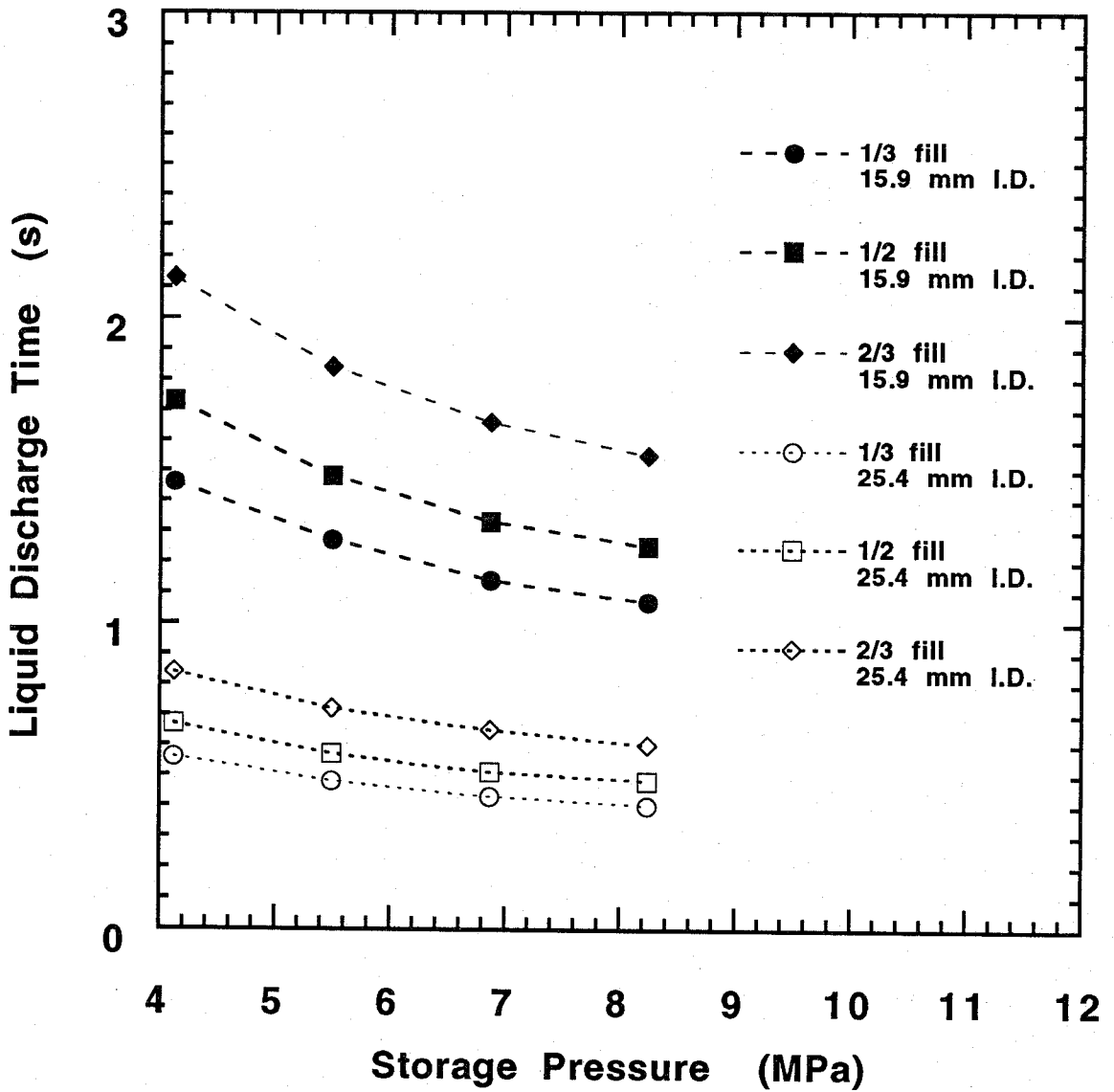


Figure 147. Calculated liquid discharge times for HFC-227ea for a various liquid fill volumes and storage pressures. The mass in the liquid-phase was held constant. Calculations assume equilibrium bottle conditions.

8.7 Concluding Remarks

Several important aspects related to agent storage and its subsequent discharge have been studied in detail. They are summarized in the following.

1. A computer program (PROFISSY) for calculating binary vapor-liquid equilibrium has been developed to aid the bottle designers by providing useful and reliable data on the pressure-temperature characteristics of the selected agent/nitrogen mixtures.
2. The dissolved nitrogen in the liquid agent was found to play a very important role in the discharge whether in a dry bay or in a piping system.
3. In simulated dry bay discharges, CF_3I has the fastest volumetric discharge rate but the slowest dispersion velocities.
4. A discharge model which incorporates nitrogen degassing has also been developed. The model predicts agent discharge times within a factor of four (usually much better) without any *a priori* information other than the initial conditions of the vessel.
5. The exploratory study using complex computer codes (*e.g.*, KIVA-II) has identified the specification of the initial spray condition and the rapid evaporation of the droplets as problem areas. Methods need to be developed further to handle the highly transient flashing process in a computationally efficient manner before the detailed velocity, temperature, and concentration field predictions which have been made can be properly interpreted.
6. A computer model based on a homogeneous two-phase flow has also been developed to facilitate transient pipe-flow calculations for engine nacelle applications. The model has been validated by the experimental results. A design exercise was given to illustrate the usefulness of the model in system hardware selection for a halon alternative.

Figure 148 typifies a generic flow chart for discharge system optimization. To optimize a new discharge system, system operational requirements (*e.g.*, amount of agent required to suppress a fire) and constraints (*e.g.*, vessel growth potential, operating temperature) have to be identified or provided to the system designers. Once these constraints are known, the designers can then proceed to size the bottle using thermodynamic data of the agent (*e.g.*, PROFISSY). After the bottle size and the allowable nitrogen pressurization have been determined, the discharge time of the agent can be estimated by using a discharge model (*e.g.*, the one developed above) for dry bay applications. For engine nacelle fire protection, the pipe-flow model discussed above can be used to size the pipe and to predict agent discharge time. These calculation processes may have to be iterated several times until all the calculated parameters meet the system constraints and operational requirements.

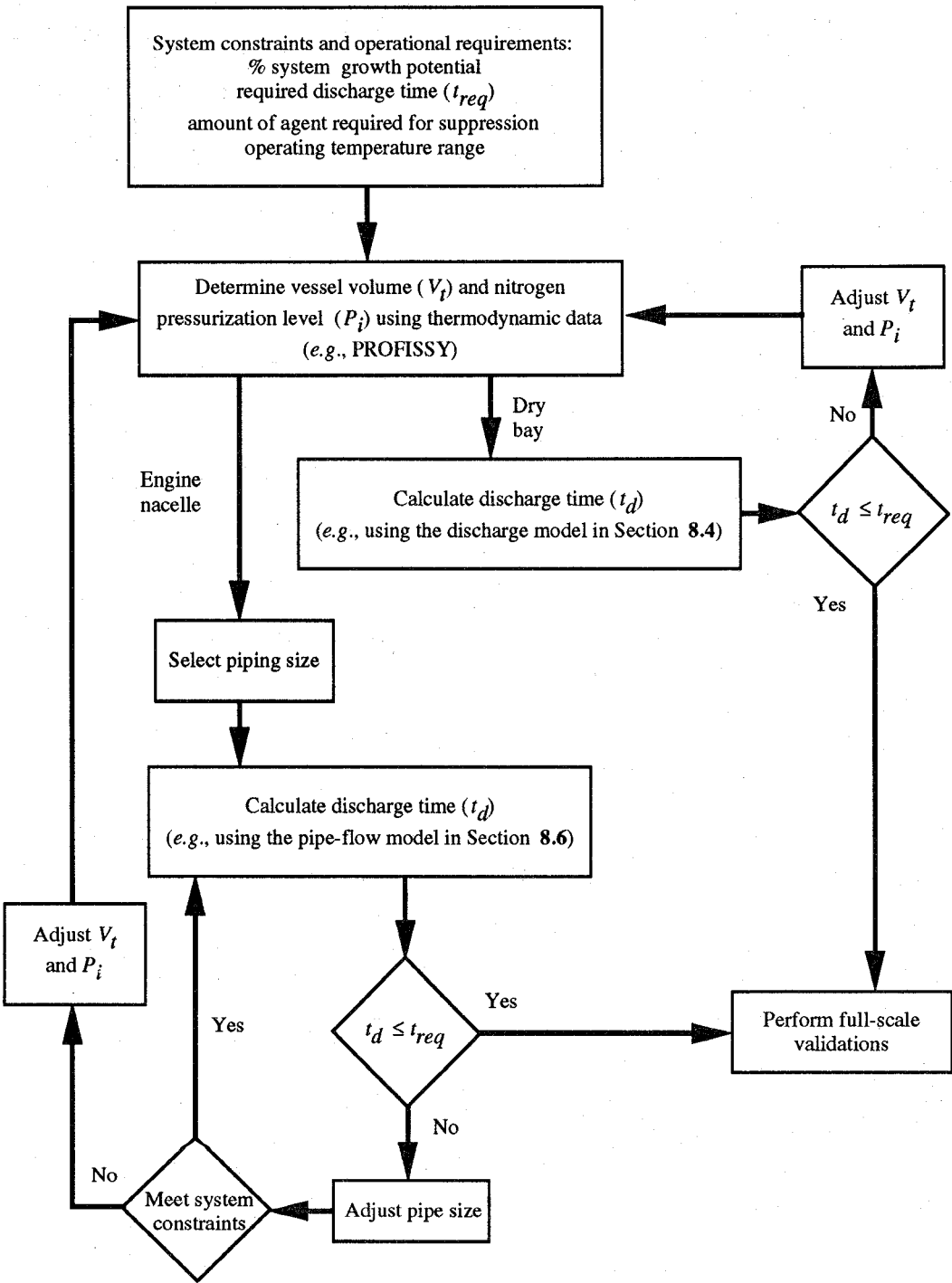


Figure 148. A generic flow chart for discharge system optimization.

8.8 Acknowledgments

This work was funded by the United States Air Force Wright Laboratory, Naval Air Systems Command, and Army Aviation and Troop Command and the Federal Aviation Administration Technical Center. Their financial support was greatly appreciated. The authors would like to thank the following BFRL, NIST staff: Dr. William M. Pitts for his constant input to the project, Mr. Roy McLane for fabricating some of the experimental hardware, and Ms. Paula Garrett for her effort in editing this section. Discussions regarding the degassing of dissolved nitrogen with Professor Charles A. Ward of the University of Toronto were very helpful. The authors would also like to acknowledge the following companies for providing the information on current halon 1301 system specifications: Boeing, Booz-Allen & Hamilton, Lockheed Martin, McDonnell Douglas, Northrop Grumman, Pacific Scientific, Systron-Donner, and Walter Kidde.

8.9 References

- Allied Signal Inc., *Selected Physical Properties: HCFC-123, HCFC-123a, HCFC-124, HFC-125, HFC-134, HFC-134a, and HFC-143a*, Allied Signal Inc., Buffalo Research Laboratory, Buffalo, NY, 1990.
- Amsden, A.A., O'Rourke, P.J., and Butler, T.D., *KIVA-II: A Computer Program for Chemically Reactive Flows with Sprays*, Los Alamos National Laboratory Report No. LA-11560-MS, 1989.
- Amsden, A.A., Butler, T.D., O'Rourke, P.J., *KIVA-III: A KIVA Program with Block-structured Mesh for Complex Geometries*, Los Alamos National Laboratory Report No. LA-12503-MS, 1993.
- ASHRAE Inc., *ASHRAE Thermodynamic Properties of Refrigerants*, ASHRAE Inc., New York, 1969.
- Balzhiser, R.E., Samuels, M.R., and Eliassen, J.D., *Chemical Engineering Thermodynamics, The Study of Energy, Entropy, and Equilibrium*, Prentice-Hall, Englewood Cliffs, NJ, 1972.
- Braker, W., and Mossman, A.L., *Matheson Gas Data Book*, 6th ed., Matheson Gas Products, New Jersey, 1980.
- Carnahan, B., Luther, H.A., and Wilkes, J.O., *Applied Numerical Methods*, John Wiley & Sons, New York, 1969.
- Carey, V. P., *Liquid-Vapor Phase-Change Phenomena: An Introduction to the Thermophysics of Vaporization and Condensation Processes in Heat Transfer Equipment*, Hemisphere Publishing Co., Washington, DC, 1992.
- Celata, G.P., Cumo, M., Farello, G.E., and Incalcaterra, P.C., "On the Critical flows of Subcooled Liquids," in *Heat Transfer 1982, Proceedings of the Seventh International Heat Transfer Conference*, Grigull, U., Hahne, E., Stephan, K., and Straub, J. (eds.), Hemisphere, New York, 1982.
- Celata, G.P., Cumo, M., Farello, G.E., Incalcaterra, P.C., and Naviglio, A., "Thermodynamic Disequilibrium in the Critical Flow of Subcooled Liquids," *Nuclear Technology* 60, 137 (1983).
- Chueh, P.L. and Prausnitz, J.M., "Vapor-Liquid Equilibria at High Pressures: Calculation of Partial Molar Volumes in Nonpolar Liquid Mixtures," *AIChE J.* 13, 1099 (1967).
- Cloutman, L.D., Dukowicz, J.K., Ramshaw, J.D., and Amsden, A.A., *Conchas-Spray: A Computer Code for Reactive Flows with Fuel Sprays*, Los Alamos National Laboratory Report No. LA-9294-MS, 1982.
- Cooper, L.Y., "The Dispersion of Fire Suppression Agents Discharged from High Pressure Vessels: Establishing Initial/Boundary Conditions for the Flow Outside the Vessel," *Proc. ICLASS-94*, Rouen, France, 1994.

Dinneno, P.J., and Budnick, E.K., *Halon 1301 Discharge Testing: A Technical Analysis*, National Fire Protection Research Foundation, Quincy, MA, 1988.

Dukler, A.E., Wicks, M., and Cleveland, R.G., "Frictional Pressure Drops in Two-Phase Flow," *AIChE J.* 10, 44 (1964).

Dukowicz, J.K., *Quasi-Steady Droplet Phase Change in the Presence of Convection*, Los Alamos Scientific Laboratory Report No. LA-7997-MS, 1979.

Dymond, J.H. and Smith, E.B., *The Virial Coefficients of Gases: A Critical Compilation*, Clarendon Press, Oxford, 1969.

Elliot, D.G., Garrison, P.W., Klein, G.A., Moran, K.M., and Zydowicz, M.P., *Flow of Nitrogen-Pressurized Halon 1301 in Fire Extinguishing Systems*, Jet Propulsion Laboratory, JPL Publication 84-62, 1984.

Ely, J.F. and Hanley, H.J.M., *A Computer Program for the Prediction of Viscosity and Thermal Conductivity in Hydrocarbon Mixtures*, NBS Technical Note 1039, U.S. Department of Commerce, Washington, DC 1981a.

Ely, J.F. and Hanley, H.J.M., "Prediction of Transport Properties. 1. Viscosity of Fluids and Mixtures," *Ind. Eng. Chem. Fundam.* 20, 323 (1981b).

Ely, J.F., "Prediction of Dense Fluid Viscosities in Hydrocarbon Mixtures," *Proc. 61st Gas Processors Association*, pp. 9-17 (1982).

Ely, J.F. and Hanley, H.J.M., "Prediction of Transport Properties. 2. Thermal Conductivity of Pure Fluids and Mixtures," *Ind. Eng. Chem. Fundam.* 22, 90 (1983).

Ely, J.F., "A Predictive, Exact Shape Factor Extended Corresponding States Model for Mixtures," *Advances in Cryogenic Engineering* 35, 1511 (1990).

Forest, T.W. and Ward, C.A., "Effect of a Dissolved Gas on the Homogeneous Nucleation Pressure of a Liquid," *J. Chem. Phys.* 66, 2322 (1977).

Friend, D.G., *NIST Standard Reference Database 14: NIST Mixture Property Database*, U.S. Department of Commerce, Washington, DC, Version 9.08, 1992.

Gallagher, J., McLinden, M., Huber, M., and Ely, J., *NIST Standard Reference Database 23: Thermodynamic Properties of Refrigerants and Refrigerant Mixtures Database (REFPROP)*, Version 3.0, U.S. Department of Commerce, Washington, DC 1991.

Gallagher, J., McLinden, M., Huber, M., and Ely, J., *NIST Standard Reference Database 23: Thermodynamic Properties of Refrigerants and Refrigerant Mixtures Database (REFPROP)*, Version 4.0, U.S. Department of Commerce, Washington, DC 1993.

Gallagher, J., Huber, M.L., Morrison, G., and McLinden, M.O., *NIST Standard Reference Database 23: Thermodynamic Properties of Refrigerants and Refrigerant Mixtures*, Version 5.0, U.S. Department of Commerce, Washington, DC, 1995 (in preparation).

Great Lakes Chemical Corporation, *FM-200TM: Environmentally Superior Fire Extinguishant for Total Flooding Applications*, Great Lakes Chemical Corporation, West Lafayette, IN, May 1993.

Grosshandler, W.L., Gann, R.G., and Pitts, W.M. (ed.), *Evaluation of Alternative In-Flight Fire Suppressants for Full-Scale Testing in Simulated Aircraft Engine Nacelles and Dry Bays*, NIST SP 861, U.S. Department of Commerce, Washington, DC, April 1994.

Henry, R.E., "Calculational Techniques for Two-Phase Critical Flow," in *Two-Phase Flow Dynamics, Japan-U.S. Seminar 1979*, Bergles, A.E. and Ishigai, S. (eds.), pp. 415-436, Hemisphere Publishing Corp., Washington, 1979.

Huber, M.L. and Ely, J.F., *NIST Standard Reference Database 4: NIST Thermophysical Properties of Hydrocarbon Mixtures*, U.S. Department of Commerce, Washington, DC, 1990.

Huber, M.L. and McLinden, M.O., "Thermodynamic Properties of R134a (1,1,1,2-tetrafluoroethane)," *Proc 1992 International Refrigeration Conference*, Purdue University, July 14-17, 453 (1992).

Huber, M.L. and Ely, J.F., "Prediction of Viscosity of Refrigerants and Refrigerant Mixtures," *Fluid Phase Equilibria* 80, 239 (1992).

Huber, M.L., Friend, D.G., and Ely, J.F., "Prediction of the Thermal Conductivity of Refrigerants and Refrigerant Mixtures," *Fluid Phase Equilibria* 80, 249 (1992).

Huber, M.L. and Ely, J.F., "A Predictive Extended Corresponding States Model for Pure and Mixed Refrigerants Including an Equation of State for R134a," *Int. J. Refrig.* 17, 18 (1994).

Jacobsen, R.T. and Stewart, R.B., "Thermodynamic Properties of Nitrogen Including Liquid and Vapor Phases from 63 K to 2000 K with Pressures to 10,000 Bar," *J. Phys. Chem. Ref. Data* 2, 757 (1973).

Kanury, A.M., *Introduction to Combustion Phenomena*, Gordon and Breach Science Publishers, New York, 1977.

Kim-E, M.E. and Reid, R.C., "The Rapid Depressurization of Hot, High Pressure Liquids or Supercritical Fluids," in *Chemical Engineering at Supercritical Fluid Conditions*, Paulaitis, M.E., Penniger, J.M.L., Gray, Jr., R.D., and Davidson, P. (eds.), pp. 81-100, Ann Arbor Science, Ann Arbor, MI, 1983.

Kudchadker, A.P., Kudchadker, S.A., Shukla, R.P., and Patnaik, P.R., "Vapor Pressures and Boiling Points of Selected Halomethanes," *J. Phys. Chem. Ref. Data* 8, 499 (1979).

Kurschat, Th., Chaves, H., and Meier, G.E.A., "Complete Adiabatic Evaporation of Highly Superheated Liquid Jets," *J. Fluid Mechanics* 236, 43 (1992).

Leach, J.W., Chapple, P.S., and Leland, T.W., "Use of Molecular Shape Factors in Vapor Liquid Equilibrium Calculations with the Corresponding States Principle," *AIChE Journal* 14, 568 (1968).

McCarty, R.D., "Mathematical Models for the Prediction of Liquified-Natural-Gas Densities," *J. Chem. Thermodynamics* 14, 837 (1982).

National Fire Codes, *NFPA 12A Standard on Halon 1301 Fire Extinguishing Systems 1992 Edition*, National Fire Protection Association, Quincy, MA, 1995.

Olujic, Ž., "Predicting Two-Phase-Flow Friction Loss in Horizontal Pipes," *Chemical Engineering*, 1985.

Perry, R.H., Green, D., and Maloney, J.O., *Perry's Chemical Engineers' Handbook*, 6th ed., McGraw-Hill, New York, NY, 1984.

Prausnitz, J.M., Anderson, T.F., Grens, E.A., Eckert, C.A., Hsieh, R., and O'Connell, J.P., *Computer Calculations for Multicomponent Vapor-Liquid and Liquid-Liquid Equilibria*, Prentice-Hall, New Jersey, 1980.

Ranz, W.E., and Marshall, W.R., "Evaporation from Drops. Part I and II," *Chemical Engineering Progress* 48, 141 & 173 (1952).

Reid, R.C., "Superheated Liquids," *American Scientist* 64, 146 (1976).

Reid, R.C., Prausnitz, J.M., and Poling, B.E., *The Properties of Gases and Liquids*, 4th ed., McGraw-Hill, New York, 1987.

SFPE Handbook of Fire Protection Engineering, First ed., Society of Fire Protection Engineers, National Fire Protection Association, Quincy, MA, 1988.

Sherman, G.J., Magee, J.W., and Ely, J.F., "PVT Relationships in a Carbon Dioxide Rich Mixture with Ethane," *Int. J. Thermophysics* 10, 47 (1989).

Sladkov, I.B., and Bogacheva, A.V., "Critical Parameters of Mixed Carbon Halides," *Zhurnal Prikladnoi Khimii* 64, 2435 (1991); 64, 2276 (1992) (English translation).

Smith, B.D. and Srivastava, R., *Thermodynamic Data for Pure Compounds. Part B Halogenated Hydrocarbons and Alcohols*, Elsevier, Amsterdam, 1986.

Smith, J.M., and Van Ness, H.C., *Introduction to Chemical Engineering Thermodynamics*, 3rd ed., McGraw-Hill, New York, 1975.

Taylor, B.N., and Kuyatt, C.E., *Guidelines for Evaluating and Expressing the Uncertainty of NIST Measurement Results*, NIST Technical Note 1297, U.S. Department of Commerce, Washington, DC, 1994.

Thompson P.A., Carofano G.C., and Kim Y.G., "Shock Waves and Phase Changes in a Large-Heat-Capacity Fluid Emerging from a Tube," *J. Fluid Mechanics* 166, 57 (1986).

Volmer, M., *Kenetik der Phasenbildung*, Edwards Brothers, Inc., Ann Arbor, MI, 1945.

Walas, S.M., *Phase Equilibrium in Chemical Engineering*, Butterworth, Boston, 1985.

Welty, J.R., Wicks, C.E., and Wilson, R.E., *Fundamentals of Momentum, Heat, and Mass Transfer*, 3rd ed., John Wiley & Sons, New York, NY, 1984.

Whalley, P.B., *Boiling Condensation and Gas-Liquid Flow*, Clarendon Press, Oxford, 1990.

Appendix A. A User's Guide to PROFISSY

There are two files (PROFISSY.EXE and PROFLIB) in the disc. The current version of PROFISSY is Version 0.08. In the following, the **bold** type style represents any text one must type. Sentences in *italic* represent the instructions given by the computer. To start a run, simply type **PROFISSY**, followed by hitting the <enter> key, from the drive or directory where the program is installed. The screen will appear as follows.

NIST Program PROFISSY - Version 0.08
PROPERTIES of FIRE Suppression SYstems

National Institute of Standards and Technology
Thermophysics Division, 838.02
M. L. Huber, 303-497-5252

Based on research sponsored by
United States Air Force, Army, and Navy, and
the Federal Aviation Administration

NOTE: NIST makes every effort to deliver a high
quality product; however --- NIST shall not be
liable for any damage that may result
from errors or omissions in this program.

The program output will be written to file OUT.DAT and to the screen.

The default units are F, lb., ft**3, Psia

Do you want to change the units ? (Yes/No)

Type **y** and hit <enter> if you want to change the default units. The Property Unit Menu will appear on the screen.

Property Unit Menu							
Property	*****options*****						current
Temperature	(K	,R	,C	,F	,	,)-	F
Pressure	(atm	,bar	,MPa	,kpf	,Psia	,mmHG)-	Psia
Volume	(liter	,m**3	,cm**3	,in**3	,ft**3	,)-	ft**3
Energy	(cal	,J	,btu	,kcal	,kJ	,)-	btu
Mass	(mol	,lb-mol	,kg	,g	,lb	,)-	lb
Velocity	(m/s	,cm/s	,ft/s	,in/s	,	,)-	ft/s
Viscosity	(uP	,cP	,uPa.s	,lb/ft.s	,lb/ft.h	,)-	lb/ft.s
Thm. Cond.	W/m.K	,cal/cm.s.K	,btu/ft.s.F	,btu/ft.h.F	,mW/m.K	,)-	btu/ft.h.F
default set options							
(1) Scientific	(K	,atm	,liter	,cal	,mol	,cm/s	,uP ,cal/cm.s.K)
(2) S.I.	(K	,MPa	,m**3	,kJ	,kg	,m/s	,uPa.s ,W/m.K)
(3) Engineering	(F	,Psia	,ft**3	,btu	,lb	,ft/s	,lb/ft.s ,btu/ft.h.F)
(4) Mixed	(K	,bar	,liter	,kJ	,mol	,m/s	,uP ,mW/m.K)
Enter the new unit or default option (X to exit) ?							

Type **C,MPa,cm**3,g,x** and hit <enter> if you want temperature in C, pressure in MPa, volume in cm³, and mass in g. The screen will appear as follows.

Please input the fire suppression agent. Choose from the following list:	
Name	Synonym
CF3I	trifluoroiodomethane
R218	perfluoropropane
R125	pentafluoroethane
R227ea	heptafluoropropane
R13b1	trifluorobromomethane

Type **cf3i** and hit <enter> if you want to run CF₃I. Follow the instructions given by the computer to input the data.

Input the amount (in g) of fire suppression agent.700 <enter>

*Input the container volume (in cm**3)500 <enter>*

Do you want to input system pressure (P) or N2 mass (M) ?p <enter>

Input the pressure (in MPa)4.12 <enter>

Input the fill temperature (in C)22 <enter>

Do you want to specify the temperature limits for the table? (Y,N)

If NO, limits will be generated automatically y <enter>

If the input is **n**, the computer will generate the table from -60 to 150 °C with 10 °C increment.

Input the Tmin, Tmax, and T increment (in C)20,40,10 <enter>

The computer will response: *please wait, computations in progress*

After the computation, the screen will appear as follows.

.....			
CF3I with nitrogen superpressure			
Pressure - Temperature Characteristics			
.....			
Agent mass	700.000(g)		
Nitrogen Mass	15.522(g)		
Container Volume	500.000(cm**3)		
Fill Temperature	22.000(C)	Fill Pressure	4.120(MPa)
Bubble point temp.	92.006(C)	Bubble point pres.	6.784(MPa)
Press Enter to Continue.			

After hit <enter>, the computer will list the calculated results on the screen. The calculated bubble point pressure and temperature are obtained at the fill conditions.

Temp. (C)	Vol. Pct. Liq. Fill	Mass Liquid CF3I (g)	Nitrogen xN2 wN2		Mass N2 (g) liquid vapor		Pressure MPa
20.0	68.99	0.6910E+03	0.085	0.013	0.9129E+01	0.6393E+01	4.1
30.0	70.83	0.6890E+03	0.088	0.014	0.9558E+01	0.5964E+01	4.3
40.0	72.90	0.6869E+03	0.093	0.014	0.1005E+02	0.5473E+01	4.6
Do you want another run? (Yes,No)							

If you do not want another run, type **n** and press <enter>.

Goodbye !

"Vol. Pct. Liq. Fill" represents the volume percent of liquid fill in the container. "xN2" and "wN2" represent the mole and mass fractions of nitrogen in the liquid mixture respectively.

Compilation of Results. For quick references, three cases with initial *pure* (before nitrogen pressurization) liquid agent volume fractions of 1/3, 1/2, and 2/3 (see Section 8.3.2.1) have been run for all the agents which the computer code currently supports and are summarized in Figures A-1 to A-15. In the calculations, the initial fill temperature is 22 °C and the three initial fill pressures are 2.75 MPa, 4.12 MPa, and 5.50 MPa.

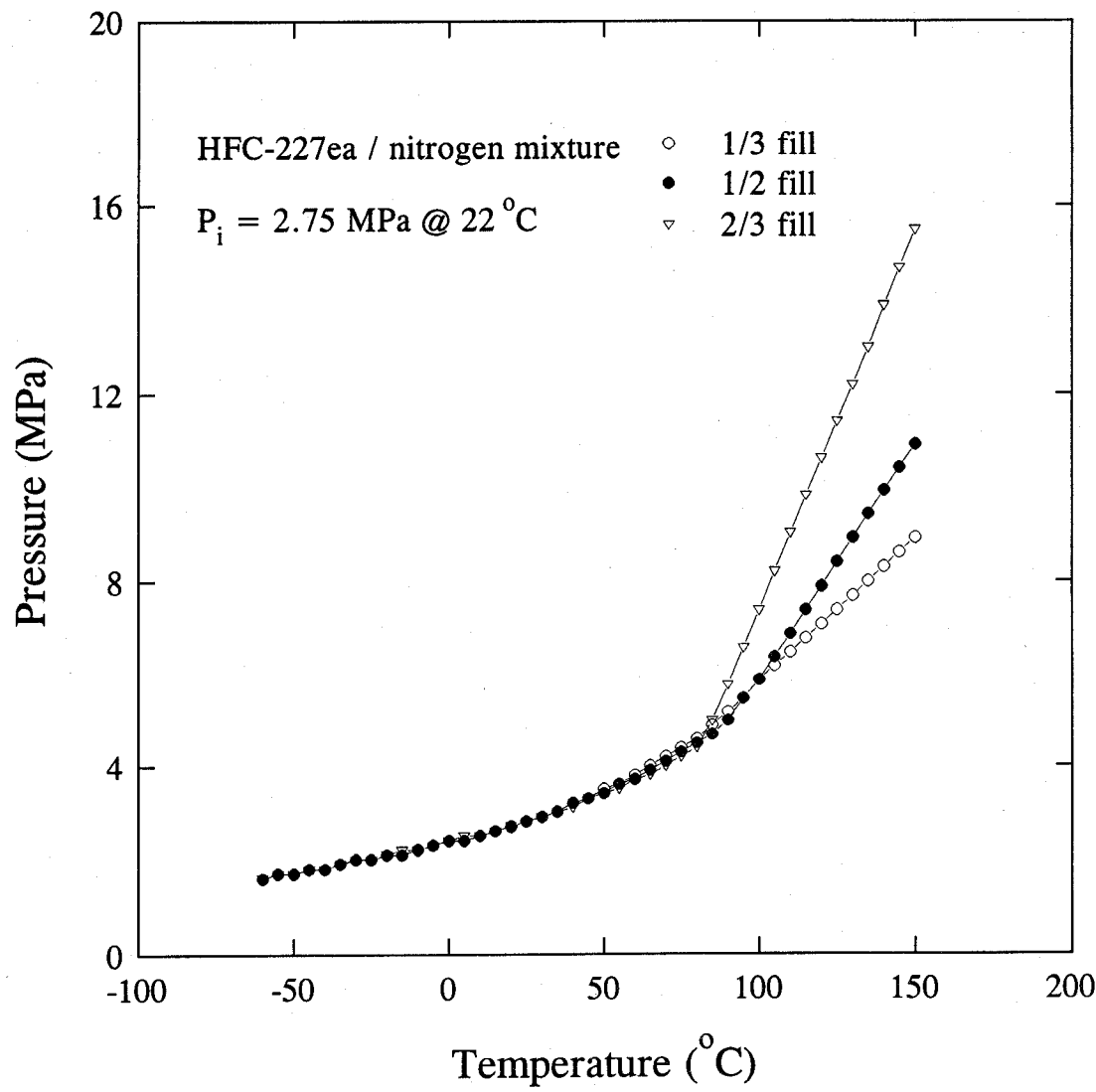


Figure A-1. Calculated pressure as a function of temperature for HFC-227ea/N₂ mixture under three fill conditions and $P_i = 2.75$ MPa.

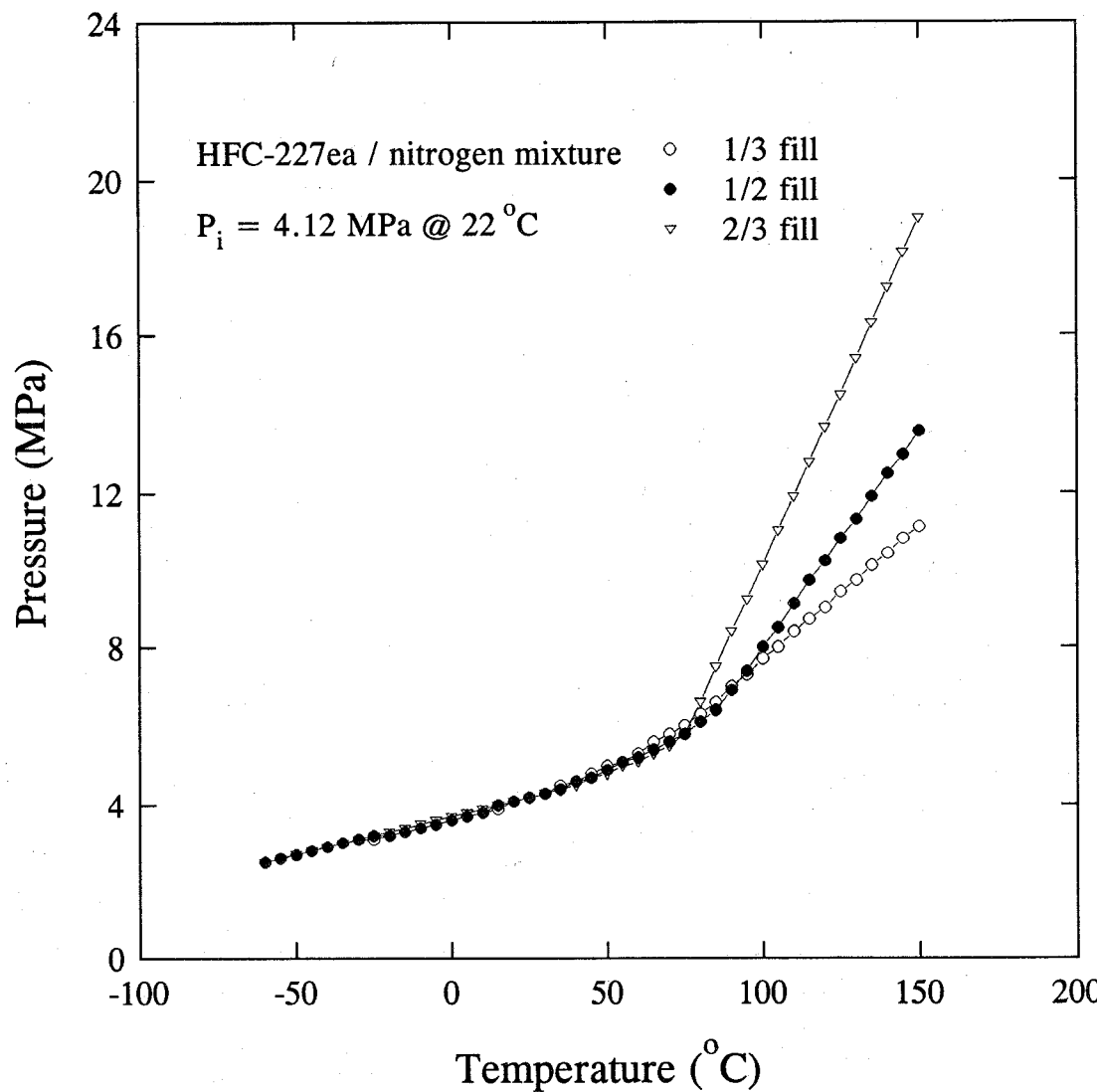


Figure A-2.

Calculated pressure as a function of temperature for HFC-227ea/ N_2 mixture under three initial fill conditions and $P_i = 4.12 \text{ MPa}$.

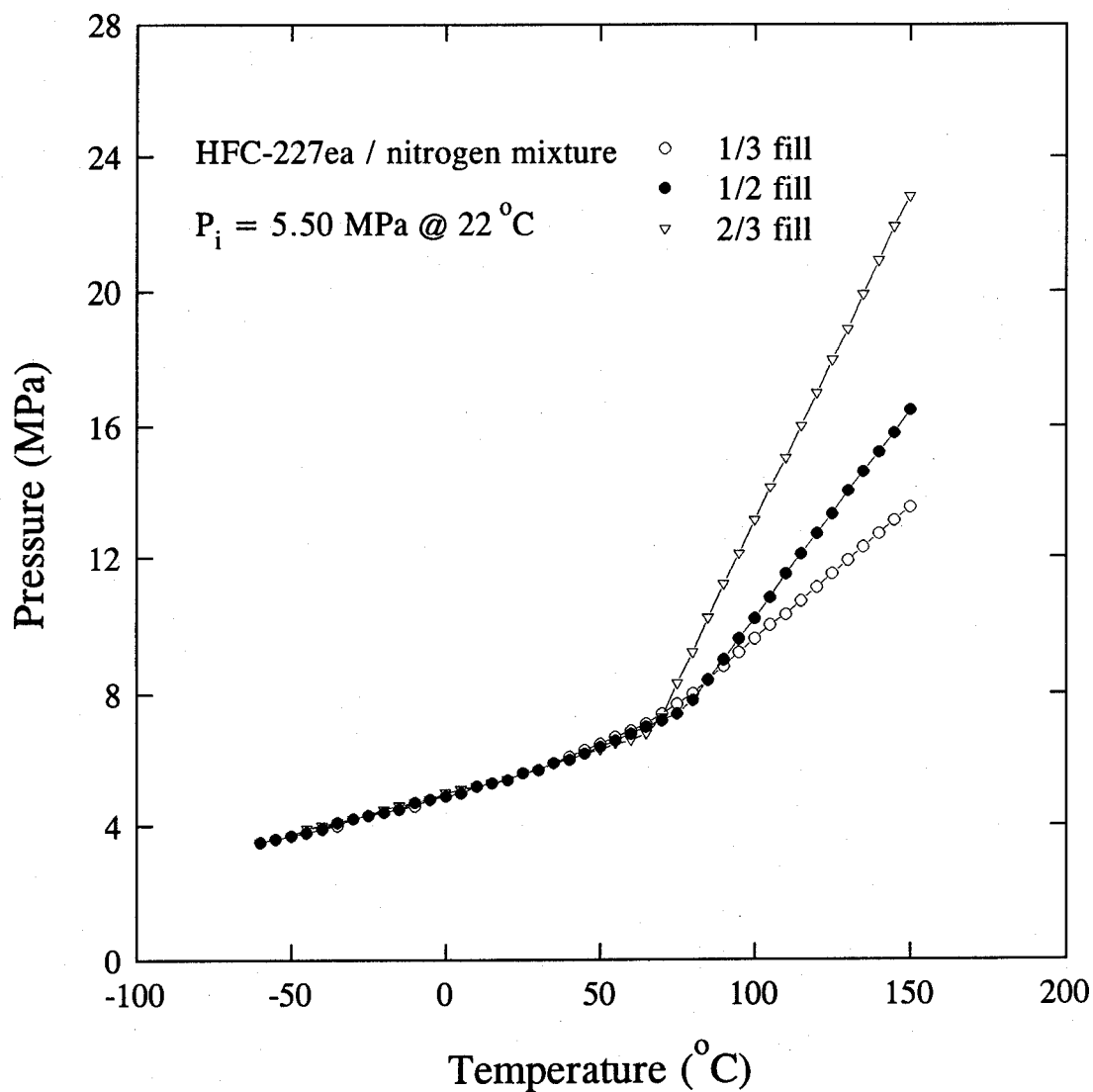


Figure A-3.

Calculated pressure as a function of temperature for HFC-227ea/N₂ mixture under three initial fill conditions and $P_i = 5.50$ MPa.

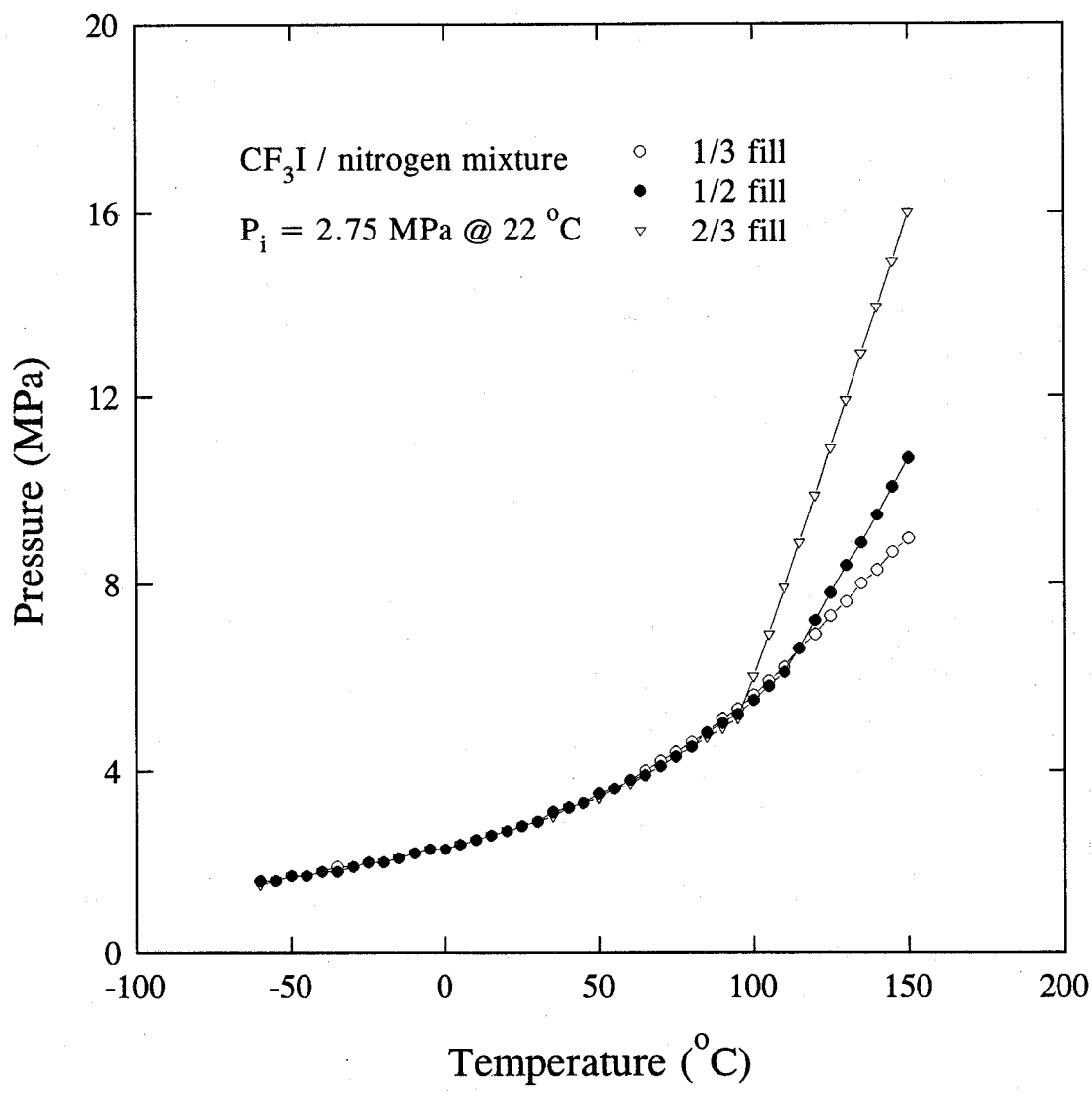


Figure A-4. Calculated pressure as a function of temperature for $\text{CF}_3\text{I}/\text{N}_2$ mixture under three initial fill conditions and $P_i = 2.75$ MPa.

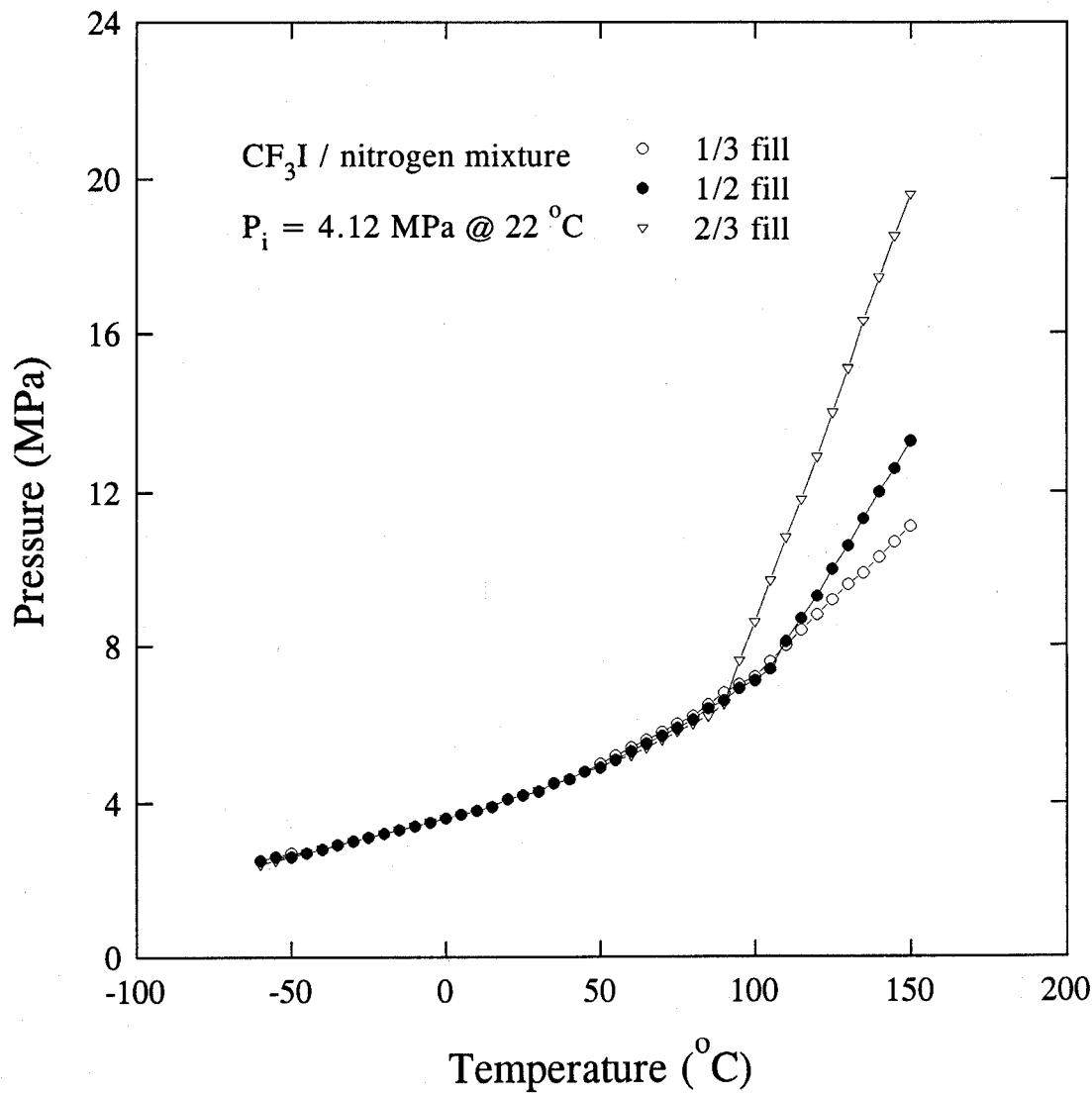


Figure A-5. Calculated pressure as a function of temperature for $\text{CF}_3\text{I}/\text{N}_2$ mixture under three initial fill conditions and $P_i = 4.12$ MPa.

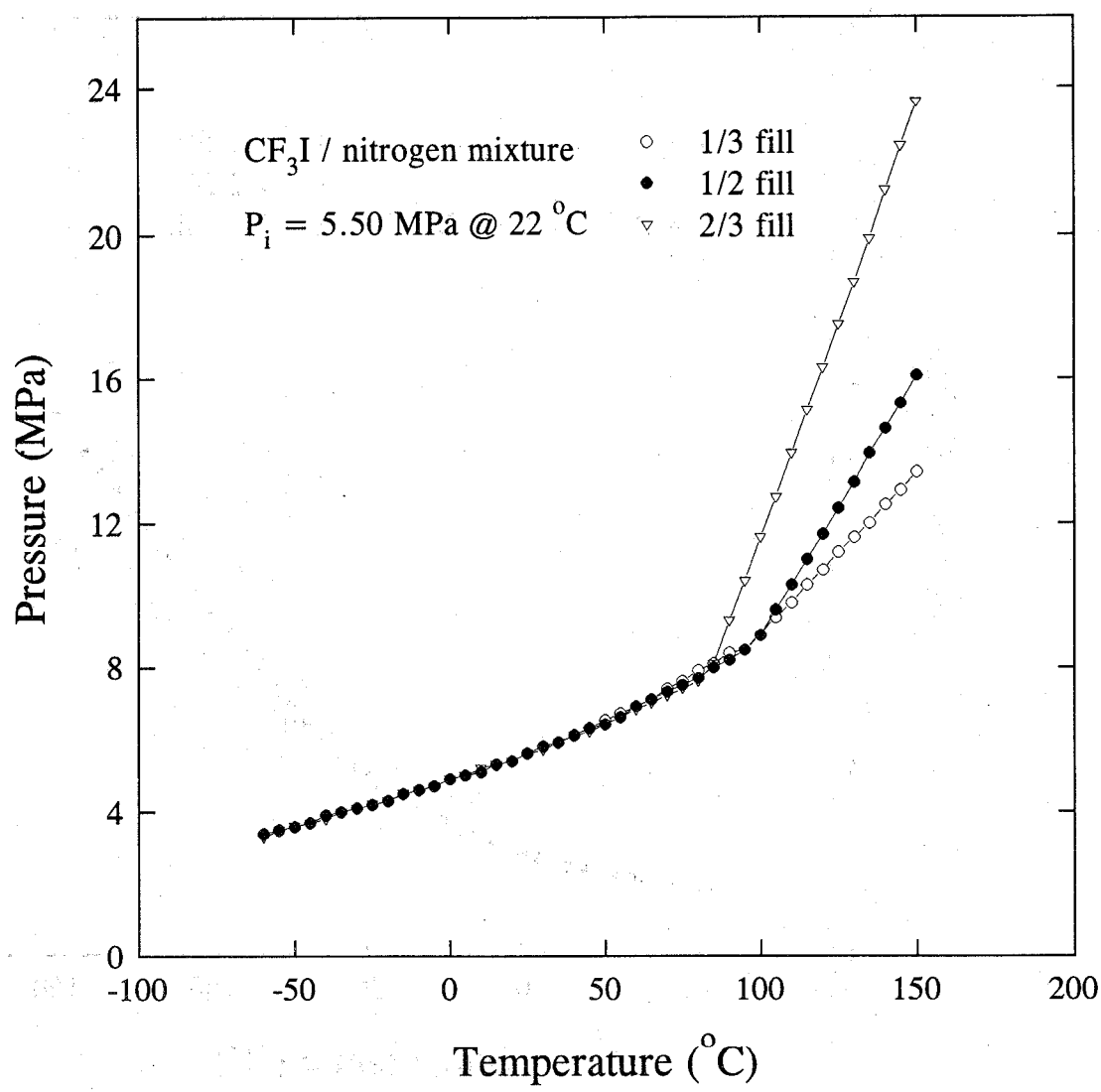


Figure A-6. Calculated pressure as a function of temperature for CF₃I/N₂ mixture under three initial fill conditions and $P_i = 5.50 \text{ MPa}$.

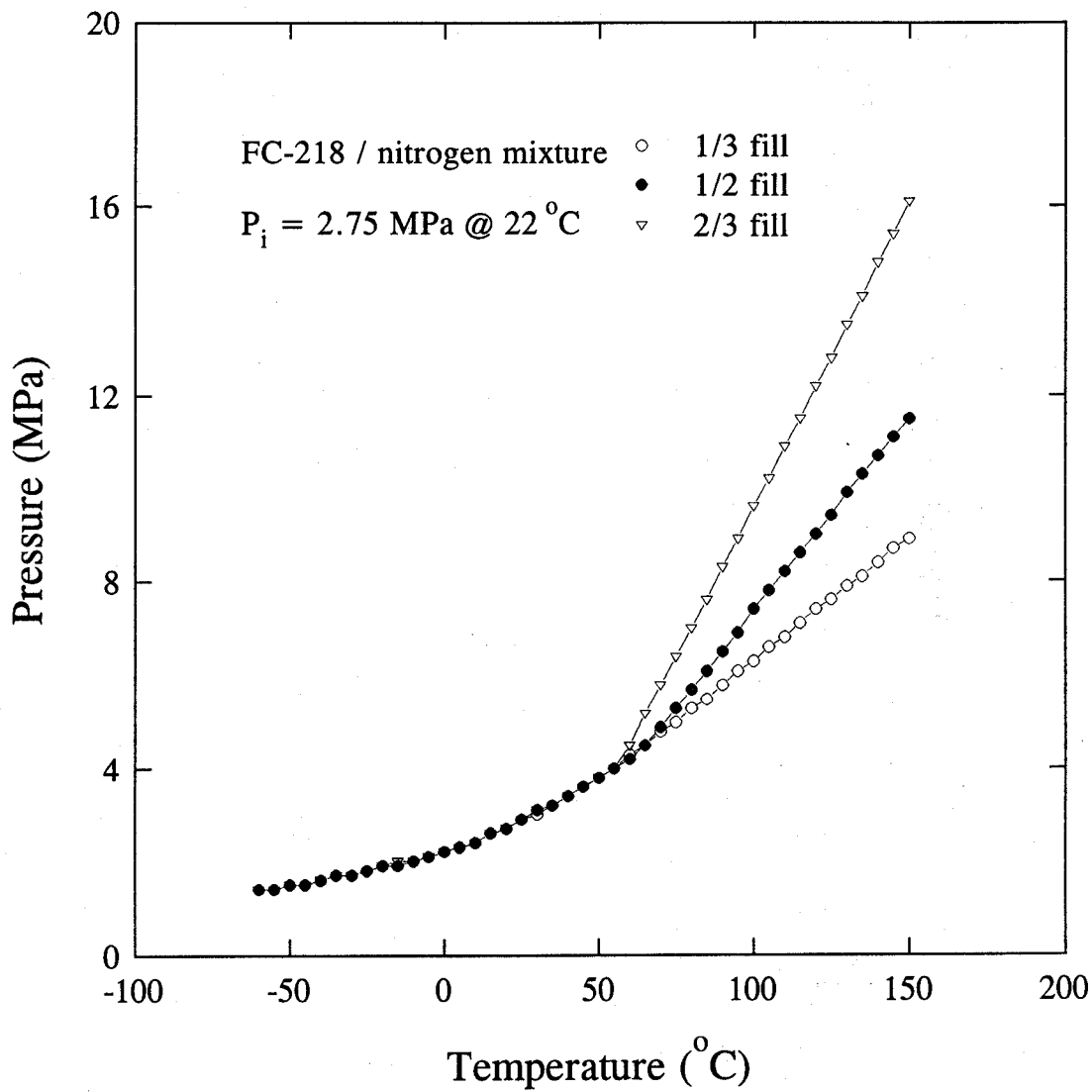


Figure A-7. Calculated pressure as a function of temperature for FC-218/N₂ mixture under three initial fill conditions and $P_i = 2.75$ MPa.

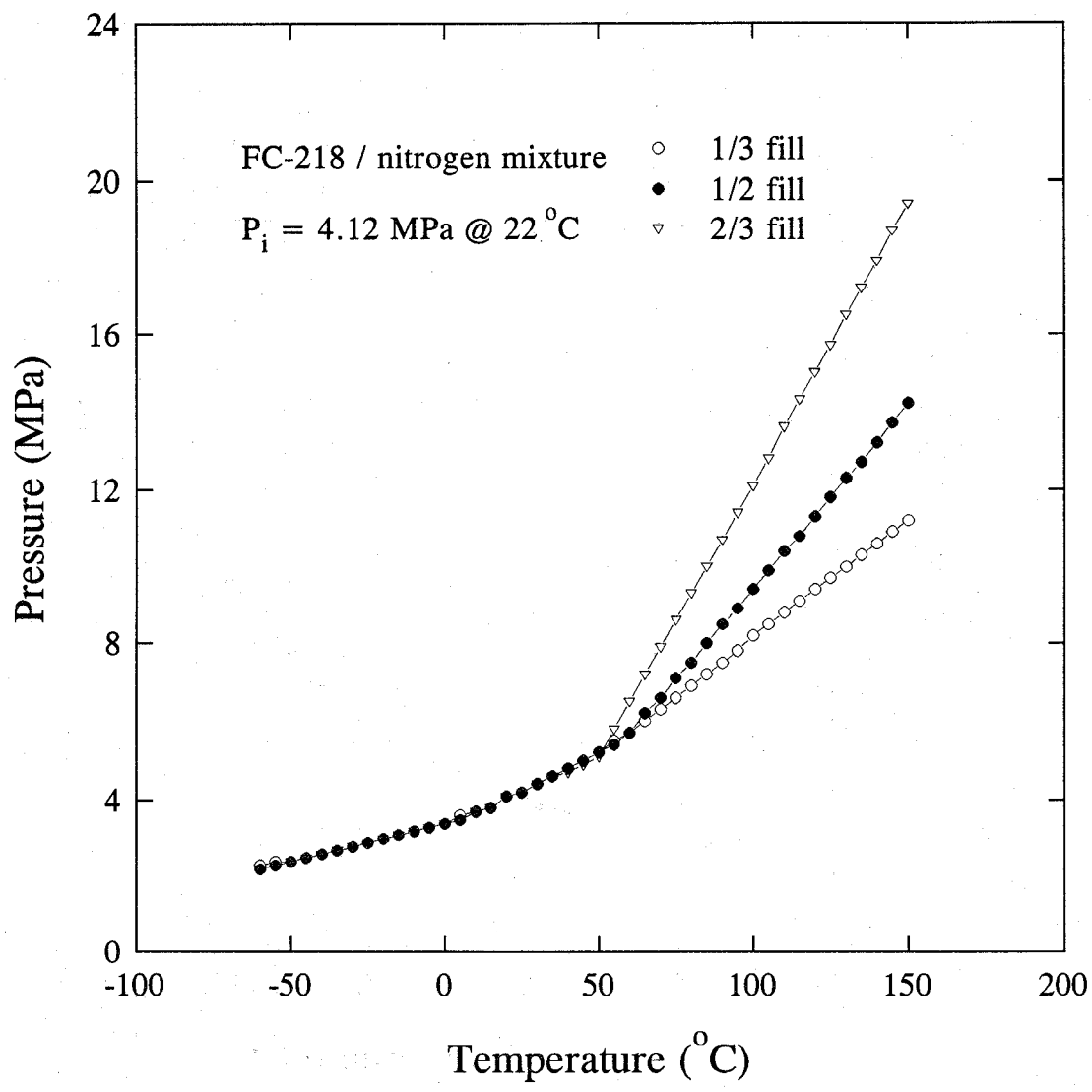


Figure A-8. Calculated pressure as a function of temperature for FC-218/N₂ mixture under three initial fill conditions and $P_i = 4.12$ MPa.

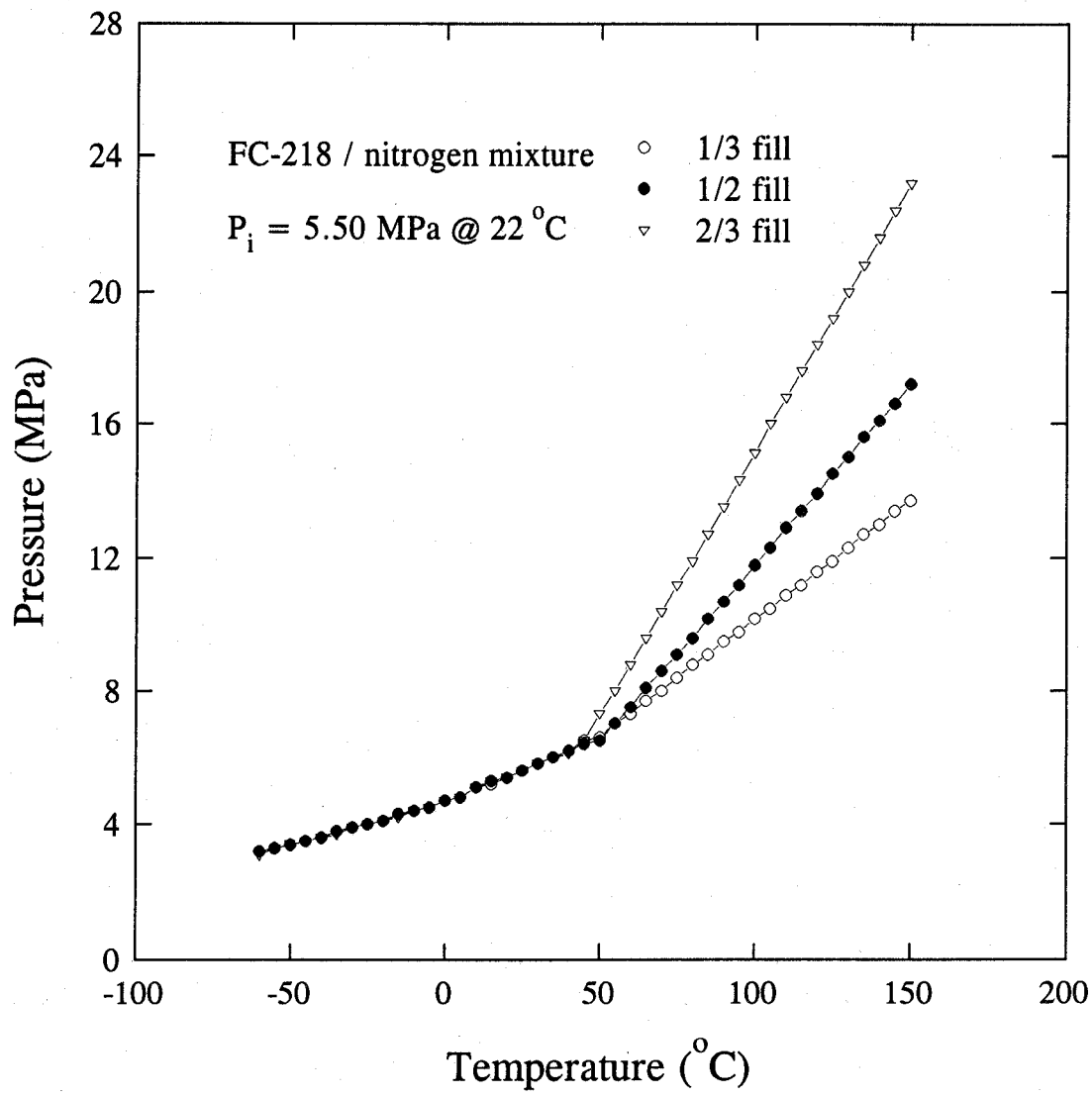


Figure A-9. Calculated pressure as a function of temperature for FC-218/ N_2 mixture under three initial fill conditions and $P_i = 5.50 \text{ MPa}$.

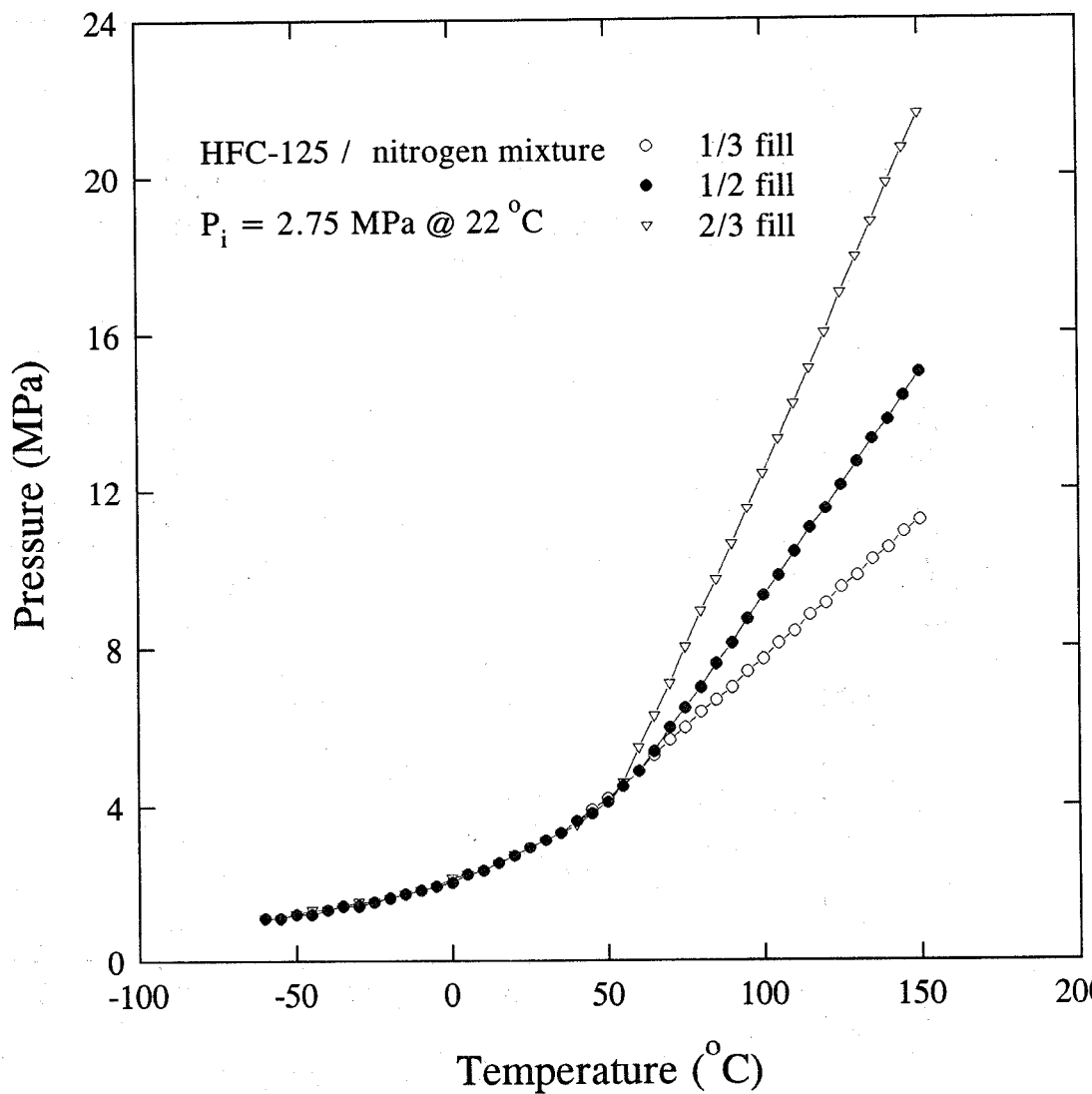


Figure A-10. Calculated pressure as a function of temperature for HFC-125/N₂ mixture under three initial fill conditions and $P_i = 2.75$ MPa.

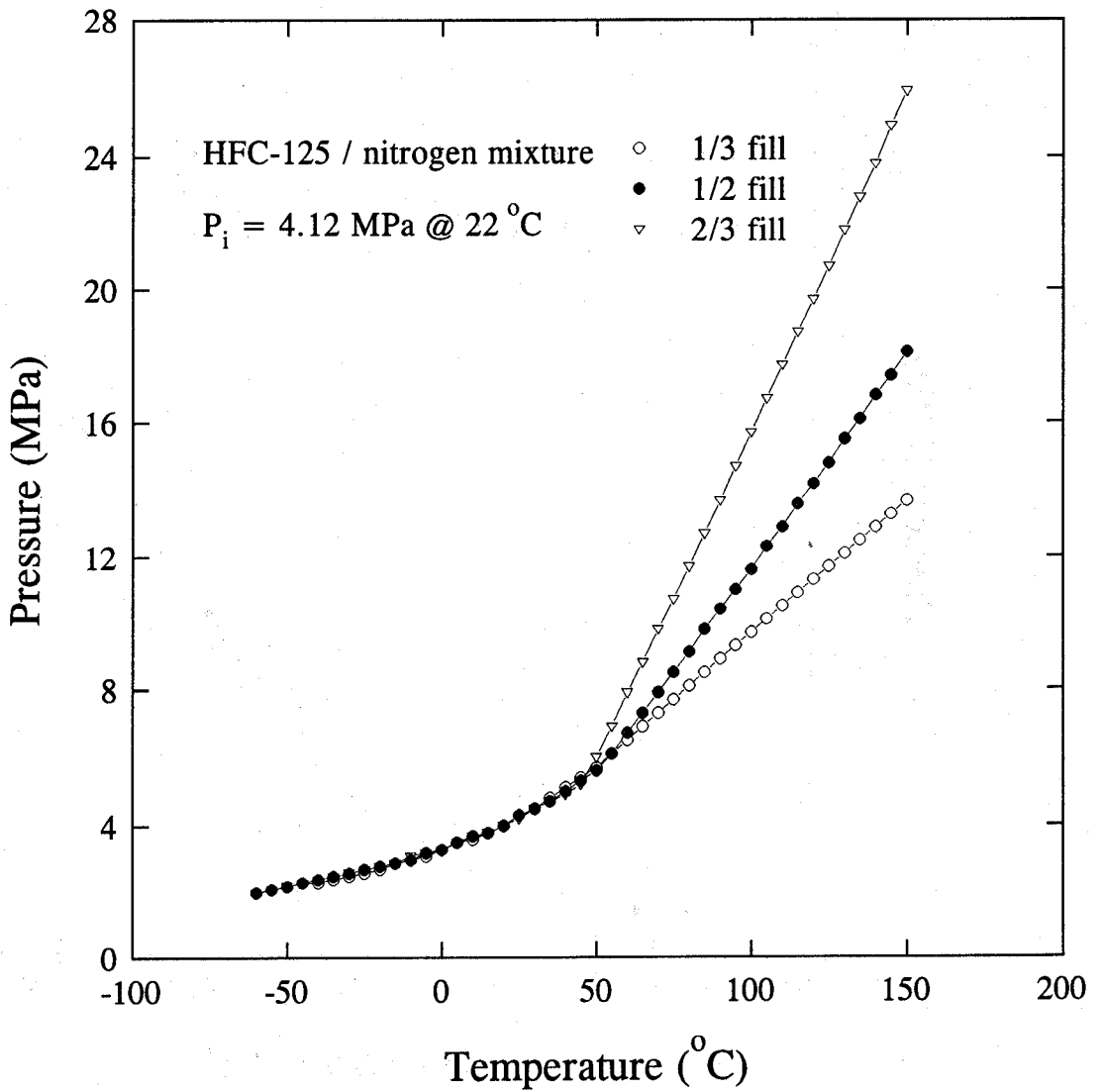


Figure A-11.

Calculate pressure as a function of temperature for HFC-125/ N_2 mixture under three initial fill conditions and $P_i = 4.12$ MPa.

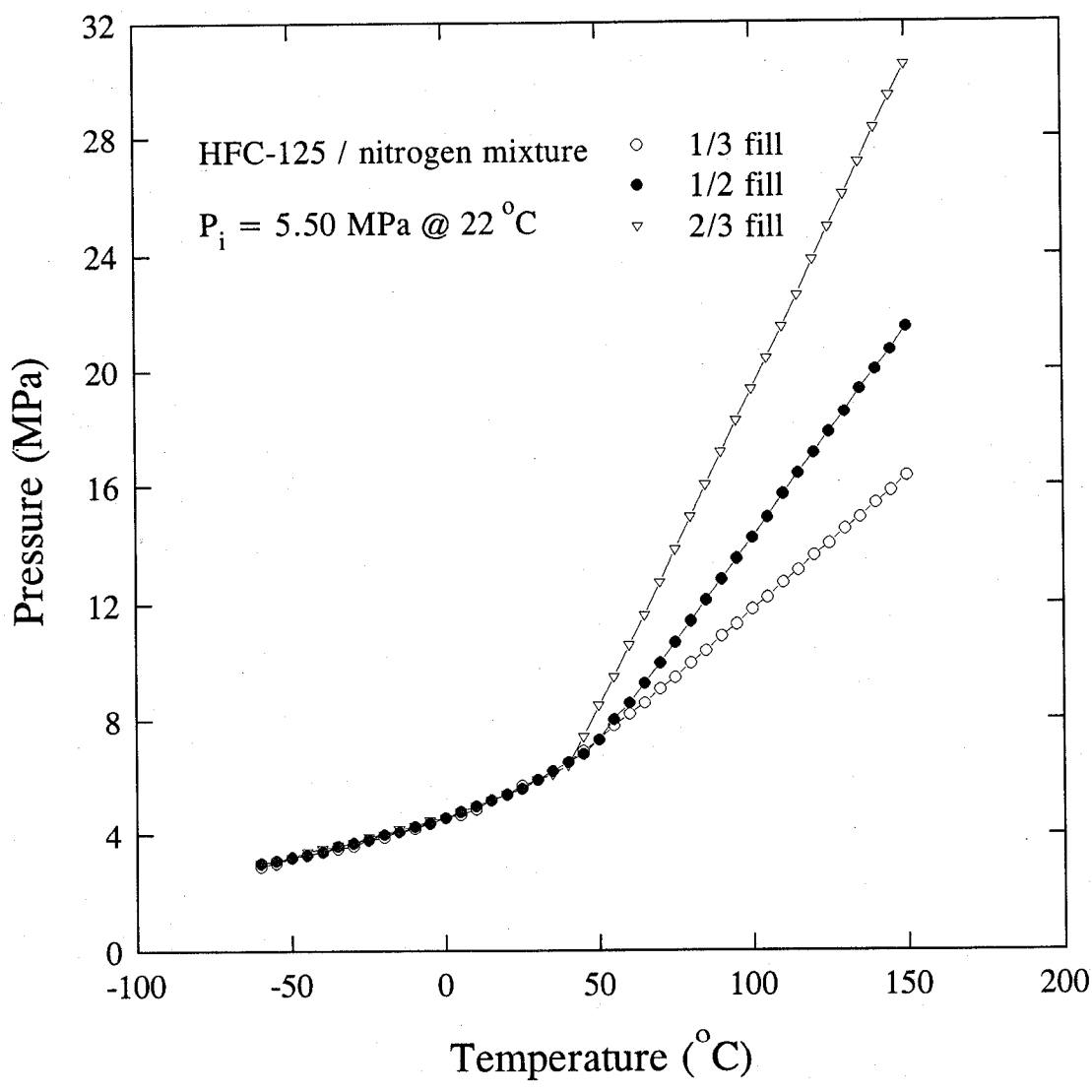


Figure A-12. Calculated pressure as a function of temperature for HFC-125/ N_2 mixture under three initial fill conditions and $P_i = 5.50 \text{ MPa}$.

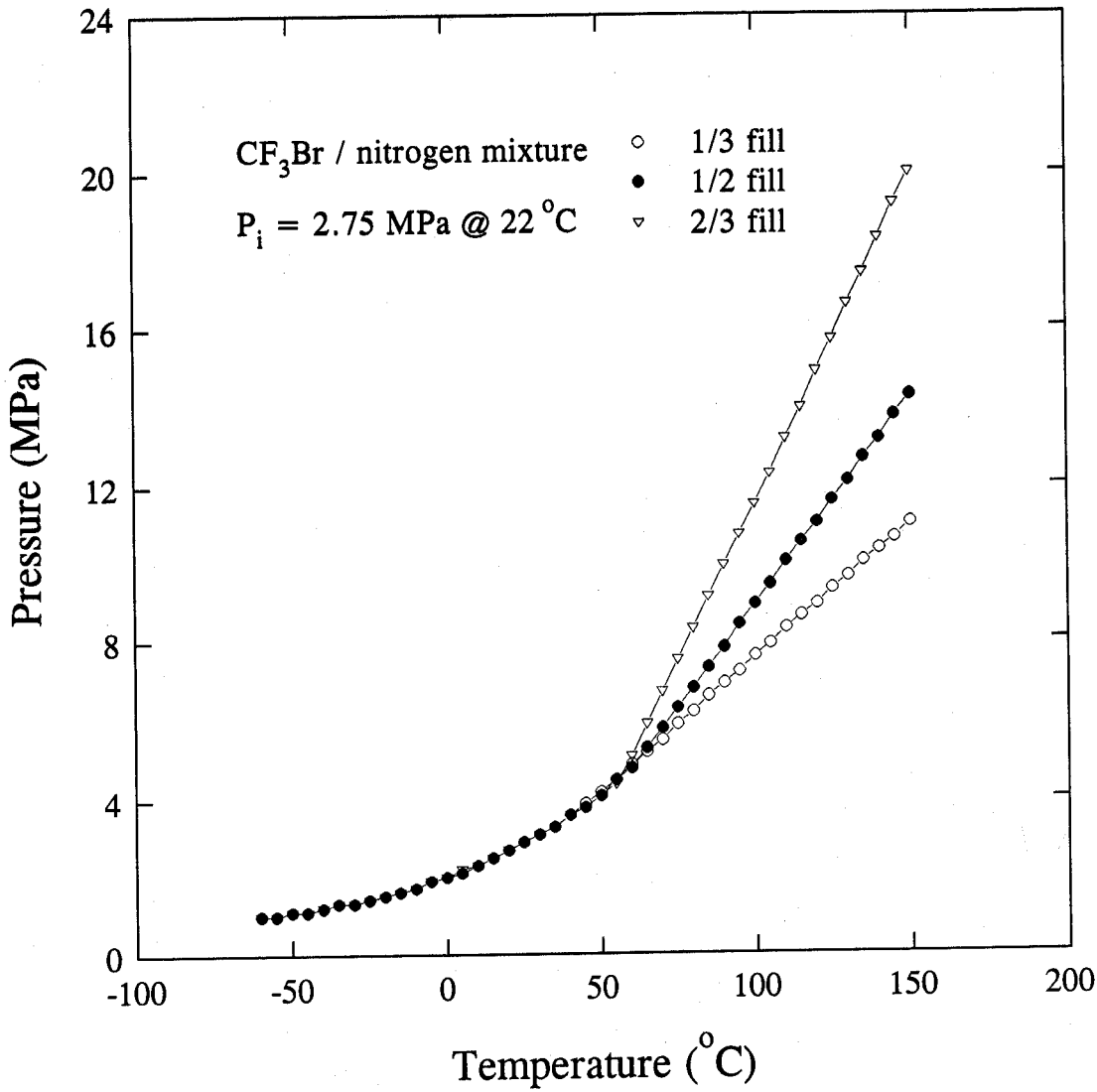


Figure A-13. Calculated pressure as a function of temperature for $\text{CF}_3\text{Br}/\text{N}_2$ mixture under three initial fill conditions and $P_i = 2.75$ MPa.

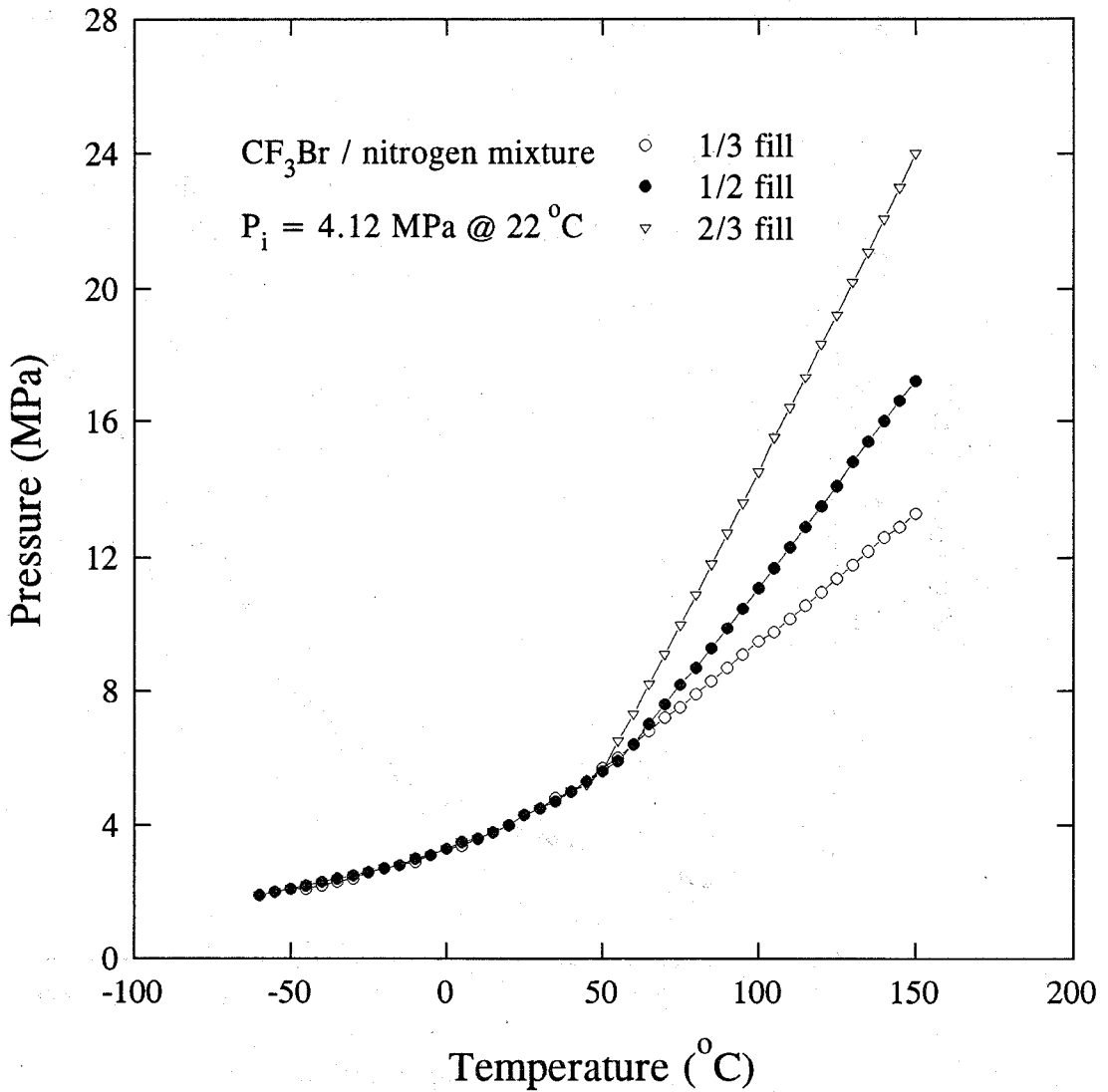


Figure A-14. Calculated pressure as a function of temperature for $\text{CF}_3\text{Br}/\text{N}_2$ mixture under three initial fill conditions and $P_i = 4.12$ MPa.

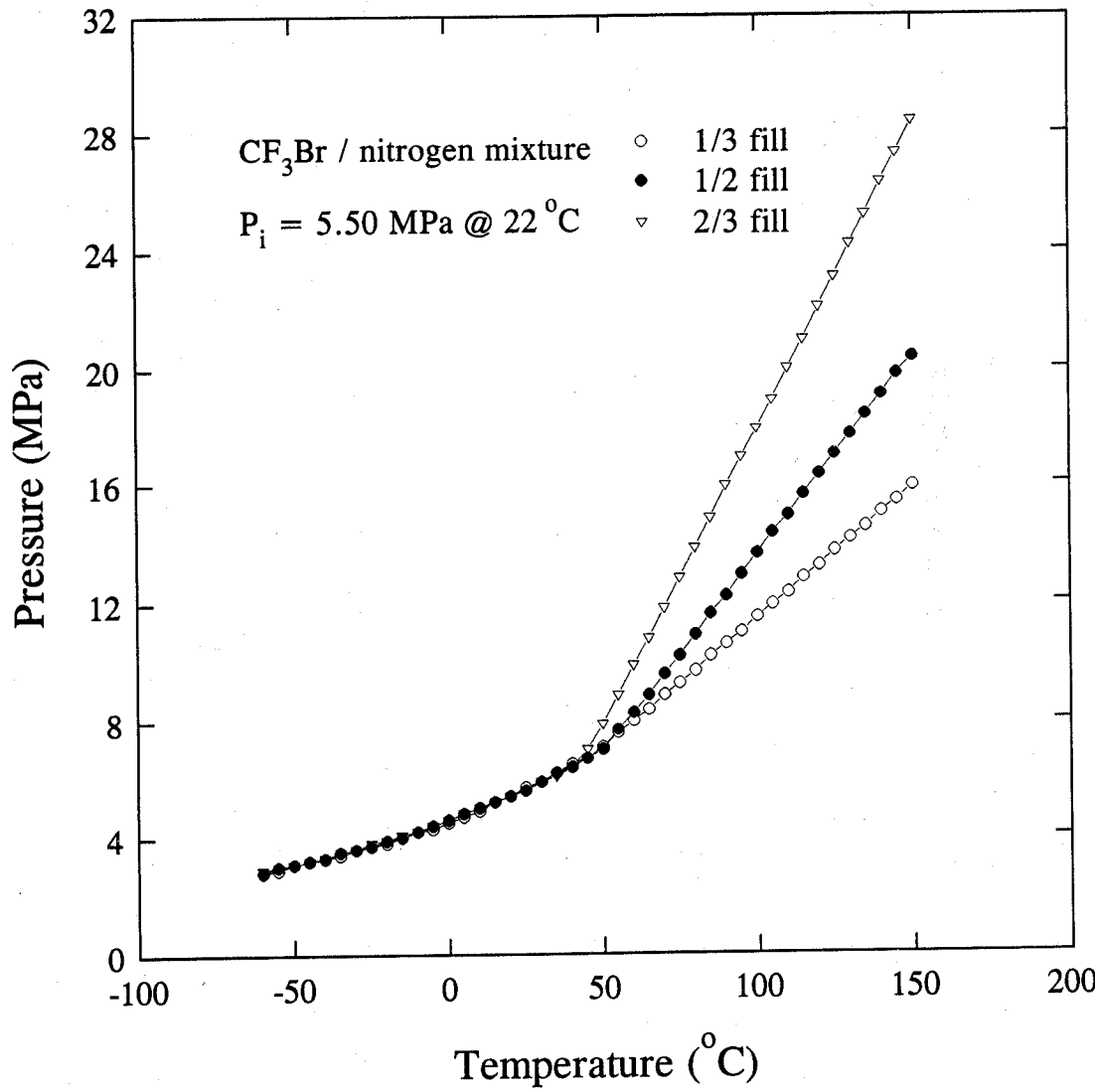


Figure A-15. Calculated pressure as a function of temperature for $\text{CF}_3\text{Br}/\text{N}_2$ mixture under three initial fill conditions and $P_i = 5.50$ MPa.

Appendix B. Tabulated fill Conditions and Pressure Traces for All Pipe Flow Discharge Tests

This Appendix lists the experimental conditions and results for all the pipe flow tests performed in this study. Table B-1 tabulates the temperatures and fill conditions for hot and cold agent discharge tests. Tables B-2 to B-5 tabulate the experimental conditions for halon 1301, HFC-125, HFC-227ea, and CF_3I , respectively. The fill volumes were estimated by the computer code, PROFISSY. The experimental results for halon 1301, HFC-125, HFC-227ea, and CF_3I are shown in Figures B-1 to B-25, Figures B-26 to B-50, Figures B-51 to B-76, and Figures B-77 to B-99, respectively. The individual pressure traces are not labeled on each figure, but follow the logical sequence of the vessel pressure being the highest, then followed in descending order by the pipe pressure traces for locations successively farther downstream. Finally, the pressure trace of the recover tank is the lowest. In some tests, not all pressures at each tap location were recorded. In those cases, the location of the tap where data was not taken is noted.

Table B-1. Temperature and fill conditions for hot and cold agent discharge tests

Agent	Figure number	Initial fill volume (%)	Liquid temp. (°C)	Gas temp. (°C)	Final pressure (± 0.05 MPa)	Equilibrium fill volume (%)	Equilibrium pressure (MPa)
CF ₃ Br	B-24	48.9	-50	4	2.20	41.8	2.0
	B-25	49.1	70	66	8.00	Single phase	7.4
HFC-125	B-49	46.4	-44	4	2.55	39.1	2.3
	B-50	49.3	68	73	7.40	Single phase	7.4
HFC-227ea	B-74	49.2	-45	4	3.00	43.5	2.8
	B-75	48.8	68	72	6.00	58.4	5.5
	B-76	49.0	70	68	5.95	59.8	5.6
CF ₃ I	B-98	50.4	-46	4	3.05	44.2	2.7
	B-99	49.7	70	70	5.70	56.7	5.7

Table B-2. Test fill conditions for halon 1301

Storage pressure (± 0.005 MPa)	Agent mass (± 0.01 kg)	Fill volume (%)	Diameter (mm)	Configuration	Figure number
2.00	3.30	N.A.	9.5	Straight pipe	B-1
2.50	3.11	N.A.	9.5	"	B-2
3.00	3.40	N.A.	9.5	"	B-3
2.77	3.26	46.6	9.5	"	B-4
4.12	2.88	40.8	9.5	"	B-5
4.15	3.00	43.1	9.5	"	B-6
4.12	3.15	45.9	9.5	"	B-7
4.12	3.39	50.4	9.5	"	B-8
4.12	4.21	65.7	9.5	"	B-9
4.12	3.31	48.9	9.5	3 m, 90° bend	B-10
4.12	3.32	49.1	9.5	4 m, 90° bend	B-11
4.12	3.28	48.3	15.9/9.5	Contraction	B-12
4.12	3.28	48.3	9.5/15.9	Expansion	B-13
2.00	4.09	N.A.	15.9	Straight pipe	B-14
2.50	3.83	N.A.	15.9	"	B-15
3.00	4.43	N.A.	15.9	"	B-16
2.75	3.52	51.1	15.9	"	B-17
4.12	3.25	47.8	15.9	"	B-18
4.12	3.35	49.6	15.9	"	B-19
4.12	4.20	65.5	15.9	"	B-20
4.12	3.30	48.7	15.9	3 m, 90° bend	B-21
4.12	3.30	48.7	15.9	4 m, 90° bend	B-22
4.12	3.26	47.9	15.9	"T" flow split	B-23
4.12	3.31	48.9	15.9	Cold	B-24
4.12	3.32	49.1	15.9	Hot	B-25

Table B-3. Test fill conditions for halon HFC-125

Storage pressure (± 0.005 MPa)	Agent mass (± 0.01 kg)	Fill volume (%)	Diameter (mm)	Configuration	Figure number
2.00	2.51	N.A.	9.5	Straight pipe	B-26
2.50	2.92	N.A.	9.5	"	B-27
3.00	2.53	N.A.	9.5	"	B-28
4.12	3.69	N.A.	9.5	"	B-29
2.76	2.62	50.4	9.5	"	B-30
4.13	2.78	56.4	9.5	"	B-31
4.16	3.33	69.9	9.5	"	B-32
4.12	2.40	47.1	9.5	3 m, 90° bend	B-33
4.12	2.44	48.1	9.5	4 m, 90° bend	B-34
4.12	2.50	49.6	15.9/9.5	Contraction	B-35
4.12	2.51	49.8	9.5/15.9	Expansion	B-36
2.00	2.72	N.A.	15.9	Straight pipe	B-37
2.55	3.29	N.A.	15.9	"	B-38
3.00	2.81	N.A.	15.9	"	B-39
2.75	2.79	54.2	15.9	"	B-40
4.12	2.50	49.6	15.9	"	B-41
4.12	2.63	52.7	15.9	"	B-42
4.12	2.64	53.0	15.9	"	<u>B-43</u>
4.12	3.17	65.9	15.9	"	<u>B-44</u>
4.14	3.82	81.8	15.9	"	<u>B-45</u>
4.12	2.47	48.8	15.9	3 m, 90° bend	B-46
4.12	2.38	46.6	15.9	4 m, 90° bend	B-47
4.12	2.70	54.4	15.9	"T" flow split	B-48
4.12	2.37	46.4	15.9	Cold	B-49
4.12	2.49	49.3	15.9	Hot	B-50

Table B-4. Test fill conditions for halon HFC-227ea

Storage pressure (± 0.005 MPa)	Agent mass (± 0.01 kg)	Fill volume (%)	Diameter (mm)	Configuration	Figure number
2.00	3.31	N.A.	9.5	Straight pipe	B-51
2.50	3.18	N.A.	9.5	"	B-52
3.00	3.24	N.A.	9.5	"	B-53
2.75	3.26	56.5	9.5	"	B-54
4.12	3.05	53.7	9.5	"	B-55
4.12	3.36	60.2	9.5	"	B-56
4.12	3.91	70.0	9.5	"	B-57
4.12	2.81	49.2	9.5	3 m, 90° bend	B-58
4.12	2.81	49.2	9.5	4 m, 90° bend	B-59
4.12	2.80	49.0	15.9/9.5	Contraction	B-60
4.12	2.80	49.0	9.5/15.9	Expansion	B-61
2.00	3.74	N.A.	15.9	Straight pipe	B-62
2.50	2.73	N.A.	15.9	"	B-63
2.50	3.65	N.A.	15.9	"	B-64
3.00	3.56	N.A.	15.9	"	B-65
2.75	3.13	54.1	15.9	"	B-66
4.12	2.77	48.4	15.9	"	B-67
4.12	2.82	49.4	15.9	"	B-68
4.12	3.23	57.1	15.9	"	B-69
4.12	3.88	69.4	15.9	"	B-70
4.12	2.82	49.4	15.9	3 m, 90° bend	B-71
4.12	2.79	48.8	15.9	4 m, 90° bend	B-72
4.12	2.77	48.4	15.9	"T" flow split	B-73
4.12	2.81	49.2	15.9	Cold	B-74
4.12	2.79	48.8	15.9	Hot	B-75
4.12	2.80	49.0	15.9	Hot	B-76

Table B-5. Test fill conditions for CF₃I

Storage pressure (± 0.005 MPa)	Agent mass (± 0.01 kg)	Fill volume (%)	Diameter (mm)	Configuration	Figure number
2.00	5.40	N.A.	9.5	Straight pipe	B-77
2.50	5.58	N.A.	9.5	"	B-78
3.00	5.22	N.A.	9.5	"	B-79
2.75	4.34	49.7	9.5	"	B-80
4.13	4.31	50.2	9.5	"	B-81
4.12	5.57	65.8	9.5	"	B-82
4.12	5.74	67.9	9.5	"	B-83
4.12	4.46	52.0	9.5	3 m, 90° bend	B-84
4.12	4.39	51.2	9.5	4 m, 90° bend	B-85
4.12	4.49	52.4	15.9/9.5	Contraction	B-86
4.12	4.60	53.8	9.5/15.9	Expansion	B-87
2.00	4.03	N.A.	15.9	Straight pipe	B-88
2.50	4.21	N.A.	15.9	"	B-89
2.50	6.27	N.A.	15.9	"	B-90
3.00	4.32	N.A.	15.9	"	B-91
2.80	4.33	49.6	15.9	"	B-92
4.13	4.19	48.7	15.9	"	B-93
4.20	5.76	68.2	15.9	"	B-94
4.17	4.24	49.4	15.9	3 m, 90° bend	B-95
4.14	4.71	55.2	15.9	4 m, 90° bend	B-96
4.12	4.29	49.9	15.9	"T" flow split	B-97
4.19	4.32	50.4	15.9	Cold	B-98
4.12	4.27	49.7	15.9	Hot	B-99

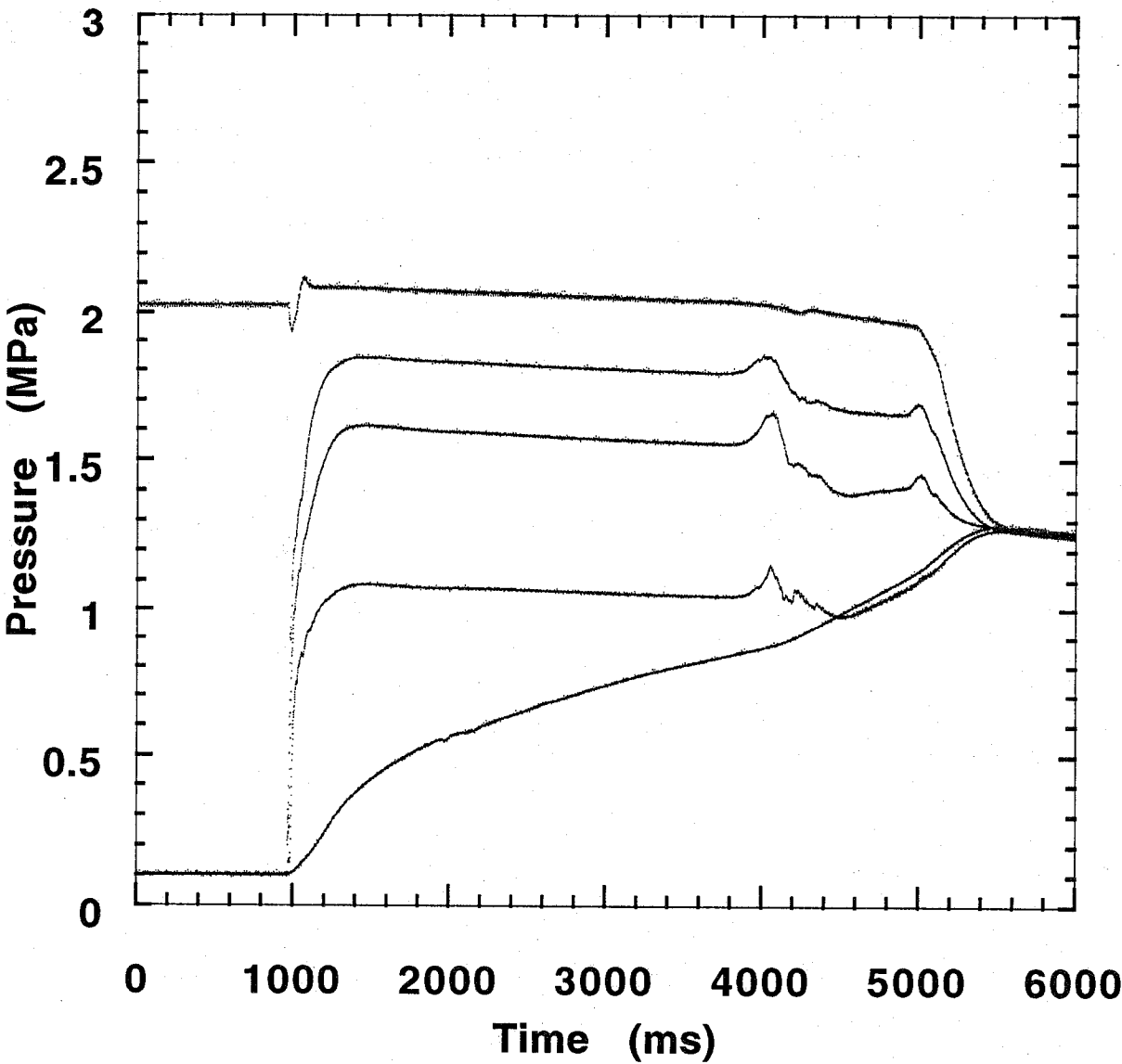


Figure B-1. Halon 1301 test. Refer to Table B-2 for experimental conditions.

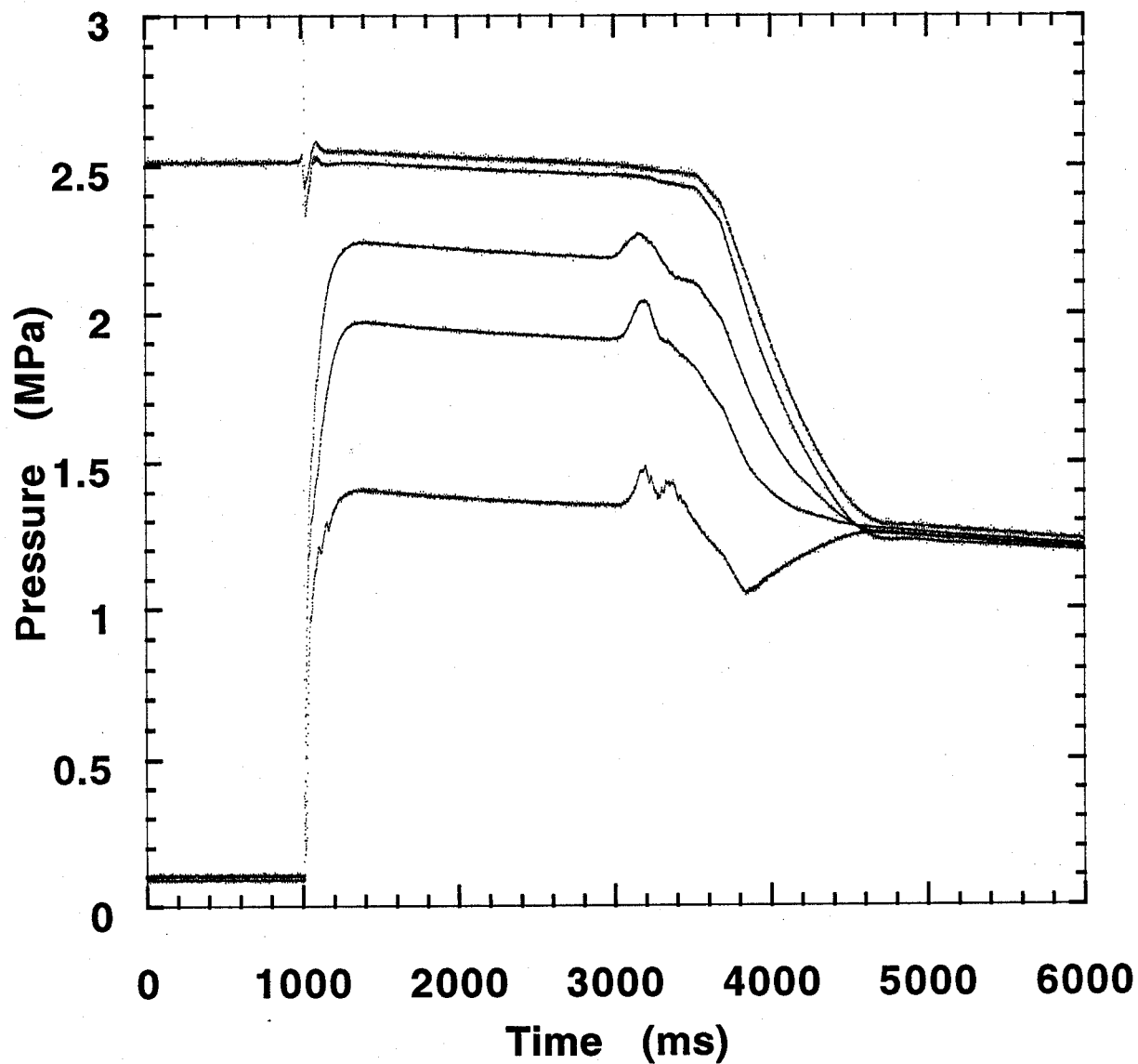


Figure B-2. Halon 1301 test. Refer to Table B-2 for experimental conditions.

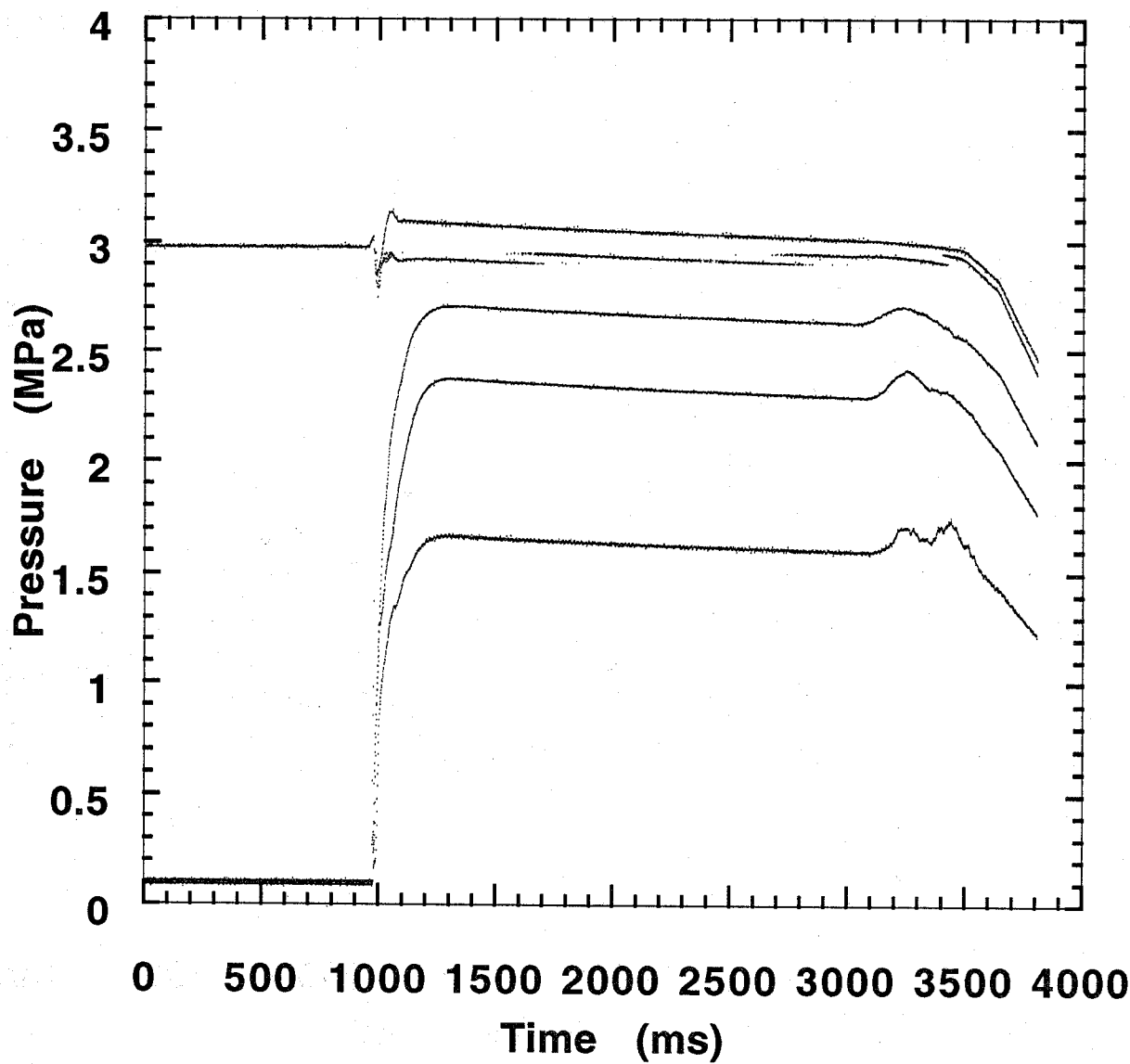


Figure B-3. Halon 1301 test. Refer to Table B-2 for experimental conditions.

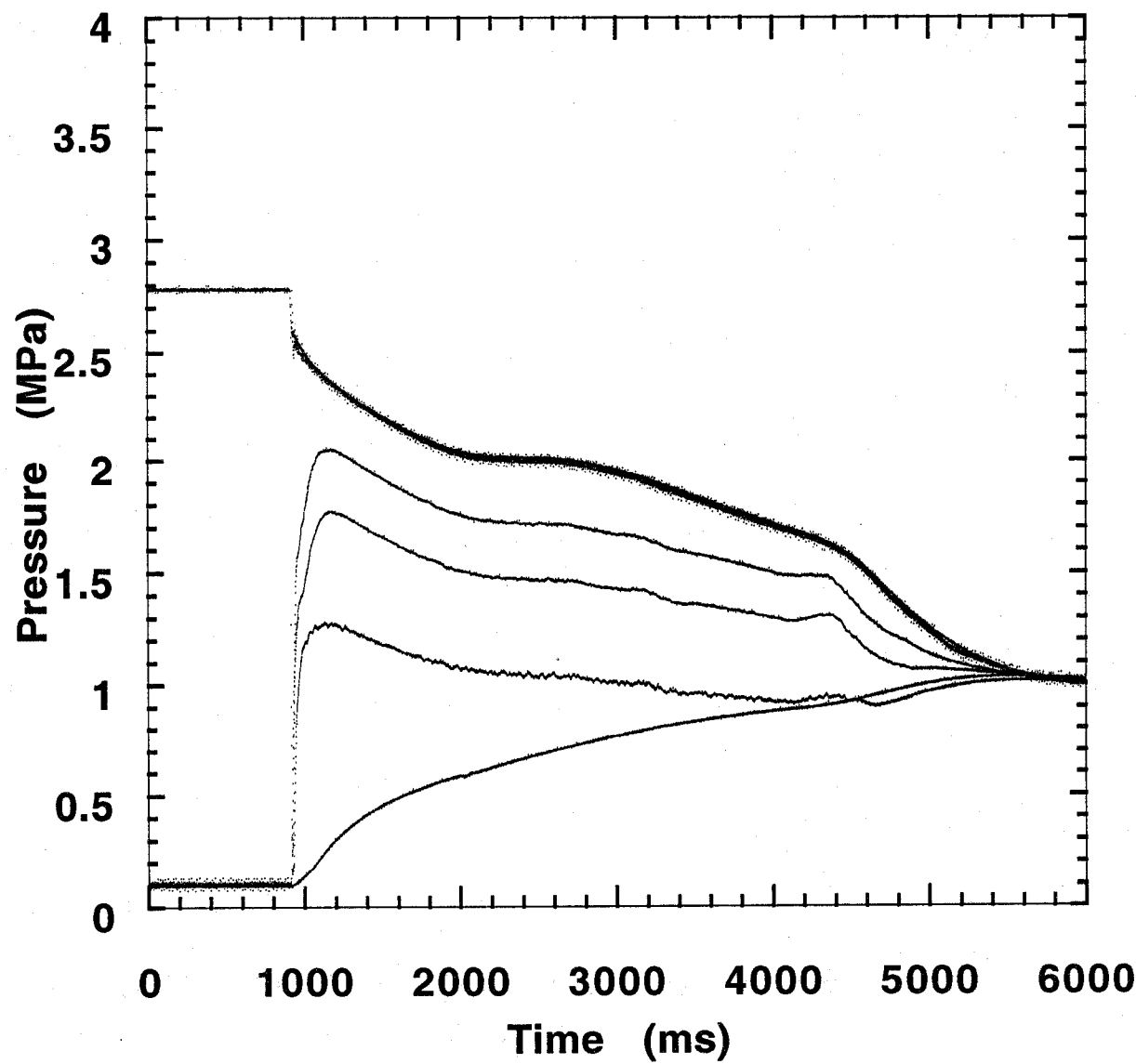


Figure B-4. Halon 1301 test. Refer to Table B-2 for experimental conditions.

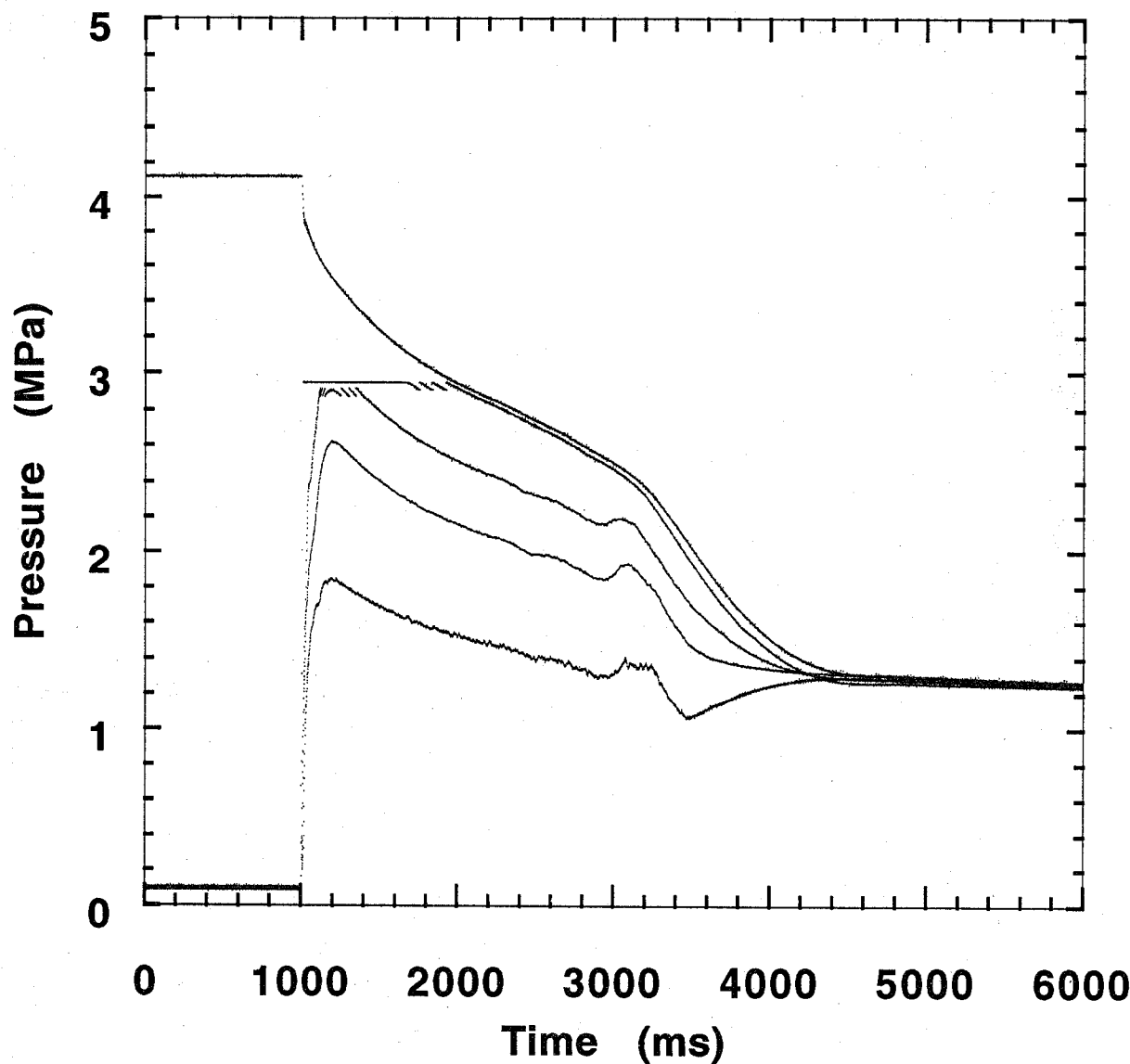


Figure B-5. Halon 1301 test. Refer to Table B-2 for experimental conditions.

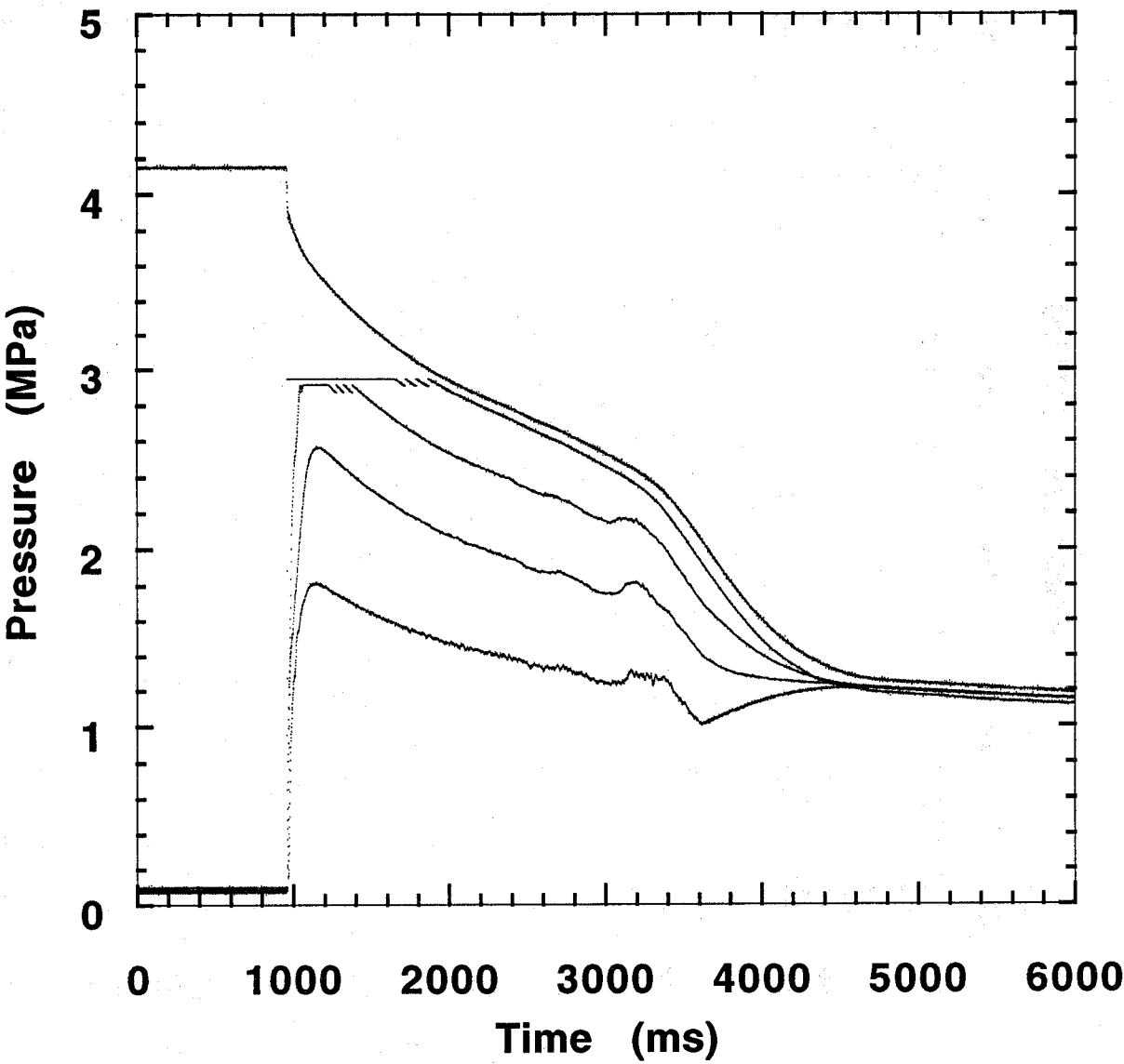


Figure B-6. Halon 1301 test. Refer to Table B-2 for experimental conditions.

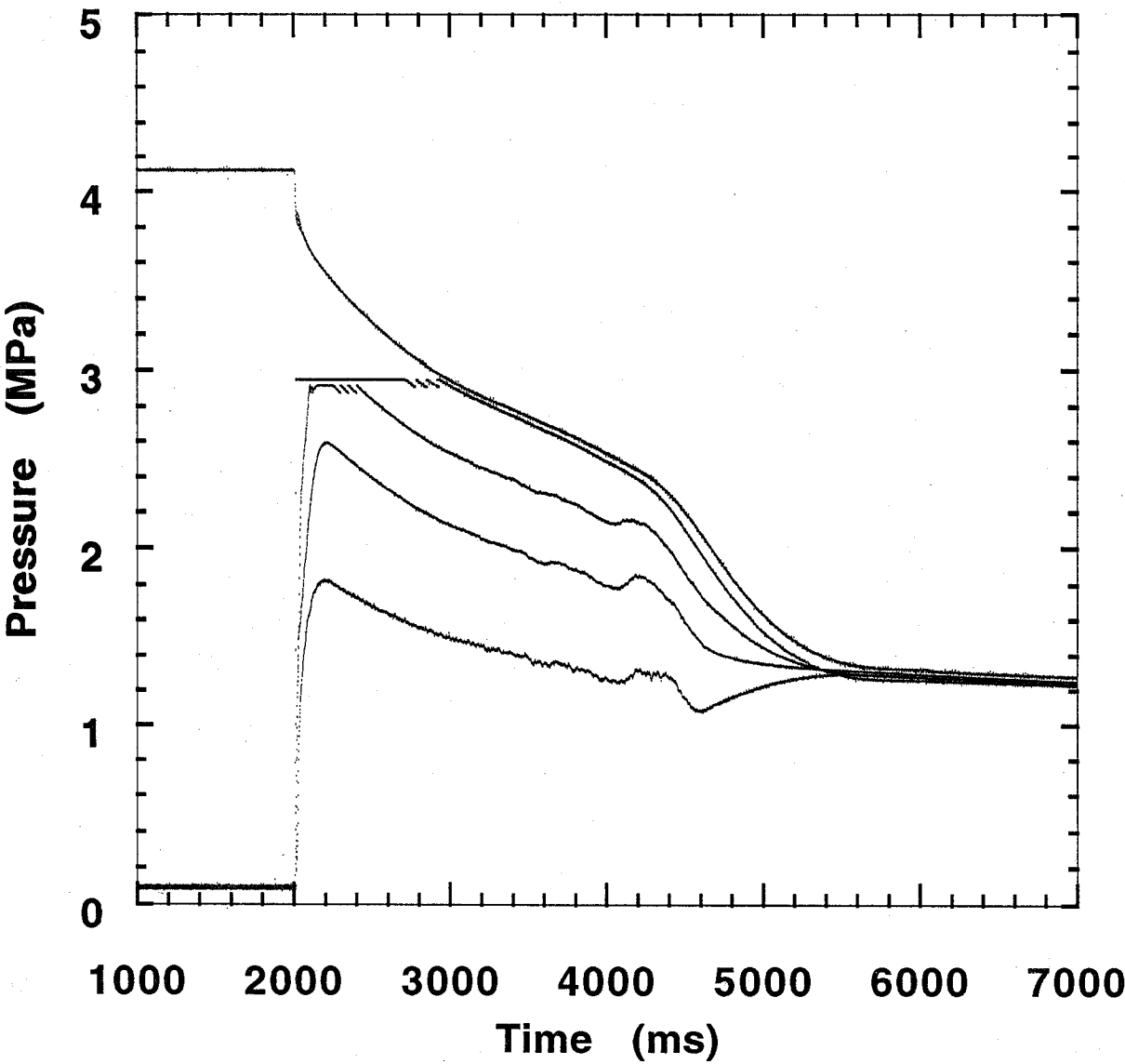


Figure B-7. Halon 1301 test. Refer to Table B-2 for experimental conditions.

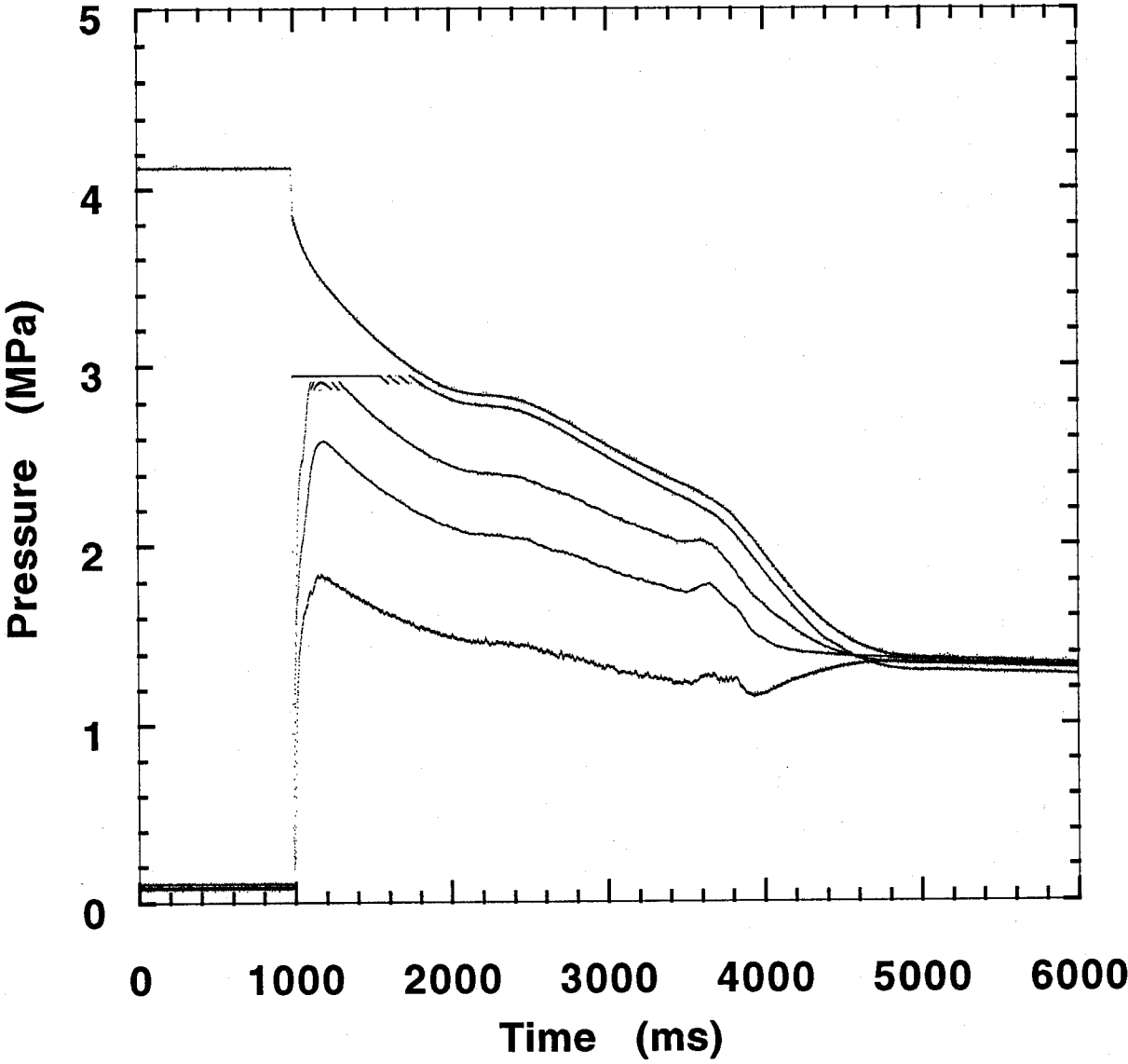


Figure B-8. Halon 1301 test. Refer to Table B-2 for experimental conditions.

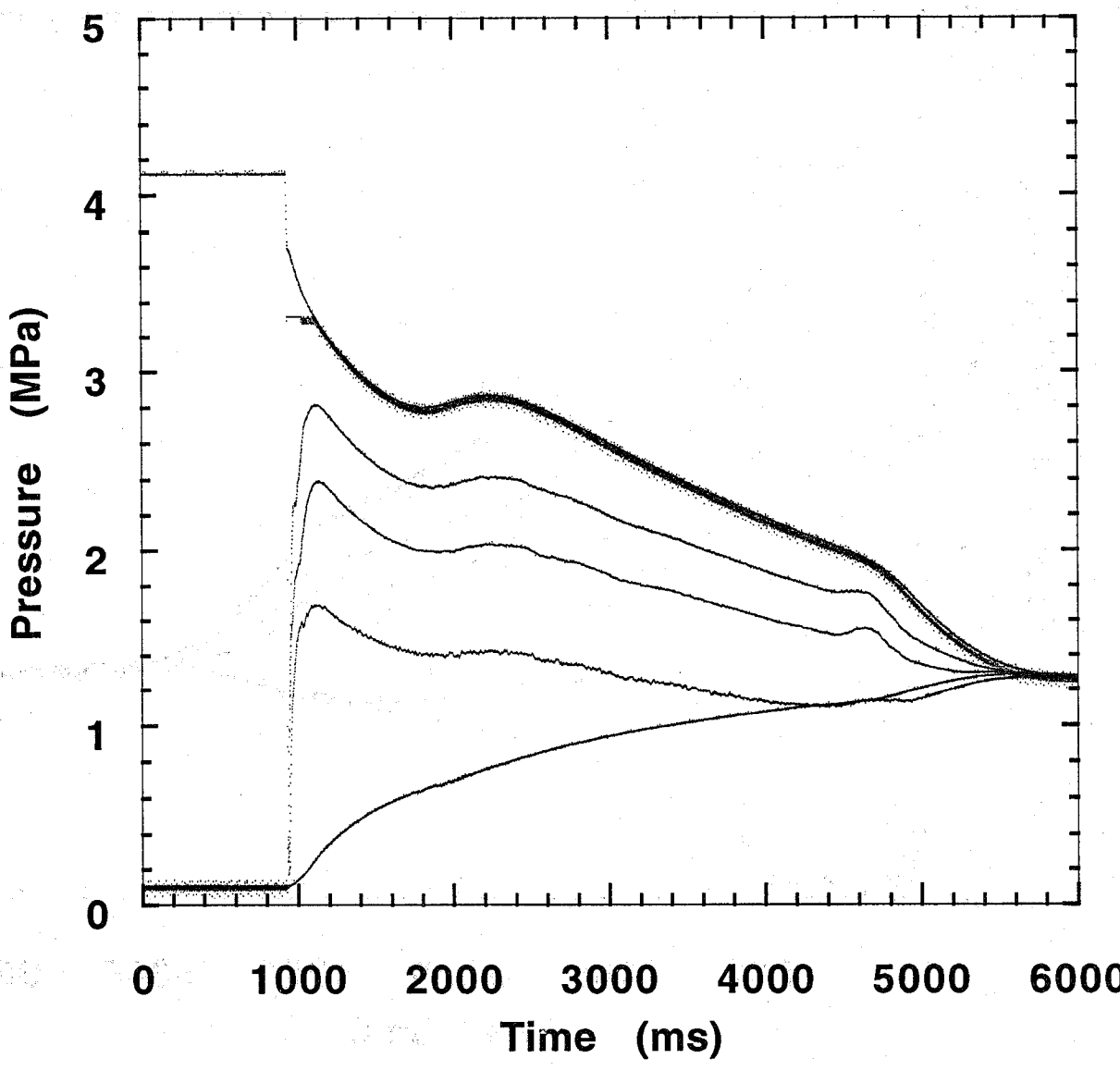


Figure B-9. Halon 1301 test. Refer to Table B-2 for experimental conditions.

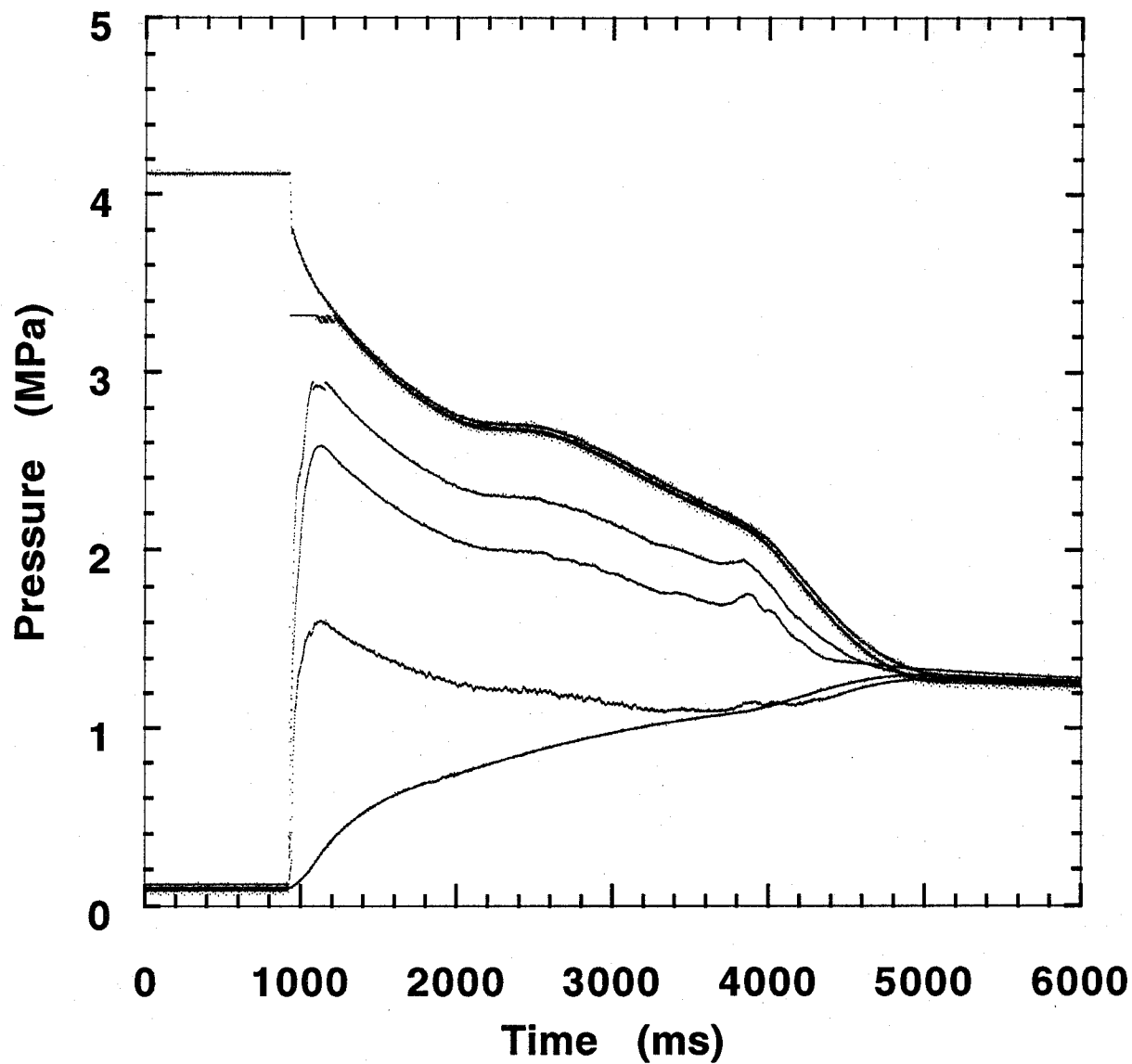


Figure B-10. Halon 1301 test. Refer to Table B-2 for experimental conditions.

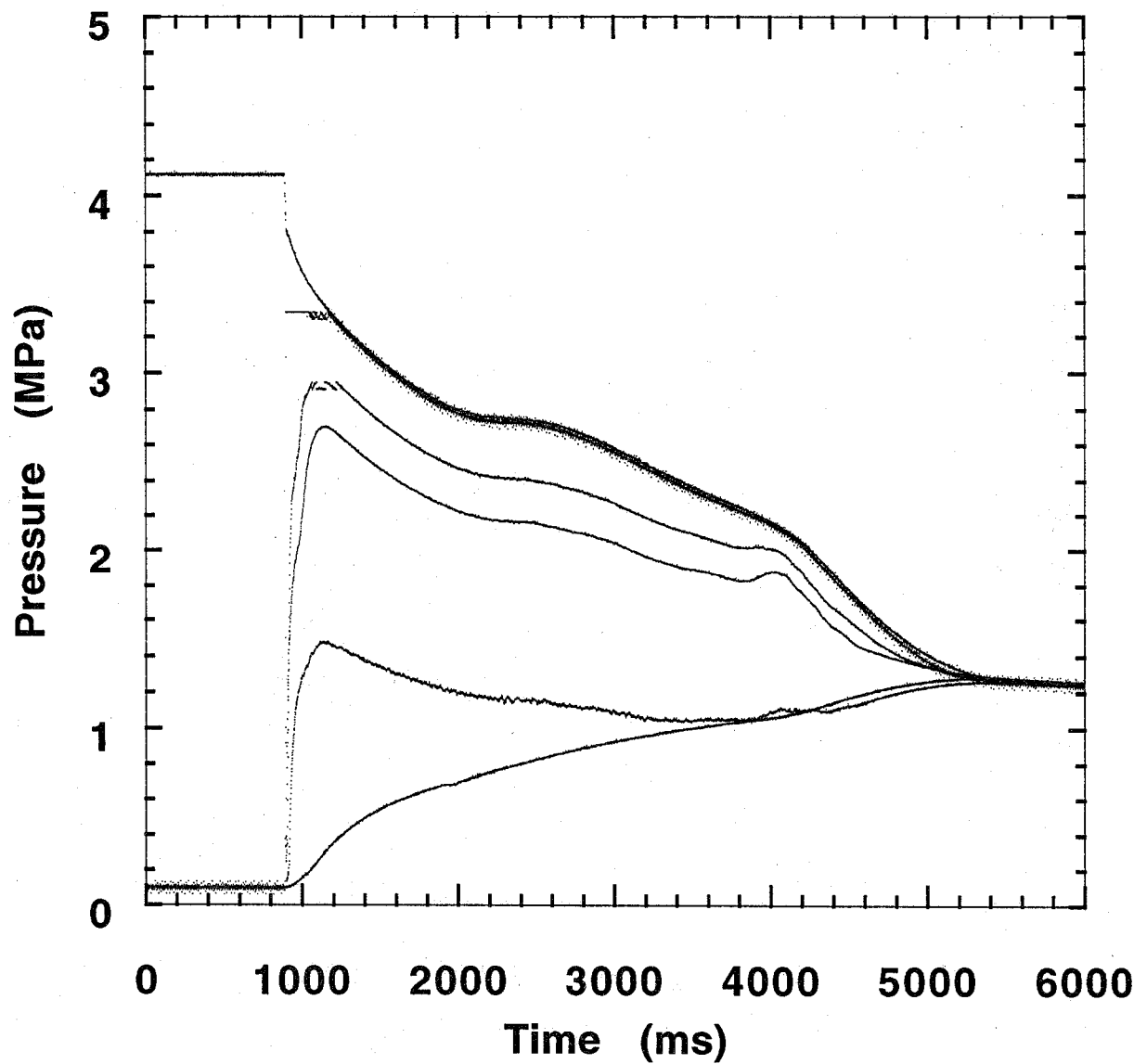


Figure B-11. Halon 1301 test. Refer to Table B-2 for experimental conditions.

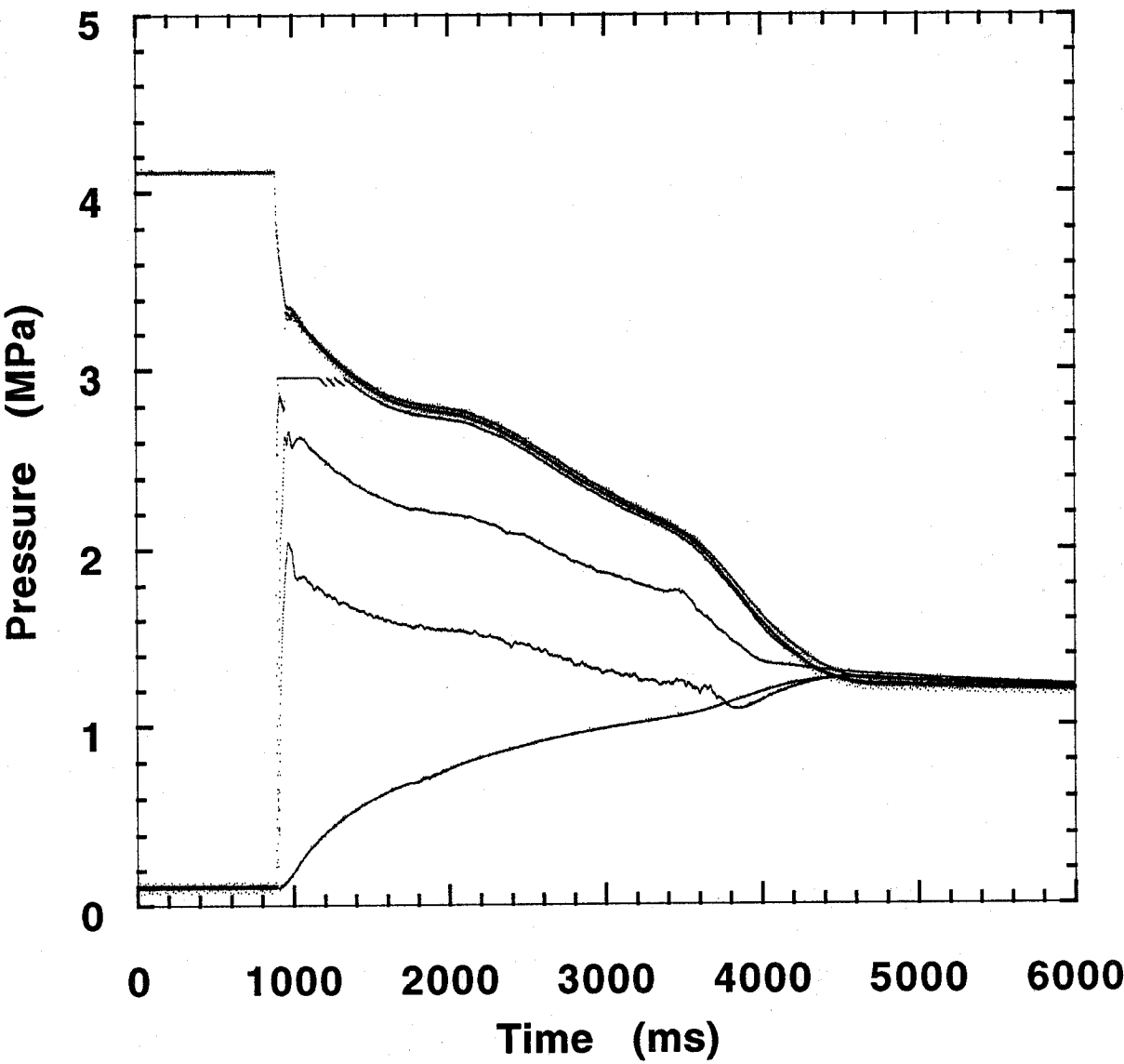


Figure B-12. Halon 1301 test. Refer to Table B-2 for experimental conditions.

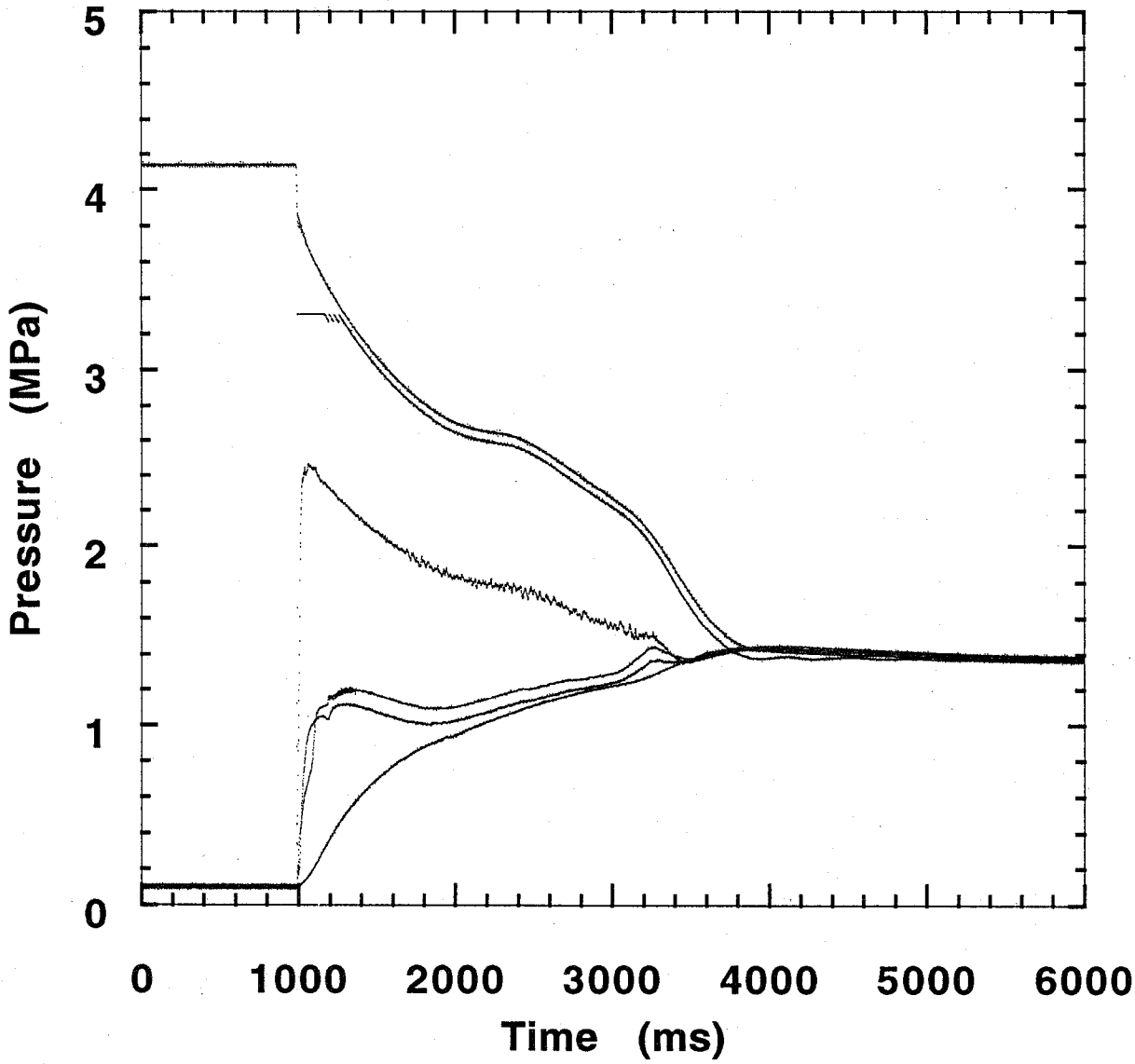


Figure B-13. Halon 1301 test. Refer to Table B-2 for experimental conditions.

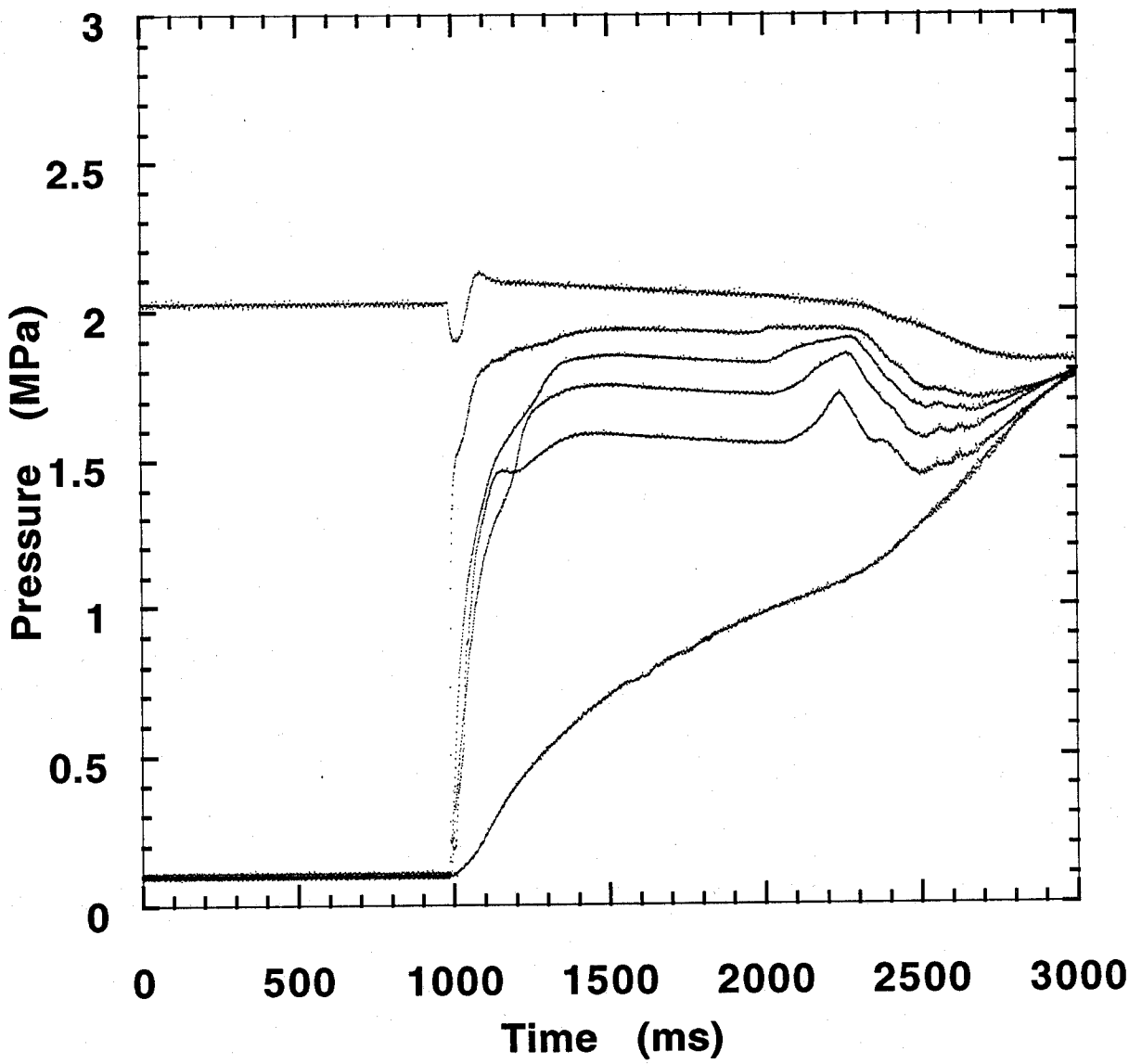


Figure B-14. Halon 1301 test. Refer to Table B-2 for experimental conditions.

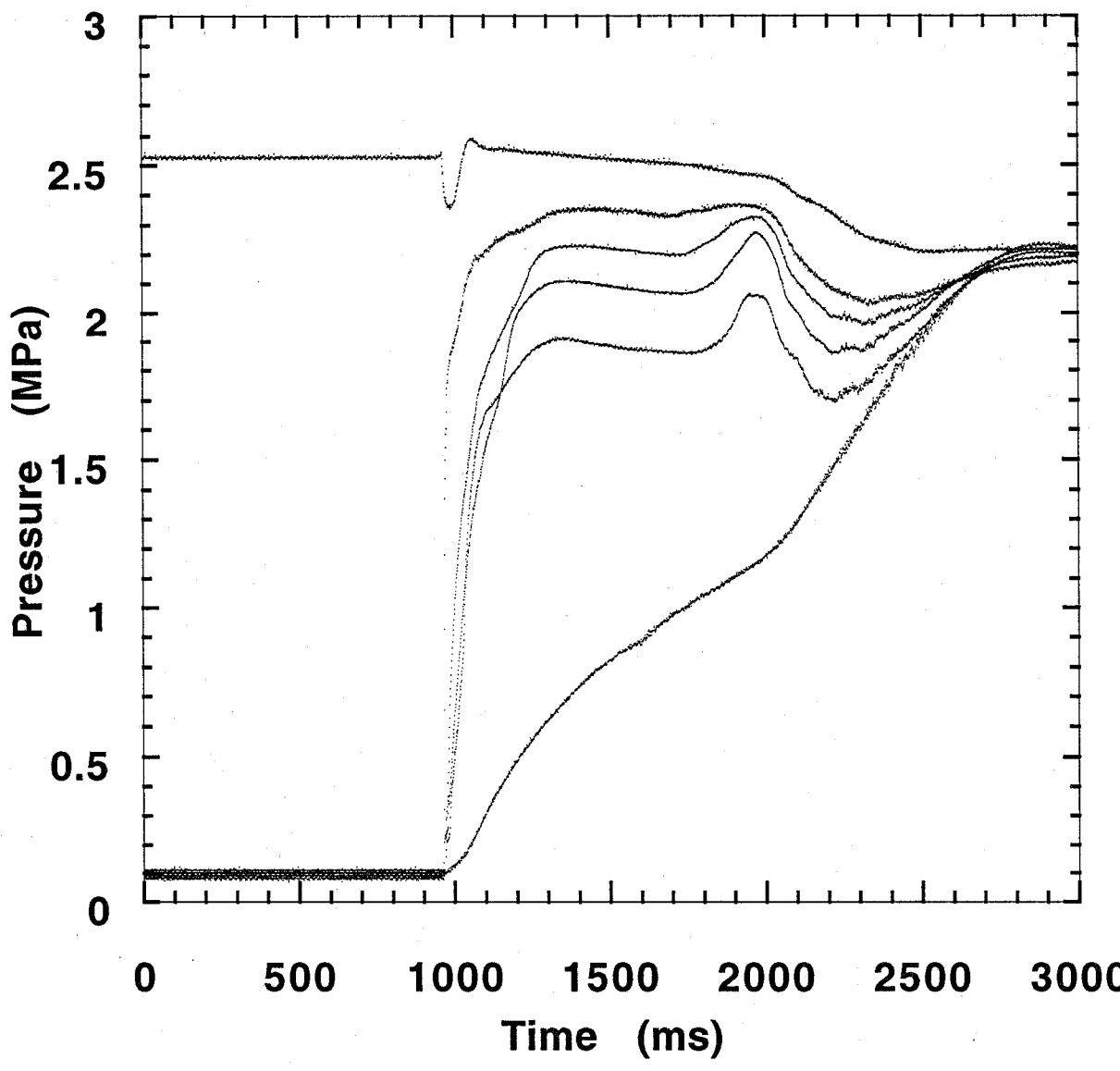


Figure B-15. Halon 1301 test. Refer to Table B-2 for experimental conditions.

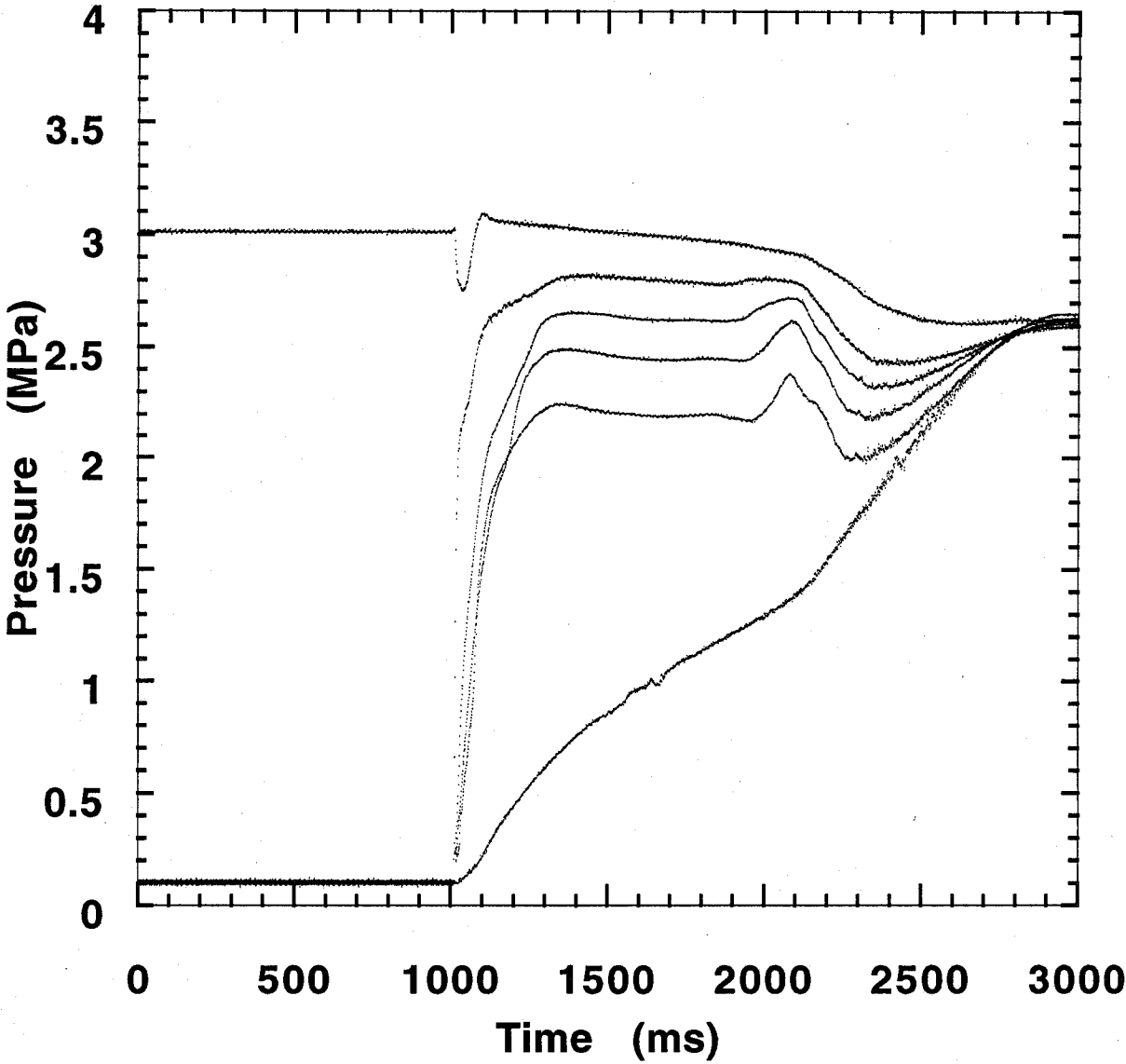


Figure B-16. Halon 1301 test. Refer to Table B-2 for experimental conditions.

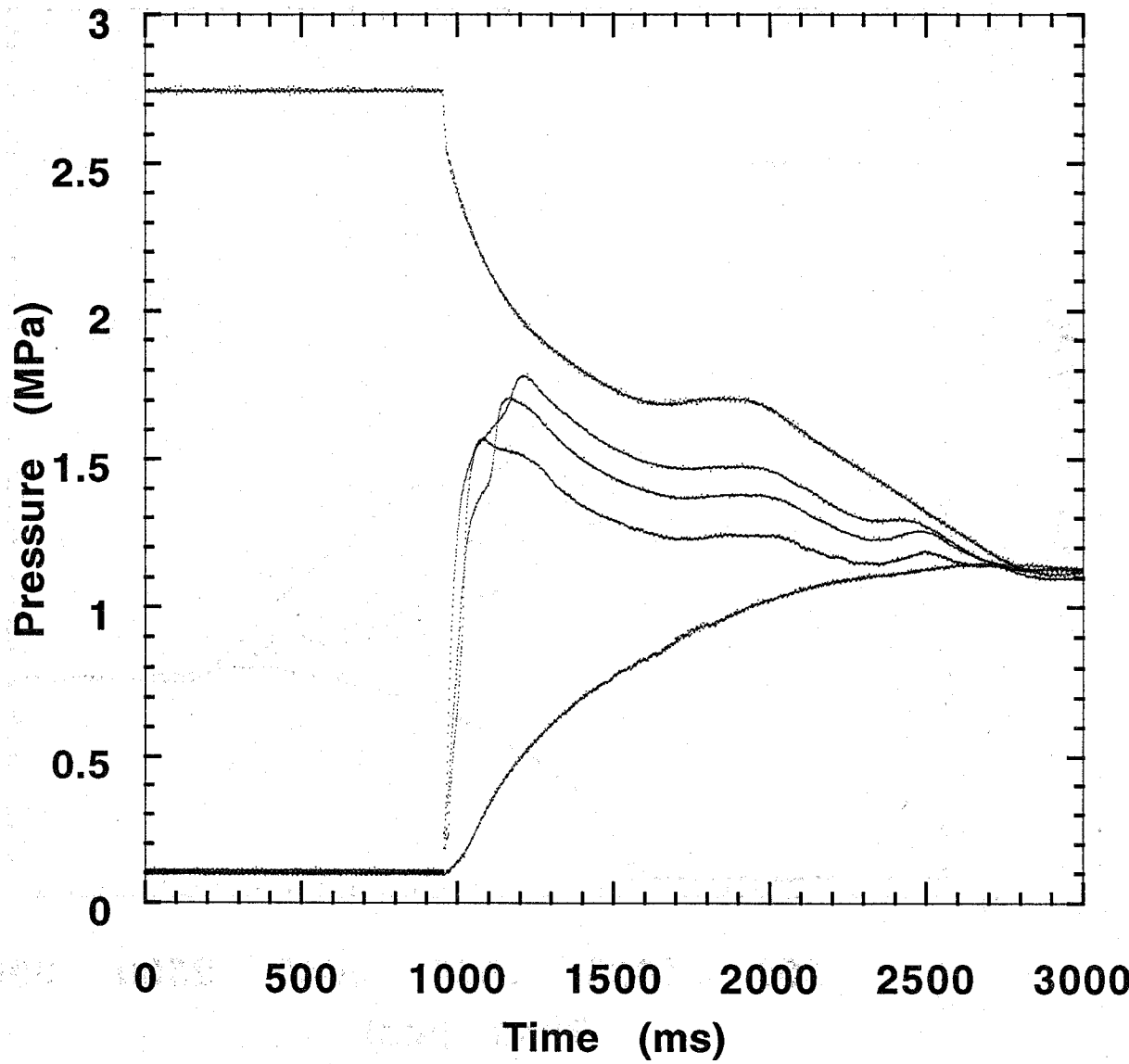


Figure B-17. Halon 1301 test. Refer to Table B-2 for experimental conditions.

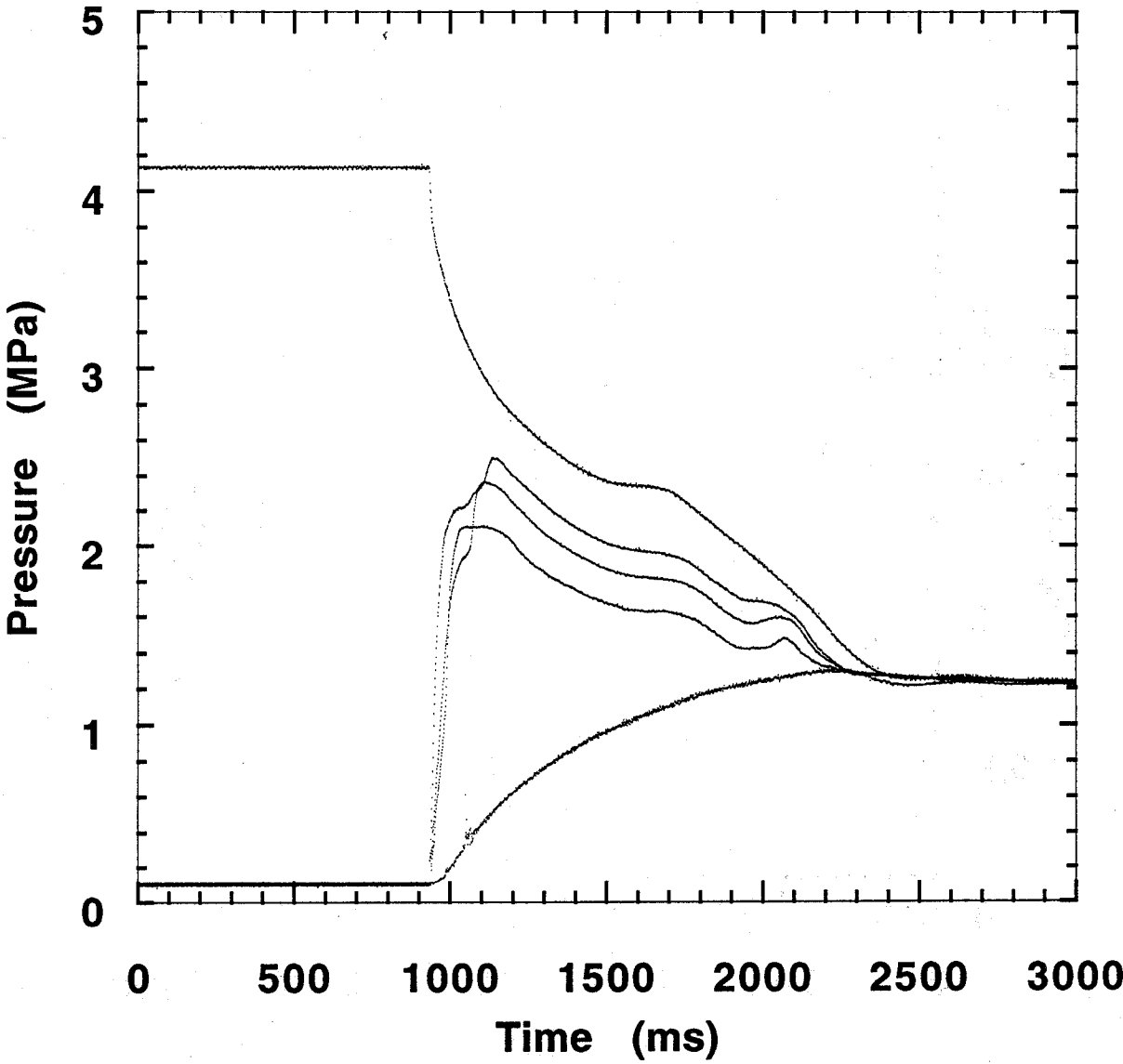


Figure B-18. Halon 1301 test. Refer to Table B-2 for experimental conditions.

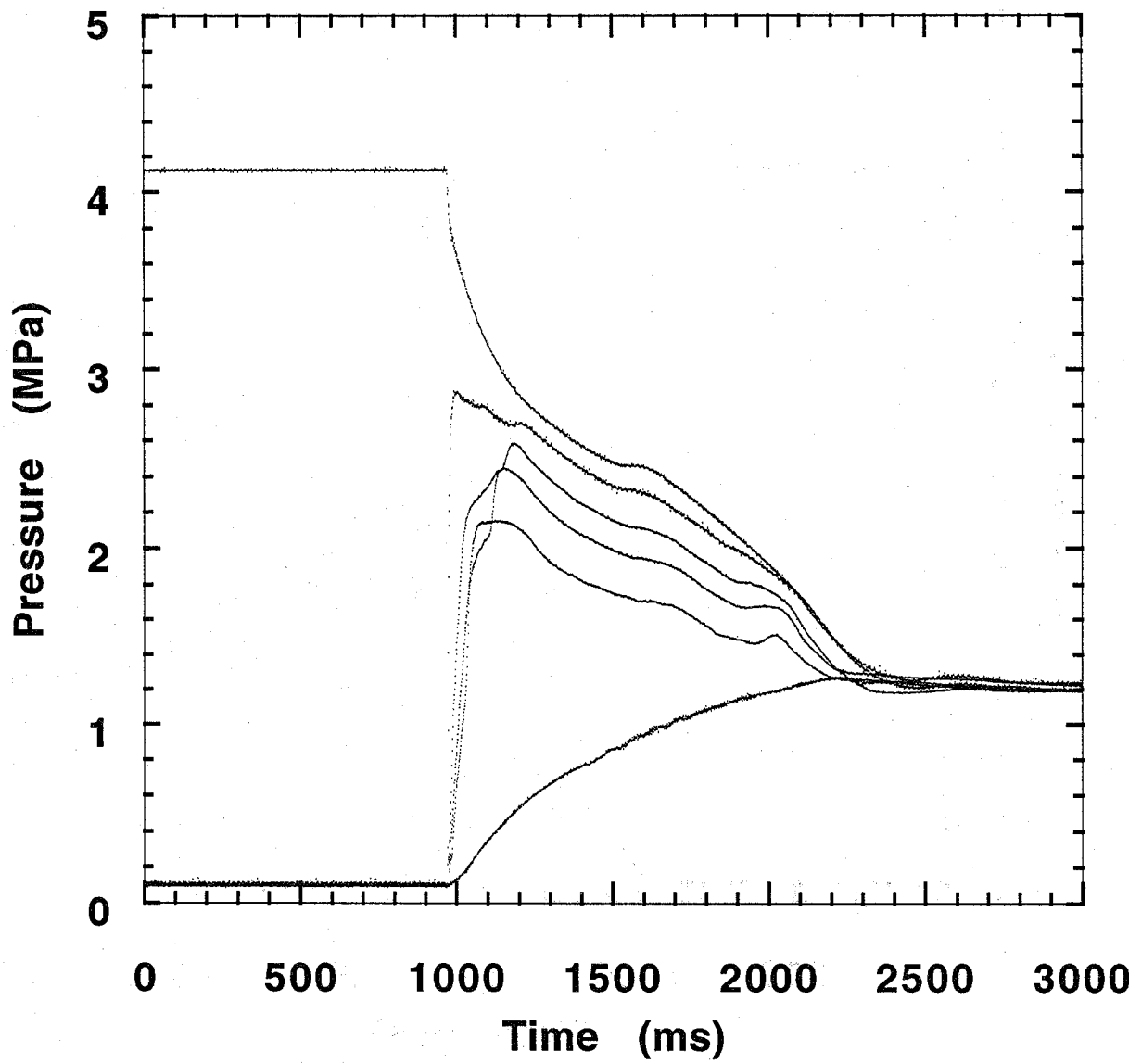


Figure B-19. Halon 1301 test. Refer to Table B-2 for experimental conditions.

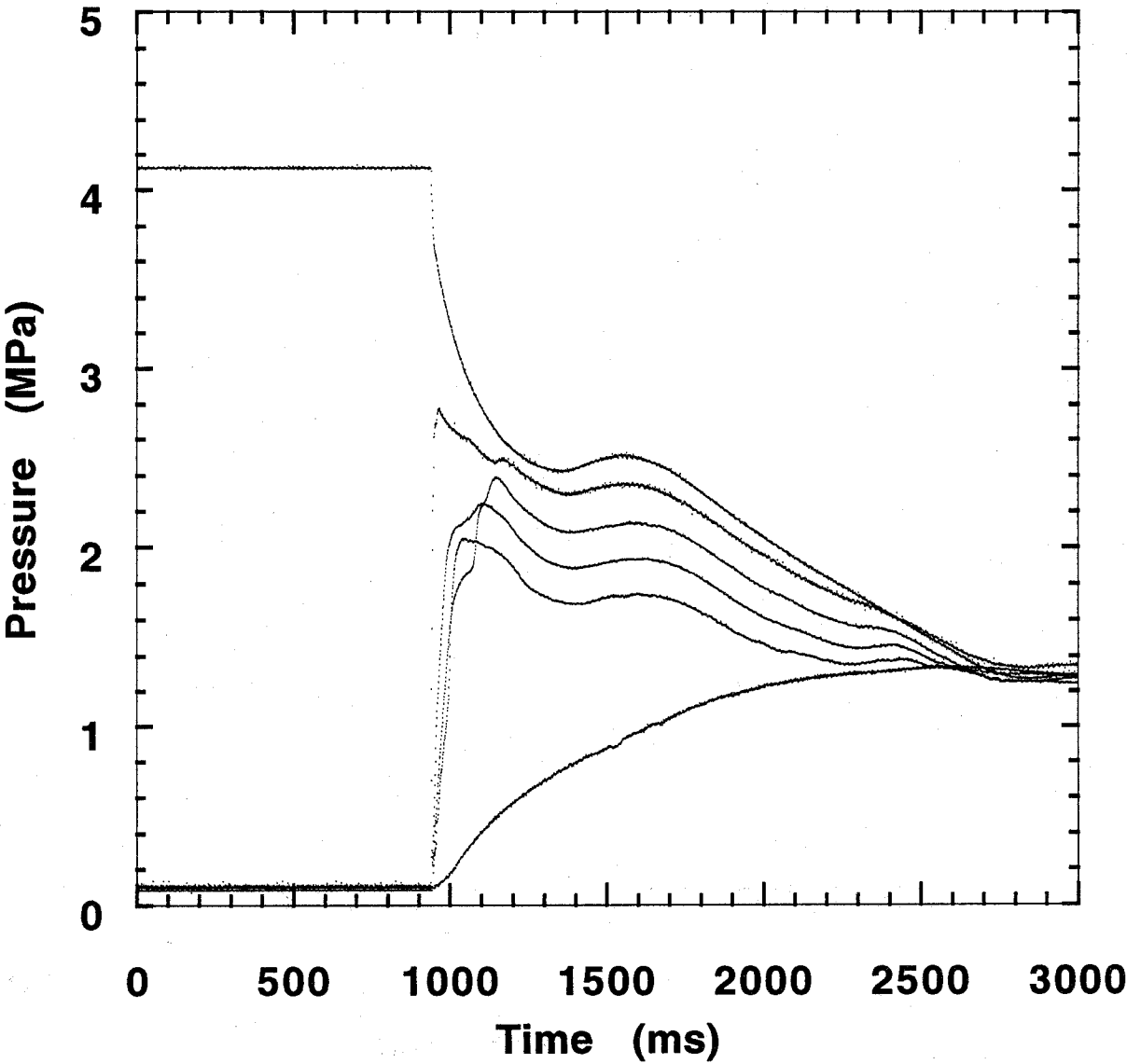


Figure B-20. Halon 1301 test. Refer to Table B-2 for experimental conditions.

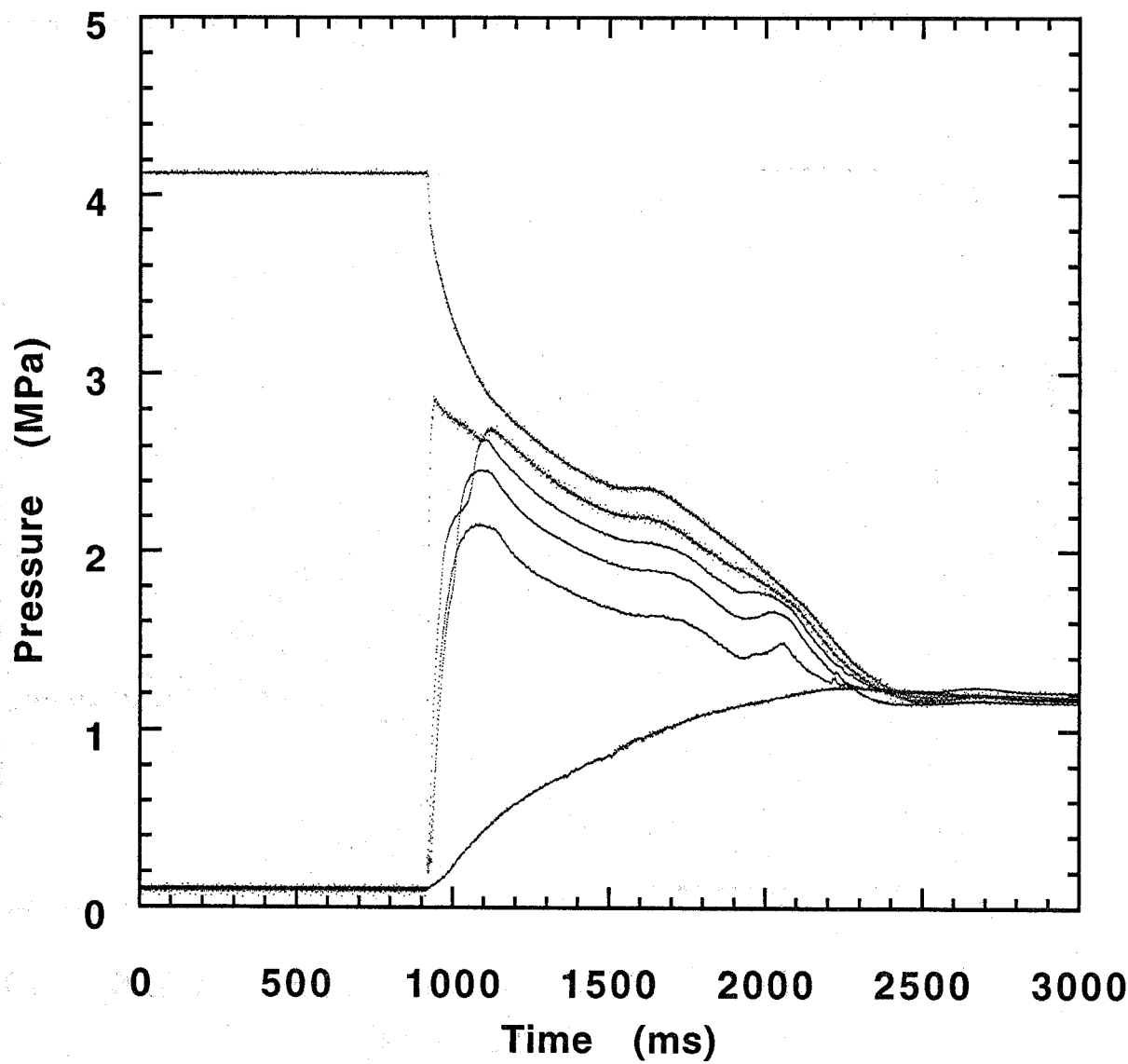


Figure B-21. Halon 1301 test. Refer to Table B-2 for experimental conditions.

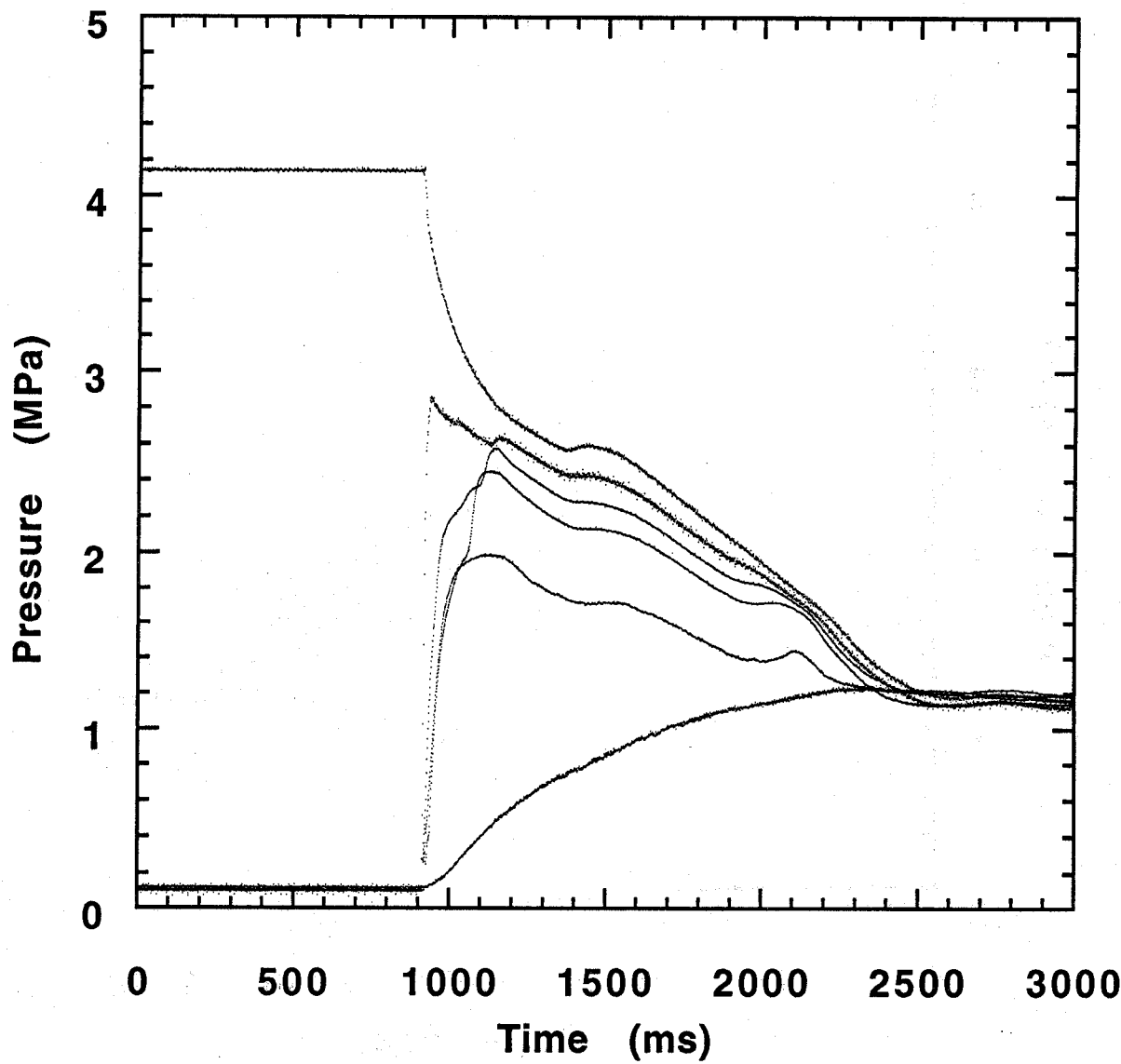


Figure B-22. Halon 1301 test. Refer to Table B-2 for experimental conditions.

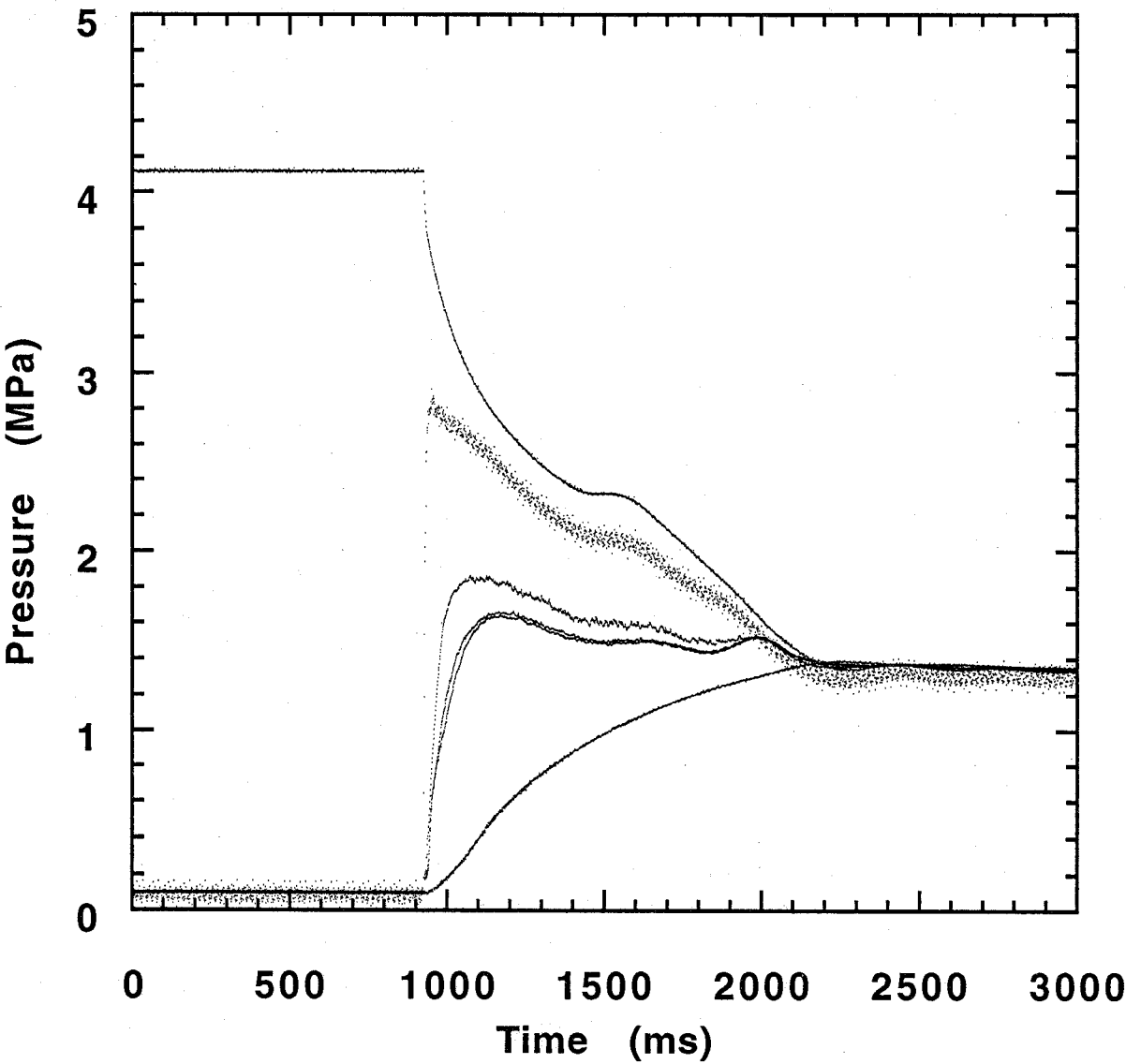


Figure B-23. Halon 1301 test. Refer to Table B-2 for experimental conditions.

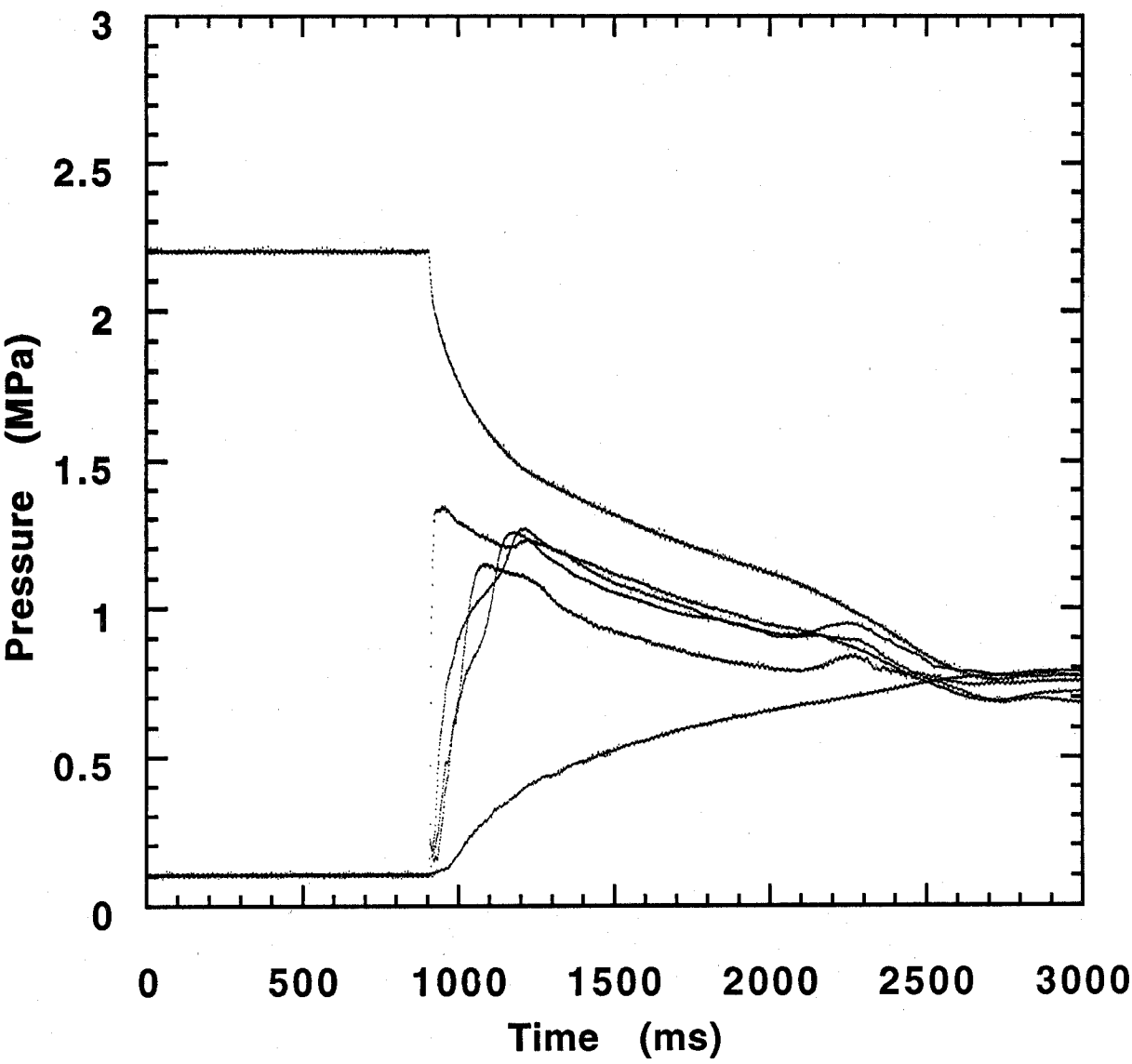


Figure B-24. Halon 1301 test. Refer to Table B-2 for experimental conditions.

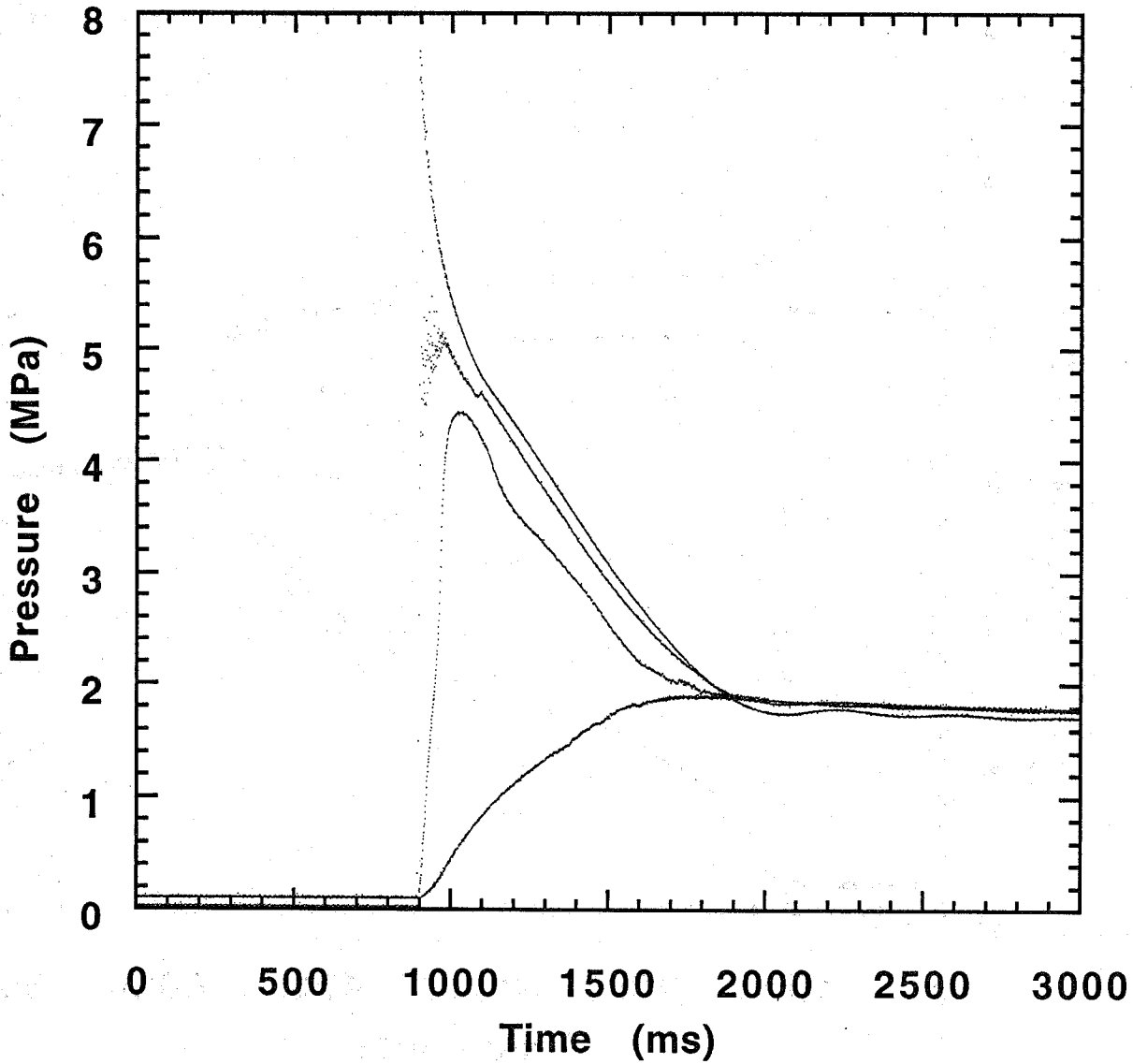


Figure B-25. Halon 1301 test. Refer to Table B-2 for experimental conditions.

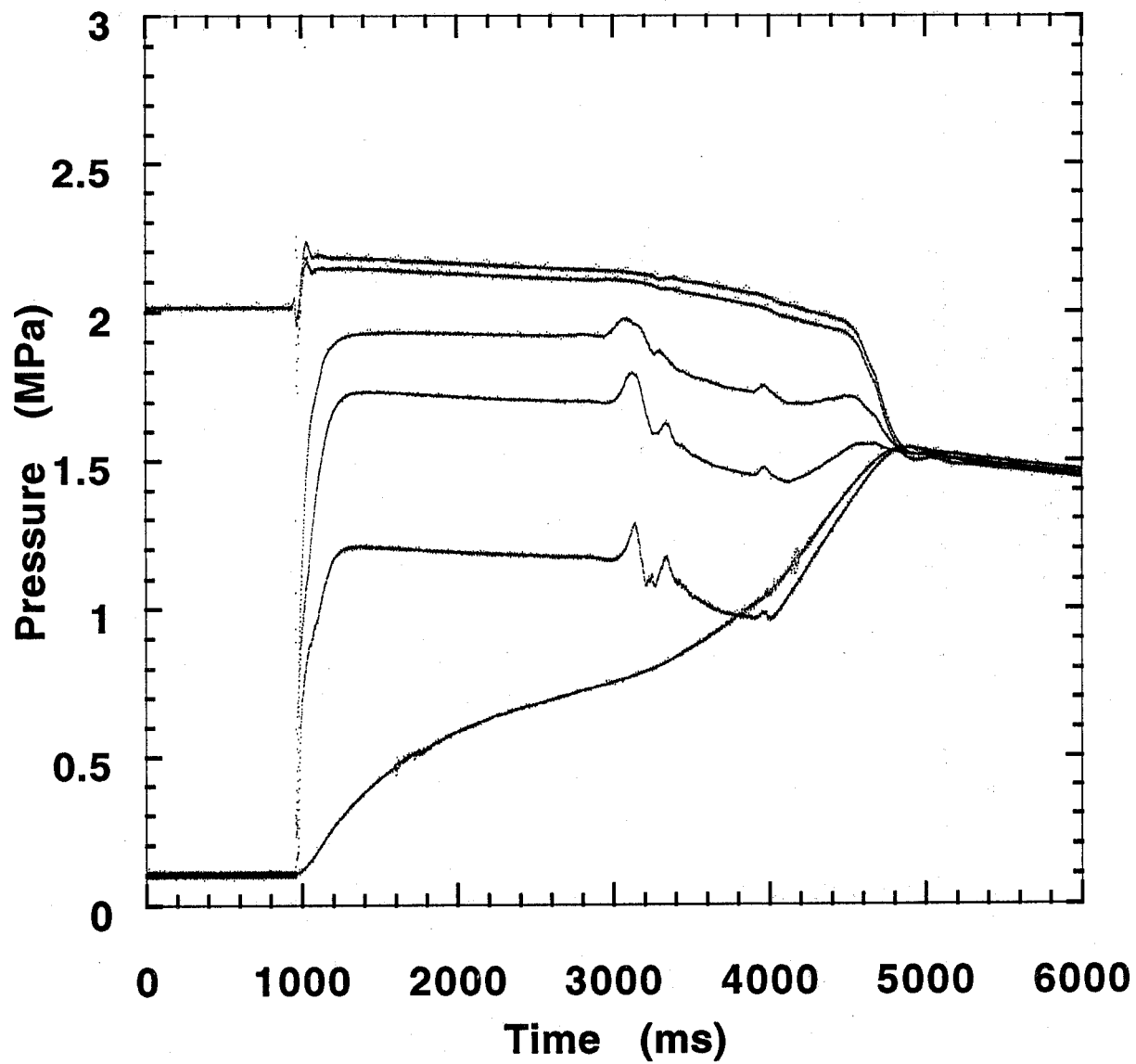


Figure B-26. HFC-125 test. Refer to Table B-3 for experimental conditions.

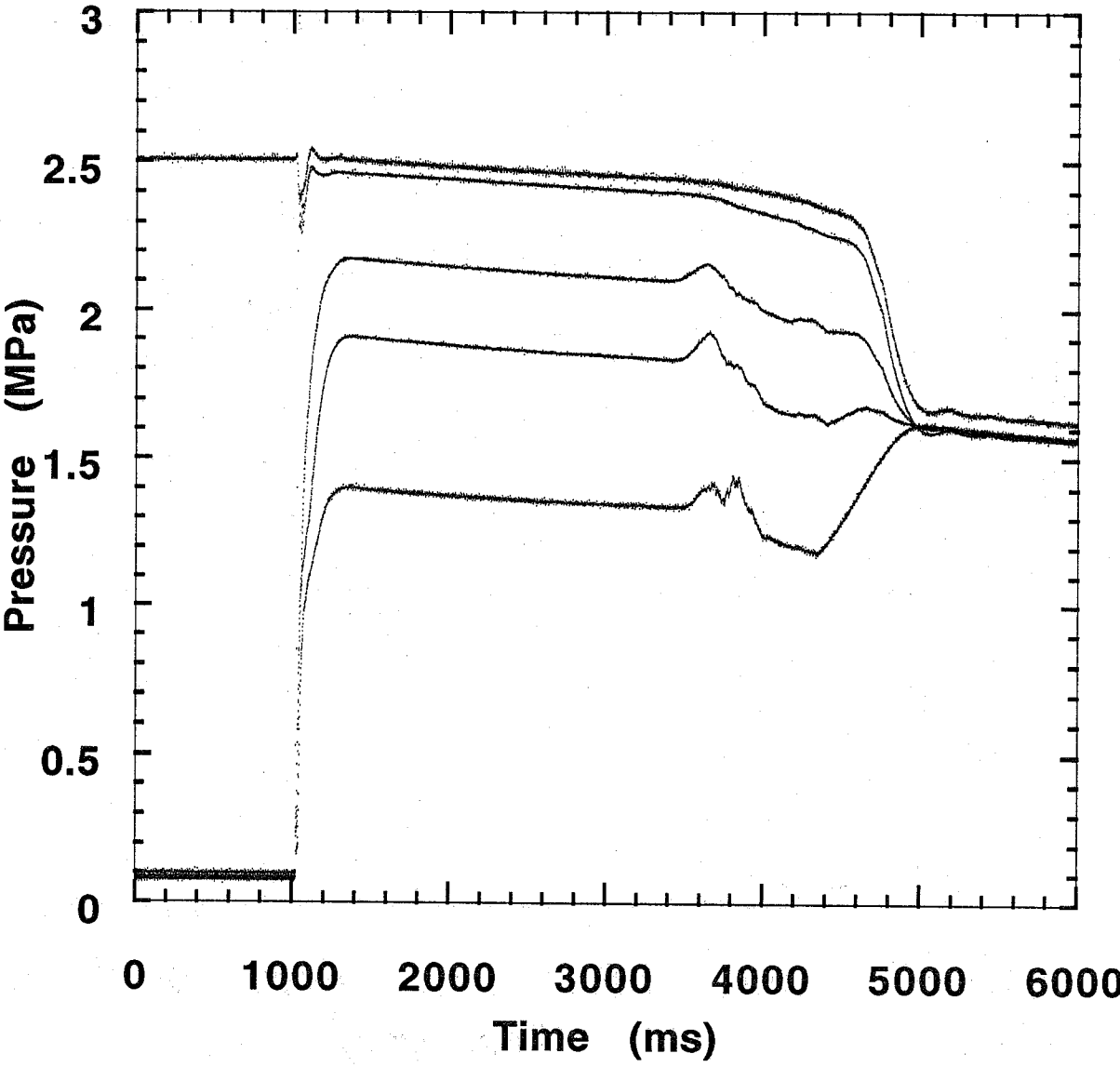


Figure B-27. HFC-125 test. Refer to Table B-3 for experimental conditions.

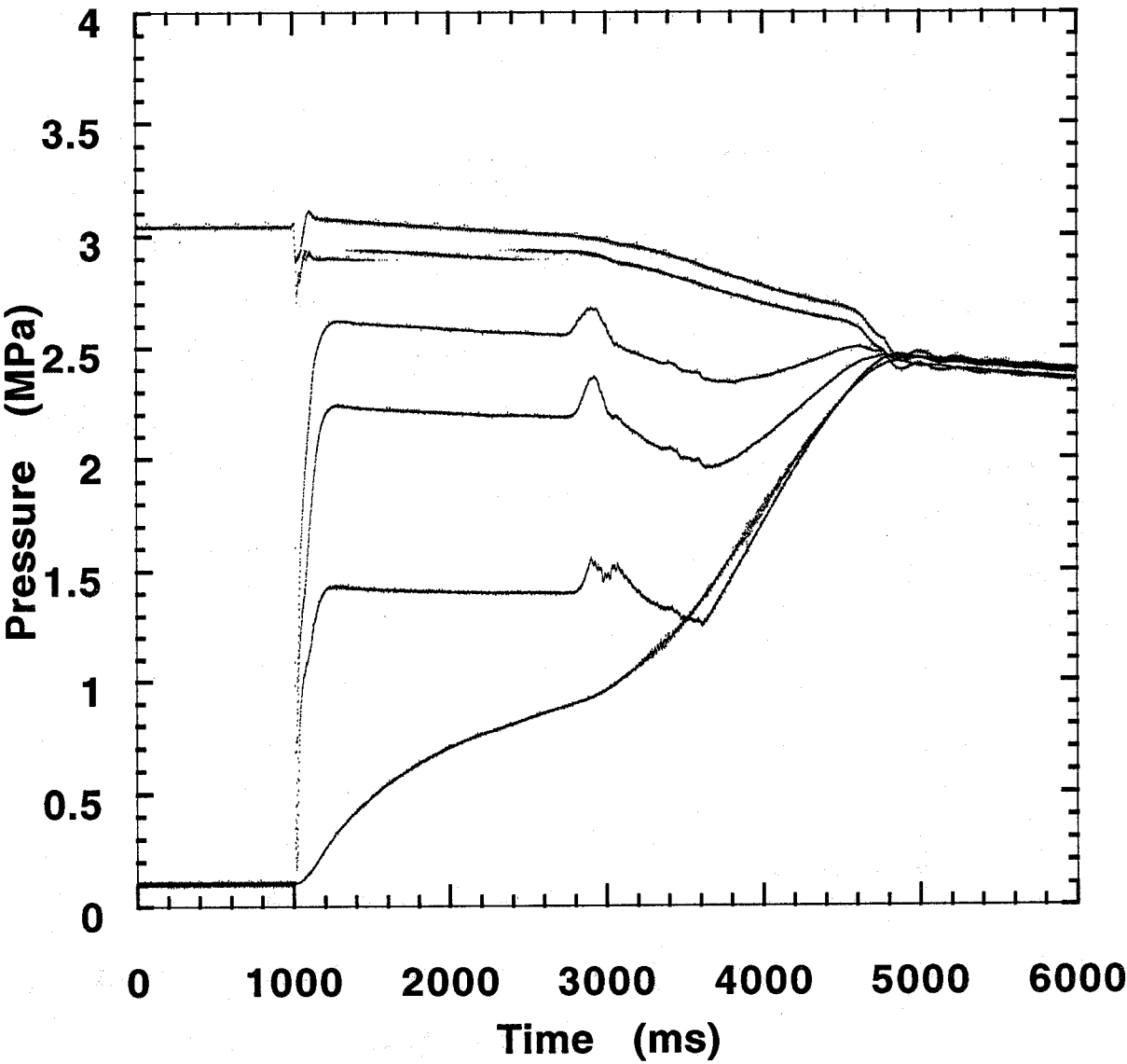


Figure B-28. HFC-125 test. Refer to Table B-3 for experimental conditions.

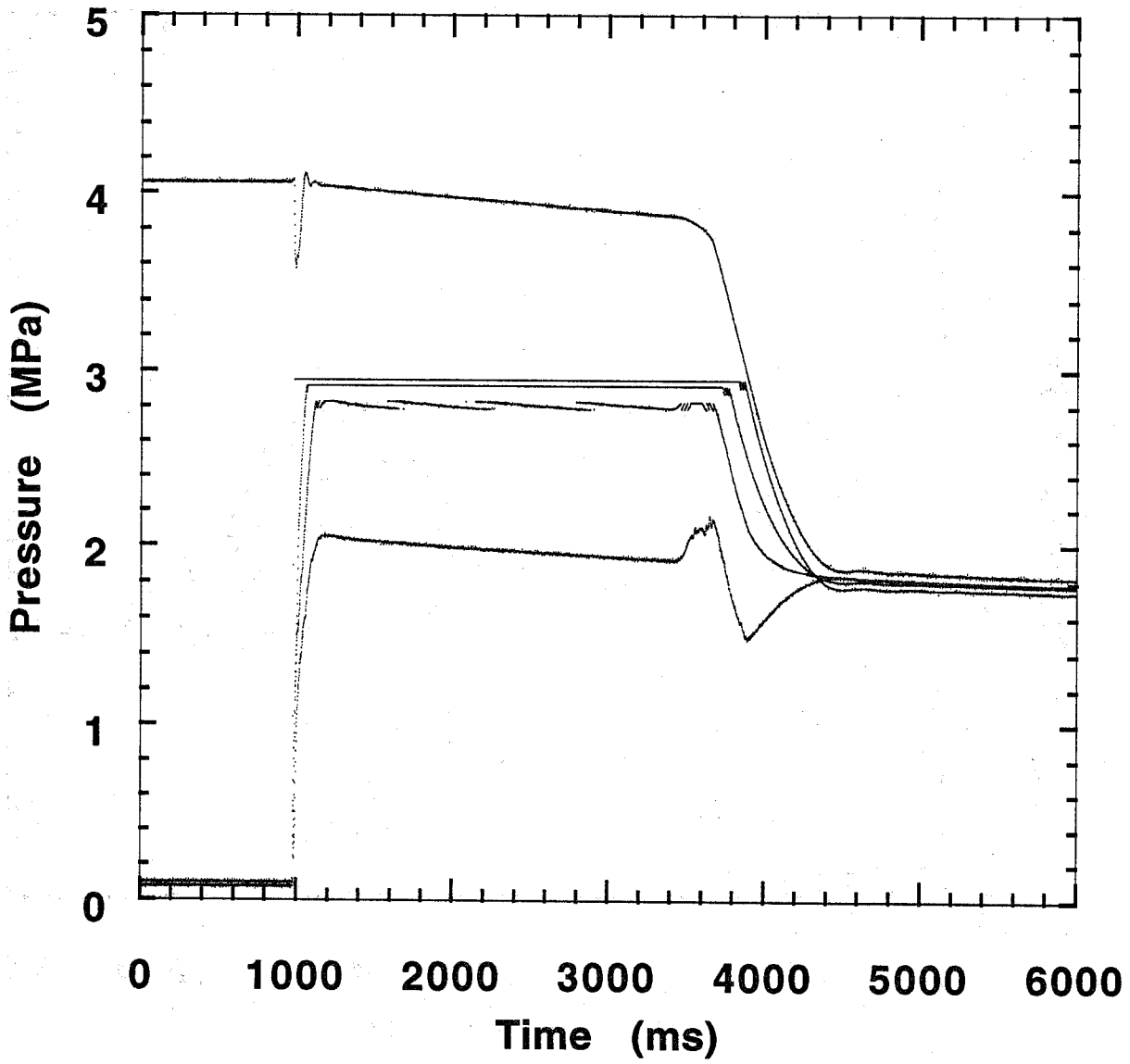


Figure B-29. HFC-125 test. Refer to Table B-3 for experimental conditions.

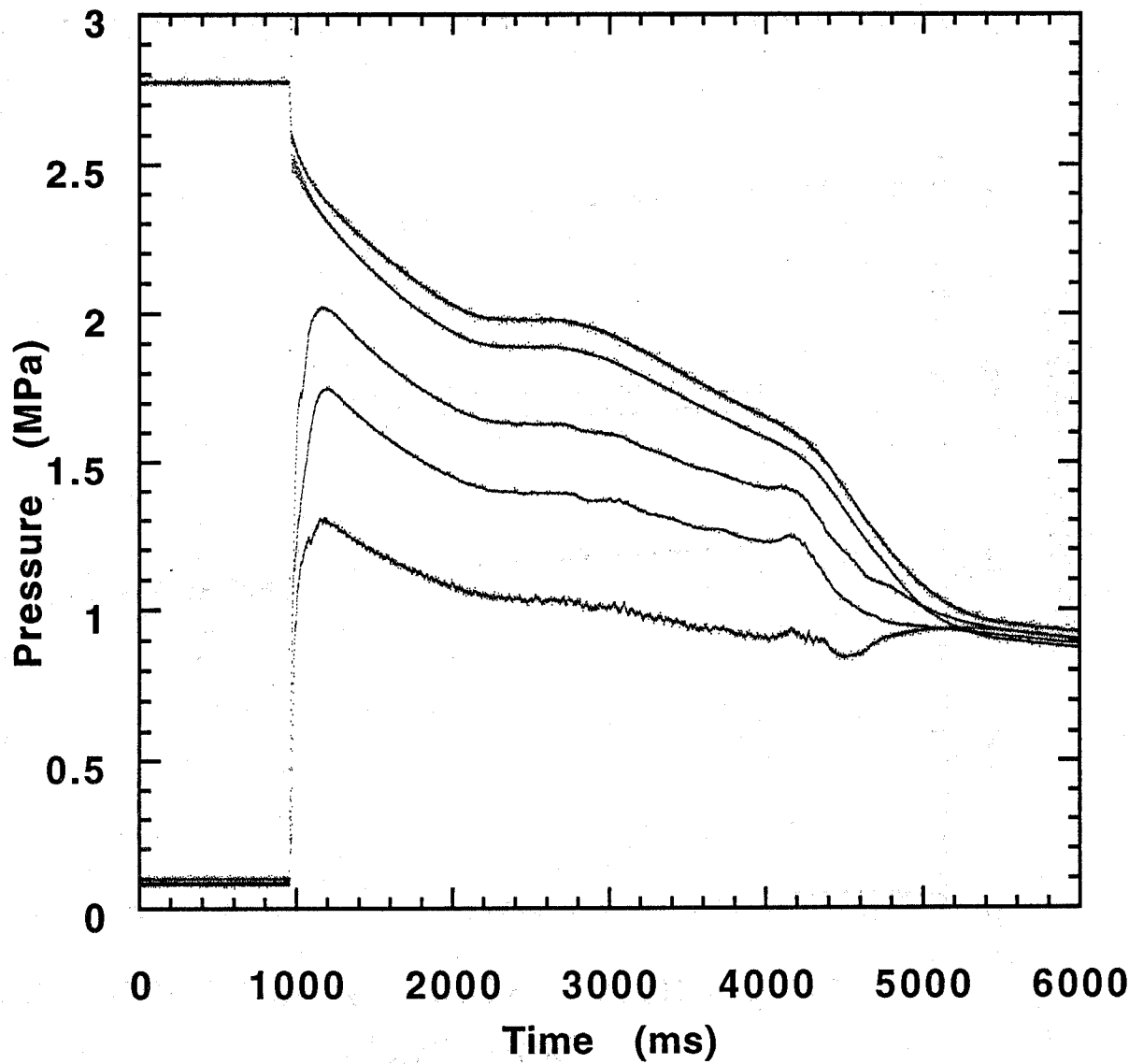


Figure B-30. HFC-125 test. Refer to Table B-3 for experimental conditions.

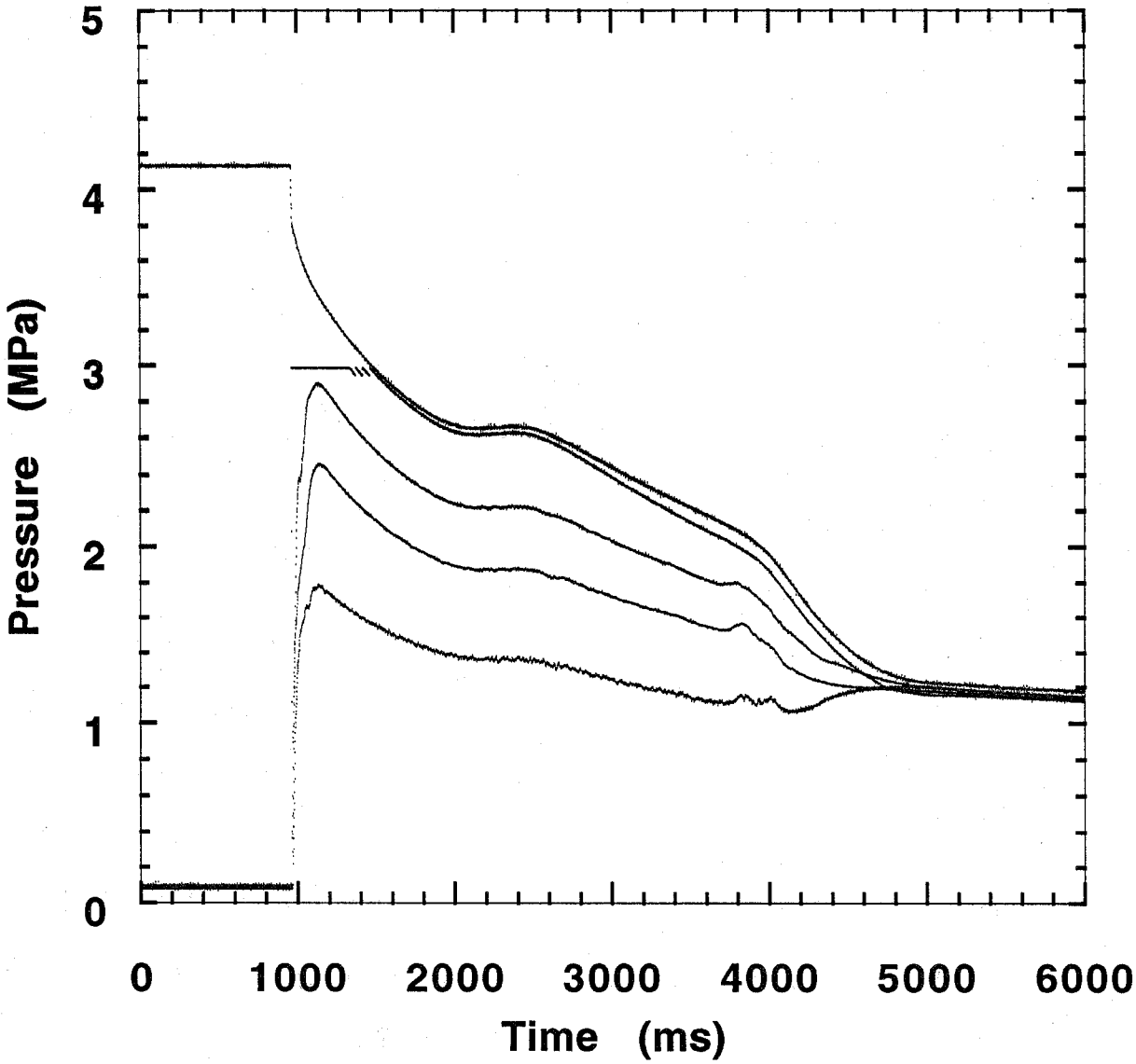


Figure B-31. HFC-125 test. Refer to Table B-3 for experimental conditions.

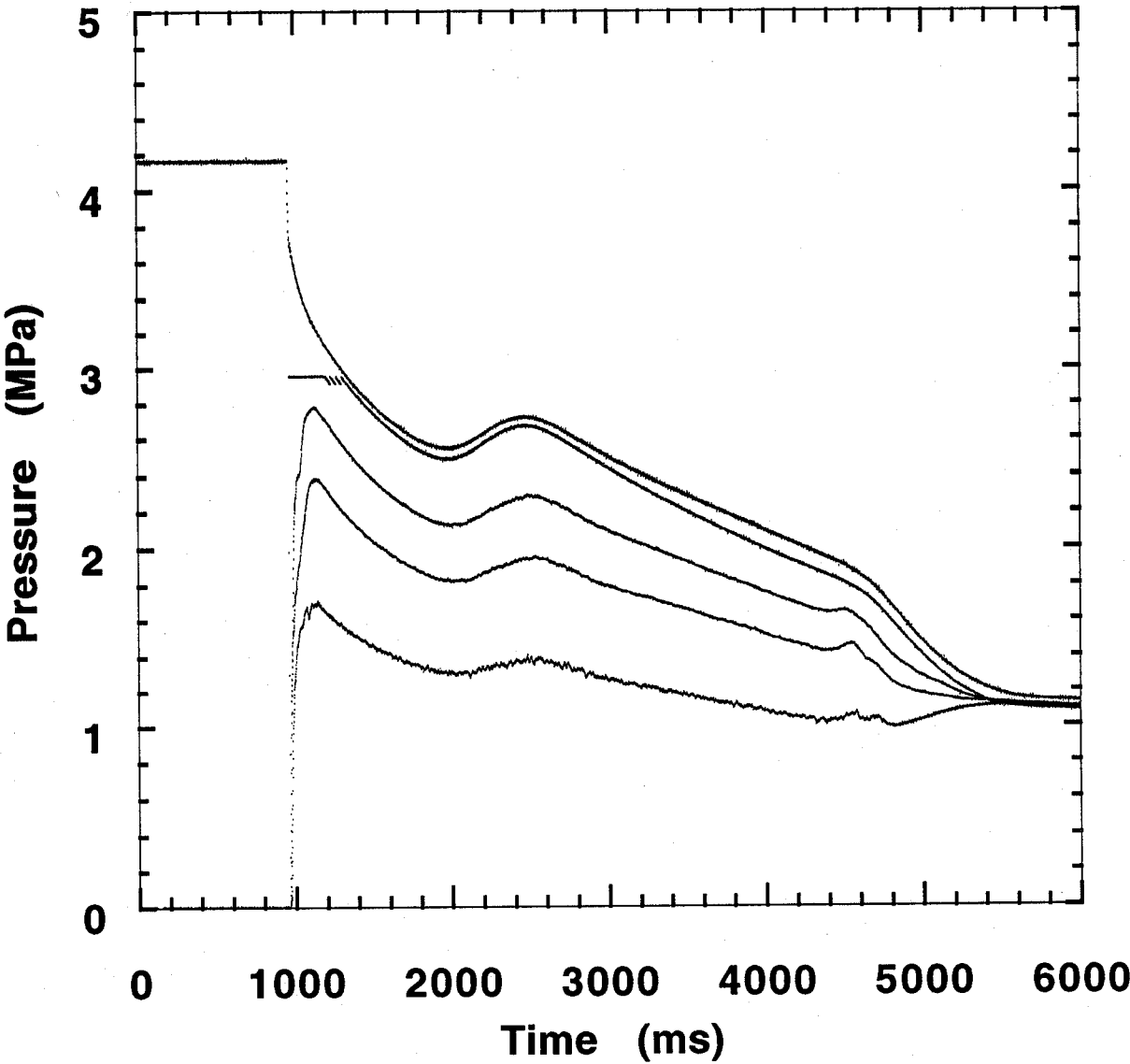


Figure B-32. HFC-125 test. Refer to Table B-3 for experimental conditions.

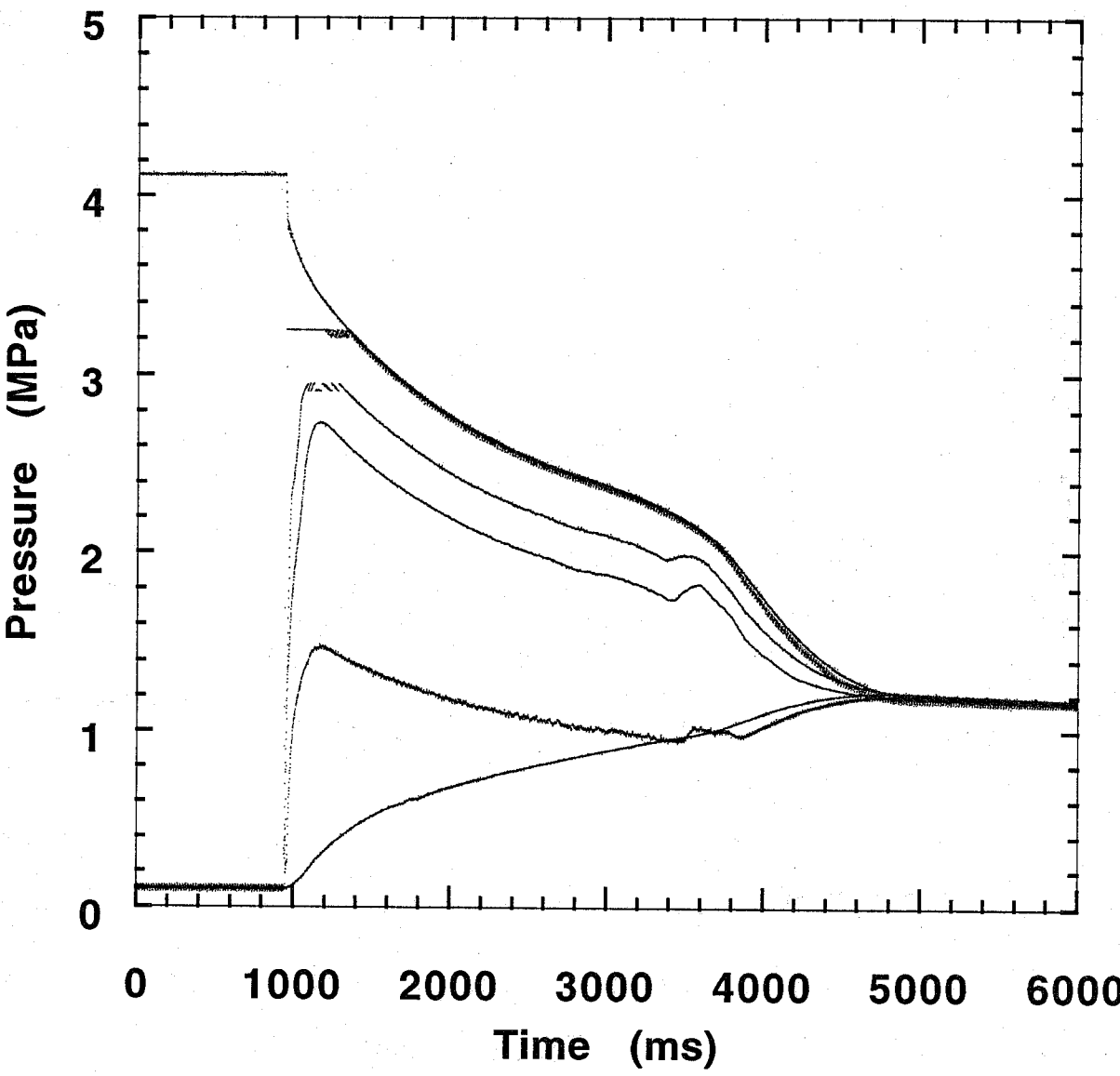


Figure B-33. HFC-125 test. Refer to Table B-3 for experimental conditions.

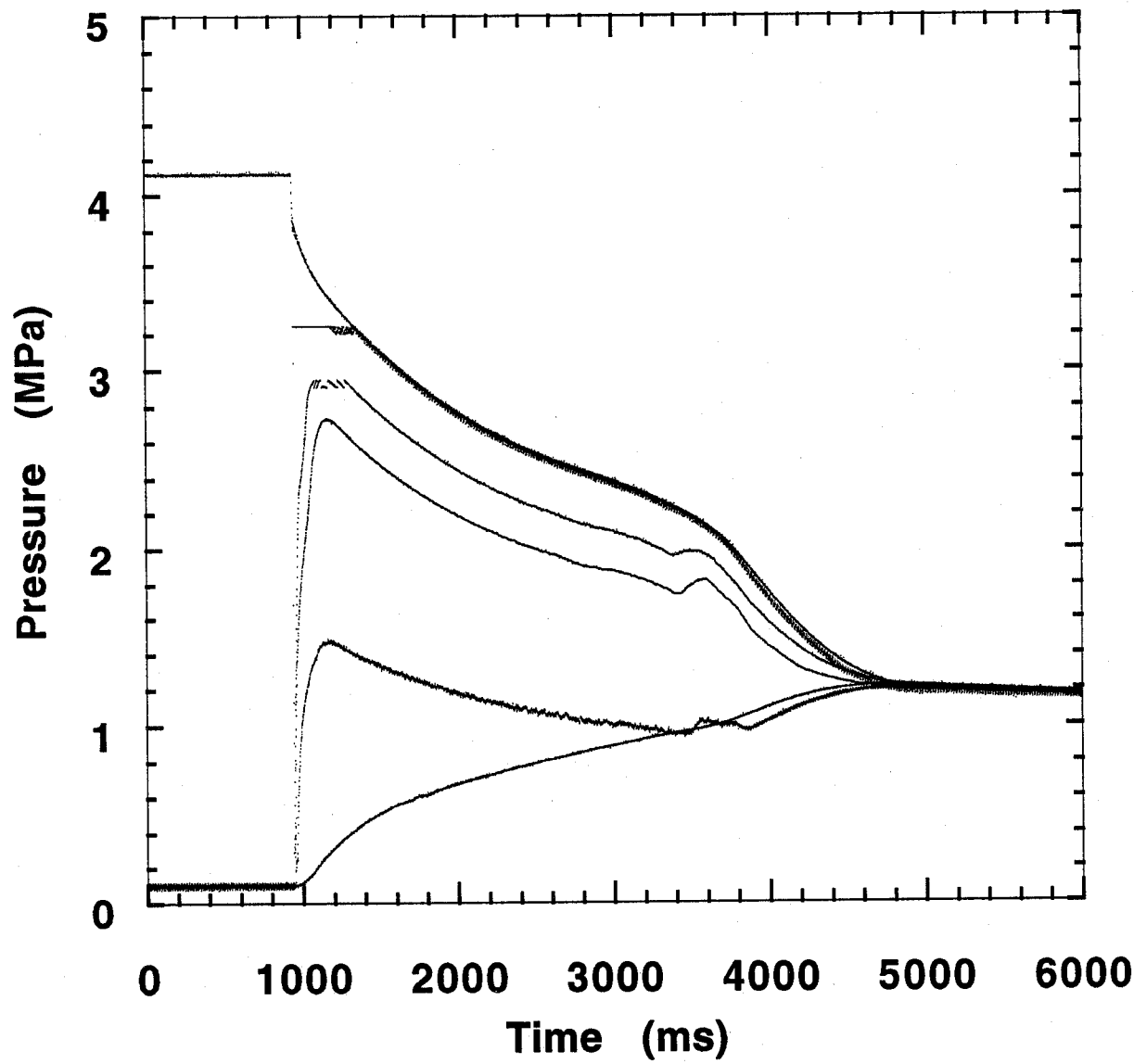


Figure B-34. HFC-125 test. Refer to Table B-3 for experimental conditions.

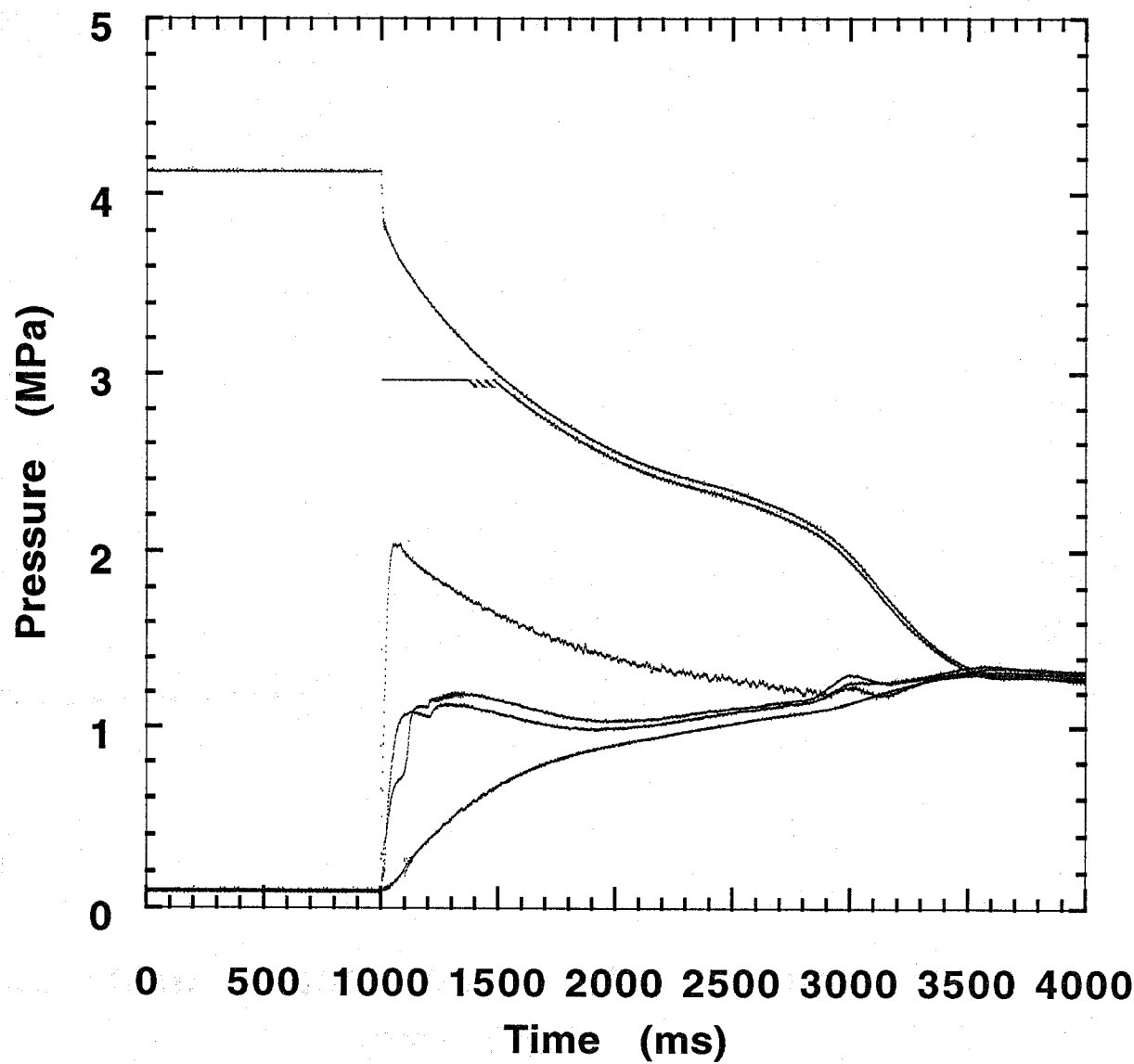


Figure B-35. HFC-125 test. Refer to Table B-3 for experimental conditions.

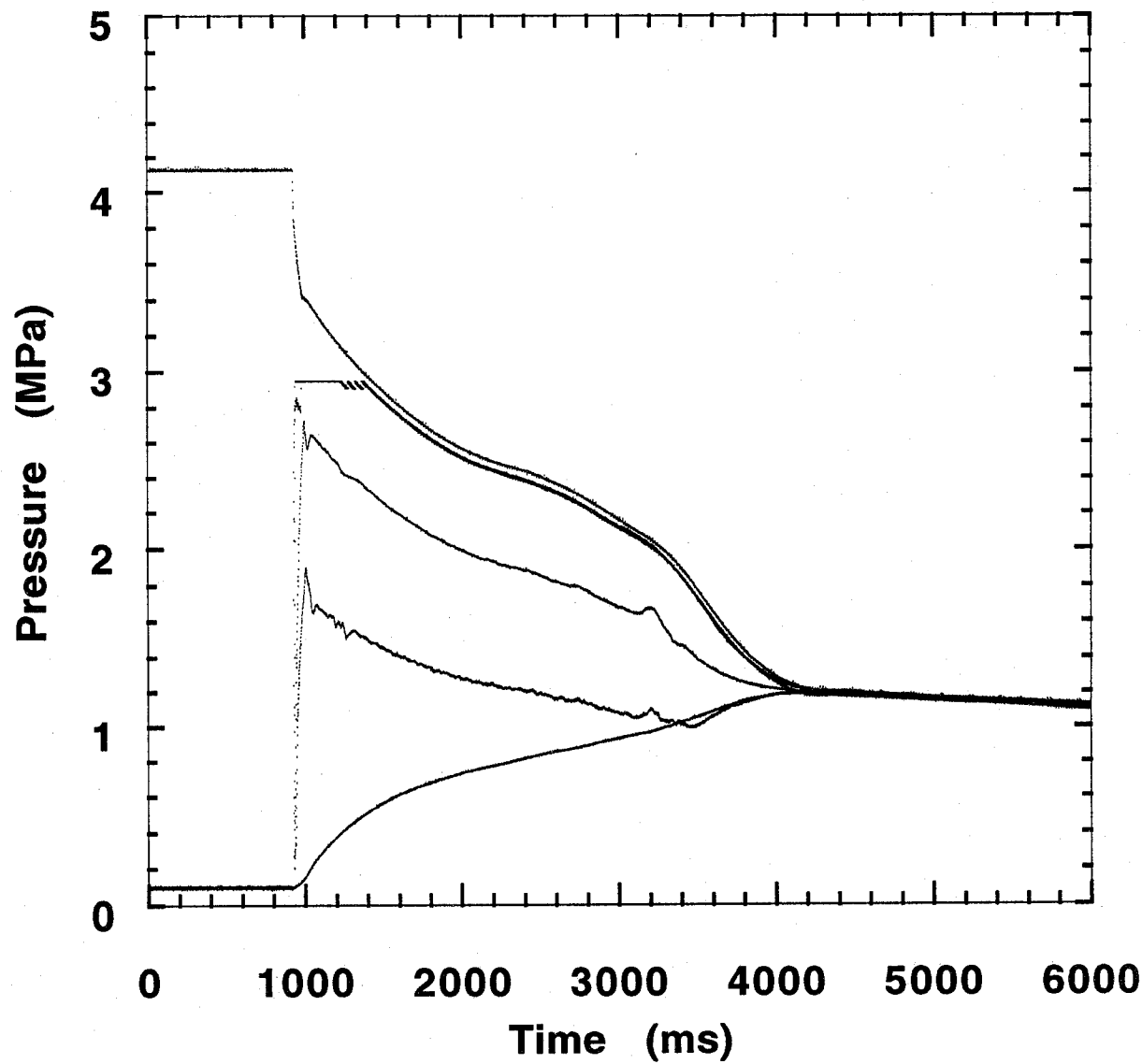


Figure B-36. HFC-125 test. Refer to Table B-3 for experimental conditions.

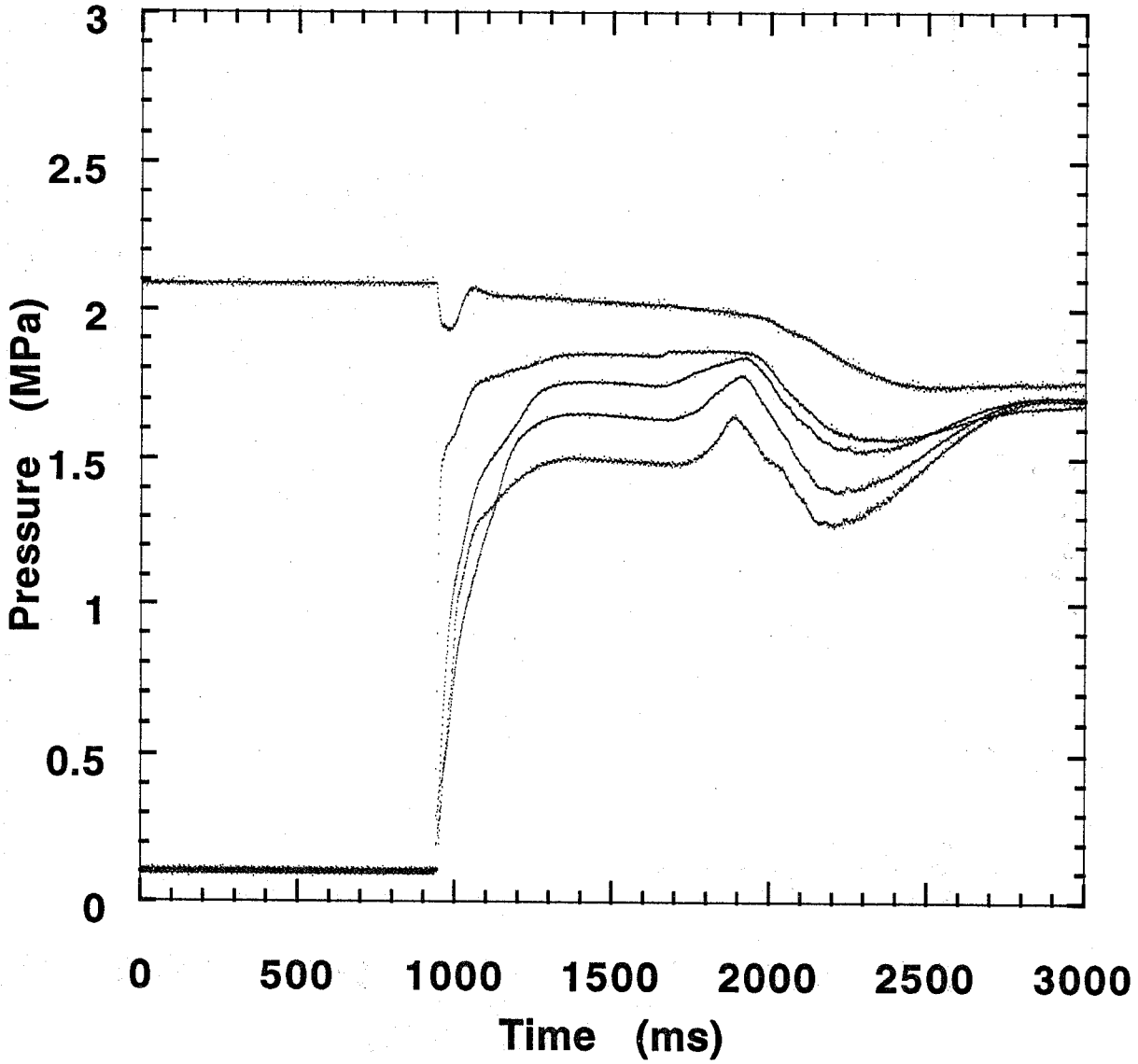


Figure B-37. HFC-125 test. Refer to Table B-3 for experimental conditions.

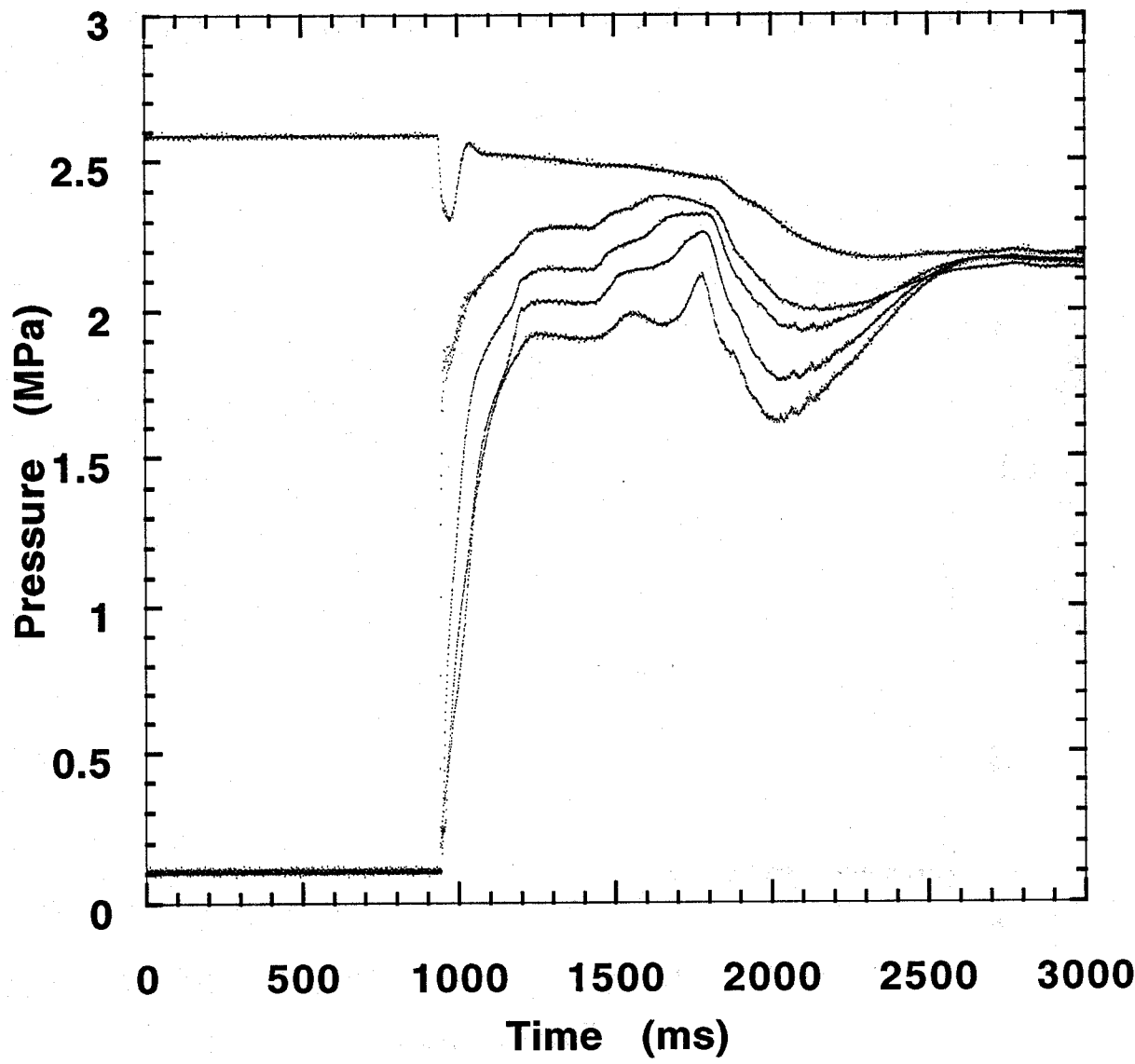


Figure B-38. HFC-125 test. Refer to Table B-3 for experimental conditions.

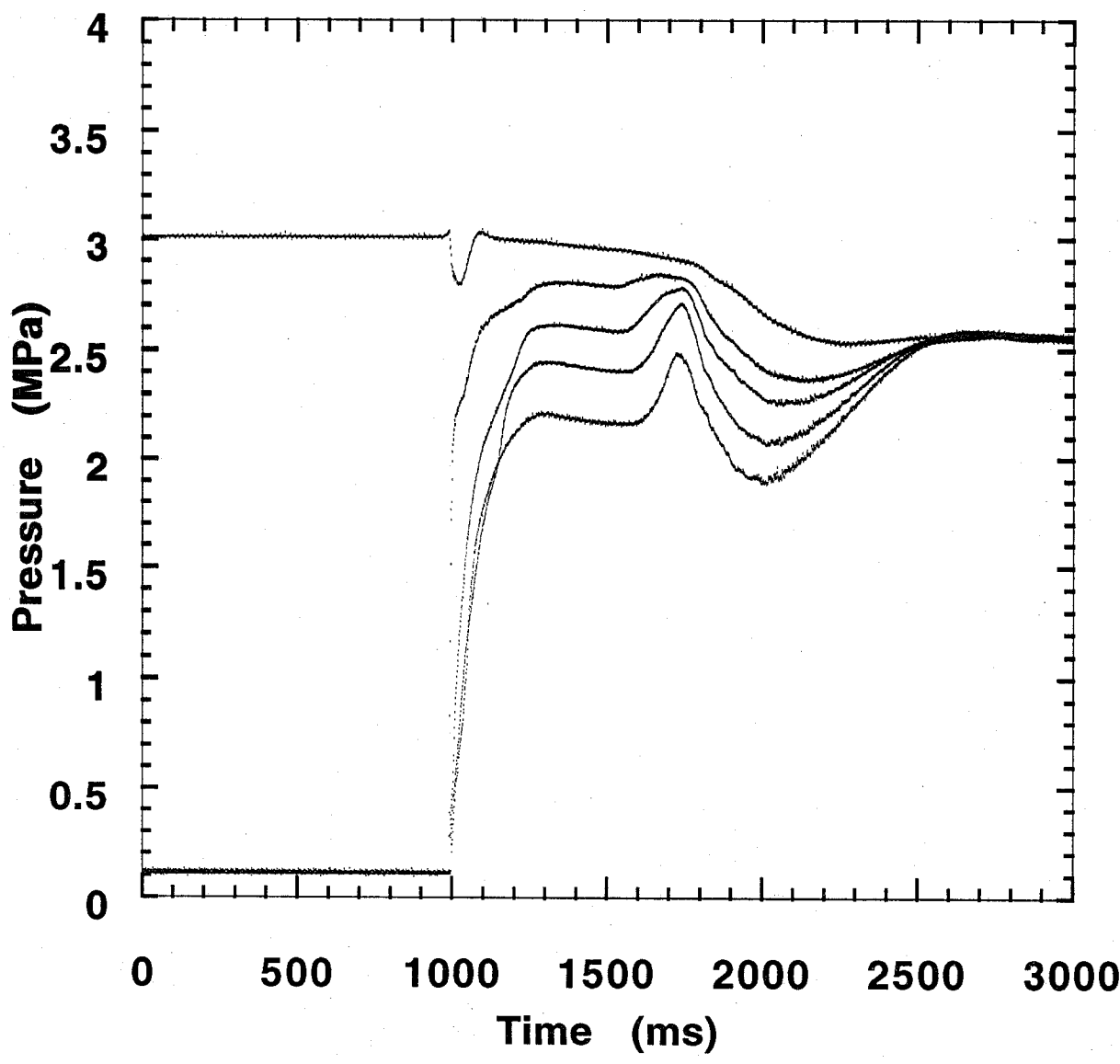


Figure B-39. HFC-125 test. Refer to Table B-3 for experimental conditions.

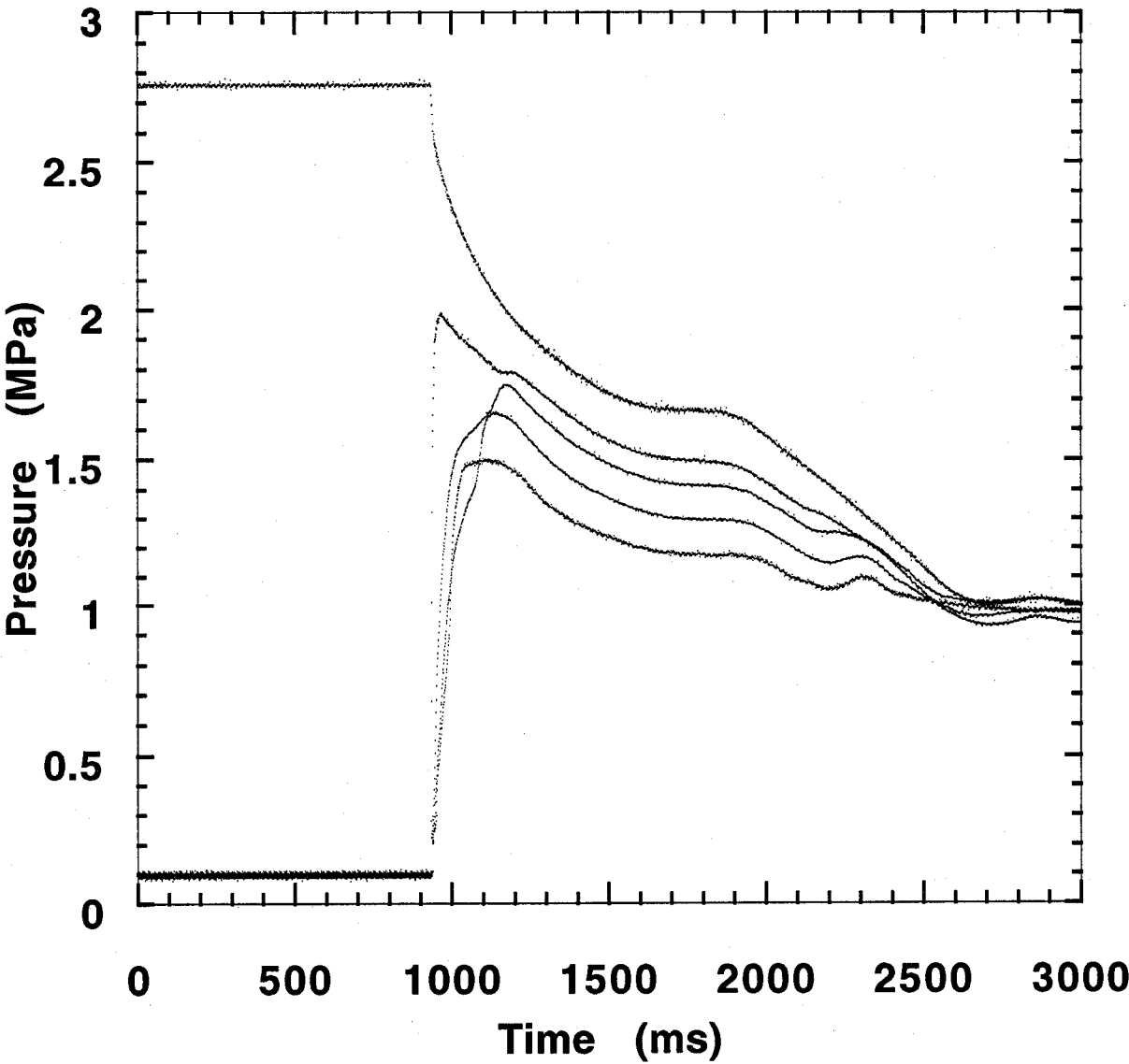


Figure B-40. HFC-125 test. Refer to Table B-3 for experimental conditions.

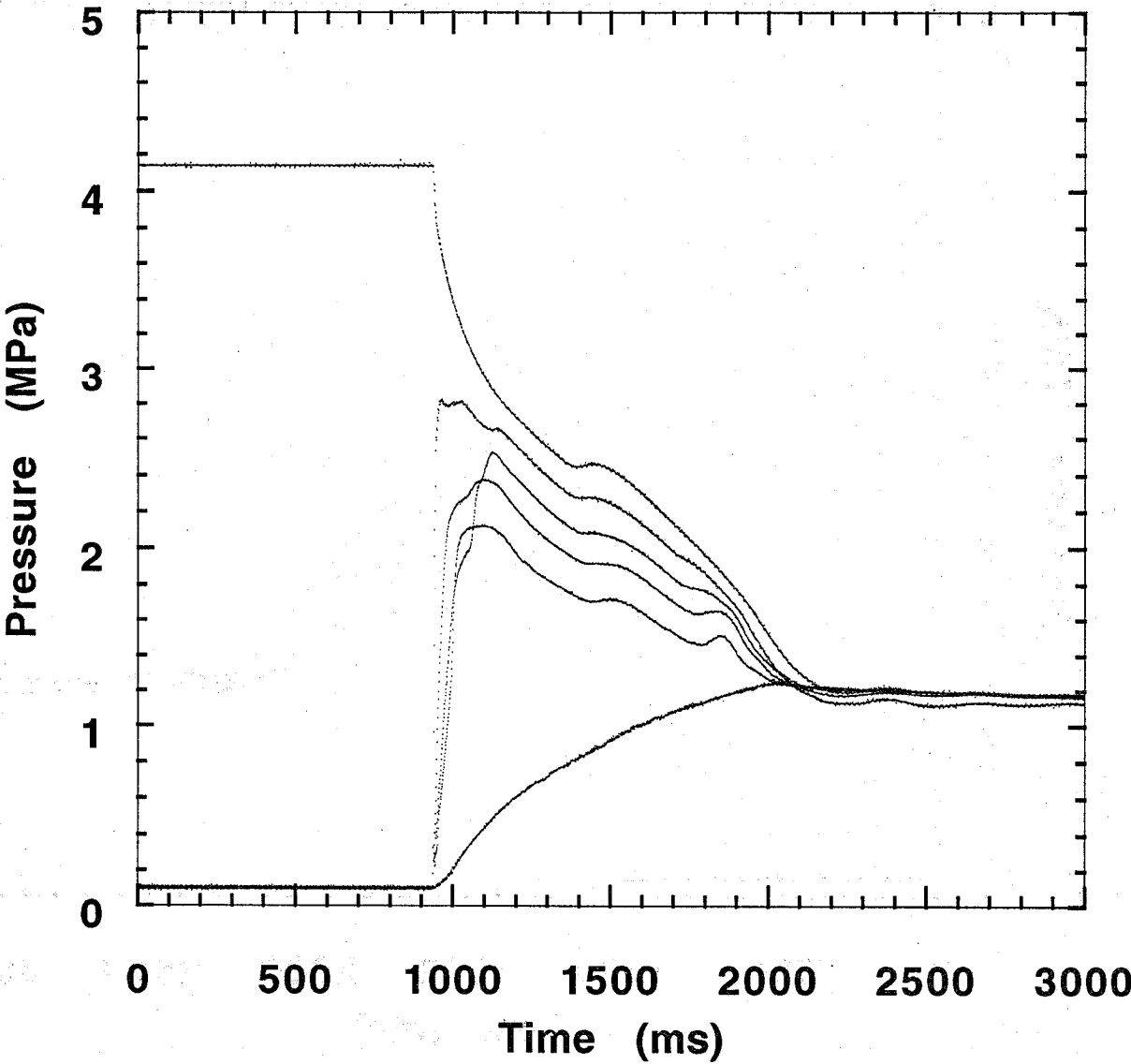


Figure B-41. HFC-125 test. Refer to Table B-3 for experimental conditions.

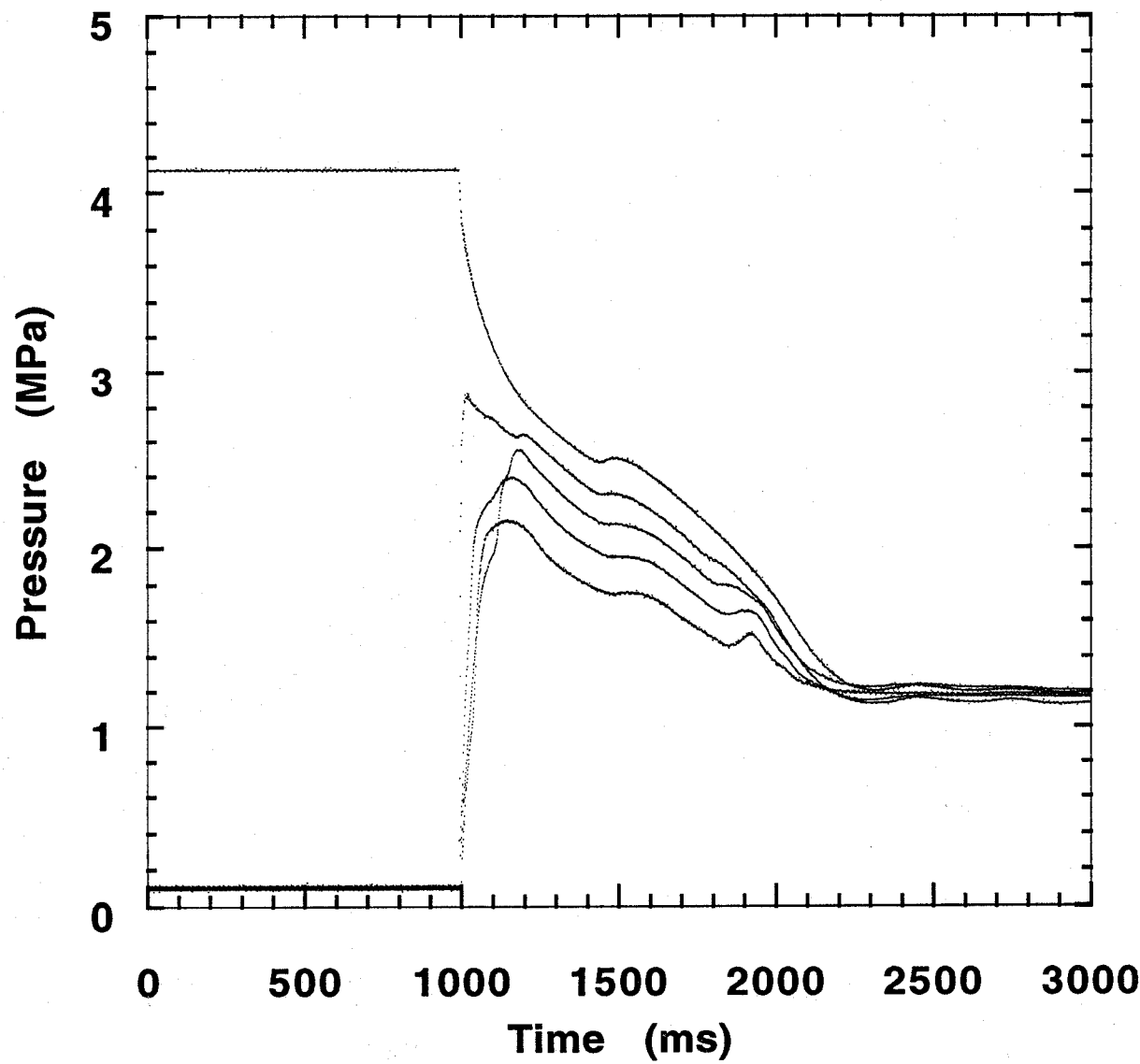


Figure B-42.

HFC-125 test. Refer to Table B-3 for experimental conditions.

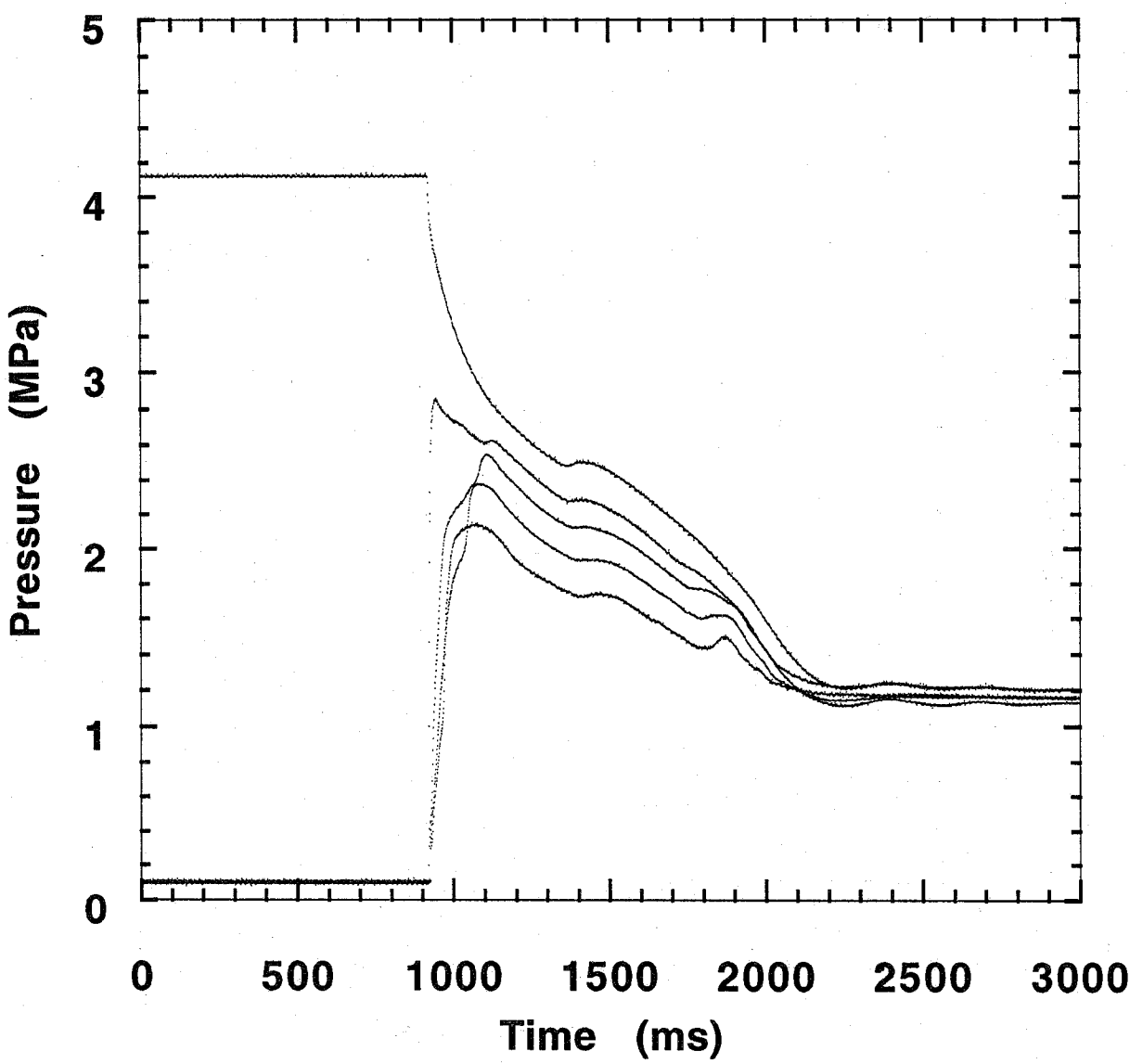


Figure B-43. HFC-125 test. Refer to Table B-3 for experimental conditions.

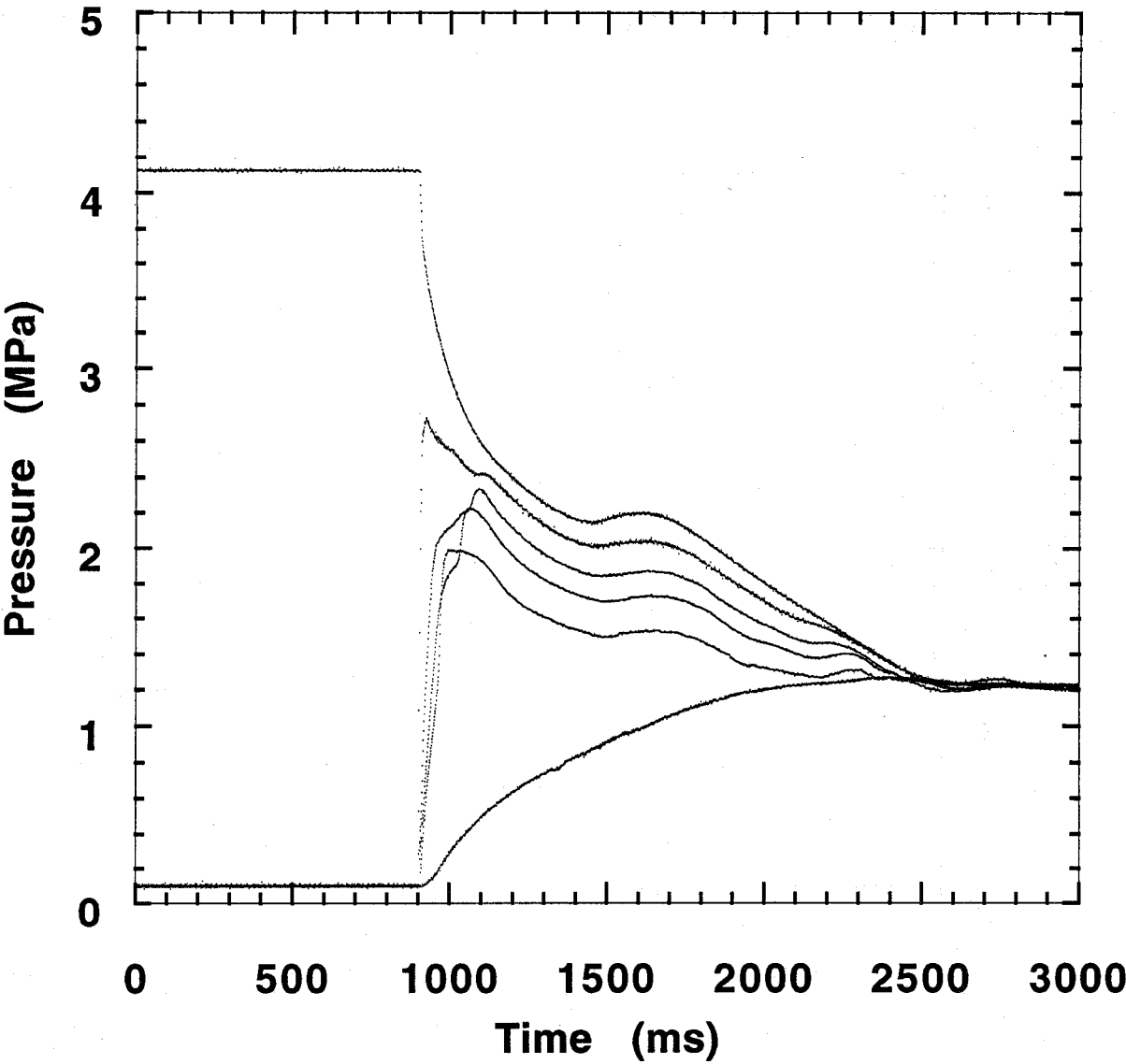


Figure B-44. HFC-125 test. Refer to Table B-3 for experimental conditions.

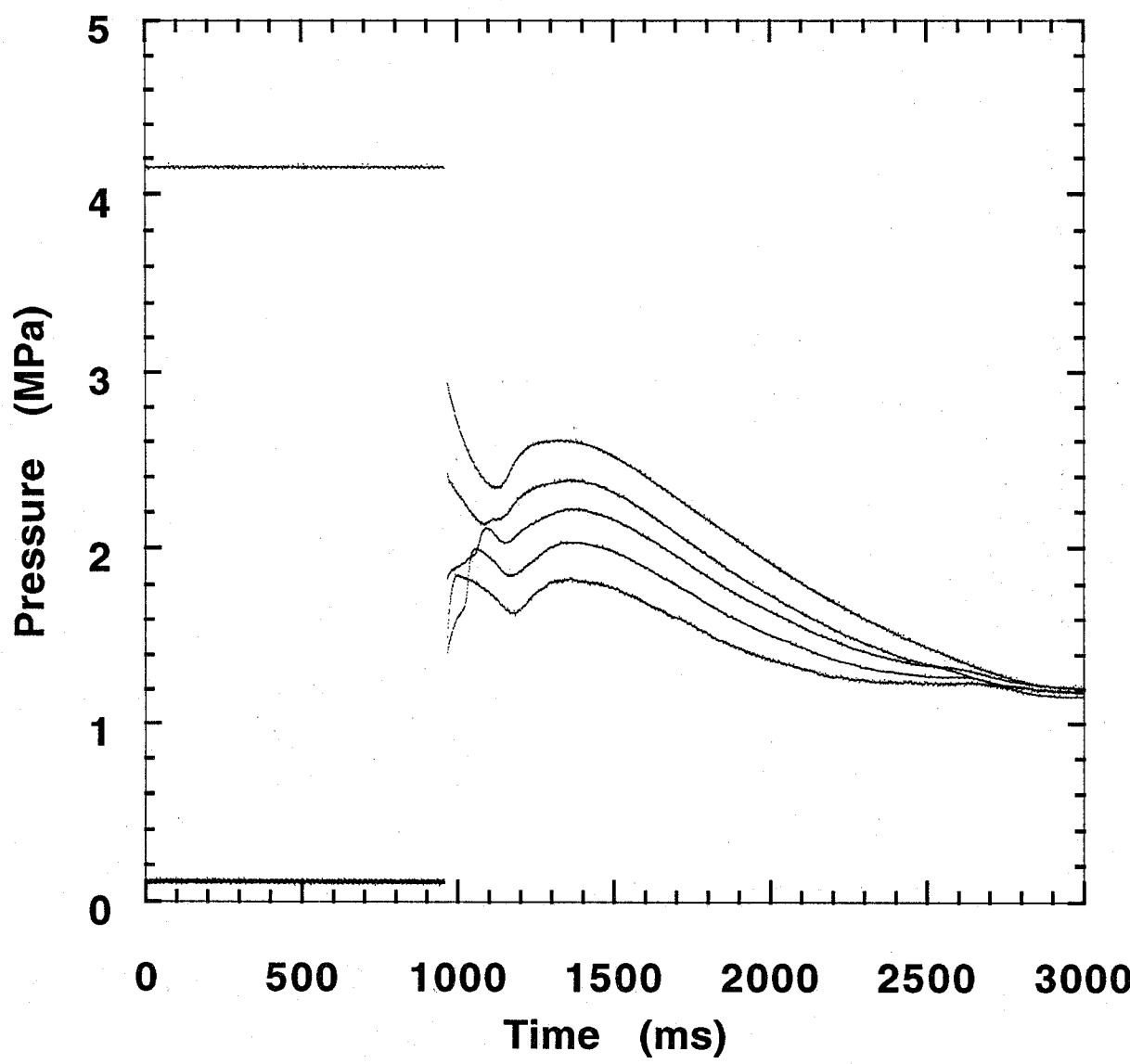


Figure B-45. HFC-125 test. Refer to Table B-3 for experimental conditions.

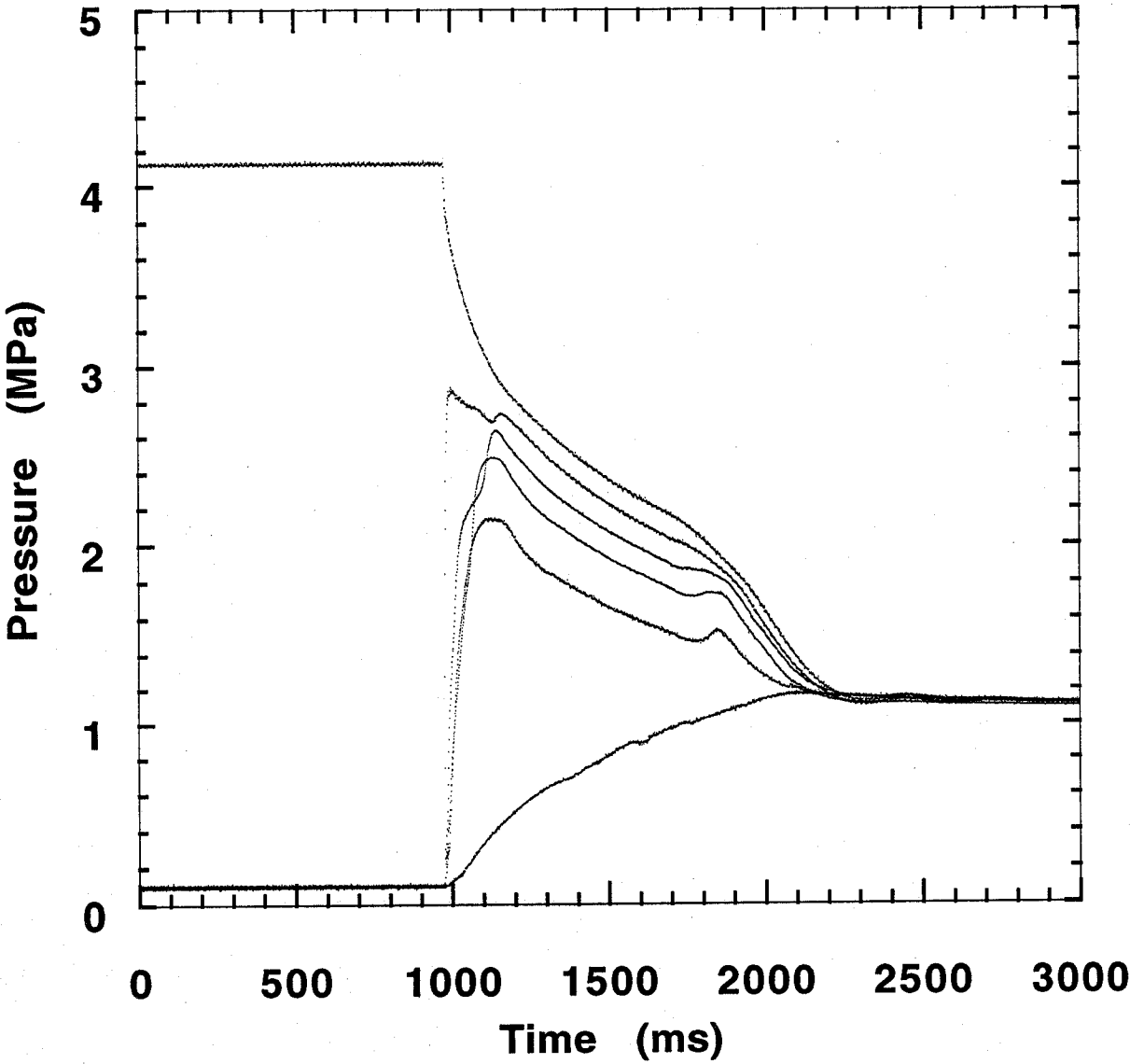


Figure B-46. HFC-125 test. Refer to Table B-3 for experimental conditions.

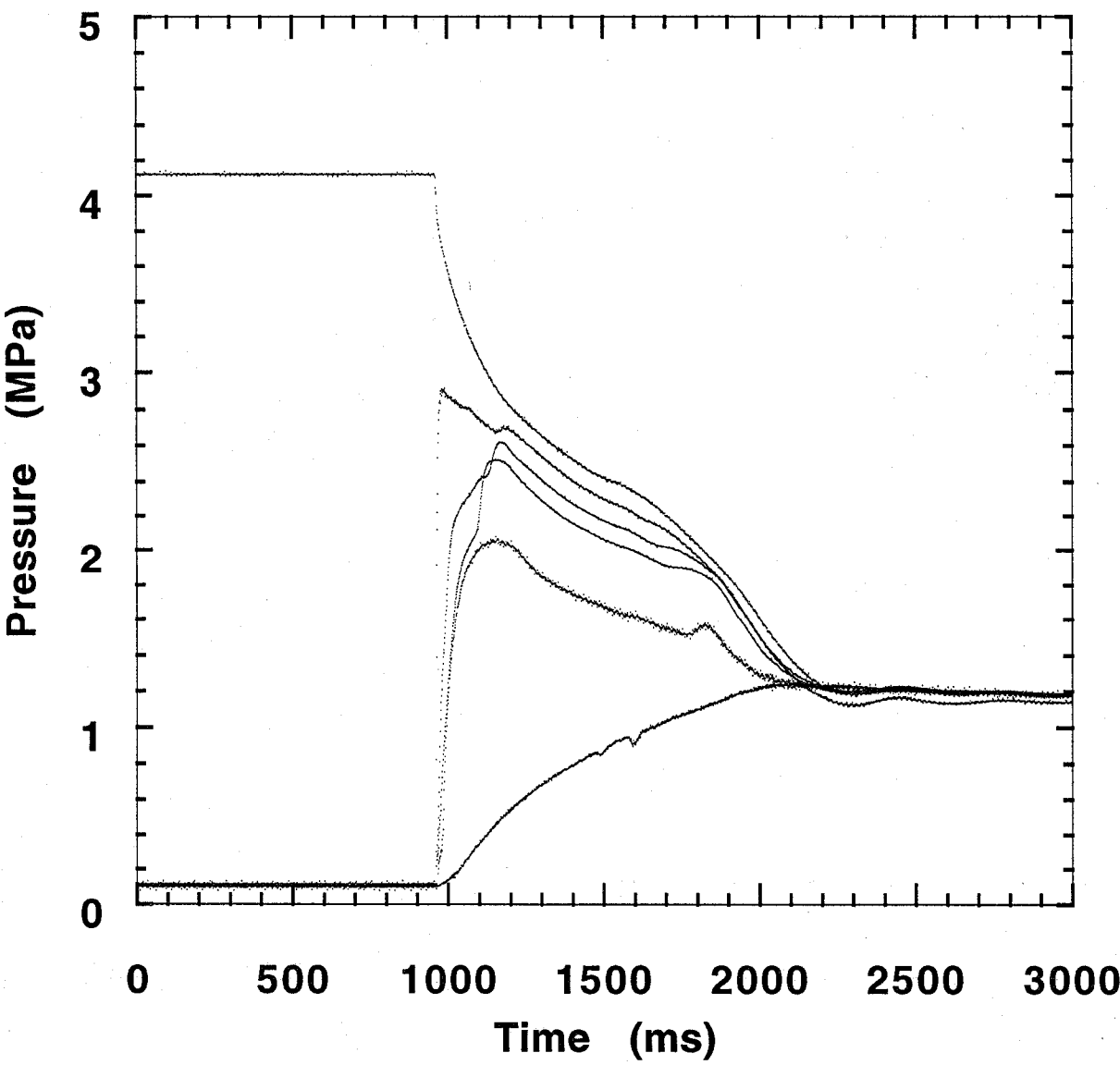


Figure B-47. HFC-125 test. Refer to Table B-3 for experimental conditions.

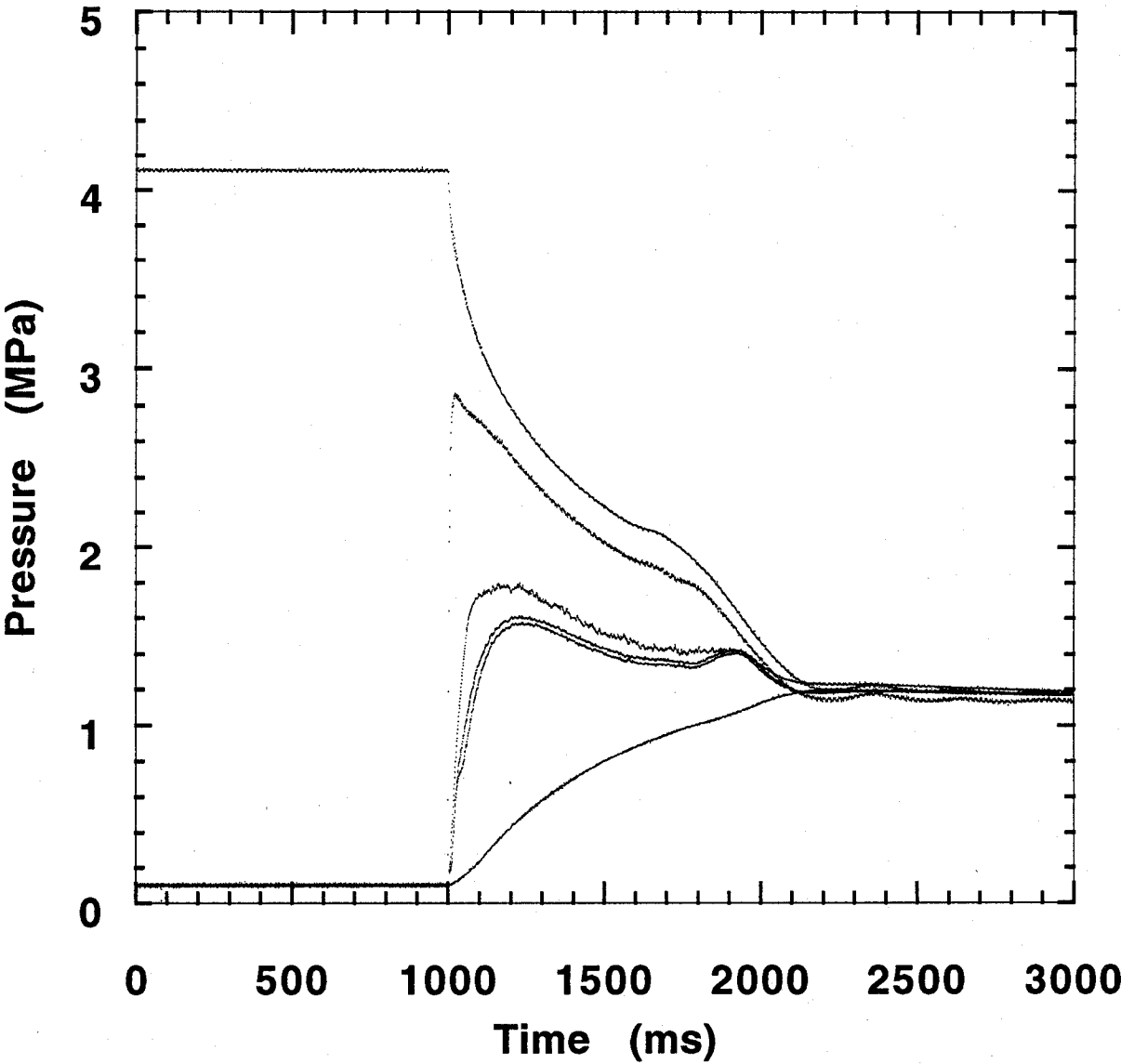


Figure B-48. HFC-125 test. Refer to Table B-3 for experimental conditions.

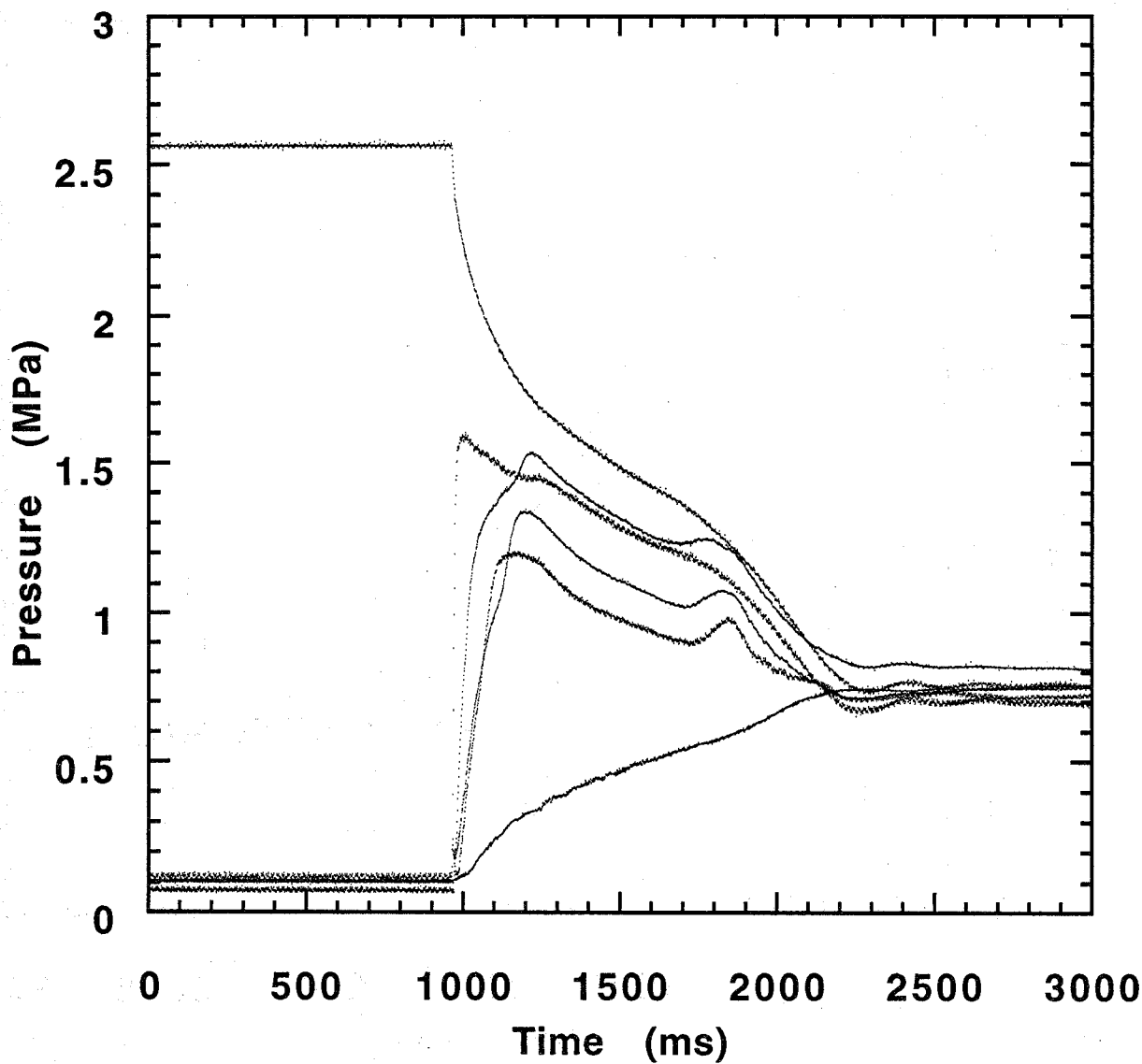


Figure B-49. HFC-125 test. Refer to Table B-3 for experimental conditions.

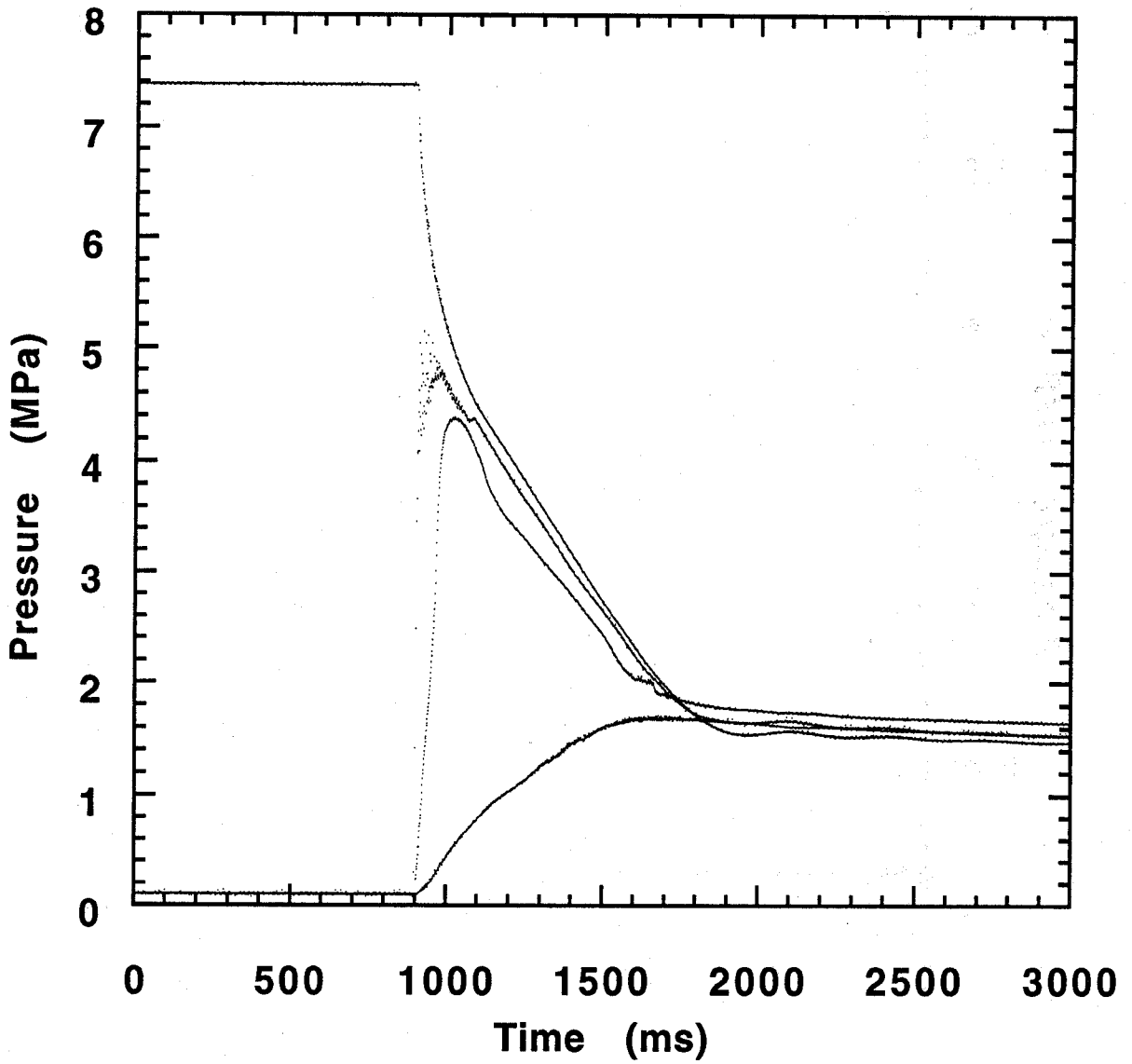


Figure B-50. HFC-125 test. Refer to Table B-3 for experimental conditions.

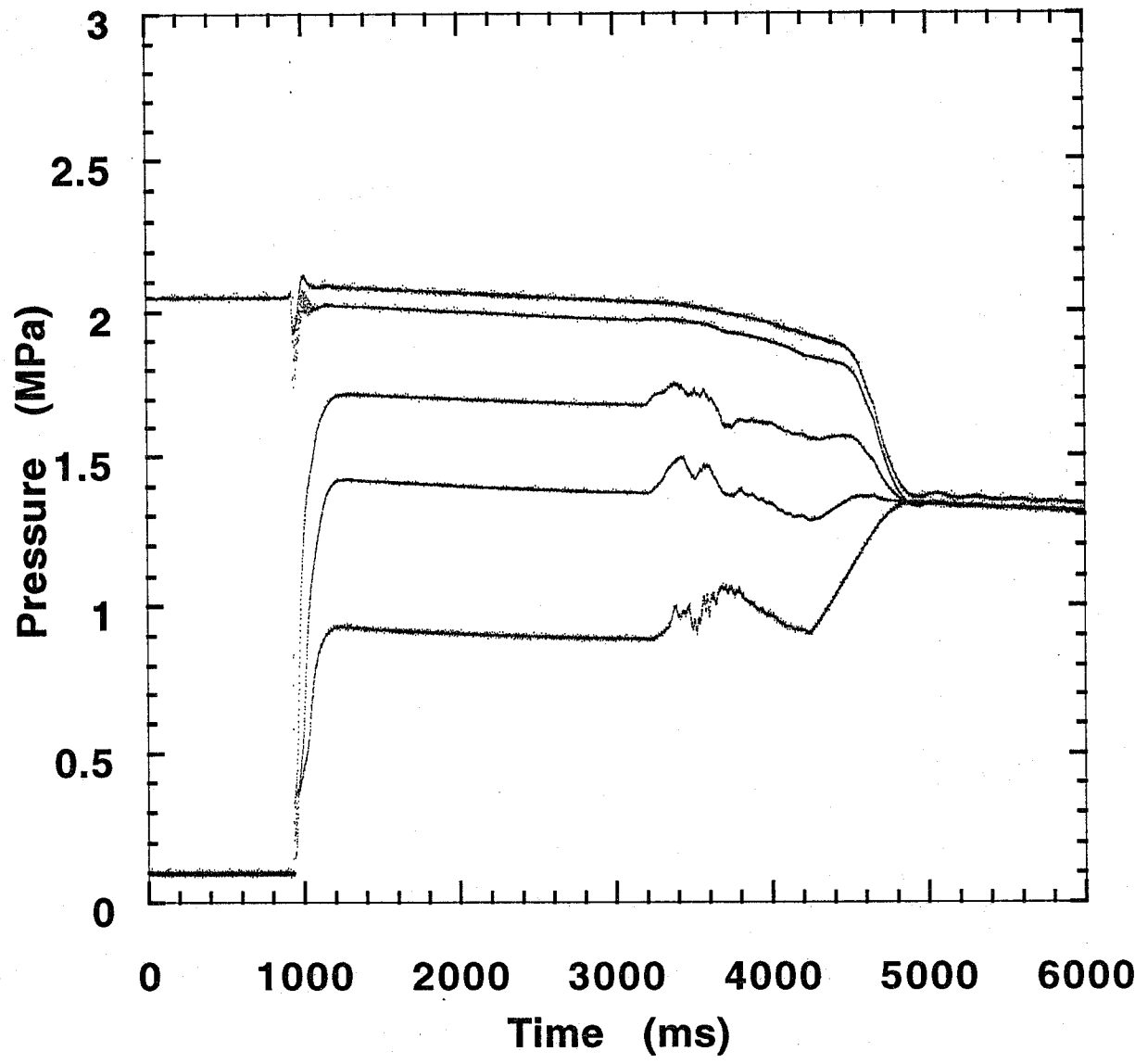


Figure B-51. HFC-227ea test. Refer to Table B-4 for experimental conditions.

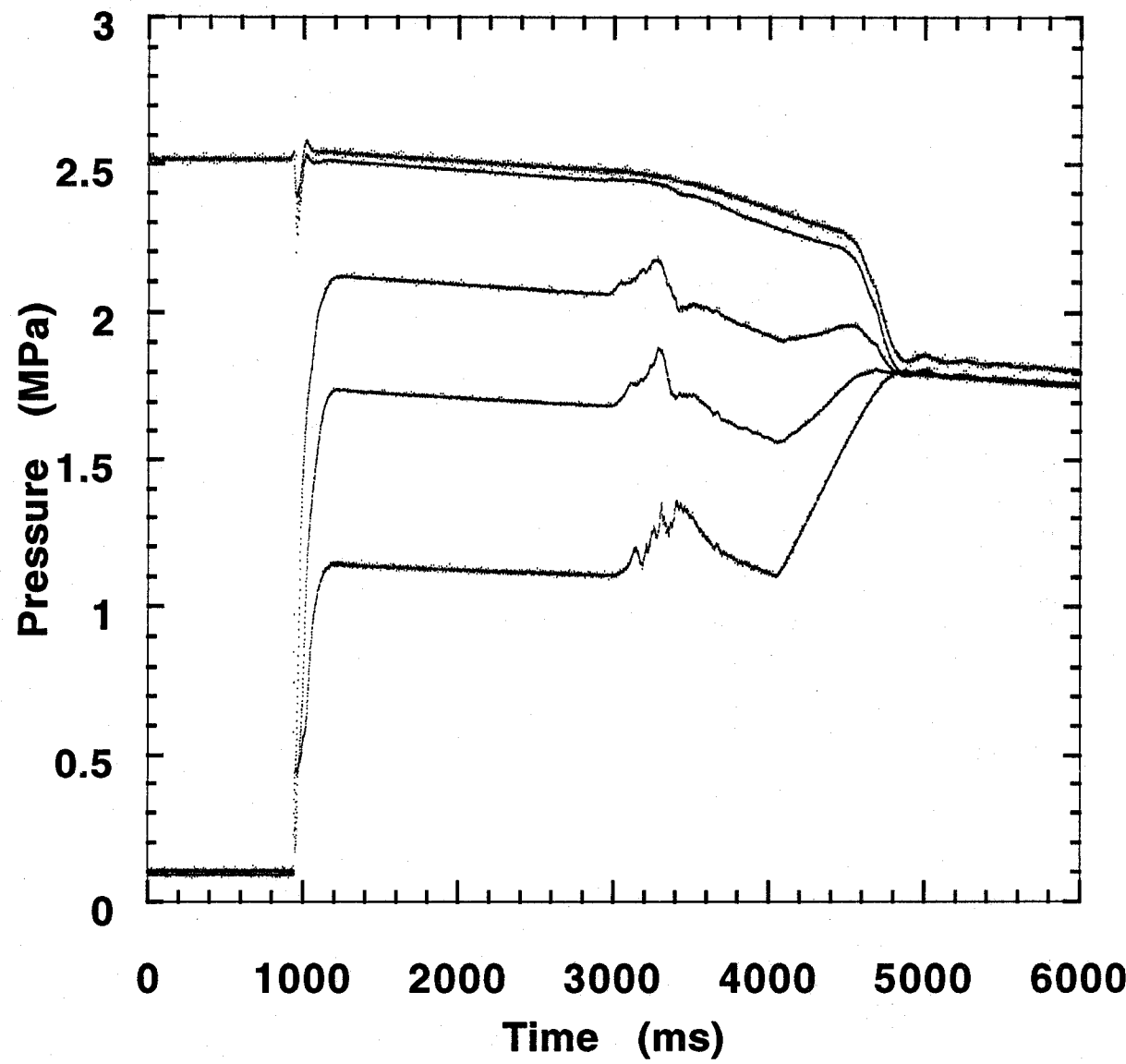


Figure B-52. HFC-227ea test. Refer to Table B-4 for experimental conditions.

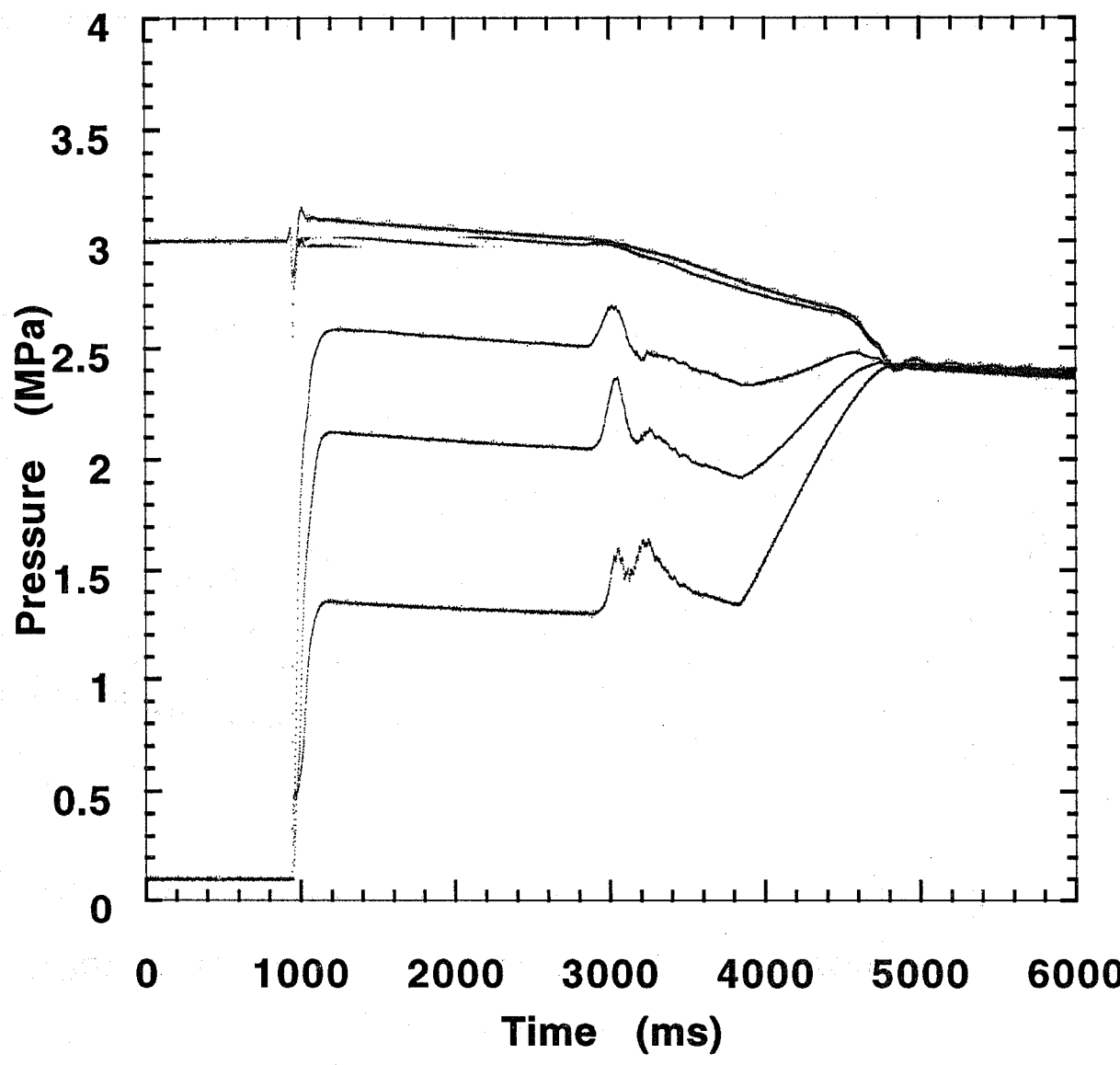


Figure B-53. HFC-227ea test. Refer to Table B-4 for experimental conditions.

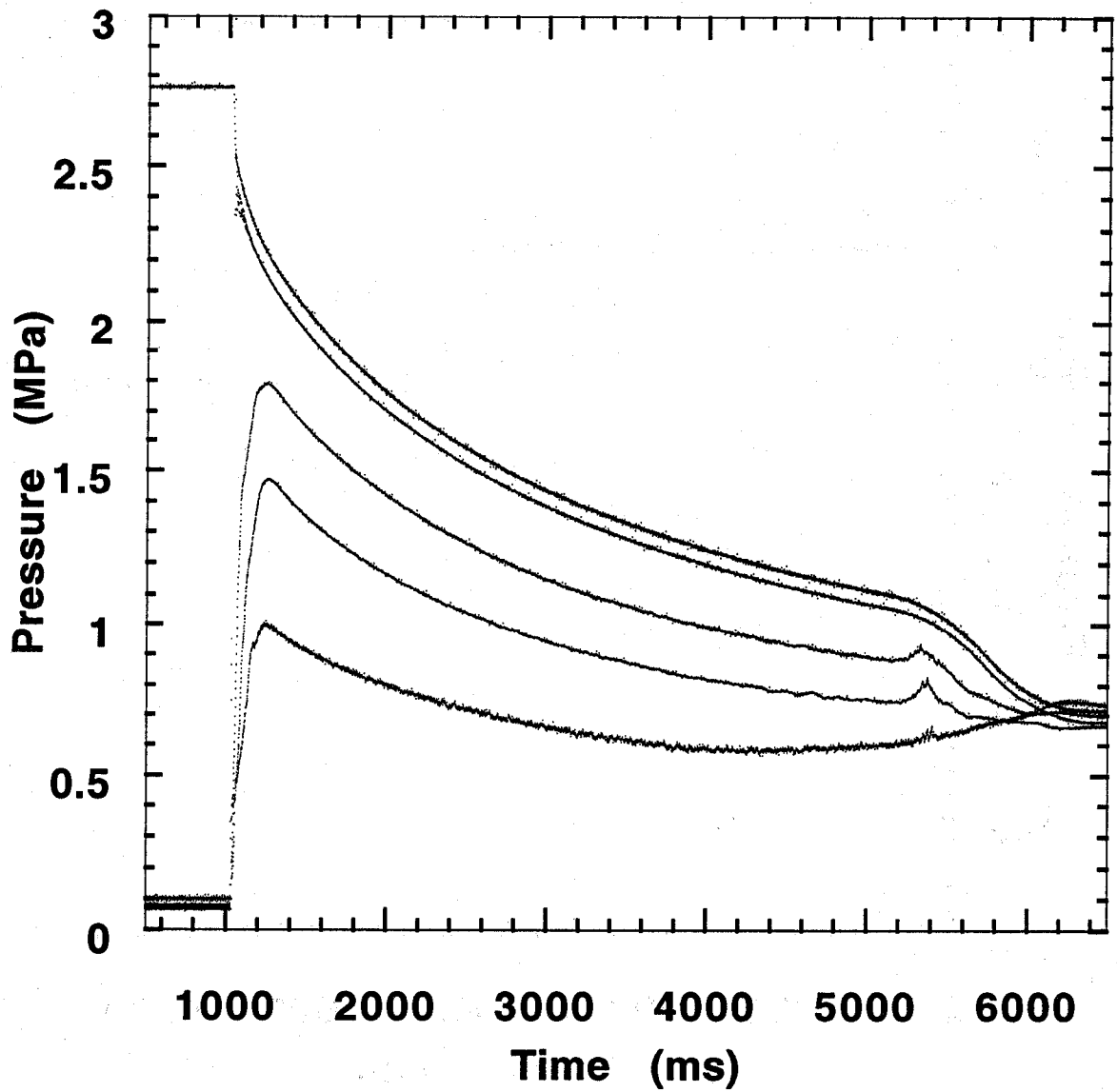


Figure B-54. HFC-227ea test. Refer to Table B-4 for experimental conditions.

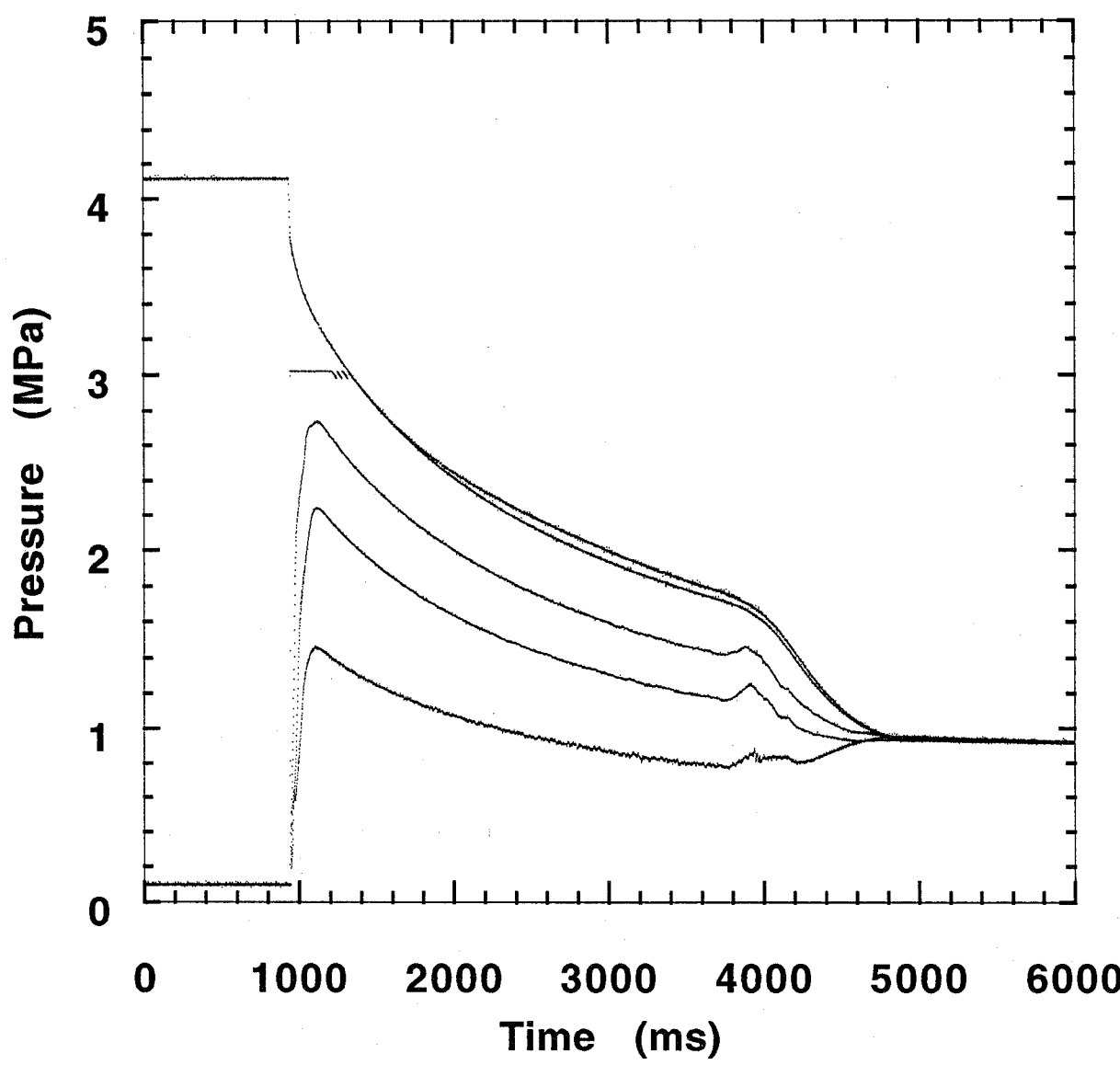


Figure B-55. HFC-227ea test. Refer to Table B-4 for experimental conditions.

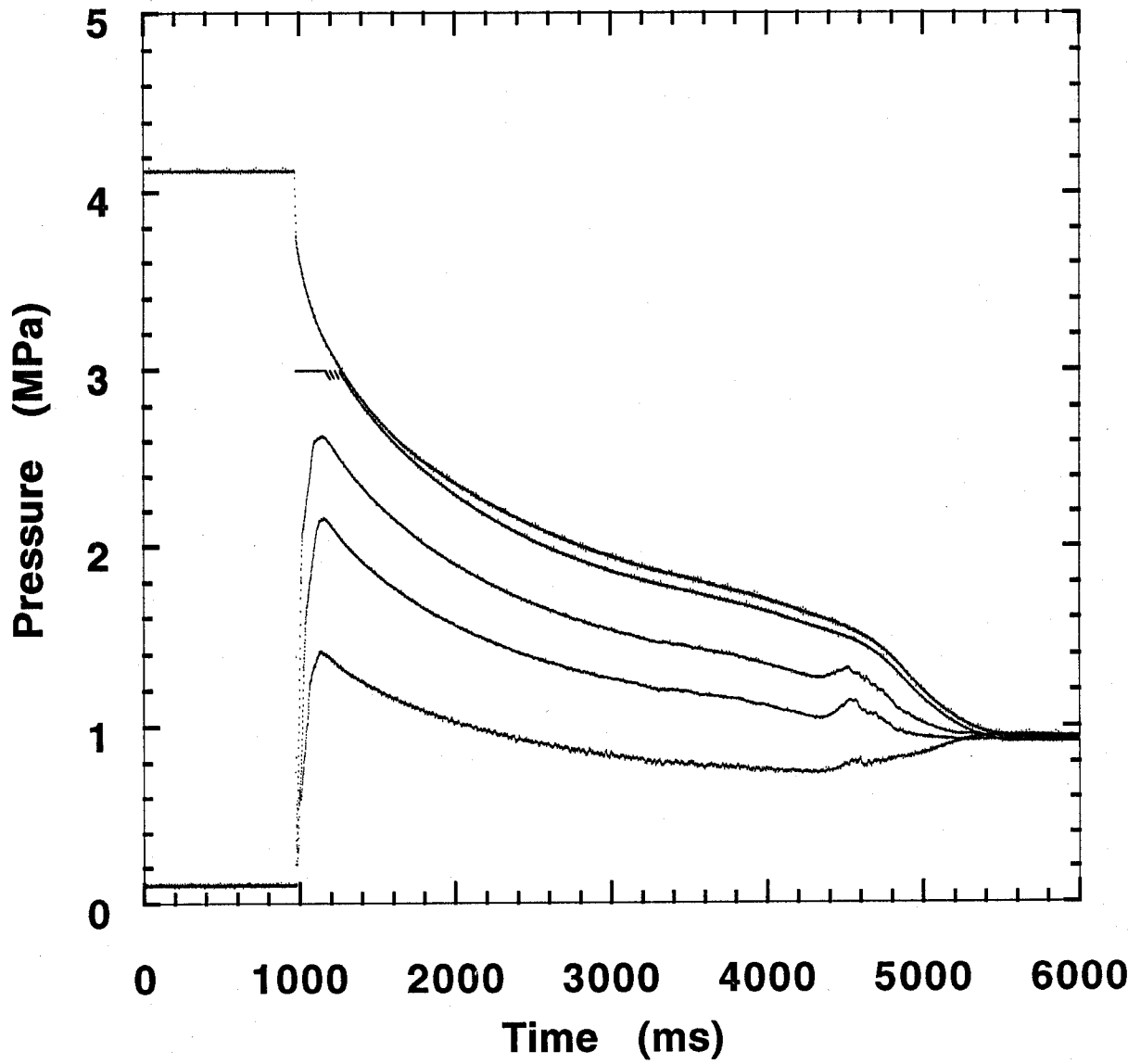


Figure B-56. HFC-227ea test. Refer to Table B-4 for experimental conditions.

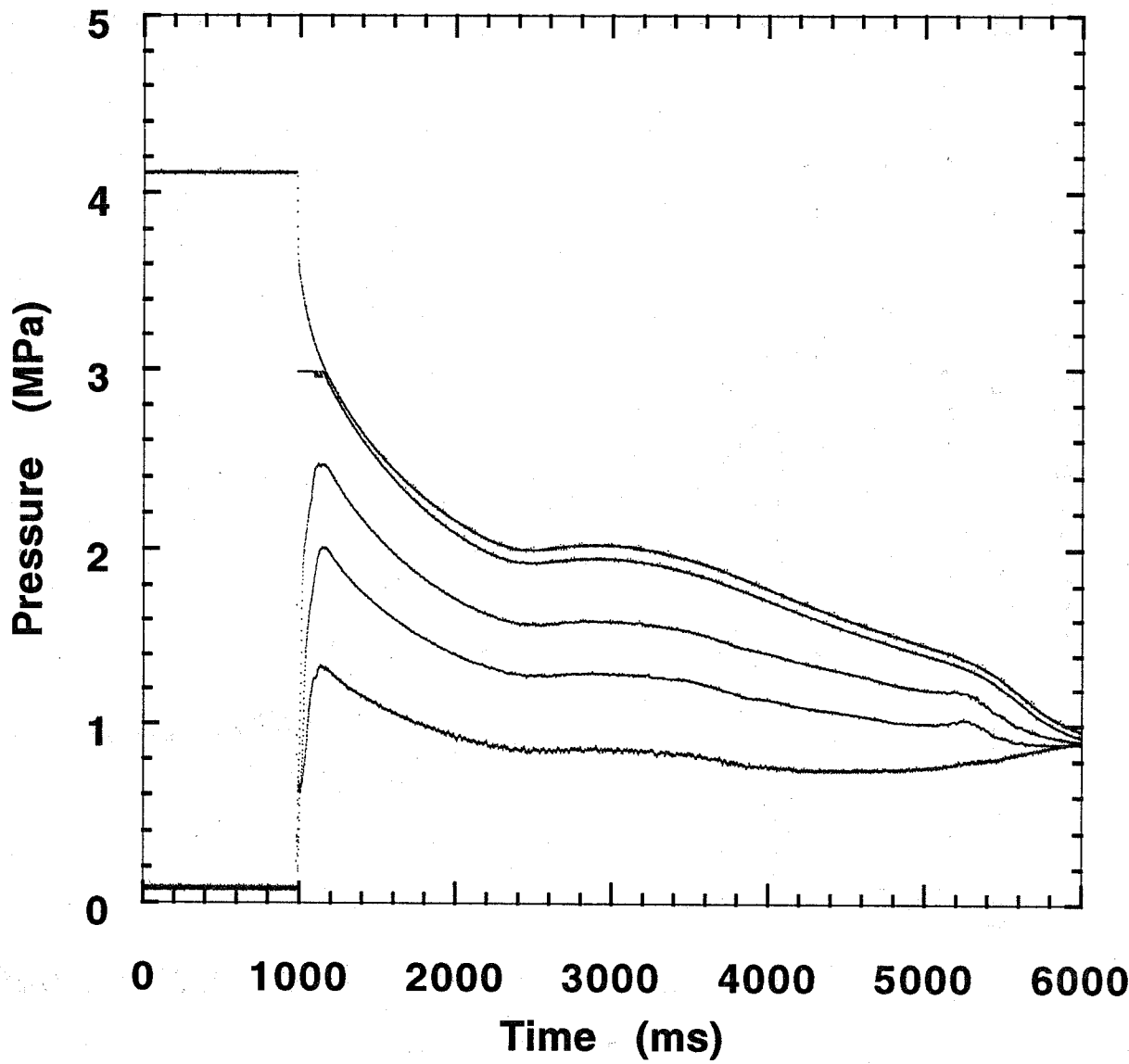


Figure B-57. HFC-227ea test. Refer to Table B-4 for experimental conditions.

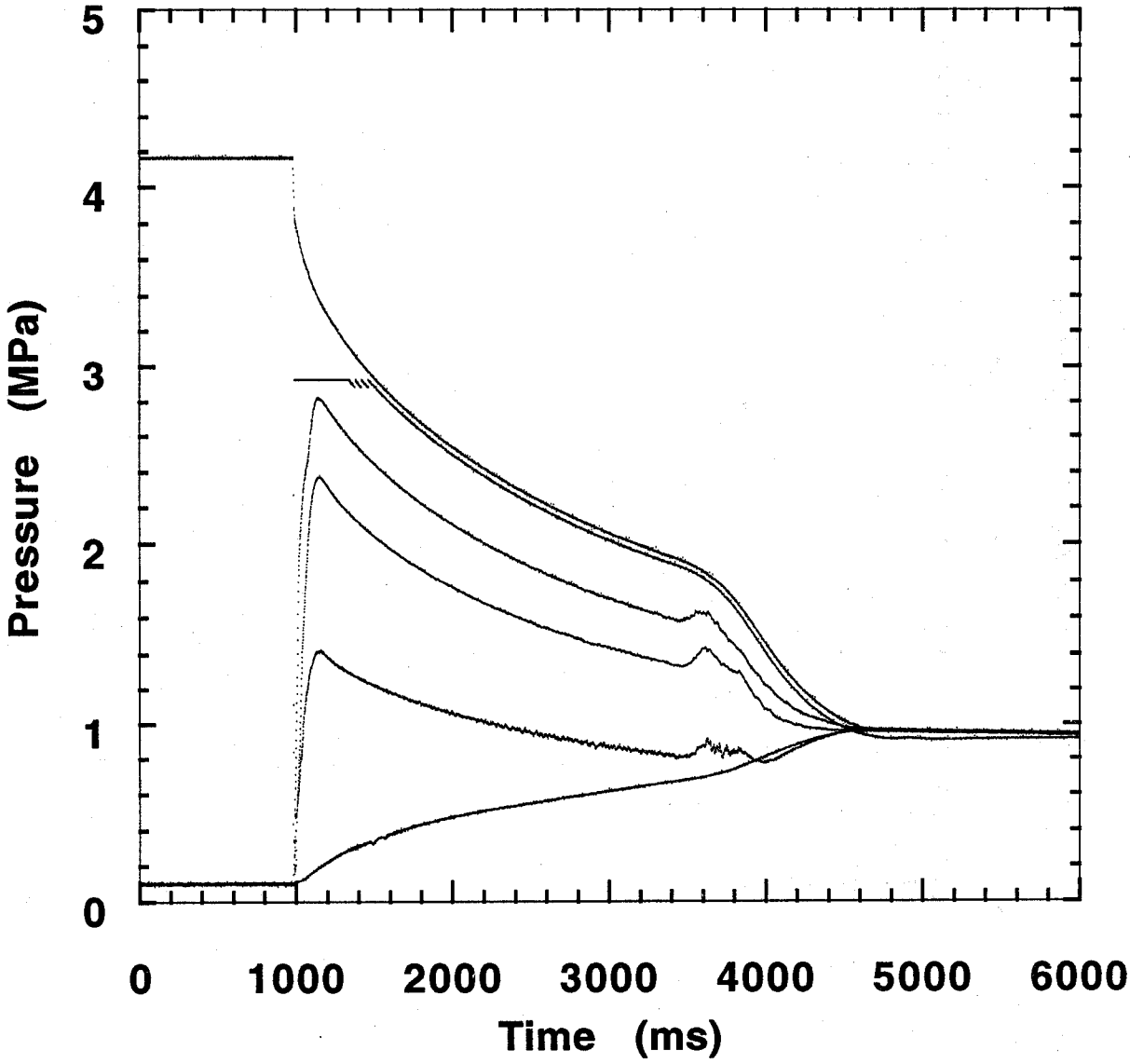


Figure B-58. HFC-227ea test. Refer to Table B-4 for experimental conditions.

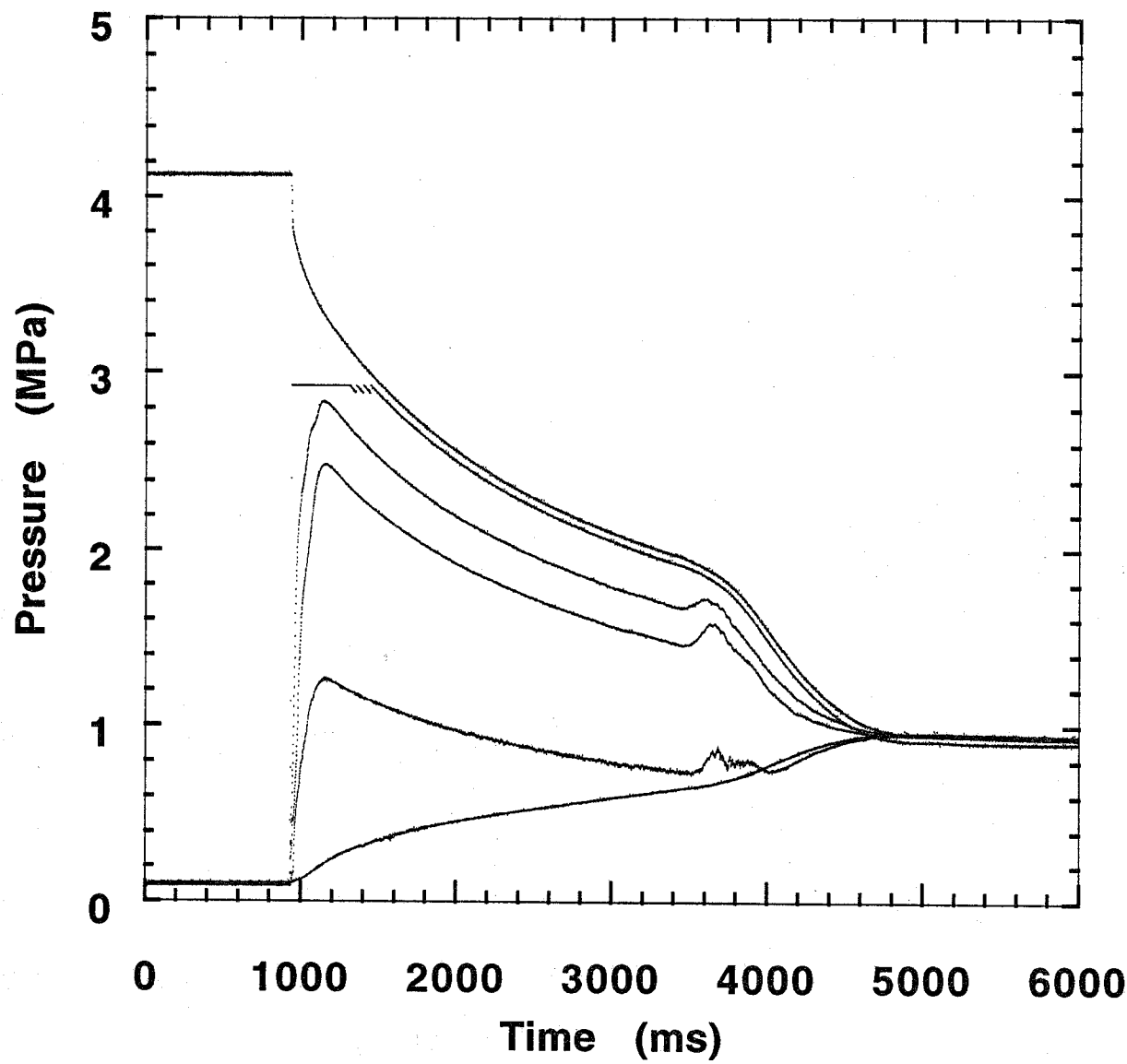


Figure B-59. HFC-227ea test. Refer to Table B-4 for experimental conditions.

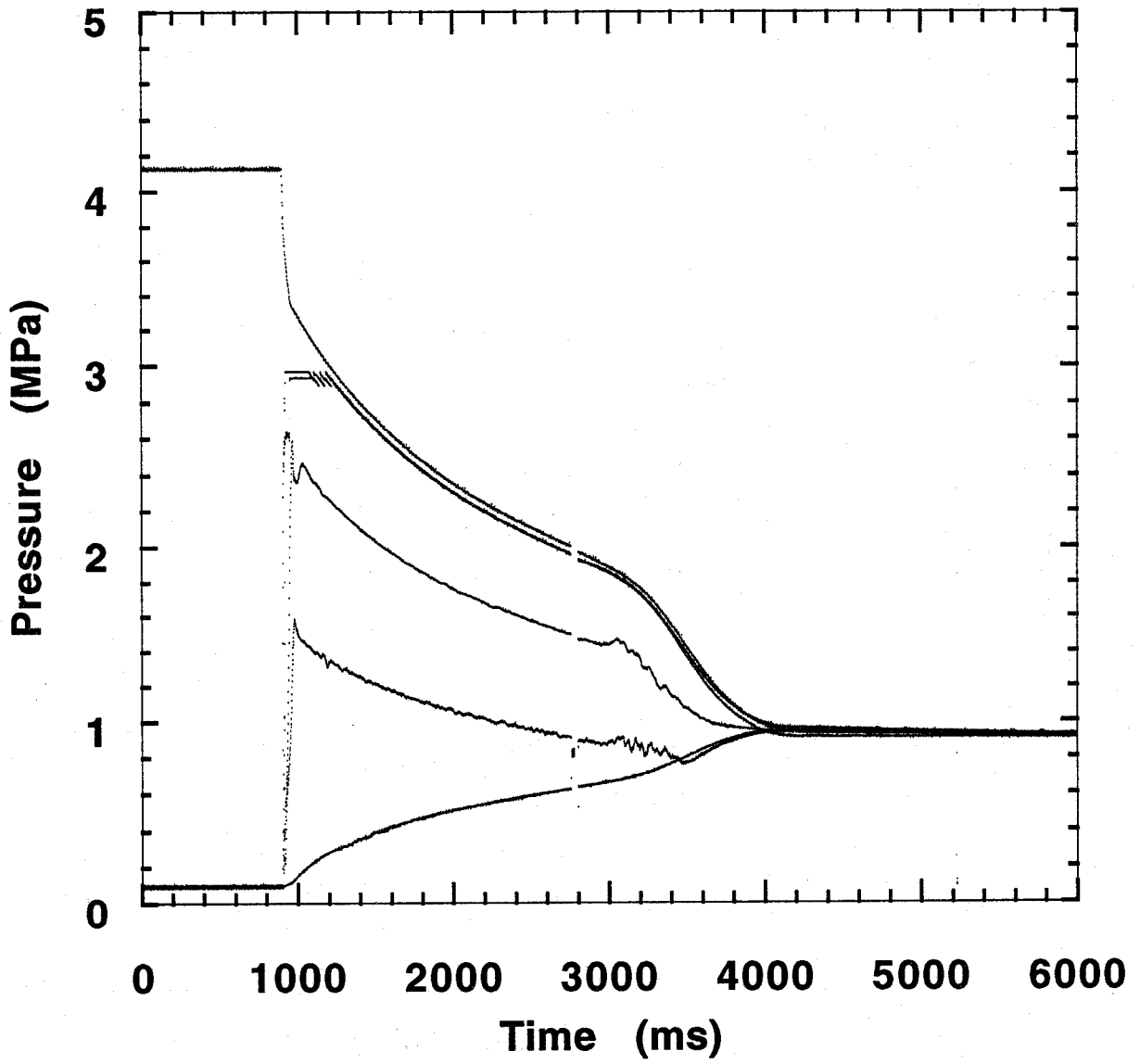


Figure B-60. HFC-227ea test. Refer to Table B-4 for experimental conditions.

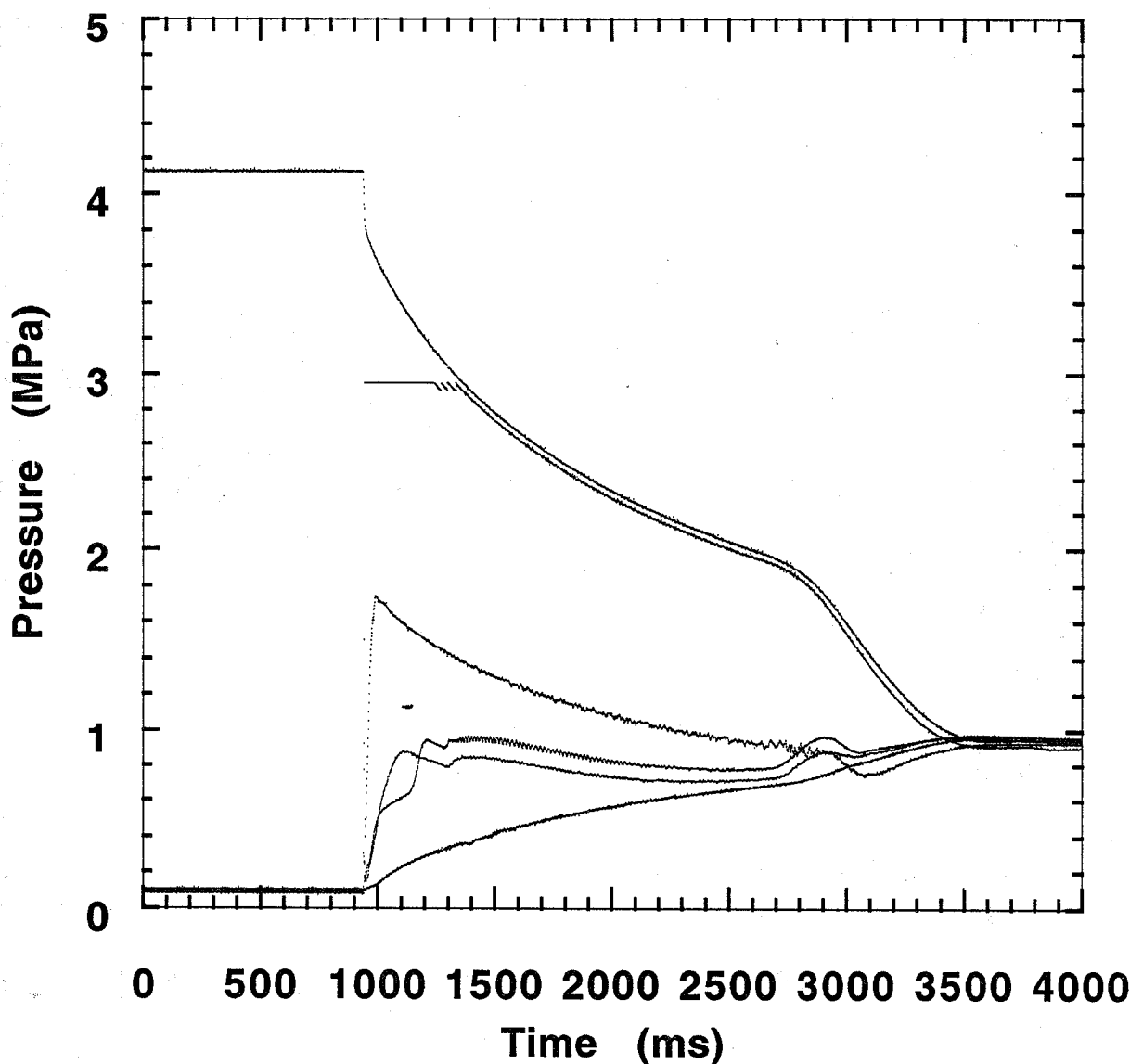


Figure B-61. HFC-227ea test. Refer to Table B-4 for experimental conditions.

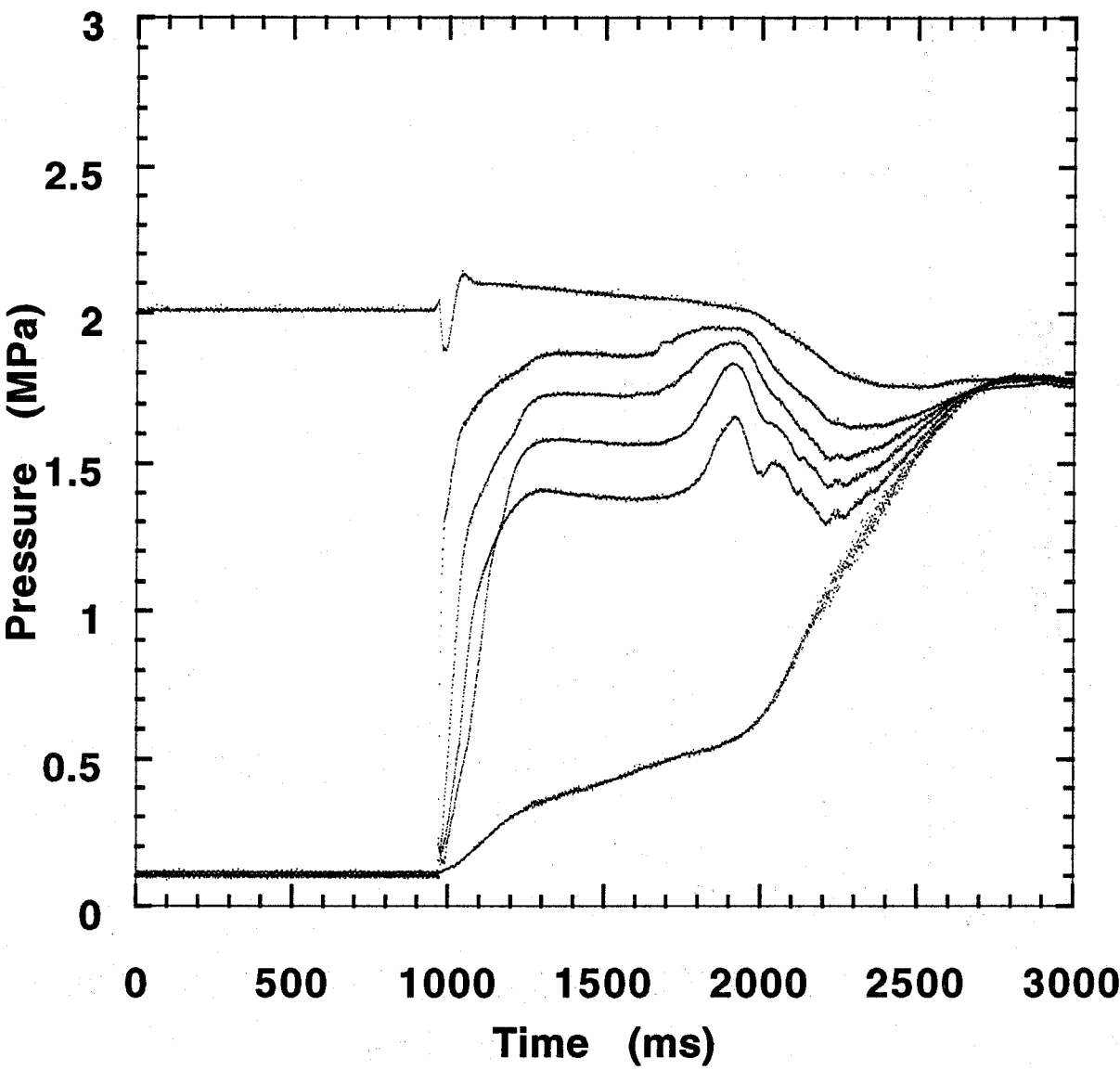


Figure B-62. HFC-227ea test. Refer to Table B-4 for experimental conditions.

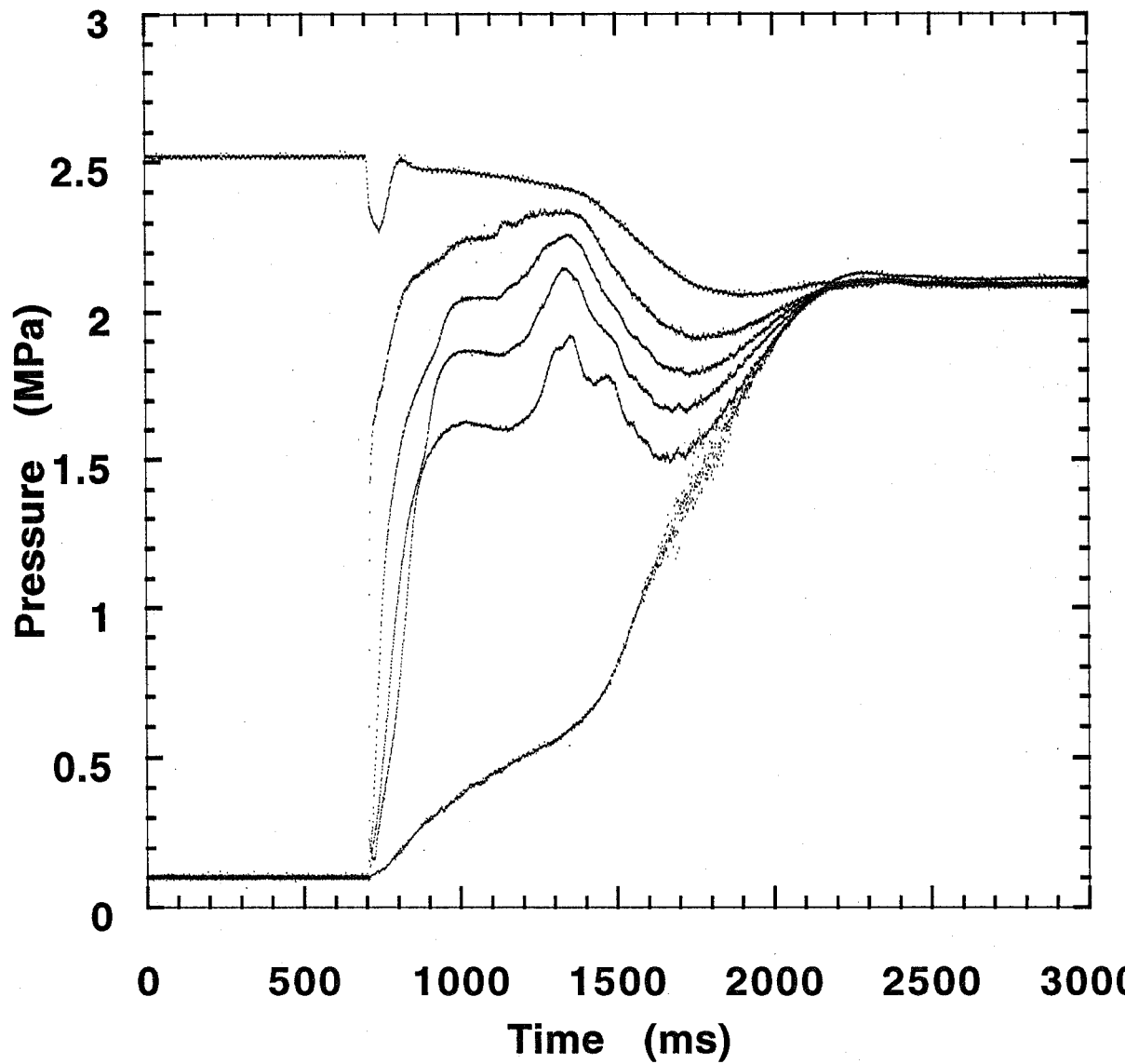


Figure B-63. HFC-227ea test. Refer to Table B-4 for experimental conditions.

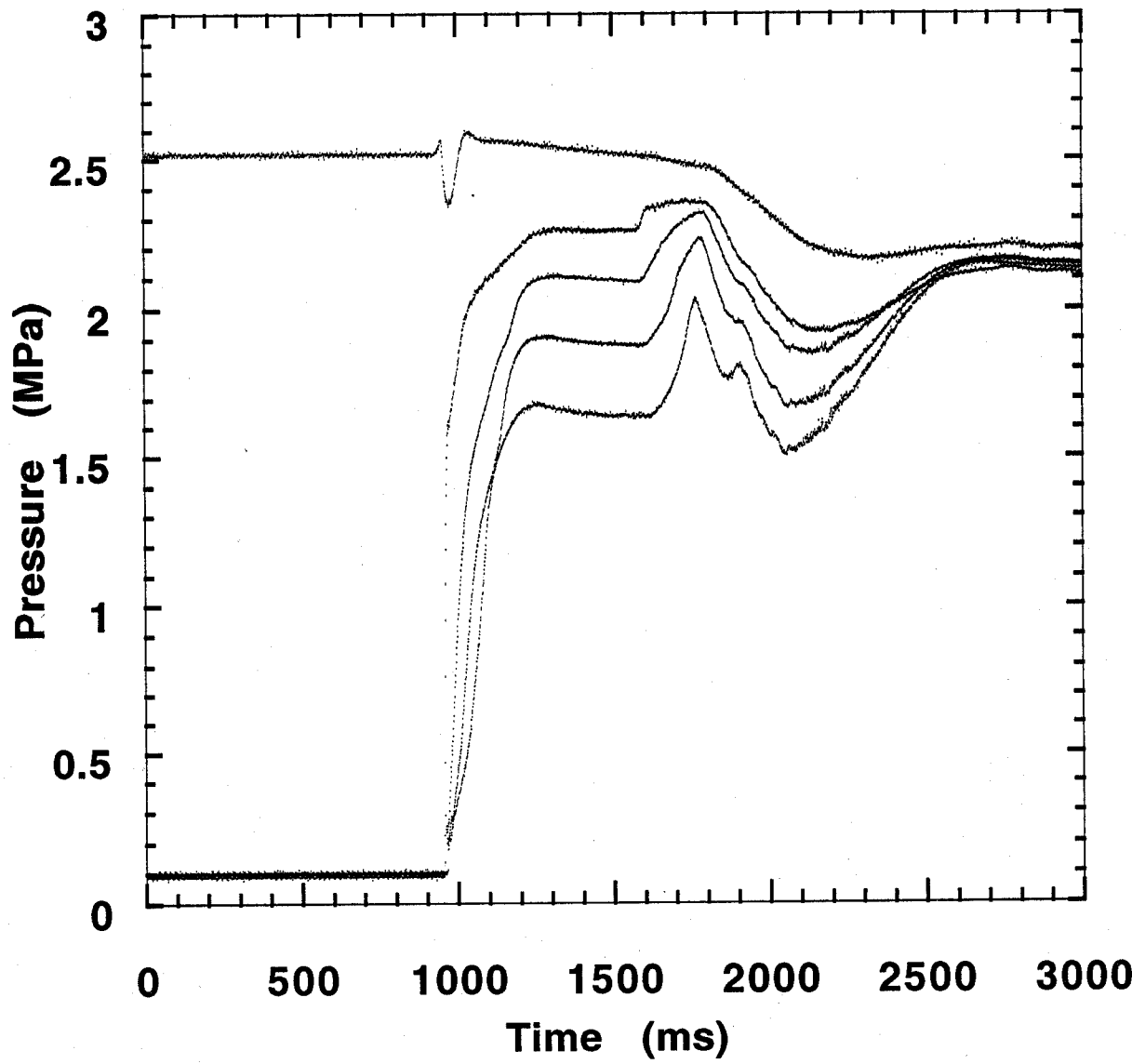


Figure B-64. HFC-227ea test. Refer to Table B-4 for experimental conditions.

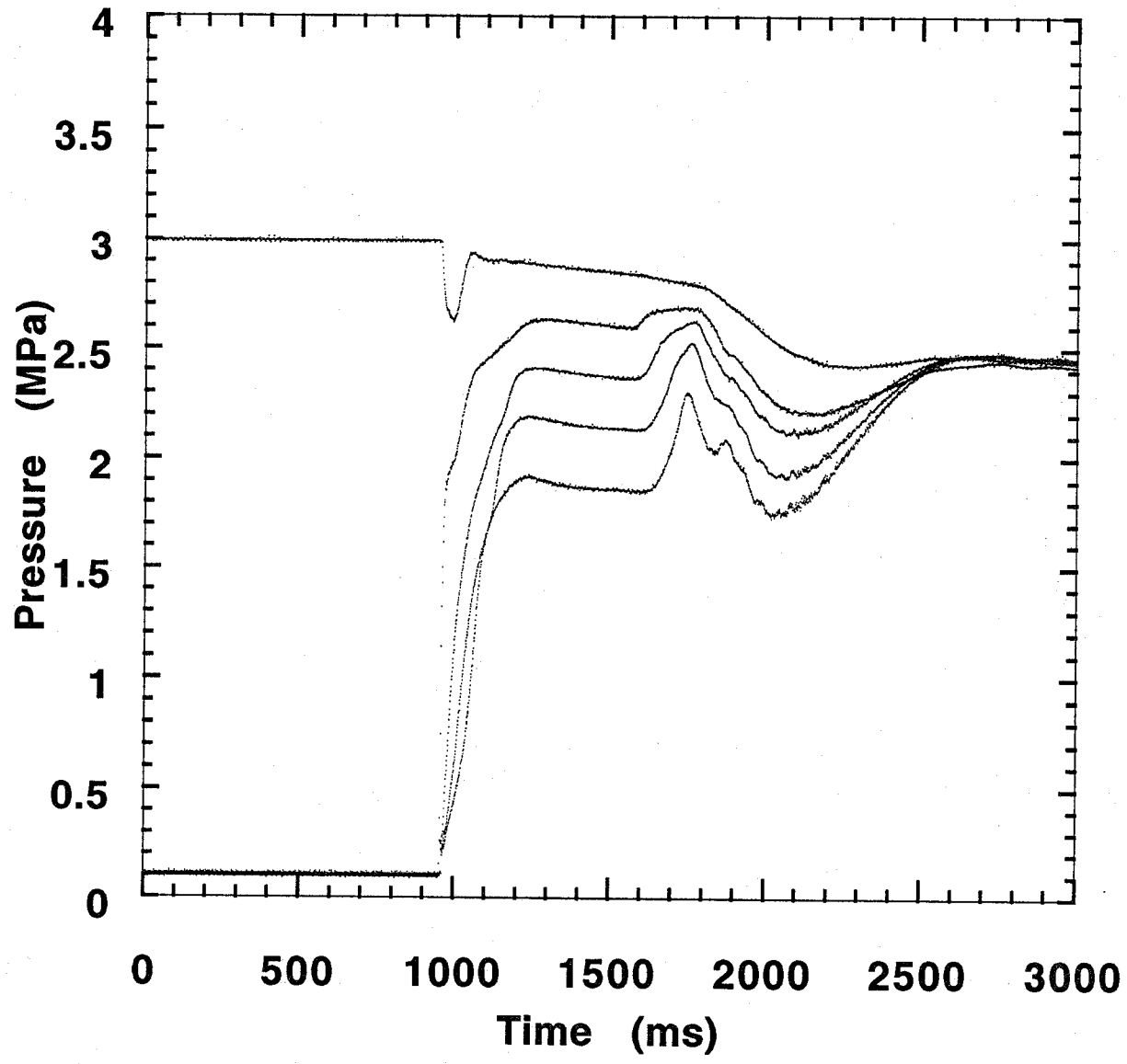


Figure B-65. HFC-227ea test. Refer to Table B-4 for experimental conditions.

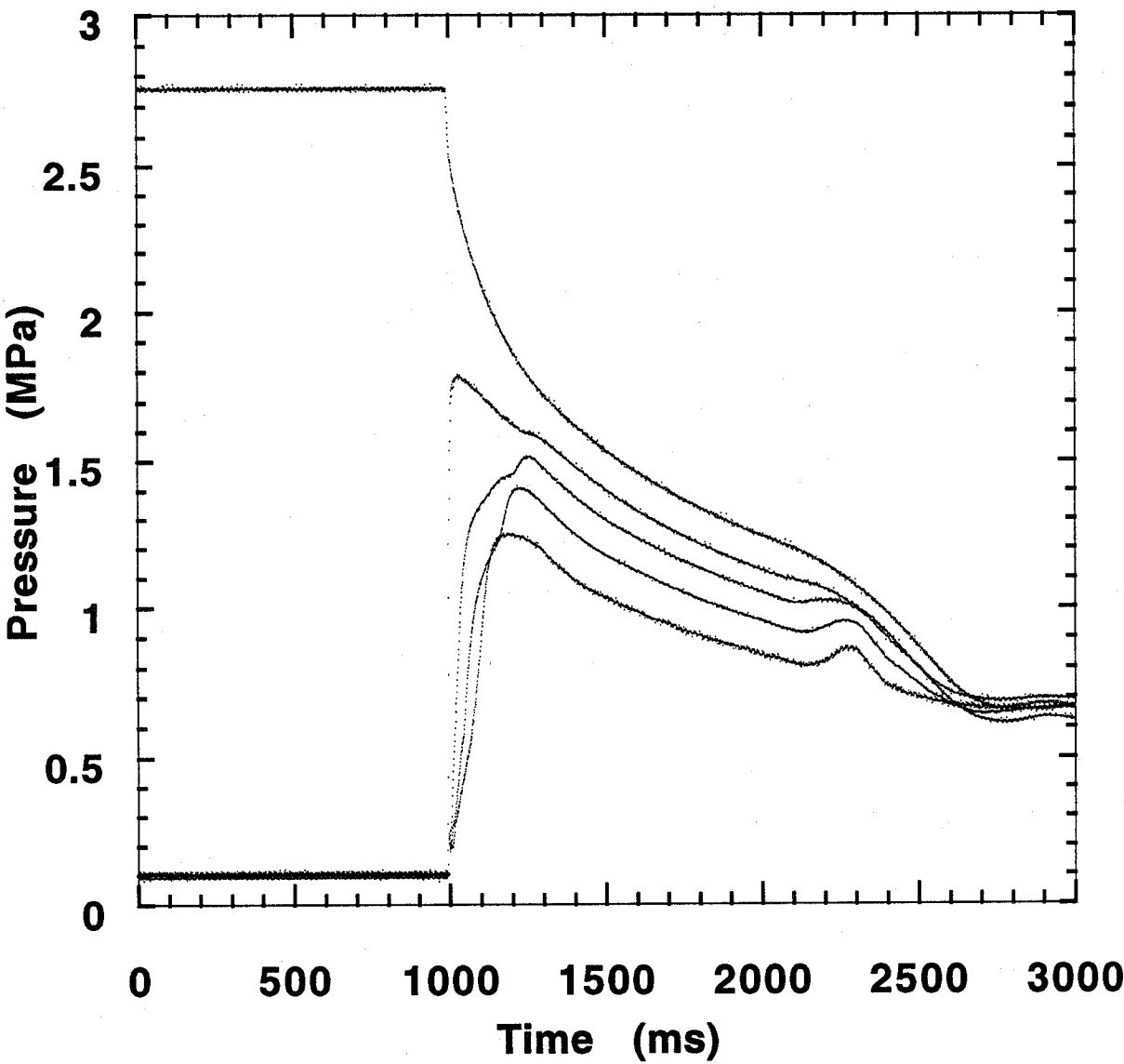


Figure B-66. HFC-227ea test. Refer to Table B-4 for experimental conditions.

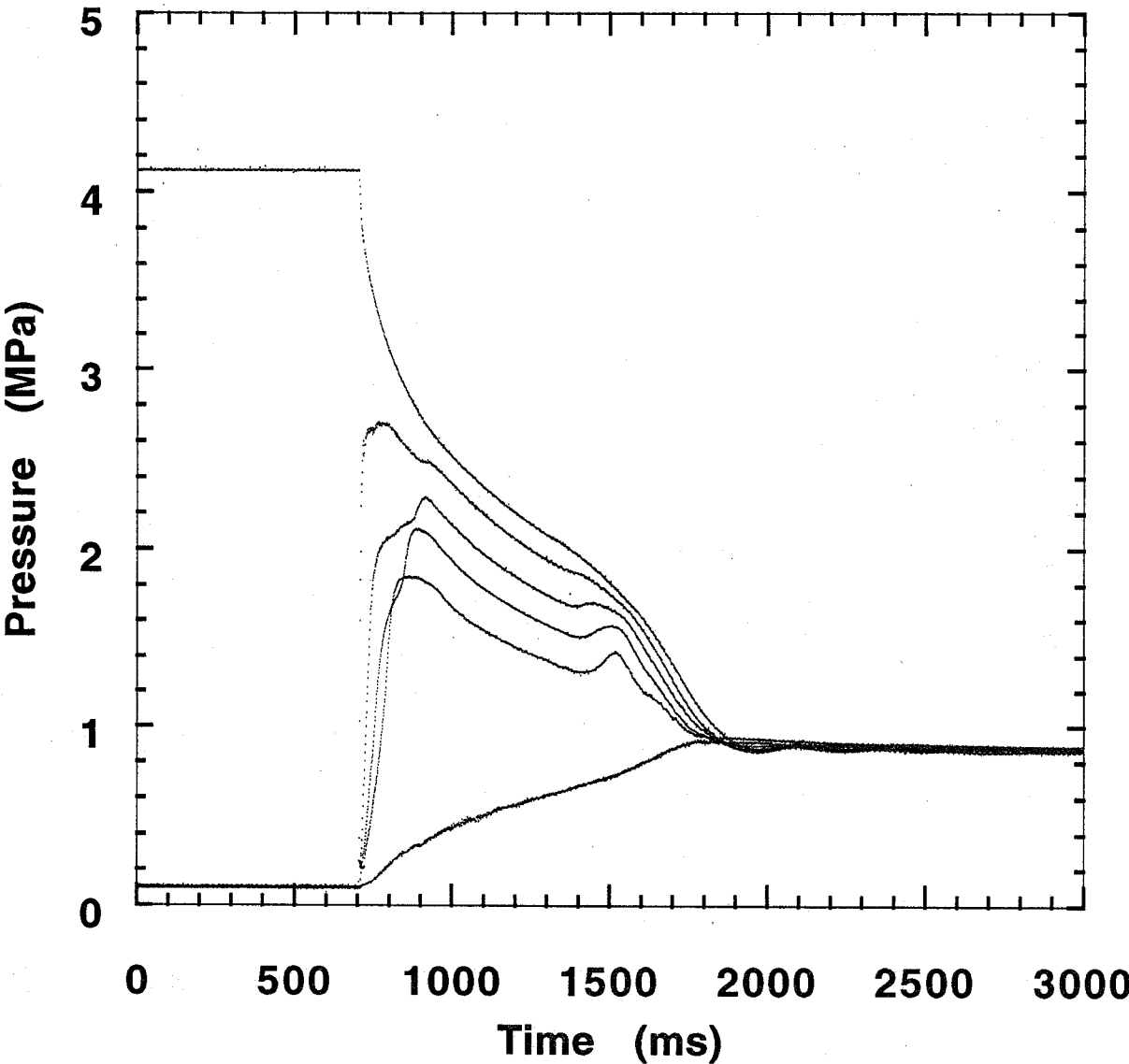


Figure B-67. HFC-227ea test. Refer to Table B-4 for experimental conditions.

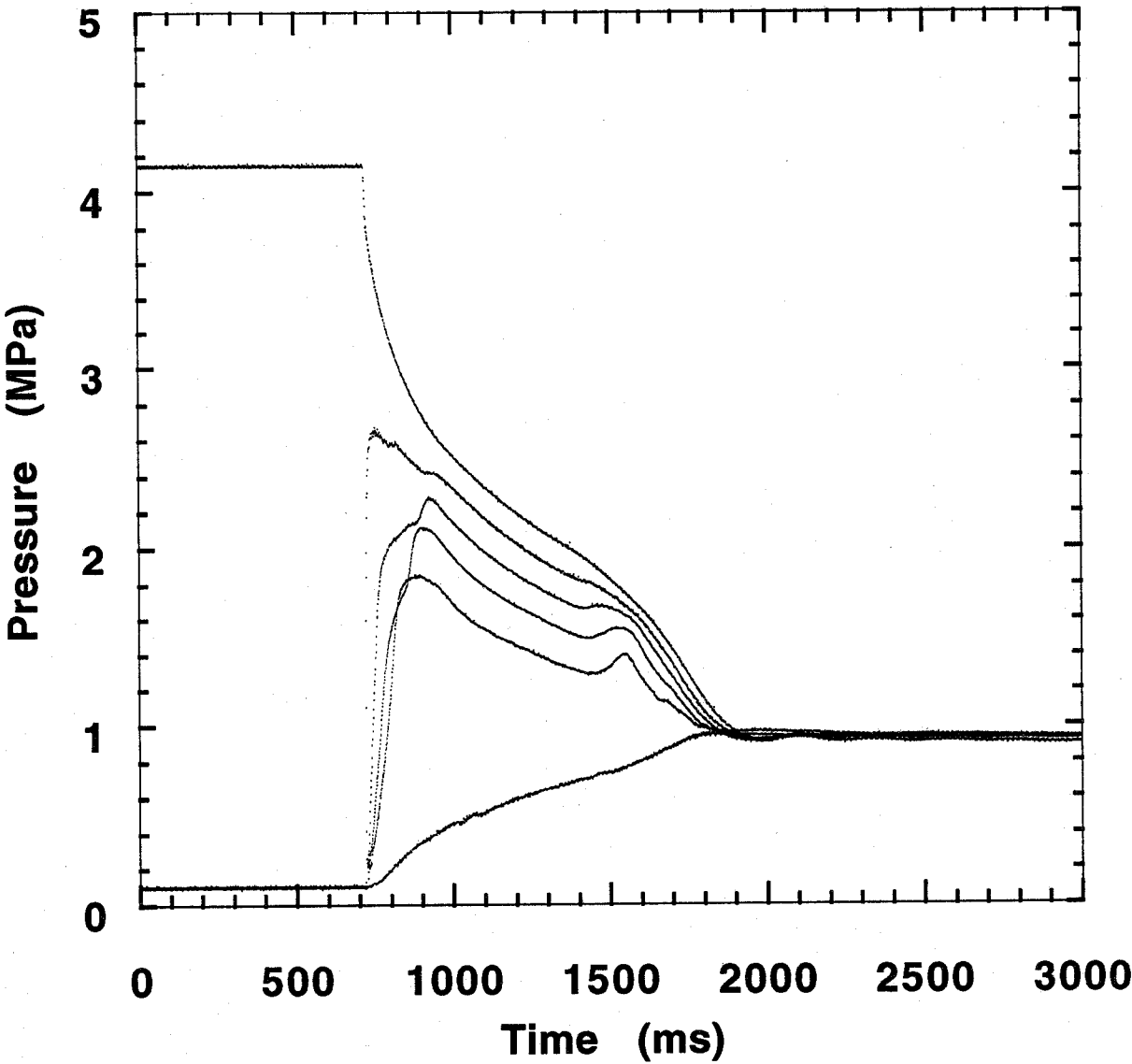


Figure B-68. HFC-227ea test. Refer to Table B-4 for experimental conditions.

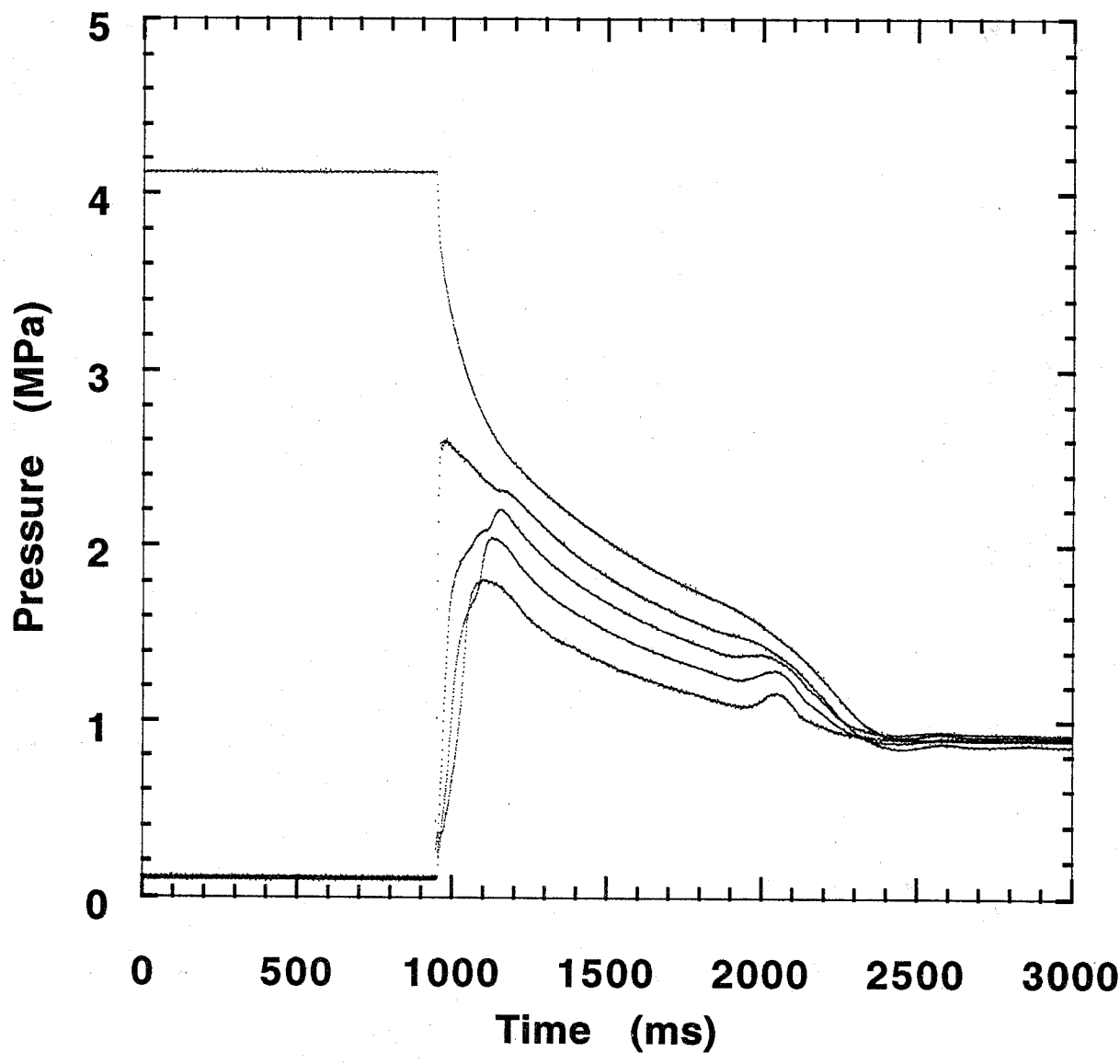


Figure B-69. HFC-227ea test. Refer to Table B-4 for experimental conditions.

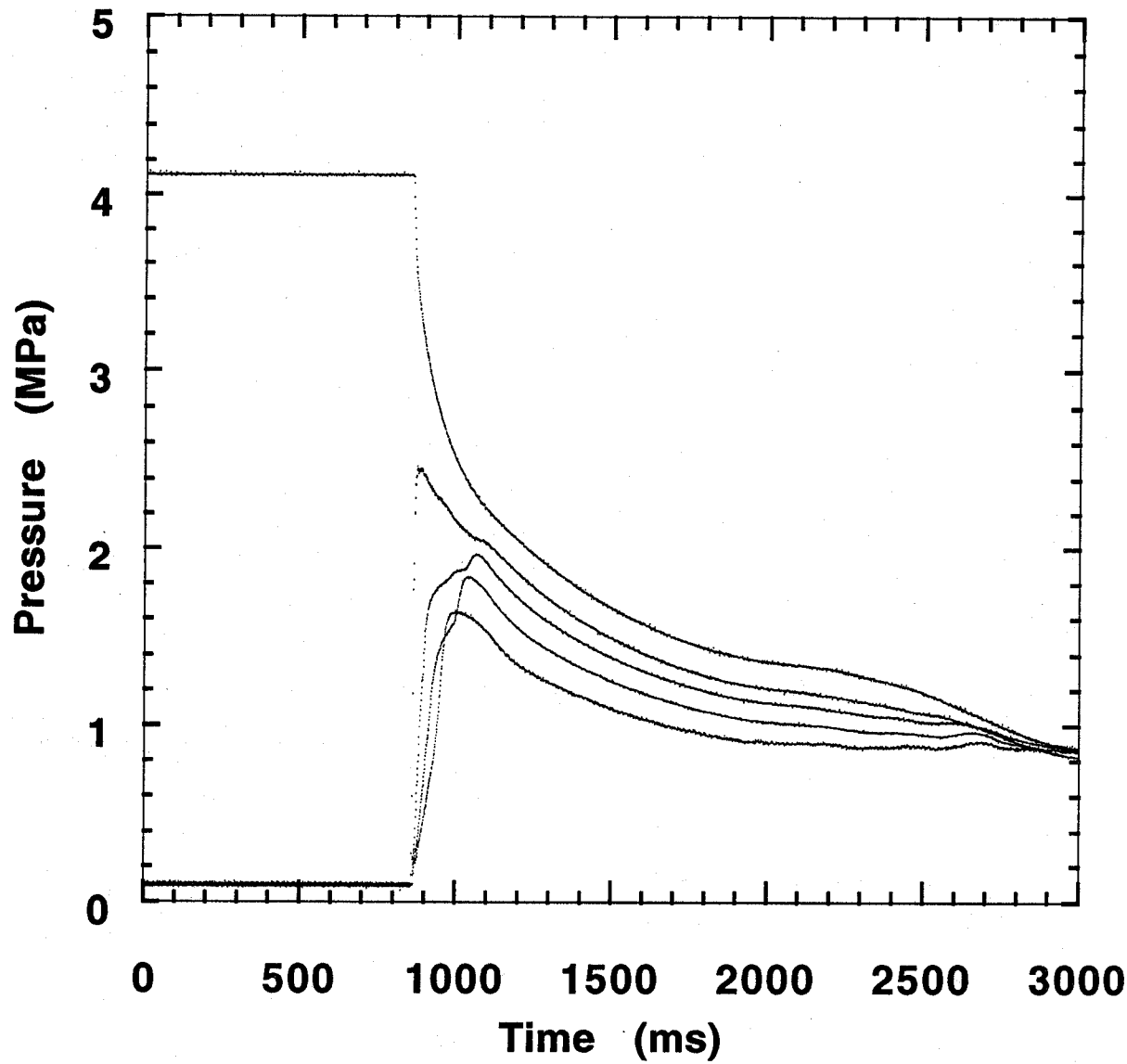


Figure B-70. HFC-227ea test. Refer to Table B-4 for experimental conditions.

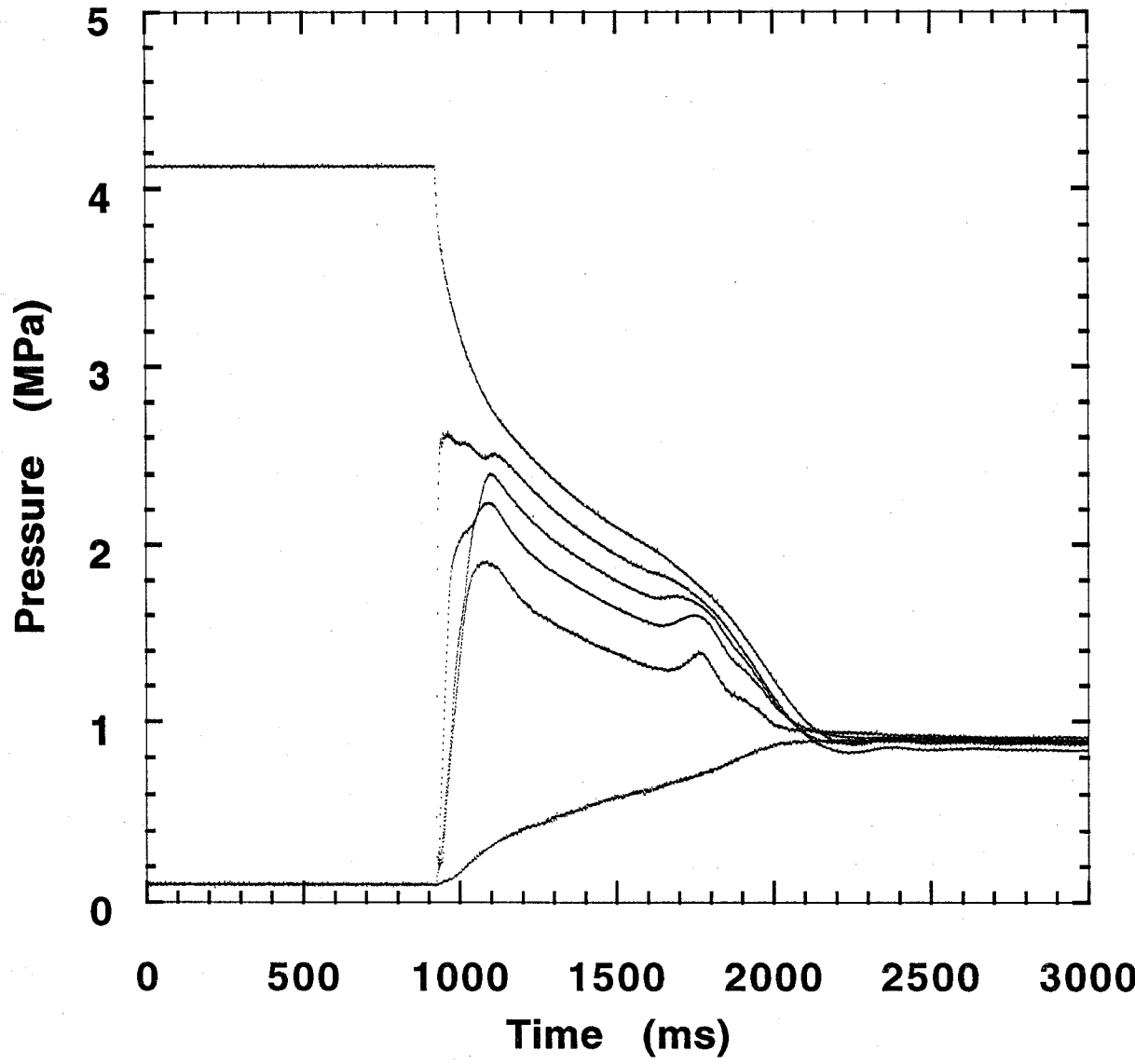


Figure B-71. HFC-227ea test. Refer to Table B-4 for experimental conditions.

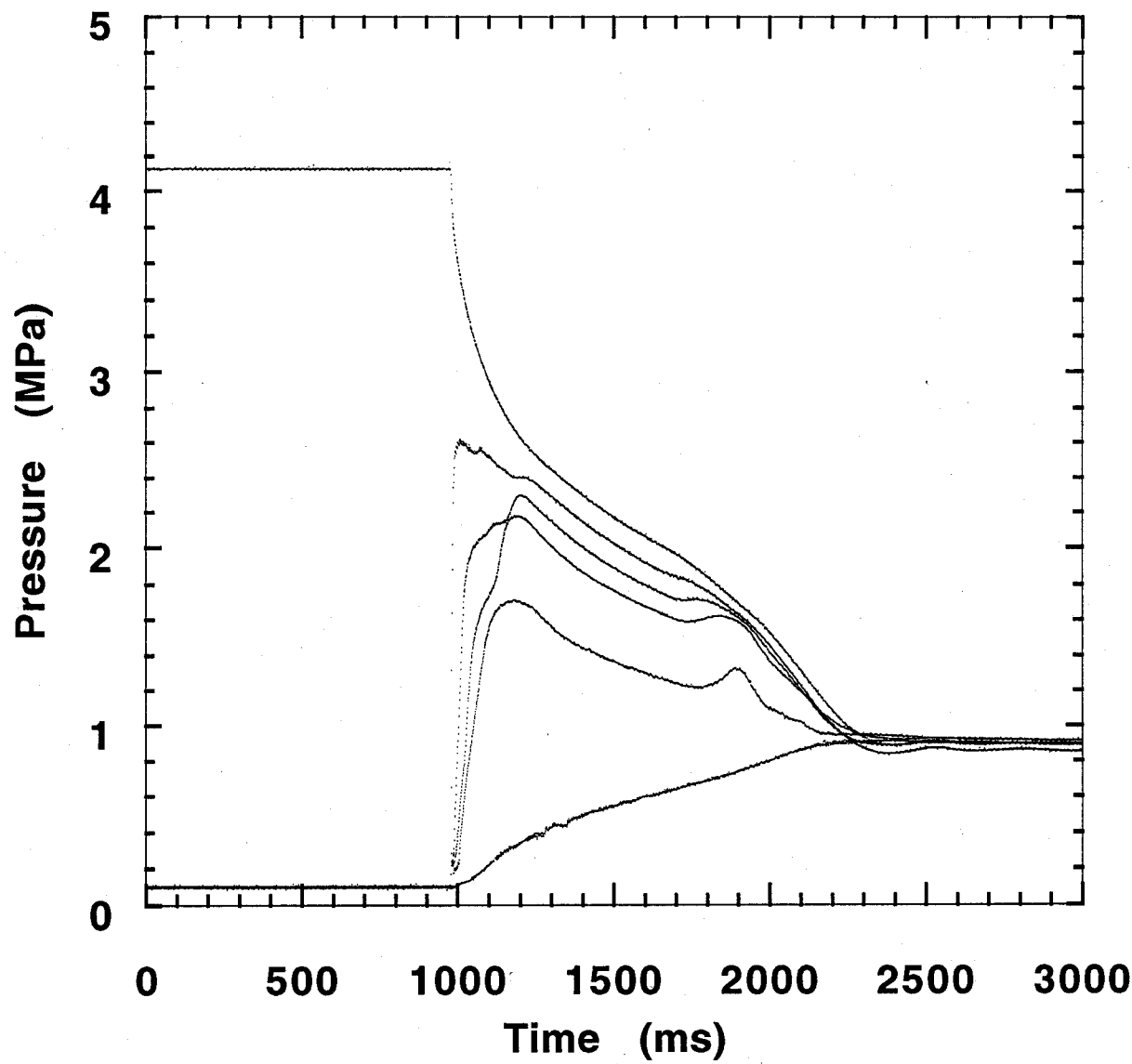


Figure B-72. HFC-227ea test. Refer to Table B-4 for experimental conditions.

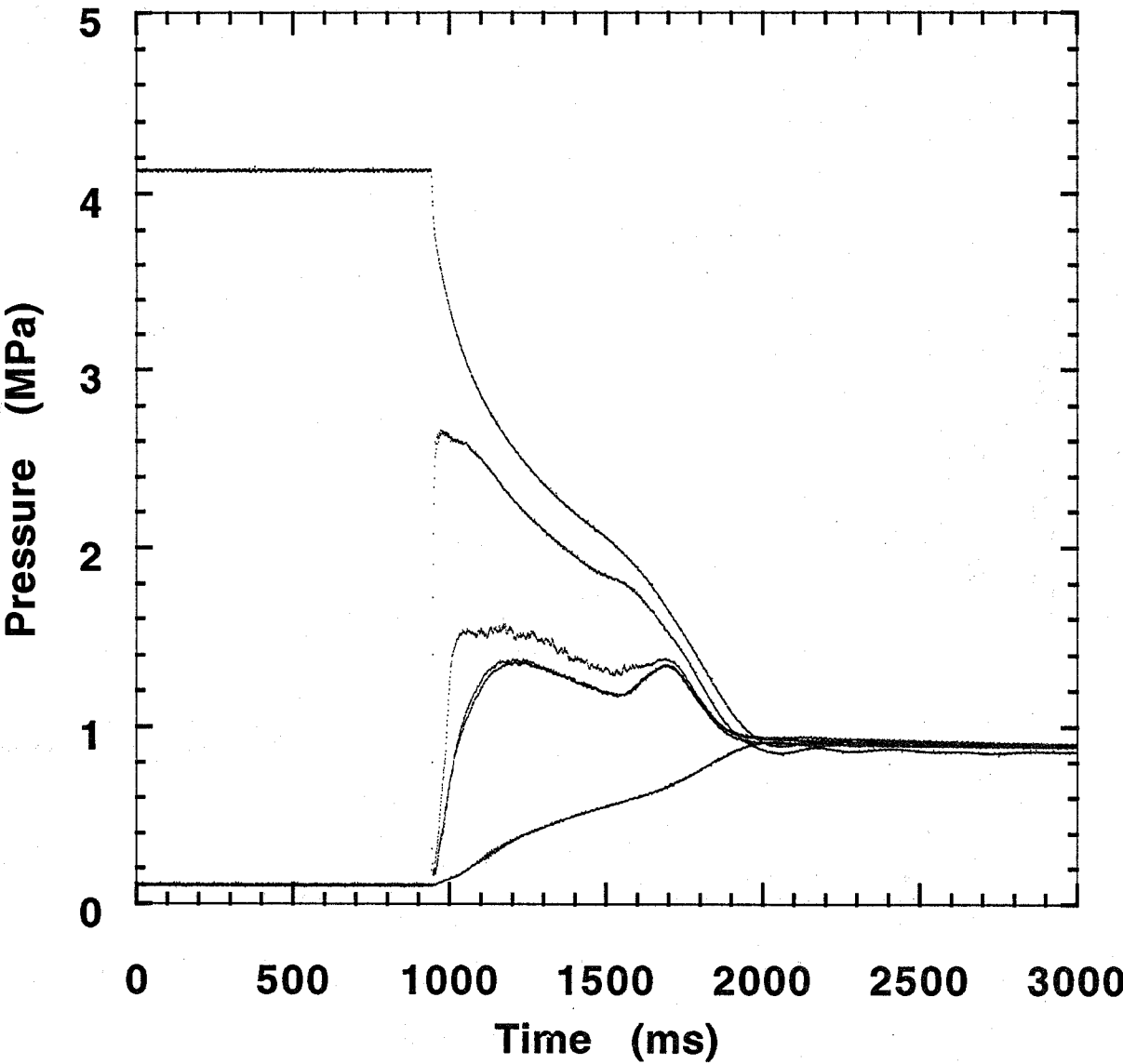


Figure B-73. HFC-227ea test. Refer to Table B-4 for experimental conditions.

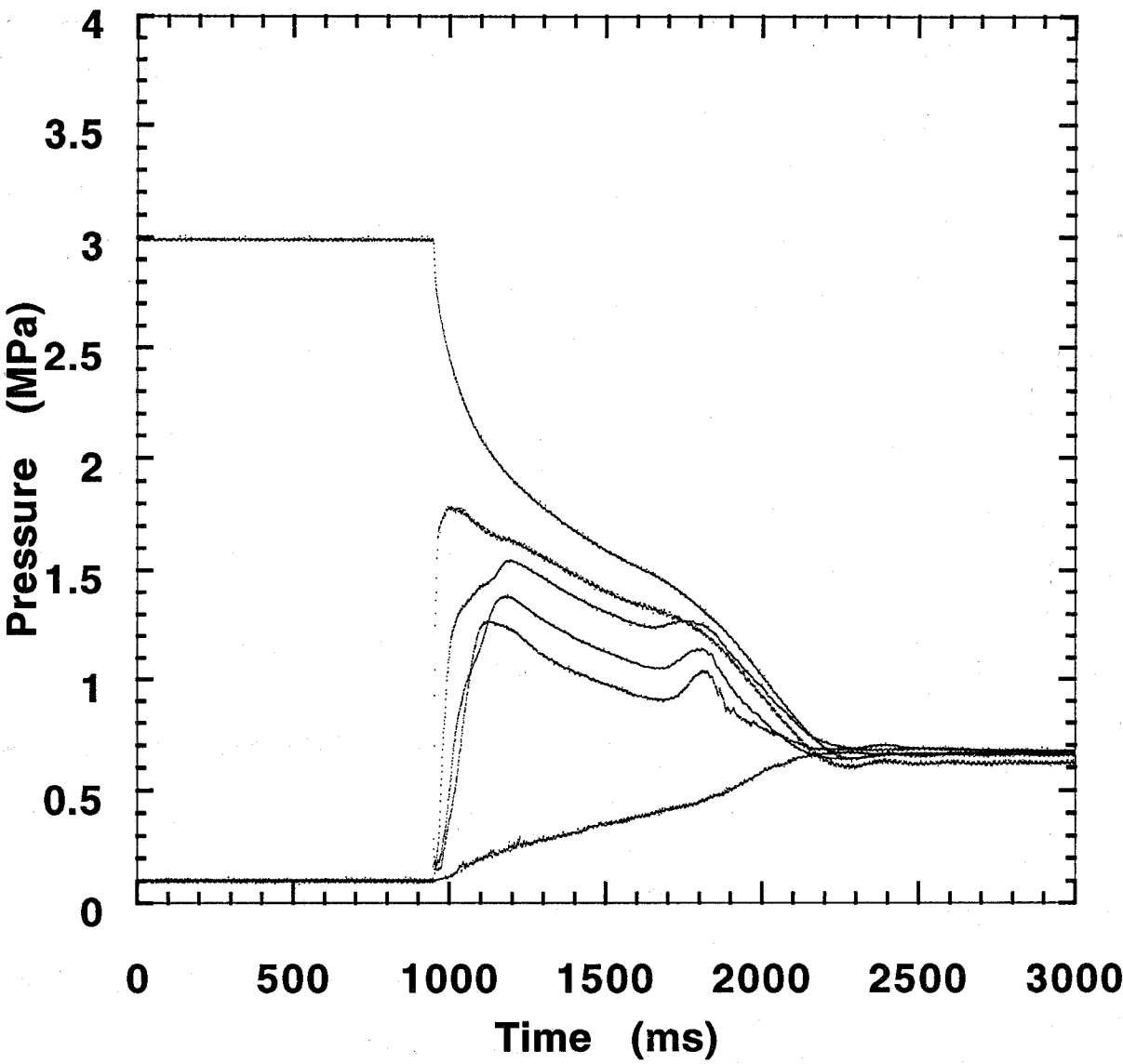


Figure B-74. HFC-227ea test. Refer to Table B-4 for experimental conditions.

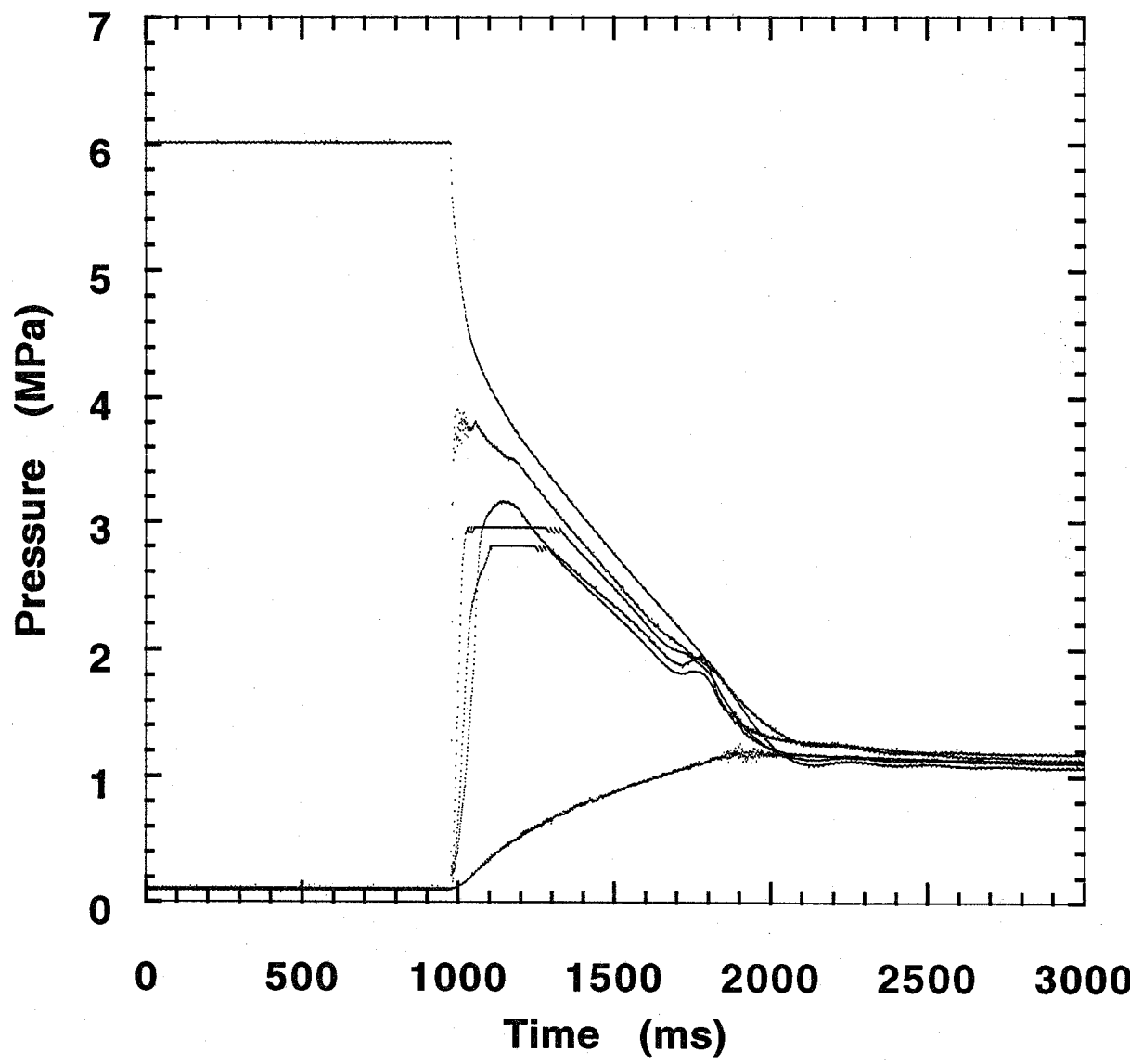


Figure B-75. HFC-227ea test. Refer to Table B-4 for experimental conditions.

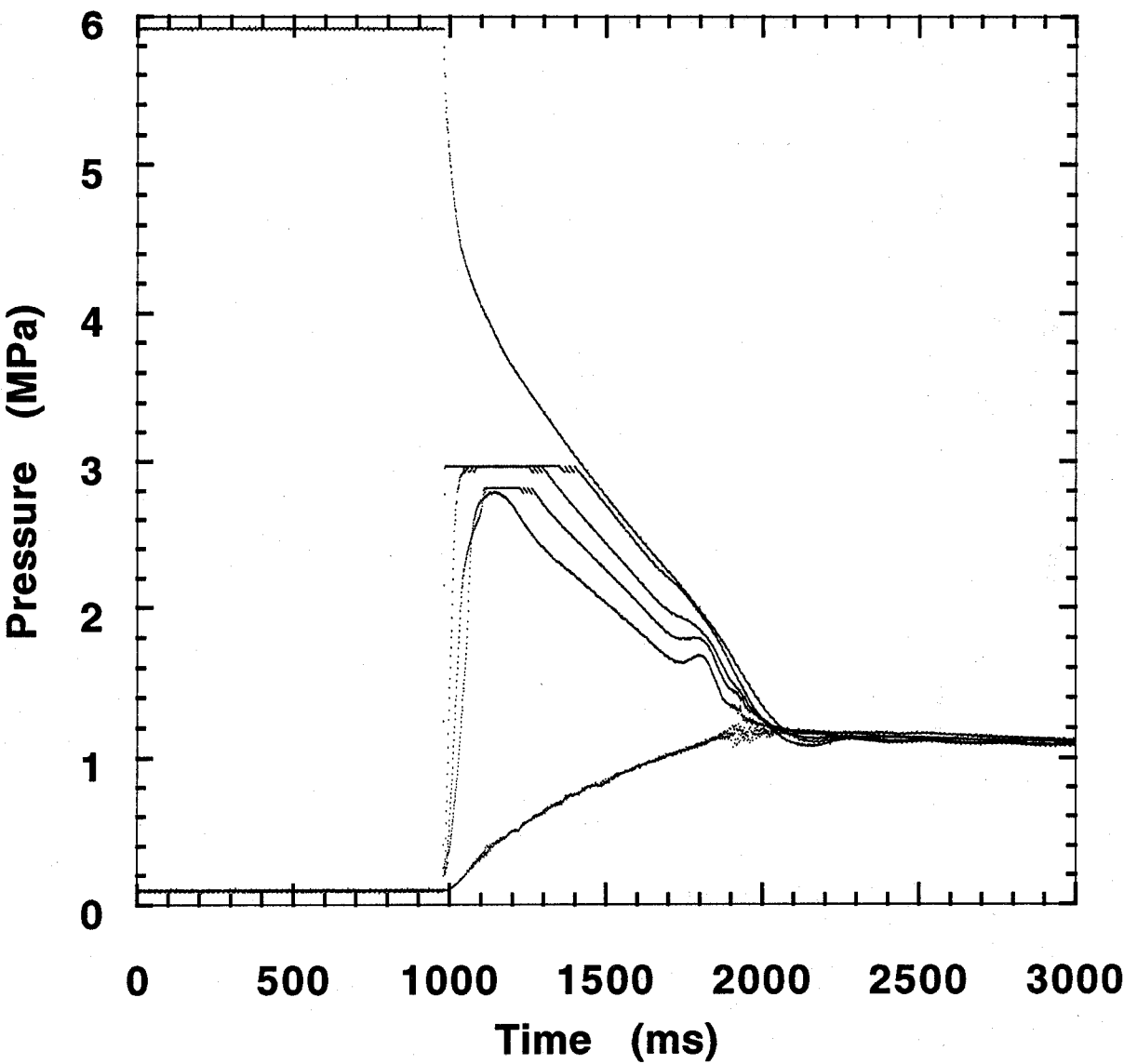


Figure B-76. HFC-227ea test. Refer to Table B-4 for experimental conditions.

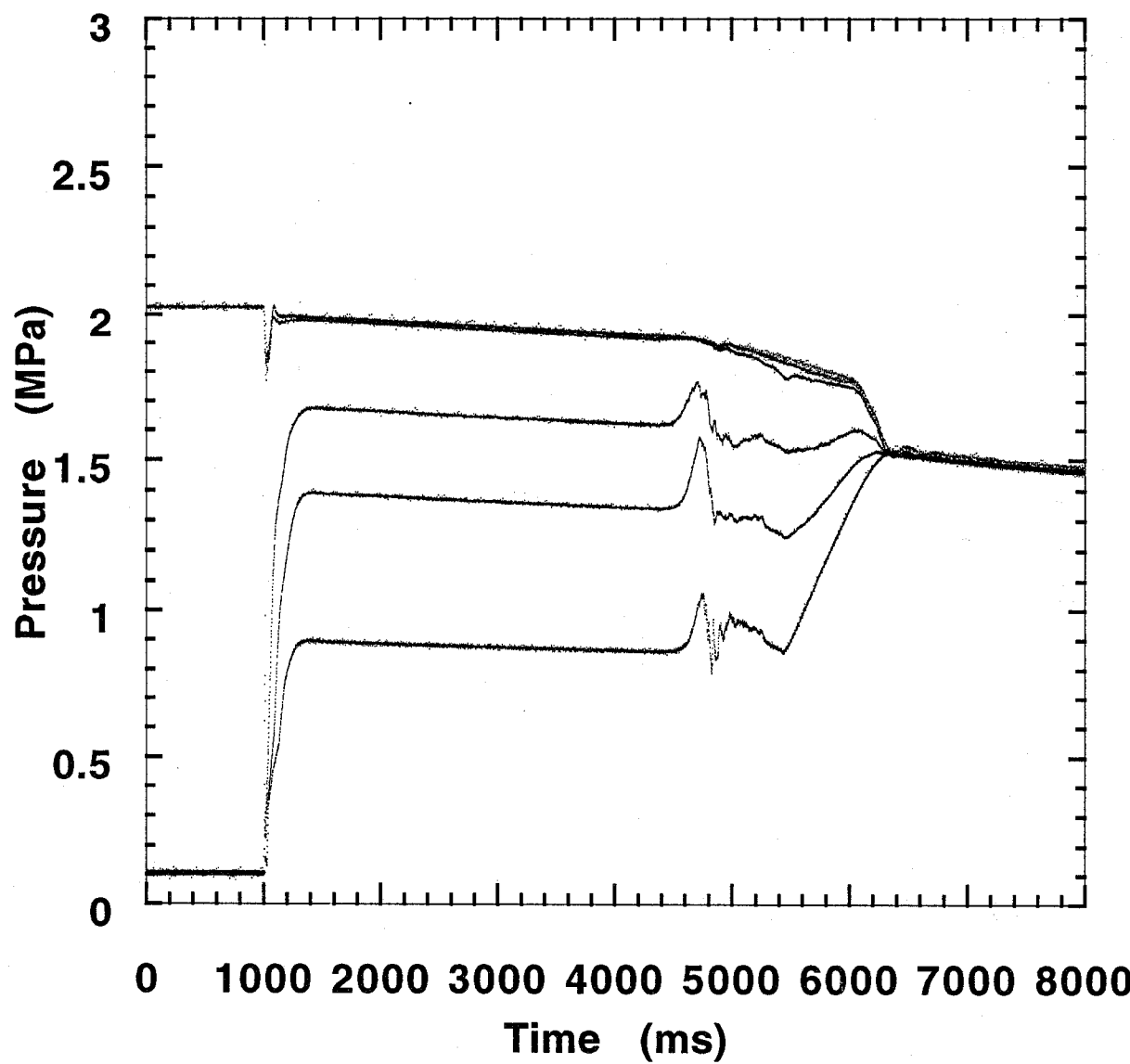


Figure B-77. CF_3I test. Refer to Table B-5 for experimental conditions.

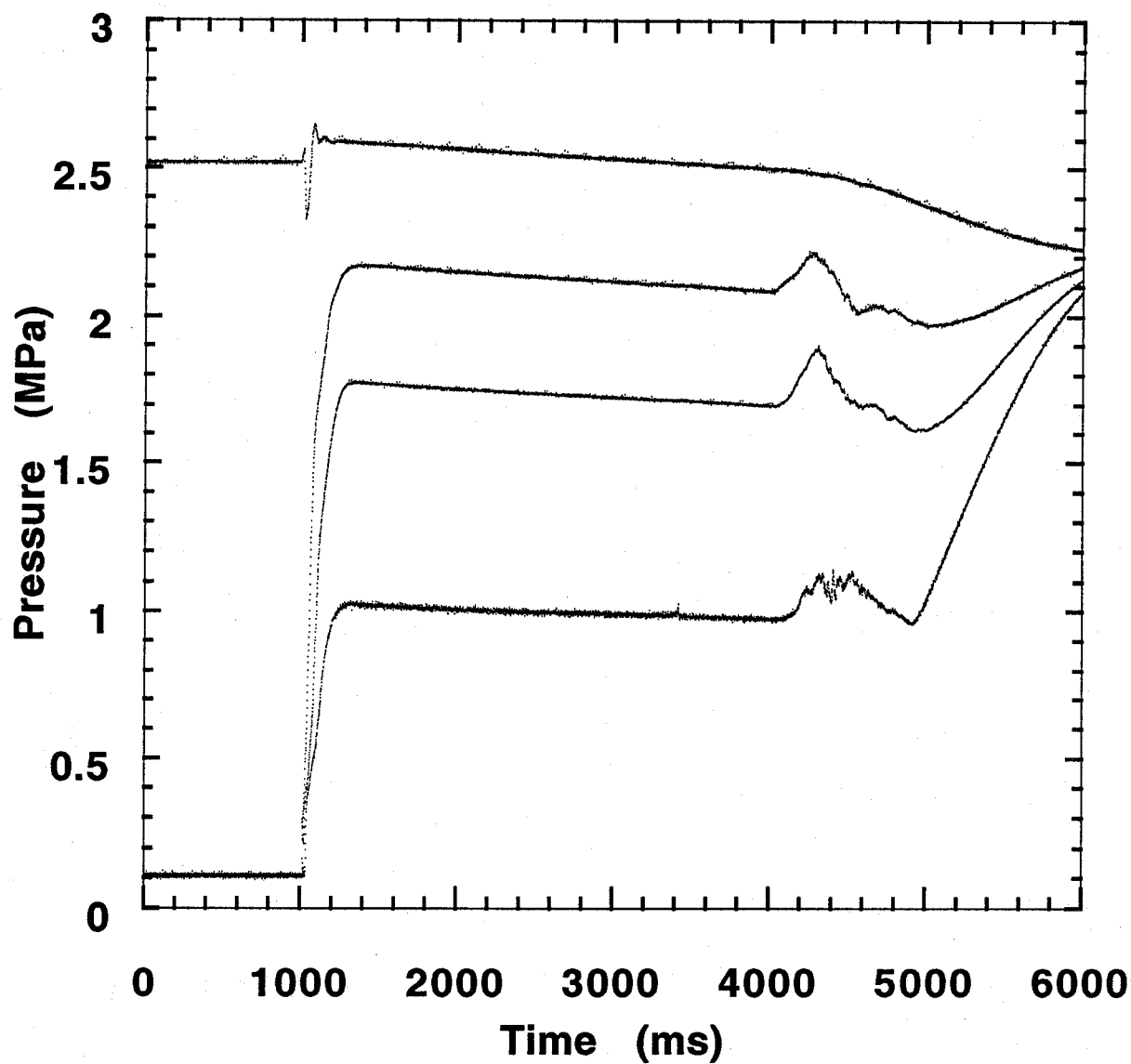


Figure B-78. CF_3I test. Refer to Table B-5 for experimental conditions.

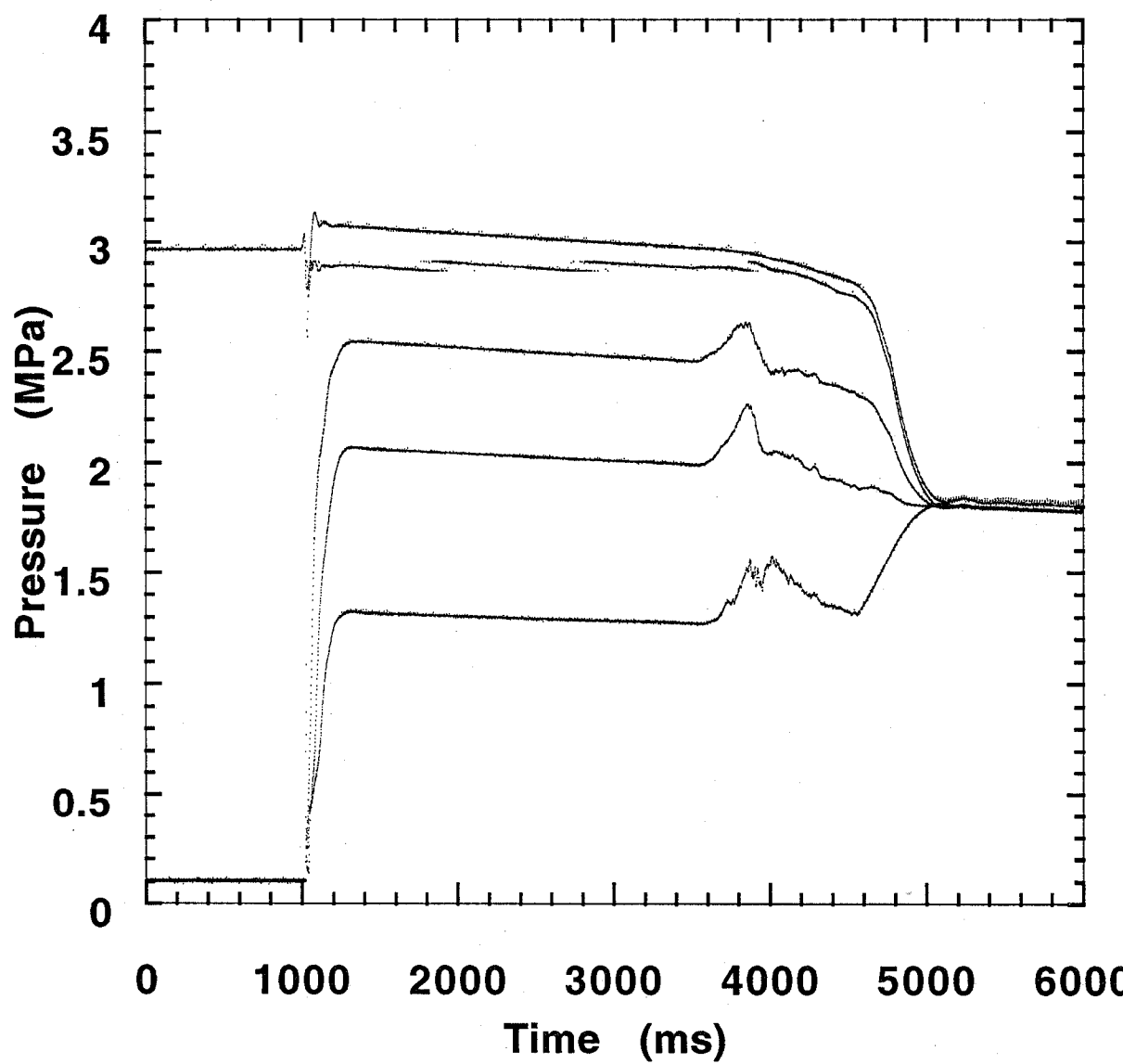


Figure B-79. CF_3I test. Refer to Table B-5 for experimental conditions.

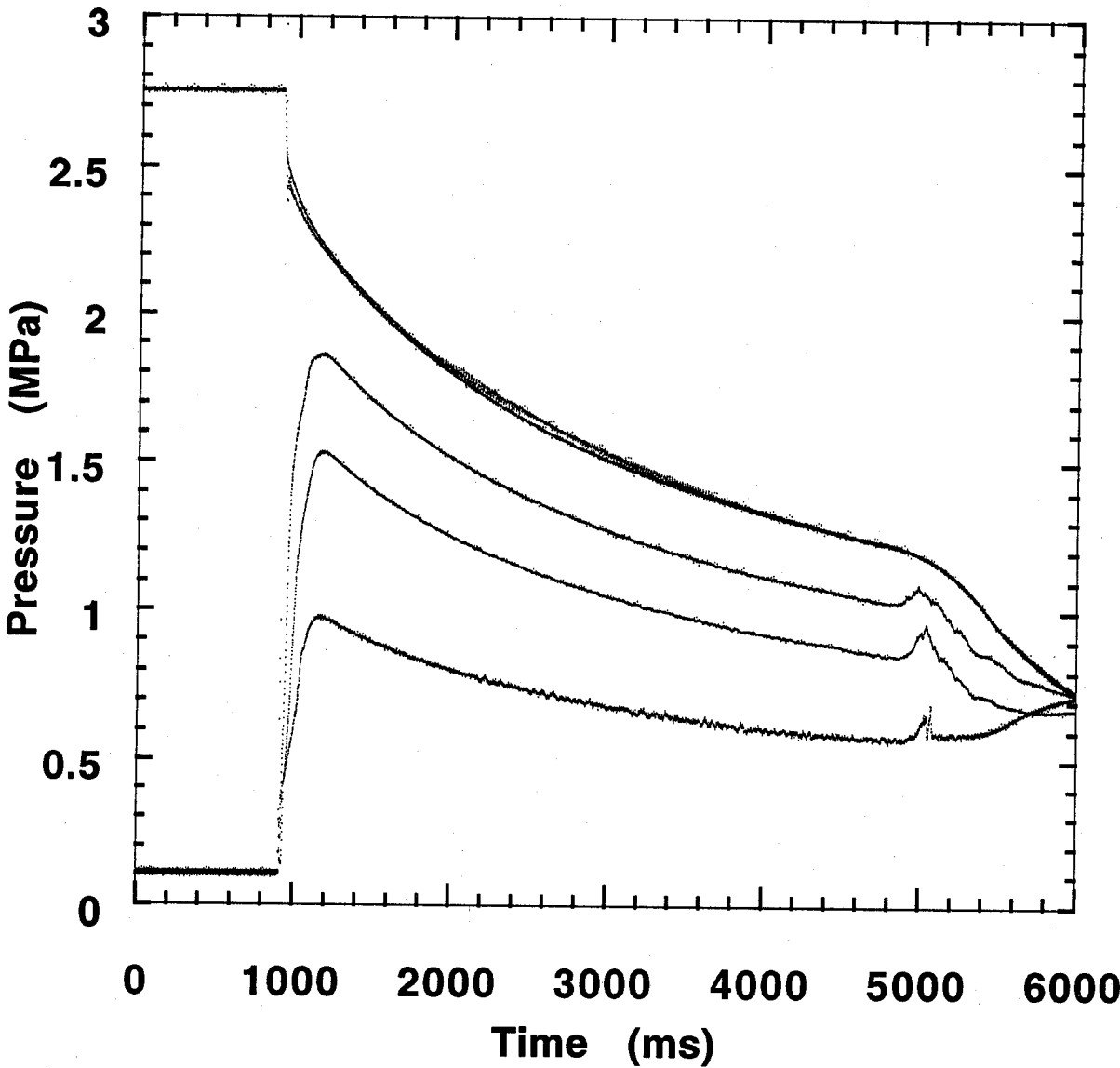


Figure B-80. CF_3I test. Refer to Table B-5 for experimental conditions.

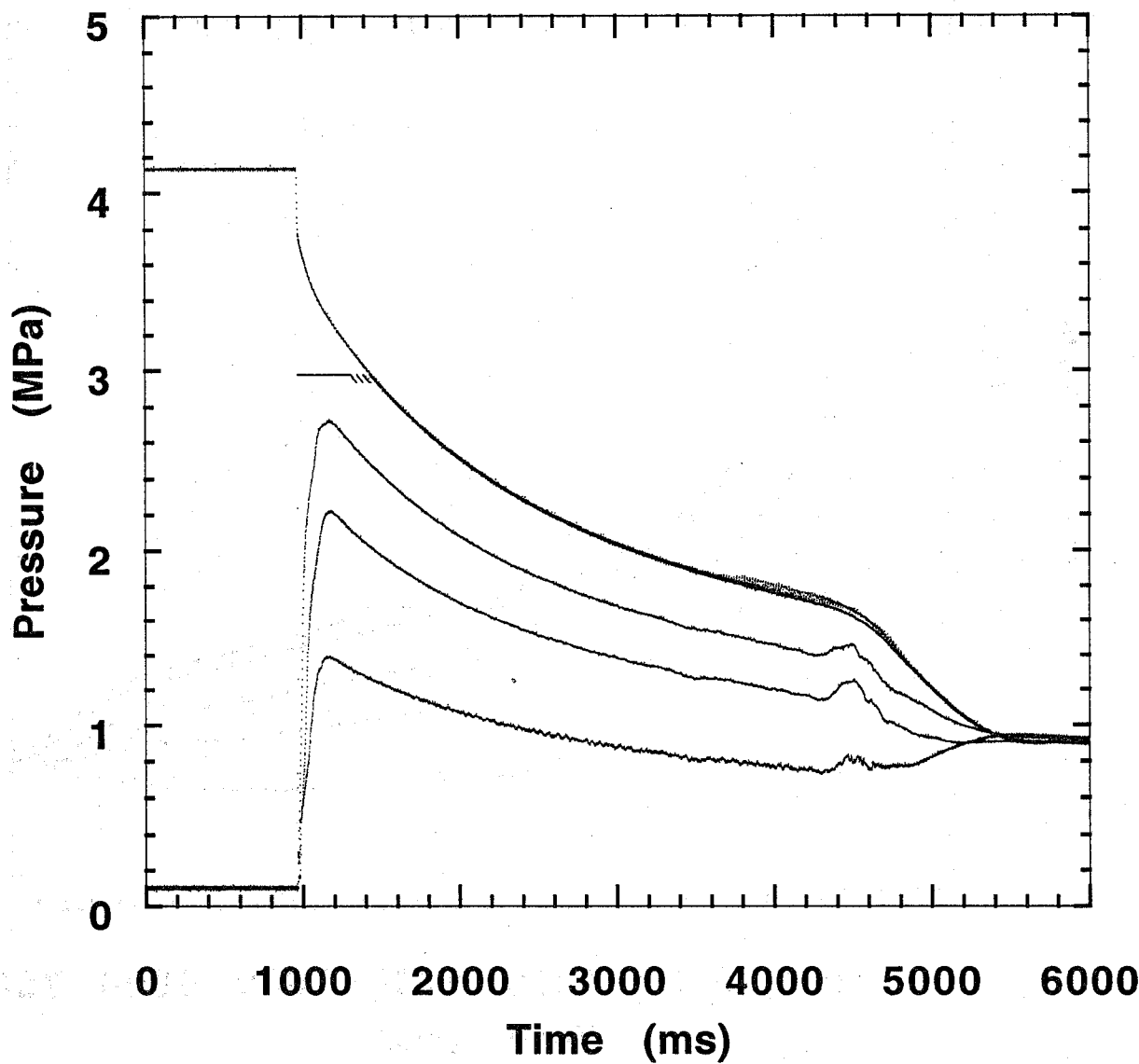


Figure B-81. CF_3I test. Refer to Table B-5 for experimental conditions.

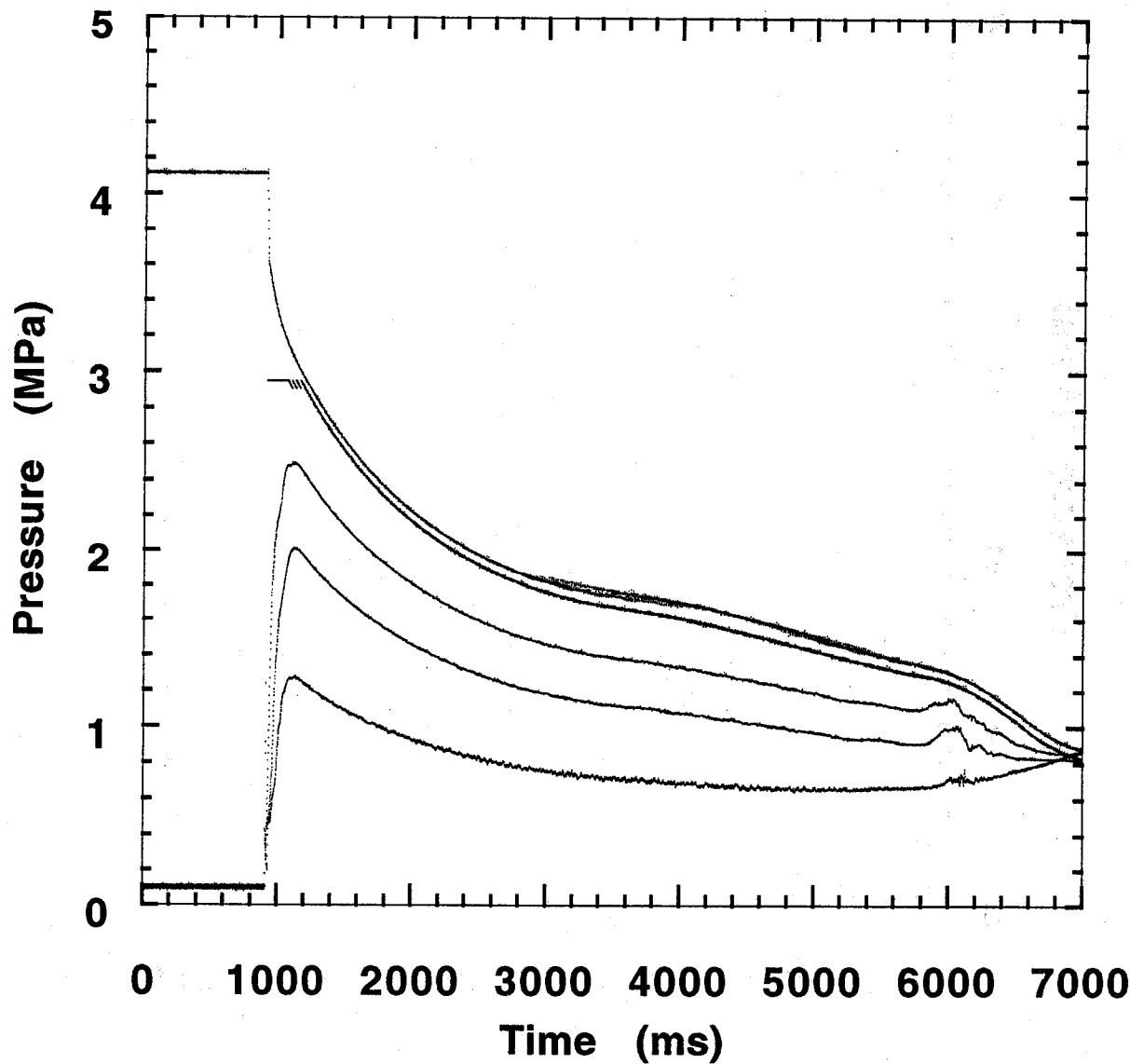


Figure B-82. CF_3I test. Refer to Table B-5 for experimental conditions.

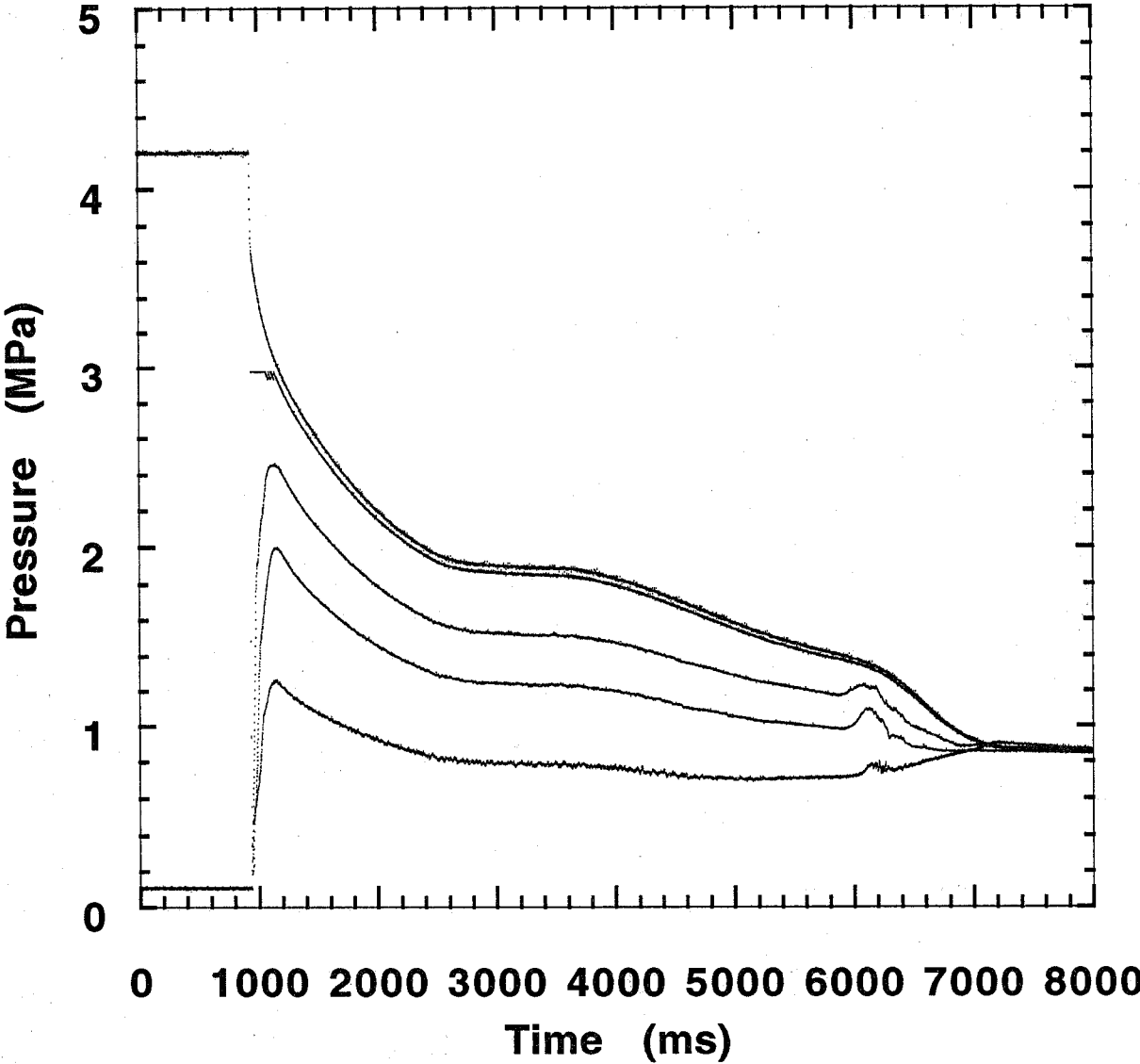


Figure B-83. CF₃I test. Refer to Table B-5 for experimental conditions.

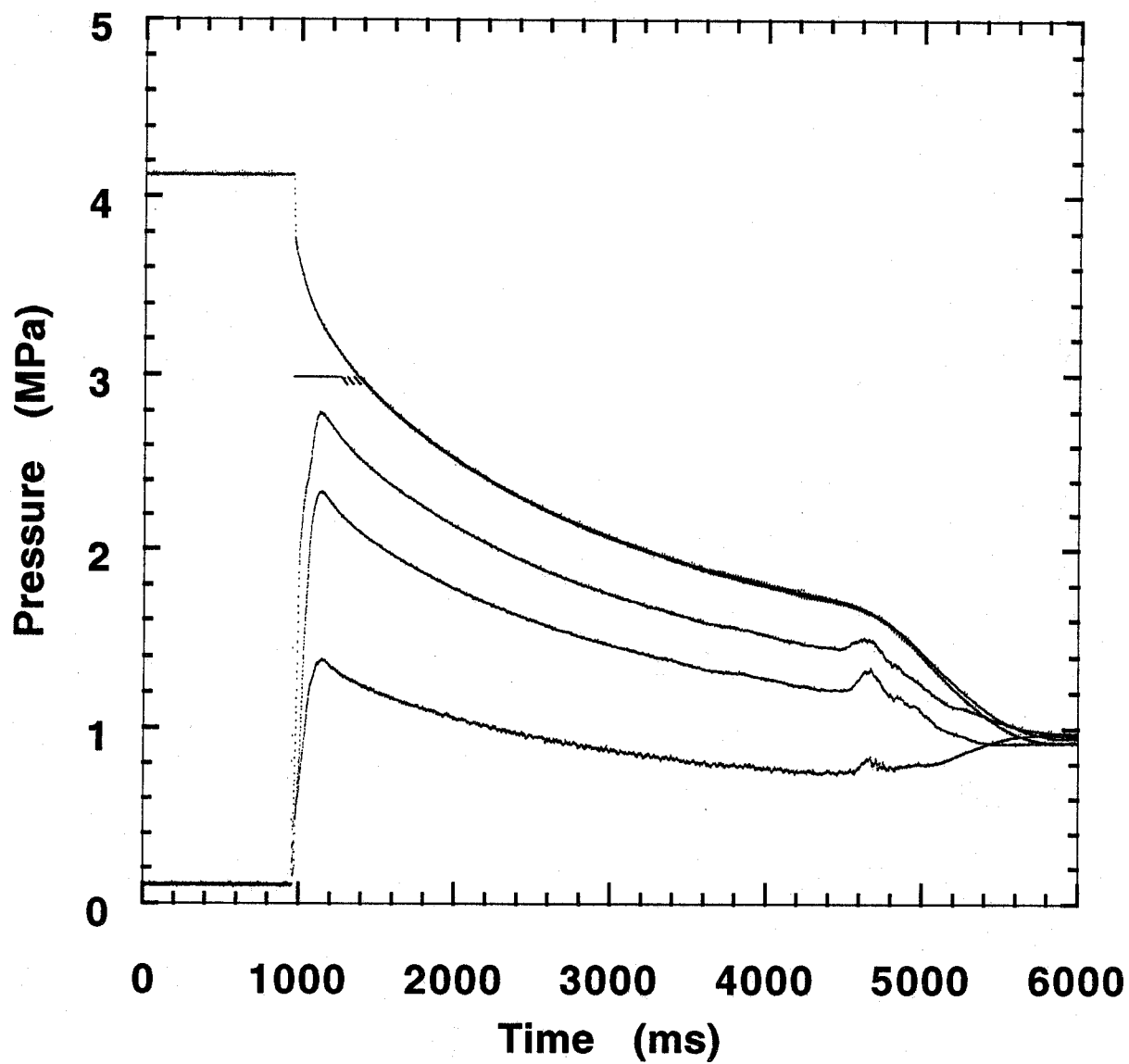


Figure B-84. CF_3I test. Refer to Table B-5 for experimental conditions.

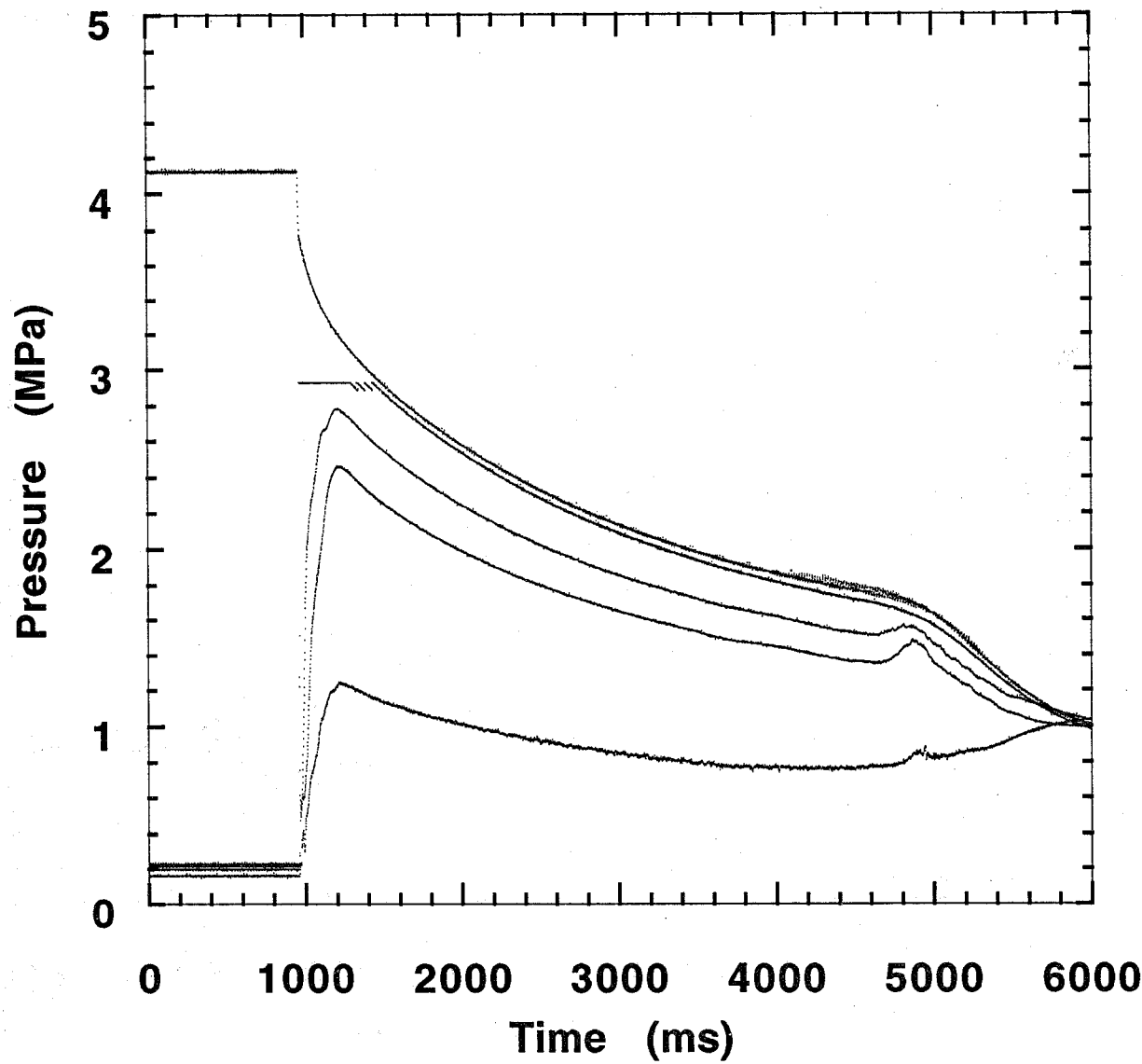


Figure B-85. CF_3I test. Refer to Table B-5 for experimental conditions.

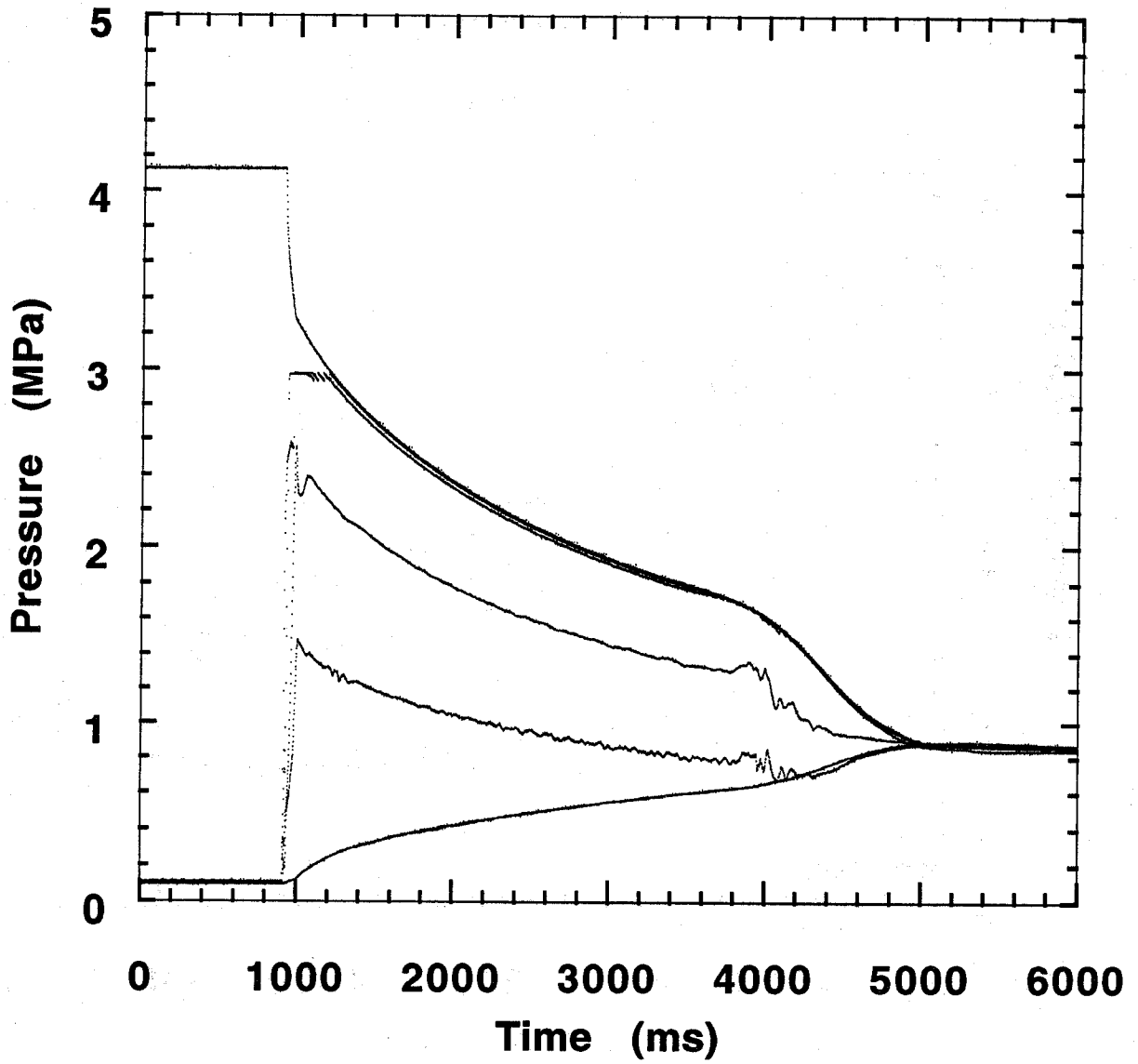


Figure B-86. CF_3I test. Refer to Table B-5 for experimental conditions.

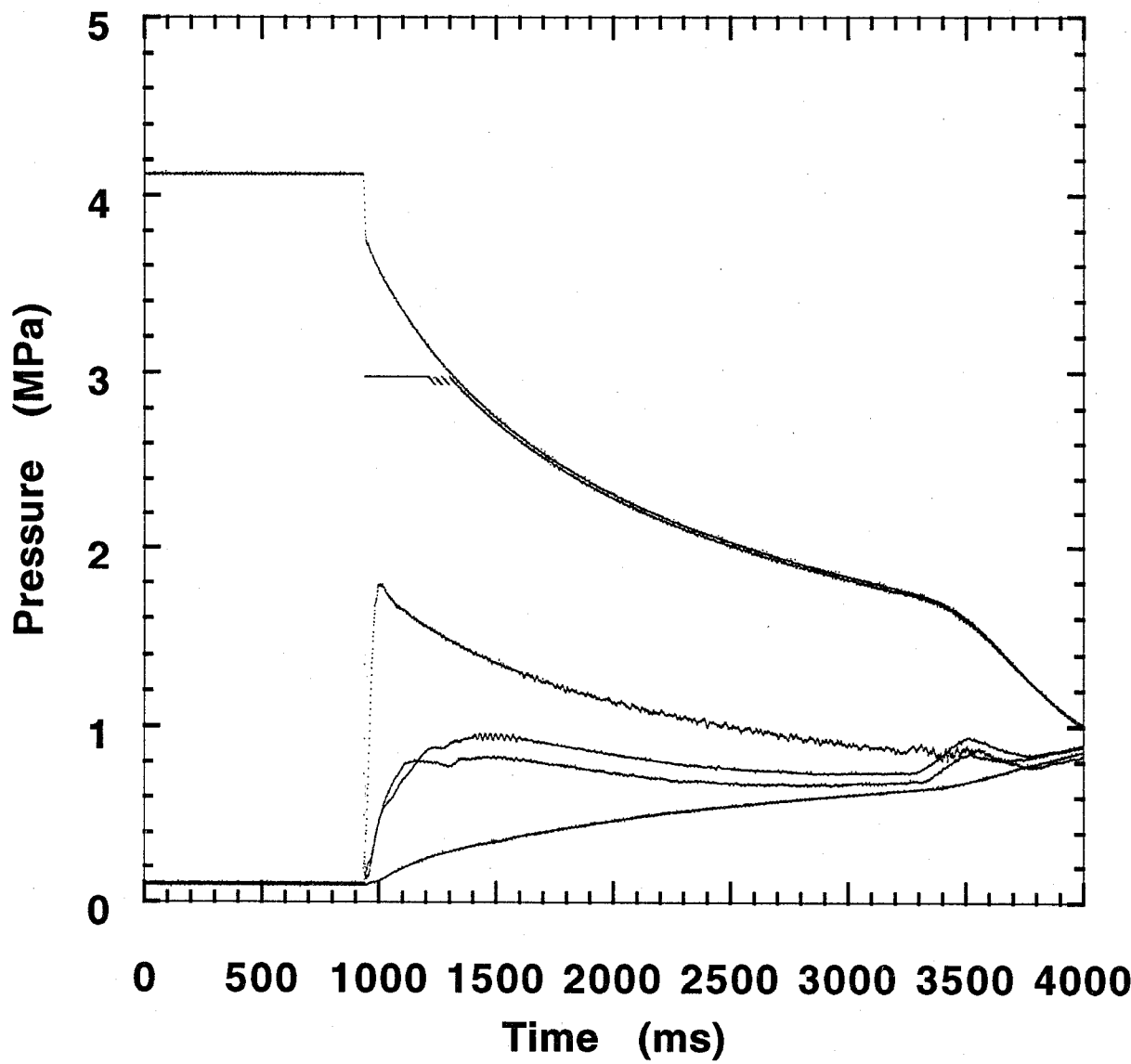


Figure B-87. CF_3I test. Refer to Table B-5 for experimental conditions.

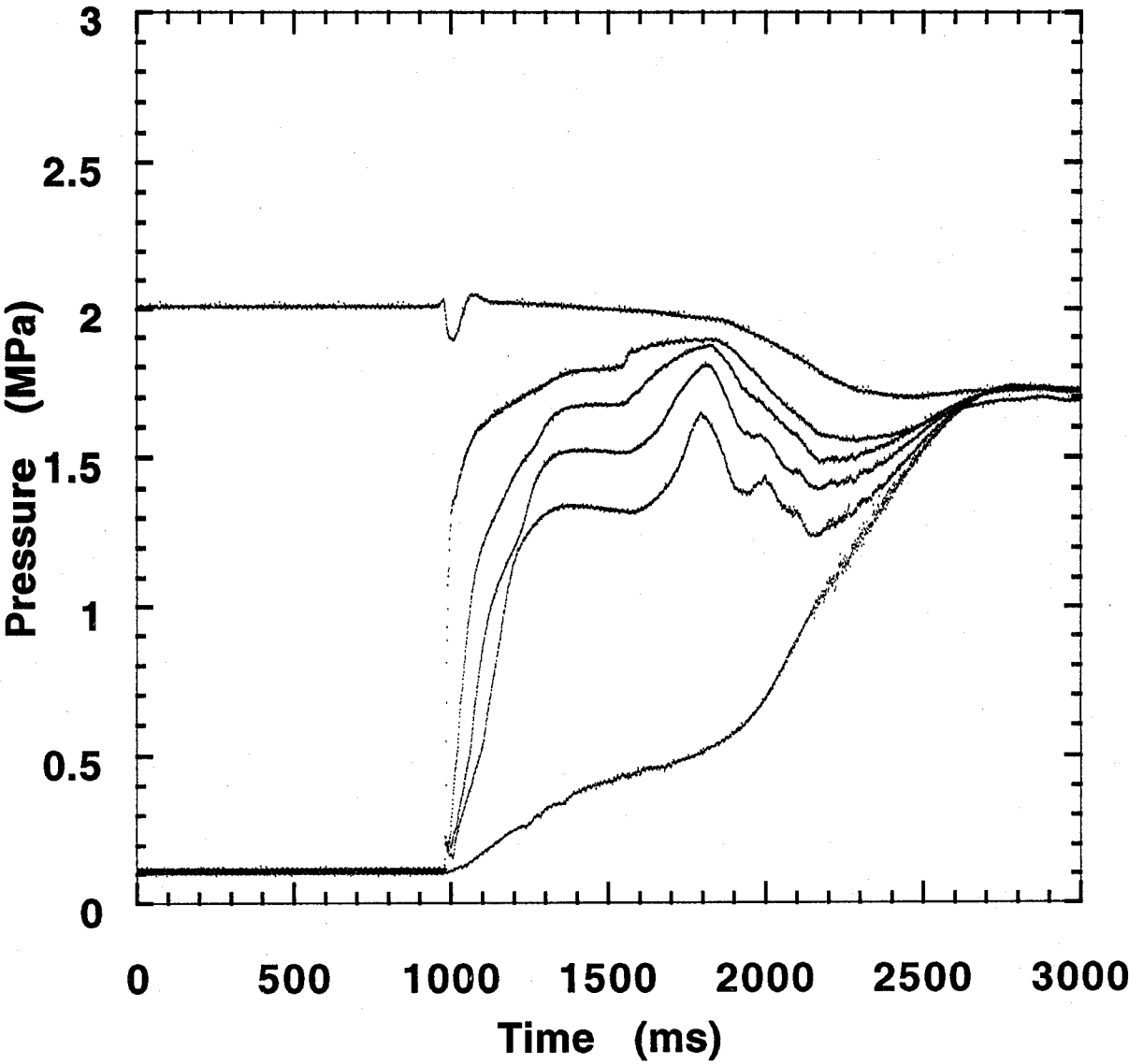


Figure B-88. CF₃I test. Refer to Table B-5 for experimental conditions.

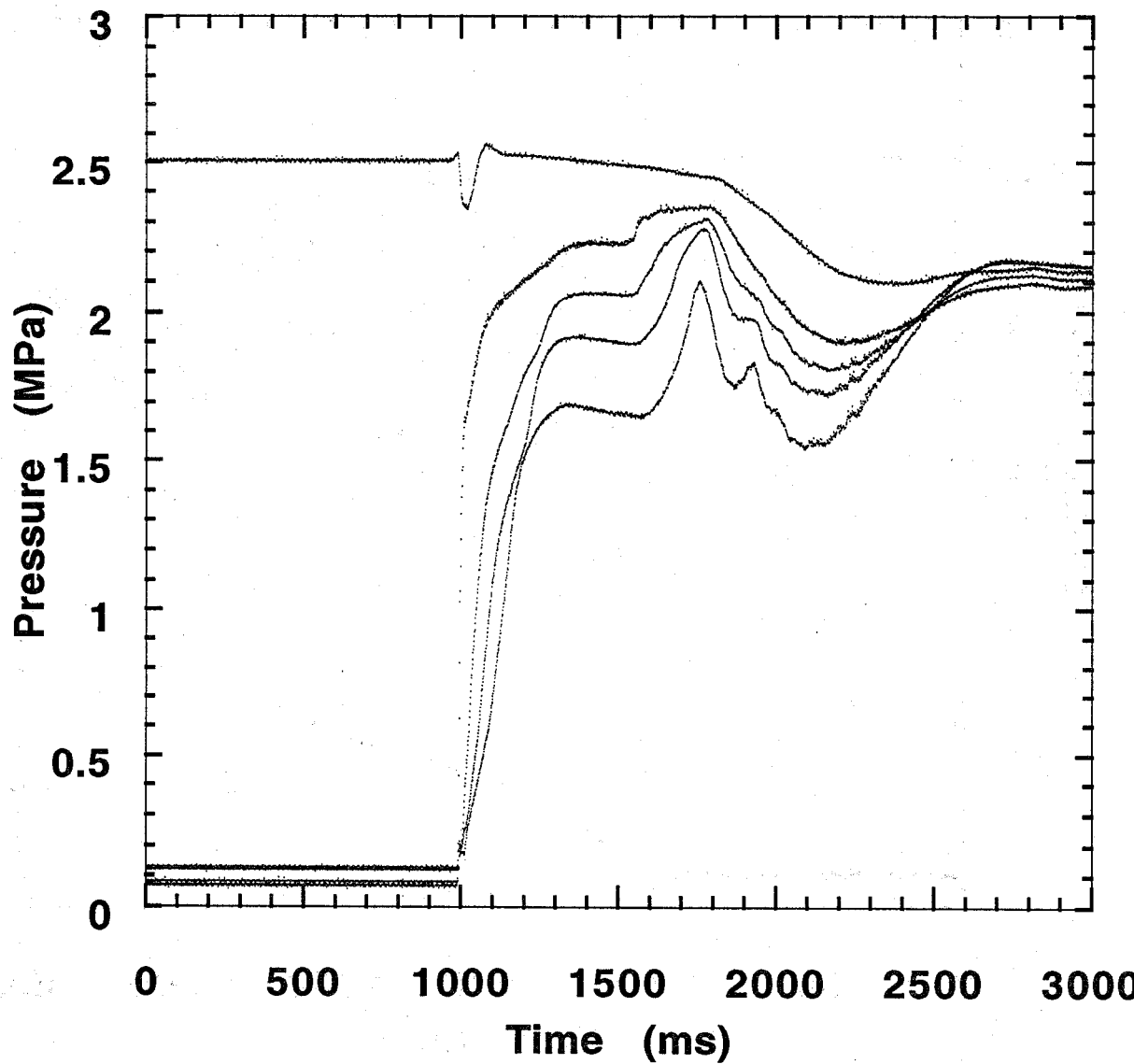


Figure B-89.

CF₃I test. Refer to Table B-5 for experimental conditions.

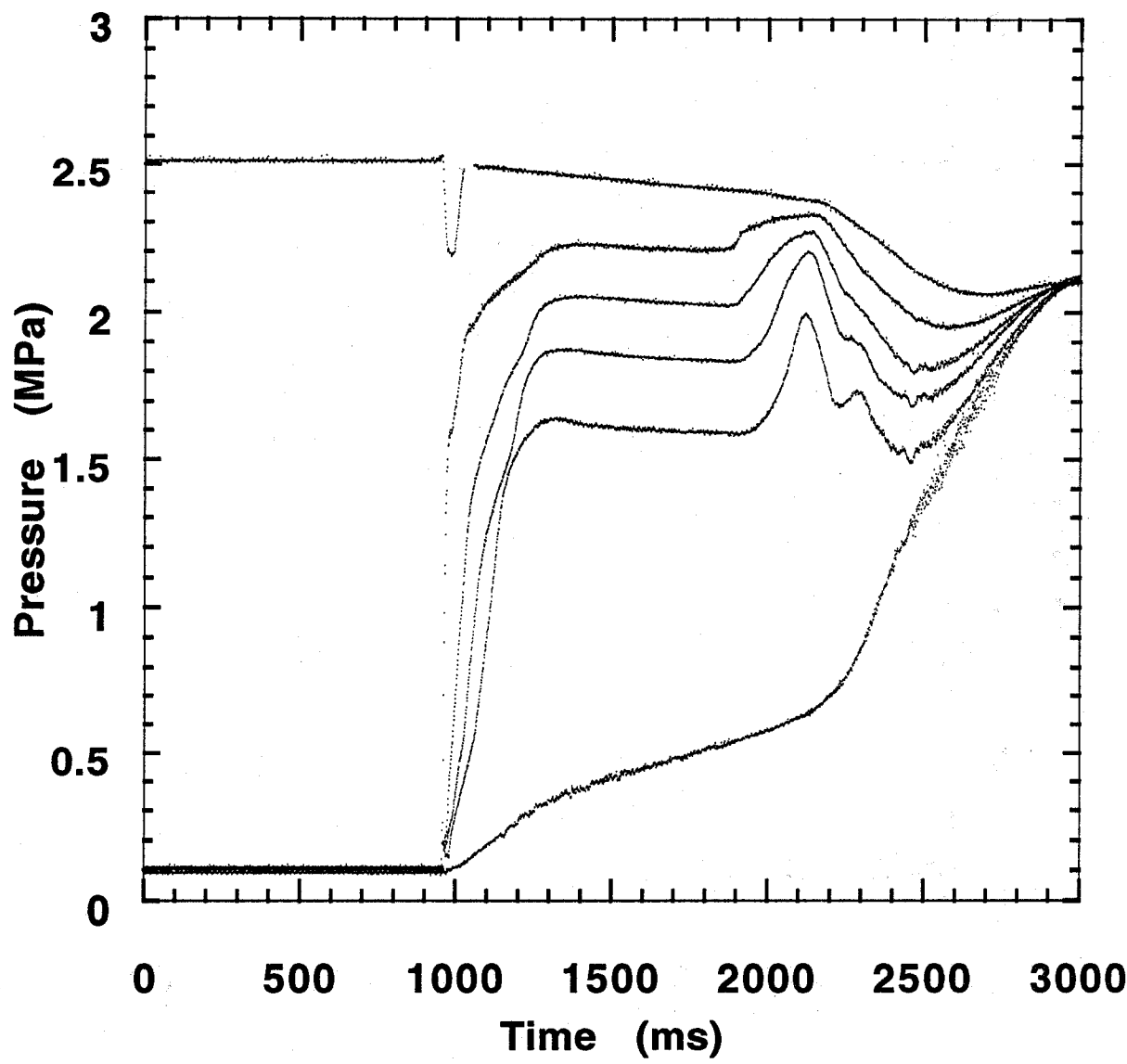


Figure B-90. CF_3I test. Refer to Table B-5 for experimental conditions.

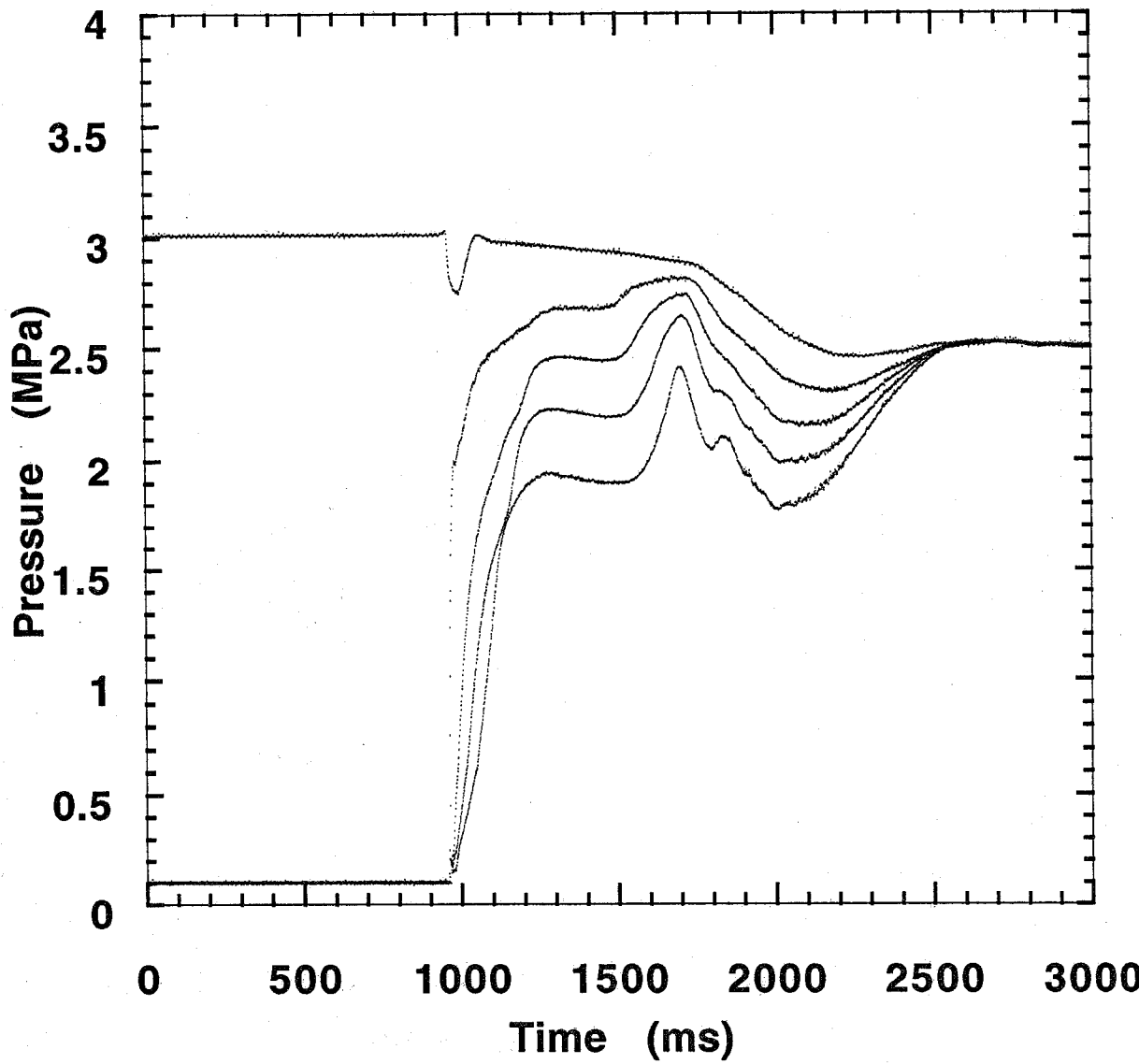


Figure B-91. CF₃I test. Refer to Table B-5 for experimental conditions.

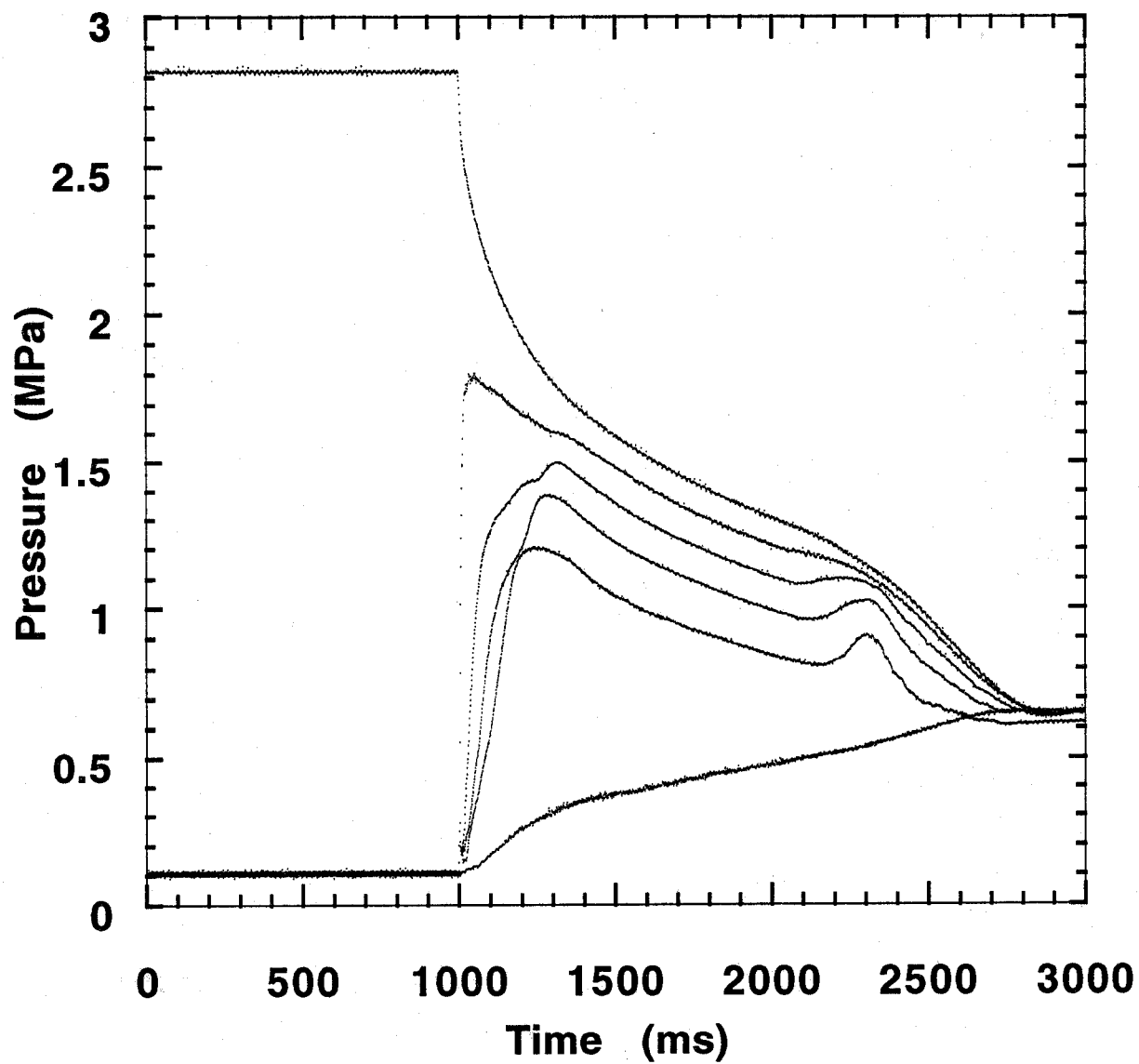


Figure B-92.

CF₃I test. Refer to Table B-5 for experimental conditions.

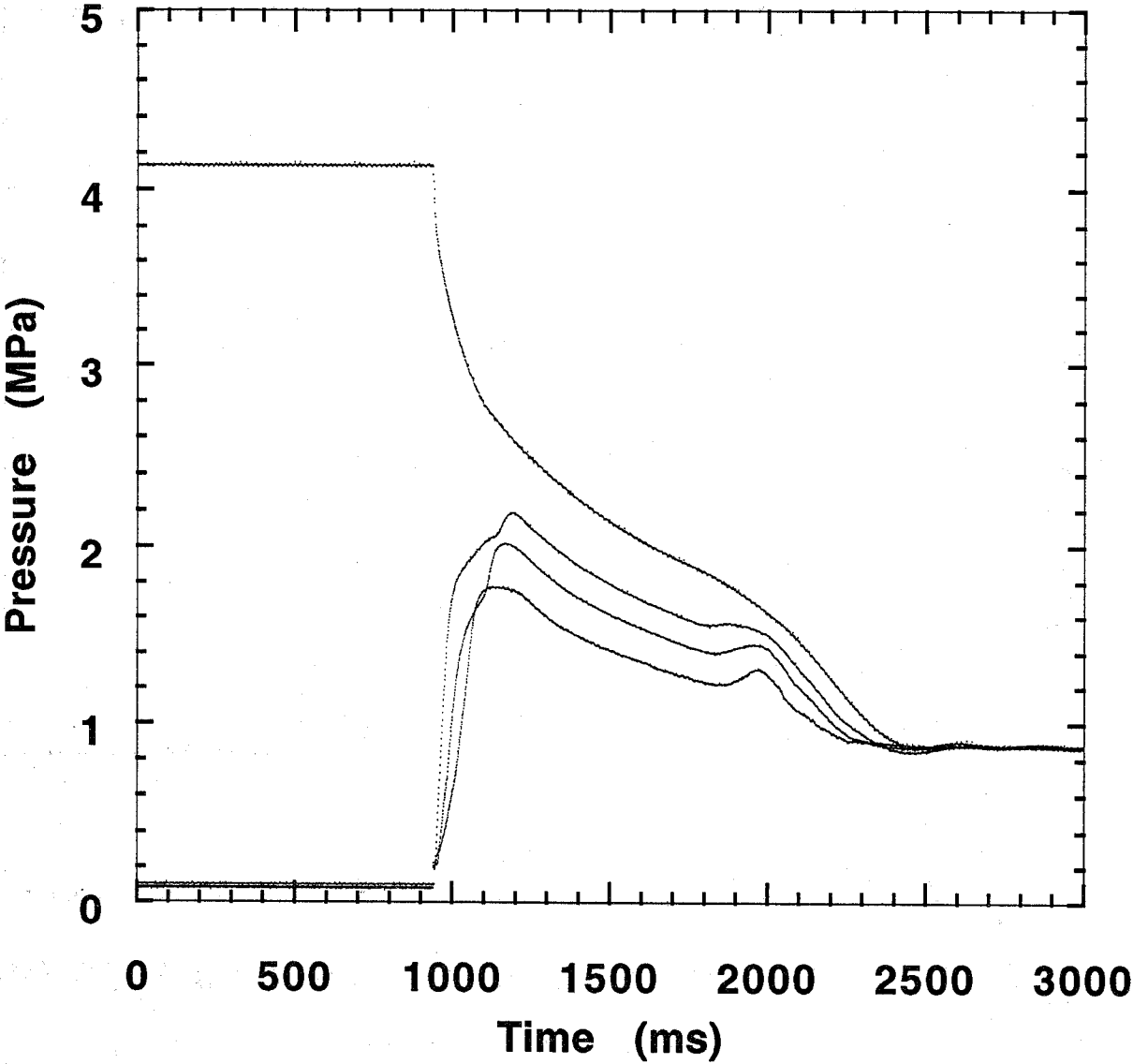


Figure B-93. CF₃I test. Refer to Table B-5 for experimental conditions.

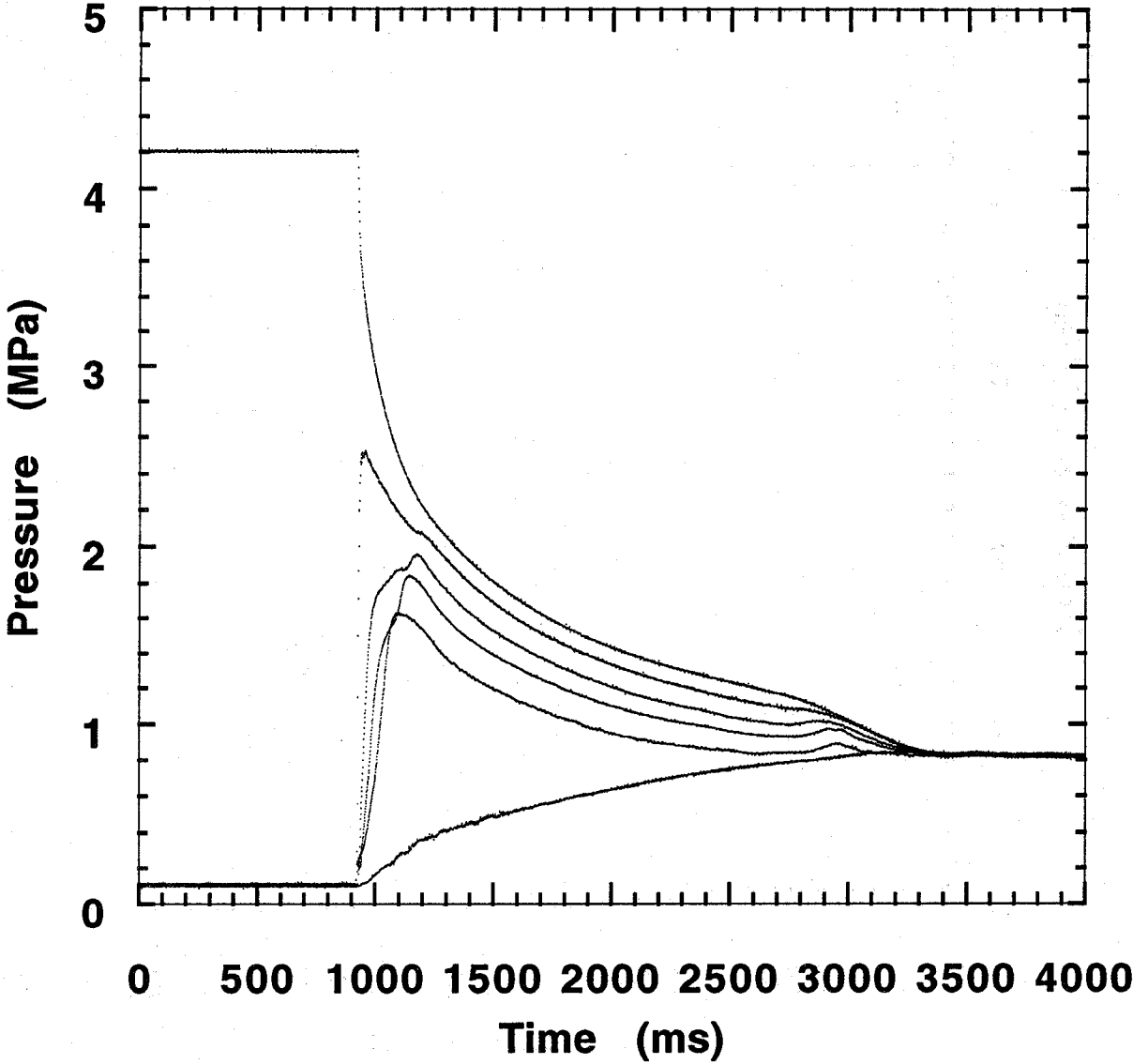


Figure B-94. CF_3I test. Refer to Table B-5 for experimental conditions.

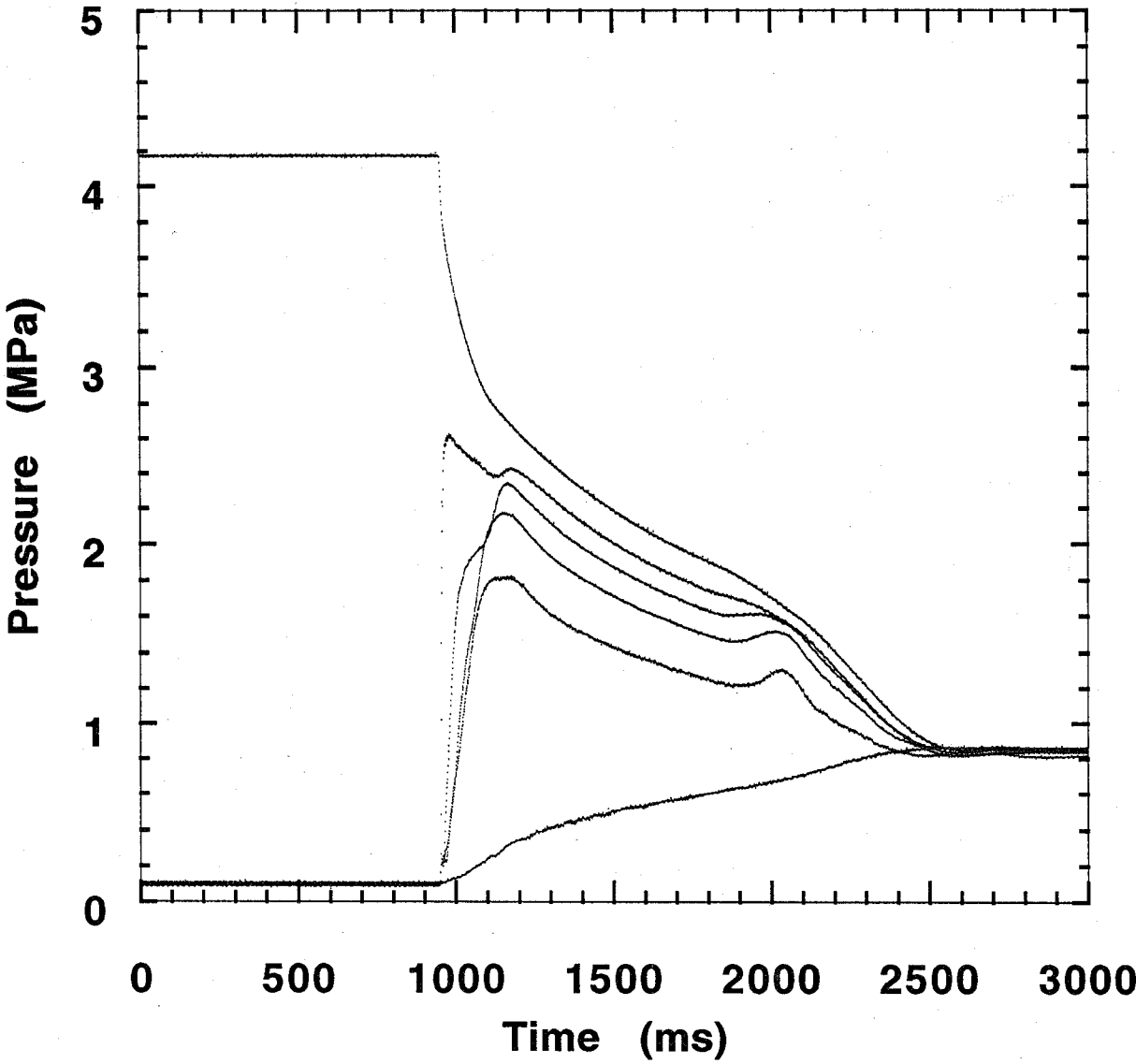


Figure B-95. CF_3I test. Refer to Table B-5 for experimental conditions.

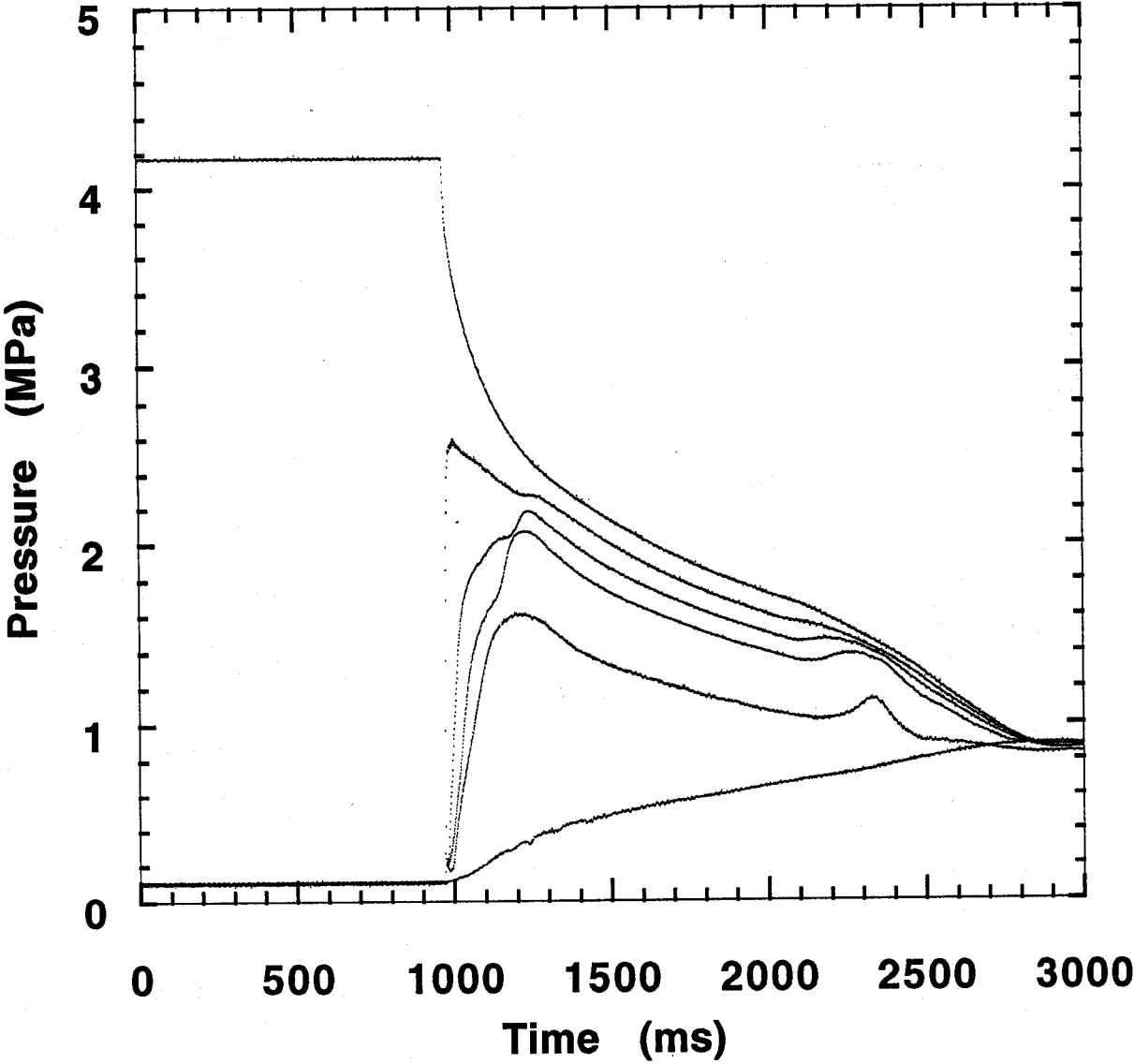


Figure B-96. CF₃I test. Refer to Table B-5 for experimental conditions.

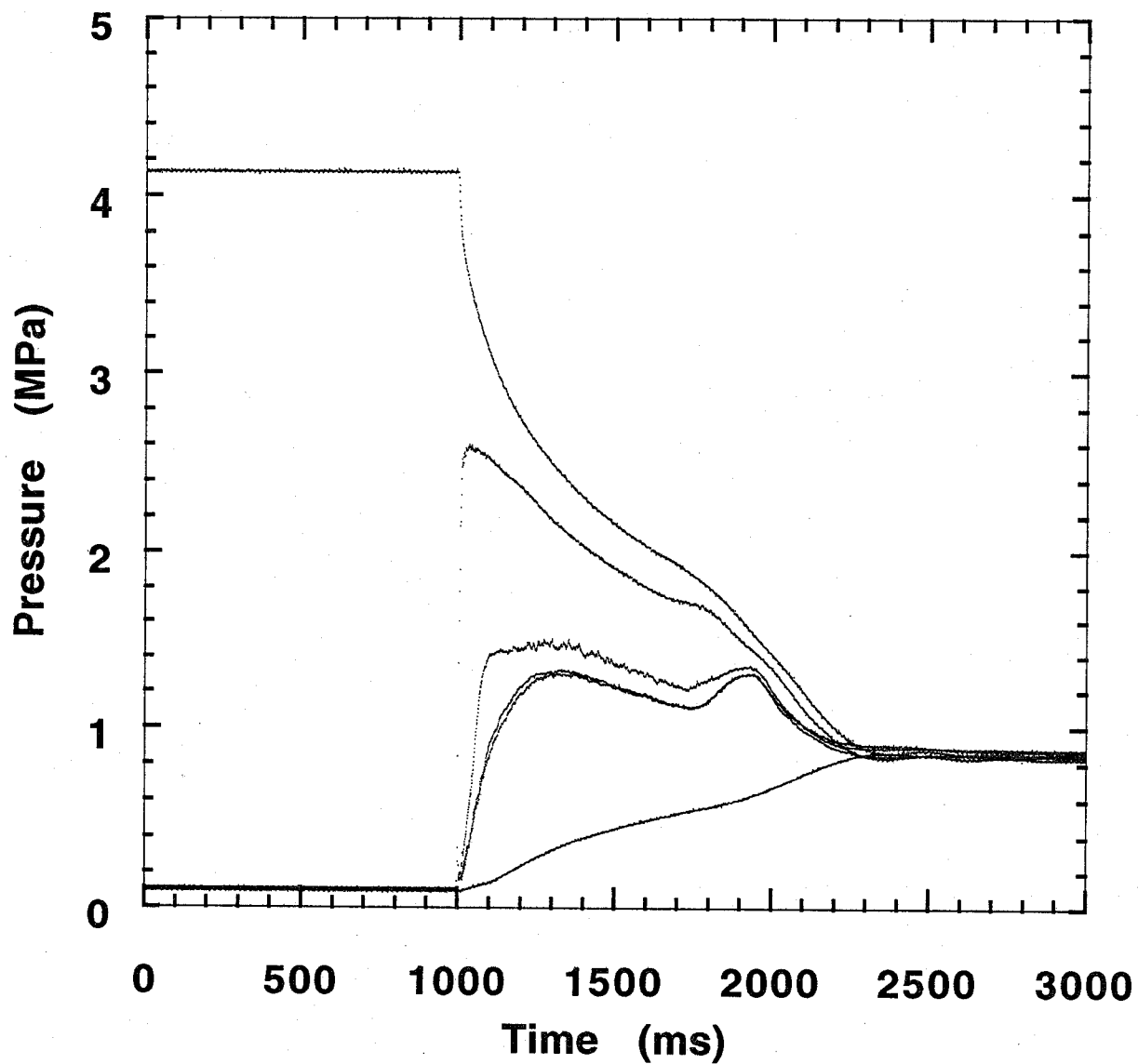


Figure B-97.

CF₃I test. Refer to Table B-5 for experimental conditions.

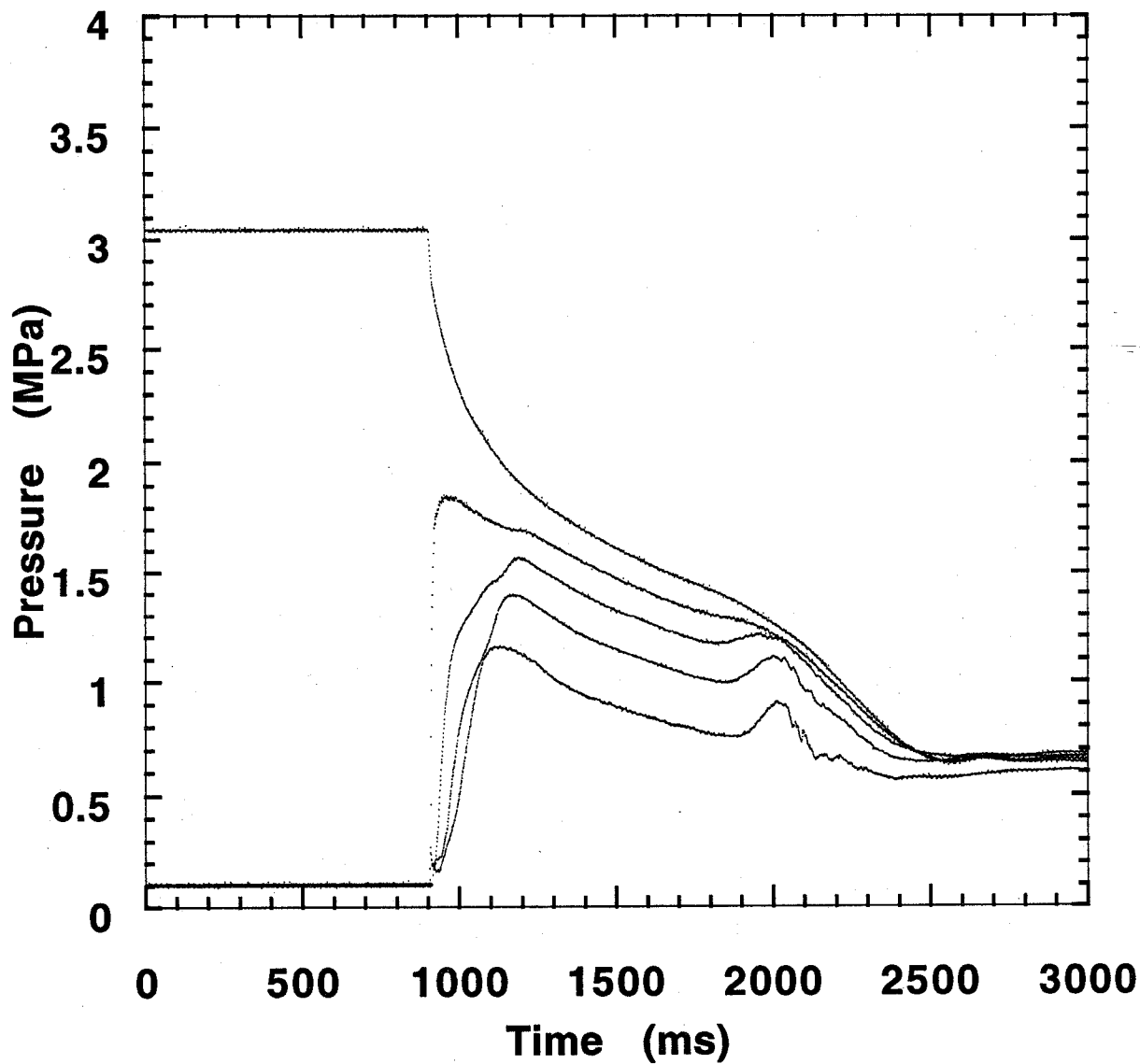


Figure B-98.

 CF_3I test. Refer to Table B-5 for experimental conditions.

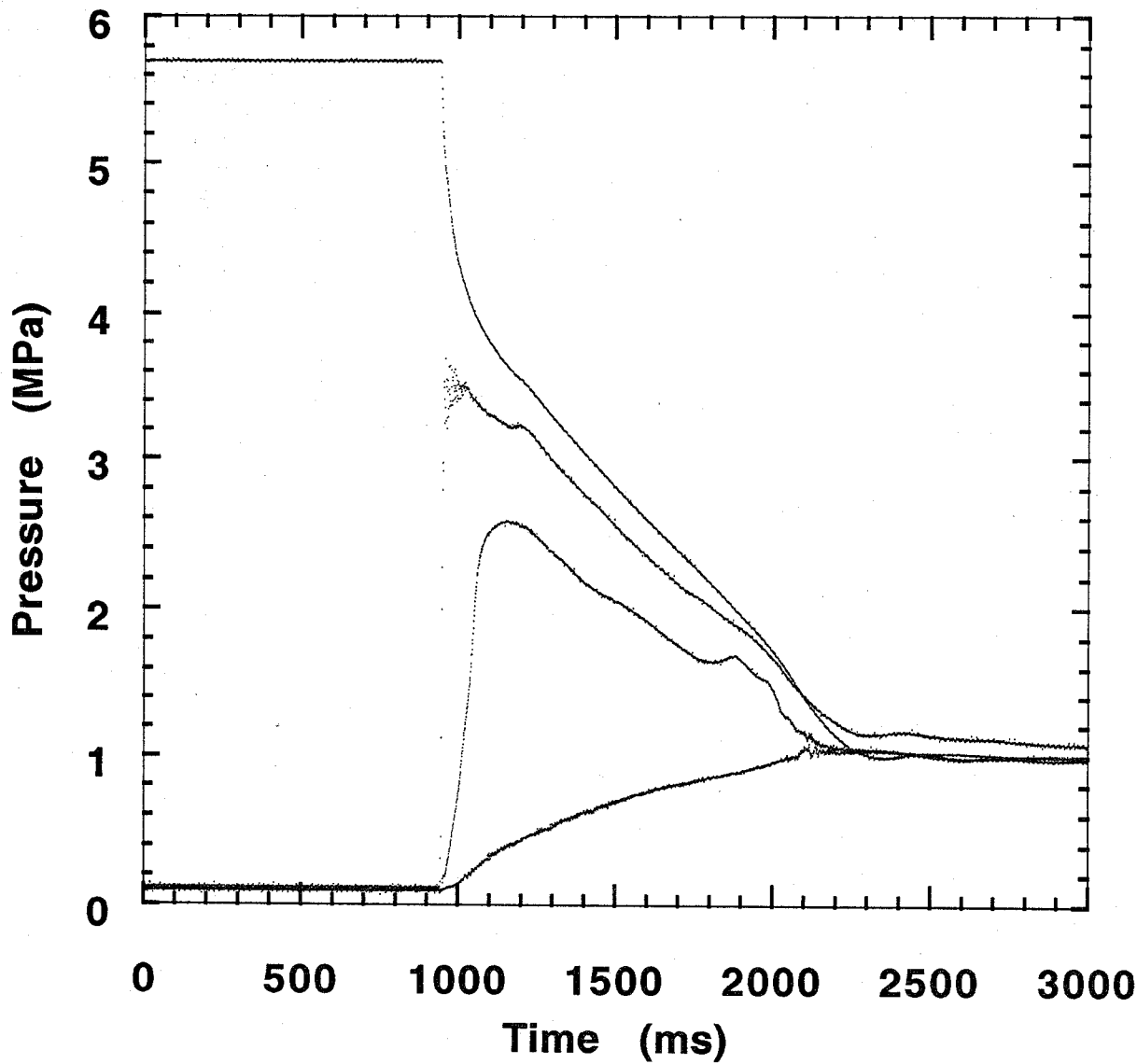


Figure B-99. CF_3I test. Refer to Table B-5 for experimental conditions.

Appendix C. Thermodynamic and Transport Properties of Agent/Nitrogen Mixtures

Coefficients to polynomial fits of calculated thermodynamic and transport properties of agent/nitrogen mixtures during isenthalpic expansion are tabulated in Tables C-1 and C-2. Figures C-1 to C-6 show the polynomial fits to the density, temperature and mass fraction results at initial pressures of 2.75 and 4.12 MPa. Figure C-7 shows the pressure/density relationships for isentropic expansion of gas-phase agent/nitrogen mixture initially at 20 °C. The curves through the data represent power-law fits to the points. In general, the exponent was not a function of initial pressure, thus the pseudo-ideal γ was taken as a constant for each agent. The values obtained for halon 1301, HFC-125, HFC-227ea, and CF_3I were 1.07, 1.12, 1.01, and 0.99 respectively.

Table C-1. Mean agent/nitrogen mixture densities

Agent	$P_{initial}$ (MPa)	$\rho_{mean} \text{ (kg/m}^3\text{)} = a_0 + a_1*P + a_2*P^2 + a_3*P^3$ $P \text{ in kPa}$			
		a_0	a_1	a_2	a_3
CF ₃ Br	2.00	-7.815	231.5	-46.81	160.8
	2.50	14.77	79.10	184.6	11.39
	2.75	18.49	66.39	189.5	-5.087
	3.00	16.36	68.25	180.4	-12.23
	4.12	3.334	118.4	81.99	-5.742
HFC-125	2.00	15.55	29.97	185.7	47.50
	2.50	17.09	5.372	226.7	-17.28
	2.75	14.32	21.18	198.0	-19.27
	3.00	9.038	47.35	153.9	-14.11
	4.12	3.586	76.32	81.13	-8.235
	5.49	-0.9375	88.697	40.26	-3.845
	6.87	-5.628	92.75	18.41	-1.511
	8.24	-7.401	85.04	7.405	-0.5212
HFC-227ea	2.00	-46.28	375.9	478.8	-159.2
	2.50	-50.25	407.1	222.5	-65.64
	2.75	-49.05	402.7	174.3	-50.13
	3.00	-56.03	418.8	98.02	-28.24
	4.12	-50.43	362.2	28.29	-8.473
	5.49	-44.59	297.1	3.781	-2.334
	6.87	-35.94	241.5	-1.419	-0.8257
	8.24	-30.56	193.6	-1.828	-0.3262
CF ₃ I	2.00	-52.59	467.7	893.7	-303.6
	2.50	-73.51	613.6	402.7	-124.6
	2.75	-80.37	648.9	269.3	-82.36
	3.00	-98.79	690.8	151.0	-49.62
	4.12	-87.52	607.0	22.44	-11.49

Table C-2. Mean agent/nitrogen mixture viscosities

Agent	$P_{initial}$ (MPa) @ 20 °C	$\mu_{mean} \text{ (g/cm s)} = a_0 + a_1 * P + a_2 * P^2 + a_3 * P^3$ $P \text{ in MPa}$			
		a_0	a_1	a_2	a_3
Halon 1301	2.75	1.456×10^{-4}	7.500×10^{-5}	1.461×10^{-4}	6.043×10^{-6}
	4.12	1.294×10^{-4}	1.192×10^{-4}	5.682×10^{-5}	6.407×10^{-8}
HFC-125	2.75	1.238×10^{-4}	6.513×10^{-5}	1.865×10^{-4}	-1.171×10^{-5}
	4.12	1.111×10^{-4}	1.194×10^{-4}	6.457×10^{-5}	-3.316×10^{-6}
HFC-227ea	2.75	2.783×10^{-5}	7.386×10^{-4}	2.947×10^{-4}	-8.376×10^{-5}
	4.12	3.707×10^{-5}	6.770×10^{-4}	4.709×10^{-5}	-1.312×10^{-5}

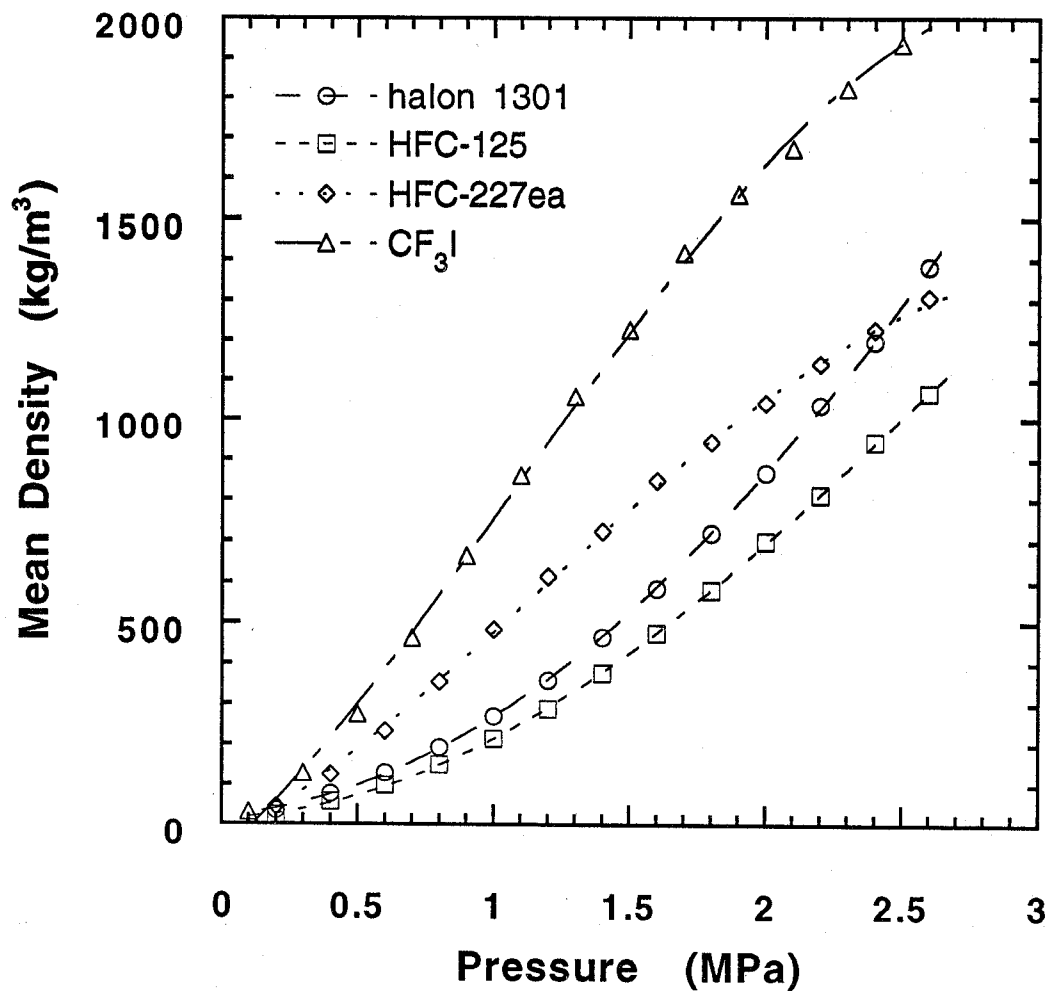


Figure C-1. Mean density as a function of pressure for initially liquid-phase agent/nitrogen mixture undergoing isenthalpic expansion. Initial pressure and temperature are 2.75 MPa and 20 °C.

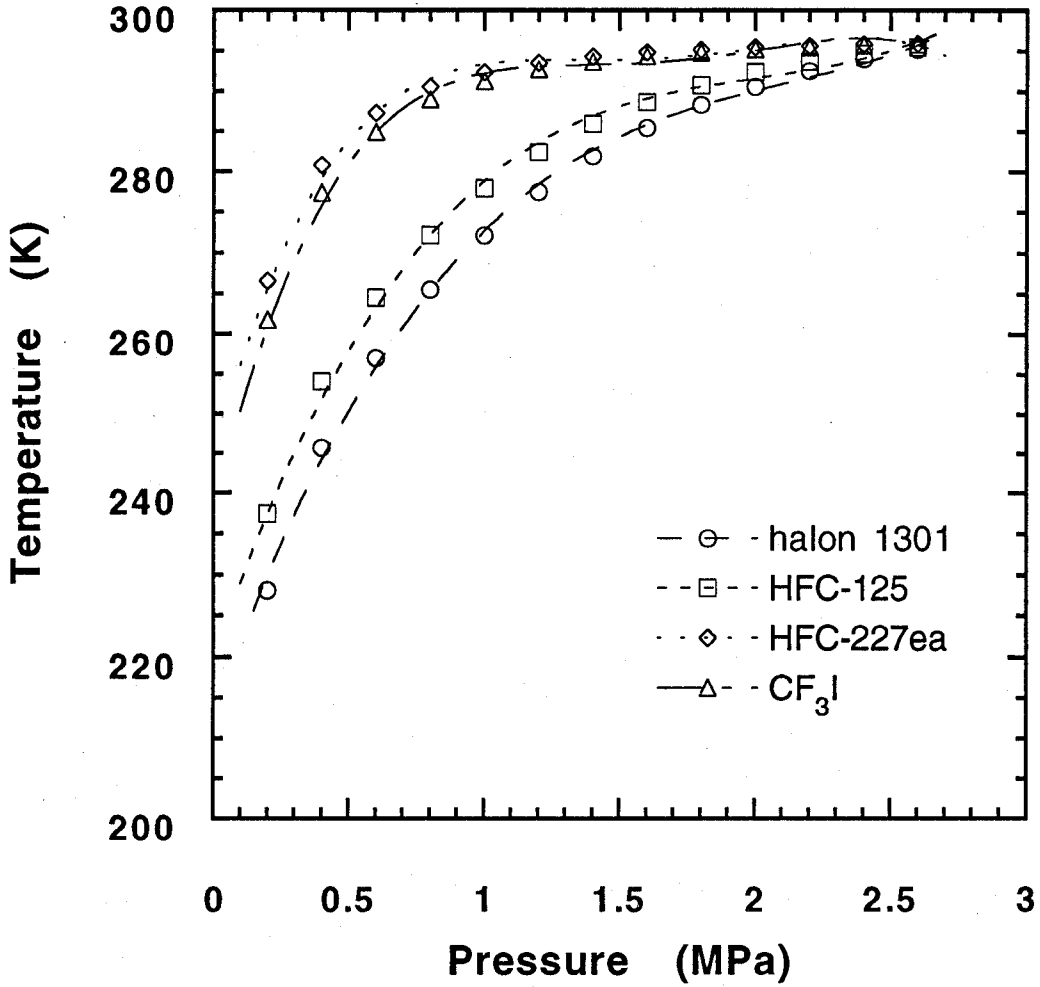


Figure C-2. Temperature as a function of pressure for initially liquid-phase agent/nitrogen mixture undergoing isenthalpic expansion. Initial pressure and temperature are 2.75 MPa and 20 °C.

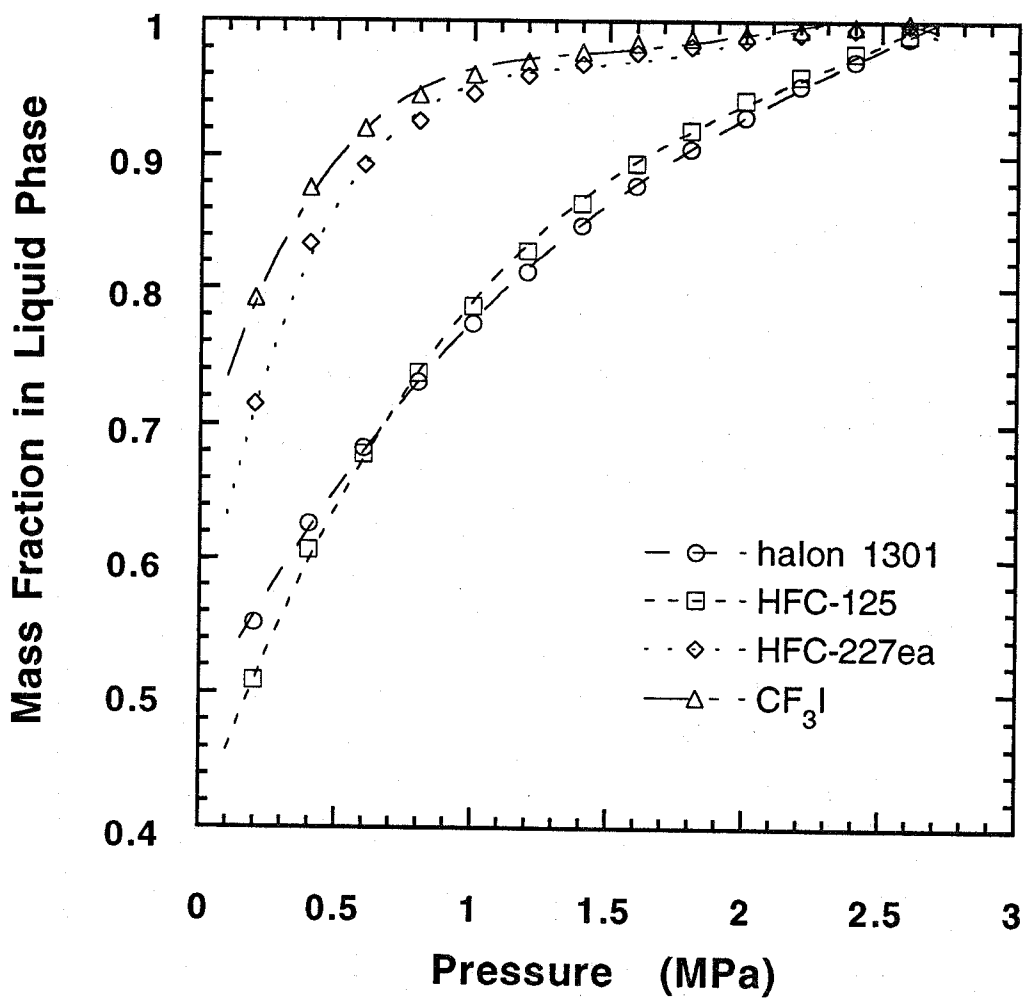


Figure C-3. Liquid-phase mass fraction as a function of pressure for initially liquid-phase agent/nitrogen mixture undergoing isenthalpic expansion. Initial pressure and temperature are 2.75 MPa and 20 °C.

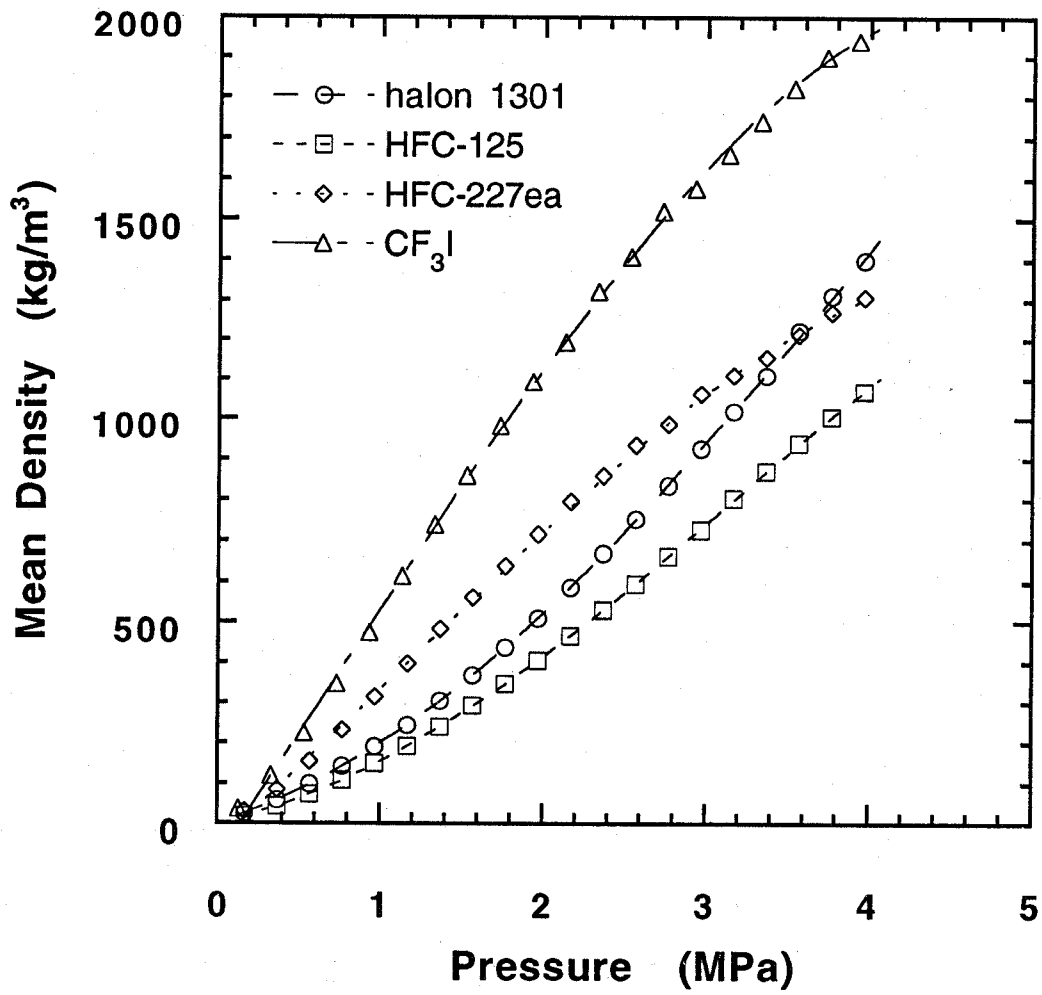


Figure C-4. Mean density as a function of pressure for initially liquid-phase agent/nitrogen mixture undergoing isenthalpic expansion. Initial pressure and temperature are 4.12 MPa and 20 °C.

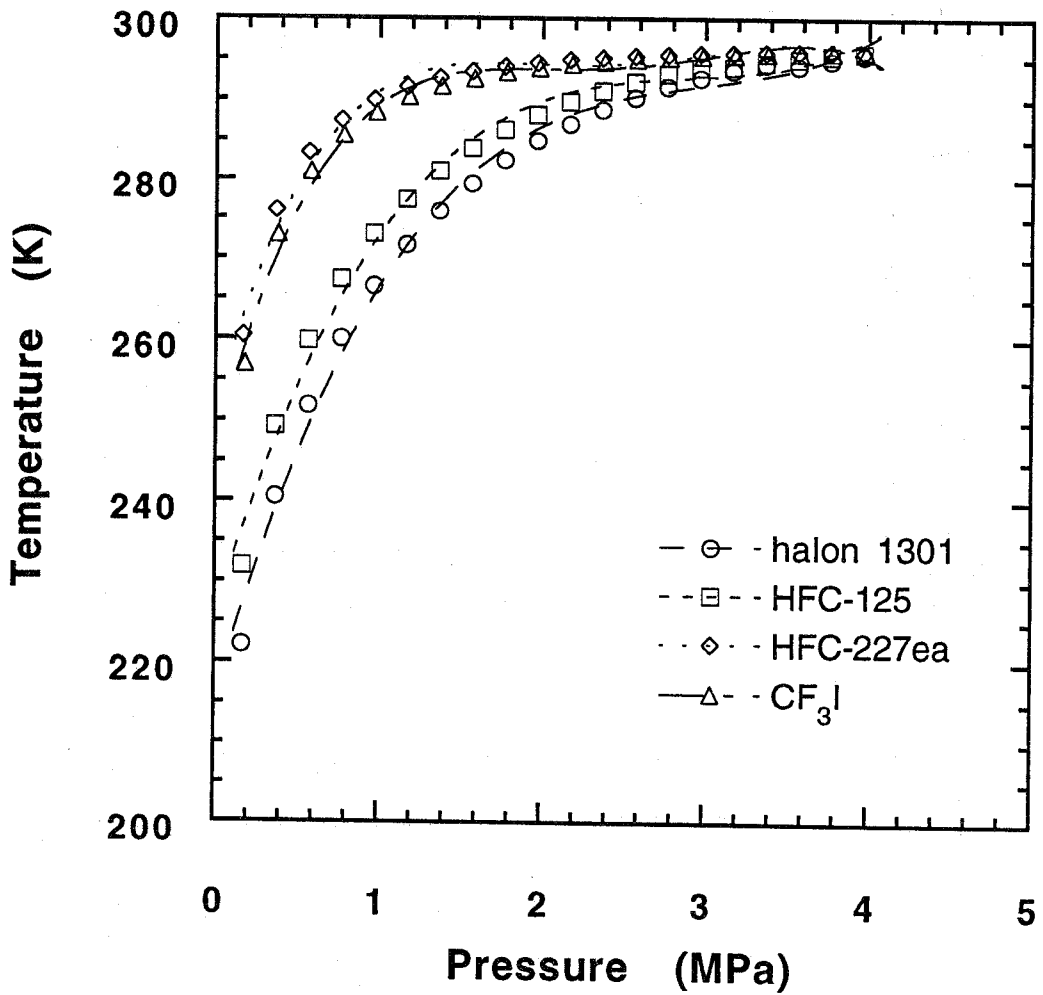


Figure C-5. Temperature as a function of pressure for initially liquid-phase agent/nitrogen mixture undergoing isenthalpic expansion. Initial pressure and temperature are 4.12 MPa and 20 °C.

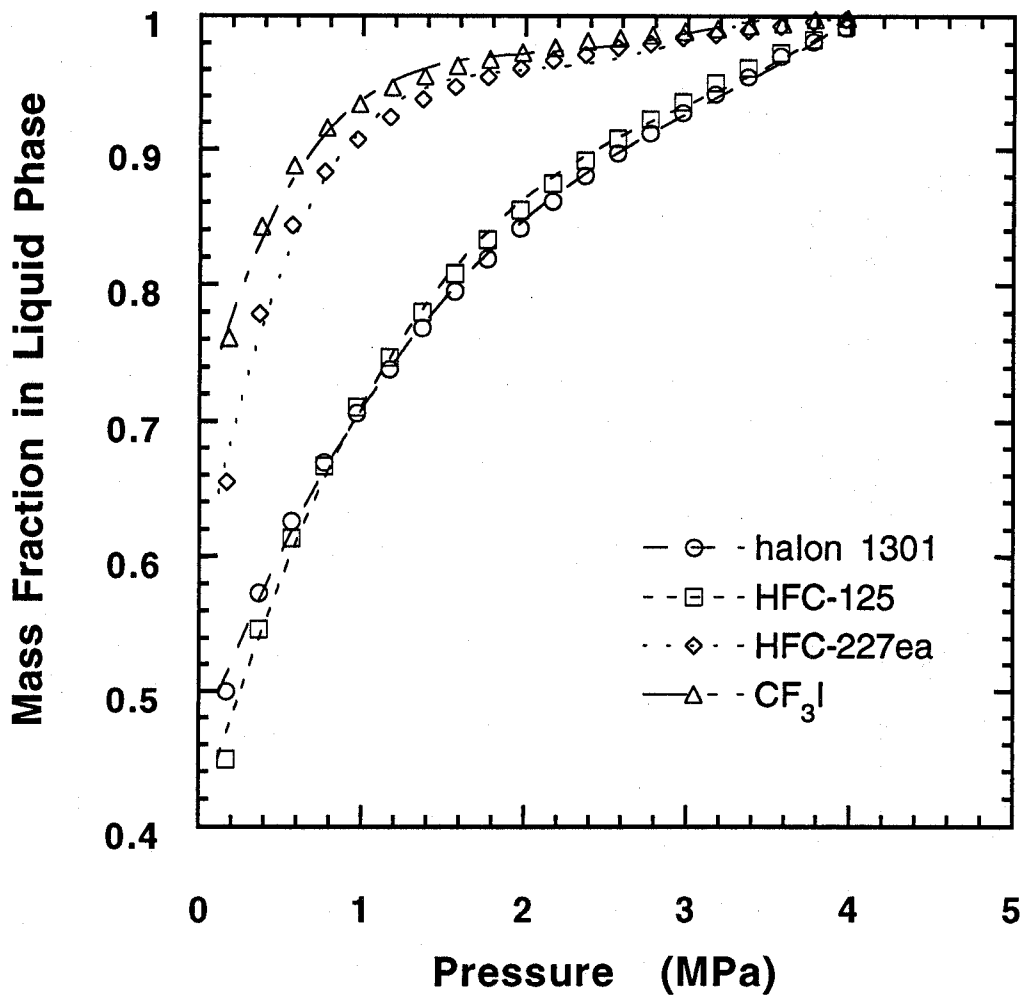


Figure C-6. Liquid-phase mass fraction as a function of pressure for initially liquid-phase agent/nitrogen mixture undergoing isenthalpic expansion. Initial pressure and temperature are 4.12 MPa and 20 °C.

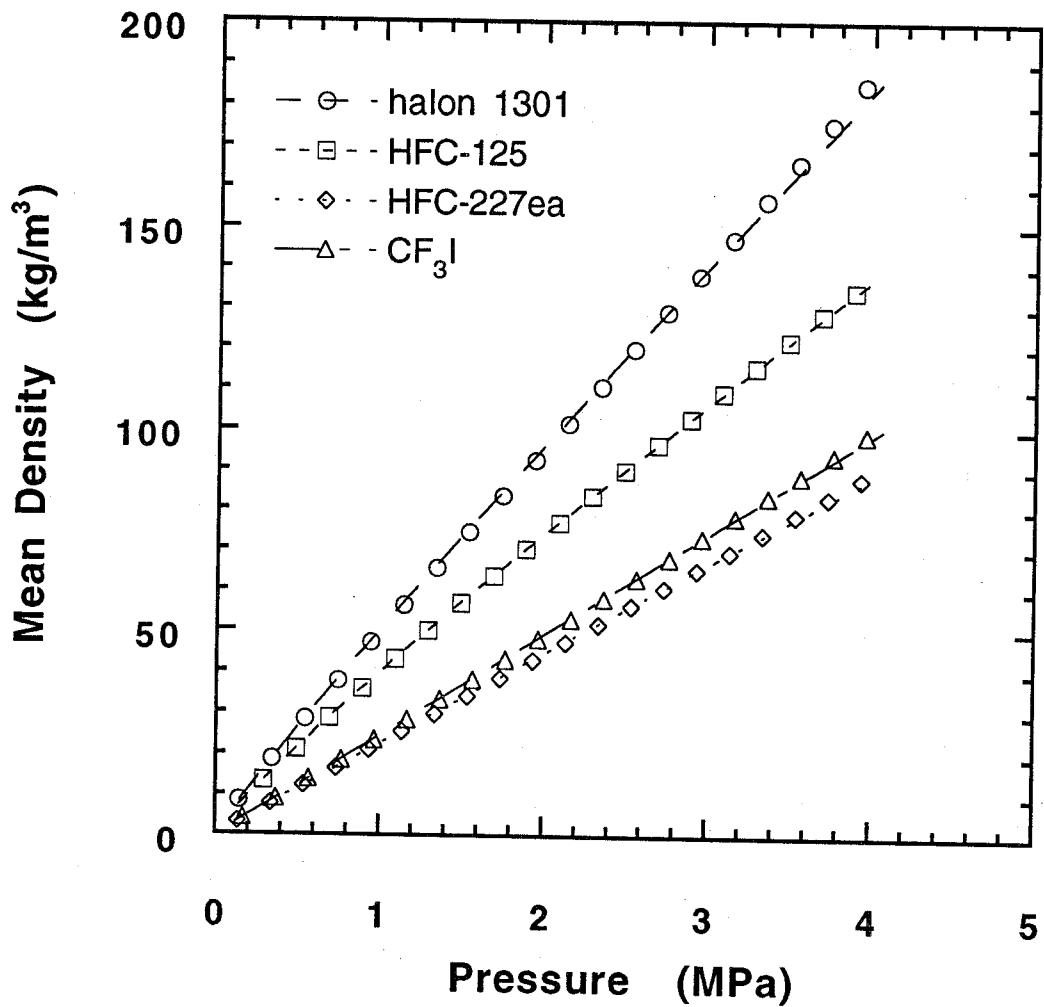


Figure C-7. Mean density as a function of pressure for initially gas-phase agent/nitrogen mixture undergoing isentropic expansion. Initial pressure and temperature are 4.12 MPa and 20 °C.